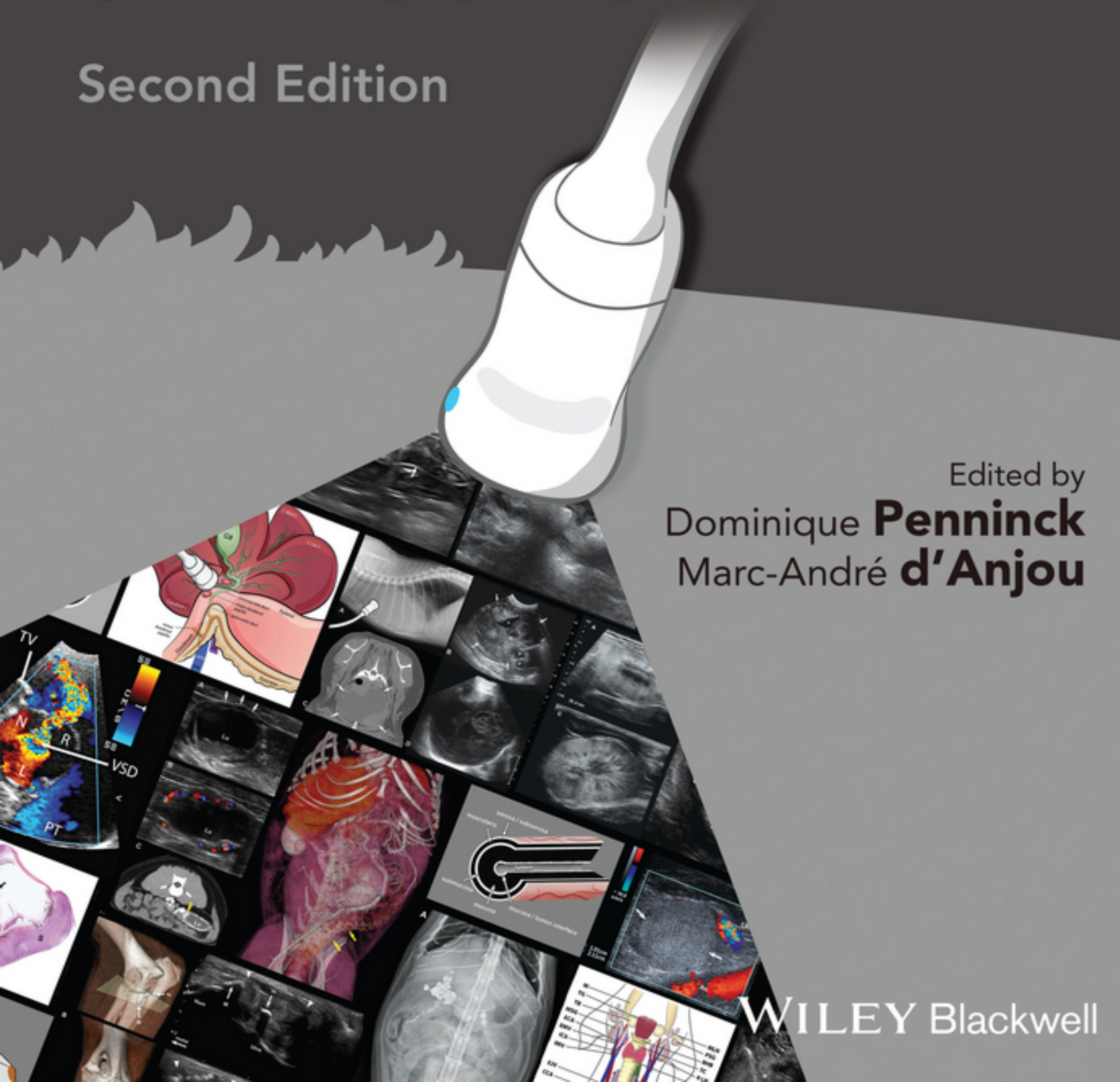
ATLAS OF SMALL ANIMAL ULTRASONOGRAPHY

Second Edition



Edited by
Dominique **Penninck**
Marc-André **d'Anjou**

WILEY Blackwell

Atlas of Small Animal Ultrasonography

Dedications

To Anaïs and Loïc, for their continued love, energy and support. They rock.

To all the students, past, present and future, for their inspiration.

In memory of my father and Vincent Dupierreux.

Dominique Penninck

To Annabelle, Olivier, and Héloïse for filling my life with sunshine.

To all students, interns, residents, and practitioners who show passion for what they do and for whom they want to become.

In memory of Charles and Leo.

Marc-André d'Anjou

Atlas of Small Animal Ultrasonography

SECOND EDITION

Edited by

Dominique Penninck

DVM, PhD, DACVR, DECVDI
Professor of Diagnostic Imaging
Department of Clinical Sciences
Cummings School of Veterinary Medicine
Tufts University
North Grafton, MA
USA

Marc-André d'Anjou

DMV, DACVR
Clinical Radiologist
Centre Vétérinaire Rive-Sud
Brossard, Québec
Canada
&
Faculté de Médecine Vétérinaire de l'Université de Montréal
Saint-Hyacinthe, Québec
Canada

Illustrations by Beth Mellor and Marc-André d'Anjou

WILEY Blackwell

This edition first published 2015
© 2015 by John Wiley & Sons, Inc.
© 2008 by Blackwell Publishing

Editorial offices: 1606 Golden Aspen Drive, Suites 103 and 104, Ames, Iowa 50010, USA
The Atrium, Southern Gate, Chichester, West Sussex, PO19 8SQ, UK
9600 Garsington Road, Oxford, OX4 2DQ, UK

For details of our global editorial offices, for customer services and for information about how to apply for permission to reuse the copyright material in this book please see our website at www.wiley.com/wiley-blackwell.

Authorization to photocopy items for internal or personal use, or the internal or personal use of specific clients, is granted by Blackwell Publishing, provided that the base fee is paid directly to the Copyright Clearance Center, 222 Rosewood Drive, Danvers, MA 01923. For those organizations that have been granted a photocopy license by CCC, a separate system of payments has been arranged. The fee codes for users of the Transactional Reporting Service are ISBN-13: 978-1-1183-5998-3/2015.

First published 2008
Second edition 2015

Designations used by companies to distinguish their products are often claimed as trademarks. All brand names and product names used in this book are trade names, service marks, trademarks or registered trademarks of their respective owners. The publisher is not associated with any product or vendor mentioned in this book.

The contents of this work are intended to further general scientific research, understanding, and discussion only and are not intended and should not be relied upon as recommending or promoting a specific method, diagnosis, or treatment by health science practitioners for any particular patient. The publisher and the author make no representations or warranties with respect to the accuracy or completeness of the contents of this work and specifically disclaim all warranties, including without limitation any implied warranties of fitness for a particular purpose. In view of ongoing research, equipment modifications, changes in governmental regulations, and the constant flow of information relating to the use of medicines, equipment, and devices, the reader is urged to review and evaluate the information provided in the package insert or instructions for each medicine, equipment, or device for, among other things, any changes in the instructions or indication of usage and for added warnings and precautions. Readers should consult with a specialist where appropriate. The fact that an organization or Website is referred to in this work as a citation and/or a potential source of further information does not mean that the author or the publisher endorses the information the organization or Website may provide or recommendations it may make. Further, readers should be aware that Internet Websites listed in this work may have changed or disappeared between when this work was written and when it is read. No warranty may be created or extended by any promotional statements for this work. Neither the publisher nor the author shall be liable for any damages arising herefrom.

Library of Congress Cataloging-in-Publication Data

Atlas of small animal ultrasonography / edited by Dominique Penninck, Marc-André d'Anjou. – Second edition.
p. ; cm.
Includes bibliographical references and index.
ISBN 978-1-118-35998-3 (cloth)
1. Veterinary ultrasonography–Atlases. I. Penninck, Dominique, editor. II. d'Anjou, Marc-André, editor.
[DNLM: 1. Ultrasonography–veterinary–Atlases. 2. Veterinary Medicine–methods–Atlases. SF 772.58]
SF772.58.A85 2015
636.089'607543–dc23

2014046407

A catalogue record for this book is available from the British Library.

Wiley also publishes its books in a variety of electronic formats. Some content that appears in print may not be available in electronic books.

Cover design by Meaden Creative

Set in 10/12.5pt PalatinoLTStd by SPi Global, Chennai, India

1 2015

Contents

Contributors vii

Preface ix

About the Companion Website xi

1. **Practical Physical Concepts and Artifacts** 1
   Marc-André d'Anjou and Dominique Penninck

2. **Eye and Orbit** 19
   Stefano Pizzirani, Dominique Penninck and Kathy Spaulding

3. **Neck** 55
   Allison Zwingenberger and Olivier Taeymans

4. **Thorax** 81
   Silke Hecht and Dominique Penninck

5. **Heart** 111
   Donald Brown, Hugues Gaillot and Suzanne Cunningham

6. **Liver** 183
   Marc-André d'Anjou and Dominique Penninck

7. **Spleen** 239
   Silke Hecht and Wilfried Mai

8. **Gastrointestinal Tract** 259
   Dominique Penninck and Marc-André d'Anjou

9. **Pancreas** 309
   Dominique Penninck and Marc-André d'Anjou

10. **Kidneys and Ureters** 331
    Marc-André d'Anjou and Dominique Penninck

11. **Bladder and Urethra** 363
James Sutherland-Smith and Dominique Penninck

12. **Adrenal Glands** 387
Marc-André d'Anjou and Dominique Penninck

13. **Female Reproductive Tract** 403
Rachel Pollard and Silke Hecht

14. **Male Reproductive Tract** 423
Silke Hecht and Rachel Pollard

15. **Abdominal Cavity, Lymph Nodes, and Great Vessels** 455
Marc-André d'Anjou and Éric Norman Carmel

16. **Clinical Applications of Contrast Ultrasound** 481
Robert O'Brien and Gabriela Seiler

17. **Musculoskeletal System** 495
Marc-André d'Anjou and Laurent Blond

18. **Spine and Peripheral Nerves** 545
Judith Hudson and Marc-André d'Anjou

Index 563

Contributors

Laurent Blond, Dr Méd Vét, MSc, DACVR
Clinique Vétérinaire Languedocia
395 rue Maurice Béjart
34080 Montpellier, France

Donald Brown, DVM, PhD, DACVM Cardiology
Vermont Veterinary Cardiology
PEAK Veterinary Referral Center
158 Hurricane Lane
Williston, VT 05495;
Adjunct Associate Professor
Department of Clinical Sciences
Tufts Cummings School of Veterinary Medicine
North Grafton, MA 01536, USA

Éric Norman Carmel, DMV, DACVR
Centre Vétérinaire Laval
4530 Highway 440
Laval, Québec, Canada, H7T 2P7
&
Centre Hospitalier Universitaire Vétérinaire / Teaching Hospital
Faculté de médecine vétérinaire de l'Université de Montréal
Saint-Hyacinthe, Québec
Canada, J2S 7C6

Suzanne Cunningham, DVM, DACVM Cardiology
Assistant Professor Cardiology
Department of Clinical Sciences
Cummings School of Veterinary Medicine,
Tufts University
200 Westborough Road
North Grafton, MA01536, USA

Marc-André d'Anjou, DMV, DACVR
Centre Vétérinaire Rive-Sud
7415 boulevard Taschereau
Brossard, Québec, Canada, J4Y 1A2
&
Faculté de médecine vétérinaire de l'Université de Montréal
Saint-Hyacinthe, Québec
Canada, J2S 7C6

Hugues Gaillot, DVM, MS, Dipl ECVDI
Clinique Vétérinaire ADVETIA
5 rue Dubrunfaut
75012 Paris, France

Silke Hecht, Dr.med.vet., DACVR, DECVDI
Associate Professor of Radiology
Department of Small Animal Clinical Sciences
University of Tennessee College of Veterinary Medicine
Knoxville, TN 37996, USA

Judith Hudson, DVM, PhD, DACVR
Professor of Diagnostic Imaging
Department of Clinical Sciences
College of Veterinary Medicine
Auburn University
Auburn, AL 35849, USA

Wilfried Mai, Dr Méd Vét, MSc, PhD
Chief, Section of Radiology, Department of Clinical Studies
Clinical Board Member, Ryan Veterinary Hospital
Associate Professor of Radiology
School of Veterinary Medicine, Section of Radiology
University of Pennsylvania
3900 Delancey Street,
Philadelphia, PA 19104, USA

Robert O'Brien, DVM, MS, DACVR
Professor
College of Veterinary Medicine, Section of Radiology
University of Illinois
1008 West Hazelwood Drive
Urbana, IL 61802, USA

Dominique Penninck, DVM, PhD, DACVR, DECVDI
Professor of Diagnostic Imaging
Department of Clinical Sciences
Cummings School of Veterinary Medicine,
Tufts University
200 Westborough Road
North Grafton, MA 01536, USA

Stefano Pizzirani, DVM, PhD, DECVS, DACVO
Associate Professor, Ophthalmology service
Department of Clinical Sciences
Cummings School of Veterinary Medicine,
Tufts University
200 Westborough Road
North Grafton, MA 01536, USA

Rachel Pollard, DVM, PhD, Diplomate ACVR
Associate Professor of Diagnostic Imaging
University of California, Davis
School of Veterinary Medicine
Department of Surgical and Radiological Sciences
Davis, CA 95616, USA

Gabriela Seiler, Dr.Med.Vet, DAVCR, DECVDI
Associate Professor
College of Veterinary Medicine
1052 William Moore Drive
Raleigh, NC 27606, USA

Kathy Spaulding
Clinical Professor Radiology
Large Animal Clinical Sciences
College of Veterinary Medicine and Biomedical
Sciences
Texas A&M University
4475 TAMU
College Station, TX 77843-4475, USA

James Sutherland-Smith, BVSc, DACVR
Assistant Professor, Diagnostic Imaging
Department of Clinical Sciences
Cummings School of Veterinary Medicine,
Tufts University
200 Westborough Road
North Grafton, MA 01536, USA

Olivier Taeymans, DVM, PhD, DipECVDI, MRCVS
Hon. Assoc. Professor in Veterinary Diagnostic
Imaging – University of Nottingham
Adj. Assoc. Professor in Veterinary Diagnostic
Imaging – Tufts University, USA
Dick White Referrals, Six Mile Bottom
Cambridgeshire, CB8 0UH, UK

Allison Zwingenberger, DVM, DACVR, DECVDI
Assistant Professor of Diagnostic Imaging
Department of Surgical and Radiological Sciences
School of Veterinary Medicine
University of California
1 Shields Avenue
Davis, CA 95616, USA

Preface

Since the first edition, ultrasound technology has continued to progress, offering the operator continuously improved image quality and additional diagnostic tools. In parallel to the technology, the scope of clinical applications has also expanded. In most institutions and veterinary practices, ultrasonography shifted from a complementary diagnostic imaging technique to a screening procedure integrated into the patient baseline medical evaluation.

Similarly to the first edition, this *Atlas of Small Animal Ultrasonography* presents a comprehensive and extensive collection of well over 800 figures incorporating high-quality sonograms and schematics of normal structures, and of common and uncommon disorders.

The goal of the second edition of *Atlas of Small Animal Ultrasonography* was not only to update the contents of the chapters of the first edition, but also to review the construction of the book in accordance with the current diagnostic imaging practice.

The main noticeable changes are the addition of two new chapters ("Practical Physical Concepts and Artifacts" and "Clinical Applications of Contrast Ultrasound"), the addition of complementary imaging modalities and histopathology where suitable, and online access to a series of video clips that best illustrate the real-time features of normal structures and common disorders (at **www.SmallAnimalUltrasonography.com**). The videos have integrated annotations and text to assist the viewer in identifying the key features therein.

All chapters have been carefully reviewed to maintain cohesion throughout the book. Many of the changes are also based on feedback we received from readers of the first edition; their input has been invaluable in designing this second edition.

Dominique Penninck and Marc-André d'Anjou

Acknowledgments

We offer warm thanks to Drs Nancy Cox, John Graham, Martin Kramer, and Erik Wisner for their invaluable contribution to the first edition. They helped to build the foundation for the second edition.

The changes to the second edition were often inspired by suggestions we received from veterinarians and students.

About the Companion Website

This book is accompanied by a companion website:

www.SmallAnimalUltrasonography.com

The website includes:

- Videos illustrating the real-time features of normal structures and common disorders

The password to access this website is gbh3972pxe.

CHAPTER ONE

Practical Physical Concepts and Artifacts

Marc-André d'Anjou[1,2] and Dominique Penninck[3]

[1] *Centre Vétérinaire Rive-Sud, Brossard, Québec, Canada*
[2] *Faculté de médecine vétérinaire de l'Université de Montréal, Saint-Hyacinthe, Québec, Canada*
[3] *Department of Clinical Sciences, Cummings School of Veterinary Medicine, Tufts University, North Grafton, MA, USA*

Fundamentals

Sound comprises a series of vibrations transmitted through an elastic solid, a liquid, or a gas. Sound waves have variable wavelengths and amplitudes, with a frequency defined as being the number of cycles repeated over a given time interval. A high-frequency sound, therefore, has a shorter wavelength and more cycles per second (cycles/s or Hz) than a low-frequency sound. The human ear can perceive sounds in the range of 20–20,000 cycles/s, or up to 20 kHz (Hangiandreou 2003). Beyond this range, it is called "ultrasound." Ultrasound frequencies used in medical imaging generally vary between 3 and 12 MHz, or 3–12 million cycles/s, which is well beyond what the human ear can perceive.

Electronic linear probes are equipped with a row of **piezoelectric crystals** whose alignment varies from flat (or linear) to convex. The material contained in each one is deformed when it receives an electrical charge, and emits a vibration – this is the initial ultrasound pulsation. The ultrasound wave travels through the tissues, generating several returning waves- or echoes-that, upon reaching the probe, make the crystals vibrate again, producing a new electric current that travels to the system's computer and provides information on each of the reflected waves. The set of all the reflected waves creates the ultrasound image.

To produce an **image**, the first piezoelectric crystals are stimulated to generate a short ultrasound pulse – comprising three to four waves – that travels through tissue interfaces to produce thousands of echoes that are sent back to the probe (Figure 1.1). Shortly afterward, a new ultrasound pulse leaves the probe at a different angle, generating a new set of echoes that return to the second series of crystals. Assuming a constant wave propagation speed of 1,540 m/s in soft tissues, each of these echoes can be located precisely along the trajectory, depending on the time interval between the departing wave and the returning echo (Hangiandreou et al. 2003). Hundreds of wave lines are produced this way, scanning tissues at high speed to produce over 30 images/s, each one containing thousands of pixels describing the acoustic characteristics of the scanned tissues.

Tissue acoustic characteristics are defined by the **acoustic impedance**, which dictates their level of ultrasound reflection and thus their echogenicity. Impedance is the product of the speed of ultrasound waves through a given tissue multiplied by its density (Table 1.1) (Bushberg 2011). Ultrasound wave reflection is stronger at interfaces of tissues that greatly differ in acoustic impedance, and weaker when traversing an interface of tissues with similar acoustic impedances. Mild variations in acoustic impedance are desirable for tissue examination, resulting in variable echogenicity and echotexture, which allow internal architectures to be compared. In fact, not only does the ultrasound system locate the origin of each echo, it also measures its intensity, which is expressed in terms of pixel brightness on the unit monitor (B mode).

Normal **tissue echogenicity**, which varies among organs and structures (Figure 1.2), and damaged tissue with altered acoustic characteristics can be compared. Normal and abnormal structures can be defined in terms of echogenicity as hypoechoic or hyperechoic to

Atlas of Small Animal Ultrasonography, Second Edition. Edited by Dominique Penninck and Marc-André d'Anjou.
© 2015 John Wiley & Sons, Inc. Published 2015 by John Wiley & Sons, Inc.
Companion website: www.SmallAnimalUltrasonography.com

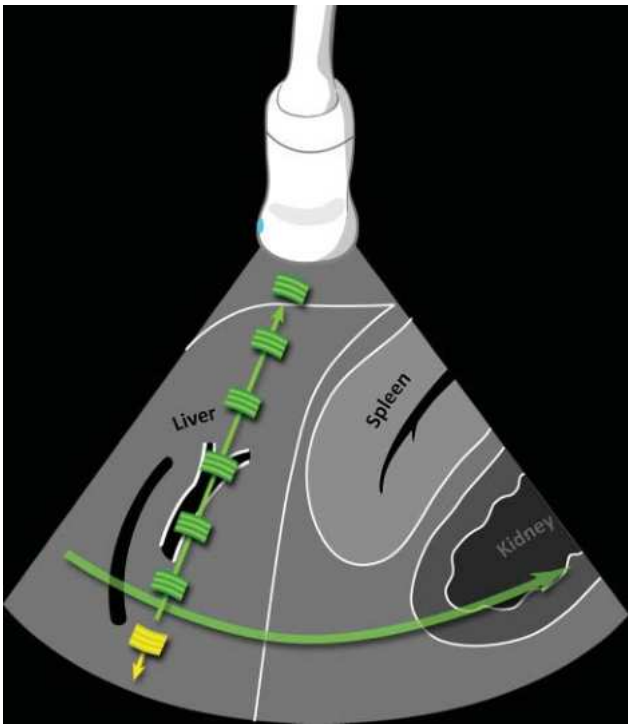


Figure 1.1. Ultrasound propagation and image formation. Each ultrasound image is formed by the addition of hundreds of individual scan lines. Each line is produced after a single ultrasound pulse (in yellow) is emitted by the transducer. As this pulse propagates through soft tissues, many echoes (in green) are generated at interfaces of different acoustic impedance (such as hepatocytes–connective tissue), producing an image of variable echogenicity and echotexture. Each echo is anatomically localized based on the time interval between the emitted pulse and its reception. After a specific time, a new pulse is emitted along an adjacent line, producing an additional scan line. Scan lines are generated very rapidly and successively, producing 15–60 images/s, allowing "real time" ultrasonography.

Table 1.1
Density and speed of sound in materials and biological tissues and resulting acoustic impedance

Material or tissue	Density (kg/m^3)	Speed (m/s)	Acoustic impedance
Air	1.2	330	0.0004×10^6
Lung	300	600	0.18×10^6
Fat	924	1,450	1.34×10^6
Water	1,000	1,480	1.48×10^6
Soft tissues (in general)	1,050	1,540	1.62×10^6
Liver	1,061	1,555	1.65×10^6
Kidney	1,041	1,565	1.63×10^6
Skull bone	1,912	4,080	7.8×10^6

Source: Bushberg et al. (2011).

their normal state, or to other structures with which they are compared. Fluids without cells or large particles are anechoic (i.e., totally black) because of the absence of reflectors.

Interactions between ultrasound waves and tissues and materials vary, dictating the intensity of echoes generated and the residual intensity of the pulse that pursues its course through tissues (Hangiandreou et al. 2003) (Figure 1.3). For instance, ultrasound waves penetrating fat result in **acoustic diffusion**, or **scattering**, as the primary interaction, reducing the intensity of the initial pulse. This type of interaction also explains the echotexture – i.e., granularity – of the parenchyma that varies among organs. On the other hand, the interaction with a smooth interface that is perpendicular to the beam axis, such as the renal capsule in Figure 1.3, causes **specular reflection**, which produces intense echoes in the opposite direction of the initial pulse. Some materials like mineral absorb a significant component of the initial pulse energy that becomes too weak to generate echoes from deeper tissues. Ultrasound **absorption** can then cause a shadow (see the section "Artifacts"). Finally, ultrasound waves may change in direction due to **refraction**. In reality, these types of interactions are often combined and their presence and relative importance is mainly influenced by the differences in acoustic impedance and by the shape of the tissue (or material) interfaces. These interactions cause the emitted ultrasound pulse energy to eventually become completely dissipated.

Ultrasound Probes and Resolution

Ultrasound probes vary in configurations for specific needs (Figure 1.4). Curved linear probes, also called convex or microconvex, have one or several rows of piezoelectric crystals aligned along a convex surface, with varying beams and tracks. These probes produce

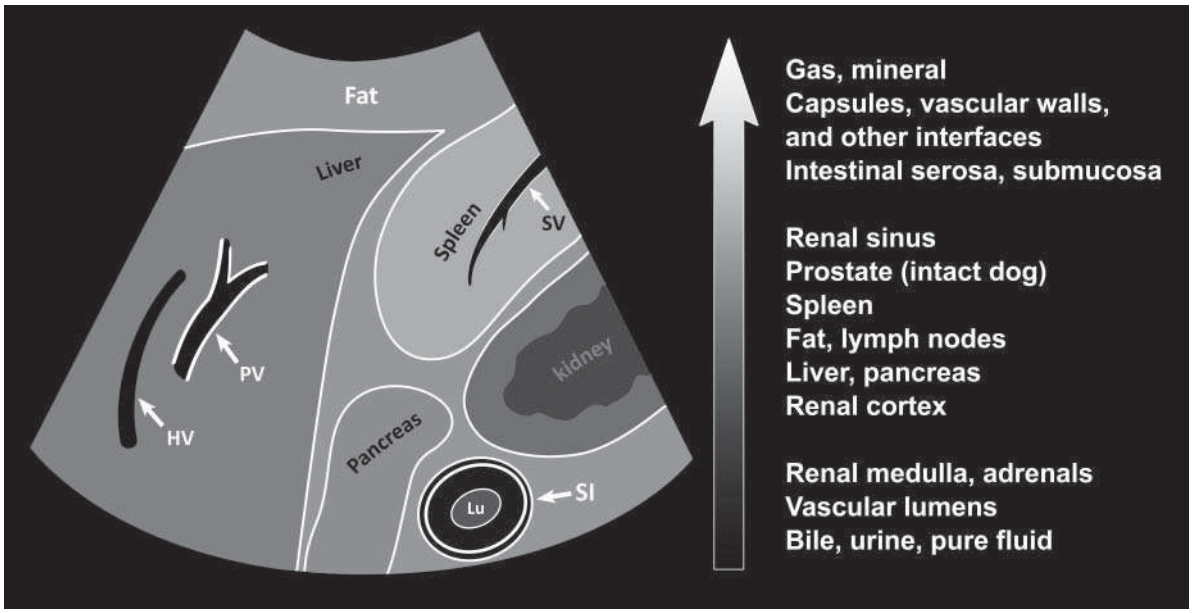


Figure 1.2. Relative echogenicity of tissues and other materials. Structures can be recognized and differentiated by their echogenicity. This figure illustrates the relative echogenicity of normal abdominal structures in dogs and cats. Note that the walls of the portal vein (PV) are hyperechoic even when this vein is not perpendicular to the insonation beam, differing from the adjacent hepatic vein (HV). The HV and splenic vein (SV) external interfaces only become hyperechoic when perpendicular to the beam. The fluid in the small intestinal (SI) lumen (Lu) is not fully anechoic because of the ingested particles. The renal cortex is often hyperechoic in normal dogs and cats and may become isoechoic to the liver and even to the spleen. The adrenal medulla may be hyperechoic in certain normal animals, sometimes exceeding the echogenicity of the renal cortex. It is important to point out that tissue echogenicity may also be influenced by several equipment-related factors, such as transducer frequency and orientation, focal zone number and position.

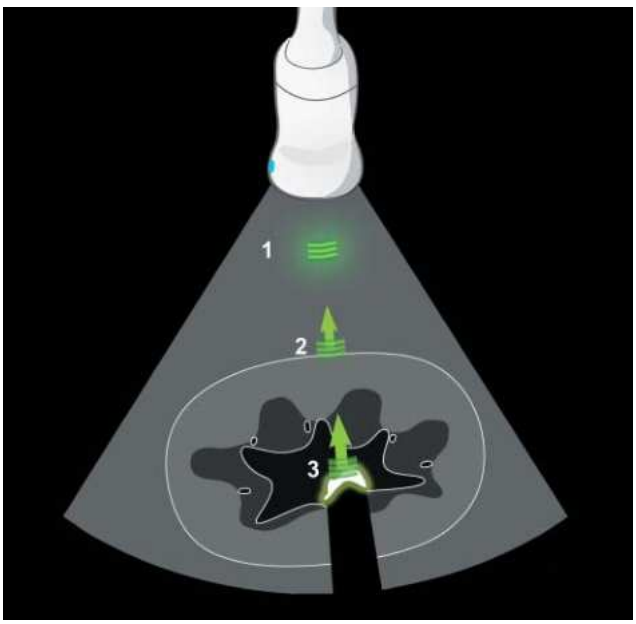


Figure 1.3. Interactions between ultrasound waves and tissues. The emitted ultrasound pulse is charged with energy. In this example, the pulse initially interacts with the abdominal fat (1), causing acoustic diffusion (green halo) and partly losing its energy as it continues its course. When interacting with a smooth, linear interface such as the renal capsule (2), a strong specular reflection occurs that generates a highly intense echo (green arrow). The weaker ultrasound pulse then reaches the renal pelvic calculus, which absorbs most of the wave energy while causing a strong reflection (green arrow). An acoustic shadow is generated and the initial pulse energy is completely dissipated.

a triangular image because of the diverging lines of ultrasound waves they generate. The main assets of this type of probe are its smaller footprint and its large scanning field, making it the ideal probe for assessing the abdomen, particularly the cranial portion along the rib cage. The piezoelectric crystals of the linear probes are distributed along a flat surface, producing a rectangular scan field. The phase interval of the impulsions can also produce a trapezoid-shaped image, allowing it to cover a larger surface. This is



Figure 1.4. Practical ultrasound transducers. Most ultrasound units are equipped with convex **(A, B)** and linear **(C)** electronic transducers with variable frequencies. A macroconvex probe **(A)** offering lower frequencies (3–8 MHz) is best suited for the abdomen of large dogs, whereas a microconvex probe **(B)** of higher frequency and smaller footprint is preferred for the abdomen of small patients and when only a small acoustic window is available (e.g., the intercostal approach of a lung lesion). A high-frequency (10–18 MHz) linear probe **(C)** is most useful for assessing superficial structures on a relatively wide and flat surface (e.g., assessing bowels in a cat, biceps tendon in a dog). A phased array transducer **(D)** offers a small flat footprint and is ideal for echocardiography.

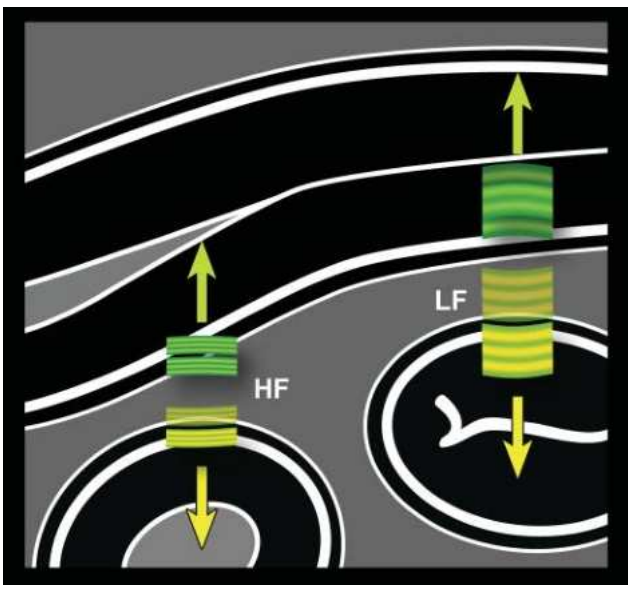


Figure 1.5. Ultrasound frequency versus axial resolution. The higher the frequency, the shorter the pulse. Because the length of the pulse does not change in depth or after interaction with tissues, high-frequency (HF) echoes (in green) that come back to the transducer are better discriminated by the system. Closely associated interfaces, such as small intestinal wall layers, are then better represented. Conversely, echoes from closely aligned layers generated by a low-frequency (LF) pulse (in yellow) partly overlap and are interpreted by the system as originating from a single interface. This phenomenon is exaggerated in this illustration for better comprehension of this important concept.

especially useful when evaluating superficial organs whose diameter may be greater than the width of the scanned area, such as the kidneys and spleen. The length of the probe's footprint indicates the width of the area it scans.

Spatial resolution is the ability of a system to recognize and distinguish two small structures located close together. For instance, optimal spatial resolution allows us to distinguish between two small nodules in the liver instead of mistaking them for only one, or missing a lesion that is adjacent to a normal structure. The spatial resolution along the path of the ultrasound beam – the *x*-axis – is determined by the length of the pulse, which in turn is related to wave frequency (Figure 1.5). As the ultrasound frequency remains constant with depth, so does the axial resolution. Conversely, lateral (*y*-axis) and slice-thickness (*z*-axis) resolutions vary with depth as the ultrasound beam changes in shape to narrow at the level of the focal zone (Figure 1.6). For a given probe, the axial resolution is

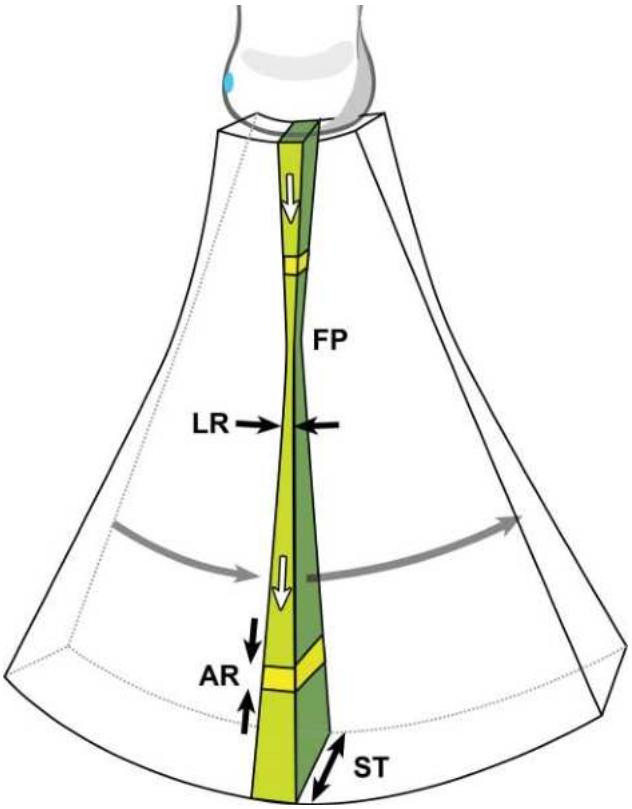


Figure 1.6. Shape of the ultrasound beam in depth. The ultrasound beam is larger at its emission point (piezoelectric elements) before narrowing at the focal point (FP), and becoming larger again further in depth. This change in shape affects the lateral resolution (LR, i.e., beam width) and slice thickness (ST, or elevational resolution), but does not affect the axial resolution (AR), which is dictated by the pulse frequency that remains constant in depth. Generally, the axial resolution is superior to the other resolutions. The white arrows represent the path of each wave line, which is repeated along the grey curved arrow to cover the entire field.

generally superior to lateral or slice-thickness resolutions, meaning that measurements should be obtained along that *x*-axis, whenever possible.

Contrast resolution is the system's ability to differentiate structures that present small differences in acoustic behavior (Figure 1.7). The influence of these two types of resolution is significant and hinges on image quality, the ability to evaluate structures and to detect and describe lesions.

As seen earlier, ultrasound waves interact with tissues in different ways, causing the initial pulse to progressively lose its intensity in depth. This attenuation limits contrast resolution in deeper areas, particularly when using high-frequency probes. Indeed, the coefficient of attenuation of ultrasound waves through tissues increases in direct proportion to wave frequency.

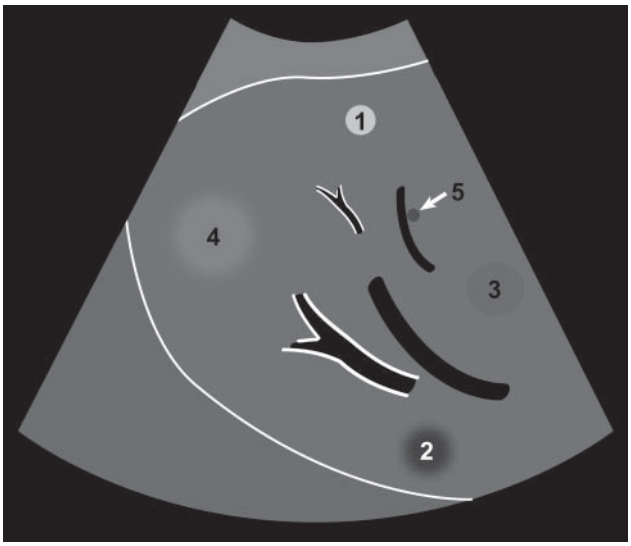


Figure 1.7. Spatial and contrast resolutions. The capacity of an ultrasound system to detect and distinguish structures of small size and similar acoustic characteristics greatly influences its diagnostic capability. In this illustration, the hyperechoic nodule 1 is clearly depicted. Its characteristics (size, echogenicity, and margin) favor its identification. The hypoechoic nodule 2 is also visualized due to its size and marked hypoechogenicity, but it has ill-defined contours. Nodules 3 and 4 are larger but less conspicuous because of their echogenicity, which is similar to the regional liver parenchyma. The contrast resolution of the system – and certain image adjustments – dictates its capacity to identify structures of characteristics that are similar to the background. The small hypoechoic nodule 5 is differentiated from the adjacent hepatic vein because of sufficient spatial resolution. Lower spatial resolution would cause this nodule to be confused with the vessel.

Excessive beam attenuation can be particularly problematic in certain animals, such as large obese dogs, or with certain disease processes (e.g., lipidosis). The use of lower-frequency probes can partially compensate for this loss of signal, but at the cost of reduced detail (lower spatial resolution). Generally, the probe offering the highest frequency but allowing all desired tissues to be imaged with sufficient signal should be selected.

System Adjustments and Image Quality

Images can be frozen to take measurements and add text prior to recording still or looped images that can be archived or submitted to a colleague for another opinion. But before being recorded, they must be optimized. Except for automatic processes, many adjustments can and should be made manually

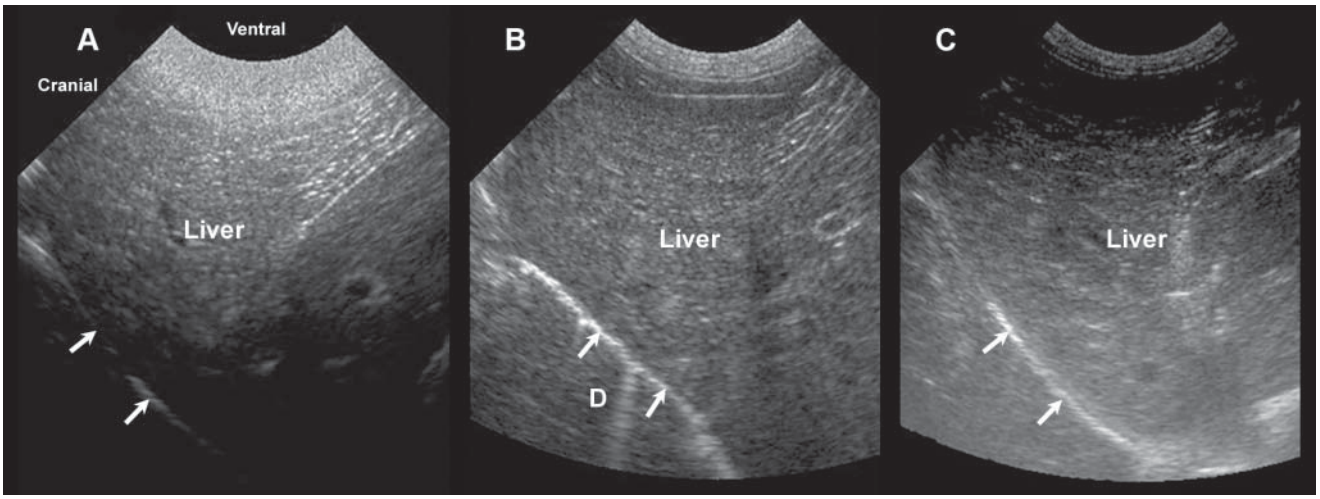


Figure 1.8. Gain setting. Because of the attenuation of the ultrasound beam as it travels through soft tissues, the amplification of echoes received must be adjusted according to tissue type and depth. This modulation can be made using time gain compensation bars or far/near/general gain knobs. These three images show the variation in echogenicity of a normal liver with excessive near gain and insufficient far gain **(A)**, well-adjusted near and far gains **(B)**, and insufficient near gain and excessive far gain **(C)**. **D**, diaphragm interface.

throughout the examination. Changes in tissue depth and acoustic properties require constant adjustments.

The **gain** determines the level of amplification of echoes to compensate for their attenuation in tissues, increasing the brightness of corresponding pixels on the screen. It can be adjusted generally, or modulated specifically in depth (Figure 1.8). Time gain compensation (TGC) is adjusted through sliding knobs, reducing superficial amplification or increasing depth amplification, for instance. As ultrasound attenuation will vary from one animal to another and from one abdominal region to another, depending on the acoustic characteristics of normal and abnormal tissues, both the general gain and TGC will have to be adjusted during the examination.

Image field **depth** determines the length of the long axis, allowing the same structure to be imaged completely, or partly. This also needs to be adjusted continually to maximize the visualization of structures in the region of interest.

The ultrasound beam can be electronically **focalized** to reduce its diameter at a specific depth. In the focal zone, the beam's width and thickness are considerably reduced, increasing the capacity of the system to depict small structures along the *y* (lateral) and *z* (slice-thickness) planes, respectively (Hangiandreou et al. 2003) (see Figure 1.6). Moreover, the intensity of the beam is concentrated over a small area, increasing the signal from tissues in that region, favoring contrast resolution. Thus, the focal zone should be adjusted during examination at the depth of the region of interest. By using two (or more) focal zones, the beam is narrowed over a greater distance, increasing the spatial and contrast resolution over a longer depth. The downside, however, is that using more zones require more time, thereby reducing the frame rate, which may limit the examination of a moving structure. Multifocal optimization is easier while evaluating structures that are completely immobile.

Noise is an inherent part of all imaging procedures and can become problematic in large patients or when using low-end systems. It results from insufficient signal (i.e., echoes) emanating from tissues and reaching the ultrasound probe, from electric interferences, from artifacts (see the section "Artifacts"), and from improper signal processing by the unit. The result is a coarse-grained textured and/or grayish image that doesn't represent normal tissue anatomy, and which limits our ability to view shades of gray (reduced contrast resolution). Noise can be partly reduced by using a higher-frequency probe, by switching to the harmonic or compound imaging modes, or by increasing output power.

Spatial compound imaging (which varies in name among brands) refers to the electronic steering of ultrasound beams from an array transducer to image the same tissue multiple times by using parallel beams oriented along different directions (Hangiandreou et al. 2003) (Figure 1.9). Tissues are scanned from different angles, simultaneously, allowing multiple echoes from the same tissue interfaces to be collected and combined, increasing the overall signal and

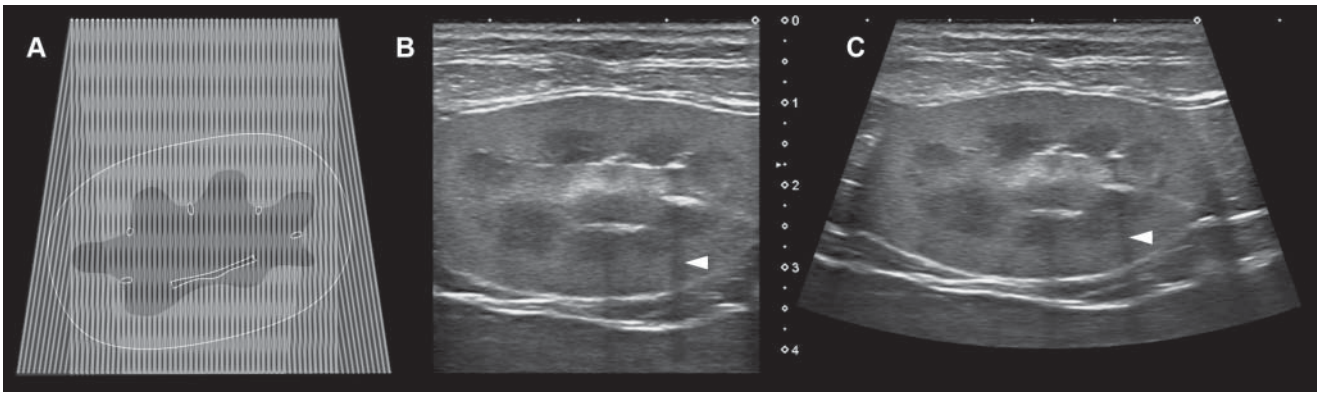


Figure 1.9. **Spatial compound imaging. A:** With this mode, the same tissue is scanned using different beam angulations (steering) to produce a trapezoidal image that is wider than the footprint of the transducer. **B, C:** Superficial structures such as this kidney may exceed the size of the image field when the standard linear mode **(B)** is used, whereas spatial compounding expands the width of the image to include the kidney, which can be fully assessed and measured **(C)**. Beam angulation also influences the shape and orientation of shadowing artifacts (arrowheads).

reducing noise. Image contrast is increased and tissue interfaces become more conspicuous. Tissues boundaries are better outlined and, because background noise is reduced, cystic lesions are fully anechoic and thus more easily differentiated from solid lesions. On the other hand, certain useful artifacts, such as acoustic shadowing – which helps in recognizing mineral, for instance – may disappear when compound imaging is used. Because multiple ultrasound beams are used to interrogate the same tissue region, more time is required for data collection, reducing the frame rate when compared with that of conventional B-mode imaging. This mode may limit the examination of moving patients.

The **harmonic mode** also increases tissue contrast by selecting echoes at a specific frequency. The term harmonic refers to frequencies that are integral multiples of the frequency of the transmitted pulse (which is also called the fundamental frequency, *f*, or first harmonic). Harmonic frequency echoes (1/2*f*, 2*f*, etc.) develop because of the distortion of the transmitted pulse as it travels through tissues (Ziegler et al. 2002). The initial pulse in fact deforms from a perfect sinusoid to a sharper, sawtooth shape, generating reflected echoes of several different frequencies. The use of higher-order harmonic echoes instead of the fundamental echoes results in improved image contrast and reduced noise, increasing normal and abnormal tissue conspicuity. The reduction of artifacts and clutter is most efficient in the near field. This may prove particularly valuable in large patients with thick abdominal walls and subcutaneous fat planes. The harmonic mode is also used for contrast-enhanced ultrasonography (see Chapter 16, "Clinical Applications of Contrast Ultrasound").

Finally, several other aspects can influence the quality of ultrasound images. As for digital radiographs, the quality of the unit monitor (size, dynamic range, brightness, calibration) can influence our ability to accurately assess ultrasound images. Several features can be used and modulated to create scanning presets, for different types of patients or body parts. Sonographers must be aware of the strengths and limitations of their system.

Doppler Ultrasound

Introduction

Doppler ultrasound provides information on the presence, direction, and speed of blood flow. A detailed description of Doppler ultrasound is beyond the scope of this practical atlas, but readers are encouraged to consult reference textbooks and articles in order to further their understanding of its concepts.

Doppler ultrasound is based on the interaction of ultrasound with particles in movement, leading to a change in the frequency of the echoes received, this phenomenon is known as the **Doppler effect** (Figure 1.10) (Boote 2003). This effect is displayed and evaluated with color schemes when using color or power Doppler modes, or graphically with spectral Doppler (Figures 1.11, 1.12). The numerous applications of these modes are highlighted in several figures throughout the book, and particularly in Chapter 6.

Flow Imaging Modes

With **color Doppler**, a color map is used to display the direction and velocity of the blood flow. The size

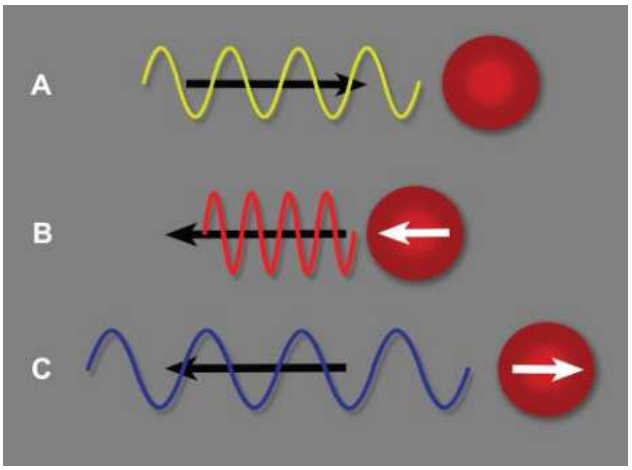


Figure 1.10. **Doppler effect. A:** The ultrasound pulse emitted by the probe moves in direction of a red blood cell (RBC) at a specific frequency. **B:** If the RBC moves toward this pulse, a positive Doppler shift occurs, increasing the frequency of the returning echo. The wavelength is reduced. **C:** If the RBC moves away from this pulse, the frequency of the returning echo is reduced and its wavelength is increased. This negative Doppler shift is displayed as a blue signal in the standard color Doppler mode, whereas blood flow moving in the direction of the probe is displayed in a red hue.

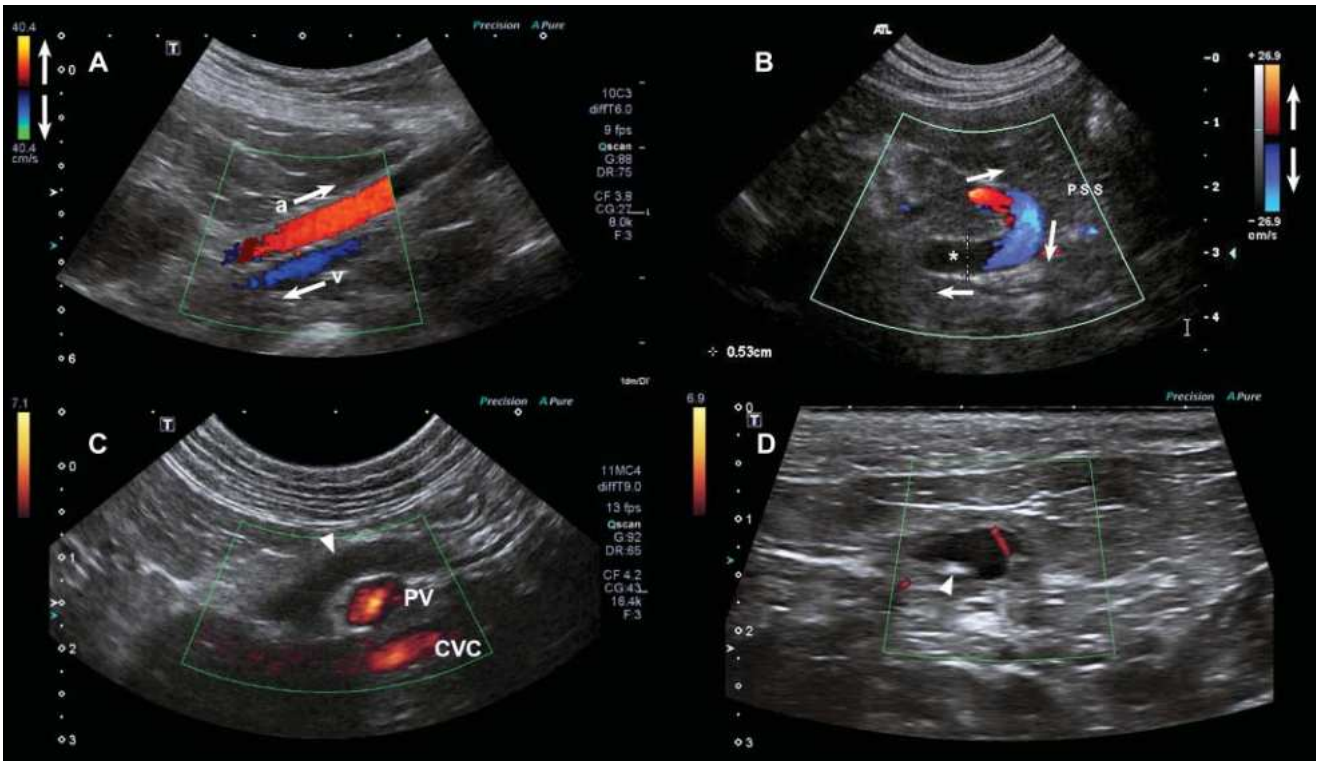


Figure 1.11. **Color and power Doppler modes. A:** With color Doppler, the direction of blood flow can be rapidly determined. In this dog, the right external iliac artery (a) and vein (v) show red and blue color hues, indicating flows directed toward and away from the probe, respectively. **B:** Color hue can change in the same vessel due to a change in direction of the flow, as demonstrated in this tortuous portosystemic shunt (PSS). The arrows indicate the direction of the flow through that shunt. When the flow becomes perpendicular to the probe, a signal void (*) appears because of the lack of Doppler shift. Power Doppler may become useful in such circumstance. **C:** Power Doppler helps to distinguish this dilated common bile duct (arrowhead) in a cat from the nearby portal vein (PV) and caudal vena cava (CVC). **D:** Power Doppler may also be used to detect a ureteral jet coming from a patent ureter, as opposed to the ipsilateral ureter which is obstructed by a small urolith (arrowhead).

and location of the interrogation box are adjusted to provide an overall view of the flow in a given region, and superimposed on the B-mode image for anatomical localization. Color Doppler is essential for cardiac evaluation (see Chapter 5), but can also serve in the assessment of other body parts. It allows rapid identification of vessels and evaluation of their flow characteristics, as well as detecting aberrant vessels such as portosystemic shunts or arteriovenous fistulas and assessing tissue perfusion. Color Doppler mode

requires that color maps and B-mode data are acquired simultaneously, limiting temporal resolution, and often reducing the spatial resolution of the underlying B-mode image. Limiting the size of the area of color investigation to the region of interest helps to increase the frame rate, thus improving temporal resolution. Color gain should also be carefully adjusted so that the color signals does not extend beyond vascular walls.

Power Doppler – also known as energy or angio-Doppler – is more sensitive to flows of low velocity as it displays the summation of all of the Doppler shift signals rather than the mean in a given area. This mode is favored for confirming or informing the presence of blood flow, particularly in smaller vessels, or to differentiate blood vessels from other tubular structures such as the common bile duct (Figure 1.11). However, as opposed to the color mode, it does not provide information on the direction or velocity of blood flow. Most newer ultrasound systems now offer a hybrid color mode combining these two modes.

Spectral (or pulsed-wave) Doppler examines blood flow at a specific site and provides detailed graphic analysis of the blood flow. The flow characteristics such as velocity, direction and uniformity can be precisely assessed over time, i.e., throughout the cardiac cycle (Figure 1.12). Flow velocities and indices can be more accurately measured than with color Doppler. In fact, the flow patterns of normal and abnormal abdominal vessels have been well described in dogs (Szatmari et al. 2001; d'Anjou et al. 2004; see also Chapter 6). Sonographers should, however, be careful to measure flow using insonation angles – which can be manually

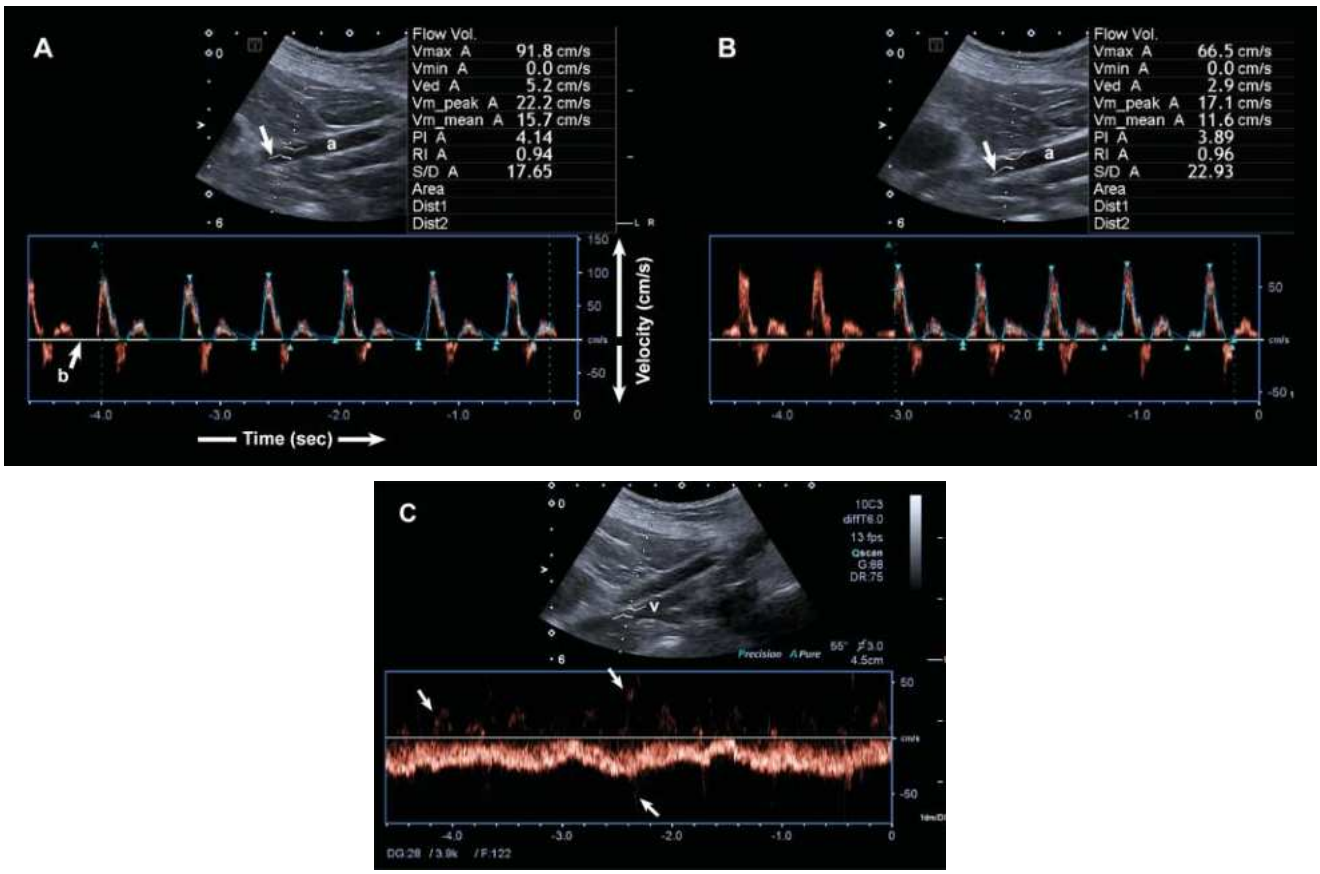


Figure 1.12. **Pulsed or spectral Doppler mode. A:** The flow in this external iliac artery (a) is mainly directed over the baseline (b), i.e., toward the probe, and pulsates according to the heartbeat. Its changes in direction and velocity are represented over time in this graph. Note that the angle cursor (arrow) is appropriately aligned to the long axis of the vessel to measure the velocity vector along that line, which reaches a maximum of 91.8 cm/s and a mean of 15.7 cm/s. **B:** Changing the angle of this line cursor results in measurement errors. The ultrasound unit estimates the flow velocities based on the measurement of the Doppler shift along that line (66.5 and 11.6 cm/s for maximal and mean velocities, respectively). **C:** The flow in the adjacent vein (v) is directed cranially, away from the probe, and is therefore represented below the baseline. It fluctuates in time (up to about 30 cm/s) but is not pulsatile as the arterial flow. A few weak peaks of the adjacent arterial flow are apparent on the graph (arrows). Note that the correction angle was of 55 degrees, which reduces the chance of errors in flow velocity estimation.

adjusted in the sampling window – well aligned to flow movement and not exceeding 60 degrees to limit measurement errors (Figure 1.12).

ARTIFACTS

Introduction

Artifacts are omnipresent in ultrasound, they are often part of the images, and may lead to misinterpretations (Kirberger 1995; Feldman et al. 2009; Hindi et al. 2013). In medical ultrasound, it is assumed that:

1. Ultrasound waves always travel in straight lines from their emitting point.
2. The lateral width and depth of the beam are narrow and constant.
3. Each interface generates a single reflection.
4. The intensity and location of echoes displayed as pixels on the monitor truly correspond to the reflecting power and anatomical location of structures being scanned.
5. The speed of the ultrasound waves and the coefficient of attenuation are constant within tissues.
6. Each echo seen on the screen comes from the most recently transmitted wave.

In reality, these assumptions are theoretical, and the sound interaction with biological tissues is complex and responsible for many explained and unexplained artifacts. Additionally, the understanding of physical properties of artifacts has been studied *in vitro* by several authors (Barthez et al. 1997; Heng and Widmer 2010), but these conditions do not represent well the complexity of numerous factors, such as probe frequency, shape, operator settings, nature, and depth of tissues evaluated.

Deleterious artifacts, such as gas-induced reverberation, can be partly controlled by adequate patient preparation, scanning methods, and system adjustments. Gastrointestinal content is responsible for most artifacts and can be partially reduced by fasting animals before their examination. Poor contact between the probe and the skin, due to hair, debris, or crusts, also limits the transmission and reception of ultrasound waves.

Although artifacts are often responsible for image degradation, they can help with interpreting images in many instances. Their recognition is used to detect and confirm the presence of calculi or tissue mineralization, gas, cysts, and foreign bodies.

Acoustic Shadowing

Shadowing is a zone of echoes with reduced amplitude beyond a highly attenuating or reflective structure. Most of the incident beam is absorbed and/or reflected at the interface. A uniformly anechoic shadow is called "clean," while the term "dirty shadowing" is used when the shadow is inhomogeneous (Rubin 1991; Hindi et al. 2013). Clean shadowing is encountered when absorption of the incident beam happens at a hyperattenuating interface, such as bone, calculi, or compact foreign material, that is larger than the ultrasound beam width (Figure 1.13A). The shadow may be

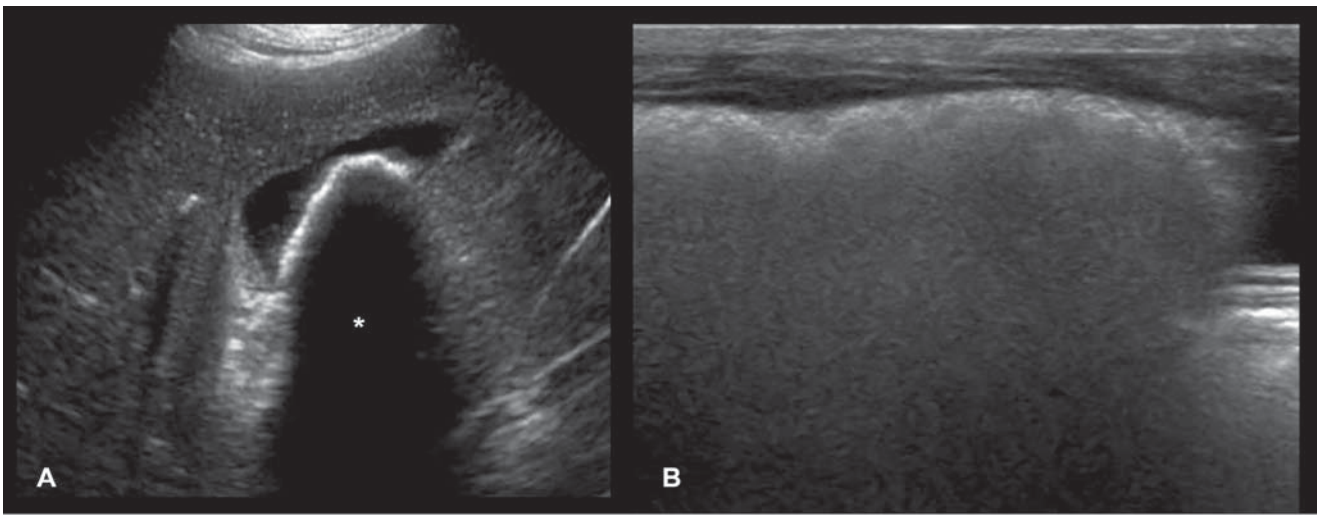


Figure 1.13. Acoustic shadowing is a poorly echoic to anechoic zone located below a highly attenuating interface. A: The clean shadow behind this large gallbladder cholelith has the triangular shape of the microconvex probe that was used. **B:** Dirty shadowing is noted associated with the mixed gas and stools present in the colon. The extensive artifact is shaped similarly to the longitudinal probe that was used.

partial behind calcifications and calculi that measure less than 0.5 mm (Hindi et al. 2013). Partial shadowing may also appear behind fat or fibrosis (Mesurolle et al. 2002; Hindi et al. 2013), depending on the size, the attenuation characteristics of the background tissue, and the equipment and settings, although this has not been well documented in veterinary medicine.

Dirty shadowing is present when the incident beam is mostly reflected, such as at a soft tissue–gas interface (Figure 1.13B).

Edge shadowing appears as discrete, triangular zones of low amplitude, at the edge of a curved structure (Figure 1.14A). When, the curved structure is fluid filled, the edge shadowing artifact borders the enhancement artifact. This type of refractive shadowing can be confusing, especially when it occurs at the cranial aspect of a fluid filled bladder, and appears as a "defect" of the wall (Figure 1.14B).

Acoustic Enhancement or Increased Through-transmission

Conversely, waves encountering a structure that allows them to pass through more easily (poorly attenuating), such as a liquid-filled cyst, remain of higher intensity when reaching the deeper tissues, allowing echoes of greater strength to return to the probe. Consequently, these deeper tissues present an artifactual increase in echogenicity (Figure 1.15). Acoustic enhancement is typically recognized deep to a fluid-filled structure in a soft tissue background, such as deep to the gallbladder or to a liver cyst, making them easy to identify and

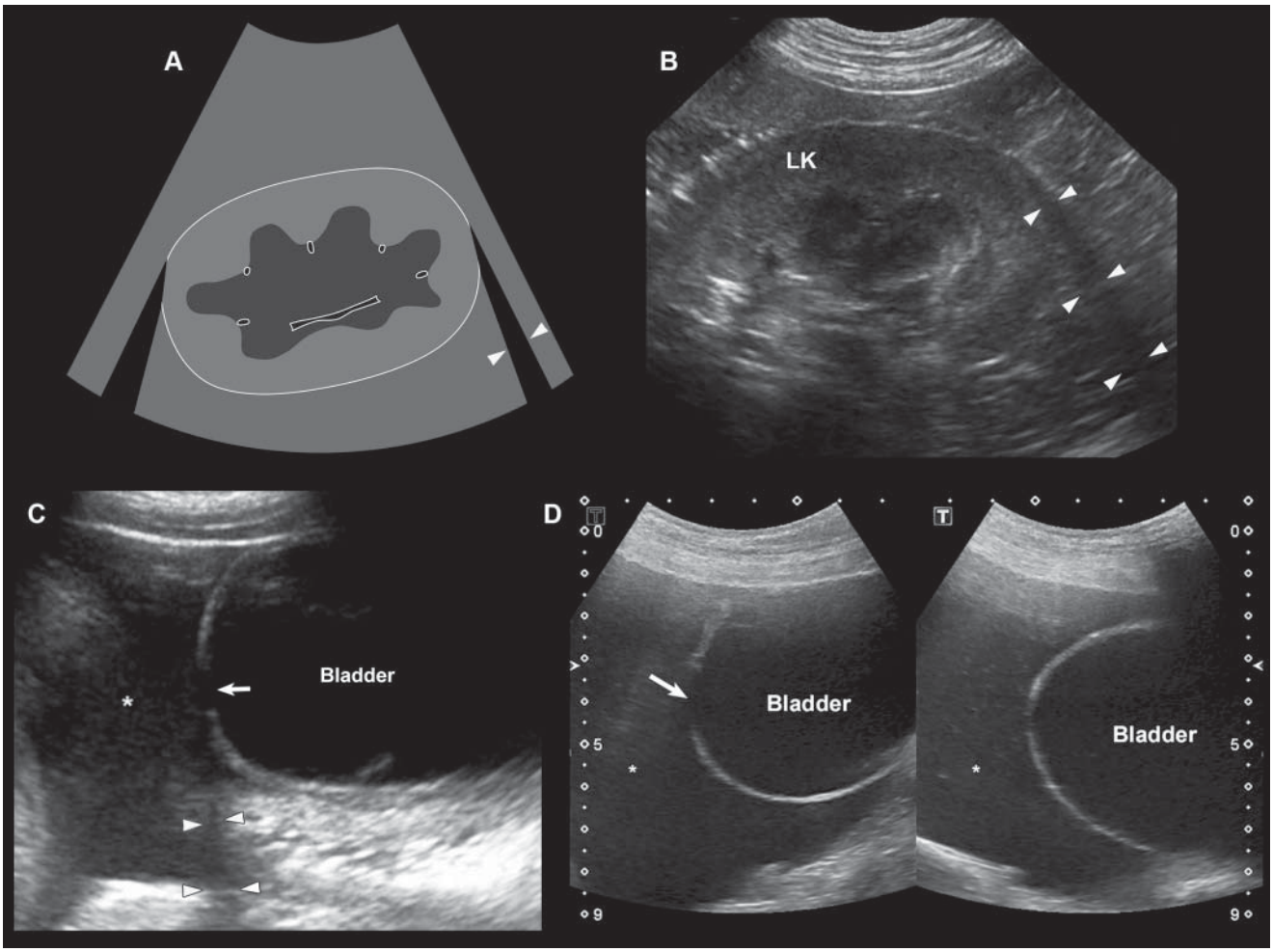


Figure 1.14. **Edge shadowing and refraction. A, B:** Edge shadowing (arrowheads) is often seen in prolongation of the renal pole. LK, left kidney. **C:** The curvature of the bladder wall causes beam refraction, which results in an acoustic shadow (arrowheads) in this dog with echogenic peritoneal effusion (*). A hole in the bladder wall (arrow) is artifactually created. **D:** In another dog with cardiac tamponade and marked peritoneal effusion (*), the artifactual hole in the bladder wall (arrow) is attenuated by repositioning the transducer with a different angulation.

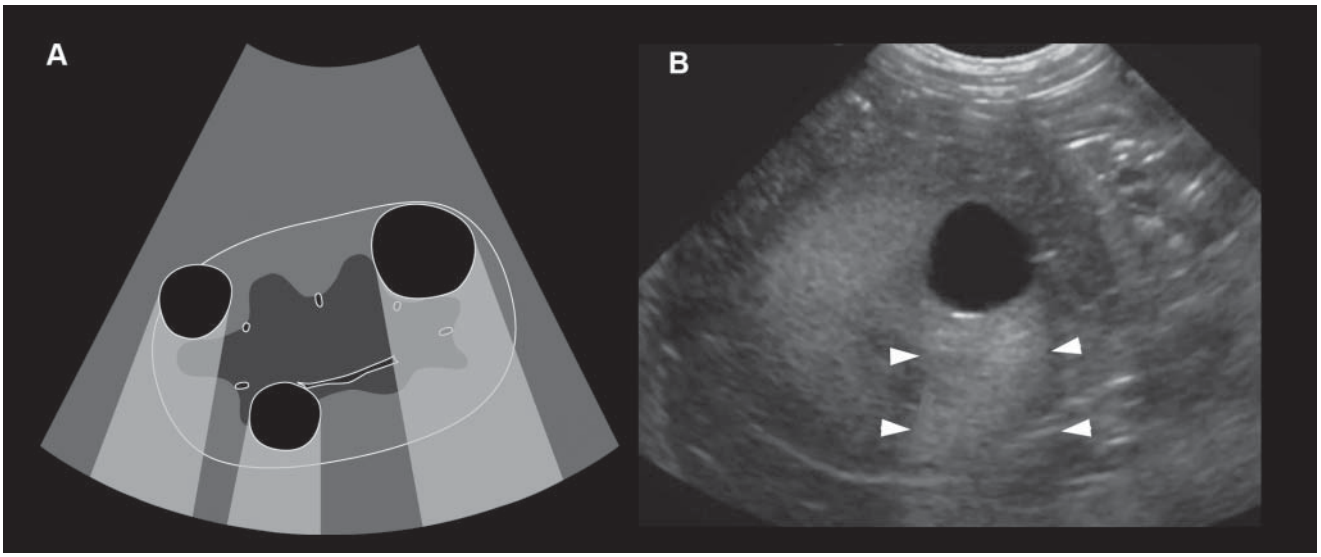


Figure 1.15. **Enhancement. A:** This artifact is represented by a zone of increased echogenicity, behind a fluid-filled structure. On this schematic drawing, several renal cysts are seen associated with distal enhancement **B:** An example of a similar cyst is present in this dog, where it is seen as a rounded, well-defined anechoic renal cyst associated with far enhancement (arrowheads).

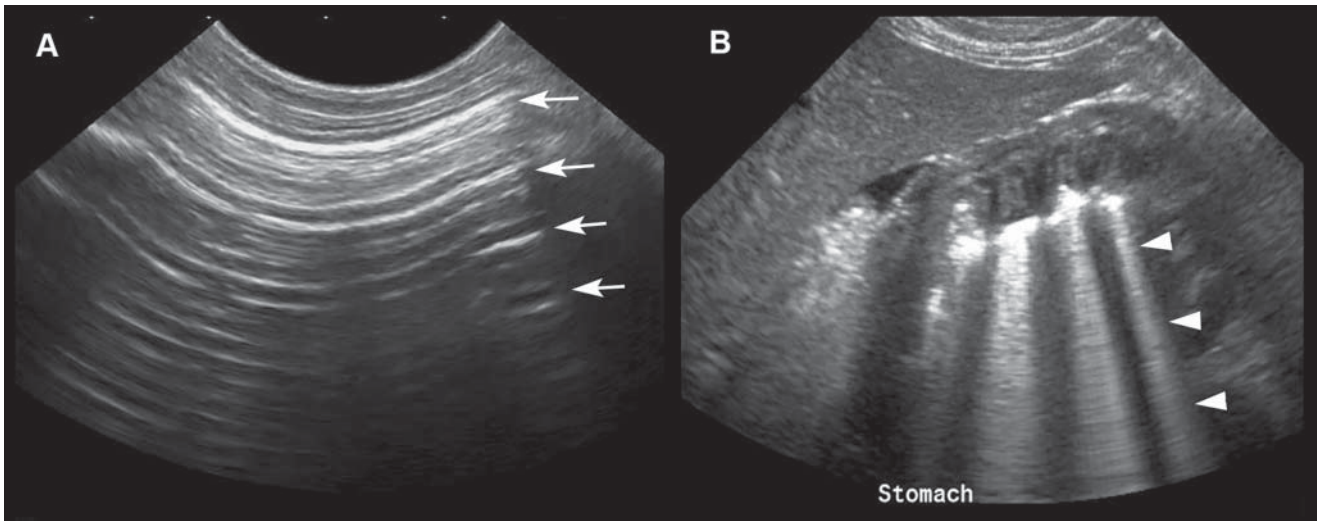


Figure 1.16. **Reverberation artifacts. A:** Reverberation appears as series of parallel and equally spaced lines (arrows), when the beam encounters a highly reflective interface such as gas. The colonic wall in the near field is barely visualized. **B:** Comet tail also appears as a series of short and very closely spaced successive echoes (arrowheads) and is often seen in the stomach.

distinguish from solid lesions. Tissues deep to the urinary bladder and organs floating in ascites often become hyperechoic.

Reverberation

Reverberation artifacts typically appear as a series of multiple, equally spaced lines (Figure 1.16A). They occur when the beam hits a highly reflective interface – such as an air pocket – and sends it back as an echo of similar intensity. The high-intensity echo is partly captured by the probe, producing a hyperechoic line at the pocket's interface, but with no echo coming from deeper tissue. The surface of the probe will reflect this high-intensity echo and send it back and forth. As part of the echo is perceived each time it returns, the computer calculates the time that has passed since the initial launch of the wave pulse and thus records

several equidistant hyperechogenic lines. There is decreasing echogenicity of the interface as it goes deeper, due to a gradual loss of wave intensity that rebounds and is attenuated during its trajectory.

Comet tail is a type of reverberation artifact – it appears as a series of short and very closely spaced successive echoes (Figure 1.16B) that typically decrease in intensity and width in depth. When gas bubbles form thin layers separated by liquid – as in the digestive tract – the waves rebound between the layers, resulting in many echoes that return to the probe at regular intervals, making a trail of echoes in the form of a shadow resembling a comet's tail. This artifact is also encountered with metallic pellets or surgical clips. **Ring down artifact** similarly appears as a series of parallel reflective lines that typically extend behind a gas collection. It happens when air bubbles resonate at the ultrasound frequency and then emit reflections. This can be seen associated with irregular lung surfaces, gastrointestinal tract, and abscesses. Practically, comet tail and ring down artifacts appear very similar on the screen, even though they result from different physical interactions.

Mirror Image

Misplacing the location of a structure often happens when a large, smooth, curvilinear, and strongly reflective interface between tissues is interposed. When this reflector is the lung surface, the most commonly encountered artifact of misplaced organ or structure, is the mirror image of the liver and/or the gallbladder on the thoracic side (Figure 1.17).

Volume Averaging

The shape of the main ultrasound beam that serves to generate images changes with depth. Indeed, the exiting ultrasound beam width is similar to the probe width, then narrows at the focal zone, and widens again deeper to the focal point. Practically, this causes more tissue to be included in areas where the beam is thickest and widest (Figure 1.18). Their echogenicities become confounded and averaged to form the brightness of the pixels being displayed in those specific regions. This may result in a pseudo-sludge in fluid-filled anechoic structures such as the gallbladder, cysts, or even the bladder, depending on their location and the quality of the probe. Volume-averaging artifact – also called slice-thickness or beam-width artifact – may then lead to errors in interpreting the content of cystic structures and may limit the conspicuity of small lesions. Using the placement of the focal zone wisely helps in reducing this artifact. Reducing the overall gain can also attenuate its appearance.

Side Lobes and Grating Lobe Artifacts

Side lobes and grating lobes are different types of secondary lobes present on the side of the primary sound beam. Side lobes are present in all transducers, and are usually of low intensity; they can create spurious echoes in the near field. Grating lobes are associated with the geometric construction of linear probes (Barthez et al. 1997). The artifacts created by secondary lobes result in misplacement of reflected echoes (Figure 1.19). In clinical situations, secondary lobe artifacts are difficult to differentiate from volume-averaging artifacts.

Speed Error and Range Ambiguity Artifacts

When the ultrasound speed is not the assumed 1,540 m/s through tissues, errors in size or location of structures may arise (Feldman et al. 2009; Hindi et al. 2013). For example, when sound travels through fat (with a velocity of about 1,450 m/s), the returning echoes will take longer to come back to the transducer and thus be displayed deeper in the image than they really are (Figure 1.20). **Speed – or propagation – error** artifacts may cause structures to be inaccurately localized or measured.

Ultrasound systems assume that all received echoes are formed form the most recent transmitted pulse. **Range ambiguity** artifact occurs when the system receives echoes from deep structures after the subsequent pulse is emitted, misplacing this structure closer to the transducer than in reality. This happens predominantly when using high pulse repetition frequency and when increasing the number of focal zones (O'Brien et al. 2001).

Anisotropy

This artifact is most commonly described in musculoskeletal ultrasound and consists of a decrease in echogenicity of the structure (such as the tendon or ligament), due to an oblique position (rather than perpendicular) of the probe on the body part being evaluated (Figure 1.21). This can be easily corrected by changing the probe angle.

Electronic Interference

Electronic interferences from devices sharing the same electrical outlet can appear as discrete radiating

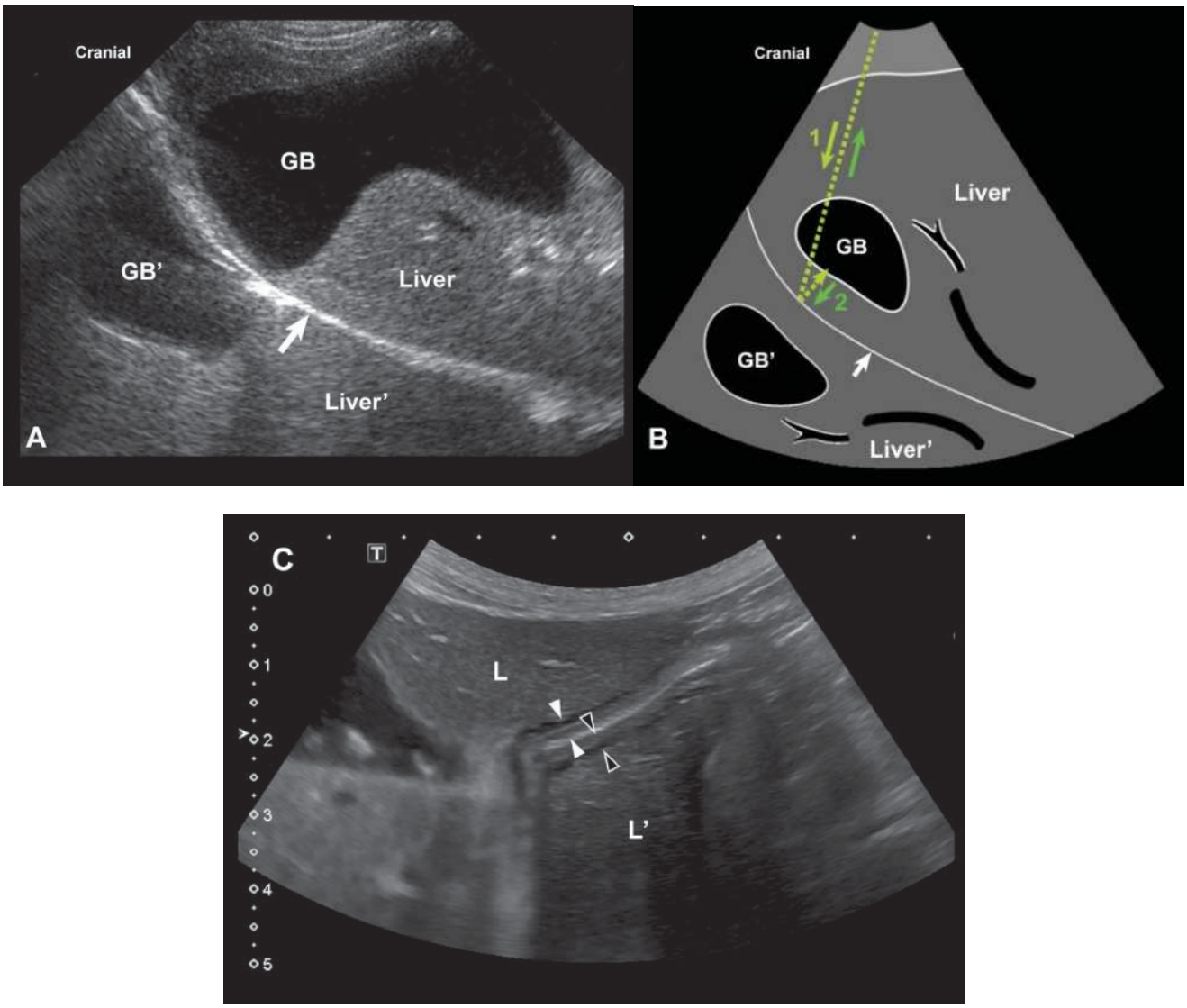


Figure 1.17. Mirror images. A-B: Sonographic **(A)** and schematic **(B)** images of a mirror artifact involving the liver in a dog. The image of the actual liver and gallbladder (GB) is obtained based on the echoes generated during "normal" ultrasound wave propagation (path 1). In this case, however, the remaining pulses are not dissipated in deeper tissues, but are almost fully reflected at the contact of the diaphragm–lung interface (arrow), which acts as strong reflector. Echoes from this reflection are thus sent back to the liver and GB, which once more reflect some of the energy back to the diaphragm/lung, before it is redirected back to the transducer (path 2). This "second set" of echoes is received long after the first set (producing the true image) and is thus interpreted by the machine as originating from the other side of the diaphragm. A mirror image of the liver (liver′) and GB (GB′) is then added on the monitor underneath the real image. **B:** In another dog, the interface of a gas-filled stomach results in a mirror image (black arrowheads) of its superficial wall (white arrowheads). A portion of the liver (L) is also mirrored distally (L′).

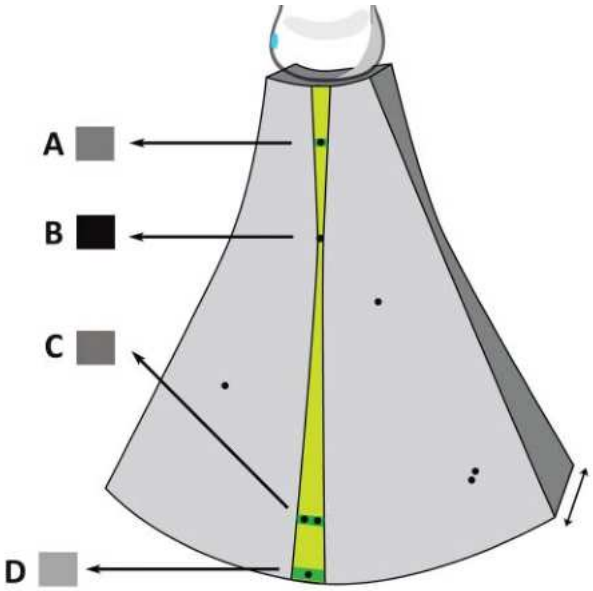


Figure 1.18. Impact of partial averaging on lesion detection. The detection of a lesion is influenced by its size, its echogenicity and its position with regard to the primary ultrasound beam. It is also influenced by the spatial resolution of the system. At a given ultrasound frequency, the lesion will be better depicted at the focal zone. Indeed, the smaller width and thickness of the beam at that level allow the lesion to completely fill the beam, resulting in anechoic pixels on the screen **(B)**. If, however, the lesion is in a larger portion of the beam **(A, C)**, the resulting image displays pixels of higher echogenicity because of the inclusion of regional liver parenchyma. The displayed pixels in fact reflect the average echogenicity of the sampled tissue. Lesions may even be confounded when multiple in a large portion of the beam (C), or with normal adjacent structures such as vessels. Moving the focal zone to the region of interest is essential when assessing small structures, such as when looking for small lesions or when measuring intestinal layers. Using more than one focal zone reduces the beam size over a greater depth.

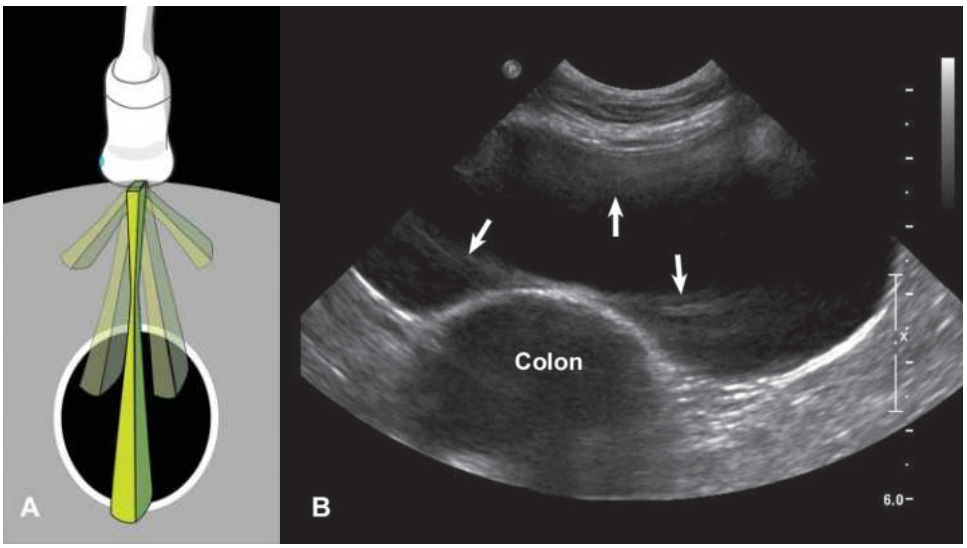


Figure 1.19. Side lobes. A: Schematic drawing of the main central beam lobe and the diverging side lobes of lower energy of a probe while imaging a fluid structure such as the bladder. **B:** Artifactual echoes are projected in the bladder, some in the near field and some in the far field. Notice that the echoes are curvilinear as they arise from the hyperreflective bladder wall interface which interacts with the side lobe beams. These echoes are erroneously interpreted to originate from the interaction with the main beam.

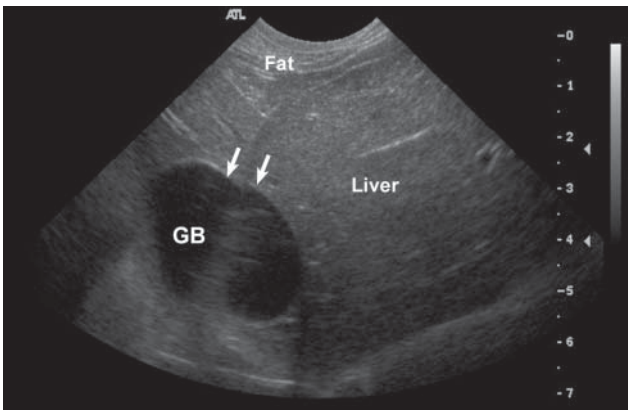


Figure 1.20. Speed error. When sound travels through fat (with a velocity of about 1,450 m/s), the returning echoes take longer to come back to the transducer and are thus displayed deeper in the image than they really are. In this normal dog, the slower velocity of ultrasound waves through fat in comparison to liver (around 1,600 m/s) results in inaccurate displacement of the GB further away from the transducer.

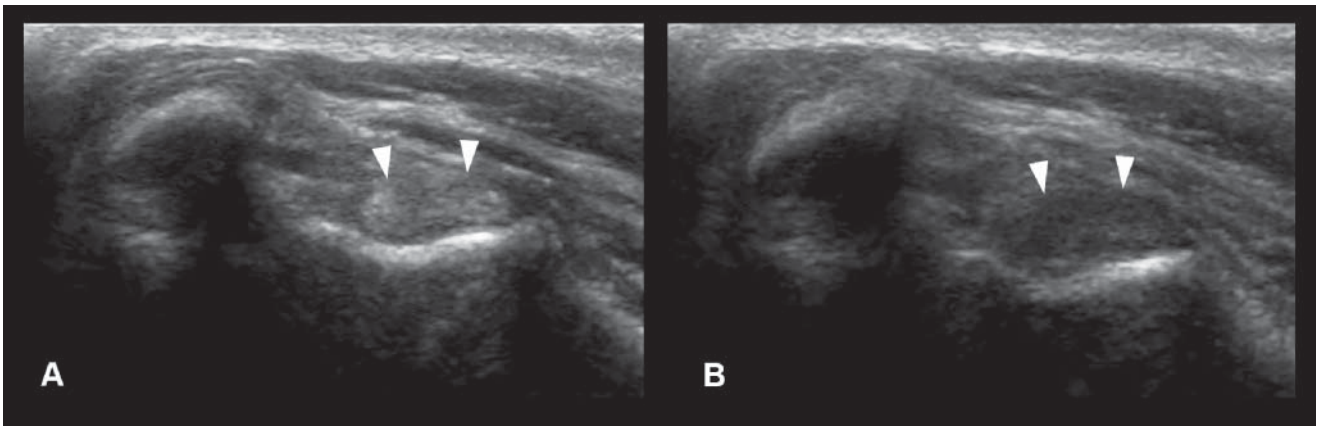


Figure 1.21. **Anisotropy. A:** Normal cross-sectional appearance of the biceps tendon (arrowheads), with the probe being perpendicular to the structure. **B:** The decrease in echogenicity of the tendon is due to an oblique position of the probe. This can be easily corrected by changing the probe angle. This artifact could be misinterpreted as a core lesion.

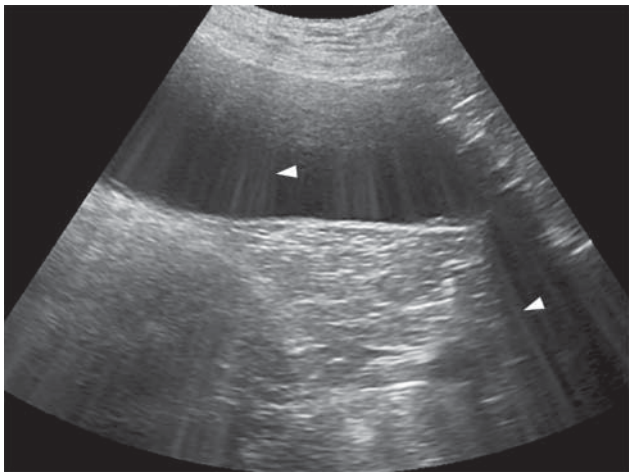


Figure 1.22. **Electronic interferences.** Discrete, highly echogenic spikes (arrowheads) are crossing the entire scan field. They are best seen when they project onto poorly echogenic structures. These were due to the use of an electrocutter in the adjacent room.

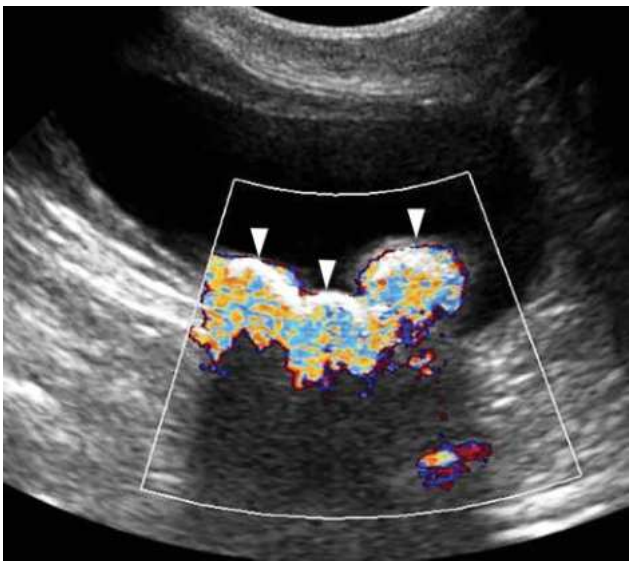


Figure 1.23. **Twinkling artifact.** Several hyperechoic interfaces associated with shadowing are present in the bladder, consistent with calculi. When activating the color flow Doppler mode, zones of rapidly changing red and blue hues (arrowheads) can be seen behind these strongly reflective structures.

echogenic spikes (Figure 1.22). This can be easily fixed by having a dedicated power outlet for the ultrasound equipment.

Twinkling Artifact

When using color flow Doppler, zones of rapidly changing red and blue hues can be seen behind strongly reflective structures, such as calculi or tissue mineralization (Figure 1.23). This artifact seems independent of the calculi composition, and it is accentuated by the size and surface of the calcification or calculus (Louvet 2006). It can be encountered with calculi in the bladder, gallbladder, or associated with any tissue mineralization.

Doppler Aliasing

This artifact occurs for a high-velocity flow when the Doppler sampling rate (i.e., pulse repetition frequency, PRF) is less than twice the Doppler frequency shift of that flow (Hindi et al. 2013). Aliasing causes the

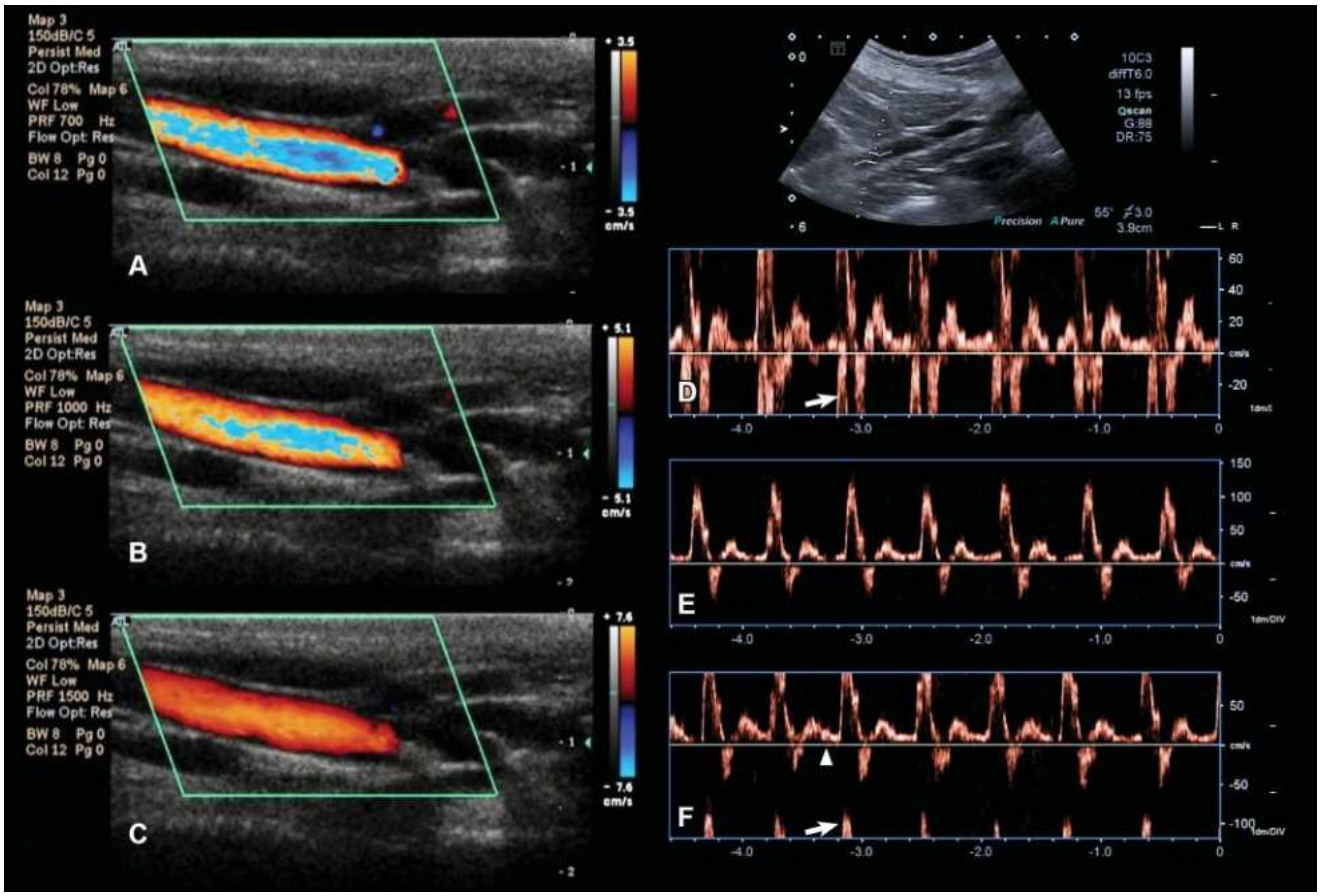


Figure 1.24. **Aliasing artifact. A:** With color Doppler, aliasing appears as a linear or mosaic hue in the center of a high-flow-velocity vessel and when the measuring scale (on the right – 3.5 cm/s in this case) is exceeded. **B:** By increasing the scale to 5.1 cm/s, the artifact is less pronounced. **C:** It disappears completely when the scale is increased to 7.6 cm/s. **D:** With spectral Doppler, aliasing manifests itself as a wraparound of the flow profile on the opposite extremity of the velocity scale. The measured maximal velocity of this iliac artery (in the direction of the transducer) exceeds 60 cm/s and is interpreted as reversed (arrow). **E:** Increasing the velocity scale (or pulse repetition frequency) to 150 cm/s allows the entire flow spectrum to be included. Note that the calculated maximal velocity of this artery exceeds 100 cm/s. **F:** The baseline (arrowhead) position can also be responsible for the onset of aliasing. In this case, it was moved to the positive side, reducing the scale on that side (maximal velocity approximating 75 cm/s), and resulting in velocity peak wraparound (arrow).

high-frequency component of the flow to wrap around the scale, from its positive or negative extremity, depending on its direction (Figure 1.24).

Aliasing can be reduced or eliminated by increasing the velocity scale (which increases the PRF), moving up or down the baseline, increasing the Doppler angle (which decreases the Doppler shift), or using a lower ultrasound frequency.

Doppler Flash Artifact

Rapid movement of the patient's body, of a structural component (e.g., heart or arterial pulsation), or of the probe might lead to Doppler shifts being interpreted by the system as blood flow. A spurious appearance of blood flow is displayed, limiting the assessment of true vessels. This artifact tends to be more apparent in fluid-filled structures and with ascites (Figure 1.25).



Visit our website at **www.SmallAnimalUltrasonography.com** for complementary video clips with annotations and text on:

- Formation of the ultrasound image
- Propagation of ultrasound waves and interaction with tissues
- Ultrasound beam and spatial resolution
- Gain and time gain compensation
- Mirror image artifact
- Shadowing artifact
- Enhancement artifact

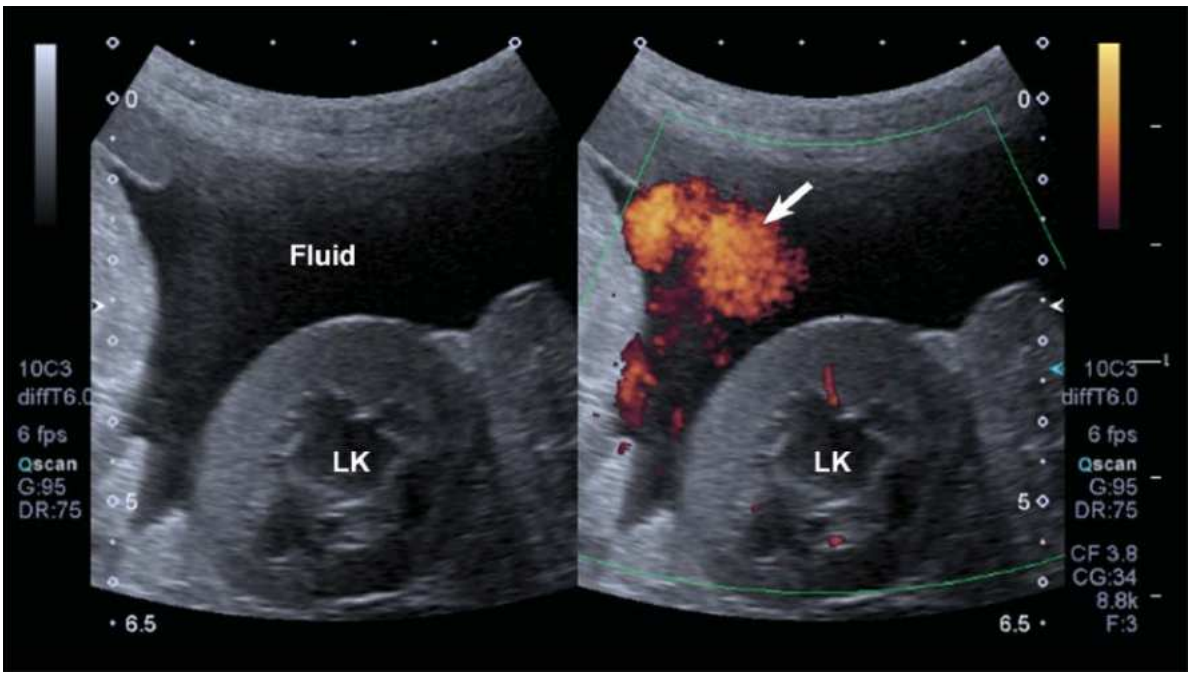


Figure 1.25. **Flash.** Spurious echoes often appear when using power Doppler in moving patients or when ascites is present, limiting the assessment the tissue perfusion in these cases. LK, left kidney.

- Reverberation artifacts
- Refraction artifact
- Speed error and range ambiguity artifacts
- Twinkling artifact

References

Barthez PY, Leveille R, Scrivani PV. Side lobes and grating lobes artifacts in ultrasound imaging. Vet Radiol Ultrasound 1997; 38:387–393.

Boote EJ (2003) AAPM/RSNA physics tutorial for residents: topics in US–Doppler US techniques: concepts of blood flow detection and flow dynamics. Radiographics 23:1315–1327.

Bushberg JT, Seibert JA, Leidholdt EM Jr., Boone JM. (2011) Ultrasound. In: The Essential Physics of Medical Imaging, 3rd edition. Philadelphia, PA: Lippincott Williams & Wilkins, pp 500–576.

d'Anjou MA, Penninck D, Cornejo L, Pibarot P (2004) Ultrasonographic diagnosis of portosystemic shunting in dogs and cat. Vet Radiol Ultrasound 45:424–437.

Feldman MK, Katyal S, Blackwood MS (2009) US artifacts. Radiographics 29:1179–1189.

Hangiandreou NJ (2003) B-mode US: basic concept and new technology. Radiographics 23:1019–1033.

Heng HG, Widmer WR (2010) Appearance of common ultrasound artifacts in conventional vs. spatial compound imaging. Vet Radiol Ultrasound 51:621–627.

Hindi A, Paterson C, Barr RG (2013) Artifacts in diagnostic ultrasound. Rep Med Imaging 6:29–48.

Kirberger RM (1995) Imaging artifacts in diagnostic ultrasound-a review. Vet Radiol Ultrasound 36:297–306.

Louvet A (2006) Twinkling artifact in small animal Color-Doppler sonography. Vet Radiol Ultrasound 47:384–390.

Mesurolle B, Ariche-Cohen M, Mignon F, Guinebretière JM, Tardivon A, et al. (2001) Small focal areas of acoustic shadowing in the breast. J Clin Ultrasound 30:88–97.

O'Brien RT, Zagzebski JA, Delaney FA (2001) Ultrasound corner: range ambiguity artifact. Vet Radiol Ultrasound 42:542–545.

Rubin JM, Adler RS, Bude RO, et al. (1991) Clean and dirty shadowing at US: a reappraisal. Radiology 181:321–236.

Szatmari V, Sotonyi P, Voros K (2001) Normal duplex Doppler waveforms of major abdominal blood vessels in dogs: a review. Vet Radiol Ultrasound 42:93–107.

Ziegler L, O'Brien RT (2002) Harmonic ultrasound: a review. Vet Radiol Ultrasound 43:501–509.

CHAPTER TWO

Eye and Orbit

Stefano Pizzirani[1], Dominique Penninck[1] and Kathy Spaulding[2]

[1]*Department of Clinical Sciences, Cummings School of Veterinary Medicine, Tufts University, North Grafton, MA, USA*

[2]*Large Animal Clinical Sciences, College of Veterinary Medicine and Biomedical Sciences, Texas A&M University, College Station, TX, USA*

Preparation and Scanning Technique

There are few standard methods for imaging the globe and the orbit.

For **globe** evaluation, high-frequency transducers can be applied directly on the cornea or at the limbus. The globe can be geometrically compared to a sphere. The planes of the sections can be changed according to the needs. Visual axis defines axial (central corneal) sections. Paraxial meridional sections are obtained when the plane of the section does not follow the visual axis, but still involves the center of the lens. If the probe is maintained on the corneal surface, using a fanning motion, the globe is scanned from one side to the other with sections that may follow the meridians (usually keeping the center of the lens in the section) or that are parallel to the visual axis plane (obtaining parallel sections).

Sections parallel to the visual axis can be achieved moving the probe without changing the scanning direction (Figure 2.1). If the position of the probe is at the limbus or in perilimbal areas, meridional (radial) or transverse (perpendicular to the visual axis and parallel to the iris plane) sections can be obtained; the probe can be then moved laterally or rostrally to caudally (Figures 2.2, 2.3). Once the standard approach is performed, ad hoc selected oblique planes can help to delineate a lesion more accurately.

Orbital evaluation is best obtained with lower-frequency probes using the transcorneal positions and/or the temporal fossa window in mesocephalic and dolicocephalic dogs. A window less commonly used exploits the space underneath the zygomatic arch. Images obtained with the transducer applied directly on the cornea are of higher quality.

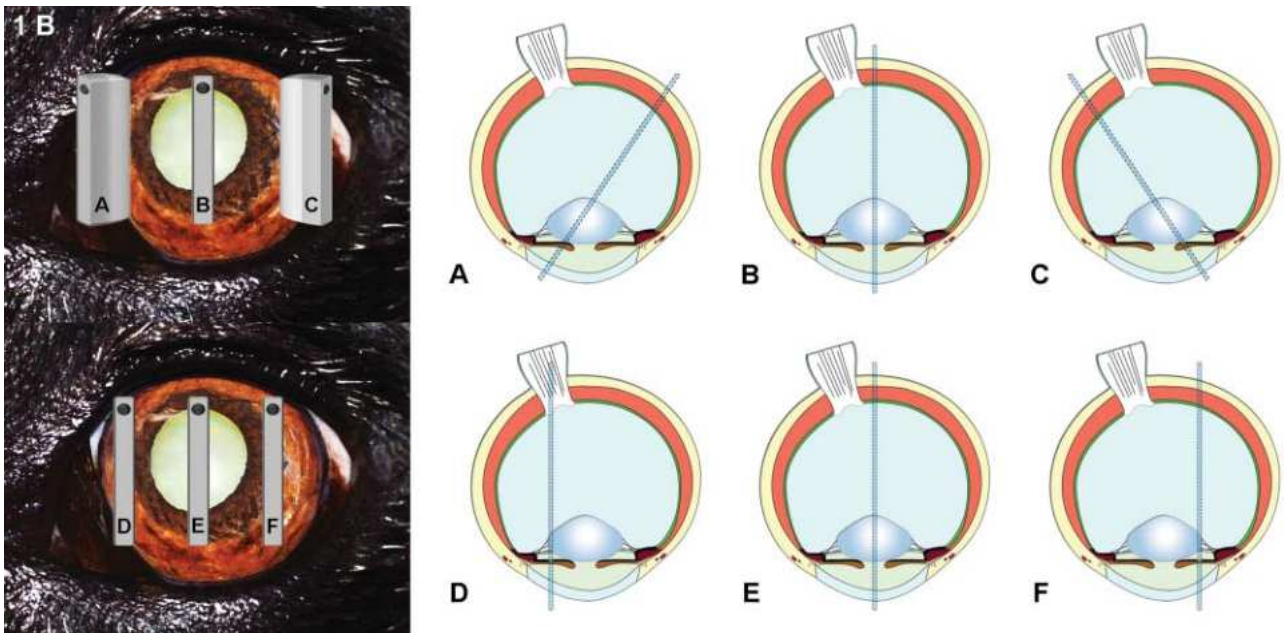
In some instances, the globe can also be scanned through the eyelid. Artifacts and image degradation may occur when imaging through the eyelid, although in breeds with thinner eyelids and eyelids that are poorly haired, using abundant coupling gel may obviate this inconvenience. The technique of imaging through the closed lid in brachycephalic dogs (or the temporal fossa approach in dolicocephalic dogs) is recommended if there is a defect in the corneal surface, recent severe globe trauma, recent ocular surgery or the patient is severely blepharospastic, or if the swelling of the periocular tissues prevents manual opening of the eyelids.

The examination is generally performed with the dogs awake. A topical anesthetic (proparacaine 0.5% eye drops) is applied at a dose of one to two drops to the cornea 1 minute before the examination. With painful eyes, the application can be repeated a few times every 30–60 seconds. Different acoustic coupling gels can be used. A sterile, water-soluble lubricating acoustic gel approved for the eye is recommended. It is important that the gel does not contain preservatives or scents. At the end of the examination, the gel should be flushed from the eye with approved sterile eyewash. For the safety of the imager and the patient, mild sedation of a non-collaborative patient may be advised if manual restraint is inadequate to securely position it. Depending on the anesthetic agent(s) used,

Atlas of Small Animal Ultrasonography, Second Edition. Edited by Dominique Penninck and Marc-André d'Anjou.
© 2015 John Wiley & Sons, Inc. Published 2015 by John Wiley & Sons, Inc.
Companion website: www.SmallAnimalUltrasonography.com



Figure 2.1. Probe placement and direction of the beam through the eye using the corneal surface. A: The probe is placed on the cornea and oriented to section ocular meridians. Schematic sections show the section through the lens center. **B:** The probe is placed on the cornea and moved laterally to produce parallel paraxial sections. These sections are helpful in evaluating the anterior chamber and iris, besides the posterior segment. For both of these orientations, vertical, horizontal and oblique sections are obtained.



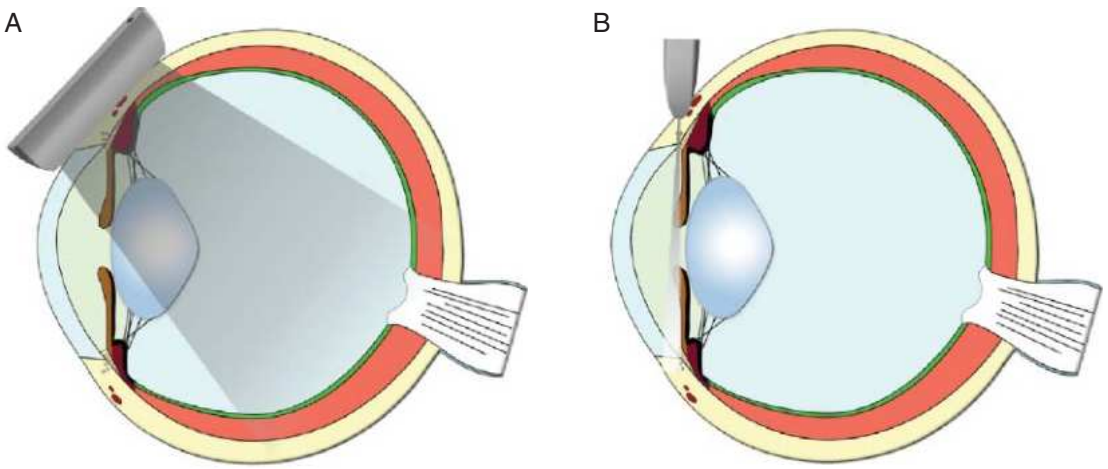


Figure 2.2. Probe placement and direction of the beam through the eye using the limbal and perilimbal approach. Radial (**A**) or transverse (**B**) sections can be obtained; the probe can be then moved rostrally to caudally. Both these sections can be oriented around the clock to produce the best imaging.

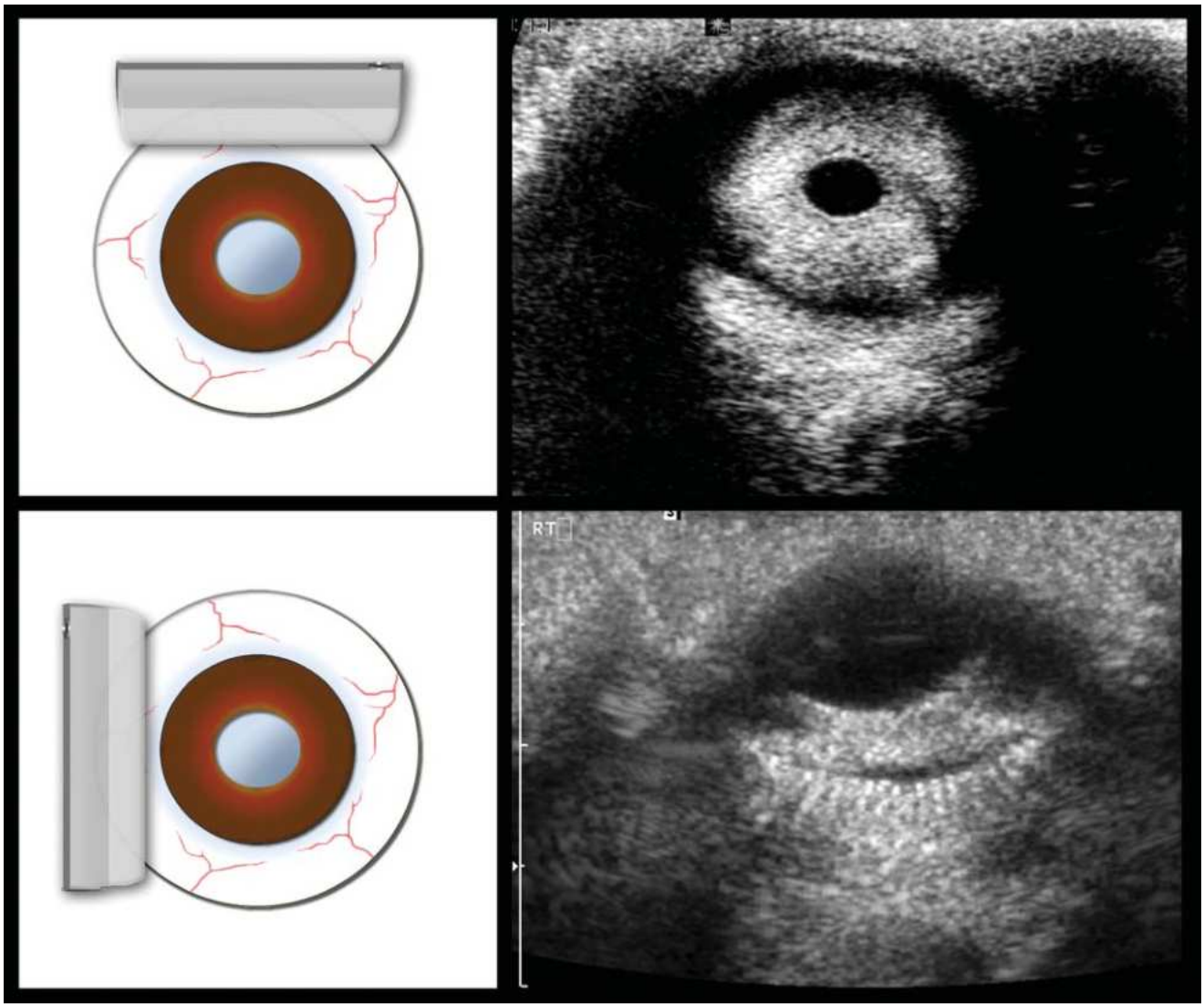


Figure 2.3. **Limbal and perilimbal approach. A:** Transverse plane through the eye allows the visualization of the iris and ciliary bodies. The iris encircles the pupil (central anechoic space, of variable size). **B:** The iris is seen in close apposition to the peripheral ciliary bodies (arrowheads). The marker should be kept nasal in the horizontal position and dorsal in the vertical position.

the globe may tend to rotate ventrally. Ventral rotation of the globe may render transducer positioning more difficult; in this case, a conjunctival forceps or a stay suture applied to the limbus in a strategic position may be necessary to move the globe in an axial alignment. When the transducer covers the surface of the globe, maintaining a specific orientation of the ocular section may be difficult.

High-frequency transducers are selected depending on the equipment available and the region of the eye and orbit to be imaged. The highest resolution available is recommended. Transducers with a range from 7.5 to 50 MHz are commonly used to image the globe and orbit. Probes with frequencies between 75 and 100 MHz have been developed (Sherar et al. 1989; Pavlin et al. 1991; Aubin et al. 2003; Bentley et al. 2003; Silverman et al. 2006) but their clinical use in veterinary ocular ultrasonography has not been yet reported.

Ultrabiomicroscopy (UBM) uses very high-resolution probes in the 35–50 MHz range, to evaluate cornea, anterior chamber, iris, ciliary body, and anterior lens. High-frequency probes can provide axial and lateral resolutions of up to 30 and 60 microns, respectively (Silverman 2009). The vitreous body and the retrobulbar area are often best imaged with the 7.5–13 MHz transducers. A linear transducer provides optimum imaging of the near-field structures, but manipulating a sector or convex probe with a

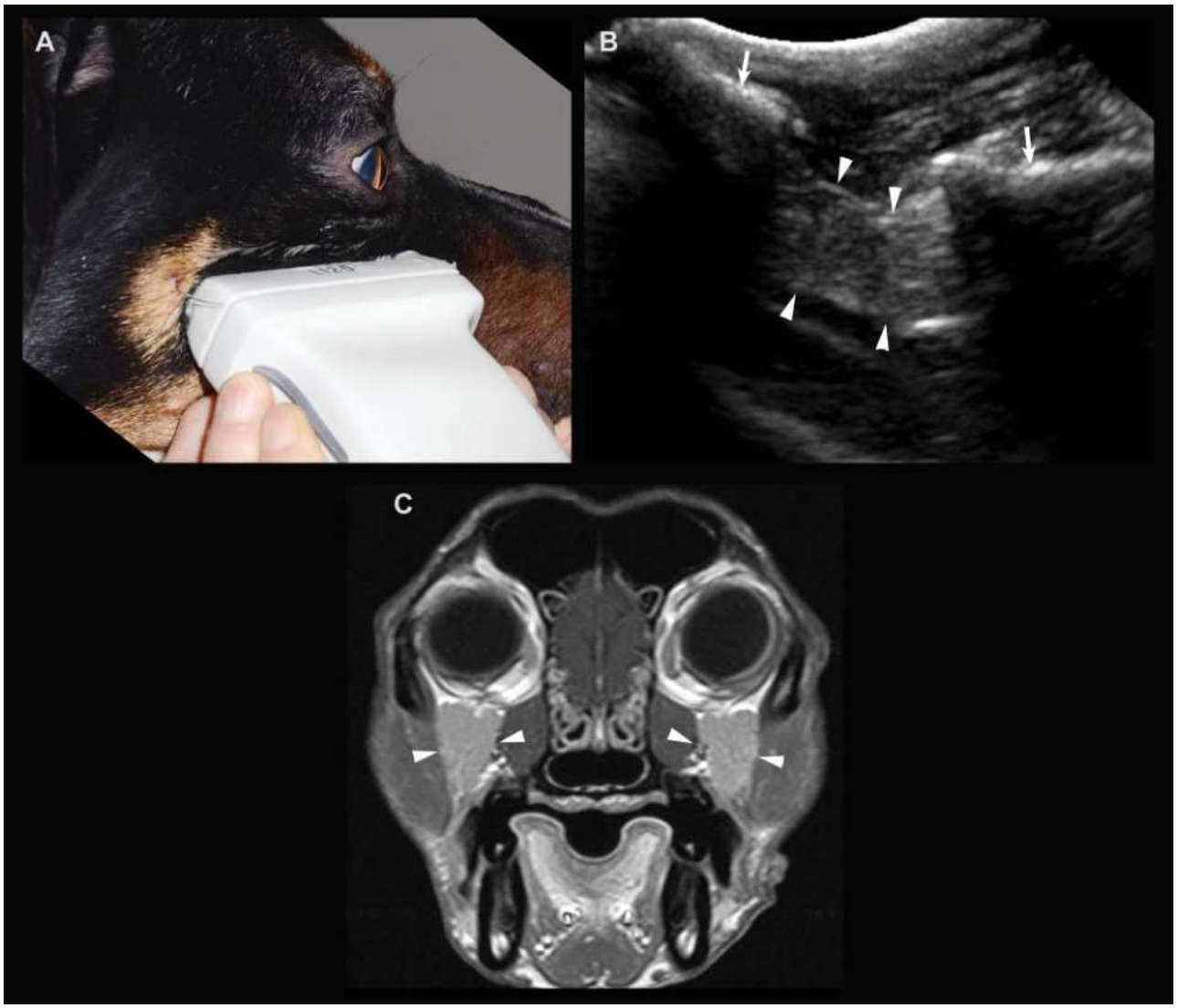


Figure 2.4. **Zygomatic gland scanning. A:** Images of the zygomatic salivary gland are obtained by placing the transducer ventral to the zygomatic arch and caudoventral to the globe. **B:** The zygomatic salivary gland is identified as a well-defined echogenic tissue (between arrowheads) located deep to the zygomatic arch depicted by the hyperechoic shadowing bone (arrows). **C:** Transverse T1-weighted contrast-enhanced magnetic resonance image. The zygomatic gland is identified by the arrowheads ventral to the eyes.

small footprint may be easier. The patient's eyelids are manually held open by the restrainer while the head is secured (Hager et al. 1987; Dziezyc et al. 1988).

Large-breed dogs, especially dolicocephalic patients, are often more difficult to image because they are naturally enophthalmic and may squint or retract the globe further into the orbit and thus limit access to the eye. This may be particularly challenging when using a linear probe. The globes of mesocephalic and brachiocephalic breeds are generally more accessible.

The zygomatic salivary gland, located ventrally to the globe, can be imaged with the probe placed ventrolaterally to the zygomatic arch (Figure 2.4). Doppler imaging or standardized A-mode scanning may provide additional vascular and measurement information.

For both globe and orbital evaluations, the probe position marker is usually placed on the left side of the image to identify the nasal (medial) aspect for a horizontal plane, and dorsal for a vertical plane (Figure 2.5).

The directional terms used with reference to the globe can be anterior and posterior, rostral to caudal, dorsal to ventral, and medial and lateral (nasal to temporal).

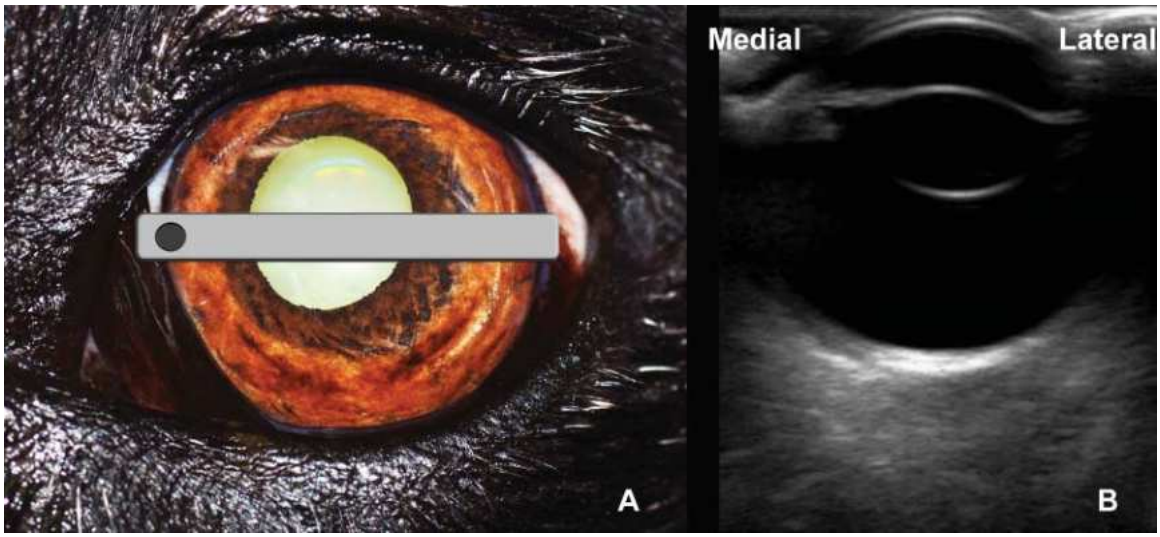


Figure 2.5. **Horizontal plane. A:** The probe is seen oriented horizontally on the cornea. The position of the marker is nasal (medial). **B:** The corresponding sonogram, displaying the medial side of the eye on the left side of the image.



Figure 2.6. **Ultrabiomicroscopy (UBM) probe.** Photograph of the fluid-filled covering cup used with 35–50 MHz UBM probes. Notice the size and shape of the transducer, which allow an easier evaluation of the dorsolateral quadrant of the eye. The reference scale is in mm.

The dimension and shape of high-frequency probes (35–50 MHz) make the dorsolateral quadrant the easier one to image (Figure 2.6).

Ultrasonographic Anatomy of the Normal Eye

Ocular ultrasonography evaluates the globe (eyeball or bulbus oculi) and orbital structures, consisting of the tissues within the periorbital cone in the retro-orbital area, including the optic nerve, extra-ocular muscles, vessels, fat, and surface of adjacent orbital bone, and the soft tissues and glands (lacrimal glands and zygomatic salivary glands) around the globe.

The spaces inside the globe are represented by the anterior and the posterior chambers, and the vitreous cavity (Figure 2.7). The globe wall is made by three layers: the outer fibrous coat (anteriorly represented by a transparent cornea and laterally and more posteriorly by the white sclera), the middle vascular coat (the uveal tissue, which consists anteriorly of the iris and ciliary body and posteriorly of the choroid) and the retina (the innermost layer) that covers only the posterior segment. The lens is positioned axially and anteriorly within the globe. It is suspended by zonular ligaments attaching to the ciliary body and divides the anterior and posterior chambers from the vitreous cavity. The lens physically supports the iris anteriorly and their close contact is responsible for the anterior bowing of the iris (Figures 2.8C, 2.13A). In the normal eye, the anterior chamber, posterior chamber, and vitreous body are anechoic, with few reflectors present (Figures 2.7, 2.8). The thickness of the cornea and various parts of the eye has been recorded in different

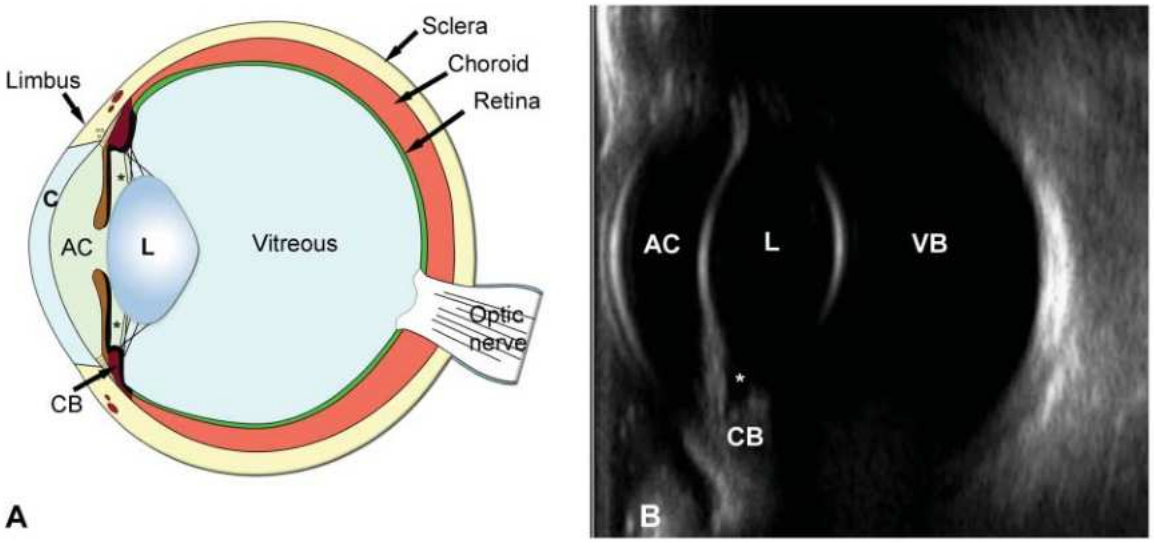


Figure 2.7. **Normal ocular globe. A:** Schematic drawing of ocular structures. **B:** Corresponding sonogram of a normal eye. The globe has a three-layered outer shell and contains the fluid-filled anterior and posterior chambers, and the vitreal chamber (filled with vitreous body); these chambers all have an anechoic appearance. The posterior chamber is marked by an asterisk (*). C, cornea; L, Lens; CB, ciliary body; AC, anterior chamber.

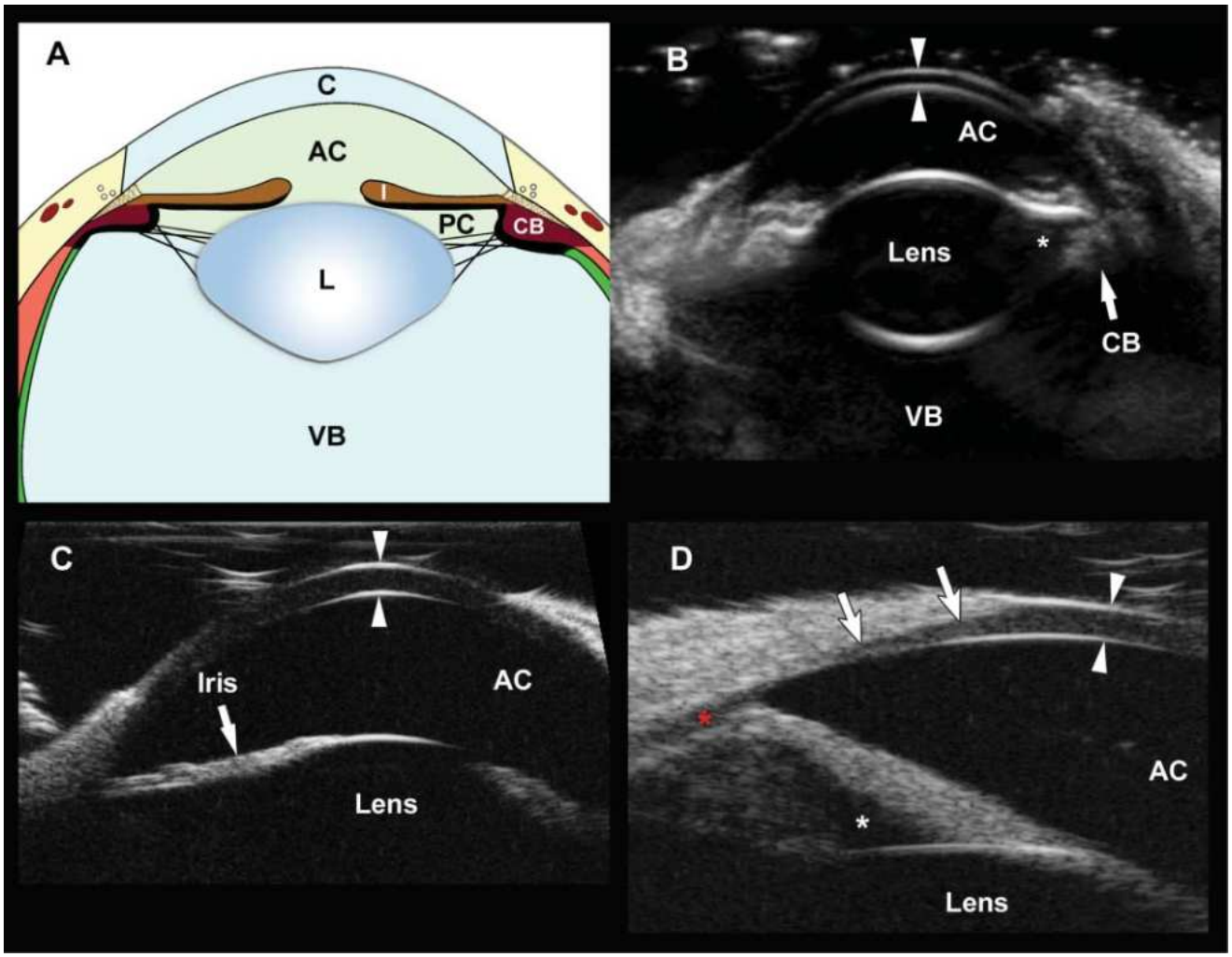


Figure 2.8. **Normal anterior segment of the eye.** (for full caption, see facing page)

species (Schiffer et al. 1982; Cottrill et al. 1989; Boroffka et al. 2006).

Depending on the probe frequency, the cornea most commonly presents as a double parallel echogenic line with a nearly anechoic center (Figure 2.8). The outer line represents the corneal epithelium and basal membrane. The stroma is anechoic and the inner line represents the Descemet's membrane and the corneal endothelium (Pavlin et al. 1995). The corneoscleral junction (limbus) is defined by the transition between the poorly reflective corneal stroma and the highly reflective scleral tissue (Figure 2.8D) and can only be accurately evaluated using UBM technology. The sclera is imaged as a highly reflective structure compared with the cornea. The sclera can usually be differentiated from the overlying episclera and the underlying ciliary body and retina.

The anterior chamber can be difficult to image because of its compressibility, size, and location in the near field. Better evaluation of the anterior chamber is provided by UBM. The depth of the anterior chamber varies with breed and age. Normal depth is usually in a range of about 3–4 mm. The cornea, the iris, and the central anterior lens capsule delineate the anterior chamber, which is distended with anechoic aqueous humor (Figure 2.8).

Perilimbar meridional or transverse sections perpendicular to the ciliary processes are used with UBM to investigate the opening of the cleft and the ciliary processes. A standard sagittal section should image the ciliary processes with a triangular shape (Figure 2.9). Besides the evaluation of the ciliary cleft, these sections are also useful for investigating the presence of iridociliary cysts or masses posterior to the iris or invading the ciliary body.

The normally shallow posterior chamber is located between the iris and the lens; it contains aqueous humor produced by the ciliary body, which flows from the posterior chamber to the anterior chamber through the pupil. The uvea is the middle vascular layer of the globe, and is made of the ciliary body and the iris anteriorly, and the choroid posteriorly (Figures 2.7).

The iris is a dynamic, stromal and muscular, contractile diaphragm with a central opening (the pupil). The size of the pupil can vary rapidly in diameter, allowing varying amounts of light to reach the retina. The muscles in the iris control the pupil size. The pupil appears as an anechoic void in the central iris. When the pupil is constricted or when the beam is off axis, the iris may be mistaken for the anterior surface of the lens. However, the iris leaflets are thicker and ill-defined, while the anterior lens capsule is a discrete, linear hyperechoic interface. The ciliary body is highly vascular and at the junction with the choroid forms the ora ciliaris retinae. This transition can't be seen with ultrasonography. The aqueous humor is produced by the non-pigmented ciliary epithelium, which lies on the inner surface of the ciliary processes. The ciliary body contains muscle fibers that regulate the position of the lens. The lens is supported by the suspensory ligaments (zonulae). The zonulae may occasionally be seen as striations that attach to the lens contour. The iris, ciliary body, and zonulae are often best imaged from a transverse or oblique view.

The lens is composed of a capsule, anterior epithelium, lens cortical (perinuclear) fibers, and nucleus. The capsule is like an envelope that encases the lens. The lens fibers that make up the majority of the lens are positioned in layers, with the cortex forming the outer layer of the lens and the nucleus located in the center. The gel-like density of the vitreous body contributes to support the lens position posteriorly.

The internal appearance of the normal lens is anechoic. Curvilinear hyperechoic interfaces appear at the anterior and posterior margins of the lens, as a result of specular reflections, when scanned perpendicularly (Figures 2.8). The surface of the lens is smooth and slightly convex. The size of the lens varies with the species and age. The anterior surface of the lens can be difficult to separate from the iris unless the pupil is dilated. The normal nucleus in a young animal has the same appearance as the cortex of the lens. With age (in dogs usually starting at 5–6 years) the nuclear density increases (nuclear sclerosis) and the nucleus becomes more visible (because it is less anechoic)

Figure 2.8. **Normal anterior segment of the eye. A:** Schematic drawing of the anterior segment of the eye. C, cornea; AC, anterior chamber; I, iris; PC, posterior chamber; L, lens; VB, vitreous body; CB, ciliary body. **B:** High-resolution (12 MHz) sonogram of the cornea, anterior and posterior chambers, ciliary bodies (CB). The cornea appears as two discrete hyperechoic curvilinear interfaces (arrowheads). The asterisk (*) indicates the posterior chamber. **C:** Normal cornea (between arrowheads) and anterior chamber imaged (AC) with a 35-MHz probe in axial section. The iris and the anterior lens capsule are in mutual contact. **D:** Perilimbal radial section with a 35-MHz probe. The ciliary cleft is visible and normally open (red asterisk). The corneal–scleral junction (arrows), anterior chamber, anterior lens capsule, part of the iris and the posterior chamber (white asterisk) can be seen.

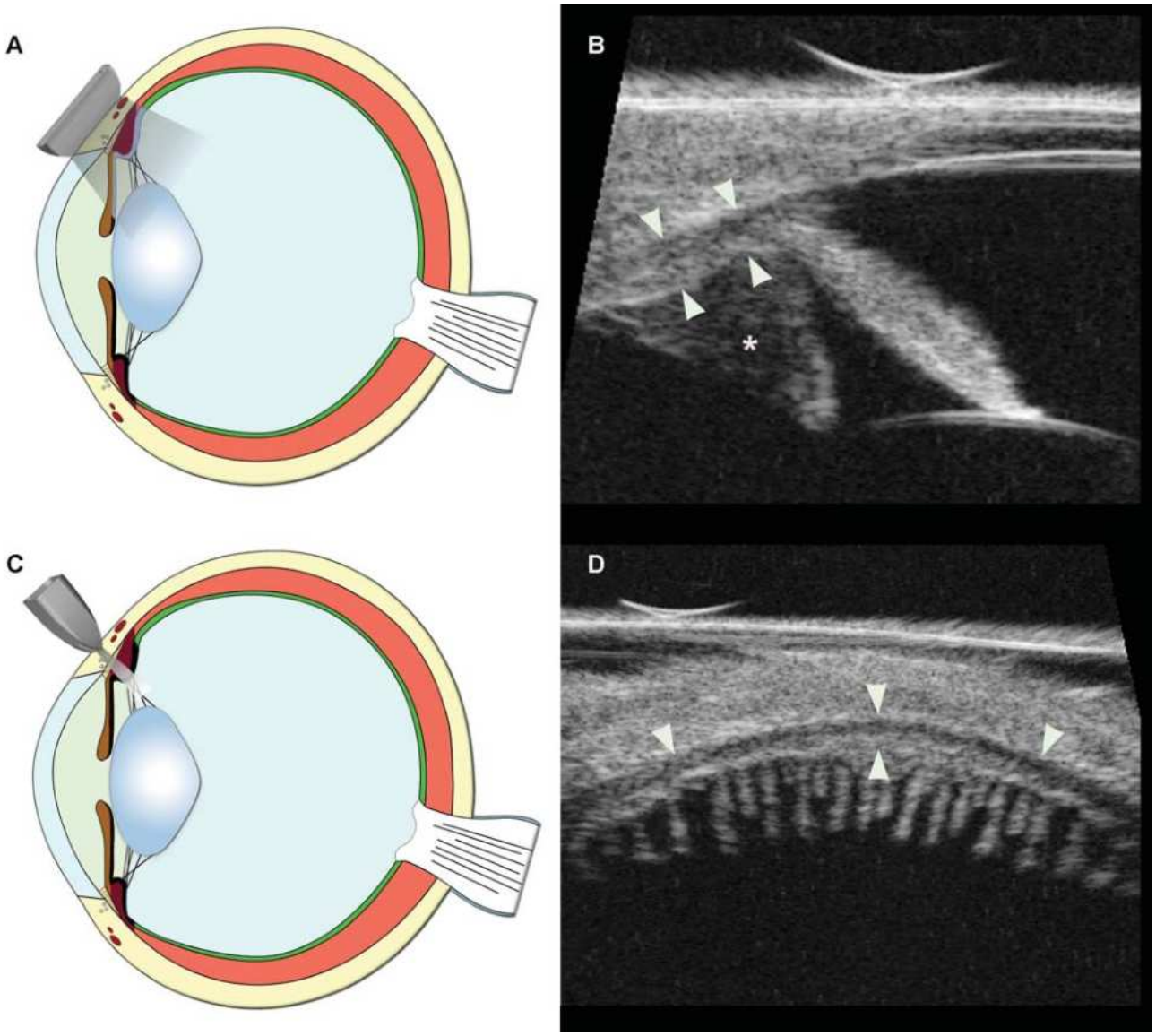


Figure 2.9. **A 35-MHz ultrabiomicroscopy (UBM) probe is used to evaluate the iridocorneal angle, the ciliary cleft and the ciliary body. A:** Schematic illustration of a limbal radial section. **B:** Note the triangular shape of the ciliary process indicating a correct position of the probe (asterisk). The ciliary cleft appears as a hypoechoic space between the sclera and the ciliary body (arrowheads). In this case, it is normally open. Attention should be paid so as not to press the probe on the ocular wall, to avoid indentation and possible change in the morphology of the angle. **C:** Transverse section, perpendicular to the ciliary body. **D:** Ultrasonographic image corresponding to probe position illustrated in C. The cleft appears as a linear hypoechoic space when normally open (arrowheads). The ciliary processes in this section appear as slender, finger-like hyperechoic structures directed to the center of the eye.

(Figure 2.10). Posterior to the lens and extending to the posterior aspect of the globe is the vitreous body, which fills the vitreal cavity. The vitreous body is a thick, acellular, gelatinous structure composed of 98% water, mucopolysaccharides, and hyaluronic acid. The vitreous cavity is bounded by the lens zonules and posterior capsule anteriorly and the retina posteriorly (Figure 2.10). The vitreous body attaches primarily at the region of the optic disc (vitreous base) and at the ora ciliaris retinae and forms the hyaloid fossa, a fibrillar dense indentation, to adapt the posterior surface of the lens. The vitreous body is densely packed at the posterior surface of the lens except at the attachment of the hyaloid canal (Cloquet's or central canal).This canal extends from the posterior surface of the lens through the vitreous body to the optic disc on the posterior surface of the globe. This potential space in the vitreous body contains the hyaloid artery in an

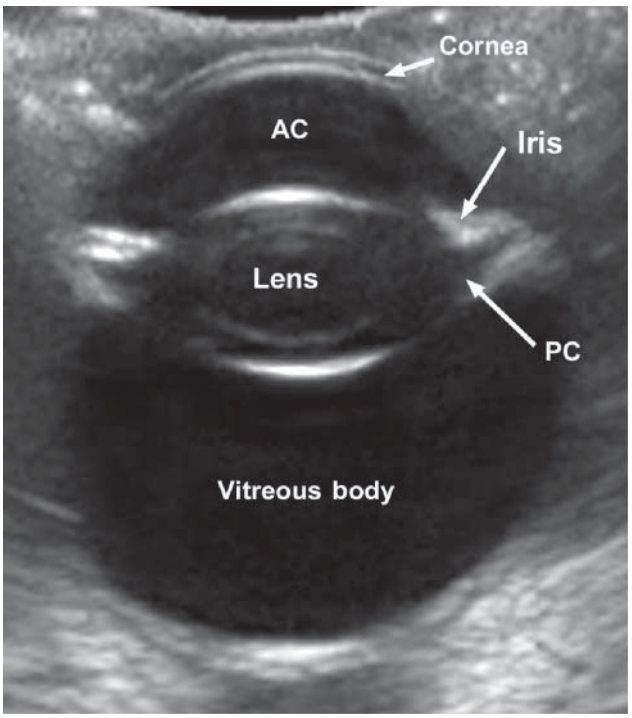


Figure 2.10. Transcorneal axial plane of a normal globe in a 7-year-old patient. The anterior chamber (AC) and vitreous body are anechoic. The lens in this older dog shows evidence of nuclear sclerosis. PC, posterior chamber.

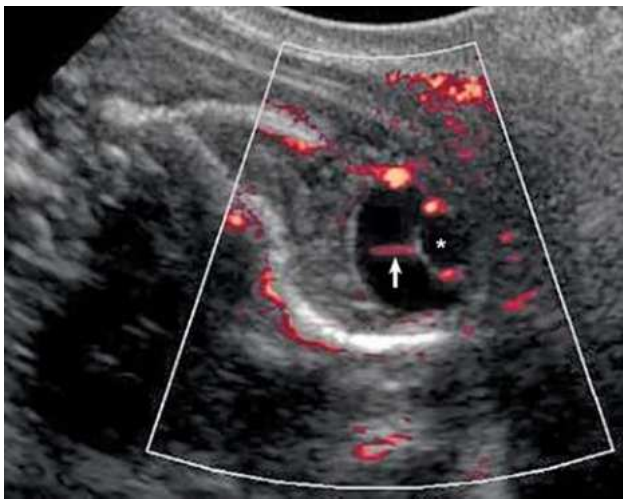


Figure 2.11. Fetal eye. This is the globe of late term fetus. Note the straight line from the posterior surface of the lens to the posterior surface of the globe (arrow). This is a patent (color flow Doppler) hyaloid vessel supplying nutrition to the lens. This vessel typically is not present after birth. The asterisk indicates the lens.

embryonic eye (Figure 2.11). Remnants of this vessel may be present in adults. The posterior surface of the vitreal body, located in close proximity to the retina, does not have a true membrane but is referred to as the posterior hyaloid membrane.

The posterior wall of the globe is formed by a thin, hyperechoic, smooth layer that represents the combined layers (from outer to inner) of the sclera, choroid, and retina. There is no clear demarcation between the three layers in the normal globe. The retina extends from the optic nerve to the ora ciliaris retinae located just posteriorly to the ciliary body. Located slightly ventrally and medially in the posterior wall of the globe in dogs and cats is the optic disc. The optic nerve courses in a straight or undulating course from the posterior surface of the globe at the optic disc into the periorbita of the retrobulbar region, to the optic canal in the sphenoid bone (Figure 2.12A).

The retrobulbar space (periorbital cone), which includes the extraocular muscles, optic nerve, arteries and veins, and periorbital fat, can also be sonographically evaluated (Figure 2.12B). The frontal bone, which forms the medial wall of the orbit, appears as a hyperechoic interface associated with shadowing. The extraocular muscles are hypoechoic linear structures that attach to the equatorial and postequatorial zones of the globe. The optic nerve is a thin, linear, hypoechoic structure outlined by adjacent hyperechoic fat. The lobular lacrimal gland, which is on the lateral (temporal) side of the orbit, and the zygomatic salivary gland, which is ventral and caudal to the globe and ventral to the orbital cone, can also be imaged (Figure 2.4).

Sonography of Ocular and Orbital Abnormalities

Cornea and Anterior Segment

The anterior segment of the eye is best evaluated using a high-resolution transducer (20MHz) or UBM, using up to 60 MHz frequency probes. The size, echogenicity, and appearance of the layers of the cornea may be disrupted with inflammation, degeneration, neoplasia, trauma, or specific corneal disorders, such as bullous keratopathy and corneal sequestra (Figure 2.13). Limbal infiltration caused by neoplasia or granulation tissue may be identified as focal thickening of the cornea and/or sclera. Determining the depth and involvement of the lesion is helpful because the prognosis is more guarded if a limbal lesion extends beyond the sclera to the ciliary body (Figure 2.14). Scleral thickening may also support scleritis or episcleritis (Figure 2.15).

The cornea and the sclera merge at the limbus or corneoscleral junction and internally form the iridocorneal

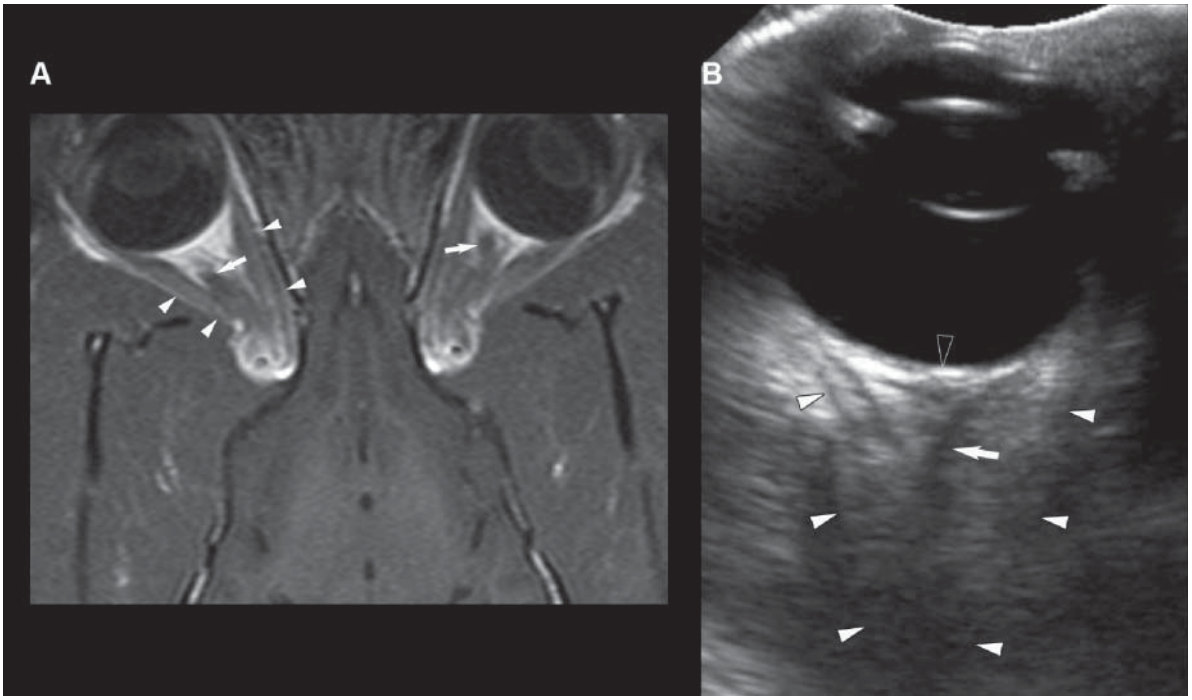


Figure 2.12. **Normal optic nerve and retrobulbar space.** (for full caption, see facing page)

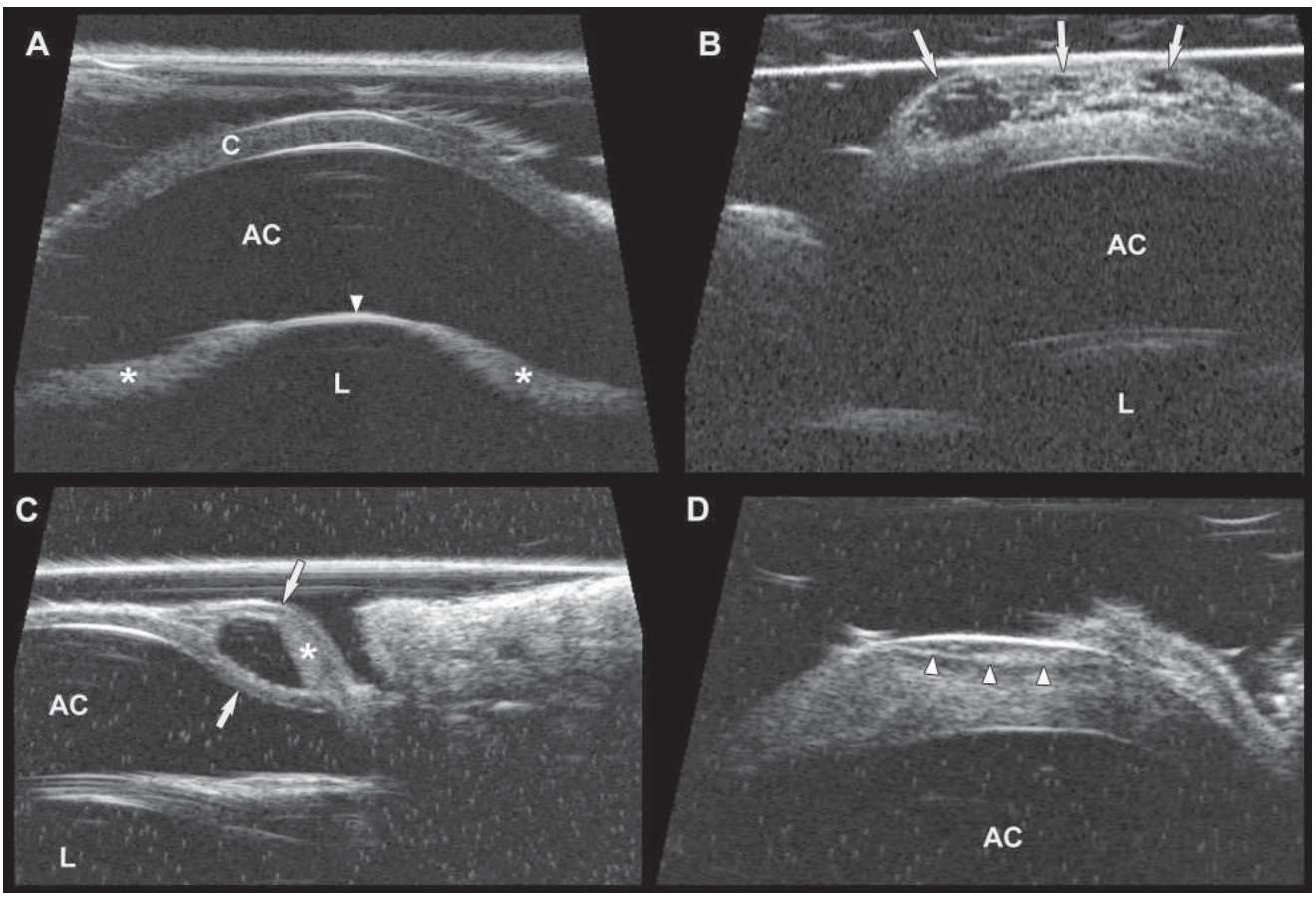


Figure 2.13. **Corneal changes in dogs and cats.** (for full caption, see facing page)

Figure 2.12. **Normal optic nerve and retrobulbar space.** The optic disc and nerve in dogs and cats are located slightly ventrally and medially on the posterior wall of the globe. **A:** This dorsal magnetic resonance (MR) image displays the extraocular muscles (arrowheads), and the optic nerve (arrows) is difficult to identify because of its wavy course. **B:** Sonogram of the retrobulbar space. The optic disc is a short discrete hyperechoic interface (black arrowhead). Posterior to it, the hypoechoic optic nerve (arrow) is partially visualized, encircled by extraocular muscles and fat present in this conical retrobulbar space (arrows).

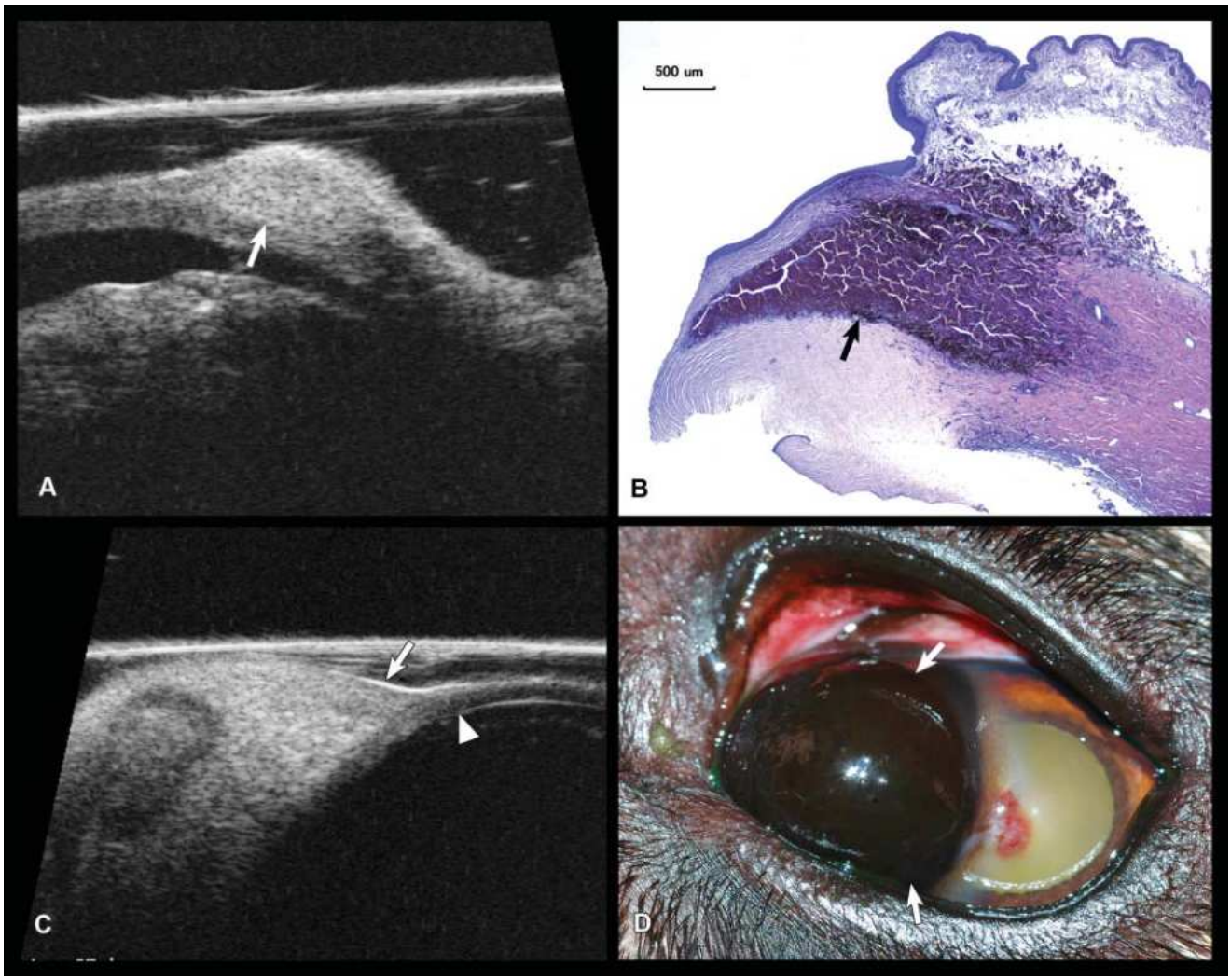


Figure 2.14. **Limbal neoplasia in two dogs.** The images illustrate two limbal melanocytomas with different levels of extension. **A:** Limbal radial section with a 35-MHz probe. The hyperechoic mass is extending to a partial depth into the corneal and scleral tissues. The arrows indicate the inner mass margin at ultrasonography **(A)** and in the corresponding histologic section **(B)**. **C:** Invasive, full-thickness limbal melanocytoma. Radial section in perilimbal/corneal position using a 35-MHz probe. The mass is extending to invade the inner portion of the cornea. The hyperechoic corneal epithelium is lifted (arrow) to follow the outer contour of the mass while the inner corneal hyperechoic Descemet membrane and endothelium disappear inner to the mass (arrowhead). **D:** Clinical photograph of the melanocytoma (arrows) illustrated in C.

Figure 2.13. **Corneal changes in dogs and cats. A:** Normal cornea. The axial transpupillary section also shows the ultrasonograhic anatomy of the anterior chamber (AC). The iris leaflets (asterisks) and the anterior lens capsule (arrowhead) are in mutual contact and the anterior bowing of the iris reflects the anterior lens curvature **B:** Feline bullous keratopathy. The anterior stroma shows multiple fluid-filled areas (arrows). The entire cornea thickness is severely increased. **C:** Vertical section of a corneal inclusion cyst in a dog. The anechoic cavity involves the midstroma. The echoic cellular component of the fluid (asterisk) is deposited at the bottom of the cavity (the left side is dorsal). **D:** Intrastromal corneal sequestrum in a cat. The cornea is thickened and the hyperechoic linear interface indicated by the arrowheads represents the sequestrum.

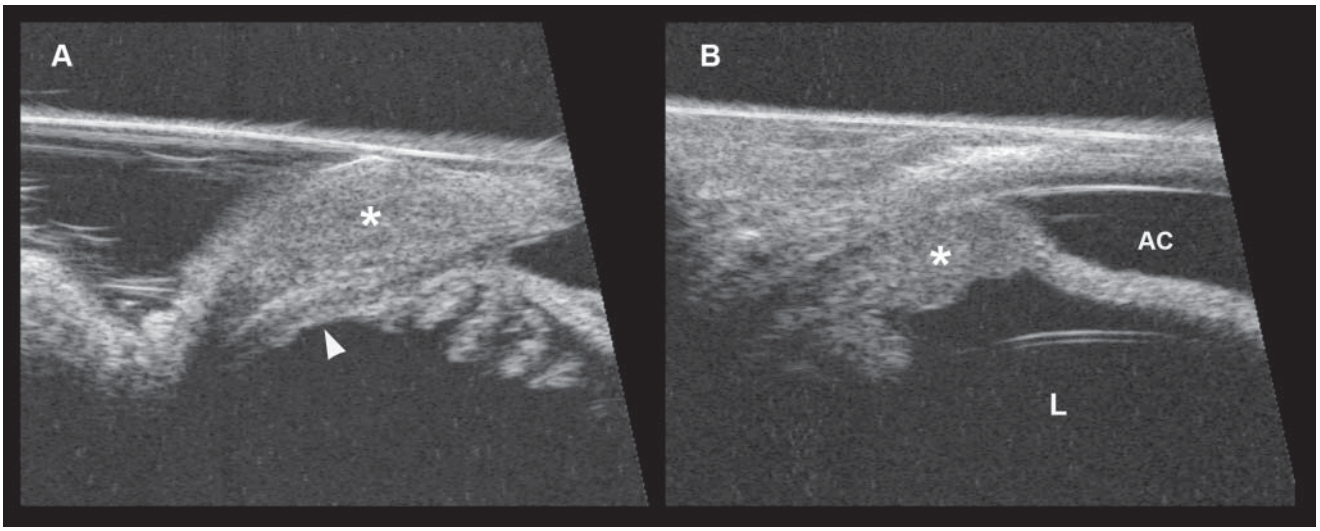


Figure 2.15. **Evaluation of lesion extension. A:** Granulomatous scleritis in a dog. The sclera appears thickened and uniformly echoic (asterisk). The ciliary cleft is respected (arrowhead) and ciliary processes are not involved. **B:** Melanocytoma of the anterior uvea. The base of the iris and the ciliary body are enlarged and uniformly echoic (asterisk). The ciliary cleft is obstructed/invaded anteriorly. The sclera shows normal consistency and thickness. AC, anterior chamber; L, lens.

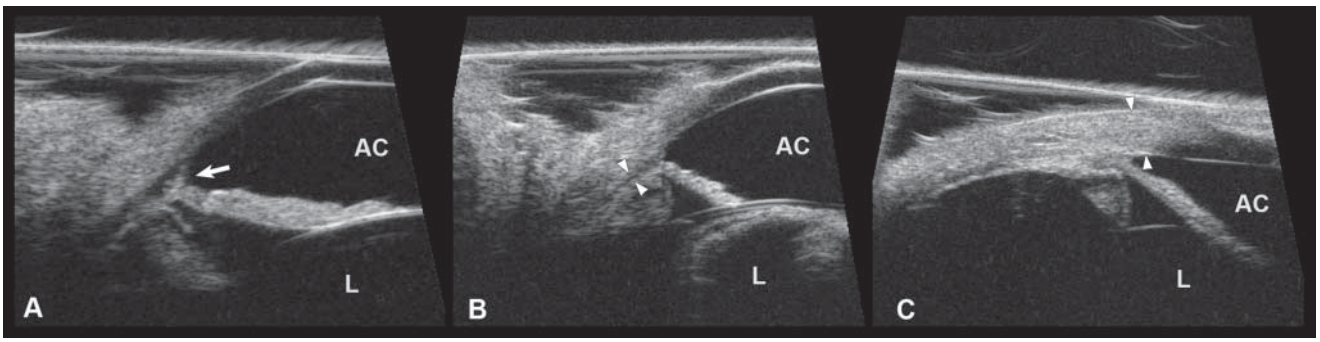


Figure 2.16. **Ultrabiomicroscopy (UBM) evaluation of the iridocorneal angle. A:** Basset Hound, 2-year-old with pectinate ligament dysplasia (arrow) but with open cleft and normal intraocular pressure. **B:** American Cocker Spaniel, 10-year-old with mature cataract and reduced opening of the cleft (arrowheads). The patient developed glaucoma 3 months after cataract surgery. **C:** American Cocker Spaniel, 8-year-old with acute glaucoma. The cleft is closed and the cornea (arrowheads) is mildly edematous.

angle with the iris. In small animals, this angle represents the site for aqueous humor outflow. Any primary or secondary change in the angle may interfere with normal flow of the aqueous humor and cause glaucoma. A perilimbal sagittal section with UBM is useful for investigating the width of the ciliary cleft and estimating the risk of glaucoma (Figure 2.16). An enlarged anterior chamber may be associated with glaucoma, aphakia, or posterior lens dislocation. A shallow anterior chamber may be associated with an intumescent cataract in diabetic patients, an anteriorly subluxated lens, vitreal expansion (brachycephalic dogs and aqueous misdirection), intraocular neoplasia, or excessive compression by the transducer (Figure 2.17).

Cells and fibrin debris within the aqueous humor often present as echogenic foci that are moved along by ocular motion (Figure 2.18). The primary abnormalities associated with the uvea include neoplasia, inflammation, and cysts. Tumors of the iris and ciliary body may present as focal echogenic nodules or as diffuse infiltrative process. Masses are usually attached to the iris, lens, or cornea (Figure 2.19). The most common intraocular tumor in dogs is benign or

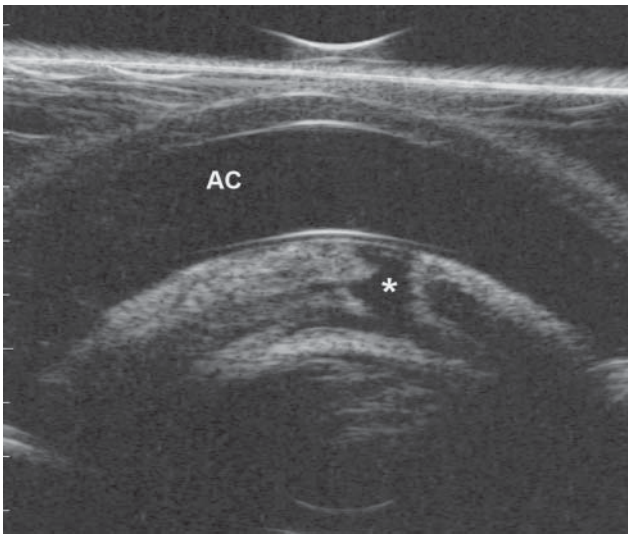


Figure 2.17. Intumescent cataract in a diabetic dog. The anterior chamber (AC) is shallower and an anechoic fracture of the anterior cortex is visible (asterisk). This is a common finding in intumescent cataracts.

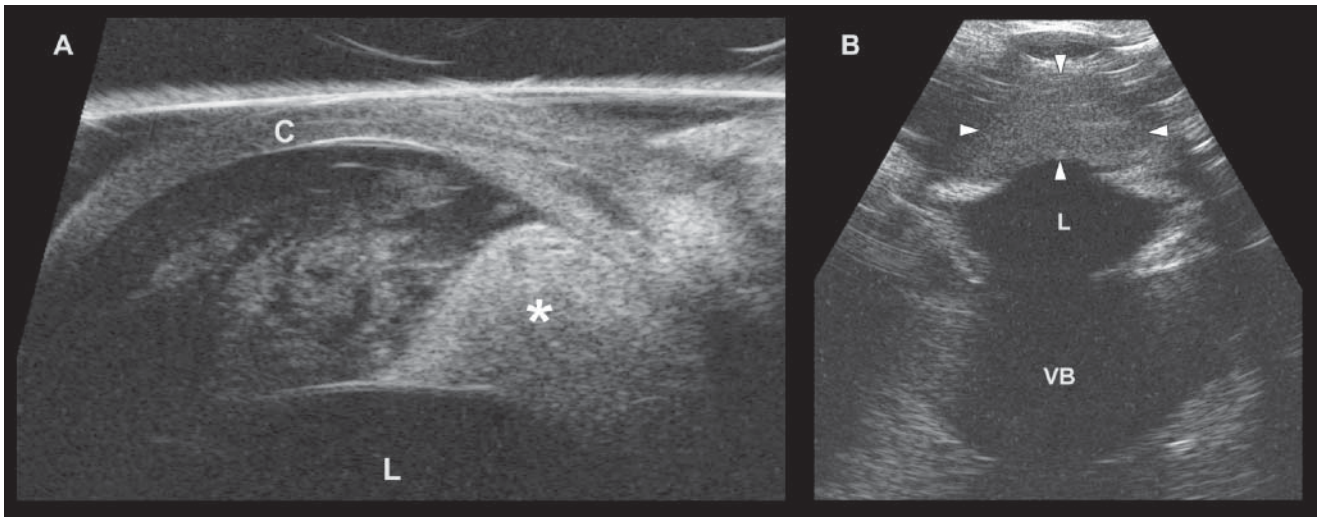


Figure 2.18. Anterior chamber abnormalities. A: Cellular debris/fibrin in anterior chamber associated with an iris mass (asterisk). C, cornea; L, lens. **B:** Anterior chamber hyphema. The hypoechoic homogeneous collection of frank blood is outlined by arrow heads. L, lens; VB, vitreal body.

malignant melanoma and is most often associated with the anterior uvea. Ciliary bodies can also be affected by other tumors, such as lymphoma, adenoma, adenocarcinoma, and medulloepithelioma or metastatic disease (Dubielzig et al. 1989; Dubielzig 2002; see Figure 2.20).

Tumors may be difficult to distinguish from blood clots or granuloma (Gallhoefer et al. 2013). The presence of vascular flow within a mass is often helpful in determining whether the mass is a blood clot or a tumor and may assist in determining the tissue of origin. Lymphoma may have very echogenic thickening of the iris and ciliary body, echoes in the anterior and posterior chambers, and thickening of the choroid, with possible retinal detachment.

Uveitis is the inflammation of the uvea – ultrasonography is not used for its diagnosis. It can be used to assess some of the complications that are associated with the condition (retinal detachment, presence of synechiae and iris bombe versus neoplasia, vitreal degeneration) (Figure 2.21). Iridociliary cysts present as singular or multiple thin-walled anechoic structures. Cysts usually form from uveal neuroepithelium in the posterior chamber and, if detached, may float into either the anterior chamber or, rarely, the vitreous body. They may occur in any breed, but Golden Retrievers, Labrador Retrievers, Great Danes, Boston Terriers and American Bulldogs are predisposed (Corcoran et al. 1993; Deehr et al. 1998; Spiess et al. 1998; Sapienza et al. 2000; Pumphrey et al. 2013). Cysts may be incidental

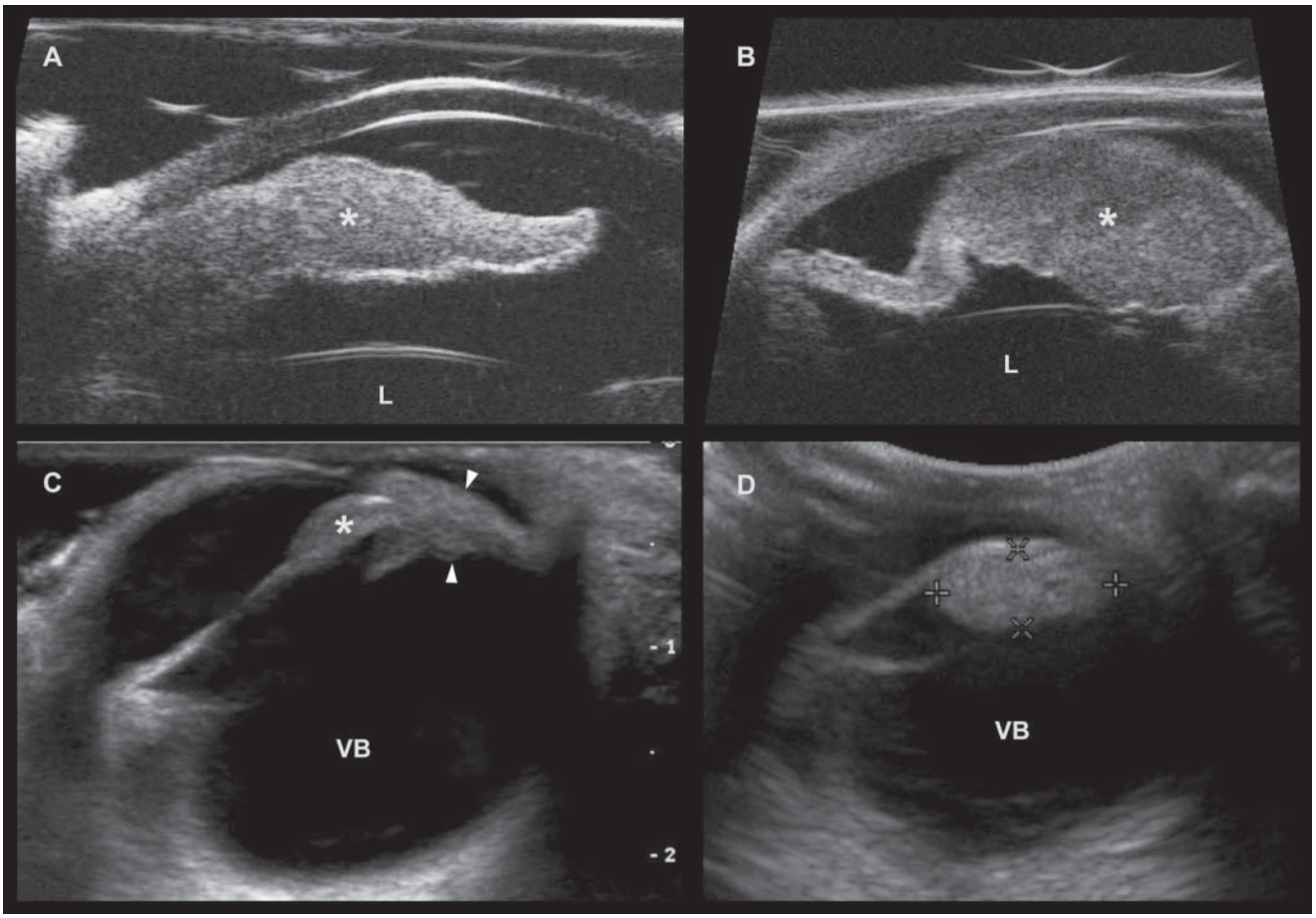


Figure 2.19. **Anterior uveal masses.** (for full caption, see facing page)

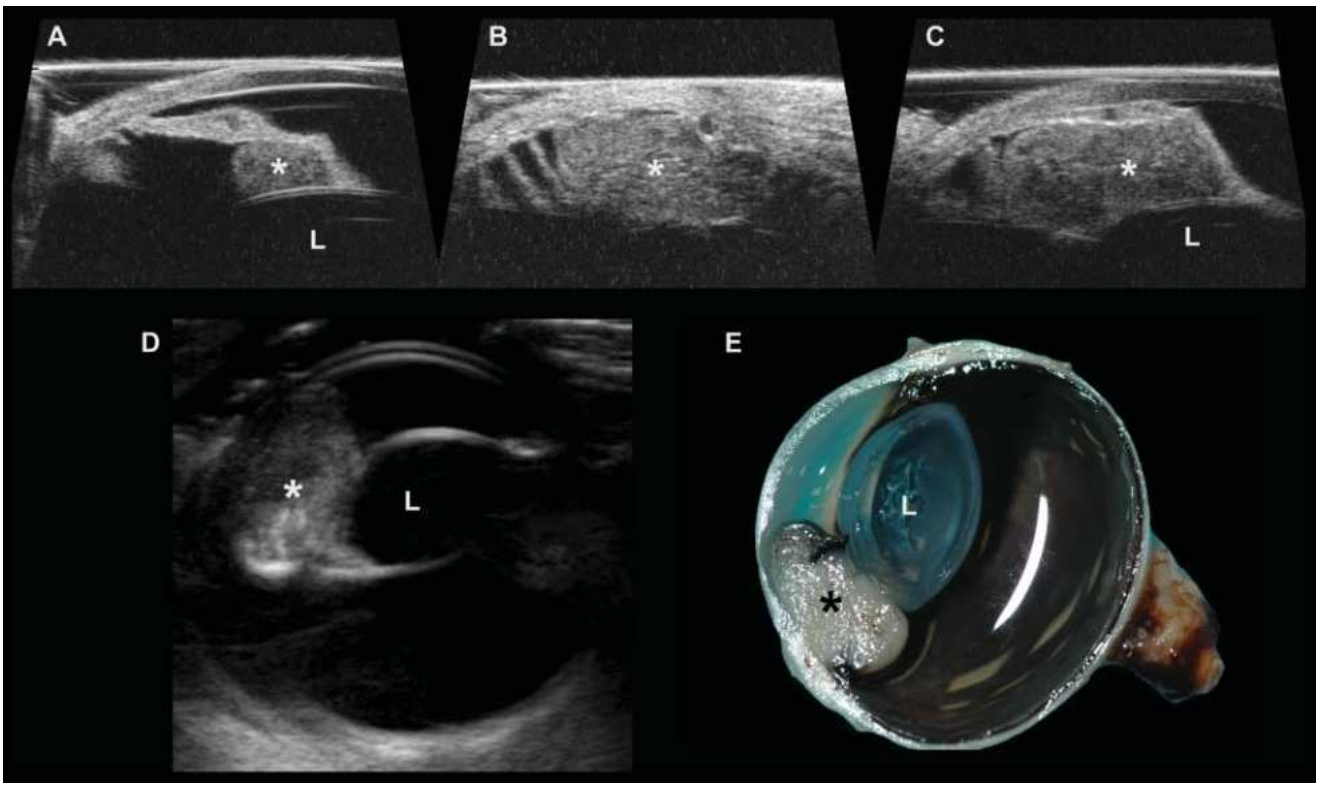


Figure 2.20. **Ciliary body adenoma in two dogs.** (for full caption, see facing page)

Figure 2.19. Anterior uveal masses. A: Iridal lymphoma in a cat. The iris is diffusely thickened by neoplastic infiltrate (*). **B:** Melanocytic neoplasia of part of the iris in a dog (*). **C:** Melanocytic neoplasia of the anterior uvea in a dog. Parasagittal section of the globe showing peripheral iris thickening (*) and extension of the neoplastic process to the ciliary body (arrowheads). VB, vitreous body. **D:** Another dog with same tumor shows posterior iridal invasion (between cursors).

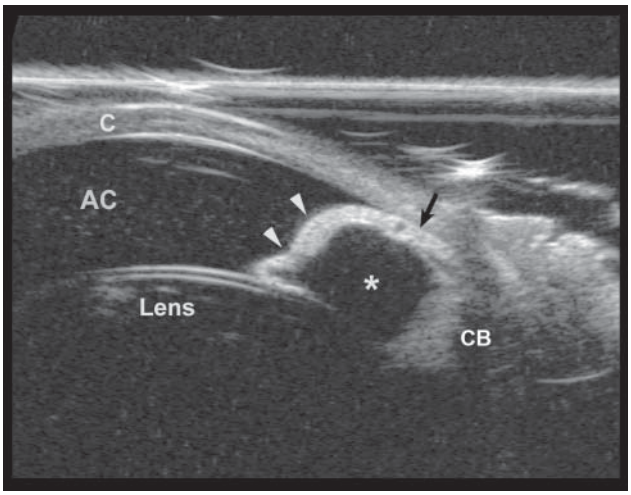


Figure 2.21. Posterior synechia and iris bombe in a dog with chronic uveitis and secondary glaucoma. Axial section with a 35-MHz ultrabiomicroscopy (UBM) probe. The iris edge is attached to the anterior lens capsule because of chronic uveitis and posterior synechia formation. The posterior chamber (asterisk) is distended and the iris is pushed forwards (arrowheads). The iridocorneal angle is obstructed by apposition of the peripheral iris and cornea (arrow) and no ciliary cleft is visible. AC, anterior chamber; C, cornea; CB, ciliary body.

findings; however, iridociliary cysts can also cause pigmentary uveitis or glaucoma (Figure 2.22).

Lens

Abnormalities of the lens include congenital anomalies (persistent pupillary membranes, remnants of the tunica vasculosa lentis or persistent hypertrophic primary vitreous [PHPV]), cataracts (cortical or nuclear), liquefaction of the cortex, intumescence (swelling) of the lens, rupture of the anterior or posterior capsule, posterior ectasia or lenticonus, retrolenticular membrane, subluxation, or dislocation.

Cataracts are degenerative changes in the solubility of lens proteins (Gelatt and MacKay 2005). A cataract produces increased echoes in various locations within a normally anechoic lens. The echogenicity, shape, and size of the lens may change with the type and stage of cataract and its duration.

The most commonly used classifications for cataracts are based on topography and stage of maturation. According to their location within the lens, cataracts will be addressed as capsular, cortical (anterior, posterior, or equatorial), perinuclear or nuclear (the core of the lens) (Figure 2.23). The classification based on the stage of progression of the cataract is clinically more useful and includes incipient, immature and mature cataract with < 10% of the volume, 10–100% of the volume with partial opacity, and 100% complete opacity, respectively. These stages usually maintain the lens volume which instead may be increased in diabetic mature hyperosmotic cataracts (intumescent). The latter may consistently reduce the depth of the anterior chamber (Figure 2.17) and increase the risk for capsular stretching and rupture. In one clinical study comparing lens morphometry in normal and cataractous lenses, diabetic cataracts had an increased axial thickness (Beam et al. 1999). Mature cataracts had a trend toward increased axial thickness, whereas immature cataracts demonstrated a trend toward reduced thickness (Williams 2004).When capsular tears occur, they usually involve the equator, which makes them more difficult to be seen at ocular examination (Figure 2.24). When moderate to severe uveitis is present or the anterior lens curvature and thickness are inhomogeneous, an equatorial tear needs to be ruled out with ultrasonography. Hypermature and Morgagnian cataracts are later stages with cortical reabsorption (Figure 2.23E). In these stages, the lens thickness is reduced and the capsules appear wrinkled;

Figure 2.20. Ciliary body adenoma in two dogs. A-C: Ciliary body tumor (*) displacing the iris leaflet forwards and involving the ciliary processes. The different sections characterize the echogenicity, shape and extension of the mass. **D, E:** Sonogram and gross section of a ciliary body adenoma (*) invading the anterior chamber in another dog.

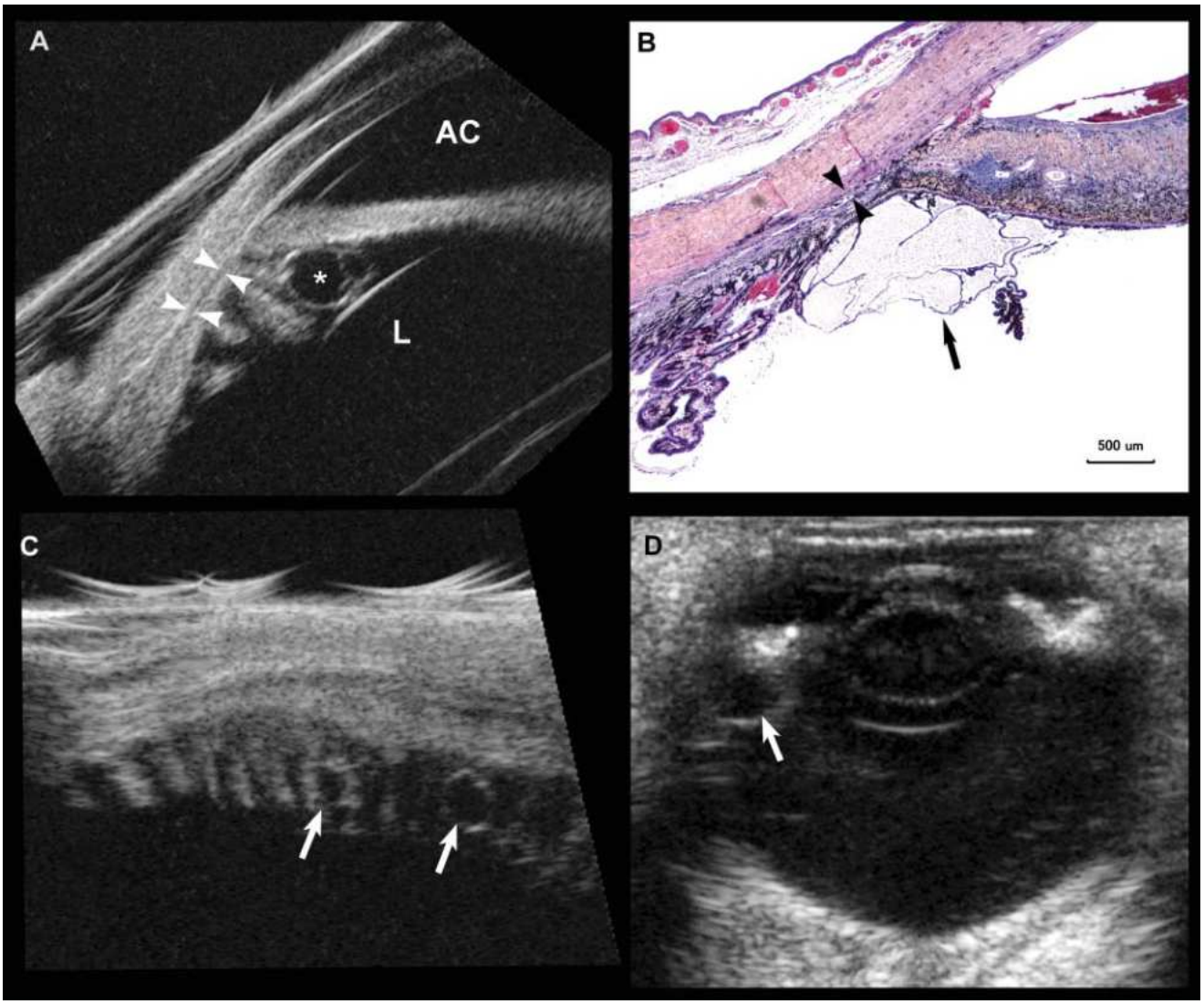


Figure 2.22. **Iridociliary cysts.** These are characterized by a round structure that has a hyperechoic membrane and an anechoic center (asterisk). **A:** Radial limbal section with a 35-MHz ultrabiomicroscopy (UBM) probe showing multiple iridociliary cysts and a collapsed cleft (arrowheads) in an American Bulldog with glaucoma. **B:** Histologic section of the ultrasonographic image shown in **A**. **C:** Transverse perilimbal section with a 35-MHz UBM probe that shows the presence of two hypoechoic ciliary cysts between ciliary processes (arrows). **D:** Axial section of a canine globe showing a large iridociliary cyst (arrow).

these changes can be assessed ultrasonographically. Resorption can be detected as a decrease in the antero-posterior width of the lens and an increased depth of the anterior chamber. In a cortical cataract, the anterior and/or posterior cortices become echogenic. The cortical sutures may become echogenic and be identified especially from a transverse plane, while they become hypoechoic when compared with the rest of the cortex in intumescent cataracts (Figure 2.17). A nucleus that becomes echogenic can be associated with aging changes (nuclear sclerosis) (Figure 2.23A) or with early-onset/congenital cataracts. Incipient or immature cataracts usually progress to involve the entire lens (Figure 2.23). A Morgagnian cataract is a late-stage disease of the lens in which the cortex becomes completely reabsorbed or liquified. Hypermature cataracts often have a decreased lens volume (Figure 2.23E). Changes in lens stifness, volume or fibrosis may stress the zonules, resulting in partial or complete rupture of the ligaments. Lens subluxation

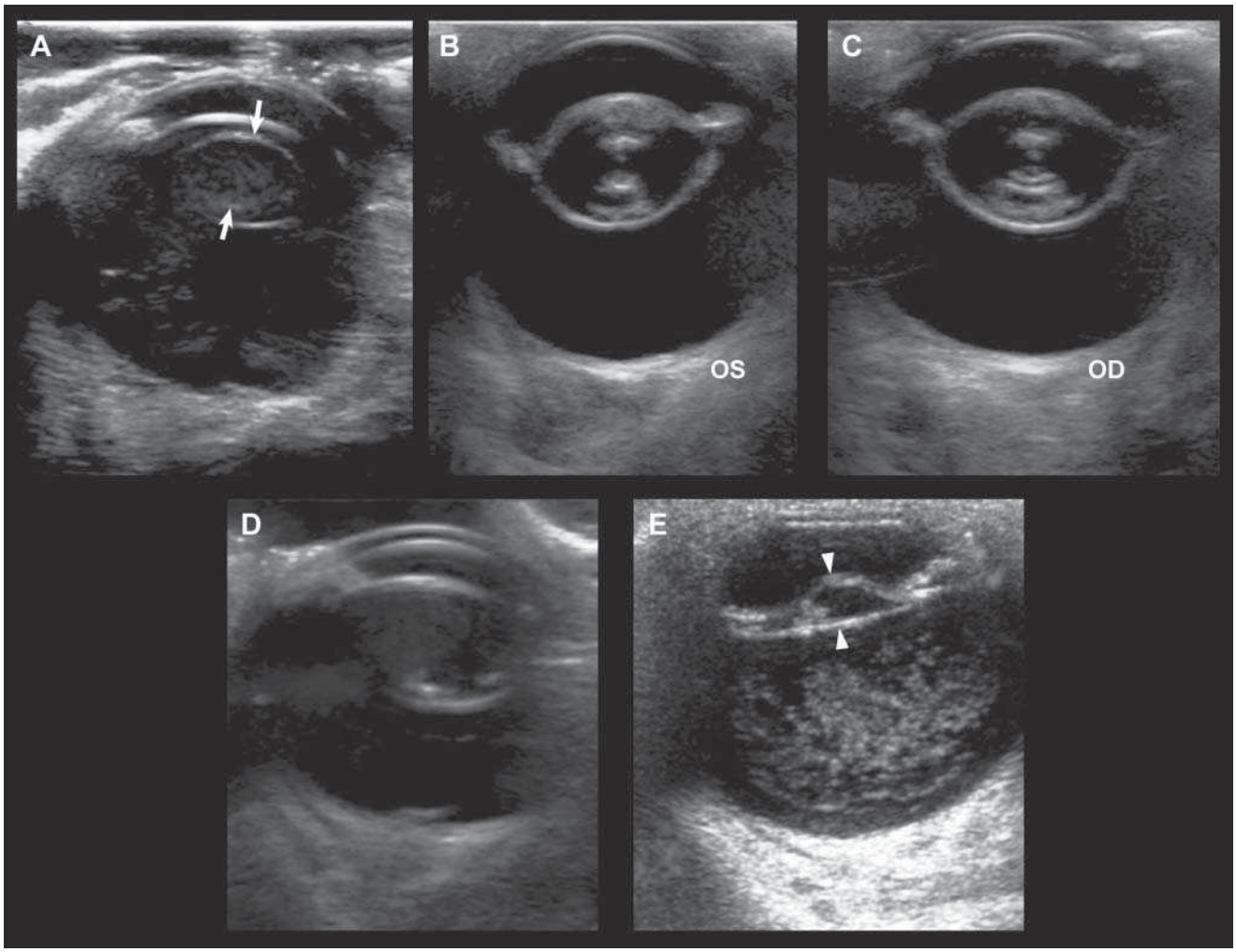


Figure 2.23. **Lens changes. A:** Dense nuclear sclerosis is noted in the eye of this 11-year-old Shih Tzu. Notice the faint curvilinear echogenic lines (arrows) bordering the nucleus. This is a common finding in the aging eye. **B, C:** Various degrees of perinuclear and cortical changes are noted in both eyes of this dog. **D:** Posterior axial cortical cataract in a 1-year-old miniature Poodle. Irregular echogenic change is noted in the posterior cortical region of the eye. **E:** Hypermature/Morgagnian cataract. Note that the lens (arrowheads) volume is greatly reduced due to lens material resorption and liquefaction. The echoes in the vitreous are consistent with degenerative changes (asteroid hyalosis).

or complete dislocation may then occur. Subluxated lenses, although partially or completely able to move, are still in front of the vitreous body and behind the iris. Flattening or posterior direction of the iris leaflets may be seen, or loss of connection between lens and iris may be visible (Figure 2.25A). Lens luxation may cause the lens to migrate into the anterior chamber or fall within the vitreal space. In anterior luxation, the anterior lens capsule is immediately posterior to the cornea (Figure 2.25B), while in posterior lens luxation, the lens may be visualized near the retina or within the vitreal space (Figure 2.25C). In focal zonular ruptures, vitreal presentation in the anterior chamber may be seen first.

Posterior lenticonus is a developmental anomaly of the lens with localized cone-shaped protrusion of the axial portion of its posterior surface (Figure 2.26). Posterior focal paraxial capsular ectasias may occur and manifest as an isolated protrusion of the posterior thin capsule without cortical herniation (Figure 2.27). The posterior capsule may appear irregular or wrinkled. This may be seen in association with a retrolenticular fibrous or fibrovascular membrane and a persistent hyperplastic primary vitreous (Figure 2.28). Posterior or peripheral capsular irregularities are important to recognize prior to surgery because they can lead to surgical complications when removal of the lens is attempted.

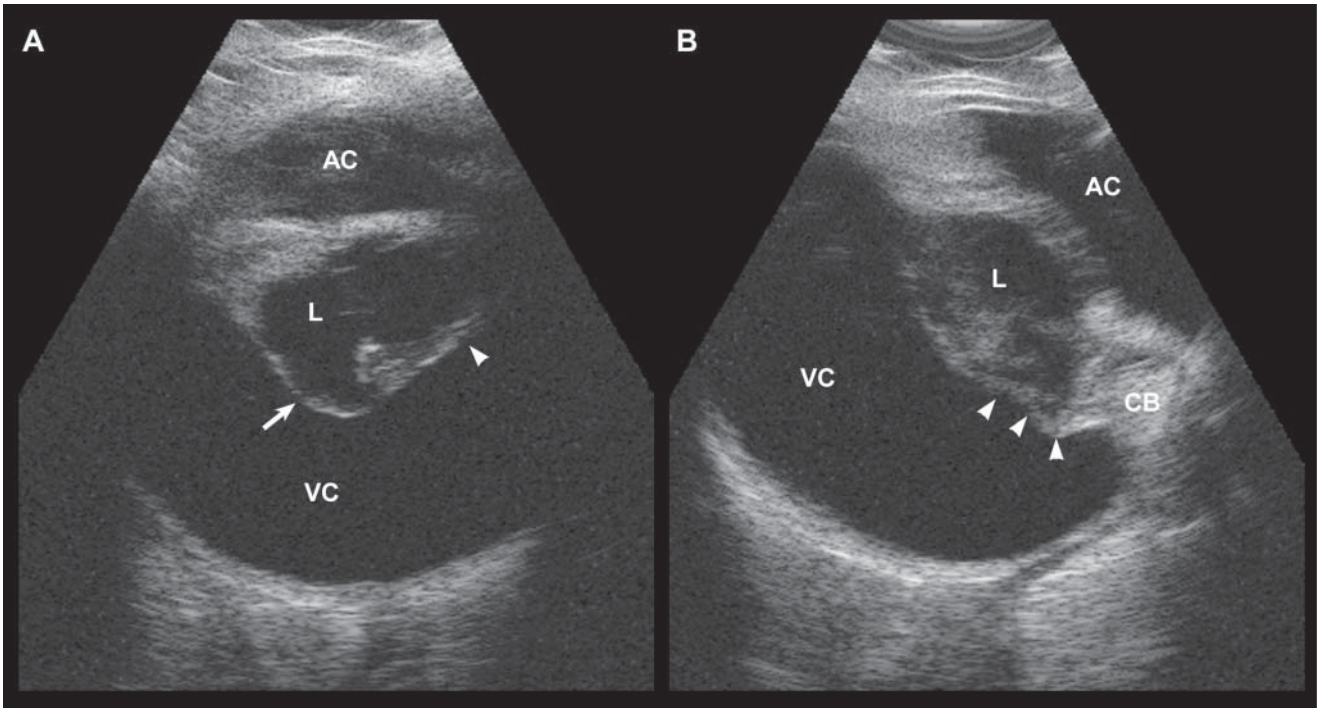


Figure 2.24. **Capsular rupture (and associated phacoclastic uveitis) in a 3-year-old Labrador. A:** Paraxial vertical section showing mild echogenicity of the lens content (L). The lens shape is abnormal, showing volumetric discrepancy between the dorsal (arrow) and ventral (arrowhead) portions. Variation in lens volume and thickness in the same eye, associated with moderate uveitis as in this case, indicate possible peripheral rupture of the capsule. **B:** Oblique paraxial section showing irregular morphology of the posterior lens capsule (arrowheads) and abnormal lens adhesion and increased echogenicity of the ciliary body (CB), supporting the diagnosis of phacoclastic uveitis because of equatorial lens capsule rupture. In this case, clinical examination also revealed a deeper anterior chamber corresponding to flattening of the anterior lens surface. AC, anterior chamber. VC, vitreal cavity.

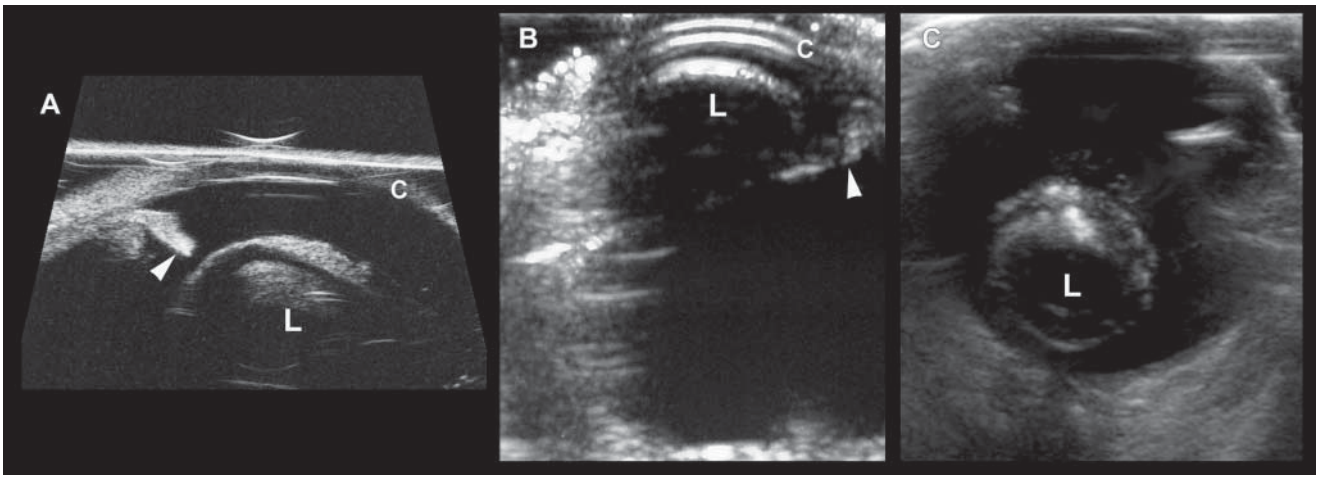


Figure 2.25. **Lens displacement. A:** Lens subluxation in a 13-year-old Lhasa Apso. The lens outer cortex and the nucleus are hyperechoic (cataract) and the lens is displaced ventrally, showing lack of contact with the iris leaflet (arrowhead). **B:** Anterior lens luxation. The hyperechoic anterior lens capsule is just posterior to the cornea, indicating that the lens (L) is clearly displaced within the anterior chamber, anteriorly to the iris and ciliary bodies (arrowhead). The two superficial hyperechoic curved lines represent the cornea (C). **C:** Posterior lens luxation. The echogenic lens (cataract) has completely dislocated into the vitreal cavity, near the optic disc. Irregular curvilinear structures are seen near the posterior lens capsule.

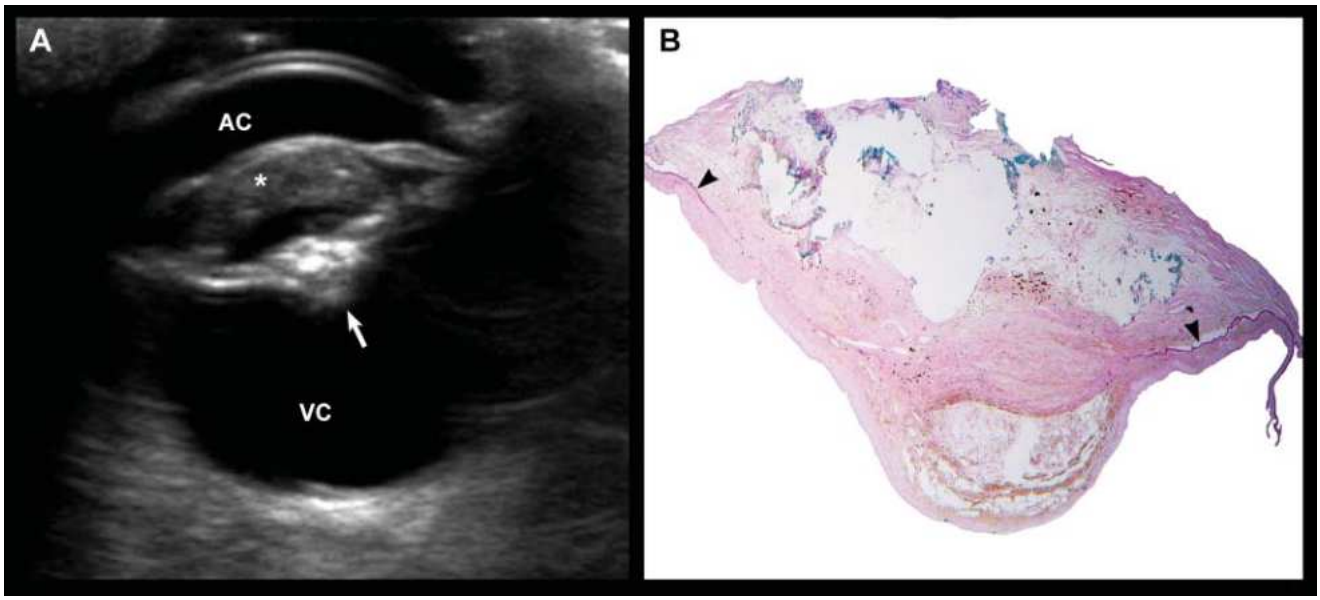


Figure 2.26. **Posterior lenticonus. A:** Axial section of a canine globe with an intralenticular organized hemorrhage and cataract. The lens opacity was preventing the clinical assessment of the posterior segment of the eye. An ultrasound showed an echoic lens (*) with a protruding posterior hyperechoic pole (arrow). AC, Anterior chamber; VC, Vitreal cavity. **B:** Histologic section (periodic acid–Schiff stain) of the posterior lenticular plaque seen at ultrasound after cataract surgery. The specimen shows fibrotic and mineralized tissue representing a congenital malformation (persistent hypertrophic primary vitreous). The posterior capsule is visible as a thin purple line (arrowheads) fading into the center of the plaque.

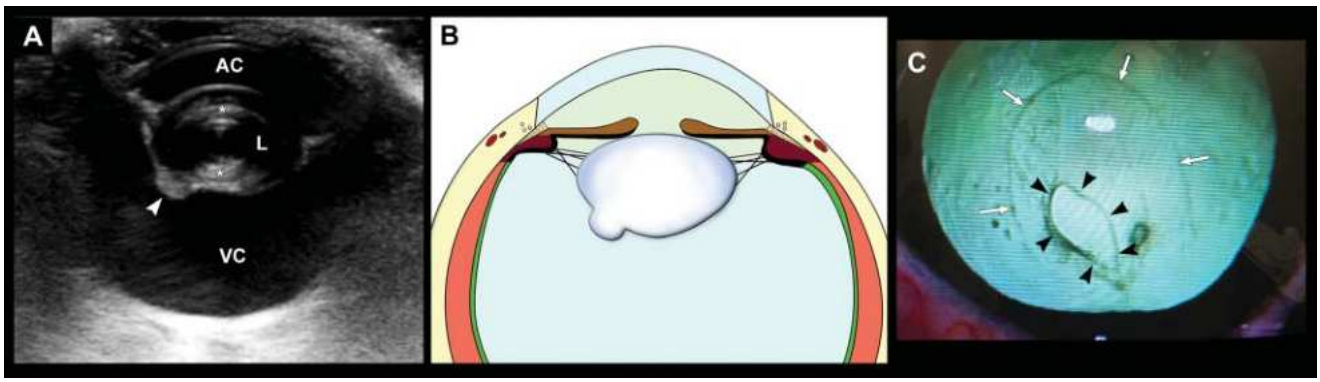


Figure 2.27. **Cataract and capsular ectasia. A:** Vertical axial section of a canine globe presented for cataract evaluation. The lens (L) is normally sized and presents anterior and posterior cortical cataracts (asterisks). In addition, a discrete rounded echoic mass is seen protruding from the posterior capsule dorsally (arrowhead). A hyperechoic line can be seen lining the mass. AC, Anterior chamber; VC, Vitreal cavity. **B:** Schematic illustration of the ultrasonographic findings of posterior capsular ectasia. **C:** Intrasurgical photograph of the case described in A and B. Posterior capsular ectasia was identified at surgery. The anterior capsulorexis is indicated by the arrows, while the arrowheads indicate the dorsal, paraxial area of capsular ectasia after fragmentation and aspiration of the lens material.

Vitreous and Retina

Sonographically visible posterior segment changes include alterations in the shape of the globe, acquired vitreous opacities (such as asteroid hyalosis, synchysis scintillans, vitreous hemorrhage, and uveitis), posterior vitreous detachment, persistence and hyperplasia of the primary vitreous or remnant of the hyaloid artery, retinal detachment, or presence of a foreign body or a mass.

The globe shape may be altered by developmental anomalies, trauma, glaucoma, an internal mass, scleral diseases or by pressure from extraocular diseases (Figures 2.29–2.31). Microphthalmos (reduction in

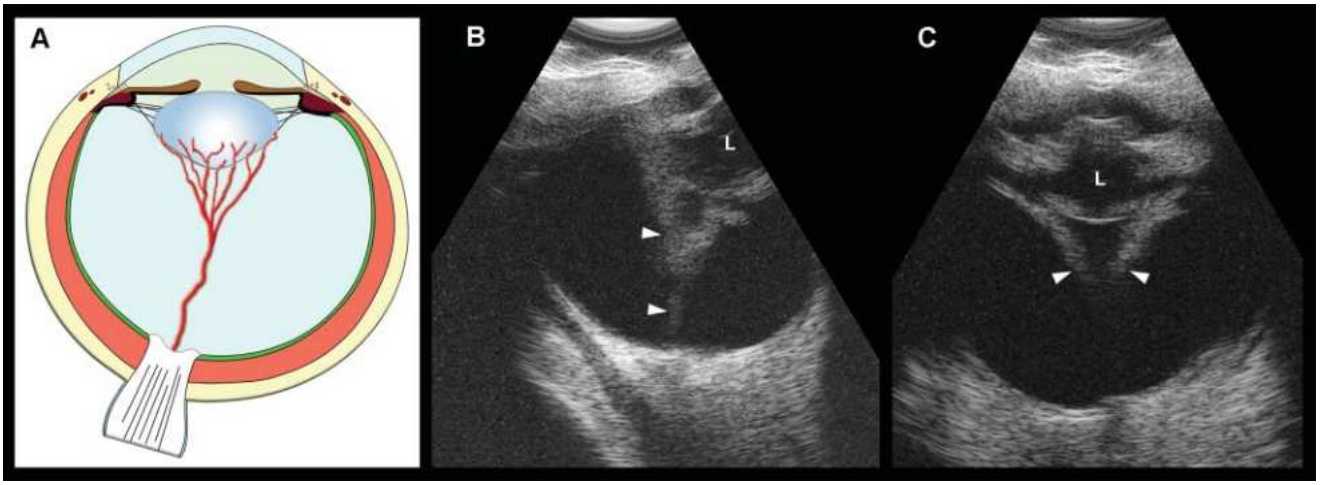


Figure 2.28. **Persistent hypertrophic primary vitreous.** (for full caption, see facing page)

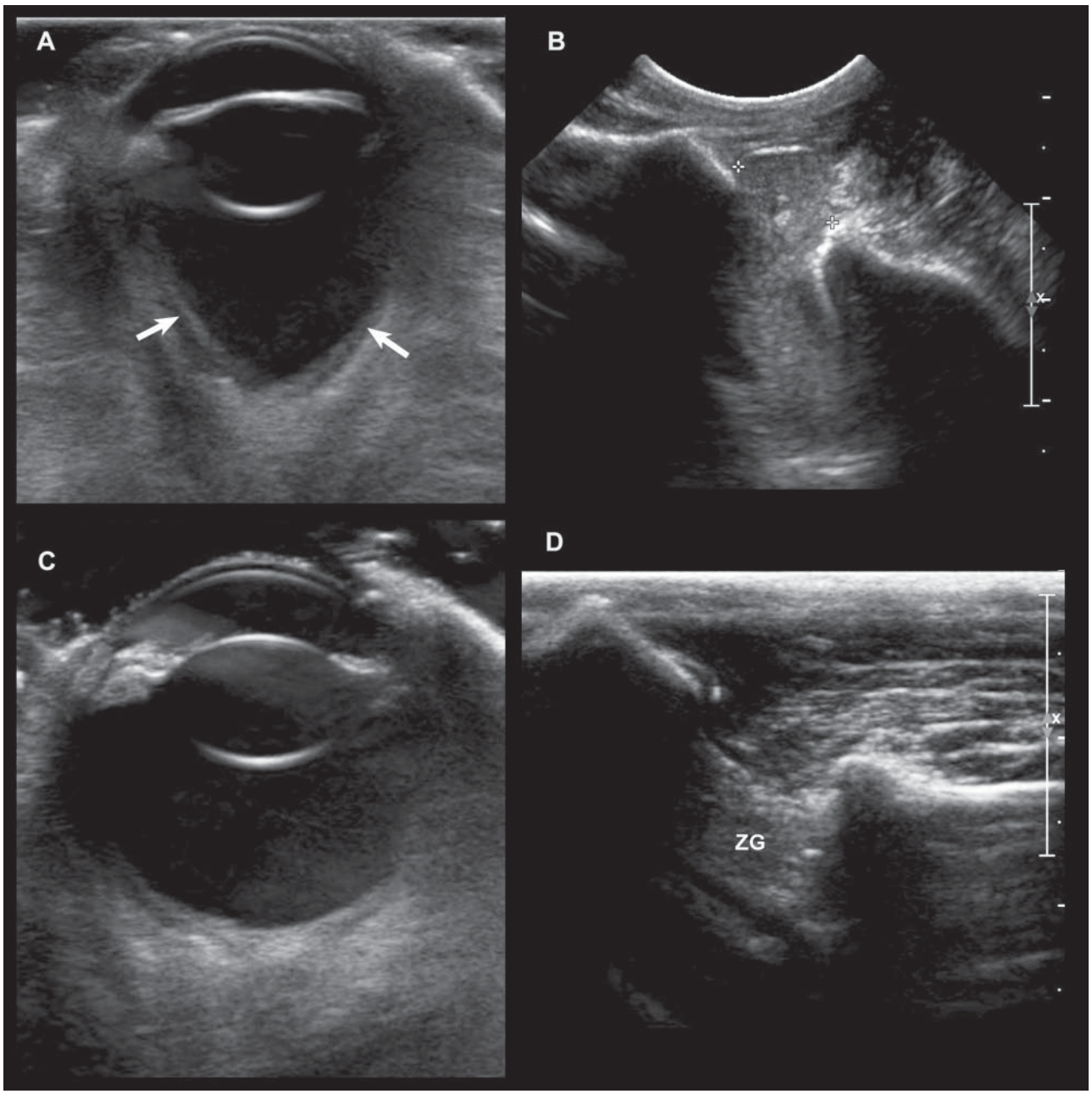


Figure 2.29. **Orbital cellulitis in a Jack Russell Terrier.** (for full caption, see facing page)

Figure 2.28. **Persistent hypertrophic primary vitreous** in a 3-month-old Boxer with bilateral cataract. **A:** Schematic drawing showing the vascular distribution of the primary vitreous in the posterior segment. **B:** Slightly oblique paraxial section showing abnormal echoic tissue (arrowheads) expanding from the posterior lens (L) to the optic nerve area in a triangular shape consistent with persistency of the fetal fibrovascular tissue **C:** Axial section showing echoic structures projecting into the posterior vitreous body posteriorly to the lens.

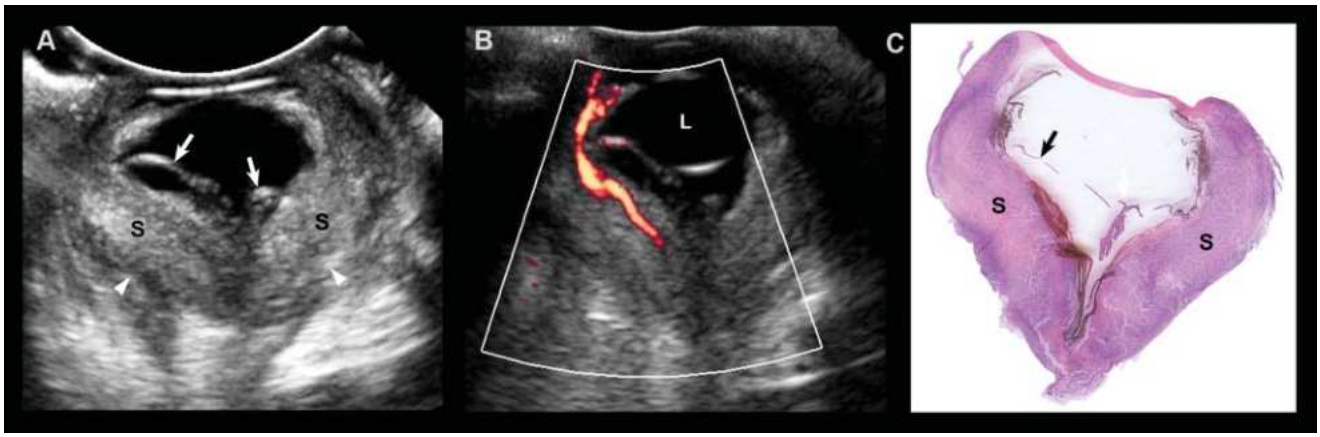


Figure 2.30. **Diffuse scleritis in a dog. A:** Paraxial section showing a severely thickened scleral wall (S). Arrowheads indicate the outer wall of the globe. A retinal detachment is present as hyperechoic linear images in the posterior cavity of the globe (arrows). **B:** Axial section. L, lens. Power angio-Doppler mode showed moderate vascular flow within a severely inflamed scleral tissue and partially in the retina. **C:** Histopathologic section of the same globe after enucleation. The scleral wall (S) is thickened and the posterior vitreal cavity deformed. Retinal detachment is present (arrows).

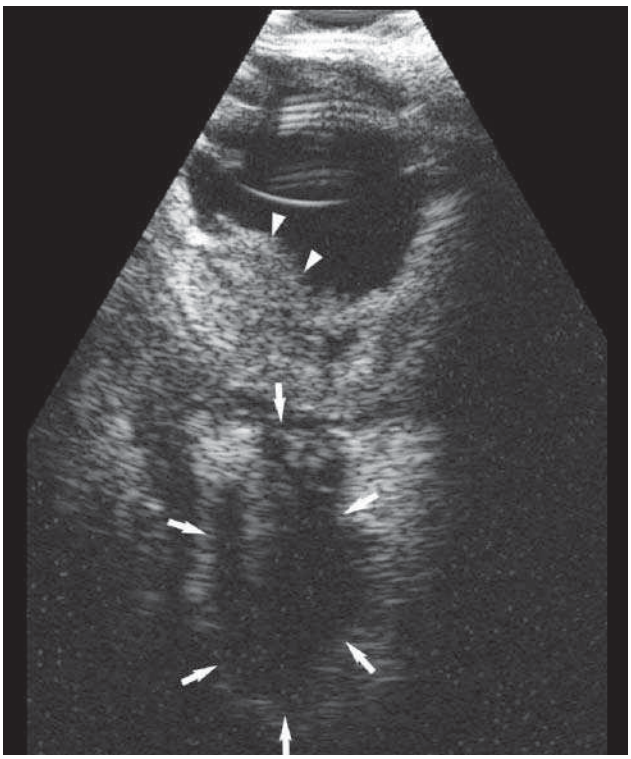


Figure 2.31. **Retrobulbar abscess.** An irregular poorly echogenic cavitary lesion (arrows) is noted in the retrobulbar space. Adjacent to the lesion, the posterior ocular wall is thickened and creates an abnormal bulge (arrowheads) into the posterior vitreous body.

Figure 2.29. **Orbital cellulitis in a Jack Russell Terrier. A**: The globe has a conical shape (arrows) secondary to compression from the inflammation affecting the surrounding orbital tissues. **B:** The zygomatic gland (between cursors) is thickened, possibly as an extension of the inflammation. **C:** A few days after treatment with a combination of oral antibiotics, the globe shape returned to its normal shape. **D:** The zygomatic gland (Z) has a normal size.

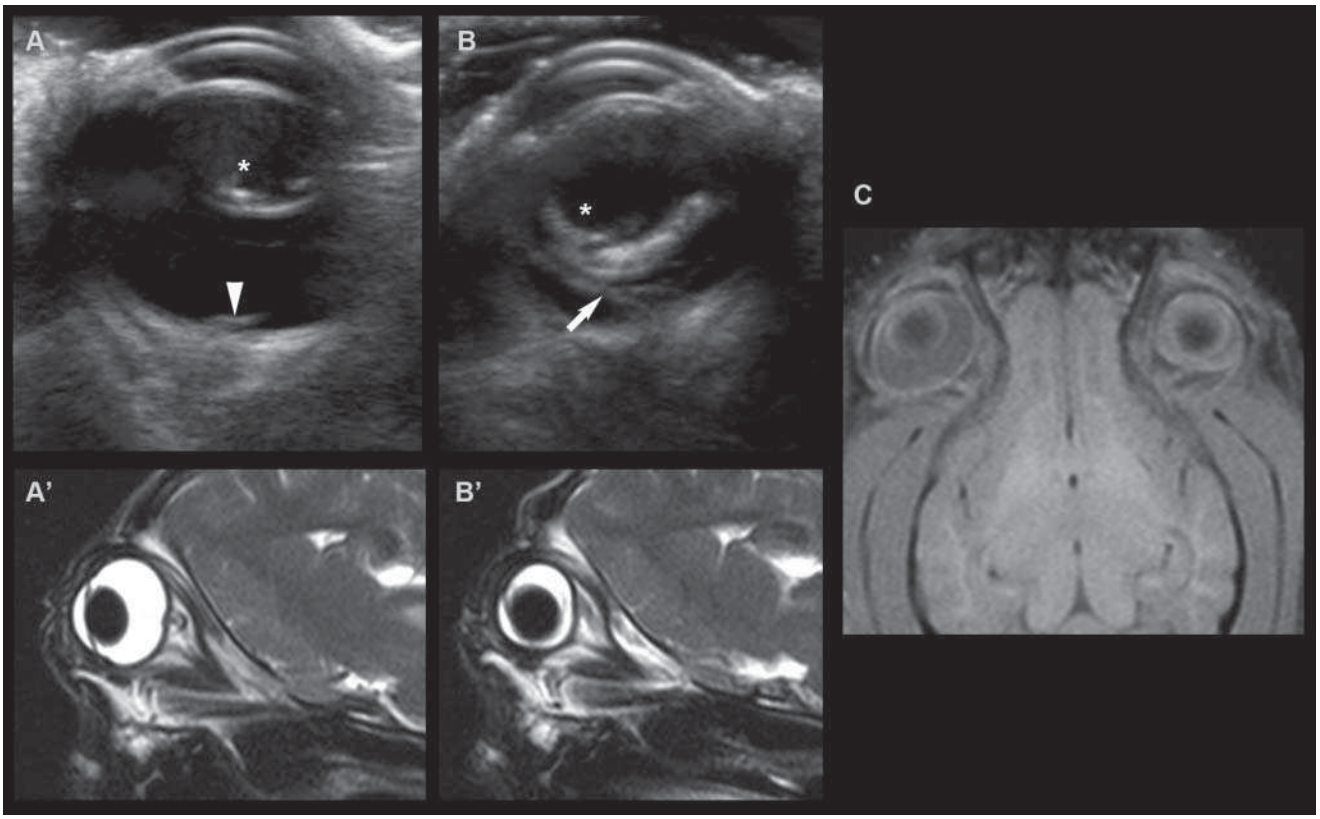


Figure 2.32. Congenital microphtalmia in a 1-year-old miniature Poodle presented for acute blindness. Sonographic **(A)** and sagittal T2 magnetic resonance image (MRI) **(A')** of the right eye. Notice the immature cataract evidenced by echoes within the lens (*). A small bulge is noted at the level of the optic disc (arrowhead), which may represent a swollen optic nerve. Sonographic **(B)** and T2 MRI image **(B')** of the left eye. This eye is smaller than the right. Echoes are also present in the lens (asterisk). In addition, a curvilinear structure (arrow) is seen obliquely crossing the vitreous body, representing the detached retina. **C:** Dorsal T1 post-contrast image of both eyes, illustrating the size asymmetry of the eyes.

eye volume) may be caused by developmental defects (Figure 2.32) or may be acquired (phthisis bulbi) secondary to chronic diseases (uveitis or end-stage glaucoma) or trauma (Figure 2.33). Buphthalmos (an enlarged globe) may instead be associated with large intraocular masses or chronic glaucoma.

Echogenic foci or debris within the vitreous are common findings in older patients and can be associated with several conditions. They appear as dot-like reflectors within the normally anechoic vitreous body. Fibrotic membranes may be imaged and appear as hyperechoic lines within the vitreous. These reflectors are more common in eyes that have sustained trauma or are affected by some chronic diseases.

Asteroid hyalosis is the most common vitreal degeneration in older patients and in specific breeds (brachycephalic and Italian Greyhounds). These small foci of 0.03–0.1 mm calcium–lipid complexes are discrete pinpoint reflectors suspended in the vitreous framework (Figure 2.34). A few may be present or a large number may be dispersed throughout the vitreous. In synchysis scintillans, the cholesterol crystals are not suspended. They sink to the bottom of the liquefied vitreous body. This is often seen in eyes with end-stage disease and vitreal syneresis (liquefaction). Vitreal degeneration is often identified in dogs with cataracts. In one study, vitreal degeneration was seen in 55%, 89%, and 100% of dogs with immature, mature, and hypermature cataracts, respectively (Dietrich et al. 1995).

A detached vitreous may appear as one or several curved lines with varying reflectivity. Anechoic fluid may accumulate between the retracted vitreal body and the retina (Figure 2.35). This may be an incidental finding in older patients. Lines are sometime difficult to differentiate from retinal detachments, although vitreal membranes are usually less echoic that retinal tissue.

Echoes within the vitreous may be caused by inflammation, infection, or hemorrhage. Hemorrhage into the vitreous may produce a multitude of echoes within the anechoic vitreous cavity, varies in appearance, and often depends on the duration, severity, and location

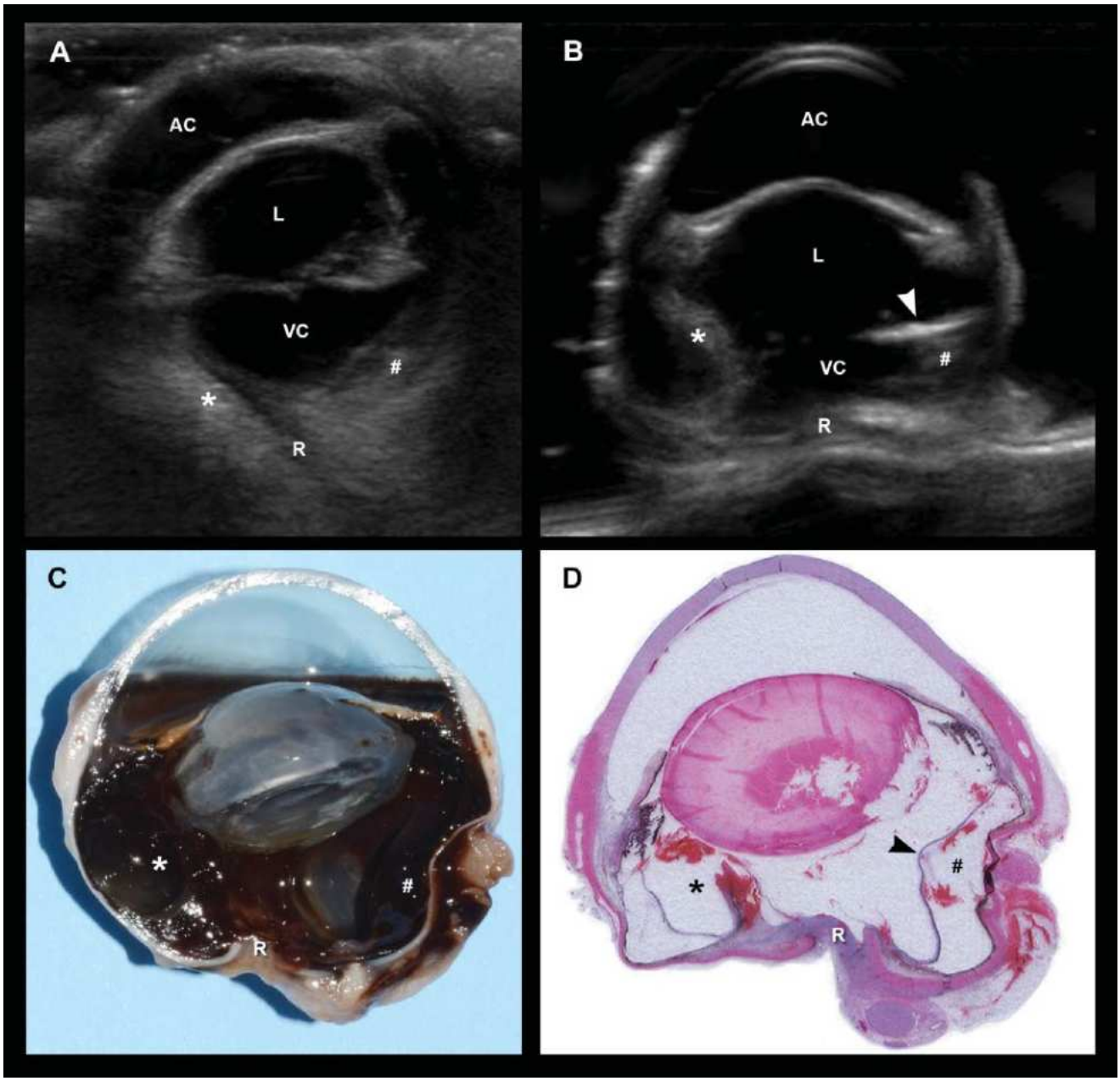


Figure 2.33. **Traumatic globe rupture in a cat. A:** Paraxial meridional sonogram. The vitreal cavity (VC) appears severely decreased when compared with the anterior chamber (AC) and lens (L). Echogenic structures of different intensity are visible in the posterior segment and were interpreted as vitreal (*) and choroidal hemorrhages (#). A lens dense area in the posterior wall was identified and suspected to correspond to a globe rupture (R). **B:** Sonogram performed on the globe after enucleation. A linear hyperechoic interface (arrowhead) confirmed retinal detachment and subretinal hemorrhage (#). Globe rupture along the posterior wall was suspected (R). **C, D:** Gross and histologic sections confirming vitreal hemorrhage (*), retinal separation (arrowhead), subretinal hemorrhage (#) and posterior globe rupture. The scleral rupture had occurred several weeks before admission of the cat and fibrous tissue is bridging the defect.

of the bleed (Figure 2.36). Hemorrhage may be seen as diffuse point-like multiple echoes. Erythrocytes often precipitate onto a pre-existing vitreous strand, acquired membrane, or the posterior hyaloid membrane. Fibrous strands may develop secondary to clot formation. These strands may cause tractional retinal detachment when they contract. Blood within the vitreous framework typically is absorbed more slowly (Zeiss and Dubielzig 2004). Blood clots into the vitreous may mimic a mass (Gallhoefer et al. 2013).

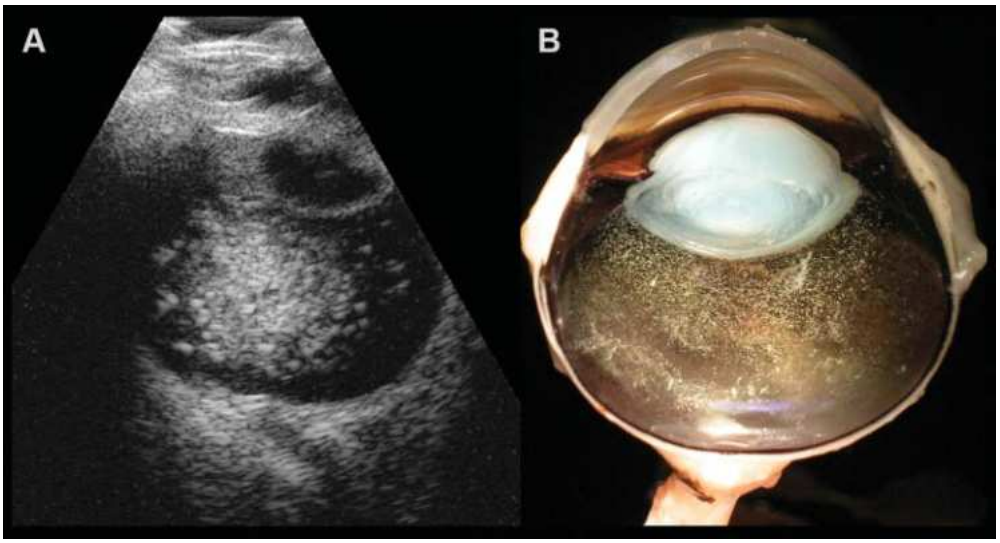


Figure 2.34. **Asteroid hyalosis. A:** The vitreal cavity contains multiple hyperechoic granular structures consistent with accumulation of vitreal degenerative bodies made of calcium and phospholipids (asteroid hyalosis). **B:** Gross section of a globe showing the corresponding disease in another dog. Multiple white bodies are visible posteriorly to the lens. Images courtesy of Dr R. Dubielzig, University of Wisconsin.

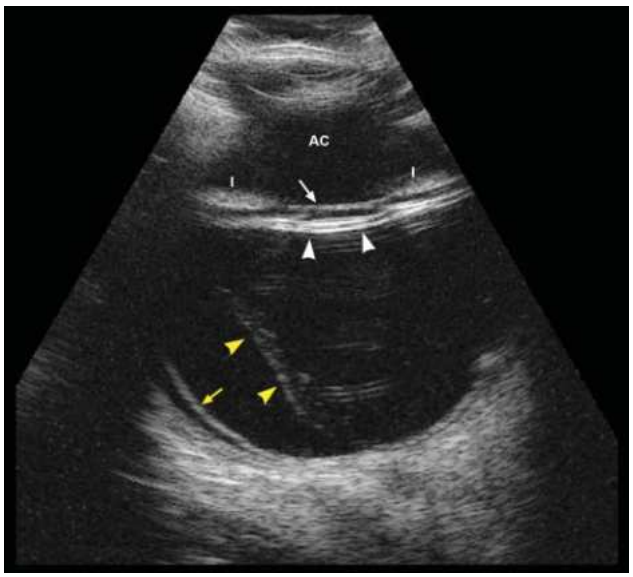


Figure 2.35. **Vitreal and retinal detachment.** Vertical axial sonogram showing vitreal detachment (yellow arrowheads) and corresponding retinal separation (yellow arrow) after cataract surgery. Note the different echogenicity of the two structures, with retinal tissue usually being more echoic than the vitreous cortex. The anterior lens capsule is indicated by the white arrow and the prosthetic intraocular lens by the white arrowheads. Multiple reverberations can be seen as linear echoic parallel lines in the vitreal body. AC, anterior chamber; I, iris.

In these cases, color flow Doppler may be useful in their differentiation.

Persistent and hyperplastic primary vitreous is a congenital condition (Bayon et al. 2001; Gemensky-Metzler and Wilkie 2004; Grahn et al. 2004) in which the primary vitreous (hyaloid artery and posterior tunica vasculosa lentis) incompletely regresses after birth. A classification of different grades has been published (Stades 1980), which includes various combinations of capsular plaques and cataracts, posterior lenticonus and connective-tissue strands (retrolenticular fibrovascular tissue) between the posterior surface of lens and the area of the optic nerve. A funnel-shaped echogenic retrolenticular structure emerging from the lens and coursing to the optic disc may be seen in these cases (Figure 2.28). The strand between the surface of the lens and the area of the optic nerve may contain patent hyaloid vessels. Color Doppler may be helpful in assessing the presence of vascular flow (Boroffka et al. 1998).

Retinal detachment is commonly diagnosed with ultrasound. However, retinal separation/detachment can be missed in 30–40% of the cases confirmed at histopathology (Gallhoefer et al. 2013).

The retina normally adheres firmly to the optic disc posteriorly and to the ora ciliaris anteriorly. In exudative retinal detachment, the retinal layers remain attached at these two points but may be separated from

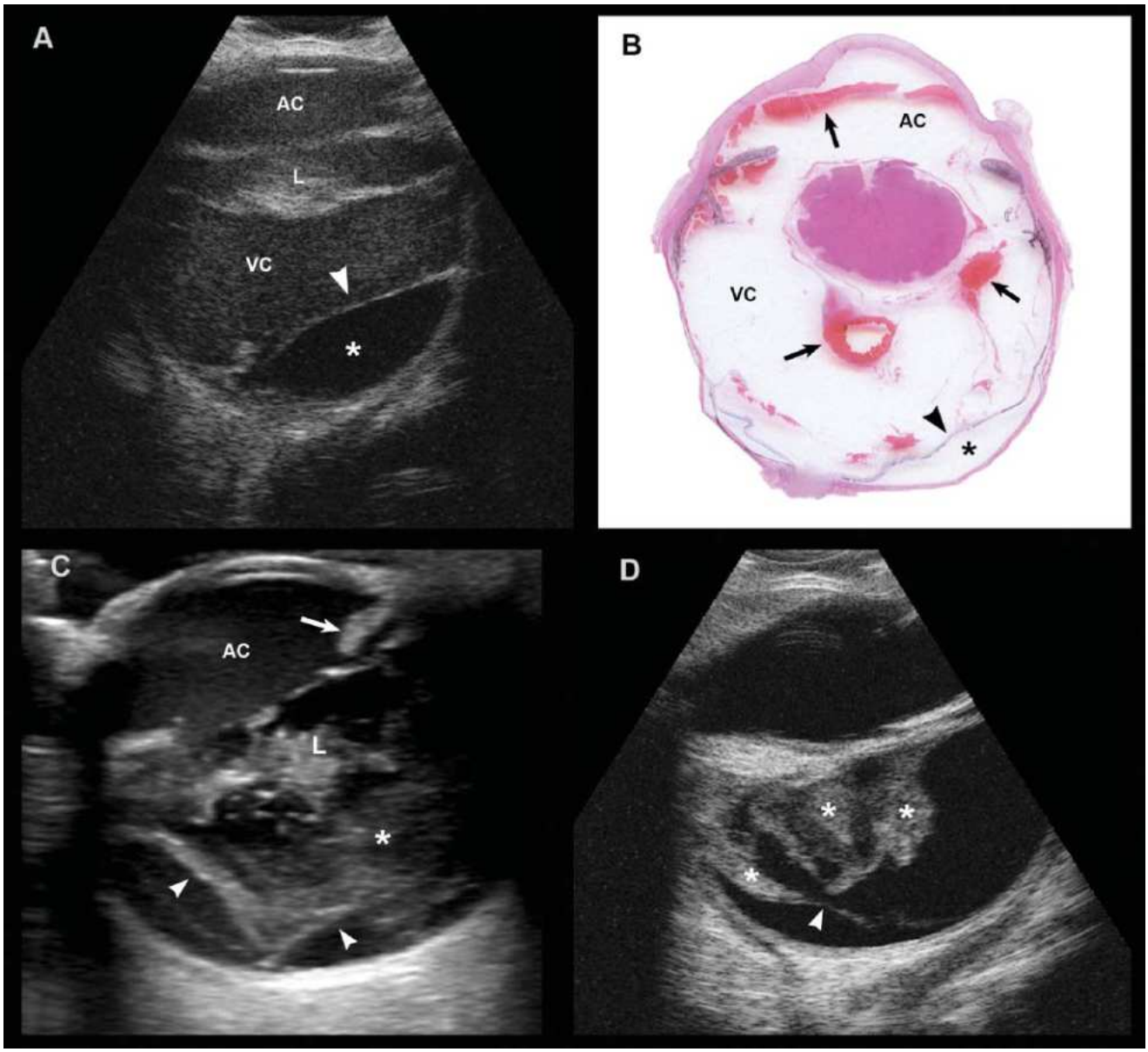


Figure 2.36. **Vitreal hemorrhage. A, B:** Sonogram and histologic section of a canine globe after severe blunt trauma and hyphema. The sonogram in A shows hypoechoic homogenous material filling the anterior chamber (AC) and the vitreal cavity (VC). A retinal separation is present (arrowhead) and the subretinal space is anechoic (*). The histologic section in B confirms the sonographic findings. Most of the fresh blood present in the ocular cavities has been lost during specimen preparation. Remnants of a frank hemorrhage are still visible (arrows). **C:** Severe ocular trauma. The anterior chamber (AC) is filled with hypoechoic material. The iris is directed posteriorly (arrow) and the lens is ruptured. The vitreal cavity contains echoic material consistent with blood (asterisk). The retina is detached (arrowheads). **D:** Organized vitreal hemorrhage in a cat several weeks after lens removal due to lens luxation. The echoic masses indicated by asterisks are fibrin and blood clots. One of them is adhering to the retina and separates it from the choroid (arrowhead).

the adjacent choroid by fluid or exudate. A detached retina commonly appears as a discrete, thin echogenic interface with an underlying anechoic space. The detachment may occur focally or along the entire surface between the optic nerve head and the ora ciliaris retinae. Such a complete retinal detachment appears as a V-shaped structure (Figure 2.37). If a giant tear occurs at the level of the ora ciliaris retinae, the retinal layers fold to the center of the posterior segment or ventrally because of gravity (Figure 2.38). Different mechanisms of retinal detachment include a retinal tear with vitreous material migrating into the subretinal

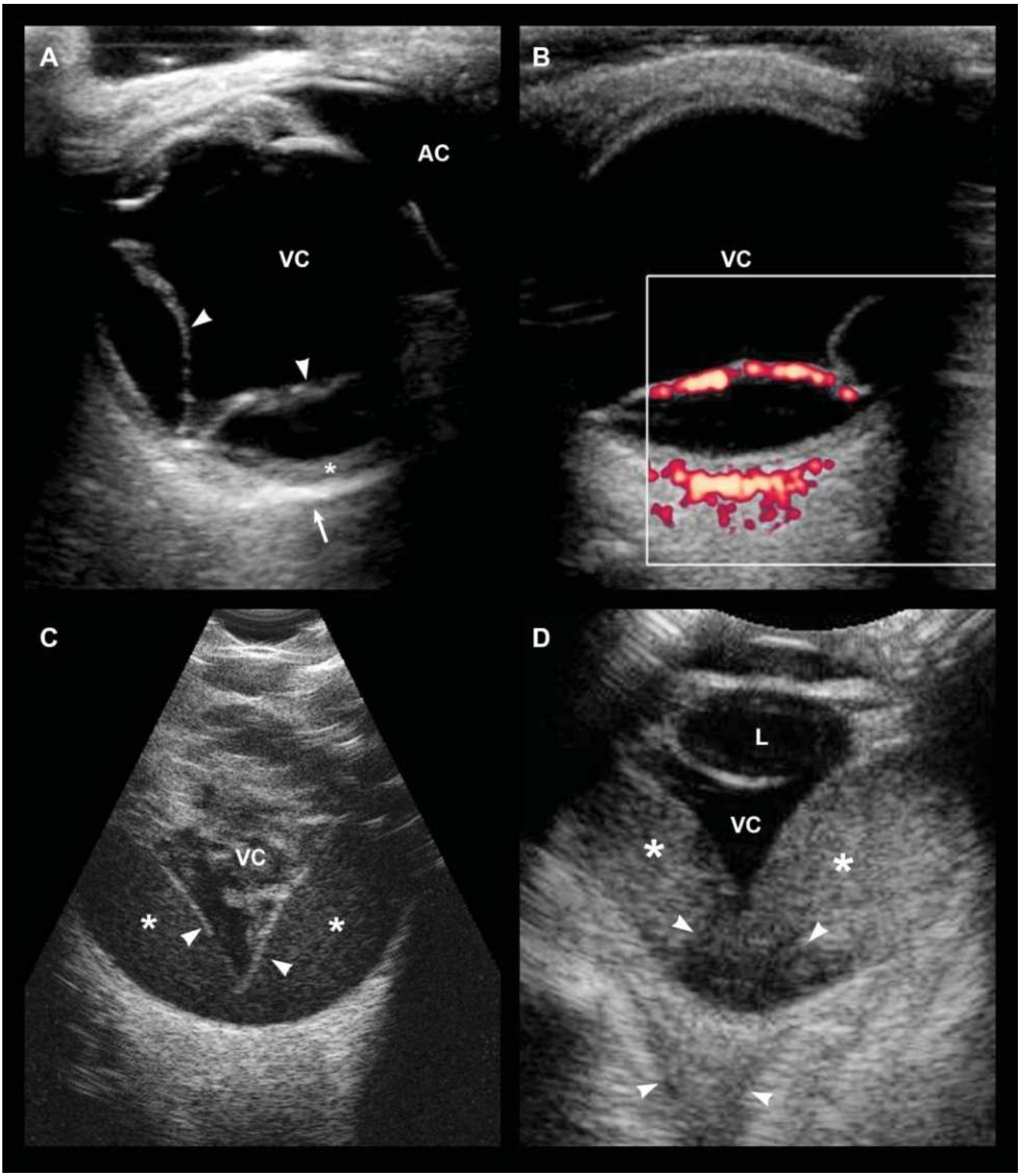


Figure 2.37. Retinal detachment. A: The retina is detached (arrowheads) and the choroid is thickened (*). The scleral wall is indicated by the arrow. AC, Anterior chamber; VC, Vitreal cavity. **B:** Color Doppler used in the same patient shown in A. Intense blood flow is detected in the retina and in the choroid and sclera. **C:** "Seagull wings" sign (arrowheads) in a dog with retinal detachment and subretinal hemorrhage (*). Echoic material consisting in vitreal hemorrhage is also present in the VC. **D:** Axial plane. Exudative retinal detachment in a dog affected with blastomycosis. Note the retina has lost some of its echoic signal due to inflammation. The subretinal space is filled with uniform echoic material (*). The less echoic areas in the posterior portion of the globe and in the retrobulbar space (arrowheads) may represent a swollen optic nerve. L, lens.

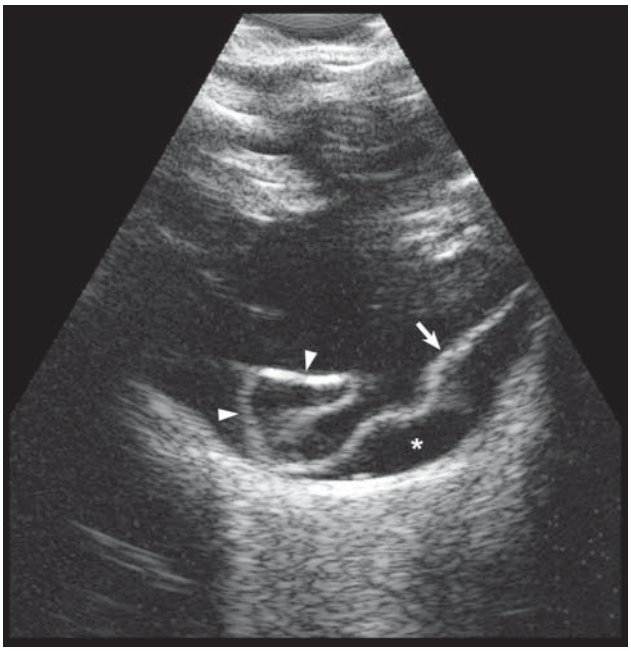


Figure 2.38. Giant retinal tear. Vertical paraxial section. The hyperechoic linear structure indicated by the arrowheads represents a torn dorsal retinal tissue folding ventrally because of gravity. The detachment has occurred peripherally at the level of the ora ciliaris retina. The ventral retina is also separated from the underlying choroid (arrow). The ventral subretinal space is visible (*).

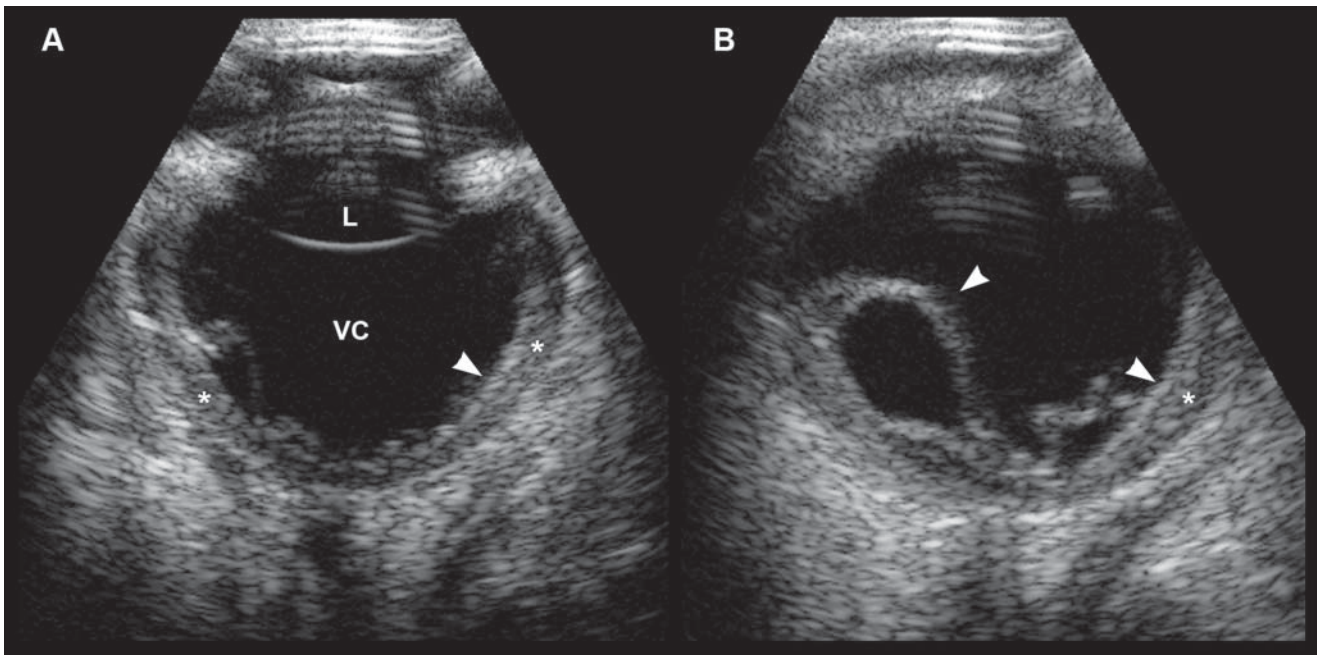


Figure 2.39. Choroiditis and retinal detachment. A, B: Axial and paraxial sections of a canine eye affected with immune mediated choroiditis. The thickened edematous choroid (*) is hypoechoic to the retinal layer. Retinal detachment is present in B. L, lens; VC, vitreal cavity.

space (rhegmatogenous detachment); traction from vitreal strands; and subretinal accumulation of fluid or inflammatory exudate. Contrast-enhanced ultrasonography has been used to differentiate retinal detachment from vitreous membrane (Labruyere et al. 2011).

The choroid is difficult to evaluate. However, when it is affected by severe inflammation and it is edematous or congested, it can be visualized as a hypoechoic layer between the outer sclera and the retina. Retinal detachment is often a result of severe choroiditis (Figure 2.39). A choroiditis may cause fluid or an exudate to accumulate between the retina and the choroid. When exudate or hemorrhage results from choroiditis, the retina is separated from the choroid and

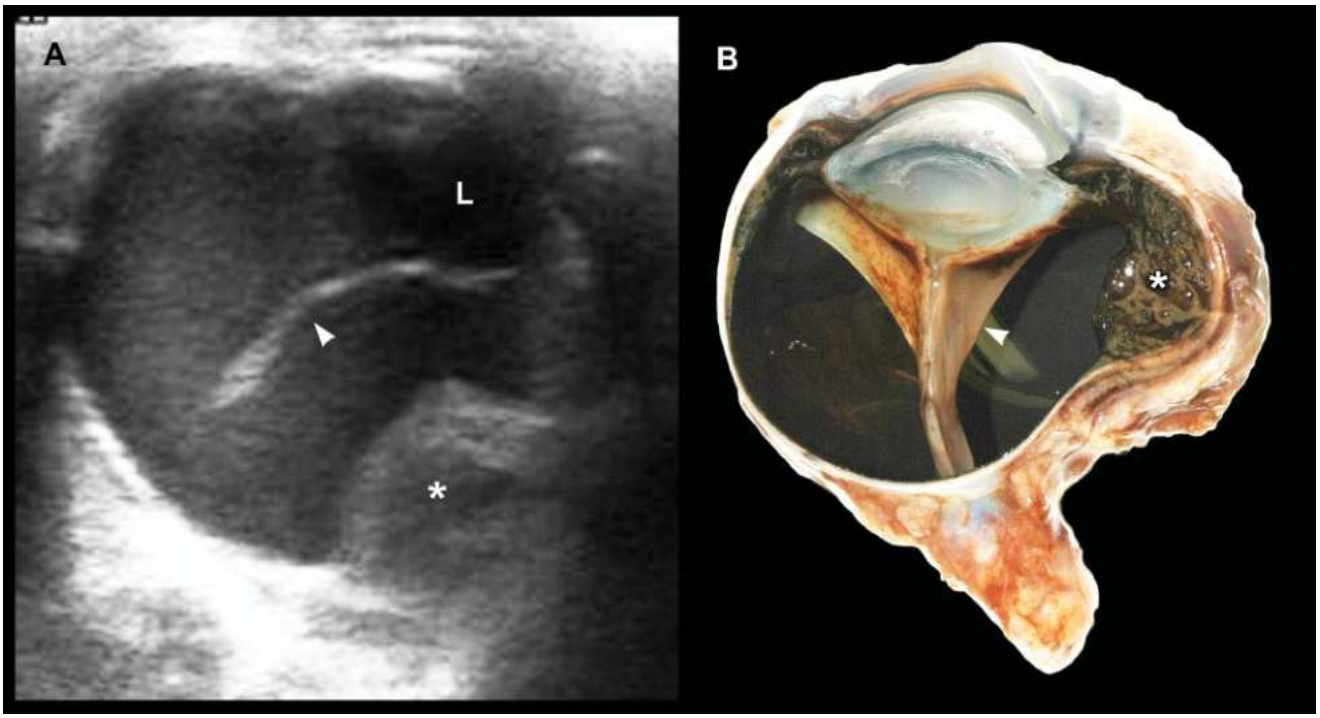


Figure 2.40. Choroidal hemangiosarcoma in a dog. A: Paraxial horizontal sonogram at presentation. The patient was admitted for acute-onset unilateral blindness in the right eye. Clinical examination revealed "morning glory" retinal detachment in the left eye. The right eye was normal. The sonogram of the left eye shows a mass affecting the lateral wall of the posterior segment (*) and complete retinal detachment (arrowhead). L, lens. **B:** Corresponding findings at gross section.

echogenic material is identified in the subretinal space (Figure 2.37).

A vitreal membrane and a detached retina may have a similar appearance. Finding an attachment to the optic disc or detecting blood flow confirms retinal origin. Hypermature cataracts have a higher incidence of retinal detachments because of the common association with vitreal degeneration and fibrosis. Trauma, inflammation, tumors (Figure 2.40), or systemic hypertension may also cause a detachment.

Tumors involving posterior segment (Figures 2.40, 2.41) are rare but should always be suspected when posterior segment examination is difficult or impossible and there is clinical presence of intraocular hemorrhage, retinal detachment, variation in the anterior chamber depth and/or increased intraocular pressure. Choroidal melanocytic neoplasia, hemangiosarcomas and ciliary adenoma/adenocarcinomas extending and invading the vitreal cavity are the most common. Post-traumatic fibrosarcomas are common in cats. Lymphomas and medulloepitheliomas are less common as neoplasia exclusively affecting the posterior segment. Astrocytomas and meningiomas arising from the optic nerve papilla are rare, but should be considered when the mass seem to involve the optic nerve area.

Intraocular and Retrobulbar Foreign Bodies

The appearance of intraocular foreign bodies varies depending on their nature, size, shape, and location. Wooden material is commonly associated with shadowing. A typical comet tail artifact is instead seen distal to a metallic foreign body (such as a pellet gun). Porcupine quills often appear as double paralleling hyperechoic lines, and few of them may be present (Figure 2.42). When present, a hypoechoic tract or cavity around the foreign body may assist in locating it.

Specular reflections from the bones forming the orbit should not be mistaken for foreign bodies. Retrobulbar foreign bodies are difficult to diagnose at ultrasonography. A combination of different modalities is often required and computed tomography (CT) and magnetic resonance imaging (MRI) offer useful information for their detection (Figure 2.43)

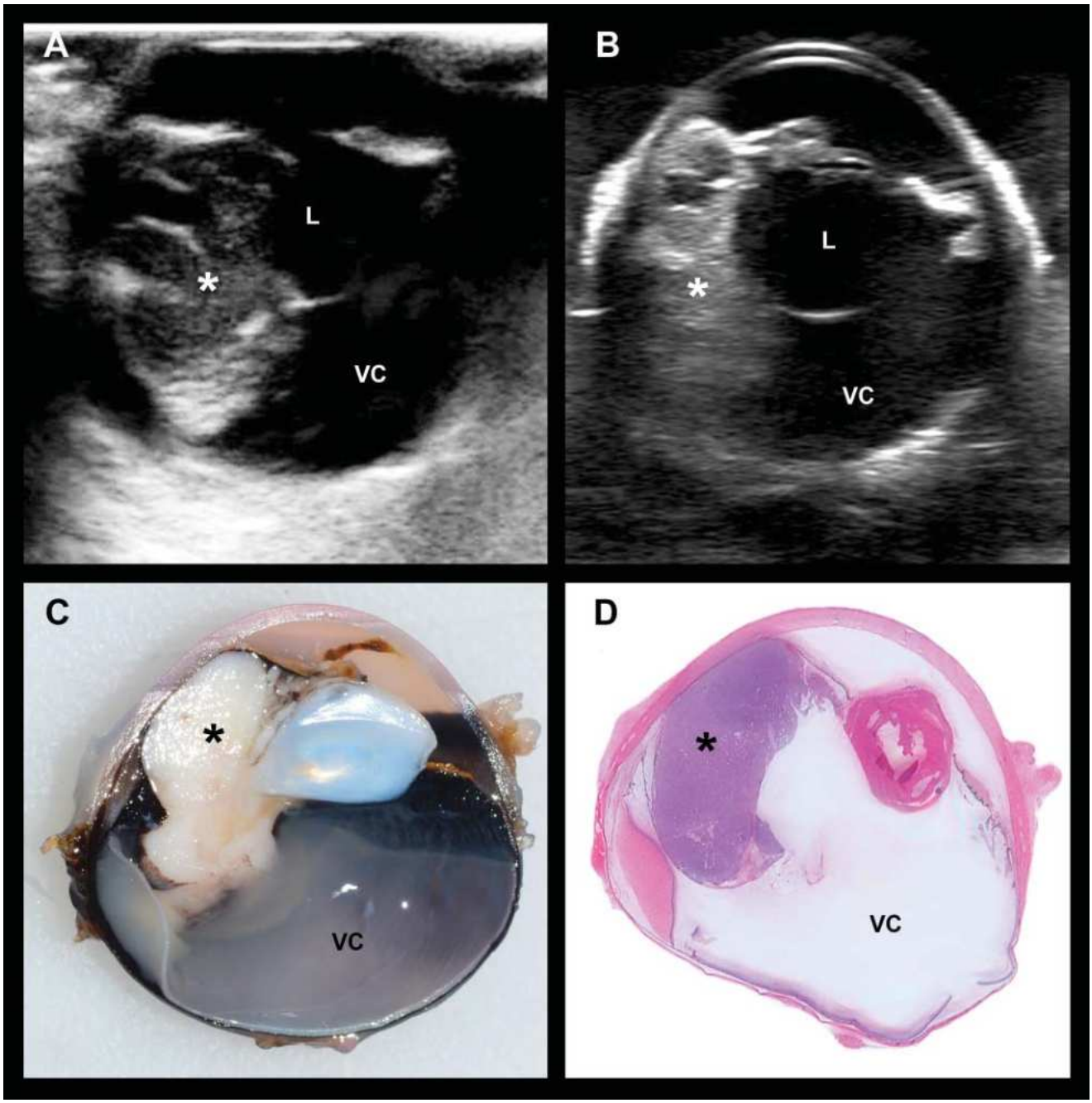


Figure 2.41. **Intraocular tumor invading the posterior segment. A–D**: Horizontal axial sections of a globe affected with a large ciliary adenoma showing as an echogenic mass on the nasal aspect of the globe (*). The tumor develops from the ciliary body, enwraps the lens (L), invading the posterior chamber and diffusely extending posteriorly into the vitreal cavity (VC).

Orbital Disease

The bone surrounding the ocular cone limits the sonographic evaluation of orbital lesions. Abnormalities include blunting of the posterior aspect of the globe; discrete, hypoechoic mass in the retrobulbar space; or discrete, highly echogenic mass/interface deforming the posterior aspect of the globe (Morgan 1989; Attali-Soussay et al. 2001). Retrobulbar malignancies present as variable echogenicity and size masses, with various degrees of deformity of the posterior aspect of the globe (Figure 2.44). Tumors involving the

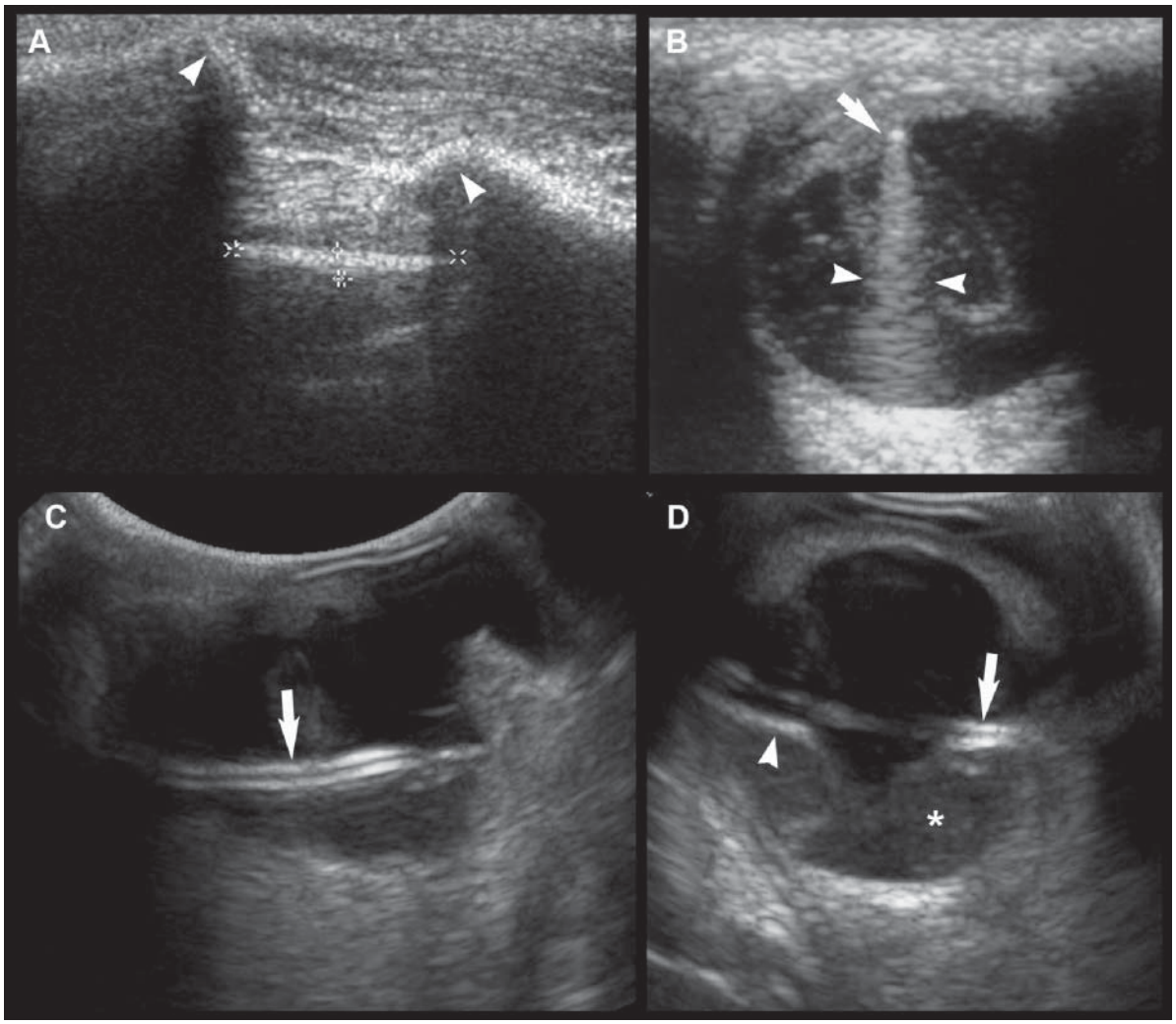


Figure 2.42. **Foreign bodies.** (for full caption, see facing page)

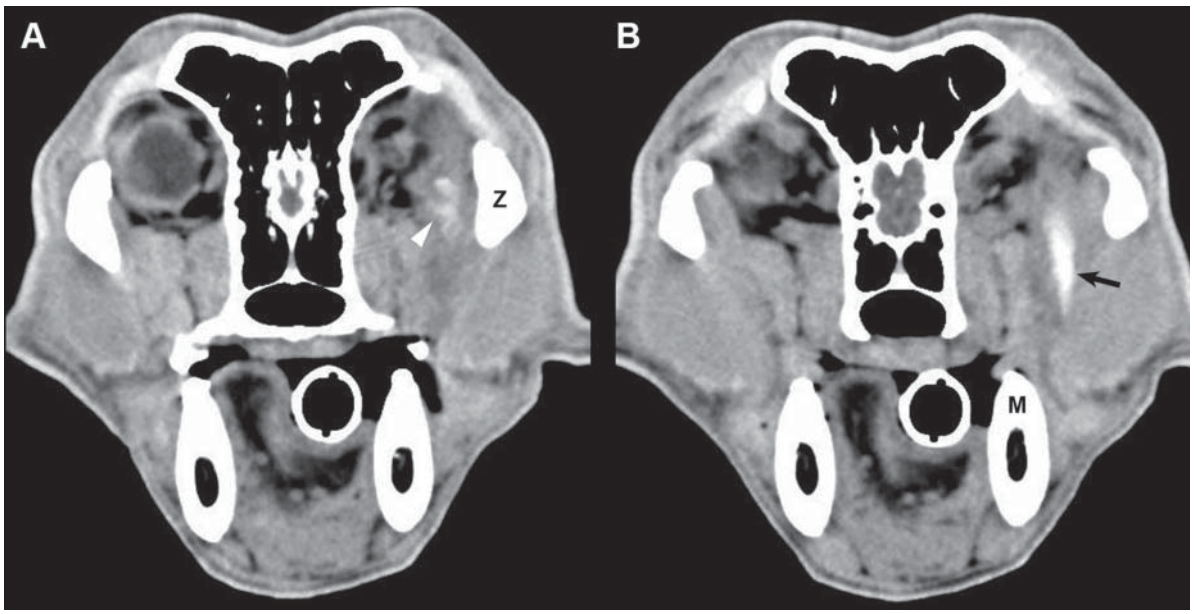


Figure 2.43. **Computed tomography (CT) of retrobulbar wooden foreign body in a 7-year-old Labrador with long-standing jaw pain.** (for full caption, see facing page)

Figure 2.42. **Foreign bodies. A:** Wooden stick. A hyperechoic line associated with shadowing is present between the margins of the zygomatic bone (arrowheads). The globe is to the left of the image. The wooden foreign body is between the cursors. **B:** Pellet-gun metallic foreign body (BBs) (arrow) with associated comet-tail artifact (arrowheads). **C, D:** Porcupine quill in a dog. Two discrete hyperechoic parallel lines (arrow) representing a porcupine quill are crossing the vitreous body, and caused the retinal detachment (arrowhead) and subretinal hemorrhage/exudate (asterisk).

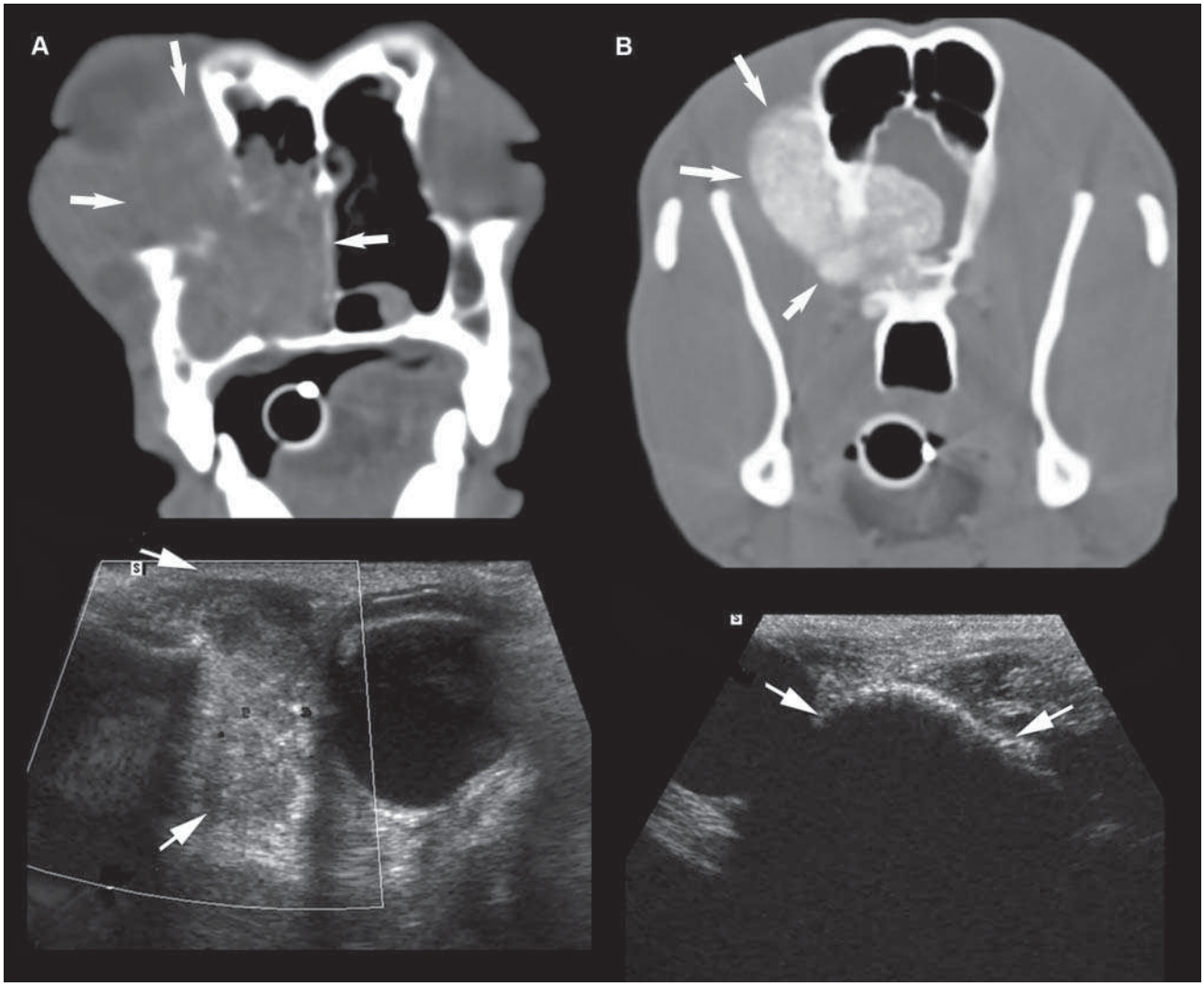


Figure 2.44. **Periocular tumors and secondary displacement of the globe.** The corresponding computed tomographic image is displayed at the top of each case. **A:** Nasal adenocarcinoma with extensive lysis of the bony orbit and extension into the periorbital tissues. The globe is displaced laterally and dorsally (arrows) in this oblique horizontal. **B:** Osteosarcoma involving the skull, with secondary ocular involvement. Note the hyperechoic and shadowing mass (arrows) displacing the globe dorsally.

Figure 2.43. **Computed tomography (CT) of retrobulbar wooden foreign body in a 7-year-old Labrador with long-standing jaw pain. A:** The tip of a hyperdense structure (arrowhead) is noted in the retrobulbar space (enucleation was performed a few months earlier), medial to the zygomatic arch (Z). **B:** This structure is about 4 cm long (arrow) and lies medial to the mandibular ramus (M). CT is useful in detecting deep-seated foreign bodies.

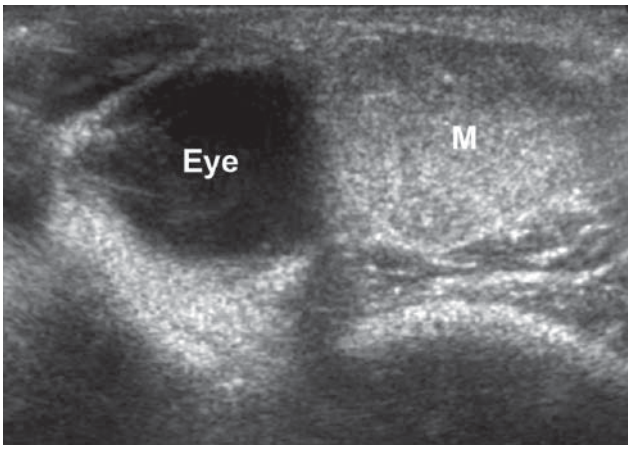


Figure 2.45. Lacrimal gland adenoma. A homogeneous echogenic mass (M) is lateral to and displacing the globe in this horizontal section.

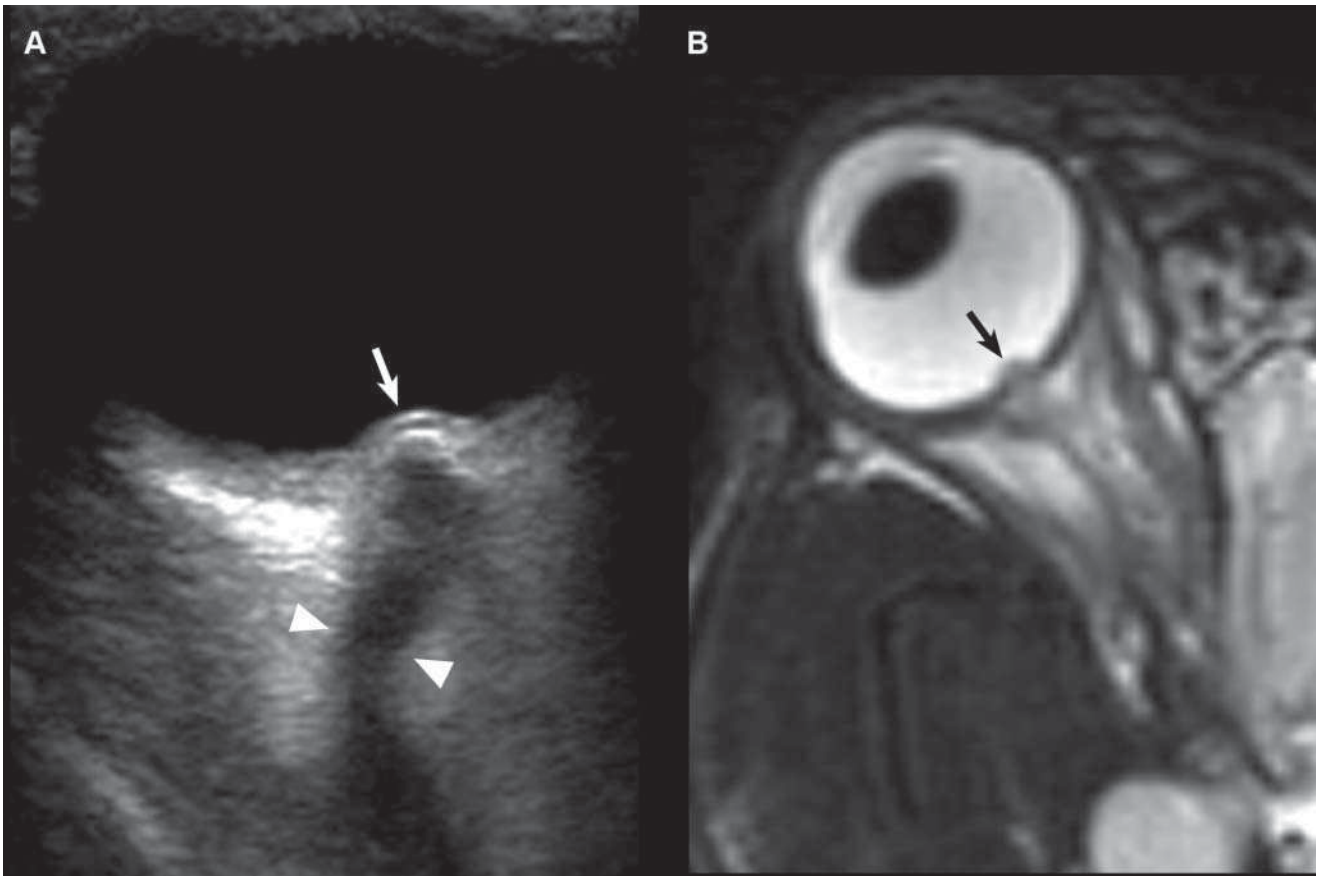


Figure 2.46. Optic neuritis. An indentation (arrows) into the globe at the optic disc is seen in both the ultrasound **(A)** and the magnetic resonance **(B)** images. The optic nerve, appearing as a less echoic linear area extending posteriorly to the globe (arrowheads), is thickened.

tissues around the eye include nasal tumors, primary benign or malignant bone tumors, oral melanomas, squamous cell carcinomas, and hemangiosarcomas. The adjacent bone may be destroyed and have an irregular appearance (Figure 2.44).

The appearance of inflammatory changes varies from a diffuse hyperechoic to a discrete hypoechoic mass (abscess) with possible blunting of the posterior aspect of the globe (Figure 2.31). Retrobulbar cellulitis results in increased echogenicity of the retrobulbar

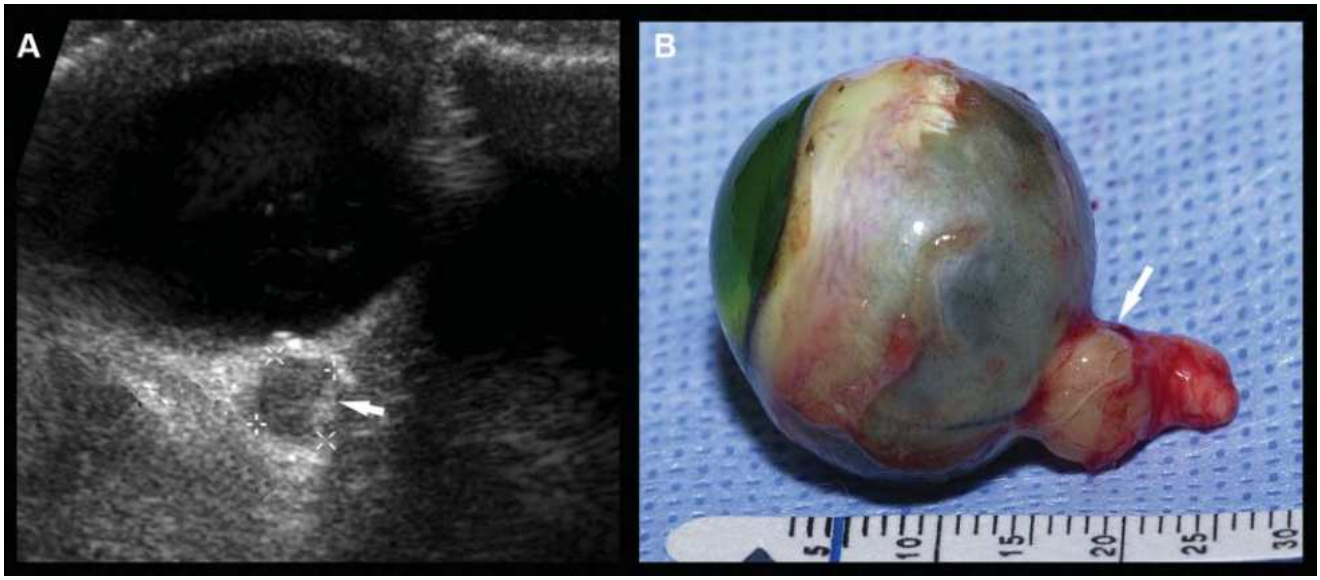


Figure 2.47. **Optic nerve meningioma. A:** Sonogram showing a poorly echogenic mass/thickening of the optic nerve. (arrow, and between cursors). **B:** Enucleated globe corresponding to the sonographic image in A. The mass involves the optic nerve (arrow).

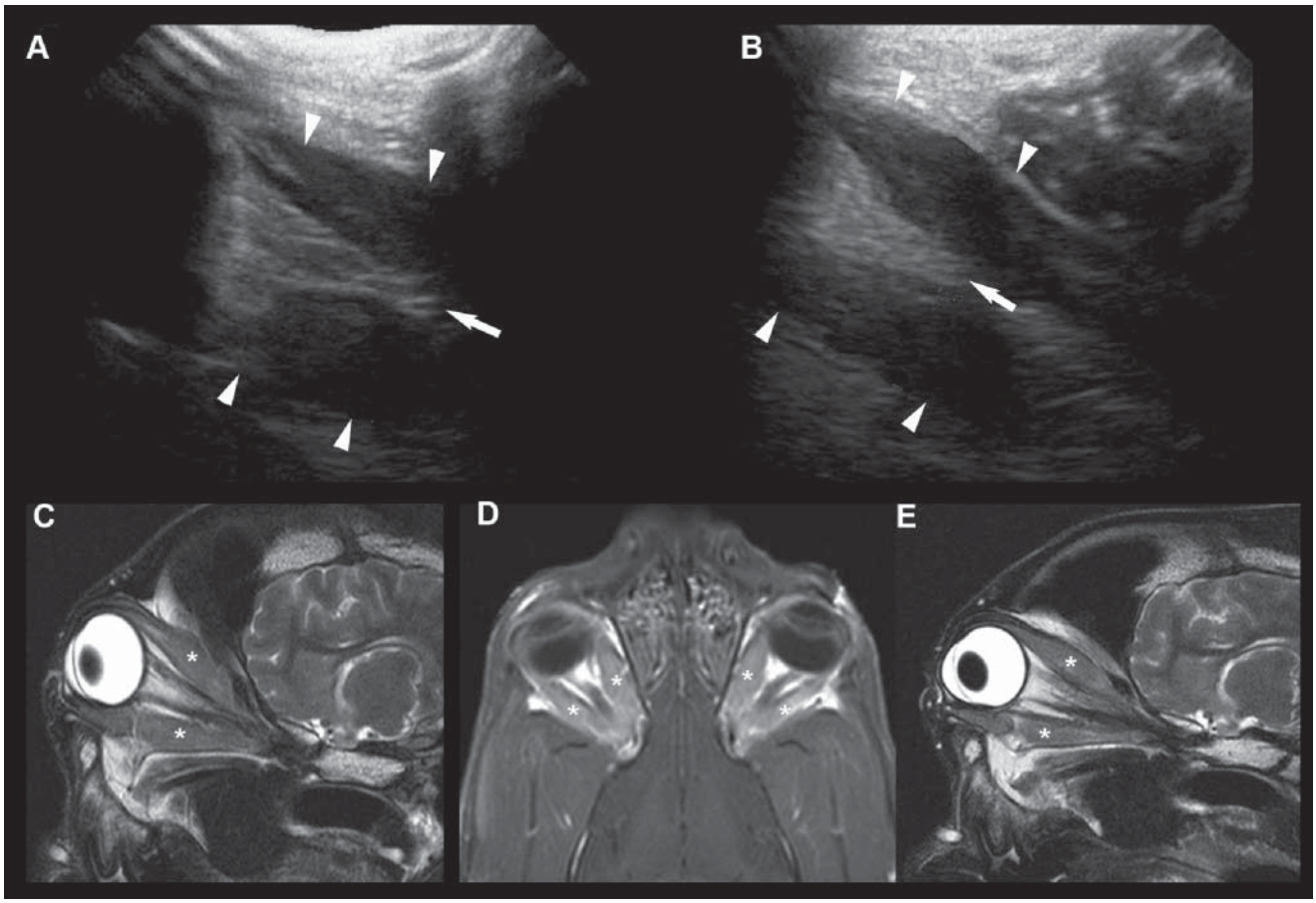


Figure 2.48. **Polymyositis of extraocular muscles associated with bilateral exophthalmia.** Longitudinal sonograms through the orbital fossa of the right **(A)** and left **(B)** retrobulbar region of a 2-year-old mixed-breed dog. Thickened extraocular muscles (arrowheads) are seen around the fat (arrow) encircling the optic nerve. **C–E:** T2 sagittal magnetic resonance (MR) image of the right orbital region, outlining the right **(C)** and the left **(E)** thickened extraocular muscles (*). In D, the dorsal T1-weighted MR image shows the symmetrical bilateral myositis, considered likely immune-mediated in this 9-month-old Labrador.

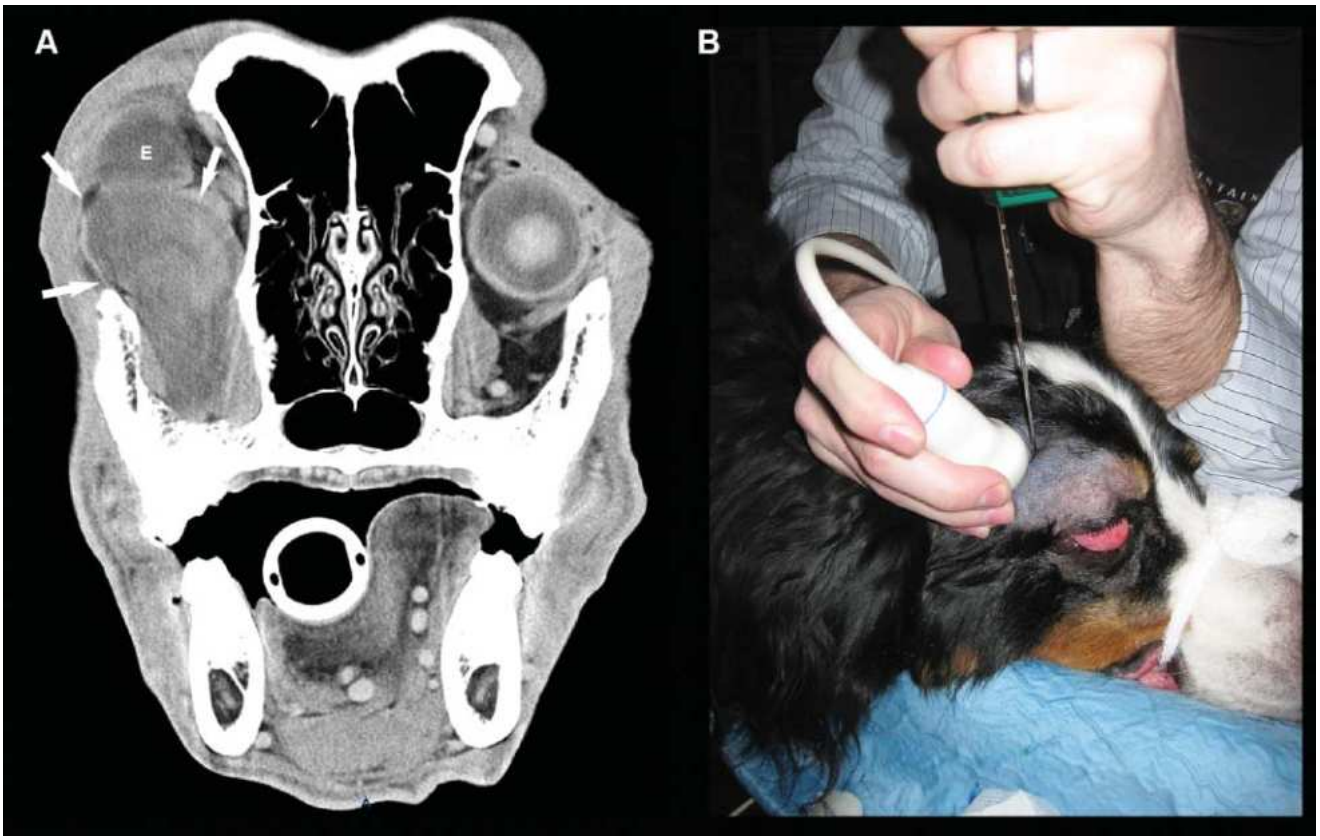


Figure 2.49. **Ultrasound-guided freehand biopsy of a retro-orbital mass. A:** Computed tomography (CT) image of the large and poorly enhancing retrobulbar mass (arrows). The eye (E) is markedly displaced dorsally. **B:** The 18-gauge core needle placed in an automated biopsy gun is engaged into the retrobulbar lesion that was diagnosed as an orbital schwanoma on histopathological evaluation.

tissues without discrete hypoechoic lesion. Retrobulbar cellulitis may or may not deform the globe (Figure 2.29).

Additional periorbital tissues that may affect the globe include the lacrimal gland and the zygomatic gland (Giudice et al. 2005). Either inflammation or neoplasia may affect the size, shape, and echogenicity of the different periorbital glands. Enlargement or a mass from the affected glands can produce a mass effect that displaces the globe (Figures 2.29B, 2.45).

The optic nerve is a curvilinear, hypoechoic structure coursing from the posterior surface of the globe into the orbital cone. Abnormalities of the nerve include neuritis (Figure 2.46) with diffuse enlargement or neoplasia with either focal or diffuse enlargement (Figure 2.47). Tumors of the optic nerve include meningioma, neurofibroma, astrocytoma, and lymphoma.

Extraocular muscles include the four rectus muscles (dorsal, medial, ventral, and lateral), the retractor bulbi muscle, and the dorsal and ventral oblique muscles. Normally the muscles attach in the equatorial zone of the globe or more posteriorly (retractor bulbi) and form a cone whose apex is at the posterior orbital bony wall. The muscles run around the optic nerve and are hypoechoic, being surrounded by hyperechoic fat. Extraocular muscle myositis is an immune-mediated condition in which ultrasonography may be helpful in diagnosis and results in finding enlarged and hypoechoic muscles (Allgoewer et al. 2000). Young Golden Retrievers seem to be predisposed (Carpenter et al.1989) (Figure 2.48).

As the orbital cone has a complex anatomy considering its neighboring structures, cross-sectional imaging techniques such as CT and MRI can assist in completing the evaluation of this region (Penninck et al. 2001).

Interventional Procedures

Ultrasound-guided fine-needle aspiration and/or core biopsies of lesions in the periorbital and retro-orbital region can be performed. This technique enables visualization of the lesion and assists the safe needle placement into the lesion. The angle at which the needle is placed relative to the direction of the

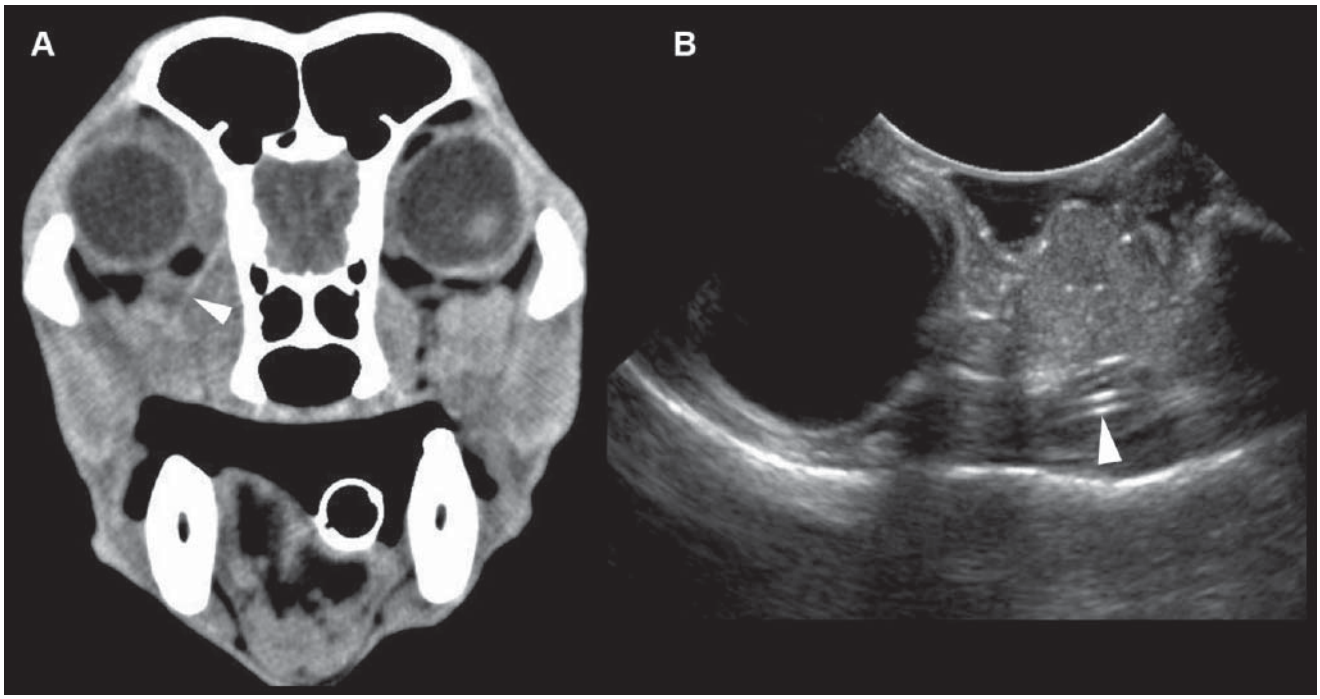


Figure 2.50. Intraoperative assistance for quill removal in a 10-year-old Jack Russell Terrier with prior porcupine quilling. **A:** On computed tomography (CT), two quills (only one is displayed in this image – arrowhead) were identified in the retrobulbar space. **B:** Careful intraoperative ultrasound evaluation allowed the quills to be identified with minimal trauma and the eye to be saved.

transducer is vital in order to position the tip of the needle accurately; this can be done with assistance from a guide or using a freehand technique. Aspiration or biopsy in the retro- or peri-orbital region with ultrasound guidance is helpful in avoiding structures such as the optic nerve, the globe, and the vessels. It is also helpful in placing the needle within the mass or infiltrate to acquire appropriate cells for cytology, or to drain the abscess cavity (Figure 2.49). Additionally, ultrasound can be useful in assisting the surgeon in locating retrobulbar foreign objects and minimizing regional trauma in order to save the eye (Figures 2.50, 2.51).



Visit our website at **www.SmallAnimalUltrasonography.com** for complementary video clips with annotations and text on:

- Normal eye: anatomy and scanning
- Asteroid hyalosis
- Cataracts
- Retinal detachment
- Lens luxation
- Lens extrusion
- Intraocular neoplasia
- Retrobulbar foreign body

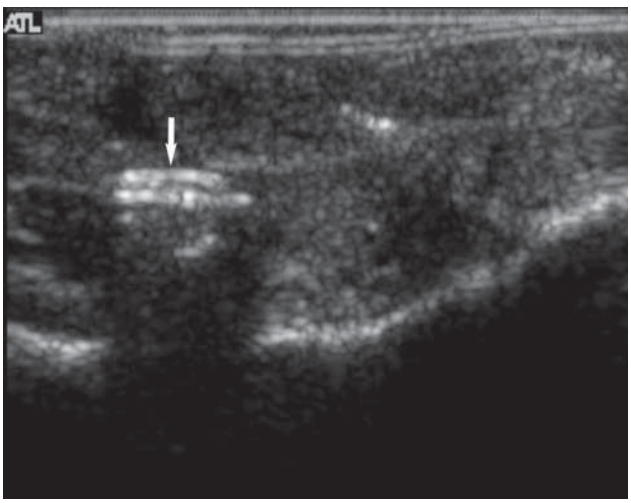


Figure 2.51. Intraoperative assistance for wooden foreign body removal in a 7-year-old Labrador with previous enucleation for wooden foreign bodies in the retrobulbar region. An intraoperative ultrasound exam was performed to assess the periorbital tissues. Additional small wooden foreign chips (arrow) were identified and removed under ultrasound guidance.

References

Allgoewer I, Blair M, Basher T, Davidson M, et al. (2000) Extraocular muscle myositis and restrictive strabismus in 10 dogs. Vet Ophthalmol 3:21–26.

Attali-Soussay K, Jegou J, Clerc B (2001) Retrobulbar tumors in dogs and cats: 25 cases. Vet Ophthalmol 4:19–27.

Aubin ML, Powell CC, Gionfriddo JR, Fails AD. (2003) Ultrasound biomicroscopy of the feline anterior segment. Vet Ophthalmol 6:15–17.

Bayon A, Tovar MC, Fernandez del Palacio MJ, Agut A (2001) Ocular complications of persistent hyperplastic primary vitreous in three dogs. Vet Ophthalmol 4:35–40.

Beam A, Correa M, Davidson M (1999) A retrospective-cohort study on the development of cataracts in dogs with diabetes mellitus: 200 cases. Vet Ophthalmol 2:169–172.

Bentley E, Miller PE, Diehl KA. (2003) Use of high-resolution ultrasound as a diagnostic tool in veterinary ophthalmology. J Am Vet Med Assoc 223:1617–1622.

Boroffka SA, Verbruggen AM, Boevé MH, Stades FC. (1998) Ultrasonographic diagnosis of persistent hyperplastic tunica vasculosa lentis/persistent hyperplastic primary vitreous in two dogs. Vet Rad Ultrasound 39:440–4.

Boroffka SA, Voorhour G, Verbruggen AM, Teske E (2006) Intraobserver and interobserver repeatability of ocular biometric measurements obtained by means of B-mode ultrasonography in dogs. Am J Vet Res 67:1743–1749.

Carpenter JL, Schmidt GM, Moore FM, Albert DM, Abrams KL, Elner VM (1989) Canine bilateral extraocular polymyositis. Vet Pathol 26:510–512.

Corcoran KA, Koch SA. (1993) Uveal cysts in dogs: 28 cases (1989–1991). J Am Vet Med Assoc 15:545–546.

Cottrill N, Banks WJ, Pechman RD (1989) Ultrasonographic and biometric evaluation of the eye and orbit of dogs. Am J Vet Res 50:898–903.

Deehr AJ, Dubielzig RR (1998) A histopathological study of iridociliary cysts and glaucoma in golden retrievers. Vet Ophthalmol 1:153–158.

Dietrich U, Kostlin R, Tassani M (1995) Ultrasonographic examination of the eyes of dogs with cataracts [Abstract]. Vet Radiol Ultrasound 36:436.

Dubielzig RR (2002) Tumors of the eye. In: Meuten D, ed. Tumors in Domestic Animals, 4th edition. Ames, IA: Blackwell, pp 739–754.

Dubielzig RR, Steinberg H, Garvin H, Deehr AJ, Fischer B (1998) Iridociliary epithelial tumors in 100 dogs and 17 cats: A morphological study. Vet Ophthalmol 1:223–231.

Dziezyc J, Hager DA (1988) Ocular ultrasonography in veterinary medicine. Semin Vet Med Surg (Small Anim) 3:1–9.

Gallhoefer NS, Bentley E, Ruetten M, Grest P, et al.(2013) Comparison of ultrasonography and histologic examination for identification of ocular diseases of animals:113 cases (2000–2010). J Am Vet Med Assoc 243:376–388.

Gelatt K, MacKay E (2005) Prevalence of primary breed-related cataracts in the dog in North America. Vet Ophthalmol 8:101–111.

Gemensky-Metzler A, Wilkie DA (2004) Surgical management and histologic and immunohistochemical features of a cataract and retrolental plaque secondary to persistent hyperplastic tunica vasculosa lentis/persistent hyperplastic primary vitreous (PHTVL/PHPV) in a bloodhound puppy. Vet Ophthalmol 7:369–375.

Giudice C, Marco R, Mirko R, Luca M, Giorgio C (2005) Zygomatic gland adenoma in a dog: Histochemical and immunohistochemical evaluation. Vet Ophthalmol 8:13–16.

Grahn BH, Storey ES, McMillan C (2004) Inherited retinal dysplasia and persistent hyperplastic primary vitreous in Miniature Schnauzer dogs. Vet Ophthalmol 7:151–158.

Hager DA, Dziezyc J, Millchamp NJ (1987) Two-dimensional real-time ocular ultrasonography in the dog: Technique and normal anatomy. Vet Radiol 28:60–65.

Labruyere JJ, Hartley C, Holloway A (2011) Contrast-enhanced ultrasonography in the differentiation of retinal detachment and vitreous membrane in dogs and cats. J Small Anim Pract 52:522–530.

Morgan RV (1989) Ultrasonography of retrobulbar diseases of the dog and cat. J Am Anim Hosp Assoc 25:393–399.

Pavlin CJ, Foster FS (1995) Ultrasound biomicroscopic anatomy of the normal eye and andexa. In: Pavlin CJ, Foster FS, eds. Ultrasound Biomicroscopy of the Eye. New York: Springer-Verlag, pp 47–60.

Penninck DG, Daniel GB, Brawer R, Tidwell AS (2001) Cross-sectional imaging techniques in veterinary ophthalmology. Clin Tech Small Anim Pract 16:22–39.

Pumphrey SA, Pizzirani S, Pirie CG, Needle DB (2013) Glaucoma associated with uveal cysts and goniodysgenesis in American Bulldogs: a case series. Vet Ophthalmol 16:377–385.

Sapienza JS, Simo FJ, Prades-Sapienza A (2000) Golden retriever uveitis: 75 cases (1994–1999). Vet Ophthalmol 3:214–246.

Schiffer SP, Rantanen NW, Leary GA, Bryan GM (1982) Biometric study of the canine eye, using A-mode ultrasonography. Am J Vet Res 43:826–830.

Sherar MD, Starkoski WB, Taylor WB, Foster FS (1989) A 100 MHz B-scan ultrasound backscatter microscope. Ultrasonic Imaging 11:95–105.

Silverman RH, Cannata J, Shung KK, Gal O, Patel M, Lloyd HO, Feleppa EJ, Coleman DJ. (2006) 75 MHz Ultrasound Biomicroscopy of Anterior Segment of Eye. Ultrasound Imaging 28:179–188.

Silverman RH (2009) High-resolution ultrasound imaging of the eye – a review. Clin Experiment Ophthalmol 37(1):54–67.

Spiess BM, Bolliger JO, Guscetti F, Haessig M, Lackner PA, Ruehli MB (1998) Multiple ciliary body cysts and secondary glaucoma in the Great Dane: A report of nine cases. Vet Ophthalmol 1:41–45.

Stades FC (1980) Persistent hyperplastic tunica vasculosa lentis and persistent hyperplastic primary vitreous PHTVL/PHPV in 90 closely related Doberman Pinschers: clinical aspects. J Am Anim Hosp Assoc 16:739–751.

Williams DL (2004) Lens morphometry determined by B-mode ultrasonograph of the normal and cataractous canine lens. Vet Ophthalmol 7:91–95.

Zeiss CJ, Dubielzig RR (2004) A morphologic study of intravitreal membranes associated with intraocular hemorrhage in the dog. Vet Ophthalmol 7:239–243.

CHAPTER THREE

Neck

Allison Zwingenberger[1] and Olivier Taeymans[2]

[1] *Department of Surgical and Radiological Sciences, School of Veterinary Medicine, University of California, Davis, CA, USA*

[2] *Dick White Referrals, Station Farm, Six Mile Bottom, Cambridgeshire, UK*

Scanning Technique

Because the ventral cervical region is anatomically complex, ultrasound is uniquely suited to evaluating cervical organs and tissues that are not readily characterized on survey or contrast radiographs. In addition to defining gross anatomy of the neck, high-resolution ultrasound can also be used to examine very small structures such as the thyroid and parathyroid glands. High-frequency (8–15 MHz) linear transducers and curvilinear transducers provide the best images of small structures and those with complex internal architecture. Tissue harmonic imaging and/or compound imaging techniques are also available on most recent machines, which can further improve image resolution by decreasing artifacts.

For ultrasonography of most structures, the animal is positioned in dorsal recumbency with the area of interest clipped (Figure 3.1A). Because many of the structures in the neck are symmetrically paired, it is useful to compare them. Positioning the patient so that the neck is as straight as possible is important to locate anatomical landmarks reliably and to compare both sides of the neck. Any structure can be investigated while the animal is in lateral recumbency (Figure 3.1B) according to operator preference or for dyspneic animals, with the caveat that anatomy may appear somewhat distorted and comparisons to the contralateral neck will be impaired. For imaging the tympanic bullae, positioning the patient in sternal recumbency (Figure 3.1C) or seated with the head held straight and extended is preferred.

Although the ultrasound beam cannot penetrate air within hollow structures such as the tympanic bullae, trachea, and larynx, the interface between air and adjacent soft tissues can still be evaluated for regularity of contours and physiological motion, as exemplified by examination of the vocal folds. Sonographic assessment of the cavities of these structures becomes possible in case of fluid accumulation or soft tissue proliferation.

In addition to two-dimensional B-mode imaging, color flow Doppler, power Doppler, and pulsed-wave Doppler imaging can be used to evaluate vascularity of organs, vessels, and tissues. Flow characteristics of large vessels such as the common carotid artery and jugular vein can be determined with color and pulsed-wave Doppler.

Normal Sonographic Anatomy

There are a few anatomical landmarks that are useful for locating cervical structures of clinical interest (Figure 3.1D). Normal size values for these landmarks are reported in Table 3.1.

Vessels and Nerves

The major neck vessels that can be seen with ultrasound are the jugular veins and their primary tributaries and the common carotid arteries and their major branches (Wisner et al. 1991). Other vessels, such as thyroid arteries and veins, are smaller and seen inconsistently. All of these structures are imaged in transverse or sagittal plane. Some may be seen from ventral midline, whereas others may be seen better with the transducer positioned lateral to midline.

Atlas of Small Animal Ultrasonography, Second Edition. Edited by Dominique Penninck and Marc-André d'Anjou.
© 2015 John Wiley & Sons, Inc. Published 2015 by John Wiley & Sons, Inc.
Companion website: www.SmallAnimalUltrasonography.com

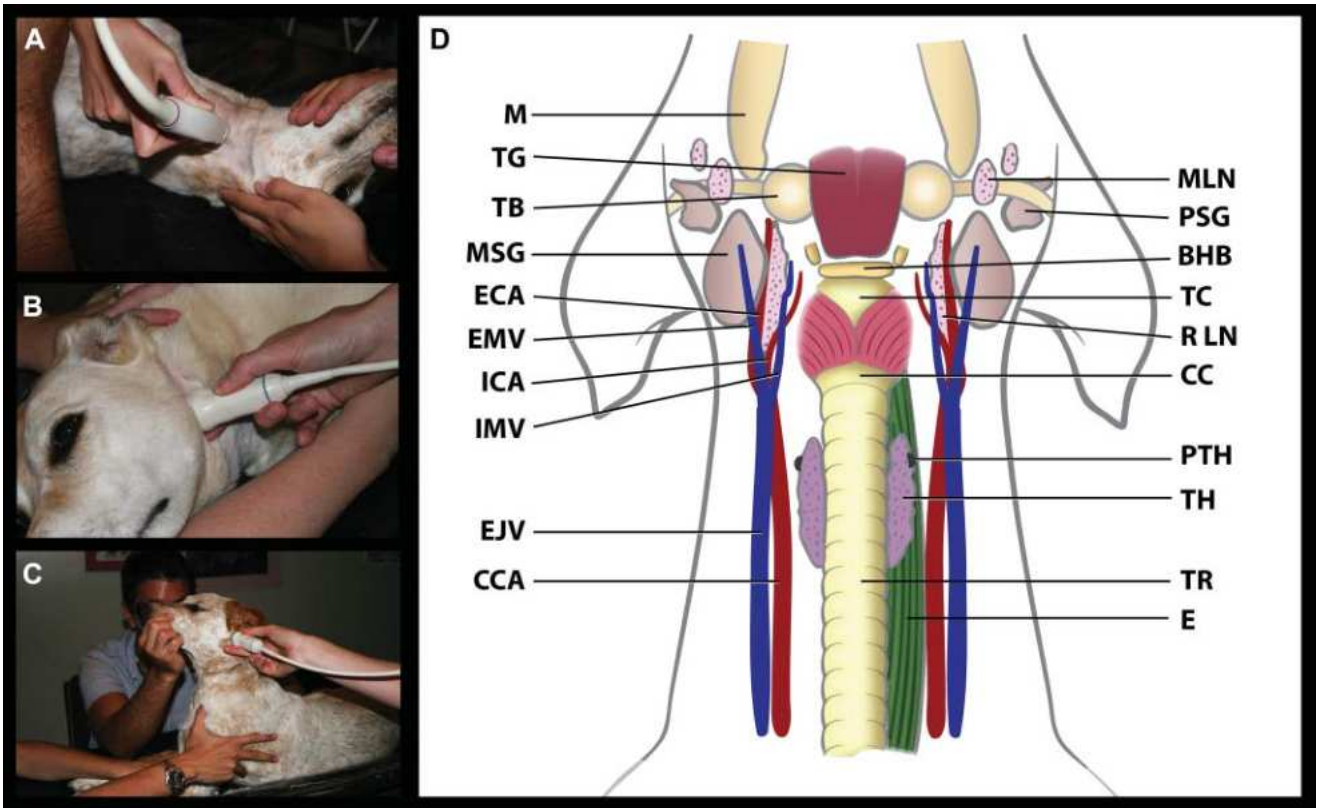


Figure 3.1. **Ultrasound approach to the neck of a dog and normal regional anatomy.** (for full caption, see facing page)

Table 3.1
Measurements of normal structures in the neck

Structure	Width/diameter (mm)	Height (mm)	Length (mm)	Volume (mm^3)
Vagosympathetic trunk	1.2 ± 0.4			
Medial retropharyngeal lymph node, canine	5		20–40	
Medial retropharyngeal lymph node, feline	3.3 (2.0–6.0)	11 (6–18)	20.7 (13.0–32.0)	
Mandibular lymph node	<5			
Thyroid, feline (single lobe)				66–103
Left		3.3 (2.5–4.1)	20.5 (18.9–22.1)	89 (66–112)
Right		3.0 (2.4–3.6)	20.3 (18.7–21.9)	80 (61–99)
Cats (total volume)				124–215
Thyroid, canine				
Mixed breed	16 (8–28)	8 (4–21)	22 (10–55)	
Beagles	5.3 (3.3–7.3)	5.3 (3.3–7.3)	24.5 (20.4–28.5)	380
Akitas				63–1912
Golden Retrievers	4.3 (3.3–6.4) Left 4.9 (3.1–8.5) Right		24.8 (18.9–32.4) Left 24.4 (18.3–33.1) Right	447 (178–805) Left 501 (132–1061) Right
Toy and Miniature Poodles				128–713
Parathyroid, Canine				
Mixed Breed	2.3 (1.3–3.3)	1.7 (0.9–3.1)	3.4 (2.1–7.6)	

Combined data from Wisner et al. (1991, 1994), Reese and Ruppert (2001), Taeymans et al. (2005), Bromel et al. (2005), Liles (2010), and Nemanic (2012).

Figure 3.1. Ultrasound approach to the neck of a dog and normal regional anatomy. A: Dorsal recumbency is convenient for imaging most of the structures of the neck. It enables comparison of bilaterally symmetrical structures, and it is easy to maintain true sagittal and transverse orientation. **B:** Lateral recumbency is an alternate position for investigating the structures of the neck. **C**: Sternal positioning for ultrasonography of the tympanic bulla. **D:** Illustration of main anatomical structures of the neck that are evaluated with ultrasound or serve as landmarks. BHB, basihyoid bone; CC, cricoid cartilage; CCA, common carotid artery; E, esophagus; ECA, external carotid artery; EMV, external maxillary vein; ICA, internal carotid artery; IMV, internal maxillary vein; EJV, external jugular vein; M, mandible; MLN, mandibular lymph node; PSG, parotid salivary gland; PTH, parathyroid gland; RLN, retropharyngeal lymph node; TH, thyroid gland; TB, tympanic bulla; TC, thyroid cartilage; TG, tongue; TR, trachea.

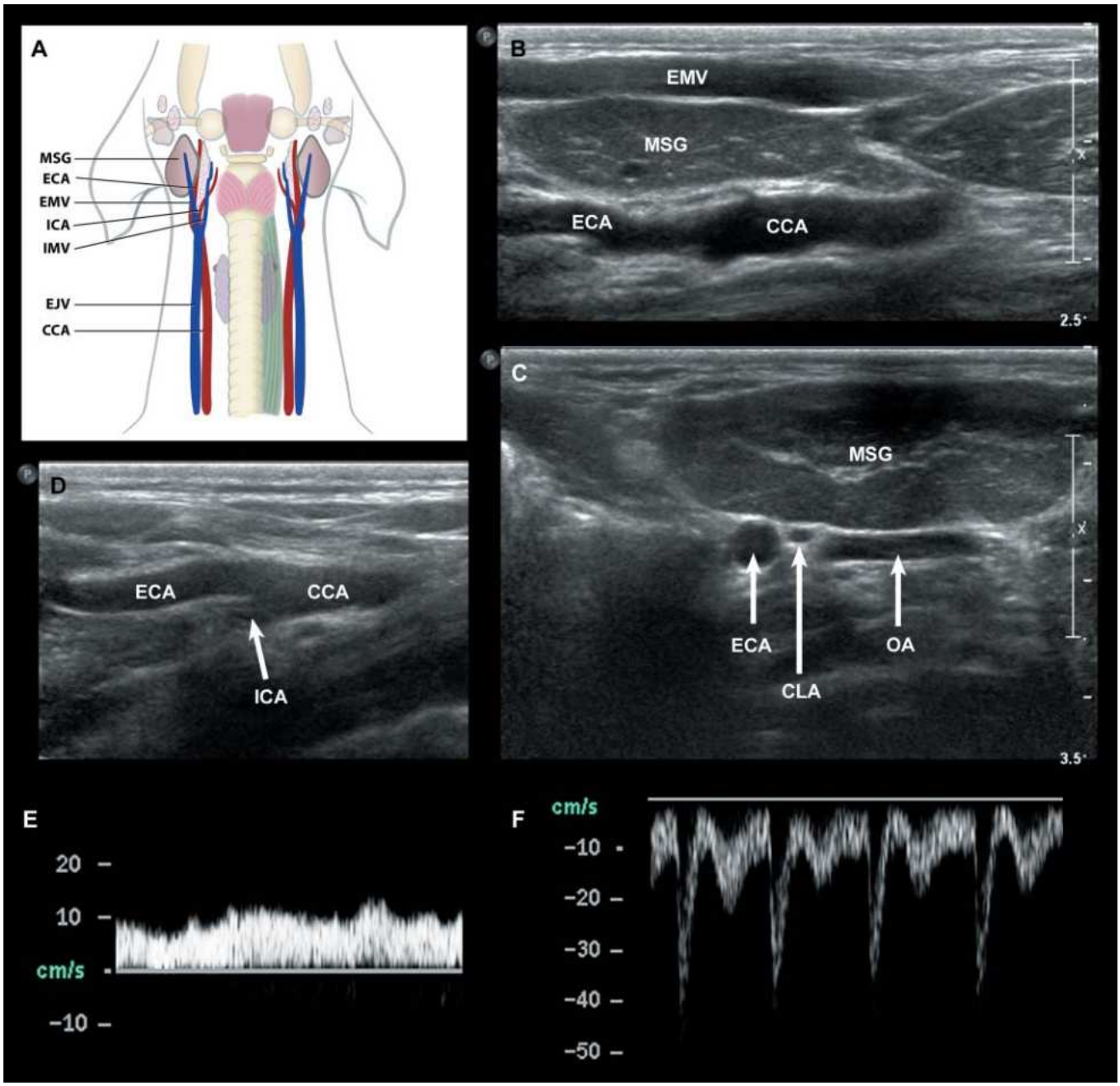


Figure 3.2. Images of the carotid arteries, jugular veins, and mandibular salivary glands of a normal dog. A: Illustration of the anatomical location of these structures in the canine neck. The common carotid artery (CCA) subdivides into the external carotid artery (ECA), ventrally, and the internal carotid artery (ICA), which extends dorsally. The external jugular vein (EJV) subdivides into the external maxillary vein (EMV), ventrally, and the internal maxillary vein (IMV), which extends dorsally. The mandibular salivary gland (MSG) lies cranial to these bifurcations. **B, C:** Sagittal (**B**) and transverse **(C)** images of the CCA, EMV, and MSG. Note the low echogenicity and coarse echotexture of the gland. CLA, cranial laryngeal artery; OA, occipital artery. **D:** Sagittal images of the common carotid artery at its site of bifurcation into the ECA and the ICA. **E, F:** Pulsed-wave Doppler signature of the external jugular vein **(E)** and common carotid artery **(F)**. The venous flow is directed toward the transducer, has lower velocity and is laminar and therefore more constant (**E**). The arterial flow is directed away from the transducer with pulsatile flow of higher velocity **(F)**.

The external jugular vein (Figure 3.2A) lies superficially within the jugular furrow. Cranially, the external and internal maxillary veins join to form the external jugular vein at the caudal aspect of the mandibular salivary gland (Figure 3.2A,B). The jugular vein is easily compressed, so very little transducer pressure should be used to image it. The transducer should be placed in the jugular furrow in a sagittal orientation and angled 45° toward the midline. The wall of the jugular vein is thin, and the lumen is anechoic. With color Doppler or pulsed-wave Doppler ultrasound, a smooth, laminar flow is seen (Figure 3.2E). This is sometimes difficult to demonstrate, because the Doppler signal is weakest when the vessel lies at nearly 90° to the beam. Slight angulation of the transducer in a caudal direction, as well as beam steering, will increase the Doppler signal and help confirm the direction of the flow. Weak pulsatile flow referred from the carotid artery will be seen occasionally.

The common carotid artery is located in close association and parallel to the trachea. The artery has a thick, hyperechoic wall and anechoic lumen (Figure 3.2B–D), with a pulsatile Doppler waveform (Figure 3.2F). Each artery is located at the dorsolateral margin of the trachea, and the sternohyoid and sternothyroid muscles are located ventromedially to them. The sternocephalicus muscle lies between the common carotid artery and the more superficial jugular vein. The common carotid artery branches into the internal and external carotid arteries medial to the mandibular salivary gland. The external carotid artery continues in a straight line from the common carotid artery, whereas the internal carotid artery is slightly smaller in diameter and travels medially and dorsally at a 30° angle (Figure 3.2B–D). The carotid bulb, a focal dilatation of the arterial lumen at the origin of the internal carotid artery, can be seen occasionally.

In transverse orientation, the carotid sheath appears hyperechoic and encompasses the common carotid artery, vagosympathetic trunk, and internal jugular vein. The vagosympathetic trunk is dorsal to the common carotid artery and appears hypoechoic. It can be seen from the laryngeal region to the thoracic inlet, and no visible vascular structures are within it. The vagosympathetic trunk is approximately 1.2 ± 0.4 mm in diameter, which varies with the weight of the animal (Reese et al. 2001).

Salivary Glands and Lymph Nodes

The mandibular salivary gland is easily visible caudal to the ramus of the mandible, and between the external and internal maxillary veins as they join to form the jugular vein (Figure 3.3A). A portion of the sublingual salivary gland shares the capsule of the rostral portion of the mandibular salivary gland, but may not be distinguished as a separate entity.

In the parasagittal imaging plane, the mandibular salivary gland is caudal to the more hypoechoic digastricus muscle, with the medial retropharyngeal lymph node medial to it (Figure 3.3A–C). To image the mandibular salivary gland in a sagittal orientation, the transducer can be rotated slightly from the parasagittal plane relative to the head and neck. It is well defined, large and ovoid in shape, with a hyperechoic capsule and linear echogenic streaks within finely textured hypoechoic parenchyma (Figure 3B,C). A large centrally located hilum is characteristic for this gland, which may sometimes be confused for a lymph node.

The medial retropharyngeal lymph nodes are dorsal to the pharynx and caudomedial to the mandibular salivary gland. The medial retropharyngeal lymph node is larger than most other cervical lymph nodes and measures around 0.5 cm in height and 4–5 cm long. The cranial portion of these nodes is typically wider than the caudal part, which is more fusiform. In cats, reference measurements are 20.7 × 12.4 × 3.7 mm (Nemanic et al. 2012). The lymph nodes decrease in size with increasing age.

Mandibular lymph nodes are very superficially located oval structures located lateral and cranial to the mandibular salivary glands and clustered around the linguofacial vein. They are typically less than 0.5 cm thick and 1–2 cm long in the dog, and are usually mildly hypoechoic to surrounding fat, although they can be isoechoic (Figure 3.3D). There are usually two to three lymph nodes on each side. The deep cervical lymph nodes are generally poorly developed and usually not seen when normal, and are located along the trachea. Mandibular and retropharyngeal lymph nodes can be seen in normal dogs. The superficial cervical lymph nodes (commonly referred to as prescapular nodes), located superficially in the lateroventral aspect of the caudal neck, cranial to the supraspinatus muscle, are often paired and significantly larger than those in the cranial cervical region. Their size is positively correlated to body weight, with a mean length of 2.26 cm, a mean width of 0.91 cm and a mean height of 0.46 cm (right side) (Silver et al. 2012).

Moving dorsally from the mandibular salivary gland by using a dorsal plane, the parotid salivary gland appears as a less distinct, heterogeneous, and poorly marginated structure lateral or caudal to the curvilinear external ear canal and tympanic bulla (Figure 3.3E, F).

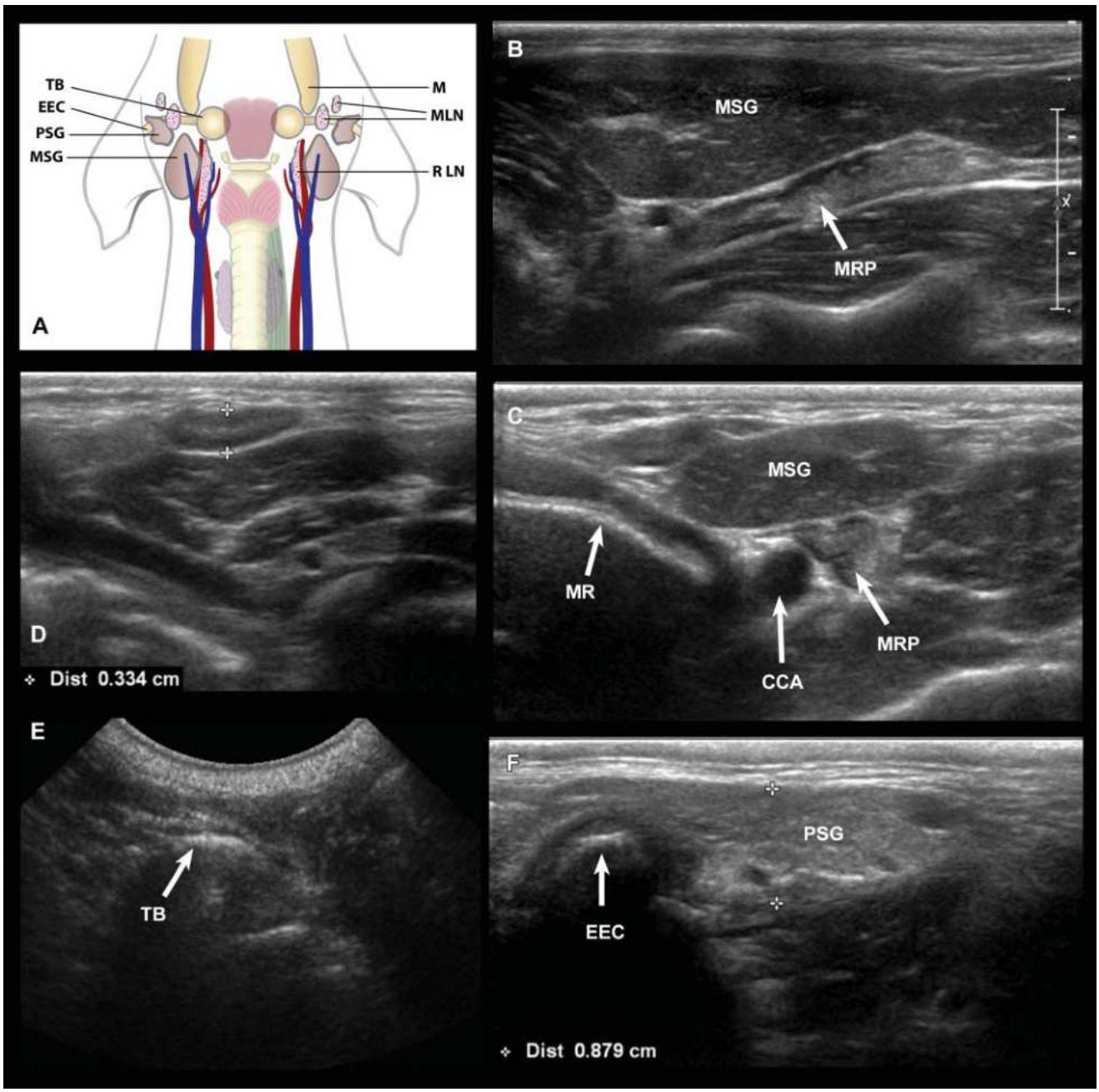


Figure 3.3. **Normal lymph nodes and salivary glands. A:** Illustration of the anatomical location of these structures in the canine neck. TB, tympanic bulla; EEC, external ear canal; PSG, parotid salivary gland; MSG, mandibular salivary gland; M, mandible; MLN, mandibular lymph nodes; RLN, retropharyngeal lymph node. **B, C:** Sagittal (**B**) and transverse (**C**) sonographic images of the MSG and medial retropharyngeal lymph nodes (MRP). Cranial is to the left of the image. The MSG has a striated echotexture with a central linear echo. It is adjacent to the more hypoechoic digastric muscle overlying the hyperechoic interface of the mandibular ramus (MR). The MRP lymph node is more echogenic and located obliquely dorsomedial to the salivary gland. The lymph node is located lateral to the common carotid artery (ECA) in the transverse plane **(C)**. **D:** Sagittal sonographic image of one of the MLNs. This node shows a hypoechoic halo in this asymptomatic dog, and is considered normal. **E:** Sagittal sonogram of the tympanic bulla. Note the hyperconvex interface with deep acoustic reverberation. **F:** Sagittal image of the normal PSG, which is located caudal to the external ear canal (EEC). Note that the gland partly encircles the canal ventrally.

Larynx, Trachea and Esophagus

Just caudal to the tongue, the thyroid and cricoid cartilages have echogenic surfaces and produce acoustic shadowing in the far field. In sagittal orientation, the epiglottis is a short echogenic line parallel to the transducer surface and dorsal to the cranial portion of the thyroid cartilage. Its motion during swallowing assists its identification.

In transverse section (Figure 3.4A), the arytenoid cartilages appear as a pair of echogenic lines oriented parallel to the transducer and within the thyroid cartilage near the lateral walls. Between the arytenoid cartilages and the true vocal folds are hypoechoic bands medial to the wall of the thyroid cartilage (Figure 3.4B). These represent the insertion of the aryepiglottic fold from the epiglottis on the ventral portion of the cuneiform process of the arytenoid cartilage and are called the false vocal folds.

Orienting the transducer transversely ventral to the thyroid cartilage shows the moving vocal folds (Bray et al. 1998). The transducer is then moved caudally to the junction of the thyroid and cricoid cartilages and directed cranially toward the vocal folds, which are attached to the vocal process of the arytenoid cartilage dorsally and the thyroid cartilage ventrally. The vocal folds consist of the vocal ligaments located craniomedially, and the vocal muscle continues laterally and caudally from it to join with the larynx. The vocal ligaments appear as vertical hyperechoic bands in the central larynx that contact each other in the ventral portion of the thyroid cartilage (Figure 3.4B). The vocal processes of the arytenoid cartilage are hyperechoic lines that join with the vocal ligaments dorsally. The air-filled space between the vocal folds is the rima glottis (Figure 3.4B). Mineralization of the laryngeal cartilages may hinder viewing of the vocal folds through the thyroid cartilages.

Normal motion of the vocal folds is abduction during inspiration and adduction during expiration. The cuneiform and vocal processes of the arytenoid cartilages also move in this manner (Figure 3.4B,C). The motion may be more apparent when an animal is panting. Motion should be evaluated for symmetry, and overall motion is minimal in normal dogs.

The trachea and esophagus can then be examined in transverse and longitudinal planes (Figure 3.5A). The trachea contains air that causes reverberation artifacts and acoustic shadowing. Consequently, only its near walls (ventral and lateral) can be examined using ultrasound. In a transverse plane, the trachea appears as a hyperechoic, convex interface with distal acoustic shadowing obscuring the lumen (Figure 3.5B). In a longitudinal view, the tracheal rings are visible as small, regularly spaced hypoechoic structures with central hyperechoic dots when partly mineralized (Figure 3.5C).

The esophagus is also sagittally oriented, but varies in position from dorsal to the trachea caudal to the larynx, to left of the trachea at the thoracic inlet.

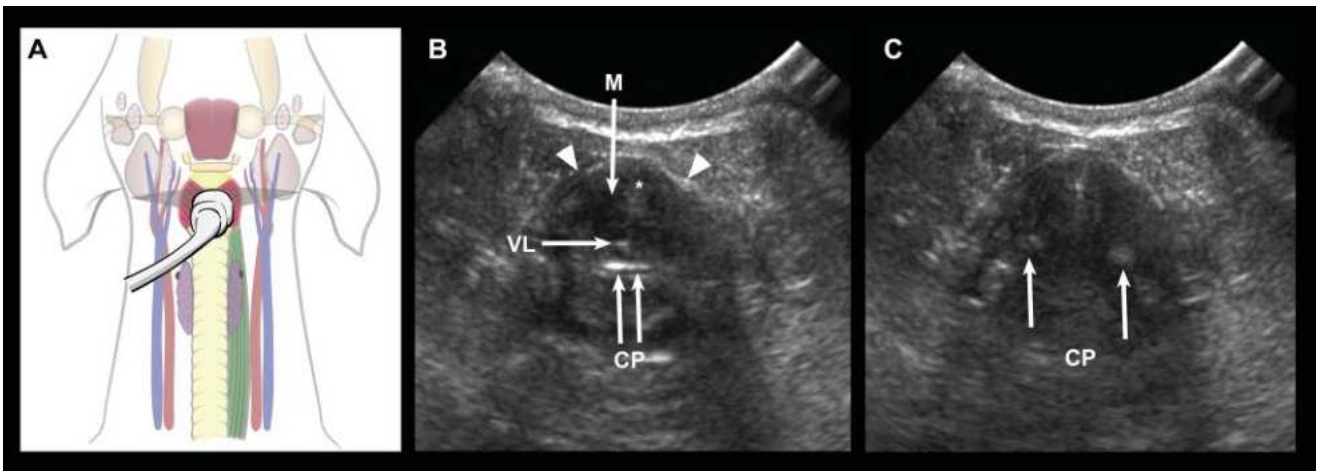


Figure 3.4. **Normal larynx in a dog. A:** Illustration of the probe placement on the ventral aspect of the larynx. **B:** Transverse sonogram of the larynx taken through the thyroid cartilage at expiration. Ventral is at the top of the image, and the right side is on the left. The thyroid cartilage is visible as a hyperechoic V-shaped line (arrowheads). The rima glottis is the air-filled space (asterisk) between the hyperechoic vocal ligaments (VL). Dorsal to the VL, the cuneiform processes of the arytenoid cartilages appear as hyperechoic dots (CP). The vocal muscles (M) are hypoechoic and fill the space between the ligaments and the thyroid cartilage on either side. **C:** Transverse image of the canine larynx taken during inspiration. The cuneiform processes move in abduction in inspiration (arrows) and in adduction in expiration (compare with B).

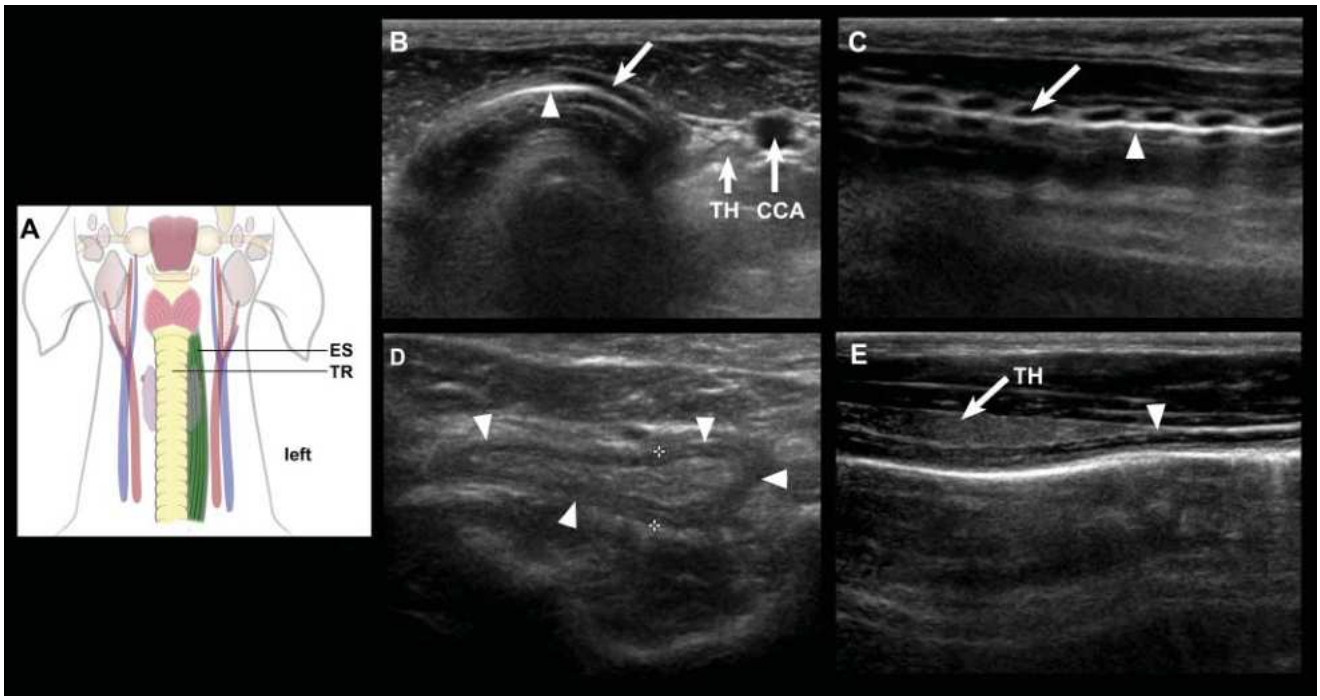


Figure 3.5. Normal trachea and esophagus of a dog. A: Illustration of the anatomical location of the trachea (TR) and esophagus (ES) in the canine neck. **B, C:** Transverse **(B)** and longitudinal **(C)** sonographic images of the trachea. The rings (arrows) are hypoechoic and delineated axially by the hyperreflective gas interface (arrowheads). TH, left thyroid gland; CCA, left common carotid artery. **D, E:** Transverse **(B)** and longitudinal **(C)** sonographic images of the esophagus (arrowheads). The muscularis, submucosa, and mucosa are hypoechoic, hyperechoic, and hypoechoic, respectively. In the longitudinal plane **(E)**, there is gas in the lumen causing a hyperechoic linear interface deep to the external wall (arrowhead).

The lumen of the esophagus may contain a small amount of gas and mucus (Figure 3.5D) and may have a star shape in transverse orientation. In sagittal orientation, the muscularis layer is visible as a hypoechoic band superficially, and gas or fluid may be seen in the lumen (Figure 3.5E). The esophagus can be seen dorsal to the left common carotid artery and left thyroid gland (Figure 3.5E).

Thyroid and Parathyroid Glands

The left and right thyroid lobes lie between the common carotid artery and the trachea and are often positioned at slightly different levels craniocaudally. The sternohyoid and sternothyroid muscles border the gland ventrally, and the esophagus usually borders the left lobe dorsally. To locate the thyroids, place the transducer in a transverse plane centered on the trachea just caudal to the larynx and move it caudally until triangular structures are seen between the trachea and carotid (Figure 3.6A). Each thyroid lobe can also be located separately by sliding the probe lateral to the trachea and following the correspondent common carotid artery on cross-section, which serves as an important landmark. Once a thyroid is located, rotate the transducer 90° to a sagittal plane, keeping the thyroid in the middle of the screen. This motion can be challenging because the thyroid gland is thin. Alternatively, the transducer may need to be angled medially from a parasagittal plane within the jugular furrow.

The thyroid is fusiform in sagittal section with a thicker and more rounded cranial pole, and oval or triangular in transverse section (Figures 3.6B–D, 3.7). Thyroid glands in dogs and cats are normally hyperechoic to isoechoic to the surrounding musculature. The glands are surrounded by a thin hyperechoic capsule, are uniformly echogenic, and have a fine echotexture. Small vessels may sometimes be seen as anechoic structures coursing through the thyroid tissue, which can be confirmed with Doppler ultrasound. Both canine and feline thyroids can be imaged by using a 10- to 13-MHz transducer for best resolution. Cats may also occasionally have ectopic thyroid tissue located in the caudal cervical region or cranial mediastinum.

Thyroid volume can be estimated by measuring the length, width, and height of the gland, and using the formula $\pi/6$ (length × width × height) to calculate volume. The thyroid gland volume is better correlated

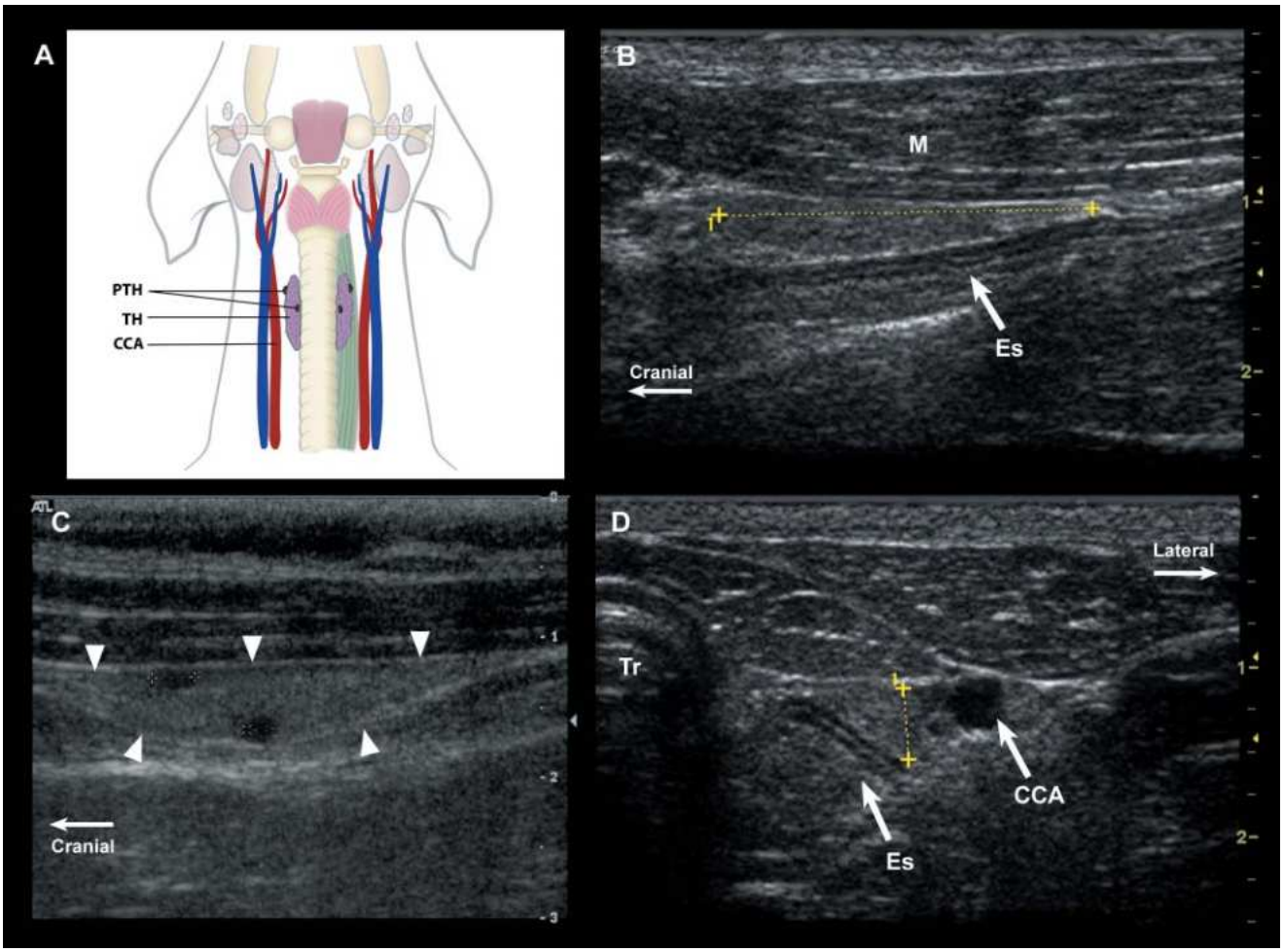


Figure 3.6. **Normal thyroid and parathyroid glands in dogs. A:** Illustration of the anatomical location of the thyroid and parathyroid glands in the canine neck. **B, C:** In these sagittal sonographic images, the normal canine thyroid (cursors in B and arrowheads in C) is fusiform to elliptical and hyperechoic to the surrounding musculature (M) and esophageal (Es) wall. **D:** The normal left thyroid (calipers) in transverse section between the trachea (Tr) and carotid artery (CCA), and adjacent to the esophagus (Es).

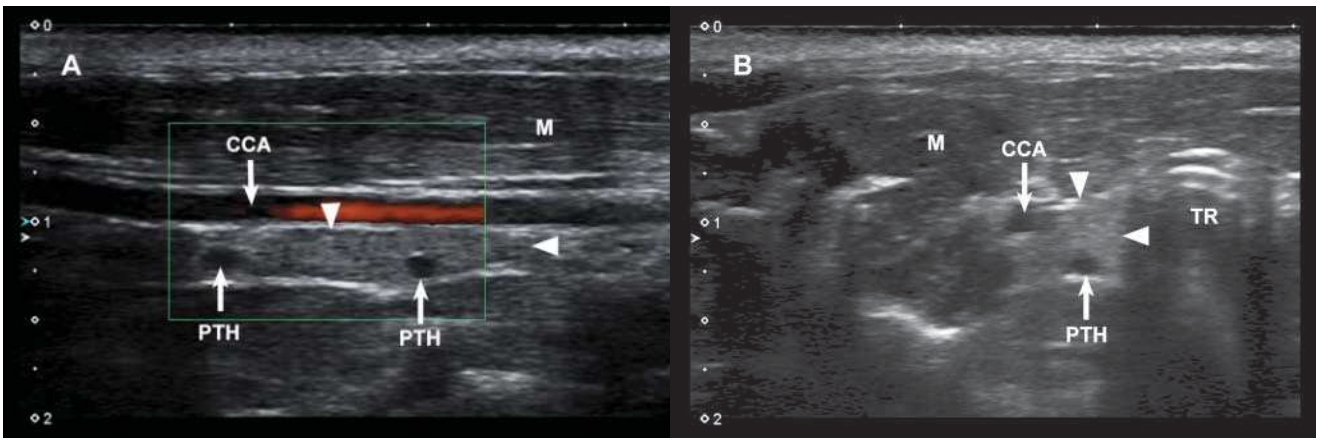


Figure 3.7. **Normal thyroid and parathyroid glands in a 9-year-old cat.** The right thyroid gland (arrowheads) is fusiform in the longitudinal plane **(A)** and triangular to oval in the transverse plane (**B**). The common carotid artery (CCA) is nearby and serves as a useful landmark for localization. Two parathyroid (PTH) glands appear as well-defined spherical to oval structures that measure 1 mm in this cat, located cranially and caudodorsally, respectively. M, muscles; TR, trachea.

with body weight and body surface area than with breed. There is more intraobserver variability in measuring the length of the glands because they taper caudally and the distal limit may be difficult to define (Table 3.1) (Taeymans et al. 2005).

On average, there are two parathyroid glands associated with each thyroid lobe, making a total of four. One is located at the cranial aspect of each thyroid lobe (external glands) and one within the thyroid gland parenchyma (internal glands) (Figure 3.6A,C). However, there is significant normal individual variation in both parathyroid numbers and distribution. Normal parathyroid glands are usually well margined, hypoechoic to anechoic, and less than 2 mm in diameter and 3.3 mm long (Reusch et al. 2000; Wisner et al. 2002) (Figures 3.6C, 3.7). All parathyroid glands are not always visible in normal dogs or cats. Thyroid lobules surrounded by connective tissue are similar in position and appearance to parathyroid glands (Liles et al. 2010) and may be mistaken for parathyroid tissue.

External Ear Canal and Tympanic Bullae

The external ear canal and tympanic bulla are best imaged with a curvilinear transducer of medium frequency (5–8 MHz) with a small footprint. The contact area for imaging these structures is small, and a higher-frequency linear transducer is often too large to position evenly on the skin. In addition, the bone of the tympanic bulla absorbs the ultrasound beam, and higher frequencies may not penetrate the bullae wall adequately to generate an image of the lumen (Dickie et al. 2003).

The external ear canal and bulla are imaged from both a lateral approach and a ventral approach (Figure 3.1B,C), with the patient in sternal, seated, or lateral recumbency. The tympanic bulla and cross-section of the external ear canal are visible as a curvilinear hyperechoic line filled with air, producing a reverberation artifact (Figure 3.3E, F). In a transverse plane with respect to the head, the external ear canal appears in a longitudinal orientation. The ear canal lies just caudal to the zygomatic arch, with the masseter muscle lateral to the arch and the sternocephalicus muscle and parotid salivary gland caudal to it (Figure 3.3F). The parotid salivary gland appears mildly echogenic to hypoechoic to the more superficial subcutaneous fat and hyperechoic to the muscles. The horizontal portion of the ear canal is imaged from a ventral position in either a longitudinal or a transverse orientation. From the longitudinal position, the transducer can be rotated slightly to view the tympanic bulla and external ear canal in the same image.

The tympanic bulla itself is composed of thin bone and is filled with air. The normal bulla wall appears as an echogenic convex line, and the air within it causes a reverberation artifact and shadow deep to the bone margin. The bone is thin enough that the ultrasound beam penetrates it, and therefore within the bulla cavity the presence of soft tissue or fluid caused by a middle ear disorder can be identified.

The maxillary artery can be identified with color Doppler caudally and laterally to the tympanic bulla at the junction of the external ear canal and the bulla.

Tongue

The tongue is attached to the paired mylohyoid and geniohyoid muscles that are attached to the ramus of the mandible and the hyoid apparatus. The mylohyoid originates from the medial side of the mandible, and the geniohyoid from the ramus of the mandible. Both muscles attach to the basihyoid bone caudally. The tongue is hyperechoic to the supporting musculature and is best approached ventrally in between the rami of the mandible with the dog positioned in dorsal recumbency (Figure 3.8).

Sonographic Features of Neck Disorders

Vessels

Abnormalities involving the carotid artery and jugular veins may include thrombosis in hypercoagulable animals (e.g., hyperadrenocorticism and protein-losing nephropathy) and may be a complication of catheter placement. The acute thrombus may be anechoic and is recognized only by a flow void in the color Doppler signal. More chronically, the thrombus becomes more echogenic and visible in B-mode imaging. Stenosis of these vessels can occur as a complication of surgery, trauma, or invasive neoplasia. Stenosis appears as a narrowing of the vessel lumen, typically with increased velocity in the center of the stenosis and turbulent flow beyond the stenosis.

Carotid-body tumors are rare neuroendocrine tumors that arise from the pressure sensors in the carotid artery. Older brachycephalic breeds may be predisposed to developing chemodectomas. Chronic hypoxia and overstimulation of the carotid bodies caused by brachycephalic syndrome may contribute to the increased prevalence of disease in these breeds. On ultrasound examination, these tumors are located at the bifurcation of the common carotid artery into the internal and external carotid arteries, dorsolateral

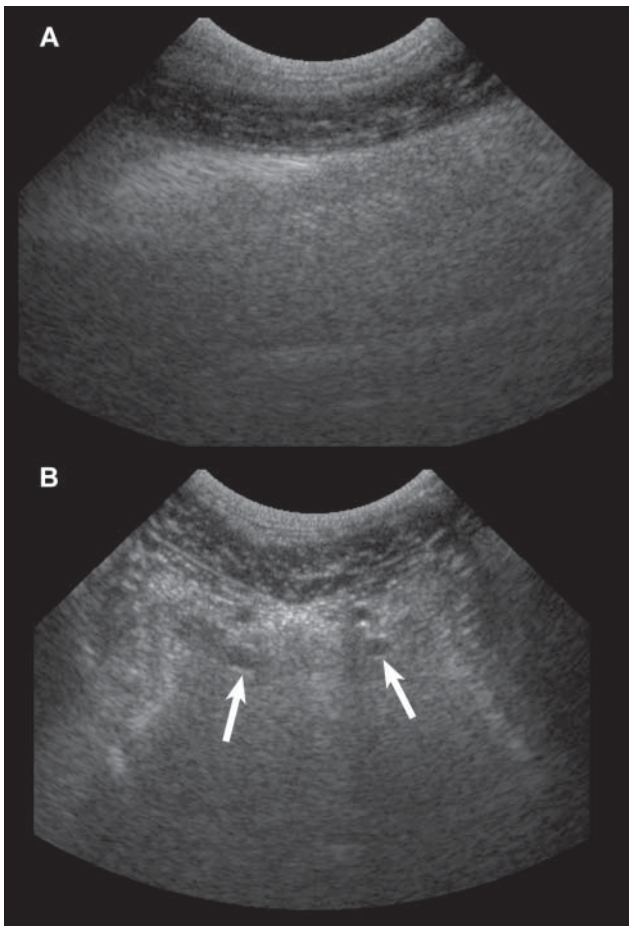


Figure 3.8. Transverse and parasagittal images of the canine tongue. A: The muscle of the tongue is hyperechoic to the more ventral geniohyoid and mylohyoid muscles. In parasagittal orientation, the fibers have a diagonal pattern. **B:** In transverse orientation, the round hypoechoic structures (arrows) represent the lingual and sublingual veins. The lingual muscles have a butterfly shape.

to the larynx (Figure 3.9). Tumors may surround the common carotid artery and its branches and are generally highly vascular. They are typically hypoechoic to surrounding tissues, lobulated, and well marginated, and can easily be confused with (ectopic) thyroid masses (Wisner et al. 1994; Fife et al. 2003; Taeymans et al. 2012) (Figure 3.15). Fine-needle aspirates should be performed with caution, considering the vascularity and proximity of major vessels.

Any invasive tumor, such as thyroid carcinoma, can cause local distortion of the vasculature. Invasion of the common carotid artery can cause erosion of the wall and massive hemorrhage (Slensky et al. 2003). Local vessels may be infiltrated by the neoplasia (Figure 3.10), recruited into the tumor, compressed, or thrombosed. Other small vessels may also distend to supply the mass. Tumors of the caudal neck and

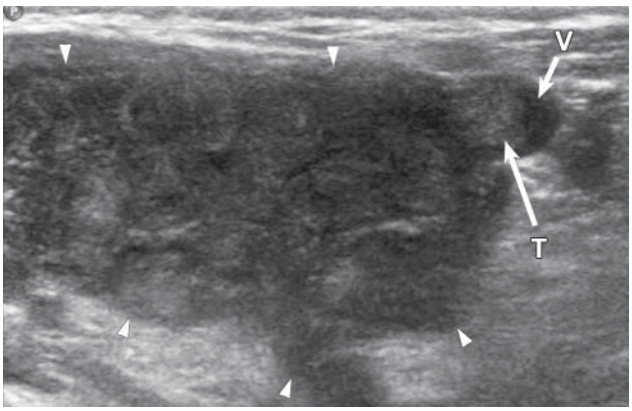


Figure 3.10. Venous invasion and thrombosis in a dog. Transverse image of a thyroid carcinoma. A large, ill-defined, hypoechoic mass (arrowheads) has replaced the thyroid gland. The tumor thrombus (T) continued into the thyroid vein (V).

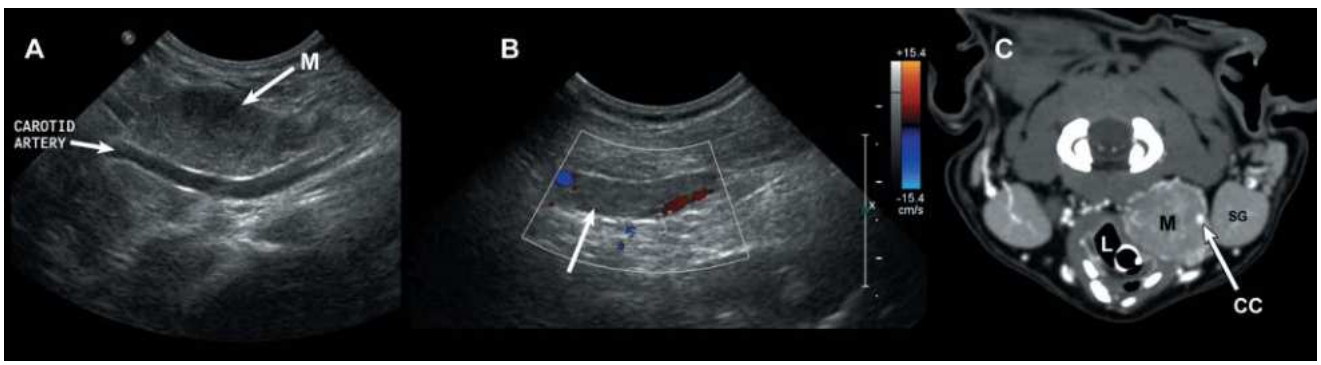


Figure 3.9. Chemodectoma in a 10-year-old dog. Sagittal B-mode **(A)** image of a neck mass, and sagittal color Doppler **(B)** of the neighboring external jugular vein. A smooth, well-circumscribed mass (M) of low echogenicity is noted ventral to the common carotid artery. A moderately echogenic thrombus (arrow) fills most of the external jugular vein. **C:** Transverse contrast-enhanced computed tomography (CT) image of the mass (M) demonstrating the characteristic position surrounding the carotid artery (CC) of a mass arising from the carotid body, and the marked vascularity of the mass. The adjacent larynx (L) is compressed. SG, mandibular salivary gland.

thoracic inlet may also invade local vessels or cause thrombosis. Thrombosis may be visible as an intraluminal heterogeneous structure, either partially or fully filling the lumen, or in the acute phase may not be visible. The use of Doppler ultrasound may demonstrate a void in flow in the vessel lumen that identifies the presence of a thrombus. If the cranial vena cava is thrombosed, distended, or occluded, veins may be seen more cranially. Obstruction of venous flow may also cause subcutaneous edema of the head and neck, which will appear as hyperechoic bands interlaced with anechoic fluid layers.

Arteriovenous fistula in association with a recurrent thyroid carcinoma has been reported in the neck (Wisner et al. 1994). These abnormal connections between the arterial system and the venous system often have multiple tortuous vessels with arterial flow characteristics. The local veins may be distended and subcutaneous edema may develop.

Cervical masses such as lymphoma and thyroid carcinoma may also involve the vagosympathetic trunk, causing Horner's syndrome (Melian et al. 1996) and laryngeal paralysis (Schaer et al. 1979). There is also a single report of a neoplastic mass originating from the vagus nerve (Ruppert et al. 2000).

Salivary Glands

Disorders that affect the salivary glands include true cyst, sialolith, sialoadenitis (Figure 3.11), sialocele/mucocele (Figure 3.12A), salivary duct cyst (Figure 3.12B), and neoplasia.

Most of these conditions are rare in dogs and cats. Localization of the lesion is based on the anatomical site and surrounding landmarks. Common findings in inflammatory or obstructive disease include enlargement and decreased echogenicity of the gland. The salivary ducts may be enlarged and fluid-filled when obstructed, and occasionally a focal shadowing sialolith is visible within the duct lumen. Zygomatic sialadenitis causes enlargement and the appearance of a retrobulbar mass of variable echogenicity (Cannon et al. 2011). Sialoceles may be associated with sialadenitis. Edema or steatitis may appear as hypoechoic or hyperechoic regions in the surrounding tissues. Sialoceles are thin-walled, fluid-filled structures with anechoic to echogenic contents. These can be difficult to trace to the origin from the salivary gland.

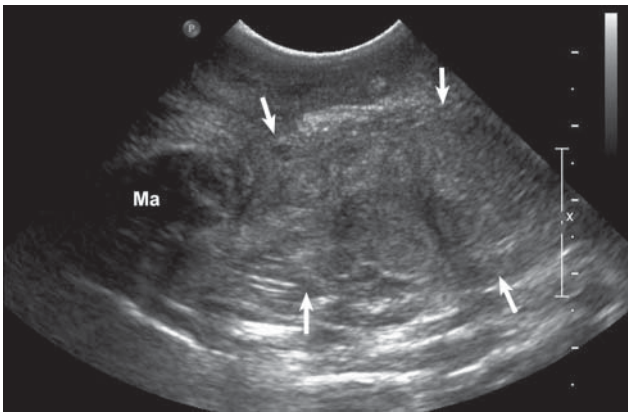


Figure 3.11. Sialoadenitis in a dog. On this sagittal image, the right mandibular gland is rounded, hypoechoic, mildly heterogeneous and enlarged (arrowheads), just caudal to the mandible (Ma).

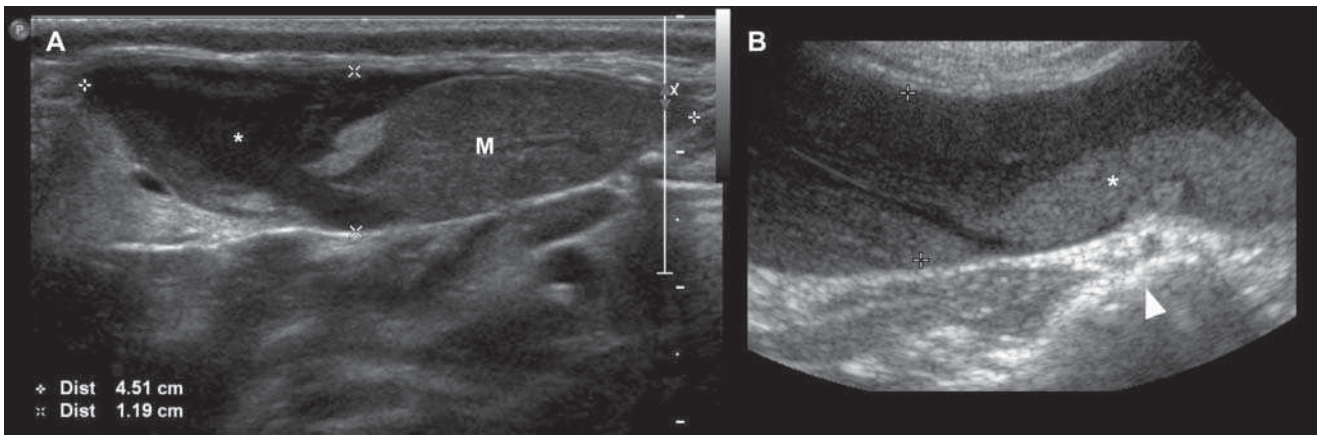


Figure 3.12. Sialocele in a dog. A: large cyst (asterisk) expands the cranial margin of the mandibular salivary gland (M, cursors). **B:** Salivary duct cyst in a cat. On this sagittal image, a well-demarcated, fluid-filled structure is ventral and lateral to the mandible (arrowhead). The cyst (between cursors) contains hyperechoic sedimenting debris (asterisk).

Neoplasms of the salivary gland may disrupt the normal capsule and normally uniform echogenicity. Cystic lesions, nodular lesions, and enlarged salivary glands can be aspirated to determine their origin.

Lymph Nodes and Soft Tissues

Enlarged mandibular, retropharyngeal, or cervical lymph nodes may be caused by local inflammation, tumoral infiltration, or regional metastatic disease. Tumors of the mouth often metastasize to the mandibular lymph nodes. Lymph nodes affected by inflammatory or neoplastic disease are enlarged, rounded, and hypoechoic (Figure 3.13B–D). The margins of the lymph nodes can be indistinct if there is local inflammation.

Cavitation can also occur in reactive nodes because of abscessation and in metastatic nodes because of

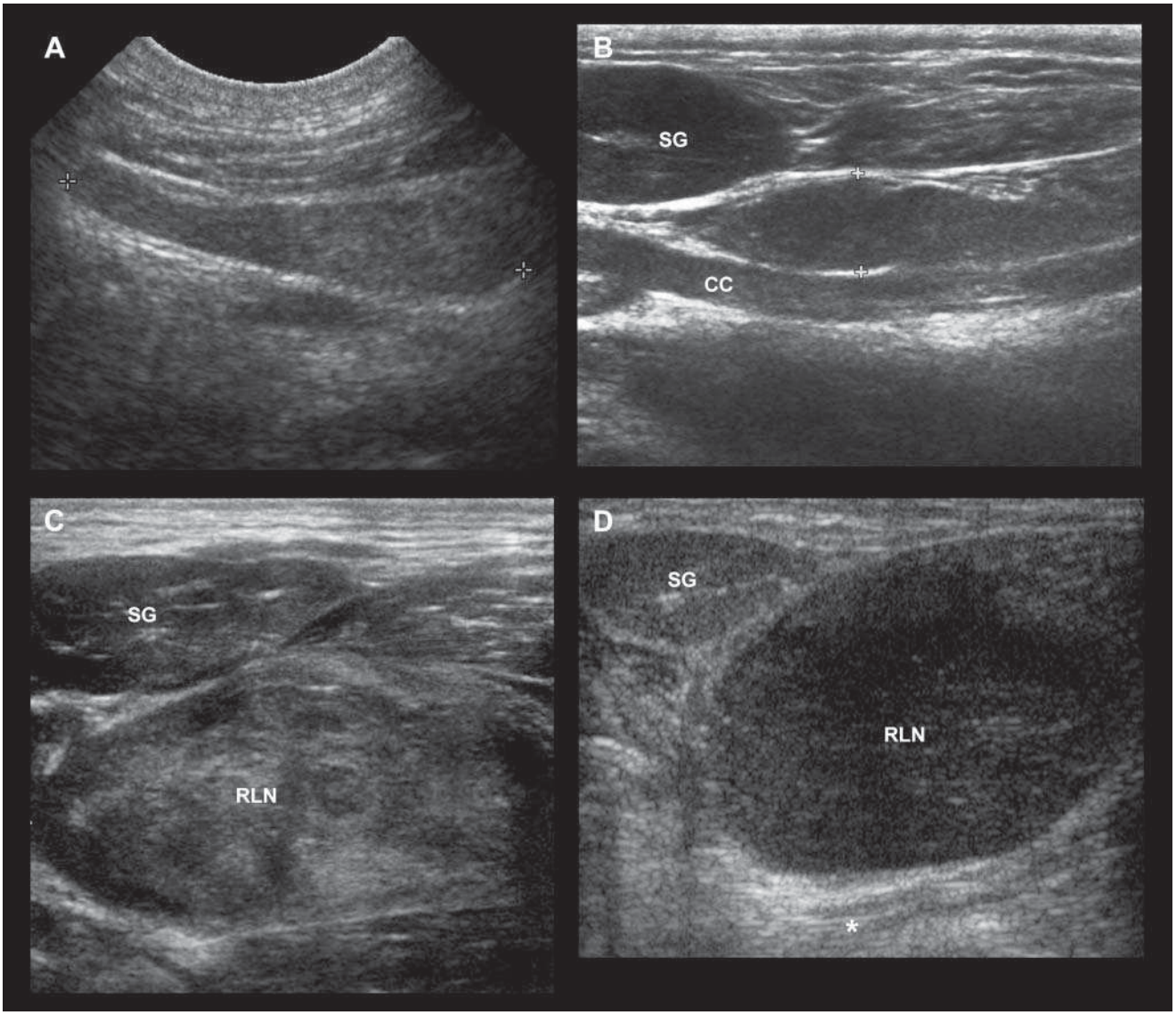


Figure 3.13. Mandibular and medial retropharyngeal lymphadenopathy in different dogs. A: Sagittal image of a normal left mandibular lymph node (calipers). It is oval and slightly hypoechoic to the surrounding tissues. **B:** Sagittal image of a reactive retropharyngeal lymph node (calipers) in another dog. It is hypoechoic and rounded, with a margin that is homogeneous in echotexture and slightly irregular. CC, common carotid artery, SG, mandibular salivary gland. **C:** Sagittal image of an enlarged retropharyngeal lymph node (RLN) with metastatic disease in another dog. The lymph node is slightly inhomogeneous and has irregular contours. **D:** Sagittal sonographic images of markedly enlarged, rounded and hypoechoic medial RLN in a dog with lymphoma. The normal SG is just cranial to the much larger medial RLN. Note the speckled echotexture in the superficial cervical nodes that are not normally seen in dogs. There is also distal acoustic enhancement deep to the lymph nodes (asterisk).

hemorrhage and necrosis. Metastatic lymph nodes can also be hypoechoic or heterogeneous without enlargement. They tend to become rounder and thicker from their normal oval or elongated shape. Reactive and metastatic lymph nodes appear very similar, and fine-needle aspiration is generally needed for a diagnosis.

Lymphoma causes generalized peripheral lymphadenopathy in dogs, but rarely in cats. Affected lymph nodes of the head and neck are enlarged and hypoechoic to nearly anechoic. The nodes may have indistinct margins and disrupted internal architecture. In dogs with lymphoma, the cervical and mandibular lymph nodes enlarge to a lesser degree than the retropharyngeal lymph nodes (Figure 3.13D). These hypoechoic lymph nodes may also have distal acoustic enhancement and be surrounded by hyperechoic tissue. The distal enhancement can cause the nodes to be confused with anechoic cysts.

Other cervical masses that are non-lymphoid, thyroid, or parathyroid in origin, such as lipomas, hemangiosarcomas, fibrosarcomas, hematomas, and abscesses, can be found in the neck and may appear solid, cystic, or complex (Gooding et al. 1977). Neoplastic masses are usually solid or complex, and hematomas are complex or cystic. Acutely, hematomas appear as hypoechoic masses with a hypoechoic center. With time, septations can develop, echogenicity increases, and a capsule may form (Wisner et al. 2002). Hematomas should become smaller with time. Lipomas are usually well marginated, elliptical, and striated and hyperechoic to the surrounding musculature. However, lipomas can be infiltrative and poorly defined. Interfascial planes or muscles can be infiltrated.

Penetrating wounds from the skin or esophagus, with or without foreign bodies, may cause diffuse or localized cellulitis of the soft tissues of the neck (Figures 3.14–3.16). Edema can be seen dissecting between fascial planes or within the subcutaneous fat as anechoic or hypoechoic areas separated by thin hyperechoic septa (Figure 3.15C). Inflamed fatty tissues are often thickened, hyperechoic, and hyperattenuating (Figure 3.15D). Abscesses are often septated, with a thick wall and echogenic fluid contents (Figures 3.15A, 3.16 and 3.17B). They can mimic neoplasia. Foreign bodies can be challenging to identify. Their detection is greatly influenced by their acoustic characteristics and their size, location, and shape (Figures 3.14A, 3.16A,B). Cystic lesions are rare and usually thyroid or branchial in origin (Wisner et al. 2002).

Larynx, Trachea and Esophagus

Neoplasia (Figure 3.18), trauma, inflammation (Figure 3.19), and cysts can affect the larynx and paralaryngeal structures. The most common neoplasia

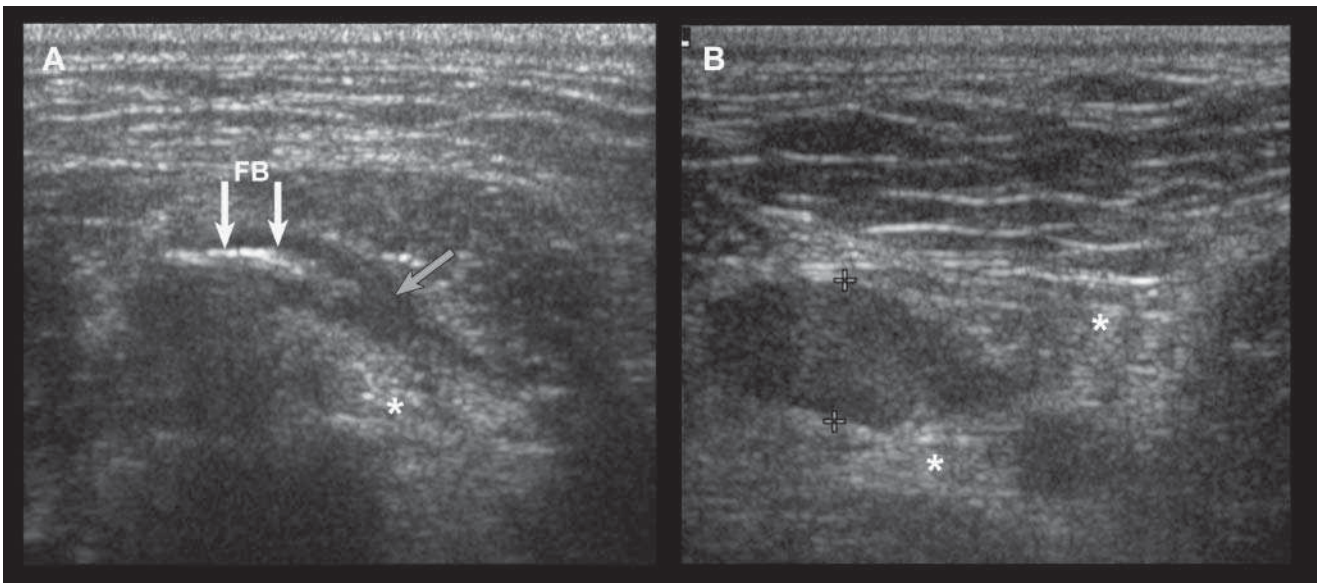


Figure 3.14. **Migrating plant foreign body in a dog. A:** Transverse image taken between the mandibles from a ventral position. There is an fusiform hypoechoic region of tissue (gray arrow) surrounding a triangular hyperechoic grass awn (FB) in the soft tissues of the neck. The hypoechoic tissue may be edema or pus, or a cast of fibrous or pyogranulomatous tissue, and the hyperechoic tissue deep to this reaction is inflamed (*). **B:** The nearby mandibular lymph nodes are reactive. They are mildly enlarged (calipers) and uniformly hypoechoic, with surrounding hyperechoic fat (*).

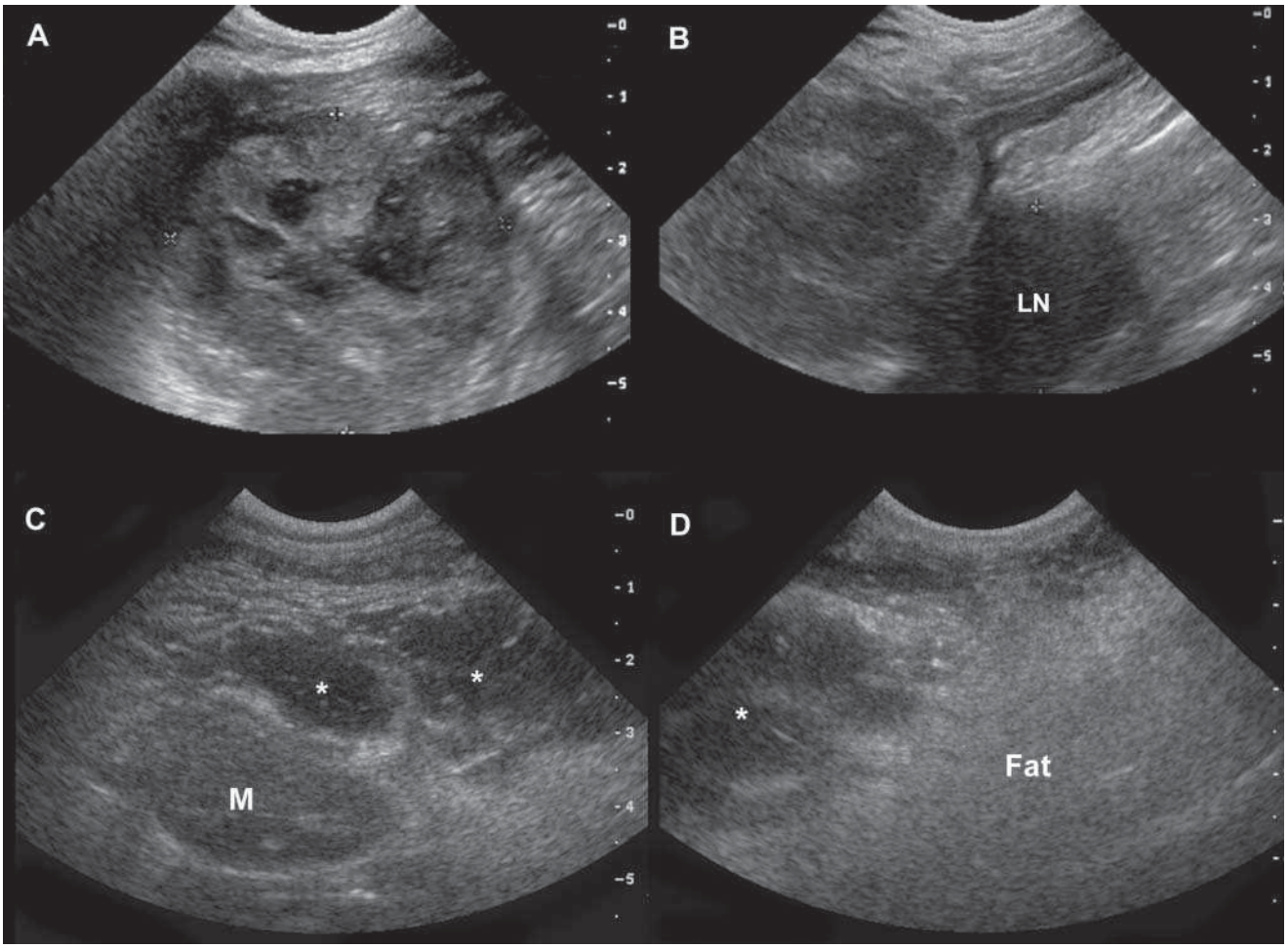


Figure 3.15. **Septic suppurative cellulitis and abscess formation in two dogs. A, B:** Sagittal images of the cranioventral neck in an 11-year-old Irish Setter, on which a multicavitated mass measuring about 4.5 × 6 cm is caudoventral to the larynx. A local lymph node is enlarged and hypoechoic (LN). **C, D:** Sagittal images obtained in another large-breed dog with a history of neck pain and swelling and inappetence. The subcutaneous fat is swollen and presents several hypoechoic, septated cavities (*) located caudal to one of the mandibular (M) salivary glands. The neighboring fat is hyperechoic and hyperattenuating. The presence of serohemorrhagic fluid and pus was confirmed by fine-needle aspirations.

of the larynx in cats is lymphoma, and in dogs is malignant epithelial neoplasia (Carlisle et al. 1991). These tumors can appear as masses in the laryngeal wall and may also distort or obliterate the normal laryngeal structures. Lymphoma in cats appears as a well-circumscribed, hypoechoic or mixed echogenic mass arising from the ventral or lateral larynx (Figure 3.18C,D). The mass may narrow the lumen of the larynx or displace the larynx to the side. Squamous cell carcinoma may appear more destructive and occurs in the ventral larynx, as well as on the vocal cords. Laryngeal cysts have been reported infrequently in dogs and cats and may originate from the epiglottis, laryngeal wall, or paralaryngeal tissues. They are seen as anechoic masses distorting the rima glottis.

Laryngeal paralysis, which is a neuropathy of the recurrent laryngeal nerve, causes unilateral or bilateral paralysis of the vocal folds. Ultrasound can be used to evaluate the motion of the vocal folds and cuneiform cartilages to diagnose the condition. The criterion for diagnosing laryngeal paralysis is reduced or asymmetrical motion of the vocal folds. This appears as lack of abduction of the cuneiform cartilages and vocal folds during inspiration on one or both sides (Figure 3.20). Approximately 50% of dogs with laryngeal paralysis have abnormal dorsal and ventral movement of the arytenoid cartilages that is caused by the unaffected contraction of the cricothyroid muscle (Rudorf et al. 2001). Signs of severe upper airway obstruction include collapse of the pharynx during inspiration, paradoxical movement of the vocal folds

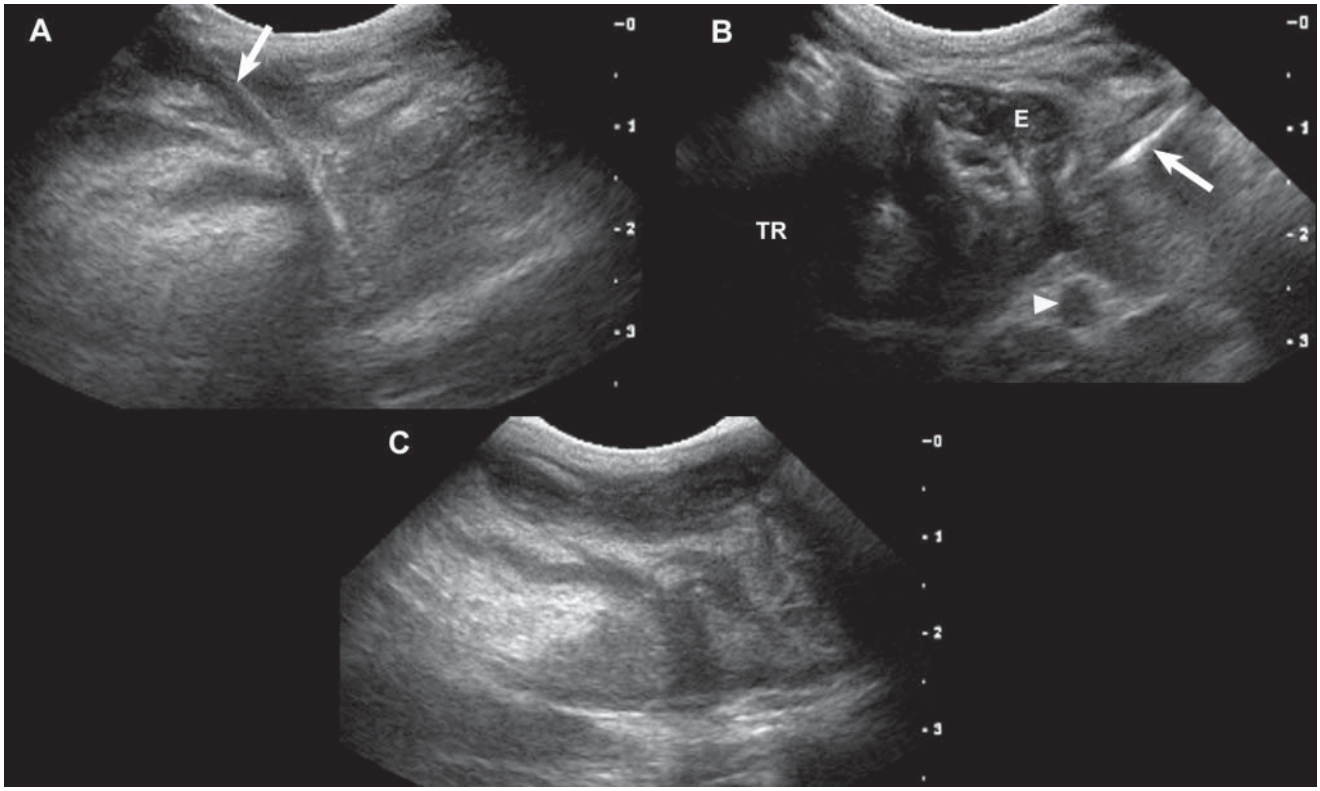


Figure 3.16. **Sewing needle and associated cellulitis in a dog. A:** The needle (arrow) appears as a discrete hyperechoic line surrounded by a poorly marginated hypoechoic area representing extensive cellulitis and edema. **B:** The needle tip (arrow) is close to the esophagus (E) and the carotid artery (arrowhead). TR, trachea. **C:** Hypoechoic arborization through the superficial and deep cervical soft tissue is noted and is often seen in abscess formation, dissecting cellulitis, and edema.

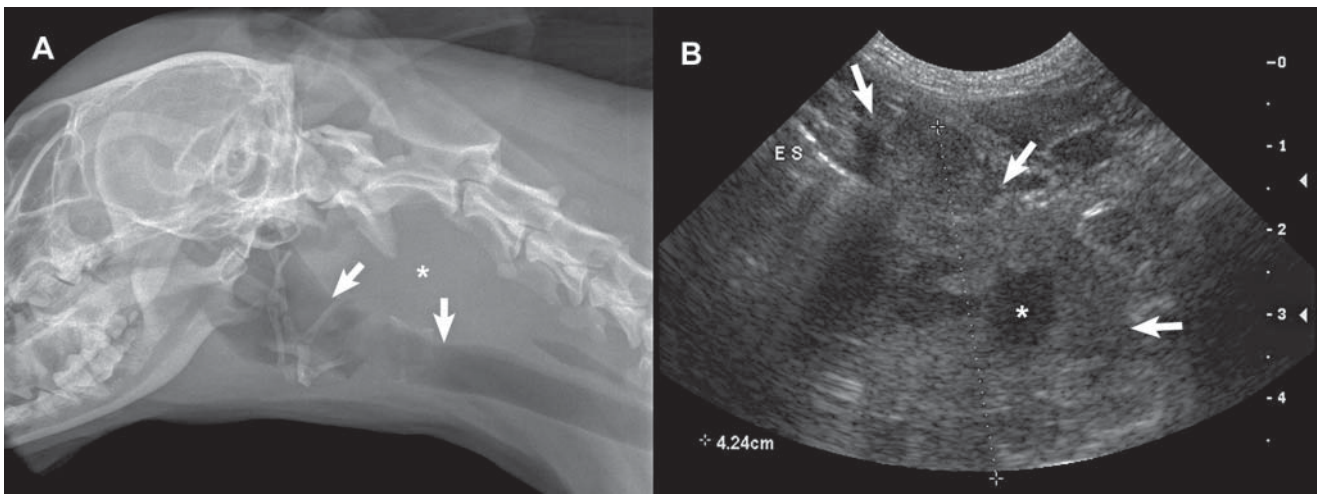


Figure 3.17. **Retropharyngeal abscess in a dog. A:** Lateral oblique radiograph of the head and neck of a dog with a history of difficulties in swallowing and of neck pain. A soft-tissue mass effect (asterisk) is in the retropharyngeal region, causing ventral displacement of the nasopharynx, larynx, and trachea (arrows). **B:** Transverse sonogram in the region of the mass. A large, irregular, moderately echogenic mass (arrows) is lateral and caudal to the esophagus (ES). This mass has a thick wall encircling an irregular cavity filled with echogenic fluid. Fine-needle aspirations and surgical biopsies confirmed the presence of a sterile, pyogranulomatous abscess of uncertain origin.

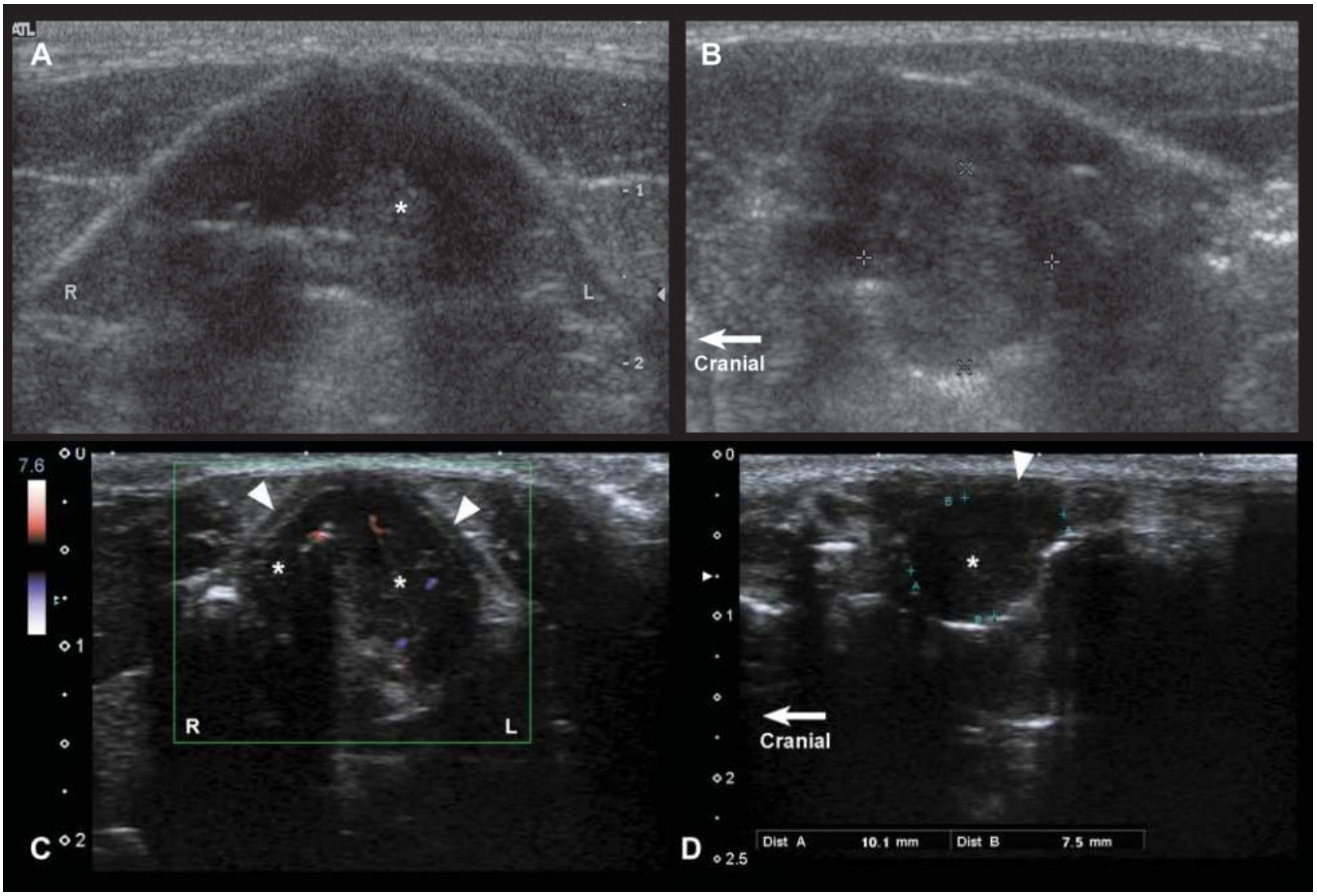


Figure 3.18. **Laryngeal neoplasia. A:** Transverse image of the larynx through the thyroid cartilage. An ill-defined soft tissue mass (asterisk) is within the left (L) side of the lumen of the larynx, corresponding to a melanoma in a dog. R, right. **B:** In left sagittal orientation, the mass is better delineated (calipers) originating from the left laryngeal wall. Cranial is to the left side of the image. **C, D**: Transverse and sagittal sonographic images of a laryngeal lymphoma in cat. The hypoechoic mass (*) invades both vocal folds, particularly on the left side, filling most of the laryngeal lumen at that level. The outside wall (arrowheads) of the larynx remains distinct. Note the vascularity of the mass in power Doppler mode, helping to distinguish it from fluid.

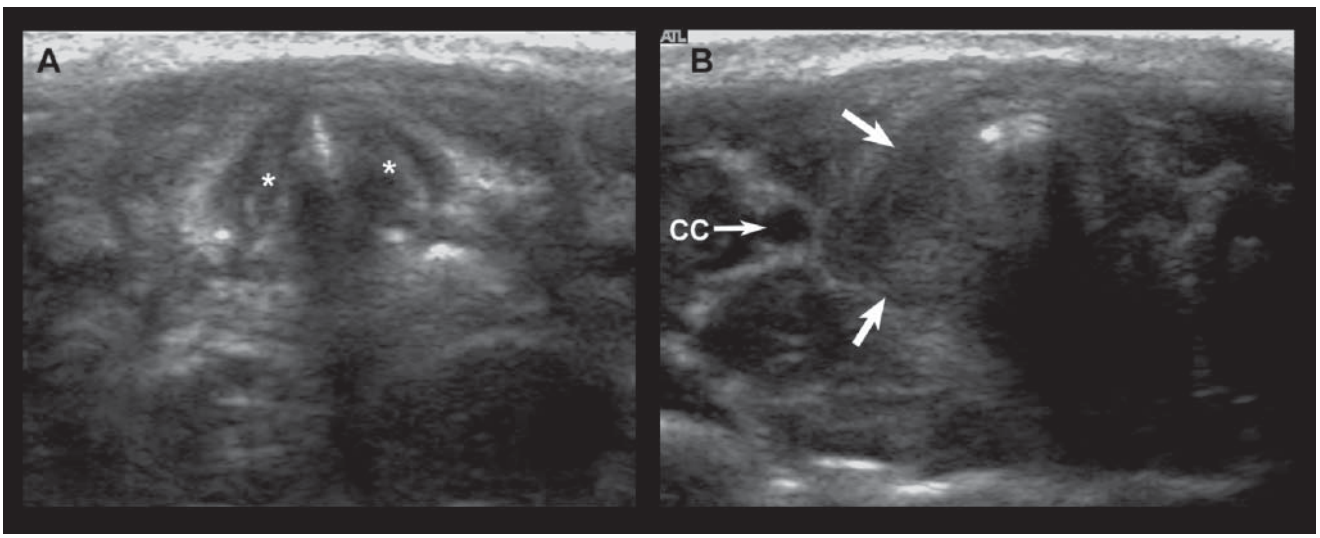


Figure 3.19. **Lymphofollicular laryngitis in a cat. A:** Transverse image of the larynx with the right side on the left of the image. The vocal folds (*) appear normal at this level. **B:** Just caudal to the vocal folds is a lobulated, hypoechoic mass (arrows) involving the right side of the larynx and trachea, in contact with the right common carotid artery (CC).

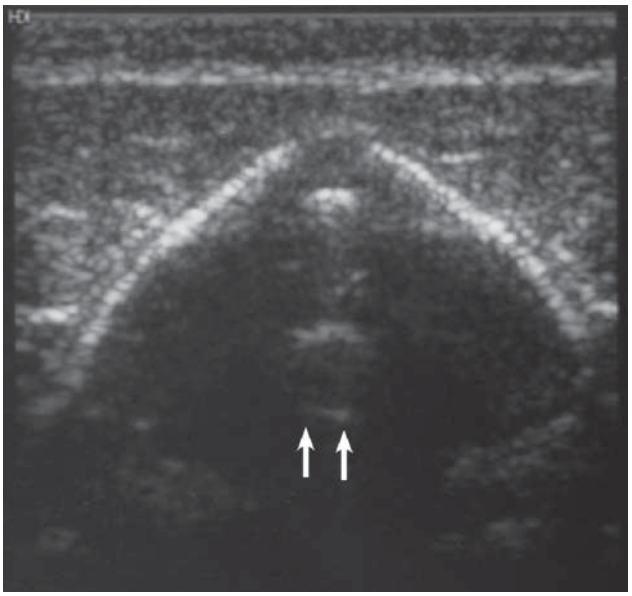


Figure 3.20. Laryngeal paralysis in a dog. The cuneiform processes of the arytenoid cartilage (arrows) fail to abduct during inspiration.

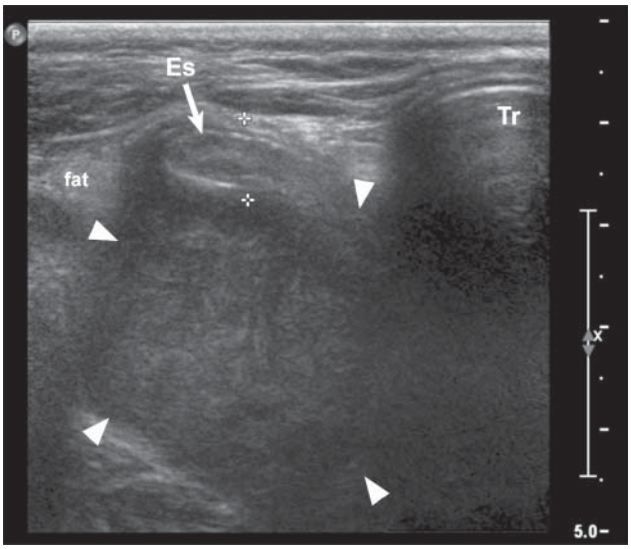


Figure 3.21. Paraesophageal abscess in a dog. The abscess appears as a large, mildly echogenic mass (arrowheads) dorsal to the esophagus (Es, between calipers), associated with regional hyperechoic fat. The cellular fluid mimics a solid soft tissue mass. Tr, trachea.

(blowing laterally during expiration), and caudal displacement of the whole larynx.

Laryngeal paralysis and vocal cord thickening have been reported in cats. Vocal cord thickening can be caused by inflammation, edema, or neoplasia. The anatomy and motion of the cuneiform cartilage are similar to those of dogs, but the smaller size of the feline larynx can cause incomplete visibility of the vocal folds.

In dogs with tracheal collapse, the hyperechoic air column appears oval to flat, depending on the severity of the collapse (Rudorf et al. 1997). The dorsal tracheal membrane is not visible directly, but this alteration in shape of the air column is indicative of redundancy. The flattening of the air column may worsen slightly with the head in an extended position. Other tracheal lesions such as masses, trauma, or tracheitis and edema may occasionally be seen (see Figure 4.28).

Ultrasonography can be used to identify mass lesions in the cervical esophagus to monitor correct placement of an endotracheal tube or to confirm megaesophagus (Wisner et al. 2002). Other lesions, such as esophageal wall thickening or paraesophageal abscess, can also be detected (Figures 3.21, 3.22).

Thyroid Glands

Hyperthyroidism caused by functional thyroid adenoma or adenomatous hyperplasia is very common in older cats (Mooney 2002). This can manifest as a discrete nodule within the thyroid gland or as diffuse thyroid enlargement with or without areas of cavitation. Ultrasound can be used to measure the volume of the thyroid glands to detect enlargement. Although this is not a functional test, as is nuclear scintigraphy, enlarged glands are indicative of thyroid disease. Both thyroid lobes are affected in 70% of cats (Mooney 2002). Hyperplastic thyroid glands are hypoechoic or isoechoic to surrounding tissue and hypoechoic to normal thyroids. In thyroid adenomas, the glands can be focally or diffusely affected, often with a lobular margin and tubular shape (Figure 3.23). A distinction between the two, however, can often not be made.

Thyroid glands occasionally contain incidental cysts showing distal acoustic enhancement. These cysts can be confused with normal parathyroid glands, which can also appear hypoechoic or anechoic but without distal acoustic enhancement. The cyst may be irregular in shape, but its margin should be visible in both planes. Thyroid and parathyroid neoplasia, such as thyroid cystadenoma and parathyroid adenocarcinoma, can also appear cystic (Phillips et al. 2003; Figure 3.23A,C). In contrast to cats, dogs are more often affected by primary hypothyroidism. On ultrasound examination in one study, hypothyroid lobes were more rounded on transverse imaging, rather than their normal triangular shape (Reese et al. 2005). However, a further study of normal dogs revealed many with a similar transverse shape, making the

Figure 3.23. **Thyroid adenoma in cats. A:** Sagittal image of the right thyroid with a cystic thyroid adenoma. The cranial third of the gland is solid, but its caudal portion is occupied by a cyst filled with anechoic fluid (F). **B:** Sagittal image of the right thyroid with thyroid adenoma. The thyroid lobe is outlined by calipers. The gland is enlarged and rounded, with an irregular border, and is isoechoic to surrounding tissue. **C:** Sagittal image of a thyroid cystic adenoma in a 16-year-old Burmese cat. The lesion is primarily cystic but filled with echogenic fluid mimicking a solid mass.

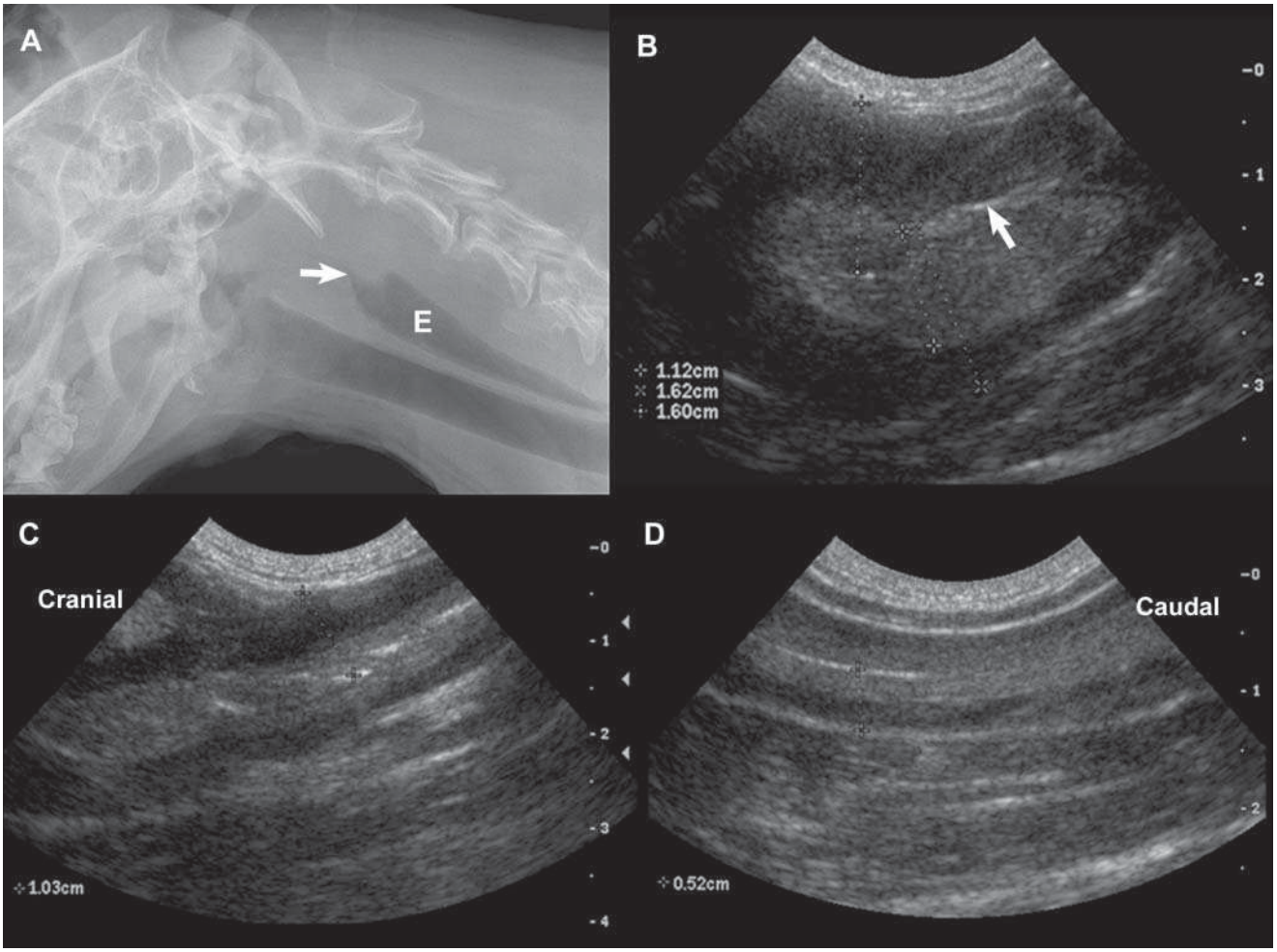


Figure 3.22. **Idiopathic esophageal hypertrophy in a dog. A:** Lateral radiograph of the cranial neck in a dog with chronic swallowing disorder. The esophagus (E) is abnormally dilated with air, and a soft-tissue mass-like projection is noted within its cranial lumen (arrow), in the region of the cricopharyngeal muscle. **B–D:** Transverse **(B)** and sagittal **(C, D)** sonograms of the diffusely and markedly thickened esophagus, involving in particular the muscular layer. The mucosa is hyperechoic and confluent with the submucosa. Cranial and caudal portions of the esophagus are represented in C and D, respectively. The arrow points to the collapsed lumen. Mucosal and muscular hyperplasia and hypertrophy, as well as non-specific inflammation, were diagnosed by means of ultrasound-guided biopsies. There was no evidence of neoplasia.

earlier observation non-specific. Hypothyroid lobes are also hypoechoic and smaller than normal lobes (Figure 3.24). They may be heterogeneous in echotexture and have an irregularly shaped capsule (Bromel et al. 2005; Taeymans et al. 2007).

Thyroid carcinoma is a rare but aggressive neoplasia that affects dogs more often than cats. It often presents at an advanced stage, with the mass involving a large area of the ventral cervical region and distorting local anatomy. This may make localizing the origin of the mass to the thyroid difficult. On ultrasound examination, the mass appears heterogeneous and hypoechoic to normal thyroid tissue, with good to poor margination (Figure 3.25). The trachea and esophagus may be

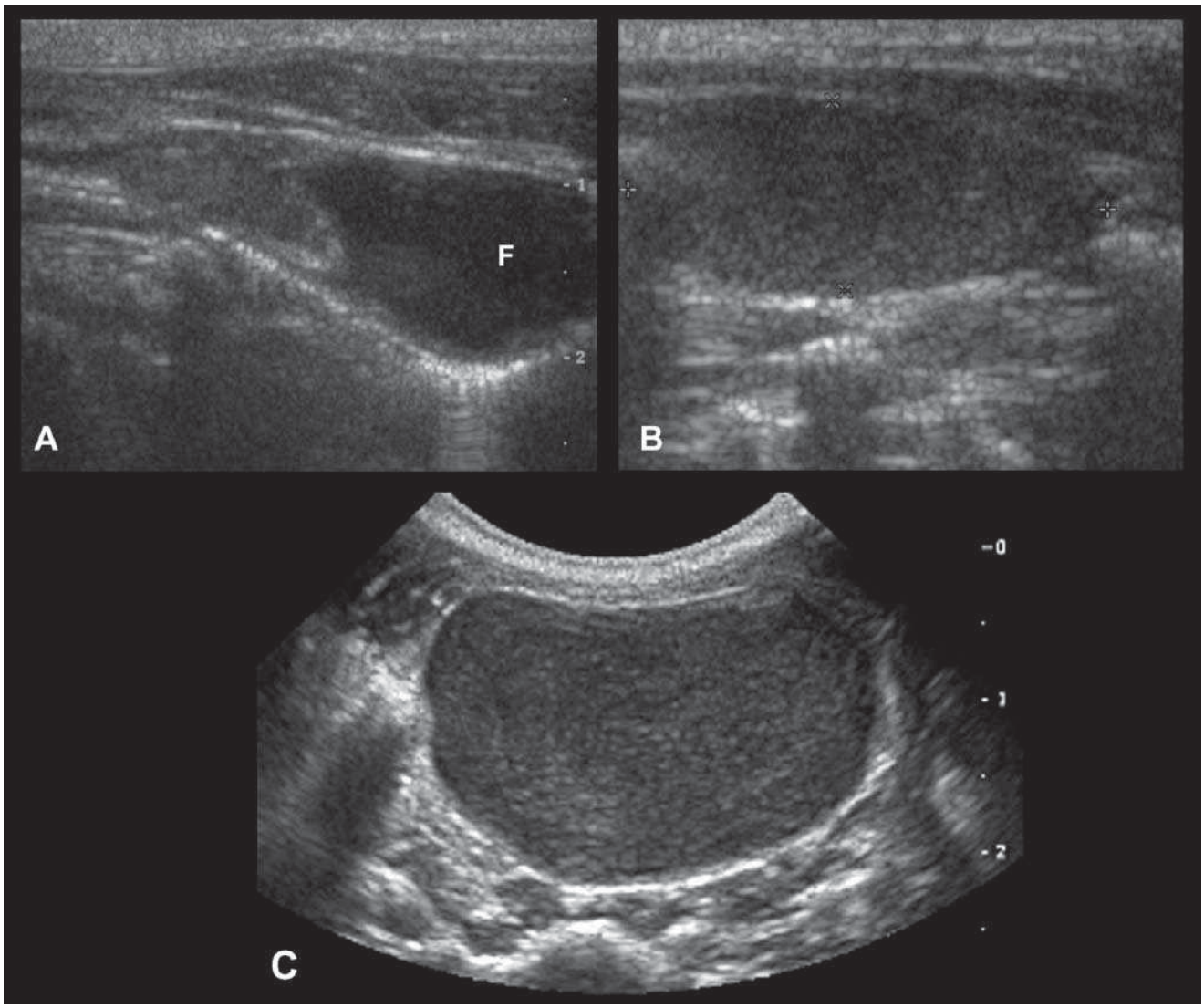


Figure 3.23. **Thyroid adenoma in cats.** (for full caption, see facing page)

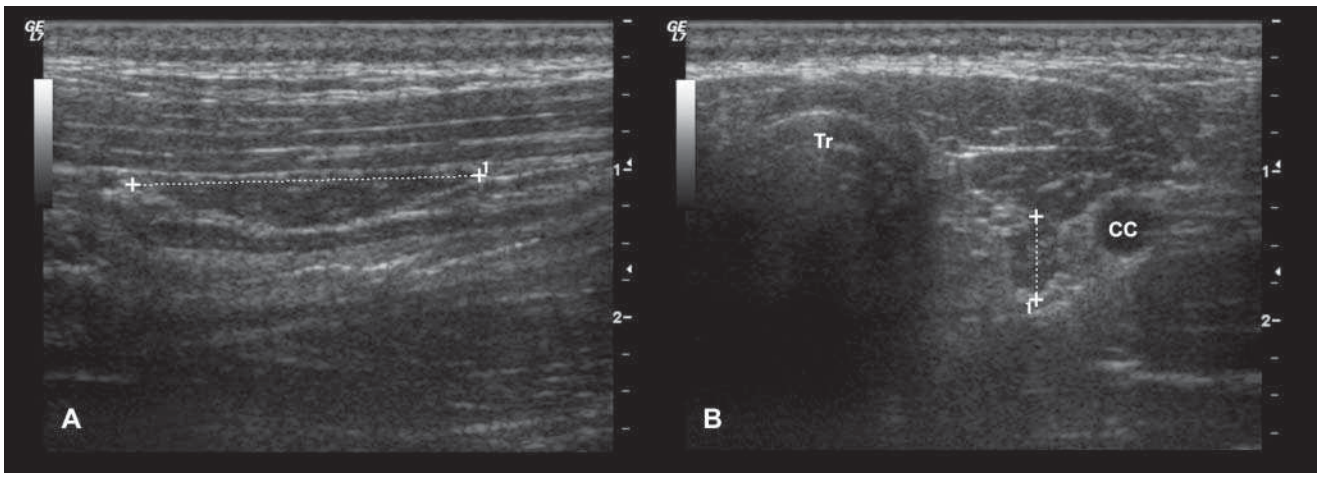


Figure 3.24. **Left thyroid lobe of a dog with hypothyroidism.** Sagittal **(A)** and transverse **(B)** images of the small thyroid lobe outlined by cursors. It is irregular and hypoechoic to the surrounding tissue (arrows). CC, common carotid artery; Tr, trachea.

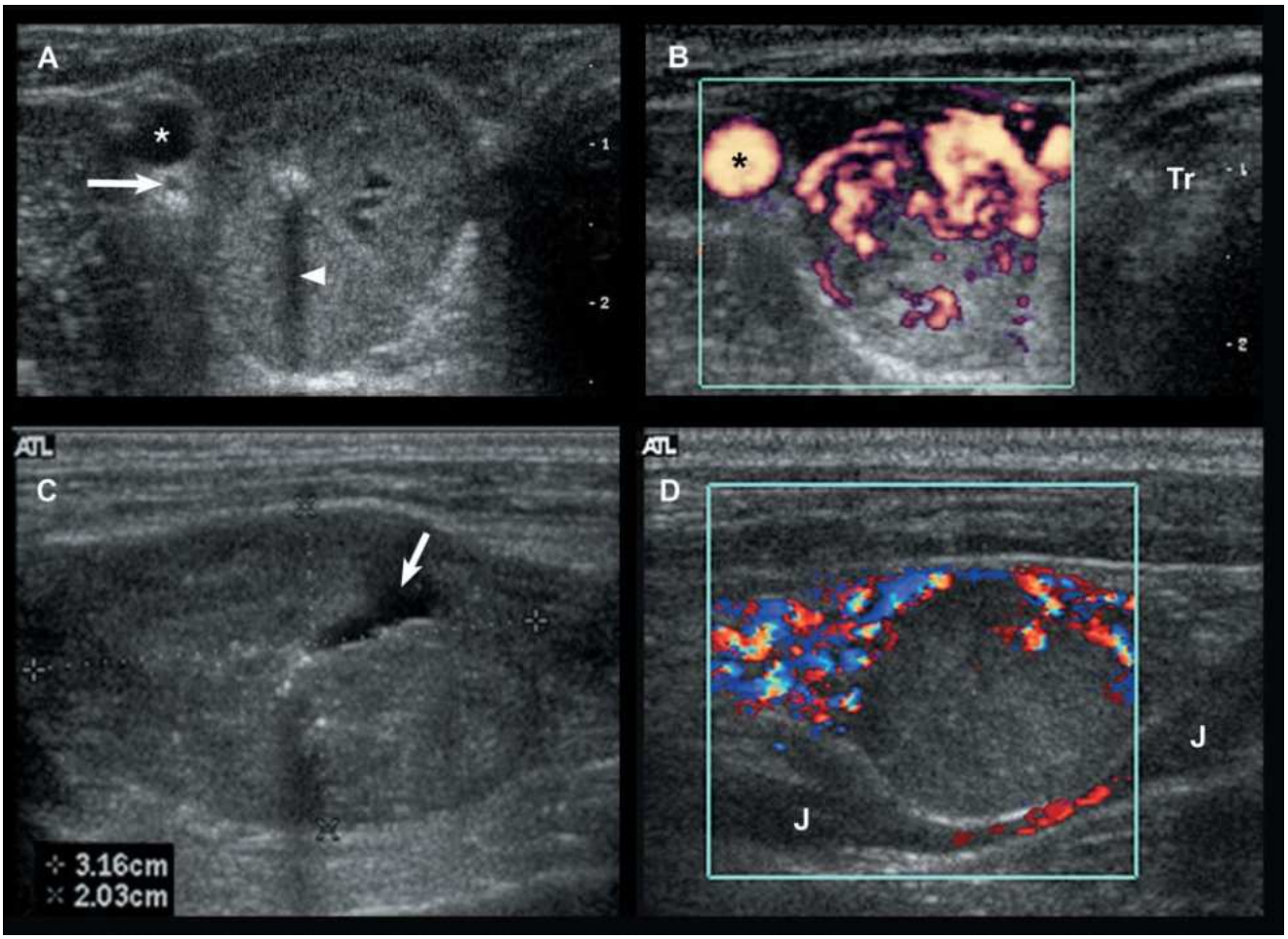


Figure 3.25. **Thyroid carcinoma in three dogs. A:** Transverse image of the left thyroid gland. The large, hypoechoic thyroid carcinoma is displacing the common carotid artery (asterisk) laterally. The trachea (Tr) is visible on the medial side of the mass. Foci of mineralization are within the mass, causing acoustic shadowing (arrowhead). The vagosympathetic trunk (arrow) is dorsal to the common carotid artery. **B:** Power Doppler of another thyroid carcinoma, which is highly vascularized. The mass is between the common carotid artery (asterisk) and the trachea (Tr). **C, D:** Sagittal B-mode and color Doppler images of another thyroid carcinoma. The mass contains discrete, hyperechoic mineral foci and a fluid cavitation (arrow). Prominent vessels are noted at the ventral periphery, and the external jugular vein (J) is displaced and compressed, but not invaded.

displaced ventrally and laterally, and the enlarging mass can cause upper airway obstruction. The local vasculature, trachea, esophagus, and fascial planes can be compressed or invaded by thyroid carcinoma. Because of their higher sensitivity and specificity, computed tomography (CT) or magnetic resonance imaging (MRI) may be the preferred modalities to diagnose these features (Figure 3.26; Taeymans 2012). Mineralization of the mass can be observed in about 50% of cases as hyperechoic foci with distal acoustic shadowing (Figure 3.25A,C), and metastasis to the medial retropharyngeal lymph nodes is not uncommon. In the absence of local tissue invasion and areas of mineralization or metastatic disease, differentiation of thyroid adenoma from other masses cannot be made with ultrasound. Malignant transformation of ectopic thyroid tissue can occur separately or concurrently to thyroid gland carcinoma (Figure 3.27). In contrast to carotid body tumors, which are laterally located, malignant transformation of ectopic thyroid tissue is typically found midline, often ventral to the larynx (Taeymans et al. 2012).

Parathyroid Glands

Dogs with hypercalcemia may have primary or secondary parathyroid disease, and ultrasonography often helps to differentiate between them (Reusch et al. 2000). Primary hyperparathyroidism is caused by hyperplasia, adenoma, or, less commonly,

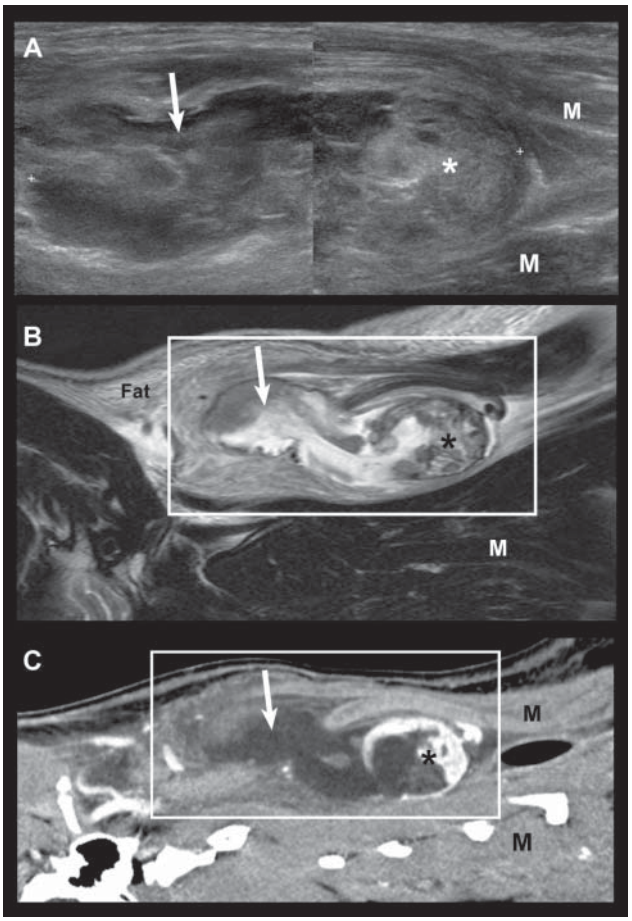


Figure 3.26. Comparative imaging for thyroid carcinoma in a dog. Sonographic images **(A)** of the hemorrhagic mass with corresponding sagittal T2-weighted magnetic resonance (MR) (**B**) and computed tomography (CT) (**C**) images. In ultrasound **(A)**, the carcinoma (*) is mixed in echogenicity, with a hemorrhagic component cranially that is mixed in echogenicity **(A)**, MR signal intensity and (**B**) and CT attenuation characteristics (**C**). M, muscles.

adenocarcinoma, and presents as a single parathyroid nodule. Rarely, two to three concurrent parathyroid nodules occur with primary hyperparathyroidism. Secondary hyperparathyroidism is caused by parathyroid hyperplasia secondary to renal disease or nutritional deficiencies, with all parathyroid glands being mildly enlarged.

Parathyroid nodules are hypoechoic and may be heterogeneous or have distal acoustic enhancement. They tend to be well circumscribed and are round or oval (Figure 3.28). Parathyroid nodules that are greater than 4 mm in diameter are more likely to be parathyroid adenomas or carcinomas, whereas those less than 4 mm in diameter are more often primary hyperplastic, or secondary to chronic renal disease or hypercalcemia of malignancy (Wisner et al. 1997). In acute renal failure, parathyroid length (median, 2.7 mm) is similar to that in normal dogs (median, 3.3 mm). In dogs with chronic renal failure, however, the parathyroid glands are longer (median, 5.7 mm) (Reusch et al. 2000). This may help to differentiate between acute and chronic renal failure, although there is likely to be some overlap between the two groups. There is little information on feline parathyroid glands; however, normal feline parathyroid glands are often not visible on ultrasound examination, and are generally less than 2 mm in width.

External Ear Canals and Tympanic Bullae

Middle ear disease is often characterized by the presence of fluid in the tympanic bulla. Fluid in the bulla appears hypoechoic, replacing the normal gas shadows. The transmission of the ultrasound beam through the fluid also renders the far wall of the bulla visible (Figure 3.29). If air and gas are present in the bulla, a dependent scanning position may be the most sensitive. Fluid in the bulla can also be found incidentally as a transient effusion rather than as a result of inflammatory or obstructive disease, so its presence should be correlated with clinical signs of middle ear disease.

Tumors and inflammatory polyps may fill the bulla and external ear canal, and extend into the peripheral soft tissues in cases of severe infection or malignant processes (Figure 3.30). Variable echogenic tissue and fluid collections may then be observed at the periphery of the bulla and ear canal. The tympanic wall may also become irregular or interrupted due to new bone formation or lysis, respectively. In such cases, severe bacterial otitis media, neoplasia, osteomyelitis, craniomandibular osteopathy, or cholesteatoma should be considered.

Experimentally, a fluid-filled external ear canal improves the visualization of canal size and cartilage thickness. The tympanic membrane cannot be seen directly; however, if the ear canal is fluid-filled and the bulla is air-filled, the membrane is probably intact. If the membrane is ruptured, the bulla is also fluid-filled.

Special Procedures

Tissue samples of neck lesions are most often obtained by using a fine-needle aspirate, although tissue-core biopsies of larger lesions are possible using ultrasound guidance (Figure 3.30C). However, because of the high vascularity of some organs and masses, such as those

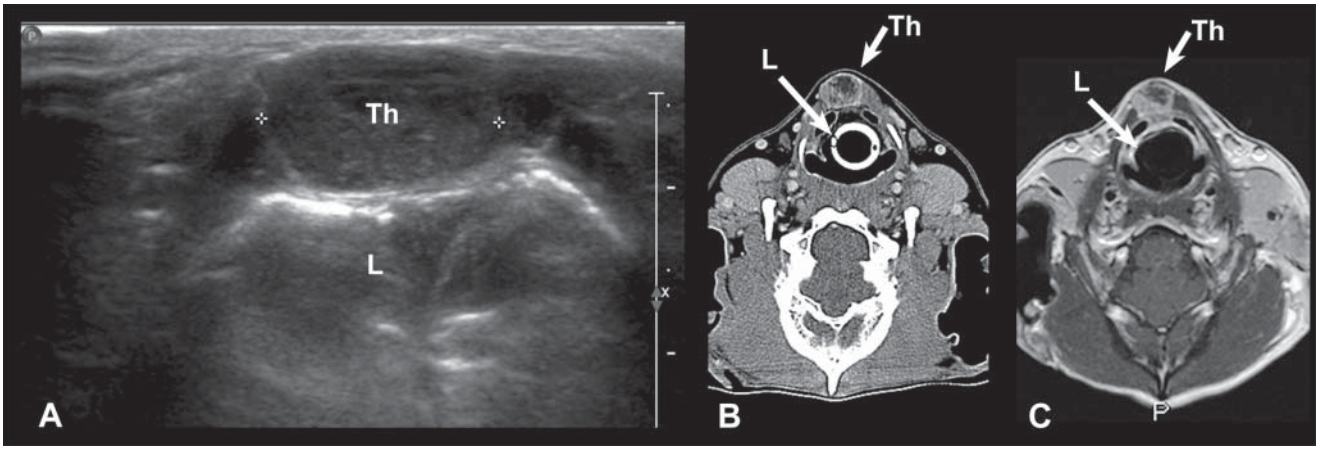


Figure 3.27. Comparative imaging of an ectopic thyroid carcinoma in a dog. Ventral is on top of these transverse ultrasound **(A)**, and post-contrast computed tomography (CT) (B) and T1-weighted magnetic resonance (MR) **(C)** images. A soft tissue mass consistent with ectopic thyroid (Th) proliferation showing peripheral contrast enhancement is noted along the midline, ventral to the larynx (L). Local invasion of the ventral laryngeal musculature is noted on the MRI.

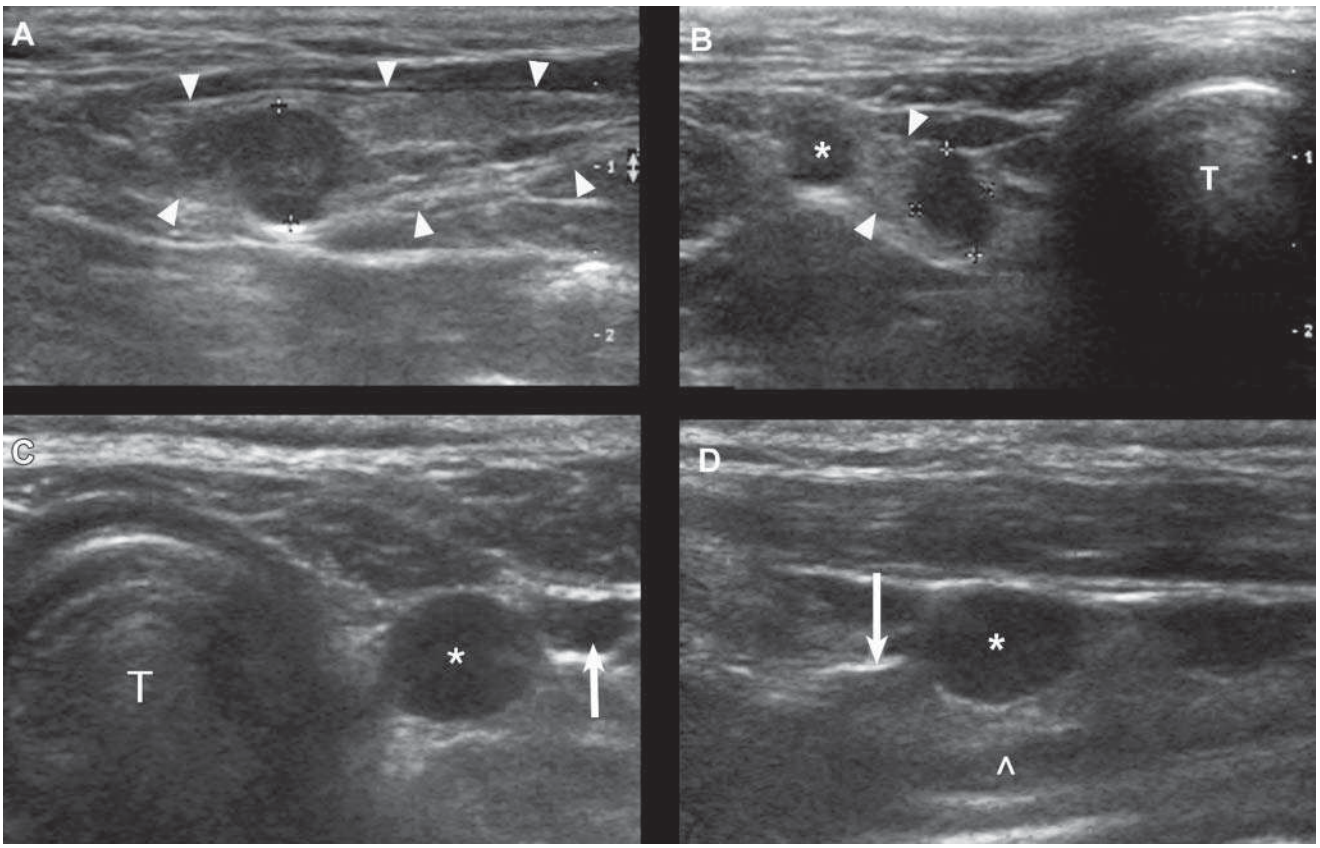


Figure 3.28. Parathyroid (chief cell) adenoma in dogs. A: Sagittal image of the right thyroid (arrowheads) and parathyroid glands of a 10-year-old English Setter. A discrete hypoechoic nodule (between cursors) measuring 7 mm in diameter is present cranially. **B:** Transverse image of the right thyroid (arrowheads) and parathyroid glands of a 10-year-old Siberian Husky. A discrete hypoechoic nodule (between the cursors) measuring 8 × 4 mm is deforming the medial contour of the thyroid gland (arrowheads). The diagnosis is parathyroid chief cell adenoma. The adjacent common carotid artery (asterisk) seen on cross-section should not be confused with a parathyroid nodule. T, trachea. **C:** Transverse image of the right parathyroid of another dog with parathyroid carcinoma. A round, hypoechoic nodule (asterisk) is between the trachea (T) and the common carotid artery (arrow) in the left neck. **D:** In the sagittal orientation, the nodule protrudes from the cranioventral aspect (arrow) of the thyroid gland. The dorsal border of the thyroid gland is marked with the caret.

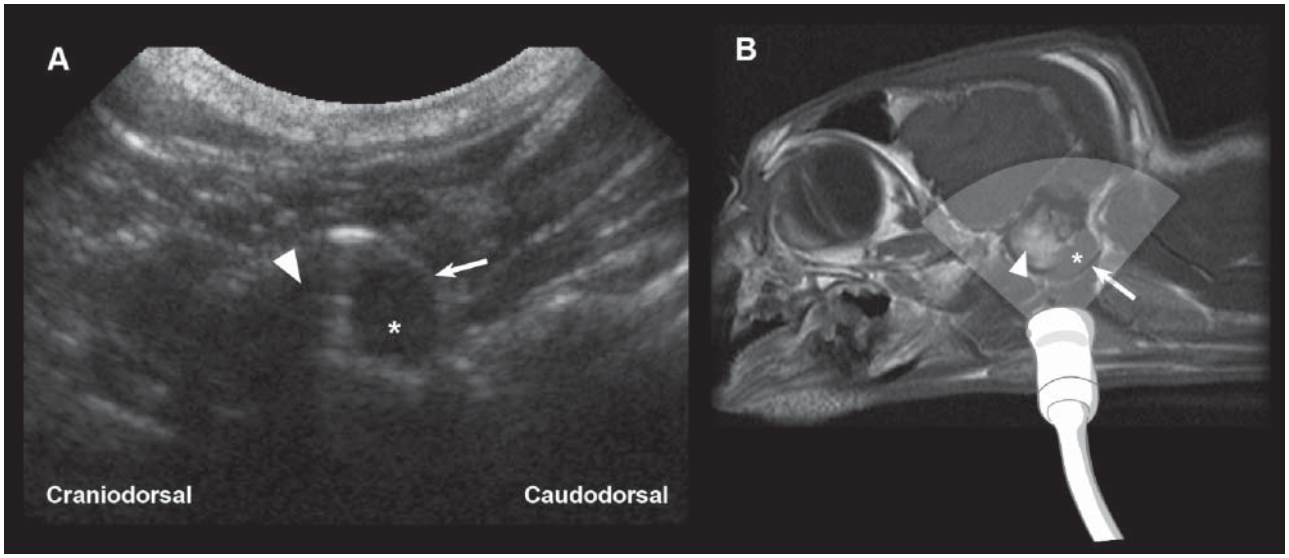


Figure 3.29. **Otitis media in a cat. A:** Sagittal image of the tympanic bulla. The sonogram is taken from the ventral position. The ventromedial compartment of the bulla is filled with anechoic fluid (*) and the near wall is seen more clearly (arrow). The far wall is also visible because the fluid has transmitted the ultrasound. The dorsolateral compartment (arrowhead) appears hypoechoic, and there is no reverberation artifact, suggesting soft-tissue content. **B:** Magnetic resonance (MR) T1-weighted post-contrast sagittal image of the tympanic bulla. The MR image confirms the presence of fluid in the ventromedial compartment (*) and contrast-enhancing soft tissue in the dorsolateral compartment (arrowhead). The arrowhead points to the caudoventral wall, as in A.

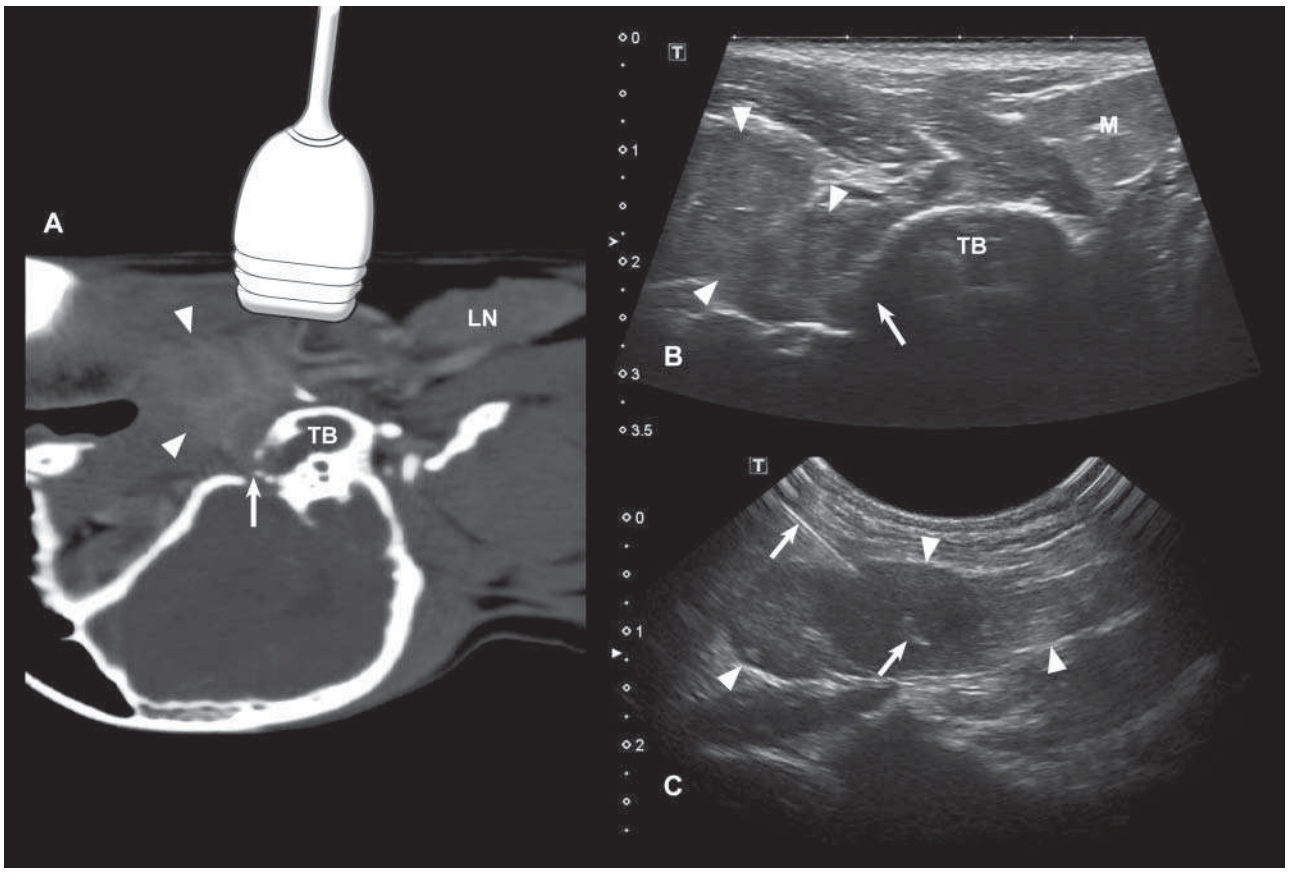


Figure 3.30. **Infiltration of the tympanic bulla by a carcinoma in a dog. A:** Computed tomography (CT) image reformatted in sagittal plane with an overlying linear probe placed to obtain image B. An ill-defined hyperattenuating mass (arrowheads) is present at the rostroventral aspect of the tympanic bulla (TB)**.** The mass is seen to invade the rostral wall of the bulla (arrow). The bulla was otherwise filled with fluid. The nearby retropharyngeal lymph node (LN) is enlarged. **B:** Corresponding sonographic image, with the dog placed in dorsal recumbency, showing a moderately echogenic mass (arrowheads) with focal lysis of the rostral wall (arrow) of the TB. **C:** The adjacent retropharyngeal lymph node (arrowheads) was fine-needle-aspirated, revealing metastasis. The arrows point to the proximal third and distal extremity of the inserted 38-mm-long, 22-gauge needle. M, mandibular salivary gland.

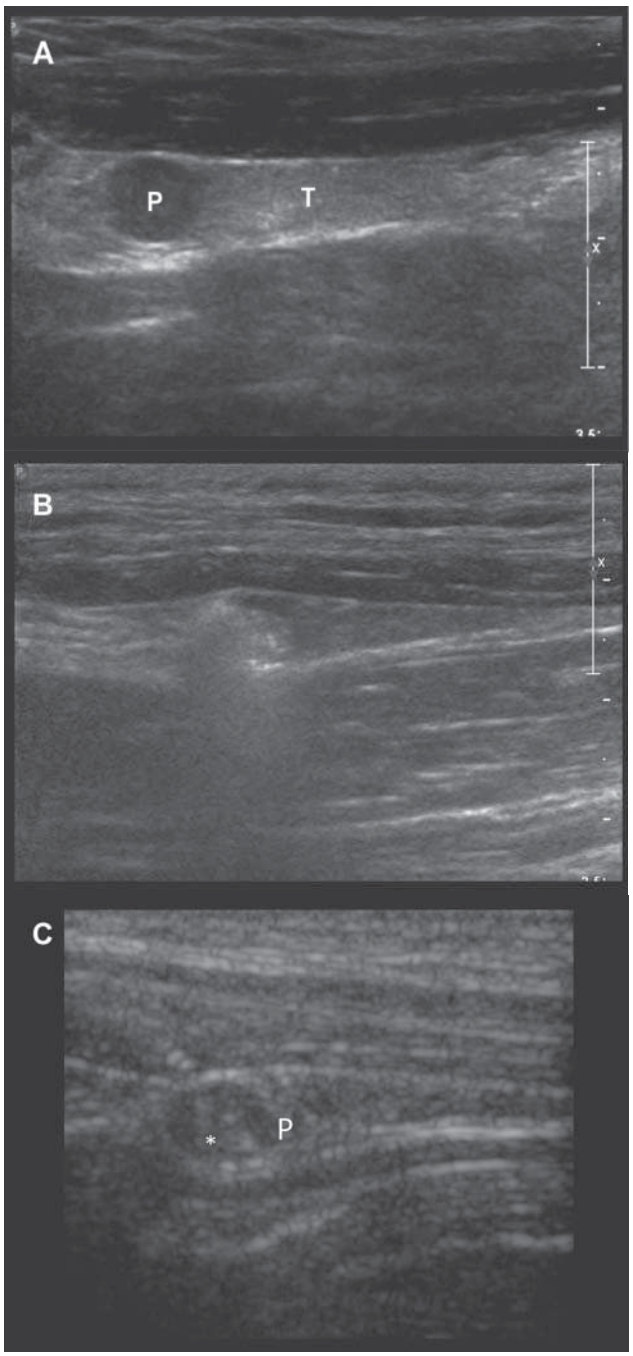


Figure 3.31. Intralesional ultrasound-guided treatment of parathyroid adenoma with ethanol (A, B) or radiofrequency ablation (C). A: Sagittal image of a parathyroid gland adenoma (P) at the cranial aspect of the thyroid gland (T). **B:** The needle originates from the left superficial aspect of the image in C. The ethanol accumulation is a round, hyperechoic area causing dirty shadowing artifact. **C:** During radiofrequency ablation, the tissue disruption appears as a hyperechoic region (asterisk) within the parathyroid gland.

of thyroid origin, and the presence of large arteries and veins often adjacent to cervical lesions, particular care should be taken when either fine-needle aspiration or tissue-core biopsy is attempted.

Vessels of masses and tissues can be identified with color and power Doppler imaging to gauge vascularity, to map vessels prior to fine-needle aspiration or biopsy, and to determine operability of a mass lesion.

Feline hyperthyroidism has been treated using both heat ablation and percutaneous ethanol ablation (Wells et al. 2001; Mallery et al. 2003) (Figure 3.31). Complications from both of these procedures include Horner's syndrome and laryngeal paralysis. Heat ablation obtained better results than ethanol ablation, with a mean euthyroid period of 4 months. The longest euthyroid period with ethanol ablation was 27 weeks, with a higher complication rate. Neither of these methods is as effective as the surgical, medical, or radiotherapeutic methods currently in use.

Parathyroid ablation has also been implemented using both chemical methods (ethanol) and radiofrequency methods (heat) (Long et al. 1999; Pollard et al. 2001) as an alternative to surgery. Both methods were safe and successful in the small clinical trials reported, with hypocalcemia requiring treatment in approximately half of dogs after ablation.

Post-surgical monitoring when swelling is present may also be useful to add. Detection of seroma, abscess, or left gauze/catheter/penrose is useful to dictate the next therapeutic step (Figure 3.32).

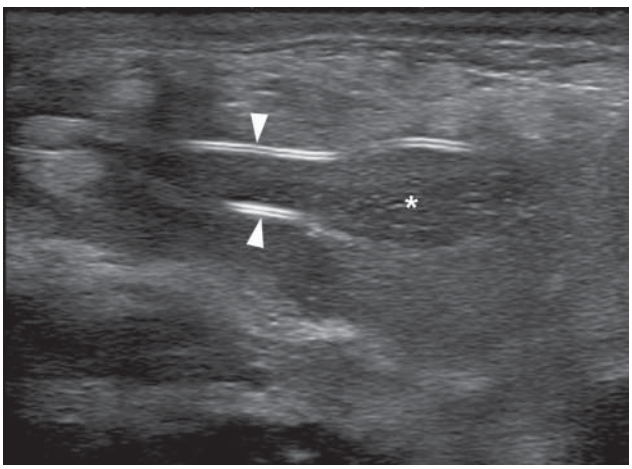


Figure 3.32. Penrose in a dog following surgical excision of a salivary gland tumor. The walls of the penrose drain appear as thin double-line structures, floating in an echogenic collection (*) that was confirmed to be an abscess at surgery.



Visit our website at **www.SmallAnimalUltrasonography.com** for complementary video clips with annotations and text on:

- Normal neck anatomy and scanning
- Thyroid carcinoma
- Parathyroid nodule
- Lymphadenopathy
- Neck abscess and foreign body
- Salivary sialocele

References

Bray JP, Lipscombe VJ, White RA, Rudorf H (1998) Ultrasonographic examination of the pharynx and larynx of the normal dog. Vet Radiol Ultrasound 39:566–71.

Bromel C, Pollard RE, Kass PH, Samii VF, Davidson AP, Nelson RW (2005) Ultrasonographic evaluation of the thyroid gland in healthy, hypothyroid, and euthyroid golden retrievers with nonthyroidal illness. J Vet Intern Med 19:499–506.

Cannon MS, Paglia D, Zwingenberger AL, Boroffka SA, Hollingsworth SR, Wisner ER (2011) Clinical and diagnostic imaging findings in dogs with zygomatic sialadenitis: 11 cases (1990–2009). J Am Vet Med Assoc 239:1211–8.

Carlisle CH, Biery DN, Thrall DE (1991) Tracheal and laryngeal tumors in the dog and cat: Literature review and 13 additional patients. Vet Radiol 32:229–235.

Dickie AM, Doust R, Cromarty L, Johnson VS, Sullivan M, Boyd JS (2003) Ultrasound imaging of the canine tympanic bulla. Res Vet Sci 75:121–126.

Fife W, Mattoon J, Drost WT, Groppe D, Wellman M (2003) Imaging features of a presumed carotid body tumor in a dog. Vet Radiol Ultrasound 44:322–325.

Gooding GA, Herzog KA, Laing FC, McDonald EJ, Jr (1977) Ultrasonographic assessment of neck masses. J Clin Ultrasound 5:248–252.

Liles, S.R., Linder, K.E., Cain, B. and Pease, A.P. (2010) Ultrasonography of histologically normal parathyroid glands and thyroid lobules in normocalcemic dogs. Vet Radiol Ultrasound 51:447–452.

Long, CD, Goldstein RE, Hornof WJ, Feldman EC, Nyland TG (1999) Percutaneous ultrasound-guided chemical parathyroid ablation for treatment of primary hyperparathyroidism in dogs. J Am Vet Med Assoc 215:217–221.

Mallery KF, Pollard RE, Nelson RW, Hornof WJ, Feldman EC (2003) Percutaneous ultrasound-guided radiofrequency heat ablation for treatment of hyperthyroidism in cats. J Am Vet Med Assoc 223:1602–1607.

Melian C, Morales M, Espinosa de los Monteros A, Peterson ME (1996) Horner's syndrome associated with a functional thyroid carcinoma in a dog. J Small Anim Pract 37: 591–593.

Mooney CT (2002) Pathogenesis of feline hyperthyroidism. J Feline Med Surg 4:167–169.

Nemanic S, Nelson NC. (2012) Ultrasonography and noncontrast computed tomography of medial retropharyngeal lymph nodes in healthy cats. Am J Vet Res. 73(9):1377–1385.

Phillips DE, Radlinsky MG, Fischer JR, Biller DS (2003) Cystic thyroid and parathyroid lesions in cats. J Am Anim Hosp Assoc 39:349–354.

Pollard RE, Long CD, Nelson RW, Hornof WJ, Feldman EC (2001) Percutaneous ultrasonographically guided radiofrequency heat ablation for treatment of primary hyperparathyroidism in dogs. J Am Vet Med Assoc 218:1106–1110.

Reese S, Breyer U, Deeg C, Kraft W, Kaspers B (2005) Thyroid sonography as an effective tool to discriminate between euthyroid sick and hypothyroid dogs. J Vet Intern Med 19:491–498.

Reese S, Ruppert C (2001) Ultrasonographic imaging of the vagosympathetic trunk in the dog. Vet Radiol Ultrasound 42:272–275.

Reusch CE, Tomsa K, Zimmer C et al. (2000) Ultrasonography of the parathyroid glands as an aid in differentiation of acute and chronic renal failure in dogs. J Am Vet Med Assoc 217:1849–1852.

Rudorf H, Barr FJ, Lane JG (2001) The role of ultrasound in the assessment of laryngeal paralysis in the dog. Vet Radiol Ultrasound 42:338–343.

Rudorf H, Herrtage ME, White RA (1997) Use of ultrasonography in the diagnosis of tracheal collapse. J Small Anim Pract 38:513–518.

Ruppert C, Hartmann K, Fischer A, Hirschberger J, Hafner A, Schmidt P (2000) Cervical neoplasia originating from the vagus nerve in a dog. J Small Anim Pract 41:119–122.

Schaer M, Zaki FA, Harvey HJ, O'Reilly WH (1979) Laryngeal hemiplegia due to neoplasia of the vagus nerve in a cat. J Am Vet Med Assoc 174:513–515.

Silver TI, Lawson JA, Mayer MN (2012) Sonographic characteristics of presumptively normal main axillary and superficial cervical lymph nodes in dogs. Am J Vet Res 73: 1200–1206.

Slensky KA, Volk SW, Schwarz T, Duda L, Mauldin EA, Silverstein D (2003) Acute severe hemorrhage secondary to arterial invasion in a dog with thyroid carcinoma. J Am Vet Med Assoc 223:649–653.

Taeymans O, Daminet S, Duchateau L, Saunders JH (2007) Pre- and post-treatment ultrasonography in hypothyroid dogs. Vet Radiol Ultrasound 48:262–269.

Taeymans O, Duchateau L, Schreurs E, Kramer M, Daminet S, Saunders JH (2005) Intra- and interobserver variability of ultrasonographic measurements of the thyroid glandin healthy beagles. Vet Radiol Ultrasound 46:139–142.

Taeymans O, Penninck DG, Peters RM (2012) Comparison between clinical, ultrasound, CT, MRI, and pathology

findings in dogs presented for suspected thyroid carcinoma. Vet Radiol Ultrasound 54:61–70.

Wells AL, Long CD, Hornof WJ et al. (2001) Use of percutaneous ethanol injection for treatment of bilateral hyperplastic thyroid nodules in cats. J Am Vet Med Assoc 218:1293–1297.

Wisner ER, Mattoon JS, Nyland TG (2002) Neck. In: Nyland TG, ed. Small Animal Diagnostic Ultrasound. Philadelphia: WB Saunders, pp 285–304.

Wisner ER, Mattoon JS, Nyland TG, Baker TW (1991) Normal ultrasonographic anatomy of the canine neck. Vet Radiol Ultrasound 32:185–190.

Wisner ER, Nyland TG, Mattoon JS (1994) Ultrasonographic examination of cervical masses in the dog and cat. Vet Radiol Ultrasound 35:310–315.

Wisner ER, Penninck D, Biller DS, Feldman EC, Drake C, Nyland TG (1997) High-resolution parathyroid sonography. Vet Radiol Ultrasound 38:462–466.

CHAPTER FOUR

Thorax

Silke Hecht[1] and Dominique Penninck[2]

[1] *Department of Small Animal Clinical Sciences, University of Tennessee College of Veterinary Medicine, Knoxville, TN, USA*

[2] *Department of Clinical Sciences, Cummings School of Veterinary Medicine, Tufts University, North Grafton, MA, USA*

Preparation and Scanning Technique

In a normal animal, evaluation of intrathoracic structures is hampered by the interposition of aerated lung tissue. However, collapsed or consolidated lung, thoracic masses, or pleural effusion can provide a suitable acoustic window. Thoracic radiography or thoracic CT should precede thoracic ultrasonography to confirm the presence of a lesion, identify a suitable acoustic window, and rule out entities, such as pneumothorax, which preclude an ultrasonographic examination (Tidwell 1998). However, ultrasonography can be used as a screening procedure to diagnose pneumothorax, especially in traumatized patients. As pleural effusion may facilitate the examination of intrathoracic structures, thoracocentesis should be postponed until the ultrasonographic examination has been performed, unless the patient has respiratory compromise (Larson 2009).

To optimize image quality, hair should be clipped in the region to be scanned, and acoustic gel should be applied. An intercostal approach is most commonly used and involves examination of the thoracic structures by positioning the transducer on the chest wall between adjacent ribs (Figure 4.1A,B). Animals are generally positioned in lateral recumbency, although scanning in sternal recumbency or while a patient is standing may be considered in compromised patients or for an initial screening. A thoracic inlet approach can sometimes help in visualizing cranial thoracic lesions (Figure 4.1C).

A subcostal (transhepatic) approach may be used to assess caudal mediastinal or pulmonary lesions. The animal is in dorsal or lateral recumbency, and the transducer is aimed cranially under the rib cage.

Some examiners prefer imaging the dependent portion of the thorax by using a cardiac table. This approach optimizes the acoustic window, because pleural fluid accumulates in the dependent portion of the thorax, and the pulmonary structures in the near field contain less air because of positional atelectasis. However, ultrasound-guided interventional procedures are difficult to perform using this approach, and the field of view is limited to the size of the table window and the ability to position the area of interest over the opening.

Usually, a curvilinear or microconvex sonographic probe with a small footprint should be selected when using an intercostal window, although a linear probe may also be used. The optimal frequency depends on the size of the animal and the location of the lesion. For the examination of the cranial mediastinum in large dogs, a 5-MHz transducer may be used, whereas examination of small superficial pulmonary lesions necessitates the use of a higher-frequency transducer (8 MHz or higher). For a transhepatic or thoracic inlet approach, curvilinear transducers are most commonly used.

The examination is performed in at least two planes, depending on the nature, size, and location of the lesion(s).

Normal Sonographic Anatomy

Intercostal Approach

The soft tissues of the thoracic wall (skin, subcutaneous fat, and muscle) appear as layered tissues of alternating echogenicity in the near field (Figure 4.2). The parietal pleura is rarely recognized as a discrete

Atlas of Small Animal Ultrasonography, Second Edition. Edited by Dominique Penninck and Marc-André d'Anjou.
© 2015 John Wiley & Sons, Inc. Published 2015 by John Wiley & Sons, Inc.
Companion website: www.SmallAnimalUltrasonography.com

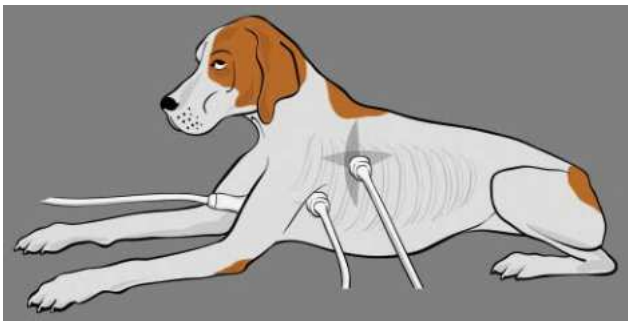


Figure 4.1. Ultrasonographic examination of the thorax. The patient can be examined while standing or in sternal, lateral, or dorsal recumbency. **A, B:** Intercostal approach. The transducer is placed on the thoracic wall in the area of interest, previously detected on radiographs or computed tomography (CT). To better evaluate the cranial mediastinum **(B)**, the thoracic limbs are pulled forward. The transducer is placed on the thoracic wall caudal to the elbows and dorsolateral to the sternum. **C:** The thoracic inlet approach can be used to evaluate the most cranial aspect of the thoracic cavity. The transducer is placed midline on the caudal neck and aimed caudally into the thorax. An initial dorsal plane view is useful to identify the trachea, esophagus, and great vessels.

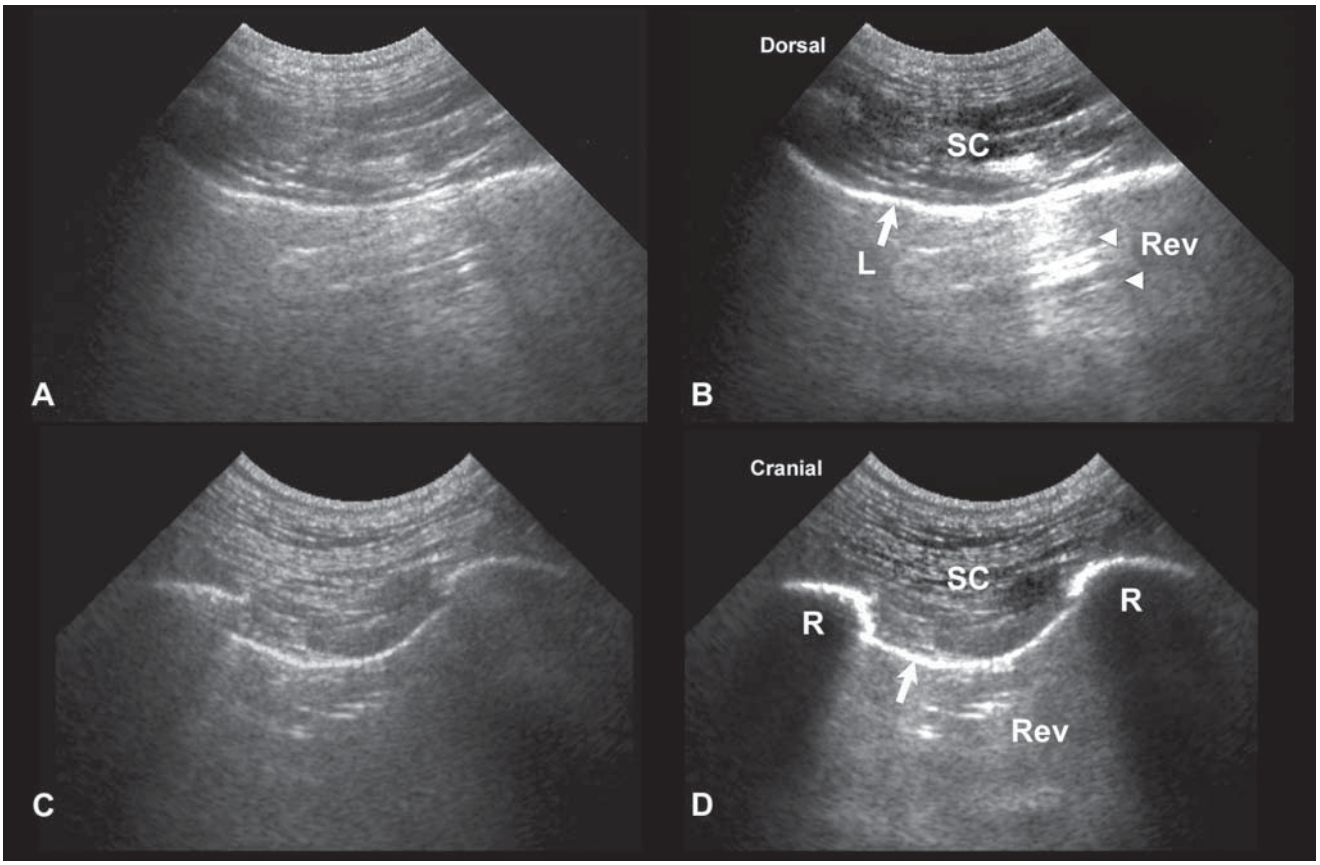


Figure 4.2. Normal thoracic wall when using an intercostal approach. Longitudinal ultrasonographic and enhanced labeled images. The subcutaneous tissues (SC), which include muscle, fat, and fascial planes, are recognized as multiple alternating hypoechoic and hyperechoic layers in the near field. The lung surface (arrow) appears as a smooth, strongly hyperechoic line. Distal to the lung surface are dirty shadowing and reverberation artifacts (Rev) that prevent evaluation of the normal air-filled lung. The ribs are visible as strongly hyperechoic curvilinear structures (R), with clean distal shadowing in the far field.

structure, but may be differentiated from the visceral pleura in real time by the sliding motion of the lung during respiration. The ribs appear as smooth, curvilinear, hyperechoic structures with distal acoustic shadowing (Figure 4.2C,D). The lung interface is seen as an echogenic linear band with distal reverberation artifacts and dirty shadowing. The pulmonary parenchyma deep to the lung surface cannot be evaluated in normal animals because of these artifacts.

Evaluation of the normal cranial and caudal mediastinum by means of an intercostal approach is often hampered by the interposition of aerated lung. However, cranial mediastinal vessels may be visualized as

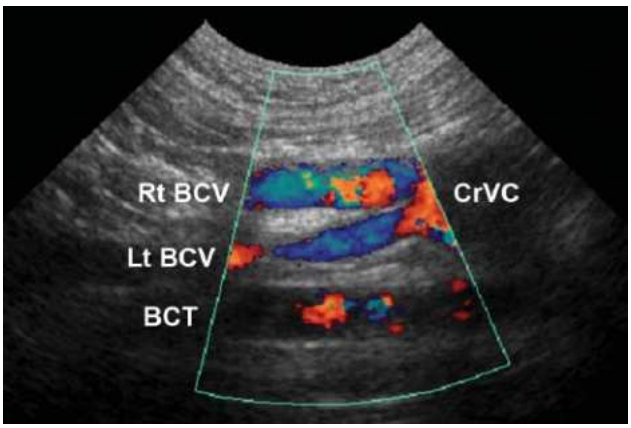


Figure 4.3. Normal cranial mediastinum in a dog when using a right intercostal approach (dorsal plane) and color Doppler. The cranial mediastinal vessels are clearly visible. The confluence of the brachiocephalic veins to form the cranial vena cava is observed. BCT, brachiocephalic trunk; CrVC, cranial vena cava; Lt BCV, left brachiocephalic vein; and Rt BCV, right brachiocephalic vein.

tubular anechoic structures that show flow on Doppler examination (Figure 4.3).

The thymus may be visible in young animals and appears as echogenic coarse well vascularized tissue in the ventral mediastinum cranial to the heart (Seiler 2011). Care must be taken not to confuse abundant mediastinal fat with intrathoracic mass lesions. Occasionally, the sternal lymph nodes can be seen in medium to large dogs.

Transhepatic (Subcostal) Approach

The diaphragm–lung interface appears as a curvilinear, strongly hyperechoic structure in the far field cranial to the liver (Figure 4.4). The diaphragm cannot be distinguished from the adjacent hyperechoic lung interface, except in cases of pleural effusion or consolidation of the caudal lung lobes. The caudal thoracic esophagus is occasionally seen traversing the diaphragm (Figure 8.3). Using this approach, the

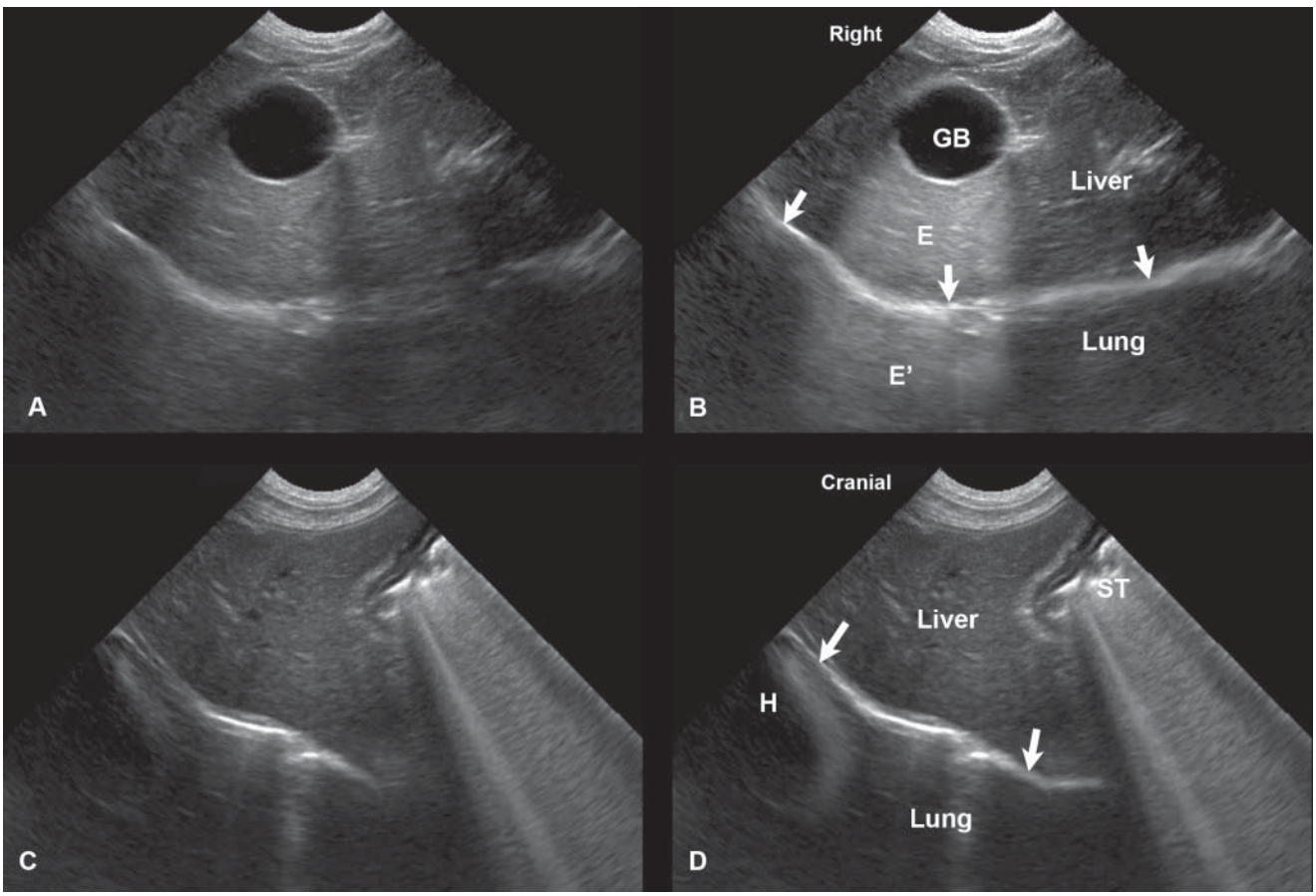


Figure 4.4. Normal caudal thorax in a dog when using a transhepatic (subcostal) approach. A, B: Transverse ultrasonographic and enhanced labeled images. The diaphragm–lung interface (arrows) appears as a curvilinear hyperechoic line cranial to the liver. A mirror image of the hyperechoic acoustic enhancement (E) deep to the gallbladder (GB) is in the lung region (E′). H, heart; ST, stomach.

examiner has to be aware of the commonly observed mirror artifact (Figure 1.17).

Thoracic Inlet Approach

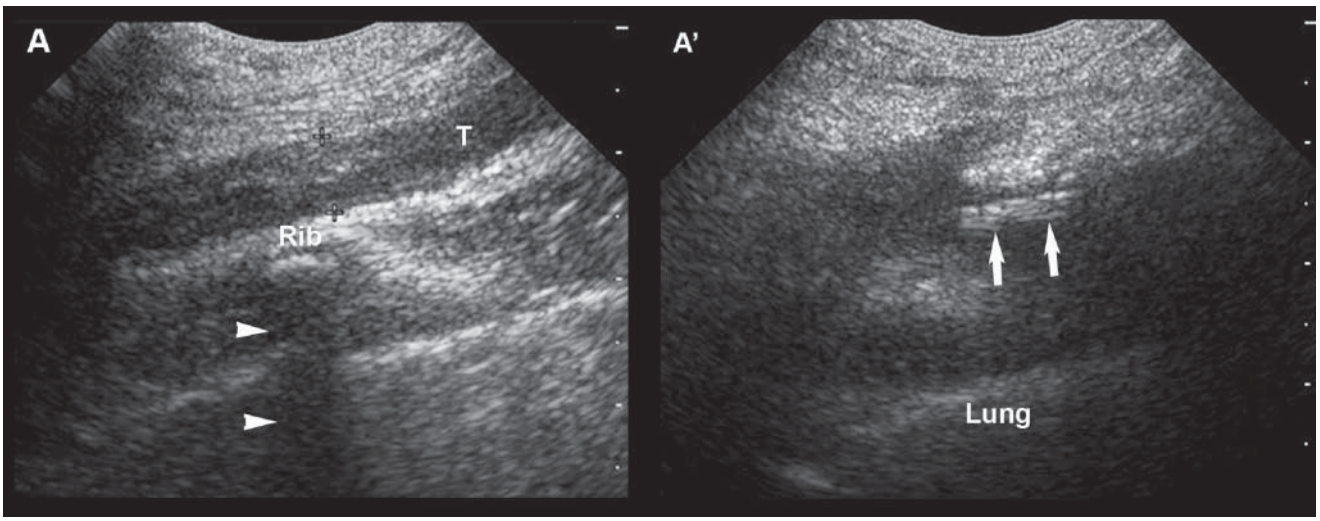
By using a thoracic inlet approach, mediastinal fat, cranial thoracic trachea, and esophagus can be seen. Cranial mediastinal vessels, and occasionally sternal or cranial mediastinal lymph nodes, may be visible.

Sonographic Features of Thoracic Disorders

Lesions of the Thoracic Wall

Thoracic wall lesions include neoplasms, inflammatory lesions, and traumatic changes. Ultrasound allows assessment of the extent and margination of a lesion, bone involvement (such as in rib neoplasms or traumatic fractures), echogenicity and echotexture (solid and/or fluid-filled), invasion of adjacent structures, and presence of foreign material or gas (e.g., in abscesses). Inflammatory lesions affecting the thoracic wall include cellulitis, abscesses, and granulomas. Ultrasound enables identification of fluid pockets. Ultrasonography has been proven to be more accurate than fistulography in the detection of foreign material in animals with chronic draining tracts or abscesses (Armbrust et al. 2003). Depending on their size and composition, foreign bodies are usually hyperechoic to the surrounding soft tissues and often cast an acoustic shadow (Schultz et al. 2008; Figure 4.5).

In cases of thoracic trauma, ultrasonography can be used as an alternative to radiography in the diagnosis of rib fractures. Findings include discontinuity of cortical alignment (Figure 4.6) as well as edge



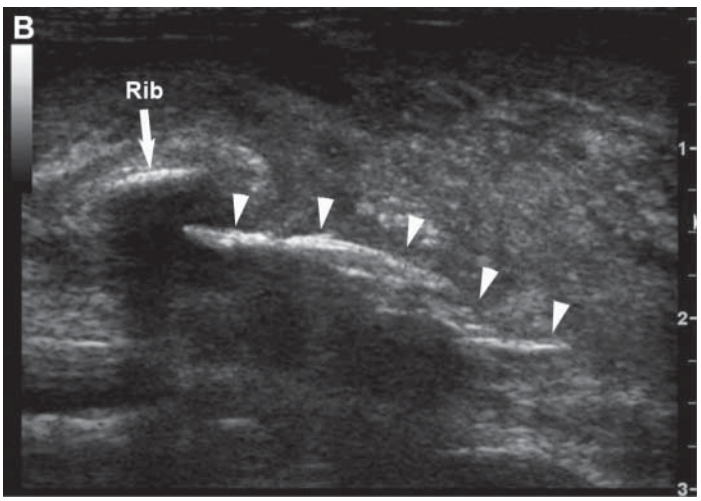


Figure 4.5. Thoracic wall foreign bodies. A, A′: In a 7-year-old German Shorthaired Pointer, with chronic draining tract, sonograms of the draining tract **(A)** and foreign body **(A′)** are shown. The draining tract (T) appears as a 6-mm-wide tubular space within the subcutaneous tissues of the thoracic wall immediately superficial to the ribs. Notice the shadowing associated with the visible rib (arrowheads). At the termination of the tract, a hyperechoic, sharp-edged structure of 9×2 mm is noted, consistent with a foreign body (arrows). The foreign body is surrounded by hypoechoic material, consistent with an abscess. A wooden splinter was identified at surgery. **B:** An irregular-shaped foreign body is present near a rib of this English Setter with a draining tract, and was suspected to represent a grass awn. The grass awn was removed under ultrasound guidance. Image courtesy of Dr Ulrich Zeyen, Centro Veterinario Specialisito, Rome, Italy.

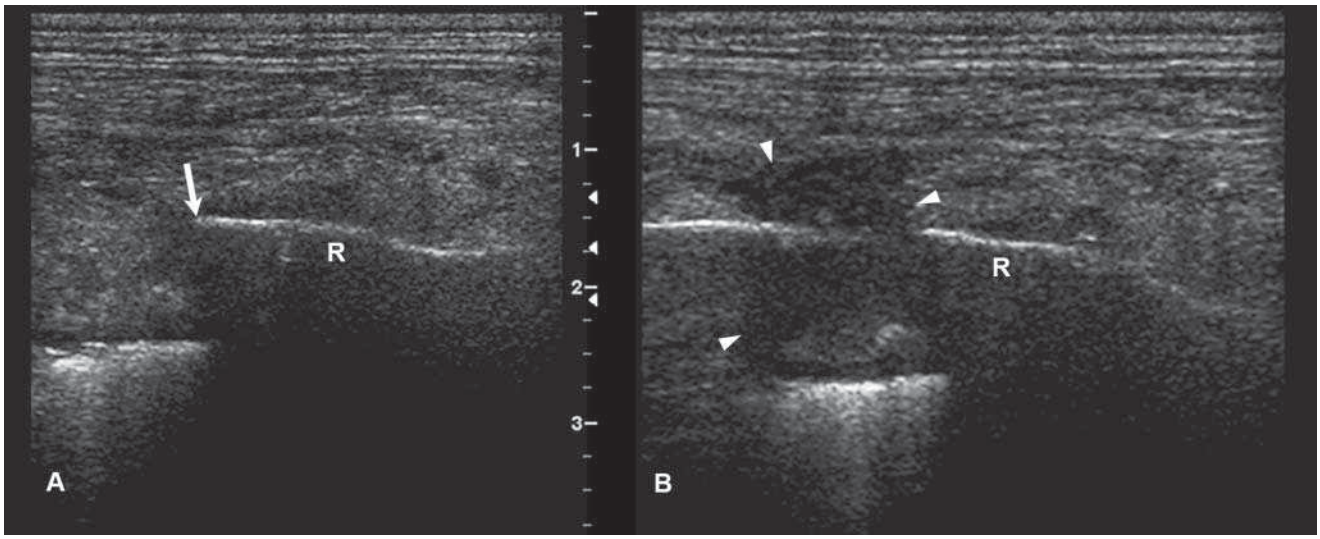


Figure 4.6. Rib fractures in a dog. Ultrasonographic images obtained in a transverse plane with respect to the thoracic cavity, which corresponds to the long axis of the ribs. A and B show two rib fractures in the same dog. **A:** There is disruption of the smooth hyperechoic contour of the rib (R), with displacement of the fracture fragments (arrow). **B:** Segmental rib fracture with medial displacement of an isolated bone fragment. The adjacent hematoma is poorly echogenic and inhomogenous (arrowheads).

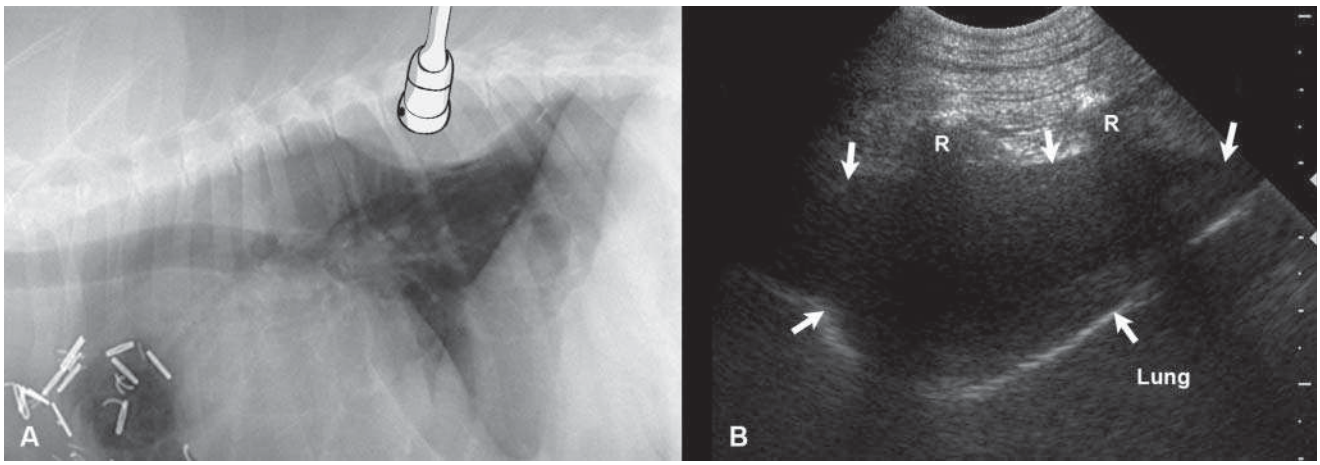


Figure 4.7. Extrapleural mass (metastatic thymoma) in a 7-year-old elkhound. A: On this right lateral radiograph there is a fusiform mass lesion associated with the caudal dorsal thorax (under the sonographic probe). This mass is in broad-based contact with the dorsal thoracic wall (extrapleural sign). Surgical hemoclips from previous removal of a cranial mediastinal mass (thymoma) are noted in the cranial ventral thorax. **B:** The mass, which is visualized by using a left dorsal intercostal approach, appears as a homogeneously hypoechoic mass lesion (arrows) forming an obtuse angle with the adjacent thoracic wall. The hyperechoic interface of the normal lung is visible in the far field, as well as acoustic shadows associated with ribs (R).

shadowing and reverberation artifacts arising from the margin of the displaced rib segment (Hurley et al. 2004). However, based on the literature on human patients, ultrasonography does not significantly increase the detection rate of rib fractures, may be uncomfortable for a patient, and is more time-consuming than radiography.

A thoracic wall mass is convex, in broad-based contact with the chest wall, and displaces the normal lung interface (**extrapleural sign**). In contrast to most mass lesions originating from the pulmonary parenchyma, the angle between the extrapleural mass and the adjacent thoracic wall is obtuse (Figure 4.7). Additionally, the dynamic visualization of lung motion underneath

thoracic wall lesions enables their extrapulmonary origin to be confirmed. In contrast to pulmonary masses, thoracic wall mass lesions only move with the chest wall during respiration.

Benign or malignant neoplastic processes, such as infiltrative lipomas or soft-tissue sarcomas, may invade the thoracic wall (Figure 4.8) and appear as masses or swelling of variable echogenicity.

Masses originating from ribs or sternum are most commonly neoplastic in etiology (e.g., chondrosarcoma or osteosarcoma). These masses cause irregular disruption of the smooth contour of the affected bone and are accompanied by an intrathoracic and extrathoracic mass lesion of variable size and echogenicity (Figures 4.9, 4.10). Metastatic disease may involve one or several bones of the thoracic

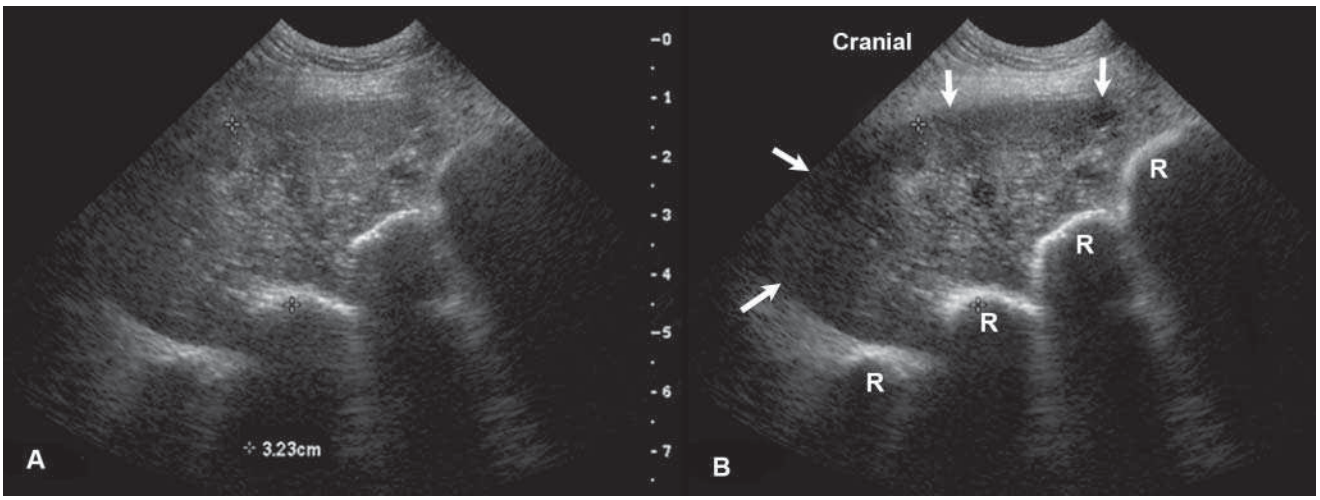


Figure 4.8. Infiltrative soft-tissue sarcoma in a large-breed dog. Ultrasonographic **(A)** and enhanced labeled **(B)** dorsal images of the thoracic wall in a dog with firm swelling on palpation. A heterogeneous, 3.2-cm-thick mass (arrows) is visible at the lateral aspect of the ribs (R), which are characterized by strongly hyperechoic surfaces and strong acoustic shadowing. This echogenic mass infiltrated the intercostal muscles and connective tissue without invading the pleural space.

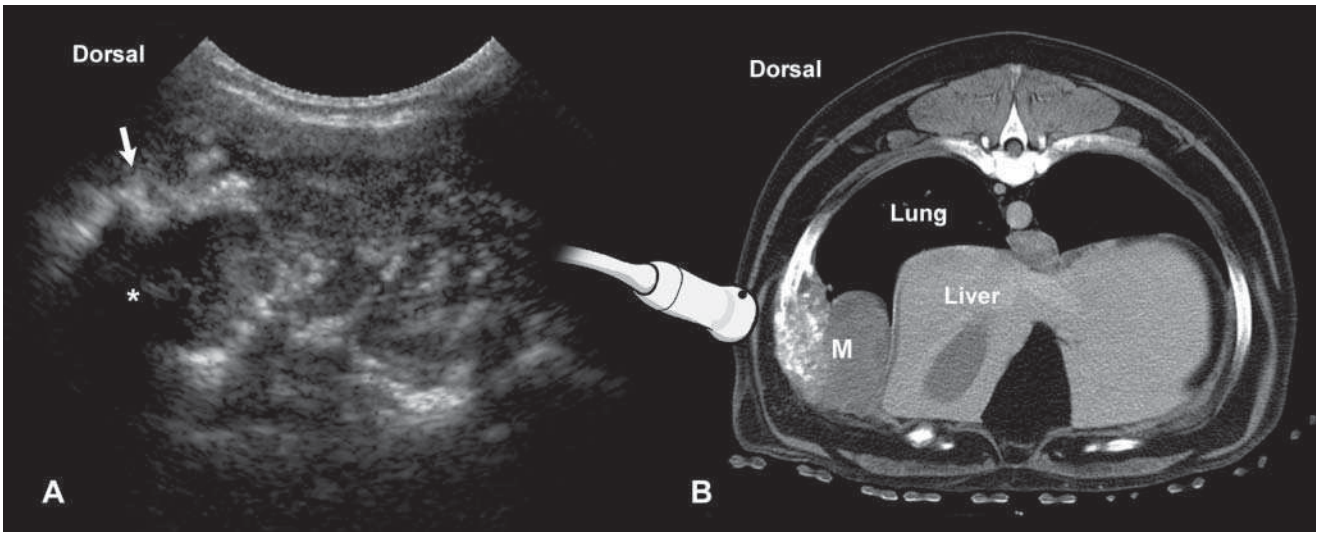


Figure 4.9. Rib osteosarcoma in a 10-year-old Rottweiler. Transverse ultrasound **(A)** and computed tomographic **(B)** images obtained at the level of the 11th rib, on which an aggressive osteolytic and osteoproliferative rib mass (M) is identified that protrudes into the right hemithorax. Ultrasonographically, the mass is mixed in echogenicity, and hyperechoic foci (arrow) are associated with acoustic shadowing (*), consistent with mineralization.

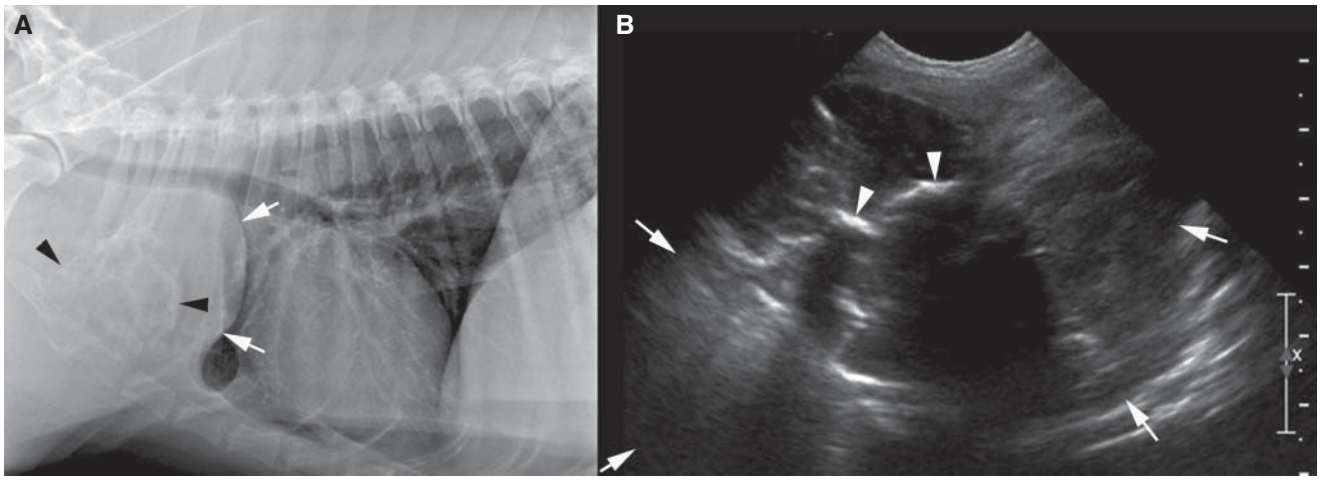


Figure 4.10. Primary rib tumor in an 11-year-old Labrador. A: On the lateral thoracic radiograph, a large soft-tissue mass (white arrows) associated with the cranial ventral thorax at the level of the costal cartilages of the second pair of ribs shows irregular amorphous mineralization (black arrowheads). **B:** Transverse plane ultrasonographic image of the rib mass (white arrows). The mass is of mixed echogenicity, with multiple hyperechoic areas (white arrowheads) corresponding to the mineralization seen radiographically. Strong acoustic shadowing is seen distal to these mineralized regions.

wall, causing variable alteration in their normal hyperechoic, shadowing surface. The osseous proliferative and/or lytic changes encountered in aggressive bone lesions are typically irregular and poorly defined when compared with benign processes such as rib fractures. In cases where there is doubt, thoracic radiographs would help to further characterize these changes.

Abnormalities of the Pleura and the Pleural Space

Pleural Effusion

Ultrasonography is useful in detecting and characterizing pleural effusion; identifying or ruling out an underlying problem, such as a cranial mediastinal mass; and guiding sampling or therapeutic thoracocentesis. Pleural effusion appears as echogenic or anechoic fluid separating the lung surface from the thoracic wall and diaphragm. The fluid echogenicity is mainly influenced by the concentration of free cells. Transudates, modified transudates, and chylous effusions can be slightly echogenic or anechoic (Figure 4.11). Exudates (e.g., pyothorax), malignant pleural effusions, or hemorrhages are usually moderately echogenic (Figures 4.11D, 4.12).

Free fluid may be differentiated from trapped fluid pockets by scanning the patient in different recumbent positions. Although free fluid accumulates in the dependent portion of the thorax, trapped fluid is not influenced by gravity and remains in the same region of the pleural space.

Chronic pleural effusion causes echogenic strands to develop within the pleural space, consistent with pleural adhesions or fibrinous bands.

Pleural Lesions

The pleural cavity can be affected by inflammation (pleuritis), in which case parietal and/or visceral thickening can be observed in association with pleural effusion (Figure 4.12).

Pleural neoplasia (such as carcinomatosis, mesothelioma, metastatic disease) can also occur. The detection of small pleural nodules and masses on radiographs is commonly hampered by the presence of pleural effusion. On ultrasonographic examination, pleural neoplasia manifests as irregular thickening, nodules, or masses of variable echogenicity associated with the pleura. Lesions arising from the parietal pleura are readily recognized, especially in the presence of pleural effusion (Figures 4.13–4.15). Even in the absence of pleural effusion, differentiation between pulmonary and parietal pleural lesions is usually possible based on real-time ultrasonography. Whereas a pulmonary mass moves with respiration, a mass arising from the parietal pleura remains stationary in comparison with the sliding lung (Mattoon and Nyland 1995).

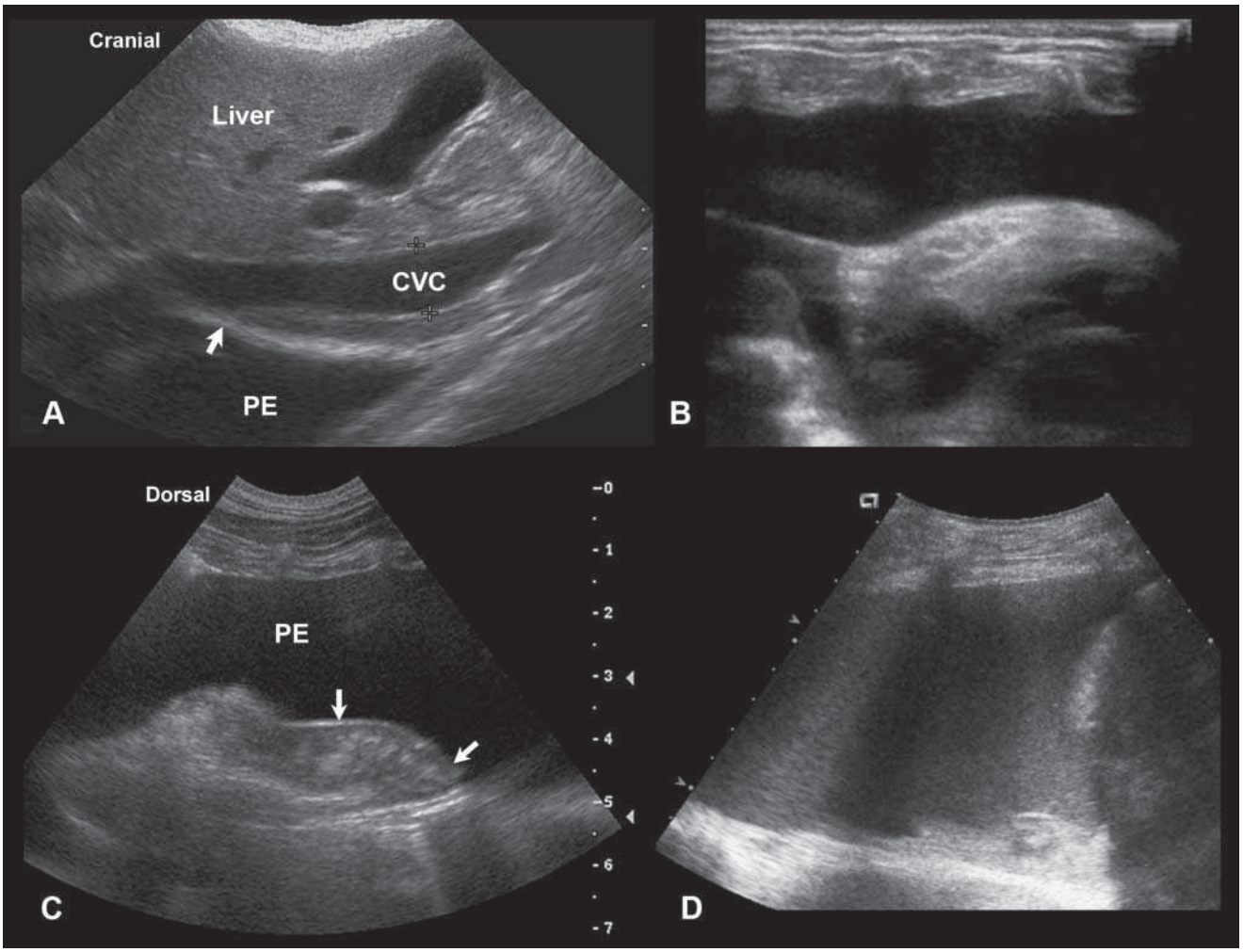


Figure 4.11. Pleural effusion (PE) in four patients. Subcostal/transhepatic (A) or intercostal approach (B-D) is used in these example to detect anechoic pleural effusion. The effusion is seen cranial to the diaphragm (arrow). Caudal vena cava (CVC) is distended in this dog with congestive heart failure **(A)**. Anechoic effusion is also noted in this 16-year-old cat with a modified transudate **(B)**, and in another cat with severe chylothorax **(C).** Notice **(B, C)** the concurrent lung lobe collapse (arrows). Markedly echogenic effusion is present in a 9-year-old Labrador Retriever with generalized lymphosarcoma **(D)**.

Nodules or masses arising from the visceral pleura cannot be easily distinguished from lesions originating from the pulmonary parenchyma (Figure 4.14).

Pneumothorax

Ultrasonography is increasingly used in emergency care as a screening procedure to diagnose or rule out pneumothorax in patients with acute respiratory compromise, especially after a reported trauma or thoracocentesis. Although radiography remains the imaging modality of choice to diagnose air within the pleural space, ultrasonographic assessment of the pleural space is recommended after interventional procedures, and the examiner should be aware of the ultrasonographic appearance of pneumothorax. Free air within the pleural space creates similar reverberation artifacts as normal lung (Figures 4.34, 4.35). However, the classic **gliding sign** of the lung against the parietal pleura is not observed. In cases of concurrent pleural effusion, a gas–fluid interface may be visualized.

Abnormalities of the Mediastinum

In animals with a wide mediastinum on radiographs, ultrasound facilitates differentiating fat accumulation from fluid or mediastinal masses. Additionally,

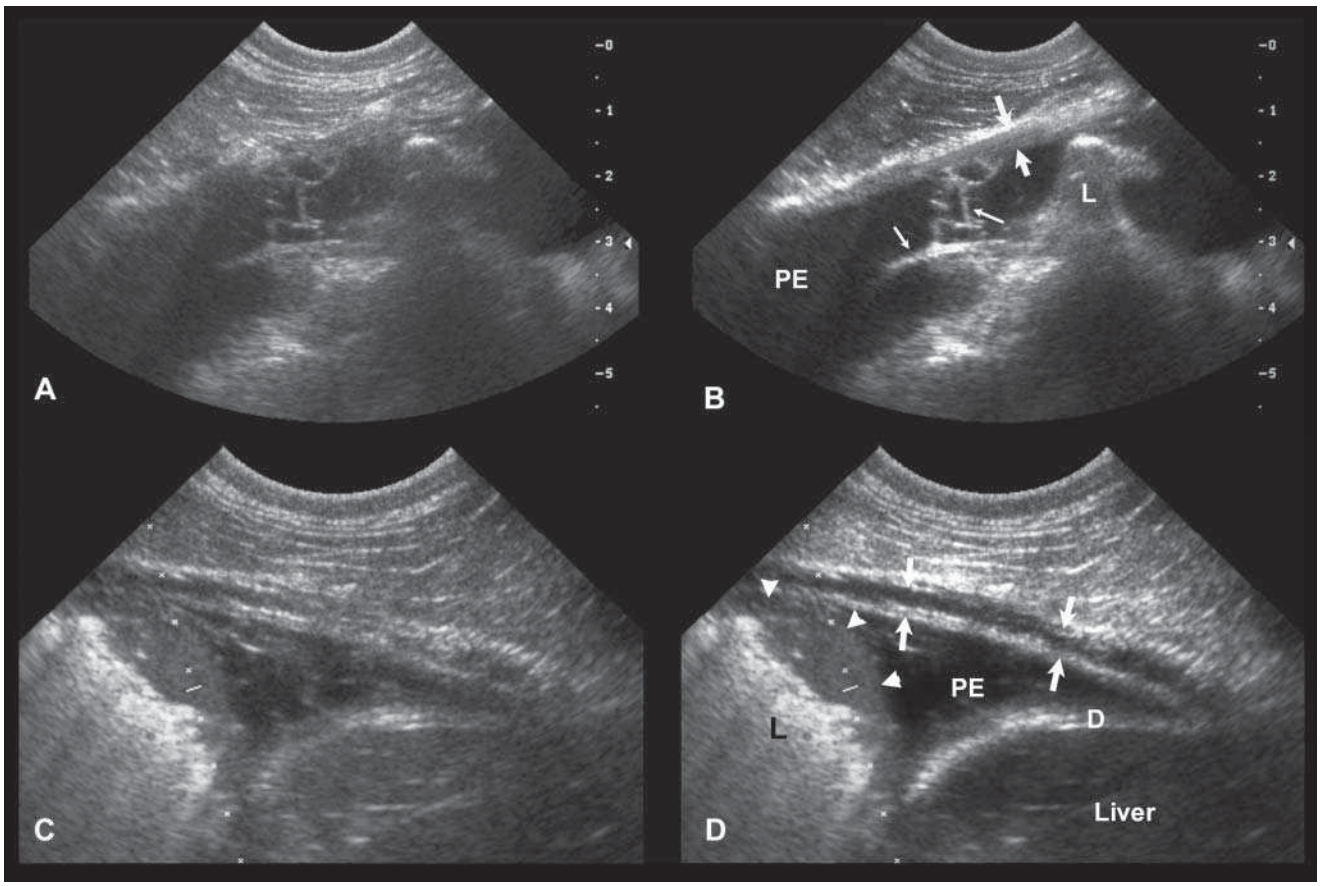


Figure 4.12. **Chronic pleuritis in a 2-year-old cat.** Ultrasonographic **(A, C)** and enhanced labeled **(B, D)** transverse images in which anechoic pleural fluid (PE) is associated with lung atelectasis (L). Hyperechoic linear strands (thin arrows) are visible within the fluid, consistent with pleural adhesions or fibrin strands and indicative of chronicity. The visceral pleura is also thickened (arrowheads). The superficial parietal pleura (arrows) is irregularly thickened, irregular, and hypoechoic. The visceral pleura of the left caudal lung lobe is also markedly thickened (arrowheads). Pleural effusion (PE) separates the lung lobe from the diaphragm (D).

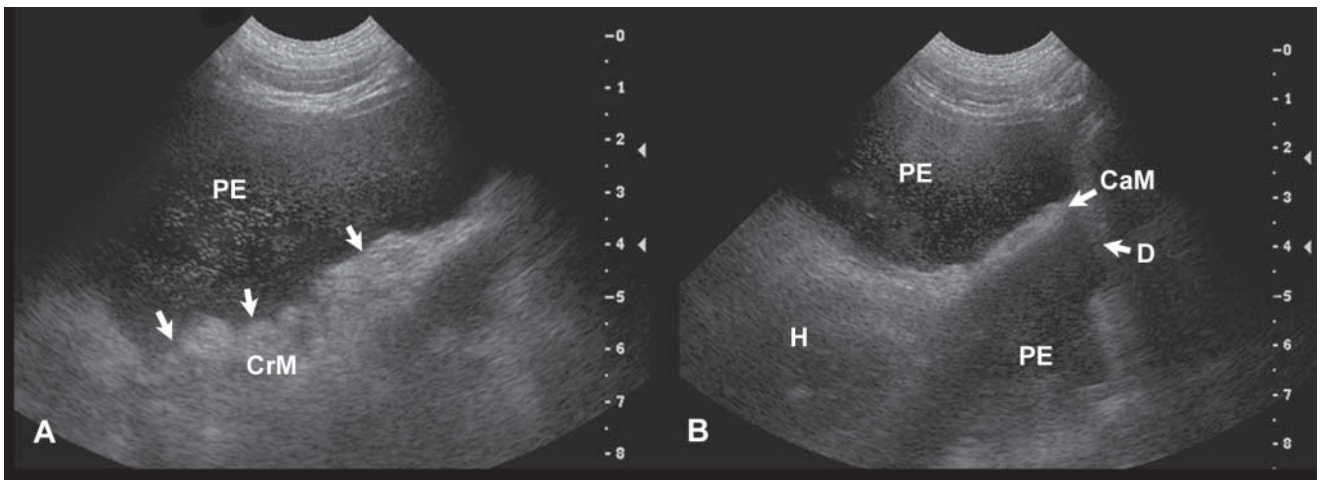


Figure 4.13. **Severe pleural effusion in a dyspneic dog with carcinomatosis.** Oblique intercostal sonographic images of the cranial thorax. A large volume of echogenic pleural effusion effusion (PE) is present in both pleural spaces, visible on each side of the caudal mediastinum (CaM). The border of the cranial mediastinum (CrM) is irregular and hyperechoic (arrows). D, diaphragm; H, heart.

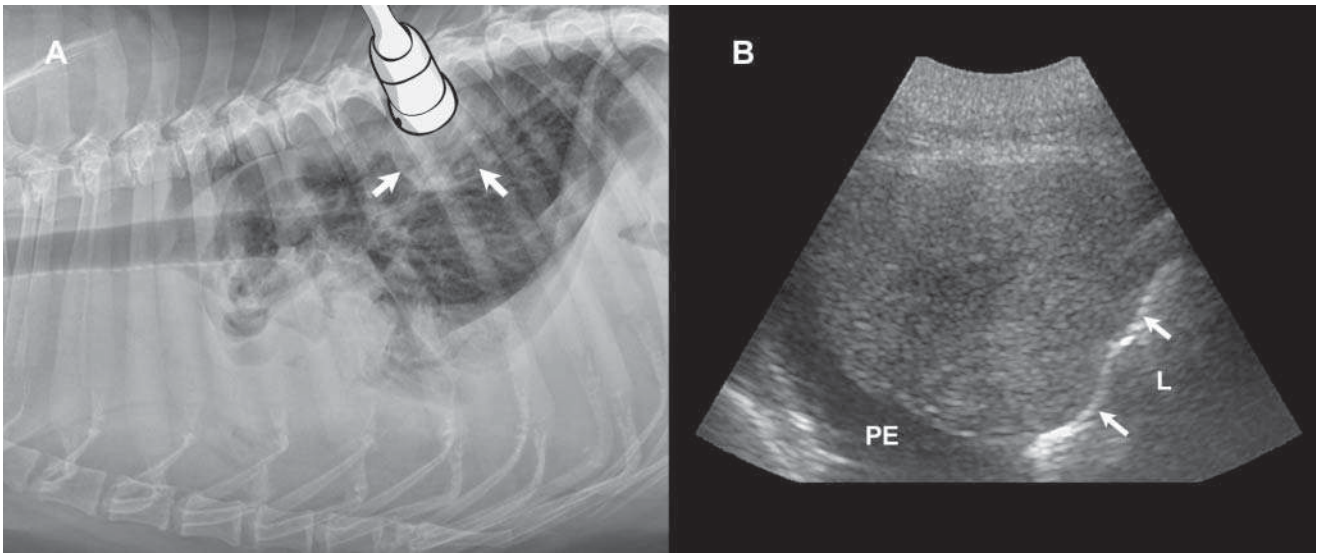


Figure 4.14. Pleural carcinomatosis and cranial mediastinal mass in a 9-year-old dog. A: Left lateral radiograph of the thorax. Moderate pleural effusion as well as a cranial mediastinal mass cause dorsal displacement of the trachea and lungs. A round soft-tissue opacity is associated with the dorsal thorax bordering the thoracic spine (arrows; under ultrasound transducer). **B:** Intercostal ultrasonographic image of the dorsal thoracic mass. The mass is seen arising from the pleura, is of moderate echogenicity and is separate from the hyperechoic lung interface (L, arrows) in the far field. Pleural effusion (PE) is also present. Fine-needle aspirates of the cranial mediastinal and pleural lesions were consistent with carcinoma.

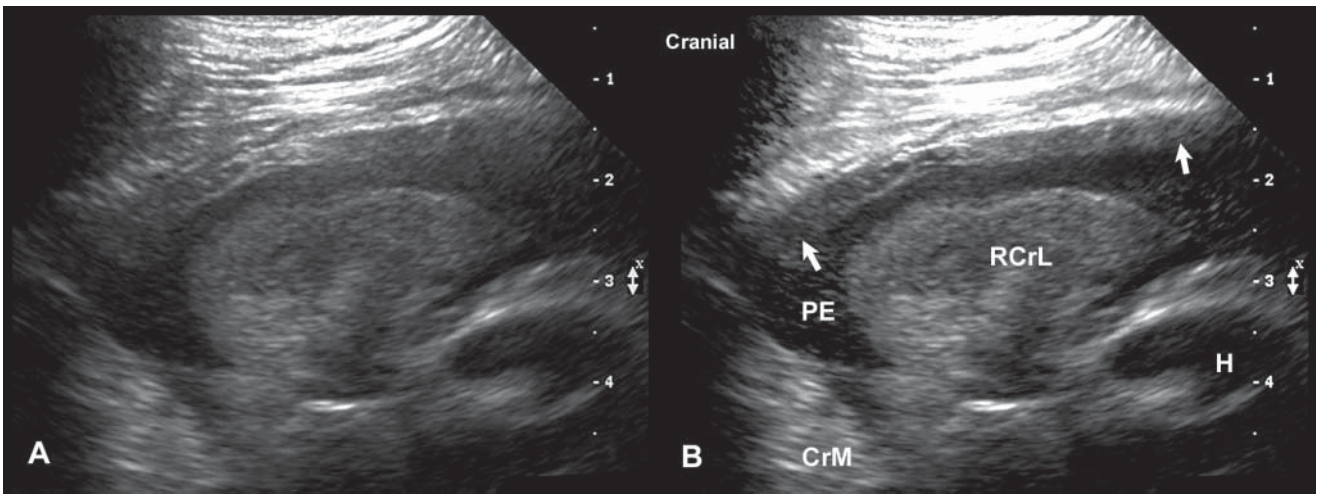


Figure 4.15. Pleural carcinomatosis and pulmonary carcinoma in a 10-year-old cat. Intercostal approach. On these dorsal ultrasonographic **(A)** and enhanced labeled **(B)** images, the right cranial lung lobe (RCrL) is rounded, irregular, and has assumed soft-tissue echogenicity because of replacement of normally air-filled parenchyma by neoplastic cells. Echogenic fluid (PE) separates the lung lobe from the parietal pleura. The parietal pleura (arrows) is thickened, slightly irregular, and unusually hypoechoic. CrM, cranial mediastinum; H, heart.

it enables identification of a cranial mediastinal mass in the presence of pleural effusion, characterization of cranial mediastinal mass lesions (cystic in contrast to solid), may allow assessment of middle or caudal mediastinal lesions, and is helpful in identifying a window suitable for interventional procedures.

Cranial Mediastinal Masses

These are most commonly found in the cranioventral mediastinum and are often accompanied by pleural effusion (Reichle and Wisner 2000). Their visualization depends on their location, size, and the presence of a suitable acoustic window. Differential diagnoses for

cranial mediastinal masses include branchial cysts, lymphadenomegaly, neoplasms (e.g., lymphoma or thymoma), inflammatory lesions (abscesses or granulomas), and hematomas. Fat accumulation may be confused with an infiltrative tumor; however, it usually does not distort the mediastinal vessels or lymph nodes.

Cranial mediastinal cysts are an occasional incidental finding in cats (Zekas and Adams 2002). They are often well circumscribed, thin-walled, and filled with anechoic fluid (Figure 4.16).

Enlarged sternal lymph nodes are recognized as rounded nodules or masses of variable size, margination, echotexture, and echogenicity immediately dorsal to the sternum (Figures 4.17–4.19). As the peritoneal cavity is partly drained by these nodes, ultrasonographic examination of the abdomen for underlying disease processes may be warranted in

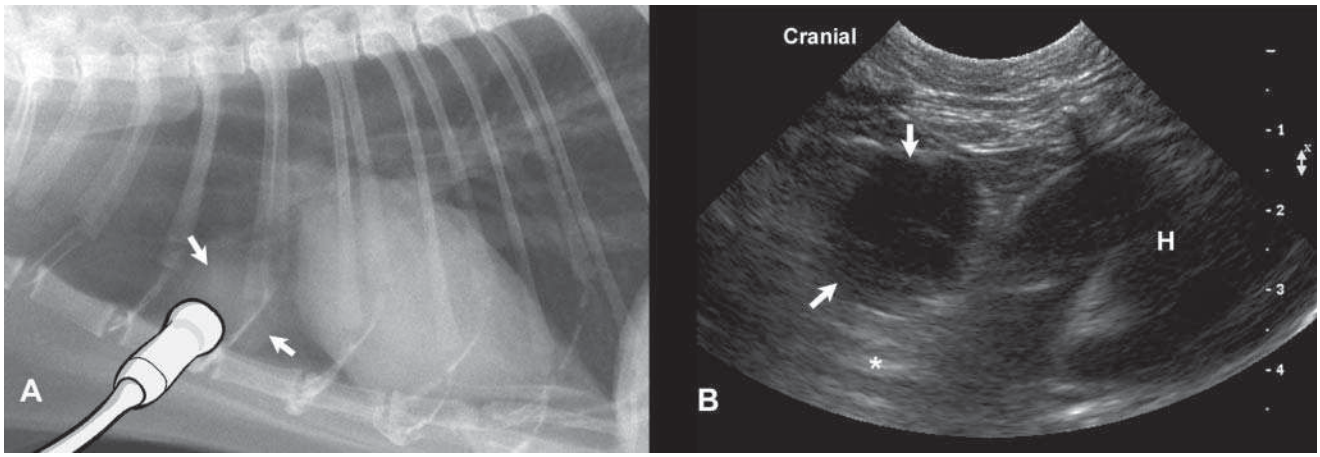


Figure 4.16. Cranial mediastinal cyst in a 9-year-old cat. A: Lateral thoracic radiograph demonstrating an ovoid area of increased opacity immediately cranial to the heart (arrows). **B:** Ultrasonographic image obtained by using an intercostal approach immediately dorsal to the sternum at the level of the fourth intercostal space. Cranial to the heart (H) is a round anechoic structure with distal enhancement (*), consistent with the presence of a cranial mediastinal cyst.

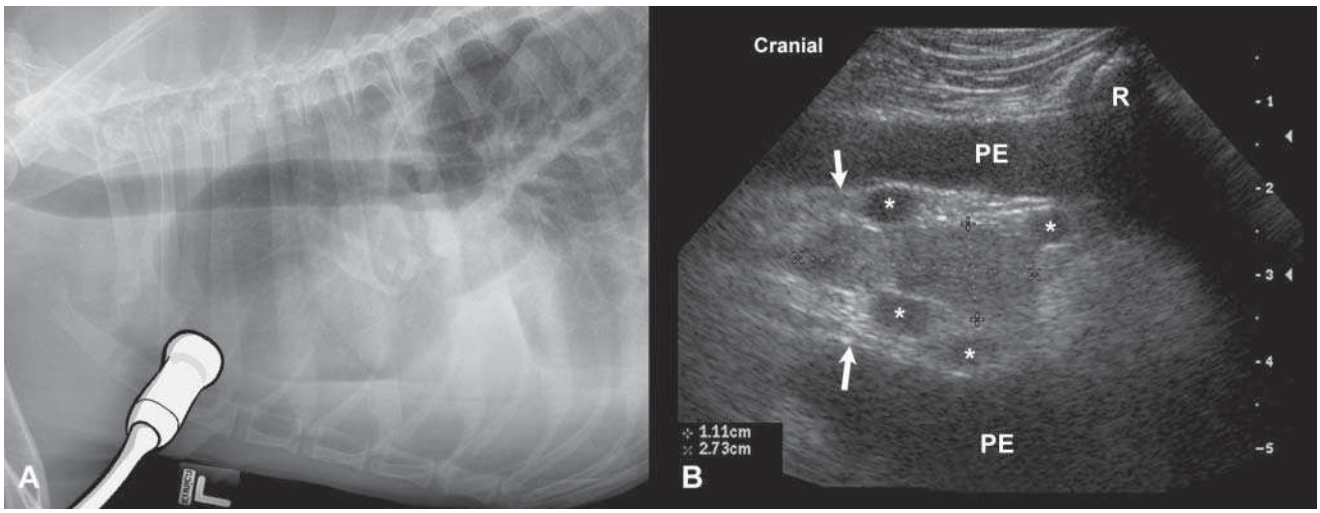


Figure 4.17. Reactive sternal lymph node in a dog with chylothorax. A: Lateral thoracic radiograph showing significant pleural effusion that masks thoracic structures including the cardiac silhouette. The lung lobes are retracted from the body wall and appear rounded, consistent with chronic effusion. **B:** Ultrasonographic image obtained at the right second intercostal space immediately dorsal to the sternum. Mildly echogenic effusion (PE) is present on both sides of the cranial mediastinum (arrows). A mildly enlarged sternal lymph node (cursors) is surrounded by hyperechoic fat and hypoechoic vessels (*). A curved hyperechoic interface casting strong shadowing, consistent with a rib (R), is identified in the near field.

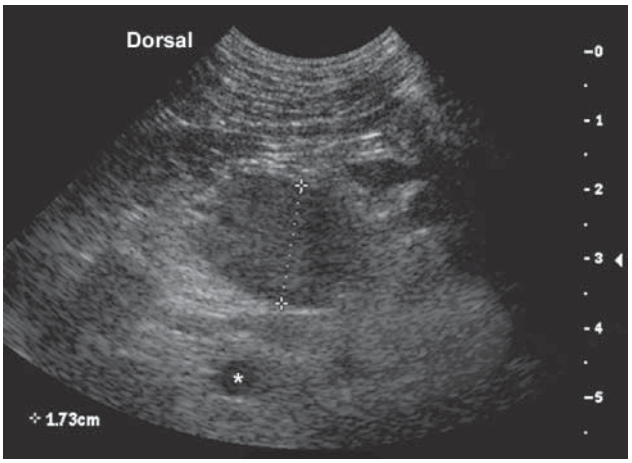


Figure 4.18. Metastatic sternal lymph node in a dog with splenic hemangiosarcoma and hemoabdomen. Transverse ultrasonographic image of an enlarged sternal lymph node (cursors) via an intercostal approach dorsal to the sternum at the level of the second intercostal space. The enlarged lymph node appears as a round hypoechoic nodule surrounded by echogenic fat and adjacent to anechoic vessels (*). The final histopathologic diagnosis was metastatic hemangiosarcoma.

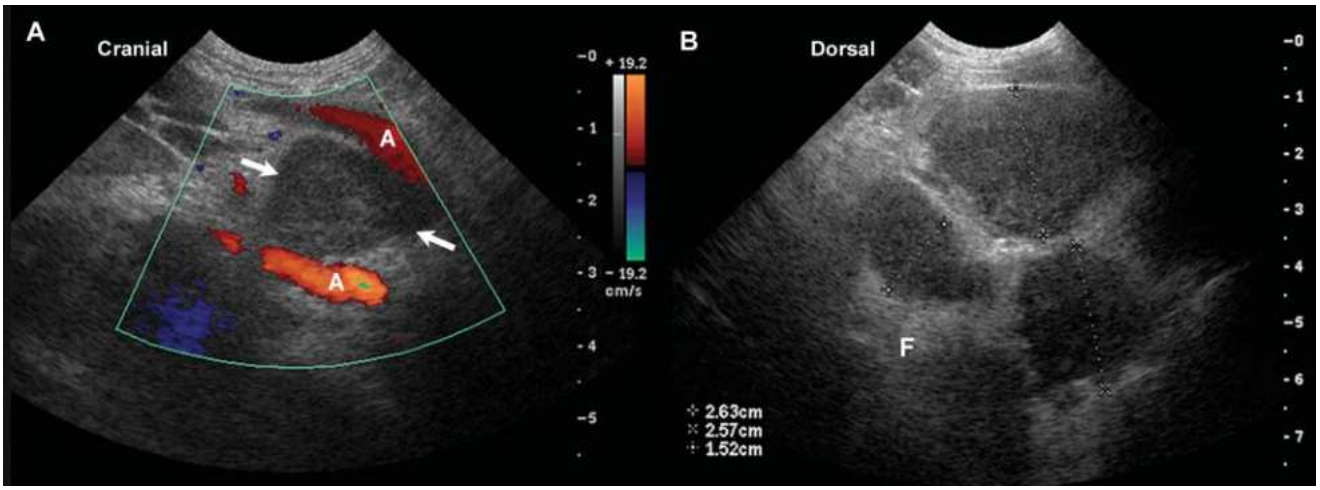


Figure 4.19. Mediastinal lymphadenopathy in a 5-year-old Bernese mountain dog with disseminated histiocytic sarcoma. Sagittal color Doppler **(A)** and transverse B-mode **(B)** intercostal sonographic images of the cranioventral thorax. A cranial mediastinal mass was suspected on radiographs. Multiple well-defined, hypoechoic nodules and masses (arrows and cursors) are surrounded by mediastinal hyperechoic fat (F) and arteries (A).

affected patients. Although reactive lymph nodes tend to be smaller than neoplastic or granulomatous lesions, ultrasonographic differentiation of these entities, and differentiation of an enlarged lymph node from cranial mediastinal mass lesions of other etiology, may not be possible.

Masses of inflammatory or neoplastic etiology may appear similarly rounded or lobulated, solid or cystic, homogeneous or inhomogeneous (Figures 4.20–4.25). Large lesions may infiltrate the surrounding structures, hampering determination of their origin. Cranial mediastinal lymphomas tend to appear as solid masses (Figure 4.20), while thymomas more commonly have a cystic component (Figure 4.21) (Tidwell 1998). However, cranial mediastinal masses cannot be differentiated based solely on their ultrasonographic appearance, and histopathology or cytology is needed to assess the nature of the lesion.

Other Mediastinal Lesions

Radiography (including contrast procedures) and thoracic computed tomography (CT) remain the imaging modalities of choice for the diagnosis of lesions

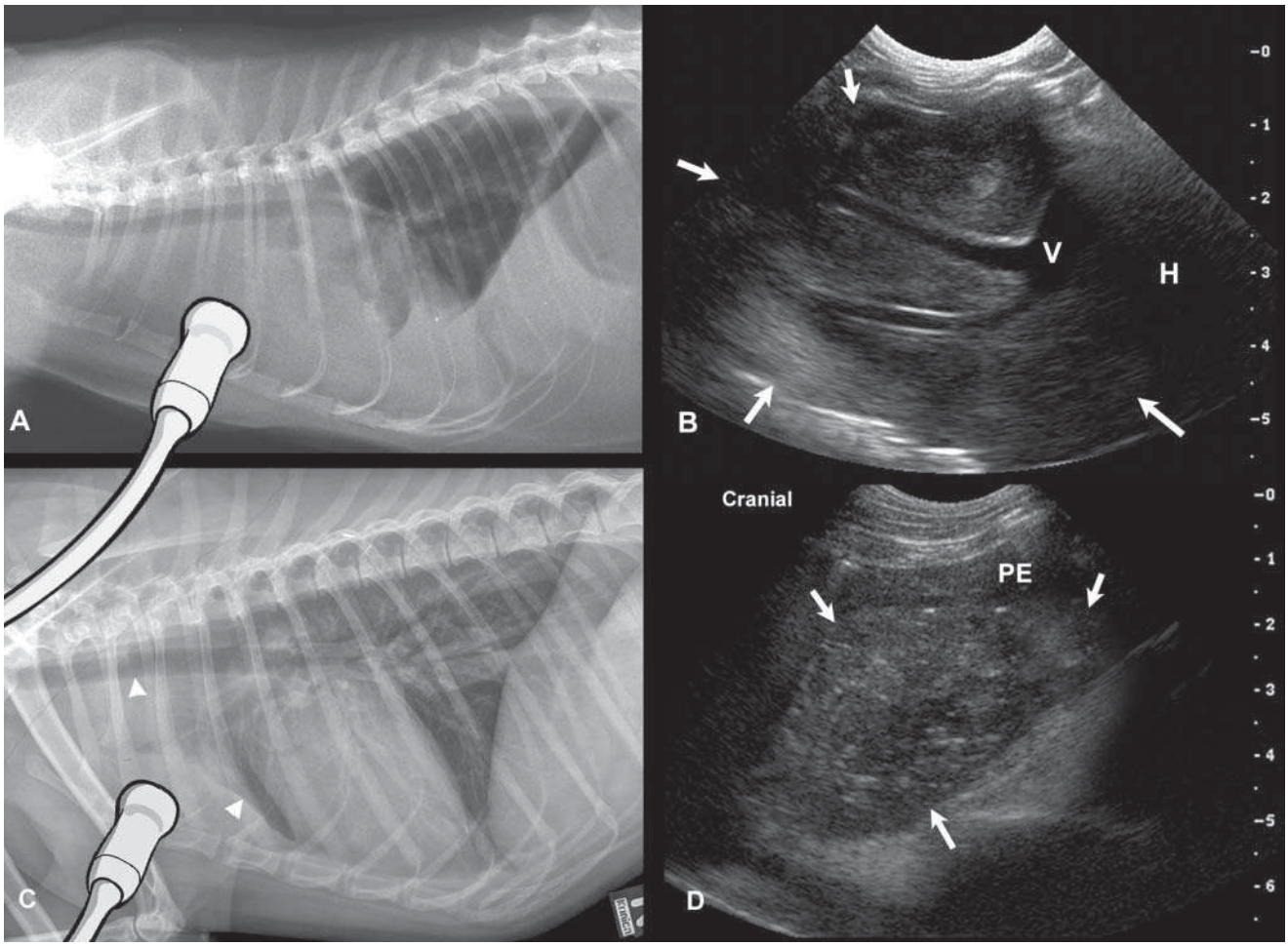


Figure 4.20. **Cranial mediastinal lymphomas. A:** On the lateral thoracic radiograph of a 4-year-old cat there is a large cranial mediastinal mass silhouetting, with the heart and displacing the trachea dorsally. Pleural effusion is also present, as indicated by scalloped fluid opacity associated with the ventral thorax, pleural fissure lines, and retraction of the caudodorsal lung lobes from the thoracic wall and diaphragm. **B:** Longitudinal sonogram via an intercostal approach. A large homogeneous mass (arrows) is associated with the cranial mediastinum and in contact with the heart (H). Large vessels are visible within this mass as anechoic tubular structures with strongly hyperechoic vessel walls (V). Lymphoma was diagnosed based on histopathology. **C:** Lateral thoracic radiograph of a large soft-tissue opacity in the cranial mediastinum of a 7-year-old Labrador Retriever. The opacity is displacing the trachea and cranioventral lung margin dorsally (arrowheads). **D:** Corresponding ultrasonographic image obtained using a dorsal oblique plane through a right intercostal window. A well-defined hypoechoic mass with hyperechoic speckles is identified in the cranial mediastinum (arrows). A small amount of anechoic pleural effusion (PE) is also observed around the mass.

associated with the dorsal mediastinum, trachea, esophagus, and heart base. Transesophageal ultrasonography may also be of great value when available. Large heart base tumors may be visualized through the heart or by using an intercostal approach (Figure 4.26). Esophageal dilation, foreign bodies, and masses (neoplasms or granulomas) may occasionally be visualized via a thoracic inlet or transhepatic approach, depending on their location and size (Figure 4.27).

Ultrasonography has been described as an alternative to fluoroscopy in the diagnosis of tracheal collapse (Rudorf et al. 1997). Additionally, it may prove useful in distinguishing between tracheal collapse and other causes of tracheal narrowing, such as tracheal wall thickening or compressive mass lesions (Figure 4.28). The ultrasonographic examination is performed using a thoracic inlet approach and is limited to the cervical and cranial thoracic trachea.

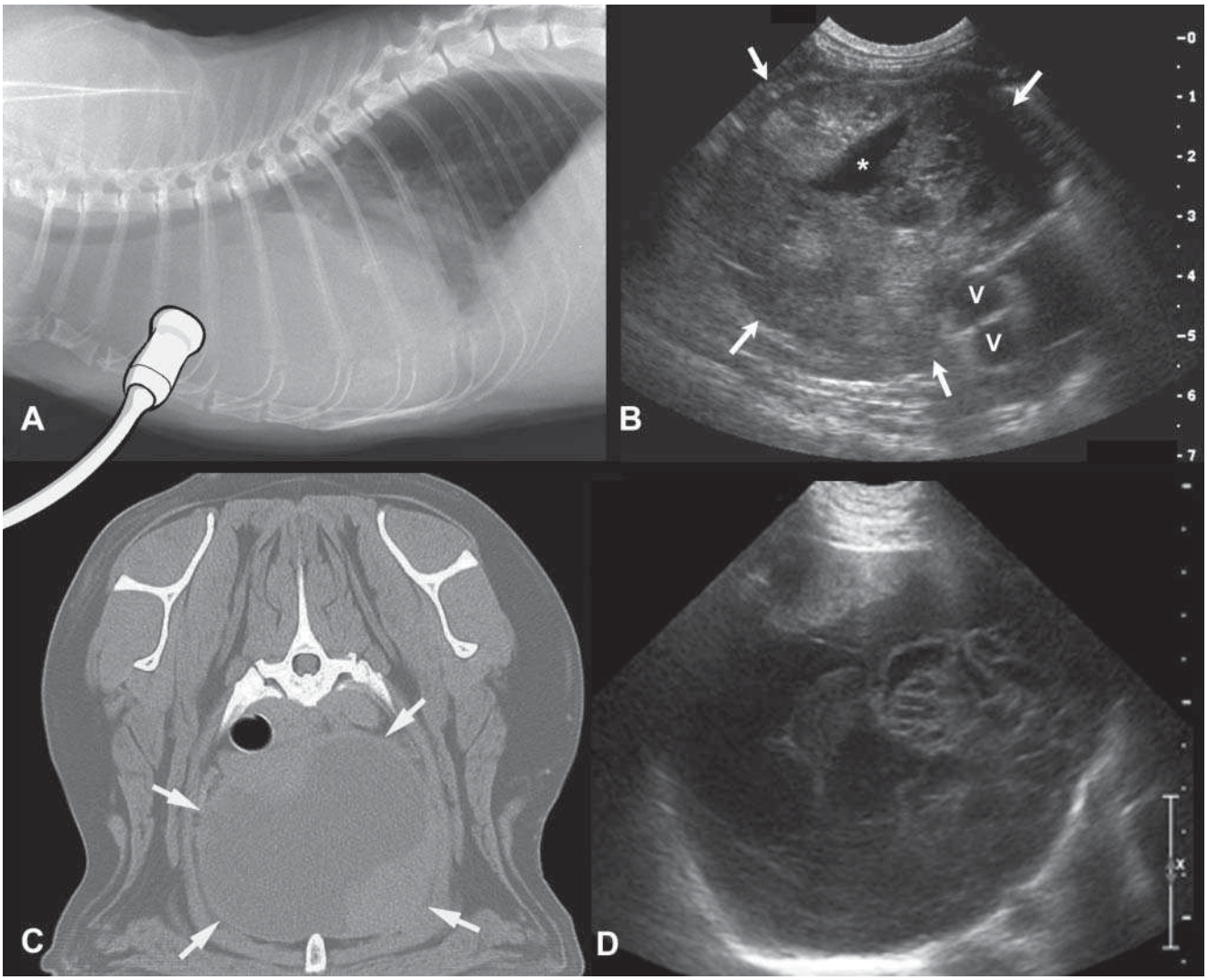


Figure 4.21. **Thymomas. A:** Lateral thoracic radiograph of a 12-year-old cat demonstrating a large cranial mediastinal mass causing dorsal displacement of the trachea and silhouetting with the cardiac silhouette. **B:** Ultrasonographic image obtained through a right cranial intercostal approach shows a large cranial mediastinal mass lesion (arrows) of mixed echogenicity, with several anechoic (cystic or cavitated) areas (*). Cranial mediastinal vessels (V) are seen in the far field in cross-section as anechoic circular structures. Thymoma was diagnosed based on ultrasonographically obtained biopsy samples. **C:** Computed tomography of an 11-year-old Labrador cross with a large cystic mediastinal mass (arrows). **D:** Ultrasonographic image of the same mass showing a large cystic component.

Pulmonary Disorders

The ability to assess pulmonary lesions depends on the location and size of the lesion, as well as the presence of a suitable acoustic window. Normally aerated lung, and lesions completely surrounded by normally aerated lung, cannot be evaluated ultrasonographically. However, when fluid or cells replace the air within alveoli and/or airways, or if a lung lobe collapses, evaluation of the affected lung becomes possible. Pulmonary abnormalities commonly detected and investigated by means of ultrasonography are atelectasis, consolidation, and pulmonary nodule/mass. When present, the pleural effusion facilitates the evaluation of lobar size, shape, and contour. A composite of the main ultrasonographic features of different pulmonary disorders is shown in Figure 4.29. Although these sonographic findings are helpful in establishing a preliminary diagnosis, fine-needle aspirations or biopsies are required in most instances to confirm.

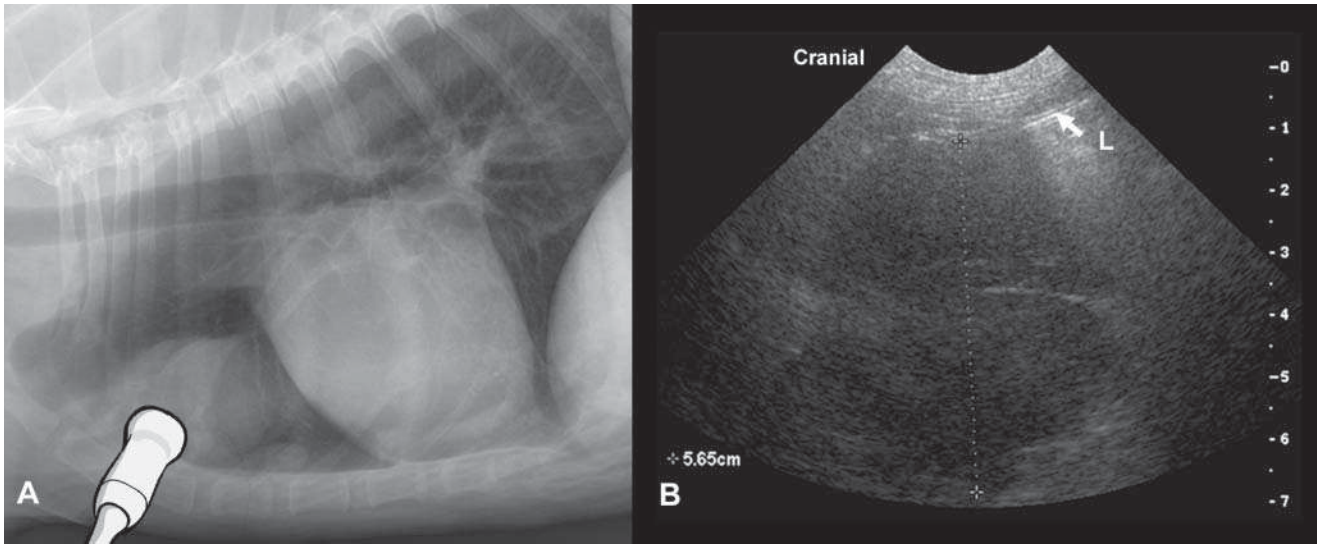


Figure 4.22. **Cranial mediastinal mass in an 11-year-old mixed-breed dog. A:** On this lateral thoracic radiograph, a well-circumscribed round soft-tissue opacity in the cranial thorax is suspected to originate from the mediastinum, supported on the ventrodorsal radiograph (not shown). **B:** Using a right parasternal intercostal approach, a lobulated hypoechoic mass is noted (between cursors). Fine-needle aspiration yielded a cytologic diagnosis of mast cell tumor. L, lung interface.

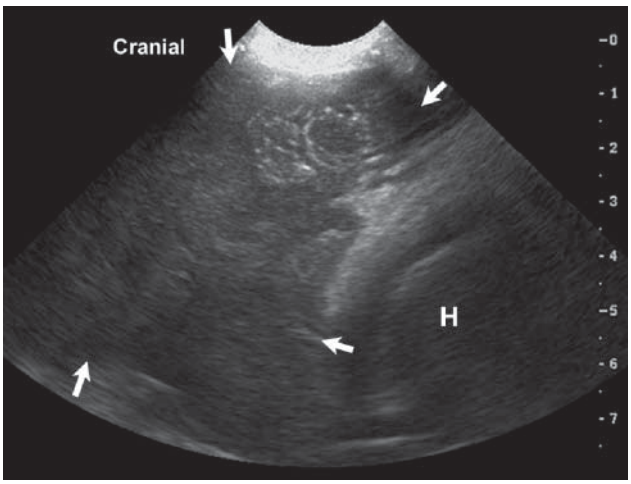


Figure 4.23. **Cranial mediastinal lymphoma in a 1-year-old Lhasa Apso.** Dorsal sonogram via a right intercostal approach. A large, ill-defined mass lesion (arrows) is cranial to the heart (H). The lesion is mainly hypoechoic, with hyperechoic foci in the near field.

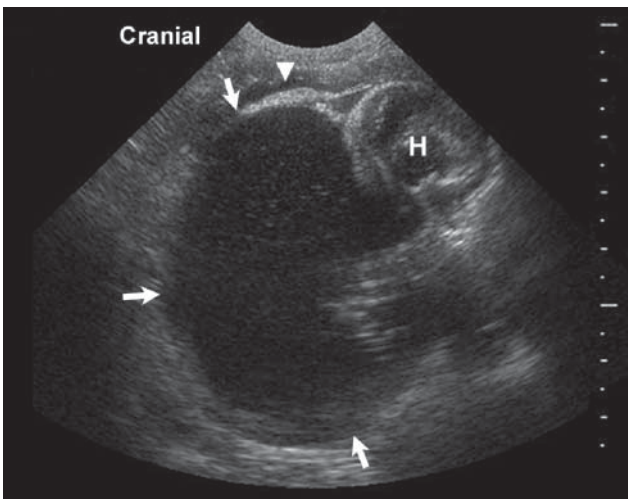


Figure 4.24. **Cranial mediastinal mass in a domestic long-hair cat.** The examination is performed by using a right intercostal approach. A large mass, mixed in echogenicity, with a large, hypoechoic cavitary component (arrows) is cranial to the heart (H). A small amount of pleural effusion is present in the near field (arrowhead). The histopathologic diagnosis was adenocarcinoma.

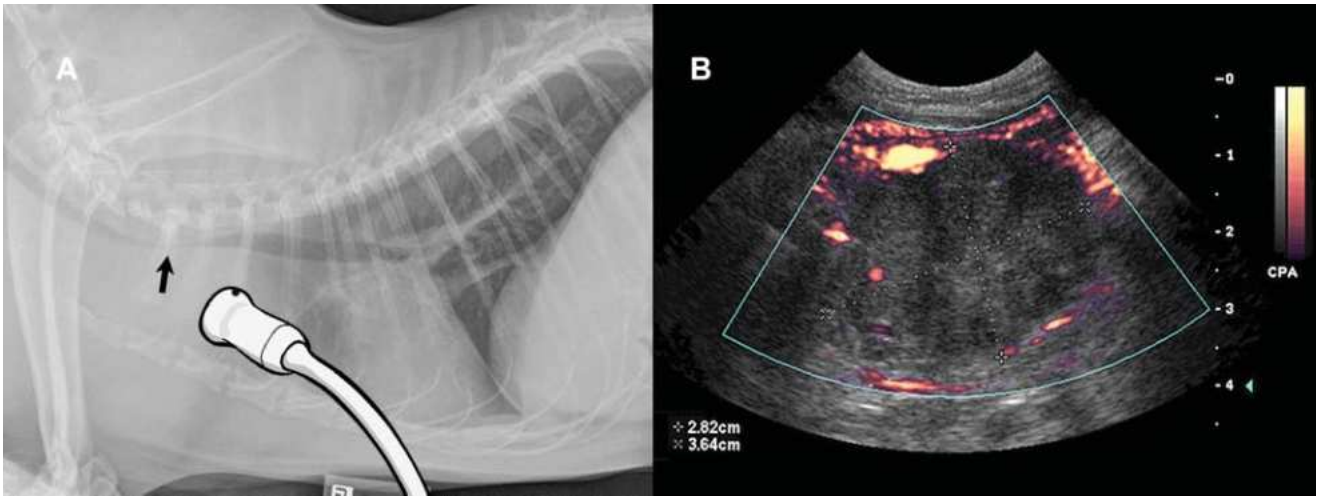


Figure 4.25. **Granulomatous cranial mediastinal mass in a cat. A:** On the lateral thoracic radiograph there is a large, ill-defined, cranial mediastinal mass displacing and compressing the trachea (black arrow). Severe swelling also extends throughout the neck. **B:** This transverse sonogram via an intercostal approach shows a large heterogeneous mass (cursors) associated with the cranial mediastinum. Increased vascularity is noted at the periphery of the mass using power Doppler. Cryptococcosis was diagnosed based on ultrasound-guided fine-needle aspiration.

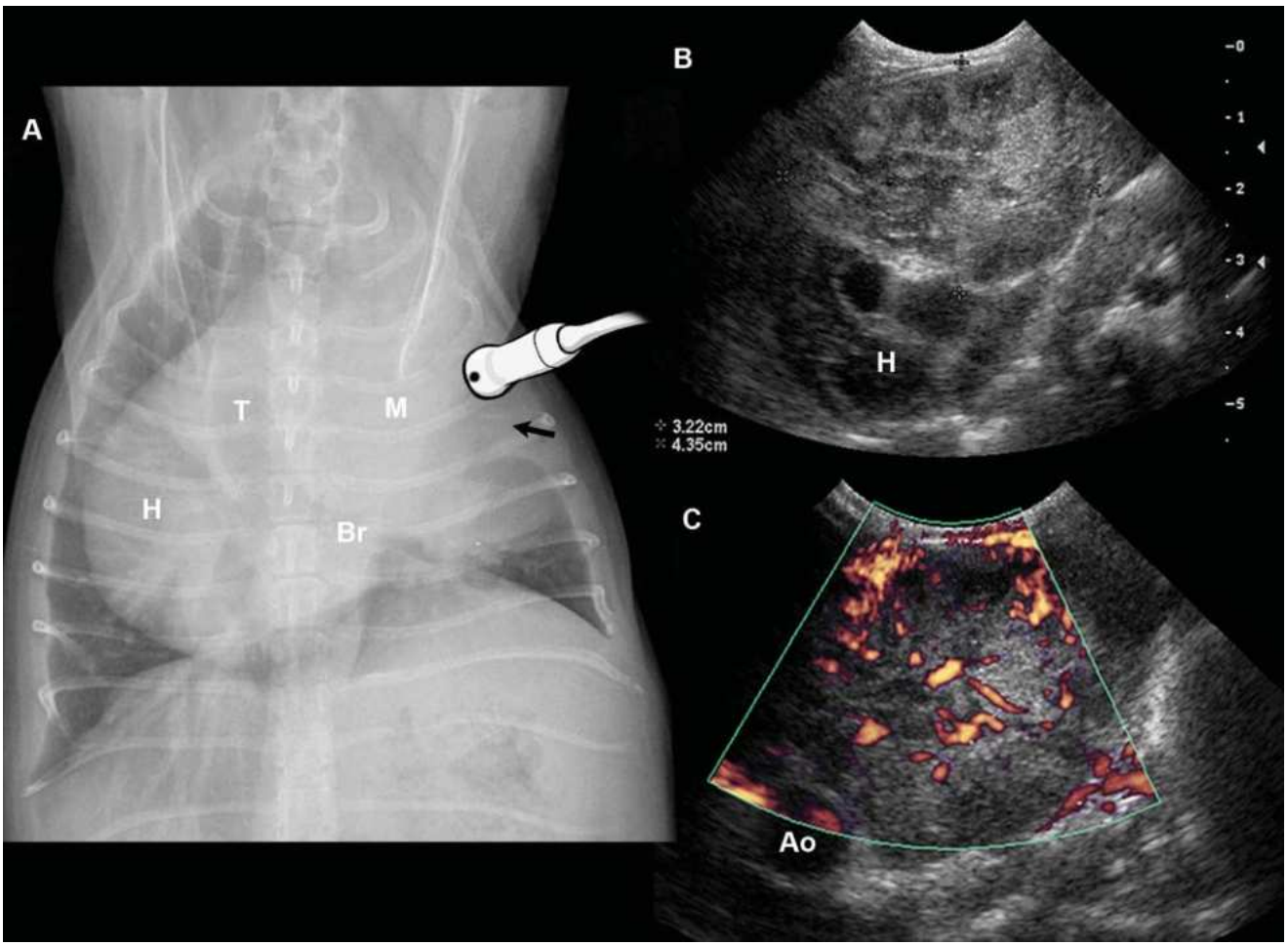


Figure 4.26. **Heart base tumor in a small-breed dog.** (for full caption, see facing page)

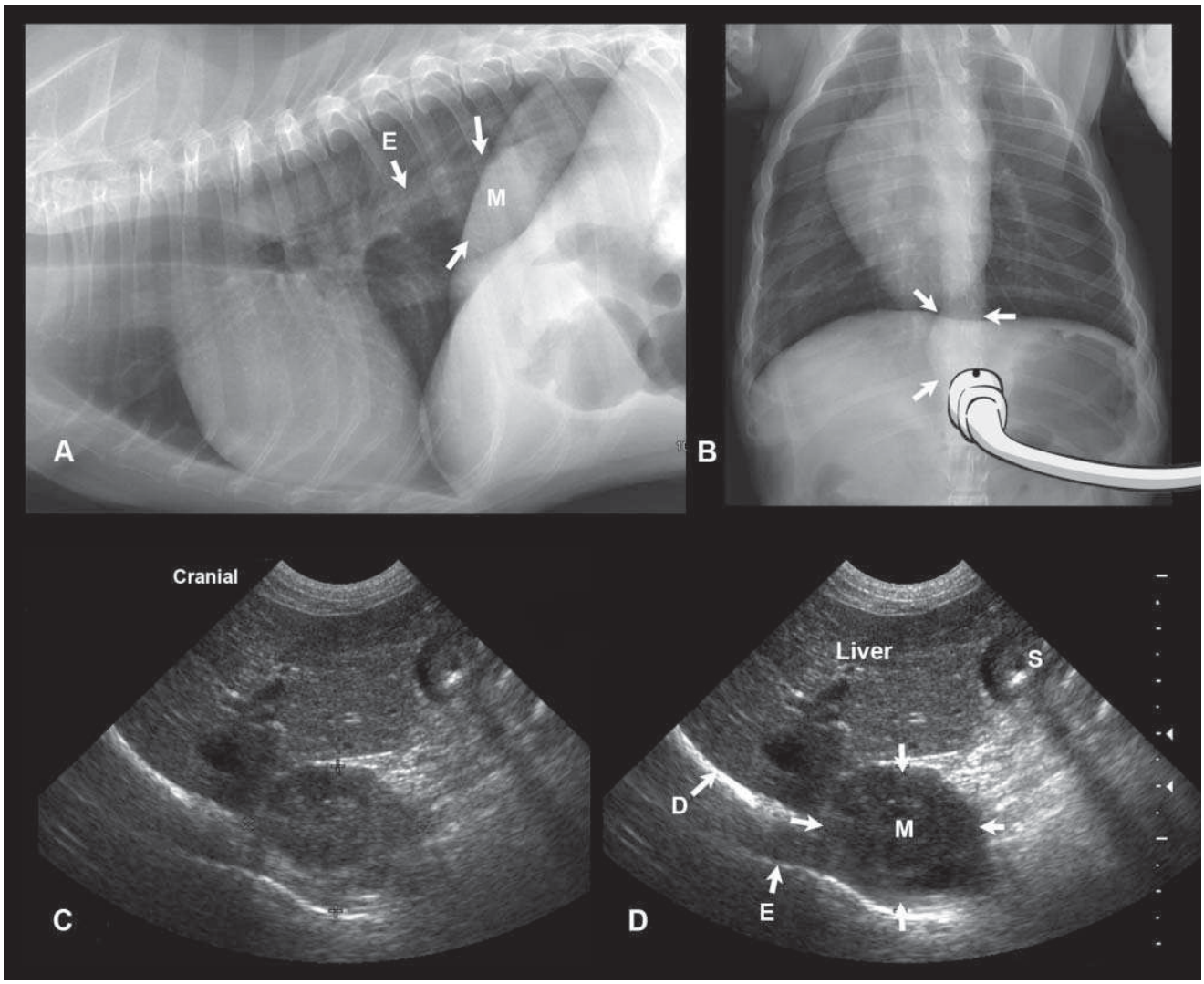


Figure 4.27. **Esophageal mass in a 14-year-old Welsh Corgi. A and B:** Thoracic radiographs reveal a homogeneous, soft-tissue opacity (M, arrows) associated with the caudal mediastinum, in the caudal region of the esophagus (E), summating with the diaphragm. The position of the ultrasound transducer is shown in **B**. **C and D:** Ultrasonographic and enhanced labeled images obtained with a ventral transhepatic approach (sagittal plane). At the level of the esophageal hiatus, the mass (M, arrows) is associated with the esophagus (E). Liver and stomach (S) are visible in the near field, and the lung-diaphragm interface (D) manifests as a curvilinear, strongly hyperechoic structure bordering the esophageal mass. **E and F:** Esophageal mass in a 16-year-old cat presented for a 6-month history of regurgitation. The sonographic image **(E)** via a transhepatic approach shows a large mass. At this location, the collapsed lumen is not visible. The rounded anechoic structure on the side of the mass is the aorta. Ultrasound-guided fine-needle aspirates were performed. The corresponding computed tomography (CT) image **(F)** shows the mass with a small amount of gas in the lumen. The trachea (*) is partially compressed.The cytological diagnosis was round-cell tumor (either histiocytic sarcoma or lymphoma).

Figure 4.26. **Heart base tumor in a small-breed dog. A:** The ventrodorsal thoracic radiograph shows a large soft-tissue mass in the left cranial hemithorax. The trachea (T) and cardiac silhouette (H) are displaced to the right, and the left mainstem bronchus (Br) is partially compressed. The increased opacity identified in the left mid-thorax adjacent to the mass (arrow) is thought to represent a focal alveolar pattern or a small-volume pleural effusion. **B:** B-mode sonogram obtained using a transverse intercostal approach (as shown in A) demonstrates a well-defined mixed echogenic solid mass (cursors) displacing the heart (H). **C:** When power Doppler is used, this mass appears strongly vascularized. The aorta (Ao) is in the far field, adjacent to the mass. A neuroendocrine tumor was highly suspected on cytological specimens obtained with fine-needle aspiration.

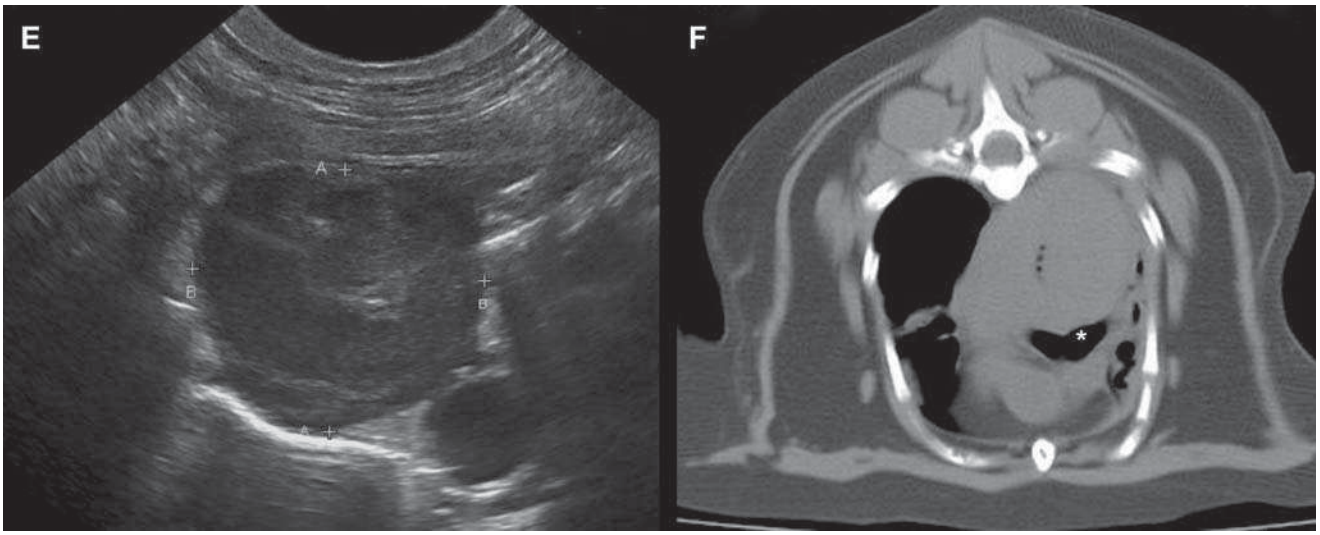


Figure 4.27. *Continued*

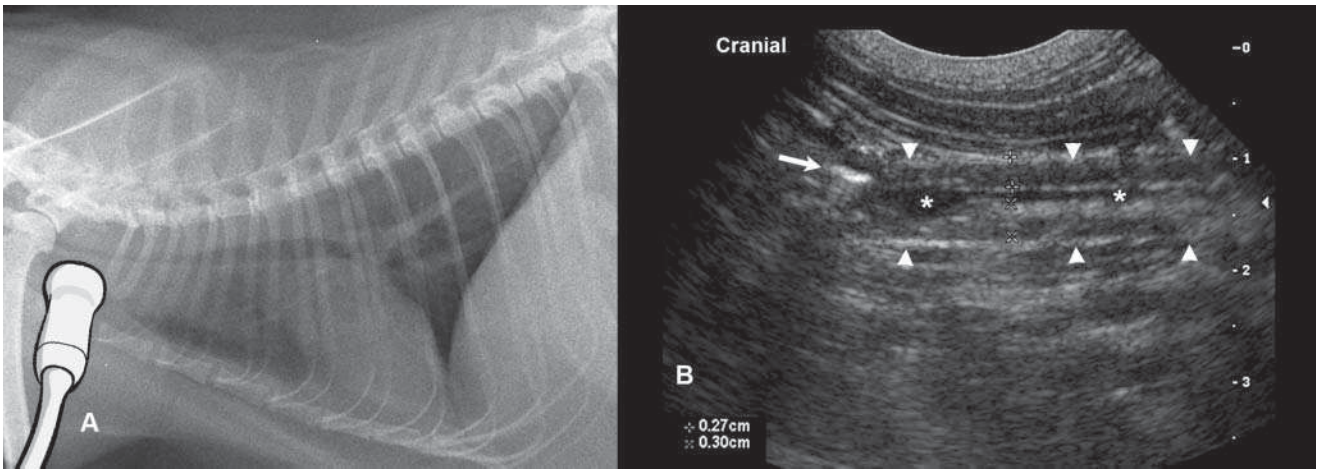


Figure 4.28. **Tracheal wall thickening caused by eosinophilic airway disease in a 4-year-old cat. A:** The lateral thoracic radiograph shows extensive narrowing of the cranial thoracic trachea. **B:** An ultrasonographic examination of the trachea (arrowheads) is performed by using a thoracic inlet approach. The tracheal wall (cursors) is thickened (0.3 cm) and hypoechoic. Anechoic material, consistent with mucus, is present within the severely narrowed tracheal lumen (*). A gas bubble is present more cranially, appearing as a reverberating hyperechoic focus (arrow).

Atelectasis

Atelectasis (pulmonary collapse) may occur secondary to increased pressure within the pleural space (pneumothorax or pleural effusion), may be a sequela to bronchial obstruction, or may result from decreased pulmonary compliance and inability of the lung to inflate properly. Ultrasonographic assessment of atelectatic lung is possible in cases of concurrent pleural effusion or adjacent compressive mass, but can be difficult if atelectasis is caused by other factors such as pneumothorax. Atelectatic lung lobes appear as small, smoothly marginated, triangular structures, outlined by pleural fluid, when present (Figure 4.29B). The echogenicity of atelectatic lung depends on the amount of residual air within the air spaces. Linear and speckled hyperechoic foci, indicating residual air within bronchi and alveoli, as well as bronchial walls, are often seen. Additionally, vessels can be visualized, particularly by means of color or power Doppler, although respiratory motion may affect the quality of the Doppler signal. Completely collapsed lung lobes tend to be similar in echogenicity and

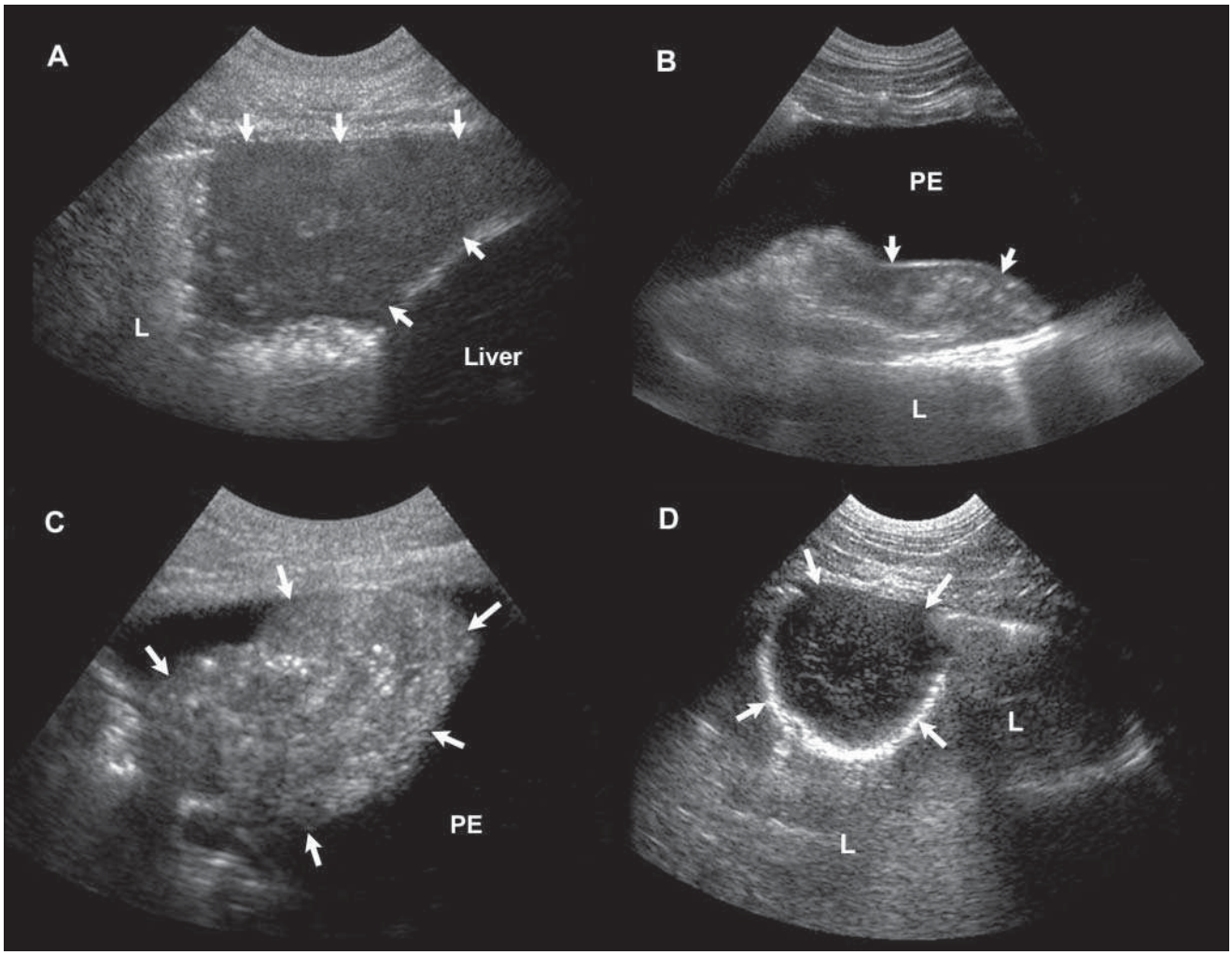


Figure 4.29. **Enhanced sonographic images of common pulmonary abnormalities. A:** Consolidation. Normal pulmonary parenchyma is filled with fluid or replaced with inflammatory or possibly neoplastic infiltrates. The affected portion (arrows) is hypoechoic when compared with the normally aerated, hyperechoic lung portion (L). The lung lobe retains its normal size, shape, and contour. **B:** Atelectasis. The lung is collapsed because of pleural effusion (PE). The affected lung lobe is significantly reduced in volume (arrows). Occasional hyperechoic foci within the collapsed lung lobe are consistent with a small amount of residual air. The reverberating interface of the contralateral air-filled lung is seen in the far field. **C:** Pulmonary mass (carcinoma). With increasing size, pulmonary mass lesions cause loss of the normal shape and margination of a lung lobe, with distortion of the pulmonary border and the normal triangular form of a lung lobe (arrows). These changes are enhanced if PE is present. The echogenicity of pulmonary mass lesions is variable. **D:** Pulmonary nodule. Lung nodules are typically rounded, hypoechoic, and well demarcated from the peripheral aerated lung (arrows). These nodules can only be detected if they are in contact with the thoracic wall. L, aerated lung.

echotexture to liver. In cases of obstructive atelectasis, ultrasonography may prove useful in identification of the obstructive lesion (e.g., mass).

Consolidation

Early or mild pulmonary infiltrative diseases result in multifocal interruption of the normal lung surface by small hyperechoic foci with distal shadowing called "comet tail" or "ring-down" artifacts (Louvet and Bourgeois 2008). In more advanced cases, when fluid or cells uniformly infiltrate the pulmonary air spaces, the lung often has an echogenicity and echotexture similar to liver (**hepatized lung**) (Schwarz and Tidwell 1999). The affected lung lobe typically retains its normal shape and volume (Figures 4.30–4.34). Air-filled

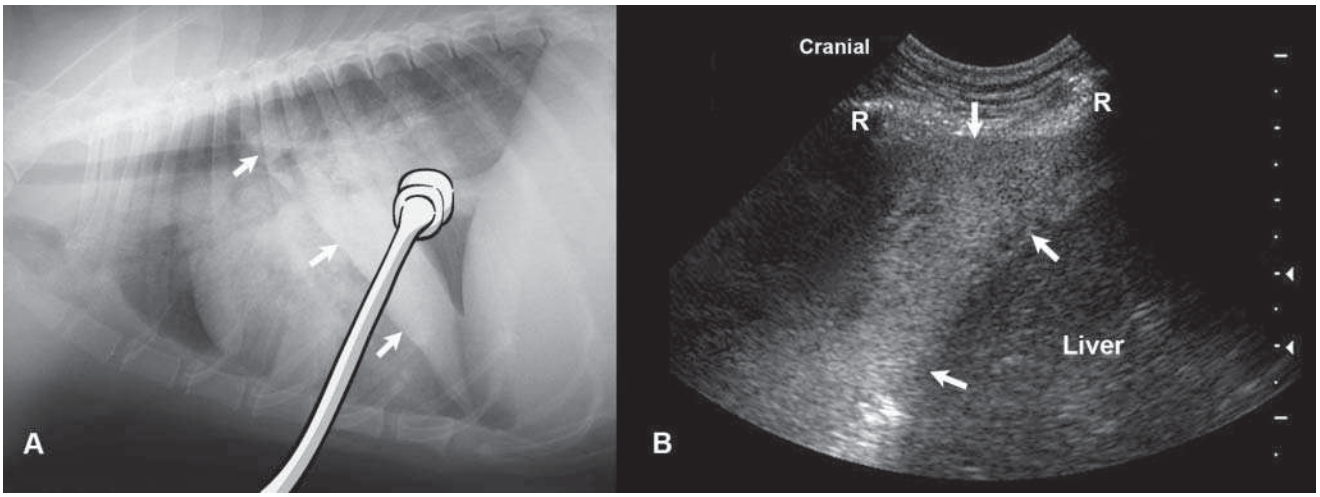


Figure 4.30. **Acute suppurative pneumonia with hemorrhage in a 10-year-old Labrador Retriever. A:** The right lateral radiograph of the thorax shows an alveolar pattern in the left caudal lung lobe and a clear border between the left cranial and caudal lung lobe (lobar margination [arrows]). There is also a mixed alveolar pattern and an interstitial pattern in the left cranial lung lobe. **B:** The ultrasonographic examination is performed in a dorsal plane using a left caudal dorsal intercostal approach. The left caudal lung lobe is homogeneously echogenic (arrows) and is hyperechoic to the hepatic parenchyma seen caudal to the diaphragm. Acoustic shadows related to superficial ribs (R) are present.

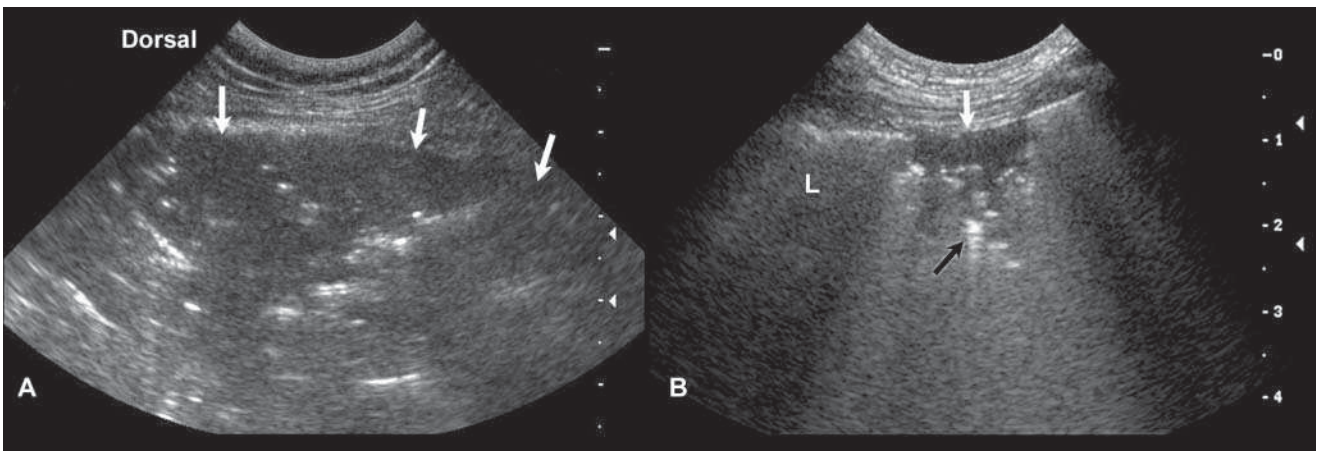


Figure 4.31. **Aspiration pneumonia in two dogs.** Both examinations are performed with a right intercostal approach. **A:** The right middle lung lobe (arrows) is homogeneous and mostly hypoechoic, with a few hyperechoic foci representing gas inclusions. The lung lobe retains its normal triangular shape and size. There is no evidence of pleural effusion. **B:** Focal pneumonia (white arrow) involving the right middle lung lobe, which appears as an irregular, hypoechoic region with gas speckles associated with comet-tail artifacts (black arrow). Deeper foci of pneumonia cannot be visualized because of overlying aerated lung (L).

bronchi appear as hyperechoic **air bronchograms** radiating from the hilus and are commonly associated with reverberation artifacts or dirty shadowing. Residual air within alveoli also remains hyperechoic (Figure 4.31). If the bronchial lumen is filled with secretions or cellular debris, **fluid bronchograms** develop, which resemble vessels but can be distinguished by means of color or power Doppler by their lack of flow (Figure 4.33). Although pulmonary consolidation is most commonly associated with pneumonia, it may also be encountered in lung contusion, lobe torsion, and infiltrative pulmonary neoplasia (Figures 4.32–4.34). Dispersed, hyperechoic, and reverberating foci, indicating vesicular emphysema, are commonly observed in the central

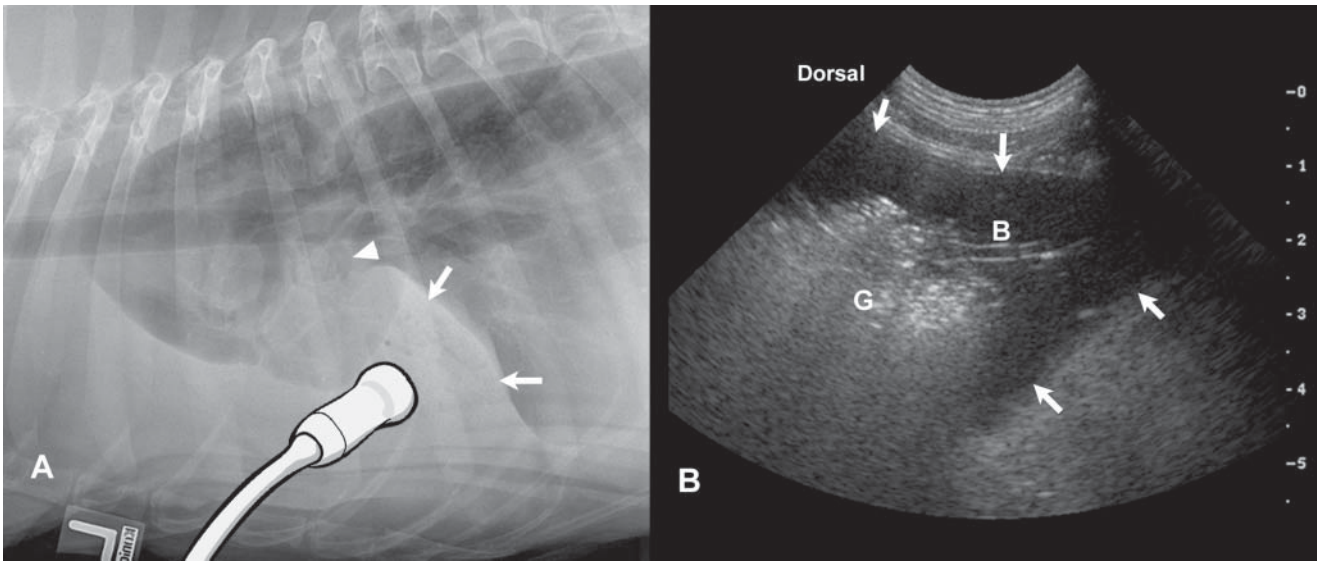


Figure 4.32. **Torsion of the right middle lung lobe in a 5-year-old mixed, large-breed dog. A:** On the lateral thoracic radiograph, marked pleural effusion is noted, as well as right middle lung lobe opacification and enlargement (arrows). The lobar bronchus is interrupted (arrowhead), and punctate and linear gas lucencies are observed in the consolidated lobe. **B:** The ultrasound examination is performed by using a right intercostal approach at the level of the sixth intercostal space. The peripheral portion of the lung lobe is hypoechoic, and dispersed hyperechoic foci in the central portion are associated with reverberation artifacts, consistent with gas (G). This pattern is commonly encountered with lung-lobe torsion. A fluid-filled bronchus (fluid bronchogram) appears in the apex of this lobe (B).

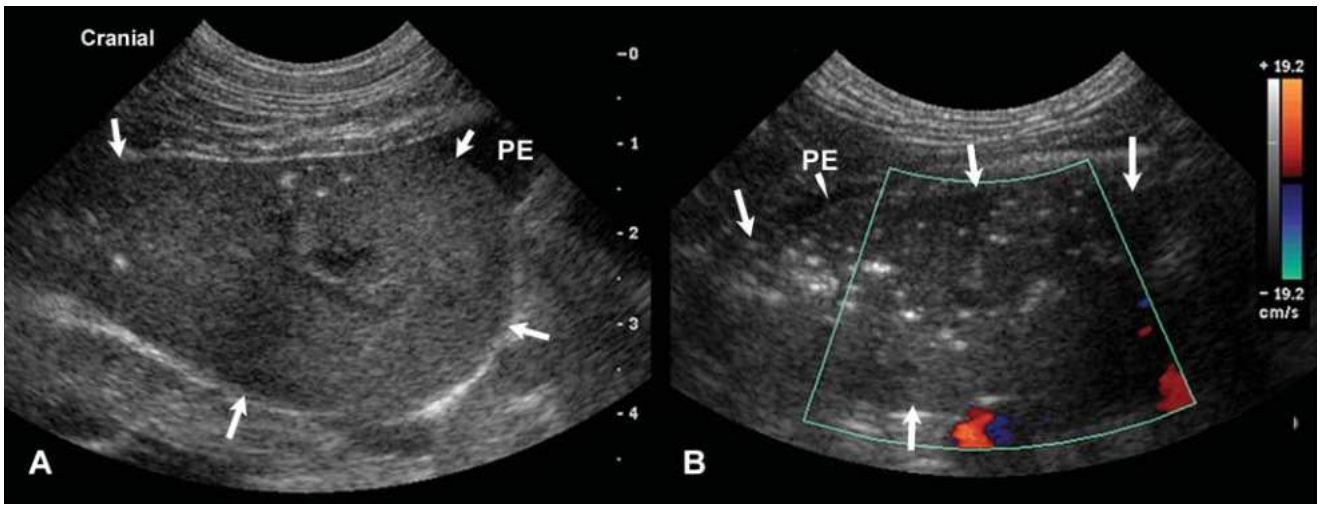


Figure 4.33. **Lung-lobe torsion in a small-breed dog. A, B:** Ultrasonographic images of different portions of the right cranial lung lobe, which appears "hepatized" and enlarged (arrows). The lobe is diffusely and mildly echogenic and presents dispersed hyperechoic foci that were consistent with gas. When color Doppler is used **(B)**, there is no evidence of any vascular flow. A small volume of hypoechoic pleural effusion (PE) is also apparent around the lobe.

portion of a twisted lung lobe (d'Anjou et al. 2005) (Figures 4.32, 4.33). Additionally, concurrent pleural effusion is more typically seen with lung-lobe torsion, as opposed to pneumonia. Color or power Doppler can prove useful in confirming the lack of flow in a twisted lobe. However, ultrasonographic differentiation of these entities, which may coexist in the same lobe, may not be possible and requires further examination with CT angiography.

Pulmonary Masses and Nodules

Although pulmonary masses in small animals are most commonly neoplastic or possibly granulomatous

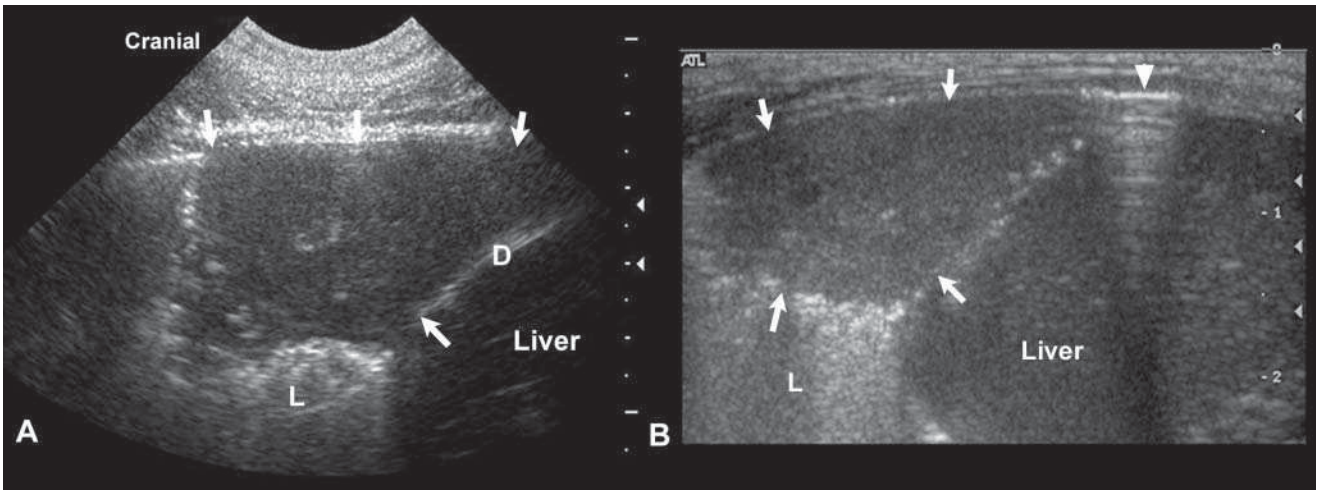


Figure 4.34. **Uniform lung consolidation in two dogs. A:** Bronchoalveolar carcinoma in a 15-year-old mixed-breed dog. Dorsal sonogram using a right intercostal approach. The tip of the right caudal lung lobe (arrows) is uniformly hypoechoic and has retained its normal triangular shape. The abnormal portion of this lobe is in contact with the diaphragm (D). The normal lung portion, which remains aerated, is seen in the far field (L). **B:** Traumatic lung contusion in another dog in which the affected portion of the right caudal lobe (arrows) is uniformly moderately echogenic. Additionally, a short linear hyperechogenicity is in the caudolateral portion of the pleural space (arrowhead), in association with a comet-tail artifact, consistent with mild pneumothorax. L, normal aerated lung.

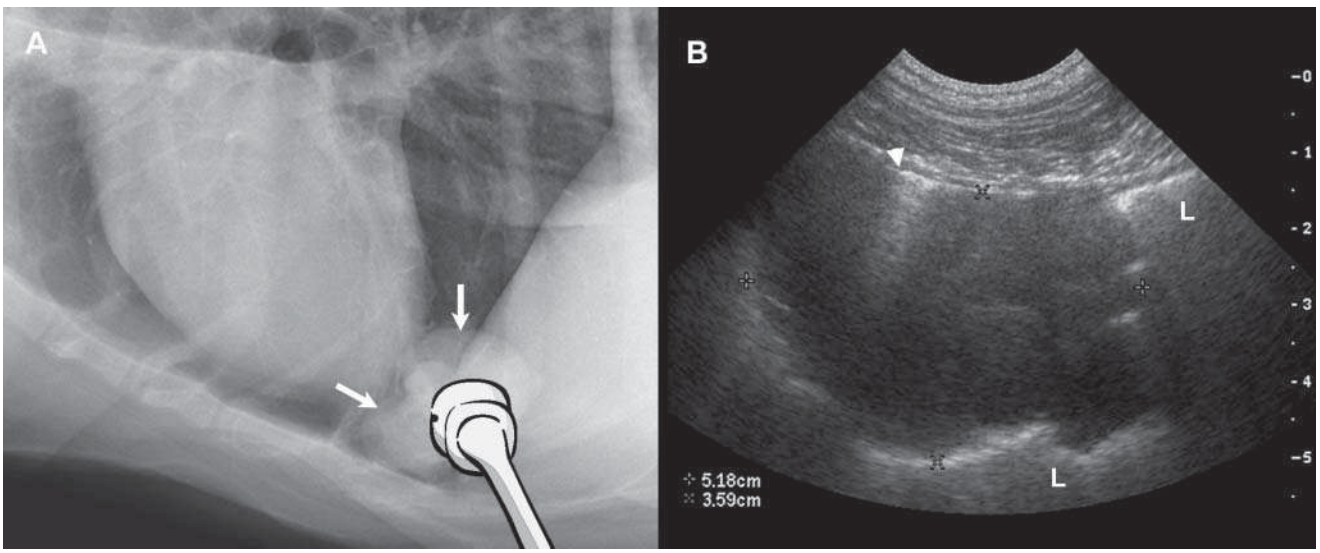


Figure 4.35. **Disseminated histiocytic sarcoma in a 6-year-old Bernese mountain dog. A:** On the left lateral radiograph of the thorax there is an approximately 5-cm soft-tissue mass in the caudal ventral thorax, summating with the diaphragm (arrows). **B:** The ultrasonographic examination of the caudal ventral thorax was performed using an intercostal approach immediately dorsal to the sternum. The mass (cursors) is irregular, homogeneous, hypoechoic, and associated with the ventral aspect of the right caudal lung lobe. The peripheral border is strongly hyperechoic and associated with reverberation artifacts, consistent with aerated portion of the lung lobe (L). On real-time examination, it was seen to be sliding with respiration. A reverberating artifact originating from the pleural space and consistent with free air is also observed in the near field (arrowhead).

in etiology, abscesses, cysts, or hematomas may also be encountered. In the absence of pleural effusion, pulmonary masses can be evaluated ultrasonographically only if located at the periphery of the lung field.

Pulmonary neoplasms and granulomas usually appear poorly echogenic or of mixed echogenicity. They cause focal disruption of the reflective lung surface and commonly form an acute angle with the thoracic wall (Figures 4.35–4.37). Lung masses or

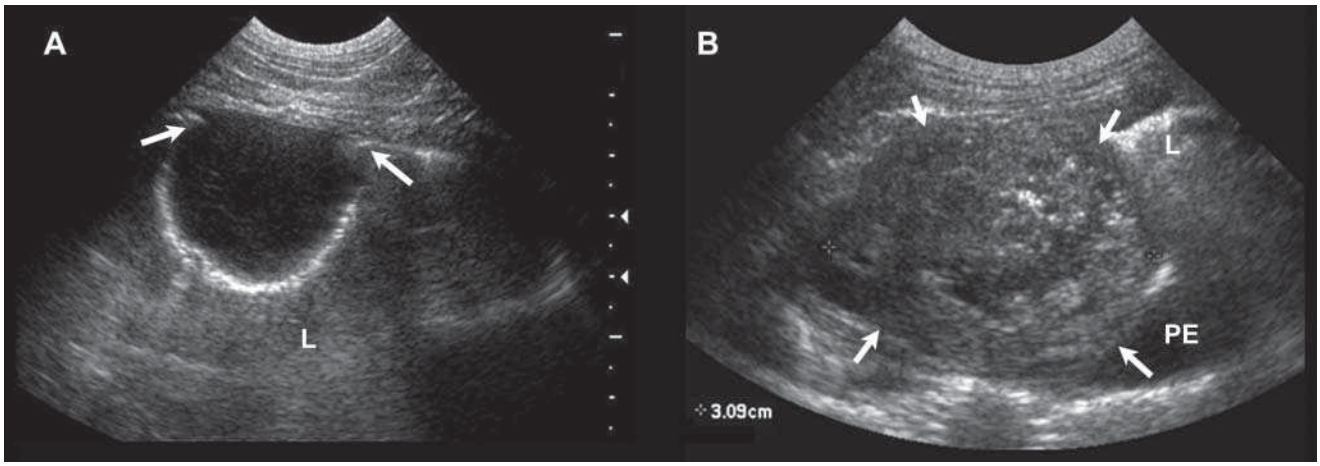


Figure 4.36. **Pulmonary carcinoma. A:** This examination in an 8-year-old Labrador Retriever was performed using an intercostal approach. The pulmonary mass is well circumscribed, almost anechoic, forms an acute angle with the thoracic wall (arrows), and is surrounded by normally aerated lung parenchyma (L). **B:** This examination was performed using an intercostal approach in a 12-year-old cat. A 3-cm mixed echogenic mass (arrows) associated with the pulmonary parenchyma distorts the normal lung margins. The adjacent normal lung is characterized by a hyperreflective interface (L). A small amount of pleural effusion (PE) is present.

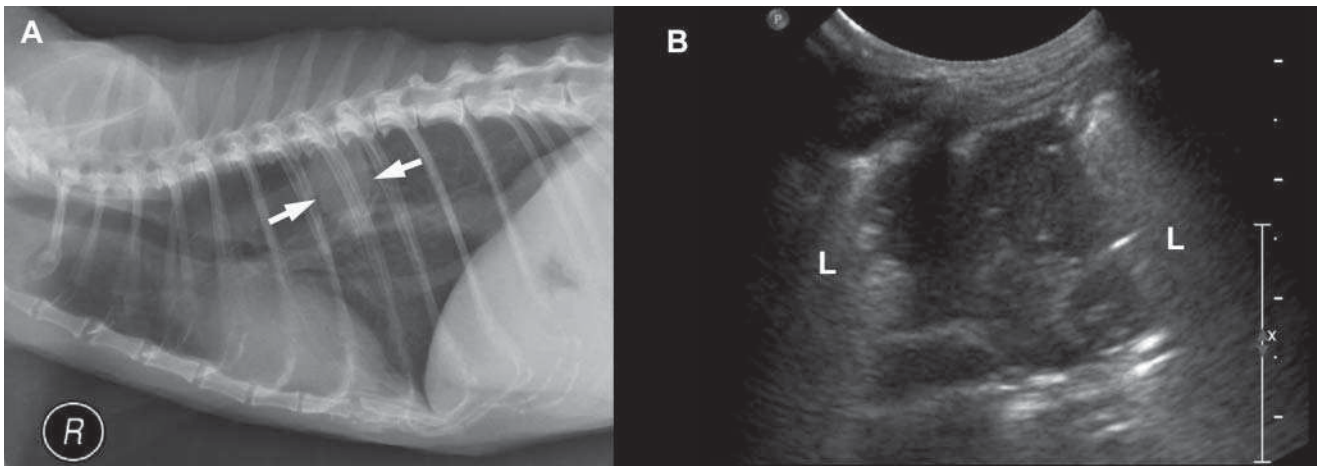


Figure 4.37. **Pulmonary lymphoma in an 18-year-old cat. A:** The right lateral thoracic radiograph shows a discrete soft-tissue mass (arrows) located in the left caudal lung lobe. **B:** The sonogram performed using a left intercostal approach shows a poorly echogenic pulmonary mass, surrounded by aerated lung (L).

nodules are easily identified as pulmonary in origin when they move with the rest of the lung during respiration. However, this feature is not observed in cases of pleural adhesions. In contrast to atelectasis or consolidation, pulmonary mass lesions frequently cause distortion of the normal contour of the affected lung lobe (Figure 4.29C,D). Central tumor necrosis can vary in appearance and may resemble a pulmonary abscess, particularly when it is poorly echoic or anechoic. Air cavities and dystrophic mineralization, appearing as hyperechoic foci with or without reverberating and shadowing artifacts, are often seen in primary lung tumors.

Pulmonary metastases may be recognized as peripherally distributed, round, hypoechoic nodules moving with the aerated lung (Figure 4.38). Larger metastases may show similar ultrasonographic features to primary pulmonary neoplasms.

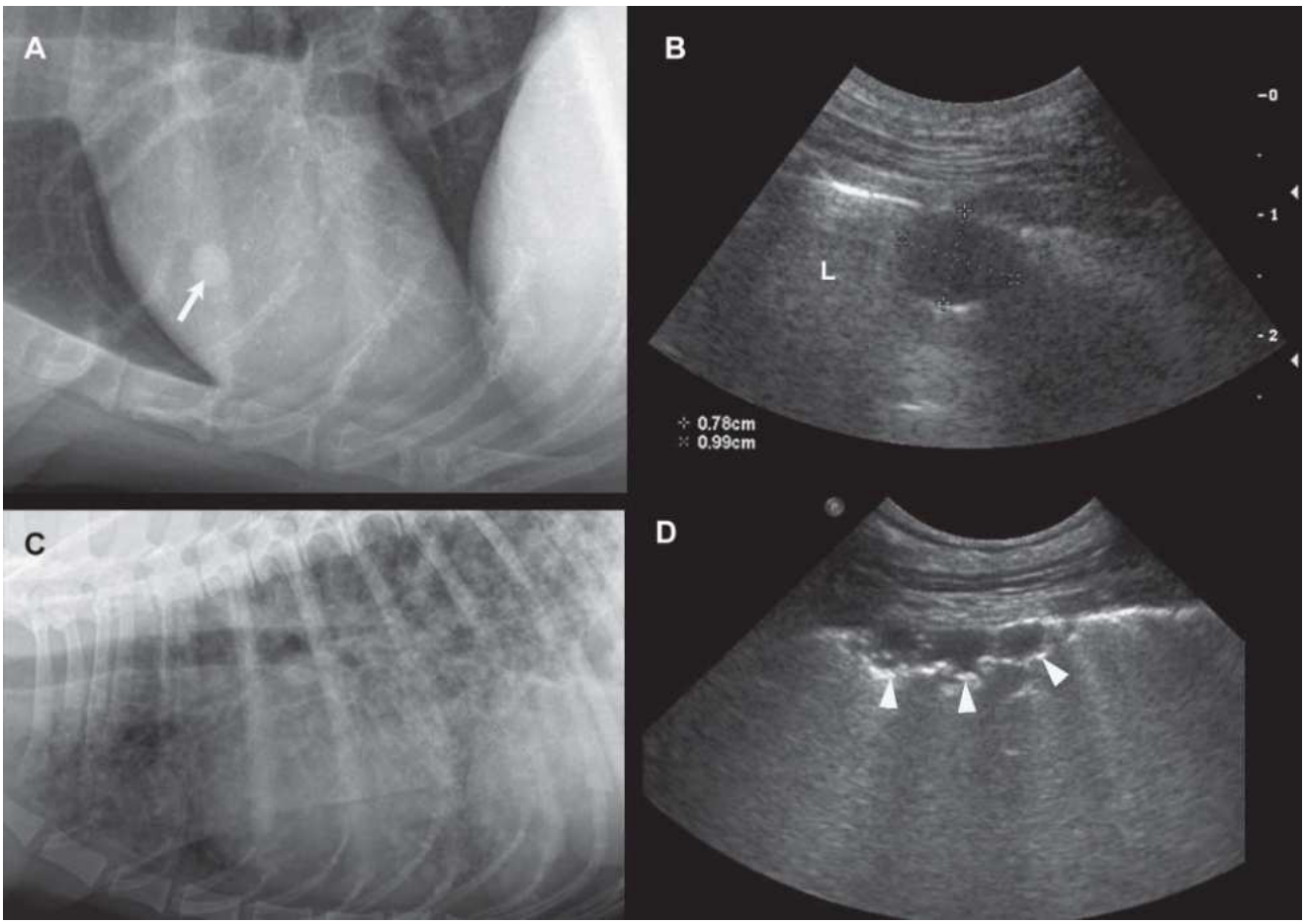


Figure 4.38. **Pulmonary metastases in two dogs. A:** A small, round, soft-tissue opacity is noted on this left lateral thoracic radiograph (arrow) of a Dalmatian with a history of weight loss. **B:** Using a left intercostal approach, a spherical hypoechoic nodule is seen at the superficial aspect of the lung (L). Ultrasound-guided fine-needle aspirate revealed a metastatic sarcoma. An abdominal fibrosacoma was also detected. **C:** This lateral thoracic radiograph in an 8-year-old Golden Retriever with a 2-week history of cough shows numerous small soft-tissue nodules affecting all lung lobes. **D:** Using both left and right intercostal approaches, numerous small, hypoechoic nodules (arrowheads) are observed at the superficial aspect of the lung. Fine-needle aspiration using ultrasound guidance revealed a histiocytic sarcoma.

Primary and metastatic neoplasms are ultrasonographically indistinguishable from granulomas, necessitating cytological or histological analysis for a definitive diagnosis (Figure 4.39). The signalment and clinical history are helpful in prioritizing the differential list.

Pulmonary cysts, acute hematomas, and abscesses can be fluid-filled. Cysts are usually thin-walled and contain anechoic fluid. Abscesses and hematomas have variable wall thickness and margination, and the echogenicity of their contents may range from anechoic to echogenic (Figures 4.40–4.42). Abscessing pneumonia may also cause lobar enlargement and marked heterogeneity, mimicking neoplasia and necrosis. Furthermore, these processes can coexist.

Diaphragmatic Disorders

Hernia

Although challenging, ultrasonography can be a useful imaging tool in diagnosing traumatic diaphragmatic hernias, true (congenital) diaphragmatic hernias, and congenital peritoneo-pericardial diaphragmatic hernias (PPDHs) (Spattini et al. 2003).

The ultrasonographic characteristics of a diaphragmatic hernia or rupture are an irregular or asymmetrical cranial aspect of the liver and the presence of abdominal viscera in the thorax (Figures 4.43–4.46), and, occasionally, visible disruption of the diaphragm.

If an ultrasonographic examination is performed to confirm or exclude a diaphragmatic hernia, the

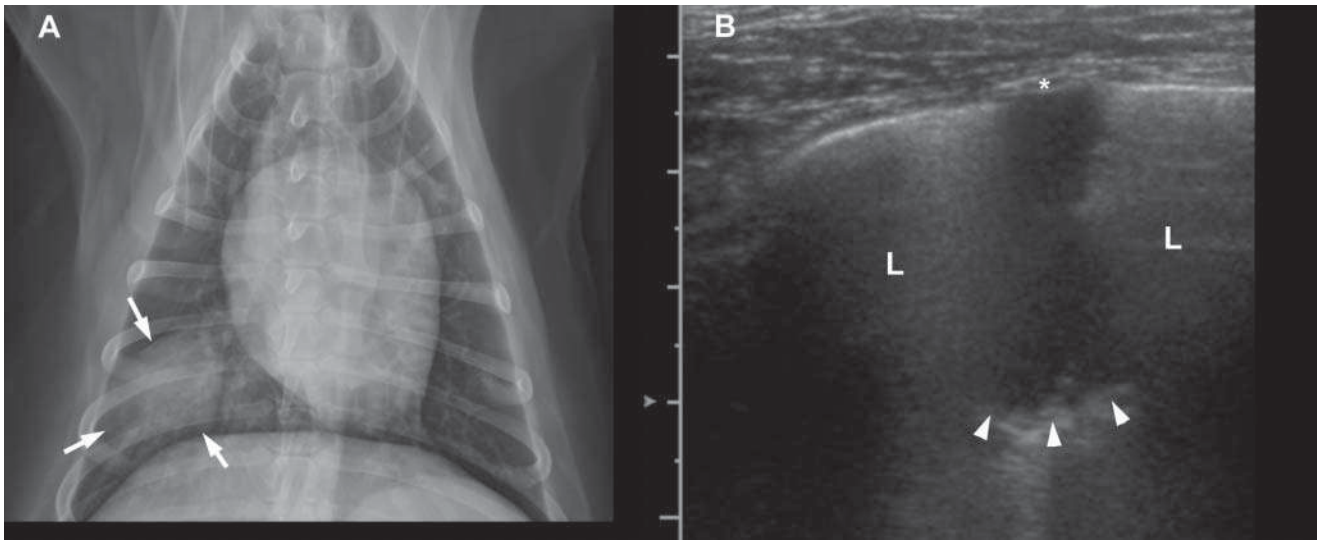


Figure 4.39. Fungal granuloma (blastomycosis) in an 11-year-old Cocker Spaniel. A: The slightly oblique ventrodorsal radiograph of the thorax reveals a soft-tissue mass associated with the right caudal lung lobe (arrows). **B:** Ultrasonographic image performed using a right dorsal intercostal approach. A small portion of the pulmonary infiltrate (arrowheads) can be seen, despite the surrounding aerated lung (L). A rib (*) is limiting the visualization of the lesion.

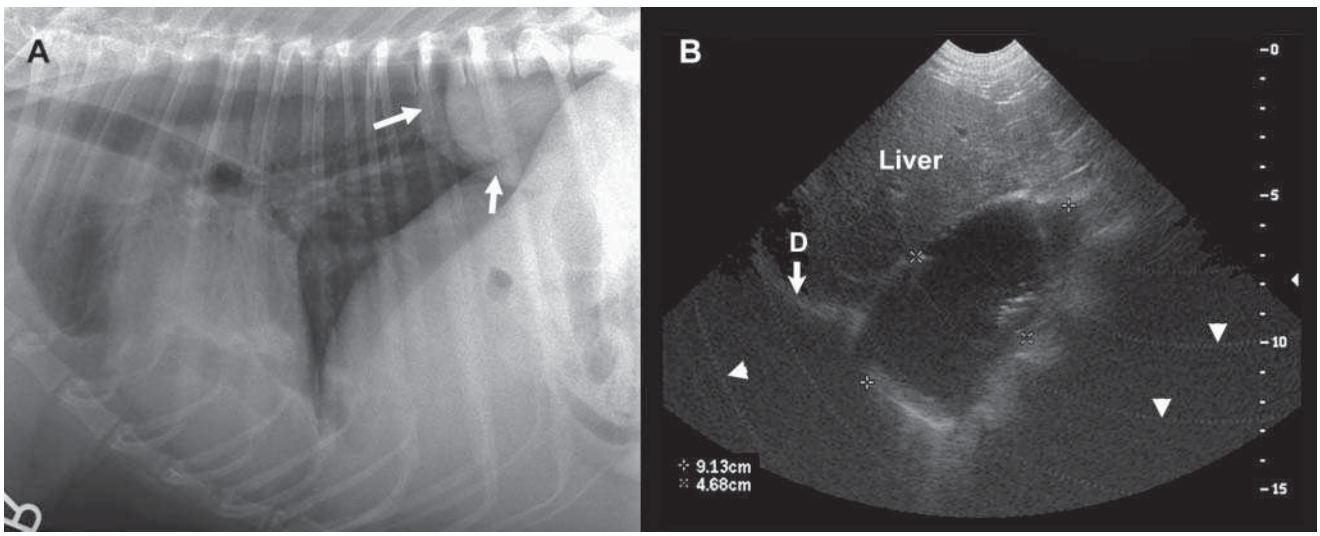


Figure 4.40. Pulmonary abscess in a 5-year-old collie. A: On the lateral thoracic radiograph there is a large, well-circumscribed, homogeneous mass lesion associated with the caudal dorsal lung fields immediately cranial to the diaphragm (arrows). **B:** Ultrasonographic examination performed by using a transhepatic approach (oblique transverse to dorsal plane). The abscess (cursors) is seen immediately cranial to the diaphragm (D). It is anechoic and surrounded by a thin, hyperechoic rim. The concentric dotted lines (arrowheads) represent an artifact likely caused by electrical interference.

examiner has to be aware of common artifacts occurring at the level of the diaphragm. If the animal has ascites, refraction of the beam at the liver surface may cause the diaphragm to appear discontinuous. The commonly seen mirror-image artifact might be mistaken for a herniation of liver into the thorax (see Figure 1.17). Adhesions between herniated organs and the pleural cavity and/or diaphragm may exist and appear as echogenic strands floating or adhering to the walls and organs. The ultrasonographic diagnosis

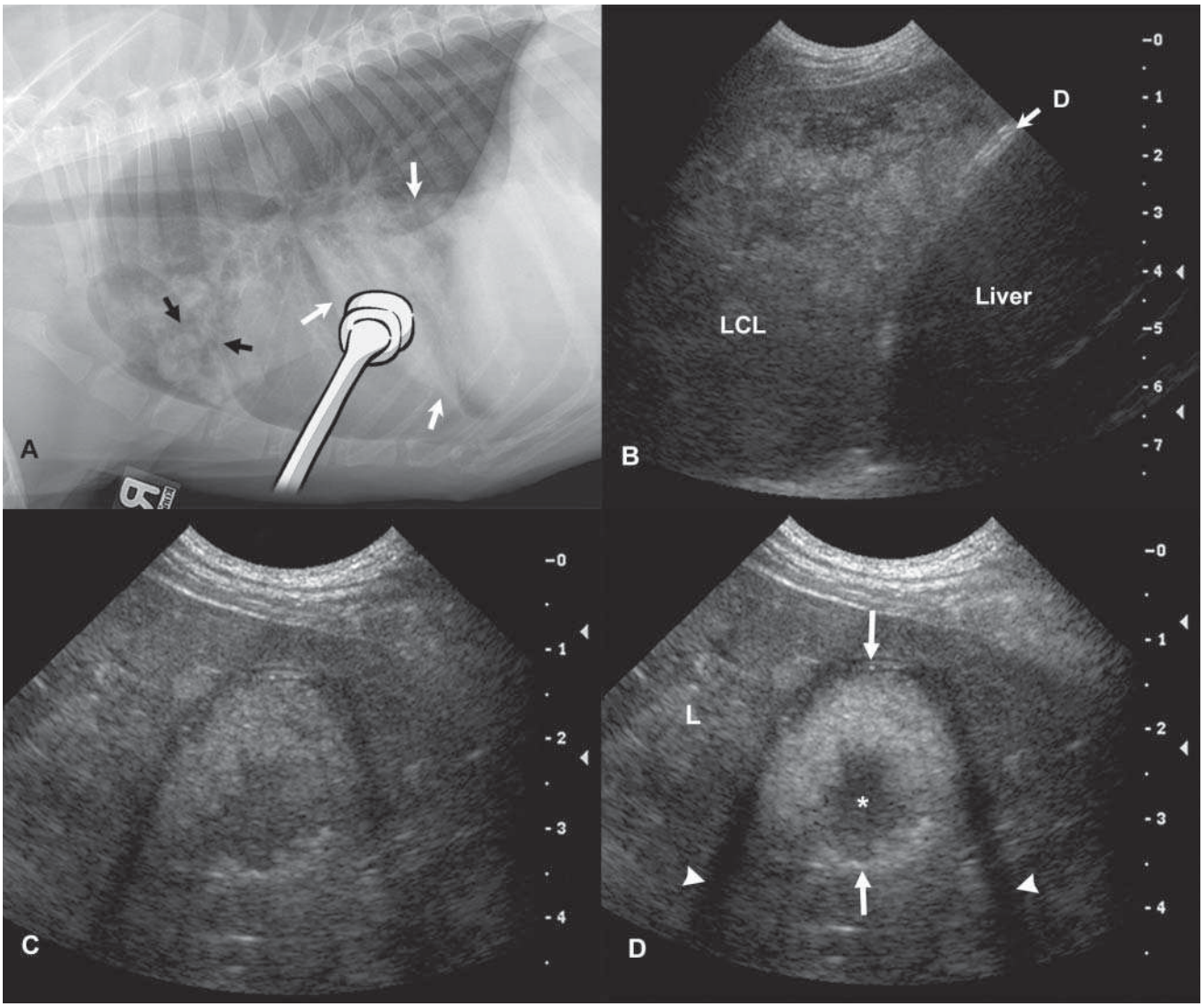


Figure 4.41. **Chronic pyogranulomatous pneumonia in a large-breed dog. A:** A soft-tissue opacity is noted in the caudoventral lung field on the right lateral radiograph (white arrows). An alveolar pattern is also apparent in the cranioventral lung field, as well as irregular, air-filled, dilated bronchi consistent with bronchiectasis (black arrows). **B:** On this ultrasonographic image obtained through the left sixth intercostal space, a large portion of the left caudal lung lobe (LCL) in contact with the diaphragm (D) is heterogeneous, moderately echogenic, and enlarged. **C, D:** Sonographic and enhanced labeled images. In a portion of this lung lobe (L) there is a spherical hyperechoic mass (arrows) with an irregular hypoechoic center (*) and a thin hypoechoic rim. Edge-shadowing artifacts indicate margins of the lesion (arrowheads). Fine-needle aspiration confirmed the presence of a pyogranuloma.

of a PPDH is usually straightforward if abdominal organs (e.g., liver or intestine) are present within the pericardial sac (Figures 4.45, 4.46).

Other Diaphragmatic Disorders

Other disorders of the diaphragm are rare. Benign or malignant mass lesions are occasionally encountered (Figures 4.47, 4.48).

Interventional Procedures

Ultrasound is very useful to aid diagnostic or therapeutic thoracocentesis, especially if only a small volume of pleural effusion is present (Figure 4.49), or when septations between fluid pockets interfere with blinded centesis. Additionally, fine-needle aspiration or biopsies of thoracic mass lesions are commonly performed. These procedures are safe and have a

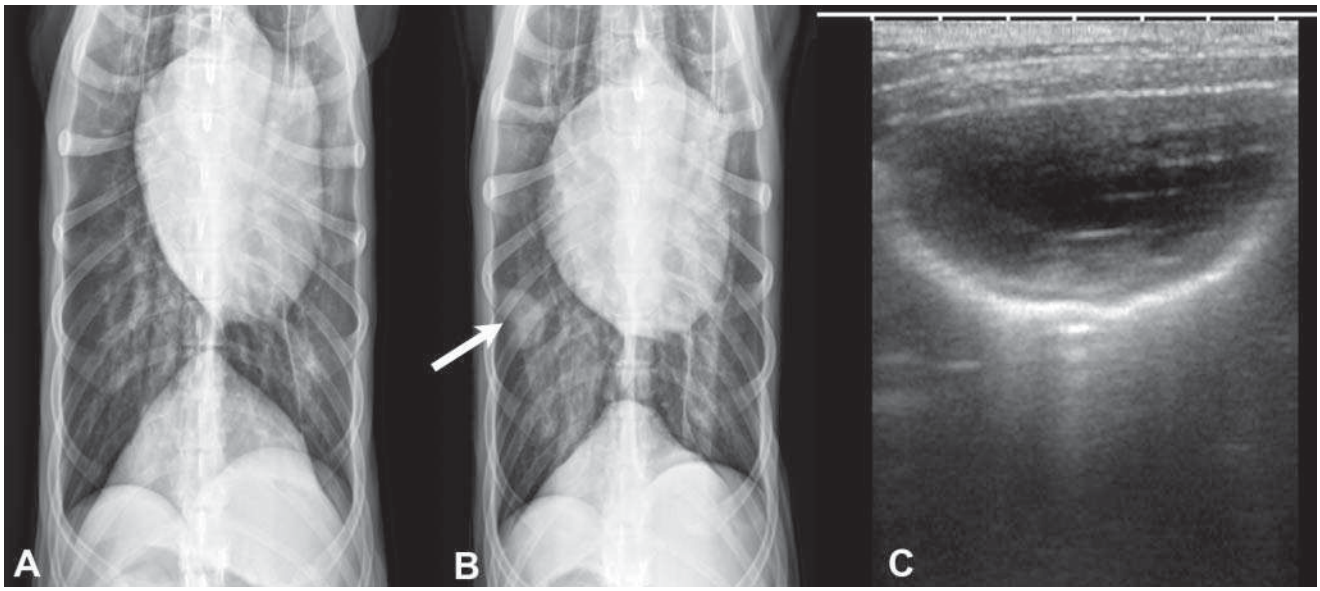


Figure 4.42. Traumatic pulmonary hematoma in a 9-year-old Scottish Deerhound. Radiographs and sonogram of the lung after bronchoalveolar lavage. **A:** The ventrodorsal radiograph, at the time of presentation, reveals a generalized unstructured interstitial pattern. No other abnormality is detected at this time. A bronchoalveolar lavage was then performed. **B:** Re-check radiographs 6 days later show a homogeneous 3-cm mass lesion associated with the right lung at the level of the sixth rib (arrow). **C:** Ultrasonographic examination performed using a linear probe with a transverse intercostal approach. An anechoic, well-circumscribed lesion of diameter 3 cm is associated with the lung. Aspiration yielded blood, consistent with a hematoma.

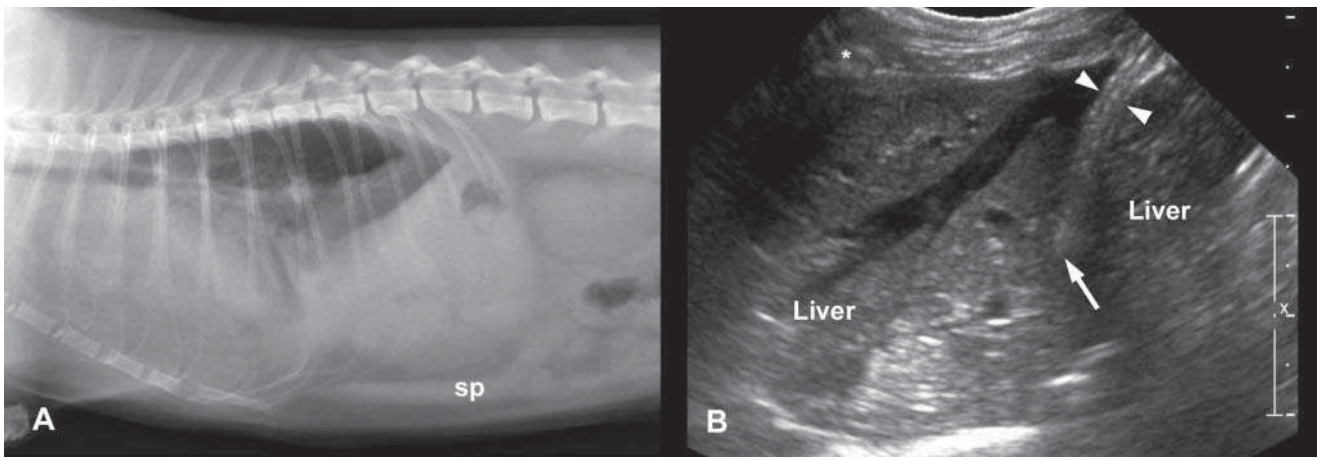


Figure 4.43. Diaphragmatic rupture in a 1-year-old cat. A: The lateral radiograph of the whole body outlines the caudal thoracic increased opacity, the indistinct diaphragm, and the displaced spleen (sp) in the cranioventral abdomen, leading to the diagnosis of traumatic hernia. **B:** Longitudinal sonogram via a left caudal intercostal approach. The liver is displaced into the thoracic cavity cranial to the diaphragm outlined by arrowheads. A small amount of anechoic pleural effusion is present between the herniated liver lobes. Part of the liver is still present in the cranial abdomen. A rib (*) in the near field is creating a strong acoustic shadow.

high diagnostic yield (Wood et al. 1998; Figure 4.50). An intercostal approach is most commonly used. Patient preparation (sedation with or without anesthesia, sterile preparation) is performed in a routine manner. Depending on the size and location of the lesion, 20- to 22-gauge injection or spinal needles are used for fine-needle aspiration, and 16- to 18-gauge biopsy needles are used to obtain core biopsy samples. Fine-needle aspiration can be performed freehand, with an extension tube or directly attached to a syringe

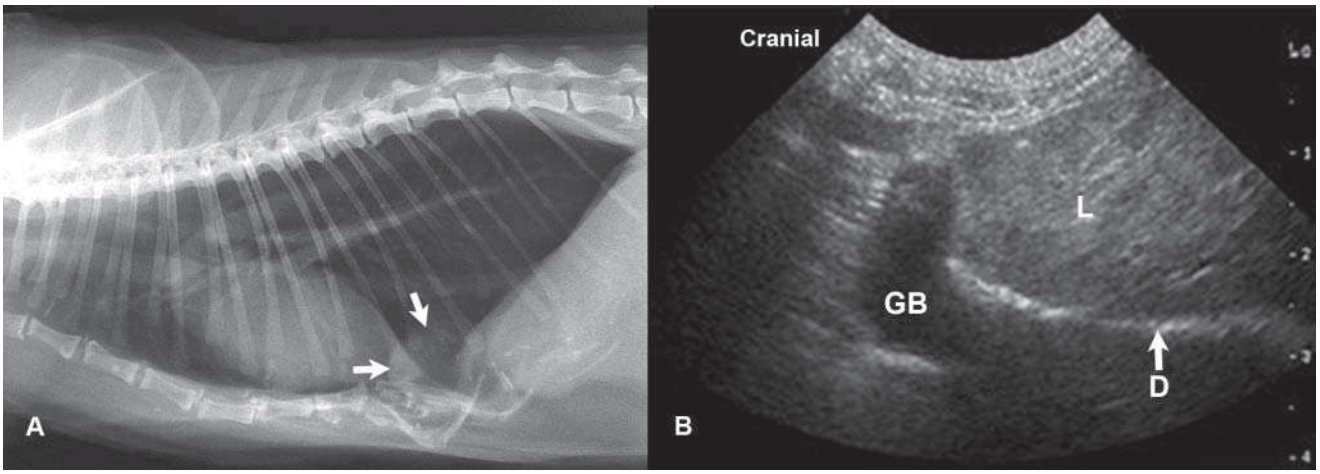


Figure 4.44. **Herniation of the gallbladder in a cat. A:** On the lateral thoracic radiograph, a well-circumscribed, round opacity (arrows) is present between the diaphragm and cardiac silhouette. **B:** The ultrasonographic examination is performed by using a right ventral intercostal approach. The diaphragm (D) is the strongly hyperechoic curvilinear structure in the far field. The diaphragm is discontinuous in the near field, with herniation of the gall bladder (GB) into the thoracic cavity L = Liver.

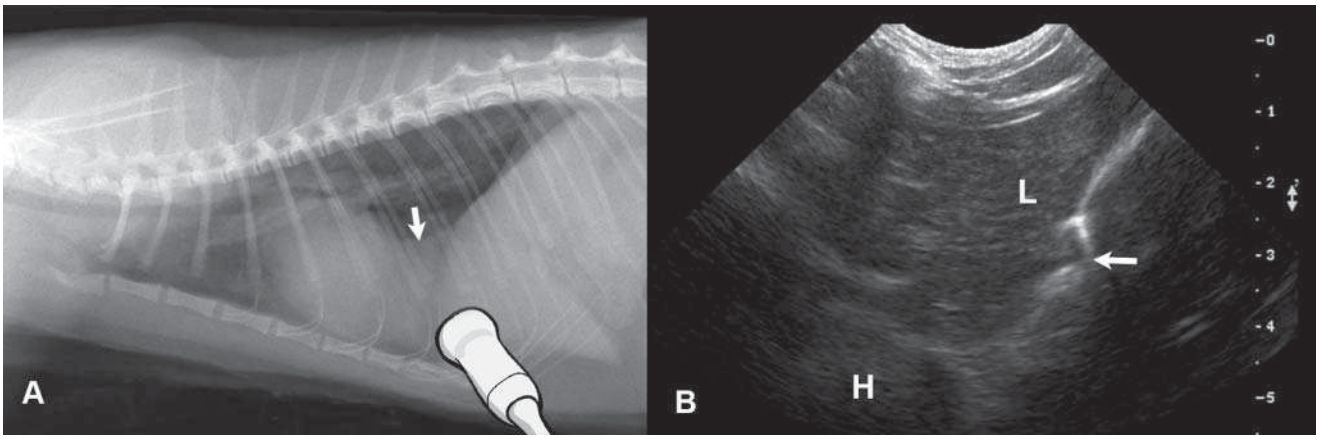


Figure 4.45. **Peritoneo-pericardial diaphragmatic hernia in a 2-year-old cat. A:** The lateral thoracic radiograph reveals loss of the ventral part of the diaphragmatic silhouette and silhouetting of abdominal and peritoneal contents. A "mesothelial remnant" sign is noted ventral to the caudal vena cava (arrow). The cardiac silhouette is enlarged. **B:** Ultrasonographic examination performed using an intercostal approach. There is discontinuity of the diaphragm (arrow), and hepatic parenchyma (L) is visible in the near field, cranial to the diaphragm and close to – and displacing – the heart (H).

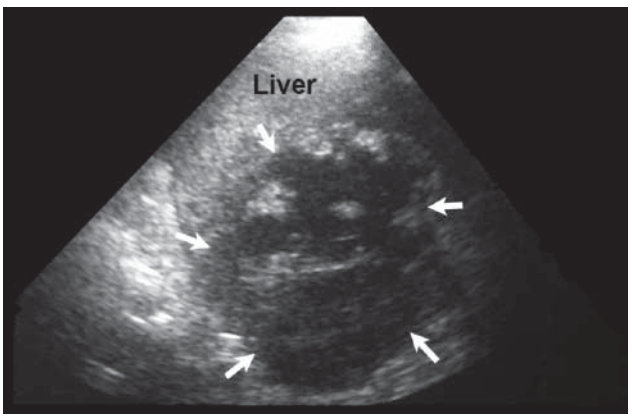


Figure 4.46. **Peritoneo-pericardial diaphragmatic hernia in an 8-year-old Rhodesian Ridgeback.** The examination is performed via a right intercostal approach. Normal hepatic parenchyma is visible in the near field. There is a 9-cm mixed echogenic hepatic mass within the pericardial sac (arrows). Histopathologic examination of the herniated liver lobe revealed hepatocellular atrophy and hepatic dysplasia caused by compression and long-standing circulatory compromise. There was no evidence of neoplasia.

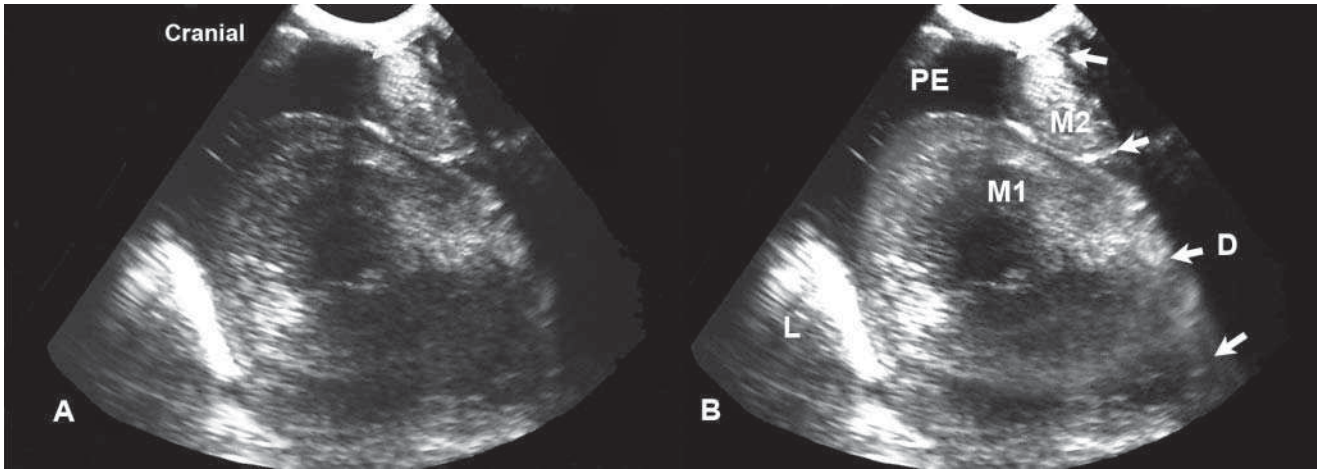


Figure 4.47. Diaphragmatic rhabdomyosarcoma in a 4-month-old cat. Ultrasonographic **(A)** and enhanced labeled **(B)** images obtained with an intercostal approach. Two mixed echogenic mass lesions (M1, M2) are arising from the diaphragm (D, arrows). The larger mass measures more than 6 cm in maximum diameter, and the smaller mass measures 2.5 cm. The lung is displaced cranially (L) and there is anechoic pleural (PE) and peritoneal effusion.

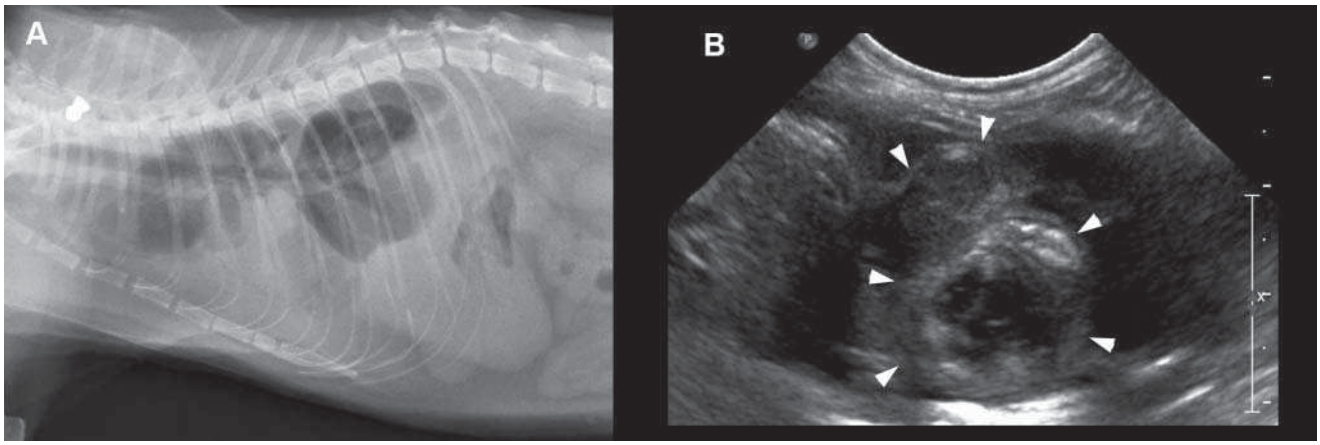


Figure 4.48. Sarcoma in a 6-year-old domestic shorthair cat. A: On this right lateral radiograph, there is a marked increased opacity in the thorax, which was confirmed on ultrasound as a combination of pleural effusion and thoracic masses. The poorly defined diaphragm appears irregular. A gun pellet is superimposed on the cranial thoracic spine. **B**: The ultrasonographic image was obtained via a subcostal approach. A complex, cavitated nodule (arrowheads) is floating in the caudal thorax, and was attached to the diaphragm. An inhomogeneously echogenic mass was noted in the left caudal lung lobe (not shown). Fine-needle aspirates of these lesions were diagnostic for sarcoma, probably metastatic from a recently removed soft-tissue sarcoma.

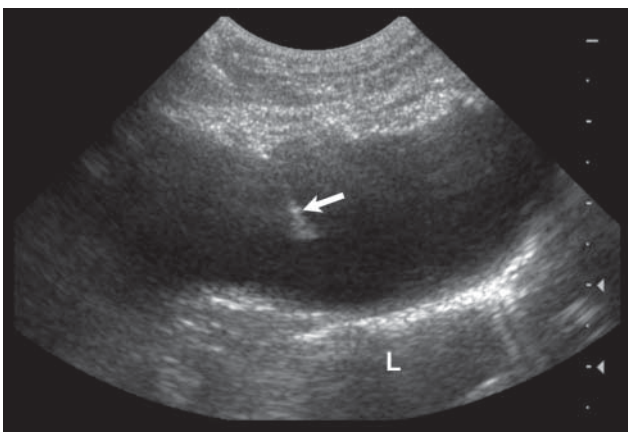


Figure 4.49. Ultrasound-guided thoracocentesis in a cat with pleural effusion. The needle is traversing the thoracic wall, and the needle tip, which appears as a hyperechoic line (arrow), is within the pleural space. The aerated lung (L) is partially retracted medially.

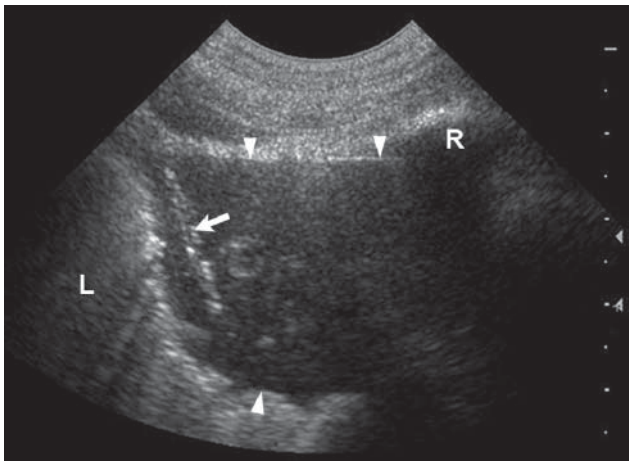


Figure 4.50. Biopsy of a pulmonary mass (bronchoalveolar carcinoma) in a dog. Two closely aligned needle tracts are visible as hyperechoic lines (arrow) in the periphery of the mass (arrowheads) adjacent to the aerated portion of the lung (L). There is no evidence of pneumothorax. There is a hyperechoic superficial margin of a rib (R) with associated acoustic shadowing in the near field.

of 5–10 ml, enabling, with practice, faster and safer interventions. Biopsy samples can also be obtained freehand or by using a biopsy guide. To facilitate fine-needle aspiration or biopsy of pulmonary lesions, it might be necessary to induce respiratory standstill for the duration of the procedure, warranting endotracheal intubation of the patient. In addition to hemorrhage, which is a potential sequela to any biopsy, fine-needle aspiration or biopsy of pulmonary lesions might also cause pneumothorax. However, this can usually be prevented when areas of tissue without gas foci are targeted. When pneumothorax occurs, severe complications necessitating therapeutic intervention are rare.

Intraoperative assistance for tracing draining tracts and foreign material dissecting the thoracic wall and possibly entering the thoracic cavity can be useful to the surgeon, as it will reduce the length of the procedure and minimize soft tissue exploration.

Visit our website at **www.SmallAnimalUltrasonography.com** for complementary video clips with annotations and text on:

- Normal lung interface
- Thoracic wall mass
- Pleural effusion
- Pulmonary tumor
- Mediastinal mass
- Branchial cyst
- Diaphragmatic hernia

References

Armbrust LJ, Biller DS, Radlinsky MG, Hoskinson JJ (2003) Ultrasonographic diagnosis of foreign bodies associated with chronic draining tracts and abscesses in dogs. Vet Radiol Ultrasound 44:66–70.

d'Anjou MA, Tidwell AS, Hecht S (2005) Radiographic diagnosis of lung lobe torsion. Vet Radiol Ultrasound 46: 478–484.

Hurley ME, Keye GD, Hamilton S (2004) Is ultrasound really helpful in the detection of rib fractures? Injury 35: 562–566.

Larson M (2009) Ultrasound of the thorax (Noncardiac). Vet Clin North Am Small Anim Pract 39:733–745.

Louvet A, Bourgeois JM (2008). Lung ring-down artifact as a sign of pulmonary alveolar-interstitial disease. Vet Radiol Ultrasound 49:374–377.

Mattoon JS, Nyland TG (1995) Thorax. In: Nyland TG, Mattoon JS, eds. Small Animal Diagnostic Ultrasound. Philadelphia: WB Saunders, pp 325–353.

Reichle JK, Wisner ER (2000) Non-cardiac thoracic ultrasound in 75 feline and canine patients. Vet Radiol Ultrasound 41:154–162.

Rudorf H, Herrtage ME, White RA (1997) Use of ultrasonography in the diagnosis of tracheal collapse. J Small Anim Pract 38:513–518.

Schultz RM, Zwingeberger A (2008) Radiographic, computer tomographic and ultrasonographic findings with migrating intrathoracic grass awns in dogs and cats. Vet Radiol Ultrasound 49:249–255.

Schwarz LA, Tidwell AS (1999) Alternative imaging of the lung. Clin Tech Small Anim Pract 14:187–206.

Seiler G (2011) Thorax. In: Barr F, Gaschen L, eds. BSAVA Manual of Canine and Feline Ultrasonography. Gloucester: BSAVA, pp 29–36.

Spattini G, Rossi F, Vignoli M, Lamb CR (2003) Use of ultrasound to diagnose diaphragmatic rupture in dogs and cats. Vet Radiol Ultrasound 44:226–230.

Tidwell AS (1998) Ultrasonography of the thorax (excluding the heart). Vet Clin North Am Small Anim Pract 28: 993–1015.

Wood EF, O'Brien RT, Young KM (1998) Ultrasound-guided fine-needle aspiration of focal parenchymal lesions of the lung in dogs and cats. J Vet Intern Med 12:338–342.

Zekas LJ, Adams WM (2002) Cranial mediastinal cysts in nine cats. Vet Radiol Ultrasound 43:413–418.

CHAPTER FIVE

Heart

Donald Brown[1], Hugues Gaillot[2] and Suzanne Cunningham[3]

[1] *Vermont Veterinary Cardiology, PEAK Veterinary Referral Center, Williston, VT, USA; Department of Clinical Sciences, Tufts Cummings School of Veterinary Medicine, North Grafton, MA, USA*
[2] *Clinique Vétérinaire ADVETIA, Paris, France*
[3] *Department of Clinical Sciences, Cummings School of Veterinary Medicine, Tufts University, North Grafton, MA, USA*

Echocardiographic Technique

Instrumentation

Echocardiographic methods differ from abdominal techniques in that transducer placement is confined to limited windows of access between the ribs and aerated lung. This limitation imposes the need for a small transducer footprint. Echocardiographic examinations are then best performed using sector or curvilinear scanning transducers, preferably with phased-array technology. Echocardiography also requires greater temporal resolution. Maximal temporal resolution is obtained by decreasing field depth and minimizing the sector angle (sector width). The ultimate in temporal resolution is obtained by using motion-mode (M-mode) echocardiography. Numerous dedicated abbreviations and conventions are used in this chapter and are listed in Table 5.1.

Suggested guidelines for transducer frequencies include 8–12 MHz for cats and similarly sized dogs, 4–8 MHz for dogs in the 5–40 kg range, and 2–4 MHz for large dogs (>40 kg). When performing an echocardiogram, a concurrent electrocardiogram may be valuable or essential, depending on the goals of the study.

Preparation of Patients

Patients are positioned in lateral recumbency, with the transducer applied to the patient from below with the aid of a table with cutouts designed for this purpose (Figure 5.1). Acoustic transmission is facilitated either by clipping the hair over the point of transducer application or by fully saturating the fur with ultrasound coupling gel.

Two-dimensional Echocardiography

Cardiac image orientation and transducer placement are referenced with respect to the heart itself (Henry et al. 1980; Thomas 1984; Bonagura et al. 1985; O'Grady et al. 1986; Thomas et al. 1993). The central left ventricular (LV) axis can be conceptualized as an imaginary line that extends between the cardiac apex and base in the center of the LV lumen. When the transducer is oriented such that the scan plane includes or is parallel to this axis, a **long-axis image** is obtained. If the scan plane is perpendicular to this axis, a **short-axis image** is obtained (Figure 5.1).

Because of impedance mismatching and ultrasound attenuation imposed by the ribs and air-filled lungs, transthoracic echocardiography is limited to relatively small windows of access. These surround the heart on both the right and left sides of the ventral thorax, i.e., next to the sternum (**parasternal**). The size of these access windows depends on individual thoracic conformation and may be increased by pulmonary under-inflation (e.g., secondary to pleural effusion or atelectasis) and decreased by overinflation as may occur with many cardiopulmonary diseases. Additional access can be gained from the subcostal (**subxiphoid**) position, imaging the heart through the liver and caudal mediastinum; limited views of the aortic arch may be available from the thoracic inlet (**suprasternal** transducer position), as well.

Atlas of Small Animal Ultrasonography, Second Edition. Edited by Dominique Penninck and Marc-André d'Anjou.
© 2015 John Wiley & Sons, Inc. Published 2015 by John Wiley & Sons, Inc.
Companion website: www.SmallAnimalUltrasonography.com

Table 5.1
Abbreviations and conventions used throughout this chapter

Anatomical designations	
AML	Anterior mitral valve leaflet
Ao	Aorta or aortic
AV	Aortic valve
CaVC	Caudal vena cava
CrVC	Cranial vena cava
CT	Chordae tendinae
IVS	Intraventricular septum
LA	Left atrium or left atrial
LAA	Left atrial appendage
LC	Left coronary cusp of the aortic valve
LPA	Left main pulmonary artery
LV	Left ventricle or left ventricular
LVOT	Left ventricular outflow tract
LVW	Left ventricular wall
MV	Mitral valve
NC	Non coronary cusp of the aortic valve
P	Pericardium
PM	Papillary muscle
PML	Posterior mitral valve leaflet
PT	Pulmonary trunk
PV	Pulmonic valve
RA	Right atrium or right atrial
RAA	Right atrial appendage
RC	Right coronary cusp of the aortic valve
RPA	Right main pulmonary artery
RV	Right ventricle or right ventricular
RVOT	Right ventricular outflow tract
RVW	Right ventricular wall
TV	Tricuspid valve
Echocardiographic modality	
CFD	Color flow Doppler
CWD	Continuous-wave Doppler
M-mode	Motion mode
PWD	Pulsed-wave Doppler
TD	Tissue Doppler
TDI	Tissue Doppler imaging
2DE	Two-dimensional echocardiography
Transducer position and orientation	
Ap	Apex
Bs	Base
Ca	Caudal
Cr	Cranial
LAp	Left apical
LPS	Left parasternal
LAx	Long-axis (orientation)
RPS	Right parasternal (position)
SAx	Short-axis (orientation)
Diseases and conditions	
AI	Aortic insufficiency
CDVD	Chronic degenerative valve disease
DCM	Dilated cardiomyopathy
HCM	Hypertrophic cardiomyopathy
LCHF	Left-sided congestive heart failure
MR	Mitral regurgitation
PI	Pulmonic insufficiency
RCHF	Right-sided congestive heart failure
TR	Tricuspid regurgitation

Right Parasternal Views

Usually there are two or more rib spaces available for right parasternal (RPS) views, including a cranial location, corresponding typically to the fourth intercostal space, and a more caudal location at the fifth (Figure 5.2).

For images suitable for LV quantification, the transducer is positioned within the selected rib space so that the central beam of the transducer is perpendicular to the LV long axis at the tips of the mitral valve leaflets. A short-axis image is obtained by twisting the transducer so that the LV cross-section is as close to circular as possible. Angulation in the base-apex direction yields a series of RPS short-axis views, depending on the transection level (Figure 5.2).

Long-axis images are obtained from the RPS position by applying a 90° counterclockwise transducer twist, relative to the short-axis orientation, and fanning so that the LV central axis lies within the scan plane; a four-chamber view results (Figure 5.3). From this view, slight cranial angulation and clockwise twisting bring the LV outflow tract and aorta into view.

Left Apical Views

Left apical position (LAp) images are best obtained with the patient in left lateral recumbency, with the transducer applied to the left ventral thorax from below (Figure 5.4). A true apical view results when the transducer is placed at an extreme ventral and caudal location, approaching a subcostal position. The transducer is angled cranially so that the central ultrasound beam is pointed toward the heart base along the LV central axis. The true apical view may be technically challenging, so a more cranial transducer position may be suitable but results in a foreshortened LV view that is unsuitable for ventricular quantification.

Cranial angulation of the transducer from the LAp four-chamber position brings the aortic root into the scan plane and enables visualization of the aortic valve. This scan plane constitutes the **apical five-chamber** image and often is suitable for aortic flow-velocity quantification. However the subcostal transducer location is typically better aligned for maximal velocity measurements in dogs (Abbott and MacLean 2003).

From the apical four-chamber view, a 90° clockwise twist yields the apical two-chamber view, including the left ventricle and atrium in the near and far fields, respectively.

Left Parasternal Views

Left parasternal position (LPS) views of the heart, also called left cranial views, are obtained preferably with the patient in left lateral recumbency. The transducer

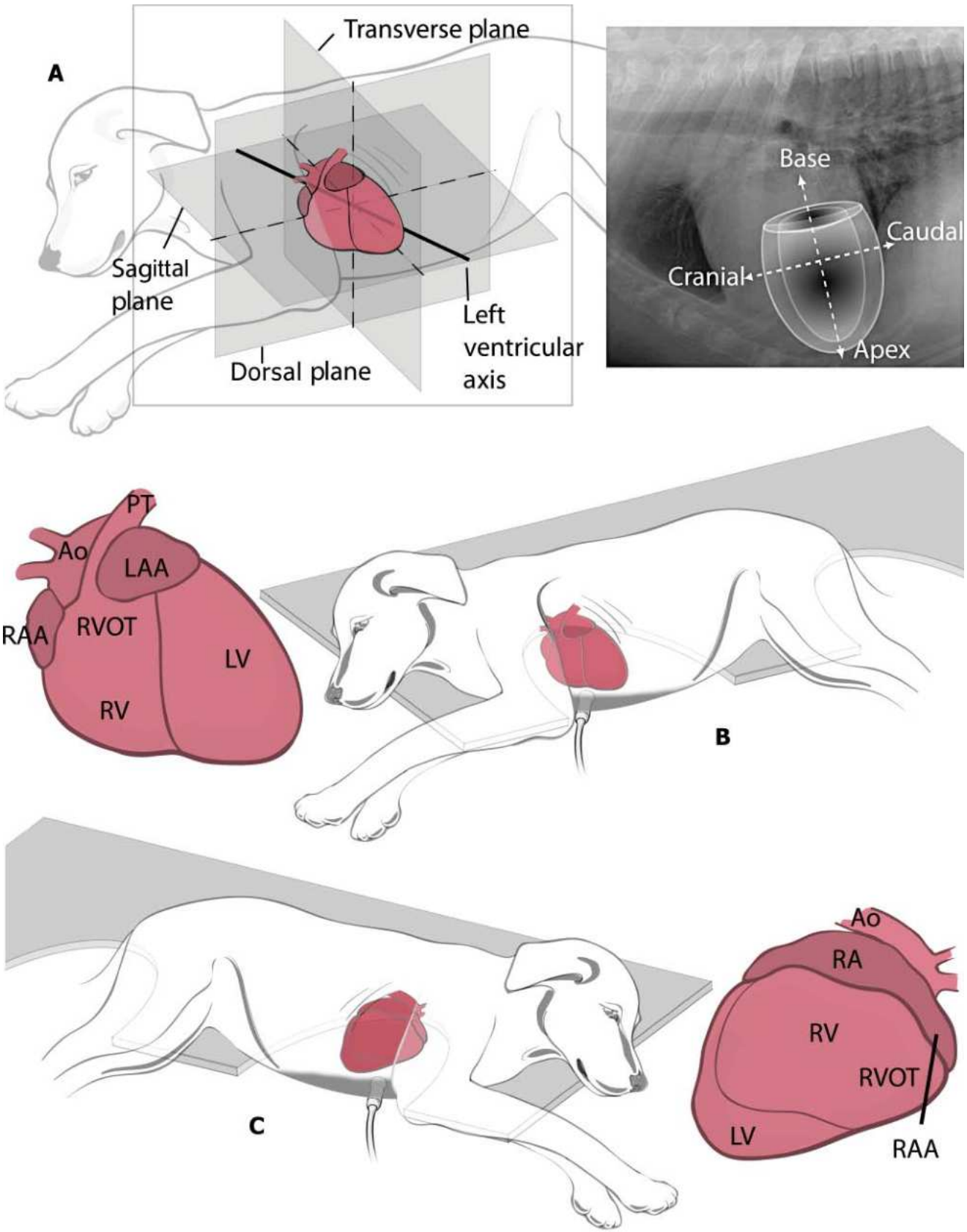


Figure 5.1. **Echocardiographic orientation and anatomy. A:** A prevailing coordinate system is defined in terms of the LV axis for the individual's heart. The terms *base* and *apex* are specific to the heart and do not usually correspond precisely with *dorsal* and *ventral* directions referenced with respect to the animal. Similarly, the *cranial-caudal* axis of the heart is perpendicular to the *base-apex* axis and does not coincide precisely with the anatomical definitions. **B, C:** The transducer is most commonly applied to recumbent patients from below with the aid of a specially designed table. **For the definition of abbreviations in the figures in this chapter, see Table 5.1**.

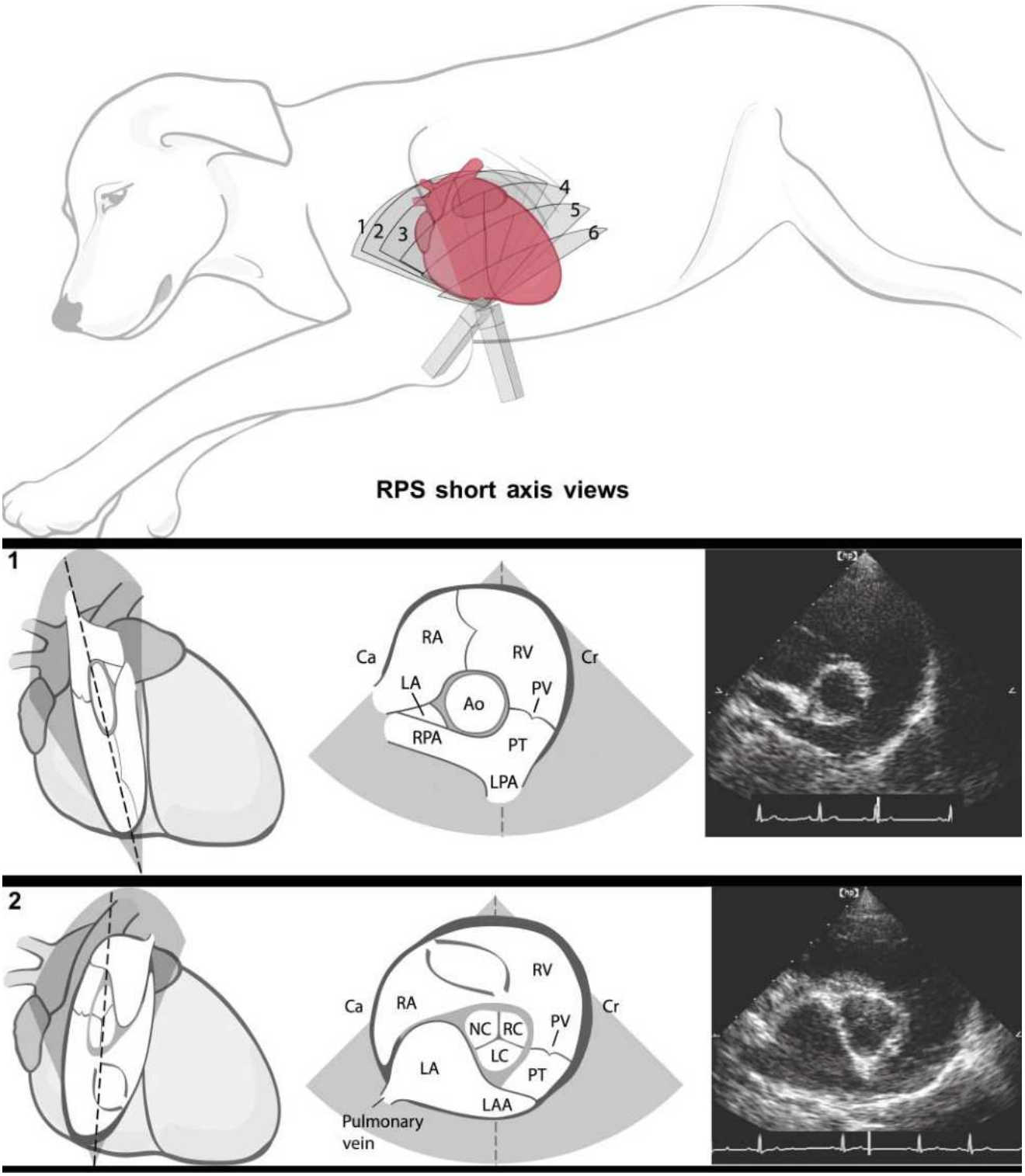


Figure 5.2. **RPS SAx scanning technique.** For RPS SAx views, the transducer is positioned so that the scan plane slices perpendicularly to the LV central axis at the level of the CT. Numbers 1–6 refer to the scan plane orientation and image obtained. Slice 6 is not shown on subsequent images. **1:** Slice 1 at the PT level. **2:** Slice 2 at the Ao root level. The right coronary (RC), left coronary (LC), and non-coronary (NC) cusps of the Ao valve may be visible. **3:** Slice 3 at the mitral level. The mitral leaflets are widely separated while blood flows between the leaflets into the LV chamber. **4:** Slice 4 at the chordal level. **5:** Slice 5 at the LV level. P, pericardium.

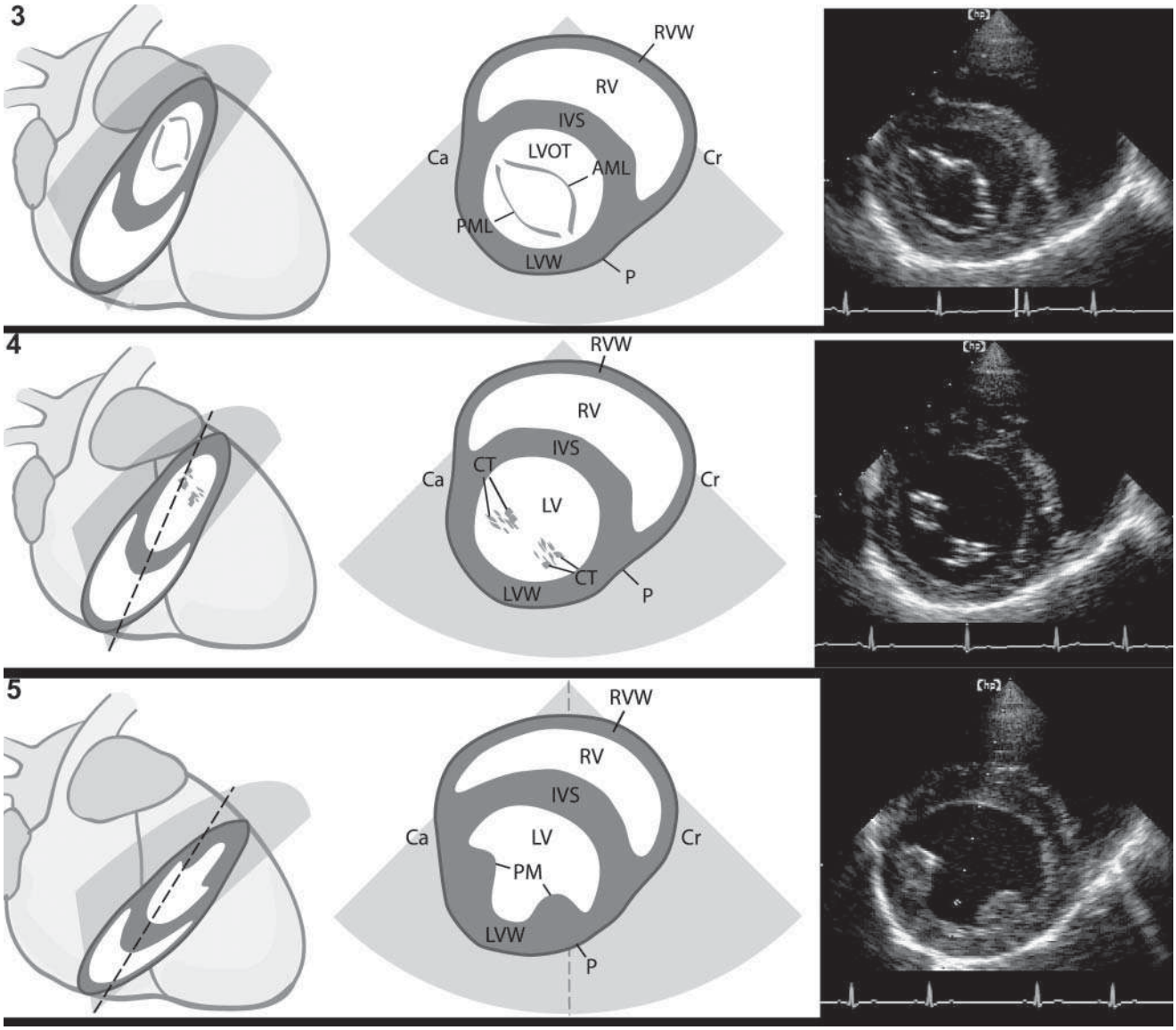


Figure 5.2. *Continued*

is positioned so that it is cranial to the heart, at the fourth to fifth intercostal space, and approximately at the level of the costal–chondral junction in the dorsal-ventral direction.

Baseline left cranial long-axis images are obtained with the scan plane oriented parallel to the ascending aorta, twisting so as to include a longitudinal view of this structure (Figure 5.5). Portions of the left ventricle and atrium, mitral valve, and right ventricular (RV) outflow tract may be visible from this position. The view is particularly useful for evaluation of heart base tumors and the RV outflow tract.

With dorsal and slightly caudal angulation of the transducer, the scan plane encounters the left atrium and ventricle, RV outflow tract, and pulmonary trunk; the pulmonary bifurcation typically can be visualized.

Relative to the initial LV outflow tract position, ventral and slightly cranial angulation causes the scan plane to transect the right atrium, right atrial (RA) appendage, tricuspid valve, and RV inflow. The RA appendage can be closely inspected from this vantage point for evidence of neoplasia.

From the initial LPS view of the LV outflow tract, a clockwise twist results in a scan plane that slices the aortic root transversely (Figure 5.6). Fanning the transducer in a cranial-dorsal direction produces a range of images for optimal viewing of the right atrium

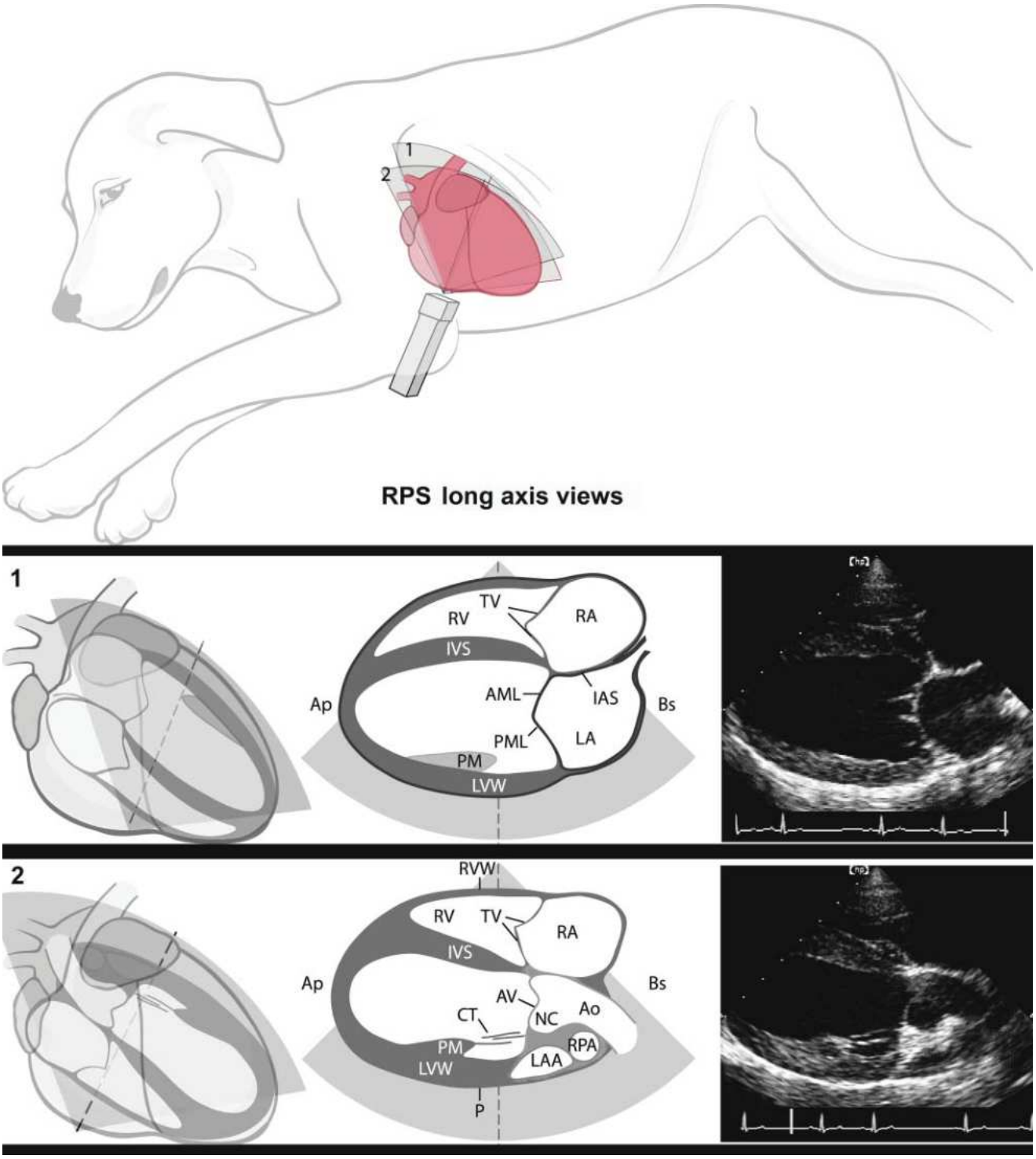


Figure 5.3. **LAx scanning technique.** For RPS LAx views, the transducer is positioned so that the scan plane contains, or is parallel to, the LV central axis. **1:** Slice 1 with a four-chamber view. **2:** Slice 2 with a LVOT view. NC is the non-coronary portion of the Ao sinus of Valsalva. IAS, interatrial septum.

Figure 5.4. **LAp scanning technique.** The transducer is positioned at the left apex of the heart. Cranial angulation brings the long axis of the heart into the scan plane. **1:** LAp four-chamber view. **2:** LAp five-chamber view. **3:** LAp two-chamber view. IAS, interatrial septum.

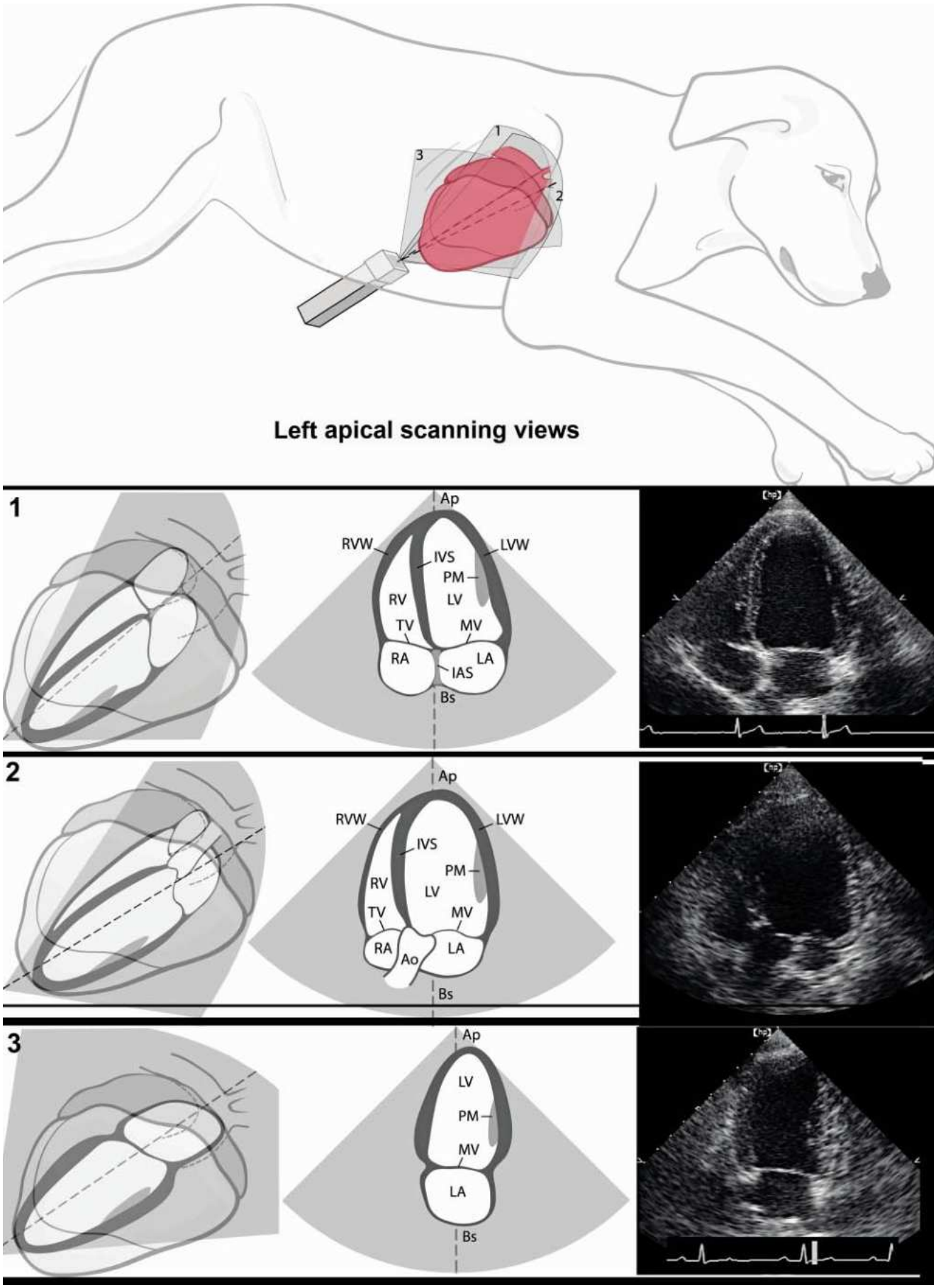


Figure 5.4. **LAp scanning technique.** (for full caption, see facing page)

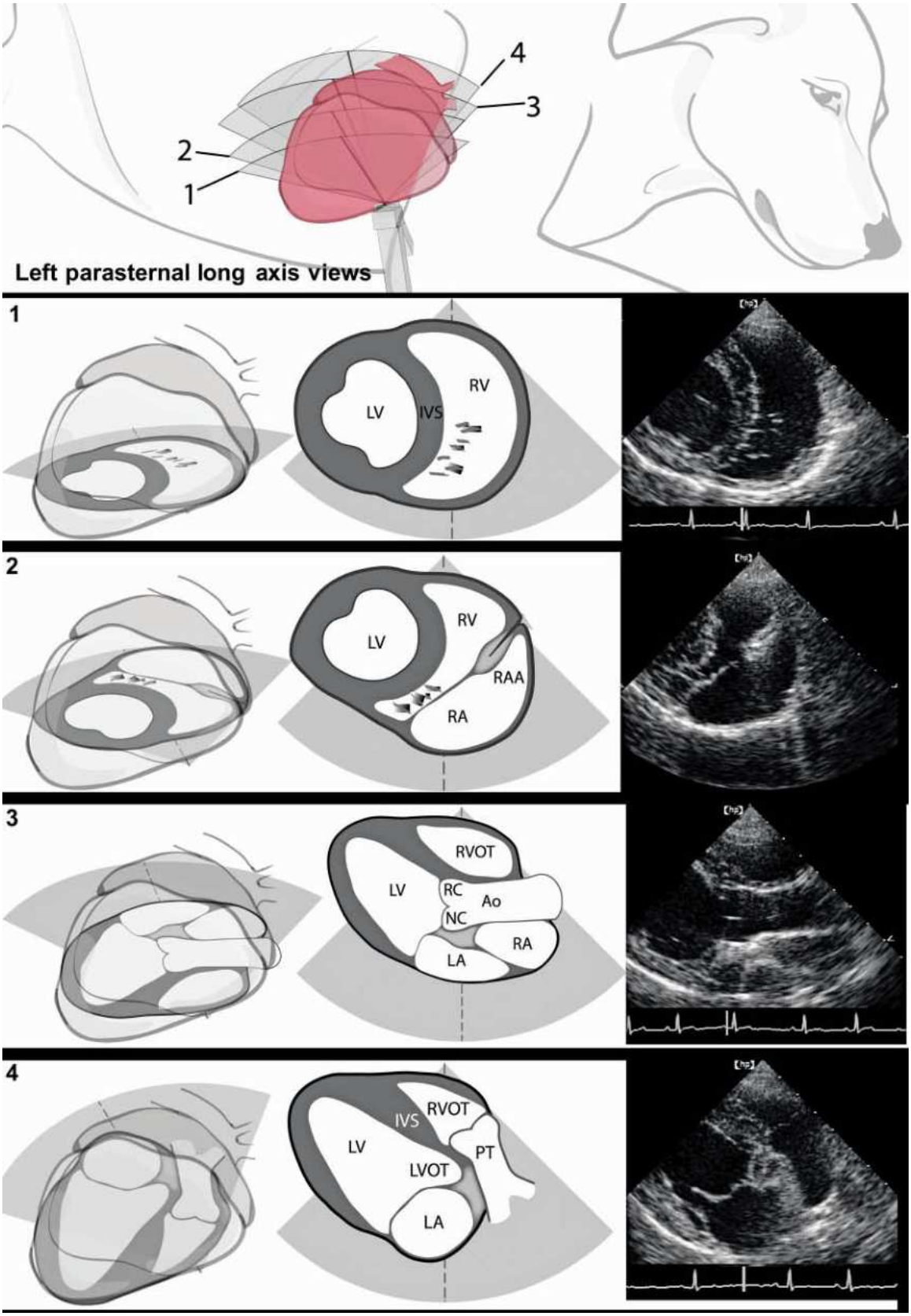


Figure 5.5. Left parasternal LAx scanning technique. The transducer is positioned near the left cranial border of the heart. Dorsal-ventral angulation yields the series of LAx images. Variable angulation in the caudal-cranial direction may be necessary as suggested by the figure. **1:** LPS LAx view at the RV. **2:** LPS LAx view at the RAA. **3:** LPS LAx view at the Ao. RC and NC refer to the right coronary and non-coronary portions of the Ao sinus of Valsalva. **4:** LPS LAx view at the RVOT, PT and LV inflow tract.

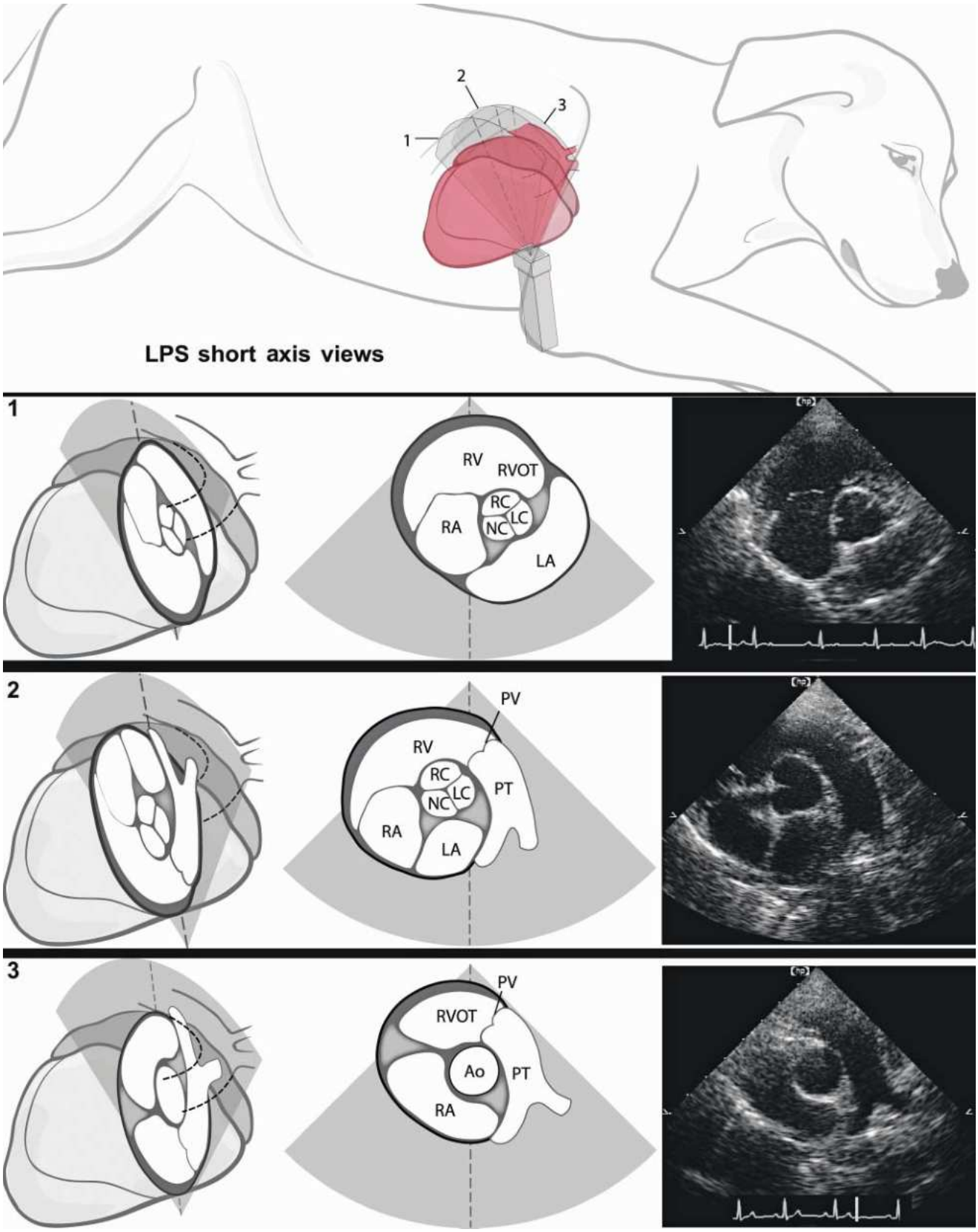


Figure 5.6. **Left parasternal SAx scanning technique.** The transducer is positioned near the left cranial border of the heart. Cranial-caudal yields the series of SAx images. Variable angulation in the dorsal-ventral direction may be necessary as suggested by the figure. **1:** LPS SAx view at the RV inflow tract. The right coronary (RC), left coronary (LC), and non-coronary (NC) cusps of the Ao valve may be visible. **2:** LPS SAx view at the RV inflow-outflow tracts. Both the inflow and outflow tracts of the right heart may be visible with subtle angulation and twist adjustments. The RC, LC, and NC cusps of the Ao valve may be visible. **3:** LPS SAx view at the PT. Division of the PT into the right and left main pulmonary arteries is seen in the far field.

and RV inflow tract, RV inflow and outflow tracts, and pulmonary trunk. The latter enables visualization of the pulmonary bifurcation, ascending aorta, and structures associated with the heart base.

Subcostal and Suprasternal Views

The suprasternal view necessitates transducer positioning at the thoracic inlet with the scan plane oriented parallel to the patient's sagittal plane. This view is best for imaging the aortic arch and is therefore valuable for quantification of aortic insufficiency. The subcostal view is obtained, with the patient in lateral recumbency, by positioning the transducer at the xiphoid process and pressing into the abdomen while pointing the transducer almost directly cranially (Figure 5.7). The twist is adjusted to be approximately parallel to the sagittal plane. For Doppler aortic velocity recordings, the transducer is fanned to include the aortic root.

Motion-mode Echocardiography (M-mode)

The majority of M-mode dimensional recordings are made from the RPS transducer position (Bonagura 1983; Bonagura et al. 1985). One of the principal applications of M-mode echocardiography is for the recording of time-dependent short-axis dimensions of the heart, and this dictates a specific external transducer location that is determined by the cardiac anatomy (Figures 5.8–5.12).

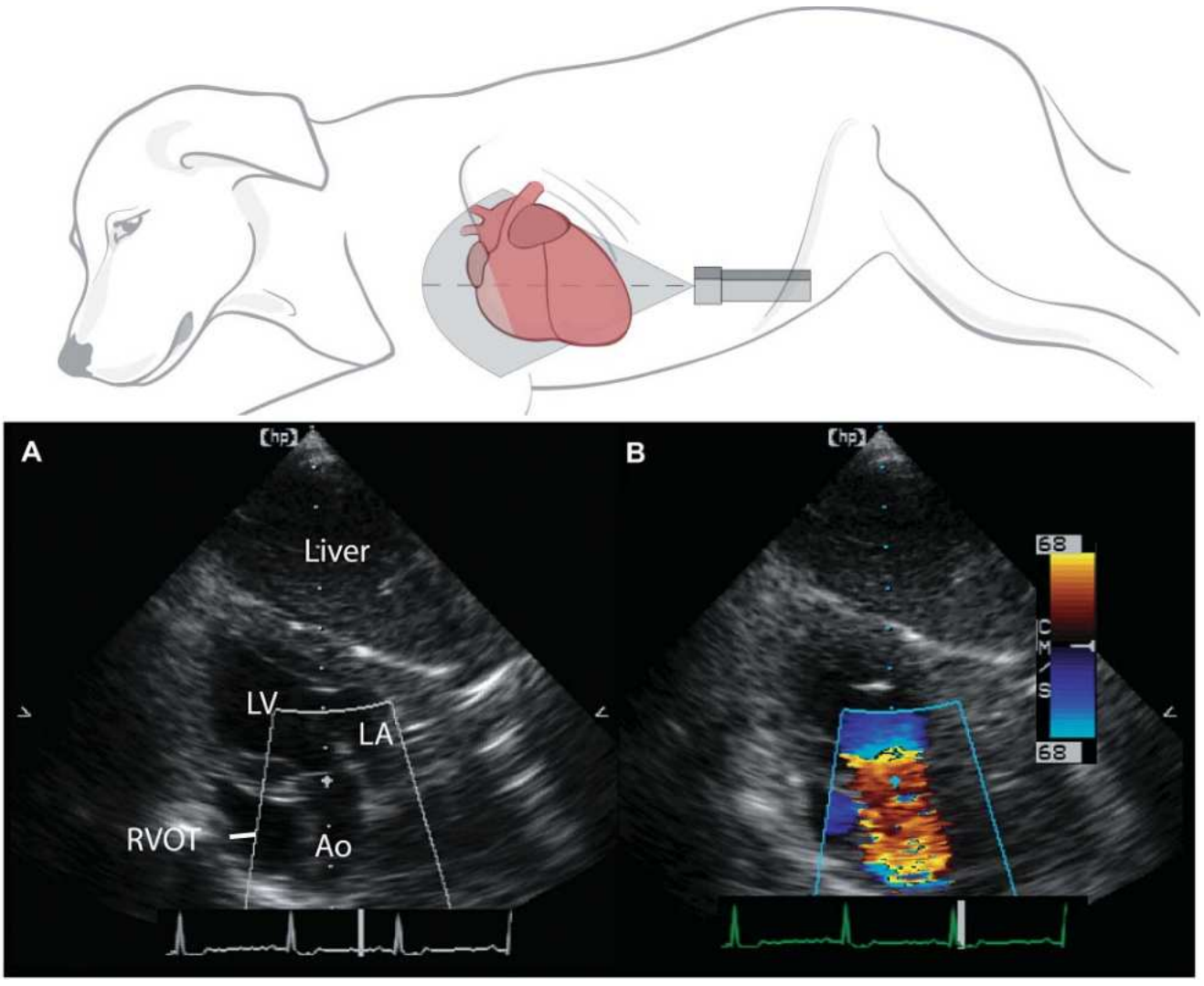


Figure 5.7. Subcostal approach. This transducer position is used principally for Doppler recordings of Ao ejection and typically yields the best alignment with flow in dogs. The liver is interposed between the transducer and heart. The CFD image **(B)** depicts Ao ejection.

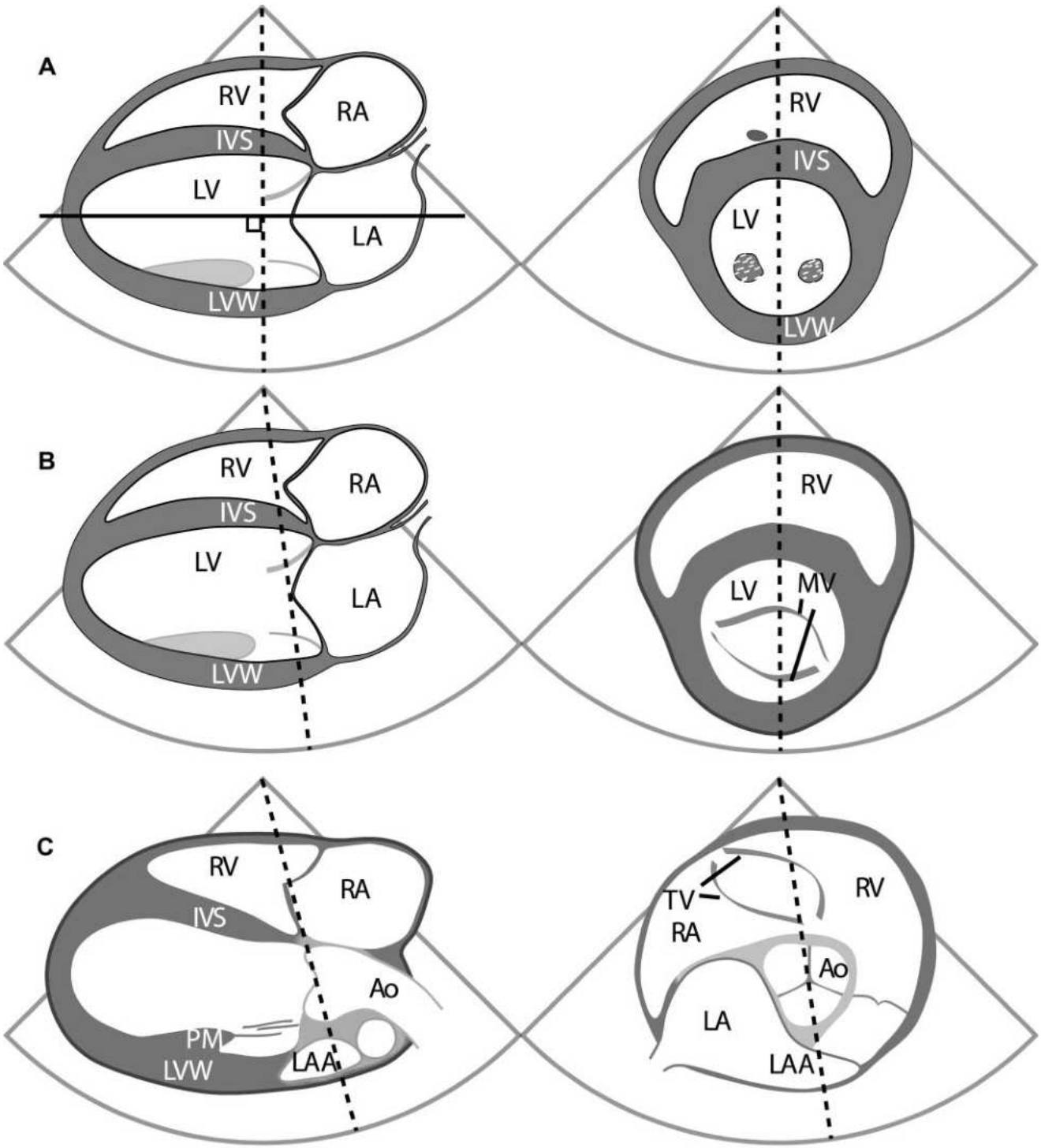


Figure 5.8. **M-mode scan-line orientation.** 2DE is used to position the transducer and orient the scan line throughout M-mode recordings as shown. Orientations are depicted for LV **(A)**, MV **(B)**, and Ao-LA **(C)** recordings.

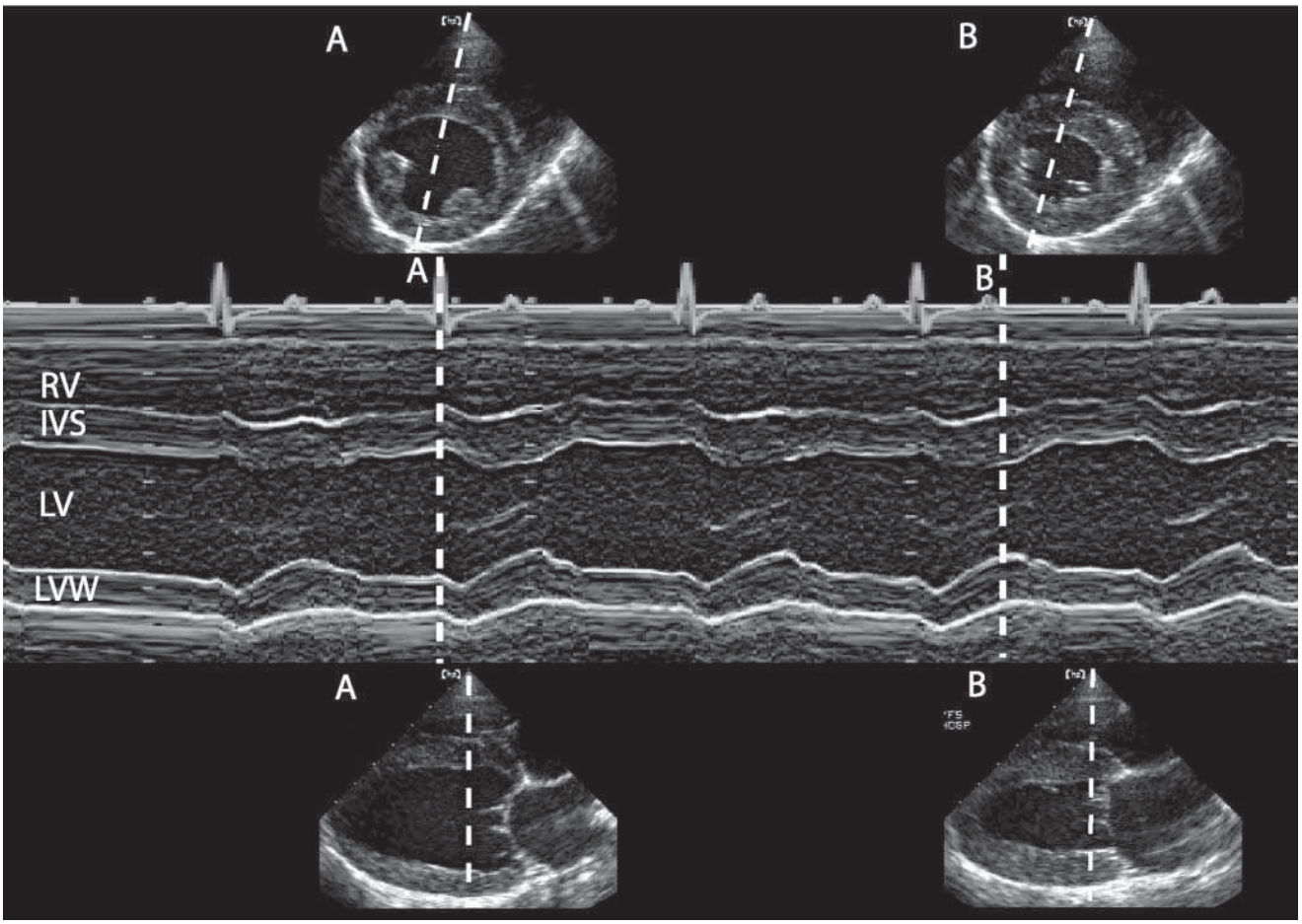


Figure 5.9. **M-mode at the LV level.** The M-mode recording (middle tier) is generated from the selected scan line shone in the RPS SAx (top tier) and LAx (bottom tier) images. Time marker A is at end diastole coinciding with the onset of the QRS complex of the electrocardiogram. Time marker B is at end systole, which coincides with the minimum LV dimension near the end of the electrocardiographic T wave.

Doppler Echocardiography

Blood Flow Doppler Imaging

Doppler echocardiography uses the Doppler principal to determine the velocity of moving blood or tissue (Darke 1992; Kirberger et al. 1992; Bonagura and Miller 1998; Bonagura et al. 1998). With **pulsed-wave Doppler** (PWD), the round-trip time of the ultrasound pulse is used to determine the tissue depth at which the velocity occurs; the maximum depth dictates a specific pulse-repetition frequency. In turn, repetitive pulsation of the ultrasound is directly responsible for the aliasing phenomenon whereby measured velocity is observed to occur at an alias velocity. The alias velocity may be a gross misrepresentation of actual velocity (Figure 5.13). In contrast to PWD, ultrasound is emitted continuously in the **continuous-wave Doppler** (CWD) modality, which does not suffer from the velocity ambiguity of PWD. There is no practical limit to the velocity magnitude that can be measured with CWD. However, this mode does not enable determination of the tissue depth from which the measured velocities arise, so the anatomical location of velocities must be inferred or determined using other means (e.g., PWD).

Color flow Doppler (CFD) is a pulsed-wave modality in which velocity characteristics are encoded to a color display, via a user-selected mapping, and overlaid onto the real-time two-dimensional echocardiography (2DE) image. This enables the ultrasonographer to visualize directly the source of velocities within the heart and great vessels within the anatomical framework of the image. Being a pulsed-wave modality, CFD is subject to velocity measurement ambiguity

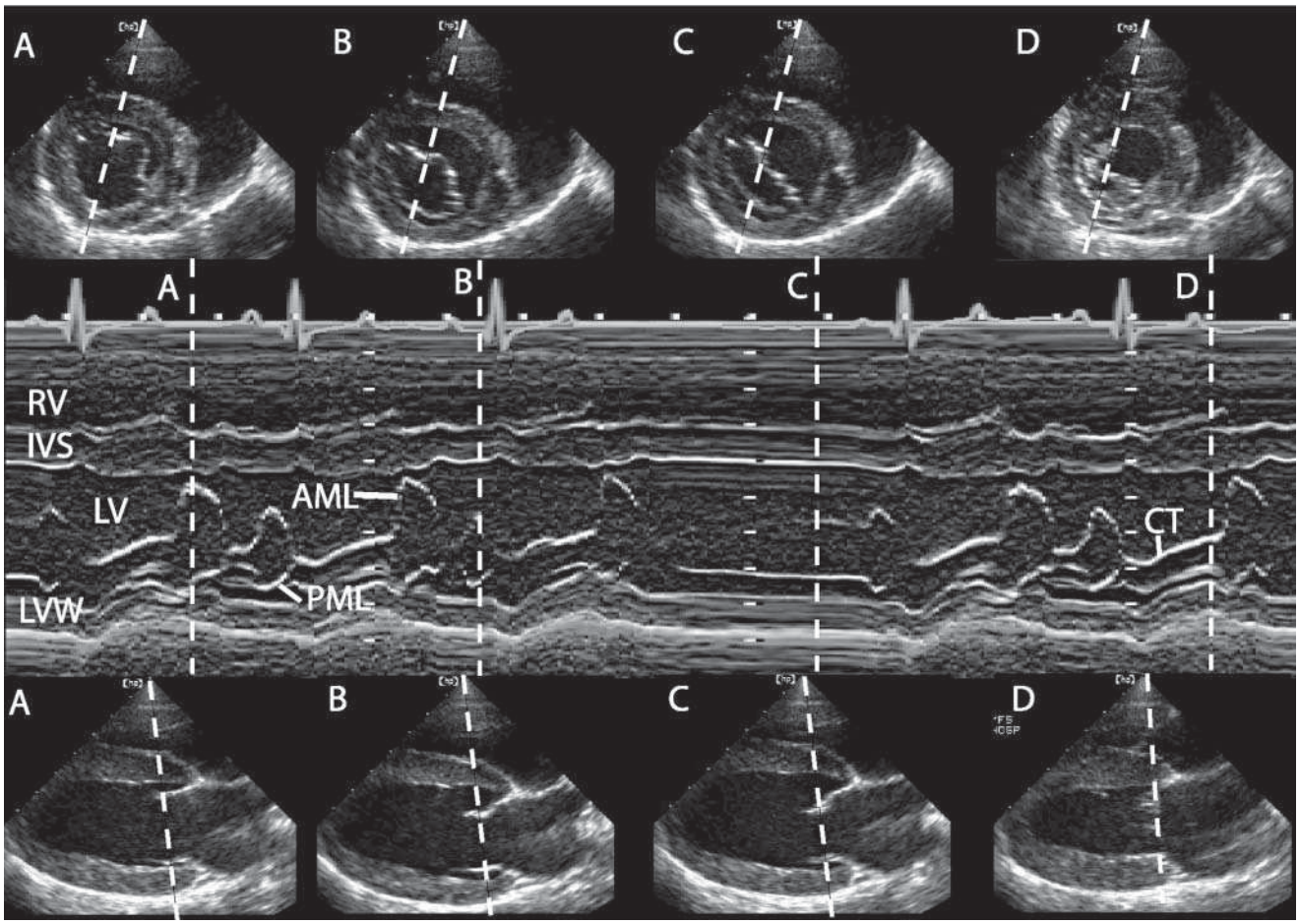


Figure 5.10. M-mode at the MV level. The M-mode recording (middle tier) is generated from the selected scan line shone in the RPS SAx (top tier) and LAx (bottom tier) images. The two primary mitral leaflets are separated from each other during diastole and apposed during systole. Time marker A is at early diastole, and marker B is at late diastole immediately after the P wave of the electrocardiogram. Marker C is at a prolonged diastasis, i.e., middiastole, and D is at end systole.

caused by aliasing (Figure 5.14). PWD and CFD are better suited than CWD for differentiation between laminar and turbulent flow patterns.

Aortic flow velocity is recorded from the subcostal or LAp transducer position for velocity quantification. The normal aortic ejection signal peaks early in the ejection cycle and may impart a dagger-like shape to the velocity envelope (Figure 5.15). By comparison, pulmonary ejection from the same individual exhibits a later peak velocity with a lower maximal value, and a longer duration of ejection (Figure 5.16). Pulmonic ejection recordings may be obtained from either the RPS or LPS transducer positions, and it may be appropriate to attempt both if quantification of maximal velocity is desired. It is normal for both the tricuspid and pulmonic valves to exhibit a small amount of insufficiency (Figure 5.17).

Mitral and tricuspid inflow velocities are usually recorded from the LAp position to best align the ultrasound beam with the direction of inflow (Figure 5.16). PWD recordings are made by placing the sample volume near the tips of the open mitral or tricuspid leaflets to include maximal velocities. Like their M-mode counterparts, velocity signals exhibit phasic changes that reflect the physiology of ventricular filling. The tricuspid inflow-velocity signal is similar to the mitral but normally exhibits diminished velocity magnitude in comparison, in part because of greater effective orifice area for the tricuspid valve. Recording of tricuspid inflow is facilitated by placing the transducer one or more rib spaces farther cranially as compared with the optimal position for mitral recordings.

Examples of normal CFD recordings are shown in Figures 5.17 and 5.18.

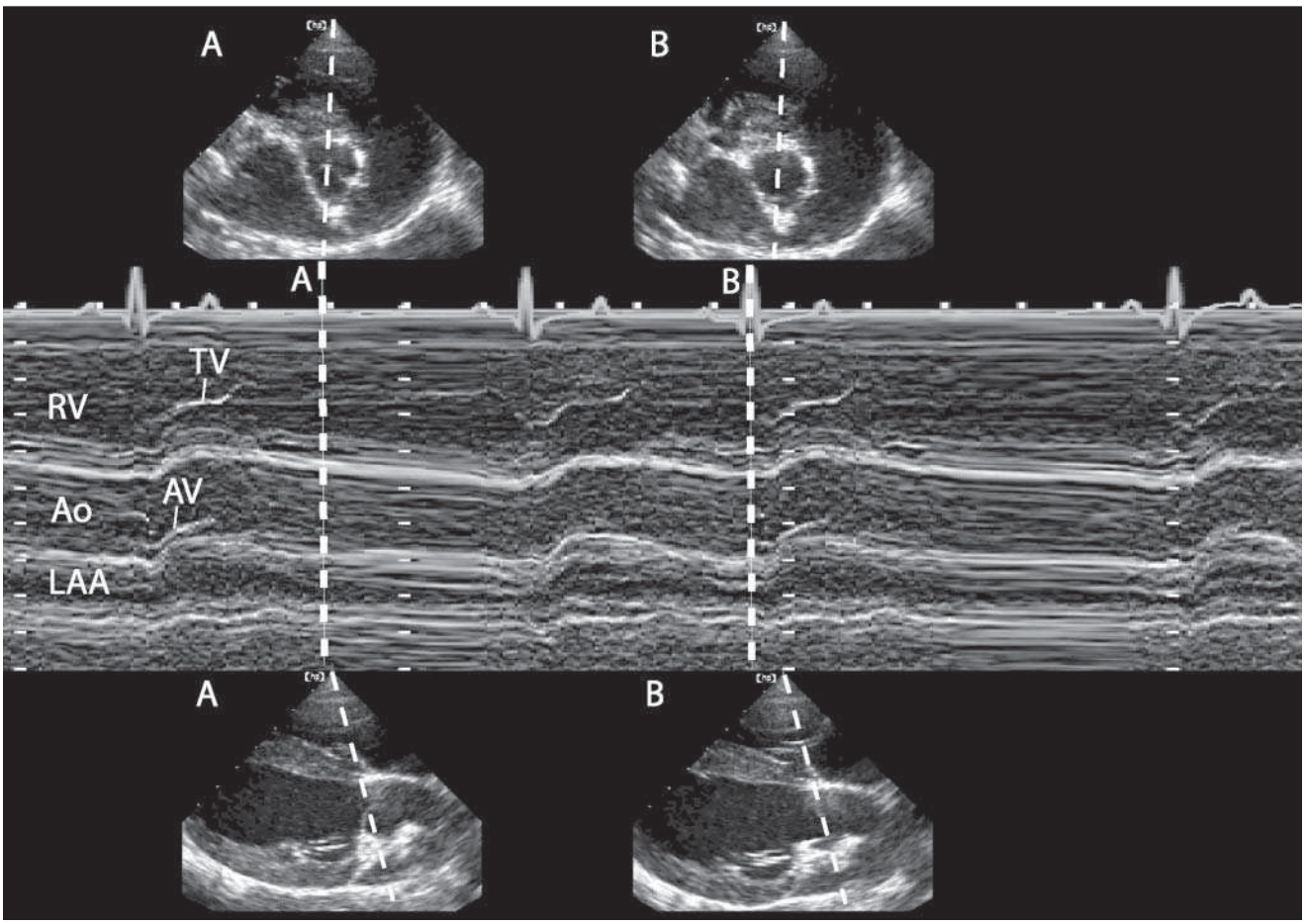


Figure 5.11. M-mode at the Ao root level. The M-mode recording (middle tier) is generated from the selected scan line shone in the RPS SAx (top tier) and LAx (bottom tier) images. Because of the orientation of the scan line, only the left coronary cusp is typically visible during systole in the dog. Time marker A is at mid-diastole, and the AV is shown closed during this phase. Time marker B coincides with systole, and the left coronary cusp is visible near the far-field Ao wall.

Tissue Doppler Imaging

Tissue Doppler imaging (TDI) is employed to quantify the velocity of motion of cardiac tissue directly. TDI may provide valuable information about both systolic and diastolic function and ventricular filling pressures, especially when used in conjunction with mitral inflow recordings. The most common use of TDI in cardiology is to record the longitudinal (base-apex) velocity of the mitral annulus from the LAp four-chamber position. Velocity recordings may be obtained from either the septal or lateral mitral annulus, adjusting transducer position so that annular motion of the chosen site is directed along the Doppler scan line to the extent possible (Figure 5.19). Longitudinal velocity recordings of the right ventricle are obtained from a segment of the internal mid-portion of the right myocardium on the LAp four-chamber view (Chetboul et al. 2005).

Echocardiographic Measurements and Indices

Besides direct visual observation, structural and functional evaluation of the heart may entail echocardiographic measurements of linear dimensions, areas, time intervals, or velocities, and calculation of performance indices from these raw data. To characterize and quantify the heart echocardiographically, the ultrasonographer must possess a detailed understanding of cardiovascular physiology, pathophysiology, and the sources of variation for observations (Table 5.2).

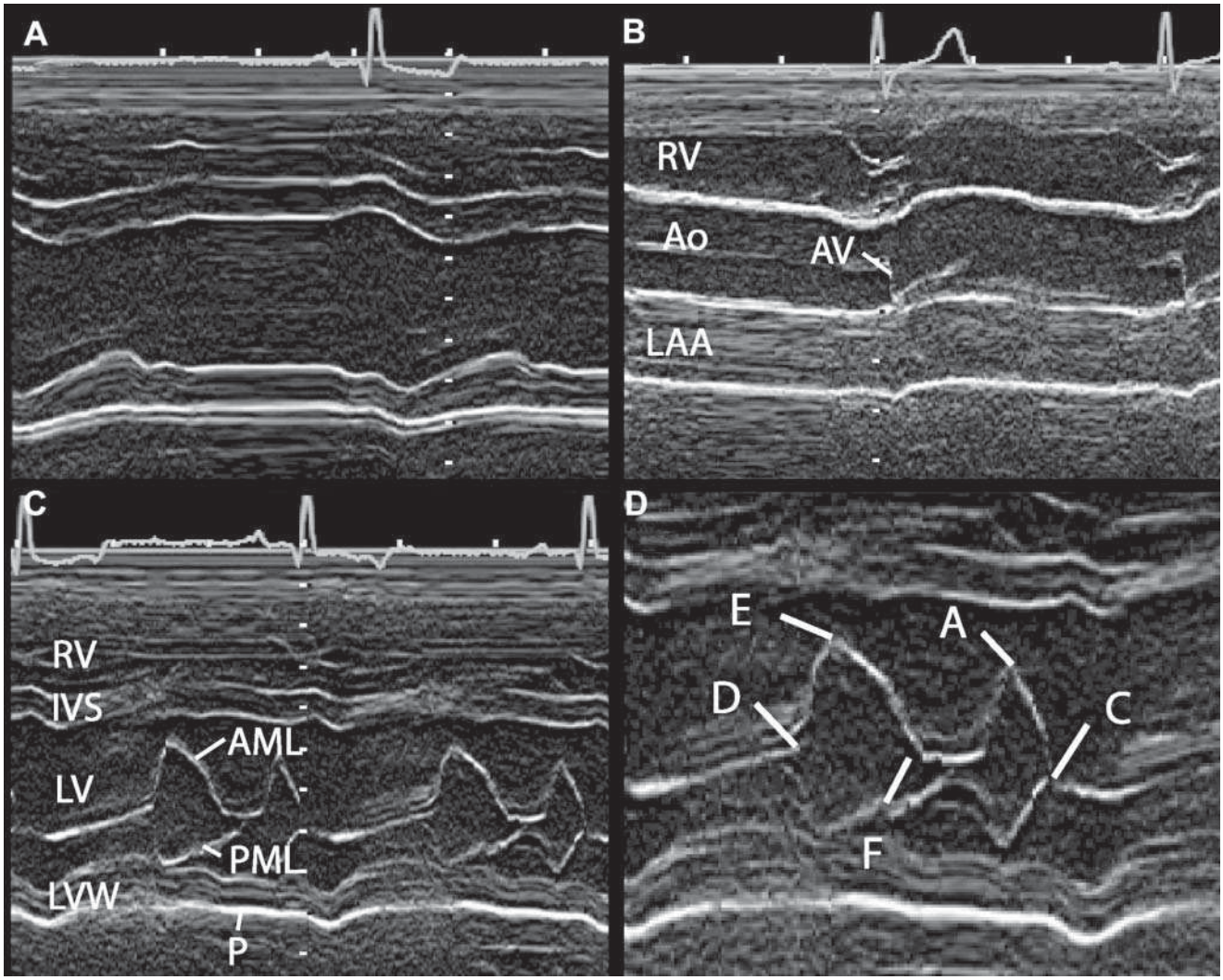


Figure 5.12. **M-mode recordings. A:** This recording is made at the LV level corresponding to the scan-line orientation shown in Figure 5.8A. Epicardial and endocardial surfaces of the IVS and LVW are well delineated throughout the recording, which is necessary for measurement accuracy. **B:** This Ao root recording corresponds to the orientation in Figure 5.8C. The AV is visible. **C:** This recording is at the MV level (Figure 5.8B). **D:** Depicted are letter designations A–F of MV motion.

Table 5.2
Sources of echocardiographic variation

Image acquisition
- Observer technique
- Instrument settings

Measurement from images
- Observer technique

Hemodynamic variation (short term)
- Autonomic balance
- Preload
- Afterload
- Contractility
- Heart rate
- Drugs

Environmental variation (long term)
- Nutrition
- Athletic training level
- Drugs

Genetic variation
- Body size
- Species variation
- Breed variation
- Individual variation

Pathophysiology
- Disease consequences
- Cardiovascular remodeling

Interpretive methods
- Observer experience
- Statistical methods
- Spectrum of normal
- Data availability

Expertise as an echocardiographer necessitates an extensive understanding of these factors and interrelationships.

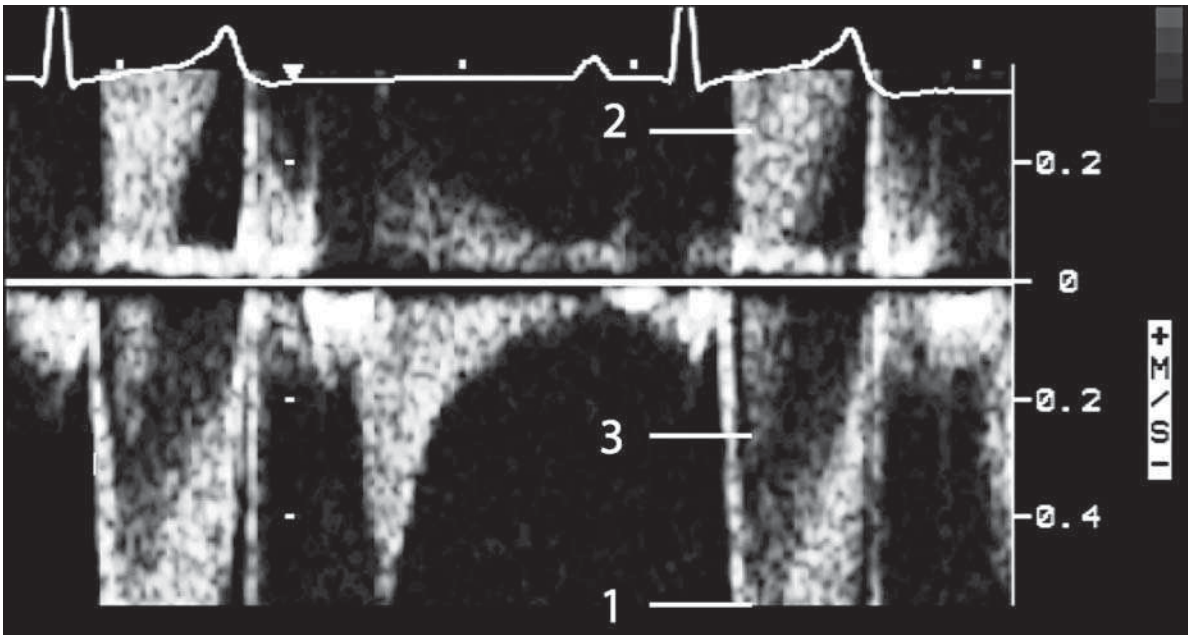


Figure 5.13. Spectral PWD aliasing. Spectral Doppler recordings represent velocity along the *y*-axis, corresponding to Doppler shift frequency, and time along the *x*-axis. In this example of Ao ejection, flow is directed away from the transducer, and velocity in this direction is depicted below the baseline. The velocity reaches the alias velocity (Nyquist limit) at position 1 and further increases, causing the signal to wrap around to the positive side of the velocity scale (position 2). Velocity continues to increase, actually passing the zero baseline to the peak velocity indicated at position 3.

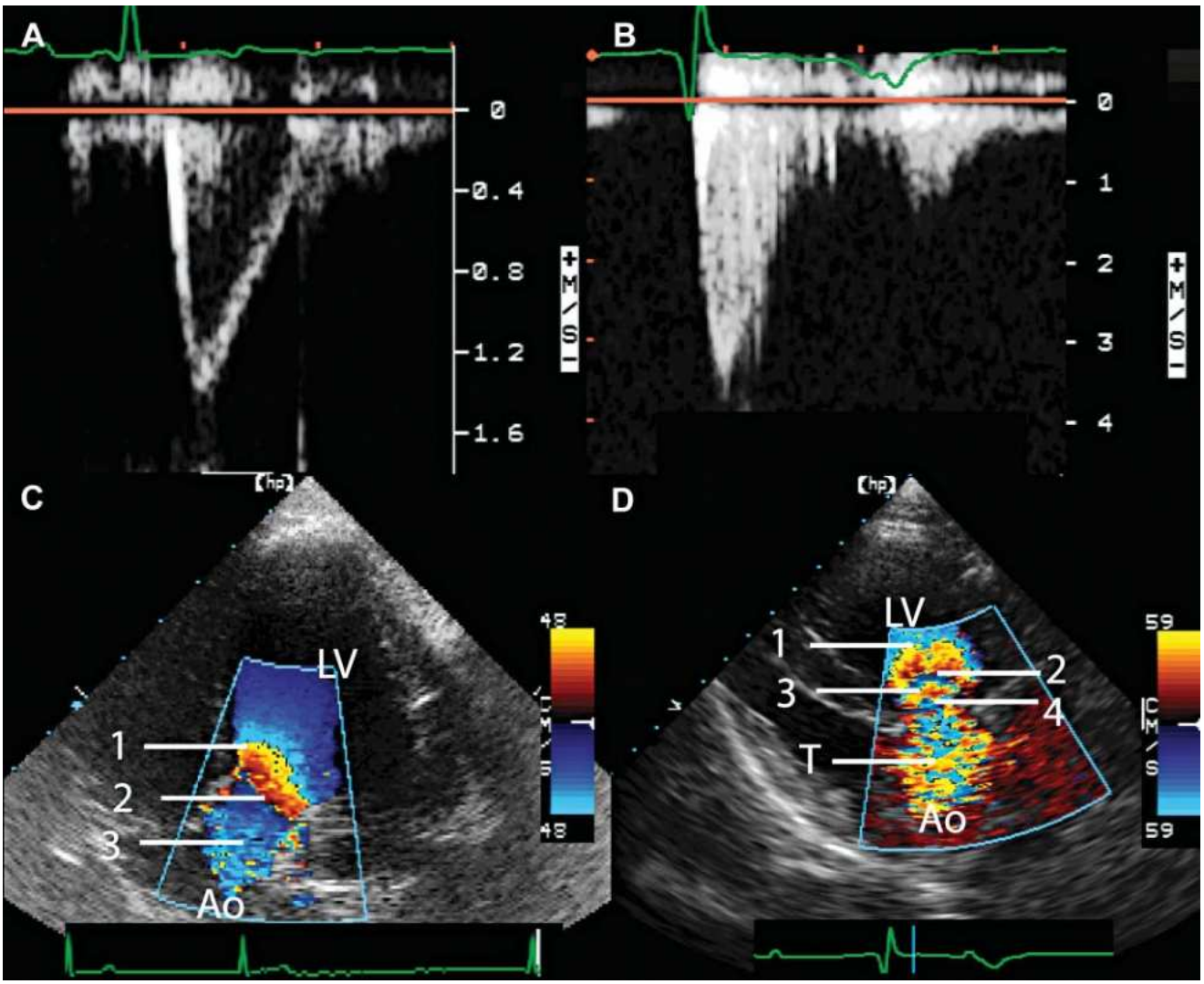


Figure 5.14. Laminar versus turbulent flow. (for full caption, see facing page)

Measurement and Index Normalization

A basic, but troublesome, aspect of veterinary cardiology has been to interpret raw measurements for the range of body size and breed variations encountered, particularly for dogs. Although no entirely satisfactory approach has been determined, a common feature of many well-normalized indices is that they derive from a ratio of two measurements with the same physical units. Echocardiographic ratio indices have long been used in cardiology, with examples dating from the beginning of the technique. Left atrial (LA) size, for example, may be expressed in terms of aortic dimension (LA/Ao_m). It is often preferable, however, to index cardiac linear dimensions in terms of the body weight (BW, in kg) raised to the one-third power. The weight-based aortic dimension, $Ao_w = 0.795 \times BW^{1/3}$, is an estimate of a dog's aortic diameter, and expectations for LA/Ao_w are similar to the index derived using the measured aortic dimension (Figure 5.20). Similarly, the aortic area can be approximated as

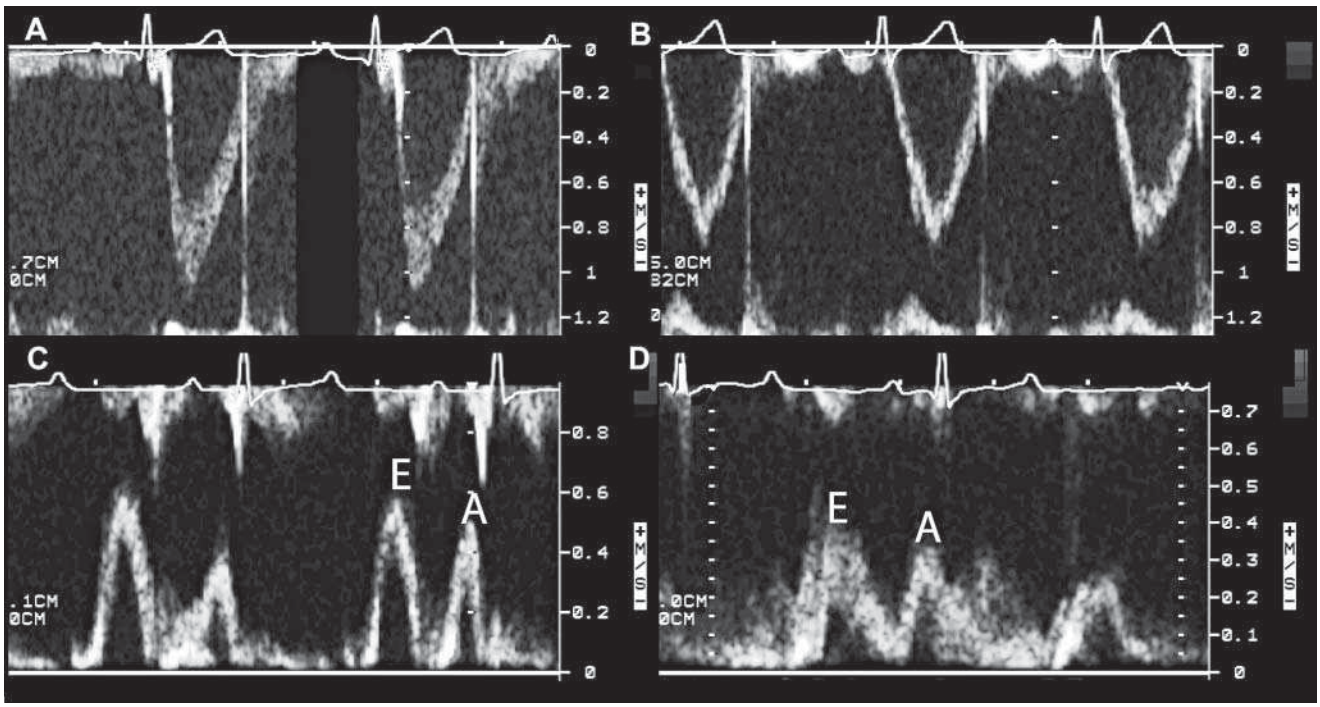


Figure 5.15. Normal PWD recordings. PWD recordings from a normal dog are shown for the Ao (**A**, LAp transducer position), pulmonic (**B**, RPS position), mitral (**C**, LAp position), and tricuspid (**D**, LAp position) valves. Characteristically, Ao ejection flow velocity peaks early in systole and may generate a dagger-shaped velocity envelope like the one shown. Inclusion of the valve itself in the velocity sampling volume generates a vertical artifact that marks the end of the ejection for both cardiac cycles shown. Normal mitral and tricuspid inflow occurs in two distinct phases (E and A waves as labeled) corresponding to M-mode designations.

Figure 5.14. Laminar versus turbulent flow. A: The PWD Ao ejection signal, recorded from the subcostal transducer position of a normal dog, demonstrates a laminar flow signal. **B:** In contrast, a CWD recording of a turbulent pattern from a dog with third-degree atrioventricular block and bradycardia, causing a marked increase in stroke volume. This results in a wide range of Doppler frequencies (i.e., velocities) at each moment during the ejection and spectral broadening of the signal; the velocity envelope is filled in (white) throughout ejection. **C:** A CFD image from the normal dog (LAp transducer position) early in the Ao ejection phase. The color pattern is laminar but depicts color aliasing that occurs at position 1. Velocity continues to increase in the direction of the outflow and has aliased to black, at position 2, wrapping around to blue again at position 3. **D:** The CFD image of Ao ejection for the bradycardic dog. Color aliasing occurs so that velocity can be seen to wrap around the color scale at least twice with a blue–yellow interface (Nyquist frequency) at positions 1 and 3, and indicated zero velocity at positions 2 and 4. A turbulent color flow pattern appears in the Ao (T), as represented by small juxtaposed islands of blue and yellow, also known as a mosaic pattern.

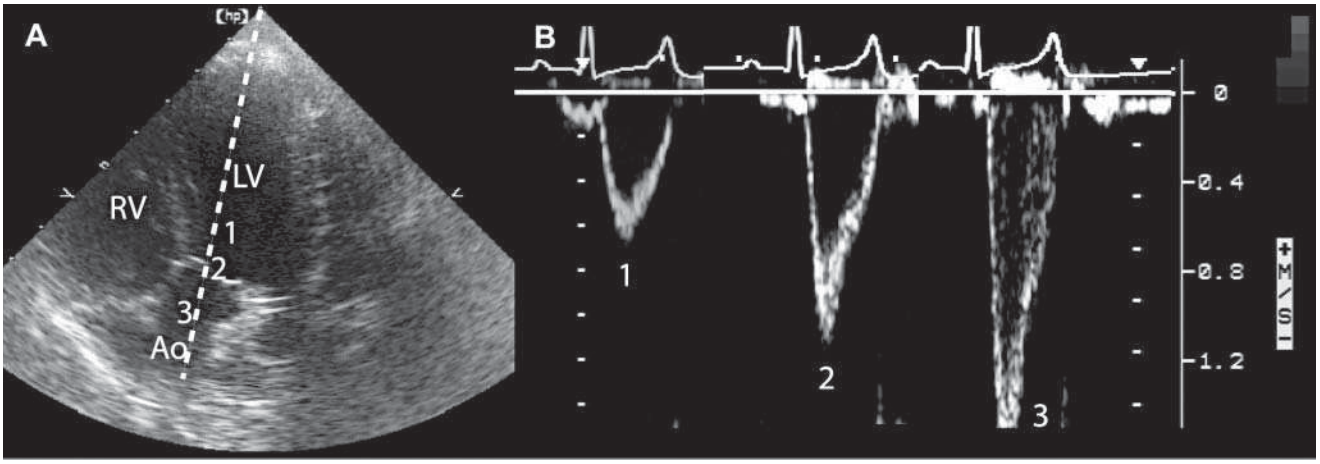


Figure 5.16. Variation of Ao ejection velocity with location. PWD recordings of Ao ejection with the LAp five-chamber image **(A)** showing sample volume locations and **(B)** corresponding PWD recordings with their relative maximum velocities. There is a marked progression of peak velocity from the subvalvular position (1) to the valvular (2) and supravalvular (3) positions. CWD recordings from the same transducer position (not shown) sample all velocities included along the chosen scan line (dotted). The envelope of the CWD recording indicates the maximum velocity along the scan line throughout ejection. There may be considerable spectral broadening because a wide range of velocities is present along the line at each moment in time, resulting in a filled velocity envelope with CWD mode.

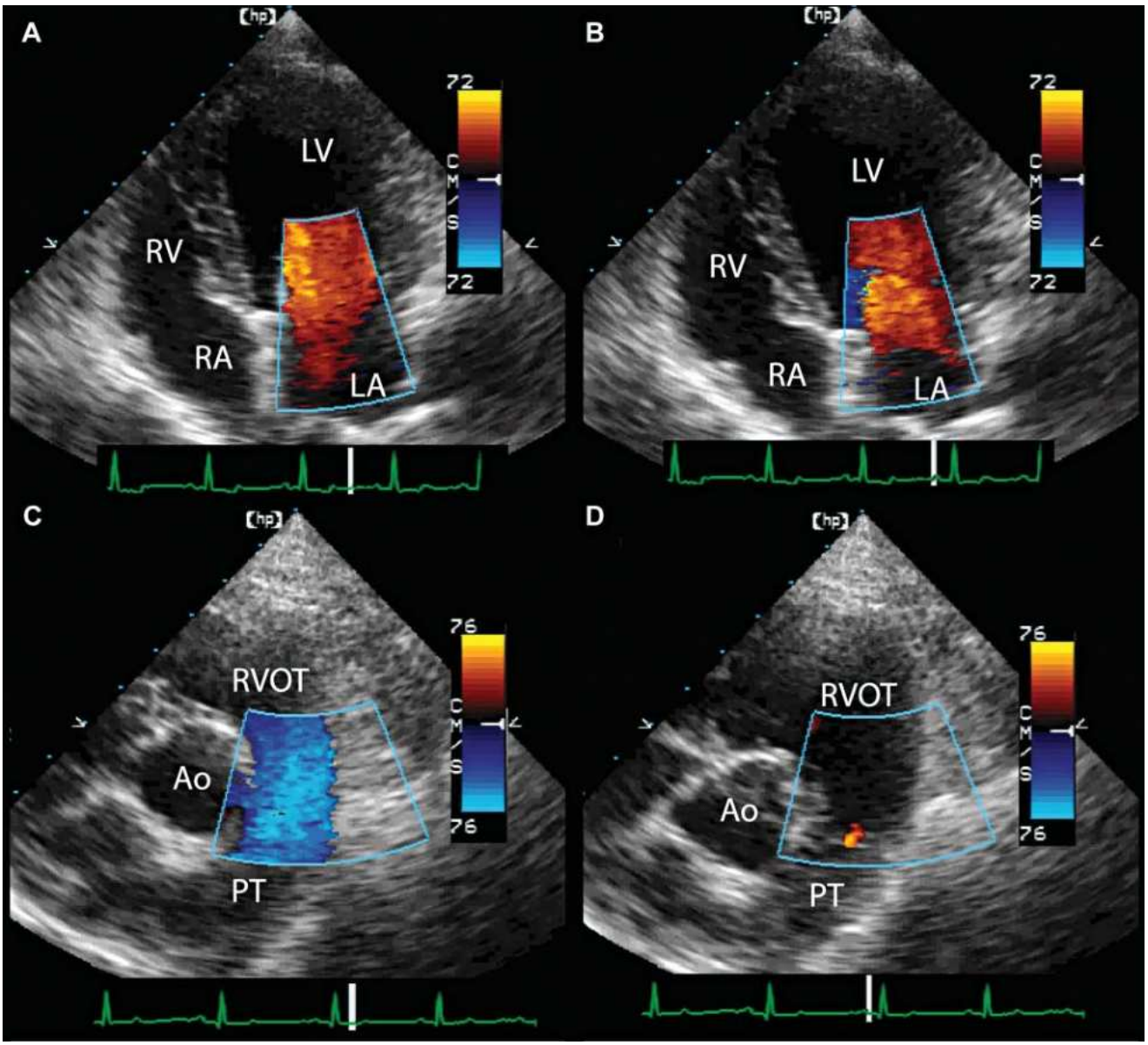


Figure 5.17. Normal CFD images of mitral and pulmonic flow. (for full caption, see facing page)

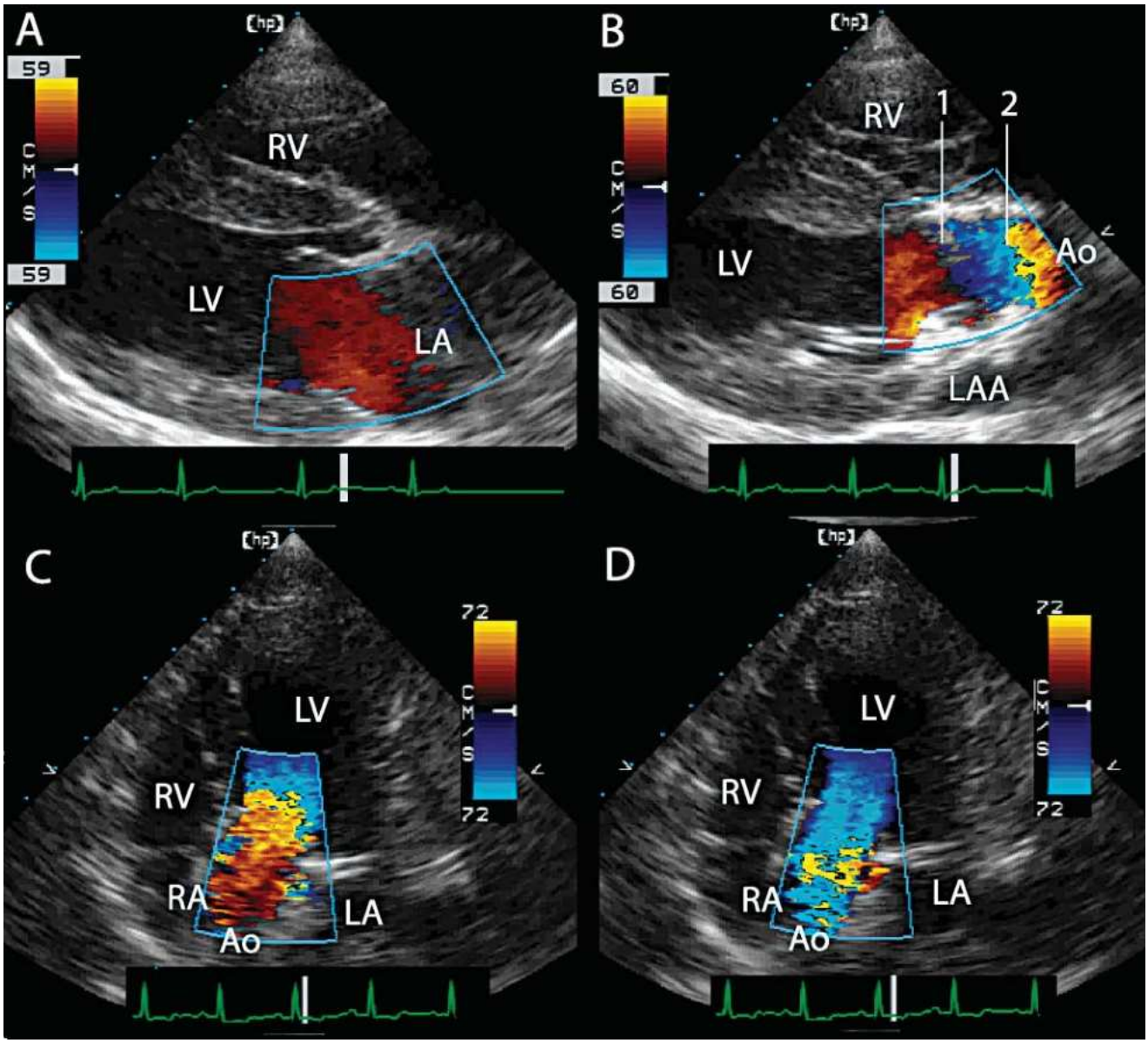


Figure 5.18. **Normal CFD images of Ao flow. A, B:** CFD images from the RPS position of a normal dog. Inflow **(A)** and outflow **(B)** velocities of the LV are not aligned with the direction of ultrasound propagation from the RPS position, and accurate quantification of these velocities is not achieved. **A:** Normal mitral inflow in early diastole is directed relatively toward the transducer and depicted in red in accordance with the color velocity map shown. **B:** LV ejection follows a bend in the Ao so that part of the flow is directed toward the transducer (red), part is directed away (blue), and velocity is completely perpendicular to the ultrasound beam at location 1, where velocity appears to be zero (black). Color aliasing occurs at location 2, where flow away from the transducer exceeds the Nyquist limit. Improved LV inflow and outflow alignment are achieved from the LAp position. **C:** Early peak Ao ejection, with color aliasing. **D:** Subsequent ejection at decreased velocity.

Figure 5.17. **Normal CFD images of mitral and pulmonic flow.** LV inflow, recorded from the LAp four-chamber view, is shown for early diastole **(A)** and for atrial kick **(B)**, corresponding to the E and A waves of mitral inflow, respectively (Figure 5.15). RPS SAx images of pulmonic flow correspond to laminar systolic ejection **(C)** and mild PI **(D)**. The latter is a normal finding.

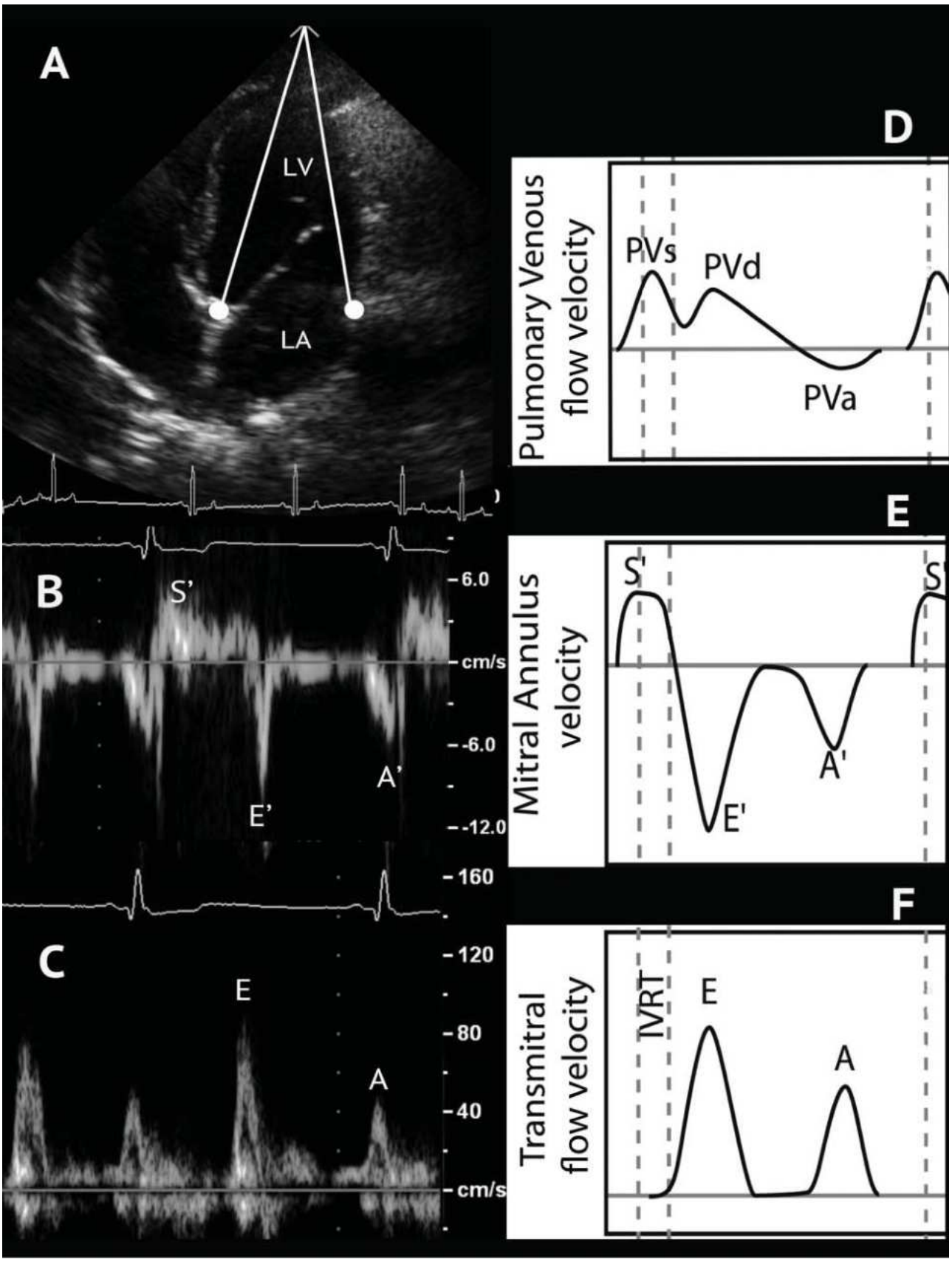


Figure 5.19. **TD recording of mitral annular velocity.** (for full caption, see facing page)

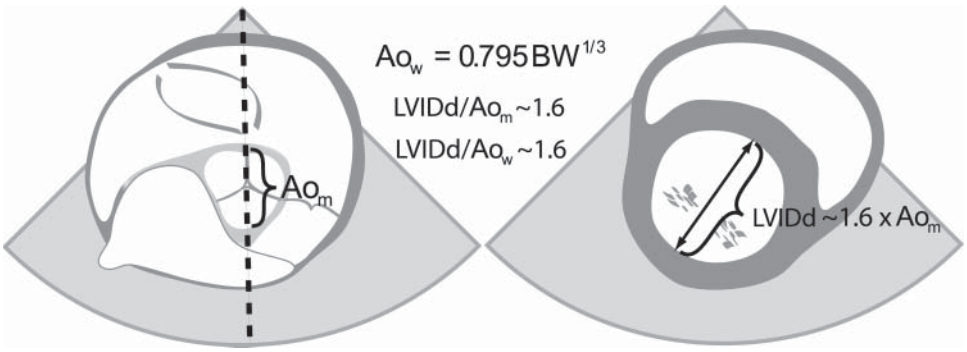


Figure 5.20. Ratio index normalization for body size. Size normalization of measured linear dimensions, area, volume, or mass can often be accomplished by using a ratio index. The measured Ao diameter (Ao_m), obtained from M-mode or 2DE recordings, has been used as a suitable reference length in echocardiography. The diastolic LV internal dimension (LVIDd), for example, ranges between 1.2 and 2.0 Ao diameters across in normal dogs, regardless of body size. However, the Ao dimension also may be estimated from body weight (kg), as shown, and often is superior statistically to Ao_m as a length standard.

$AoA_w = \pi Ao_w^2/4$, the area of a circle with radius $Ao_w/2$, and incorporated into various area ratio indices. In normal dogs, for example, LA area in the RPS short-axis orientation (SAx) image is approximately two to four aortic areas in size, regardless of body size (LA area/AoA_w = 2–4).

The majority of published cardiac dimensional data for dogs and cats are from M-mode recordings. Many of these may be recast into the form of a ratio index that enables interpretation independent of body weight (Hall et al. 2008). Normal values for raw echocardiographic measurements and ratio indices are tabulated in the Appendix at the end of this chapter.

Linear Dimensions

Motion-mode recordings suitable for accurate and reproducible linear measurements require 2DE guidance, for both transducer placement and cursor alignment. For LV measurements, the M-mode scan line should transect the LV central axis perpendicularly near the tips of the open mitral leaflets (Sahn et al. 1978; O'Rourke et al. 1984). M-mode linear measurements are made vertically along the *y*-axis of the strip chart, i.e., at a specific instant in time (Figure 5.21). A simultaneous electrocardiogram facilitates timing of the cardiac cycle where the QRS complex signals the end of diastole. It is typical for the maximum LV internal dimension to occur during the QRS complex, and it is often possible to observe a slight presystolic distension induced by atrial contraction. End systole occurs near the end of the electrocardiographic T wave, but the timing of the systolic measurement is determined from the echocardiogram itself at the occurrence of the minimum LV internal dimension. Normally, the interventricular septum moves away from the transducer during systole while the LV wall moves toward it, but motion may be slightly dyssynchronous in normal animals. There may be a brief interval near end systole where the septum and LV wall both move toward the transducer. Consequently, the minimal internal dimension need not coincide with maximal wall excursions with respect to the transducer. Linear measurement can be accomplished alternatively from single frame images of the 2DE, and this is preferable whenever M-mode cursor alignment is not attainable (O'Grady et al. 1986; Schiller et al. 1989) (Figure 5.22).

Left atrial size embodies relevant diagnostic and prognostic information, but quantification is

Figure 5.19. TD recording of mitral annular velocity. Velocity sampling locations are depicted in the LAp four-chamber image **(A)** to record either septal or lateral mitral annulus velocity **(B)**. Diastolic annular velocity measurements recapitulate the mitral inflow pattern with two distinct phases of filling. The LV expands longitudinally in both early and late diastole, resulting in annular velocity away from the transducer and generation of the E′ and A′ waves, respectively. LV contraction entails a longitudinal component that is directed toward the transducer and generation of the systolic TD wave S′. In **(C)** the PWD recording of the transmitral inflow shows the two distinct phases of the diastolic flow (E and A) corresponding to the diastolic longitudinal mitral annular velocities (E′ and A′). **D–F:** Schematic representations of pulmonary venous flow velocity, longitudinal mitral annular velocity and mitral blood inflow velocity, respectively.

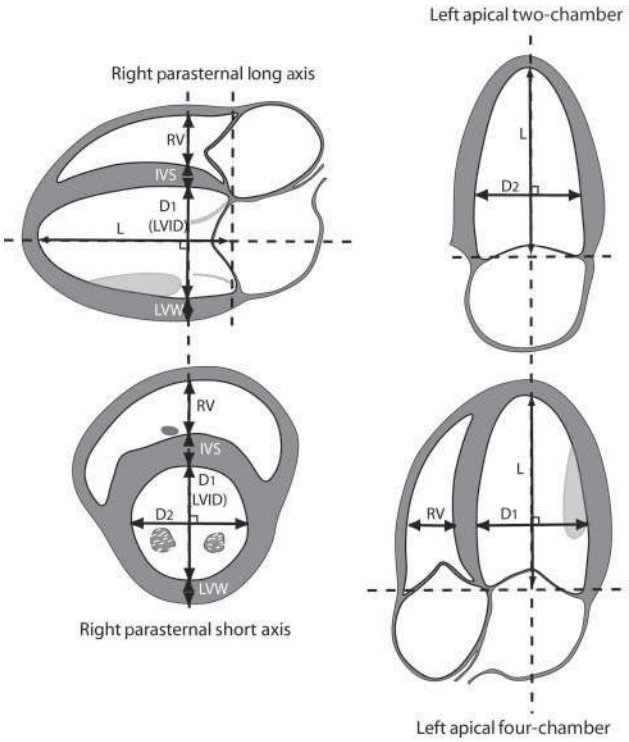


Figure 5.21. Linear ventricular measurements from 2DE. The D_1 short-axis dimension corresponds to the LV internal dimension (LVID) from M-mode, whereas D_2 must be determined from 2DE, from either the RPS SAx or LAp two-chamber image, as shown. LV length (L) is measured from the plane of the mitral annulus to the LV apex along the central LV axis. Source: Schiller et al. (1989).

problematic because of the irregular three-dimensional shape (Rishniw and Erb 2000; Hansson et al. 2002). The original measurement derived from M-mode recordings exemplifies this issue because it includes only a small portion of the structure – the atrial appendage – plus a variable thickness of adipose tissue that lies between the aorta and appendage. Body-size normalization of the M-mode measurement in dogs has been accomplished through division by the measured aortic dimension (Ao_m). Mean values of this ratio are near 1.0 across the entire body-size spectrum but with normal maximum values up to 1.4, depending on breed (see Appendix). The upper limit for the raw measurement in cats ranges from 1.2 to 1.7 cm, depending on the study (see Appendix). Linear 2DE LA measurements from SAx and LAx images afford advantages in sensitivity over M-mode determinations (Figure 5.23). Like their M-mode counterparts, maximal 2DE LA size determinations are made at end systole, just prior to the mitral valve opening. The ratio of 2DE SAx LA diameter to SAx Ao diameter should be less than 1.6 in normal dogs (Rishniw and Erb 2000) and cats (Abbott and MacLean 2006).

Measurements of aortic and pulmonary trunk diameter may be used to evaluate these outflow tracts for narrowing, stenosis, or dilation, and are also used for estimations of ventricular stroke volume and cardiac output in conjunction with Doppler velocity measurements (Figure 5.24).

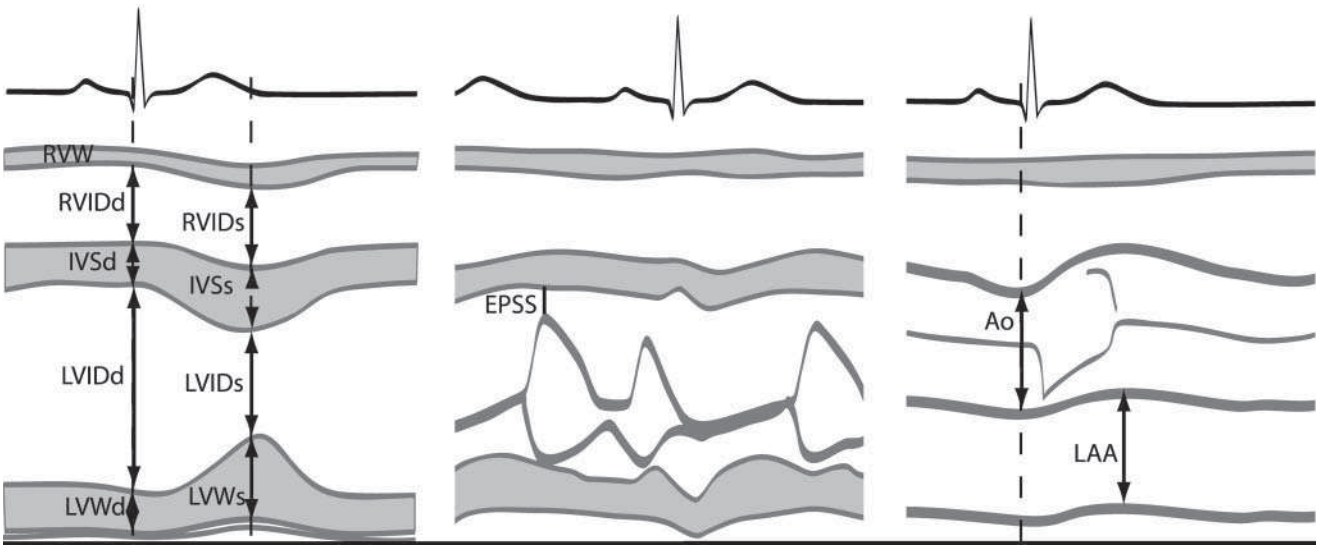


Figure 5.22. Linear ventricular measurements from M-mode echocardiography. 2DE guidance for transducer placement and M-mode scan-line selection is paramount for accurate and reproducible results. Subscripts "d" and "s" refer to diastolic and systolic determinations, respectively, where end diastole coincides with the greatest LV internal dimension (LVID), typically shortly after the onset of the QRS complex, and systole coincides with the smallest LVID. The Ao measurement is made at end diastole, coincident with maximal distance of the Ao from the transducer, and the LAA measurement is made at its maximal dimension in time, coinciding with end systole. Linear measurements are made vertically across the strip chart. EPSS, end point to septal separation distance; RVID, RV internal dimension.

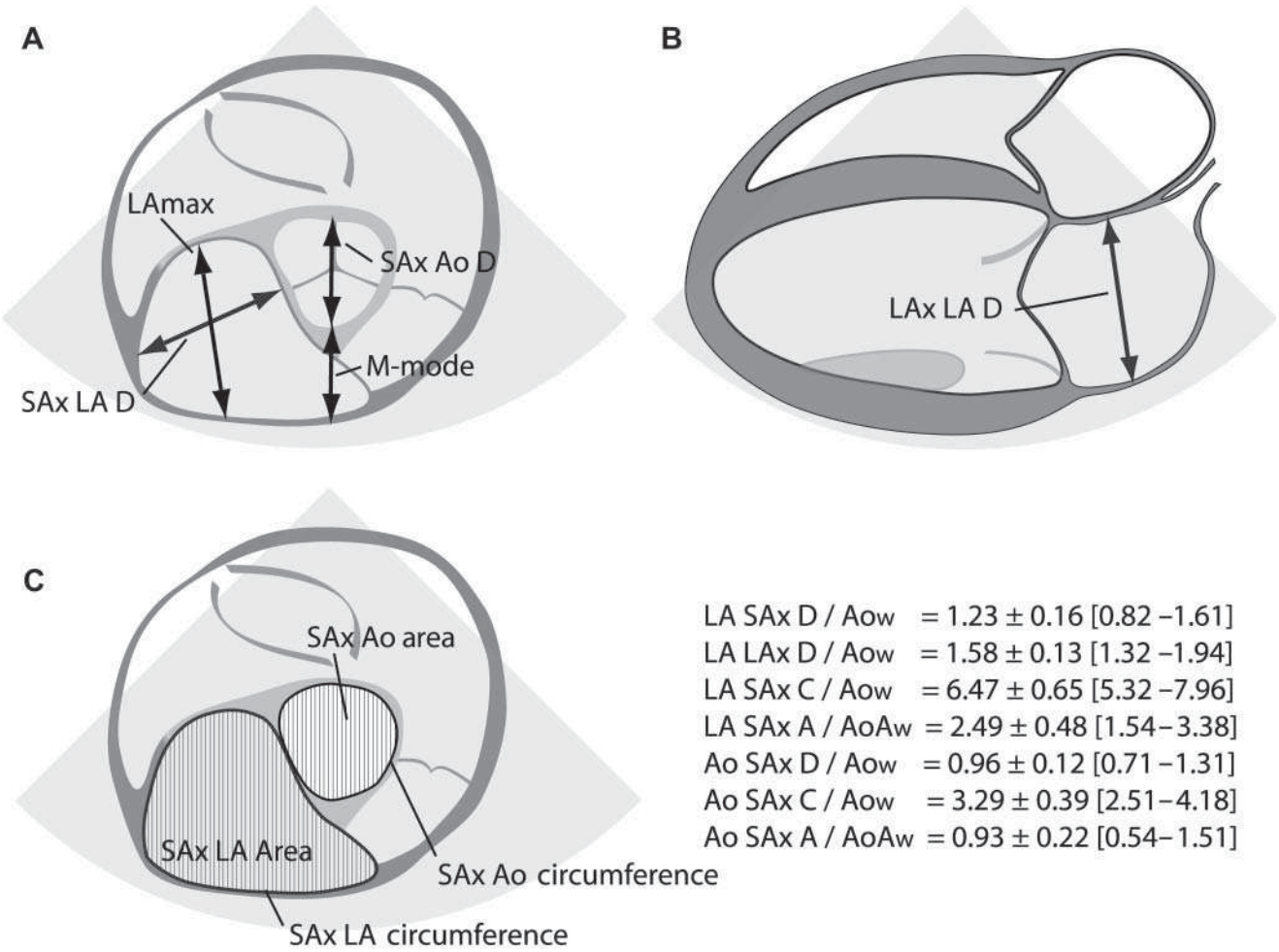


Figure 5.23. LA size determination. LA size determination is problematic because of the irregular three-dimensional shape. In dogs, the standard M-mode measurement includes only a small portion of the LA, i.e., the LAA **(A)**. Linear measurements made from the 2DE RPS SAx **(A)** and LAx **(B)** are more representative of atrial size but still suffer from angular dependence. The planimetered SAx LA area and circumference are less dependent on angle **(C)**. LA measurements studied by Rishniw and Erb may be conveniently expressed as a ratio index, dividing linear dimensions by the weight-based Ao diameter ($Ao_w = 0.795 \times BW^{1/3}$) and area measurements by the weight-based Ao area ($AoA_w = \pi Ao_w^2/4$). Each index exhibits minimal dependence on body size. Mean ± standard deviation and, in brackets, range for each index are shown. Original data supplied by Rishniw and Erb (2000). A, area; BW, body weight; C, circumference; D, diameter; max, maximum.

Cardiac Volume and Mass

Numerous mathematical formulas have been proposed for the estimation of ventricular volume, which pertains importantly to cardiovascular diagnosis and prognosis.

Ejection fraction is a ratio index calculated from ventricular volume as (EDV – ESV)/EDV, where EDV and ESV are the end-diastolic volume and the end-systolic volume, respectively (Schiller et al. 1989). Many cardiologists use the terms ejection fraction and systolic function synonymously. The one-dimensional analog of ejection fraction is the fractional shortening, FS = (LVIDd – LVIDs)/LVIDd, determined usually from M-mode short-axis measurements of diastolic (LVIDd) and systolic (LVIDs) LV internal dimension. LV stroke volume (SV) may be estimated from the difference between diastolic and systolic volumes. A body-size normalized ratio index, wΔA (Table 5.3), is the estimated LV SAx stroke area divided by the weight-based aortic area. Values derived from M-mode measurements range from 0.8 to 2.8 in dogs and may be somewhat breed- and body size-dependent (see Appendix). The M-mode index is simplistic but valuable for clinical quantification of LV volume overload

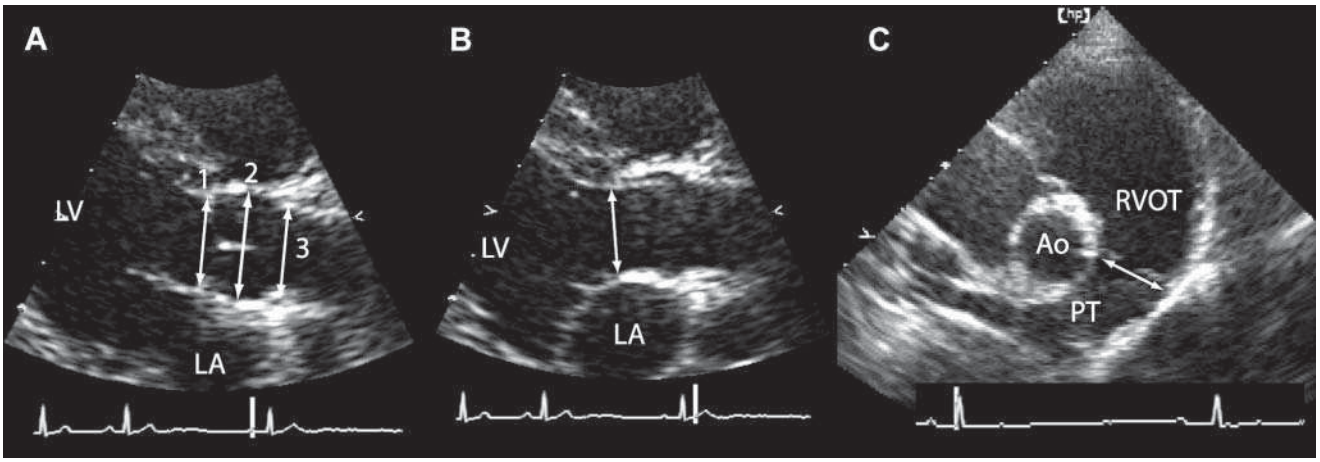


Figure 5.24. LVOT and RVOT diameters. RPS LAx **(A, B)** and SAx **(C)** images are shown. Measurements are made perpendicular to the vessel axes, and longitudinal vessel images show how dimensions vary in diameter with axial location. **A:** Position 1 depicts the Ao root diameter in diastole. **B:** The systolic dimension, where the measurement can be made between the right coronary cusp and Ao root wall to quantify the flow diameter. Position 2 in **A** corresponds to the dilation that occurs at the sinus of Valsalva, and position 3 is the sinotubular junction, a local minimum for the Ao diameter. **C:** The diameter of the PV orifice. Accurate determination of RVOT diameter is problematic because the ultrasound beam is nearly parallel to the reflecting surfaces.

Table 5.3
Weight-based echocardiographic ratio indices

Index	Calculation	Description
wAo	Ao_m/Ao_w	Indexed aortic root dimension
wIVSd	$IVSd/Ao_w$	Indexed interventricular septal thickness, diastole
wLVIDd	$LVIDd/Ao_w$	Indexed left ventricular internal dimension, diastole
wLVWd	$LVWd/Ao_w$	Indexed left ventricular wall thickness, diastole
wIVSs	$IVSs/Ao_w$	Indexed interventricular septal thickness, systole
wLVIDs	$LVIDs/Ao_w$	Indexed left ventricular internal dimension, systole
wLVWs	$LVWs/Ao_w$	Indexed left ventricular wall thickness, systole
wLA	LA/Ao_w	Indexed left atrial dimension
wLVODd	$(IVSd + LVIDd + LVWd)/Ao_w$	Index of left ventricular outer dimension, diastole
wWTd	$(IVSd + LVWd)/Ao_w$	Index of combined septal and left ventricular wall thickness, diastole
wLVODs	$(IVSs + LVIDs + LVWs)/Ao_w$	Index of left ventricular outer dimension, systole
wWTs	$(IVSs + LVWs)/Ao_w$	Index of combined septal and left ventricular wall thickness, systole
wΔA	$(LVIDd^2 - LVIDs^2)/Ao_w^2$	Index of change in left ventricular internal area, i.e., short-axis stroke area
wWAd	$(LVODd^2 - LVIDd^2)/Ao_w^2$	Index of left ventricular short-axis myocardial wall area, diastole, i.e., hypertrophy
wWAs	$(LVODs^2 - LVIDs^2)/Ao_w^2$	Index of left ventricular short-axis myocardial wall area, systole, i.e., hypertrophy

A ratio index normalizes raw echocardiographic measurements for body size. Ao_w is the weight-based aortic dimension calculated as $Ao_w = kBW^{1/3}$ where k is a species-dependent constant equal to 0.795 in dogs and 0.567 in cats.

or underload in the authors' experience. Relative echocardiographic ratio indices of the left ventricle and interventricular septum are defined in Table 5.4.

Left ventricular mass may be estimated by calculating the external volume of the left ventricle and subtracting the internal volume (Schiller et al. 1989) (Figure 5.25). Myocardial mass is normally proportional to body weight and thus requires normalization. Ratio indices wWAd and wWAs correspond to normalized LV short-axis wall area in diastole and systole, respectively, where myocardial wall area is divided by the weight-based aortic area (Table 5.3). Normal

Table 5.4
Relative echocardiographic ratio indices

Index	Calculation	Description
FS	(LVIDd – LVIDs)/LVIDd	Fractional shortening. Relative left ventricular internal wall motion or LV short axis deformation.
FWTd	(IVSd + LVWd)/LVODd	Fractional left ventricular myocardial wall thickness, diastole. Relative left ventricular wall thickness in diastole.
FWTs	(IVSs + LVWs)/LVODs	Fractional left ventricular myocardial wall thickness, systole. Relative left ventricular wall thickness in systole.
FΔA	$(LVIDd^2 - LVIDs^2)/LVIDd^2$	Fractional change in left ventricular internal area. Relative left ventricular internal wall motion or left ventricular short-axis deformation.
FWAd	$(LVODd^2 - LVIDd^2)/(LVODd^2)$	Fractional left ventricular myocardial wall area (short axis), diastole. Relative left ventricular wall area in diastole.
FWAs	$(LVODs^2 - LVIDs^2)/(LVODs^2)$	Fractional left ventricular myocardial wall area (short axis). Relative left ventricular wall area in systole.
IVSFT	(IVSs – IVSd)/IVSd	Intraventricular septum fractional thickening. Relative thickening of interventricular septum.
LVWFT	(LVWs – LVWd)/LVWd	Left ventricular wall fractional thickening. Relative thickening of left ventricular wall.
RWTd	2 LVWd/LVIDd	Relative left ventricular wall thickness, diastole. Relative left ventricular wall thickness to chamber dimension, diastole.
RWTs	2 LVWs/LVIDs	Relative left ventricular wall thickness, systole. Relative left ventricular wall thickness to chamber dimension, systole.

Fractional shortening is a better-known ratio index derived by dividing the change in left ventricular internal dimension by the diastolic value; it is common practice to multiply the result by 100 and express the value as a percentage (%ΔD). Relative ratio indices are normalized for some aspect of heart size, not for the size of the individual.

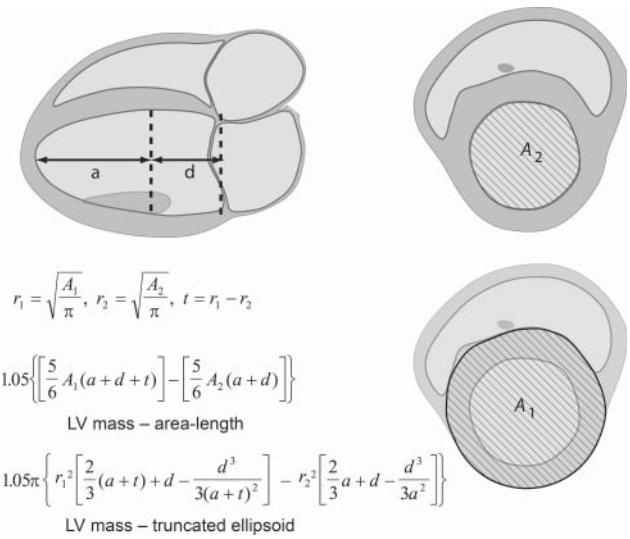


Figure 5.25. LV mass estimation by 2DE methods. Short-axis external (A_1) and internal (A_2) areas are determined by planimetry at the level of the mitral CT and used to determine geometric mean radii, both outer (r_1) and inner (r_2); constant wall thickness (t) is assumed. The major axis of the ellipsoid (a) is measured along the LV axis from the apex to the point of maximal radius, as shown; the distance (d) comprises the remainder of the LV length from the apex to the mitral annulus. The constant ($1.05\,g/cm^3$) is the density of normal soft tissue. LV mass values obtained by either equation require normalization for body size. Source: Schiller et al. (1989).

values of wWAd in dogs range roughly from 1.8 to 5.5 but with significant breed dependency; upper values in Italian Greyhounds, Whippets, and Greyhounds range from 5.0 to 6.0 (see Appendix). These are clinical indices derived from M-mode or planar 2DE measurements that do not estimate true myocardial mass. However, they may be superior indicators of hypertrophy compared with simple measurements of wall thickness, which can depend strongly on hemodynamic conditions. Three-dimensional echocardiography entails fewer geometric assumptions and affords superior estimates of ventricular volume and

myocardial mass; the method does not circumvent the body-size normalization issue.

Doppler Measurements and Systolic Function

Much of the quantitative value of Doppler studies stems from the application of fluid dynamic principles to the interpretation of measured velocities through the modified Bernoulli equation (Hatle and Angelsen 1985). The modified Bernoulli equation is expressed as $\Delta P = 4V^2$ for many clinical applications, where velocity (V) is in meters per second (m/s) and the calculated pressure is in millimeters of mercury (mmHg). Optimized velocity recordings are accomplished at the time of the recording by diligent positioning of the transducer at the appropriate body wall location, aided by cues from the CFD image and both visual and auditory feedback from the spectral Doppler display (Darke et al. 1993). Transducer position varies with the specific lesion to be evaluated, e.g., aortic stenosis versus mitral regurgitation (MR), as well as nuances specific to the individual.

Besides pressure gradients, valuable functional information is derived from spectral Doppler signals that enable the timing of cardiac cycle events and estimation of blood flow rate (Figure 5.26). Systolic time intervals have been employed for many years to evaluate cardiac function, predating the ultrasonic era, but Doppler signals are ideal for obtaining the required measurements. Systolic time intervals are determined from time measurements of the cardiac cycle and consequently are indices of global function; determinations are most commonly used to evaluate LV function. A ratio index of pre-ejection period (PEP) to LV ejection time (PEP/LVET) is often used to help normalize raw time measurements for body size and heart rate. An additional index, the velocity of circumferential shortening, is equivalent to the fractional shortening divided by LV ejection time (FS/LVET) and so relates to the rate of cardiac deformation. Additional determinations made from either aortic or pulmonary flow-velocity signals include the acceleration time (AT) and the velocity time integral (VTI). AT is related to both myocardial function and afterload (Figure 5.26).

The aortic or pulmonary VTI is the planimetered area under the flow-velocity envelope. It has physical units of length (e.g., cm), corresponding to the integration of velocity with respect to time, and also has been termed the **stroke length** (Figure 5.32). Multiplication

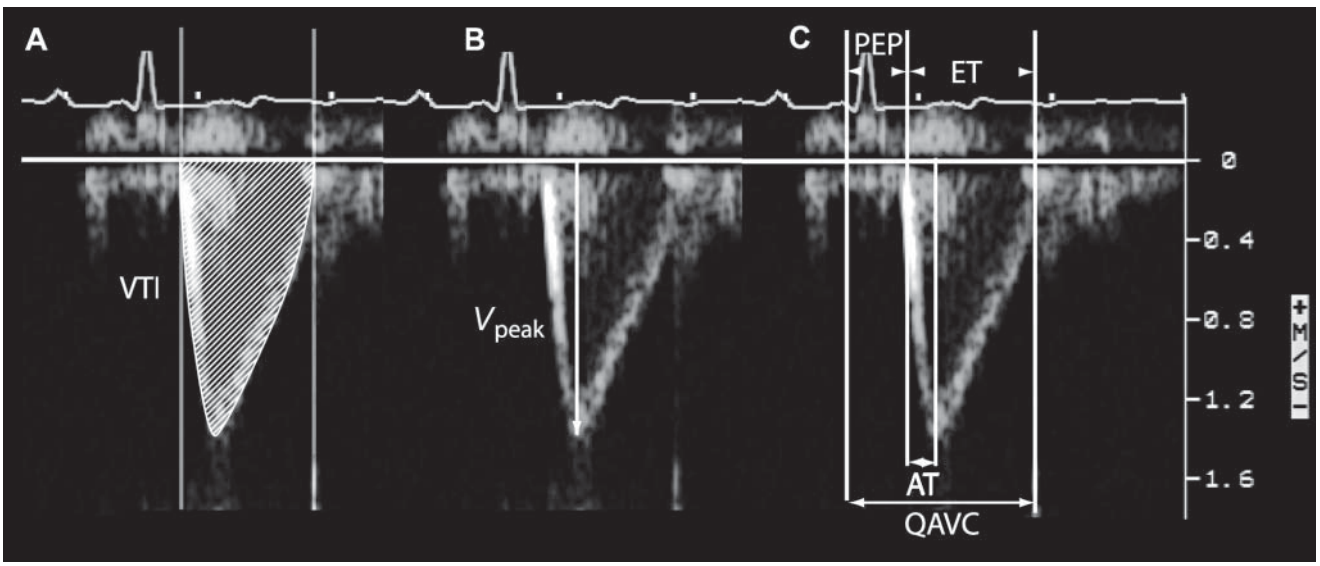


Figure 5.26. **Measurements from Ao spectral Doppler signals A:** Planimetry of the area under the flow-velocity envelope yields the velocity–time integral (VTI), which has units of length (e.g., cm). **B:** Measurement of the temporal peak velocity (V_{peak}). **C:** Determination of timing intervals. The pre-ejection period (PEP) is from the onset of the electrocardiographic QRS complex to the onset of ejection. Measurement of the ejection time (ET) is facilitated by inclusion of the Ao valve in the velocity sampling volume so that valve motion artifacts delineate the interval. Total electrical-mechanical systole is from the onset of the QRS to Ao valve closure (QAVC) and is the sum of PEP and ET. The acceleration time (AT) is the interval from the beginning of the ejection to the peak flow velocity. Average flow velocity (e.g., cm/s) can be determined by dividing the VTI by ET. The terminology also applies to RV outflow signals.

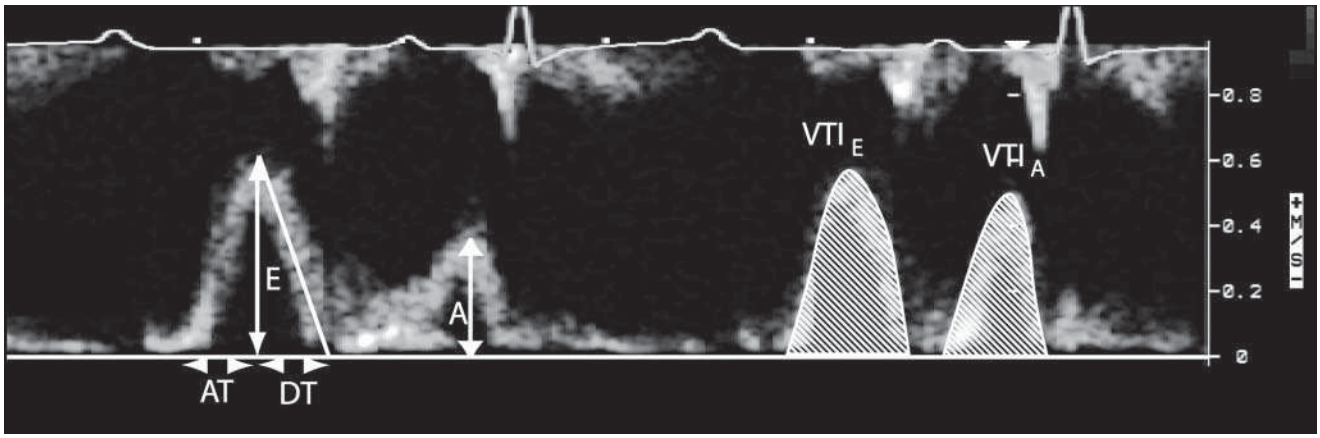


Figure 5.27. Measurements from mitral inflow signals. Measurements include peak velocities for the E and A waves and the velocity–time integrals (VTIs) of each. The E:A peak velocity ratio, normally less than 1.0, or VTI_E/VTI_A may be used to quantify relative contributions of each to ventricular filling. Peak velocities are related to the peak atrial-ventricular pressure gradient through the Bernoulli equation and so may suggest valvular stenosis or increased LA pressure. The acceleration time (AT) is the interval from opening of the MV to peak velocity. The deceleration time (DT) is determined by extrapolating from peak E-wave velocity to baseline along the flow-velocity envelope, as shown; it is common for the A wave to intervene without the velocity envelope reaching zero. The slope of the deceleration may also be recorded.

of the VTI by the effective orifice area (A_E) gives the volume of blood passing through the orifice during the ejection, i.e., the forward stroke volume (SV = VTI × A_E). Multiplication of the stroke volume by heart rate gives the cardiac output. The effective orifice area (A_E) may be estimated from 2DE images as just described for aortic and pulmonary outflow tracts by using the measured diameter (D) to compute the area of a corresponding circle ($A = \pi D^2/4$) (Figure 5.24).

Doppler Measurements and Diastolic Function

Measurements from mitral and tricuspid inflow-velocity signals include the velocity magnitude of the E and A waves and the planimetered area (VTI) for each (Figure 5.27). Factors affecting the form of inflow velocities are complex and pertain to diastolic ventricular function and ventricular filling pressures (Figure 5.28). The ratio between peak velocity of early mitral inflow (E) and peak early TDI annular velocity (E′) (E:E′) has received considerable attention as a predictor of LV filling pressure in the human literature; however, this ratio has been less robust in predicting CHF in dogs (Schober et al. 2010). In dogs with left-sided congestive heart failure (LCHF) due to chronic valvular disease or dilated cardiomyopathy measurement of the isovolumic relaxation time (IVRT), the ratio of mitral E wave to IVRT (E:IVRT), or a composite measure of diastolic functional class based on mitral inflow and TDI parameters are better predictors of CHF (Figure 5.29). The E:IVRT has also been identified as the best Doppler predictor of reduced filling pressures in response to treatment of dogs with both pacing-induced and naturally occurring CHF (Schober et al. 2008, 2011).

Transesophageal and Three-dimensional Echocardiography

Transesophageal echocardiography (TEE) is a complementary echocardiographic approach used to image the heart from within the thoracic esophagus of anesthetized patients (Loyer and Thomas 1995). TEE may provide superior images of structures at the heart base and allows for enhanced visualization of valvular lesions and more precise characterization of congenital cardiac defects. TEE is particularly well suited to intraoperative monitoring of cardiac structure and function, and the utility of TEE in guiding transcatheter closure of patent ductus arteriosus has been described in dogs (Pariaut et al. 2004; Saunders et al. 2010). A newer echocardiographic modality, three-dimensional echocardiography, is used extensively for preoperative planning of cardiac surgery in people and may also have utility in more completely characterizing valvular and congenital defects and assessing the feasibility of surgical correction in dogs (Jung et al. 2012).

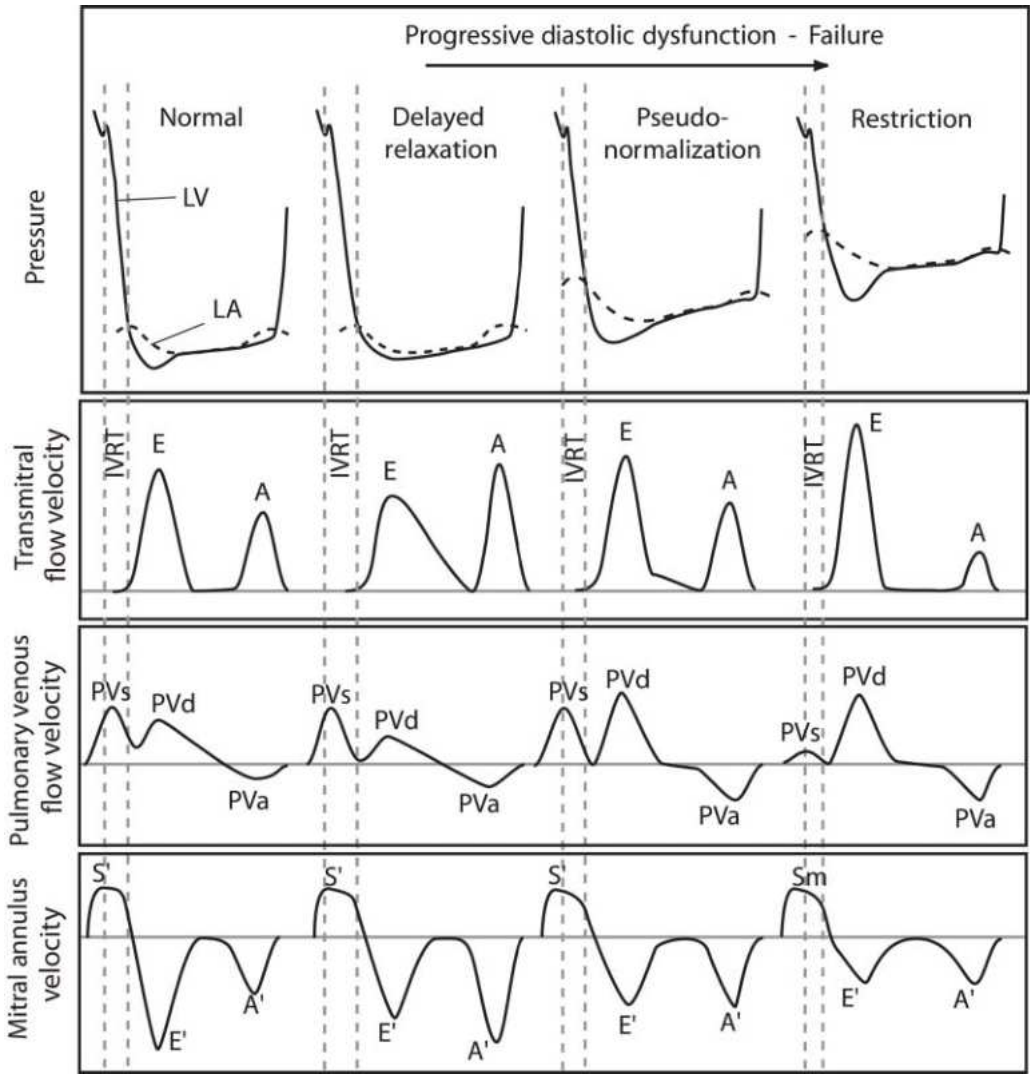


Figure 5.28. **Diastolic dysfunction.** A schematic overview of diastology can be encapsulated in terms of left ventricular (LV) and left atrial (LA) pressures (top tier), mitral blood inflow velocity patterns, pulmonary venous flow velocity, and longitudinal mitral annular velocity. In the early stages of diastolic dysfunction, delayed relaxation of the LV increases the isovolumic relaxation time (IVRT) and there are decreases in both the early diastolic transmitral pressure gradient and the size of the Doppler E wave relative to A, and E wave deceleration time may be increased. Diastolic pulmonary venous flow (PVd) may be somewhat diminished relative to systolic (PVs) and the early relaxation phase of mitral velocity (E′) is diminished relative to motion associated with atrial systole (A′). With the onset of congestion, IVRT, mitral inflow and pulmonary venous flow patterns are returned towards normal (pseudo-normalization) in association with the compensatory increase in LA and venous pressure which act to restore the early filling phase. This condition is difficult to differentiate from normal by mitral flow pattern alone but is distinguished by further decreases in E′, equalization of E′ and A′, an increase in PVd relative to PVs, and prolongation of atrial reversal flow (PVa), potentially with increased velocity as well. End-stage restrictive physiology characteristically includes an increased transmitral pressure gradient early in diastole, associated with an increased Doppler E wave magnitude, but inflow is terminated abruptly as the incompliant ventricle reaches its elastic limit and atrial-ventricular pressure equalization occurs. A shortened E wave deceleration time is characteristic, along with a further increase in duration of PVa. The incompliant ventricle can accept little additional volume with atrial systole and the A wave is small or diminutive. Further decreases in mitral annular velocity coincide with the impaired relaxation. Features of the classic description may depend dramatically on hemodynamic circumstances, e.g., preload and heart rate.

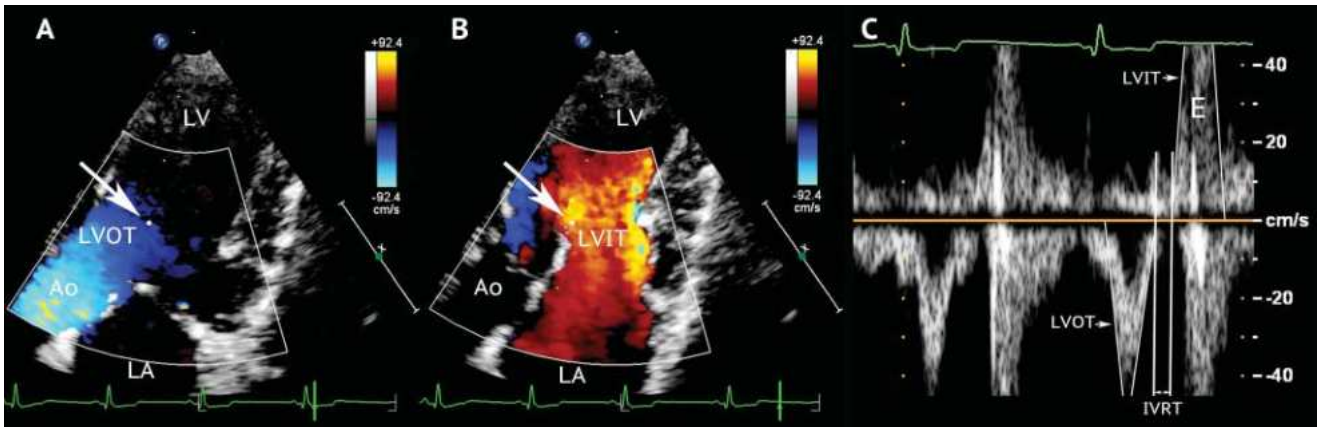


Figure 5.29. PWD recording of isovolumic relaxation time of the LV. From the LAp five-chamber view, a 5–10 mm sample volume is positioned into the LV in an intermediate position between the LV outflow tract (LVOT) (**A**) and the LV inflow tract (LVIT) (**B**) as indicated by the arrows in **A** and **B**. **C**: The isovolumic relaxation time (IVRT) of the LV is measured as the time interval between the end of the aortic systolic ejection flow wave recorded from the LVOT to the onset of the early diastolic mitral flow wave recorded from the LVIT (E). Note the filled spectral display of the early mitral inflow (E), indicating spectral broadening due to the selected large sample volume (axial dimension of 10 mm not shown).

Congenital Heart Disease

Valvular Diseases

Aortic Stenosis

Aortic stenosis (AS) signifies an obstruction to LV outflow. It may be valvular, subvalvular (subaortic stenosis, SAS), or supravalvular. SAS is the most common congenital defect of large-breed dogs. Moderate to severe SAS causes characteristic, but variable, 2DE abnormalities, including discrete or diffuse narrowing of the LV outflow tract, post-stenotic aortic dilation, and thickening of the aortic and anterior mitral valve leaflets (Figure 5.30). On the RPS LAx image, a subvalvular obstruction may appear as an echogenic ridge on the septum, mitral apparatus, or both, corresponding to a complete or incomplete hyperechoic ring of fibrocartilaginous tissue encircling the outflow tract (Bonagura and Herring 1985b). AS causes LV pressure overload and concentric hypertrophy of the left ventricle as quantified by septal and LV wall thickness and other indices of absolute or relative hypertrophy. The extent of hypertrophy is variably correlated with the severity of obstruction. Severe obstruction also may be accompanied by increased echogenicity of the papillary muscles and/or sub-endocardial myocardium, possibly secondary to ischemia of these regions and subsequent fibrosis or calcification. In severely affected cases, M-mode echocardiography of the aortic root may demonstrate premature systolic closure of the aortic valve.

Color flow Doppler of the LV outflow tract in systole reveals a region of flow acceleration proximal to the obstructive lesion, and turbulent or disturbed flow with increased velocity distally (Moise 1989) (Figure 5.31). Arbitrary prognostic categories based on the pressure gradient are mild (<50 mmHg), moderate (50–75 mmHg), severe (75–100 mmHg), and very severe (>100 mmHg). The aortic flow-velocity envelope also becomes more rounded, and its acceleration time increases, i.e., there is delayed peak velocity with increasing severity (Figure 5.32). The pressure gradient and peak velocity are flow-dependent indices of severity.

In the absence of shunts, concurrent pulmonic stenosis or significant semilunar valve insufficiency, the aortic to pulmonary VTI ratio (VTI_A/VTI_P) approximates the ratio of effective orifice areas (EOA) of the two tracts (EOA_p/EOA_A) and is corrected for body size and flow rate. In the authors' experience, VTI_A/VTI_P is <1.6 in normal dogs (PWD at the valve level). This ratio is theoretically less flow-dependent than pressure gradient or flow velocity alone and may be helpful for differentiating normal from mild SAS (Figure 5.32) (Brown et al. 1991). Bicuspid aortic valve is a common congenital defect in human patients but a rare cause of stenosis in dogs and cats (Figure 5.33).

Pulmonic Stenosis

Pulmonic stenosis (PS) is the third most common congenital cardiac defect in dogs but is uncommon

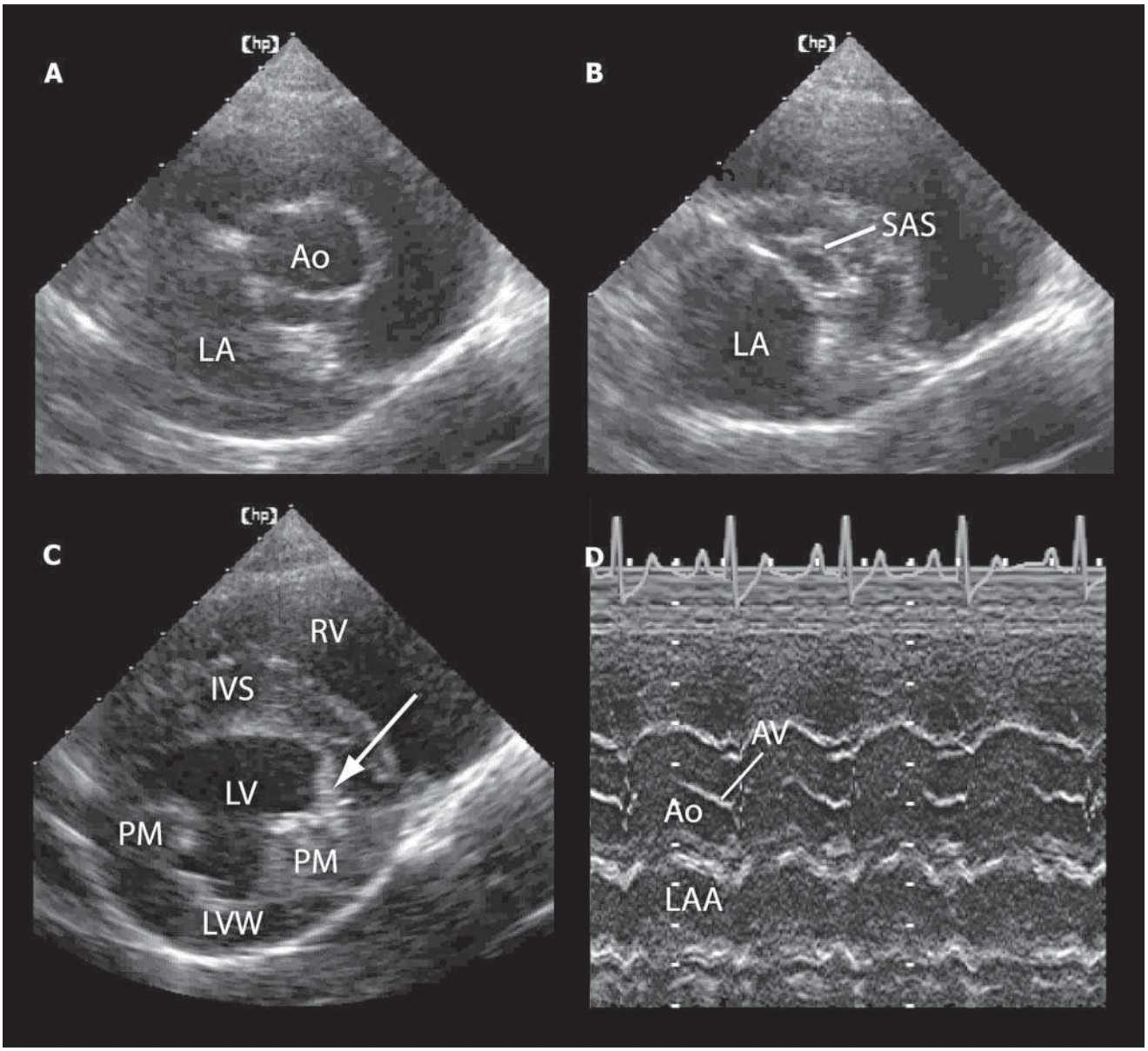


Figure 5.30. RPS SAx images from a dog with subaortic stenosis (SAS). The maximum Ao dimension normally occurs at the level of the Ao sinus of Valsalva **(A)**; valve leaflets are evident. The obstruction in SAS is most typically at the immediate subvalvular location, and the short-axis view may suggest the anatomical severity in terms of cross-sectional area relative to the Ao root **(B)**. **C:** Thickened LVW and IVS, caused by concentric hypertrophy, are evident. There is an increase in subendocardial echogenicity (arrow), which is thought to represent fibrosis, secondary to ischemia. **D:** M-mode through the Ao root depicts Ao valve leaflets (AV) that separate partially in early systole, only to quickly return to the closed position. The leaflets may inscribe a diamond or double diamond within the confines of the Ao root.

in cats. PS signifies an obstruction to RV outflow and may occur at subvalvular, supravalvular, or valvular locations, the latter being the most common site in dogs. Potential echocardiographic features in common with all forms of PS include RA enlargement, post-stenotic dilation of the pulmonary trunk, and concentric hypertrophy of the right ventricle with increased thickness of the septum and RV wall. The RV papillary muscles may become prominent, as do trabeculae carnae, imparting an uneven appearance to the RV endocardial surface and contributing to obstruction. Increased echogenicity of the RV

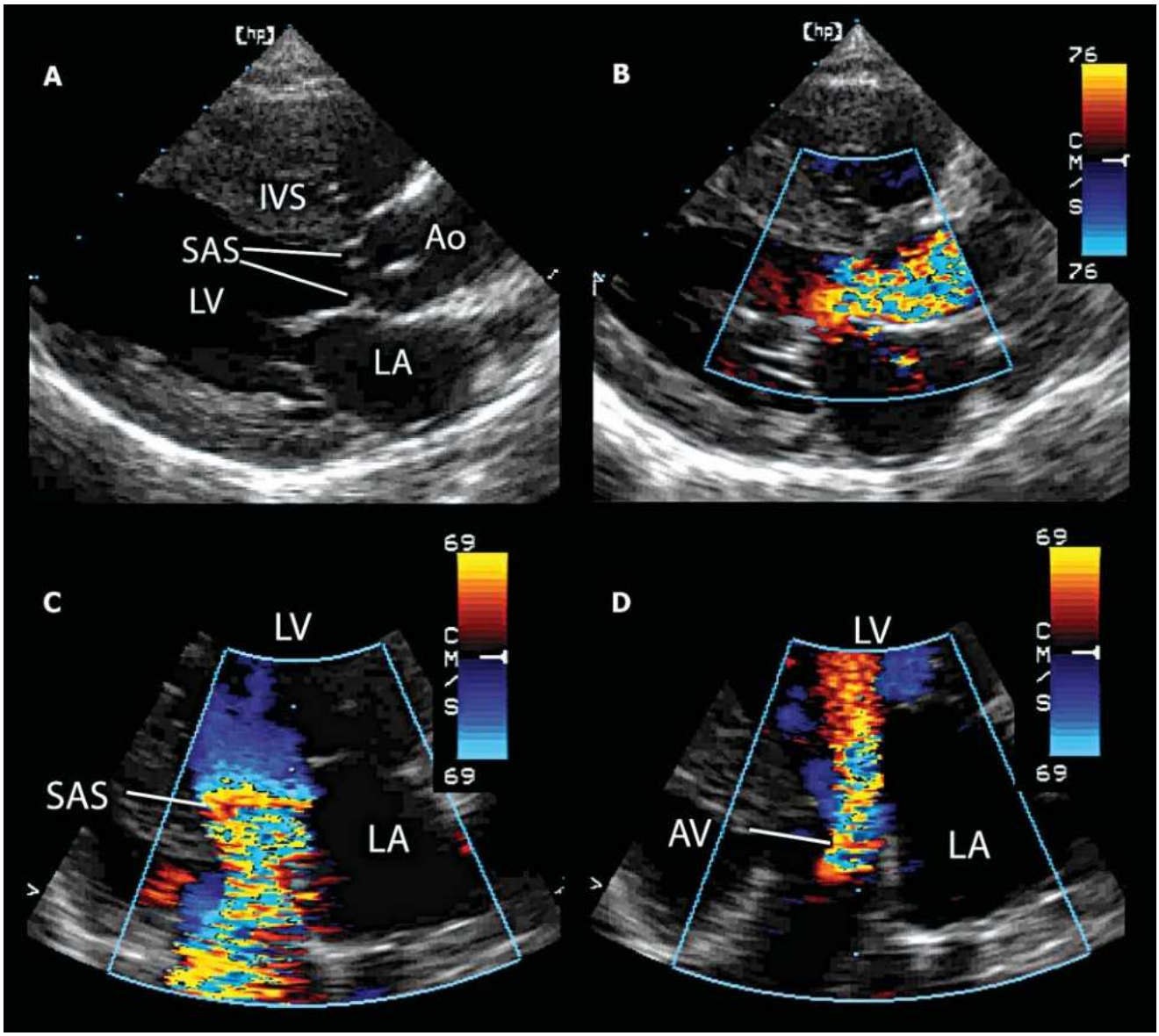


Figure 5.31. **CFD images from a dog with subaortic stenosis (SAS). A:** This RPS LAx 2DE image depicts the location of the obstruction immediately proximal to the AV and is confirmed by CFD in **B**. Although the example shown includes both septal and mitral aspects of the encircling obstruction, neither may be clearly evident, depending on the extent and location of the collar. **C, D:** CFD images obtained from the LAp five-chamber position. During systole **(C)**, the color halo of a *flow convergence zone* appears where flow acceleration and color aliasing occur proximal to the obstruction. A turbulent mosaic pattern is apparent distally in the Ao. **D:** Ao insufficiency present in the same patient during diastole. Here the flow convergence zone is in the Ao as blood accelerates toward the transducer at the location of the AV. CFD clearly demonstrates that the location of the obstruction is proximal to the valve in this instance. Mild to moderate Ao insufficiency commonly accompanies SAS.

myocardium may be associated with severe obstruction and presumed ischemic myocardial damage. Severe RV pressure overload causes flattening of the interventricular septum and an ovoid LV cross-section in the short-axis plane. LV volume underload in this circumstance may suggest concentric LV hypertrophy erroneously (pseudohypertrophy) with increased LV wall thickness and decreased LV and LA internal dimensions (Figure 5.34).

In valvular PS, leaflets may be thickened and/or fused at the commissures such that leaflet separation is impaired; the fused leaflets may form a valvular

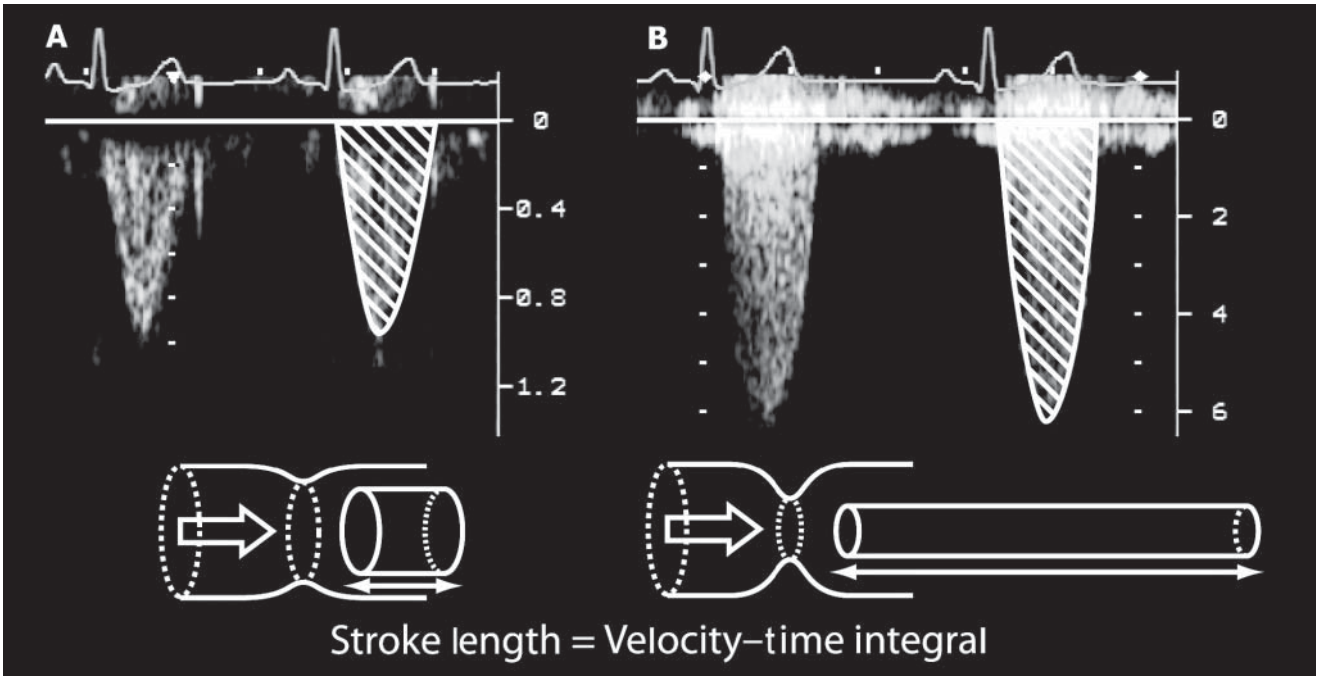


Figure 5.32. Spectral Doppler recordings in subaortic stenosis. Recordings from the pulmonary (**A**, RPS position) and Ao (**B**, subcostal position) outflow tracts of a dog. A temporal peak velocity of 6 m/s for the stenosis corresponds to a maximum pressure gradient of $4 \times 6^2 = 144$ mmHg and a very severe stenosis. The area under each phasic velocity curve, indicated by hatching, is termed the *velocity–time integral* (VTI) and has physical units of length (e.g., cm). This quantity has also been termed the *stroke length*, corresponding to the length of a figure whose volume equals the cardiac stroke volume, and whose cross-sectional area is the effective orifice area the ventricle ejects through. If the stroke volumes of the two ventricles are the same, then the ratio of VTIs approximates the ratio of effective orifice areas and is an index of stenosis severity that is relatively flow-independent.

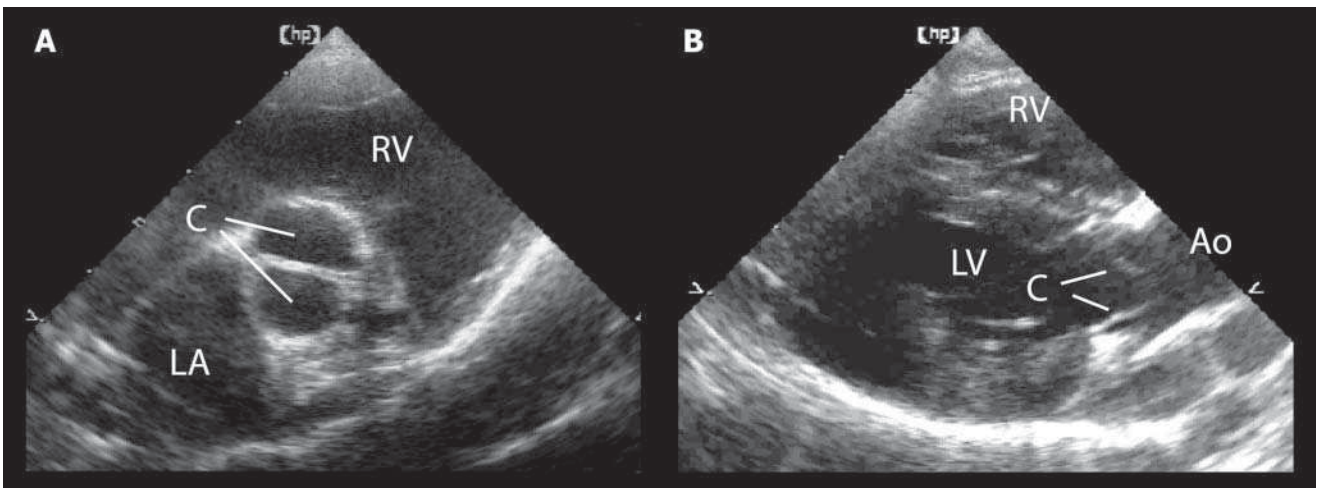


Figure 5.33. Valvular Ao stenosis. 2DE RPS SAx **(A)** and LAx **(B)** images from a dog with a bicuspid Ao valve. **A:** Only two cusps (C) are evident where there are normally three. **B:** A maximal opening excursion of the leaflets. Significant stenosis accompanied this unusual abnormality, as evidenced by the Doppler recordings (not shown).

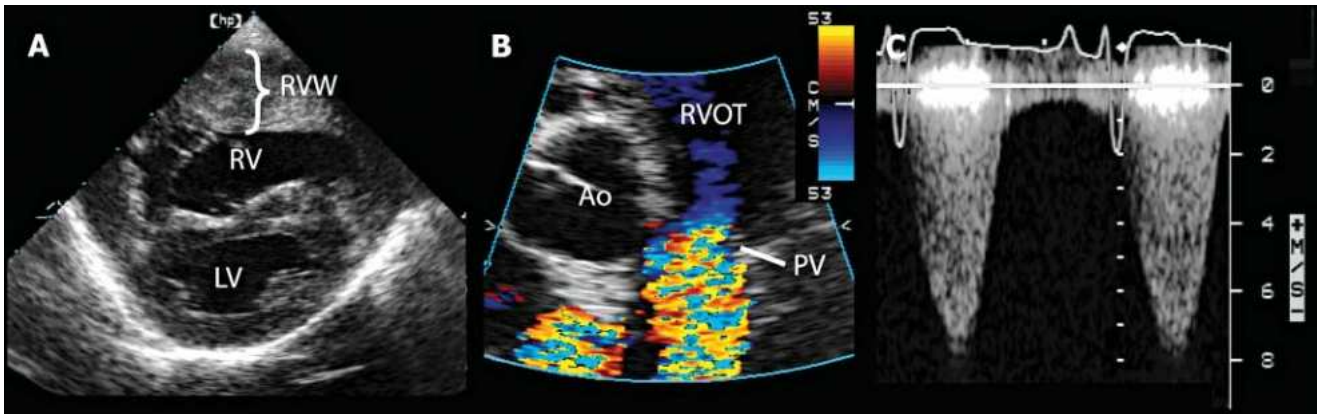


Figure 5.34. Valvular pulmonic stenosis in a dog. RPS SAx 2DE image **(A)**, RPS CFD at the PV **(B)**, and CWD of the pulmonic flow jet **(C)** from a dog with severe valvular pulmonic stenosis. The RVW is extremely thickened at more than twice that LVW thickness. The increased echogenicity of the myocardium is thought to be caused by ischemia and fibrosis. The septum is displaced toward the LV, thus causing an ovoid LV cross-section because of the flattened septum. CFD confirms the location of the obstruction at the valve. A velocity of nearly 8.0 m/s corresponds to a peak pressure gradient of $4 \times 8^2 = 250$ mmHg and severe obstruction.

dome as they bulge into the pulmonary artery during systole. The outflow tract itself may be hypoplastic and echogenic in conjunction with valvular lesions. Some dogs with pulmonic stenosis, particularly brachiocephalic breeds such as Bulldogs and Boxers, may have an anomalous pre-pulmonic (cranial) coronary artery originating from a single left or right coronary ostium, encircling the pulmonary trunk and contributing to the obstruction (Buchanan 2001; Visser et al. 2013). The coronary anatomy must be closely scrutinized in any dog anticipated to undergo balloon valvuloplasty (Fonfara et al. 2010), as an aggressive dilation procedure in a dog with aberrant coronary anatomy may result in avulsion of the coronary and immediate death of the dog (Figure 5.35). Optimal visualization of the coronary arteries may be difficult to achieve echocardiographically in some dogs, particularly English Bulldogs. Aortic root angiography or selective coronary angiography should then be considered in such patients prior to balloon valvuloplasty. An unusual form of subvalvular PS is caused by a discrete fibromuscular partition separating the RV outflow tract from the RV; this condition has also been termed **double-chamber right ventricle** (Figure 5.36). Supravalvular obstructions also may be visualized.

Combined Doppler examination of the RV outflow tract enables peak gradient quantification (CWD) and confirms the location of the obstruction, indicated by the velocity step up (PWD) or flow convergence zone (CFD) just proximal to the lesion. Suggested prognostic categories based on the pressure gradient are mild (<50 mHg), moderate (50–100 mm Hg), and severe (>100 mmHg). Specificity and sensitivity of these categories for specific outcomes have not been determined; however, dogs with severe PS are likely to benefit from balloon valvuloplasty. Mild to

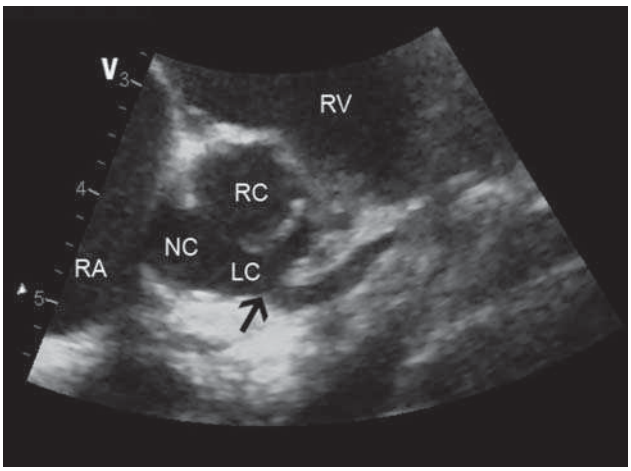


Figure 5.35. Single left coronary ostium in a Boxer puppy with pulmonic stenosis. RPS Sax 2DE image at the level of the heart base in a dog with valvular pulmonic stenosis. At the level of the aortic valve, three distinct aortic valve leaflets and a single left coronary ostium can be seen (black arrow). The single left coronary ostium gives off an anomalous pre-pulmonic right coronary artery that is seen encircling the pulmonic trunk. Screening for coronary abnormalities in dogs with pulmonic stenosis is essential prior to intervention to avoid the risk of coronary avulsion during valvuloplasty. NC, non-coronary cusp; RC, right coronary cups; LC, left coronary cusp.

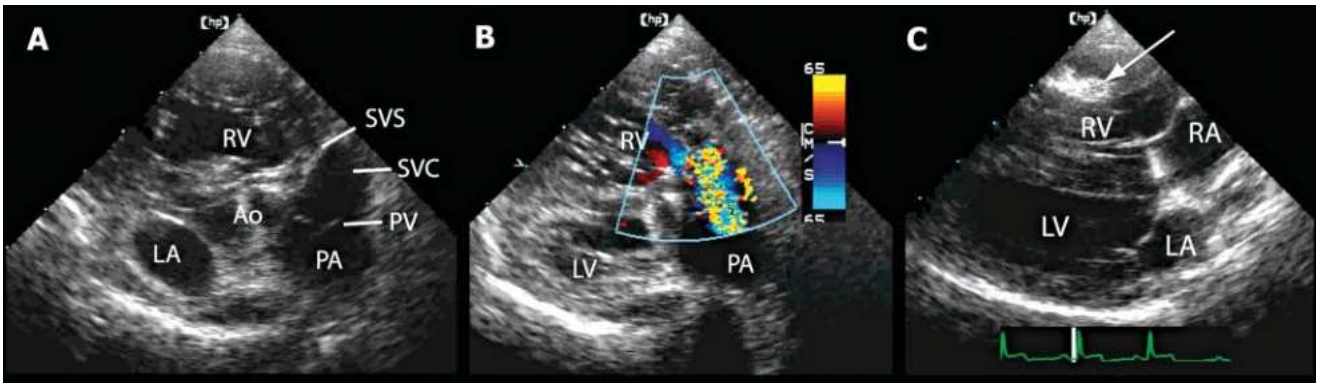


Figure 5.36. Subvalvular pulmonic stenosis in a dog. RPS SAx 2DE **(A)** and CFD **(B)** from the pulmonary outflow tract of a dog with *double-chamber RV*, a variant of subvalvular pulmonic stenosis. The PV is of normal thickness, but a discrete subvalvular stenosis (SVS) divides the RV proper from a subvalvular chamber (SVC). CFD confirms the location of the obstruction, proximal to the valve. **C:** This RPS LAx image illustrates marked thickening of the RVW and an area of increased echogenicity secondary to myocardial hypertrophy and fibrosis (arrow).

moderate tricuspid regurgitation and patent foramen ovale (PFO) with right-to-left shunt (Fujii et al. 2012) commonly coexist with significant pressure overload of the right heart. Significant tricuspid regurgitation as well as a pressure gradient through the PS of more than 60 mmHg may be associated with a worse outcome in dogs with PS (Francis et al. 2011). CWD evaluation of the tricuspid regurgitation jet velocity sometimes provides supplemental quantitative information, particularly when alignment with the PS jet is problematic.

Tricuspid Dysplasia

Dysplasia of the tricuspid valve may entail a wide range of structural abnormalities. The condition is transmitted genetically in Labrador Retrievers, the most frequently affected canine breed. Echocardiographic findings may include abnormal numbers or arrangement of papillary muscles; chordae tendinae may be foreshortened or papillary muscles may attach directly to a valve leaflet. Tricuspid leaflets may be elongated (Figure 5.37) or shortened and abnormally tethered to the septum or RV wall, thereby restricting motion and function; leaflet fusion may cause stenosis (Figure 5.38). The entire tricuspid apparatus may be displaced toward the cardiac apex, similar to Ebstein's malformation in human patients. Tricuspid dysplasia may cause valvular regurgitation and variable degrees of RV volume overload with dilation of the right ventricle and right atrium. Doppler examination reveals tricuspid regurgitation; the origin of this jet, determined from the flow convergence zone, may be displaced toward the RV apex.

Increased tricuspid regurgitation jet velocity (e.g., >3.0 m/s) should prompt consideration of concurrent pulmonary hypertension or PS, and atrial septal defect may also accompany the condition (Figure 5.37). Tricuspid stenosis may also be caused by dysplasia of this valve leading to a diastolic jet (e.g., > 2.0 m/s) into the right ventricle.

Mitral Dysplasia

Mitral valve dysplasia (MD) may entail a wide range of structural and functional abnormalities, including abnormal numbers or origins of papillary muscles; excessively shortened, lengthened, or thickened chordae tendinae; and abnormal chordal attachments to nonvalvular structures (Figures 5.39, 5.40).

Clinically relevant forms of MD cause hemodynamically significant MR (most commonly), mitral stenosis, or aortic outflow obstruction. The authors have encountered several cases of MD causing SAS directly where the anterior mitral leaflet was tethered to the septum. Subsequent rupture of the abnormal chordae caused spontaneous resolution of the stenosis.

Patent Ductus Arteriosus

Left-to-right patent ductus arteriosus (PDA) is the first or second most common congenital heart defect in dogs. Echocardiographic features of the condition include LV and LA dilation, LV hypertrophy, and increased stroke volume (volume overload)

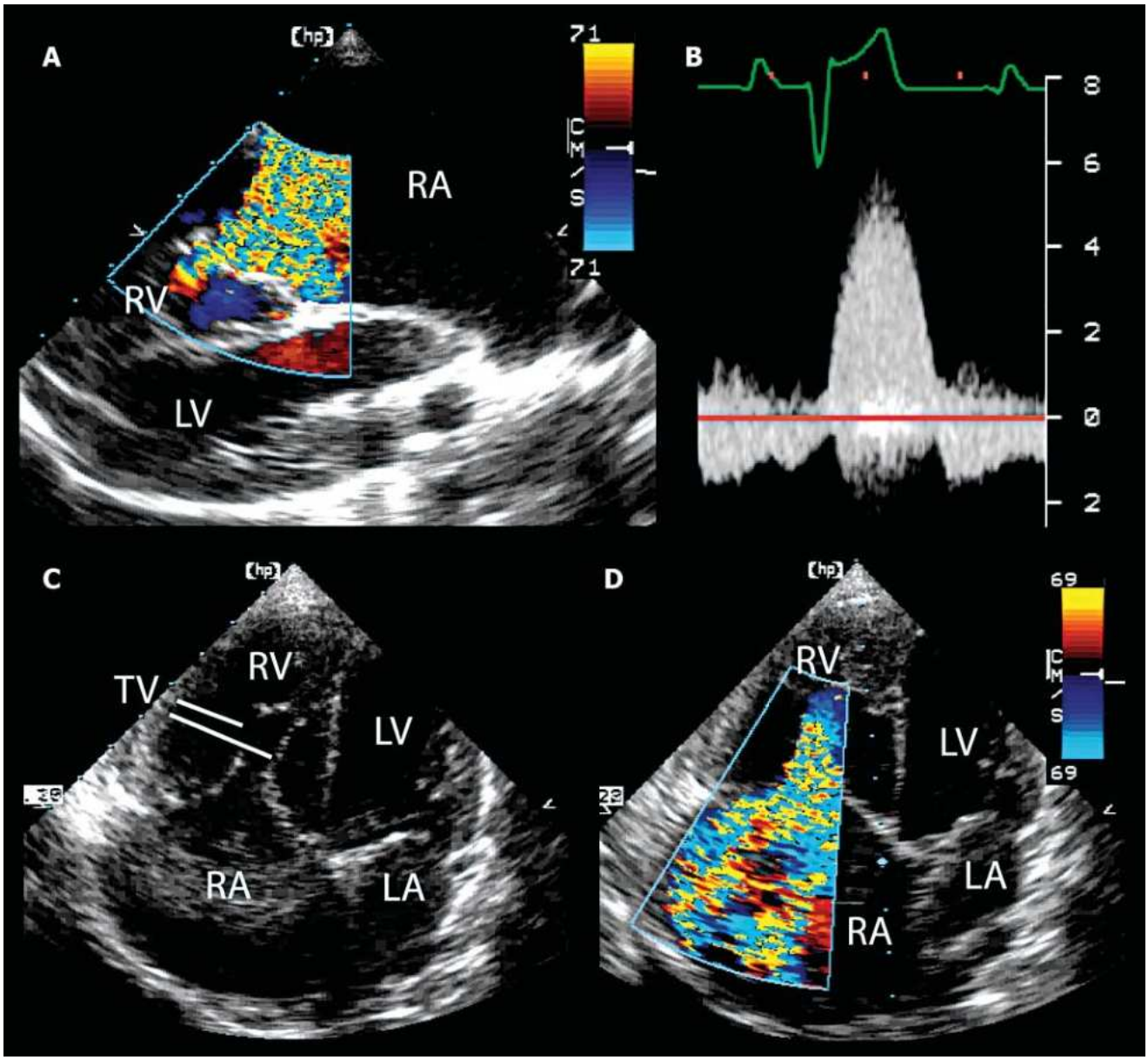


Figure 5.37. Tricuspid dysplasia and pulmonic stenosis in a Labrador Retriever with right-sided congestive heart failure (RCHF). The RPS LAx CFD image **(A)** demonstrates marked TR. Unusually, the extreme RA dilation caused the RPS position to be suitable for TR velocity quantification with the jet directed toward the transducer **(B)**. A TR jet velocity of 5.0 m/s suggests a driving pressure of $4 \times 5^2 = 100$ mmHg and is incompatible with normal RV pressure. In this case, RV pressure overload caused by pulmonic stenosis was responsible (not shown). The LAp four-chamber view **(C)** demonstrates extreme dilation of both the RA and RV. The TV leaflets are overlong and displaced toward the apex (compare with the position of the mitral leaflets). The CFD image from the same location **(D)** demonstrates marked TR and apical displacement of the flow convergence zone into the RV. Frame-by-frame visualization of the tricuspid apparatus revealed direct attachment of PMs to the tricuspid leaflets and a network of abnormal interconnecting CT, tethering the TV leaflets to the myocardial wall.

(Figure 5.41). Both the aorta and pulmonary trunk may be dilated in conjunction with increased blood flow. CFD examination of the pulmonary trunk reveals continuous turbulent flow and is useful in establishing the site of the ductus itself. Continuous-wave spectral Doppler velocity quantification reveals continuous flow into the pulmonary trunk and a peak velocity during systole of roughly 4.5–5.5 m/s, corresponding to the normal systolic aortic–pulmonic gradient of 80–120 mmHg (Moise 1989). Velocities significantly

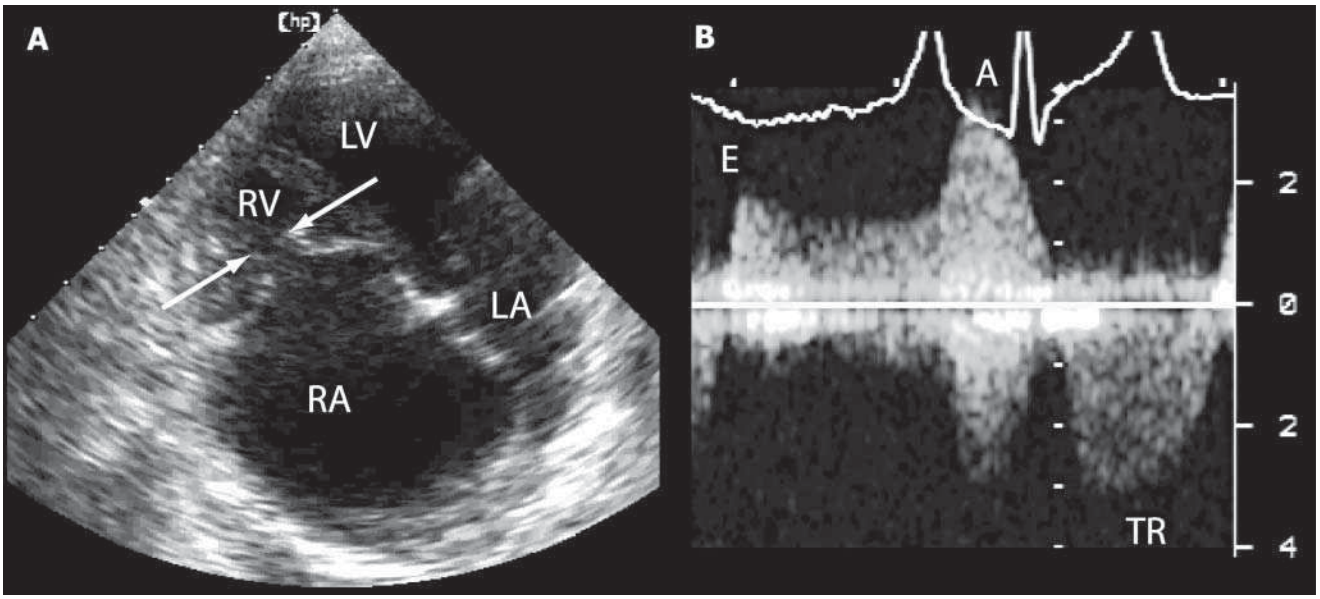


Figure 5.38. **Tricuspid dysplasia with valvular stenosis and regurgitation.** 2DE LAp four-chamber image **(A)** and CWD recording **(B)** from a Labrador Retriever. Arrows indicate the position of tricuspid leaflets at maximal separation during diastole. A TR velocity < 3.0 m/s **(B)** is consistent with relatively normal TR driving pressure (RV pressure – RA pressure = 36 mmHg). However, actual peak RV pressure may be substantially greater in this case, because the RA pressure is probably increased. The inflow recording demonstrates abnormal spectral broadening, and the velocity is elevated throughout diastole. A peak inflow gradient of $4 \times 3.5^2 = 50$ mmHg occurs at the Doppler A wave following a large P wave on the electrocardiogram. The E–F slope is flattened because of delayed pressure equalization between the atrium and ventricle.

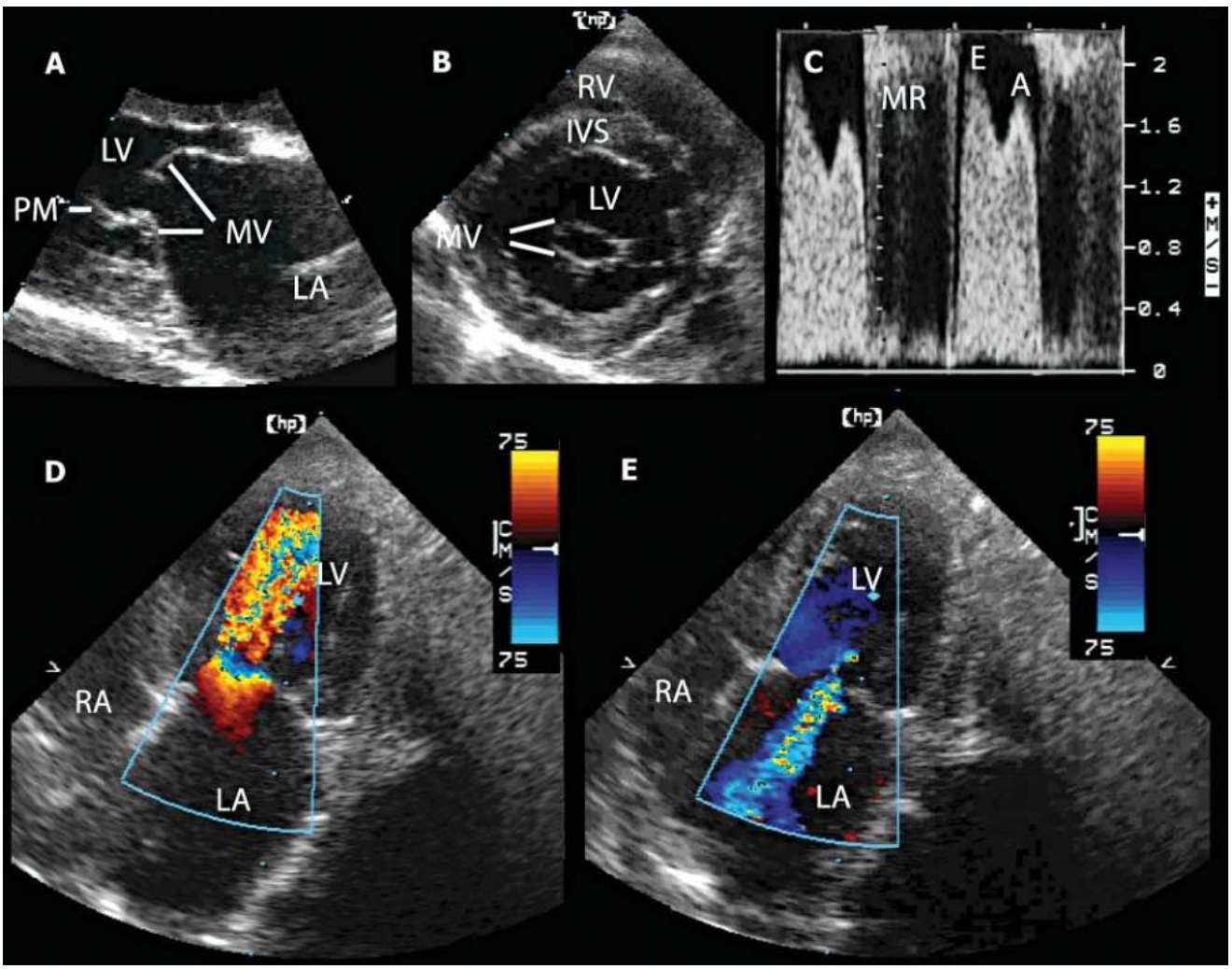


Figure 5.39. **Mitral dysplasia with valvular stenosis and regurgitation in a cat.** (for full caption, see facing page)

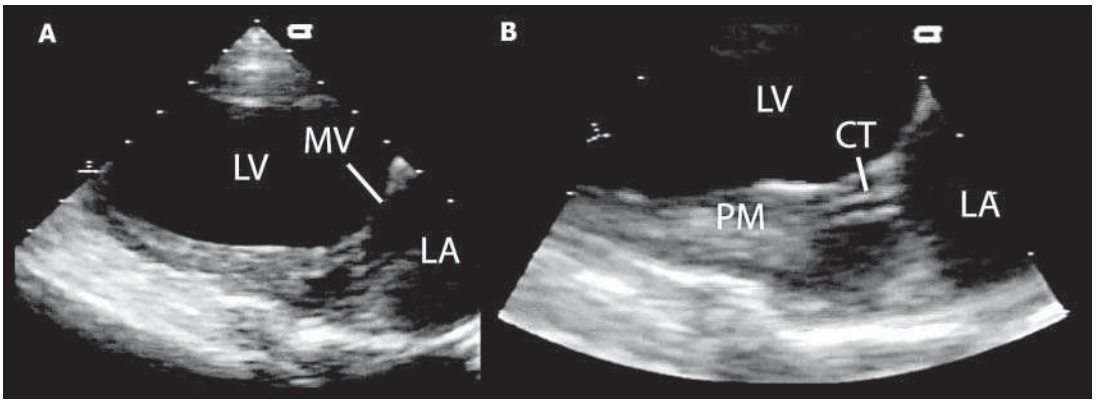


Figure 5.40. Mitral dysplasia in a Rottweiler puppy. A, B: The RPS LAx images depict marked LV and LA dilation. On the close-up **(B)**, a PM is visible, giving rise to shortened CT that distract the MV abnormally toward the LVW. There was dramatic MR (not shown).

lower than this value may suggest pulmonary hypertension or a more complex lesion. It is valuable to image the ductus directly and to determine carefully its suitability for interventional closure by coil embolization or ductal occluder device (Figure 5.42)

Right-to-left shunting patent ductus arteriosus (reverse PDA or RPDA) is uncommon but most typically occurs in dogs with a large ductus and persistent fetal circulation. Failure of the normal reduction of pulmonary vascular resistance at birth produces pulmonary pressures that approach or exceed aortic values and consequent reversal of the shunt flow direction and arterial desaturation, which may persist from birth. This scenario is consistent with echocardiographic findings of a thickened RV wall and septum typical of a RV pressure overload (Figure 5.43). The alternate RPDA scenario, i.e., left-to-right PDA producing progressive pulmonary hypertension and eventual shunt reversal, occurs less commonly. The latter would be expected to include LV dilation secondary to LV stroke volume overload.

Reverse PDA is suspected when there is clinical and echocardiographic evidence of RV pressure overload in the absence of an obstructive pulmonary lesion. The diagnosis may be confirmed by an echocontrast study (bubble study), if necessary (Goodwin and Holland 1995). The method consists of injecting echogenic aerated saline into a peripheral vein (e.g., cephalic vein) while imaging the heart or great vessels. This technique enables one to determine which vessels or cardiac chambers receive unoxygenated flow. In the case of RPDA, the abdominal aorta receives echocontrast within a few seconds of injection, having traversed the vena cava, right heart, pulmonary trunk, and ductus.

Abnormalities of Cardiac Septation

Failure of cardiac septation during embryogenesis results in a defect between the right and left sides of the heart, including atrial septal defect (ASD), ventricular septal defect (VSD), or a combination of the two.

Figure 5.39. Mitral dysplasia with valvular stenosis and regurgitation in a cat. RPS LAx **(A)** and SAx **(B)** images obtained during maximal diastolic separation of the MV leaflets. **A:** The tip of the anterior leaflet is tethered, so that the valve cannot open normally, and bows toward the septum because of increased LA pressure. A PM attaches directly to the parietal (posterior) leaflet (i.e., extreme shortening of CT). **B:** The diminished maximal orifice area is suggested by the cross-sectional image at the level of the valve tips. **C:** The PWD recording (LAp transducer position) demonstrates a turbulent diastolic inflow signal, and the E wave approaches 2 m/s, corresponding to a 16 mmHg gradient across the MV (modified Bernoulli equation). A turbulent MR signal with aliasing is also present. This example demonstrates a relatively mild case of stenosis, as suggested the peak inflow velocity and also the rapid decline of velocity after the peak of the E wave (compare with E–F slope of the tricuspid dysplasia example in Figure 5.38). **D:** The LAp CFD image obtained during diastole demonstrates a flow convergence zone at the atrial side of the MV and a turbulent inflow jet within the LV. The systolic image **(E)** demonstrates the MR jet into the enlarged LA.

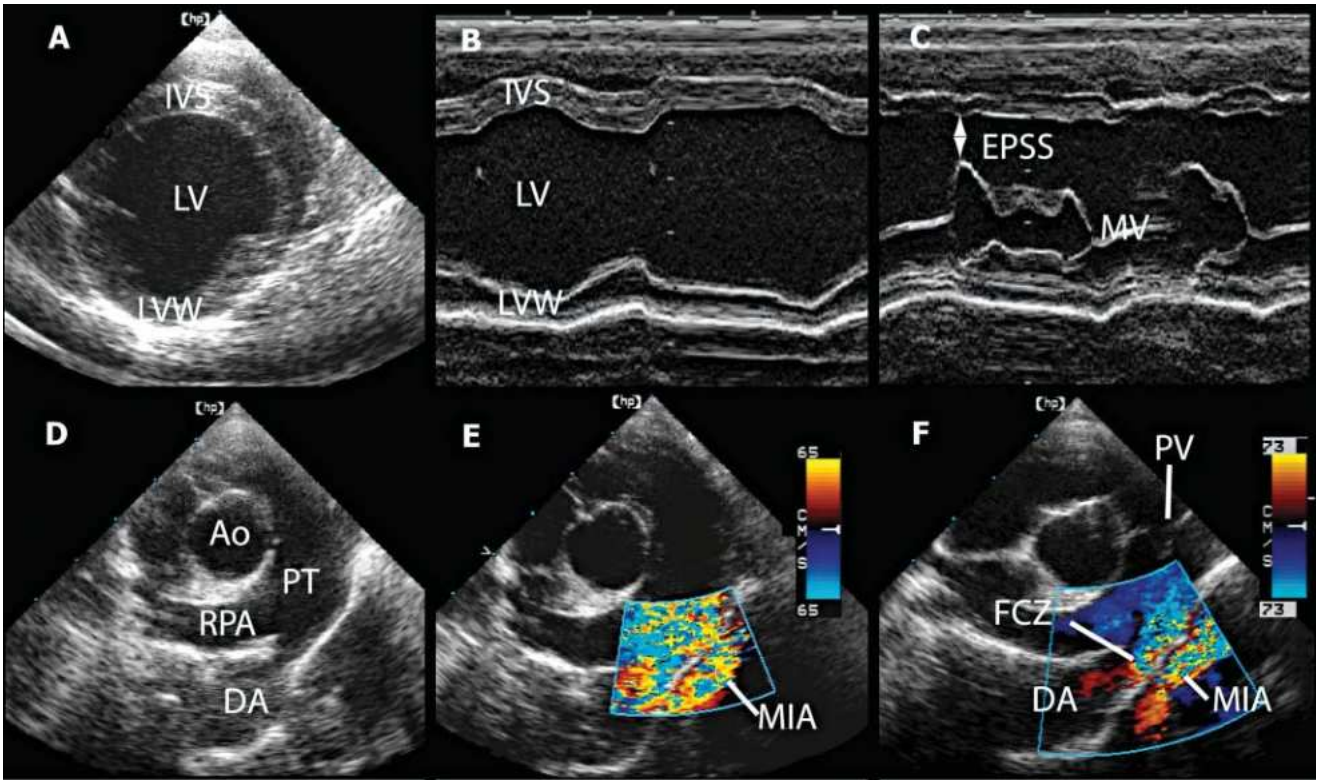


Figure 5.41. **Left-to-right shunting patent ductus arteriosus (PDA).** As suggested by the 2DE SAx LV image **(A)** and M-mode **(B)**, PDA causes LV dilation and stroke volume overload. Fractional shortening was depressed in this case, and the end point to septal separation distance (EPSS) was increased **(C)**, suggestive of marked ventricular remodeling and deteriorating myocardial function. RPS SAx images **(D–F)** enable visualization of a large ductus (DA) that narrows at its entry into the pulmonary circulation. CFD images in systole **(E)** and diastole **(F)** facilitate the diagnosis by showing continuous flow from the PDA causing turbulence in the PT. A prominent CFD mirror-image artifact (MIA) is evident. Visualization and evaluation of the PDA is facilitated by the occurrence of a flow convergence zone (FCZ).

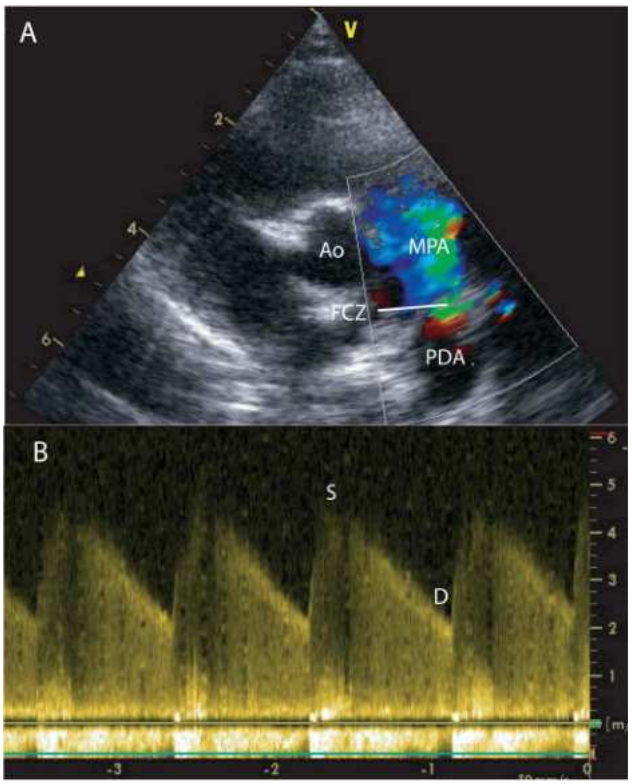


Figure 5.42. **Patent ductus arteriosus (PDA) CWD. A:** The 2DE/CFD image depicts the orientation of the PDA and CWD orientation from the LPS Sax position. The diameter of the vessel can be measured and the shape visualized. In this instance, there is an obvious constriction and flow convergence zone (FCZ) that facilitates coil occlusion. **B:** CWD recording made from this position demonstrates a typical velocity pattern due to continuous left-to-right flow through the ductus from the aorta to the main pulmonary artery (MPA). A systolic velocity of 4.5 m/s suggests an appropriate systolic pressure gradient between the two vessels (80 mmHg).

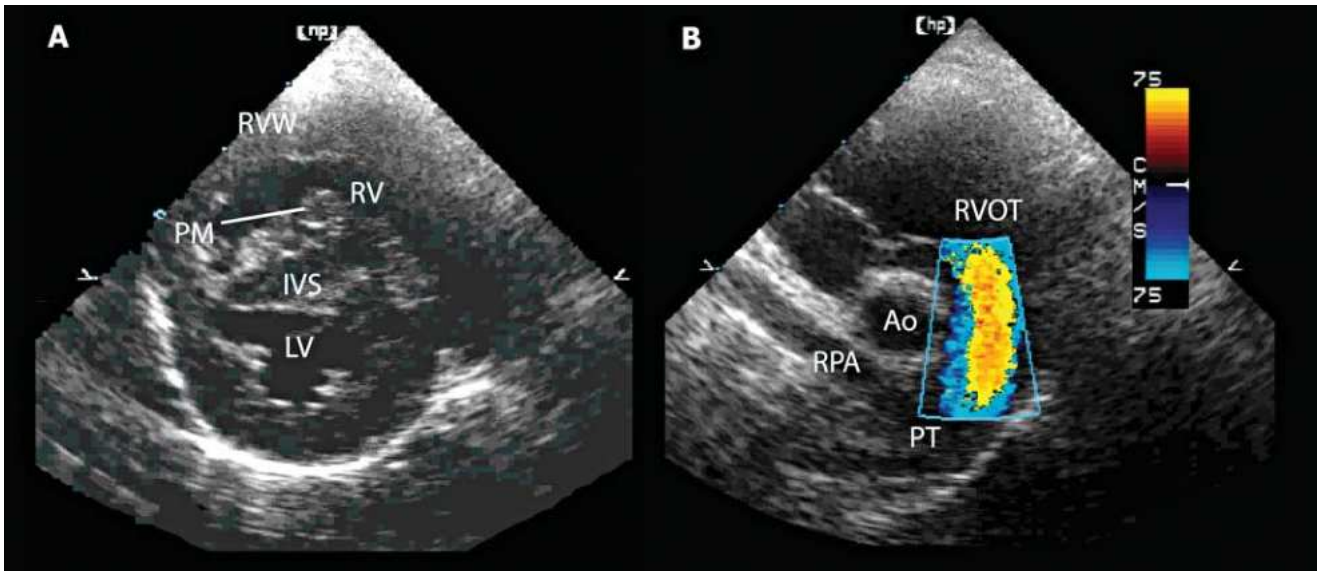


Figure 5.43. Reverse patent ductus arteriosus (RPDA or right-to-left PDA). The RPS SAx image **(A)** depicts marked RV hypertrophy, including dramatic thickening of the RVW and the trabecular and papillary muscles (PMs) of the interventricular septum. The LV appears somewhat small and thick-walled because of volume underload and distortion by the RV. **B:** CFD imaging at the PV level depicts a laminar flow pattern with color aliasing in the central flow core. CFD interrogation of the RVOT, PT, and RPA yielded no evidence of stenosis, yet a dramatic increase in TR velocity confirmed increased RV pressure and pulmonary hypertension (not shown). 2DE echocontrast imaging of the abdominal Ao, following venous injection of micro-aerated saline, can be used to confirm the lesion if necessary.

Septation abnormalities may cause a wide spectrum of functional disease. Because of the normal distributions of intracardiac pressure and chamber compliance, both ASD and VSD most typically cause left-to-right shunting of blood and pulmonary overcirculation. Under these circumstances, ASD causes volume overload and consequent dilation of the right ventricle, whereas VSD necessitates increased stroke volume of the left ventricle. These abnormalities depend on the magnitude of the shunt.

Atrial Septal Defect

Deficiency of the septum secundum (septum secundum ASD) causes a defect near the normal position of the fossa ovalis in the midatrial wall (Figures 5.44, 5.45). In distinction, a septum primum defect (septum primum ASD, endocardial cushion defect, or atrioventricular canal ASD) is located near the atrioventricular canal and may cause ASD, VSD, or both (Figure 5.46). **Sinus venosus ASD**, which is rare in small animals, occurs near the junction of the cranial vena cava. **Patent foramen ovale** is not an anatomical defect, but results when functional closure of the foramen ovale at birth is not permanent. ASD flow is typically generated by a small pressure gradient with jet velocity <0.5 m/s.

Ventricular Septal Defect

Ventricular septal defect also occurs with a range of anatomical and functional types. One aspect of classification relates to whether the VSD is small and **restrictive**, where the pressure gradient between the right and left ventricles is maintained and jet velocity is greater than 4 m/s, in contrast to **nonrestrictive**, where the large size of the defect approximates a single ventricle with pressure equilibration between the right and left sides (e.g., <3 m/s).

The most common form of VSD in dogs and cats is caused by a defect in the membranous (or conoventricular) septum located just proximal to the aortic root (Figure 5.47). Conversely, a defect in the conotruncal septum causes a VSD that is located distal to the crista supraventricularis (supracristal VSD, outlet VSD, or doubly committed VSD), including the specific type associated with tetralogy of Fallot (Figure 5.48). In the latter, the outlet septum is malaligned with the trabecular septum of the right ventricle, creating a septation defect (malalignment VSD) and disproportionate sizes of the two outflow tracts. The muscular outflow septum obstructs the RV outflow tract, causing a subvalvular PS, and the aorta is enlarged and straddles (overrides) the interventricular

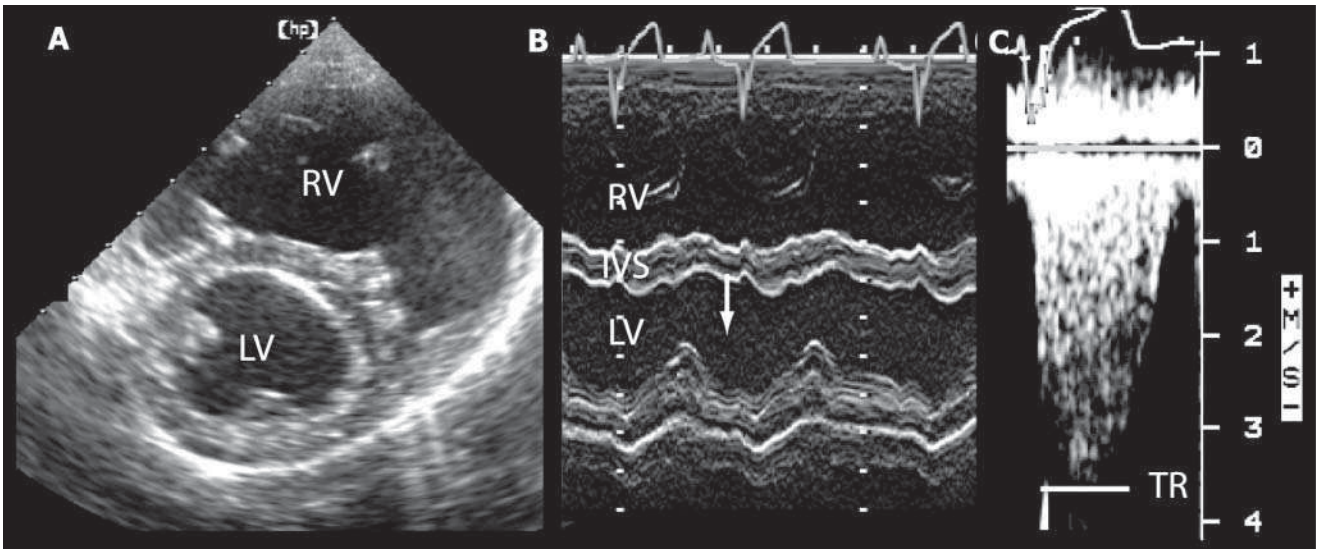


Figure 5.44. Secundum atrial septal defect (ASD). RPS SAx 2DE image **(A)** from a dog with a large-secundum-type ASD demonstrating RV dilation secondary to volume overload. The RV dilation is also apparent on the M-mode recording **(B)**, as is *paradoxical septal motion* (arrow) caused by displacement of the septum away from the transducer with diastolic filling of the enlarged RV. A CWD recording **(C)** of TR in this dog demonstrates a peak TV gradient of 4×3.5^2 m/s ~50 mmHg, consistent with either pulmonic stenosis or pulmonary hypertension. No pulmonic stenosis was evident, and pulmonary hypertension is a well-known sequela to chronic pulmonary overcirculation.

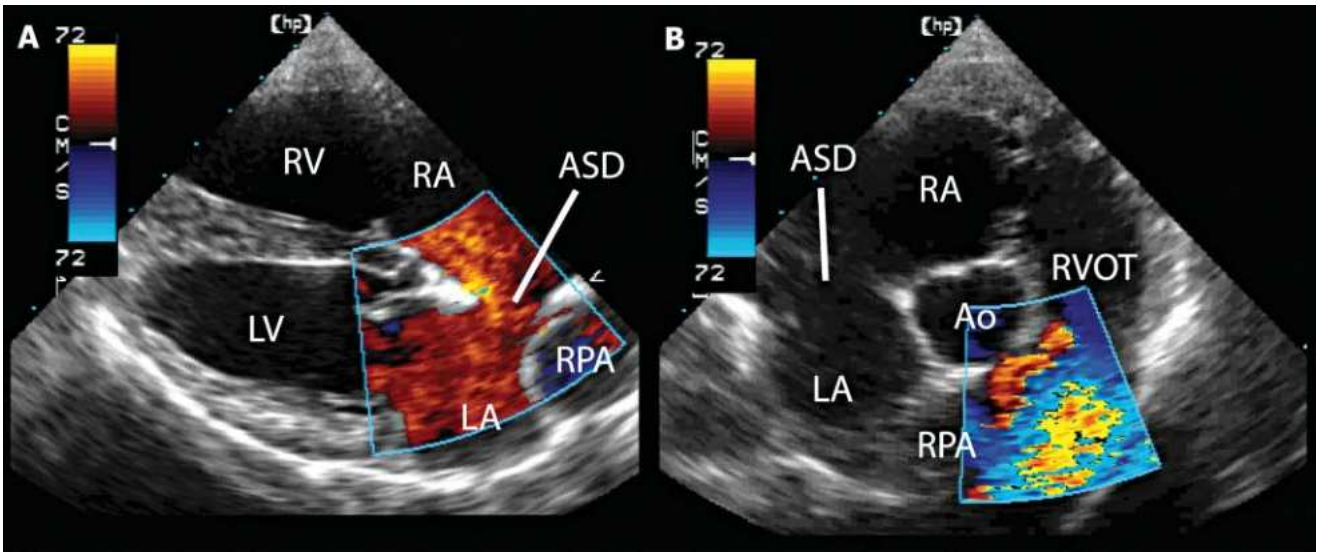


Figure 5.45. Secundum atrial septal defect (ASD). CFD RPS LAx **(A)** and SAx **(B)** images from the dog with secundum ASD in Figure 5.44. The RV and RA are dramatically dilated because of the volume overload generated by the defect, and the pulmonary overcirculation is suggested by marked enlargement of the RPA and increased velocity of blood flow in the main pulmonary artery. The LAx image demonstrates retrograde flow across the defect from the LA into the RA. Apparent ASD flow at this location must be differentiated from a retrograde CaVC flow into the RA.

septum. Tetralogy of Fallot is the most common cyanotic congenital cardiac defect in small animals but is part of a spectrum of conditions ranging from mild outflow tract abnormalities to pseudotruncus arteriosus with pulmonary atresia, where conotruncal septal malalignment is so marked that the pulmonary outflow tract is functionally obliterated (Figure 5.49).

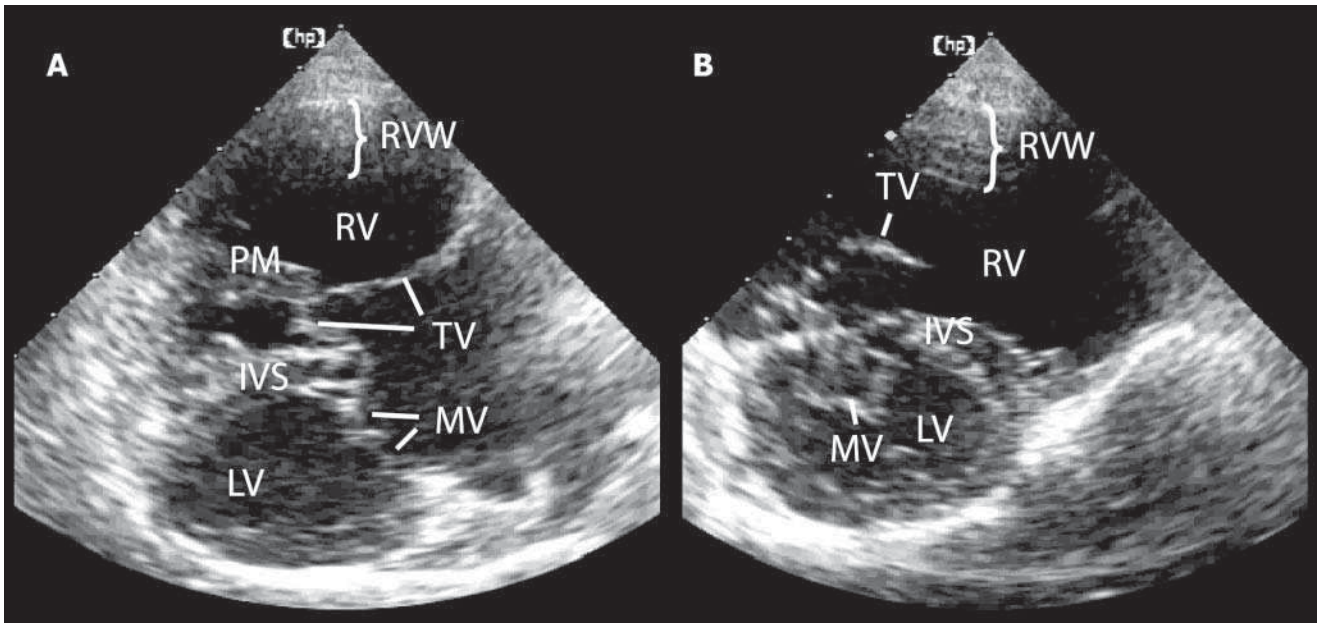


Figure 5.46. Primum atrial septal defect (ASD). LAx **(A)** and SAx **(B)** 2DE RPS images from a dog with a large-septum-primum ASD causing a so-called *common atrium*. The RV is dramatically enlarged because of volume overload, and a hypertrophied PM attaches directly to an elongated TV leaflet. RV hypertrophy is secondary to pulmonary overcirculation and hypertension in this case. The tricuspid and mitral apparatuses communicate through the defect, which involves the atrioventricular canal portion of the ventricular septum as well (inlet VSD).

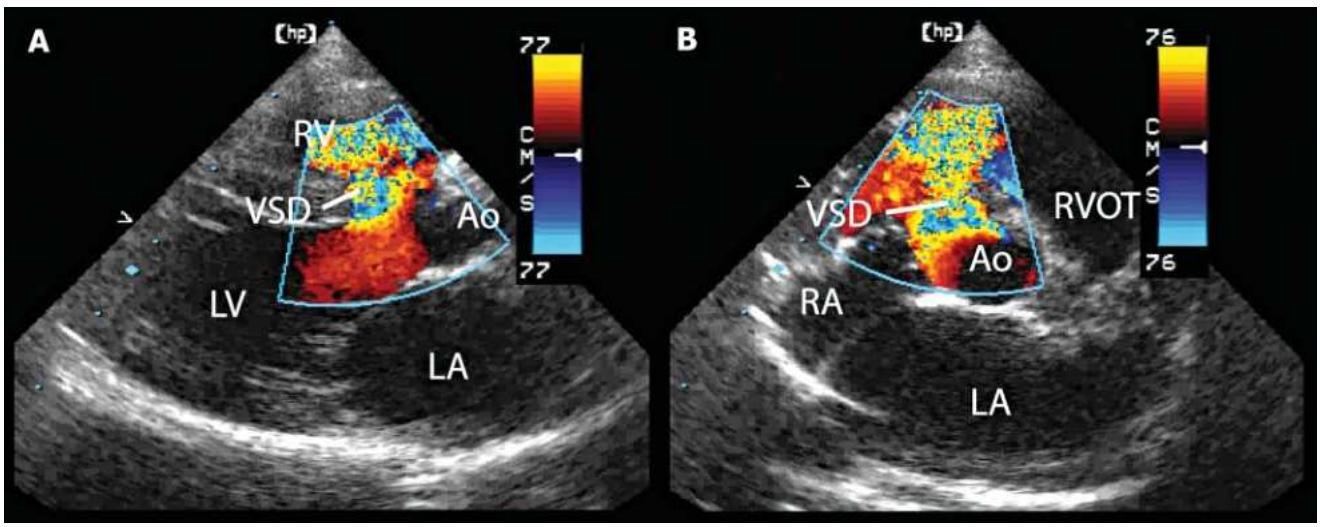


Figure 5.47. Membranous ventricular septal defect (VSD) in a cat. LAx **(A)** and SAx **(B)** CFD RPS images from a cat with membranous (or perimembranous) VSD. The location of the defect is identified by the color halo of the flow convergence zone, caused by color aliasing, where the blood accelerates through the defect; a turbulent mosaic color flow pattern is visible in the RV. The defect is immediately proximal to the Ao valve. This is the most common type of VSD in small animals.

Miscellaneous and Complex Congenital Disease

A wide range of cardiac congenital defects and combination defects is possible, with varying severity and clinical importance of each. Echocardiographic principles are applied in each case to determine the presence of connections between vessels and chambers and pressure gradients between the connections.

Cor triatriatum is an unusual condition characterized by the presence of an accessory atrial chamber, separated from the atrium proper by a perforated

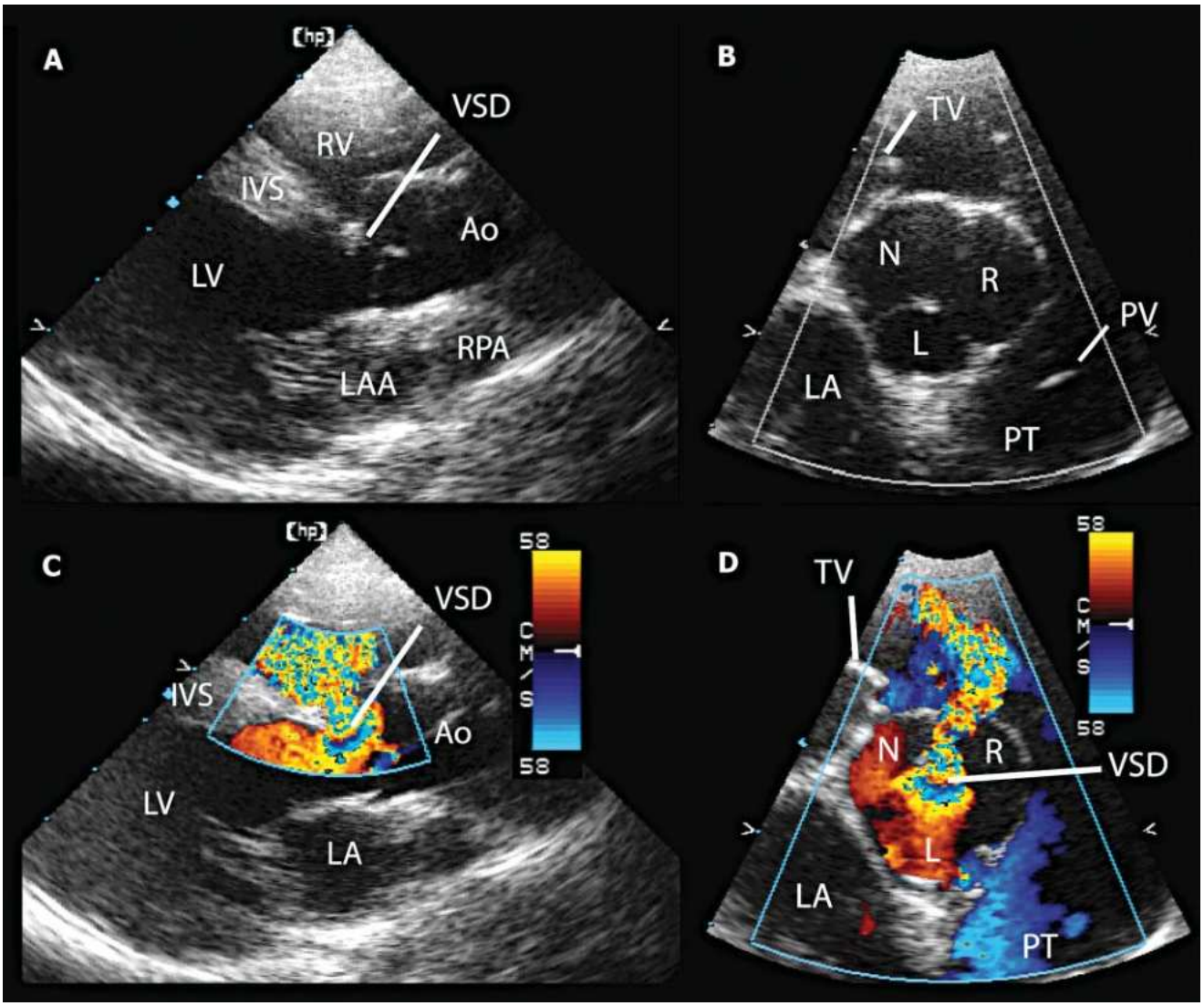


Figure 5.48. Outlet ventricular septal defect (VSD). LAx **(A, C)** and SAx **(B, D)** 2DE **(A, B)** and CFD **(C, D)** RPS images from a dog with a left-to-right restrictive VSD in conjunction with an Ao that straddles the septum **(A)** (i.e., *overriding Ao*). The location of the defect is identified by the color halo of the flow convergence zone, caused by color aliasing, where the blood accelerates through the defect. Because the Ao straddles the septum, the defect lies directly beneath the Ao valve, which is particularly evident in **D**.

membrane partition (Figure 5.50). Blood received by the accessory chamber must flow through the perforation, which may be restrictive. A significant pressure gradient across the membrane implies congestion of tissues and organs with venous drainage to the accessory chamber. Cor triatriatum may occur for the right atrium (cor triatriatum dexter) or the left (cor triatriatum sinister).

Peritoneal-pericardial diaphragmatic hernia, which implies a communication between the pericardial space and the abdominal cavity, is probably related to abnormal fetal development of the septum transversum or pleuroperitoneal folds. The condition is most common in cats and may be diagnosed subsequent to the incidental discovery of an enlarged cardiac silhouette on thoracic radiography. Echocardiography reveals a range of abdominal organs within the pericardial space. Often, cardiac function is little affected, and determining whether clinical signs are related to the hernia may be difficult (Figure 5.51; see also Chapter 4 and Figures 4.45, 4.46).

Eisenmenger physiology is caused by a shunt defect (ASD, VSD, or PDA) that results in right-to-left shunting subsequent to pulmonary vascular disease.

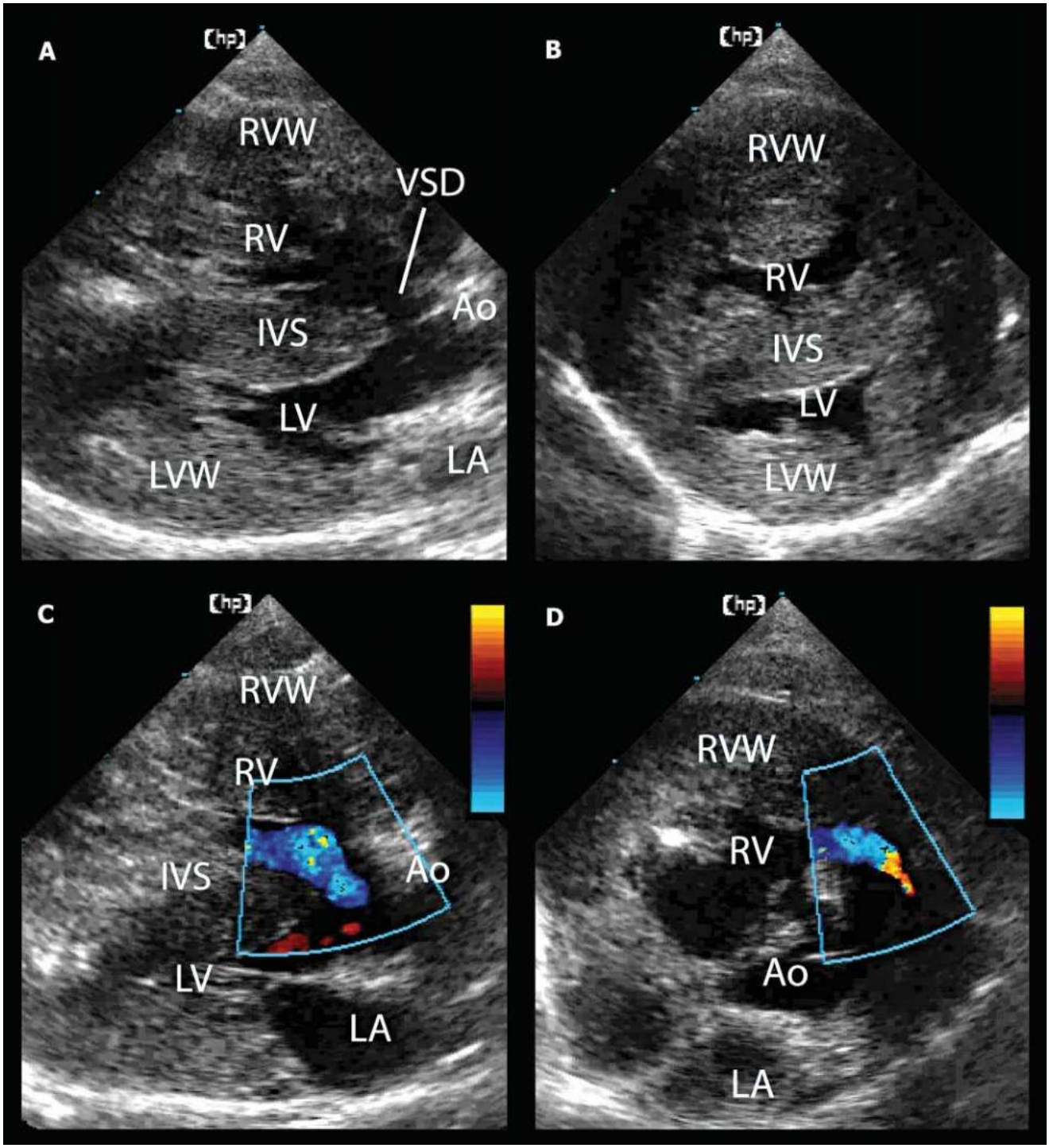


Figure 5.49. Tetralogy of Fallot (TF) in a cat. RPS 2DE LAx **(A)** and SAx **(B)** images depict extreme hypertrophy of the RVW. The LV cavity appears small and the LVW comparatively thickened because of distortion and underloading caused by the extreme RV disease. The overriding Ao is demonstrated in image **A** where the Ao root appears to straddle the IVS immediately distal to the ventricular septal defect (VSD). **C, D:** Corresponding CFD images. The VSD was somewhat restrictive in this case, and image **C** demonstrates moderate velocity flow from the RV into the Ao caused by a significant pressure gradient. Hypertrophy was extreme to the extent that the RVOT could not be fully visualized. However, image **D** demonstrates flow convergence caused by infundibular stenosis.

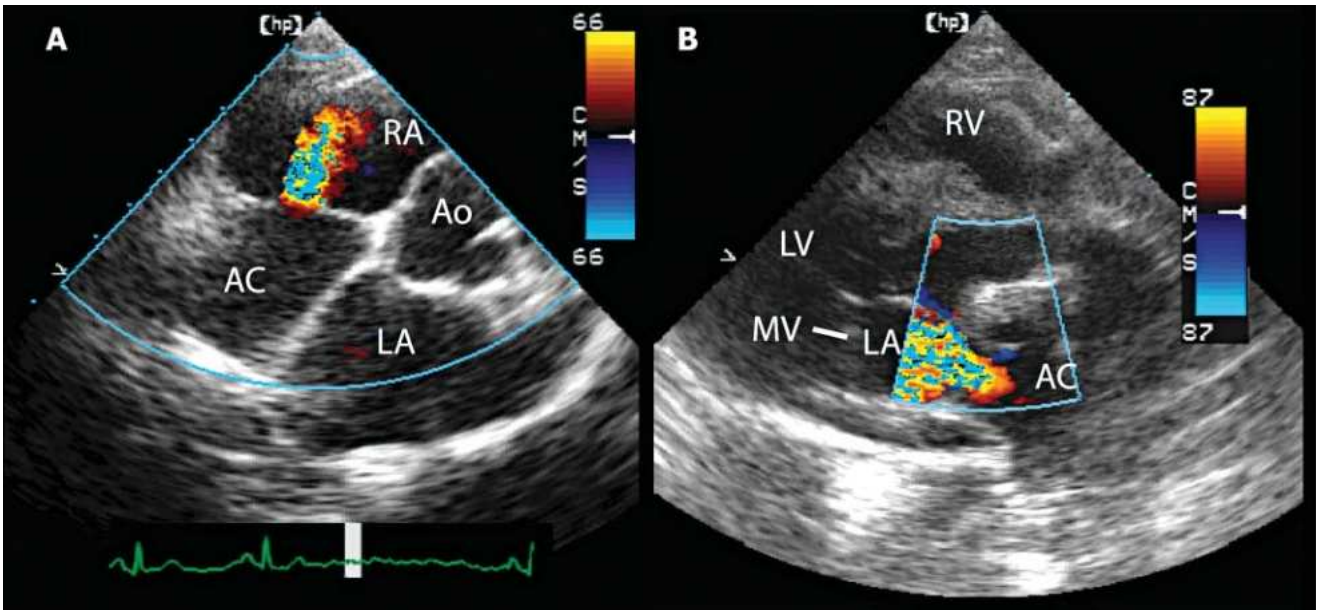


Figure 5.50. Cor triatriatum. RPS SAx CFD image of cor triatriatum dexter in a Labrador Retriever **(A)** and LAx image of cor triatriatum sinister in a young cat **(B)**. In each case, an accessory chamber (AC) is separated from the atrium by a restrictive membrane. **A:** The dog also had tricuspid dysplasia, so the TV was displaced into the ventricle and is not visible. **B:** The MV is visible, and the flow convergence zone depicts the location of the restrictive membrane.

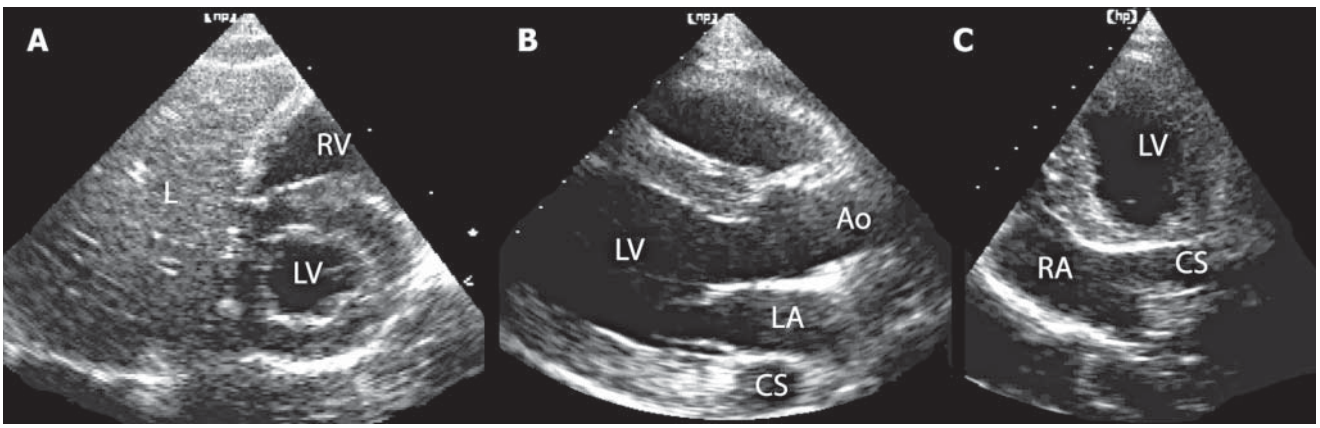


Figure 5.51. Miscellaneous and incidental abnormalities. A: The RPS SAx view from a cat with peritoneal-pericardial diaphragmatic hernia (PPDH). The liver (L) is juxtaposed to the heart, where normally there is intervening lung tissue and the diaphragm. The P does not appear to enclose the heart. The cat was presented for signs of respiratory distress, and a thoracic radiograph revealed a markedly enlarged cardiac silhouette, prompting cardiac evaluation. Respiratory signs were caused by bronchial disease and unrelated to the congenital pericardial abnormality. PPDH is often an incidental finding. **B, C:** RPS LAx **(B)** and LAp with caudal angulation **(C)** from a dog with marked dilation of the coronary sinus (CS), causing a persistent left CrVC. The view in C shows the CS entering the RA at the caudal aspect of the heart.

High-volume pulmonary overcirculation from a left-to-right shunt may initiate a well-described sequence of pulmonary vascular changes that ultimately causes elevation of right-sided pressures and shunt reversal. RV hypertrophy is present, and Doppler or echocontrast studies may assist in identifying the location and direction of the shunt.

Diagnosis of complex congenital heart disease is one of the most challenging applications of echocardiography and largely beyond the scope of this chapter. Potential abnormalities may include hypoplastic cardiac chambers, atretic great vessels, and situs inversus at the level of the abdomen, ventricles, or great vessels (Figure 5.52).

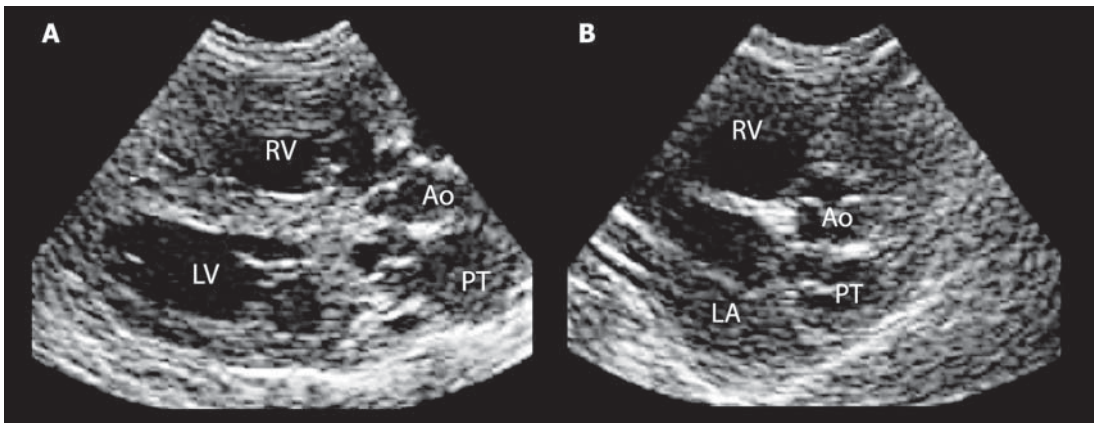


Figure 5.52. Uncorrected transposition of the great vessels (TGV). RPS LAx **(A)** and SAx **(B)** 2DE images from a rare case of uncorrected TGV in a cyanotic kitten (aorticopulmonary situs inversus). **A:** The Ao is evident leaving the RV while the PT joins the LV. Post-stenotic dilation of the PT is visible because of a constriction at the junction of this vessel with the LV. **B:** This SAx image reveals simultaneous transverse views of both the Ao and PT. This does not occur in a normal heart because the two semilunar valves do not normally lie in the same plane. An atrial septal defect was the location of bidirectional shunting in this case. A shunt is necessary for survival beyond birth in uncorrected TGV because the pulmonary and systemic circulations are otherwise isolated from each other.

Acquired Heart Disease

Acquired Valvular Heart Disease

Endocardiosis

Endocardiosis, also known as chronic degenerative valve disease (CDVD), is the most common acquired heart disease of dogs and is particularly prevalent among smaller breeds. The mitral valve is the one most commonly affected, but the tricuspid valve may be affected concurrently and/or preferentially in individuals. Exemplary 2DE echocardiographic findings of mitral CDVD include thickening, increased echogenicity, and prolapse of the valvular leaflets (Bonagura and Herring 1985a). Characteristic remodeling changes secondary to MR include progressively increasing LA and diastolic LV dimensions (Brown et al. 2005) (Figure 5.53). The end-systolic LV internal dimension (LVIDs) is characteristically preserved with the condition. This remodeling pattern coincides with a normal to increased fractional shortening, which is, consequently, a poor index for staging disease severity. In late-stage disease, LVIDs and E-point septal separation may begin to increase; these findings have been interpreted as evidence of myocardial dysfunction or failure (Kittleson et al. 1984). Although advanced Doppler techniques can be utilized to evaluate ventricular diastolic function and filling pressures (Bonagura and Schober 2009), interpretation of these methods may be rendered ambiguous by age-related changes in diastolic function and the influence of increased preload on most of the Doppler parameters. Diastolic functional class, IVRT, and E:IVRT are the best predictors of LCHF in dogs with CDVD (Schober et al. 2010, 2011).

Echocardiographic techniques for the evaluation of MR range from qualitative measures to semiquantitative. One of the simplest methods is to evaluate the MR jet size by visual inspection on a CFD image. Alternatively, a ratio can be calculated (i.e., planimetered jet area divided by LA area) to provide a seemingly quantitative estimate of MR severity. Unfortunately, the extent of the MR jet is highly dependent on CFD control settings, jet and chamber geometry, and ambient hemodynamic conditions (Figure 5.54).

A semiquantitative Doppler method of MR evaluation involves estimation of the regurgitant fraction by using the proximal isovelocity surface area (PISA), which focuses on the flow convergence zone on the LV side of the regurgitant orifice (Kittleson and Brown 2003). Instantaneous blood flow rate across any hemisphere is simply the product of blood velocity at that radius and the area of the hemisphere, $A = 2\pi r^2$. Radius and velocity are both determined from a CFD image, the radius being the distance from the orifice to the aliasing velocity (Figure 5.54). The PISA method is very sensitive to the radius measurement, and determining the location of the valvular

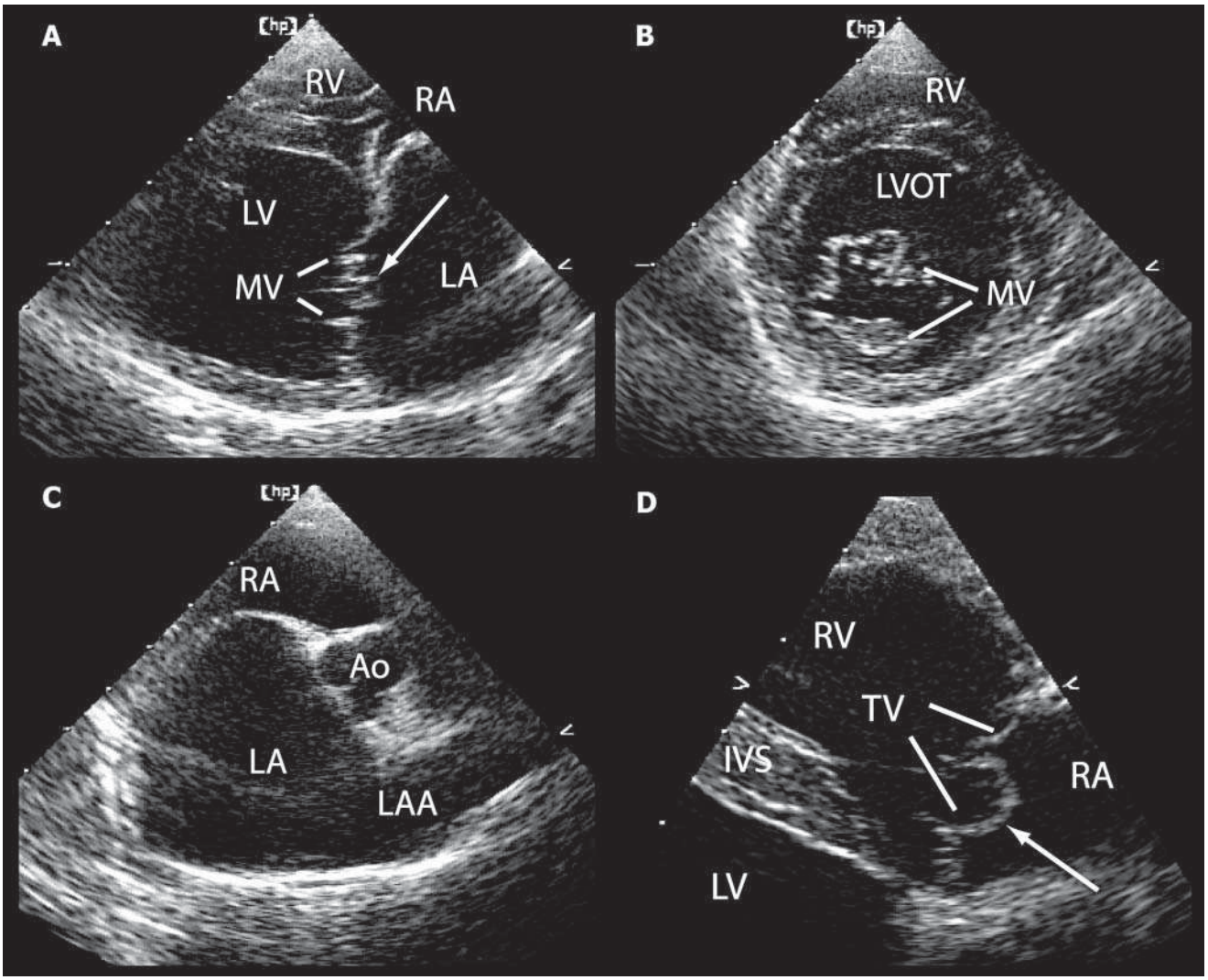


Figure 5.53. **Chronic degenerative valve disease (CDVD [endocardiosis]). A:** This RPS LAx view in early systole demonstrates dilation of the LV and LA along with prolapse of the AML, which appears as a displacement into the LA (arrow). **B:** This diastolic RPS SAx view portrays dramatic thickening of the leaflets. **C:** This SAx view at the level of the Ao root demonstrates dramatic LA dilation. **D:** This RPS LAx view of the TV demonstrates prolapse into the RA (arrow).

orifice accurately can be difficult. Color M-mode can be helpful in increasing temporal resolution and enabling visual averaging of the radius during the regurgitant flow.

Using the maximal regurgitant flow rate (Q_r [PISA method]), the peak regurgitation velocity (V_p), and the VTI of the MR, the MR volume (V_r) can be calculated as follows: $V_r = (Q_r/V_p) \times VTI_r$. This value is used to calculate the regurgitant fraction after the LV forward stroke volume has been estimated ($V_{SV} = area_{Ao} \times VTI_{Ao}$). The regurgitant fraction is $V_r/(V_r + V_{SV})$ (Kittleson and Brown 2003).

Infective Endocarditis

Infective endocarditis is an unusual, but potentially devastating, consequence of bacteremia and/or sepsis most commonly affecting medium-sized and large dogs. Lesions most typically involve the aortic and/or mitral valves but can also extend to surrounding myocardial tissue, with possible periannular abscessation (Figure 5.55).

Nonspecific echocardiographic signs include thickened hyperechoic aortic and mitral valve leaflets, chordal rupture, and diastolic mitral valve fluttering or oscillation (Lombard and Buergelt 1983a). The

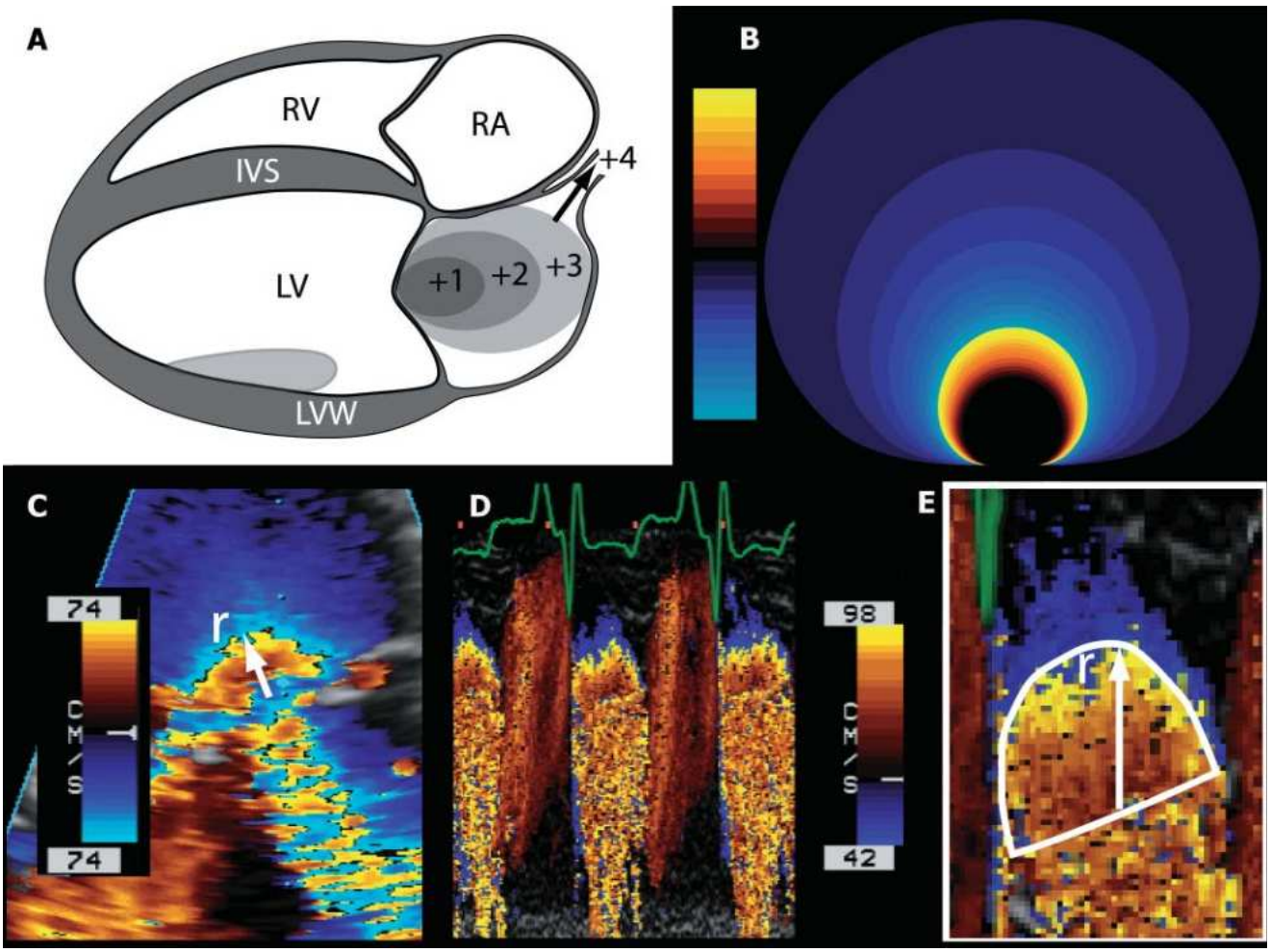


Figure 5.54. **MR severity.** Qualitative evaluation of MR can be made from CFD assessment of jet size **(A)**. +4 MR is associated with retrograde jet extension into the pulmonary veins. Semiquantitative methods assume that the regurgitant flow rate (cm^3/s) is approximated as the surface area of the hemispherical flow convergence zone ($A = 2\pi r^2$) multiplied by the aliasing velocity (proximal isovelocity surface area method [PISA]). However, the computed mathematical solution of the assumed flow **(B)** results in infinite velocity at the infinitesimal orifice (inner black zone); PISA assumptions are not valid unless the hemisphere radius is large with respect to the orifice size. **C:** This LAp CFD image, which is from the regurgitant orifice of a dog with severe MR, was recorded at an aliasing velocity of 74 cm/s; the estimated radius of the hemisphere (r) is not large enough compared with the orifice. Requirements for the PISA determination are improved by adjusting the color baseline in the direction of flow, downward in this case, which decreases the aliasing velocity and increases the distance from the aliasing velocity contour to the orifice. This has been done for the color M-mode recording in image **D**, decreasing the aliasing velocity to 42 cm/s and increasing the hemisphere radius; the radius also can be estimated from the color M-mode recording **(E)**.

diagnosis of endocarditis might be difficult if lesions are small or involve only the mitral valve of dogs predisposed to endocardiosis. Echocardiographic follow-up may be useful in these cases by revealing rapid valvular changes. Chronic vegetations may appear hyperechoic, with acoustic shadowing indicating calcification.

Large vegetative lesions may cause valvular stenosis or insufficiency, or both. The volume overload (insufficiency, either valve) or pressure overload (AS) is often acute. Hence, cardiac remodeling may not be apparent even though marked functional compromise is present. Doppler echocardiography enables confirmation and quantification of the valvular dysfunction.

Endocarditis is the most likely cause of substantial aortic insufficiency in dogs. Echocardiographic evidence of severe aortic insufficiency includes premature

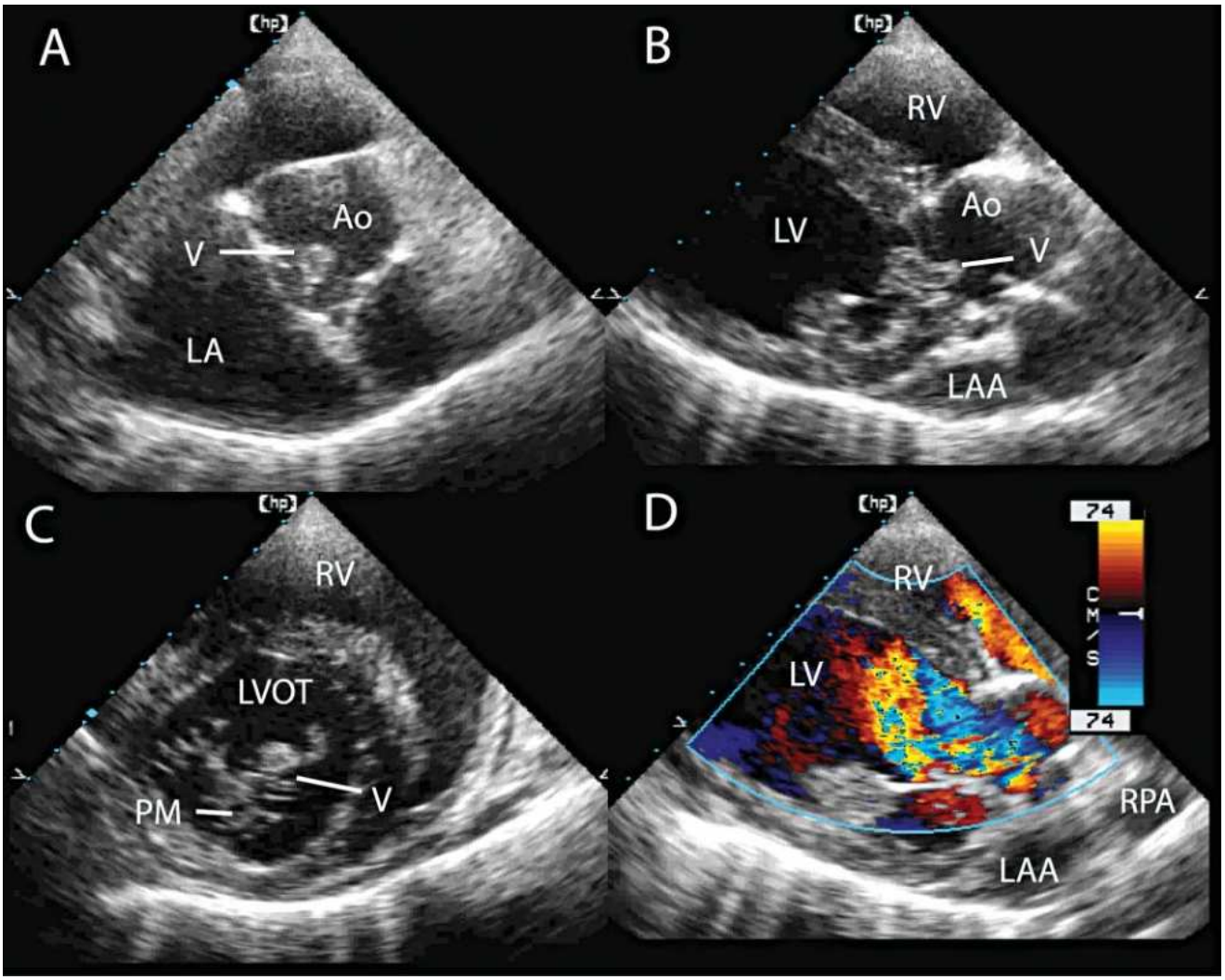


Figure 5.55. Endocarditis of the Ao and MVs. RPS SAx **(A, C)** and LAx **(B, D)** images from a dog with mitral and Ao endocarditis. The largest component of the vegetative lesion (V) is on the anterior leaflet of the MV and extends into the LVOT during systole. Nevertheless, the principal functional deficit in this case was Ao insufficiency, evident on the CFD image **(D)** as dramatic diastolic flow into the LV from the Ao.

systolic mitral valve closure, an increasingly negative diastolic slope of the aortic regurgitation Doppler velocity envelope, and flow reversal in progressively distal segments of the aorta (Figure 5.56).

Myocardial Disease

Dilated and Arrhythmogenic Right Ventricular Cardiomyopathy

Cardinal echocardiographic features of dilated cardiomyopathy (DCM) include chronically increased LV dimensions particularly in systole, and depressed fractional shortening and ejection fraction (Calvert et al. 1982) (Figure 5.57). Another fundamental diagnostic criterion is a decrease in the ratio of wall thickness to chamber dimension representing the inability of the myocardium to thicken appropriately. This decrease in relative wall thickness imparts the visual impression of dilation on 2DE images. Increased mitral E-point to septal separation distance is also noticed as a consequence of LV dilation, systolic dysfunction, and decreased peak mitral inflow.

Left ventricular echocardiographic changes are often most readily observed, but anatomical, pathological, and functional abnormalities are typically biventricular. As the name implies, the pathology of arrhythmogenic RV cardiomyopathy (ARVC) is initiated in the right heart but may cause global cardiac

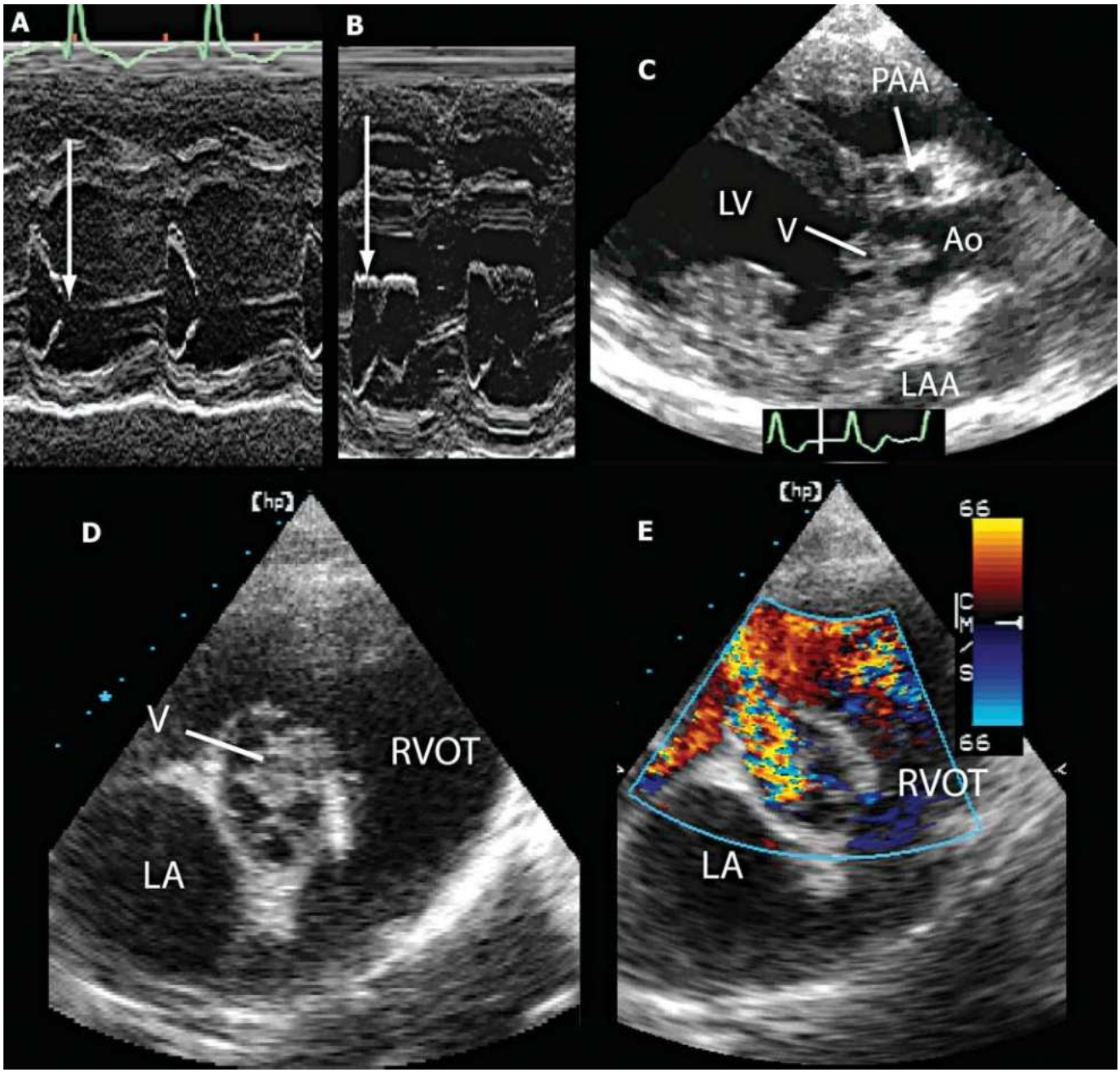


Figure 5.56. **Miscellaneous findings with infective endocarditis. A:** M-mode depicts early systolic closure of the MV (arrow) caused by severe Ao insufficiency, leading to early diastolic equilibration of LV and LA pressures. **B:** Diastolic MV fluttering (arrow) is caused by the turbulent flow of Ao insufficiency past the valve. **C:** This RPS LAx image depicts a large vegetation (V) on the Ao valve and a para-annular abscess (PAA). **D, E:** These RPS SAx images (2DE and CFD, respectively) are from a dog with Ao valve endocarditis, vegetative lesions (V), and rupture of the sinus of Valsalva causing an acquired shunt. Continuous (systole and diastole) left-to-right flow occurred across this defect because of the persistent pressure gradient between the Ao and RV.

disease resembling the typical DCM (Baumwart et al. 2005). ARVC is common in Boxers as a familial disease (previously termed Boxer cardiomyopathy) characterized by malignant ventricular arrhythmias, and may also be seen in cats with otherwise unexplained right ventricular enlargement (Harvey et al. 2005).

Doppler studies most commonly demonstrate atrioventricular valve regurgitation in DCM relating to cardiac dilation and consequent dysfunction of the mitral and/or tricuspid apparatus (Figure 5.58). Typically, atrioventricular valvular regurgitation in DCM is not as voluminous as in CDVD, but both

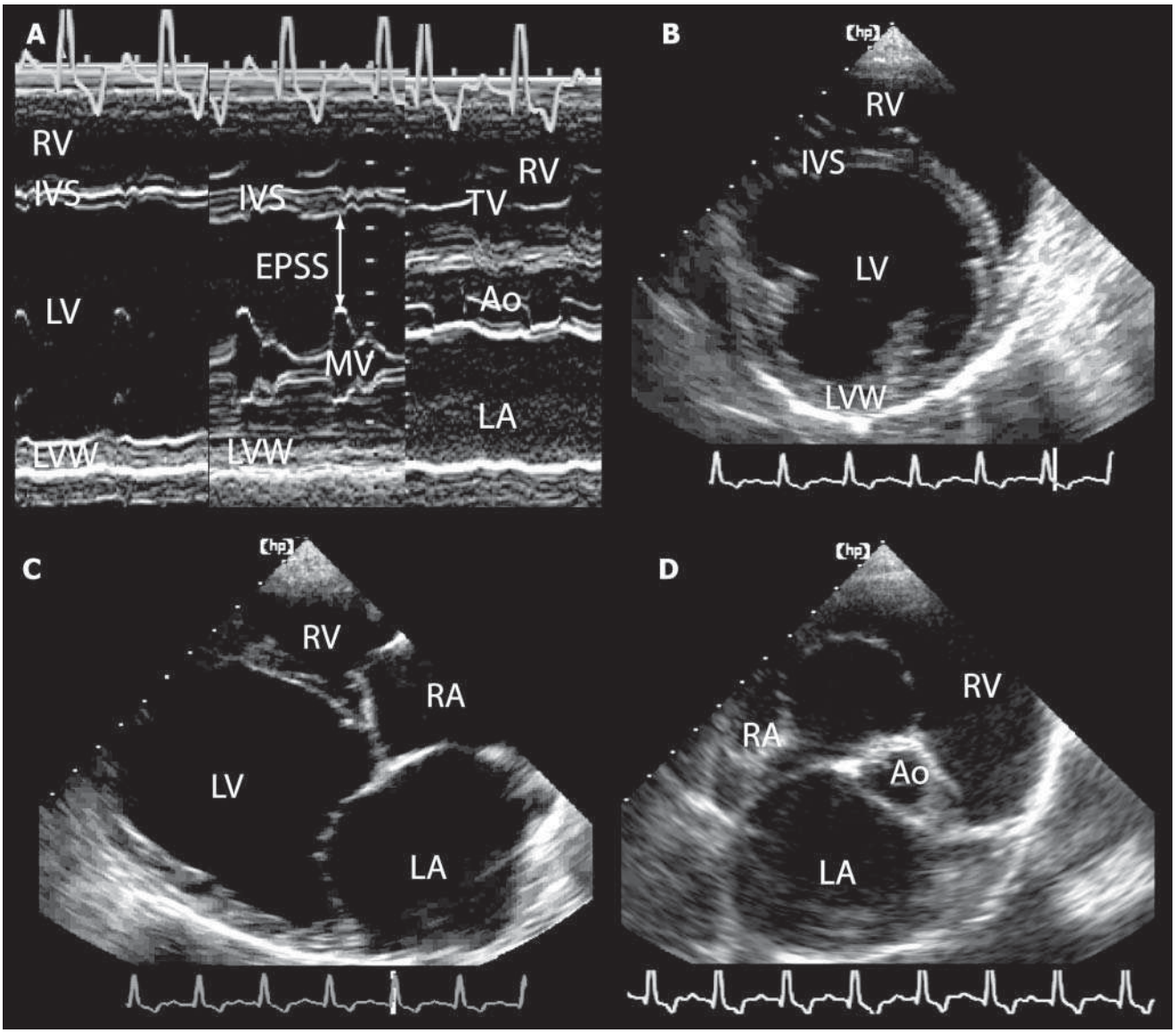


Figure 5.57. **DCM in a Boxer. A:** RPS M-mode recordings demonstrate dramatic LV dilation and decreased fractional shortening. The end point to septal separation distance (EPSS) is markedly increased, as is LA/Ao. RPS SAx **(B, D)** and LAx **(C)** 2DE images depict marked dilation of all chambers.

diseases may occur in some individuals and produce a mixed echocardiographic pattern.

Hypertrophic Cardiomyopathy

Hypertrophic cardiomyopathy (HCM), defined as a primary myocardial abnormality, is the most common acquired heart disease in cats and is reported as a rare condition in dogs (Fox 1999). Echocardiographic abnormalities caused by feline HCM relate principally to myocardial hypertrophy including increased absolute (interventricular septum [IVS] or LV wall [LVW]) or indexed wall thickness (wWT, wIVS, or wLVW), increased wall thickness relative to chamber dimension (RWT, FWT, or FWA – defined in Table 5.4), and indices suggestive of an actual increase in muscle mass (wWA) (Moise et al. 1986; see also Appendix). Increasing functional severity is commonly accompanied by progressive LA dilation (Figure 5.59). Although fractional shortening is typically normal to hyperdynamic in the early stages of the disease, cats with end-stage HCM may exhibit progressive systolic dysfunction and thinning of LV walls, probably secondary to myocardial ischemia and fibrosis (Cesta et al. 2005).

Motion-mode echocardiography is useful in quantifying HCM changes but also suffers from certain

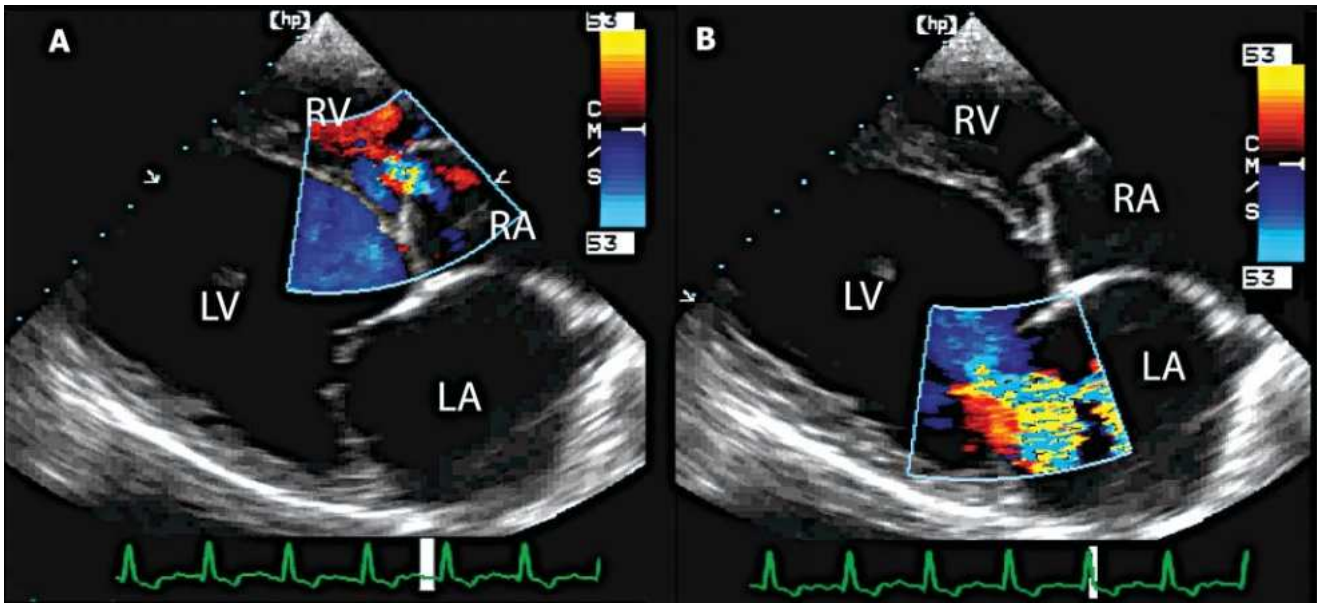


Figure 5.58. **Valvular regurgitation with DCM.** RPS LAx CFD images from the Boxer in Figure 5.57. Marked cardiac dilation contributes to TR **(A)** and MR **(B)**, which are commonly evident with the disease.

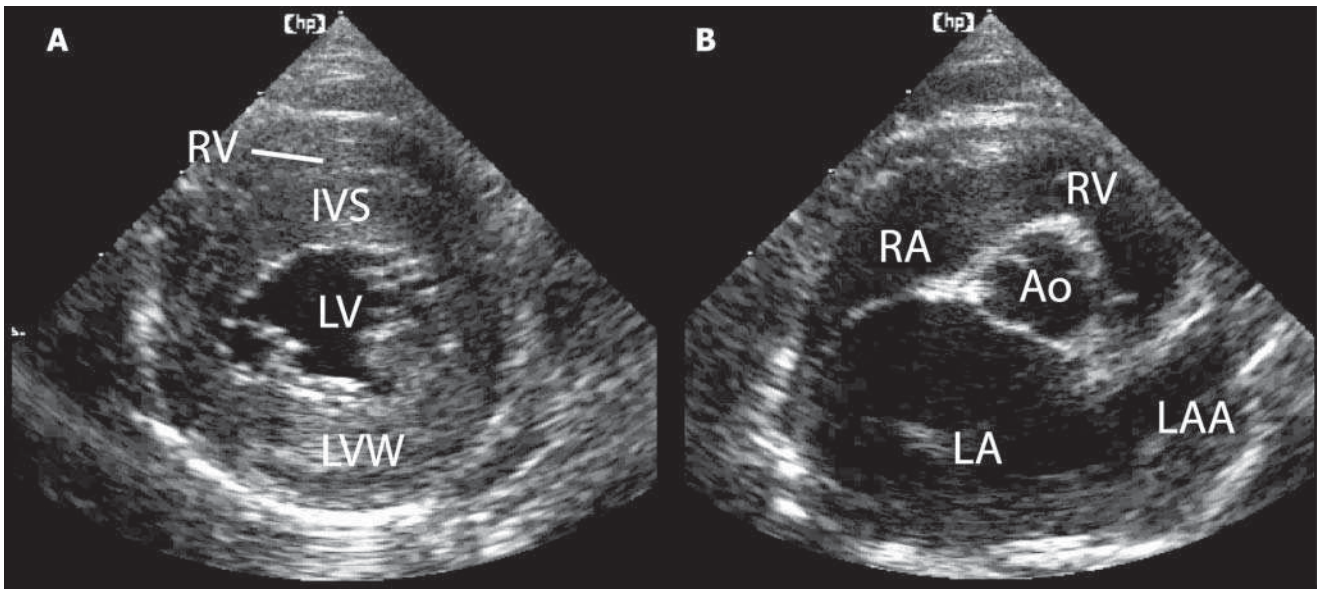


Figure 5.59. **HCM.** RPS SAx CFD images from a cat with HCM as suggested by thickening of the IVS and LVW, a decrease in LV internal dimension, and LA dilation.

limitations. The LV wall thickness in diastole (LVWd) is less than 0.55 cm normally, and values greater than 0.60 cm are suggestive of hypertrophy. However, subtle papillary muscle hypertrophy in mild cases (Adin and Diley-Poston 2007) or regional disparity in wall thickness may have no representation in an M-mode study. Systolic anterior motion (SAM) of the mitral valve is a functional abnormality, readily identified on M-mode recordings, that typifies obstructive HCM. The result is dynamic LV outflow obstruction and subvalvular AS (Figure 5.60).

The obstructive aspect of HCM is best assessed with the addition of Doppler methods. While SAM is a common source of outflow obstruction, hypertrophy of papillary muscles or muscular trabeculae may cause intraventricular obstruction, observed as a turbulent

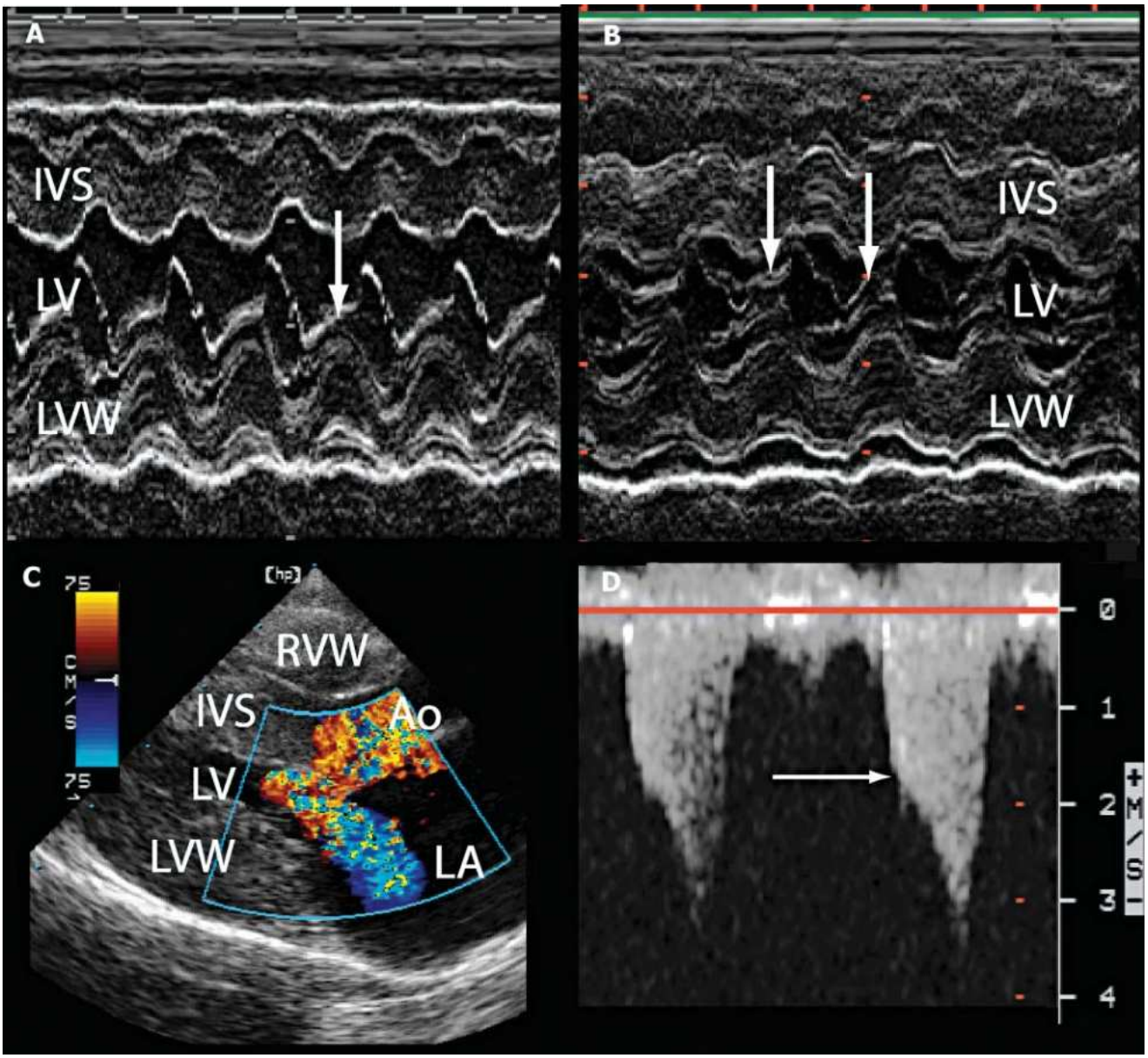


Figure 5.60. Dynamic LV outflow obstruction with HCM. M-mode recordings from cats with **(B)** and without **(A)** dynamic outflow obstruction secondary to HCM. There is pronounced thickening of the IVS and LVW in both cases. Arrows in both indicate the location of the MV during systole. **A:** Adequate separation between the IVS and MV coincides with an unobstructed LVOT. **B:** There is systolic anterior motion (SAM) of the MV; the MV is displaced into the LVOT and obstructs outflow. **C:** This RPS LAx CFD image displays the functional result of systolic obstruction, including both intra-Ao turbulences, caused by dynamic stenosis, and MR due to or accentuated by the SAM of the anterior MV leaflet. **D:** This LAp CWD recording from the LVOT depicts spectral broadening caused by turbulence, increased peak velocity, and a dagger-shaped velocity envelope. Increasing proximity of the MV to the interventricular septum, beginning at the arrow, causes an abrupt change in the envelope as the degree of obstruction increases.

systolic jet emanating from within the ventricular chamber. CWD recording establishes the outflow tract blood flow velocity associated with an obstruction. Study of mitral inflow velocities may suggest impaired diastolic function and/or elevated filling pressures (see the next section).

The development of intracardiac thrombi can sometimes be observed echocardiographically, particularly within the LA appendage (Figure 5.61). Stagnant blood flow can manifest echocardiographically as spontaneous echo contrast, so-called "smoke" within the left atrium, suggesting a high propensity for

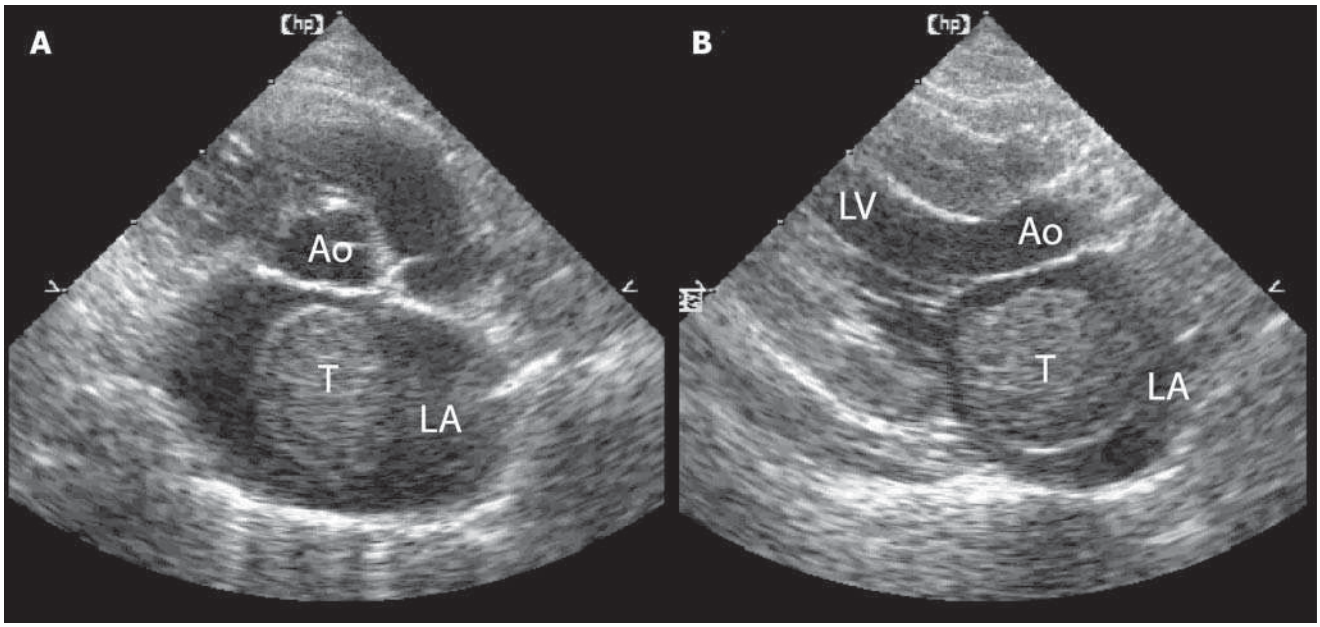


Figure 5.61. LA thrombus. RPS SAx **(A)** and LAx **(B)** images from a cat with restrictive cardiomyopathy demonstrating a free-floating echogenic thrombus (T) within the LA.

thrombus formation. Measurement of LA appendage flow velocity may also help to identify stagnant left atrial flow conditions in cats with cardiomyopathy, with velocities < 0.25 m/s having predictive value for cats at risk of spontaneous echo contrast and possible thrombus formation (Schober and Maerz 2006).

Restrictive and Unclassified Cardiomyopathy

Restrictive cardiomyopathy (RCM) includes a diverse array of diseases that can cause loss of ventricular compliance, restrictive physiology and, ultimately, severe signs of CHF (Fox 2004). The source of restriction in RCM may reside within the myocardium (myocardial RCM) or be localized to the endocardium (endomyocardial RCM).

Feline myocardial RCM is associated with a restrictive flow pattern characterized in severe cases by increased velocity of the mitral E wave followed by an abrupt termination of inflow with a shortened deceleration time (Figure 5.62; see also Figure 5.28). This pattern may occur in the presence of normal fractional shortening and ejection fraction and normal wall thicknesses or only mild hypertrophy. Atrial dilation is often dramatic in RCM, particularly involving the left chamber, and predisposes patients to thromboembolic events (Figure 5.61). The LV endomyocardial form, also known as endomyocardial fibrosis, may include increased endocardial thickness and echogenicity, distortion and dysfunction of the mitral apparatus, or strands of echogenic tissue that bridge the ventricular chamber walls. RCM is often diagnosed by exclusion of typical DCM and HCM morphological characteristics in the presence of clearly significant heart disease. Hence, echocardiographic findings may entail a wide range of features, and a notable fraction of feline cardiomyopathies are not readily classified morphologically (**unclassified cardiomyopathy**).

Pulmonary Hypertension, Cor Pulmonale, and Heartworm Disease (Dirofilariasis)

Pulmonary hypertension (PHT) is excessive pulmonary arterial pressure and may be caused by chronically elevated pulmonary venous pressure (left-sided CHF, pulmonary venous obstruction, mitral stenosis, or cor triatriatum sinister), pulmonary overcirculation (left-to-right shunts), or increased pulmonary vascular resistance (pulmonary thromboembolism, dirofilariasis, chronic respiratory disease and alveolar hypoxia, external vascular compression, vascular obliteration, persistent fetal circulation, or idiopathic PHT).

Cor pulmonale is RV hypertrophy and dysfunction caused by PHT not due to congenital heart disease or left heart failure causes. Evidence from 2DE of cor pulmonale may include thickening of the RV wall, papillary muscles, and trabeculae. RV and/or RA dilation may occur, particularly if significant tricuspid regurgitation results. The pulmonary trunk and main branches

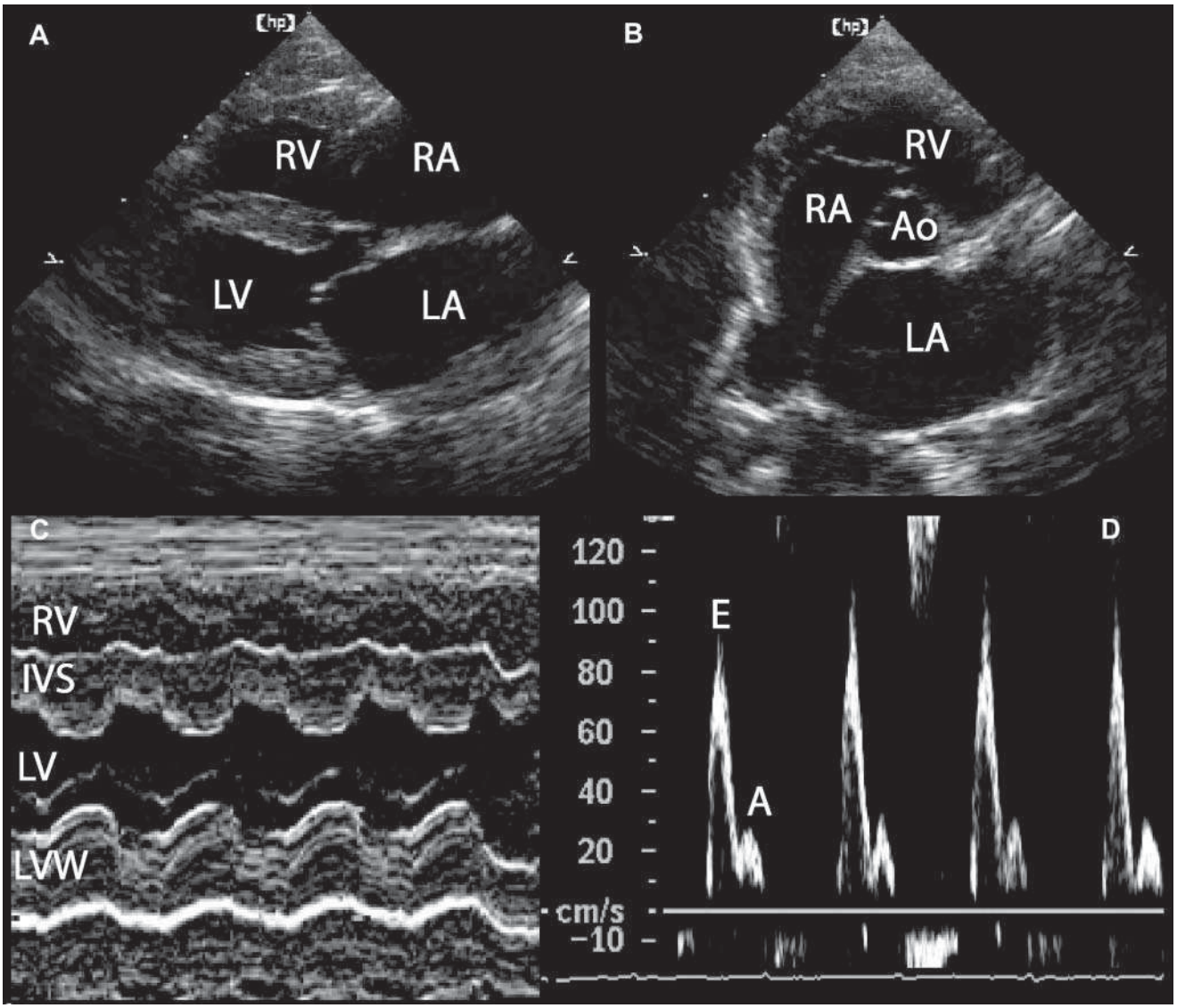


Figure 5.62. Restrictive cardiomyopathy (RCM). 2DE LAx **(A)** and SAx **(B)** images and M-mode **(C)** and PWD mitral inflow **(D)** recordings from a cat with RCM. There is dramatic atrial enlargement on the 2DE images, particularly of the left chamber; significant RV dilation is also present **(A)**. Nevertheless, wall thicknesses of all chambers are normal to mildly increased, while the LV internal chamber dimensions and fractional shortening are within normal limits **(C)**. The PWD recording **(D)** demonstrates a restrictive flow pattern. In this example, the E wave of mitral inflow is prominent, with mildly increased velocity, and the A wave is nearly absent; atrial contraction causes little additional ventricular filling because of loss of compliance (i.e., restriction).

may be dilated, which is an assessment made by comparison with the aorta. The left ventricle may appear ovoid in cross-section in the RPS short-axis image, with septal flattening because of compression and distortion imposed by the right heart; pseudohypertrophy of the left ventricle may occur from left-sided volume underload and septal hypertrophy (Figure 5.63). Paradoxical septal motion may be evident on M-mode recordings as systolic LV pressure distends the septum toward the transducer.

Doppler confirmation of PHT is made by CWD or at times by PWD quantification of tricuspid regurgitation or pulmonary insufficiency velocity; either or both may be caused by the excessive pressures and geometric distortion imposed by PHT (Figure 5.63). PHT might be associated with a modified flow-velocity pattern in the pulmonary artery (Figure 5.64). Different types of modified pattern suggestive of PHT have been described. However, these findings are of limited diagnostic value as they do not provide an accurate

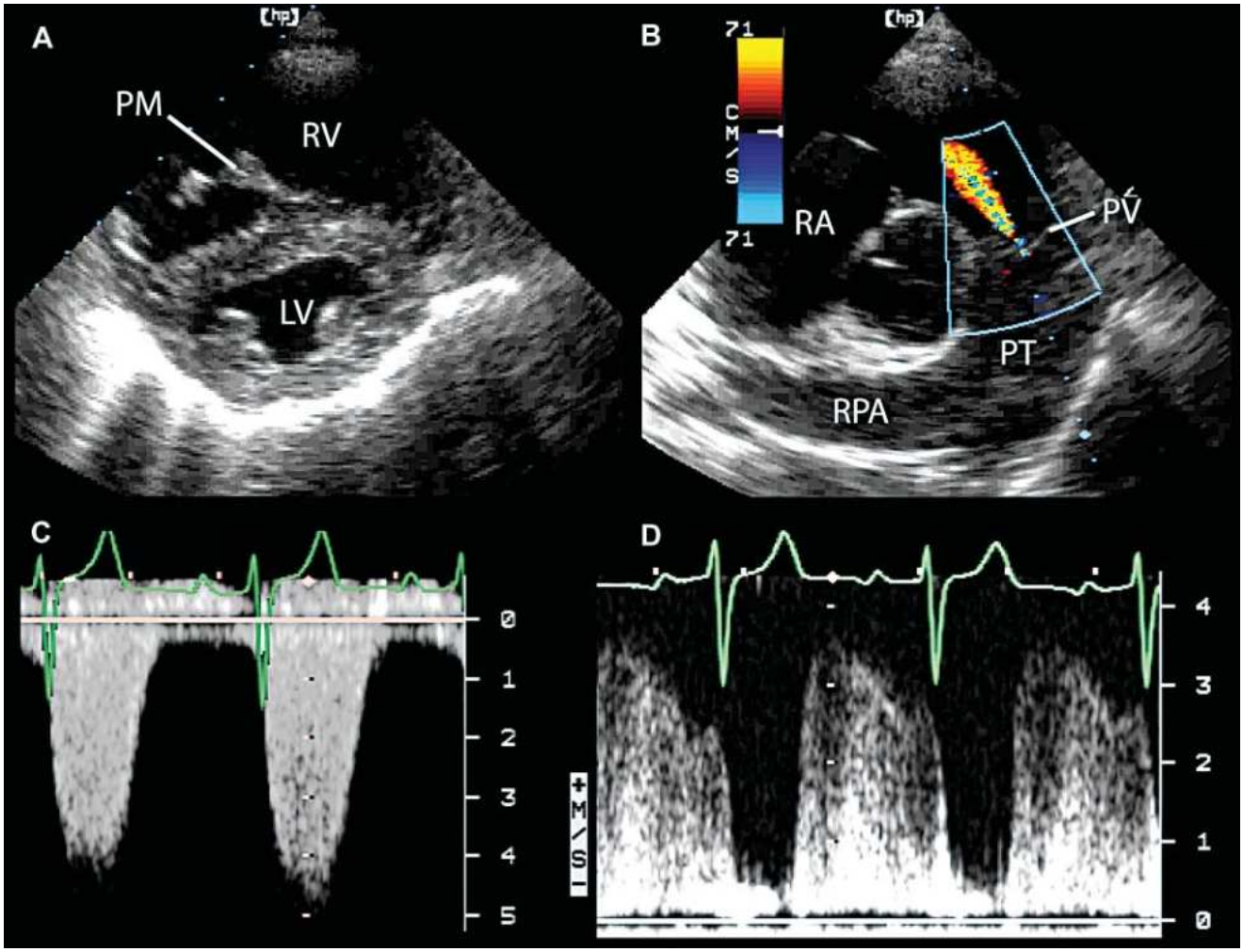


Figure 5.63. **Cor pulmonale in a dog with chronic respiratory disease. A:** This RPS SAx image depicts RV dilation, flattening of the IVS, and a small LV chamber. The RV PM is prominent because of hypertrophy, but RVW thickening is not dramatic. **B:** This CFD image demonstrates PV insufficiency, a normal finding except for the extent of the jet in this case, and dilation of the PT and RPA. CWD recordings of TR **(C)** and pulmonary insufficiency **(D)** confirm pulmonary hypertension in systole and diastole respectively. The peak TR velocity is greater than 4.5 m/s, which corresponds to a systolic driving pressure of greater than 80 mmHg and peak pulmonary insufficiency velocity of 3.5 m/s, with a diastolic driving pressure of about 50 mmHg.

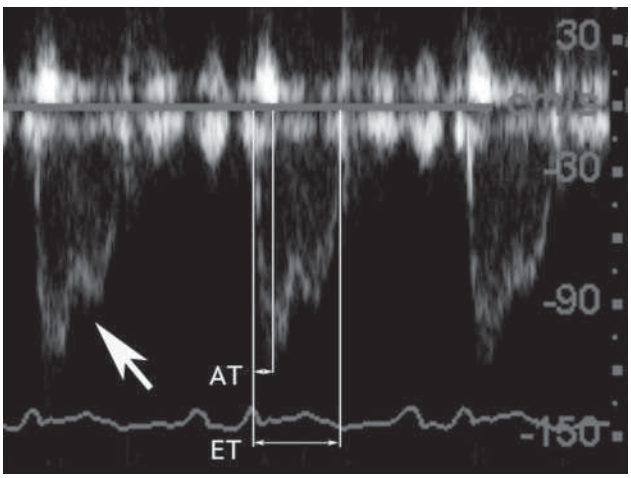


Figure 5.64. **Doppler flow pattern of pulmonary artery flow in a dog with pulmonary hypertension (PHT).** The AT is reduced (35 ms), as indicated by the steep slope of the acceleration phase, which resembles aortic flow acceleration pattern. The AT:ET ratio is also reduced (0.28 with ET of 135 ms). Such low values (under 58 ms and 0.31 respectively) are considered predictive for PHT. This dog had a peak TR velocity of 4.9 m/s, corresponding to a systolic pressure gradient of 96 mmHg (not shown). Given a fixed right atrial pressure estimate of 5 mmHg, the calculated PA pressure is 101 mmHg. Notice the notched envelope in the deceleration phase of the PA flow that might be seen with severe PHT (arrow).

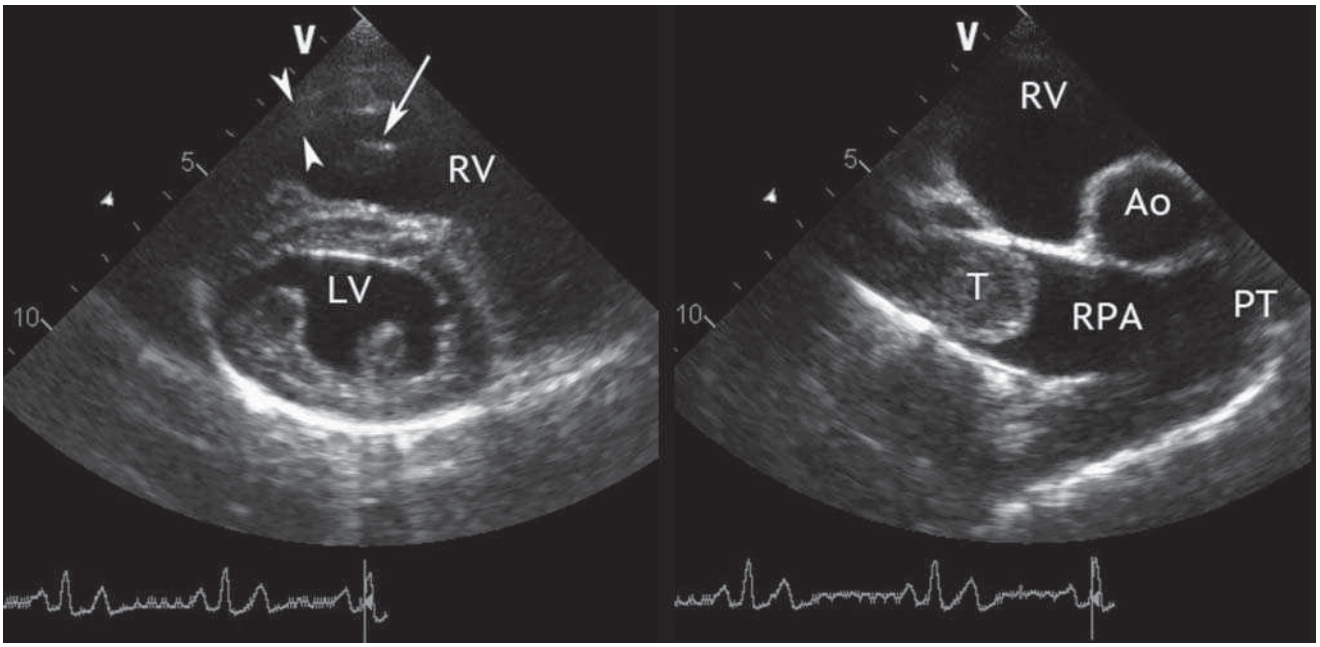


Figure 5.65. **Core pulmonale in a dog with pulmonary thromboembolism. A:** This 2DE RPS SAx image illustrates ventricular morphological changes secondary to PHT: RV dilation, papillary muscle (arrow) and RV wall (arrowheads) hypertrophy (suggesting chronicity), flattening of the interventricular septum and a small LV due to volume underloading. **B**: 2DE RPS SAx at the PT level. A large homogeneous and moderately echoic thrombus (T) is seen occluding the RPA lumen 2 cm distal to the PT branching. Notice the RPA and PT dilation: diameters of these vessels are larger than the Ao diameter.

estimation of the pulmonary arterial pressure (Uehara 1993). Several TDI-derived variables of the right ventricule have been proposed as indirect markers of PHT. These variables are particularly useful in the absence of measurable tricuspid regurgitation. A right ventricular AT of <58 ms and an AT:ET ratio of < 0.31 (Schober and Baade 2006) as well as a ratio of peak right myocardium velocities in early (E′) and late (A′) diastole (E′:A′ ratio) of <1.12 (Serres et al. 2007) have been found to be predictive of PHT (Figure 5.64).

Pulmonary thromboembolism can occasionally be confirmed echocardiographically as the cause of PHT (Figure 5.65) (Venco et al. 1998).

Heartworm disease (HWD or dirofilariasis) is an important cause of PHT and cor pulmonale in dogs. In addition to the echocardiographic abnormalities already noted, adult parasites may be visualized directly within the pulmonary arteries, right ventricle or right atrium, or vena cavae (Lombard and Buergelt 1983b) (Figure 5.66). Echocardiography is an insensitive test for HWD in dogs because parasites may reside entirely within lobar and distal pulmonary arteries, which are inaccessible to 2DE examination. Nevertheless, when adults may be visualized in more proximal locations of the pulmonary circulation, 2DE facilitates qualitative evaluation of a parasite burden that becomes moderate to marked. **Vena cava syndrome** is characterized by a dramatic parasite burden within the right ventricle, right atrium, and vena cava.

Adult heartworms have a distinctive echocardiographic appearance because of the echogenicity of the parasite's cuticle relative to the gut (Figure 5.66). Although still an insensitive test, echocardiography is an important adjunct for the diagnosis of HWD in cats where visualization of a single adult parasite confirms the condition.

Pericardial Disease

Pericardial effusion (PE), which is the most common disorder involving the pericardium, is readily recognized echocardiographically. Effusions may be idiopathic (*benign idiopathic* PE), neoplastic, cardiogenic (CHF), inflammatory, infectious, or hemorrhagic in origin. PE typically appears as an anechoic or variably echogenic space between the epicardial surface of the heart and the echogenic parietal pericardium (Bonagura and Pipers 1981). Any significant fluid accumulation within the pericardium should prompt the ultrasonographer to search for a cause (advanced heart disease, neoplasia, or potential cardiac rupture) before completing the study. Cardiac tamponade

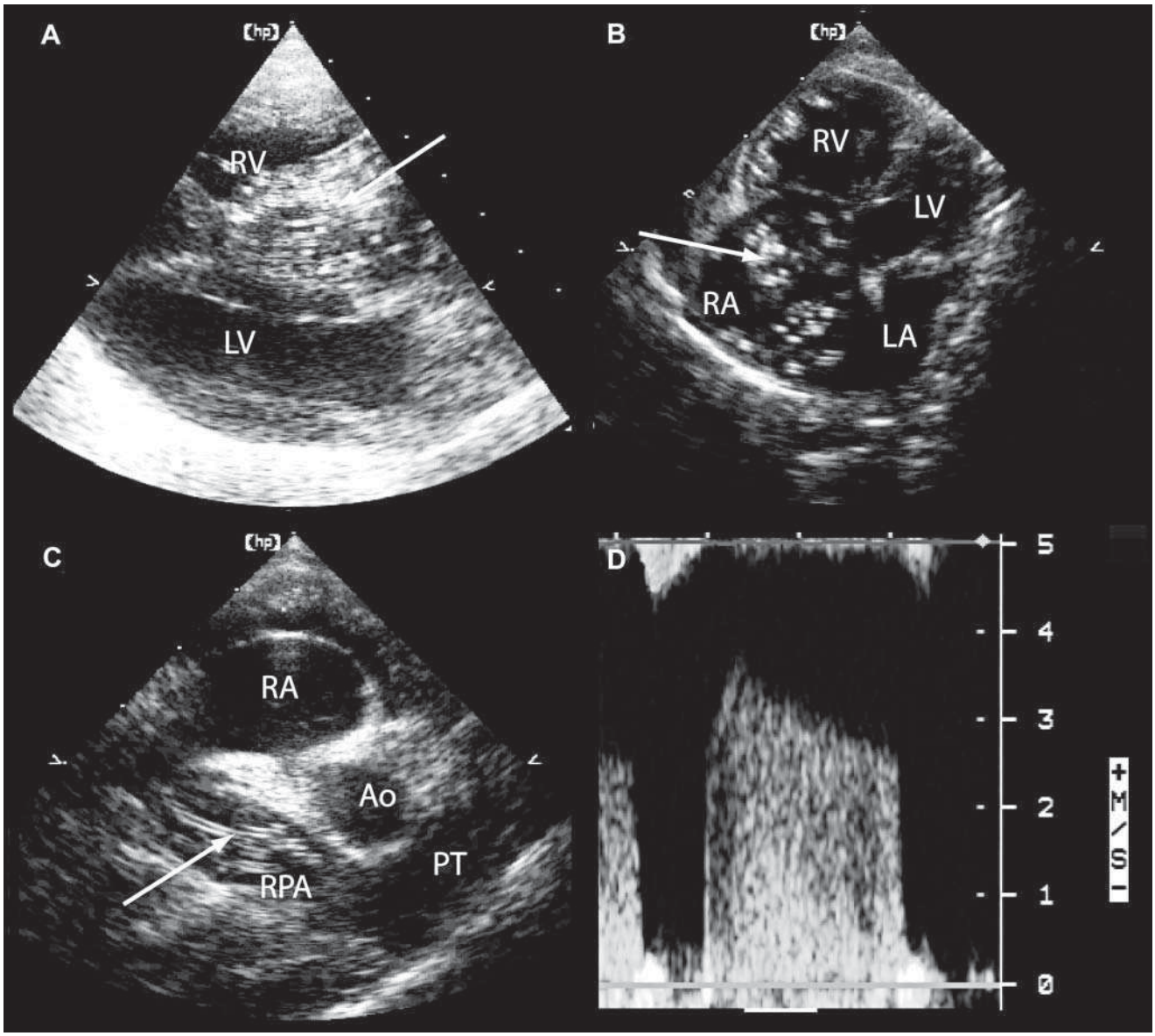


Figure 5.66. **Heartworm disease (dirofilariasis). A:** This RPS LAx image from a dog with vena cava syndrome depicts an extensive bolus of parasites flowing from the RA into the RV in early diastole (arrows indicate adult parasites in panels A–C). **B:** This LAp four-chamber image is from a rare case of vena cava syndrome in a cat with concurrent feline immunodeficiency virus infection. The RV and RA are dilated in both panels A and B. **C:** This RPS SAx image of the heart base demonstrates parasites in a more typical location within the RPA. A continuous-wave Doppler recording of PI demonstrates a peak diastolic velocity of 3.5 m/s between the PT and the RV, consistent with a driving pressure of 4×3.5^2 ~50 mmHg and pulmonary hypertension.

results when PE accumulation is sufficient to elevate the intrapericardial pressure at the level of or above the right heart filling pressure. Tamponade is characterized echocardiographically by decreased ventricular size and early diastolic collapse of the right atrium, right ventricle, or both. With large effusions, the heart may exhibit a swinging motion within the pericardial space, typically on an every-other-beat basis. This motion coincides with the electrocardiographic occurrence of electrical alternans and is heart rate dependent (Figure 5.67).

Cardiac Neoplasia

Echocardiography is well suited for the diagnosis of cardiac neoplasia, which is common in dogs and a

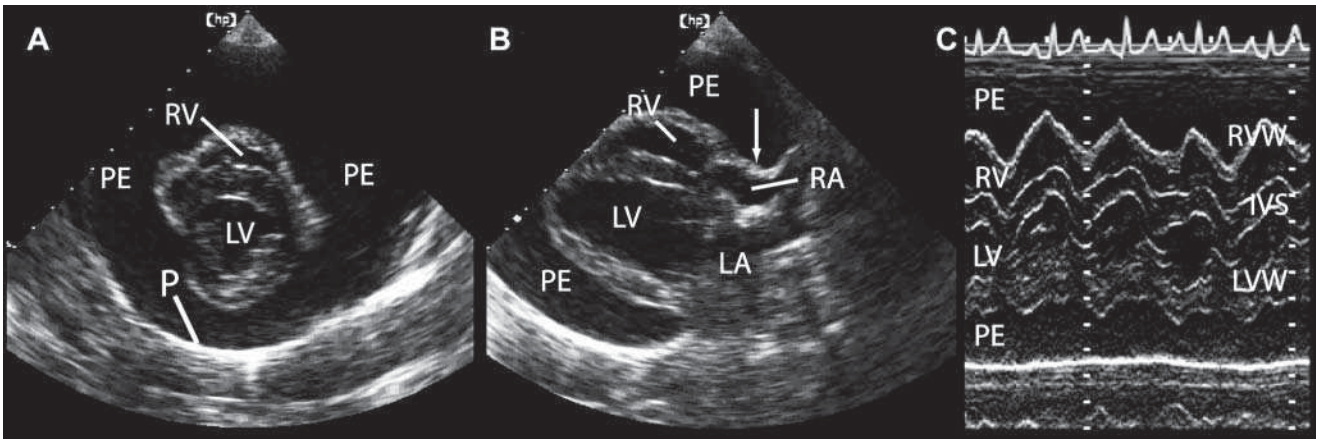


Figure 5.67. Pericardial effusion (PE) and tamponade. RPS SAx **(A)** and LAx **(B)** images from a dog with PE causing cardiac tamponade. There is a large anechoic space between the heart and the echogenic P. The LV and RV chambers are decreased in size. The RA exhibits early diastolic collapse in the LAx image (**B**, arrow). 2DE is superior for establishing the presence or absence of PE. However M-mode **(C)** is sometimes valuable for timing cardiac cycle events.

frequent cause of PE (Thomas et al. 1984). Hemangiosarcoma is the most common cardiac malignancy, with a strong site predilection for the RA appendage, right atrium, and RV wall. Small tumors on the RA appendage may often be visualized from either the LPS or RPS transducer positions, and visualization may be improved by placing the transducer at the most cranial aspect of the imaging window. Neoplasia cannot be ruled out by echocardiography, however, and multiple transducer positions should be attempted if a tumor is suspected. PE may improve tumor visualization, providing an echo-free zone for contrast. Hemangiosarcoma may appear mottled or cavitated because of hypoechoic collections of blood within the tumor (Figure 5.68).

Chemodectoma (aortic body tumor), which is a common tumor of brachiocephalic breeds, arises from aortic chemoreceptor cells that are often situated near the base of the heart (heart base tumor) (Thomas et al. 1984). Chemodectomas range in appearance from a small nodule, seemingly adherent to the ascending aorta, to a large mass that partially or completely surrounds the great vessel. Tumors are most often biologically benign and cause clinical signs from PE or compression of the trachea or heart. Echocardiographic examination of a heart base tumor may necessitate imaging the ascending aorta far dorsal to the heart (Figure 5.69).

Thyroid carcinoma may arise from ectopic thyroid tissue, typically located at the heart base or within the RV outflow tract. Tumors may cause PE or obstruction of the RV outflow tract (Figure 5.69).

Mesothelioma involving the pericardium may be difficult to diagnose echocardiographically because it does not typically produce a discrete, echogenic mass. Pericardial and/or pleural effusion of unexplained origin must include this cell type as a differential.

Cardiac neoplasia in cats is uncommon. Lymphoma may occur within the heart, as one or more discrete masses or as a diffuse, infiltrative lesion causing altered and irregular echogenicity and/or PE.

Miscellaneous Acquired Disease

Echocardiography is an insensitive method for the detection of **pulmonary thromboembolism**, but may provide evidence of chronicity (cor pulmonale) or hemodynamic severity (right-sided pressures, acute dilation, and RV stroke volume). Occasionally, thrombi may be visible in the pulmonary trunk or main branches (Figure 5.65). CFD or echocontrast may be valuable in delineating a thrombus, thereby improving diagnostic accuracy.

Systemic hypertension (SHT), which is common in both dogs and cats, may cause nonspecific echocardiographic changes because of left-sided pressure overload. LV wall thickness and indices of LV hypertrophy may be increased with chronic SHT. Alterations can resemble mild to moderate HCM in cats and thus require blood pressure determination for differentiation. Inconsistently, the aortic root and proximal aorta may be dilated with mild to moderate aortic insufficiency. In the absence of LV outflow obstruction, peak MR velocity > 6.3 m/s suggests SHT with peak systolic pressure > 160 mmHg.

Hyperthyroidism is the most common endocrinopathy in cats, and concurrent, nonspecific echocardiographic abnormalities are often observed. LV wall

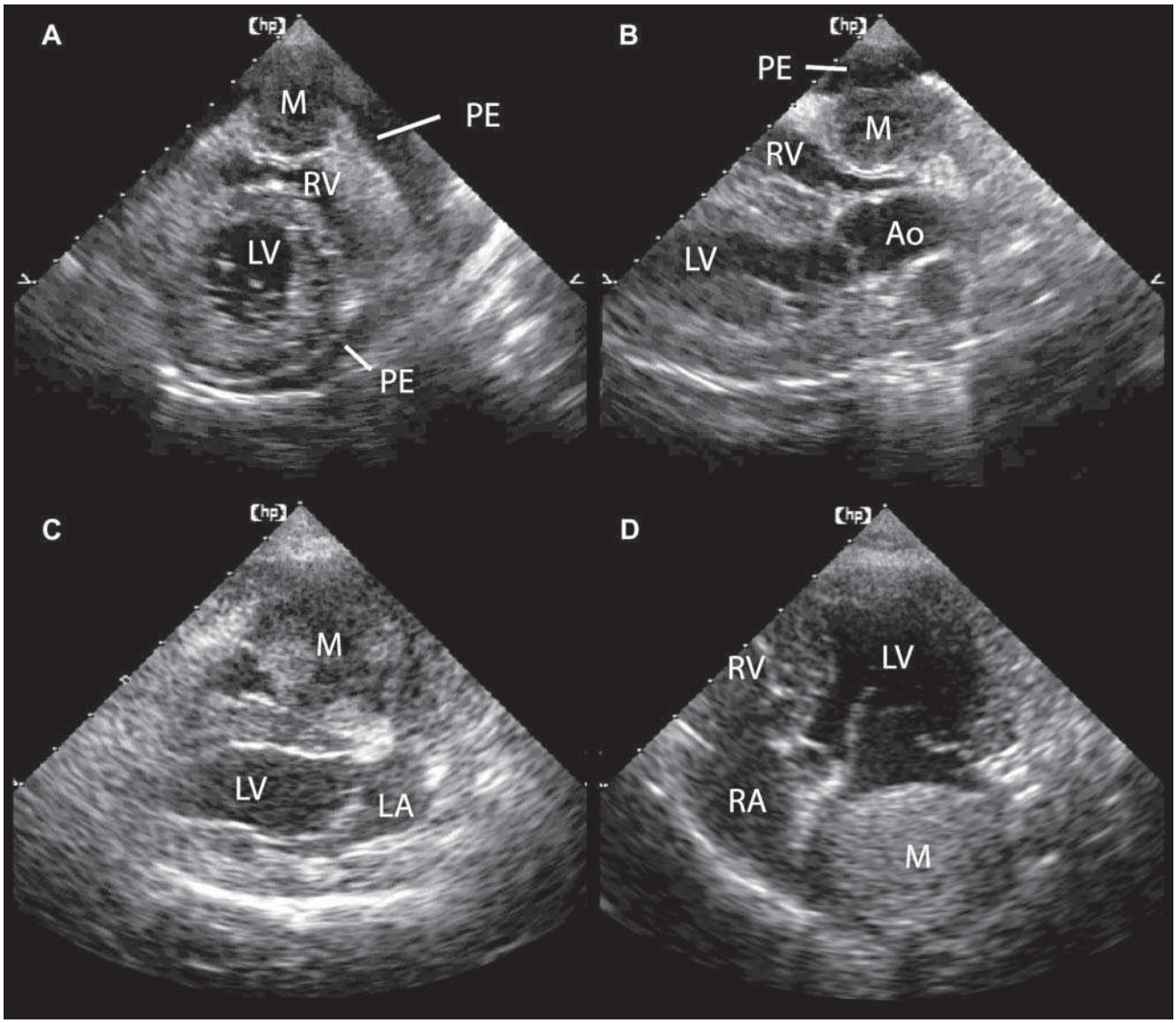


Figure 5.68. Hemangiosarcoma (HSA). RPS SAx **(A)** and LAx **(B)** 2DE images illustrate the typical location for HSA in a dog. A large mass (M) appears at the junction of the RVW and RA in this case. A small amount of pericardial effusion is evident (PE) because of extension of the tumor and bleeding into the pericardial space. **C, D:** Two variations of atypical cardiac HSA: a large mass (M) fills the RV and RA in the RPS LAx image **(C)**; a mass fills the LA in the LAp four-chamber view **(D)**.

thickening and hypertrophy may occur, and the condition may resemble HCM of mild to moderate severity echocardiographically (Moise et al. 1986). Tachycardia and increased indices of stroke volume (e.g., wΔA) may result, with variable dilation of all cardiac chambers. Atrioventricular valvular regurgitation may accompany the condition if there is sufficient remodeling of the heart to impair valve function, and CHF with pulmonary edema and/or pleural effusion may occur in severe cases. Hyperthyroid cats are occasionally seen with cardiac changes resembling DCM, including marked chamber dilation and depressed fractional shortening.

Interventional Procedures

Pericardiocentesis (PC) is both a therapeutic and a diagnostic procedure. Pericardial effusion (PE) associated with clinical signs due to cardiac compression (tamponade) is the major indication for PC. PC is also indicated in obtaining a sample of PE for diagnostic analysis.

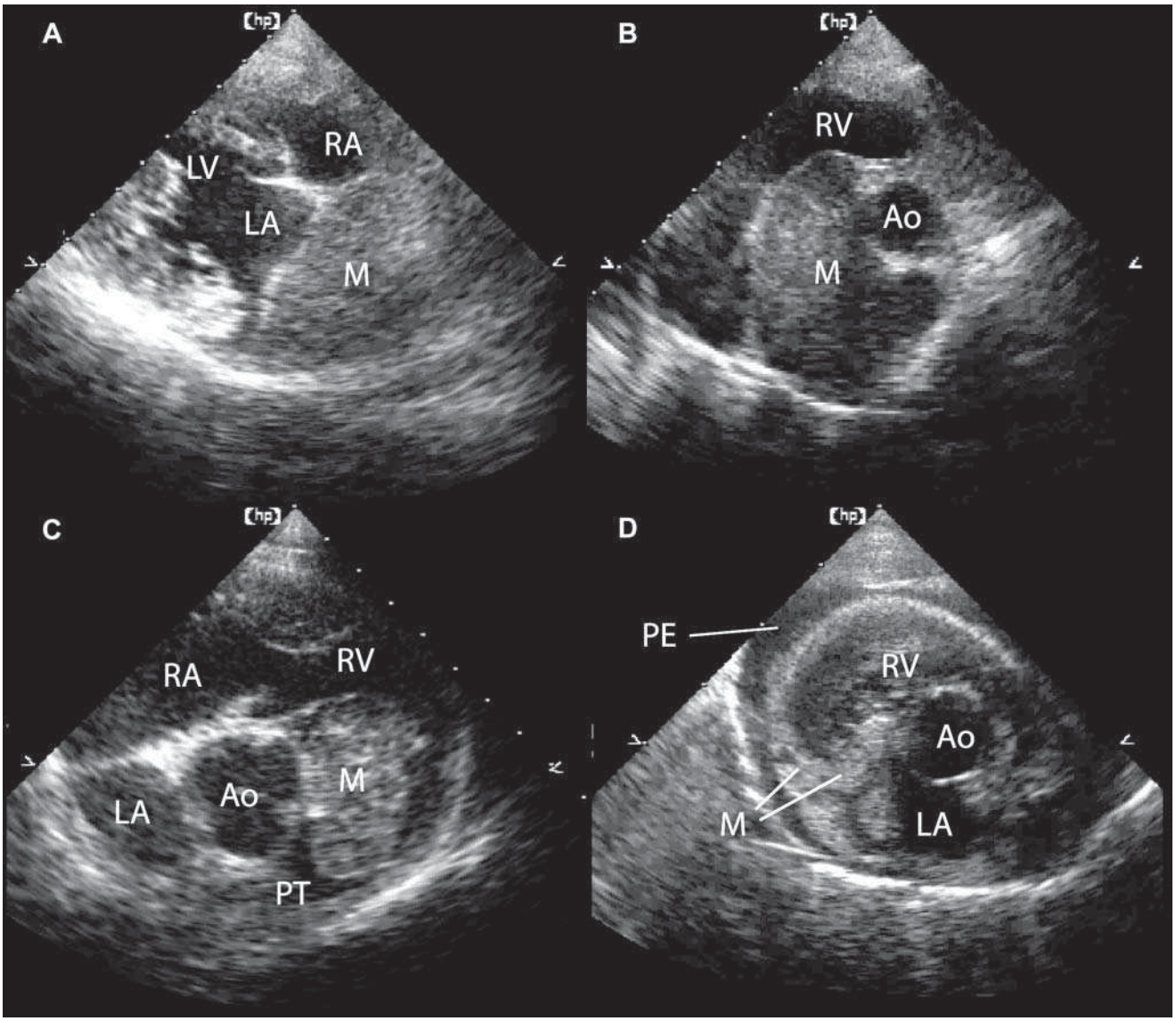


Figure 5.69. **Cardiac neoplasia. A, B:** RPS LAx and SAx views from a dog with a large mass (M) at the heart base. **C:** A thyroid carcinoma (M) is apparent on this RPS SAx view at a typical location in the RVOT. **D:** A SAx RPS image from a cat with echogenic cardiac metastases (M) from a carcinoma. A small amount of pericardial effusion (PE) is also evident.

Insufficient PE volume is the main contraindication for PC if the risk of the procedure outweighs the potential benefits. Relative contraindications include hemorrhagic PE secondary to bleeding disorders or atrial tear, because reducing the pericardial pressure may perpetuate hemorrhage. Distension of the pericardium by solid tumors or abdominal contents as seen in peritoneal-pericardial diaphragmatic hernia is also a contraindication for PC. The most common cause of pericardial effusion in cats is CHF, and pericardiocentesis is rarely indicated in these cases (Hall et al. 2007).

The required equipment list includes a 14- to 18-gauge over-the-needle catheter (2–5 inches [5.08–12.7 cm], depending on patient size), syringes (3–50 mL), three-way stopcock, extension tubing, and collection tubes or apparatus for cytology (ethylenediaminetetraacetic acid, EDTA) and culture submission.

Sedation and local analgesia are useful and can be obtained with diazepam (0.2 mg/kg) intravenous (IV) in combination with either butorphanol (0.2 mg/kg) IV or oxymorphone (0.1 mg/kg) IV. Agents promoting hypotension must be avoided (e.g., acepromazine).

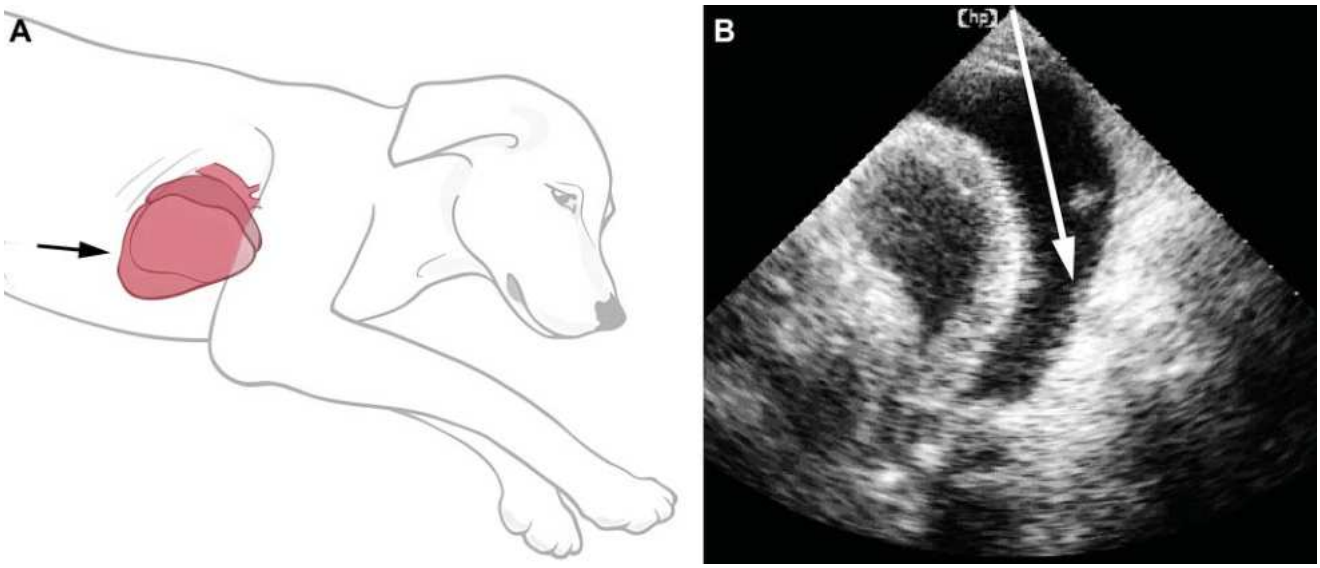


Figure 5.70. **Pericardiocentesis in a dog. A:** The catheter is placed at the fifth to seventh intercostal spaces of the right ventral thorax, at the level of the costochondral junction (arrow). **B:** The arrow indicates the orientation and position of an imaginary needle within the fluid-filled pericardial sac.

The patient is usually positioned in left lateral or sternal recumbency. Electrocardiographic monitoring for heart rate and rhythm during the procedure is essential. The catheter entry location is at the fifth to seventh intercostal space of the right ventral thorax, at the level of the costochondral junction (Figure 5.70). Ultrasound guidance is highly useful in directing the catheter, in confirming the distribution and amount of PE, in establishing the optimal catheter entry point and direction, and in confirming the catheter position. Needle entry should be near the center of the rib space to avoid puncture of the intercostal vessels and also catheter kinking and obstruction by a rib as the patient breathes.

Using aseptic technique, the operator attaches a sterile 3-ml syringe to the catheter, positions the point of the catheter at the predetermined location, and orients the direction of the catheter dorsocranially. The entire apparatus is advanced through the skin and thoracic wall while mild negative pressure (suction) is applied with the syringe. A burst of ventricular premature complexes on the electrocardiogram suggests that the catheter tip is in contact with the epicardium; this requires catheter retraction until the dysrhythmia resolves. The flexible catheter is advanced off the stylus into the pericardial space, and the metal catheter stylus is then fully withdrawn. Extension tubing is attached directly to the flexible catheter end, leading to a large syringe and interposed three-way stopcock operated by an assistant.

With tamponade, decompression of the pericardial space by even a small amount often causes an observable decrease in heart rate. A continual decrease in heart rate throughout the procedure is suggestive of correct catheter placement, whereas any trend toward increased heart rate should prompt the operator to interrupt aspiration and re-evaluate catheter position. Once the catheter tip positioning within the pericardial space is assured, complete and rapid evacuation of PE may proceed (exceptions: atrial tear or bleeding disorder). Significant ventricular arrhythmias should prompt catheter repositioning and/or partial withdrawal. Intravenous administration of a 2% lidocaine bolus (2–4 mg/kg = 1–2 ml per 10 kg) should be considered if the dysrhythmia does not abate promptly.

Potential complications of PC include puncture of cardiac chambers or great vessels, cardiac dysrhythmia, coronary laceration, exsanguination, pulmonary laceration or hemorrhage, and pneumothorax. Complications are minimized by careful preparation and technique.



Visit our website at **www.SmallAnimalUltrasonography.com** for complementary video clips with annotations and text on:

- Normal short and long axes of the heart (dog)
- Normal short and long axes of the heart (cat)
- Chronic degenerative valvular disease
- Hypertrophic cardiomyopathy in a cat
- Dilated cardiomyopathy in a dog
- Pulmonary hypertension/cor pulmonale in a dog
- Idiopathic pericardial effusion and tamponade in a dog

- Cardiac tumor
- Patent ductus arteriosus in a dog
- Pulmonic stenosis in a dog
- Ventricular septal defect in a cat

References

Abbott JA, MacLean HN (2003) Comparison of Doppler-derived peak aortic velocities obtained from subcostal and apical transducer sites in healthy dogs. Vet Radiol Ultrasound 44:695–698.

Abbott JA, MacLean HN (2006) Two-dimensional echocardiographic assessment of the feline left atrium. J Vet Intern Med 20:111–119.

Adin DB, Diley-Poston L (2007) Papillary muscle measurements in cats with normal echocardiograms and cats with concentric left ventricular hypertrophy. J Vet Intern Med 21(4):737–741.

Baumwart RD, Meurs KM, Atkins CE, Bonagura JD, et al. (2005) Clinical, echocardiographic, and electrocardiographic abnormalities in Boxers with cardiomyopathy and left ventricular systolic dysfunction: 48 cases (1985–2003). J Am Vet Med Assoc 226:1102–1104.

Bonagura JD (1983) M-mode echocardiography: Basic principles. Vet Clin North Am Small Anim Pract 13:299–319.

Bonagura JD, Herring DS (1985a) Echocardiography: Acquired heart disease. Vet Clin North Am Small Anim Pract 15:1209–1224.

Bonagura JD, Herring DS (1985b) Echocardiography: Congenital heart disease. Vet Clin North Am Small Anim Pract 15:1195–1208.

Bonagura JD, Miller MW (1998) Doppler echocardiography II: Color Doppler imaging. Vet Clin North Am Small Anim Pract 28:1361–1389.

Bonagura JD, Miller MW, Darke PGG (1998) Doppler echocardiography I. Pulsed-wave and continuous-wave examinations. Vet Clin North Am Small Anim Pract 28:1325–1359.

Bonagura JD, O'Grady MR, Herring DS (1985) Echocardiography: Principles of interpretation. Vet Clin North Am Small Anim Pract 15:1177–1194.

Bonagura JD, Pipers FS (1981) Echocardiographic features of pericardial effusion in dogs. J Am Vet Med Assoc 179:49–56.

Bonagura JD, Schober KE (2009) Can ventricular function be assessed by echocardiography in chronic canine mitral valve disease? J Small Anim Pract 50(Suppl. 1):12–24.

Brown DJ, Knight DH, King RR (1991a) Use of pulsed-wave Doppler echocardiography to determine aortic and pulmonary velocity and flow varables in clinically normal dogs. Am J Vet Res 52:543–550.

Brown DJ, Rush JE, MacGregor J, Ross JN Jr, et al. (2005) Quantitative echocardiographic evaluation of mitral endocardiosis in dogs using ratio indices. J Vet Intern Med 19:542–552.

Buchanan JW (2001) Pathogenesis of single right coronary artery and pulmonic stenosis in English Bulldogs. J Vet Intern Med 15:101–104.

Calvert CA, Chapman WL Jr, Toal RL (1982) Congestive cardiomyopathy in Doberman pinscher dogs. J Am Vet Med Assoc 181:598–602.

Cesta MF, Baty CJ, Keene BW, Smoak IW, et al. (2005) Pathology of end stage remodeling in a family of cats with hypertrophic cardiomyopathy. Vet Pathol 42:458–67.

Chetboul V, Carlos Sampedrano C, Gouni V, Concordet D, et al. (2005) Quantitative assessment of regional right ventricular myocardial velocities in awake dogs by Doppler tissue imaging: Repeatability, reproducibility, effect of body weight and breed, and comparison with left ventricular myocardial velocities. J Vet Intern Med 19:837–844.

Darke PGG (1992) Doppler echocardiography. J Small Anim Pract 33:104–112.

Darke PGG, Bonagura JD, Miller M (1993a) Transducer orientation for Doppler echocardiography in dogs. J Small Anim Pract 34:2–8.

Fonfara S, Martinez Pereira Y, Swift S, Copeland H, et al. (2010) Balloon valvuloplasty for treatment of pulmonic stenosis in English Bulldogs with an aberrant coronary artery. J Vet Intern Med 24:354–359.

Fox PR (1999) Feline cardiomyopathies. In: Fox PR, Sisson D, Moise NS, eds. Textbook of Canine and Feline Cardiology: Principles and Clinical Practice, 2nd edition. Philadelphia: WB Saunders, pp 621–678.

Fox PR (2004) Endomyocardial fibrosis and restrictive cardiomyopathy: pathologic and clinical features. J Vet Cardiol. 2004 6:25–31.

Francis AJ, Johnson MJ, Culshaw GC, Corcoran BM, et al. (2011) Outcome in 55 dogs with pulmonic stenosis that did not undergo balloon valvuloplasty or surgery. J Small Anim Pract 52:282–288.

Fujii Y, Nishimoto Y, Sunahara H, Takano H et al. (2012) Prevalence of patent foramen ovale with right-to-left shunting in dogs with pulmonic stenosis. J Vet Intern Med 26:183–185.

Goodwin JK, Holland M (1995) Contrast echoartography as an aid in the diagnosis of right-to-left shunting patent ductus arteriosus. Vet Radiol Ultrasound 36:157–159.

Hall DJ, Shofer F, Meier CK, Sleeper MM (2007) Pericardial effusion in cats: a retrospective study of clinical findings and outcome in 146 cats. J Vet Intern Med. 21:1002–1007.

Hall DJ, Cornell CC, Crawford S, Brown DJ (2008a) Meta-analysis of normal canine echocardiographic dimensional data using ratio indices. J Vet Cardiol 10:11–23.

Hansson K, Haggstrom J, Kvart C, Lord P (2002) Left atrial to aortic root indices using two-dimensional and M-mode echocardiography in cavalier King Charles spaniels with and without left atrial enlargement. Vet Radiol Ultrasound 43:568–575.

Harvey AM, Battersby IA, Faena M, Fews D, et al. (2005) Arrhythmogenic right ventricular cardiomyopathy in two cats. J Small Anim Pract 46:151–156.

Hatle LK, Angelsen B (1985) Physics of blood flow. In: Doppler Ultrasound in Cardiology: Physics, Principles, and Clinical Applications, 2nd edition. Philadelphia: Lea and Febiger, pp 8–31.

Henry WL, DeMaria A, Gramiak R, King DL, et al. (1980) Report of the American Society of Echocardiography Committee on Nomenclature and Standards in Two-dimensional Echocardiography. Circulation 62:212–217.

Jung S, Orvalho J, Griffiths LG (2012) Aortopulmonary window characterized with two- and three-dimensional echocardiogram in a dog. J Vet Cardiol 14:371–375.

Kirberger RM, Bland-van den Berg P, Grimbeek RJ (1992a) Doppler echocardiography in the normal dog. Part II: Factors influencing blood flow velocities and a comparison between left and right heart blood flow. Vet Radiol Ultrasound 33:380–386.

Kittleson MD, Brown WA (2003) Regurgitant fraction measured by using the proximal isovelocity surface area method in dogs with chronic myxomatous mitral valve disease. J Vet Intern Med 17:84–88.

Kittleson MD, Eyster GE, Knowlen GG, Olivier NB, et al. (1984) Myocardial function in small dogs with chronic mitral regurgitation and severe congestive heart failure. J Am Vet Med Ass 184:455–459.

Lombard CW, Buergelt CD (1983a) Vegetative bacterial endocarditis in dogs: Echocardiographic diagnosis and clinical signs. J Small Anim Pract 24:325–339.

Lombard CW, Buergelt CD (1983b) Echocardiographic and clinical findings in dogs with heartworm-induced cor pulmonale. Compend Contin Educ Pract Vet 5:971–979.

Loyer C, Thomas W (1995) Biplane transesophageal echocardiography in the dog: technique, anatomy and imaging planes. Vet Radiol Ultrasound 36:212–226.

Moise NS (1989) Doppler echocardiographic evaluation of congenital cardiac disease. J Vet Intern Med 3:195–207.

Moise NS, Dietze AE, Mezza LE, Strickland D, et al. (1986) Echocardiography, electrocardiography, and radiography of cats with dilatation cardiomyopathy, hypertrophic cardiomyopathy, and hyperthyroidism. Am J Vet Res 47:1476–1486.

O'Grady MR, Bonagura JD, Powers JD, Herring DS (1986) Quantitative cross-sectional echocardiography in the normal dog. Vet Radiol Ultrasound 27:34–49.

O'Rourke RA, Hanrath P, Henry WN, Hugenholts PG, et al. (1984) Report of the Joint International Society and Federation of Cardiology/World Health Organization Task Force on recommendations for standardization of measurements from M-mode echocardiograms. Circulation 69:854A–857A.

Pariaut R, Sydney Moïse N, Kraus MS, Gelzer AR, et al. (2004) Use of transesophageal echocardiography for visualization of the patent ductus arteriosus during transcatheter coil embolization. J Vet Cardiol 6:32–39.

Rishniw M, Erb HN (2000) Evaluation of four 2-dimensional echocardiographic methods of assessing left atrial size in dogs. J Vet Intern Med 14:429–435.

Sahn DJ, DeMaria A, Kisslo J, Weyman A (1978) Recommendations regarding quantitation in M-mode echocardiography: Results of a survey of echocardiographic measurements. Circulation 58:1072–1083.

Saunders AB, Achen SE, Gordon SG, Miller MW 2010 Utility of transesophageal echocardiography for transcatheter occlusion of patent ductus arteriosus in dogs: influence on the decision-making process. J Vet Intern Med 24:1407–1413.

Schiller NB, Shah PM, Crawford M, DeMaria A, et al. (1989) Recommendations for quantitation of the left ventricle by two-dimensional echocardiography. American Society of Echocardiography Committee on Standards, Subcommittee on Quantitation of Two-dimensional Echocardiograms. J Am Soc Echocardiogr 2:358–367.

Schober KE, Baade H (2006) Doppler echocardiographic prediction of pulmonary hypertension in West Highland white terriers with chronic pulmonary disease. J Vet Intern Med 20:912–920.

Schober KE, Hart TM, Stern JA, Li X, et al. (2010) Detection of congestive heart failure in dogs by Doppler echocardiography. J Vet Intern Med 24:1358–1368.

Schober KE, Stern JA, DaCunha DN, Pedraza-Toscano AM, et al. (2008) Estimation of left ventricular filling pressure by Doppler echocardiography in dogs with pacing-induced heart failure. J Vet Intern Med 22:578–585.

Schober KE, Hart TM, Stern JA, Li X, et al. (2011) Effects of treatment on respiratory rate, serum natriuretic peptide concentration, and Doppler echocardiographic indices of left ventricular filling pressure in dogs with congestive heart failure secondary to degenerative mitral valve disease and dilated cardiomyopathy. J Am Vet Med Assoc 239: 468–479.

Schober KE, Maerz I (2006) Assessment of left atrial appendage flow velocity and its relation to spontaneous echocardiographic contrast in 89 cats with myocardial disease. J Vet Intern Med 2006 20:120–130.

Serres F, Chetboul V, Gouni V, Tissier R, et al. (2007) Diagnostic value of echo-Doppler and tissue Doppler imaging in dogs with pulmonary arterial hypertension. J Vet Intern Med. 21:1280–1289.

Thomas WP (1984) Two-dimensional, real-time echocardiography in the dog. Vet Radiol Ultrasound 25:50–64.

Thomas WP, Gaber CE, Jacobs GJ, Kaplan PM, et al. (1993) Recommendations for standards in transthoracic two-dimensional echocardiography in the dog and cat. J Vet Intern Med 7:247–252.

Thomas WP, Sisson D, Bauer TG, Reed JR (1984) Detection of cardiac masses in dogs by two-dimensional echocardiography. Vet Radiol Ultrasound 25:65–72.

Uehara Y (1993) An attempt to estimate the pulmonary artery pressure in dogs by means of pulsed Doppler echocardiography. J Vet Med Sci 55:307–312.

Venco L, Calzolari D, Morini S (1998) Pulmonary thromboembolism in a dog with renal amyloidosis. Vet Radiol Ultrasound 39:564–565.

Visser LC, Scanse BA, Schober KE (2013) Single left coronary ostium and an anomalous prepulmonic right coronary artery in 2 dogs with congenital pulmonary valve stenosis. J Vet Cardiol 15:161–169.

APPENDIX

Canine breed-specific M-mode reference values: unindexed

Reference	Breed	N	BW (kg)	LVIDd (cm)	LVIDs (cm)	IVSd (cm)	IVSs (cm)	LVWd (cm)	LVWs (cm)	Ao (cm)	LA (cm)
Morrison et al. 1992	Miniature Poodle	20	3.0[b] [1.4–9.0]	2.00[b] [1.60–2.80]	1.00[b] [0.80–1.60]	0.50[b] [0.40–0.60]	0.80[b] [0.60–1.00]	0.50[b] [0.40–0.60]	0.80[b] [0.60–1.00]	1.00[b] [0.80–1.30]	1.20b [0.80–1.80]
Della Torre et al. 2000[a]	Italian Greyhound	20	5.4 ± 1.5 [3.2–8.4]	2.22 ± 0.27 [1.63–2.66]	1.28 ± 0.28 [0.84–1.76]	0.64 ± 0.11 [0.44–0.85]	0.91 ± 0.13 [0.69–1.15]	0.71 ± 0.09 [0.49–0.92]	1.02 ± 0.08 [0.86–1.19]		
Haggstromaa Cornell et al. 2004	Cavalier King Charles Spaniel	57	8.9 ± 1.4 [5.5–11.9]	2.92 ± 0.31 [2.20–3.55]	1.96 ± 0.25 [1.50–2.70]			0.70 ± 0.09 [0.50–0.85]		1.60 ± 0.15 [1.20–2.00]	1.60 ± 0.19 [1.10–2.25]
Crippa et al. 1992	Beagle	20	8.9 ± 1.5 [5.9–11.9]	2.63 [1.95–3.31]	1.57 [0.89–2.25]	0.67 [0.45–0.89]	0.96 [0.66–1.26]	0.82 [0.44–1.20]	1.14 [0.76–1.52]		
Pedersen[a] Cornell et al. 2004	Dachshund	33	9.5 ± 1.9 [6.2–16.0]	2.84 ± 0.33 [2.20–3.60]	1.88 ± 0.29 [1.20–2.60]	0.70 ± 0.10 [0.50–0.80]	0.95 ± 0.11 [0.70–1.20]	0.68 ± 0.13 [0.40–0.90]	1.01 ± 0.14 [0.70–1.20]	1.82 ± 0.18 [1.50–2.30]	1.63 ± 0.23 [1.00–2.10]
Baade et al. 2002	West Highland White Terrier	24	10.3 ± 0.9 [8.5–12.1]	2.88 [1.74–4.02]	2.00 [1.26–2.74]	0.69 [0.41–0.97]	1.02 [0.52–1.52]	0.64 [0.40–0.88]	0.98 [0.72–1.24]		
Gooding et al. 1986	English Cocker Spaniel	12	12.2 ± 2.4 [8.5–15.8]	3.38 ± 0.35 [2.90–4.00]	2.23 ± 0.29 [1.90–2.80]	0.82 ± 0.14 [0.50–0.90]		0.79 ± 0.12 [0.50–0.90]			
Morrison et al. 1992	Welsh Corgi	20	15.0[b] [8.0–19.0]	3.20[b] [2.80–4.00]	1.90[b] [1.20–2.30]	0.80[b] [0.60–0.90]	1.20[b] [1.00–1.40]	0.80[b] [0.60–1.00]	1.20[b] [0.80–1.30]	1.80[b] [1.50–2.20]	2.10[b] [1.20–2.40]
Sisson and Schaeffer 1991	English Pointer	16	19.2 ± 2.8 [13.6–24.9]	3.92 ± 0.24 [3.44–4.40]	2.53 ± 0.24 [2.05–3.01]	0.69 ± 0.11 [0.47–0.91]	1.06 ± 0.10 [0.86–1.26]	0.71 ± 0.07 [0.57–0.85]	1.15 ± 0.13 [0.89–1.41]	2.41 ± 0.17 [2.07–2.75]	2.26 ± 0.20 [1.86–2.66]
Morrison et al. 1992	Afghan Hound	20	23.0[b] [17.0–36.0]	4.20[b] [3.30–5.20]	2.80[b] [2.00–3.70]	1.30[b] [0.80–1.80]	1.30[b] [0.80–1.80]	0.90[b] [0.70–1.10]	1.20[b] [0.90–1.80]	2.60[b] [2.00–3.40]	2.60[b] [1.80–3.50]
Page et al. 1993	Greyhound	16	26.6 ± 3.5 [20.7–32.5]	4.41 ± 0.30 [4.00–4.90]	3.25 ± 0.35 [2.90–3.80]	1.06 ± 0.17 [0.80–1.40]	1.34 ± 0.26 [1.00–1.70]	1.21 ± 0.17 [0.90–1.40]	1.53 ± 0.22 [1.20–1.80]		
Della Torre et al. 2000[a]	Greyhound	20	26.9 ± 3.3 [21.7–31.5]	4.27 ± 0.28 [3.88–4.92]	3.21 ± 0.25 [2.84–3.66]	1.19 ± 0.13 [0.9–1.51]	1.57 ± 0.13 [1.33–1.85]	1.29 ± 0.11 [1.13–1.49]	1.71 ± 0.13 [1.54–2.04]		
Snyder et al. 1995[a]	Greyhound	11	29.1 ± 3.7 [24.9–36.3]	4.69 ± 0.30 [3.98–4.98]	3.33 ± 0.26 [2.84–3.63]	1.34 ± 0.17 [1.04–1.61]		1.16 ± 0.17 [0.82–1.34]			
Vollmar[a] Cornell et al. 2004	Boxer	75	31.0 ± 4.8 [22.5–43.0]	4.13 ± 0.38 [3.27–5.08]	2.78± 0.31 [2.0–3.59]	0.97 ± 0.16 [0.65–1.27]	1.38 ± 0.22 [1.00–1.90]	0.98 ± 0.13 [0.66–1.26]	1.46 ± 0.18 [1.08–1.95]	2.28 ± 0.22 [1.82–3.00]	2.46 ± 0.31 [1.72–3.46]
Morrison et al. 1992	Golden Retriever	20	32.0[b] [23.0–41.0]	4.50[b] [3.70–5.10]	2.70[b] [1.80–3.50]	1.00[b] [0.80–1.30]	1.40[b] [1.00–1.70]	1.00[b] [0.80–1.20]	1.50[b] [1.00–1.90]	2.40[b] [1.40–2.70]	2.70[b] [1.60–3.20]
Calvert and Brown 1986	Doberman Pinscher	21	36.0 [31.0–42.0]	4.68 ± 0.42 [4.10–5.50]	3.08 ± 0.33 [2.50–3.60]	0.96 ± 0.06 [0.80–1.00]	1.43 ± 0.07 [1.30–1.50]	0.96 ± 0.06 [0.90–1.00]	1.41 ± 0.08 [1.30–1.50]	2.99 ± 0.23 [2.80–3.50]	2.66 ± 0.15 [2.20–2.80]
Bayon et al. 1994	Spanish Mastiff	12	52.4 ± 3.3 [45.8–59.0]	4.77 ± 0.14 [4.50–5.04]	2.90 ± 0.11 [2.69–3.11]	0.98 ± 0.04 [0.89–1.06]	1.56 ± 0.05 [1.46–1.66]	0.97 ± 0.04 [0.90–1.04]	1.52 ± 0.04 [1.43–1.60]	2.76 ± 0.08 [2.61–2.91]	2.85 ± 0.09 [2.67–3.03]
Koch et al. 1996	Newfoundland	27	61.0 [47.0–69.5]	5.00 [4.40–6.00]	3.55 [2.90–4.40]	1.15 [0.70–1.50]	1.50 [1.10–2.00]	1.00 [0.80–1.30]	1.50 [1.10–1.60]	2.90 [2.60–3.30]	3.00 [2.40–3.30]
Koch et al. 1996	Great Dane	15	62.0 [52.0–75.0]	5.30 [4.40–5.90]	3.95 [3.40–4.50]	1.45 [1.20–1.60]	1.65 [1.40–1.90]	1.25 [1.00–1.60]	1.60 [1.10–1.90]	2.95 [2.80–3.40]	3.30 [2.80–4.60]
Vollmar[a] Cornell et al. 2004	Irish Wolfhound	144	63.5 ± 8.3 [45.0–91.0]	5.07 ± 0.37 [4.30–5.97]	3.35 ± 0.33 [2.55–4.09]	1.11 ± 0.19 [0.56–1.67]	1.55 ± 0.22 [1.03–2.13]	1.06 ± 0.16 [0.66–1.44]	1.58 ± 0.19 [1.19–2.21]	3.29 ± 0.30 [2.71–4.13]	3.18 ± 0.31 [2.47–3.89]
Koch et al. 1996	Irish Wolfhound	20	68.5 [50.0–80.0]	5.00 [4.60–5.90]	3.60 [3.30–4.50]	1.20 [0.90–1.45]	1.50 [1.10–1.70]	1.00 [0.90–1.30]	1.40 [1.10–1.70]	3.00 [2.90–3.10]	3.10 [2.20–3.50]

[a]Original data supplied by investigators. All others from referenced sources.

[b]Mean or median ± standard deviation [range].

Ao, aorta; BW, body weight; IVSd, interventricular septal thickness, diastole; IVSs, interventricular septal thickness, systole; LA, left atrium; LVIDd, left ventricular internal dimension, diastole; LVIDs, left ventricular internal dimension, systole; LVWd, left ventricular wall thickness, diastole; and LVWs, left ventricular wall thickness, systole.

Canine breed-specific M-mode reference values indexed for body size (weight-based ratio indices)

Reference	Breed	N	BW (kg)	wLVIDd	wLVIDs	wIVSd	wIVSs	wLVWd	wLVWs	wAo	wLA
Morrison et al. 1992	Miniature Poodle	20	3.0[b] [1.4–9.0]	1.74[b] [1.40–2.44]	0.87[b] [0.70–1.40]	0.44[b] [0.35–0.52]	0.70[b] [0.52–0.87]	0.44[b] [0.35–0.52]	0.70[b] [0.52–0.87]	0.87[b] [0.70–1.13]	1.05[b] [0.70–1.57]
Della Torre et al. 2000[a]	Italian Greyhound	20	5.4 ± 1.5 [3.2–8.4]	1.61 ± 0.18 [1.17–1.88]	0.93 ± 0.17 [0.62–1.22]	0.46 ± 0.06 [0.34–0.57]	0.66 ± 0.07 [0.52–0.80]	0.51 ± 0.05 [0.42–0.65]	0.74 ± 0.07 [0.61–0.86]		
Haggstroma[a] Cornell et al. 2004	Cavalier King Charles Spaniel	57	8.9 ± 1.4 [5.5–11.9]	1.78 ± 0.16 [1.40–2.16]	1.19 ± 0.14 [0.91–1.60]			0.42 ± 0.05 [0.34–0.52]		0.98 ± 0.09 [0.78–1.19]	0.97 ± 0.10 [0.76–1.24]
Crippa et al. 1992	Beagle	20	8.9 ± 1.5 [5.9–11.9]	1.60 [1.18–2.01]	0.95 [0.54–1.37]	0.41 [0.27–0.54]	0.58 [0.40–0.76]	0.50 [0.27–0.73]	0.69 [0.46–0.92]		
Pedersen[a] Cornell et al. 2004	Dachshund	33	9.5 ± 1.9 [6.2–16.0]	1.70 ± 0.19 [1.32–2.37]	1.12 ± 0.16 [0.72–1.51]	0.42 ± 0.05 [0.29–0.53]	0.57 ± 0.06 [0.41–0.66]	0.41 ± 0.07 [0.24–0.53]	0.61 ± 0.08 [0.42–0.75]	1.08 ± 0.09 [0.90–1.25]	0.98 ± 0.14 [0.60–1.18]
Baade et al. 2002	West Highland White Terrier	24	10.3 ± 0.9 [8.5–12.1]	1.66 [1.01–2.32]	1.16 [0.73–1.58]	0.40 [0.24–0.56]	0.59 [0.30–0.88]	0.37 [0.23–0.51]	0.57 [0.42–0.72]		
Gooding et al. 1986	English Cocker Spaniel	12	12.2 ± 2.4 [8.5–15.8]	1.85 ± 0.14 [1.62–2.04]	1.22 ± 0.14 [1.02–1.41]	0.45 ± 0.08 [0.25–0.55]		0.44 ± 0.08 [0.25–0.55]			
Della Torre et al. 2000[a]	Whippet	20	14.5 ± 2.1 [10.8–20.2]	1.86 ± 0.12 [1.56–2.03]	1.25 ± 0.14 [0.96–1.49]	0.44 ± 0.05 [0.32–0.52]	0.64 ± 0.06 [0.45–0.72]	0.46 ± 0.05 [0.40–0.60]	0.67 ± 0.10 [0.56–0.92]		
Morrison et al. 1992	Welsh Corgi	20	15.0[b] [8.0–19.0]	1.63[b] [1.43–2.04]	0.97[b] [0.61–1.17]	0.41[b] [0.31–0.46]	0.61[b] [0.51–0.71]	0.41[b] [0.31–0.51]	0.61[b] [0.41–0.66]	0.92[b] [0.76–1.12]	1.07[b] [0.61–1.22]
Sisson and Schaeffer 1991	English Pointer	16	19.2 ± 2.8 [13.6–24.9]	1.84 ± 0.11 [1.62–2.07]	1.19 ± 0.11 [0.96–1.41]	0.32 ± 0.05 [0.22–0.43]	0.50 ± 0.05 [0.40–0.59]	0.33 ± 0.03 [0.27–0.40]	0.54 ± 0.06 [0.42–0.66]	1.13 ± 0.08 [0.97–1.29]	1.06 ± 0.09 [0.87–1.25]
Wey[a] Cornell et al. 2004	Generic	47	20.8 ± 13.0 [2.2–47.4]	1.75 ± 0.16 [1.45–2.09]	1.16 ± 0.19 [0.62–1.42]	0.40 ± 0.06 [0.28–0.54]	0.56 ± 0.11 [0.38–0.92]	0.40 ± 0.05 [0.29–0.50]	0.57 ± 0.09 [0.39–0.78]		
Morrison et al. 1992	Afghan Hound	20	23.0[b] [17.0–36.0]	1.86[b] [1.46–2.30]	1.24[b] [0.88–1.64]	0.57[b] [0.35–0.80]	0.57[b] [0.35–0.80]	0.40[b] [0.31–0.49]	0.53[b] [0.40–0.80]	1.15b [0.88–1.50]	1.15b [0.80–1.55]
de Madron 1983	Generic	27	24.4 ± 19.2 [2.7–95.0]	1.91 ± 0.16 [1.49–2.16]	1.29 ± 0.16 [0.99–1.68]	0.36 ± 0.08 [0.23–0.54]	0.52 ± 0.07 [0.36–0.65]	0.33 ± 0.07 [0.22–0.52]	0.51 ± 0.09 [0.32–0.72]	1.06 ± 0.15 [0.81–1.38]	1.05 ± 0.17 [0.39–1.26]
Brown et al. 2003	Generic	50	25.2 ± 17.4 [2.3–76.4]	1.59 ± 0.15 [1.30–1.85]	1.04 ± 0.16 [0.78–1.36]	0.44 ± 0.06 [0.28–0.57]	0.59 ± 0.09 [0.40–0.79]	0.41 ± 0.06 [0.29–0.57]	0.60 ± 0.08 [0.43–0.76]	1.00 ± 0.12 [0.81–1.43]	1.01 ± 0.11 [0.76–1.26]
Page et al. 1993	Greyhound	16	26.6 ± 3.5 [20.7–32.5]	1.86 ± 0.12 [1.69–2.06]	1.37 ± 0.15 [1.22–1.60]	0.45 ± 0.07 [0.34–0.59]	0.56 ± 0.11 [0.42–0.72]	0.51 ± 0.07 [0.38–0.59]	0.64 ± 0.09 [0.51–0.76]		

(*Continued*)

Canine breed-specific M-mode reference values indexed for body size (weight-based ratio indices) (*Continued*)

Reference	Breed	N	BW (kg)	wLVIDd	wLVIDs	wIVSd	wIVSs	wLVWd	wLVWs	wAo	wLA
Della Torre et al. 2000[a]	Greyhound	20	26.9 ± 3.3 [21.7–31.5]	1.79 ± 0.13 [1.62–2.05]	1.35 ± 0.10 [1.22–1.58]	0.05 ± 0.04 [0.43–0.62]	0.66 ± 0.04 [0.54–0.74]	0.54 ± 0.04 [0.49–0.60]	0.72 ± 0.05 [0.65–0.90]		
Goncalves et al. 2002[a]	Generic	70	27.7 ± 19.5 [3.9–97.7]	1.52 ± 0.14 [1.21–1.79]	0.95 ± 0.13 [0.61–1.24]	0.52 ± 0.08 [0.38–0.70]	0.70 ± 0.09 [0.54–0.93]	0.42 ± 0.11 [0.29–1.15]	0.63 ± 0.10 [0.45–0.91]	0.93 ± 0.12 [0.71–1.48]	1.13 ± 0.14 [0.89–1.50]
Snyder et al. 1995[a]	Greyhound	11	29.1 ± 3.7 [24.9–36.3]	1.92 ± 0.12 [1.68–2.12]	1.37 ± 0.11 [1.20–1.54]	0.55 ± 0.07 [0.44–0.67]		0.48 ± 0.06 [0.34–0.55]			
Lombard[a] Cornell et al. 2004	Generic	23	30.1 ± 7.8 [21.0–44.0]	1.76 ± 0.17 [1.37–2.01]	1.10 ± 0.13 [0.82–1.34]			0.42 ± 0.04 [0.35–0.53]		1.01 ± 0.08 [0.80–1.17]	0.98 ± 0.13 [0.62–1.14]
Vollmar[a] Cornell et al. 2004	Boxer	75	31.0 ± 4.8 [22.5–43.0]	1.66 ± 0.14 [1.39–2.09]	1.12 ± 0.12 [0.84–1.43]	0.39 ± 0.06 [0.27–0.50]	0.55 ± 0.08 [0.41–0.77]	0.40 ± 0.05 [0.26–0.52]	0.59 ± 0.07 [0.42–0.81]	0.92 ± 0.08 [0.79–1.16]	0.99 ± 0.11 [0.73–1.30]
Morrison et al. 1992	Golden Retriever	20	32.0[b] [23.0–41.0]	1.78[b] [1.47–2.02]	1.07[b] [0.71–1.39]	0.40[b] [0.32–0.51]	0.55[b] [0.40–0.67]	0.40[b] [0.32–0.48]	0.59[b] [0.40–0.75]	0.95[b] [0.55–1.07]	1.07[b] [0.63–1.27]
Calvert and Brown 1986	Doberman Pinscher	21	36.0 [31.0–42.0]	1.78 ± 0.16 [1.56–2.09]	1.17 ± 0.13 [0.95–1.37]	0.37 ± 0.02 [0.30–0.38]	0.54 ± 0.02 [0.50–0.57]	0.37 ± 0.02 [0.34–0.38]	0.54 ± 0.03 [0.50–0.57]	1.14 ± 0.09 [1.07–1.33]	1.01 ± 0.06 [0.84–1.07]
Bayon et al. 1994	Spanish Mastiff	12	52.4 ± 3.3 [45.8–59.0]	1.60 ± 0.05 [1.51–1.69]	0.97 ± 0.04 [0.90–1.05]	0.33 ± 0.01 [0.30–0.36]	0.53 ± 0.02 [0.49–0.56]	0.33 ± 0.01 [0.30–0.35]	0.51 ± 0.01 [0.48–0.54]	0.93 ± 0.03 [0.88–0.98]	0.96 ± 0.03 [0.90–1.02]
Koch et al. 1996	Newfoundland	27	61.0 [47.0–69.5]	1.60 [1.41–1.92]	1.13 [0.93–1.41]	0.37 [0.22–0.48]	0.48 [0.35–0.64]	0.32 [0.26–0.42]	0.48 [0.35–0.51]	0.93 [0.83–1.05]	0.96 [0.77–1.05]
Koch et al. 1996	Great Dane	15	62.0 [52.0–75.0]	1.68 [1.40–1.87]	1.26 [1.08–1.43]	0.46 [0.38–0.51]	0.52 [0.44–0.60]	0.40 [0.32–0.51]	0.51 [0.35–0.60]	0.94 [0.89–1.08]	1.05 [0.89–1.46]
Vollmar[a] Cornell et al. 2004	Irish Wolfhound	144	63.5 ± 8.3 [45.0–91.0]	1.60 ± 0.12 [1.33–1.88]	1.06 ± 0.11 [0.83–1.29]	0.35 ± 0.06 [0.19–0.51]	0.49 ± 0.07 [0.32–0.67]	0.33 ± 0.05 [0.21–0.47]	0.50 ± 0.06 [0.37–0.65]	1.04 ± 0.09 [0.89–1.30]	1.01 ± 0.11 [0.73–1.26]
Koch et al. 1996	Irish Wolfhound	20	68.5 [50.0–80.0]	1.54 [1.41–1.81]	1.11 [1.01–1.38]	0.37 [0.28–0.45]	0.46 [0.34–0.52]	0.31 [0.28–0.40]	0.43 [0.34–0.52]	0.92 [0.89–0.95]	0.95 [0.68–1.08]

[a]Original data supplied by investigators. All others estimated from referenced sources.
[b]Mean or median, ± standard deviation [range].
Index formulas from Table 5.3.

Canine breed-specific M-mode functional and relative indices

Reference	Breed	N	BW (kg)	FS	EF	wAA	FWTd	FWAd	wWAd	wWAs
Della Torre et al. 2000[a]	Italian Greyhound	20	5.4 [3.2–8.4]	0.43 [0.32–0.56]	0.80 [0.68–0.92]	1.75 [0.98–2.25]	0.38 [0.30–0.45]	0.61 [0.51–0.70]	4.11 [2.63–5.20]	4.58 [3.17–6.08]
Haggstrom[a] Cornell et al. 2004	Cavalier King Charles Spaniel	57	8.9 [5.5–11.9]	0.33 [0.21–0.44]	0.69 [0.50–0.82]	1.74 [0.94–2.59]				
Crippa et al. 1992	Beagle	20	8.9 [5.9–11.9]	0.40 [0.22–0.58]						
Pedersen[a] Cornell et al. 2004	Dachshund	33	9.5 [6.2–16.0]	0.34 [0.19–0.53]	0.70 [0.46–0.89]	1.63 [0.86–4.35]	0.33 [0.25–0.39]	0.55 [0.44–0.62]	3.51 [1.71–4.36]	4.01 [1.90–5.13]
Baade et al. 2002	West Highland White Terrier	24	10.3 [8.5–12.1]	0.35 [0.21–0.49]						
Gooding et al. 1986	English Cocker Spaniel	12	12.2 [8.5–15.8]	0.34 [0.29–0.43]	0.71 [0.64–0.82]	1.95 [1.52–2.53]	0.32 [0.20–0.38]	0.54 [0.36–0.62]	4.09 [2.26–5.33]	
Della Torre et al. 2000[a]	Whippet	20	14.5 [10.8–20.2]	0.33 [0.25–0.47]	0.69 [0.57–0.85]	1.88 [1.45–2.36]	0.33 [0.29–0.42]	0.55 [0.49–0.66]	4.20 [3.36–5.08]	4.96 [3.97–5.72]
Maschiro et al. 1976	Generic	16	17.6 [11.3–24.0]	0.31 [0.24–0.39]	0.67 [0.57–0.77]	1.72 [1.14–2.13]	0.25 [0.22–0.29]	0.44 [0.39–0.50]	2.59 [2.07–3.39]	
Sisson and Schaeffer 1991	English Pointer	16	19.2 [13.6–24.9]	0.36 [0.28–0.44]						
Wey[a] Cornell et al. 2004	Generic	47	20.8 [2.2–47.4]	0.34 [0.23–0.59]	0.69 [0.54–0.93]	1.71 [0.91–2.71]	0.31 [0.25–0.37]	0.53 [0.43–0.61]	3.47 [2.50–4.90]	3.91 [2.46–6.37]
de Madron 1983	Generic	27	24.4 [2.7–95.0]	0.33 [0.22–0.46]	0.69 [0.53–0.84]	1.99 [1.20–2.60]	0.26 [0.19–0.32]	0.46 [0.35–0.54]	3.15 [1.95–5.12]	3.72 [2.21–5.25]
Brown et al. 2003	Generic	50	25.2 [2.3–76.4]	0.34 [0.25–0.50]	0.71 [0.58–0.87]	1.44 [0.78–2.01]	0.35 [0.28–0.44]	0.57 [0.48–0.68]	3.40 [2.21–5.05]	3.94 [2.63–5.13]
Della Torre et al. 2000[a]	Greyhound	20	26.9 [21.7–31.5]	0.25 [0.18–0.32]	0.57 [0.44–0.68]	1.40 [0.87–2.01]	0.37 [0.32–0.42]	0.60 [0.53–0.66]	4.83 [3.87–5.30]	5.62 [4.48–6.32]
Goncalves et al. 2002[a]	Generic	70	27.7 [3.9–97.7]	0.38 [0.30–0.57]	0.75 [0.66–0.92]	1.43 [0.80–2.21]	0.38 [0.30–0.54]	0.61 [0.52–0.79]	3.77 [2.44–7.31]	4.30 [2.81–5.88]
Snyder et al. 1995[a]	Greyhound	11	29.1 [24.9–36.3]	0.29 [0.24–0.37]	0.64 [0.56–0.75]	1.82 [1.39–2.30]	0.35 [0.32–0.40]	0.57 [0.54–0.64]	4.99 [4.04–5.98]	
Lombard[a] Cornell et al. 2004	Generic	23	30.1 [21.0–44.0]	0.38 [0.30–0.49]	0.75 [0.66–0.87]	1.93 [0.95–2.75]				
Vollmar[a] Cornell et al. 2004	Boxer	75	31.0 [22.5–43.0]	0.33 [0.26–0.41]	0.69 [0.59–0.79]	1.50 [0.94–2.35]	0.32 [0.24–0.39]	0.54 [0.42–0.63]	3.23 [1.93–4.47]	3.85 [2.58–5.72]
Bayon et al. 1994	Spanish Mastiff	12	52.4 [45.8–59.0]							
Koch et al. 1996	Newfoundland	27	61.0 [47.0–69.5]	0.30 [0.22–0.37]						
Koch et al. 1996	Great Dane	15	62.0 [52.0–75.0]	0.25 [0.18–0.36]						
Vollmar[a] Cornell et al. 2004	Irish Wolfhound	144	63.5 [45.0–91.0]	0.34 [0.25–0.45]	0.71 [0.58–0.84]	1.45 [0.95–2.36]	0.30 [0.20–0.36]	0.51 [0.36–0.59]	2.68 [1.56–4.30]	3.09 [1.94–4.19]
Koch et al. 1996	Irish Wolfhound	20	68.5 [50.0–80.0]	0.28 [0.20–0.34]						

[a]Original data supplied by investigators. All others from referenced sources.
[b]Mean or median, ± standard deviation [range].
Index formulas from Table 5.3.

Feline M-mode echocardiographic reference values

	References						
	Jacobs et al. 1985	**Pipers et al. 1979**	**Sisson et al. 1991**	**Moise et al. 1986**	**Allen and Downey 1983**	**Allen 1982**	**Fox et al. 1985**
Conditions	Unanesthetized	Unanesthetized	Unanesthetized	Unanesthetized	Xylazine-sodium pentobarbital	Sodium pentobarbital	Ketamine hydrochloride
N	30	25	79	11	8	10	30
BW (kg)	[1.96–6.26]	[2.30–6.80]	[2.70–8.20]	4.30 ± 0.50	3.50 ± 0.41	3.64 ± 0.66	[2.05–6.80]
HR (/min)	[147–242]	[120–240]	[120–240]	182 ± 22	163 ± 13	175 ± 20	[160–300]
RVIDd (cm)	[0.00–0.70]						[0.12–0.75]
IVSd (cm)	[0.22–0.40]	[0.28–0.60]	[0.30–0.60]	0.50 ± 0.07		0.40 ± 0.03	[0.22–0.49]
LVIDd (cm)	[1.20–1.98]	[1.12–2.18]	[1.08–2.14]	1.51 ± 0.21	1.29 ± 0.09	1.30 ± 0.12	[1.07–1.73]
LVWd (cm)	[0.22–0.44]	[0.32–0.56]	[0.25–0.60]	0.46 ± 0.05		0.40 ± 0.40	[0.21–0.45]
RVWs (cm)	[0.23–0.43]						
RVIDs (cm)	[0.27–0.94]						
IVSs (cm)	[0.47–0.70]		[0.40–0.90]	0.76 ± 0.12			
LVIDs (cm)	[0.52–1.08]	[0.64–1.68]	[0.40–1.12]	0.69 ± 0.22	0.88 ± 0.08	0.86 ± 0.16	[0.49–1.16]
LVWs (cm)	[0.54–0.81]		[0.43–0.98]	0.78 ± 0.10			
Ao (cm)	[0.72–1.19]	[0.40–1.18]	[0.60–1.21]	0.95 ± 0.15		0.90 ± 0.07	[0.71–1.15]
LA (cm)	[0.93–1.51]	[0.45–1.12]	[0.70–1.70]	1.21 ± 0.18		1.00 ± 0.07	[0.72–1.33]
LA/Ao	[0.95–1.65]		[0.88–1.79]	1.29 ± 0.23			[0.73–1.64]
FS	[0.39–0.61]	[0.23–0.56]	[0.40–0.67]	0.55 ± 0.10	0.31 ± 0.47	0.35 ± 0.25	[0.30–0.60]
EPSS (cm)	[0.00–0.21]		[0.00–0.20]	0.04 ± 0.07			

Mean ± standard deviation [range].

Canine Doppler outflow reference values

	References						
	Kirberger et al. 1992	**Kirberger et al. 1992**	**Brown et al. 1991**	**Darke et al. 1993**	**Gaber 1987**	**Yuill and O'Grady 1991**	**Bonagura and Miller 1989**
Method	CWD	PWD	PWD		PWD	CWD	PWD
Aortic V_{peak} (m/s)	1.49 ± 0.27 [0.99–2.10]	1.57 ± 0.33 [1.06–2.29]	1.06 ± 0.21 [0.65–1.37]	1.19 ± 0.24	1.19 ± 0.18	1.18 ± 0.11 [1.04–1.38]	1.20 [–1.70]
Aortic VTI (m)			0.146 ± 0.029				
Aortic AT (s)		0.055 ± 0.015		0.050 ± 0.010			
Aortic ET (s)		0.182 ± 0.029	0.205 ± 0.015				
Aortic PEP (s)		0.058 ± 0.012					
Aortic PEP/ET				0.22 ± 0.06			
Aortic acceleration (cm/s)		32.00 ± 14.00		34.00 ± 16.00			
Pulmonic V_{peak} (m/s)	1.25 ± 0.26 [0.60–1.91]	1.20 ± 0.20 [0.88–1.20]	0.84 ± 0.17 [0.34–1.29]	0.99 ± 0.22	1.00 ± 0.15	0.98 ± 0.09 [0.76–1.22]	1.07 [–1.30]
Pulmonic VTI (m)			0.131 ± 0.028				
Pulmonic AT (s)		0.08 ± 0.02		0.07 ± 0.02			
Pulmonic ET (s)		0.184 ± 0.028	0.219 ± 0.018				
Pulmonic PEP (s)		0.051 ± 0.010					
Pulmonic PEP/ET				0.14 ± 0.03			

Mean ± standard deviation [range].

Canine Doppler inflow reference values

	References					
	Yuill and O'Grady 1991	**Gaber 1987**	**Kirberger et al. 1992**	**Darke et al. 1993**	**Bonagura and Miller 1989**	**Yamamoto and Masuyama 1993**
Mitral E_{peak} (m/s)	0.86 ± 0.10 [0.70–1.08]	0.75 ± 0.12	0.91 ± 0.15 [0.59–1.18]	0.65 ± 0.18	0.76 [−1.00]	0.56 ± 0.18
Mitral A_{peak} (m/s)			0.63 ± 0.13 [0.33–0.93]	0.43 ± 0.13	0.49 [−0.75]	0.44 ± 0.11
Mitral E_{peak}/A_{peak}			1.48 ± 0.31 [1.04–2.42]	1.55 ± 0.36		1.30 ± 0.30
Mitral VTI (m)						0.094 ± 0.032
Tricuspid E_{peak} (m/s)	0.69 ± 0.08 [0.52–0.92]	0.56 ± 0.16	0.86 ± 0.20 [0.49–1.31]	0.57 ± 0.15	0.60 [−0.80]	
Tricuspid A_{peak} (m/s)			0.58 ± 0.16 [0.33–0.94]	0.37 ± 0.15	0.48 [−0.60]	
Tricuspid E_{peak}/A_{peak}			1.60 ± 0.56 [0.69–3.08]	1.62 ± 0.36		

Systolic time interval reference values (canine and feline)

	References		
	Boon et al. 1983	**Atkins and Snyder 1992**	**Atkins and Snyder 1992**
Species	Canine	Canine	Feline
HR (/min)	98 ± 24	124 ± 23	226 ± 25
LVET (s)	0.178 ± 0.017	0.159 ± 0.015	0.116 ± 0.019
PEP (s)	0.057 ± 0.018	0.054 ± 0.007	0.046 ± 0.005
PEP/LVET	0.32 ± 0.11	0.24 ± 0.05	0.40 ± 0.05
Vet (/s)	2.21 ± 0.40	2.48 ± 0.50	4.00 ± 0.90

Appendix References

Allen DG (1982) Echocardiographic study of the anesthetized cat. Can J Comp Med 46:115–122.

Allen DG, Downey RS (1983) Echocardiographic assessment of cats anesthetized with xylazine–sodium pentobarbital. Can J Comp Med 47:281–283.

Atkins CE, Snyder PS (1992) Systolic time intervals and their derivatives for evaluation of cardiac function. J Vet Intern Med 6:55–63.

Baade H, Schober K, Oechtering G (2002) Echocardiographic reference values in West Highland White Terriers with special regard to right heart function. Tierarztl Prax 30:172–179.

Bayon A, Fernandez del Palacio MJ, Montes AM, Gutierrez Panizo C (1994) M-mode echocardiography study in growing Spanish mastiffs. J Small Anim Pract 35: 473–479.

Bonagura JD, Miller MW (1989) Veterinary echocardiography. Am J Cardiovasc Ultrasound Allied Tech 6:229–264.

Boon J, Wingfield WE, Miller CW (1983) Echocardiographic indices in the normal dog. Vet Radiol 24:214–221.

Brown DJ, Knight DH, King RR (1991b) Use of pulsed-wave Doppler echocardiography to determine aortic and pulmonary velocity and flow variables in clinically normal dogs. Am J Vet Res 52:543–550.

Brown DJ, Rush JE, MacGregor J, Ross JN, Brewer B, Rand W (2003) M-mode echocardiographic ratio indices in normal dogs, cats, and horses: A novel quantitative method. J Vet Intern Med 17:653–662.

Calvert CA, Brown J (1986) Use of M-mode echocardiography in the diagnosis of congestive cardiomyopathy in Doberman pinschers. J Am Vet Med Assoc 189:293–297.

Cornell CC, Kittleson MD, Della Torre P, et al. (2004) Allometric scaling of M-mode variables in normal adult dogs. J Vet Intern Med 18:311–321.

Crippa L, Ferro E, Melloni E, Brambilla P, Cavalletti E (1992) Echocardiographic parameters and indices in the normal beagle dog. Lab Anim 26:190–195.

Darke PGG, Fuentes VL, Champion SR (1993b) Doppler echocardiography in canine congestive cardiomyopathy. In: 11th ACVIM Forum, pp 531–534.

de Madron E (1983) M-mode echocardiography in the dog (L'echocardiographie en mode M chez le chien normal) 76: Ecole Nationale Veterinaire d'Alfort.

Della Torre PK, Kirby AC, Church DB, Malik R (2000) Echocardiographic measurements in greyhounds, whippets, and Italian greyhounds: Dogs with similar conformation but different size. Aust Vet J 78:49–55.

Fox PR, Bond BR, Peterson ME (1985) Echocardiographic reference values in healthy cats sedated with ketamine hydrochloride. Am J Vet Res 46:1479–1484.

Gaber C (1987) Normal pulsed Doppler flow velocities in adult dogs. In: 5th ACVIM Forum, p 923.

Goncalves AC, Orton EC, Boon JA, Salman MD (2002) Linear, logarithmic, and polynomial models of M-mode echocardiographic measurements in dogs. Am J Vet Res 63:994–999.

Gooding JP, Robinson WF, Mews GC (1986) Echocardiographic assessment of left ventricular dimensions in clinically normal English cocker spaniels. Am J Vet Res 47:296–300.

Hall DJ, Cornell CC, Crawford S, Brown DJ (2008b) Meta-analysis of normal canine echocardiographic dimensional data using ratio indices. J Vet Cardiol 10:11–23.

Jacobs G, Knight DH (1985) M-mode echocardiographic measurements in nonanesthetized healthy cats: Effects of body weight, heart rate, and other variables. Am J Vet Res 46:1705–1711.

Kirberger RM, Bland-van den Berg P, Grimbeek RJ (1992b) Doppler echocardiography in the normal dog: Part II. Factors influencing blood flow velocities and a comparison betwen left and right heart blood flow. Vet Radiol Ultrasound 33:380–386.

Koch J, Pedersen HD, Jensen AL, Flagstad A (1996) M-mode echocardiographic diagnosis of dilated cardiomyopathy in giant breed dogs. J Vet Med 43:297–304.

Maschiro I, Nelson RR, Cohn JN, Franciosa JA (1976) Ventricular dimensions measured noninvasively by echocardiography in the awake dog. J App Physiol 41:953–959.

Moise NS, Dietze AE, Mezza LE, Strickland D, Erb HN, Edwards NJ (1986) Echocardiography, electrocardiography, and radiography of cats with dilatation cardiomyopathy, hypertrophic cardiomyopathy, and hyperthyroidism. Am J Vet Res 47:1476–1486.

Morrison SA, Moise NS, Scarlett J, Mohammed H, Yeager AE (1992) Effect of breed and body weight on echocardiographic values in four breeds of dogs of differing somatotype. J Vet Intern Med 6:220–224.

Page A, Edmunds G, Atwell RB (1993) Echocardiographic values in the greyhound. Aust Vet J 70:361–364.

Pipers FS, Reef V, Hamlin RL (1979) Echocardiography in the domestic cat. Am J Vet Res 40:882–886.

Sisson D, Schaeffer D (1991) Changes in linear dimensions of the heart, relative to body weight, as measured by M-mode echocardiography in growing dogs. Am J Vet Res 52:1591–1596.

Sisson DD, Knight DH, Helinski C, et al. (1991) Plasma taurine concentrations and M-mode echocardiographic measures in healthy cats and in cats with dilated cardiomyopathy. J Vet Intern Med 5:232–238.

Snyder PS, Sato T, Atkins CE (1995) A comparison of echocardiographic indices of the nonracing healthy greyhound to reference values from other breeds. Vet Radiol Ultrasound 36:387–392.

Yamamoto K, Masuyama TJT (1993) Effects of heart rate on the left ventricular filling dynamics: Assessment from simultaneous recordings of pulsed Doppler transmitral flow velocity pattern and haemodynamic variables. Cardiovasc Res 27:935–941.

Yuill CDM, O'Grady MR (1991) Doppler-derived velocity of blood flow across the cardiac valves in the normal dog. Can J Vet Res 55:185–192.

CHAPTER SIX

Liver

Marc-André d'Anjou[1,2] and Dominique Penninck[3]

[1] *Centre Vétérinaire Rive-Sud, Brossard, Québec, Canada*
[2] *Faculté de médecine vétérinaire de l'Université de Montréal, Saint-Hyacinthe, Québec, Canada*
[3] *Department of Clinical Sciences, Cummings School of Veterinary Medicine, Tufts University, North Grafton, MA, USA*

Preparation and Scanning Technique

Hair clipping of animals should cover the entire cranial abdomen and ideally the last one or two intercostal spaces, particularly in deep-chested dogs or if microhepatia is suspected. Animals can be scanned in dorsal, left, or right recumbency after acoustic gel application. The ability to visualize the liver in small animals is related to body conformation, liver size, and overlying gastrointestinal content. In small dogs and cats, the liver can usually be entirely scanned in transverse and longitudinal planes by means of a subcostal approach (Figure 6.1), as long as the stomach is not overly distended with ingesta or gas. The transverse colon can also limit hepatic visibility, particularly if filled with gas or feces, or if the liver is small. In these instances, an intercostal approach can provide a useful alternative. In large, deep-chested dogs, the liver is completely hidden by the rib cage, routinely requiring the use of an intercostal approach to reach all parts of the liver. In these dogs, and especially if the liver is atrophied, several other structures, such as the spleen, can move under the costal arch and should not be confused for a portion of the liver. In obese animals, the presence of a large amount of falciform fat can also reduce hepatic visibility by increasing the distance between the sonographic probe and the organ and by degrading image quality because of beam scattering.

The appropriate probe must be chosen based on the size and depth of the liver. In small or medium-sized dogs and cats, a medium-frequency probe (5 MHz and higher) can be use, whereas a probe with more penetration (lower than 5 MHz) is often required in larger dogs. Sectorial or convex probes are preferred over linear probes because of the triangular-shaped scanned field of view that enables larger portions of the liver to be imaged. A smaller footprint also enables most parts of the liver to be reached through limited acoustic windows such as intercostal spaces. Gain settings and focal zones must be constantly adjusted during the exam in order to optimize ultrasonographic penetration and image quality (see Figure 1.8).

Ultrasonographic Anatomy of the Normal Liver

Parenchyma and Size

In dogs and cats, the liver is composed of four lobes, four sublobes, and two processes – left lobe (lateral and medial), quadrate lobe, right lobe (lateral and medial), and caudate lobe (caudate and papillary processes) (Evans 1993a; Hudson and Hamilton 1993) – which cannot be easily distinguished unless separated by peritoneal effusion (Figure 6.2).

The left lobe forms a third to nearly half of the entire liver and contacts the left portion of the gallbladder (GB). The quadrate lobe is relatively central and partially encircles the GB. The right portion of the GB is in contact with the right medial lobe. The caudate process of the caudate lobe is the most caudal extension of the liver, on the right side, and extends to the level of the right kidney. The hepatic and portal veins (PVs) of each of these hepatic lobe divisions are relatively constant in

Atlas of Small Animal Ultrasonography, Second Edition. Edited by Dominique Penninck and Marc-André d'Anjou.
© 2015 John Wiley & Sons, Inc. Published 2015 by John Wiley & Sons, Inc.
Companion website: www.SmallAnimalUltrasonography.com

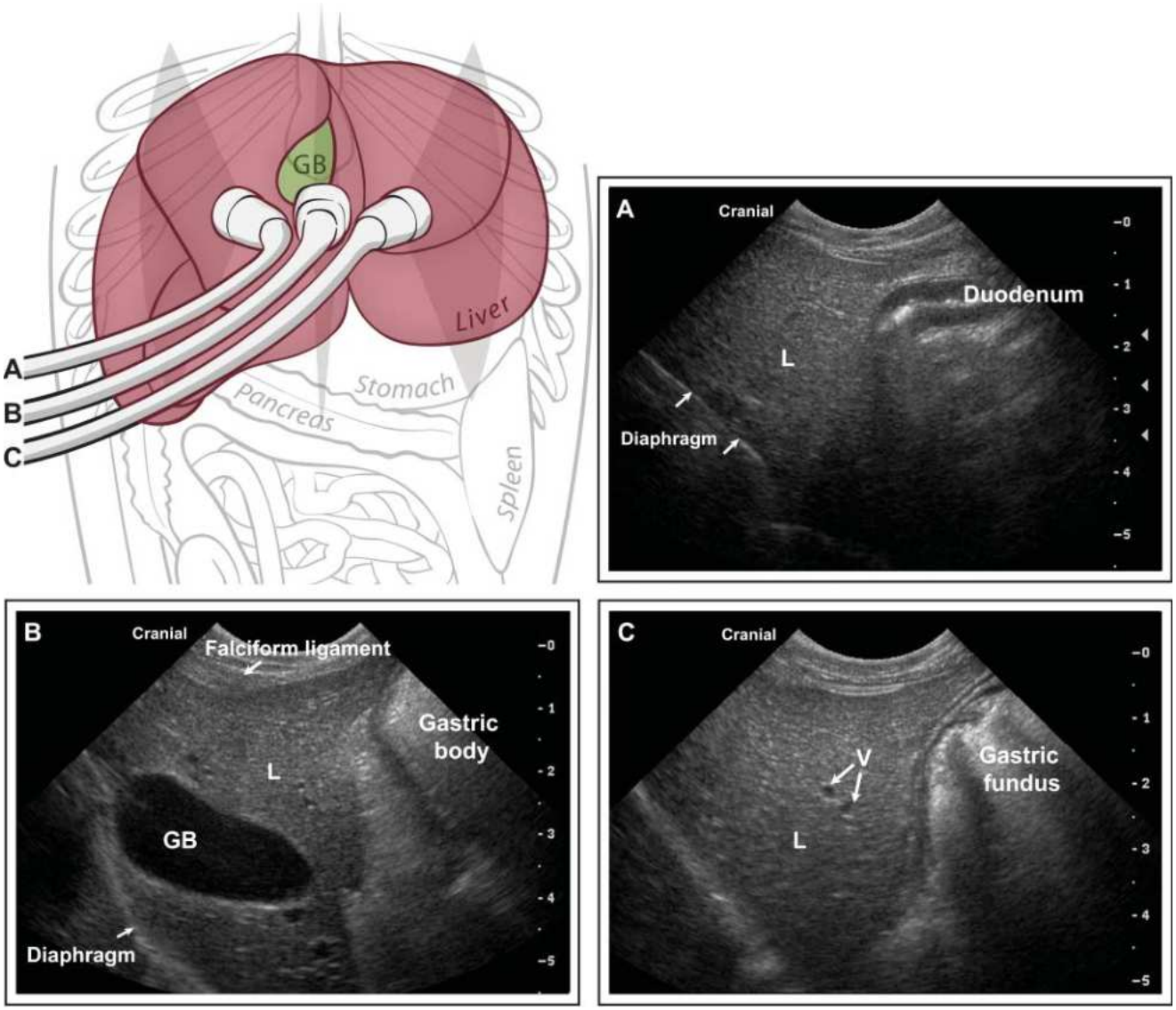


Figure 6.1. Ultrasonographic approach and anatomy of the normal liver. Illustration of the scanning technique using a subcostal approach with a dog or a cat in dorsal recumbency. The ultrasound probe must be moved in order to cover the entire liver, sequentially in the sagittal **(A–C)** and transverse **(D–F)** planes. The additional use of oblique planes, as well as an intercostal approach, is necessary in some patients. **A–C:** Using a longitudinal plane in a dog, the probe is sequentially moved from the right **(A)** to the left **(C)** of the liver (L). The intimate relationship between the duodenum-stomach and the liver is visualized. The falciform ligament, which can vary in size because of fat deposition, is in the near field. Hepatic vessels (V) appear as round, anechoic structures on cross-section. The gallbladder (GB), located to the right of the midline, is a useful landmark. **D–F:** By using a transverse plane, the liver is also entirely scanned, from its cranioventral portion **(D)** to its caudodorsal portion **(F)**. The gallbladder is seen on the right in the mid-portion of the liver **(E)**. Branching portal veins (PV) with hyperechoic boundaries are also recognized.

dogs and can represent useful ultrasonographic landmarks (Carlisle et al. 1995).

A large part of the liver is beneath the costal arch, just cranial to the stomach, in dogs and cats. Its cranial margin lies against the diaphragm and lung interface. The diaphragm appears as a curved hyperechoic line, often associated with artifacts such as a mirror-image artifact (Figure 1.17).

Caudally, the liver is often in contact with the spleen on the left side and with the right kidney at the level of the renal fossa of the caudate lobe. The hepatic volume is difficult to evaluate objectively in cats and dogs, mainly because of the variability in body conformation. As with radiography, the costal arch and location of the stomach can help in subjectively evaluating liver size, taking into account body conformation.

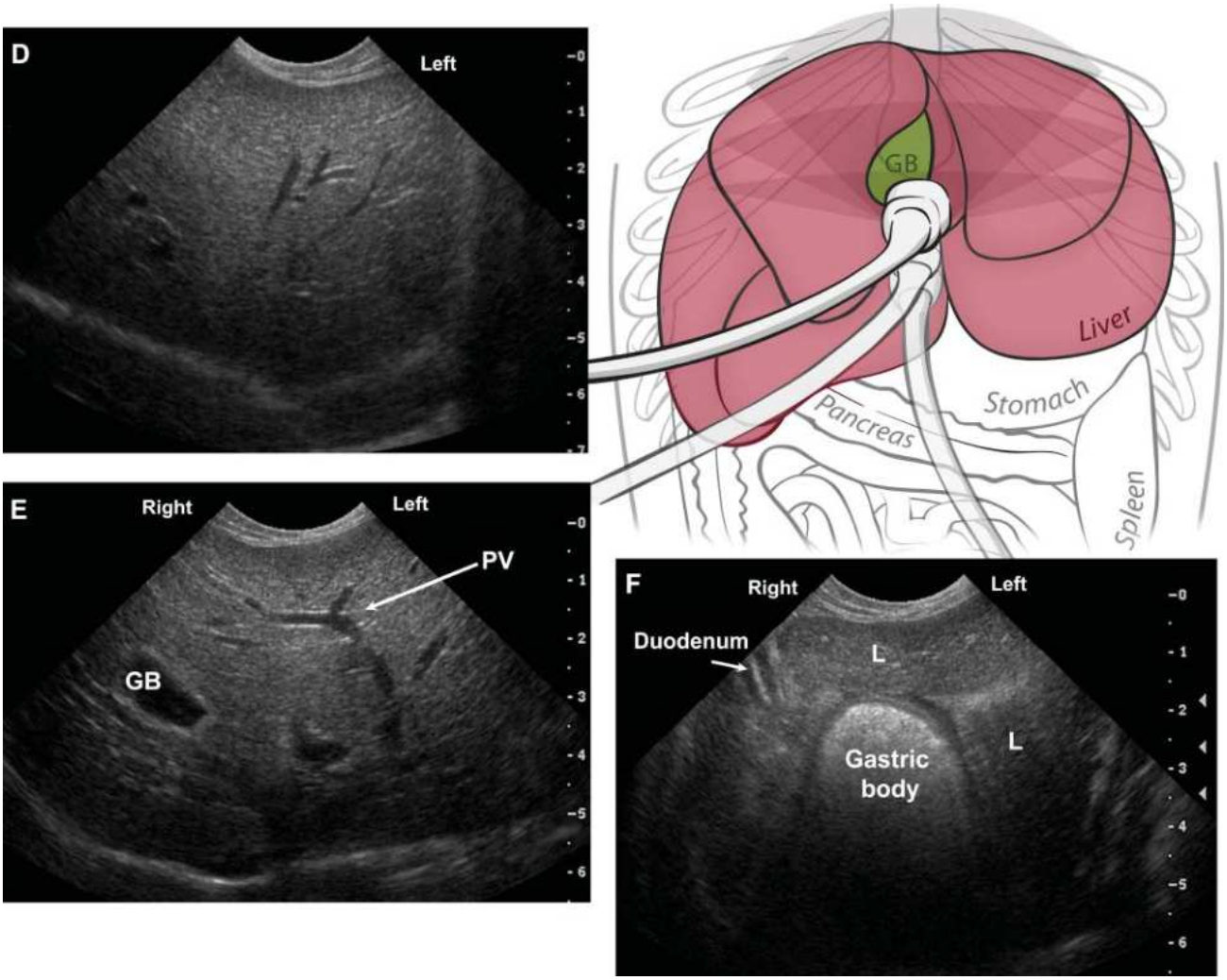


Figure 6.1. *Continued*

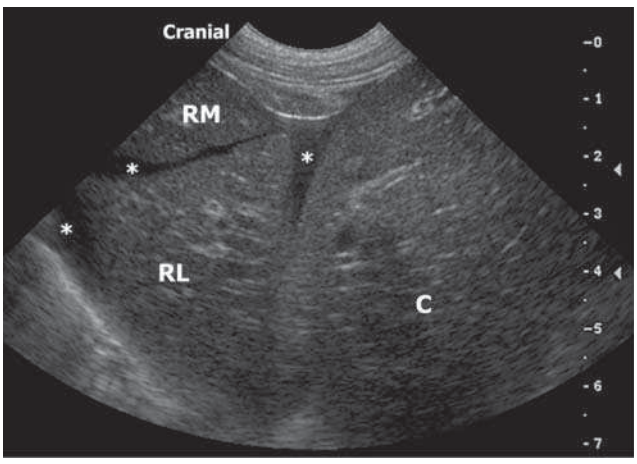


Figure 6.2. Effusion separating hepatic lobes. Longitudinal oblique image of the right portion of the liver with three distinct separate lobes well outlined by peritoneal effusion (*). C, caudate lobe; RL, right lateral; RM, right medial.

The caudal extension of the hepatic lobes can be compared with the location of the last pair of ribs (Figure 6.3A). In deep-chested dogs, the liver does not usually reach the costal arch, and the stomach often interferes with its evaluation. Conversely, in small dog breeds and in cats, the liver normally extends to the costal arch. It may also extend beyond that point in some small breeds of dogs, particularly in puppies. The caudal tips of the hepatic lobes are normally pointed. With hepatomegaly, these tips are rounded and can extend beyond the right kidney and/or reach the left kidney, depending on the symmetry of the enlargement (Figure 6.3B).

The falciform ligament filled with a variable amount of fat is ventral to the liver and protrudes between the right and left portions, dorsal to the xiphoid process (Figure 6.4). This poorly defined structure is usually isoechoic or slightly hyperechoic to the liver and presents a coarse echotexture relative to the

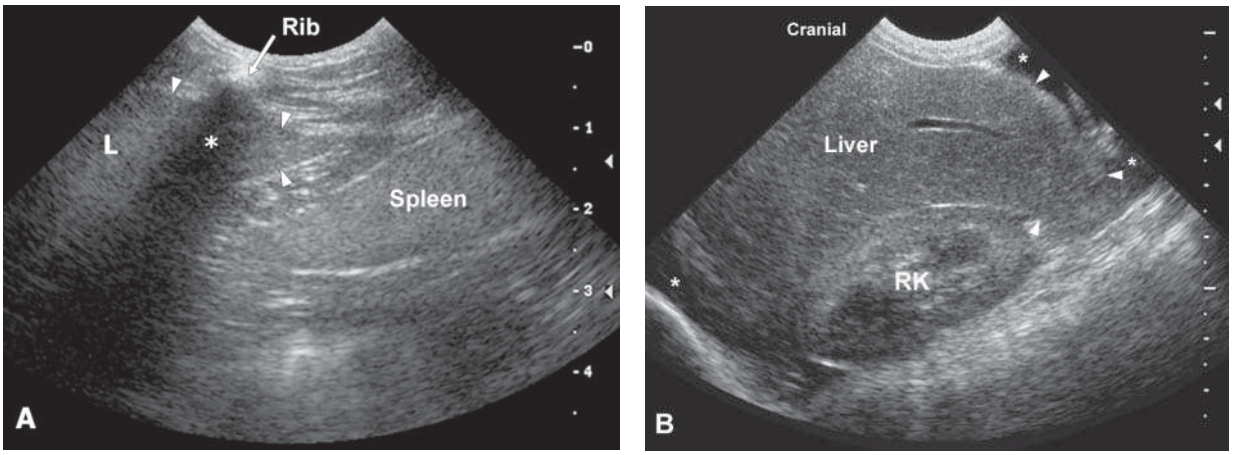


Figure 6.3. **Evaluation of liver size. A:** Normal liver. Left parasagittal image of the cranial abdomen in a normal small-breed dog with the caudal tip of the liver (L and arrowheads) extending slightly beyond the last rib. Acoustic shadowing (*) is noted deep to this hyperattenuating structure. The tip of the liver appears smooth and pointy. **B:** Hepatomegaly. On this sagittal image of the liver obtained in the right cranial abdomen of a dog, a liver lobe (arrowheads) extends caudal to the right kidney (RK) and has a rounded tip consistent with enlargement. Passive hepatic congestion was diagnosed, and peritoneal effusion (*) was also detected.

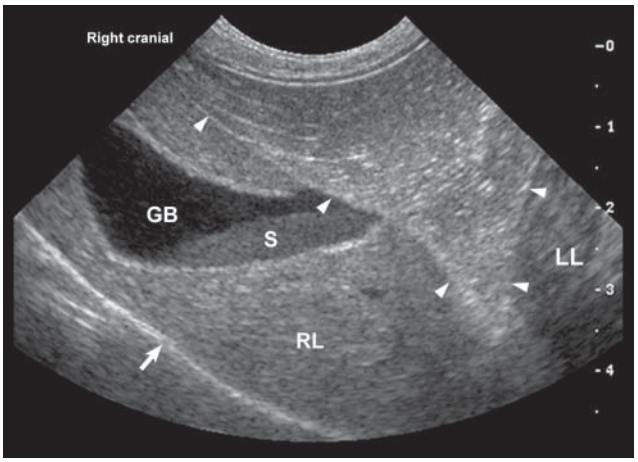


Figure 6.4. **Falciform fat.** On this sagittal oblique ultrasonographic image of the liver, the falciform fat (arrowheads) appears as a triangular hyperechoic structure with a coarse echotexture protruding between the right and left portions of the liver. The gallbladder (GB) contains a small amount of biliary sludge (S) in its dependent portion (dorsal recumbency). The arrow points to the lung–diaphragm interface. LL, left liver; RL, right liver.

liver. However, obese cats may have a liver that is hyperechoic to the falciform fat (Nicoll et al. 1998). The normal hepatic parenchyma is uniformly hypoechoic, with a coarser echotexture, when compared with the spleen. Its echogenicity relative to the renal cortices is more variable, although usually hyperechoic to isoechoic (Figure 6.5).

Biliary System

The biliary system is relatively similar in dogs and cats. The GB, occasionally bilobed in cats, represents the bile reservoir and is an anechoic teardrop-shaped structure with a conical extension: the cystic duct (Figure 6.6). GB volume can be estimated using the ellipsoid method (Figure 6.7) (Penninck et al. 2010). It can vary markedly in size and become quite large in anorexic patients, so that GB volume alone cannot be used as a reliable sign of biliary obstruction. Yet, monitoring its reduction postprandially may help to rule out outflow obstruction. In cats, GB width can be used to predict its postprandial change in volume (Diana et al. 2012).

The wall of the normal GB is thin and smooth, measuring less than 1 mm thick in cats (Hittmair et al. 2001) and dogs. Biliary sludge is often recognized in the GB of asymptomatic dogs (Bromel et al. 1998), although there is growing evidence that this may indicate a delay in GB emptying (Tsukagoshi et al. 2012). GB sludge in cats can be predictive of increased liver enzymes and total bilirubin (Harran et al. 2011) (Figure 6.8), but it may also be encountered without evidence of biliary disease. The hyperechoic sludge is mobile, but may sometimes give the impression of an aggregate mimicking a soft-tissue mass. The movement of the sludge should respond to gravity after the animal is repositioned, although this may take more time in some dogs. Additionally, because of the relatively low attenuation of the ultrasound beam through the bile, acoustic

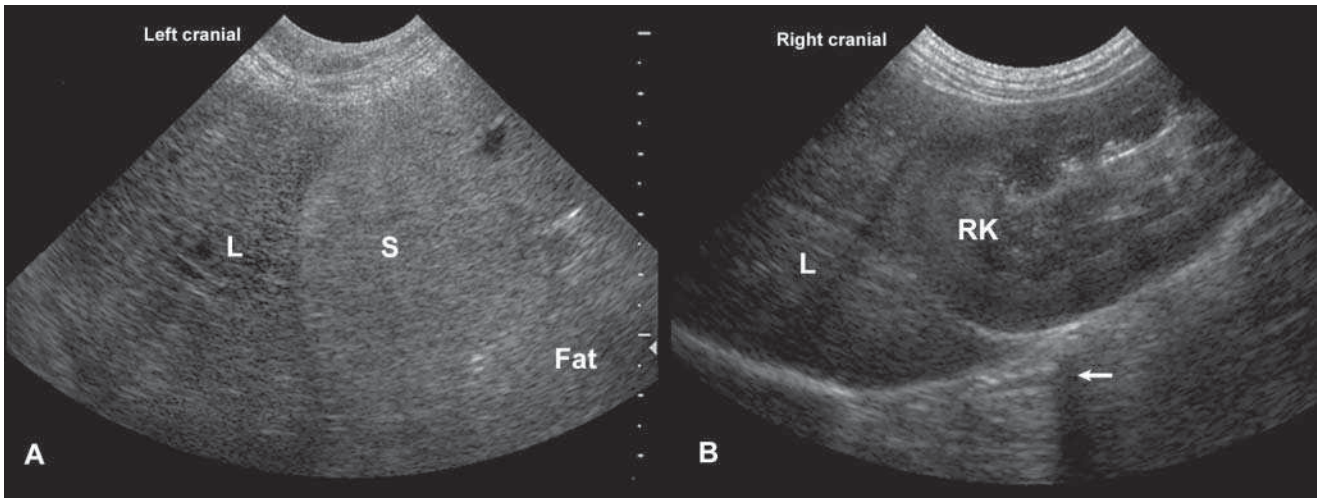


Figure 6.5. **Liver, spleen, and kidney relative echogenicities and echotextures. A:** Sagittal image obtained in the left cranial abdomen of a normal dog. The liver (L) is in contact with the spleen (S), and is relatively hypoechoic and more granular in echotexture. **B:** Sagittal image obtained in the right cranial abdomen of a normal dog. The liver (L) appears relatively isoechoic to the cortex of the right kidney (RK). Acoustic shadowing (arrow) is caused by one of the last ribs.

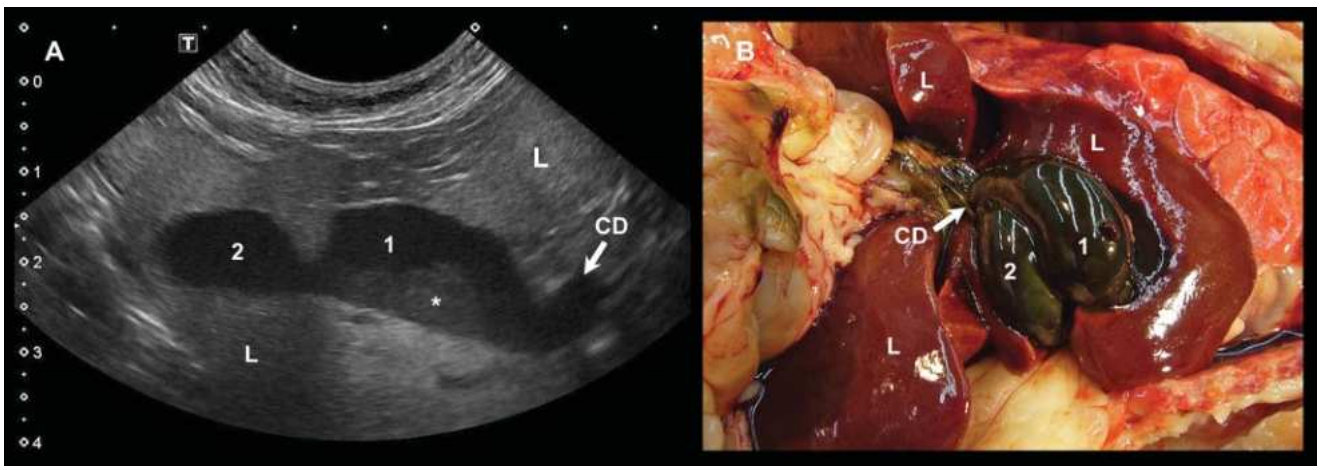


Figure 6.6. **Bilobed gallbladder in a cat.** Sonographic **(A)** and gross anatomical **(B)** images of the gallbladder that is partially divided into two compartments (1 and 2), sharing the same cystic duct (CD). This usually represents an incidental finding in cats, although hepatic lipidosis and biliary sludge (*) were identified in this cat. The liver parenchyma (L) was hyperechoic in A.

enhancement is commonly observed beyond the GB (see Figure 1.15).

The intrahepatic biliary tree, composed of biliary canaliculi and larger biliary ducts, is not seen in normal patients. The common bile duct (CBD), which represents the continuation of the connecting GB cystic duct and biliary ducts, can be seen more easily in normal cats than in normal dogs. The CBD can be visualized between the proximal duodenum (ventrally) and the PV (dorsally) (Figure 6.9). It can measure up to 4 mm wide in normal cats (Léveillé et al. 1996) and is considered normal by the authors when up to 3 mm (luminal diameter) in dogs. It parallels the PV over a few centimeters before entering into the duodenum through the major duodenal papilla. The wall of the CBD, as for the GB, is often barely visualized and should not exceed 1 mm.

Hepatic Vasculature

The afferent vascular flow to the liver is dual, with a larger proportion coming from the PV (80%) and the rest coming from the hepatic arteries (Evans 1993a) (Figure 6.10). The efferent flow follows the hepatic

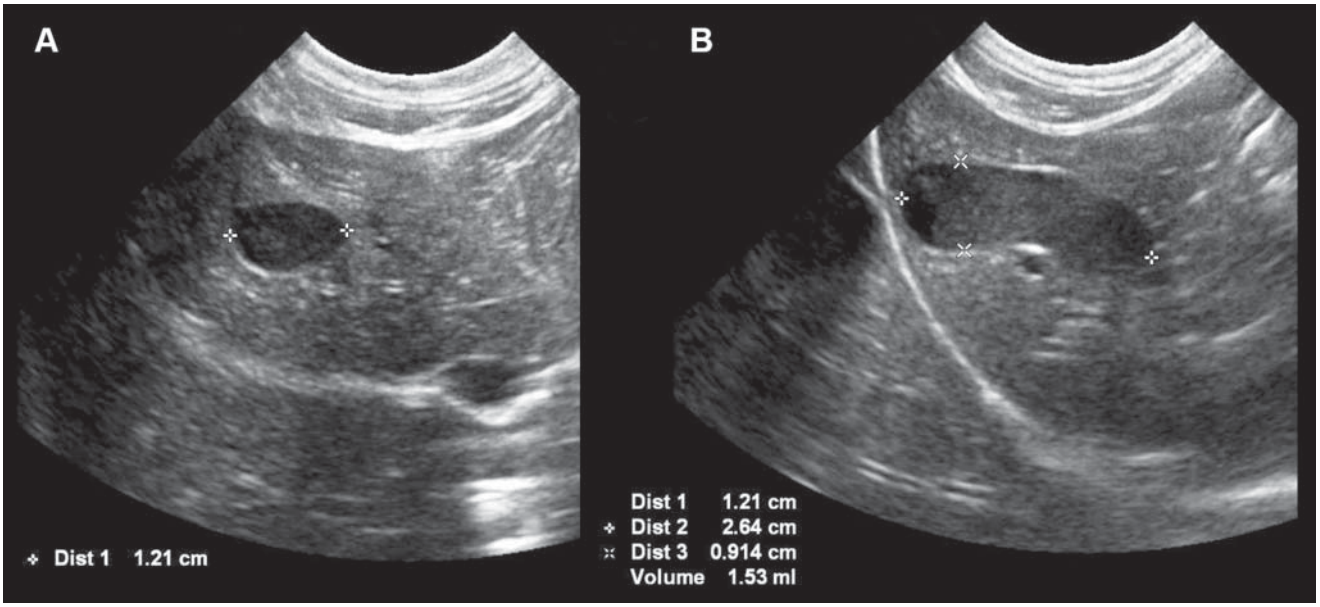


Figure 6.7. Gallbladder volume estimation using the ellipsoid method. Transverse **(A)** and longitudinal **(B)** sonograms of the gallbladder with three sets of measurements (length, height, and width) contribute in obtaining the estimated volume of the gallbladder of 1.5 ml in this 15-year-old cat.

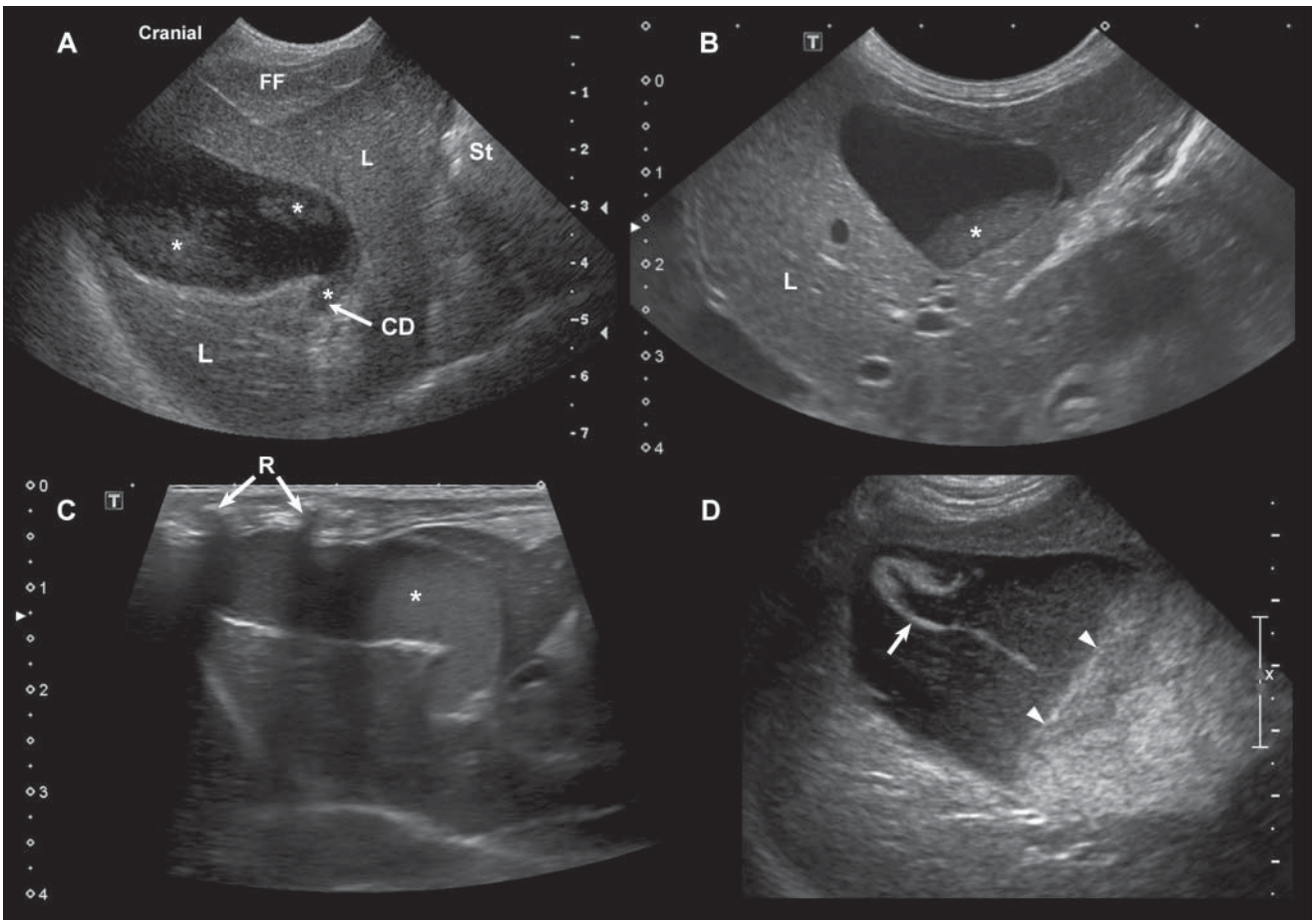


Figure 6.8. Biliary sludge in dogs and cats. A: Longitudinal image of the right-central portion of the liver of a normal dog with the gallbladder and cystic duct (CD) containing poorly defined echogenic material consistent with biliary sludge. The mobility of this sludge was confirmed by repositioning the animal during the exam. FF, falciform fat; L, liver; St, stomach. **B:** In this cat with normal liver enzymes, the biliary sludge (*) accumulates in the dependent portion of the gallbladder. **C**: In another cat with cholangiohepatitis, the gallbladder is filled with sludge (*). **D**: In this 12 year-old Golden Retriever, hyperchoic sludge is collecting in the dependent portion of the gallbladder. The orientation of the sediment (arrowheads) is oblique because of the orientation of the probe. Sludge can also form floating layers (arrow).

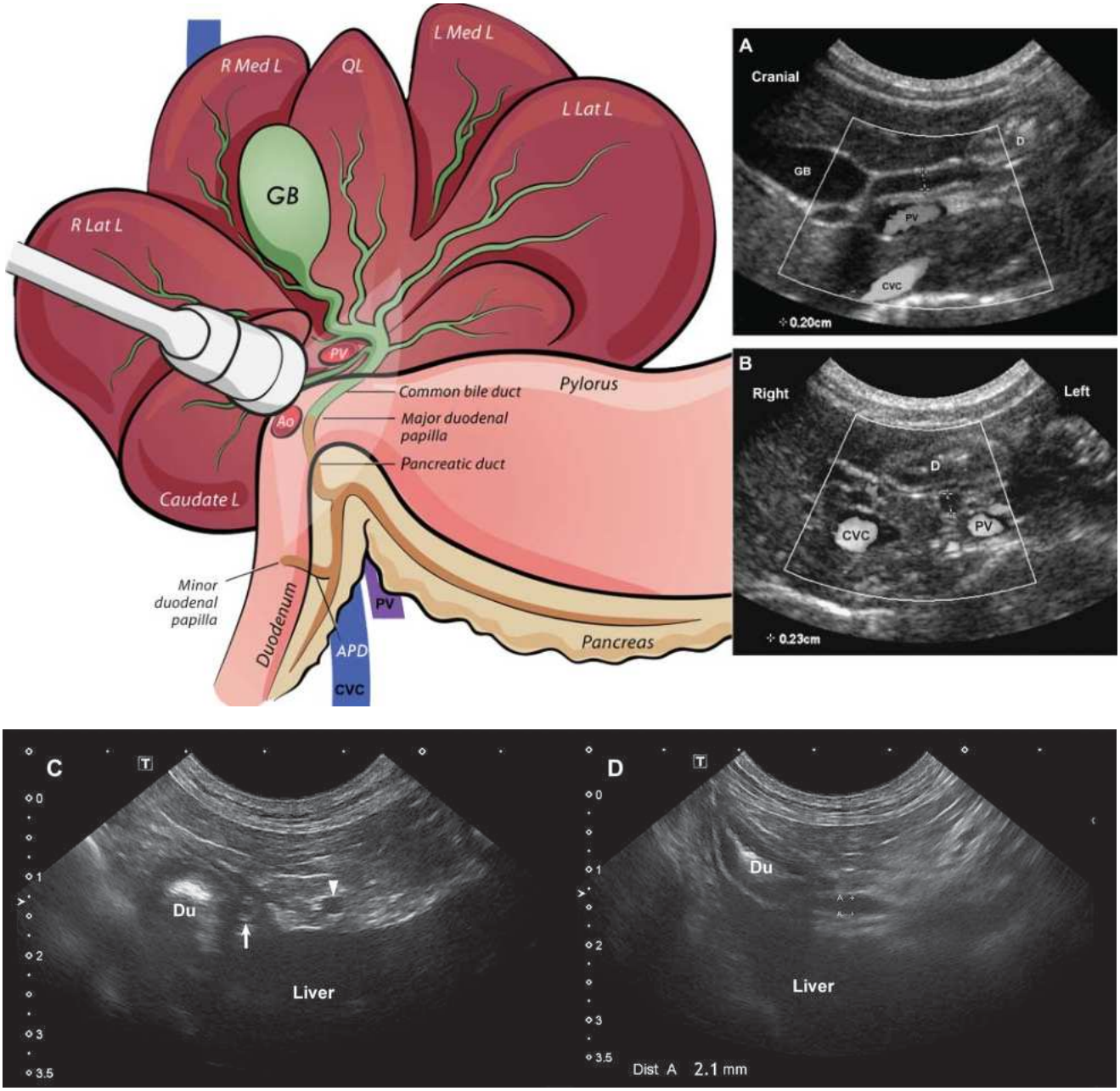


Figure 6.9. **Scanning technique for the common bile duct in a cat.** Schematic representation of the regional anatomy and landmarks of the biliary tract in the cat, with the ultrasound probe placed to obtain a longitudinal view **(A)** of the common bile duct. The probe is then rotated to obtain a transverse plane **(B)**. The common bile duct (2 mm wide) is found just ventral to the portal vein (PV) and dorsal to the proximal duodenum (D). This duct can sometimes be followed to the level of the major duodenal papilla, at the same level as the pancreatic duct termination. CVC, caudal vena cava; GB, gallbladder; R Lat L, right lateral lobe; R Med L, right medial lobe; QL, quadrate lobe; L Med L, left medial lobe; L Lat L, left lateral lobe; APD, accessory pancreatic duct; Ao, aorta. **C, D**: Normal common bile duct in a Lhasa Apso dog. The common bile duct (CBD) can sometimes be recognized in dogs as it enters the duodenal (Du) papilla (arrow in C). In this dog, the lumen of the CBD measures 2.1 mm **(D)**. Color Doppler may serve in distinguishing the duct from the nearby pancreaticoduodenal vein (arrowhead in C). Image C was obtained with a transverse plane in relation to the duodenum, whereas the probe was oriented obliquely to highlight the CBD in a longitudinal plane **(D)**.

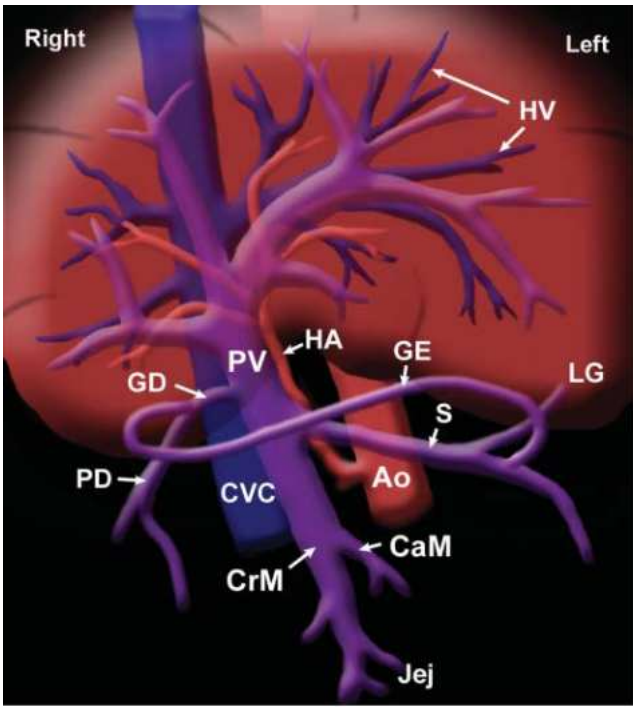


Figure 6.10. **Portal vascular system.** Schematic illustration of the hepatic vasculature and extrahepatic portal system of dogs and cats, as seen from a ventral approach. The liver receives its vascular supply through the portal vein (PV) and hepatic arteries (HA). The PV receives several smaller veins draining most abdominal viscera. The relationship with the caudal vena cava (CVC) and aorta (Ao) is also illustrated. HV, hepatic veins. Veins of the portal system: CaM, caudal mesenteric; CrM, cranial mesenteric; GD, gastroduodenal; GE, gastroepiploic; Jej, jejunal; LG, left gastric, PD, pancreaticoduodenal; S, splenic.

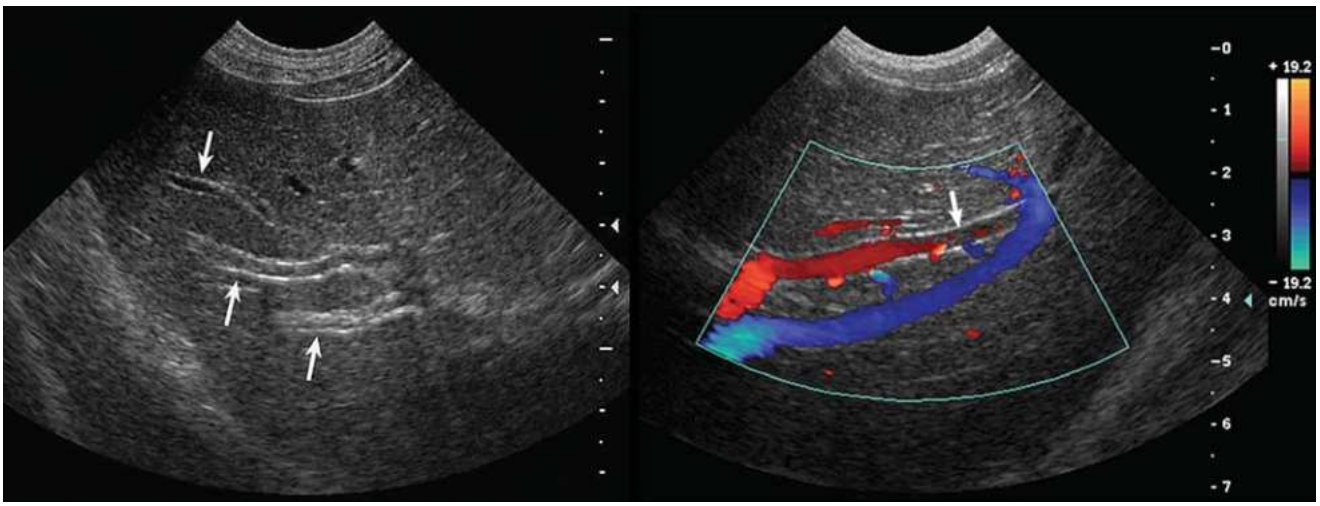


Figure 6.11. **Hepatic vasculature.** Portal veins can be differentiated from hepatic veins because of the consistent hyperechogenicity of their walls (arrows), regardless of the ultrasound beam orientation. With conventional color Doppler, portal venous flow appears as a red signal directed toward the transducer, compared with a blue signal for the hepatic veins that drain in the caudal vena cava (i.e., away from the transducer).

veins into the caudal vena cava (CVC). This particular vascular pattern is divided into all hepatic lobes and can aid in distinguishing these lobes. When using B-mode imaging, only the hepatic and PVs (larger than the arteries) can be seen as anechoic, branching, smoothly tapering tubular structures. The walls of the PVs appear hyperechoic, regardless of the orientation of the ultrasonographic beam, facilitating their identification (Figure 6.11). However, the walls of the hepatic veins can also appear hyperechoic when the ultrasonographic beam is directed perpendicularly (see Figure 6.74).

The visibility of the larger and smaller branches of these veins is influenced by patient size, vascular luminal diameter, portal flow, pressure in the CVC, hepatic parenchymal echogenicity, and image quality

and resolution. When measured at the same depth, the hepatic and portal branches should be relatively similar in diameter (Figure 6.11B).

The use of color Doppler facilitates the identification and distinction of hepatic vessels. When using standard color-map settings, portal flow directed from the center to the periphery appears as a red signal, whereas hepatic venous flow appears as a blue signal (Figure 6.11B). Arterial flow, also directed from the center to the periphery, can also demonstrate a red signal, depending on the size of the arteries and the Doppler settings, such as gain and filtration threshold.

Extrahepatic Portal Vasculature

The extrahepatic portion of the PV is relatively central in the abdomen, ventral to the CVC, and ventral and to the right of the aorta (Figure 6.12). The main PV is more

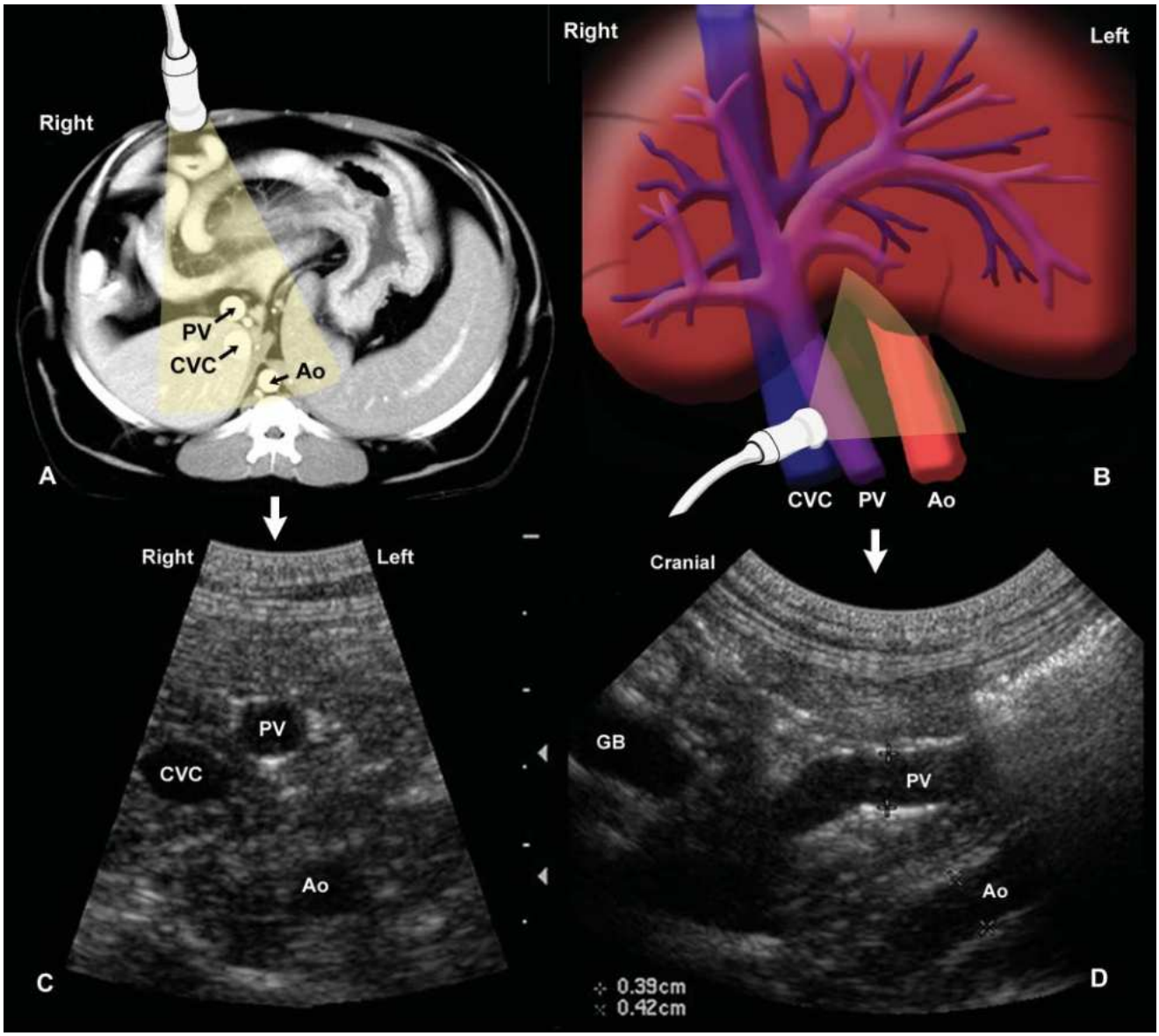


Figure 6.12. Ultrasonographic approach to the hepatic vasculature. Transverse computed tomographic image **(A)** and ventral schematic image **(B)** of the hepatic vasculature showing the relationship between the portal vein (PV), caudal vena cava (CVC), and aorta (Ao). On transverse **(C)** and longitudinal **(D)** ultrasonographic images obtained at the porta hepatis, these three vessels can usually be well visualized in normal dogs and cats, and should be similar in size. When measured at the caudal margin of the liver, the portal vein should not be less than 65% of the diameter of the aorta. GB, gallbladder. Computed tomographic image courtesy of Matthew Winter, University of Florida.

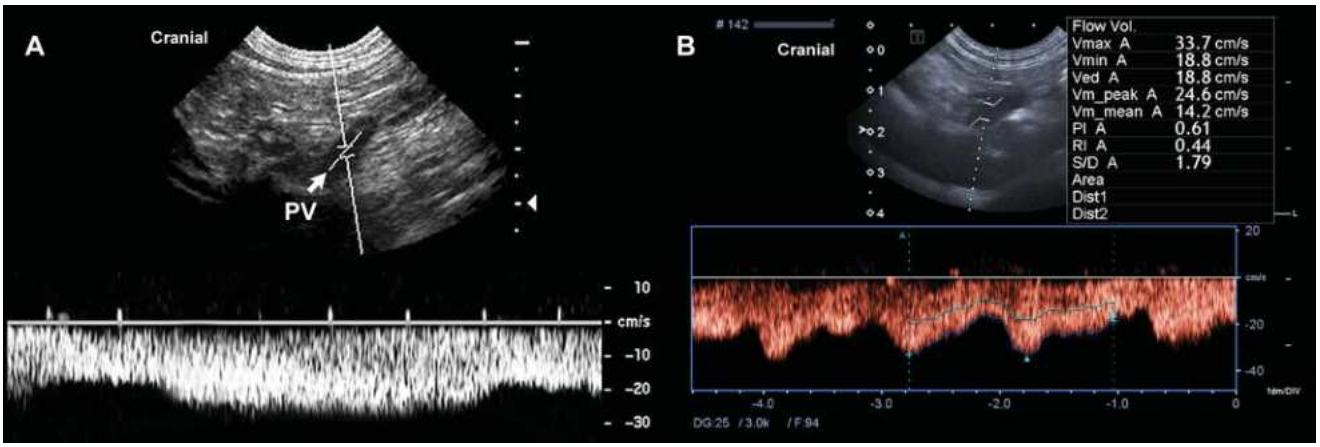


Figure 6.13. Spectral Doppler pattern of the portal flow in two normal dogs. With spectral Doppler, the flow within the portal vein (PV) can be assessed after placing the sample-volume gate in the center of the vascular lumen and correcting for the angle of flow direction. **A**: The flow spectrum observed in this dog is broad and relatively linear, with some variations occurring because of movement of the sample volume during respiration in relation to the center of the vessel, where maximal velocity is reached. Mean flow velocity is calculated by multiplying the maximal velocity (25 cm/s) by a factor of 0.57, which equals 14.3 cm/s. The angle of sample volume correction was 50°. **B**: In this other dog, the flow is more irregular because of rapid respiration. Using the automated flow velocity measuring tool in this other ultrasound machine, the flow maximum (Vmax), minimum (Vmin) and mean (Vm) velocities can be measured in a segment of the spectral profile.

tortuous than the CVC and aorta, and curves slightly to the right side before entering the liver.

When measured at the level of the porta hepatis, its luminal diameter varies between 3.4 and 5.0 mm in normal cats and between 3.3 and 10.5 mm in normal dogs. When comparing the maximal luminal diameter of the PV and the aorta, PV/aorta ratios of 0.71–1.25 are normally expected in these two species (d'Anjou et al. 2004).

The main PV is formed by the confluence of the cranial and caudal mesenteric veins and splenic vein, and therefore drains most abdominal organs (Evans 1993b) (Figure 6.10). It also receives a smaller tributary, the gastroduodenal vein, only a few centimeters caudal to the hepatic entrance. The gastroduodenal vein connects to the right-ventral aspect of the PV after receiving the pancreaticoduodenal and gastroepiploic veins. A few centimeters more caudally, the main PV receives the splenic vein on the left side, which follows the left limb of the pancreas after receiving the left gastric vein. The cranial mesenteric vein receiving all jejunal branches represents the caudal extension of the main PV after the entry of the smaller caudal mesenteric vein another few centimeters caudal to the splenic vein. These portal tributaries enlarge as they approach the main PV, and the flow of all is directed toward the liver (**hepatopetal flow**). The portal flow contained in these tributaries, as well as in the main PV, is normally parabolic and relatively constant, giving a characteristic spectral Doppler pattern (Figure 6.13). Portal flow mean velocity can be measured with spectral Doppler, after the use of an insonation angle correction of less than 60°. Portal flow mean velocity can be calculated by the ultrasound system by using the uniform insonation technique, which requires the application of a sample gate volume that fills the entire width of the main PV. Alternatively, a sample gate volume that fills approximately half of the vessel lumen placed in its center can be used to obtain maximal flow velocity. Because of the parabolic behavior of the portal flow, mean portal flow velocity can then be estimated by multiplying this result by 0.57. Mean portal flow velocities have been reported to vary between 15 ± 3 and 18 ± 8 cm/s in normal dogs and 10–18 cm/s in normal cats (Nyland and Fisher 1990; Lamb and Mahoney 1994; Lamb 1998; d'Anjou et al. 2004). However, these measurements are susceptible to inaccurate estimations, especially with higher correction angles (more than 60°), and must therefore be used cautiously.

Ultrasonographic Features of Hepatic Disorders

Several hepatic disorders are found in dogs and cats and cause focal, multifocal, or diffuse parenchymal alterations. The evaluation of the liver must include

several parameters: liver size and contour, parenchymal echogenicity, ultrasound-beam attenuation, as well as the distribution of abnormalities. Although some of these disorders have characteristic ultrasonographic features, most changes are not pathognomonic of one particular process. A more definite diagnosis is usually based on the combination of clinical presentation, blood test results, ultrasonographic findings, and cytological or histopathologic results.

Diffuse Hepatic Parenchymal Disorders

Diffuse hepatic disorders can be difficult to differentiate from poorly defined multifocal diseases. Typically, these disorders affect all lobes, although not always uniformly. The parenchymal echogenicity can be increased, reduced, or unaffected. These disorders can also affect the parenchymal uniformity and distort the hepatic margin. The evaluation of the liver contour is facilitated by the presence of peritoneal effusion (Figure 6.2). With the exception of congenital portal vascular anomalies, such as portosystemic shunting, chronic hepatitis, and cirrhosis, most disorders tend to be associated with symmetrical or asymmetrical hepatomegaly. Two or more hepatic disorders, such as hepatitis, vacuolar hepatopathy, or nodular hyperplasia, can be found in the same patient, complicating the ultrasonographic diagnosis. The correlation between ultrasound findings and cytological and histopathological results is relatively poor for diffuse parenchymal diseases, justifying fine-needle aspiration cytology, or ideally biopsy, in most cases (Feeney DA et al. 2008; Guillot et al. 2009; Warren-Smith et al. 2012; Kemp et al. 2013). Table 6.1 lists the typical diagnostic differential for diffuse changes in hepatic parenchymal echogenicity, and Table 6.2 lists the causes of diffuse or focal/asymmetrical hepatomegaly.

Vacuolar Hepatopathies and Nodular Hyperplasia

Hepatic lipidosis, and steroid-induced and other vacuolar hepatopathies are among the most common

Table 6.1
Diagnostic differentials for diffuse alterations in hepatic parenchymal echogenicity

Diffuse Hyperechogenicity	Diffuse Hypoechogenicity	Mixed Echogenicity
Steroid hepatopathy	Passive congestion	Steroid hepatopathy associated with benign hyperplasia, or other combinations of processes
Lipidosis	Acute hepatitis or cholangiohepatitis	Hepatitis
Other vacuolar hepatopathies	Lymphoma	Lymphoma
Chronic hepatitis	Leukemia	Hepatocellular carcinoma
Fibrosis	Histiocytic neoplasms	Metastasis
Cirrhosis	Amyloidosis	Necrosis
Lymphoma		Amyloidosis
Mast cell tumor		

Table 6.2
Diagnostic differentials for alterations in hepatic volume

Diffuse Hepatomegaly	Focal or Asymmetrical Hepatomegaly	Small Liver
Steroid hepatopathy	Primary or metastatic neoplasia	Congenital portosystemic shunting
Lipidosis	Abscess	Microvascular dysplasia or primary portal vein hypoplasia
Hepatitis or cholangiohepatitis	Cyst(s)	Cirrhosis
Passive congestion	Granuloma	Fibrosis
Round-cell neoplasia: lymphoma, malignant histiocytosis, and mast cells	Thrombosis	Severe hypovolemia
Massive hepatocellular carcinoma or metastases	Lobar torsion	
Amyloidosis	Hematoma	

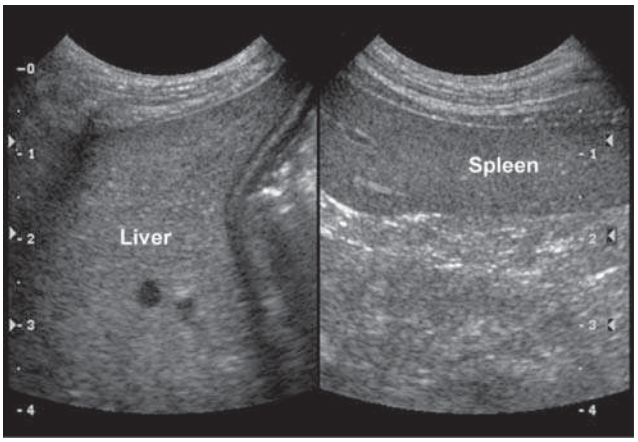


Figure 6.14. **Hyperechoic liver.** Dual images of the liver and spleen of a dog that were obtained with identical settings (depth, gain, and focus), allowing hepatic and splenic parenchymal echogenicities to be compared. Hepatic lipidosis that caused a diffusely hyperechoic liver, isoechoic to the spleen, was diagnosed.

diffuse parenchymal disorders in cats and dogs, respectively. Degenerative vacuolar hepatopathy is often present with other primary disorders in dogs (Wang et al. 2004). These hepatopathies are usually associated with a diffuse increase in parenchymal echogenicity and hepatomegaly (Figures 6.14–6.16). The parenchyma can also appear hyperattenuating, i.e., result in excessive sound-beam attenuation (Figures 6.15, 6.16). Consequently, the far gain must be increased (or bottom time gain compensation cursors moved to the right) in many of these patients to be able to evaluate the deepest portions of the liver. Additionally, the parenchyma can appear heterogeneous or contain hypoechoic or hyperechoic nodular foci, possibly because of concurrent nodular hyperplasia or regenerative nodules (Figure 6.16).

Hepatitis, Cholangitis/cholangiohepatitis, and Cirrhosis

Diffuse hepatic inflammatory processes can show variable ultrasonographic features. In cats, cholangitis/cholangiohepatitis was reported to be commonly associated with a decrease in parenchymal echogenicity and an increased visibility of the portal vasculature (Newell et al. 1998), although the liver may appear normal, hyperechoic or heterogeneous (Penninck et al. 1997; Marolf et al. 2012) (Figure 6.17). Additionally, this process is often associated with biliary anomalies, such as biliary sludge, cholelithiasis, or wall thickening, and with pancreatitis. In dogs, acute hepatitis also tends to cause diffuse liver hypoechogenicity, as seen with leptospirosis (Figure 6.18A, B).

Chronic liver inflammatory processes, on the other hand, tend to be associated with fibrosis, which typically results in increased echogenicity (Figure 6.19). The presence of chronic active inflammation, consisting of a mixture of inflammatory cells, edema, fibrosis, necrosis, as well as regenerative nodules (hyperplasia) can cause a markedly heterogeneous liver with variable echogenicity (Figure 6.20). Although cirrhosis classically causes the

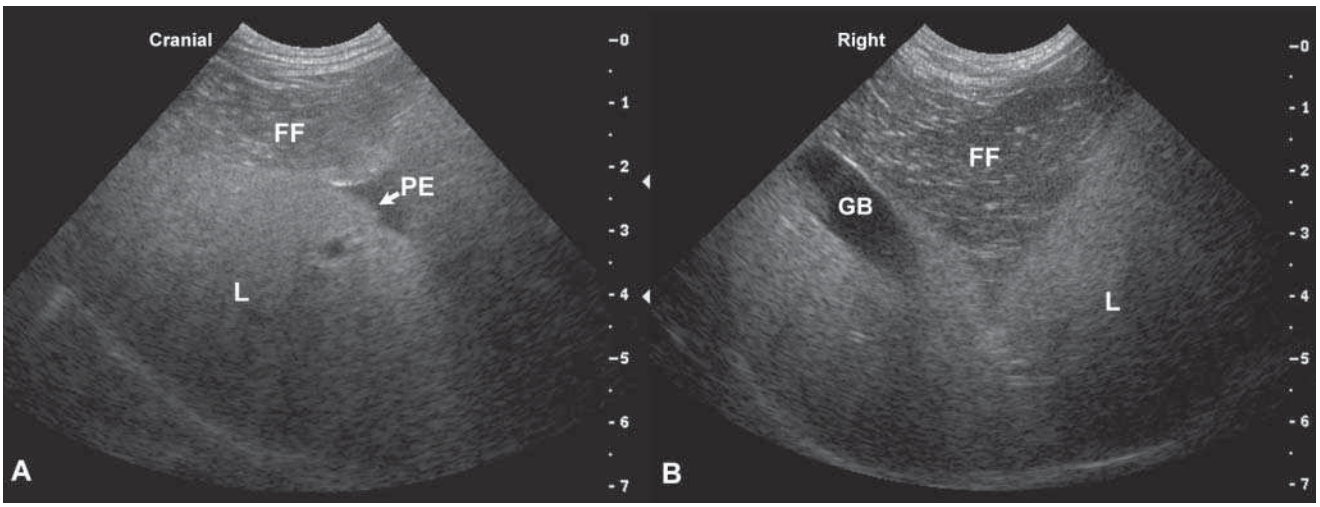


Figure 6.15. **Feline hepatic lipidosis.** Sagittal **(A)** and transverse **(B)** images of the liver in a cat with diffuse hyperechogenicity and ultrasonographic beam hyperattenuation. The liver (L) is markedly hyperechoic to the falciform fat (FF), at least superficially. The echoes coming from the deepest portions of the liver were reduced and could only be partially compensated for by increasing far gain. A small volume of peritoneal effusion (PE) is noted between liver lobes. GB, gallbladder.

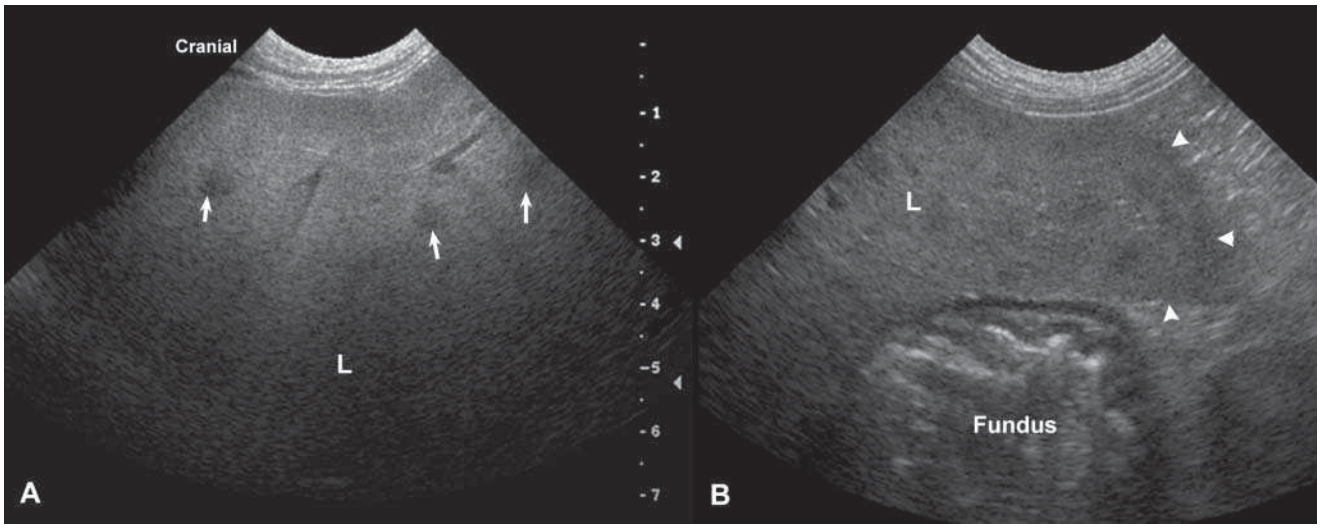


Figure 6.16. **Steroid hepatopathy.** Longitudinal images of the left portion of the liver in a dog with pituitary-dependent hyperadrenocorticism. The liver (L) is enlarged, diffusely hyperechoic, and heterogeneous. Multiple hypoechoic nodular foci, less than 1 cm wide, are noted in the liver **(A)** (arrows). **B:** The liver contour is rounded (arrowheads) and extends beyond the gastric fundus. In **A**, the deep portion of the liver is difficult to assess because of increased ultrasound-beam attenuation. Ultrasound-guided biopsy indicated vacuolar hepatopathy and benign nodular hyperplasia.

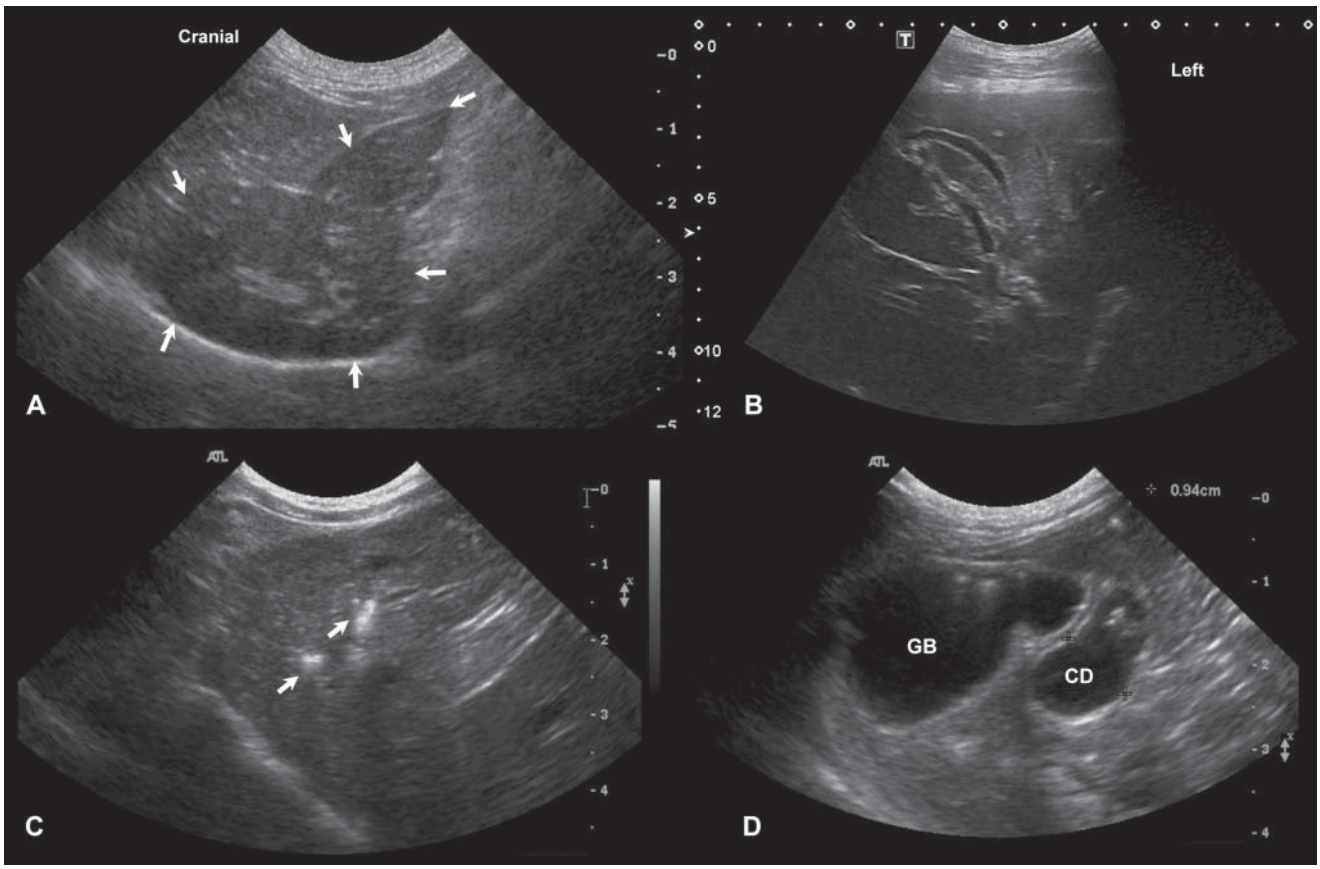


Figure 6.17. **Feline cholangiohepatitis. A:** Longitudinal image of the left portion of the liver (arrows) of a cat with fever and icterus. The liver parenchyma is diffusely hypoechoic, and the portal vein margins appear prominent. These features are suggestive of cholangiohepatitis or cholangitis in cats. **B:** Dorsal oblique image of the left portion of the liver in another cat with cholangiohepatitis. Similar features are observed. The liver (L) is enlarged and hypoechoic when compared with the falciform fat (FF) located ventrally. Arrows in **A** delineate the cranial hepatic border. **C, D**: Chronic, severe suppurative cholangiohepatitis and cholelithiasis (arrows) in an 8-year-old cat. The liver parenchyma in this case is hyperechoic. The cystic duct (CD) is also dilated and tortuous. GB, gallbladder.

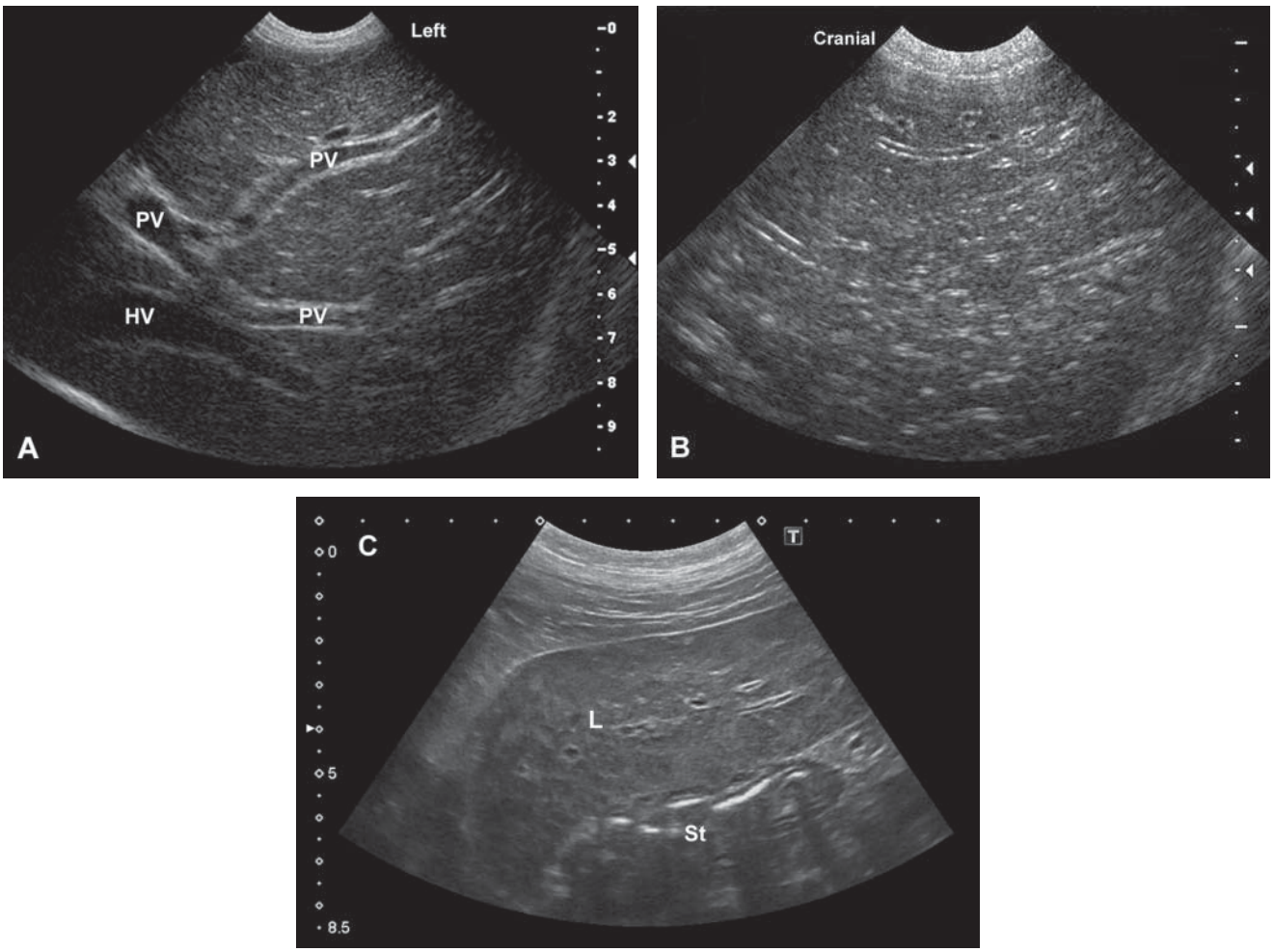


Figure 6.18. **Canine hepatitis. A:** Transverse oblique image of the left side of the liver in a dog with acute hepatitis with prominent portal veins (PV) because of diffuse parenchymal hypoechogenicity. The main left hepatic vein (HV) is also observed, but its wall is less apparent. The prominence of the PV boundaries may have also been related to the inflammatory process. **B:** Leptospirosis. Ultrasonographic image of a portion of the liver in a dog with acute leptospirosis. The liver is diffusely hypoechoic, and its portal walls are prominent, appearing as double lines and "donuts" throughout the parenchyma. These findings are common in dogs with leptospirosis. **C**: Chronic suppurative hepatitis. In this 6-year-old Labrador, the liver (L) is heterogeneously hyperechoic. St, stomach.

liver to appear small, hyperechoic, and irregular in contour, its appearance can vary and sometimes mimic neoplasia (Figure 6.21). However, chronic hepatitis and its ultimate outcome, cirrhosis, usually do not cause hepatic enlargement, as opposed to massive neoplastic infiltration.

Hepatic Neoplasia

Although several primary and secondary neoplastic processes can affect the liver in dogs and cats, diffuse hepatic involvement is less common and is usually caused by diffuse round-cell infiltration. Hepatomegaly is expected in most types of diffuse neoplasia, although its magnitude can vary with the level of infiltration.

Lymphoma can involve the liver without detectable ultrasonographic changes or cause diffuse parenchymal hypoechogenicity, hyperechogenicity, or mixed echogenicity, with or without hypoechoic nodules (Whiteley et al. 1989; Lamb et al. 1991) (Figure 6.22). Histiocytic neoplasms are more commonly associated with hypoechoic nodules and masses, although diffuse hepatic hypoechogenicity has been reported (Cruz-Arambulo et al. 2004) (Figure 6.34B). Conversely, mast cell infiltration of the liver tends to cause

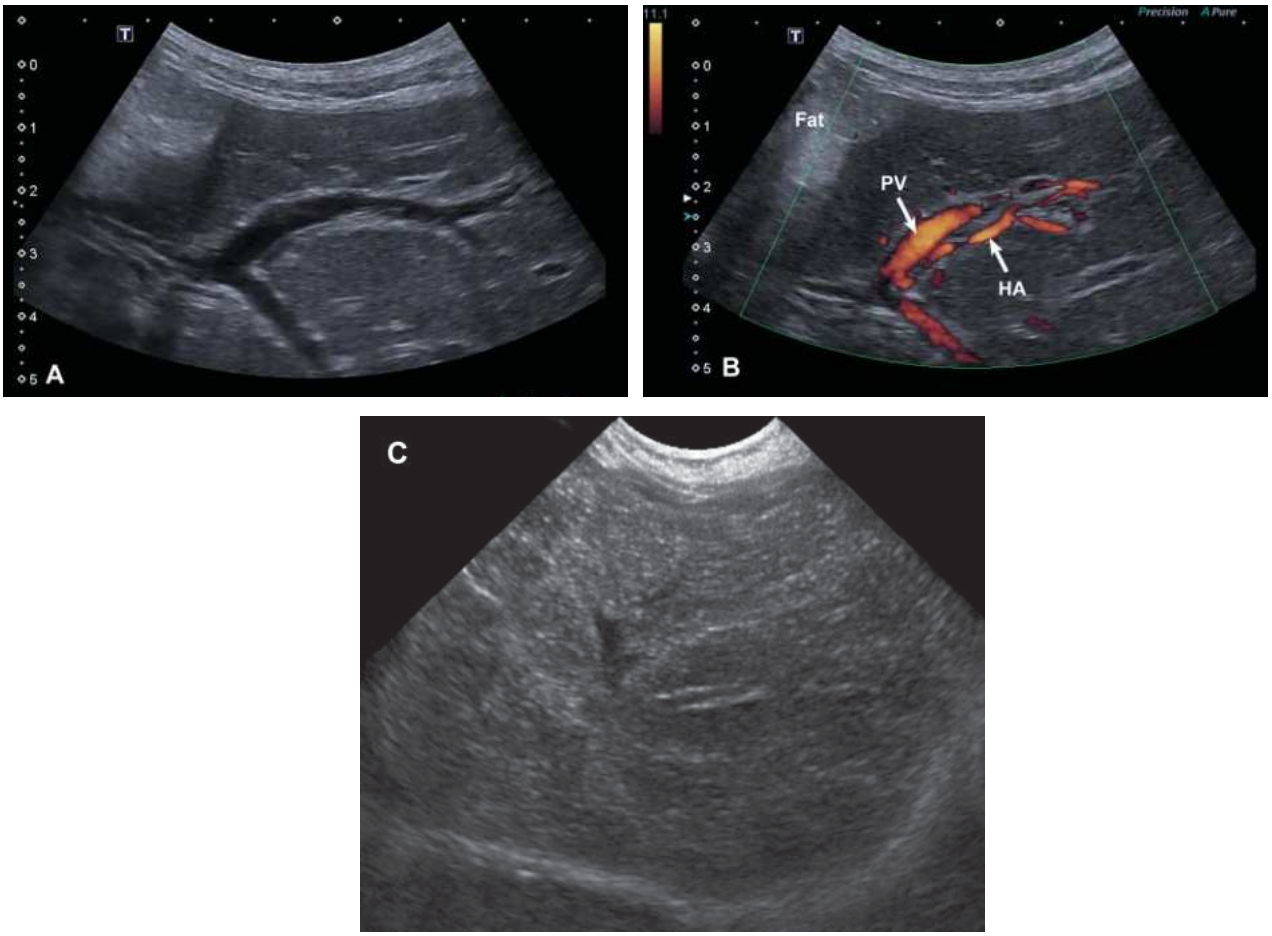


Figure 6.19. **A, B: Severe granulomatous cholangiohepatitis in a dog with mildly elevated alanine aminotransferase (ALT).** In these longitudinal B-mode **(A)** and Power Doppler **(B)** images, the periportal spaces are thickened and irregular and the hepatic arterial (HA) flow is increased. These arteries are not normally seen. The falciform fat is hyperechoic. Surgical biopsies revealed severe inflammation primarily involving the portal triads and periportal tissues of unknown etiology (normal cultures and copper level). PV, portal vein. **C**: Parasitic infestation (Heterobilharzia americana) in a 6-year-old Dachshund with increased liver enzyme elevation detected on a lab work screening before an elective dental procedure. The liver is very coarse and core biopsies revealed multifocal granulomatous cholangitis and moderate hepatocellular hypertrophy. In the centre of many of the granulomas were foci of mineral and/or degenerate parasites. See Figure 8.32 for intestinal changes in the same dog.

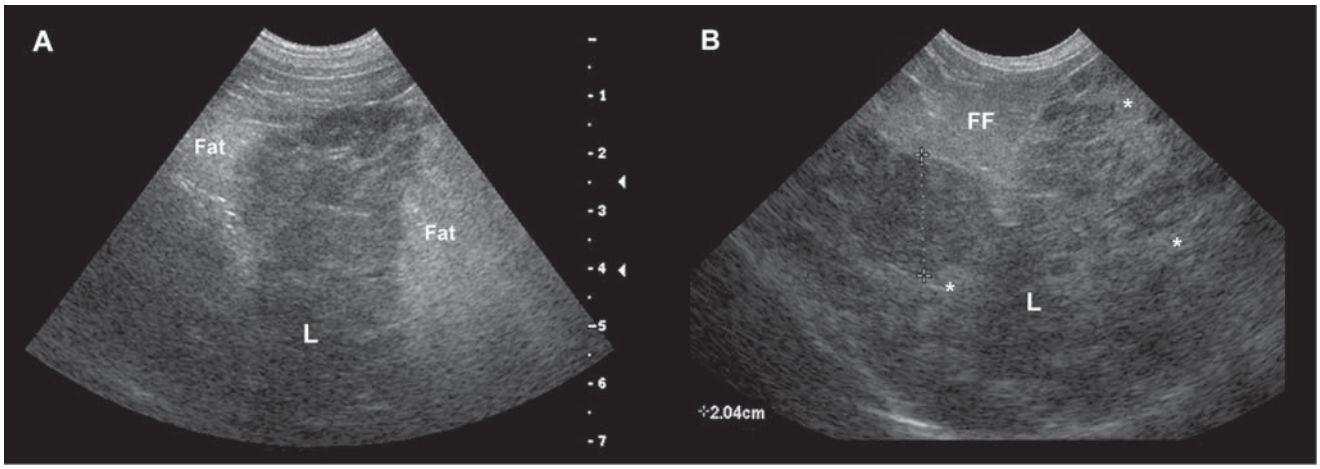


Figure 6.20. **Chronic active hepatitis and nodular hyperplasia. A:** Longitudinal image of the left portion of the liver (L), which appears diffusely hypoechoic, and with irregular and ill-defined contours. The adjacent fat is hyperechoic. Chronic active hepatitis was diagnosed on fine-needle aspiration and ultrasound-guided biopsy. **B:** Transverse image of the left portion of the liver (L) in another dog with diffuse parenchymal heterogeneity. Several hypoechoic coalescing nodules are found that reach up to 2 cm, as well as hyperechoic patches (*). Ultrasound-guided biopsy confirmed chronic hepatitis with fibrosis and nodular hyperplasia. FF, falciform fat.

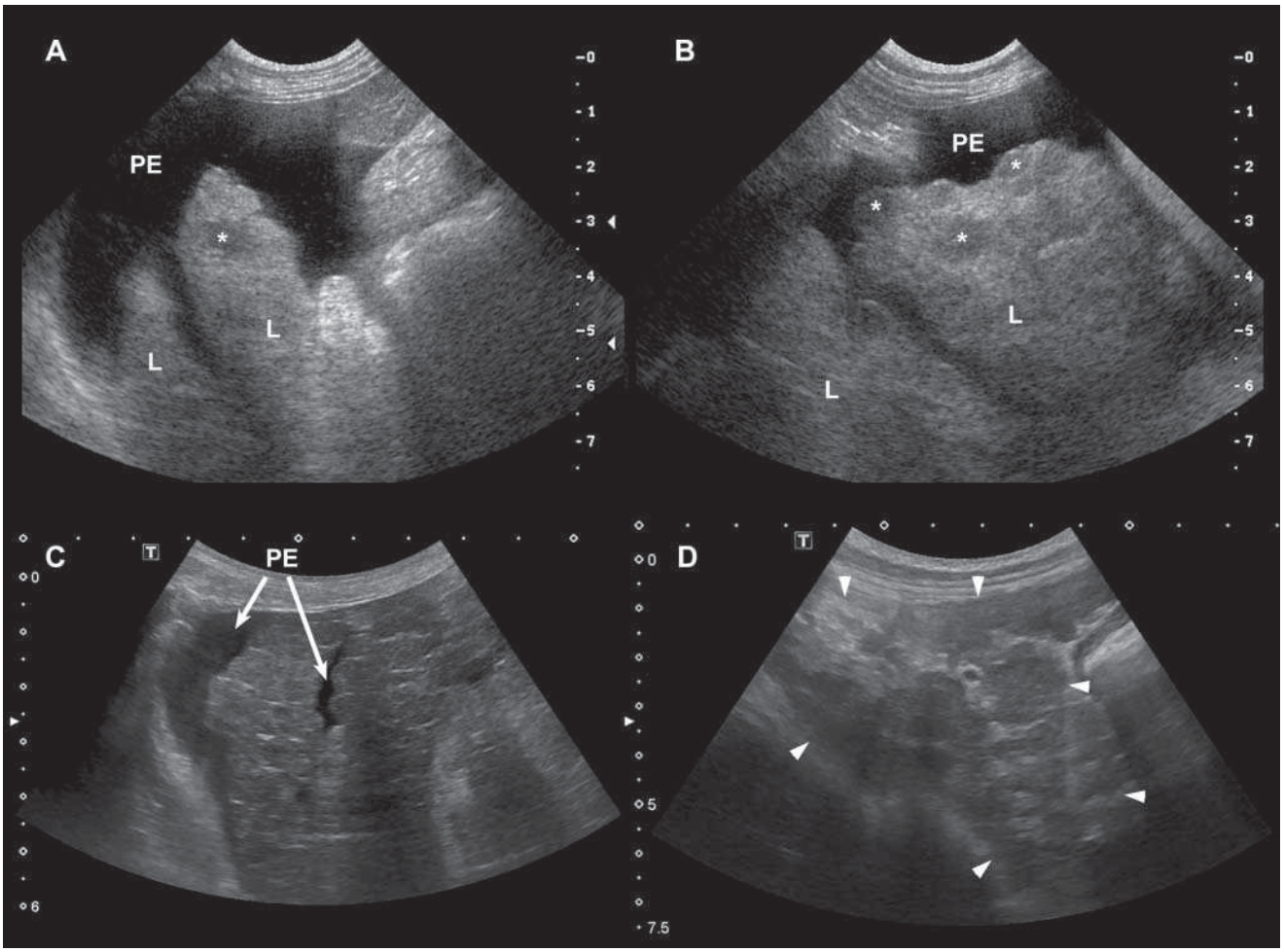


Figure 6.21. Hepatic cirrhosis in three dogs. Transverse oblique images of the right **(A)** and left **(B)** portions of the liver (L) in a dog with chronic hepatic insufficiency. All lobes are small and hyperechoic. Hypoechoic nodules (*) are found throughout the parenchyma, irregularly deforming its contours. These contours are visualized because of the presence of a large volume of anechoic peritoneal effusion (PE). These findings are common in end-stage cirrhosis in dogs. **C**: In this Cocker Spaniel, the liver is more uniformly echogenic, with nodular contours that are made evident by the presence of PE. **D**: The liver (arrowheads) of this other small-breed dog is more heterogeneous with hyperechoic areas. A small volume of effusion was present but not seen in this image.

diffuse hyperechogenicity (Sato and Solano 2004), although, as for other round-cell infiltrations, several manifestations are possible (Figure 6.23). Hepatic carcinomas can also be diffuse, or involve multiple lobes, with a variable ultrasonographic appearance that depends on the presence of necrosis, inflammation, hemorrhage, or cavitation. A mixed pattern of echogenicity is common with these malignant tumors (Figure 6.24).

Miscellaneous Diffuse Hepatic Disorders

Other types of hepatopathies can be encountered in small animals, although less commonly. Amyloidosis, primarily affecting Shar-peis and Abyssinian and Siamese cats, can cause hepatic enlargement and parenchymal ultrasonographic changes. In cats, the liver tends to become diffusely heterogeneous with mixed hyperechoic and hypoechoic foci

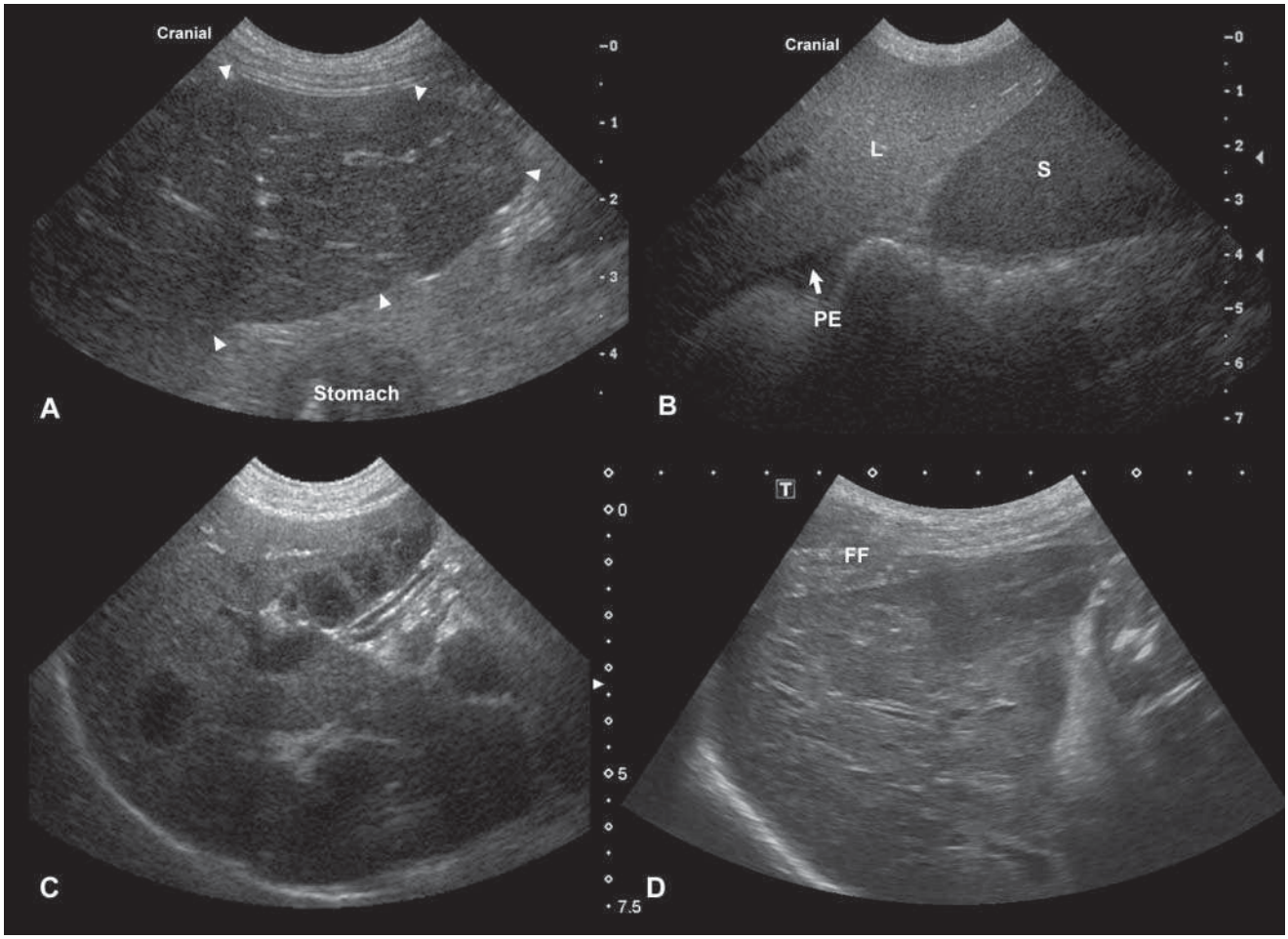


Figure 6.22. **Canine lymphoma. A:** Transverse oblique image of the left portion of the liver in a dog with multicentric lymphoma. The portal vein walls are prominent because of diffuse parenchymal hypoechogenicity. The left lateral hepatic lobe is enlarged (arrowheads), extending several centimeters caudal to the stomach, and its caudal tip is rounded. **B:** Lymphoma can also cause diffuse hepatic hyperechogenicity (L), as seen in another dog. The spleen (S) is relatively hypoechoic. Both organs are enlarged and their borders are rounded. Peritoneal effusion is also present (PE). **C:** In another dog with lymphoma, multiple, well-defined, hypoechoic nodules (*) are noted throughout the liver. **D**: The liver of this other dog is heterogeneous. FF, falciform fat.

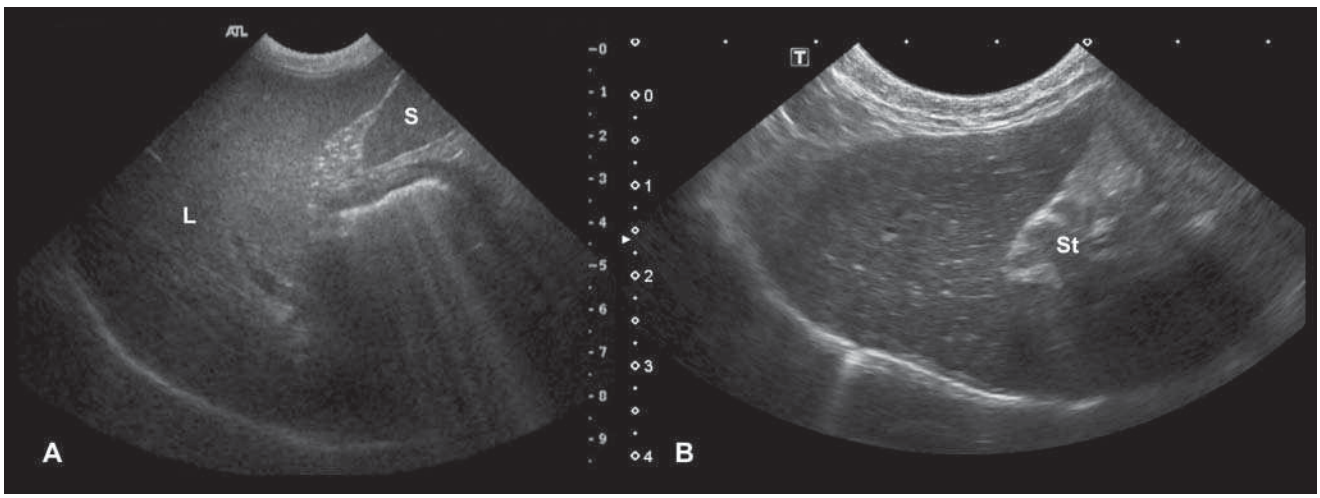


Figure 6.23. **Mast cell infiltration in a dog (A) and a cat (B). A:** In this dog, the liver (L) is uniformly hyperechoic. S, spleen. **B**: In this cat, by contrast, the liver was hypoechoic, confirming that round-cell infiltrations can manifest variable echogenic patterns.

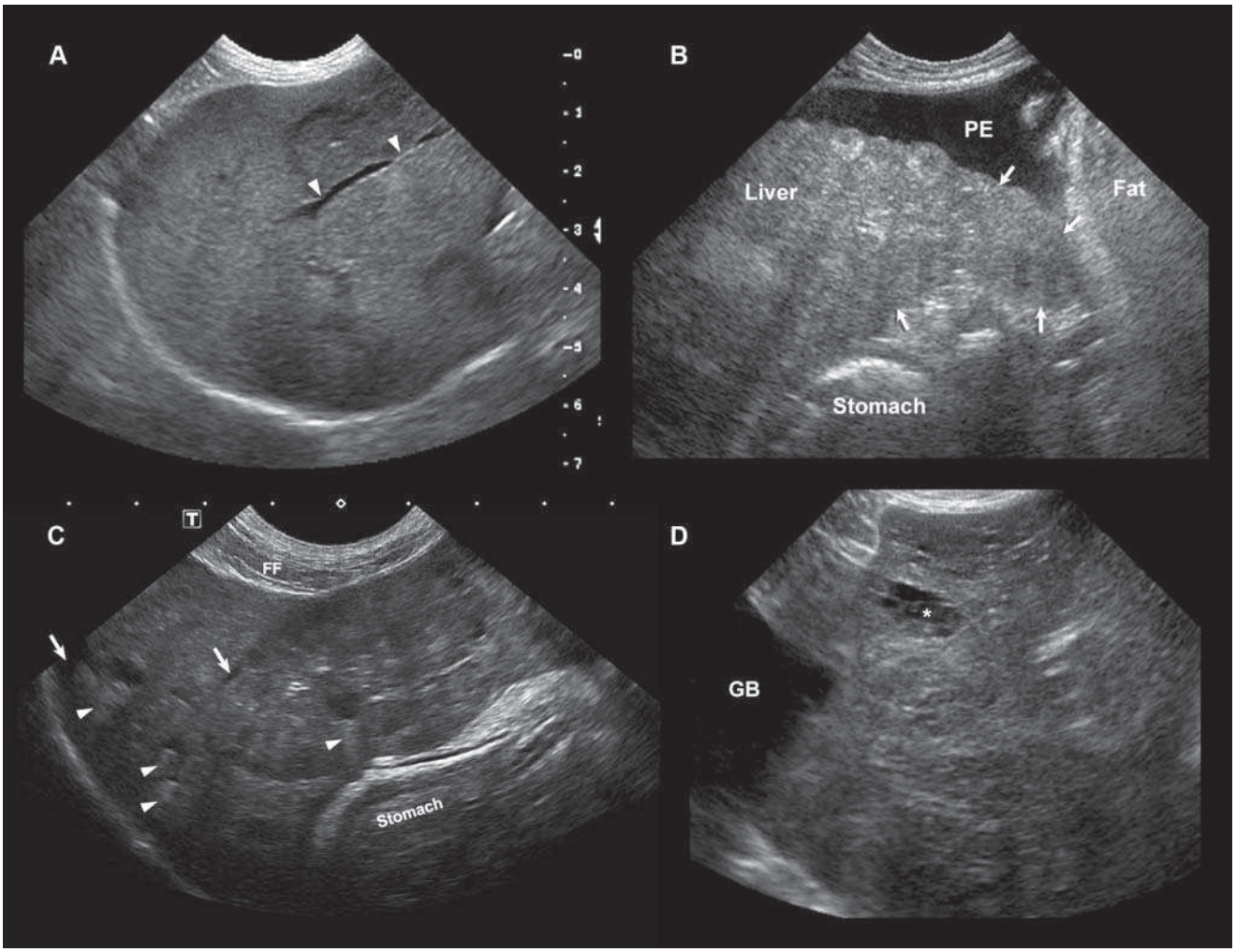


Figure 6.24. **Diffuse hepatic carcinoma and hemangiosarcoma. A:** Hepatic adenocarcinoma in a cat. The liver is moderately enlarged and mildly inhomogeneous, with several ill-defined hypoechoic areas. The neoplastic infiltration deforms the vasculature (arrowheads). **B:** Hepatocellular carcinoma in a dog. Longitudinal image of the left lateral hepatic lobe in a dog with diffuse hepatocellular carcinoma. This lobe extending caudal to the stomach (arrows) is hyperechoic and presents a nodular border. Marked peritoneal effusion is also evident ventrally (PE). **C**: In this 11-year-old cat with weight loss and increased liver enzymes, fine-needle aspiration revealed malignant epithelial cells. The liver is heterogeneous and presents several anechoic cavitary areas, some of which are associated with acoustic enhancement (arrowheads). Peritoneal effusion (arrows) is also present between liver lobes and along the diaphragm. FF, falciform fat. **D**: Diffuse hemangiosarcoma in a dog. The infiltrative process mimicked benign vacuolar hepatopathy with biliary cystic (*) changes. GB, gallbladder.

(Beatty et al. 2002). Spontaneous hepatic rupture and hemoabdomen can also be caused by massive hepatic amyloidosis. In dogs with hepatocutaneous syndrome (superficial necrolytic dermatitis), the liver can become highly hyperechoic with diffusely distributed 0.5–1.5 cm-wide hypoechoic regions, producing a honeycomb pattern (Nyland et al. 1996) (Figure 6.25).

Focal Hepatic Parenchymal Disorders

The improvement in ultrasound equipment technology has increased the sensitivity of ultrasonography in detecting focal hepatic lesions. It has been suggested that well-differentiated carcinomas (also called hepatomas) exceeding 5 mm can be detected in ideal imaging conditions in people (Nyman et al. 2004). The conspicuity of a focal lesion is also greatly influenced by its imaging characteristics. Hence, for a given size, an anechoic cyst is more likely to be detected than a soft-tissue nodule of echogenicity similar to one of adjacent normal parenchyma. Although many different types of focal lesions can be detected with ultrasonography, the appearance of several of these processes is quite variable, resulting in limited diagnostic specificity. The advances in contrast harmonic

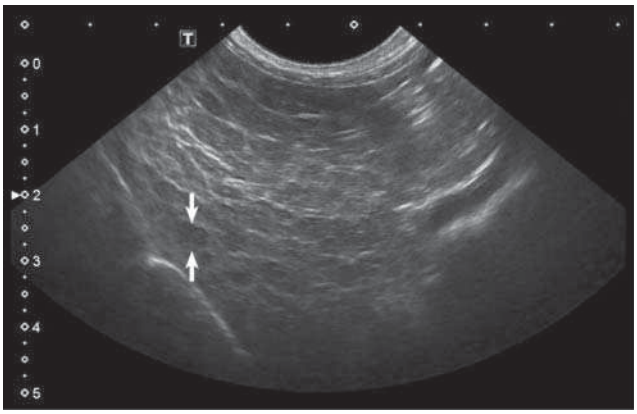


Figure 6.25. Hepatocutaneous syndrome. Sagittal image of the left central portion of the liver of a dog with superficial necrolytic dermatitis. Diffusely distributed hypoechoic irregular foci (arrows) are surrounded by hyperechoic parenchyma, giving a honeycomb pattern.

ultrasonography have helped to increase the overall diagnostic accuracy and may prove to be useful in clinical settings (Nyman et al. 2004; O'Brien et al. 2004) (see Chapter 16).

Table 6.3 lists the diagnostic differential for focal hepatic lesions, based on their typical appearance. Although some trends in ultrasonographic appearance have been reported for some of these processes, a definitive diagnosis usually requires fine-needle aspiration or biopsy.

Benign Hyperplasia and Neoplasia

Benign nodular hyperplasia is common, particularly in dogs, and accounts for many focal hepatic lesions identified with ultrasonography. Although these regenerative nodules can vary in echogenicity and size, they tend to appear as hypoechoic nodules measuring less than 5–15 mm wide (Stonewater et al. 1990; O'Brien et al. 2004) (Figure 6.26). As for most other types of focal lesions, their margin can be well or poorly defined. Benign hepatic adenomas cannot be differentiated from carcinomas or hepatomas appear as masses of variable size and are usually isoechoic to hyperechoic, although they may also present cavities (O'Brien et al. 2004) (Figure 6.27).

Malignant Neoplasia

The liver is a common target for metastases, mainly through the portal system, which drains most abdominal structures. Primary hepatic neoplasms such as hepatocellular carcinomas can also be seen as focal or multifocal masses, although less frequently than metastasis. The variable tissue characteristics of primary and metastatic neoplastic processes, including tissue density, vascular pattern, necrosis, liquefaction, and calcification, cause variable ultrasonographic appearances (Whiteley et al. 1989; O'Brien et al. 2004) (Figures 6.28–6.32, 6.36–6.38). Focal hypoechoic lesions with a hyperechoic center, also termed **target lesions**, are usually predictive of metastases (Figures 6.30, 6.33), although benign processes, such as nodular hyperplasia, can cause a similar pattern (Cuccovillo and Lamb 2002; O'Brien et al. 2004) (Figure 6.40C). It has been reported that the finding of at least one target lesion in the liver or spleen had a positive predictive value of 74% for malignancy in small animals (Cuccovillo and Lamb 2002). Other features supportive of malignancy include lesion size (>3 cm) and presence of peritoneal effusion (Guillot et al. 2009; Murakami et al. 2012). Additional features distinguishing malignant from benign hepatic masses may be found with triple-phase computed tomography (CT) (Kutura et al. 2013).

Table 6.3
Diagnostic differentials for focal hepatic lesions with ultrasonography

Anechoic	Hypoechoic	Hyperechoic	Mixed Echogenicity
Cyst	Nodular hyperplasia	Nodular hyperplasia	Nodular hyperplasia
Cystic tumor	Metastasis	Primary neoplasia	Primary neoplasia
Necrosis	Lymphoma	Metastasis	Metastasis
Abscess	Primary hepatic neoplasia	Mineralization or cholelithiasis	Abscess
Hematoma	Abscess	Abscess	Hematoma
	Necrosis	Fat or myelolipoma	
	Hematoma	Granuloma	
	Complex cyst	Gas	
		Metallic clip	

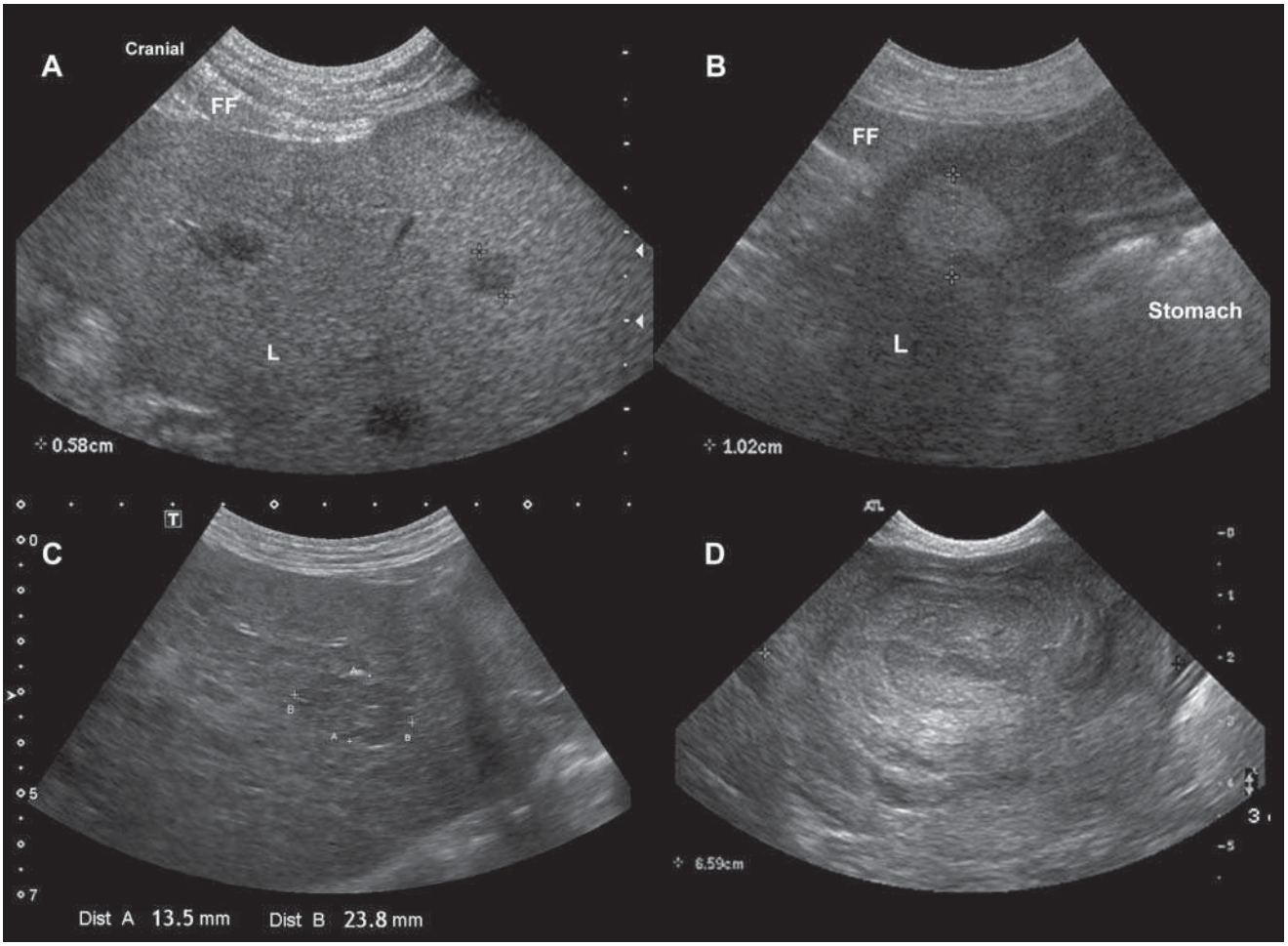


Figure 6.26. **Nodular hyperplasia in four dogs. A:** Several poorly defined hypoechoic foci measuring less than 1 cm wide are noted in a liver (L) that is otherwise hyperechoic. FF, falciform fat **B:** The regenerative nodule in this other dog is hyperechoic and well defined. **C**: Nodular hyperplasia (between cursors) can also appear more heterogeneous. **D**: Nodular hyperplasia with acute and chronic hemorrhage and necrosis forming a 6.6 cm heterogeneous mass in this 11-year-old Pomeranian dog.

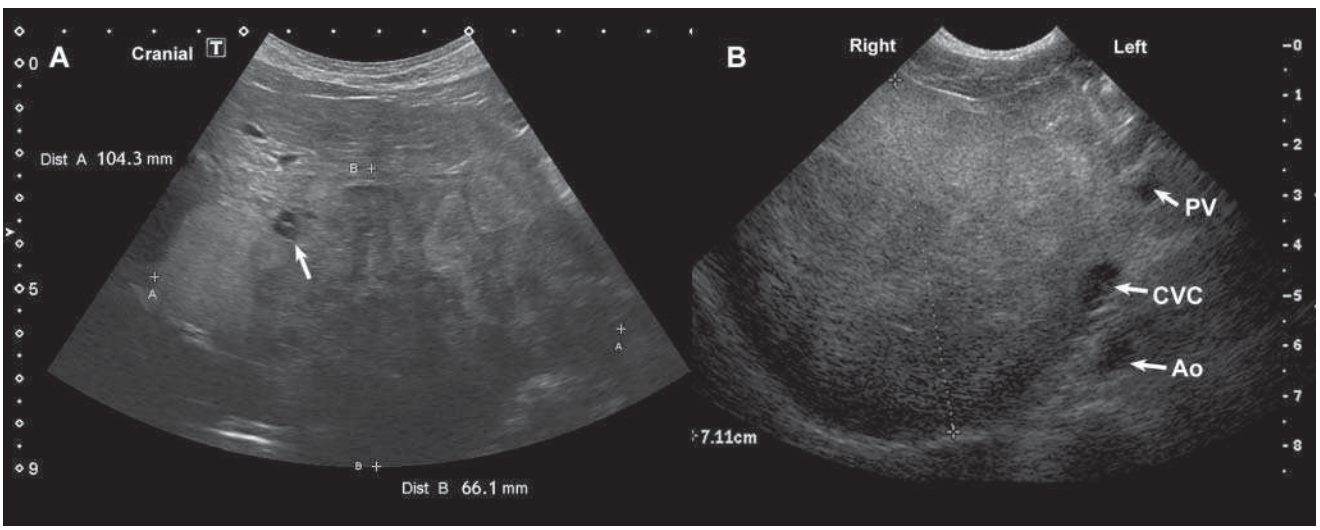


Figure 6.27. **Hepatomas (or well-differentiated carcinomas).** (for full caption, see facing page)

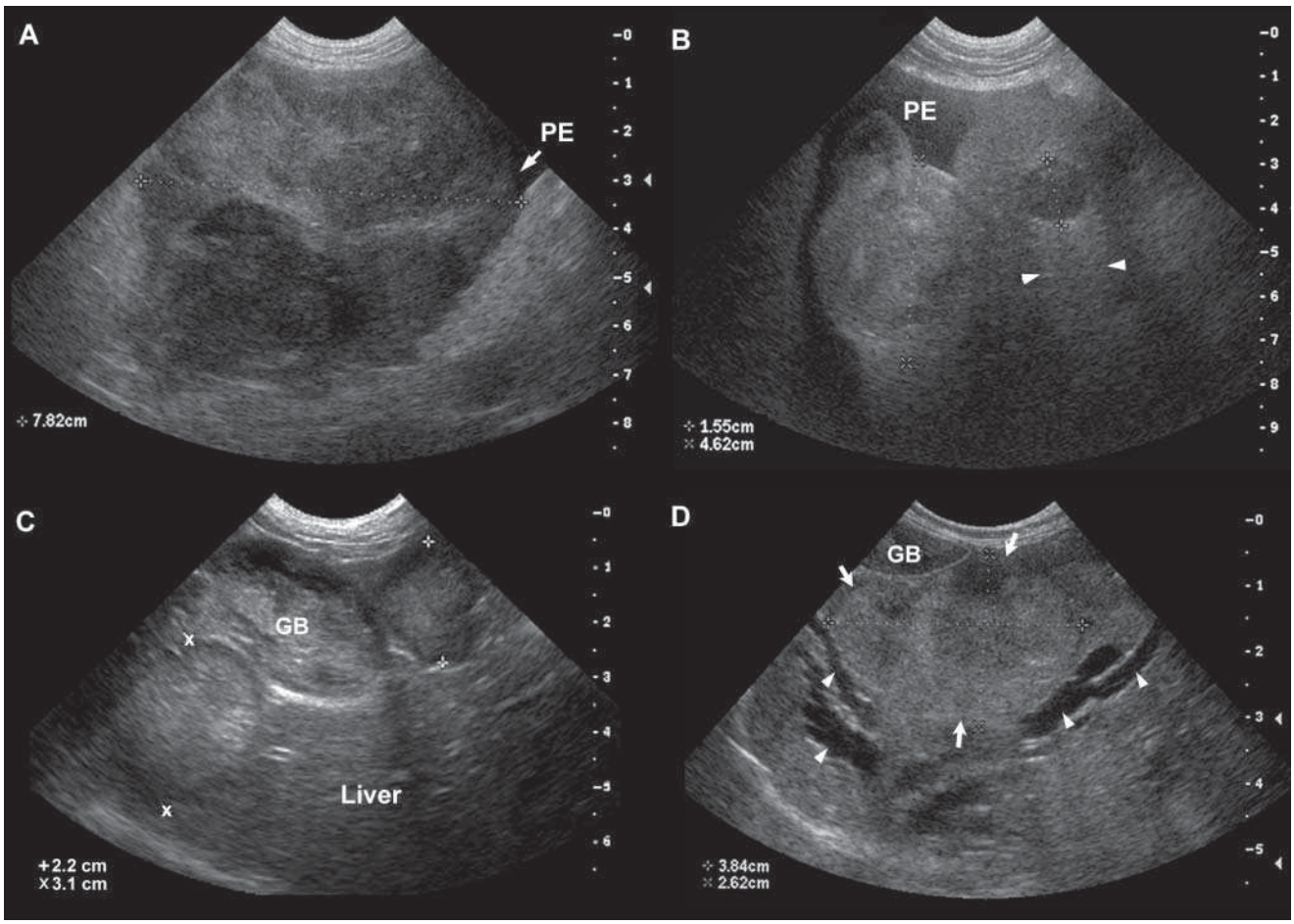


Figure 6.28. **Primary liver carcinomas. A:** Hepatocellular carcinoma in a dog. Transverse image obtained in the right cranial abdomen of a dog with a hemoabdomen. An irregular, inhomogeneous and poorly defined mass (7.8 cm wide) is deforming the architecture of a liver lobe. A small amount of peritoneal effusion (PE) is noted around the mass. **B:** Hepatic adenocarcinoma and metastasis in a dog. A spherical, hyperechoic mass (4.6 cm) is deforming the contour of a liver lobe and surrounded by mildly echogenic PE. Another small, hypoechoic nodule (1.6 cm) in the same lobe is associated with acoustic enhancement in the far field (arrowheads). **C:** Neuroendocrine carcinoma in a dog. Multiple mildly hyperechoic masses (2.2–3.1 cm) demonstrating a hypoechoic halo were found in the liver of this dog, with a histological diagnosis of neuroendocrine carcinoma. GB, gallbladder. **D:** Biliary carcinoma in a cat. Transverse image of the liver in a cat with icteria. A lobulated, mildly hyperechoic, inhomogeneous mass (arrows and cursors) is displacing the gallbladder (GB) ventrally. Irregular, anechoic, tubular structures (arrowheads) are also noted throughout the liver, consistent with dilated intrahepatic biliary ducts.

Figure 6.27. **Hepatomas (or well-differentiated carcinomas). A**: Irregular and poorly defined mass in the left portion of the liver of this 12-year-old small breed dog. The mass (between cursors) is moderately echogenic and mildly heterogeneous, with a few small cavities (arrow indicates one present in this image) . **B**: Transverse image of the right portion of the liver of another dog with increased liver enzymes. A large, mildly hyperechoic and mildly heterogeneous mass measuring at least 7 cm wide is in the right portion of the liver and in contact with the portal vein (PV) and caudal vena cava (CVC), and close to the aorta (Ao). The extent of this mass and the lack of vascular invasion could not be confirmed with the ultrasonographic exam and required computed tomography.

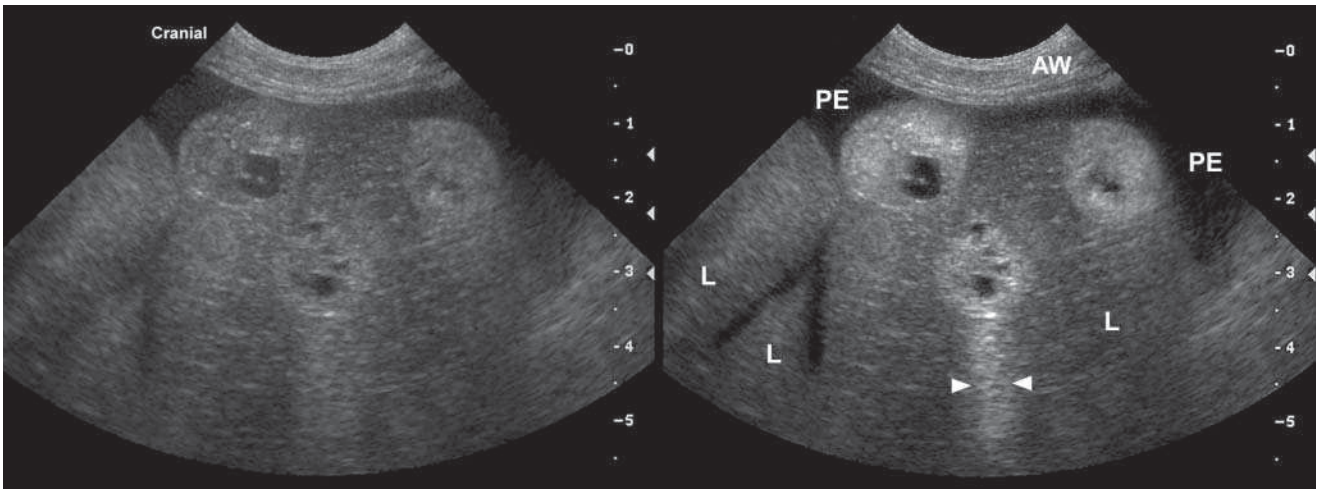


Figure 6.29. **Hepatic metastases.** On these ultrasonographic and corresponding enhanced images, three irregular hyperechoic nodules, 1.0–1.5 cm wide, are found in the liver of a dog with splenic hemangiosarcoma. Hypoechoic to anechoic cavitary foci are found in some of these nodules and are associated with far enhancement (arrowheads). Peritoneal effusion (PE) delineates the liver lobes (L). Hepatic metastases were confirmed at surgery. AW, abdominal wall.

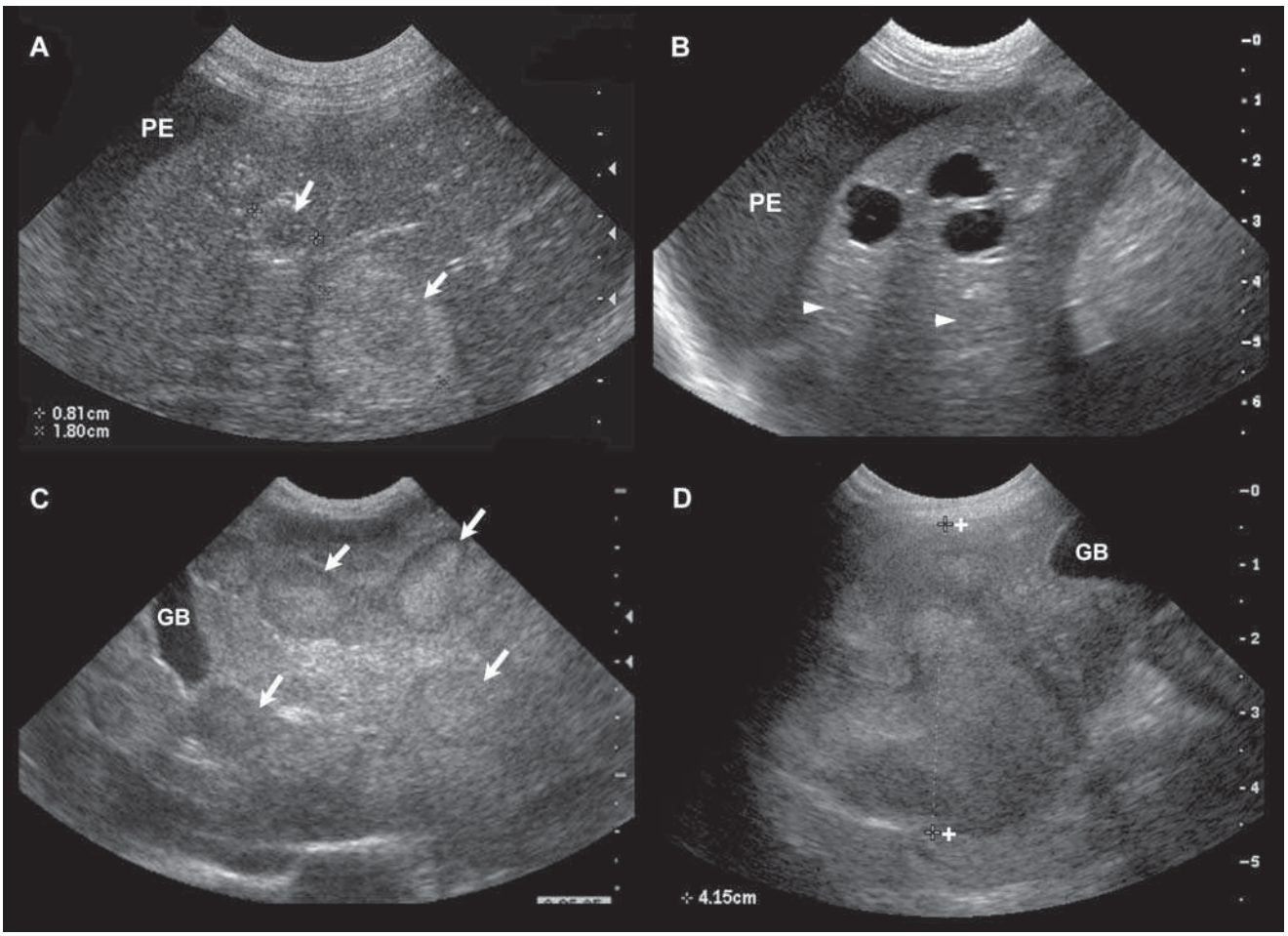


Figure 6.30. **Hepatic metastases. A:** Pancreatic adenocarcinoma. Oblique image of the left hepatic lobe with two distinct metastatic nodules (arrows). A smaller hypoechoic nodule with a thin hyperechoic rim and a larger hyperechoic nodule are present, measuring 0.8 and 1.8 cm wide, respectively. Mildly echogenic peritoneal effusion (PE) is present. **B:** Splenic hemangiosarcoma. Well-defined, anechoic cavitary metastases are seen in the liver of another dog with splenic hemangiosarcoma and severe, echogenic PE consistent with hemorrhage. Acoustic enhancement (arrowheads) is noted distal to these fluid-filled lesions. **C:** Thyroid carcinoma. Multiple "target" lesions (arrows) are seen throughout the liver of this dog with thyroid carcinoma. The hypoechoic halo seen at the periphery of these rather hyperechoic nodules is a feature that is most commonly observed with metastases. GB, gallbladder. **D:** Pancreatic adenocarcinoma. A 4-cm inhomogeneous mass is in the liver of this other dog with malignant pancreatic neoplasia. The findings on fine-needle aspiration supported a diagnosis of pancreatic metastasis. GB, gallbladder.

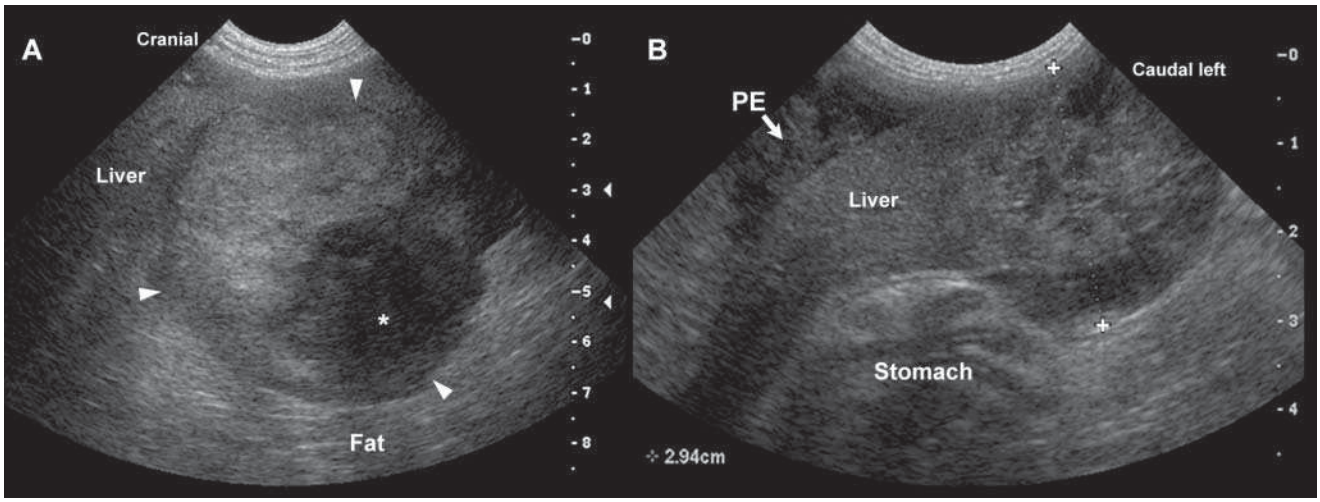


Figure 6.31. **Hepatic hemangiosarcoma. A:** Longitudinal image obtained of the left portion of the liver in a dog with acute hemoabdomen. A large hyperechoic mass (arrowheads) with a hypoechoic necrotic area (*) involves the margin of a hepatic lobe. These features are common with malignant tumors. **B:** Oblique image of the left portion of the liver in a cat with hemoabdomen. A 3-cm-wide inhomogeneous mass with small anechoic cavitary portions is at the caudal tip of the left lateral liver lobe. Peritoneal effusion (PE) with echogenic floating structures is identified in the cranioventral abdomen, consistent with hemorrhage.

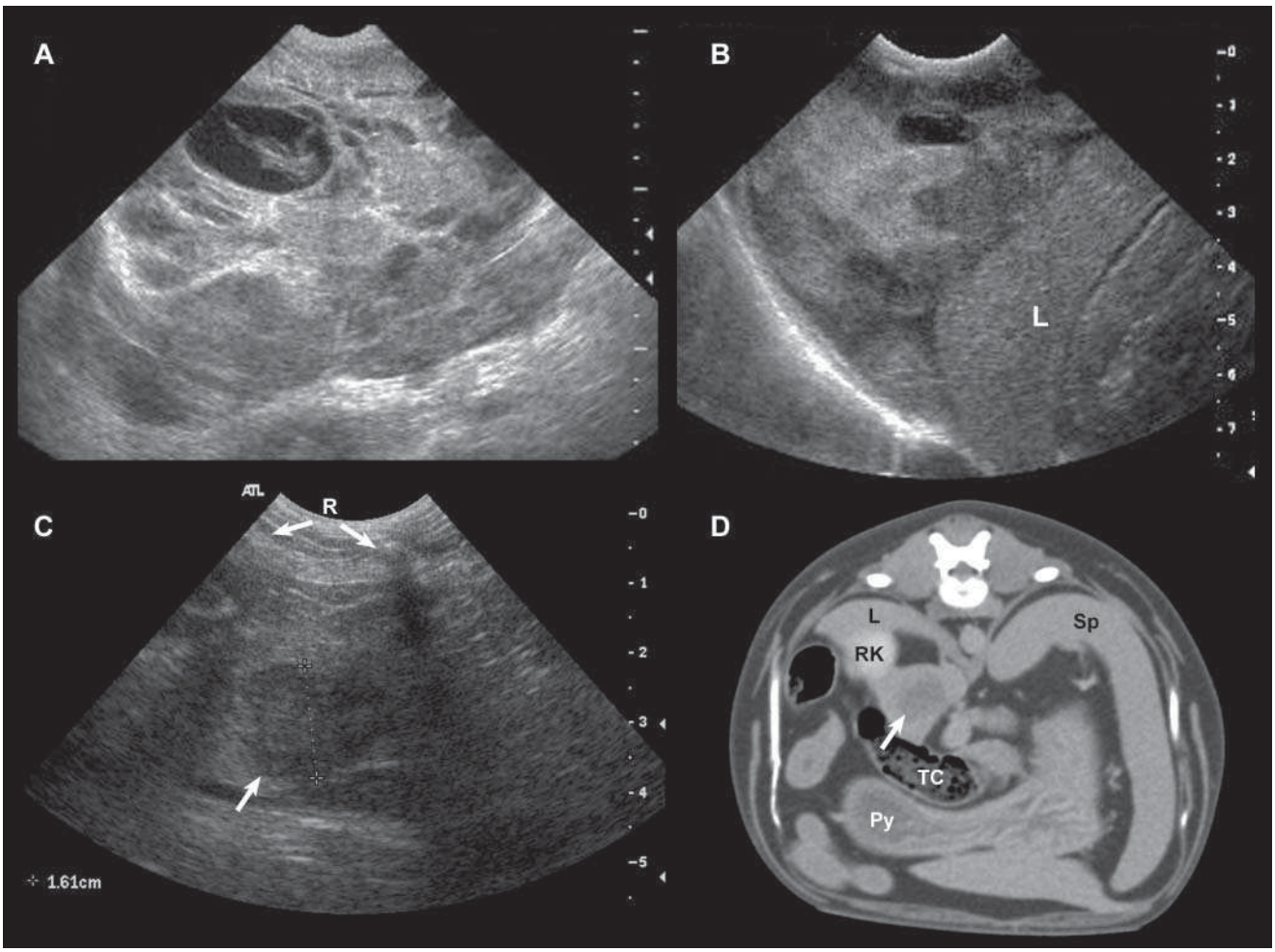


Figure 6.32. **Unusual liver tumors in two dogs. A, B:** Myxosarcoma. A large, markedly heterogeneous, cavitated mass in the liver of this dog **(A)** is disturbing most of the hepatic architecture. The same tumor was reimaged 3 months later **(B)**. In this image, a clear distinction is made between the heterogeneous mass and the normal liver (L). **C, D**: In another dog with hypoglycemia, a small *insulinoma-like tumor* was identified in the caudate liver lobe (arrows). A longitudinal sonographic image **(C)** was obtained from a right intercostal approach. R, ribs. Computed tomography **(D)** was used to confirm the location of this mass. RK, right kidney. L, liver. Sp, spleen. TC, transverse colon. Py, pyloric antrum.

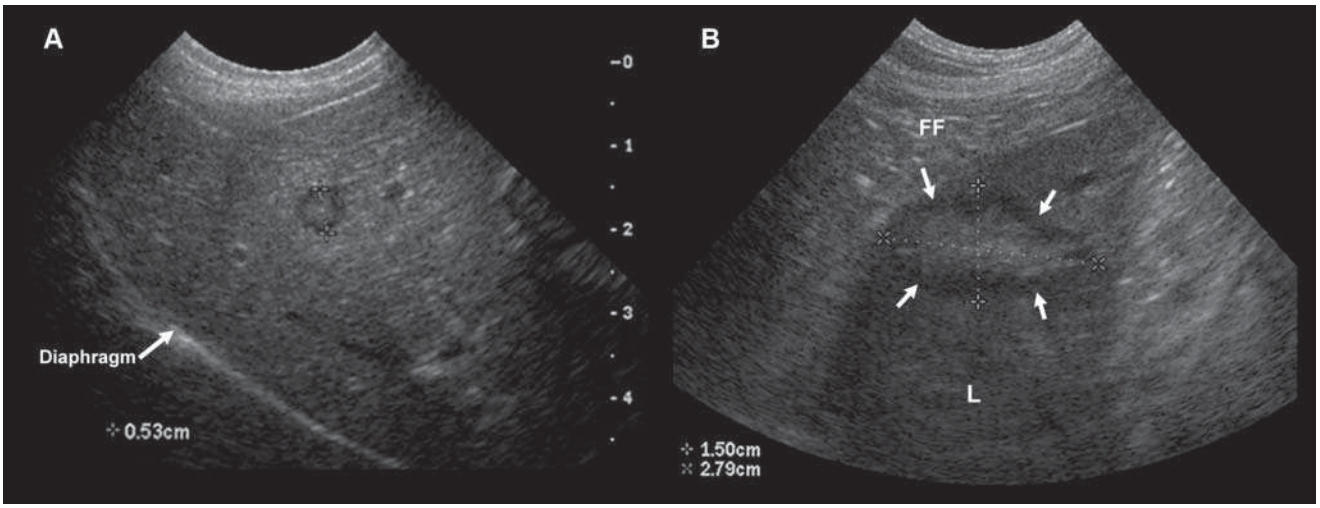


Figure 6.33. **Target lesions. A:** Longitudinal image of the mid-portion of the liver in a dog with intestinal carcinoma, on which a small nodule outlined by a peripheral hypoechoic halo is seen. The central portion of this lesion is more echogenic, giving the impression of a target. **B:** Longitudinal oblique image of the left portion of the liver of a dog with a primary hepatocellular carcinoma identified in the right lateral lobe. An ovoid nodule with a peripheral hypoechoic halo and a more echogenic center (arrows), consistent with a metastasis, is in the liver (L). Smaller but similar target lesions were found in the rest of the liver. FF, falciform fat.

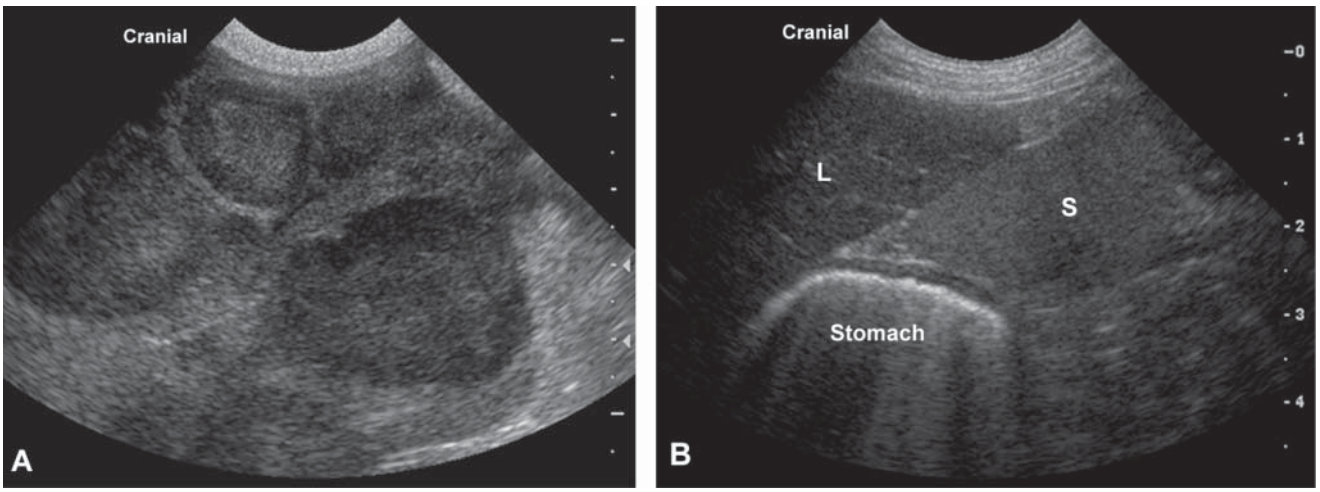


Figure 6.34. **Disseminated histiocytic sarcoma (malignant histiocytosis). A:** Multiple hypoechoic nodules and masses (more than 3 cm wide) are in the liver of this Bernese Mountain Dog. These lesions are relatively well circumscribed and have a mildly echogenic center. The liver was also enlarged. **B:** In another dog with disseminated histiocytic sarcoma, the liver (L) is uniformly hypoechoic and enlarged. The difference between the hepatic and splenic (S) echogenicities was considered excessive.

Histiocytic neoplasms and lymphoma can demonstrate similar imaging characteristics. Although findings do vary, particularly with lymphoma, multifocal nodules or masses, hypoechoic or mixed in echogenicity, are commonly found with these processes (Cruz-Arambulo et al. 2002; Ramirez et al. 2002) (Figures 6.34, 6.35). Significant hepatic lymphadenopathy is also common with these neoplasms of round-cell origin and their presence often helps in diagnosing these processes.

Cavitary Lesions

Hepatic and biliary cysts are sometimes identified in dogs and cats and appear as well circumscribed, regular or irregular, anechoic foci, typically associated

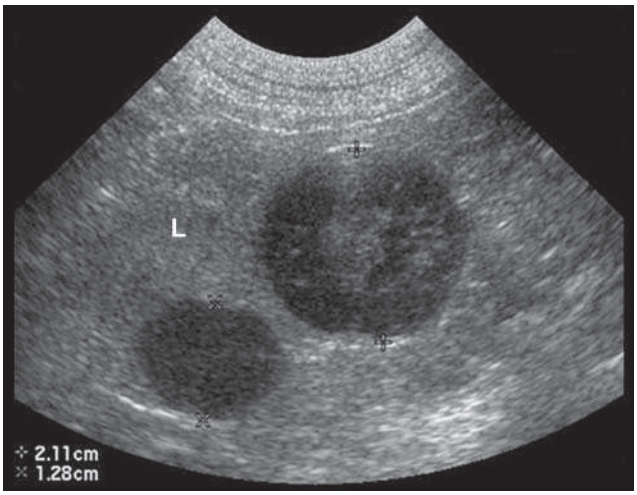


Figure 6.35. **Lymphoma.** Close-up longitudinal image of the left portion of the liver (L) of a dog with multicentric lymphoma. Two well-defined hypoechoic nodules, reaching 2.1 cm wide, are present, and the central portion of the largest nodule is more echogenic. These features are commonly recognized with lymphoma and malignant histiocytosis (see Figure 6.34A) in dogs. Round-cell neoplasms can however result in variable features (see Figures 6.22, 6.23).

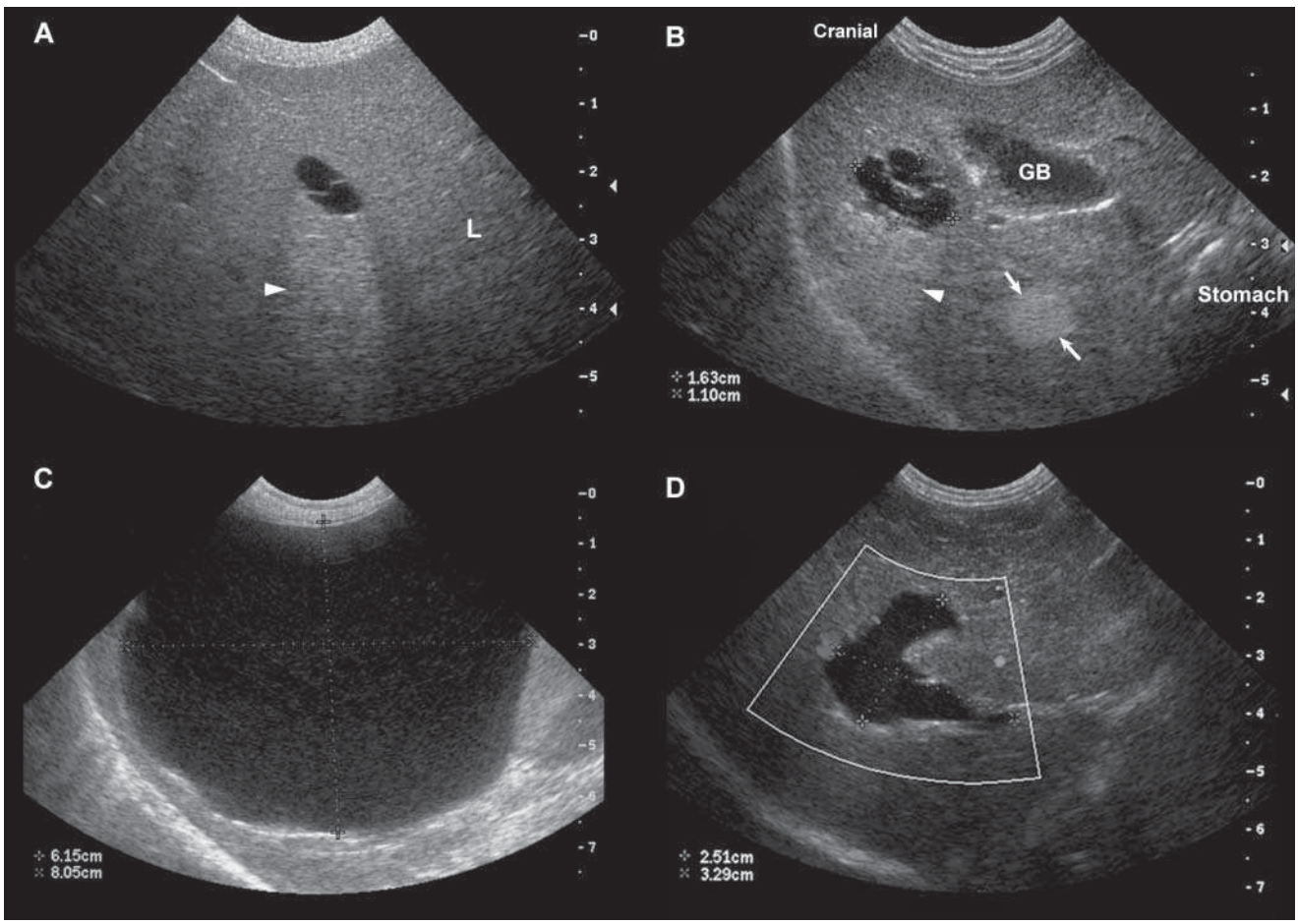


Figure 6.36. **Benign hepatic cyst-like lesions. A:** Transverse image of the liver (L) of a dog with a discrete anechoic structure (approximately 1 cm wide) that is septated and associated with far acoustic enhancement (arrows), consistent with hypoattenuating content. A clear fluid was aspirated with ultrasound guidance. The peripheral hepatic parenchyma is homogeneous. **B:** Longitudinal image of the liver of a dog with a well-circumscribed, loculated, anechoic structure. Irregular contours and far enhancement (arrowheads) are present. Bile was aspirated. The clinical significance of this finding was not determined in this patient. A hyperechoic regenerative nodule (arrows) is also present. The gallbladder (GB) wall is thickened and irregular, presumably because of cholecystitis. **C,D:** Ultrasound images of a large liver cyst in a dog with abdominal pain that were obtained before **(C)** and after **(D)** ultrasound-guided drainage. The peripheral liver parenchyma is normal.

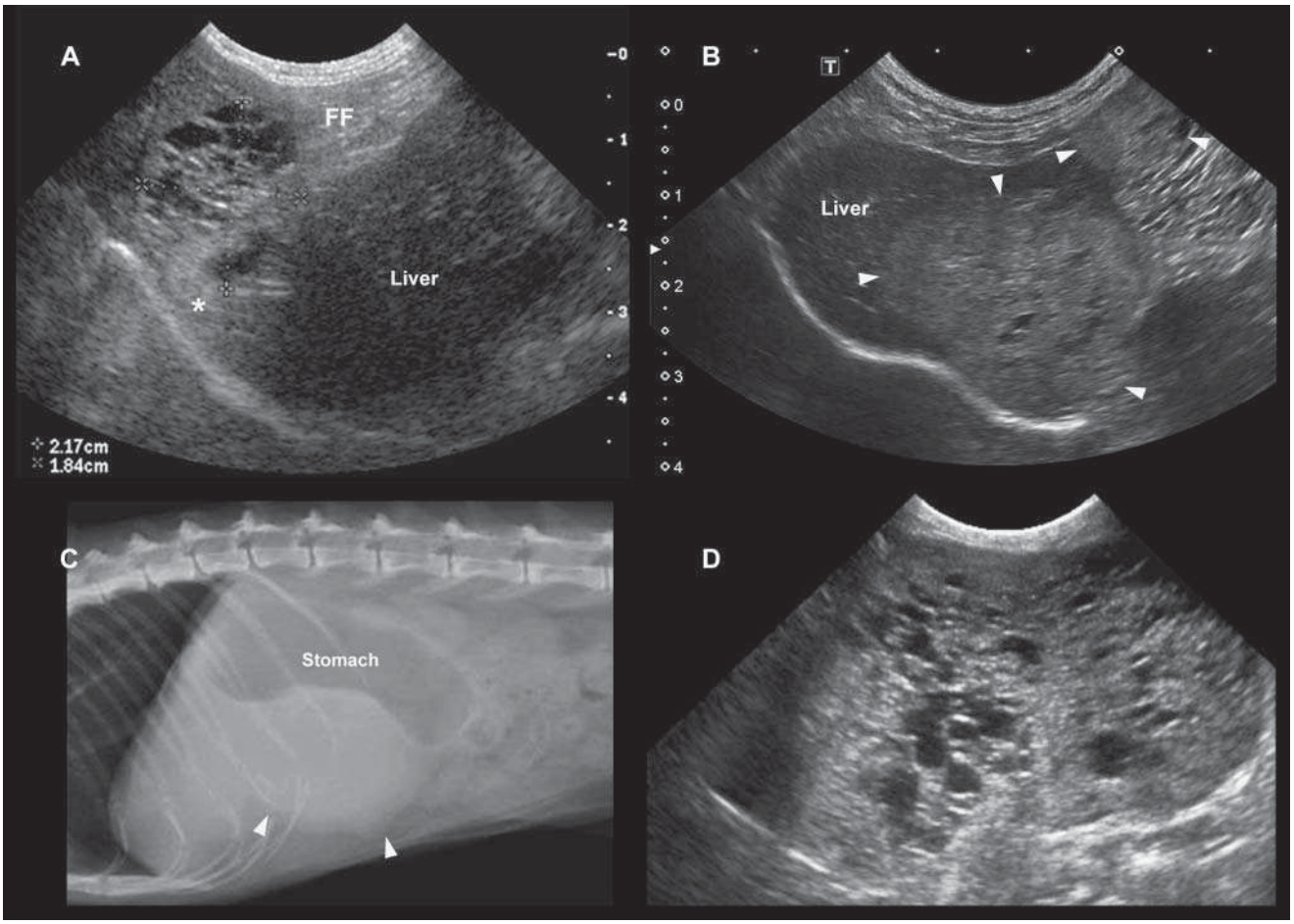


Figure 6.37. **Biliary cystadenomas and cystadenocarcinomas in cats. A**: Transverse ultrasonographic image of the liver of a cat with increased hepatic enzymes. A multiloculated mass (cursors) is identified in the right portion of the liver. Far acoustic enhancement is noted (*) because of the presence of hypoattenuating fluid-filled cavities. Biliary cystadenocarcinoma was confirmed through ultrasound-guided biopsy. FF, falciform fat. **B**: In this other 13-year-old domestic shorthair cat, several hyperechoic masses (arrowheads) filled with small anechoic cavities are detected in the liver, with a presumptive diagnosis of malignant epithelial tumor on fine-needle aspirations **C, D**: In this cat, a large hepatic soft-tissue mass (arrowheads) displaces the gas-distended stomach on the radiograph. The cystadenoma appears as a moderately echogenic mass filled with numerous anechoic cavities.

with far-enhancement artifact (Figure 6.36). In these benign cysts, the adjacent parenchyma is usually normal. These cavitary lesions must be differentiated from cystic tumors, such as biliary cystadenomas and cystadenocarcinomas, commonly demonstrating a multilocular pattern and a change in tissue appearance around the anechoic cavitations (Nyland et al. 1999) (Figure 6.37). Although more common in cats, cystic or cavitary tumors are also seen in dogs (Figure 6.38).

Hepatic abscesses, which are uncommon in dogs and cats, tend to appear as poorly marginated, round to oval, regular or irregular, hypoechoic lesions, which are often cavitated (Schwarz et al. 1998). Enhancement artifact, abdominal effusion, regional lymphadenopathy, and hyperechoic perihepatic fat are commonly seen in affected animals (Figure 6.39A). Abscesses can also show pus sedimentation in the central cavitations or appear as complex or more echogenic masses (Figure 6.39B). Hyperechoic foci with reverberation consistent with gas can also be observed (Figure 6.39C). Cellular debris or hemorrhage accumulating in benign hepatic cysts can mimic abscesses, although these lesions typically show a thinner, more well-defined rim. Parasitic cysts occurring with liver flukes or

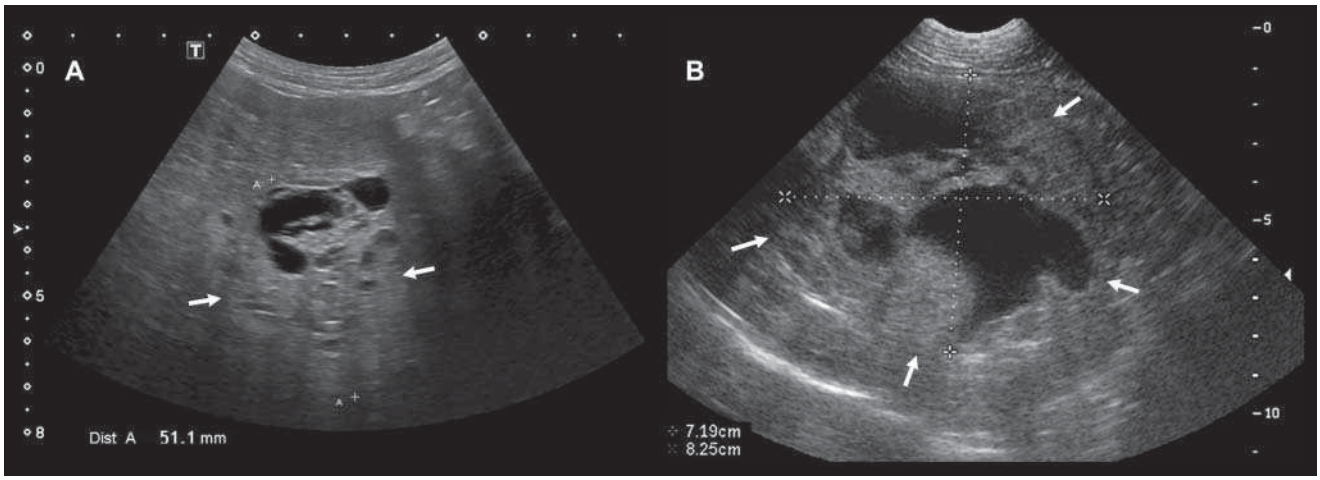


Figure 6.38. **Biliary carcinomas in two dogs. A**: A poorly defined, 5-cm hyperechoic mass (between cursors and arrows) with irregular anechoic cavities is identified in this 9-year-old dog. Histology revealed biliary cystadenocarcinoma. **B**: Longitudinal image of the right portion of the liver in an icteric dog with a large cavitated mass. This poorly defined mass (arrows) contains irregular hypoechoic and anechoic cavitations. The findings on ultrasound-guided fine-needle aspiration of the more solid portions of the mass were suggestive of biliary carcinoma.

hydatid disease can look similar to abscesses with the addition of mineralization (Nyland et al. 1999). Fine-needle aspiration can be useful in confirming the nature of the fluid contained in cavitary lesions and enabling drainage of abscesses.

Granulomas, Hematomas, and Mineralization

Hepatic granulomas or pyogranulomas can sometimes occur in dogs and cats, particularly with fungal diseases, with feline infectious peritonitis or with feline eosinophilic fibroplasia (Weissman et al. 2012) (Figure 6.40). Granulomatous lesions tend to be hyperechoic and inhomogeneous, as is the case in humans (Mills et al. 1990). Hepatic hemorrhage is rare in dogs and is usually related to hemangiosarcoma or trauma (Whiteley et al. 1989). Hepatic hematomas can also develop following ultrasound-guided procedures such as biopsies and demonstrate variable ultrasonographic changes related to clot organization and resorption (Figure 6.41). With time, hematomas tend to develop a cystic component following clot lysis. This feature, as well as the progressive reduction in size on follow-up exams, should help in differentiating spontaneous hematomas from neoplastic processes. Hepatic mineralization other than cholelithiasis can accompany benign processes (such as hematoma or granuloma) or malignant processes. Mineralization typically appears as strongly hyperechoic foci associated with acoustic shadowing (Figure 6.42).

Hepatic Lobe Torsion, Infarction, and Gas

Liver lobe torsion, which leads to lobar congestion, hemorrhage, and necrosis, can show variable signs that can mimic neoplasia or abscess formation. In a reported series, the affected lobe was commonly hypoechoic or mixed in echogenicity, and Doppler assessment of the lobe revealed reduced vascularity in many dogs (Hinkle Schwartz et al. 2006) (Figure 6.43). Spontaneous infarction is less common in the liver when compared with the spleen, but can show a similar pattern of an irregular and poorly echogenic area with reduced flow on color Doppler or power Doppler (Figure 6.44). Hyperechoic foci associated with reverberating artifact, consistent with gas, can be seen in the liver, most often in the biliary tract, following surgery. Gas can also form because of bacterial infection (Figures 6.39 and 6.45). Metallic clips used with surgical biopsies appear as short, strongly hyperechoic lines with reverberation, mimicking gas. A radiograph can be used, if needed, to differentiate gas from metal.

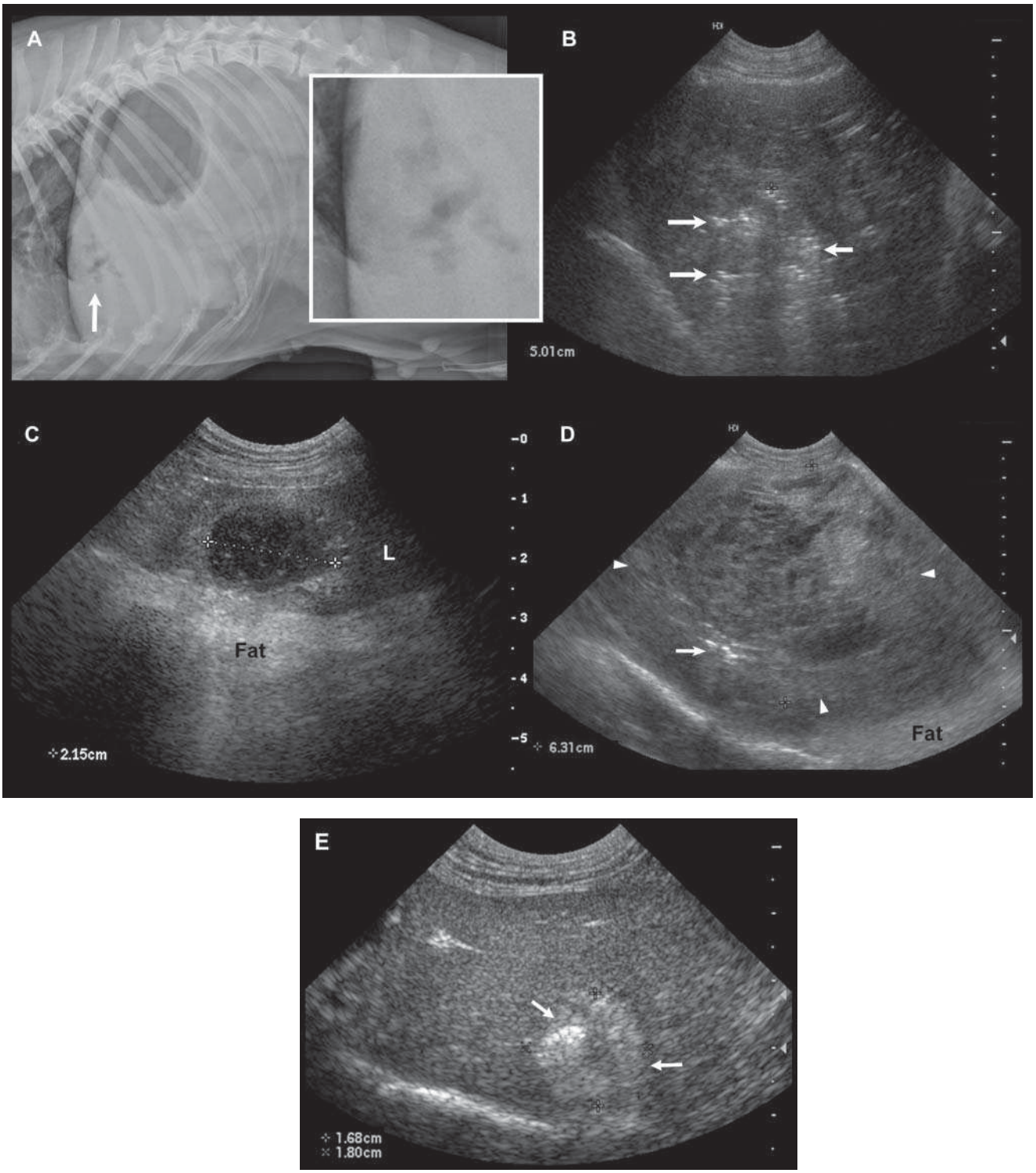


Figure 6.39. **Hepatic abscesses.** Lateral radiograph (**A**) and longitudinal sonographic image (**B**) of the liver of a medium sized dog in which a hepatic abscess was identified. The abscessed region (arrows), deep in the liver, is poorly marginated and contains several reverberating, hyperechoic foci consistent with gas, which are evident on the radiograph. **C:** Longitudinal image of the left portion of the liver in a febrile dog with abdominal pain. An irregular hypoechoic lesion (arrowheads) can be seen. The abdominal fat adjacent to the liver (L) border is hyperechoic and hyperattenuating, suggesting steatitis. Ultrasound-guided fine-needle aspiration confirmed the presence of an abscess. **D:** In this other dog with abdominal pain and fever, there is a complex mass (arrowheads). Intraparenchymal reverberating hyperechoic foci consistent with gas are noted dorsally (arrow). **E:** Longitudinal oblique image of the left portion of the liver in a febrile dog. A poorly defined hyperechoic nodule (arrows) with a hypoechoic center is found at the dorsal margin of this lobe, which was supportive a septic abscess.

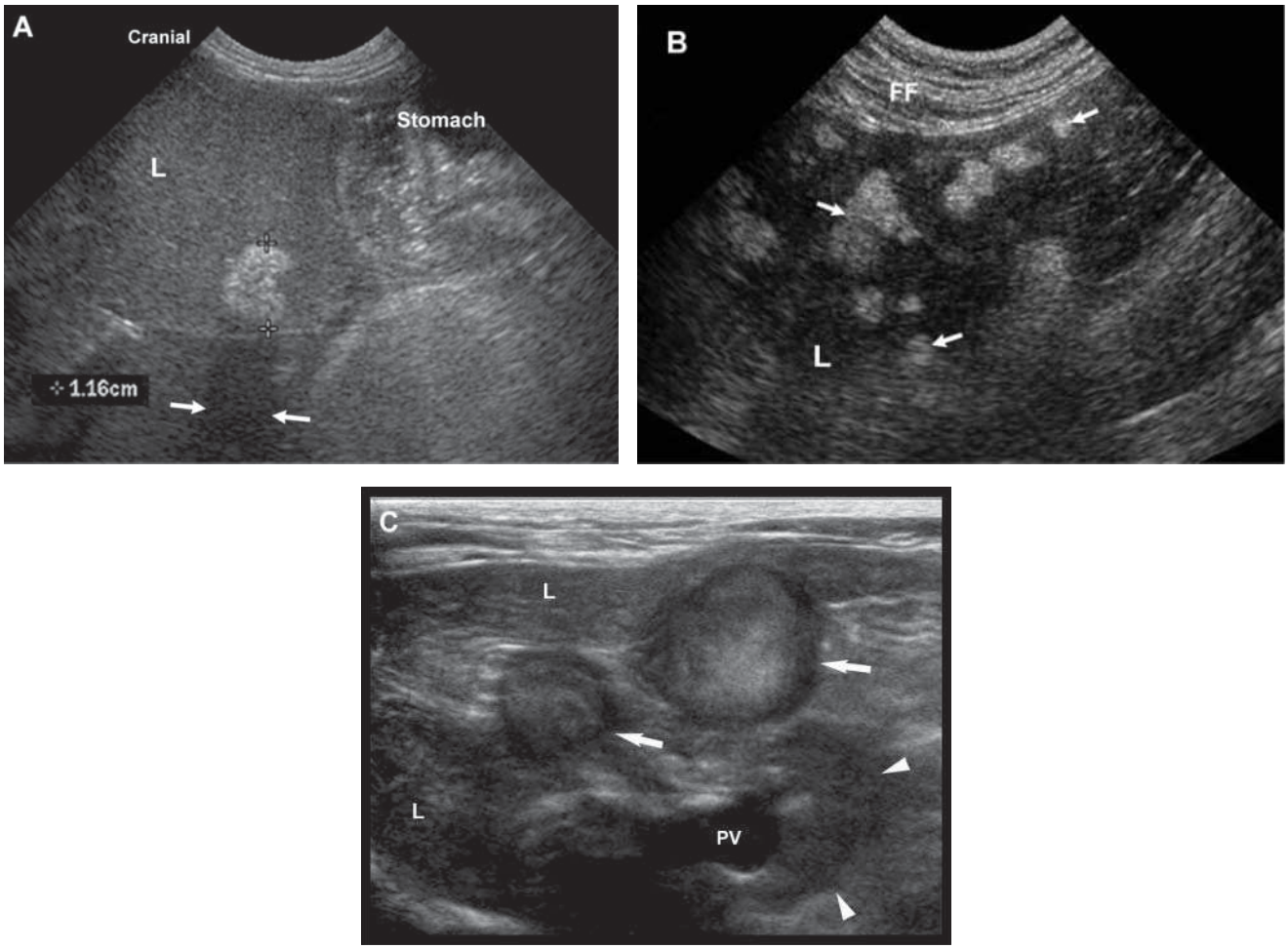


Figure 6.40. **Hepatic granulomas. A:** Longitudinal image of the left portion of the liver (L) in a dog with a relatively well-defined hyperechoic focus associated with acoustic shadowing (arrows). A granuloma was diagnosed, although no underlying etiology could be identified. This granuloma was thought to be an incidental finding. **B:** Longitudinal image of the right portion of the liver in an icteric cat with irregular hyperechoic nodules (arrows) dispersed within a hypoechoic liver (L). The diagnosis was pyogranulomatous cholangiohepatitis in relation to feline infectious peritonitis. FF, falciform fat. **C**: Longitudinal sonogram of the liver of an 8-year-old cat, showing three inhomogeneous nodules diagnosed as eosinophilic sclerosing hyperplasia. Two of them (arrows) were clearly originating from the liver (L) during the real-time evaluation, while the third nodule (arrowheads) was located near the porta hepatis and was suspected to originate from either the hepatic lymph node or liver. PV, portal vein.



Figure 6.41. **Hepatic hematoma.** Longitudinal image of the left portion of the liver in small-breed dog that was bitten by a large dog 3 days earlier. An ill-defined, irregular area of mixed echogenicity (arrows and cursors), consistent with a traumatic hematoma, is found in the superficial portion of the liver.

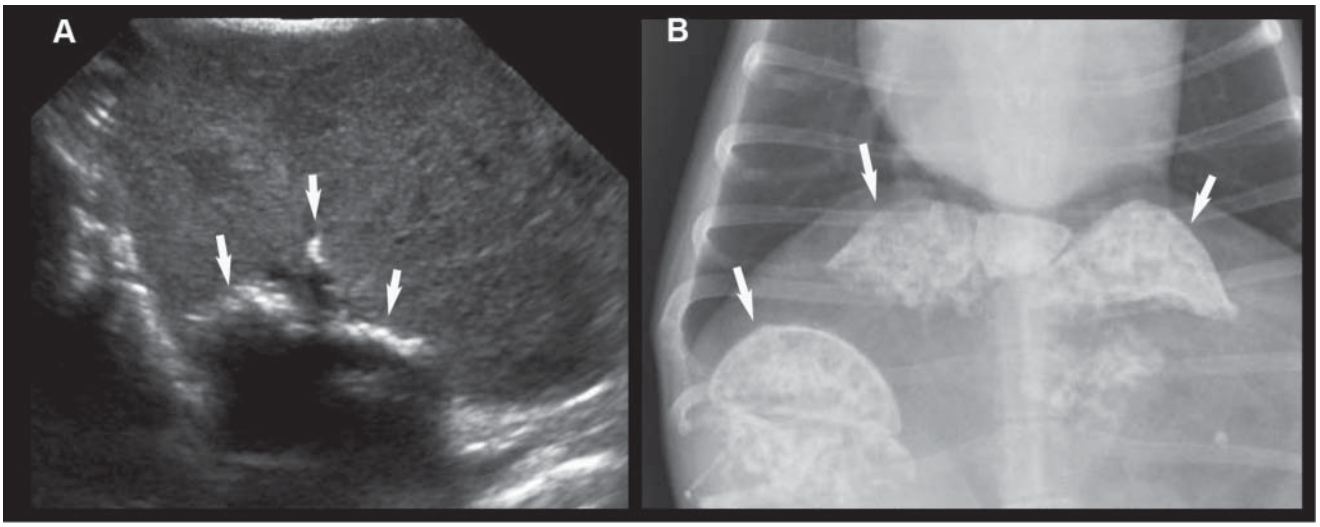


Figure 6.42. **Parenchymal mineralization in a 14-year-old Shih Tzu with chronic hepatopathy with lithiasis. A:** Numerous irregular hyperechoic interfaces (arrows) associated with strong shadowing are noted throughout the liver**.** The visible liver parenchyma is coarse with several small, ill-defined hypoechoic nodules. **B:** On this ventrodorsal radiograph, the extent of the hepatic mineralization (arrows) is more obvious.

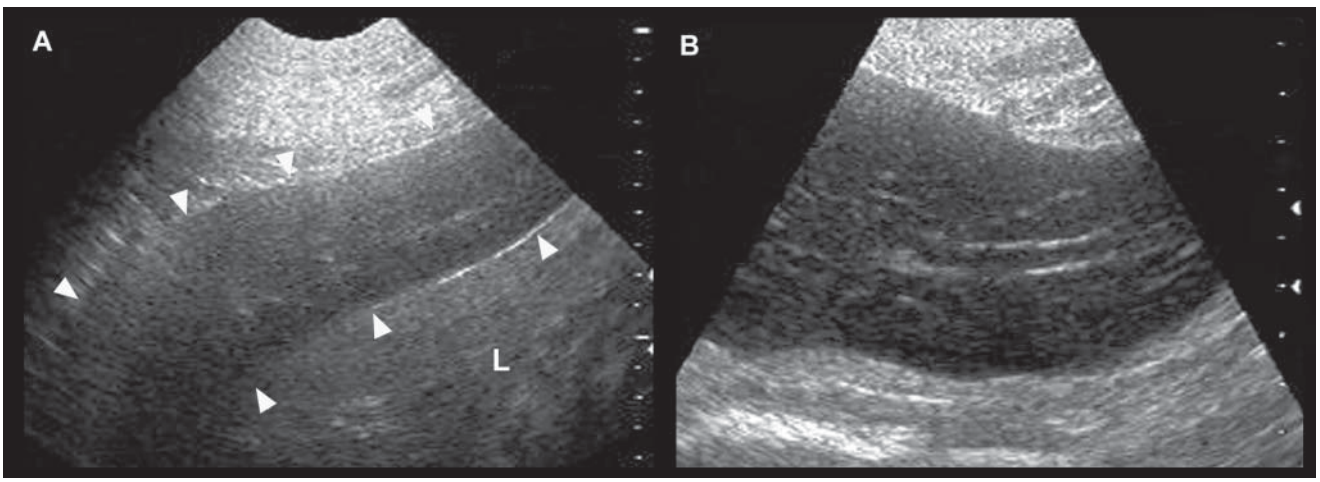


Figure 6.43. **Hepatic lobe torsion. A:** The twisted left lateral liver lobe is diffusely hypoechoic (arrowheads), contrasting with the underlying left medial lobe (L). **B:** A close-up view of the affected lobe. There was no evidence of flow through the visible vessels. The lobe margins are rounded. The surrounding fat is hyperechoic.

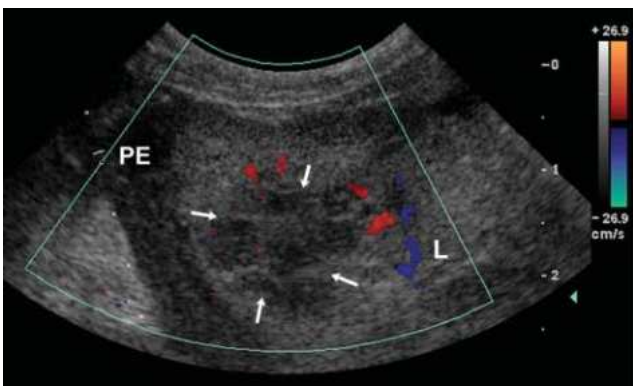


Figure 6.44. **Hepatic infarction.** Longitudinal oblique image of the left portion of the liver (L) of a dog with increased liver enzymes. Within the liver is an irregular hypoechoic region (arrows) with peripheral vascular signal. Ultrasound-guided biopsy revealed infarction of uncertain origin. Peritoneal effusion (PE) is also noted.

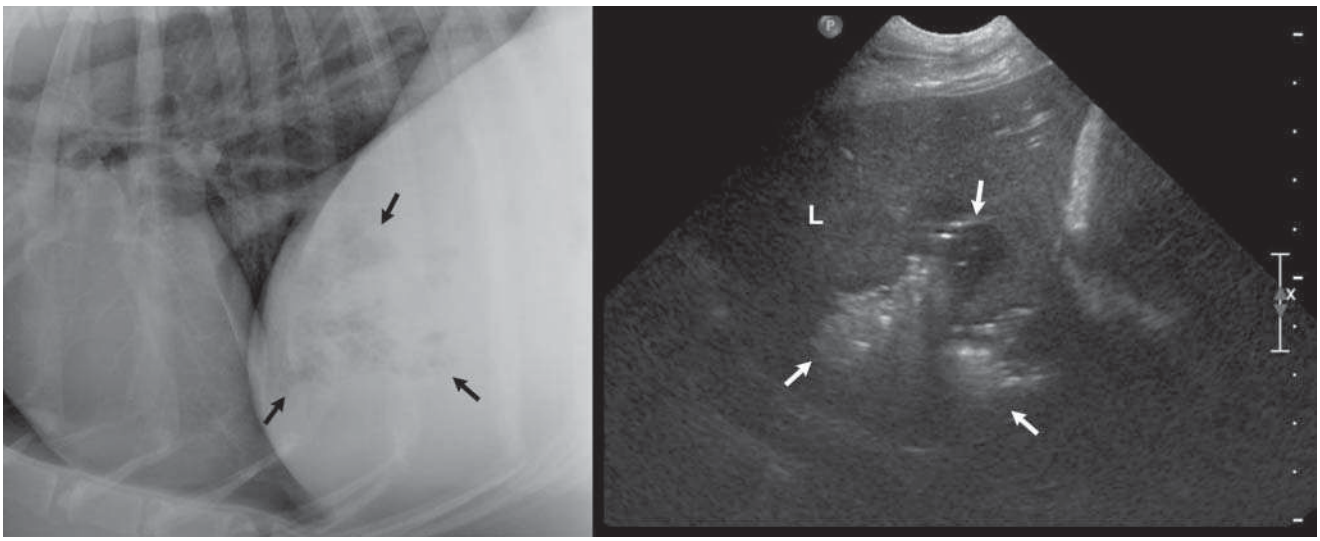


Figure 6.45. Emphysematous hepatitis. Corresponding lateral abdominal radiograph and sonogram of a dog with emphysematous hepatitis. Gas foci (arrows) are radiotransparent on the radiograph and hyperechoic with reverberation artifacts on the ultrasound image. The affected lobe (L1) is enlarged, hyperechoic, and heterogeneous when compared with an adjacent lobe (L2).

Disorders of the Biliary System

Congenital Cystic Anomalies of the Biliary Tree

Congenital cystic changes of the biliary tree can affect any portion of the biliary tree, including the intra-, and extrahepatic biliary ducts. They are originating from malformations of the ductal plate (Santiago et al. 2012). When the lesions are centered on the larger bile ducts and the extrahepatic ducts, they are categorized under Caroli's disease (Last et al. 2006) or choledochal cyst if they affect the pancreatico-biliary ductal junction (Best et al. 2010) (Figure 6.46). The anatomical complexity of these lesions makes it difficult to differentiate them from obstructive biliary disease, but clinically they have no evidence of obstructive biliary disorders. Identification of a GB and the connection of the extrahepatic bile ducts to the CBD are paramount in diagnosing these anomalies. Commonly, these segmental dilations are associated with inflammation or infection. Thickening of the biliary duct walls and echogenic bile are then noted (Figure 6.47).

Congenital polycystic disease involving the kidneys, liver and pancreas is well reported in cats (Bosje et al. 2010). The concurrent presence of multiple cysts in the kidneys assists in the diagnosis of this condition.

Agenesis of the GB is rare and the segmentally dilated CBD is often confused for the GB, but identifying the extrahepatic ducts' connection to the dilated CBD is useful (Figure 6.48). At times, CT or magnetic resonance imaging (MRI) may assist in further characterizing the distribution of these lesions.

Biliary Obstruction and Other Causes of Biliary Ectasia

Ultrasonography has become an important investigative tool in assessing icteric dogs and cats with biliary obstruction. After complete obstruction of the CBD, retrograde dilatation is expected that initially affects the CBD and GB, followed by the extra- and intrahepatic ducts (Nyland and Gillett 1982). With extrahepatic biliary obstruction, the cystic duct and CBD dilate and often become tortuous proximal to the site of obstruction (Figures 6.49–6.53). A CBD more than 4–5 mm wide is usually predictive of obstruction in cats (Léveillé et al. 1996; Gaillot et al. 2007). This is probably also true in dogs, although it has not been described. Within 5–7 days, irregular and tortuous anechoic tubes with hyperechoic walls can be found in the liver, following the more linear PVs and unassociated with color flow, indicating dilated hepatic ducts. This sign, also referred to as the "too many tubes" sign, is usually indicative of complete

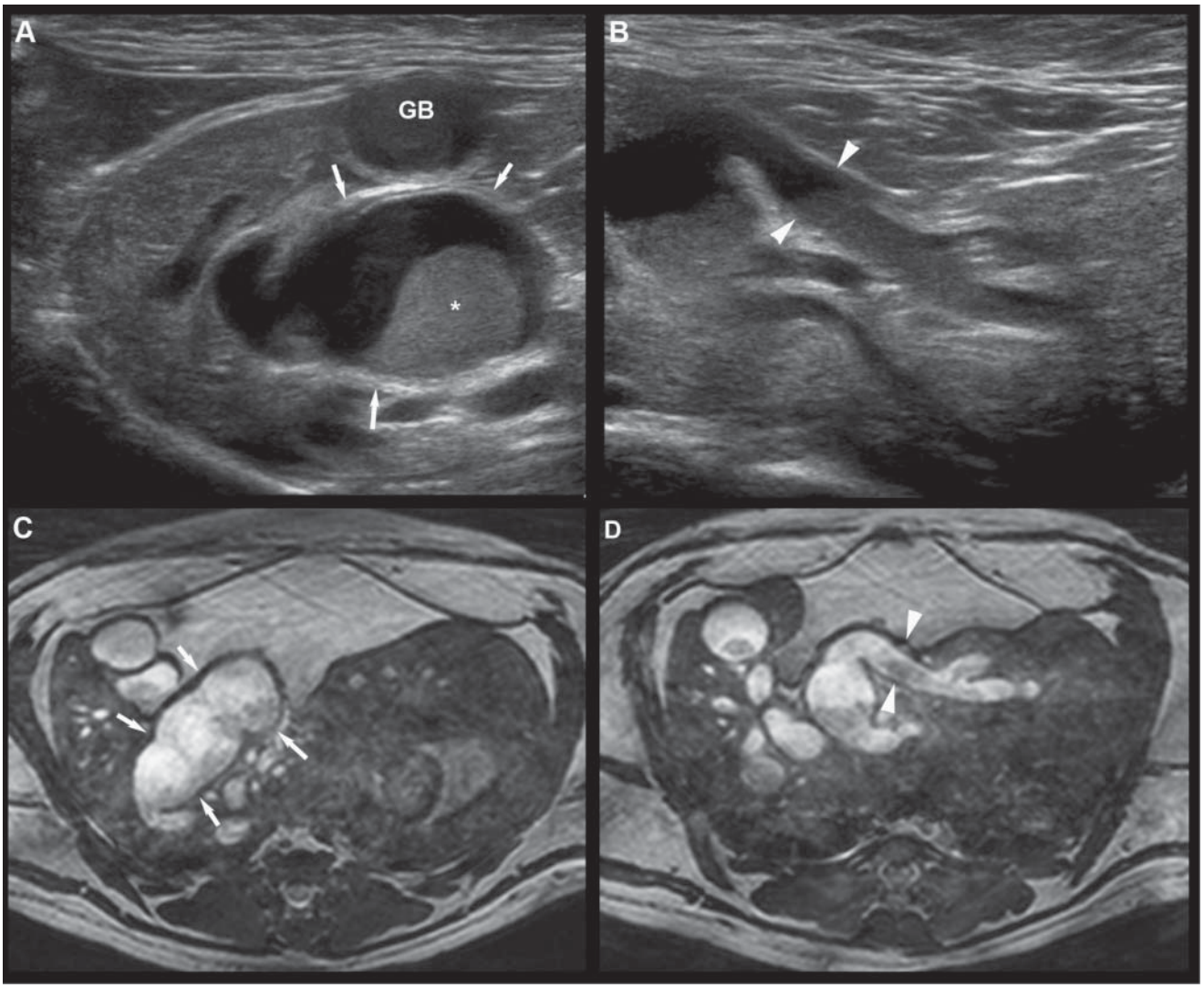


Figure 6.46. Choledochal cyst in a 7-year-old cat with chronic cholangiohepatitis and inflammatory bowel disease. A, B: Sonograms of the markedly dilated common bile duct segment – choledochal cyst (arrows) – containing a large amount of echogenic material (*). Several dilated extrahepatic ducts (arrowheads) are connecting the choledochal cyst **(B)**. **C, D**: Transverse T2 HASTE magnetic resonance images of the choledochal cyst (arrows) and dilated extrahepatic ducts (arrowheads). GB, gallbladder.

obstruction (Figures 6.28D, 6.50). Additionally, these anechoic tubes can be associated with acoustic far enhancement, which is not expected with vessels that contain a more attenuating cellular fluid (Nyland and Gillett 1982). Although the GB can be dilated with biliary obstruction (Figure 6.51C), wall contraction or inflammation possibly associated with fibrosis can limit its capacity to distend. Furthermore, reduced compliance of the peripheral liver parenchyma may limit GB dilatation. Gallbladder dilatation was in fact seen in < 50% of cats with extrahepatic biliary obstruction (Gaillot et al. 2007). Thus, the absence of GB distension should not be used to rule out biliary obstruction.

Extrahepatic biliary obstruction more commonly involves the CBD, mainly in its distal segment, in proximity to the major duodenal papilla. Pancreatitis is often responsible for CBD obstruction, particularly in dogs, because of edema, inflammation, and fibrosis involving the duodenal wall and major papilla and/or

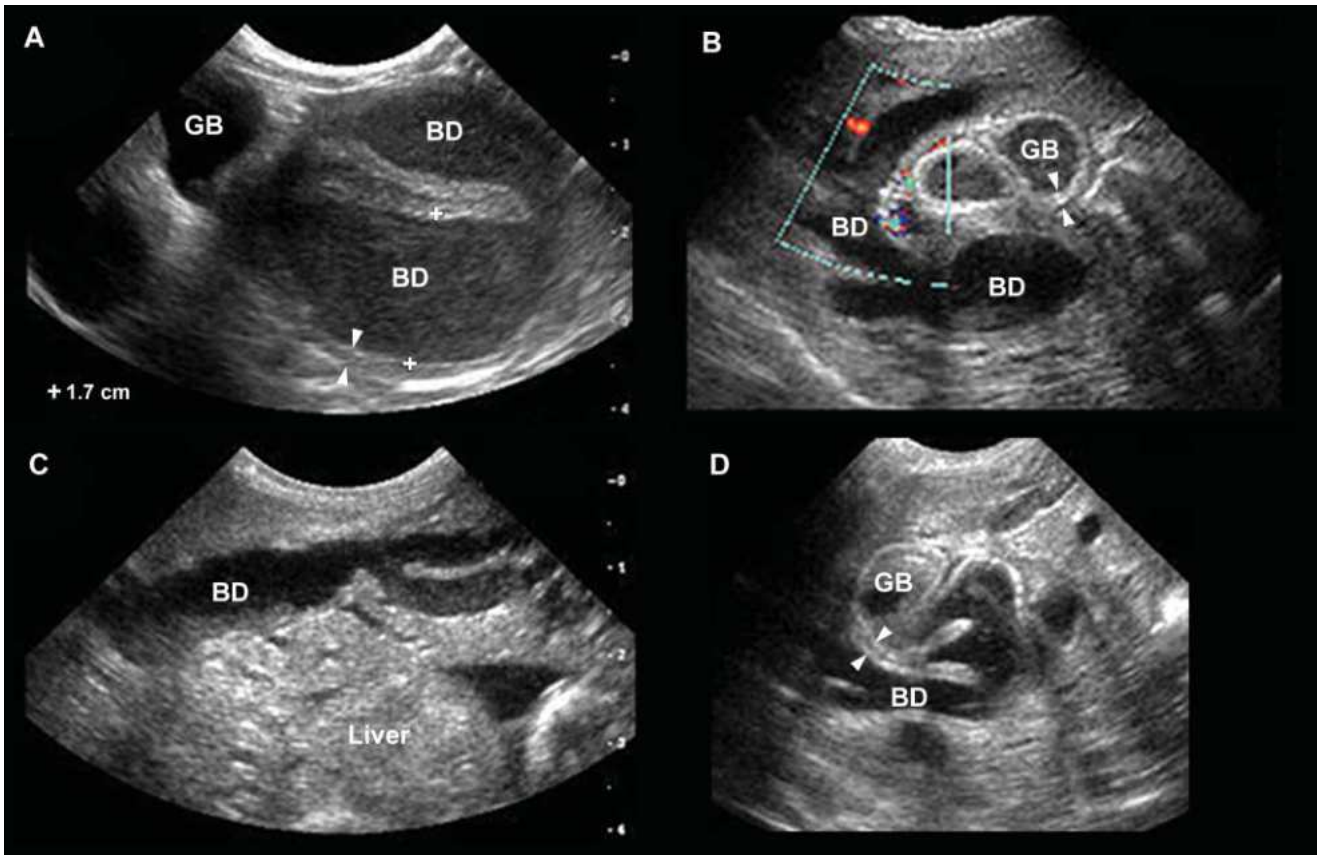


Figure 6.47. Congenital malformation with biliary ectasia in two cats. A: Sagittal image at the porta hepatis in a 2-year-old cat with biliary obstruction. Numerous bile ducts (BD), including the common bile duct, are markedly dilated (lumen between the cursors) and show a thickened wall (arrowheads). The bile content is also more echogenic than normal. Extensive biliary tree fibrosis and stenosis were identified, and an underlying congenital defect was suspected. GB, gallbladder. **B–D:** Similar changes observed in a 8-month-old cat. The bile ducts are distended and irregular. The GB contains echogenic sludge and shows a thickened, hyperechoic wall (arrowheads). Color Doppler **(B)** was used to confirm the absence of flow in these bile ducts (BD), distinguishing those from hepatic vessels. A congenital defect such as hypoplasia or atresia of the common bile duct was suspected at necropsy.

the CBD (Fahie and Martin 1995; Léveillé et al. 1996; Mayhew et al. 2002) (Figures 6.49D, 6.51). Chronic duodenitis or cholecystitis can also be associated with fibrous tissue proliferation and subsequent stenosis of the distal CDC or duodenal papilla. Inflammatory processes involving the biliary tract can be associated with amorphous plugs and cholelithiasis, although it is often difficult to determine what came first (Mayhew et al. 2002). The CBD must be evaluated thoroughly for the presence of echogenic amorphous plugs and choleliths, which may or may not cause acoustic shadowing (Figure 6.52A). Choleliths and plugs were found to be responsible for the obstruction in seven out of 30 cats in a study by Gaillot et al. (2007).

Several types of neoplasia (predominantly carcinomas) involving the biliary tract, the duodenum, or the pancreas can cause biliary obstruction (Fahie and Martin 1995). Nodules or masses of variable echogenicity, sometimes with a cystic component, can be observed (Figure 6.52). Evaluation of the rest of the abdomen, especially the liver parenchyma and lymph nodes, can help in differentiating benign from malignant processes, although tumor and inflammation often share similar sonographic features (Gaillot et al. 2007). Fine-needle aspiration or biopsy is recommended if the abnormal tissue can be safely reached. Regional tissues (liver, lymph nodes) should also be targeted if abnormal.

Figure 6.49. **Extrahepatic biliary obstruction. A:** Longitudinal image obtained through the last intercostal spaces on the right to identify the common bile duct (CBD) in a dog with gallbladder mucocele. The CBD wall is thickened (2.3 mm) and the lumen is dilated (5.4 mm). PV, intrahepatic portal vein. R, 12th and 13th ribs. **B:** Longitudinal subcostal image in another dog with duodenal carcinoma causing biliary obstruction. The CBD is dilated, as well as well as the cystic duct (CD) and one of the extrahepatic biliary ducts (EHD) that terminates into the CDC. The pylorus (Py) is nearby. **C:** Longitudinal image obtained in the central perihilar region of the liver of an icteric cat. Tortuous hypoechoic to anechoic tubular structures representing the dilated hepatic duct (HD), the CD, and the CBD indicate extrahepatic biliary obstruction. **D:** Longitudinal image of a 6-year-old Miniature Schnauzer with severe pancreatitis. The CBD is dilated up to an area of inflamed hyperechoic fat. Proximally, the cystic duct (CD) and two EHDs are also distended. Py, pylorus.

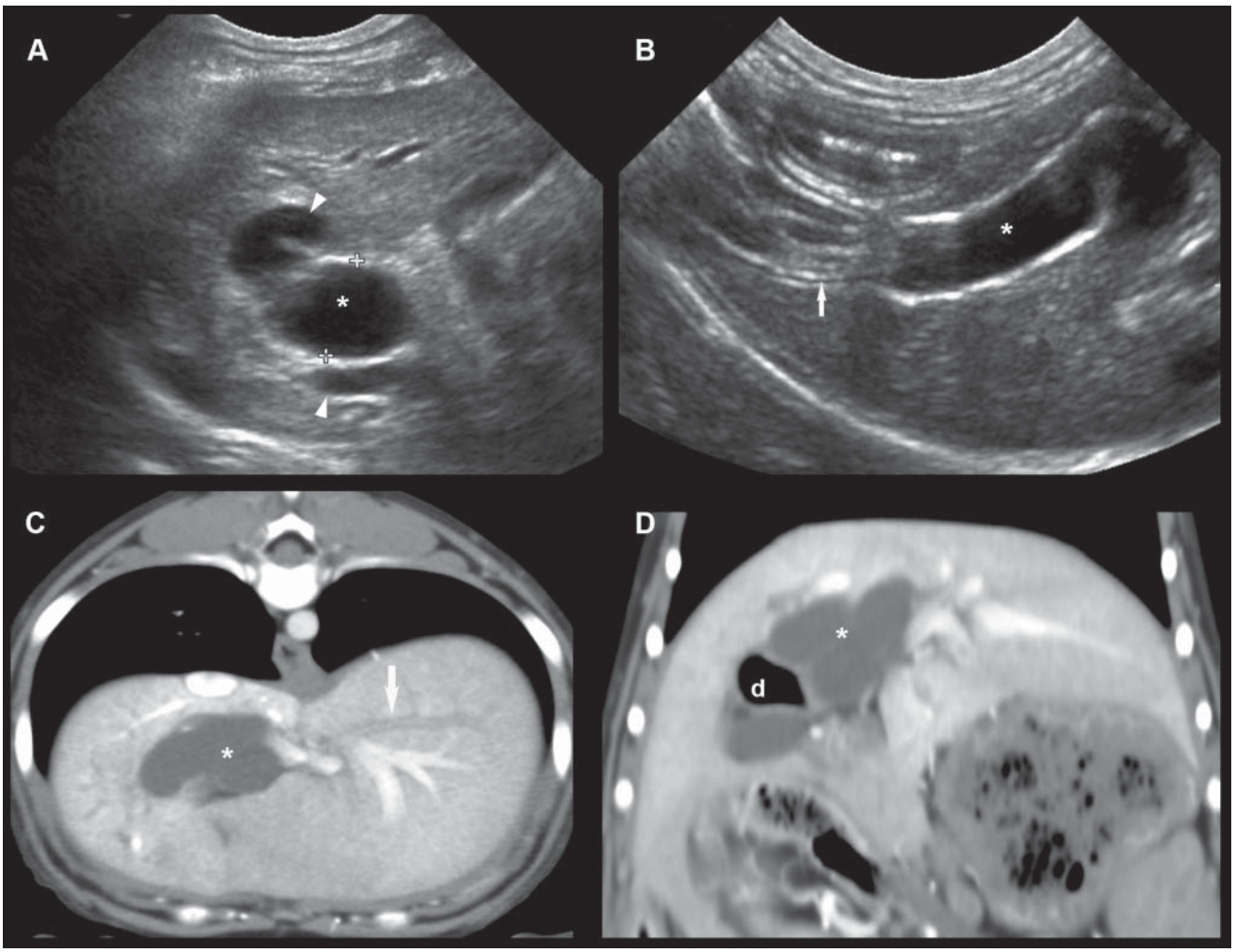


Figure 6.48. **Gallbladder agenesis in a 4-month-old Australian sheepdog presented with increased liver enzymes and bile acids. A:** Sonogram of the slightly hyperechoic liver and the dilated common bile duct (CBD, *), to which the extrahepatic ducts (arrowhead) are connected. **B**: Sonogram of the distal portion of the CBD, near the duodenal papilla (arrow). **C**: Transverse CT showing the dilated CBD (*) and one of the dilated hepatic ducts (arrow). Note the adjacent vessels filled with contrast. **D**: Dorsal CT of the lobulated and dilated CBD (*), near the duodenum (d).

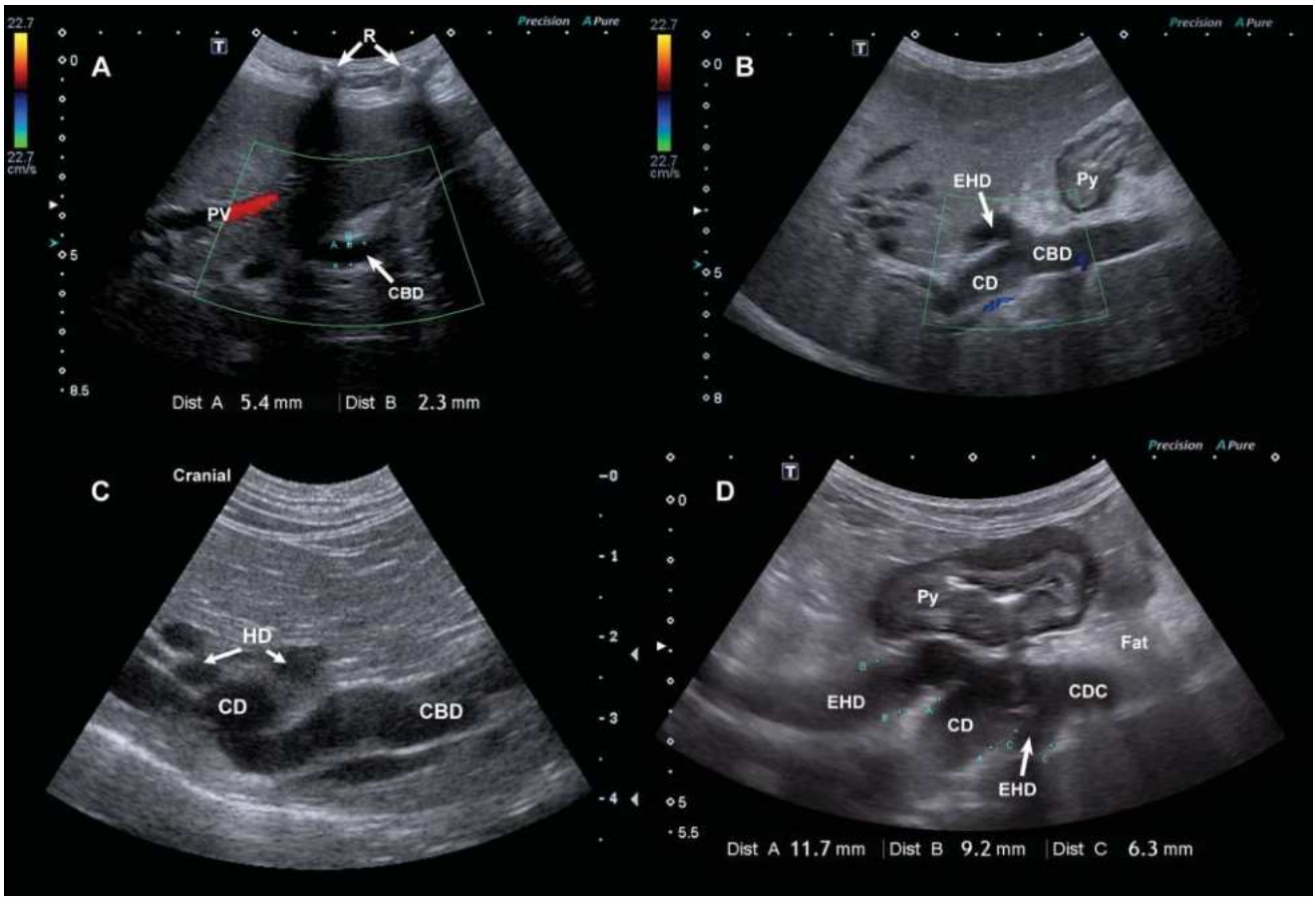


Figure 6.49. **Extrahepatic biliary obstruction.** (for full caption, see facing page)



Figure 6.50. **Chronic extrahepatic biliary obstruction.** Sonographic images of the liver in a dog **(A)** and a cat **(B)** in which intrahepatic biliary ducts (arrows) are dilated and tortuous, and lack Color Doppler signal compared with nearby hepatic vessels. Another distinctive feature is that acoustic enhancement artifacts (*) are present in the far field. This is not expected with vessels.

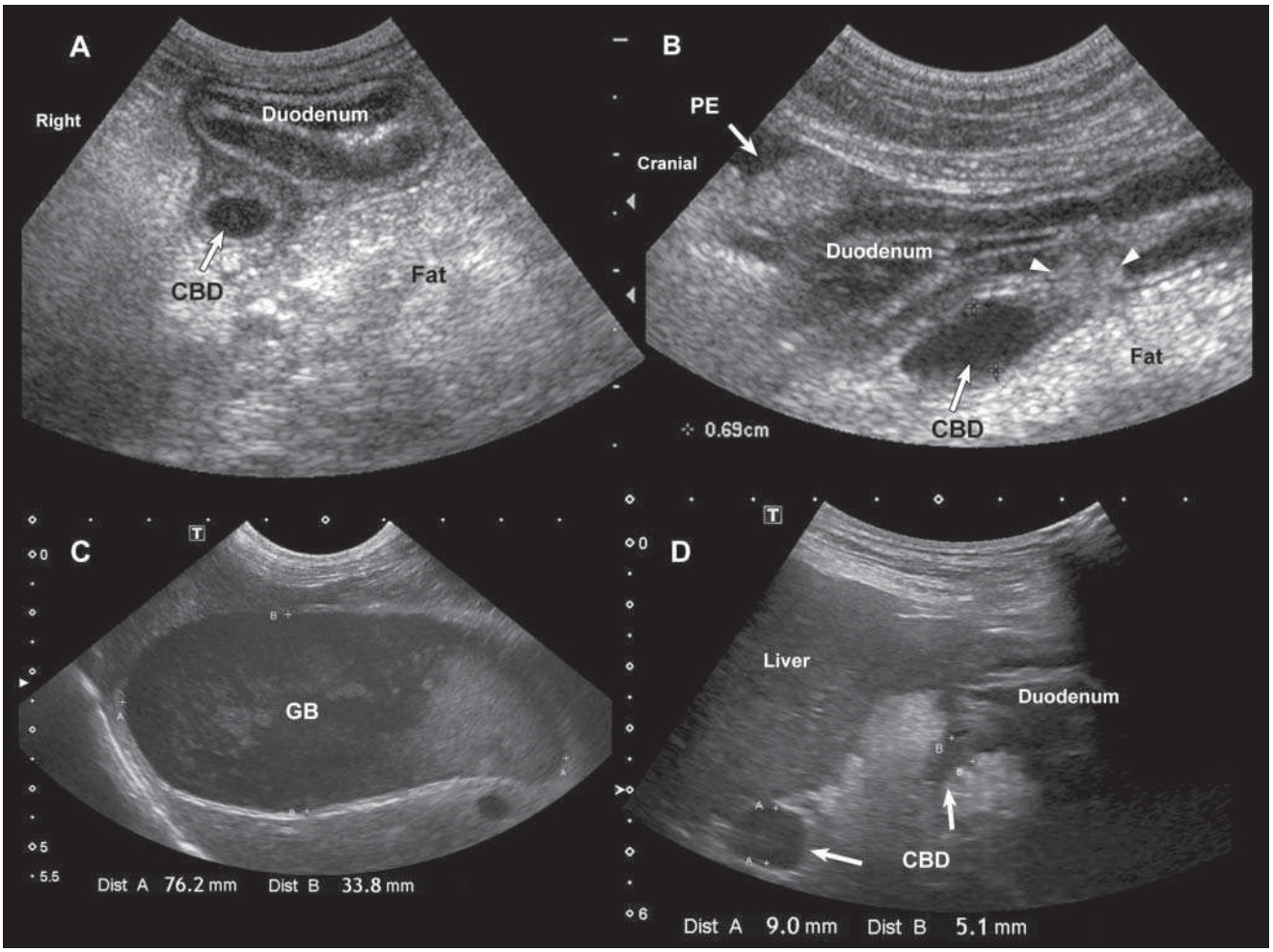


Figure 6.51. Pancreatitis and biliary obstruction. Transverse **(A)** and longitudinal **(B)** images of the proximal duodenum of a dog with pancreatitis. The distal portion of the common bile duct (CBD) is dilated. The peripheral fat is markedly hyperechoic, and a small amount of peritoneal effusion (PE) is noted. The duodenal papilla (arrowheads) is hyperechoic and subjectively enlarged, and the wall of the common bile duct appears thickened. These changes suggest an extension of the inflammatory process to these structures which causes biliary obstruction. **C, D:** In another dog with chronic severe pancreatitis, the gallbladder (GB) is distended, contains sludge and its wall is mildly thickened. The common duct is inflamed and thickened (up to 5 mm) distally in proximity to the duodenal papilla and severely dilated more proximally (9 mm).

Gallbladder and Common Bile Duct Wall Anomalies

Gallbladder wall thickening (>1 mm) can be caused by inflammation (cholecystitis/cholangitis/cholangiohepatitis), edema (portal hypertension, hypoalbuminemia, biliary obstruction, or inflammation), cystic mucosal hyperplasia, or, rarely, neoplasia (Spaulding 1993; Hittmair et al. 2001). In case of GB inflammation, the chronicity and severity of the process influence the appearance of the wall. The thickened wall may have a double-rim pattern (particularly in acute cases) or diffuse wall hyperechogenicity, sometimes associated with dystrophic mineralization. (Figure 6.53). The double-rim pattern is often seen in wall edema (Figure 6.54).

Thickening of the CBD wall and luminal dilatation are common with cholecystitis/cholangitis/cholangiohepatitis) (Figures 6.49A, 6.51, 6.52D). In cats, CBD dilation (>4 mm) appears to be a more reliable indicator of extrahepatic biliary obstruction than the GB distension (Gaillot et al. 2007). However, at times it can be difficult to differentiate obstructive dilation of the CBD from dilatation associated with stasis secondary to chronic inflammation of the biliary system (Léveillé et al. 1996). In these cases, regular

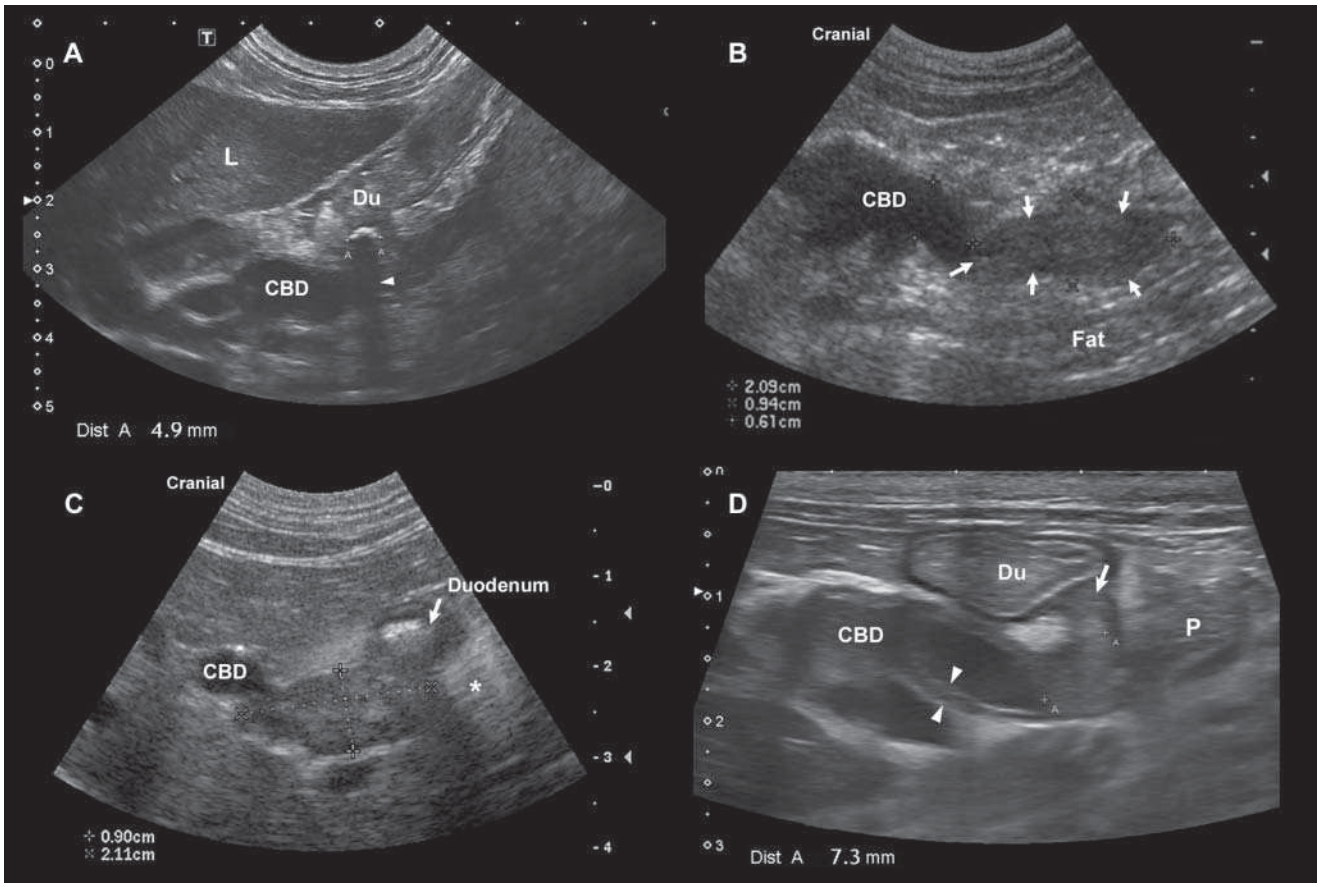


Figure 6.52. **Biliary obstruction by a cholelith or a mass. A:** Obstructive cholelith. Longitudinal ultrasonographic image obtained in a cat with icterus. A 4.9-mm hyperechoic structure, consistent with a cholelith (between cursors), is lodged in the distal portion of the common bile duct (CBD). The CBD and cystic duct (CD) are dilated and thickened because of cholecystitis and biliary obstruction. The stone is casting an acoustic shadow (arrowhead). Du, duodenum. **B:** Biliary carcinoma in a cat. Longitudinal image of a cat's CBD with a uniform, mildly echogenic mass (arrows and cursors) obliterating the lumen of the CBD. These features can indicate chronic cholecystitis with fibrosis, or a neoplastic process. Biliary carcinoma was identified at surgery. **C:** Chronic cholecystitis in a cat. Longitudinal image of the CBD in a cat with chronic suppurative cholangiohepatitis and cholecystitis. Within the distal CBD is a mass (cursors) that suggests a neoplastic process. However, this mass was confirmed to represent pyogranulomatous inflammation associated with fibrous tissue. Adjacent hyperechoic fat (*) is consistent with steatitis. **D**: Chronic cholangitis and pancreatitis in a cat. The CBD is dilated and its wall is thickened (arrowheads). A small, moderately echogenic mass is present in the distal CBD, just proximal to the duodenal (Du) papilla (arrow). Surgical exploration confirmed the presence of fibrous tissue causing the stenosis, associated with adjacent chronic pancreatitis (P).

ultrasound rechecks along with biochemical follow-up can be useful. In chronic outflow obstruction, the CBD can remain dilated even after the cause of obstruction has been alleviated. In dogs with extrahepatic biliary distension, the GB distension is seen more often than in cats, and at times, the CBD, although dilated, may be difficult to trace.

Gallbladder mucoceles typically affect older dogs of small and medium-sized breeds and represent an important cause of biliary obstruction, although they are commonly found incidentally in dogs (Besso et al. 2000; Choi et al. 2013). They have also been reported in cats (Woods et al. 2012). This complex pathology is characterized by an excessive accumulation of mucus within the GB lumen, progressively leading to overdistension and wall necrosis and rupture. Intraluminal mucinous plugs can extend or migrate into the CBD and cause obstruction. In affected GB, a characteristic accumulation of hypoechoic mucus is collected along the inner margin of the wall, centrally displacing the echogenic biliary sludge, which becomes immobile. As the mucocele is

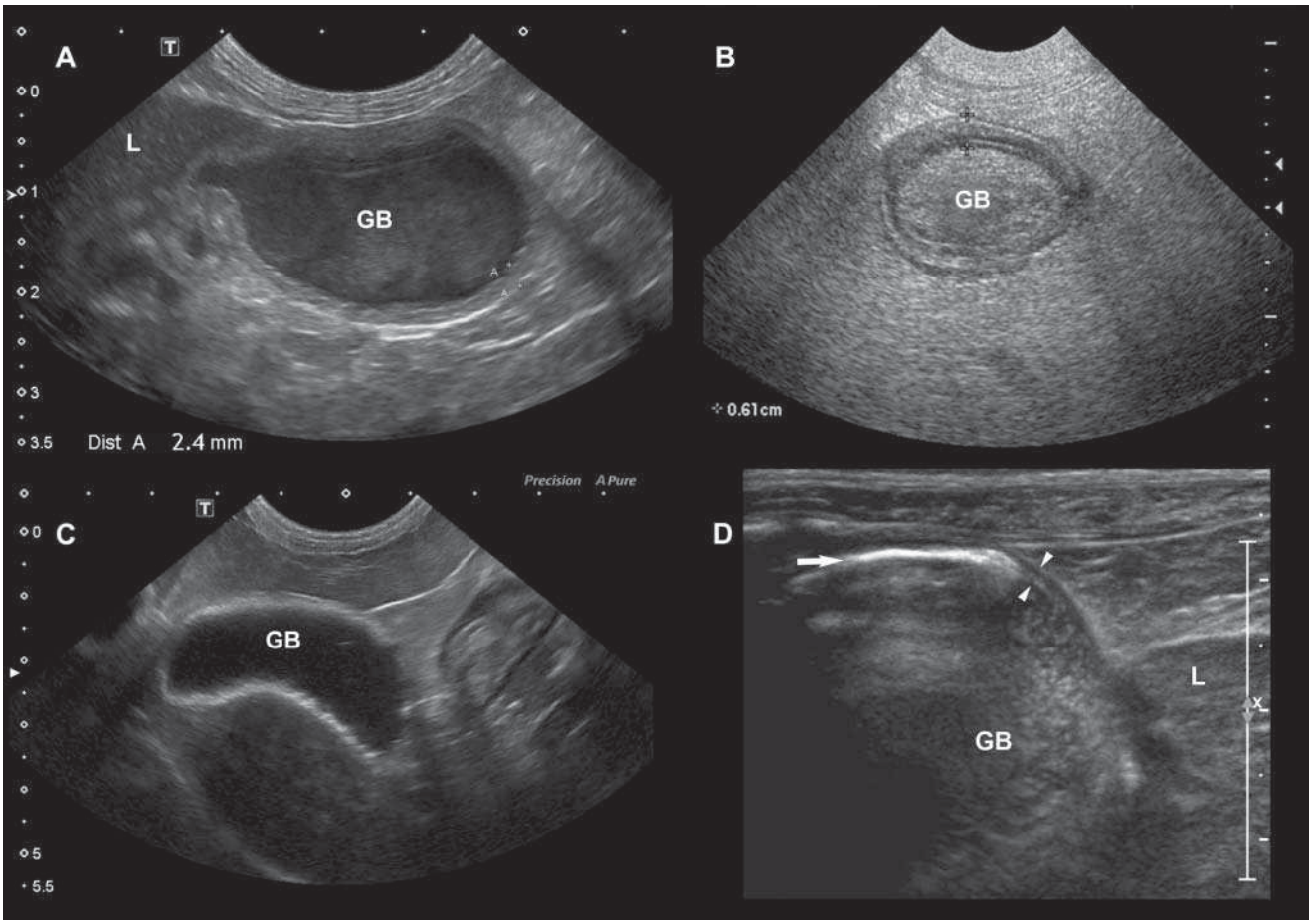


Figure 6.53. **Cholecystitis. A:** Longitudinal image of the gallbladder (GB) of a febrile cat. The GB wall is thickened (2.4 mm) and its lumen is filled with echogenic sludge. L, liver. Ultrasound-guided cholecystocenthesis yielded a positive bacterial culture. **B:** Transverse image of the GB of a dog with a clinical history of fever and increased liver enzymes. The GB wall is thickened and associated with a multilayered pattern because of severe wall inflammation, edema, and necrosis. **C:** Longitudinal image of the right-central portion of the liver of a febrile cat. The GB is thickened and has a hyperechoic, irregular wall with ill-defined margins (arrows). **D:** Emphysematous cholecystitis in a 8-year-old Rat Terrier with immune-mediated thrombocytopenia, anemia and increased liver enzymes. Gas (arrow) is dissecting the GB wall (arrowheads). The GB is moderately filled with echogenic sludge, and the liver (L) is enlarged and inhomogeneously decreased in echogenicity.

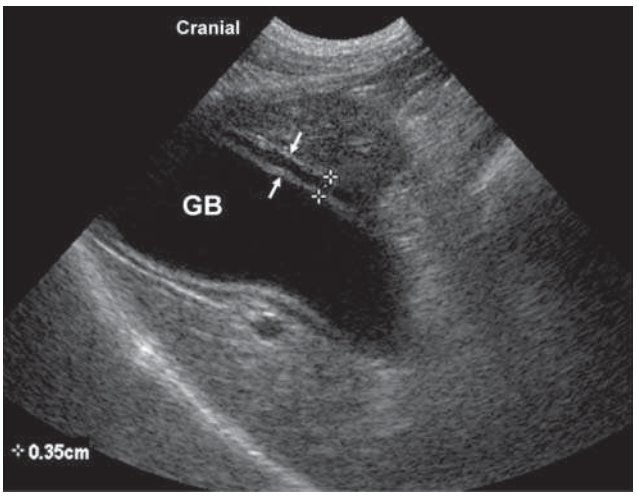


Figure 6.54. **Gallbladder wall edema.** Longitudinal image of the GB in a dog with hypoalbuminemia. The GB wall is thickened, with a double rim (arrows) consistent with edema. Cholecystitis could be not excluded based on the image (see Figure 6.52B).

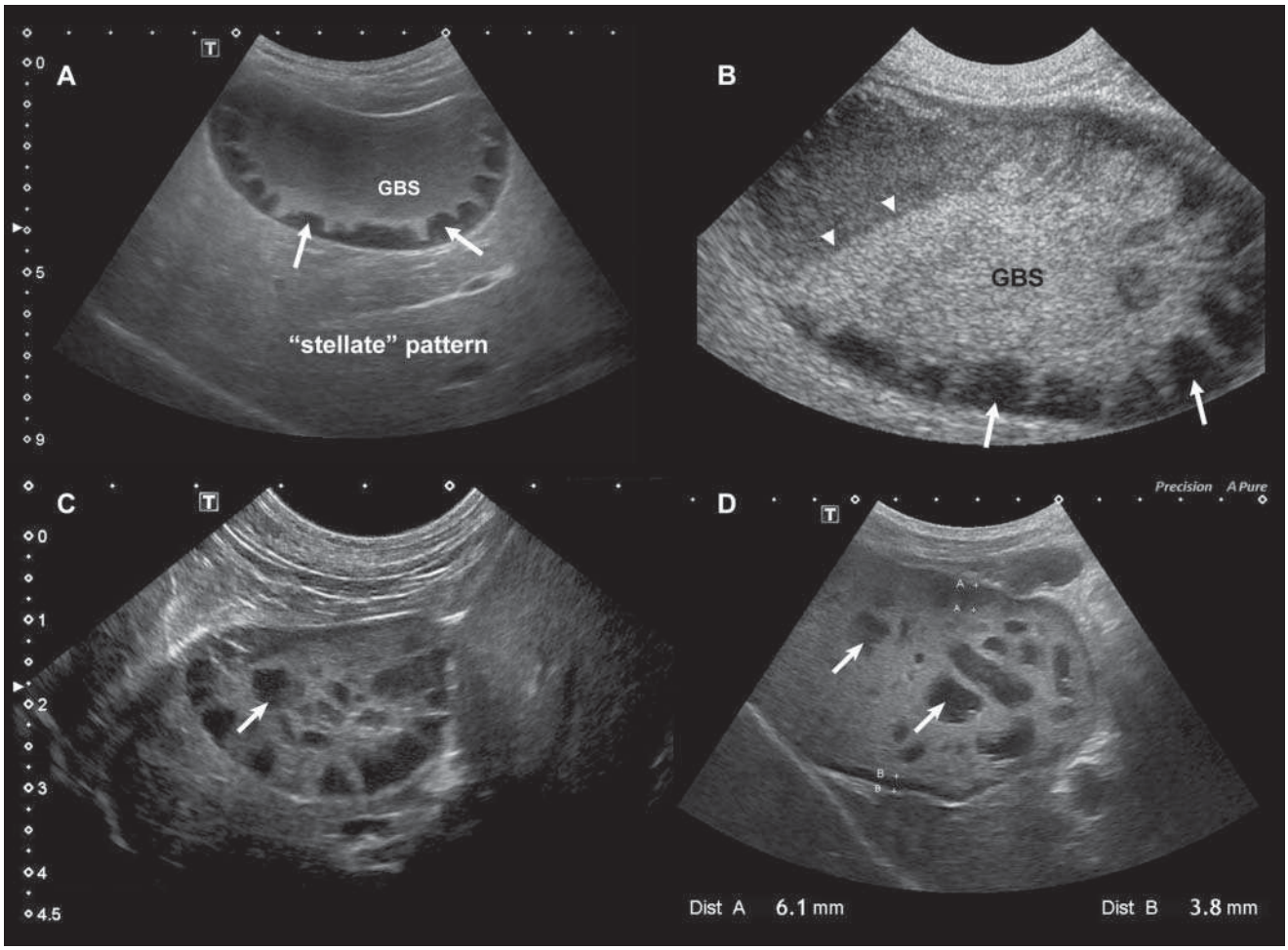


Figure 6.55. Partial or immature gallbladder mucocele in dogs. Transverse **(A)** and longitudinal **(B)** images of the gallbladder of two dogs with increased liver enzymes. The gallbladder is distended with echogenic biliary sludge (GBS) in the dependent portion of the lumen (arrowheads at the horizontal level). An interrupted and irregular, hypoechoic to anechoic rim is visible at the inner periphery of the gallbladder, consistent with mucus. The triangular shape of these hypoechoic foci (arrows) has been referred as the *stellate pattern*. **C, D**: Mucus fragments may detach from the wall and appear as hypoechoic floating structures (arrows) – often geometrical in shape – surrounded with hyperechoic sludge. A stellate pattern is present in dog C, whereas the mucus rim (between cursors) is smoother in D.

progressively formed in the GB, a **stellate pattern** is seen initially, followed by the appearance of immobile hyperechoic radiating striations that lead to a **kiwi fruit-like pattern** (Figures 6.55–6.57) (Besso et al. 2000). Mucus fragments may also detach from the wall and appear as anechoic to hypoechoic structures floating in hyperechoic biliary sludge. The GB wall may also appear thickened, hyperechoic, and irregular because of edema, inflammation, and/or necrosis. A discontinuity in the GB wall is an important sign of rupture, along with the presence of hyperechoic fat at the periphery of the GB and the presence of peritoneal effusion (Figure 6.57). These signs generally indicate a surgical emergency. Fragments of mucoceles may also migrate within the peritoneal cavity (Figure 6.57B). In a study on GB mucoceles in 30 dogs, ultrasound proved to be 86% sensitive for the detection of wall rupture (Pike et al. 2004). Most affected dogs have concurrent clinical evidence of hepatobiliary disease, but GB mucoceles can also be found incidentally on ultrasound. Although surgery is generally recommended (Choi et al. 2013), GB mucoceles may respond to medical management (Walter et al. 2008).

Gallbladder wall polyps and malignant neoplastic processes, although rarely seen in dogs and cats, can be associated with biliary obstruction. Although it can be

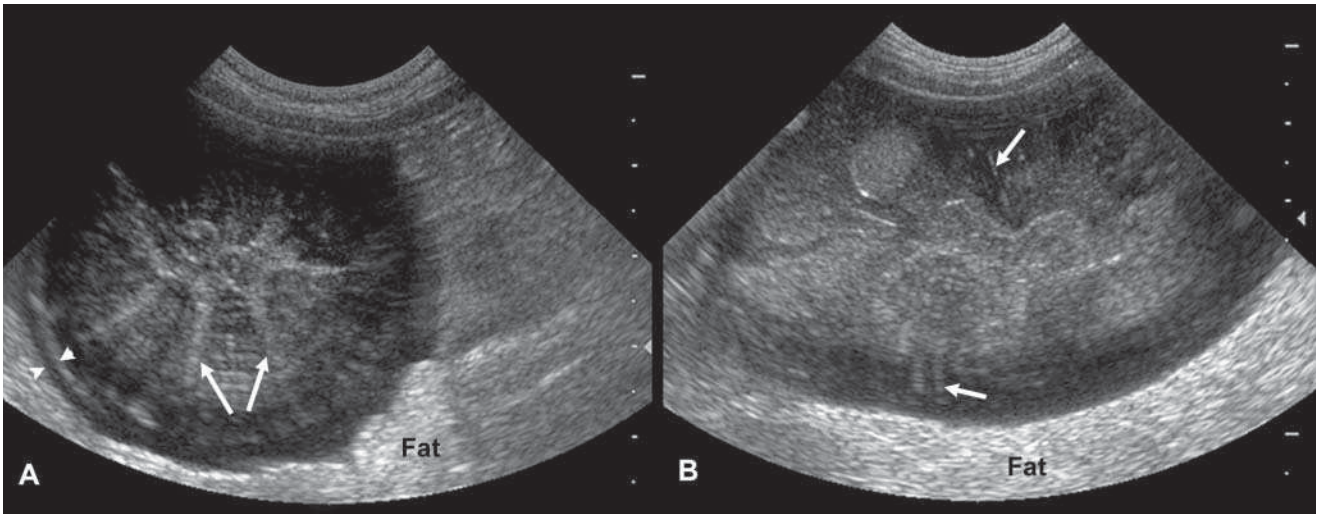


Figure 6.56. Complete or mature gallbladder mucocele. Transverse **(A)** and longitudinal **(B)** images of the gallbladder of a dog with icterus and acute abdominal pain. The gallbladder is distended and shows a pattern of hyperechoic striations (arrows) radiating toward its center. The central hyperechoic area is heterogeneous and completely immobile. These features are described as a *kiwifruit-like pattern*, which is a pathognomonic sign for gallbladder mucocele. The gallbladder wall is also thickened (arrowheads) and the adjacent fat is hyperechoic, suggesting imminent or recent wall rupture.

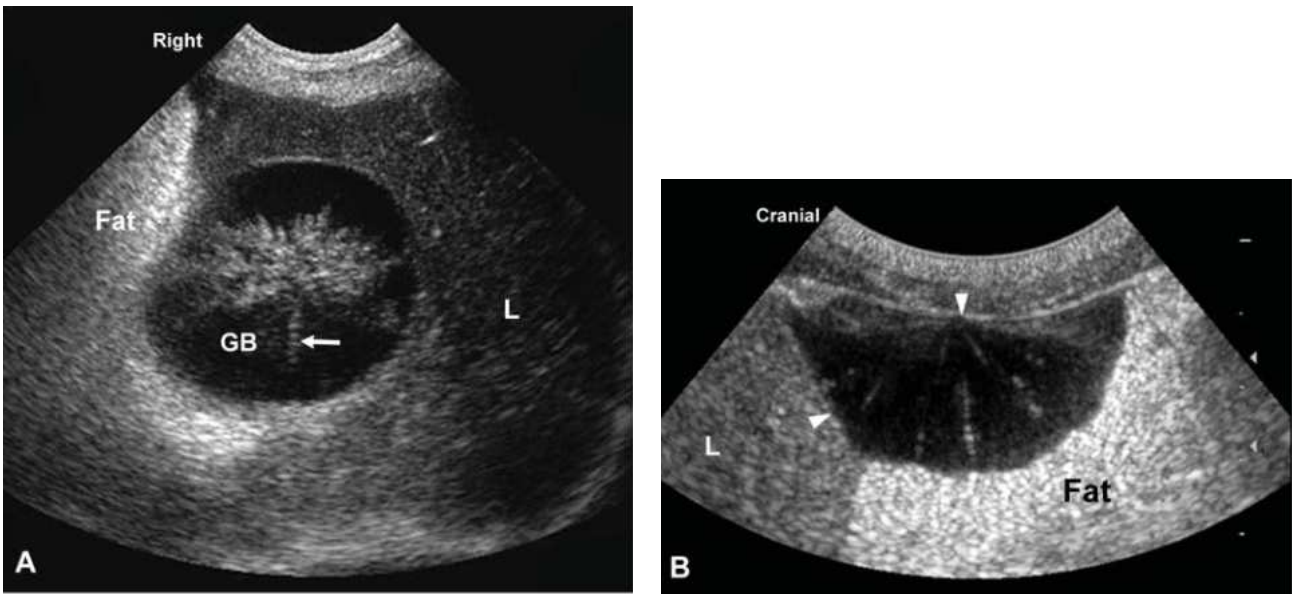


Figure 6.57. Gallbladder rupture. A: Transverse image of the gallbladder in a dog with signs of acute abdominal pain. A *kiwifruit-like pattern* of striations, consistent with mucocele, is noted (arrow) in the gallbladder (GB). The fat at the right and ventral aspects of the GB is markedly hyperechoic and hyperattenuating, highly suggestive of wall perforation and was confirmed with surgical exploration. L, liver. **B:** Migrating mucocele. Longitudinal image of the region just caudoventral to the liver (L) in a dog with GB mucocele. A crescent-shaped anechoic structure with fine radiating striations (arrowheads) is found at the caudal margin of the liver. This structure represents a fragment of mucocele that migrated after GB rupture. Consecutive bile peritonitis was present, associated with hyperechoic fat.

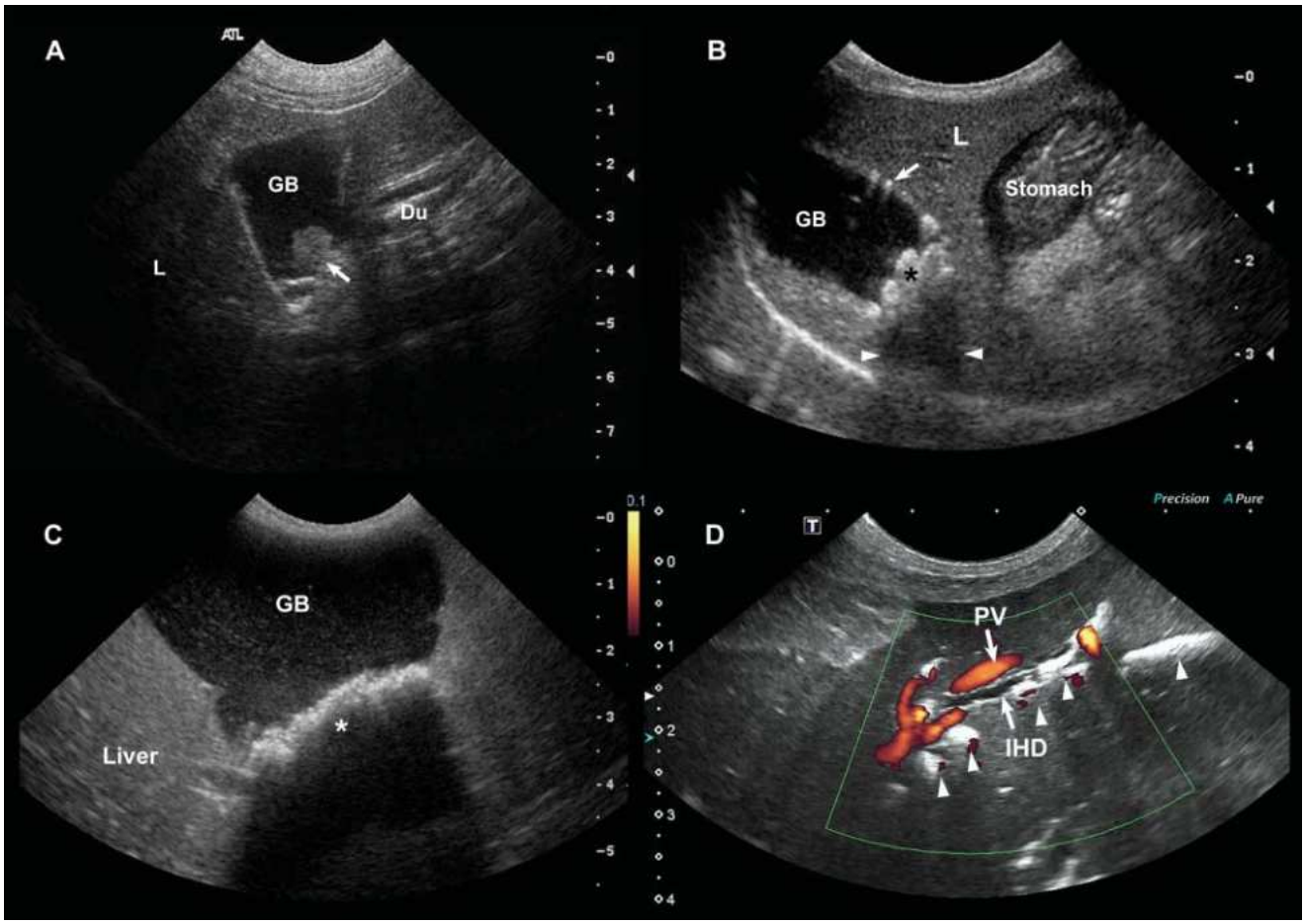


Figure 6.58. **Biliary polyp and cholelithiasis. A:** In this medium-sized mixed-breed dog, a 1-cm irregular structure of moderate echogenicity is attached to the wall of the gallbladder (GB). Its structure remained fixed in position regardless of patient positioning and followed over serial examination, presumed to represent a polyp. **B:** Longitudinal image of the central portion of the liver (L) in a small dog with acute pancreatitis. Several rounded hyperechoic structures (*) associated with acoustic shadowing (arrowheads), consistent with choleliths, are in the GB neck. Small hyperechoic foci, associated with some reverberation (arrow), are in the non-dependent ventral region of the GB. These foci could indicate small choleliths adhered to the wall or indicate gas. There was no increase in liver enzymes in this dog. The gallstones were not considered clinically significant. **C:** A larger volume of cholelithiasis (*) is in the dependent portion of the GB of this other larger dog with Cushing's disease. Similar ultrasound features are observed. **D:** Transverse oblique power Doppler image of the left portion of the liver of a dog with increased liver enzymes. Several linear hyperechoic tracts and mineral fragments (arrowheads), causing partial acoustic shadowing, are present in the intrahepatic biliary ducts (IHD) in proximity to the portal veins (PV).

difficult to differentiate these processes, pedunculated echogenic masses protruding into the GB lumen are more typical of polyps (Figure 6.58A).

Cholelithiasis

Choleliths are often incidental within any portion of the biliary tract in dogs and cats. An underlying or concurrent inflammatory process (cholecystitis or cholangiohepatitis) is commonly recognized in cats (Eich and Ludwig 2002). These calculi typically appear as well-defined, hyperechoic, shadowing foci with a tendency to form linear tracts when located in the hepatic ducts or a sediment in the GB lumen and cystic duct (Figure 6.58C,D). Subsequent intrahepatic or extrahepatic biliary obstruction can be observed, although choleliths may also form because of an obstruction (Mayhew et al. 2002).

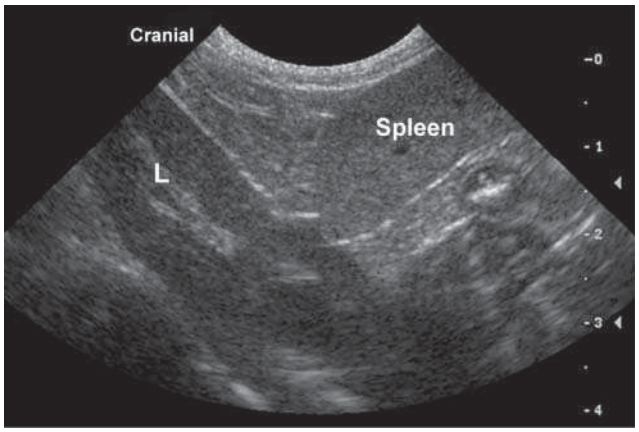


Figure 6.59. Microhepatica. Longitudinal image of the central portion of the liver (L) of a dog with a congenital extrahepatic portosystemic shunt. Because of the significant reduction in hepatic volume, the spleen is displaced cranially and the portal vein cannot be easily followed to the liver.

Disorders of the Hepatic and Portal Vasculature

Congenital Portosystemic Shunts

Portosystemic shunts (PSSs), which represent one of the most common vascular anomalies in dogs and cats, connect the portal system to the systemic circulation through the CVC or azygos vein. The use of ultrasonography in the detection and characterization of these anomalies has been well described (Lamb 1996; Lamb et al. 1996a; d'Anjou et al. 2004; Szatmari et al. 2004; d'Anjou 2007). Most PSS are congenital in dogs and cats, and more commonly detected in juvenile animals; however, a certain number of these shunts can remain undetected for several years in dogs and particularly in cats.

Because of the common reduction in hepatic volume in affected animals, a complete evaluation of the intrahepatic and extrahepatic portal vasculature can be challenging to achieve (Figure 6.59). A right-lateral approach through the 11th or 12th intercostal spaces may be required in order to visualize the liver and porta hepatitis, as well as the region of the CVC, without overlying gastrointestinal content.

Congenital PSSs are most often single. Double-shunting loops anastomosing before entering the systemic circulation were reported to be more common with shunts originating from the right gastric vein in dogs (Szatmari et al. 2004). Schematic morphological differences among congenital PSS are depicted in Figure 6.60.

Extrahepatic portosystemic shunts, arising from the main PV or a tributary (e.g., the splenic, right gastric, left gastric, or gastroepiploic vein), represent the most common type of PSS and are most prevalent in small breeds of dogs and in cats (Lamb 1996; Lamb et al. 1996a; d'Anjou et al. 2004; Szatmari et al. 2004). An anomalous tortuous vessel, containing hepatofugal flow and with a maximal diameter similar to the one of the aorta, is typically seen originating from a branch of the portal system (Figure 6.61). A termination into the CVC is often visualized in association with focal flow turbulence that appears as a mosaic pattern on color Doppler (Lamb 1996; d'Anjou et al. 2004) (Figure 6.61B).

Portocaval shunts typically terminate in the CVC cranial to the right renal vein (Figure 6.61C). The shunt termination can be more difficult to visualize when a shunt connects to the azygos vein. Portoazygos shunts typically dive craniodorsally, in the direction of the aortic hiatus, after originating from one of the portal branches (Figure 6.62). The anomalous vessel can be followed dorsally and cranially to the transverse colon and stomach, unless this window is blocked by acoustic shadowing and/or reverberation caused by the presence of gas, ingesta, or feces. In some cases, a dilated vessel adjacent and parallel to the aorta can be seen that contains venous flow directed cranially. The visualization of such a vessel, which can indicate either the shunt or a dilated azygos vein, is considered specific for portoazygos shunting (Figure 6.62C).

Intrahepatic PSSs are more prevalent in large-breed dogs and are defined as left-divisional, central divisional, or right-divisional. Left-divisional shunts, caused by a patent ductus venosus, represent the most common form of intrahepatic shunt (Szatmari et al. 2004) (Figure 6.60). With this type of PSS, a large tortuous vessel is seen originating from the intrahepatic PV and curving into the left portion of the liver before entering the CVC (Figure 6.63A). Morphologically, these shunts typically connect to the left hepatic vein, which drains into the CVC. Right-divisional shunts often appear as a mirror image of patent ductus venosus PSS, but instead curve into the right liver before connecting to a right hepatic vein or to the CVC (Figure 6.63B,C). Central divisional shunts often present as a window-type shunt between a closely aligned intrahepatic PV and CVC. The PV is commonly dilated at the site of the foramen, and flow turbulence can be observed in the CVC (Figure 6.63D).

The PV size has a significant predictive value in shunt investigation. In fact, because of flow diversion, the size of the PV cranial to the shunt origin is significantly reduced (d'Anjou et al. 2004; Szatmari et al. 2004) (Figures 6.61A, 6.64). A congenital extrahepatic shunt

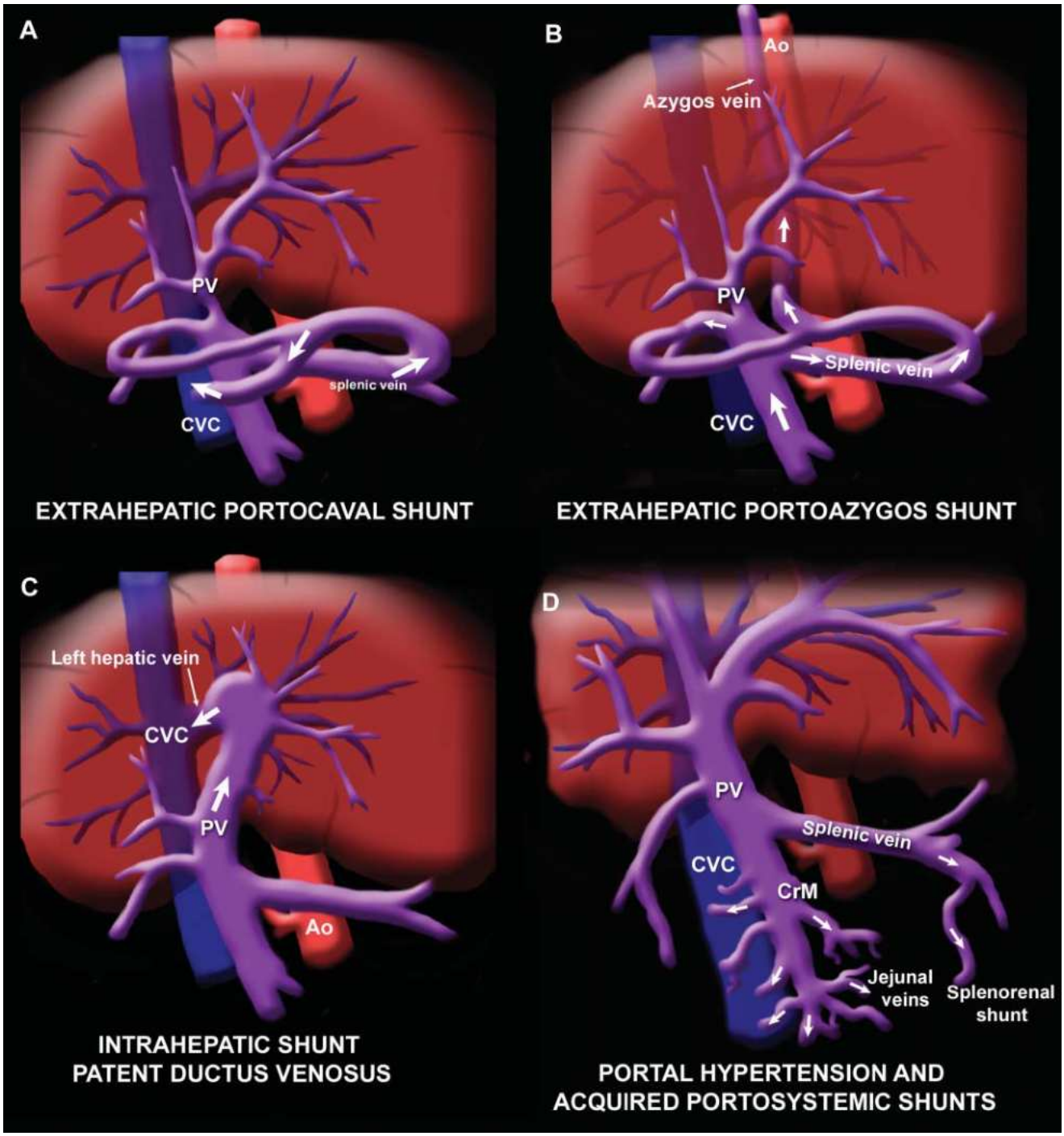


Figure 6.60. **Categories of portosystemic shunts.** Schematic illustrations of typical categories of portosystemic shunts showing the direction of shunting flow (arrows) in dogs and cats. **A, B:** Congenital extrahepatic shunts can terminate into the caudal vena cava or azygos vein. In either case, the diameter of the portal vein (PV) cranial to the origin of the shunt is significantly reduced because of flow diversion. A portoazygos shunt can be followed in the direction of the aortic hiatus, along the aorta (Ao), but its termination can be difficult to visualize. On the other hand, most portocaval shunt terminations can be seen with ultrasonography. **C:** Left-sided intrahepatic shunts (patent ductus venosus) represent the most common type of intrahepatic shunts. This shunt typically terminates into an "ampula" formed by the confluence of this shunt and a left hepatic vein, just before the caudal vena cava (CVC). **D:** Multiple acquired shunts most commonly are caused by chronic liver disease and secondary portal hypertension. Small tortuous vessels can usually be identified in the central abdomen around the CVC, as well as between the spleen and the left kidney (splenorenal anastomosis). Intrahepatic veins can also be distorted and reduced in diameter. With chronic hepatitis or cirrhosis, the liver is typically irregular in contour and heterogeneous. CrM, cranial mesenteric vein.

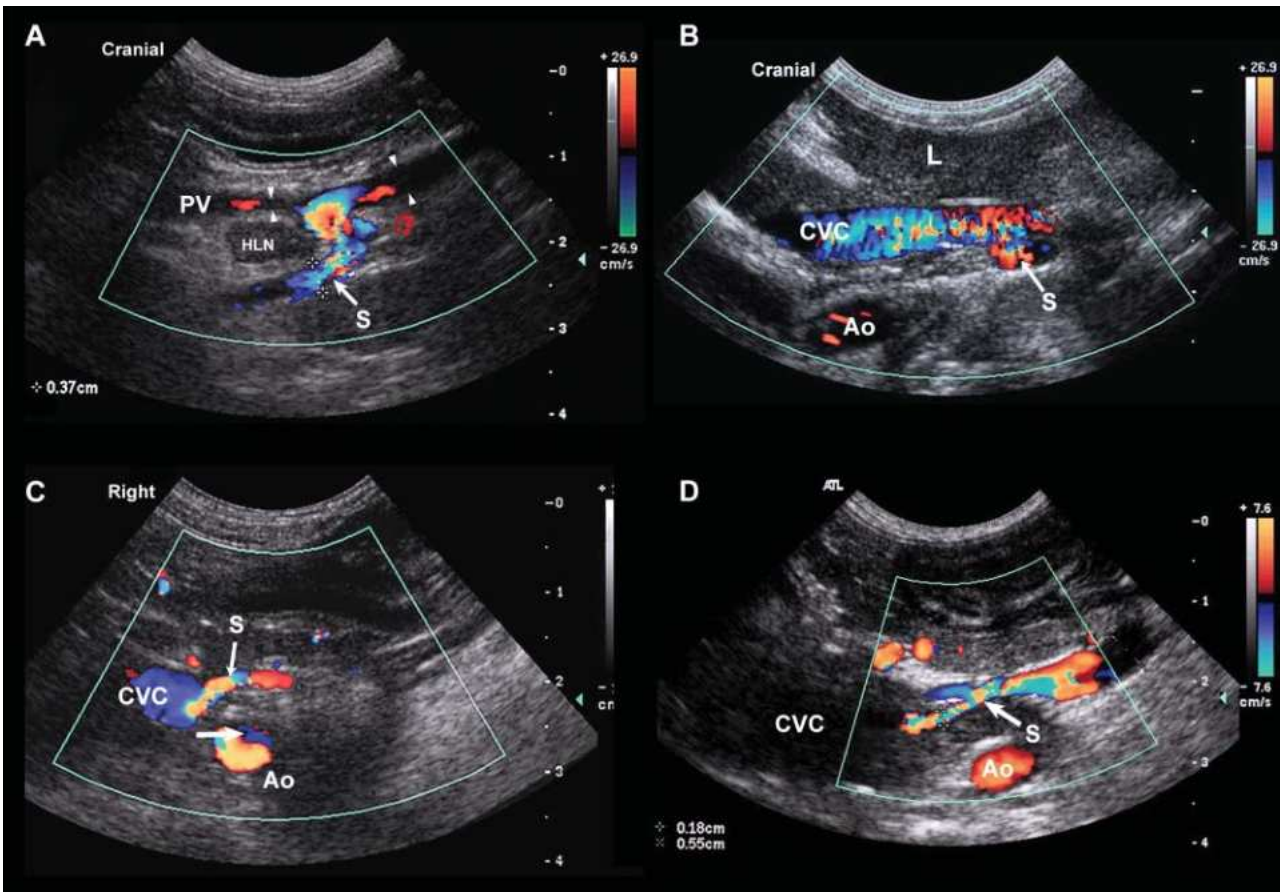


Figure 6.61. **Extrahepatic portocaval shunts. A:** Longitudinal color Doppler image of the abdomen of a Yorkshire Terrier. An anomalous shunting vein (S) just caudal to the stomach is seen originating from the main portal vein (PV). This vessel contains hepatofugal flow and is directed craniodorsally. The PV diameter is significantly reduced cranial to the shunt origin (arrowheads). **B:** Longitudinal color Doppler ultrasound image obtained in the craniodorsal abdomen of a dog with extrahepatic portocaval shunting. A mosaic pattern observed in the caudal vena cava (CVC) is consistent with flow turbulence at the site of shunt termination (S). Ao, aorta; L, liver. **C:** Transverse color Doppler image obtained in the craniodorsal abdomen of an 8-year-old small dog with a small aberrant vessel (S) connecting to the CVC, just cranial to the site of the right renal vein. This shunting vessel was followed to the splenic vein compatible with an extrahepatic splenocaval shunt. **D:** In another small-breed dog, a sinusoid congenital extrahepatic shunt (S) was found to connect to the CVC close to the porta hepatis.

is suspected if the main PV is smaller in diameter when compared with its tributaries. The search for the origin of the PSS is focused on the region where the PV, or a tributary, abruptly diminishes in size. A ratio comparing the luminal diameter of the PV, just before entering the liver, with the maximal luminal diameter of the aorta, obtained in the cranial abdomen, was investigated to predict the likelihood of an extrahepatic PSS in dogs and cats (d'Anjou et al. 2004). Based on these results, a PV-aorta ratio of ≤ 0.65 predicts the presence of an extrahepatic shunt (Figure 6.64), whereas a ratio ≥ 0.8 excludes this type of PSS. However, a low PV/aorta ratio could also be found in dogs with primary PV hypoplasia (idiopathic noncirrhotic portal hypertension), leading to multiple acquired PSS because of portal hypertension. PV/aorta ratios ≥ 0.8 are seen only in animals with a normal portal system, microvascular dysplasia, intrahepatic PSS, or portal hypertension caused by chronic liver disease.

Several other findings can be observed in dogs and cats affected with congenital PSS. Besides the microhepatia observed in most patients (particularly in dogs), the visibility of intrahepatic portal branches is often reduced because of hypoperfusion. When evaluated with spectral Doppler, the portal flow is commonly irregular because of cardiac cycle influence on the normally relatively constant portal flow (Lamb 1996; d'Anjou et al. 2004) (Figure 6.65). Comparing flow velocities in different sections of the portal vein

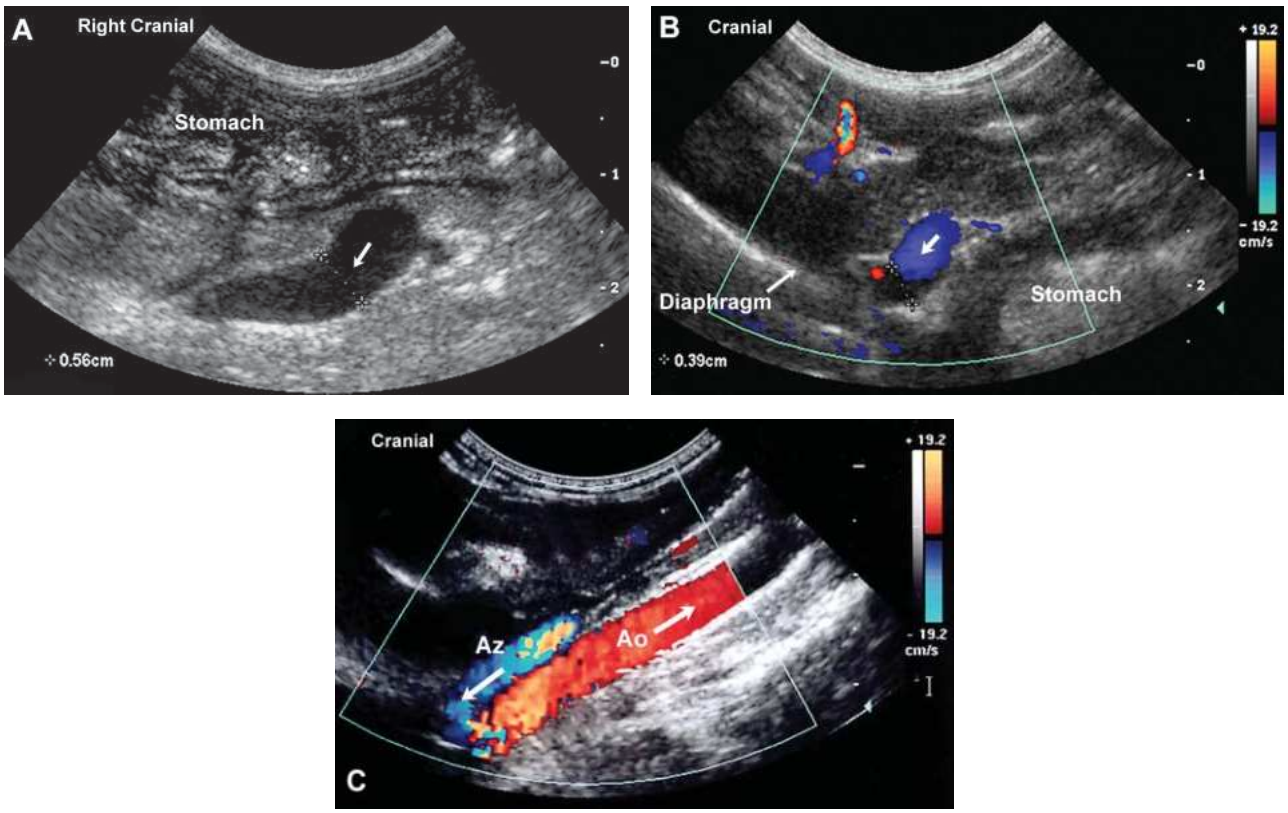


Figure 6.62. **Portoazygos shunts. A:** Transverse image obtained in the craniodorsal abdomen of a small-breed dog with a large vessel dorsal to the stomach in the direction of the aortic hiatus. This vein contained hepatofugal flow (arrow) and could be followed to the diaphragm. A portoazygos shunt was confirmed at surgery. **B:** Longitudinal oblique color Doppler image obtained in the craniodorsal abdomen of a young Yorkshire Terrier. An aberrant vein with hepatofugal flow (short arrow) is next to the gastric cardia and diaphragm. A portoazygos shunt was surgically confirmed. **C:** Longitudinal color Doppler image obtained in the craniodorsal abdomen of a young cat with a right azygos vein (Az) abnormally apparent. A shunt was detected connecting to this vein in the mid-abdomen. Ao, aorta.

and tributaries may also help to identify an anomalous vessel with increased flow (Figure 6.66). The kidneys are commonly enlarged, especially in dogs, and uroliths are often recognized. The combination of microhepatica, renomegaly, and urolithiasis is highly predictive of PSS in young dogs with clinically suspected shunting (d'Anjou et al. 2004).

A systematic approach is recommended in the detection of congenital and acquired PSS in animals (Figure 6.67).

Ultrasound is also an useful tool for monitoring the patency of PSS in dogs after surgical ligature of PSS or placement of occluding devices (Figure 6.68)

Portal Hypertension and Acquired Portosystemic Shunts

Chronic liver disease, particularly involving fibrosis and diffuse nodular regeneration (cirrhosis) or infiltrative neoplasia, can cause reduced PV compliance and increased pressure. Portal hypertension can also be caused by congenital or developmental PV hypoplasia (also termed noncirrhotic portal hypertension), arterioportal fistula, portal thrombosis, or PV compression from an extraluminal mass. Ultrasonographically, portal hypertension can be manifested by the presence of ascites and signs of edema involving several structures, such as the GB wall and pancreas. Portal hypertension is suspected when the portal flow is significantly reduced in velocity (mean $<10\,cm/s$) or reversed (**hepatofugal**), especially if the vein is normal in size or dilated (Nyland and Fisher 1990; d'Anjou et al. 2004) (Figures 6.65B, 6.69). However, flow reduction or reversal may not be observed at the time of the exam.

Sustained portal hypertension leads to the opening of pre-existing collateral vessels that connect the portal system to the systemic circulation (Figure 6.60D). Of these collaterals in dogs, a splenorenal anastomosis is commonly observed that originates from the splenic vein and has a flow directed caudally and

Figure 6.64. **Reduced portal vein/aorta ratio. A**: Transverse sonographic image obtained at the porta hepatis of a 6-month-old Beagle dog with suspected portosystemic shunt (PSS). The portal vein (PV) measures less than half of the diameter of the aorta (Ao), for a ratio of 0.47, which is consistent with the presence of a congenital extrahepatic PSS. The hepatic artery (HA) is well visualized, which is also typical of PSS. LN, hepatic lymph node. **B, C**: In these longitudinal images of the PV **(B)** and aorta **(A)**, obtained at the level of the porta hepatis, the PV appears significantly smaller. The PV/aorta ratio was calculated as 0.52. A congenital extrahepatic shunt was detected caudal to the site of measurement of the PV. The caudal vena cava (CVC) can be collapsed easily during the exam (arrow).

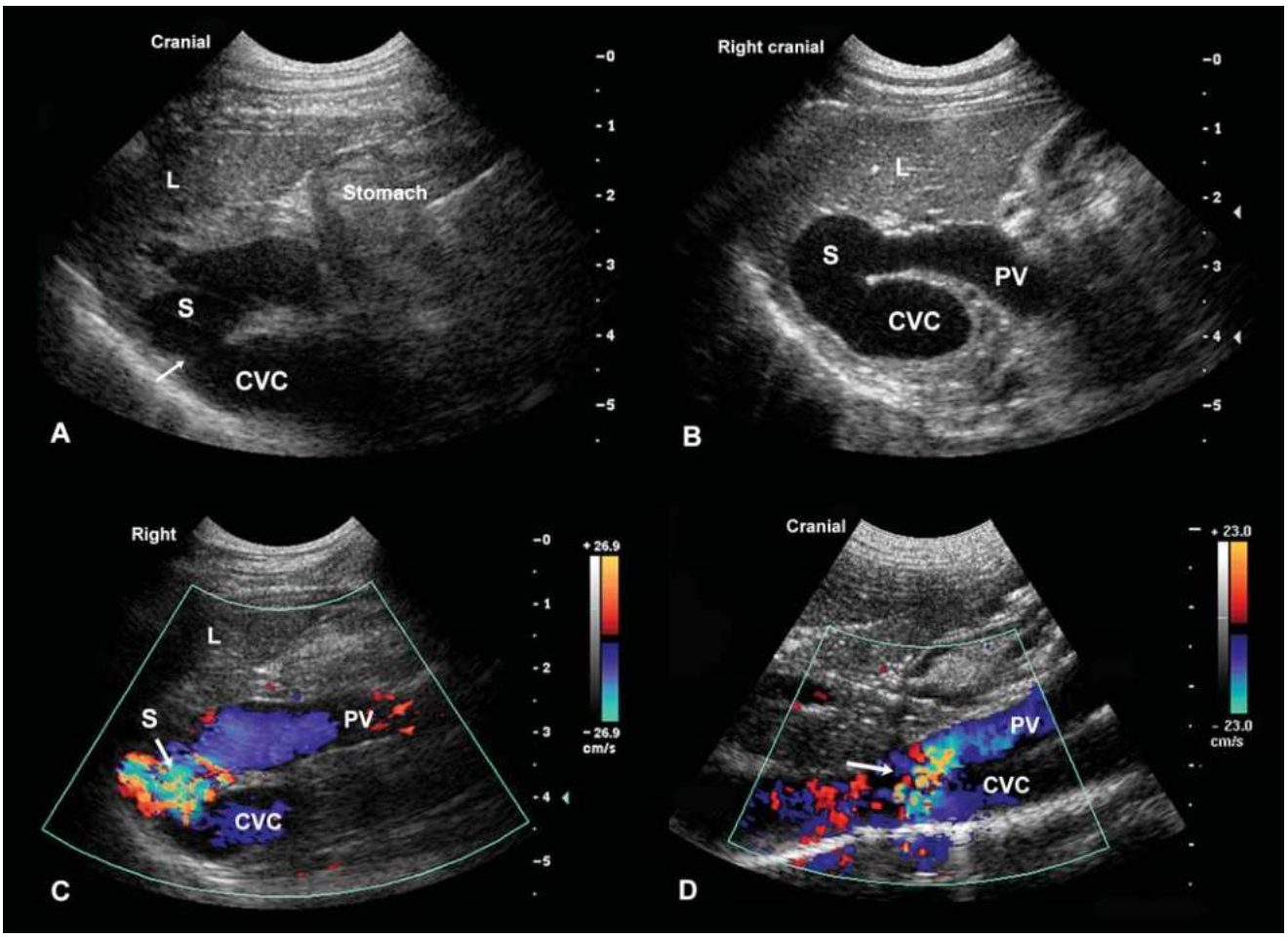


Figure 6.63. **Intrahepatic shunts. A:** Patent ductus venosus. Longitudinal oblique ultrasound image obtained in the left cranial abdomen of a young Golden Retriever. A large tortuous vein apparent in the liver connects to the caudal vena cava (CVC and arrow). Hepatofugal flow observed on color Doppler was consistent with a left-divisional intrahepatic shunt (S). The liver (L) is also reduced in volume. **B:** Right-divisional shunt. Transverse ultrasound image of the liver (L) obtained through the right 12th intercostal space (S) in a young Bernese Mountain Dog with suspected portosystemic shunting. A large, intrahepatic, tortuous vein connects the portal vein (PV) to the CVC. **C: Right-divisional shunt.** Longitudinal oblique ultrasound image obtained through the right 12th intercostal space in a young Akita with suspected portosystemic shunting. A large tortuous vein (S) is between the PV and the CVC in the liver (L). Turbulent flow is obvious, as manifested by a mosaic pattern on color mode at the site of communication of the shunt (arrow) with the caudal vena cava. **D:** Central divisional intrahepatic shunt. Longitudinal color Doppler image obtained in the craniodorsal abdomen of a young large-breed dog with suspected portosystemic shunting. The intrahepatic PV dives dorsally and a "window" (arrow) containing turbulent flow (mosaic pattern) is seen connecting to the CVC.

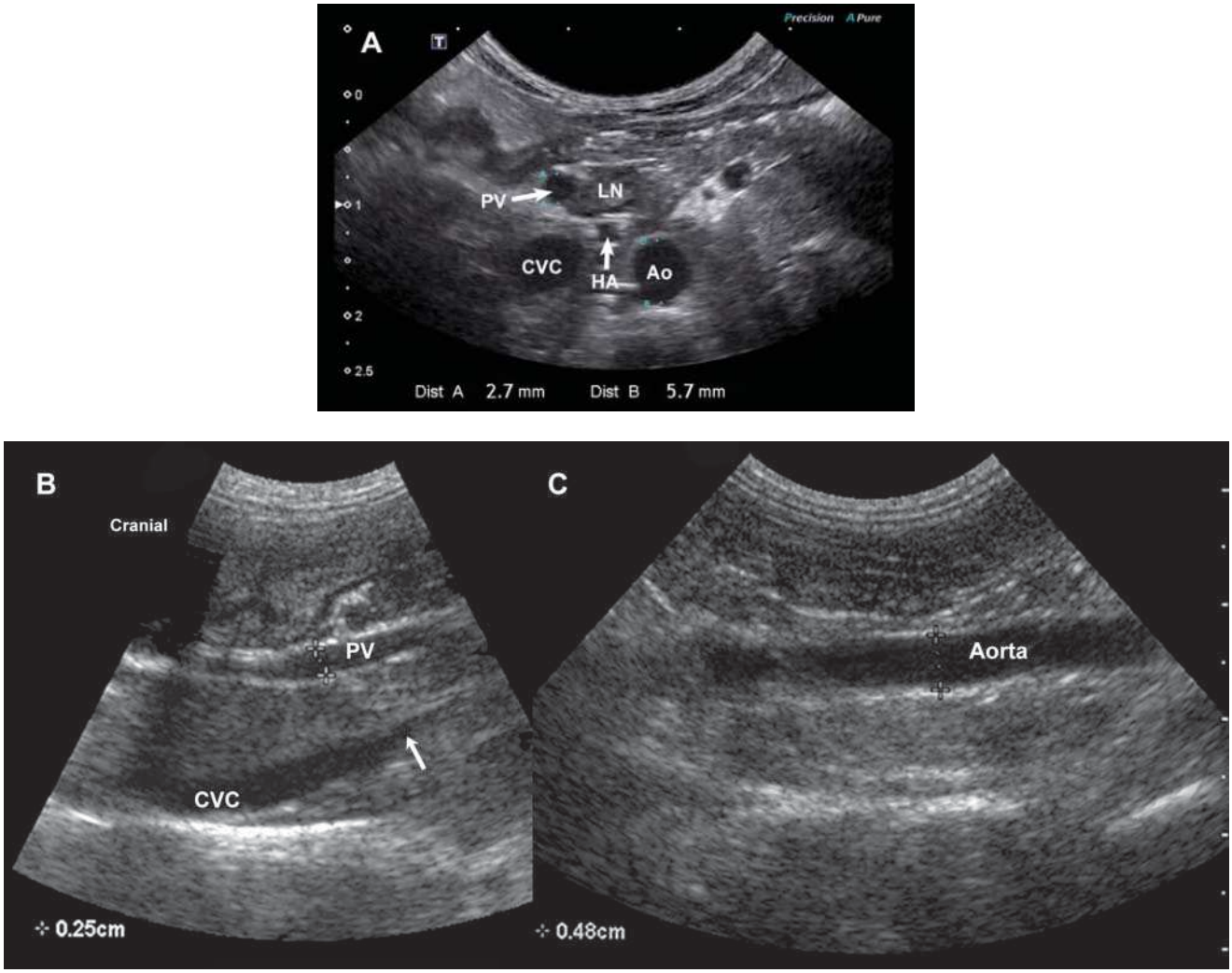


Figure 6.64. **Reduced portal vein/aorta ratio.** (for full caption, see facing page)

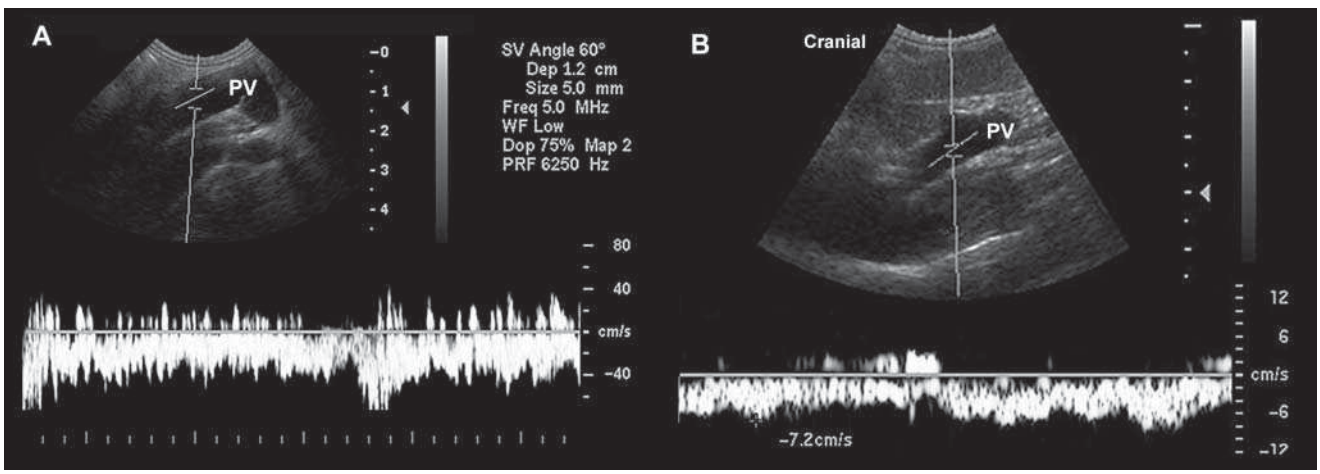


Figure 6.65. **Portal flow alterations. A:** Intrahepatic shunt. Spectral Doppler evaluation of the portal flow characteristics in a dog with intrahepatic shunting. The flow velocity is markedly irregular in the main extrahepatic portal vein (PV) because of the retrograde influence of pressure variations in the caudal vena cava. **B:** Portal hypertension. Spectral Doppler evaluation of the portal flow in a dog with chronic liver disease. The flow velocity is reduced (maximal 7.2 cm/s) in the extrahepatic PV because of intrahepatic hypertension. Multiple acquired shunts were detected.

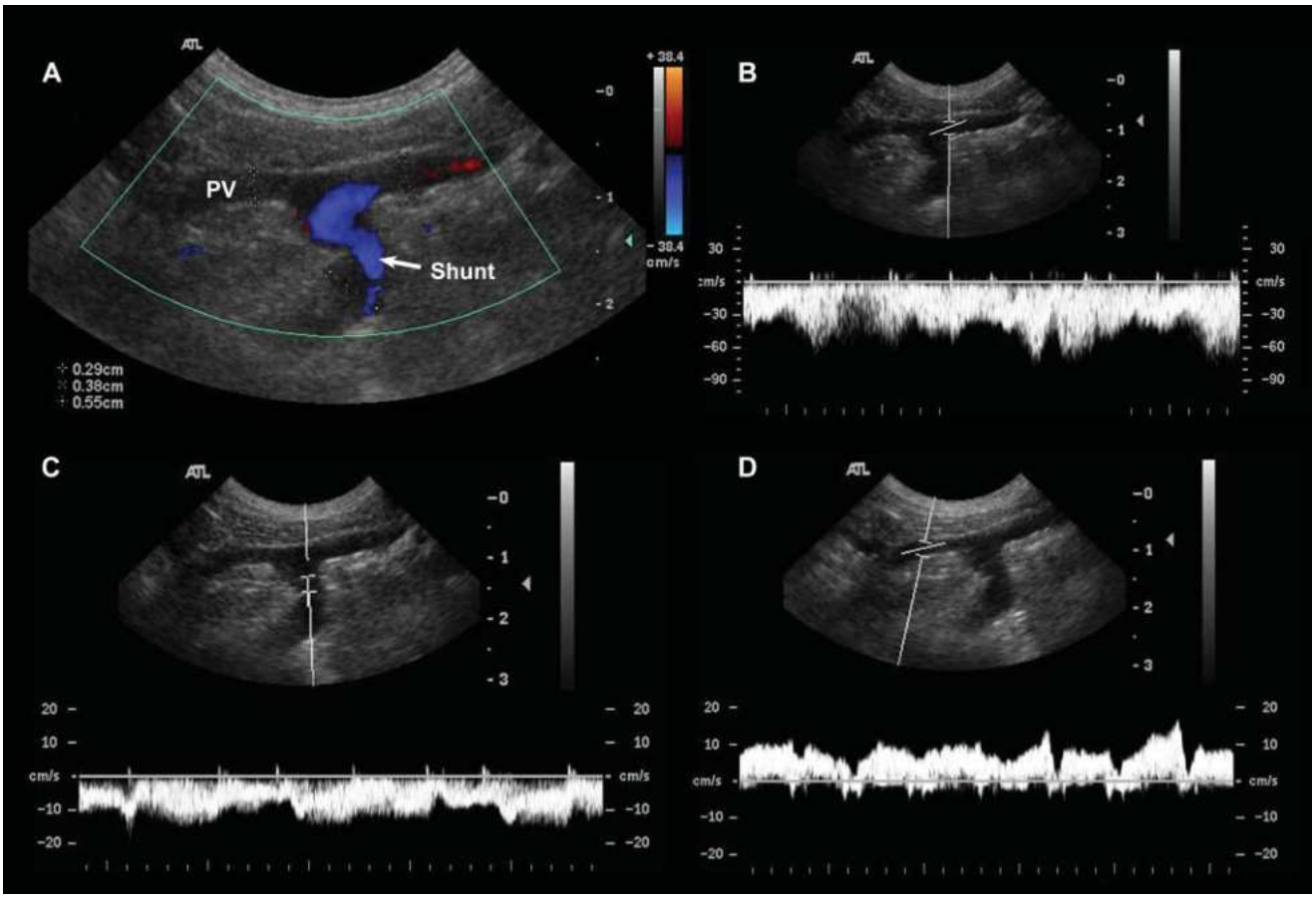


Figure 6.66. Portal flow velocities before and after shunt origin. A: Color Doppler evaluation of the extrahepatic shunt originating from the proximal portal vein (PV). The blue color signal indicates hepatofugal flow in the anomalous vessel. No color flow is identified in the PV cranial to the shunt origin, mainly because of its perpendicular position in regard to the insonation angle. **B–D**: Spectral Doppler assessment of the flow velocities in the PV proximal to the shunt **(A)**, within the shunt **(B)**, and in the PV distal to the shunt **(C)**. The flow is irregular and becomes hepatofugal (i.e., reversed) in the PV distal to the origin of the shunt **(D)**.

coursing caudally along the dorsal splenic border (Figure 6.70A) (d'Anjou et al. 2004). The caudal termination of this collateral can be difficult to visualize. However, in the same region, multiple small tortuous vessels are often seen that connect to the left renal vein or directly to the CVC (Figure 6.68B). The visualization of a vein connecting to the left renal vein, or to the CVC near the junction with the left renal vein, is consistent with a dilated gonadal vein indicating the termination of the splenorenal anastomosis. It has been described as a specific sign of acquired PSS (Szatmari et al. 2004; Figure 6.70D). Splenorenal shunts have recently been described in cats (Palerme et al. 2013). These are more common in older female cats and are often associated with hepatopathy, although they may be found incidentally (Figure 6.71).

Small, tortuous, aberrant vessels can also be observed in the mesentery and surrounding the CVC, particularly when color or power Doppler is used (Figure 6.68C). Flow turbulence is typically seen in the CVC at the site of shunt entry.

Arterioportal Fistulas

Congenital or acquired connections between PVs and hepatic arteries, termed arterioportal fistulas, can dramatically increase the pressure within the portal system and lead to rapidly progressive hypertension and the eventual opening of portosystemic collaterals (acquired PSS). Ultrasonographically, the PV can become markedly enlarged, and flow reversal can be observed with Doppler (Szatmari et al. 2004) (Figure 6.72). Intrahepatic portal branches typically become dilated and tortuous in the affected lobe, which can be more difficult to identify.

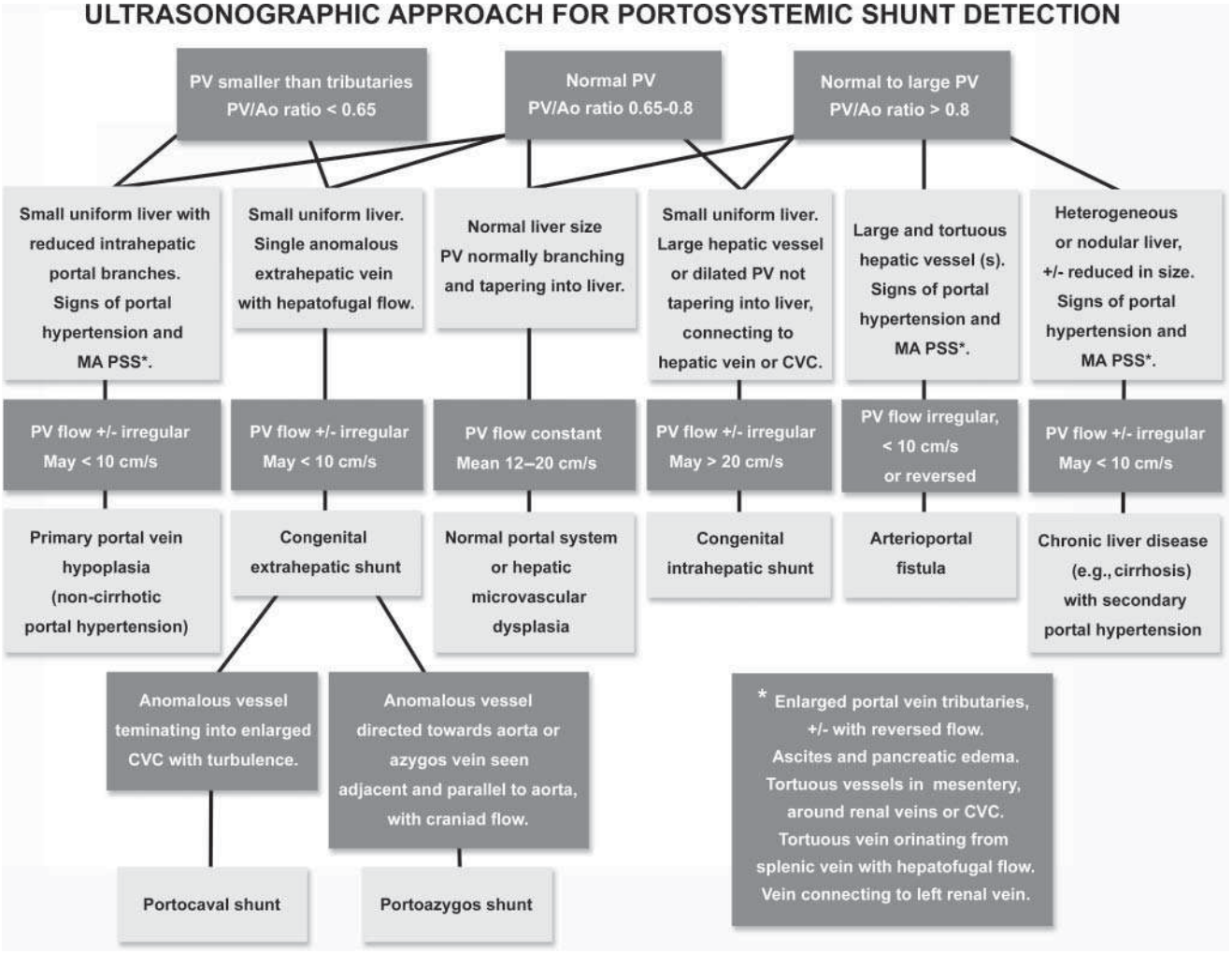


Figure 6.67. **Portosystemic shunt search algorithm.** Typical findings observed with different categories of portosystemic shunts (PSS) are shown. The main portal vein (PV) is evaluated and measured just caudal to its insertion into the liver. In that process, care must be taken not to confuse a portal tributary or an aberrant vein for the main portal vein. CVC, caudal vena cava; MA PSS, multiple acquired portosystemic shunts; and PV/Ao (aorta) ratio, ratio between the luminal diameter of the main portal vein and aorta.

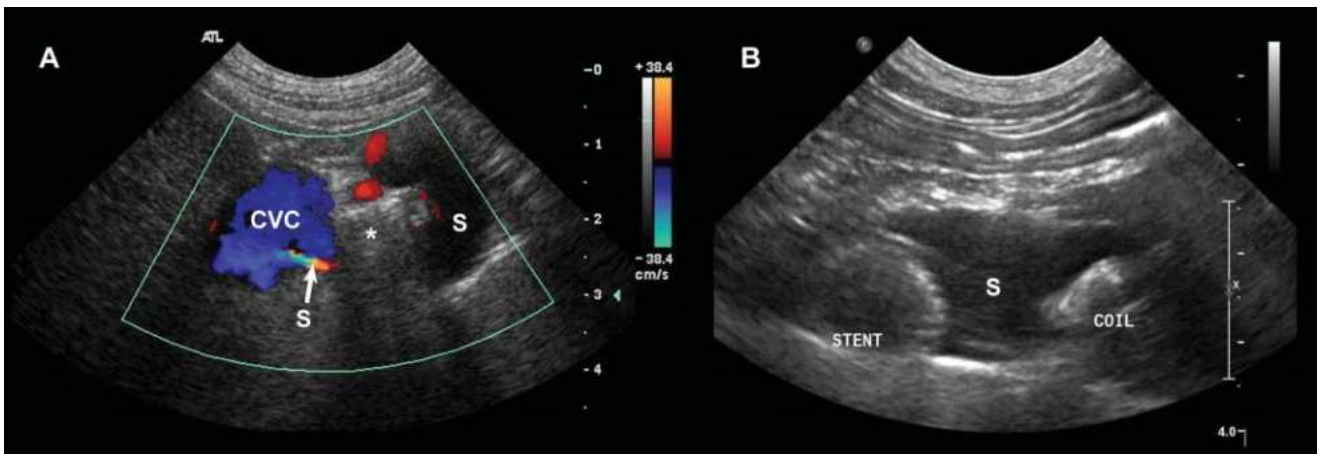


Figure 6.68. **Follow-up of portosystemic shunt (PSS) after surgical occlusion. A**: In this dog, an ameroid contrictor device (*) was placed at the site of termination of a congenital extrahepatic portocaval shunt. One week after the surgery, the shunt (S) remained patent, but it closed completely after 4 weeks. The ameroid causes acoustic shadowing and reverberation artifacts. **B**: In this 9-month-old Beagle with an intrahepatic shunt, a stent was placed into the caudal vena cava, allowing coils to be safely expanded into the shunt.

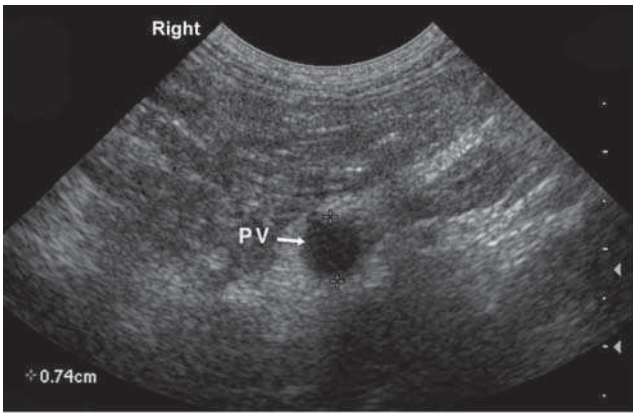


Figure 6.69. Portal hypertension. Transverse image obtained in the midcranial abdomen, caudal to the liver, of a small-breed dog. The portal vein (PV) is enlarged. The flow velocity is reduced because of portal hypertension. Hepatic cirrhosis was diagnosed.

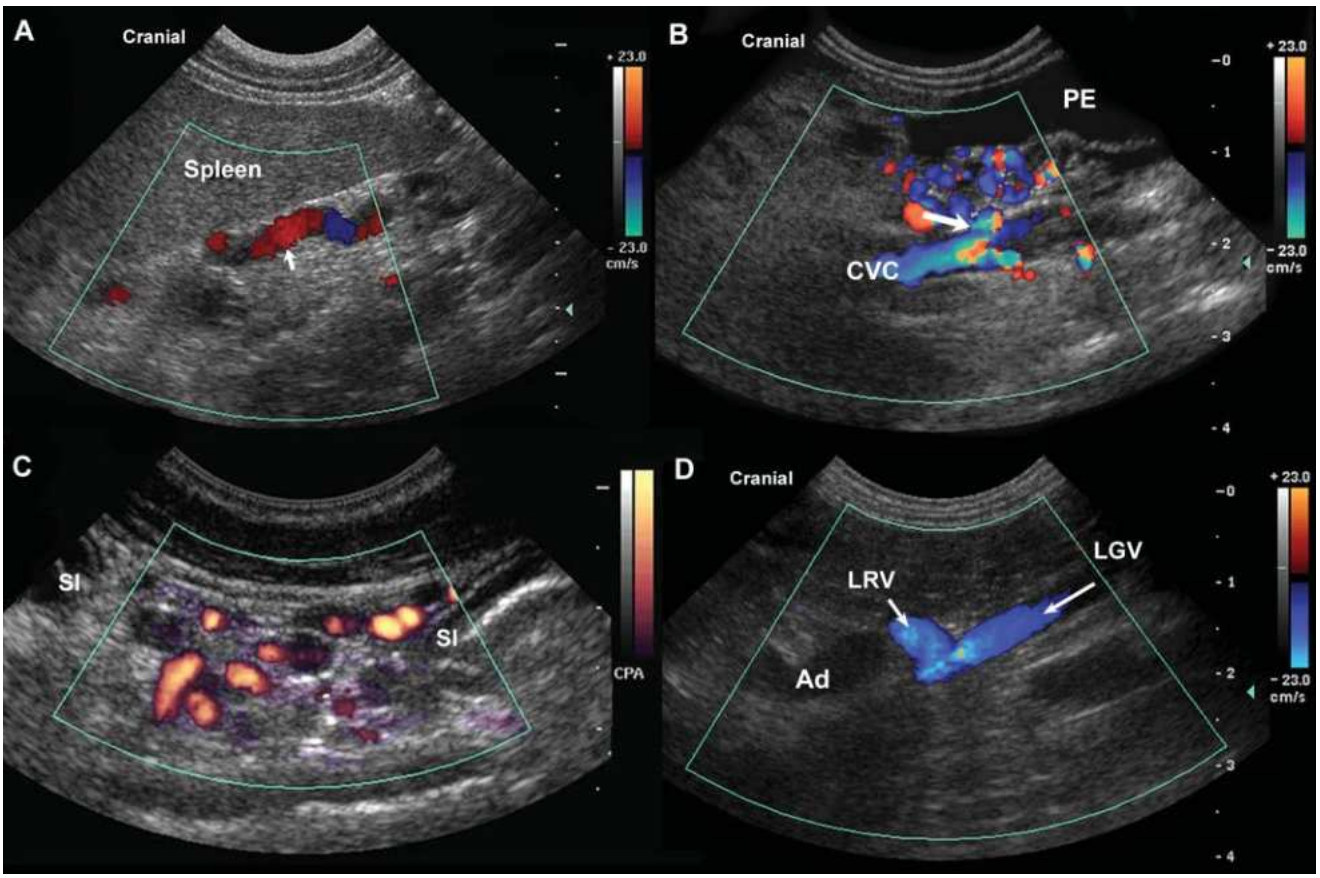


Figure 6.70. Multiple acquired portosystemic shunts. A: Longitudinal image obtained at the level of the spleen. A tortuous vein (arrow) containing flow directed caudally was connected to the splenic vein cranially and could be followed to the level of the right renal vein, caudally, consistent with an acquired splenorenal anastomosis. This dog had primary portal vein hypoplasia. **B:** Longitudinal image of a dog with portal hypertension obtained in the mid-abdomen, at the level of the caudal vena cava (CVC). Multiple small tortuous vessels are seen in the mesentery, in proximity to the CVC, with a direct connection observed (arrow). Anechoic peritoneal effusion (PE) is also detected. **C:** Longitudinal image obtained in the mid-abdomen, at the level of the omentum and small intestine (SI), of a dog with portal hypertension. Multiple small tortuous vessels are seen in the mesentery. **D:** Longitudinal image obtained at the level of the left adrenal gland (Ad) in a dog with portal hypertension caused by portal venous thrombosis. An aberrant vein is seen connecting with the left renal vein (LRV), consistent with an enlarged left gonadal vein (LGV). This feature is specific of acquired portosystemic shunt in dogs.

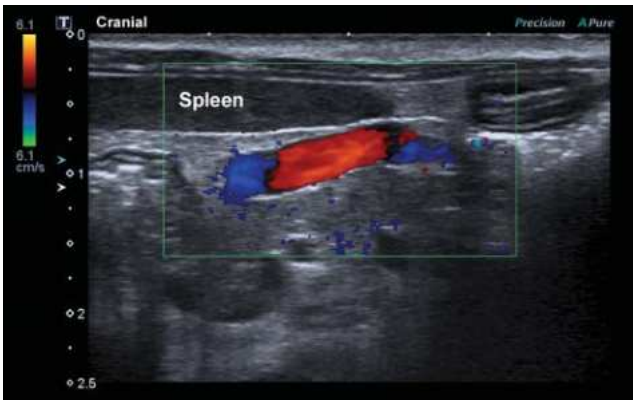


Figure 6.71. Incidental splenosystemic shunt in a cat. Longitudinal image obtained in the left lateral abdomen of a 12-year-old cat with chronic renal disease. A relatively large anomalous vessel with hepatofugal flow (red color signal) extends caudally, along the dorsal border of the spleen. The liver was mildly inhomogeneous, but clinical signs of hepatic insufficiency were lacking to justify further investigation. Image courtesy of Guy Beauregard, Centre Veterinaire Rive-Sud, Canada.

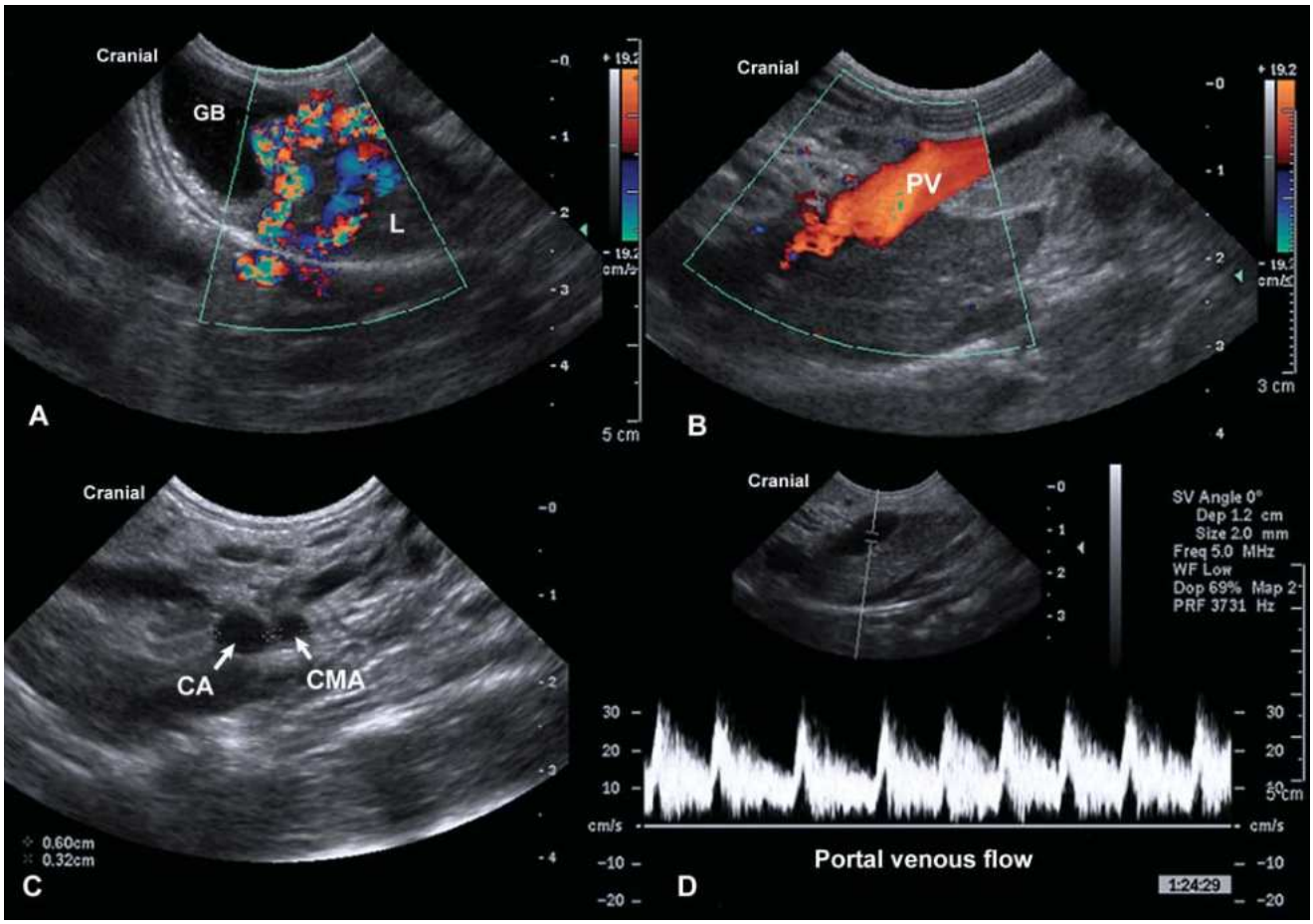


Figure 6.72. Arterioportal fistula. A: On this longitudinal color Doppler image obtained in a young dog with suspected portosystemic shunting, a markedly tortuous vascular structure with turbulent flow is observed within the liver (L), just caudal to the gallbladder (GB). The portal vein (PV) is distended and associated with reversed flow (hepatofugal; red signal) on color Doppler **(B)** and abnormal pulsatility on spectral Doppler **(D)**. These signs indicate the presence of an arterioportal fistula in the liver. **C:** Additionally, the celiac artery (CA) is noted to be much larger than the cranial mesenteric artery (CMA). Multiple acquired shunts were detected during the exam (not shown).

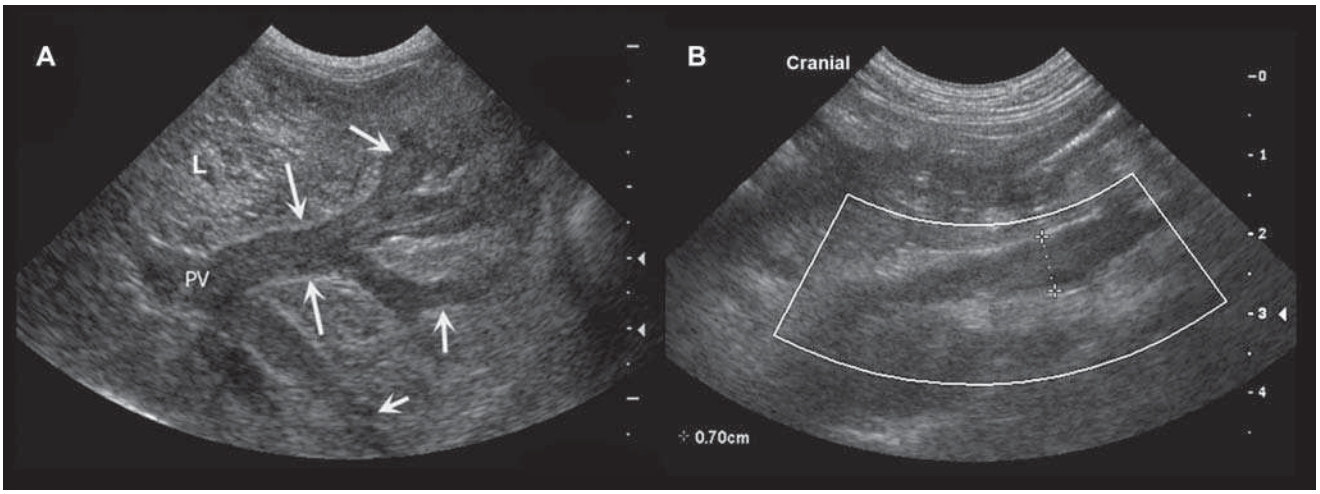


Figure 6.73. **Portal venous thrombosis. A:** Transverse image of the left portion of the liver (L) in a dog with severe chronic hepatitis. The intrahepatic portal venous lumens (arrows) appear hyperechoic. Color Doppler confirmed the absence of flow and the presence of massive thrombosis. Secondary portal hypertension was also identified. PV, portal vein. **B:** Longitudinal image of the portal vein in a small dog with protein-losing nephropathy and signs of portal hypertension. The portal vein is enlarged (cursors) and presents a mildly hyperechoic luminal content without evidence of flow on color Doppler, indicating thrombosis. The surrounding fat is mildly hyperechoic. Multiple acquired shunting vessels were also identified.

Portal Venous Thrombosis

Thrombosis can form because of a hypercoagulable state, vascular stasis, or damage to the vascular endothelium (Lamb et al. 1996b). Portal vein thrombosis is commonly associated with hepatic disease and should be considered in dogs presenting with abdominal pain, ascites, and thrombocytopenia (Respess et al. 2012). Significant portal thrombosis causes portal hypertension and consequently the formation of multiple acquired PSS, particularly if the thrombosis is long-standing. Portal thrombosis can also extend caudally into the cranial mesenteric vein or splenic vein and cause congestion that can lead to life-threatening infarction. Ultrasonographically, thrombi are characterized by a lack of flow in the affected region of the vein, as well as by the presence of an immobile, mildly echogenic structure within the vessel lumen (Lamb et al. 1996b) (Figure 6.73). The vein can be dilated, particularly caudal to the stenosis and involving the peripheral portal tributaries. Vascular congestion can be better assessed with spectral Doppler. Color Doppler and power Doppler are also useful in confirming the magnitude of the thrombosis, particularly when thrombi are initially formed and poorly echogenic. Power Doppler, which is more sensitive and not direction-dependent, helps to better assess the presence of flow around or within the thrombus, particularly when the vessel is aligned perpendicularly to the probe or if the flow is significantly reduced.

Hepatic Congestion

Hepatic venous congestion is more commonly caused by right-sided heart insufficiency, such as cardiac tamponade, leading to increased pressure within the CVC and consequently within hepatic veins. The CVC and hepatic veins appear dilated, and the liver is typically enlarged and diffusely hypoechoic (Figure 6.74).

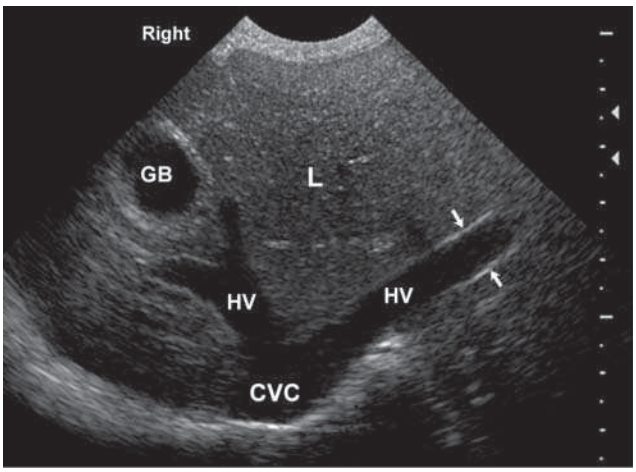


Figure 6.74. **Passive hepatic venous congestive.** Transverse image of the central portion of the liver (L) of a dog with cardiac tamponade. The caudal vena cava (CVC) and hepatic veins (HV) are dilated, and the hepatic parenchyma is diffusely mildly hypoechoic. The gallbladder (GB) wall has a double rim because of edema. The left HV has hyperechoic walls (arrows) because of their perpendicular position relative to the ultrasound beam.

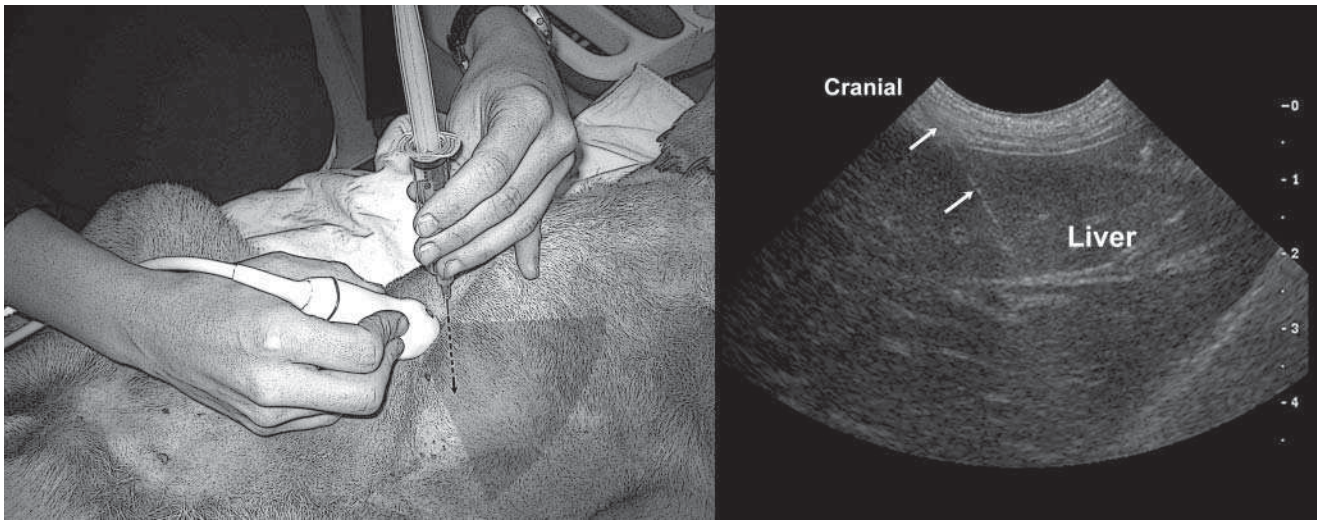


Figure 6.75. Ultrasound-guided fine-needle aspiration. In the photograph, a freehand, ultrasound-guided, fine-needle aspiration is performed. The needle is inserted through the skin just caudal to the xiphoid process and costal arch, and through the left portion of the liver. This technique is preferred when diffuse processes are suspected, because it prevents inadvertent gallbladder puncture. The corresponding ultrasound image is also shown. The hyperechoic fine needle can be seen obliquely into the parenchyma (arrows).

Interventional Procedures

Ultrasound-guided fine-needle aspiration and biopsy have become routine procedures complementing hepatic ultrasonography (Penninck and Finn-Bodner 1998). The choice of needle size (gauge) and length depends on the size, the vascularity, and the depth of the targeted tissue. Typically, 20- to 22-gauge needles are used for fine-needle aspiration, and 14- to 18-gauge needles are used for automated core biopsy. Fine-needle aspiration can usually be performed with patients under minimal sedation, whereas biopsy usually requires general anesthesia. Aspiration can be performed with a customized biopsy-needle guide placed on the probe or by using a freehand technique. The latter, which is more commonly used especially on superficial lesions, can usually be performed more quickly and limits possible lacerations (Figure 6.75). Although freehand aspiration is relatively safe and easy to perform in cases of diffuse hepatic disorders, it can be more challenging if small, deep lesions are targeted. With the assisted technique, the needle is placed through the biopsy guide tunnel and introduced along a precise path, which, however, cannot be modified (Figure 6.76).

Vacuolar hepatopathies, such as lipidosis and hyperadrenocorticism, are reliably diagnosed through cytological specimens obtained with fine-needle aspiration (Wang et al. 2004). Some neoplastic processes, such as lymphoma, and inflammatory processes can also be diagnosed through cytological examination, although a more confident diagnosis may require biopsy. Fine-needle drainage of cavitary lesions, such as cysts or abscesses, can also be performed as a diagnostic and/or therapeutic procedure.

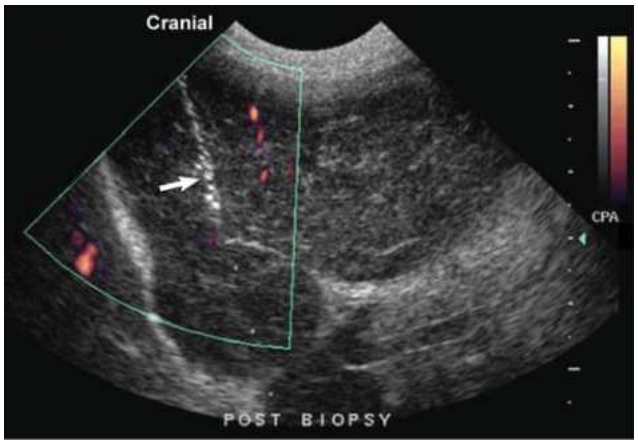


Figure 6.76. Ultrasound-guided percutaneous biopsy. Longitudinal image obtained using power Doppler after biopsy of the left portion of the liver of a dog with suspected hepatitis. A hyperechoic needle tract can be seen along the biopsy guide path (small aligned dots at the arrow) without evidence of hemorrhage. The left portion of the liver was chosen to avoid the gallbladder.

Hemorrhage represents the most common complication observed with ultrasound-guided aspiration and biopsy, particularly if the liver is friable and/or if a

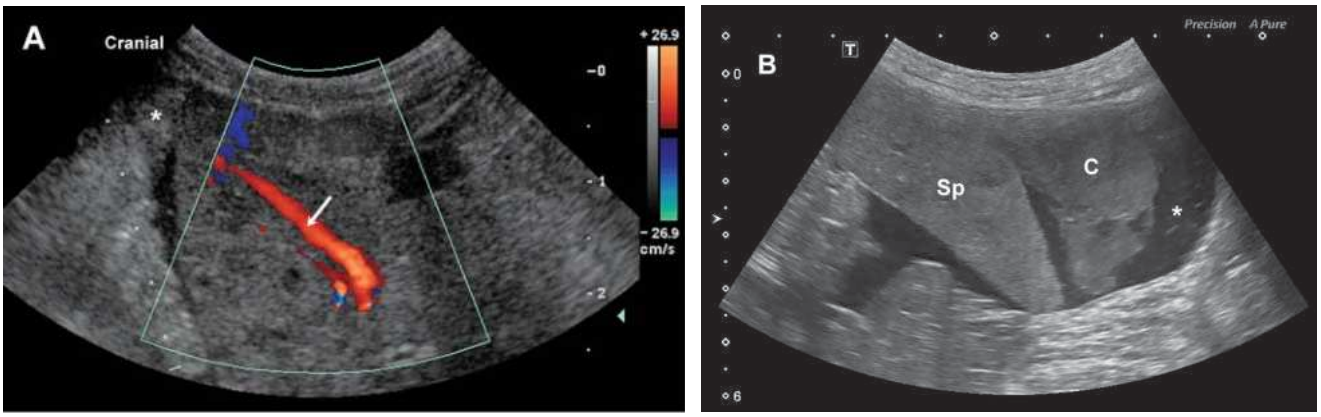


Figure 6.77. Post-biopsy hemorrhage. A: Longitudinal image obtained after ultrasound-guided biopsy of the left portion of the liver of a dog with chronic active hepatitis. A red-signal linear tract (arrow), consistent with retrograde hemorrhage, is observed along the biopsy tract. Echogenic peritoneal effusion is at the cranial aspect of the biopsy site (*), consistent with peritoneal hemorrhage. **B**: In this other dog with a severe degenerative hepatopathy, biopsies resulted in prolonged hemorrhage (*). A blood clot (C) eventually formed next to the spleen (Sp).

coagulopathy is present. Preinterventional coagulation profiles are recommended in most cases. Additionally, postinterventional ultrasonographic examination should be performed to monitor the presence of hemorrhage (Figure 6.77).

Needle tract implantation of neoplastic or infectious processes, although not well investigated in small animals, can represent a limiting factor, particularly if surgical excision is planned.

Ultrasound-guided cholecystocentesis can be used to obtain a sample of bile for culture or for GB decompression in animals with extrahepatic biliary obstruction secondary to an inflammatory process, such as pancreatitis (Herman et al. 2005) (Figure 6.78).

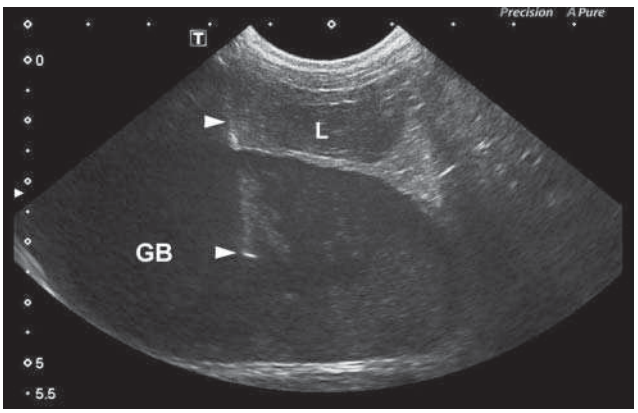


Figure 6.78. Ultrasound-guided cholecystocenthesis. In this dog with extrabiliary obstruction due to severe pancreatitis, gallbladder (GB) pressure was reduced by removing nearly 50 ml of bile. This resulted in short-term clinical improvement. Arrowheads point to the needle traversing the liver (L) parenchyma before entering the distended GB.

Although infrequent, bile leakage and subsequent peritonitis, as well as peritoneal hemorrhage, are potential complications. Risks of complications are increased if the GB is distended or if its wall is diseased. The transhepatic approach is suggested to be the safest percutaneous method of bile aspiration, enabling the liver parenchyma to seal the area of GB puncture (Center 1996).

Intraoperative ultrasonography can also help in the localization of an intrahepatic shunt and assist surgical ligation or placement of embolization coils.

Visit our website at **www.SmallAnimalUltrasonography.com** for complementary video clips with annotations and text on:

- Normal liver and biliary system
- Normal portal system
- Lipidosis
- Steroid-induced and other vacuolar hepatopathies
- Nodular hyperplasia
- Chronic active hepatitis
- Cholangitis/Cholangiohepatitis in cats
- Cirrhosis
- Hepatocellular carcinoma
- Hepatic metastases
- Hepatic lymphoma
- Cystadenoma
- Gallbladder mucocele
- Extrahepatic biliary obstruction
- Gallbladder sludge
- Cholelithiasis
- Portosystemic shunts

References

Beatty JA, Barrs VR, Martin PA, et al. (2002) Spontaneous hepatic rupture in six cats with systemic amyloidosis. J Small Anim Pract 43:355–363.

Besso JG, Wrigley RH, Gliatto JM, Webster CRL (2000) Ultrasonographic appearance and clinical findings in 14 dogs with gallbladder mucocele. Vet Radiol Ultrasound 41:261–271.

Best EJ, Bush DJ, Dye C (2010) Suspected choledochal cyst in a domestic shorthair cat. J Feline Med Surg 12:814–817.

Bosje JT, van den Ingh TS, van der Linde-Sipman JS (1998) Polycystic kidney and liver disease in cats. Vet Q 20:136–139.

Bromel C, Barthez PY, Léveillé R, Scrivani PV (1998) Prevalence of gallbladder sludge in dogs as assessed by ultrasonography. Vet Radiol Ultrasound 9:206–210.

Carlisle CH, Wu JX, Heath TJ (1995) Anatomy of the portal and hepatic veins of the dog: A basis for systematic evaluation of the liver by ultrasonography. Vet Radiol Ultrasound 36:227–233.

Center SA (1996) Diseases of the gallbladder and biliary tree. In: Guilford WG, Center SA, Strombeck DR, Williams DA, Meyer DJ, eds. Strombeck's Small Animal Gastroenterology, 3rd edition. Philadelphia: WB Saunders, pp 860–882.

Choi J, Kim A, Keh S, Oh J, Kim H, Yoon J (2013) Comparison between ultrasonographic and clinical findings in 43 dogs with gallbladder mucoceles. Vet Radiol Ultrasound 55:202–207.

Cruz-Arambulo R, Wrigley R, Powers B (2004) Sonographic features of histiocytic neoplasms in the canine abdomen. Vet Radiol Ultrasound 45:554–558.

Cuccovillo A, Lamb CR (2002) Cellular features of sonographic target lesions of the liver and spleen in 21 dogs. Vet Radiol Ultrasound 43:275–278.

d'Anjou MA, Penninck D, Cornejo L, Pibarot P (2004) Ultrasonographic diagnosis of portosystemic shunting in dogs and cat. Vet Radiol Ultrasound 45:424–437.

d'Anjou, MA (2007) The sonographic search for portosystemic shunts. Clin Tech Small Anim Pract 22:104–114.

Diana A, Guglielmini C, Specchi S, Di Tommaso M, et al. (2012) Ultrasonographic evaluation of preprandial and postprandial gallbladder volume in healty cats. Am J Vet Res 73:1583–1588.

Eich CS, Ludwig LL (2002) The surgical treatment of cholelithiasis in cats: A study of nine cases. J Am Anim Hosp Assoc 38:290–296.

Evans HE (1993a) Chapter 7: The digestive apparatus and abdomen. In: Evans HE, Christensen GC, eds. Miller's Anatomy of the Dog, 3rd edition. Philadelphia: WB Saunders, pp 385–462.

Evans HE (1993b) Veins. In: Evans HE, Christensen GC, eds. Miller's Anatomy of the Dog, 3rd edition. Philadelphia: WB Saunders, pp 682–716.

Fahie MA, Martin RA (1995) Extrahepatic biliary tract obstruction: A retrospective study of 45 cases (1983–1993). J Am Anim Hosp Assoc 31:478–482.

Feeney DA, Anderson KL, Ziegler LE, Jessen CR, et al. (2008) Statistical relevance of ultrasonographic criteria in the asessment of diffuse liver disease in dogs and cats. Am J Vet Res 69:212–221.

Gaillot HA, Penninck DG, Webster CR, Crawford S (2007) Ultrasonographic features of extrahepatic biliary obstruction in 30 cats. Vet Radiol Ultrasound 48:439–447.

Guillot M, d'Anjou MA, Alexander K, Bédard C, et al. (2009) Can sonographic findings predict the results of liver aspirates in dogs with suspected liver disease? Vet Radiol Ultrasound 50:513–518.

Harran N, d'Anjou MA, Dunn M, Beauchamp (2011) Gallbladder sludge on ultrasound is predictive of increased liver enzymes and total bilirubin in cats. Can Vet J 52:999–1003.

Herman BA, Brawer RS, Murtaugh RJ, Hackner SG (2005) Therapeutic percutaneous ultrasound-guided cholecystocentesis in three dogs with extrahepatic biliary obstruction and pancreatitis. J Am Vet Med Assoc 227:1782–1786.

Hinkle Schwartz SG, Mitchell SL, Keating JH, Chan DL (2006) Liver lobe torsion in dogs: 13 cases (1995–2004). J Am Vet Med Assoc 228:242–247.

Hittmair KM, Vielgrader HD, Loupal G (2001) Ultrasonographic evaluation of gallbladder wall thickness in cats. Vet Radiol Ultrasound 42:149–155.

Hudson LC, Hamilton WP, eds. (1993) Atlas of Feline Anatomy for Veterinarians, 1st edition. Philadelphia: WB Saunders, 287 pp.

Kemp SD, Panciera DL, Larson MM, Werre SR (2013) A comparison of hepatic sonographic features and histopathologic diagnosis in canine liver disease: 138 cases. J Vet Intern Med 27:806–813.

Kutura K, Seki M, Ishikawa C, Sakai M, Kagawa Y et al. (2013) Triple-phase helical computed tomography in dogs with hepatic masses. Vet Radiol Ultrasound 55:7–15.

Kvitko-White HL, Sayre RS, Corapi WV, Kathy A. Spaulding KA (2011). Imaging diagnosis – Heterobilharzia americana infection in a dog Vet Radiol Ultrasound 52:538–541.

Lamb CR (1996) Ultrasonographic diagnosis of congenital portosystemic shunts in dogs: Results of a prospective study. Vet Radiol Ultrasound 37:281–288.

Lamb CR, Forster-van Hijfte MA, White RN, McEvoy FJ, Rutgers HC (1996a) Ultrasonographic diagnosis of congenital portosystemic shunt in 14 cats. J Small Anim Pract 35:205–209.

Lamb CR, Hartzband LE, Tidwell AT, Pearson SH (1991) Ultrasonographic findings in hepatic and splenic lymphosarcoma in dogs and cats. Vet Radiol Ultrasound 32:117–120.

Lamb CR, Mahoney PN (1994) Comparison of three methods for calculating portal blood flow velocity in dogs using duplex-Doppler ultrasonography. Vet Radiol Ultrasound 35:190–194.

Lamb CR, Wrigley RH, Simpson KW, et al. (1996b) Ultrasonographic diagnosis of portal vein thrombosis in four dogs. Vet Radiol Ultrasound 37:121–129.

Last RD, Hill JM, Roach M, Kaldenberg T (2006) Congenital dilatation of the large and segmental intrahepatic bile ducts

(Caroli's disease) in two Golden retriever littermates. J S Afr Vet Assoc 77(4):210–214.

Léveillé R, Biller DS, Shiroma JT (1996) Sonographic evaluation of the common bile ducts in cats. J Vet Intern Med 10:296–299.

Marolf AJ, Leach L, Gibbons DS, Bachand A, and Twedt A (2012) Ultrasonographic findings of feline cholangitis. J Am Anim Hosp Assoc 48:36–42.

Mayhew PD, Holt DE, McLear RC, Washabau RJ (2002) Pathogenesis and outcome of extrahepatic biliary obstruction in cat. J Small Anim Pract 43:247–253.

Mills P, Saverymuttu S, Fallowfield M, Nussey S, Joseph AE (1990) Ultrasound in the diagnosis of granulomatous liver disease. Clin Radiol 41:113–115.

Murakami T, Feeney DA, Bahr KL (2012) Analysis of clinical and ultrasonographic data by use of logistic regression models for prediction of malignant versus benign causes of ultrasonographically detected focal liver lesions in dogs. Am J Vet Res 73:821–829.

Newell SM, Selcer BA, Girard E, Roberts GD, Thompson JP, Harrison JM (1998) Correlations between ultrasonographic findings and specific hepatic diseases in cats: 72 cases (1985–1997). J Am Vet Med Assoc 213:94–98.

Nicoll RG, O'Brien R, Jackson MW (1998) Quantitative ultrasonography of the liver in obese cats. Vet Radiol Ultrasound 39:47–50.

Nyland TG, Barthez PY, Ortega TM, Davis CR (1996) Hepatic ultrasonographic and pathologic findings in dogs with canine superficial necrolytic dermatitis. Vet Radiol Ultrasound 37:200–205.

Nyland TG, Fisher PE (1990) Evaluation of experimentally induced canine hepatic cirrhosis using duplex Doppler ultrasound. Vet Radiol Ultrasound 31:189–194.

Nyland TG, Gillett NA (1982) Sonographic evaluation of experimental bile duct ligation in the dog. Vet Radiol Ultrasound 23:252–260.

Nyland TG, Koblik PD, Tellyer SE (1999) Ultrasonographic evaluation of biliary cystadenomas in cats. Vet Radiol Ultrasound 40:300–306.

Nyman HT, Kristensen AT, Flagstad A, McEvoy FJ (2004) A review of the sonographic assessment of tumor metastases in liver and superficial lymph nodes. Vet Radiol Ultrasound 45:438–448.

O'Brien RT, Iani M, Delaney F, Young K (2004) Contrast harmonic ultrasound of spontaneous liver nodules in 32 dogs. Vet Radiol Ultrasound 45:547–553.

Palerme J-S, Brown JC, Marks SL, Birkenheuer AJ (2013) Splenosystemic shunts in cats: a retroscpetive of 33 cases (2004-2011) J Vet Intern Medic 27:1347–1353.

Penninck D, Finn-Bodner ST (1998) Updates in interventional ultrasonography. Vet Clin North Am Small Anim Pract 28:1017–1040.

Penninck D, Brisson JO, Webster CR (2010) Sonographic assessment of gallbladder volume in cats. Vet Radiol Ultrasound 51:665–666.

Penninck DG, Berry C (1997) Diagnostic imaging of the feline liver. Semin Vet Med Surg (Small Animals): Feline Liver Disease 12:10–21.

Pike FS, Berg J, King NW, Penninck DG, Webster CR (2004) Gallbladder mucocele in dogs: 30 cases (2000–2002). J Am Vet Med Assoc 10:1615–1622.

Ramirez S, Douglass JP, Robertson ID (2002) Ultrasonographic features of canine abdominal malignant histiocytosis. Vet Radiol Ultrasound 43:167–170.

Respess M, O'Toole TE, Taeymans O, Rogers CL, Johnston A, and Webster CRL (2012) Portal vein thrombosis in 33 dogs: 1998–2011. J Vet Intern Med 26:230–237.

Santiago I, Loureiro R, CUrvo-Semedo L, Marques C, et al. (2012) Congenital cystic lesions of the biliary tree. AJR 198:825–835.

Sato A, Solano M (2004) Ultrasonographic findings in abdominal mast cell disease: A retrospective study of 19 patients. Vet Radiol Ultrasound 45:51–57.

Schwarz LA, Penninck DG, Leveille-Webster C (1998) Hepatic abscesses in 13 dogs: A review of the ultrasonographic findings, clinical data and therapeutic options. Vet Radiol Ultrasound 39:357–365.

Spaulding KA (1993) Ultrasound corner gallbladder wall thickness. Vet Radiol Ultrasound 34:270–272.

Stonewater JL, Lamb C, Shelling SH (1990) Ultrasonographic features of canine hepatic nodular hyperplasia. Vet Radiol Ultrasound 31:268–272.

Szatmari V, Rothuizen J, van den Ingh GA, van Sluijs FJ, Voorhout G (2004) Ultrasonographic findings in dogs with hyperammonemia: 90 cases (2000–2002). J Am Vet Med Assoc 224:717–727.

Tsukagoshi T, Ohno K, Tsukamoto A, Fukushima K, et al. (2012) Decreased gallbladder emptying in dogs with biliary sludge or gallbladder mucocele. Vet Radiol Ultrasound 53:84–91.

Walter R, Dunn ME, d'Anjou MA, Lécuyer M (2008) Nonsurgical resolution of gallbladder mucocele in two J Am Vet Med Assoc 11:1688–1693.

Wang KW, Panceria DL, Al-Rukibat RK, Radi AZ (2004) Accuracy of ultrasound-guided fine-needle aspiration of the liver and cytologic findings in dogs and cats: 97 cases (1990–2000). J Am Vet Med Assoc 224:75–78.

Warren-Smith CMR, Andrew S, Mantis P, Lamb CR (2012) Lack of associations between ultrasonographic appearance of parenchymal lesions of the canine liver and histological diagnosis. J Small Anim Pract 53: 168–173.

Weissman A, Penninck D, Wester C, Hecht S, Keating J, Craig LE (2012) Ultrasonographic and clinicopathological features of feline gastrointestinal eosinophilic sclerosing fibroplasia in 4 cats. J Feline Med Surg 15: 148–154.

Whiteley MB, Feeney DA, Whiteley LO, Hardy RM (1989) Ultrasonographic appearance of primary and metastatic canine hepatic tumors: A review of 48 cases. Ultrasound Med 8:621–630.

Woods, K, Brisson BA, Defarges AMN, Oblak Ml (2012) Congenital dupplex gallbladder and biliary mucocele associated with partial hepatic cholestasis and cholelithiasis in a cat. Can Vet J 53:269–273.

CHAPTER SEVEN

Spleen

Silke Hecht[1] and Wilfried Mai[2]

[1] *Department of Small Animal Clinical Sciences, University of Tennessee College of Veterinary Medicine, Knoxville, TN, USA*

[2] *School of Veterinary Medicine, Section of Radiology, University of Pennsylvania, Philadelphia, PA, USA*

Preparation and Scanning Technique

Ultrasonographic examination of the spleen is usually performed with the animal in dorsal recumbency. For evaluation of the craniodorsal extremity (head) of the spleen in large and deep-chested dogs, it may be beneficial to position the dog in right lateral recumbency and use a left intercostal approach. The abdomen and, if necessary, the left caudal thoracic wall are clipped, and acoustic coupling gel is applied. Depending on the size of the animal, a 5- to 10-MHz curvilinear or convex transducer is routinely used. Alternatively, because of the superficial location of the spleen, use of a linear transducer may be feasible, particularly in small dogs and in cats.

The craniodorsal extremity (head) of the spleen is located in the left craniodorsal abdomen immediately caudal to the stomach and adjacent to the body wall. Its position varies with gastric filling. The position of the splenic body and caudoventral extremity (tail) as well as the size of the spleen are highly variable in dogs, necessitating modification of the ultrasonographic approach in individual patients (Figure 7.1). After examination of the craniodorsal extremity of the spleen through an abdominal retrocostal or left intercostal approach, the spleen is traced to the hilus and caudal extremity, which can be done by positioning the transducer in a plane transverse to the long axis of the spleen. However, as the spleen extends beyond the transducer's field of view in most dogs, a thorough examination of the abdomen with meandering probe movement is usually necessary to facilitate examination of the entire organ. In cats, the spleen is smaller and more consistent in size and location in the left cranial abdomen.

Sonographic Anatomy of the Normal Spleen

The spleen is elongated and tongue-shaped in the long axis, and triangular or lenticular in cross-section. The head is in a very dorsal location and commonly seen to form a "hook" between the gastric fundus and left kidney (Figure 7.2). The splenic parenchyma is homogeneous and of a fine echotexture and is covered by a thin, very hyperechoic capsule (Figure 7.3). In comparison with liver and renal cortices, the spleen is often described as hyperechoic (Nyland et al. 1995) (Figure 7.4) in dogs; however, its relative echogenicity can be isoechoic or mildly hyperechoic to the renal cortex in cats (Reese et al. 2013). Branches of the splenic vein are seen as tubular anechoic structures within the splenic parenchyma and exit the spleen at the hilus (Figure 7.5). Splenic arteries are usually not seen unless color-Doppler imaging is used.

Splenic size is often evaluated subjectively. In a recent study, the mean thickness of the spleen in normal cats was reported to be 8.2 mm (SD 1.4 mm), and the width to be 26.7 mm (SD 4.4mm) on transverse images (Reese et al. 2013).

The size and even echogenicity of the spleen can be affected by some tranquilization or anesthesia (O'Brien et al. 2004; Reese et al. 2013).

Sonographic Findings in Splenic Disorders

Diagnostic differentials for diffuse alterations in splenic parenchymal echogenicity, or focal and multifocal lesions of the spleen can be found in Tables 7.1 and 7.2.

Atlas of Small Animal Ultrasonography, Second Edition. Edited by Dominique Penninck and Marc-André d'Anjou.
© 2015 John Wiley & Sons, Inc. Published 2015 by John Wiley & Sons, Inc.
Companion website: www.SmallAnimalUltrasonography.com

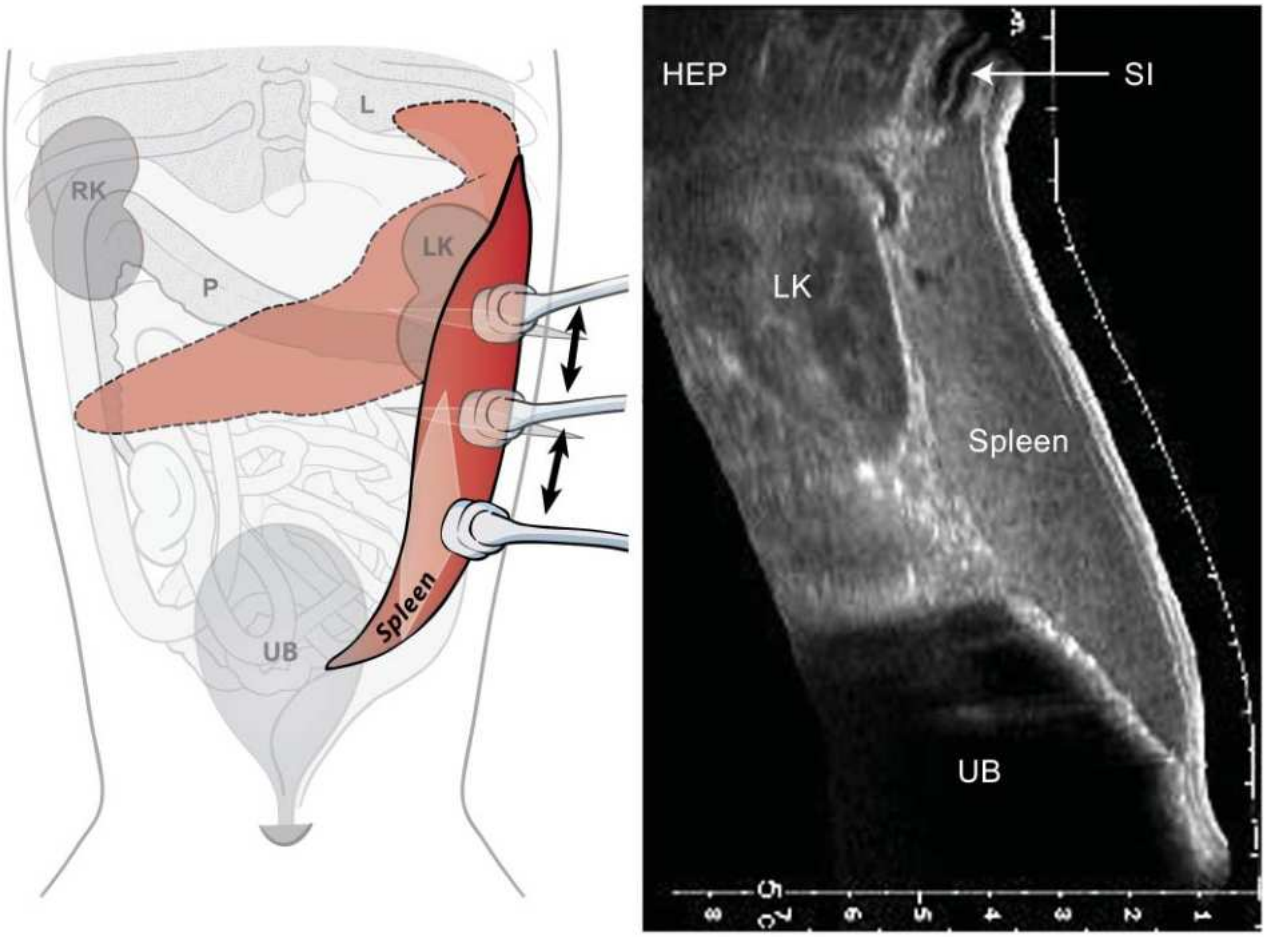


Figure 7.1. **Normal anatomy and scanning technique in a dog. Left:** A schematic representation of the spleen and its variable position in the abdomen. Ultrasound-probe positioning has to be adapted to accommodate the situation in the individual patient. LK, left kidney; UB, urinary bladder. **Right:** A panoramic ultrasonographic view of the spleen, displaying its relationship to the liver (HEP), small intestine (SI), left kidney (LK), and urinary bladder (UB).

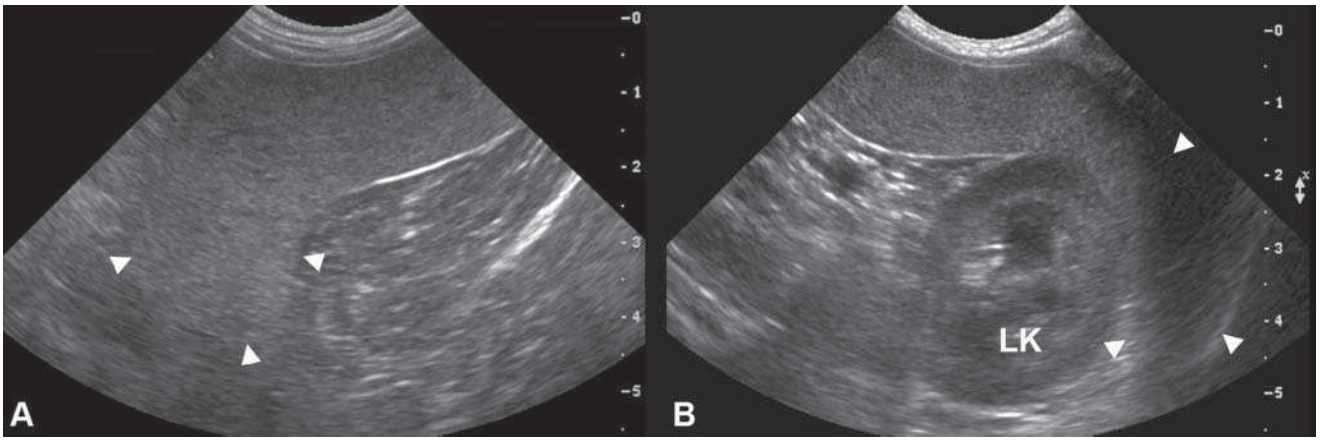


Figure 7.2. **Normal ultrasonographic appearance of the craniodorsal extremity of the spleen in a dog. A:** Image obtained with sagittal transducer orientation. The cranial portion of the spleen courses dorsally (arrowheads). Part of the central portion of the spleen is in the near field. **B:** Image obtained with transverse transducer orientation. The cranial extremity of the spleen (arrowheads) courses along the left abdominal wall laterally to the left kidney (LK), which is visible on cross-section. The central portion of the spleen is seen in the near field.

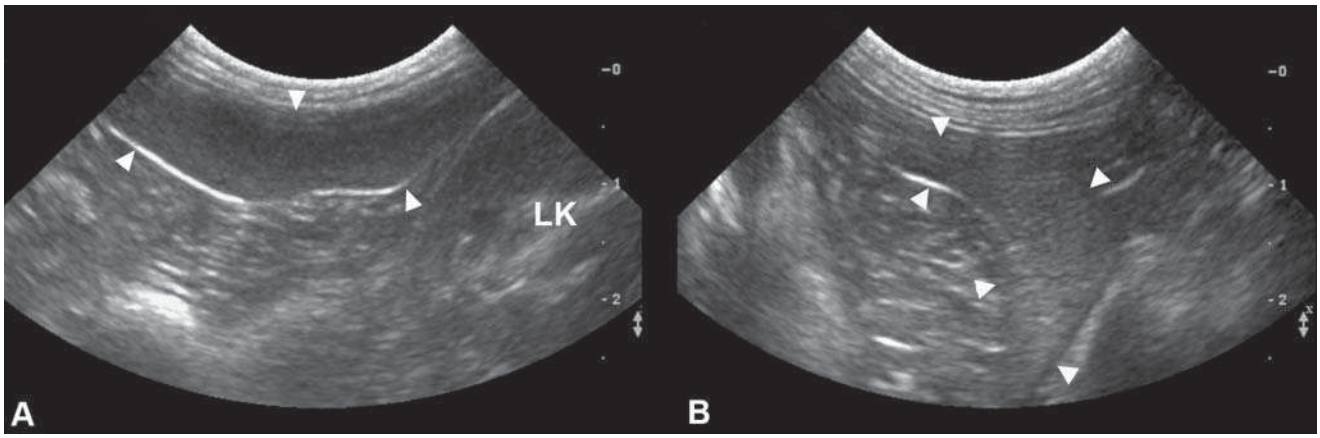


Figure 7.3. **Normal feline spleen. A:** Sagittal sonogram of a normal spleen. The spleen (arrowheads) is visible in the near field as a homogeneous tongue-shaped organ with a very hyperechoic capsule. The caudal extremity of the spleen is to the right of the image, close to the left kidney (LK). **B:** Transverse sonogram of a normal spleen. The spleen (arrowheads) appears as a sharply marginated triangular structure of homogeneous echotexture in the left cranial abdomen. Its capsule becomes prominent when perpendicular to the orientation of the ultrasound beam due to specular reflection.

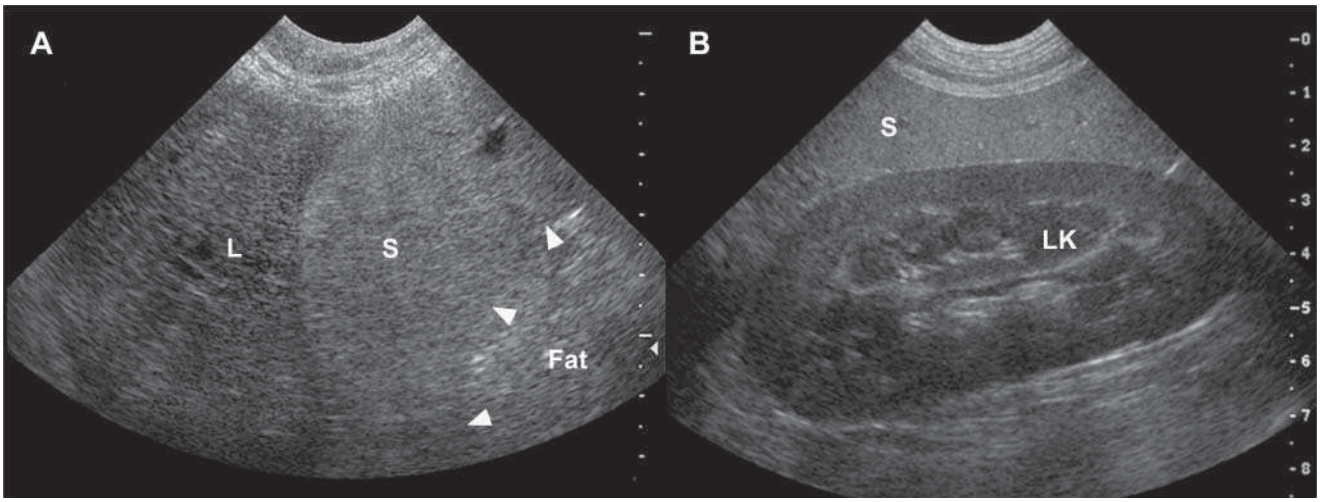


Figure 7.4. **Normal splenic echogenicity in a 3-year-old large-breed dog. A:** Comparison between normal splenic and hepatic parenchyma. The cranial extremity of the spleen (S and arrowheads) curves dorsally along the liver (L) and is relatively hyperechoic to this organ. Its echotexture is also finer than the one of the liver. **B:** Comparison between normal splenic and renal echogenicity. The spleen (S) in the near field is hyperechoic to the left kidney (LK).

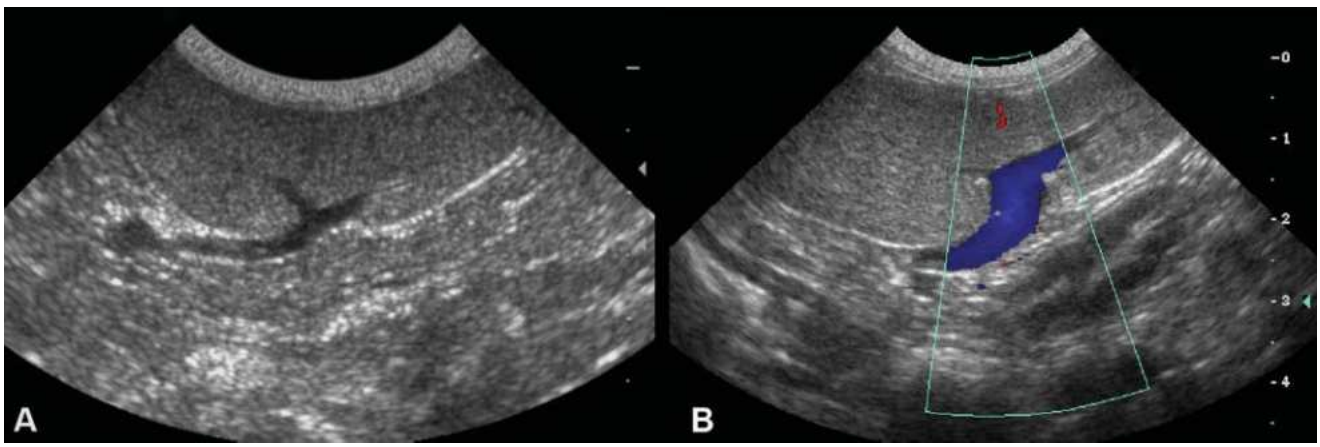


Figure 7.5. **Normal splenic veins in two dogs. A:** Normal spleen in a 13-year-old Shi Tzu. A branch of the splenic vein leaves the spleen at the splenic hilus. **B:** Color Doppler image of a branch of the splenic vein leaving the hilus in a 12-year-old springer spaniel. There is normal low-velocity flow without evidence of turbulence or thrombosis. As it moves away from the transducer, this flow appears blue on the color map.

Table 7.1
Diagnostic differentials for diffuse alterations in splenic parenchymal echogenicity

Normoechoic splenomegaly	Heterogeneous splenomegaly	Hypoechoic splenomegaly
Sedation	Extramedullary hematopoiesis	Torsion (often lacy pattern)
Extramedullary hematopoiesis	Benign lymphoid hyperplasia	Massive infarction (often lacy pattern)
Benign lymphoid hyperplasia	Neoplastic infiltration (round-cell tumor)	Lymphoma (or other round cell)
Splenic torsion (acute)	Splenitis	
Diffuse malignant infiltration (round cell tumor)		

Table 7.2
Diagnostic differentials for focal and multifocal lesions of the spleen

Hyperechoic nodular lesions	Hypoechoic nodular lesions	Mixed echogenicity nodular lesions	Anechoic lesions	Masses
Myelolipomas	**Multiple hypoechoic nodules ("Swiss-cheese appearance", "spotted spleen", "honeycomb spleen"):**	**"Target-like" lesions:**	Abscess	**Anechoic cavities with heterogeneous septations/solid components:**
Calcified hematomas	Lymphoma	Metastasis (but can also represent benign conditions such as extramedullary hematopoiesis or nodular hyperplasia)	Splenic pseudocysts (post-hematoma)	Hematoma
Also possible with:	Histiocytic sarcoma		Cyst (uncommon)	Hemangiosarcoma, possible with other neoplasms
Benign nodular hyperplasia	Extramedullary hematopoiesis	**Also possible with:**		Abscess
Extramedullary hematopoiesis	**Focal hypoechoic, territorial, wedge-shaped, lacy pattern:**	Benign nodular hyperplasia		**Solid masses, heterogeneous echotexture:**
Granuloma	Infarct	Extramedullary hematopoiesis		Solid form of hemangiosarcoma
Hematoma	**Also possible with:**	Hematoma		Other neoplasia (round-cell tumors, fibrosarcoma …)
Infection (splenitis, abscess)	Benign nodular hyperplasia	Infection (splenitis, abscess)		Benign nodular hyperplasia
Neoplasia (primary or metastatic)	Extramedullary hematopoiesis	Neoplasia (primary or metastatic)		
	Hematoma			
	Infection (splenitis, abscess)			
	Neoplasia (primary or metastatic)			

Splenomegaly (Normal Echogenicity)

Ultrasonographic assessment of splenic size is subjective. In dogs with splenomegaly, the margins of the spleen appear rounded, and the organ extends further caudally and to the right side of the abdomen. In cats, folding of the spleen upon itself indicates splenic enlargement (Hanson et al. 2001). In the authors' experience and based on a recent study (Reese et al. 2013), a spleen measuring more than 1.0 cm thick in cats supports splenomegaly. Splenomegaly with homogeneous echotexture is a frequent finding in dogs sedated with acepromazine, thiopental (O'Brien et al. 2004), ketamine, and diazepam (Wilson et al. 2004) (Figure 7.6). However, it may also be encountered secondary to extramedullary hematopoiesis, infectious diseases, splenic torsion, splenic vein thrombosis or malignant infiltration, such as occurs in lymphoma and mast cell tumors (Nyland et al. 1995; Saunders et al. 1998; Hanson et al. 2001; Sato and Solano 2004) (Figure 7.7).

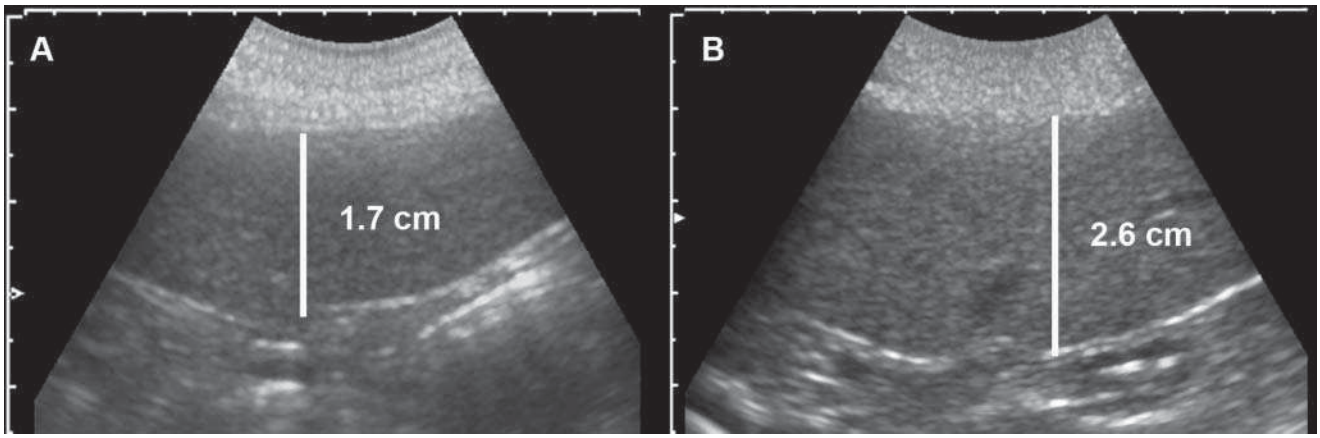


Figure 7.6. **Splenomegaly following sedation in a 7-year-old mixed-breed dog. A:** Image of the spleen prior to sedation. The maximum thickness of the spleen is 1.7 cm. **B:** Splenic enlargement is seen approximately 15 min after administration of acepromazine. The maximum thickness of the spleen is 2.6 cm.

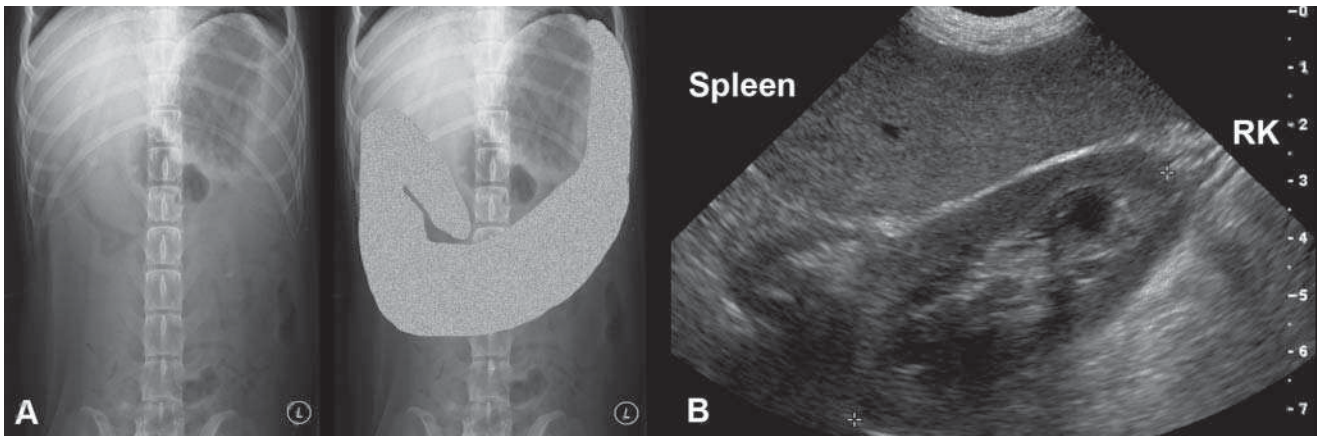


Figure 7.7. **Splenomegaly in a 7-year-old mixed-breed dog with lymphoma. A:** On the ventrodorsal radiograph of the abdomen, the spleen extends across the midline into the right abdomen and folds on itself at the level of the right kidney. **B:** Ultrasonographic image of the spleen at the level of the right kidney (RK). The spleen is enlarged, within normal limits for echogenicity, and smoothly marginated.

Diffuse Echogenic Changes of the Splenic Parenchyma

Generalized splenomegaly with parenchymal heterogeneity or hypoechogenicity can be observed in a variety of splenic disorders, including extramedullary hematopoiesis, benign lymphoid hyperplasia, neoplastic infiltration (e.g., round-cell tumors) (Figures 7.8, 7.9), infection (Figure 7.10), and vascular compromise (Figures 7.11–7.13). A diffuse, lacy, hypoechoic echotexture of the spleen is commonly encountered in dogs with splenic torsion (Saunders et al. 1998). However, the appearance of the spleen may vary with the degree of torsion and change over time.

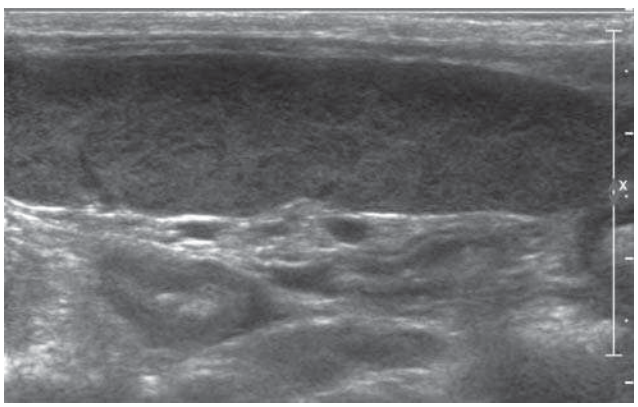


Figure 7.8. **Lymphoma in a 12-year-old domestic shorthair cat.** The spleen is enlarged (more than 1 cm in thickness) and has an inhomogeneous echotexture. A fine-needle aspirate confirmed the diagnosis of lymphoma.

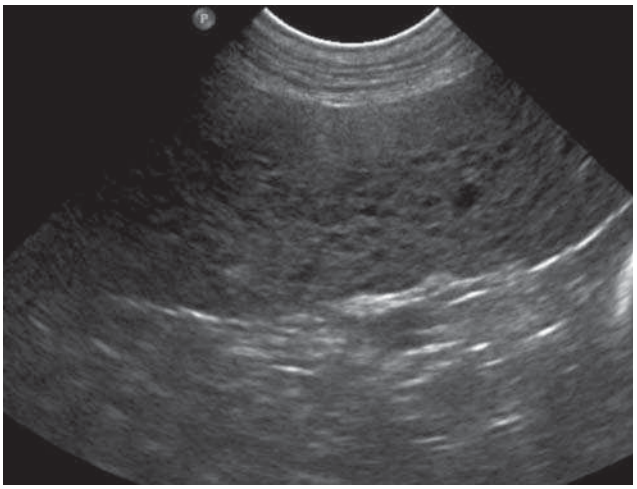


Figure 7.9. Splenic lymphoma in a 10-year-old mixed-breed dog. The spleen is enlarged, inhomogeneous, irregular, and hypoechoic.

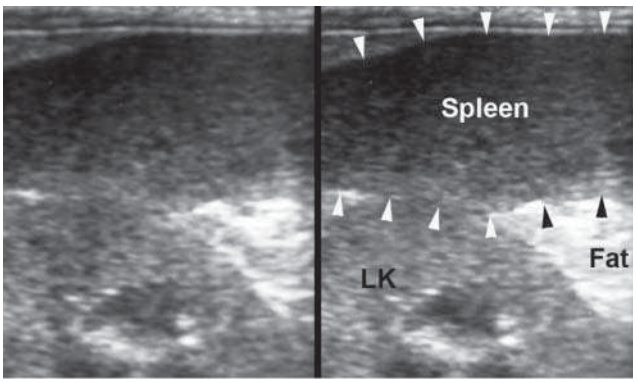


Figure 7.10. Splenic histoplasmosis in an 11-year-old domestic shorthair cat. The spleen is enlarged and inhomogeneous, with multiple tiny hypoechoic nodules. LK, left kidney.

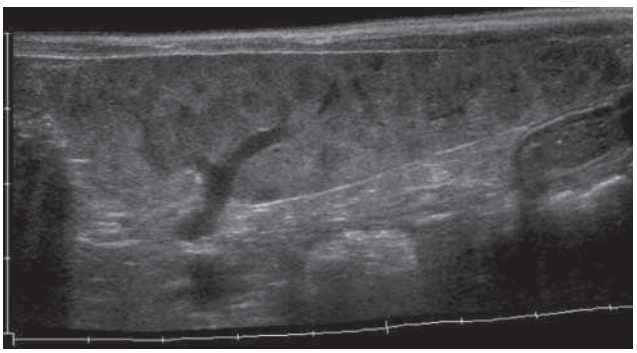


Figure 7.11. Mutifocal splenic infarctions and necrosis in an 11-year-old German shepherd. On this panoramic sonogram, the spleen is enlarged and inhomogeneous with numerous poorly echogenic nodular areas. The numerous infarctions associated with thrombi were of undetermined etiology.

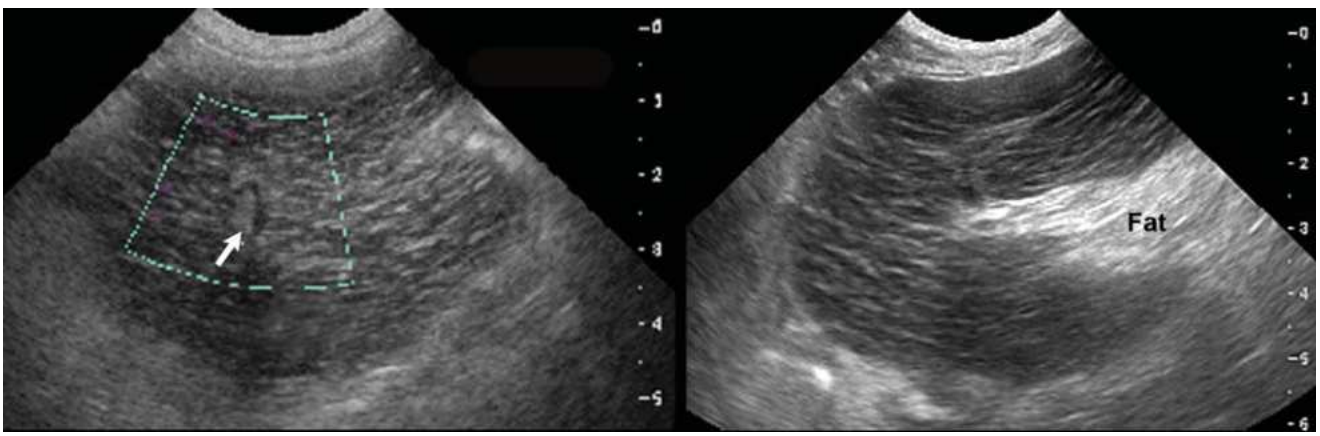


Figure 7.12. Splenic torsion in a 9-year-old standard Poodle. Left: Sonographic image of the spleen at the hilus, showing an echogenic thrombus obliterating the vessel lumen. Upon Doppler examination, no flow was detected in the splenic veins. **Right:** Sonographic image of the splenic parenchyma. The spleen is enlarged and has a diffuse lacy hypoechoic to anechoic echotexture. The adjacent abdominal fat is hyperechoic.



Figure 7.13. Splenic torsion in a 10-year-old Labrador Retriever with acute abdominal pain. B-mode and power Doppler images of the torsed spleen. Several regions show a characteristic hypoechoic to anechoic, lacey echotexture consistent with infarction and necrosis. Power Doppler revealed reduced blood flow.

Focal and Multifocal Abnormalities of the Splenic Parenchyma

Splenic nodules of variable echogenicity and size are a common and non-specific finding. Differential diagnoses include nodular hyperplasia, fibrous histiocytic nodule, extramedullary hematopoiesis (Figures 7.14, 7.15), hematoma (Figure 7.16), infection (Figures 7.17, 7.18), infiltrative neoplasia such as lymphoma, mast cell disease, disseminated histiocytic or poorly differentiated sarcoma (Figures 7.19, 7.20), and metastatic disease (Figures 7.21–7.23) (Wrigley et al. 1988; Lamb et al. 1991; Crevier and Wrigley 2000; Hanson et al. 2001; Ramirez et al. 2002; Sato and Solano 2004; Crabtree et al. 2010; Book et al. 2011).

A spotted (or "honeycomb-like" or "Swiss-cheese") echotexture of the spleen with multiple small hypoechoic nodules is highly suggestive of lymphoma (Figure 7.24), although it can also be seen in benign and other malignant conditions (Figure 7.23).

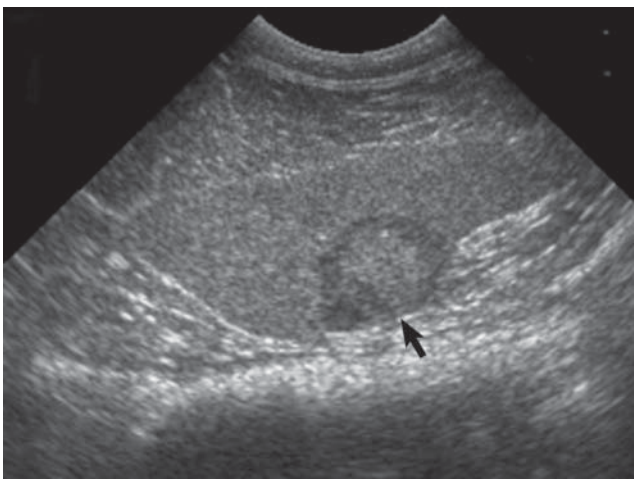


Figure 7.14. Extramedullary hematopoiesis in a 12-year-old Rottweiler. Ultrasonographic images of the spleen obtained during abdominal staging for mast cell tumor. Several nodular lesions were noted in the spleen. One of the nodules (arrow) has a smooth, well-defined, mildly hypoechoic border displacing the splenic capsule. Fine-needle aspiration revealed the presence of extramedullary hematopoiesis involving all the nodules.

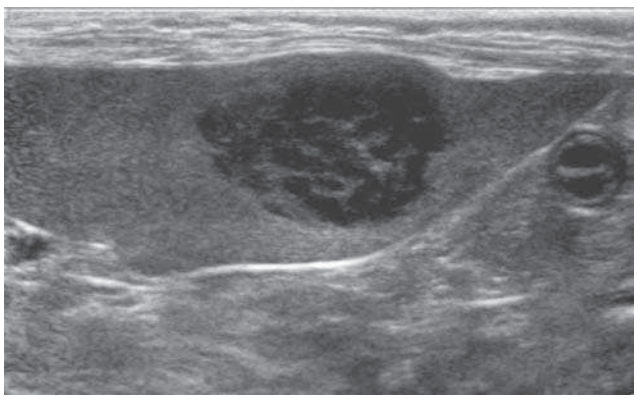


Figure 7.15. Fibrous histiocytic nodule in a cat. On the longitudinal sonographic image, there is a well-defined, hypoechoic nodule approximately 1 cm in diameter in the splenic parenchyma and deforming its contour.

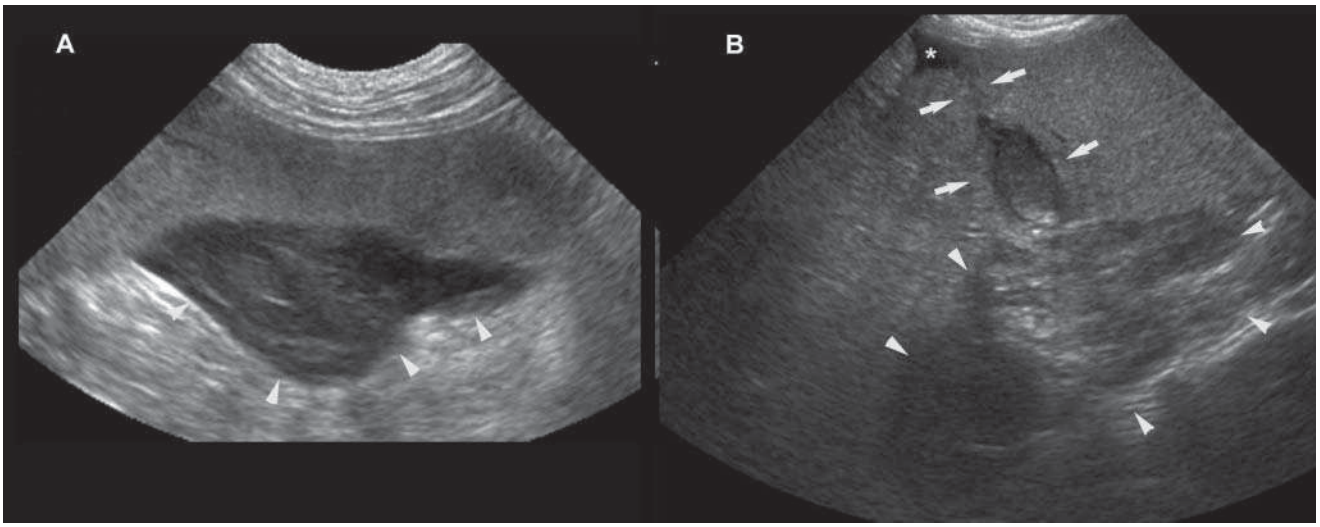


Figure 7.16. Splenic hematomas in two dogs. A: Longitudinal sonogram of the distal tip of the spleen, outlined on its visceral surface by an irregularly hypoechoic region (arrowheads). This lesion represents a subcapsular hematoma in this dog recently hit by a car. **B:** Splenic hematoma in a Bernese Mountain Dog with recent blunt trauma to the abdomen. A large, amorphous echogenic structure (arrowheads) representing a blood clot is bordering the spleen. The faint linear hypoechoic area in the spleen and the inhomogeneous oval region near the hilus likely correspond to the fractured spleen. Small peritoneal effusion is present (*).

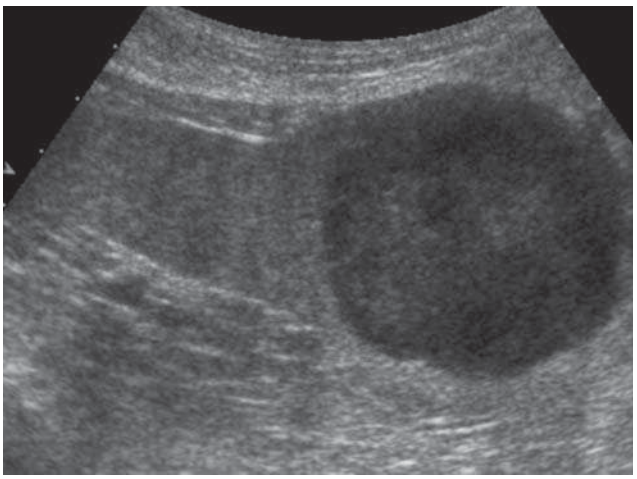


Figure 7.17. Pyogranulomatous splenitis in a 9-year-old Weimaraner. A single homogenous hypoechoic mass is associated with the splenic parenchyma. Fine-needle aspiration yielded a diagnosis of pyogranulomatous inflammation with necrosis and hemorrhage. Fungal or bacterial etiology was considered most likely; however, an underlying infectious agent was not identified on routine and special stains.

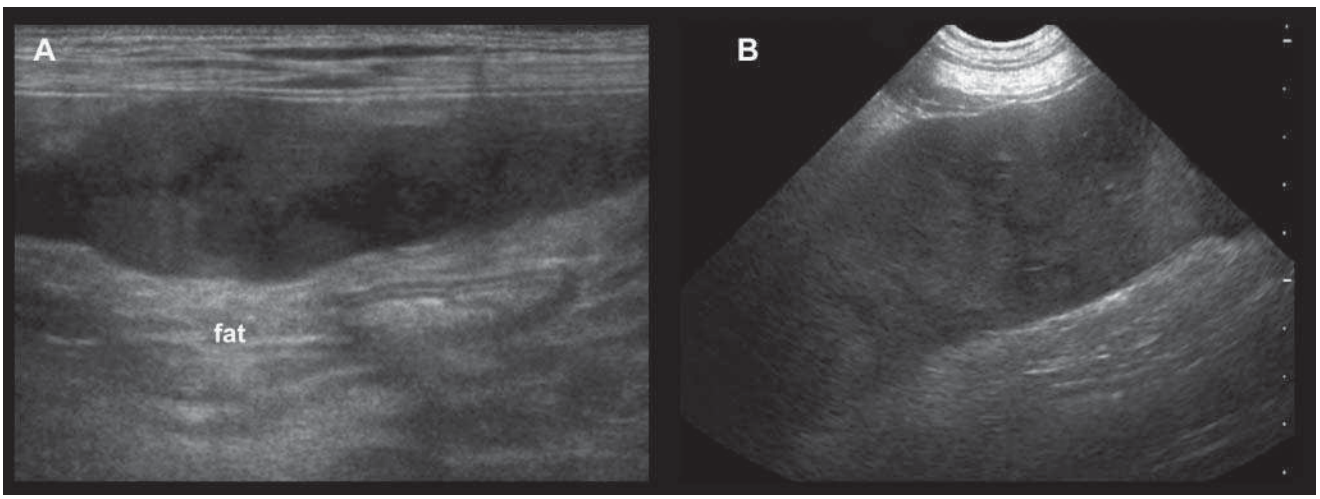


Figure 7.18. Splenitis in two dogs. A: Bacterial splenitis in a 13-year-old Bichon Frise with a history of *E. coli* septicemia. On sagittal image the spleen is irregular in contour, with multiple hypoechoic to anechoic areas and nodules. The adjacent mesenteric fat is hyperechoic. **B:** The spleen of an 8-year-old Rhodesian Ridgeback is enlarged and very inhomogeneous with irregular contour and is surrounded by hyperechoic fat. A splenectomy was performed and necro-suppurative splenitis with lymphoid hyperplasia was diagnosed. An infectious etiology was considered likely in this dog presented for fever of unknown origin.

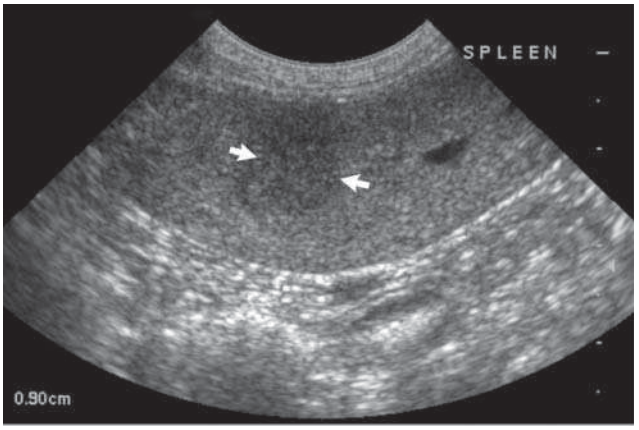


Figure 7.19. Lymphoma in a Shi Tzu. There is a 0.9-cm hypoechoic nodule (arrows) associated with the spleen.

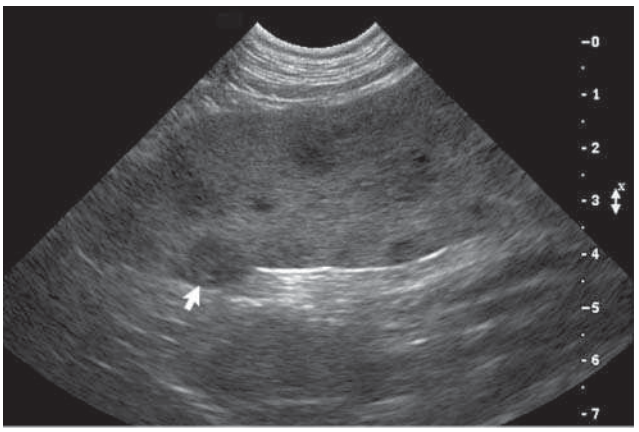


Figure 7.20. Disseminated histiocytic sarcoma in a 7-year-old Bernese Mountain Dog. There are multiple hypoechoic nodules throughout the spleen, some of which deform the splenic border (arrow).

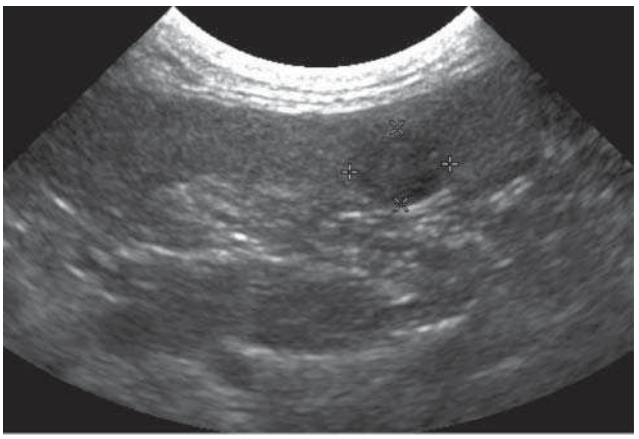


Figure 7.21. Malignant splenic epithelial neoplasm (presumably metastatic) in a cat. Several hypoechoic nodules were associated with the spleen. The one displayed on this image measures 0.8 × 0.6 cm (between the cursors).

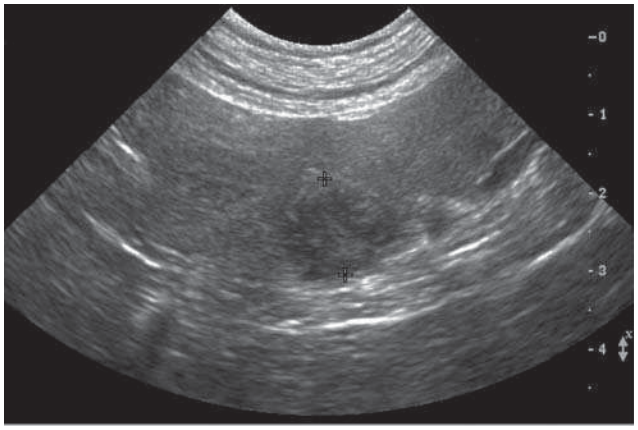


Figure 7.22. Malignant splenic epithelial neoplasm (presumably metastatic) in a 10-year-old Golden Retriever. There were several hypoechoic nodules associated with the spleen, one of which is shown and measures 1.3 cm in diameter (between the cursors).

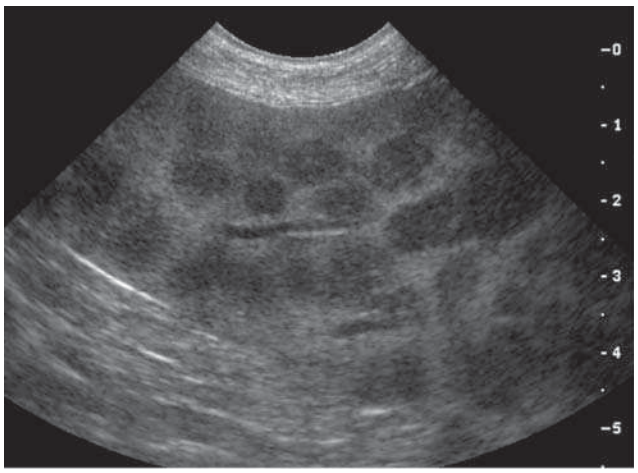


Figure 7.23. Metastatic anal sac adenocarcinoma in a dog. The spleen is enlarged and has extensively distributed hypoechoic nodules. Fine-needle aspiration revealed epithelial metastatic disease throughout the spleen, liver, and abdominal lymph nodes, although lymphoma was initially expected based on the ultrasonographic features.

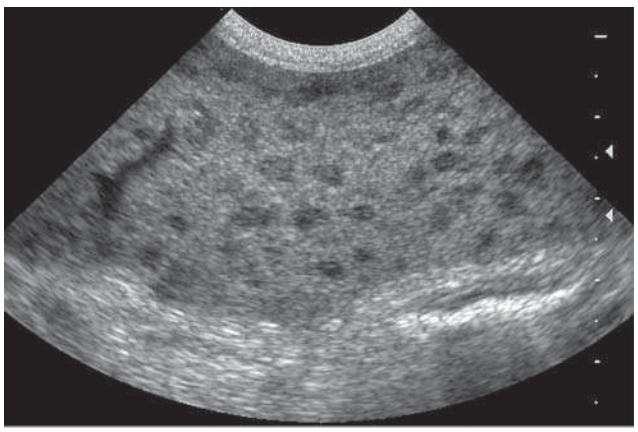


Figure 7.24. Lymphoma in a 6-year-old pit Bull Terrier. There are numerous small hypoechoic nodules throughout the spleen, causing a spotted echotexture. This pattern is most commonly seen with lymphoma.

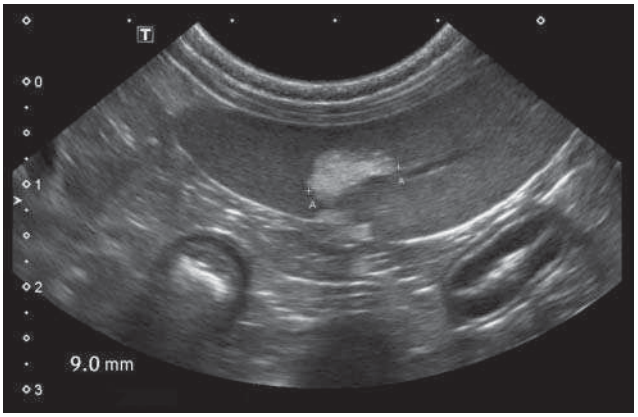


Figure 7.25. Splenic myelolipoma in a 10-year-old mixed-breed dog. Close to a branch of the splenic vein, there is a large, focal, strongly hyperechoic area.

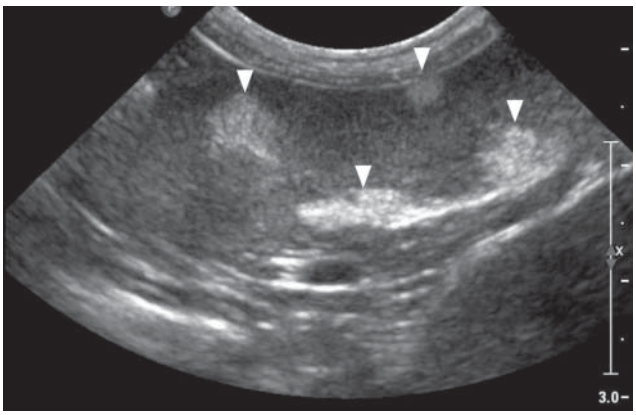


Figure 7.26. Splenic myelolipomas in a corgi. Multiple strongly hyperechoic and irregular nodules (arrowheads) are seen on the margins of the spleen and within the parenchyma.

Strongly hyperechoic nodules along the mesenteric border of the spleen, with or without distal acoustic shadowing, are a common incidental finding, especially in older dogs and cats. These lesions represent myelolipomas (Schwarz et al. 2001) (Figures 7.25–7.27). These benign lesions can also appear deeper in the splenic parenchyma, commonly along vessels. Their size and number vary greatly. In rare instances, these lesions can reach considerable size (Figure 7.27).

Splenic masses cause deformation of the splenic border. They are of variable shape, margination, and echogenicity and may be cavitated (Saunders 1998). As in the case of splenic nodules, splenic masses may be benign or malignant and cannot be differentiated based on their ultrasonographic appearance. Differential diagnoses include benign lesions such as nodular hyperplasia (which can reach sizes up to more than 15 cm (Day et al. 1995)) and hematomas (Figures 7.28–7.31), and malignancies such as hemangiosarcoma, other sarcomas, round-cell neoplasms, and metastases (Figures 7.32–7.41). Benign splenic mass lesions are more common than malignant mass lesions in dogs (Fife et al. 2004). Although rupture of a splenic mass with subsequent hemoabdomen is more frequently encountered in cases of splenic malignancies (Figures 7.33, 7.37, 7.40, 7.41), it also

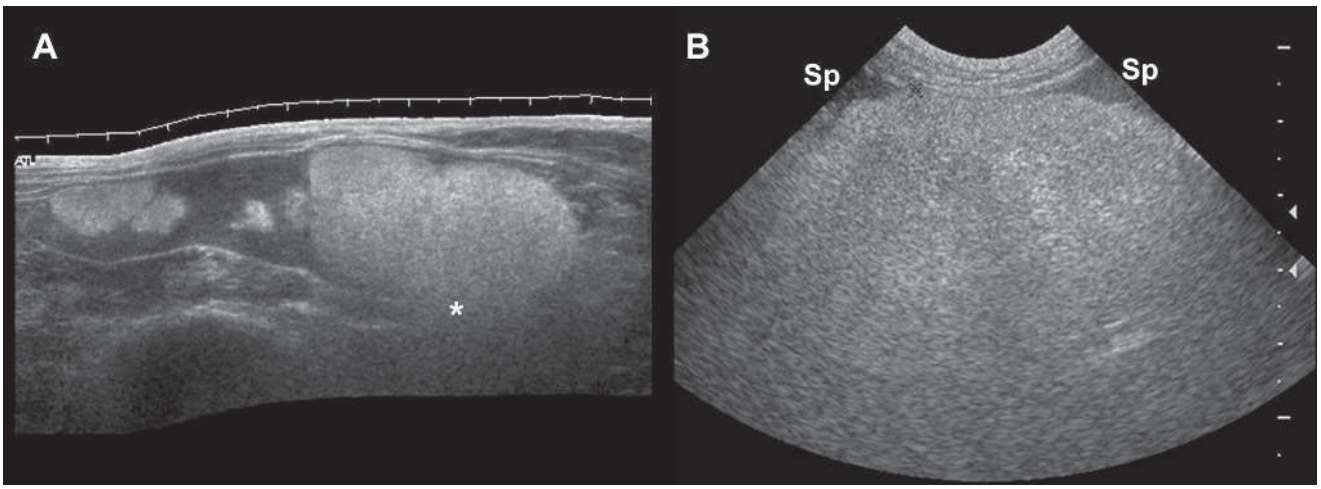


Figure 7.27. Large splenic myelolipomas in a cat and a dog. A: Panoramic view of the spleen of a 8-year-old domestic shorthair cat. Multiple strongly hyperechoic nodules and mass lesions are associated with the splenic parenchyma, deforming the capsule. The largest of these masses is associated with acoustic dirty shadowing in the far field (*), blurring the dorsal border of the spleen and mass. **B:** A similar but larger hyperechoic mass originating from the spleen (Sp) is seen in this dog referred for a possible splenic hemangiosarcoma. A benign myelolipoma of 13 cm diameter was confirmed histologically after splenectomy.

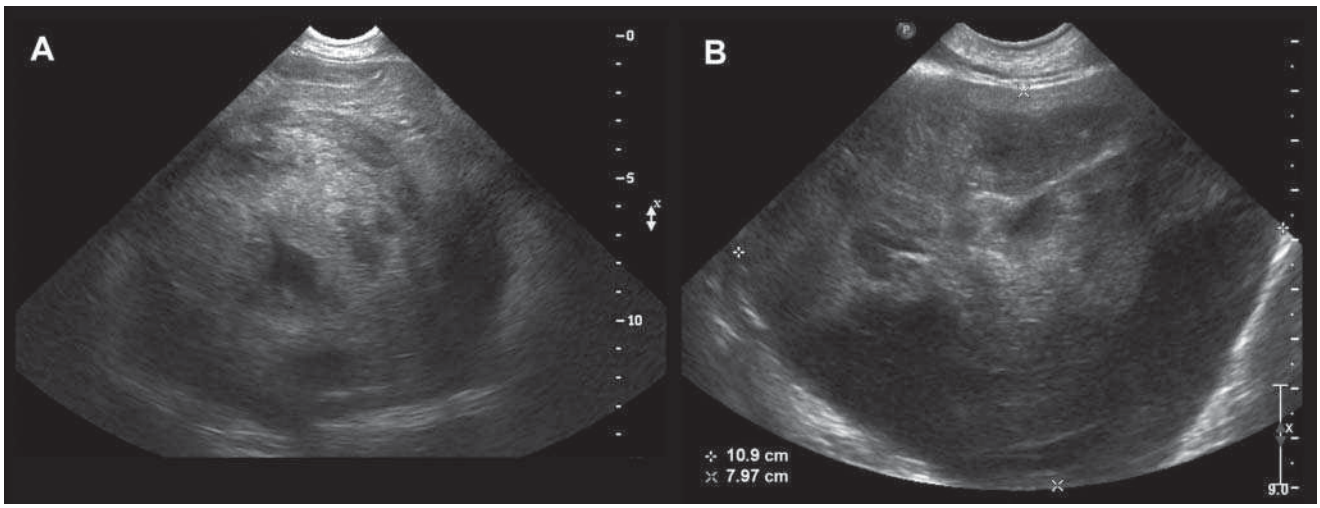


Figure 7.28. Large benign splenic masses in two dogs. A: Splenic nodular hyperplasia in an 11-year-old Labrador Retriever. An approximately 15-cm mixed echogenic mass is associated with the cranial extremity of the spleen. Histopathologic examination indicated no evidence of malignancy. **B:** Splenic nodular hyperplasia intermixed with extramedullary hematopoiesis and associated with a large hematoma and active hemorrhage in an 11-year-old Rottweiler dog. A more than 12-cm-diameter (between cursors) mixed echogenic and cavitary mass is associated with the spleen. A small amount of effusion was also noted (not shown).

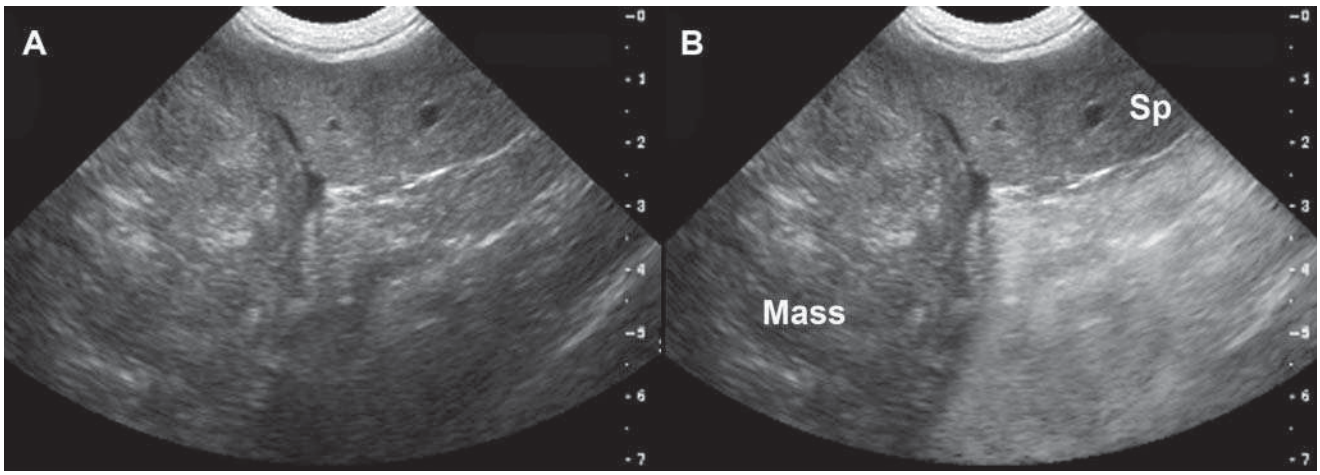


Figure 7.29. Large benign splenic mass in a dog. Longitudinal sonographic **(A)** and schematic **(B)** images of a large splenic mass. Sp, normal spleen. The histopathologic diagnosis was nodular hyperplasia and extramedullary hematopoiesis.

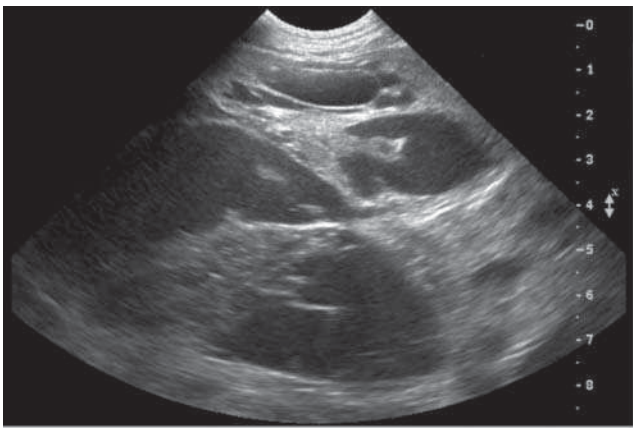


Figure 7.30. Splenic nodular hyperplasia, hemorrhage, and infarction in a 9-year-old Labrador Retriever. An ill-defined, > 10 cm, mixed echogenic and cavitated mass is associated with the spleen. There was no evidence of malignancy on histopathologic examination.

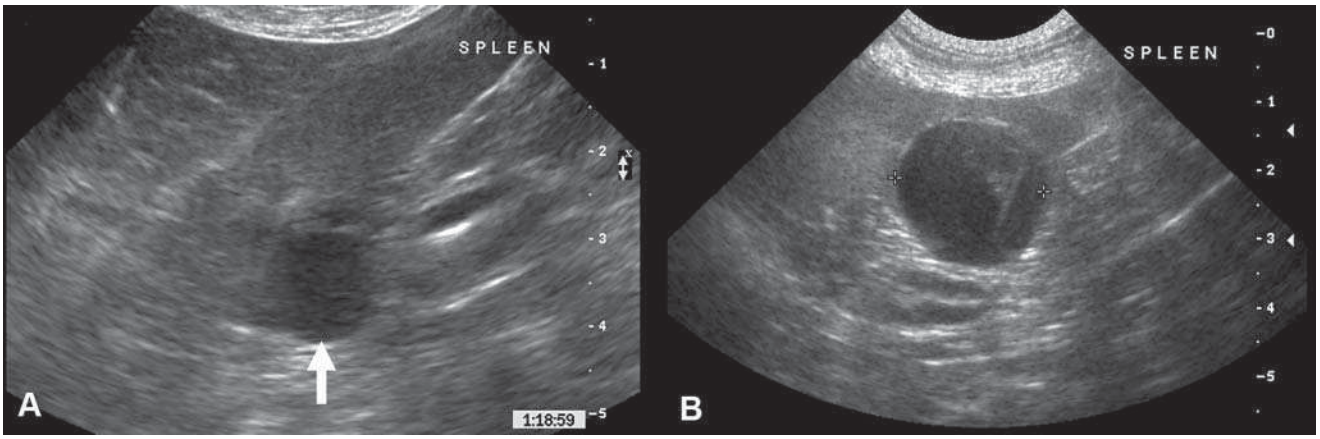


Figure 7.31. **Splenic nodular hyperplasia and hemorrhage in a 13-year-old Labrador Retriever previously diagnosed with hemangiosarcoma of the thoracic wall. A:** The initial examination shows a well-circumscribed hypoechoic nodule of approximately 1 cm diameter associated with the spleen (arrow). **B:** Examination 3 weeks later shows that the nodule (between the cursors) has doubled in size (2.2 cm diameter) and is almost anechoic, indicating cavitation. There was no evidence of malignancy on histopathologic examination.

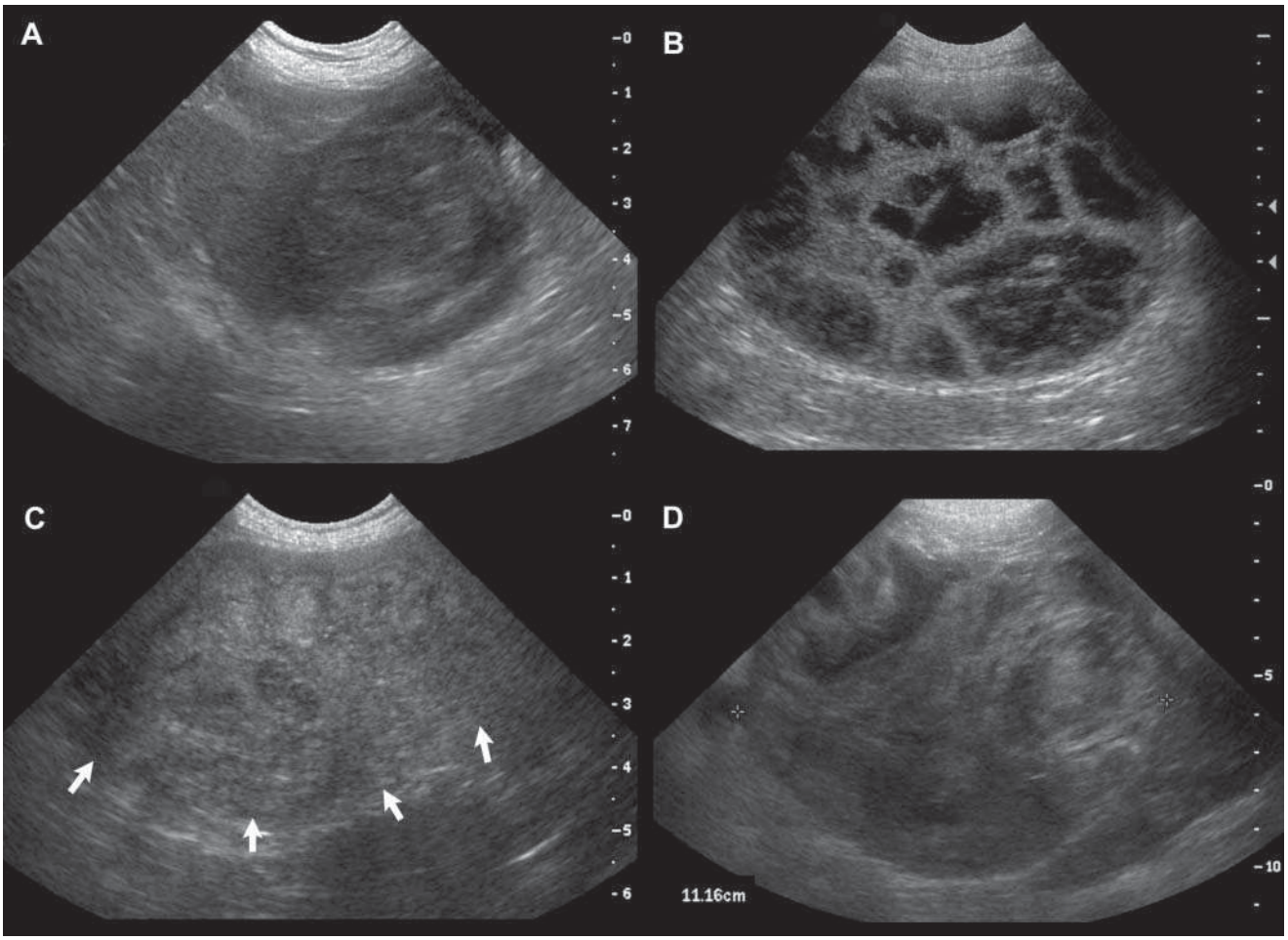


Figure 7.32. **Variable appearances of splenic hemangiosarcoma in dogs. A:** Approximately 6-cm-diameter, mixed echogenic and mainly hypoechoic mass in a 12-year-old Border Collie. **B:** A round, well-circumscribed, mixed echogenic and cavitated mass of 8 cm diameter in a 4-year-old Golden Retriever. **C:** Ill-defined, mixed echogenic mass (arrows) associated with the spleen of a 9-year-old Golden Retriever, replacing most of the normal parenchyma. **D:** Mixed echogenic mass of more than 11 cm diameter associated with the spleen (between the cursors) in an 8-year-old German Shepherd Dog.

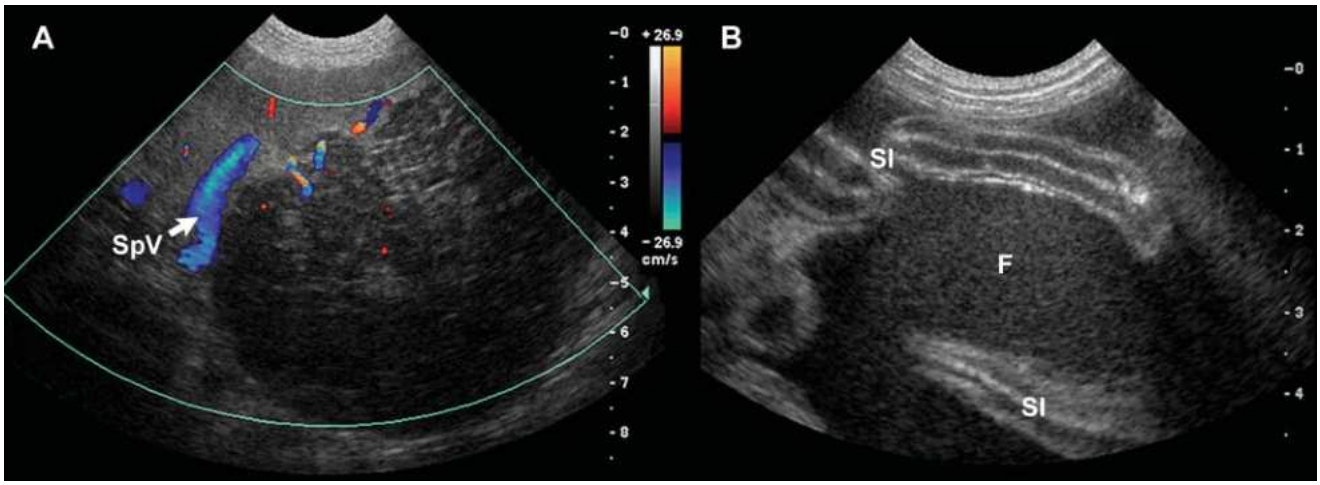


Figure 7.33. Splenic hemangiosarcoma and hemoabdomen in a large-breed dog in which an abdominal mass was palpated. A: Ultrasound image of the spleen in which an irregular, well-defined, hypoechoic mass of approximately 7 cm diameter is attached to spleen. Using color Doppler, numerous short vessels connecting the mass with the spleen are seen in the near field, which confirms the origin of this mass. The main splenic vein (SpV) is displaced. **B:** Severe, echogenic, peritoneal effusion (F) is present, consistent with hemorrhage. SI, small intestine.

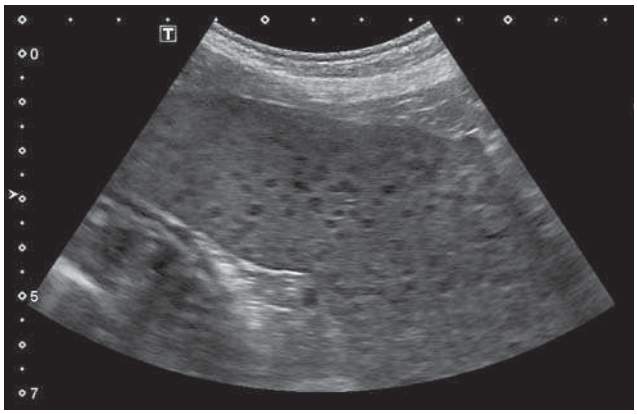


Figure 7.34. Histiocytic sarcoma in a Bernese Mountain Dog. On this sonogram, numerous hypoechoic nodules are disseminated throughout the splenic parenchyma.

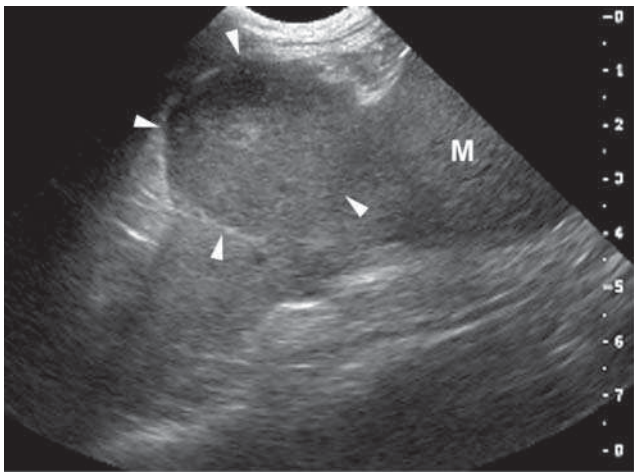


Figure 7.35. Histiocytic sarcoma in a 9-year-old Golden Retriever. A large, nearly isoechoic splenic mass (M) and a similar echogenic nodule (arrowheads) deform the splenic contour.

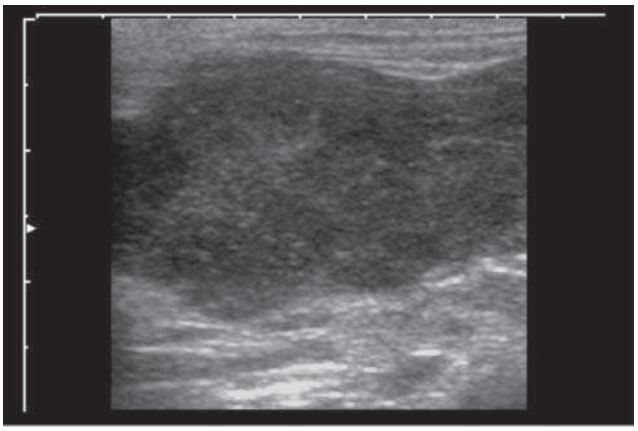


Figure 7.36. Presumptive malignant fibrous histiocytoma in a 12-year-old cat. There are multiple hypoechoic nodules in the spleen, each measuring up to 2 cm in maximum diameter.

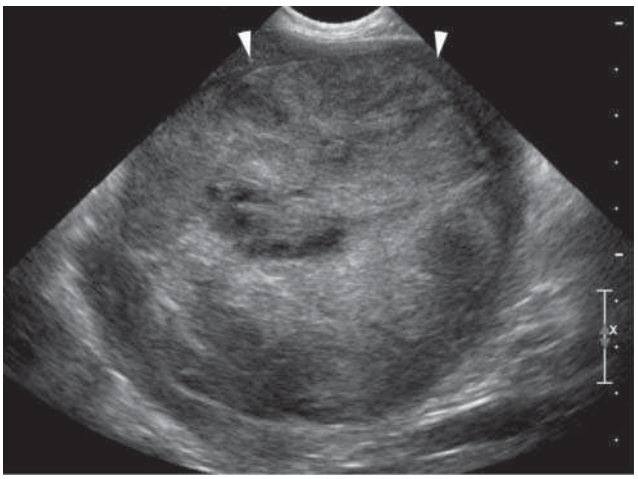


Figure 7.37. High-grade soft-tissue sarcoma in a dog. There is an approximately 8 cm mainly inhomogeneous mass associated with the spleen. Normal spleen is present in the near field (arrowhead).

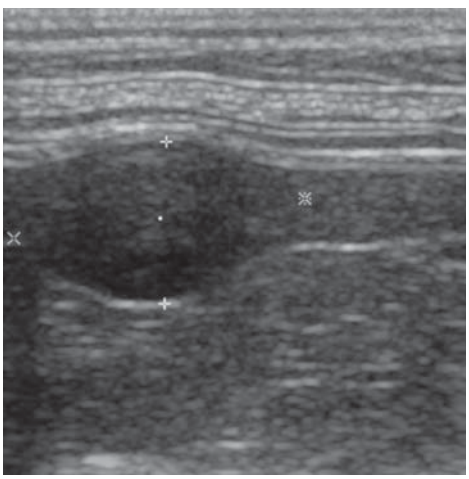


Figure 7.38. Splenic sarcoma in a 10-year-old cat. A homogeneous hypoechoic nodule (between the cursors) associated with the spleen is deforming the splenic border.

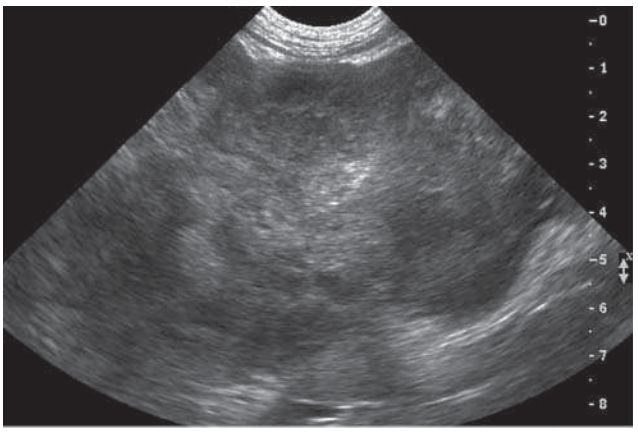


Figure 7.39. Round-cell tumor of the spleen in a 10-year-old coonhound. There is severe generalized splenomegaly, and the normal parenchyma is replaced by numerous ill-defined mass lesions of variable echogenicity.

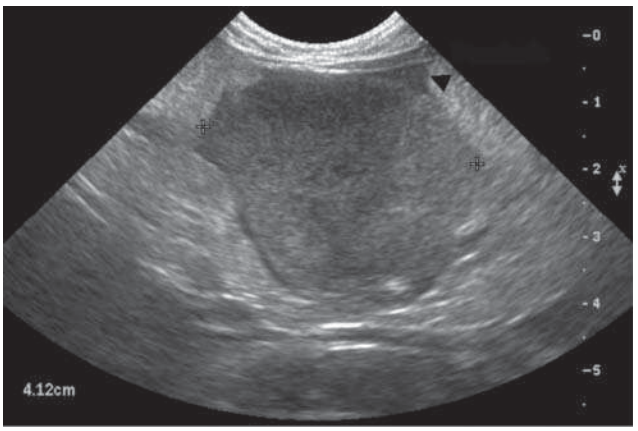


Figure 7.40. Splenic mast cell tumor in a cat. A more than 4 cm homogeneous mass of medium echogenicity is associated with the spleen (between the cursors). A small volume of abdominal effusion is noted in the periphery of this mass, particularly in the near field (arrowhead).

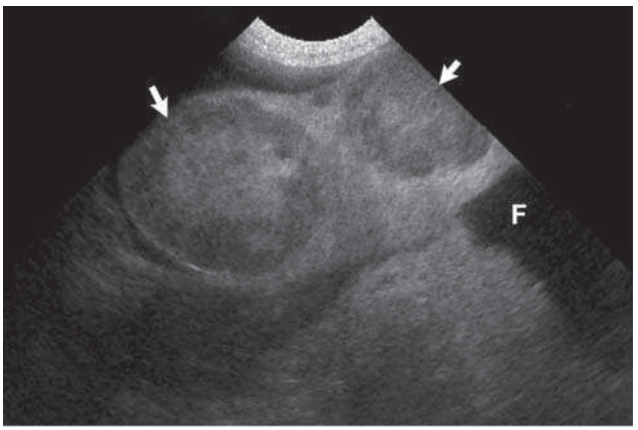


Figure 7.41. Splenic hemangiosarcoma and hemoabdomen in an 8-year-old Labrador Retriever. There are two masses (arrows), which are characterized by a hypoechoic rim and a hyperechoic center (target lesions). A large volume of echogenic abdominal effusion (F) is noted.

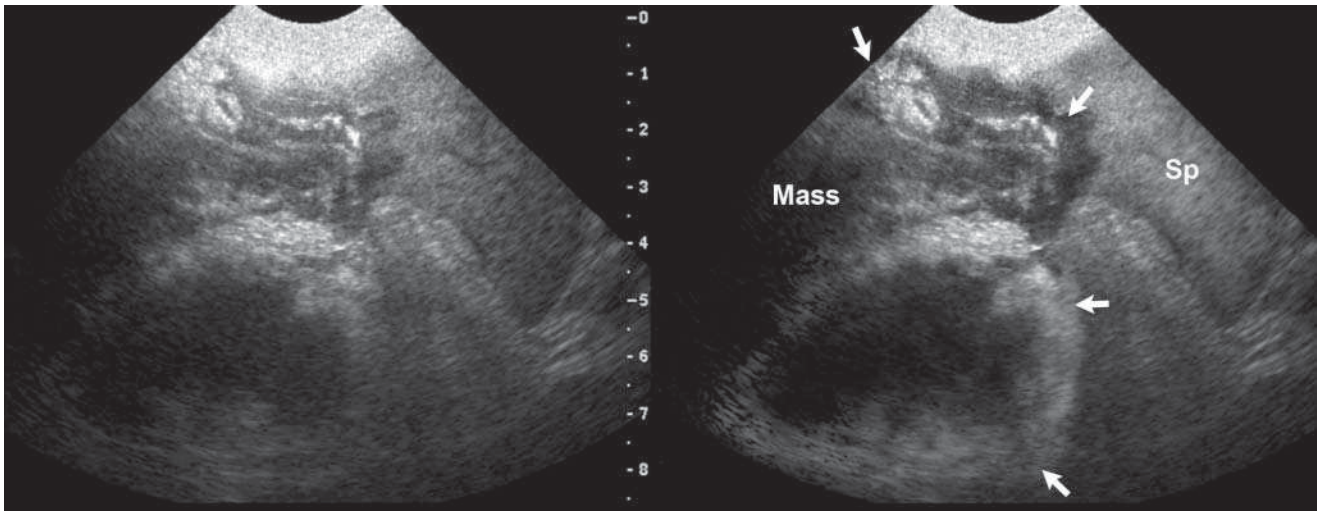


Figure 7.42. Poorly differentiated carcinoma in a 7-year-old Labrador Retriever. The ultrasonographic image (left) with the corresponding enhanced and labeled sonogram (right) show an ill-defined mixed echogenic mass suspected to be infiltrating the adjacent hyperechoic mesentery (arrows). Sp, spleen.

occurs in benign lesions. Splenic cysts and abscesses are rare and manifest as fluid-filled cavities of variable echogenicity within the splenic parenchyma, similar to hepatic cysts and abscesses. When complex in appearance, these cannot be differentiated from hematomas or cavitated masses based on their ultrasonographic appearance.

Nodules or masses with a hypoechoic rim and a hyperechoic to isoechoic center (often referred to as target lesions) are more commonly associated with malignant processes such as metastasis (Cuccovillo and Lamb 2002) (Figure 7.41). However, they may also be seen with benign processes such as nodular hyperplasia. Malignant neoplasms and less commonly benign lesions such as nodular hyperplasia may occasionally disrupt the splenic capsule and invade the adjacent mesentery (Day et al. 1995) (Figure 7.42).

Color and power Doppler ultrasound were shown to not be able to differentiate between malignant and benign splenic lesions (Sharpley et al. 2012), but contrast-enhanced ultrasound has shown initial promising results in characterizing splenic lesions in dogs (Ohlerth et al. 2008). This technique is covered elsewhere (see Chapter 16).

Vascular Disorders

Thrombosis of the splenic vein and splenic vein branches may indicate a variety of concurrent disease processes and conditions, including neoplasia, exogenous corticosteroid administration, systemic inflammatory response syndrome, disseminated intravascular coagulation, pancreatitis and immune-mediated disease (Hardie et al. 1995; Laurenson et al. 2010). It manifests as echogenic material within the otherwise anechoic lumen of the vessel. Thrombi may remain inconsequential if occlusion of the vessel is incomplete or collateral vessels provide venous drainage of the affected areas (Figures 7.43, 7.44). Occasionally, malignant splenic tumors invade splenic vessels and cause splenic vein thrombosis and splenic infarction (Figure 7.45).

When splenic infarction occurs, the affected areas appear hypoechoic to anechoic, at times with a lacy pattern, sharply demarcated from the adjacent parenchyma, and show decreased or absent blood flow on color or power Doppler examination. In contrast to splenic masses, infarcts do not tend to distort the normal organ contour, although this can occasionally be seen (Figures 7.46–7.48).

Splenic torsion is a rare disorder in dogs. Usually, there is progressive enlargement of the spleen, with decreased to absent blood flow. The parenchymal echogenicity and echotexture vary as the congestion, hemorrhage, or infarction progresses. The parenchyma is typically mottled, and lacy anechoic to hypoechoic areas are observed, focally or diffusely, throughout the spleen (Saunders et al. 1998; Mai 2006) (Figures 7.12, 7.13, 7.49). Static, echogenic thrombi can sometimes

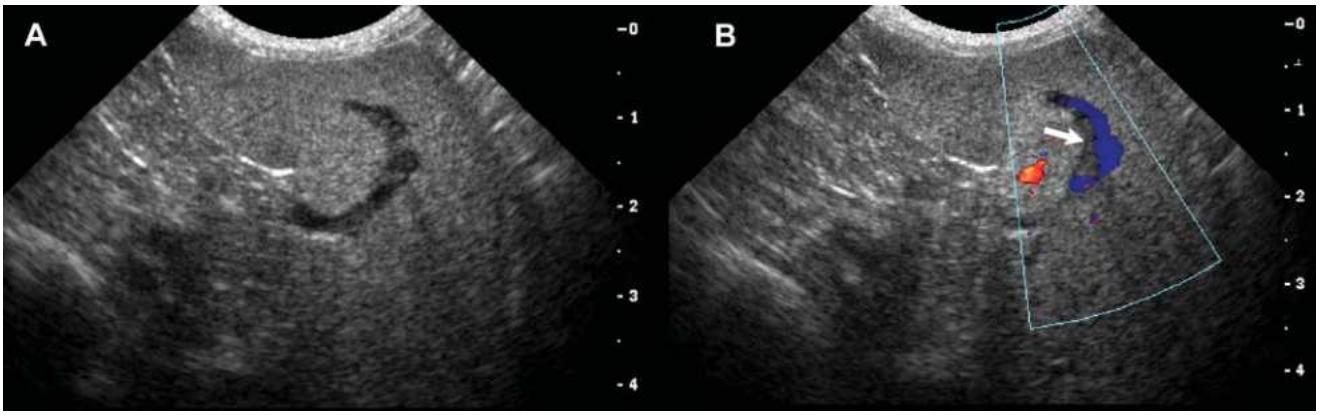


Figure 7.43. Splenic vein thrombus without evidence of splenic infarction in a 12-year-old springer spaniel. A: Echogenic material is associated with one of the branches of the splenic vein. The splenic parenchyma is within normal limits. **B:** On color Doppler examination, blood flow is noted around the thrombus (arrow), indicating incomplete vascular occlusion.

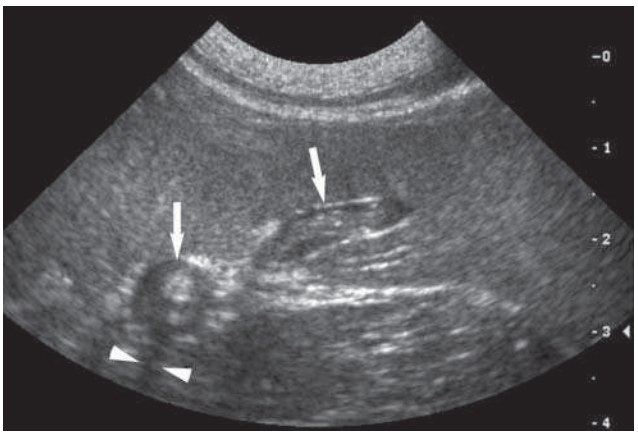


Figure 7.44. Chronic splenic vein thrombosis in an 11-year-old Labrador Retriever. Strongly echogenic material is within the lumen of the splenic vein branches (arrows). Ultrasound-beam attenuation is seen distal to one of the thrombi (arrowheads), indicating mineralization of the clot. There is no parenchymal changes supportive of infarction.

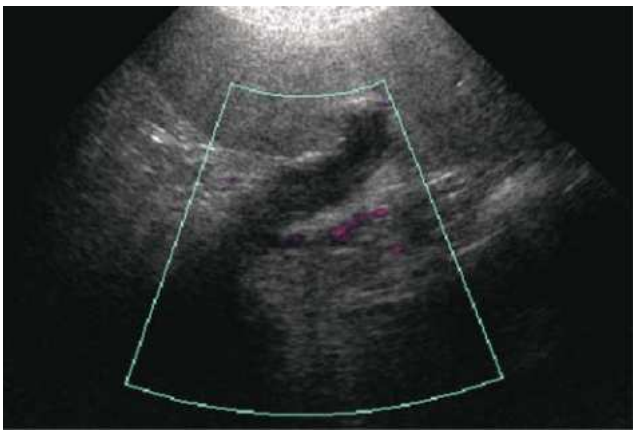


Figure 7.45. Poorly differentiated carcinoma with vascular invasion in a 7-year-old Labrador Retriever. On power Doppler examination, no blood flow is detected within the affected splenic vein branch, even though the lumen appears hypoechoic.

be seen in the lumen of splenic vessels (Figure 7.49). Additionally, the bordering fat can become hyperechoic, and a hilar, perivenous, hyperechoic triangle has been described as a supportive sign of acute splenic torsion in dogs (Mai 2006) (Figure 7.50). However, these changes can also be found with extensive venous thrombosis and/or diffuse neoplastic infiltration (e.g., lymphoma).

Other Abnormalities

In some animals, accessory spleens (splenunculi) can be found in the immediate vicinity of the spleen; these represent areas of normal ectopic splenic tissue, supplied by branches of the splenic artery, and can be congenital or secondary to auto-implantation of splenic tissue following surgery or trauma (Figure 7.51). They are usually located between the spleen, stomach, pancreas, and left lobe of the liver, and should not be confused with focal peri-splenic lesions such as enlarged splenic lymph nodes, pancreatic nodules, or mesenteric abscess or granuloma. Accessory spleens are round to triangular, 1–3 cm in size, isoechoic to the normal spleen and often surrounded by hyperechoic fat (Rossi et al. 2010).

Normal splenic lymph nodes are usually not seen ultrasonographically. Enlarged lymph nodes may be visualized in cases of metastatic or infiltrative neoplasia as isoechoic to hypoechoic, rounded, soft-tissue

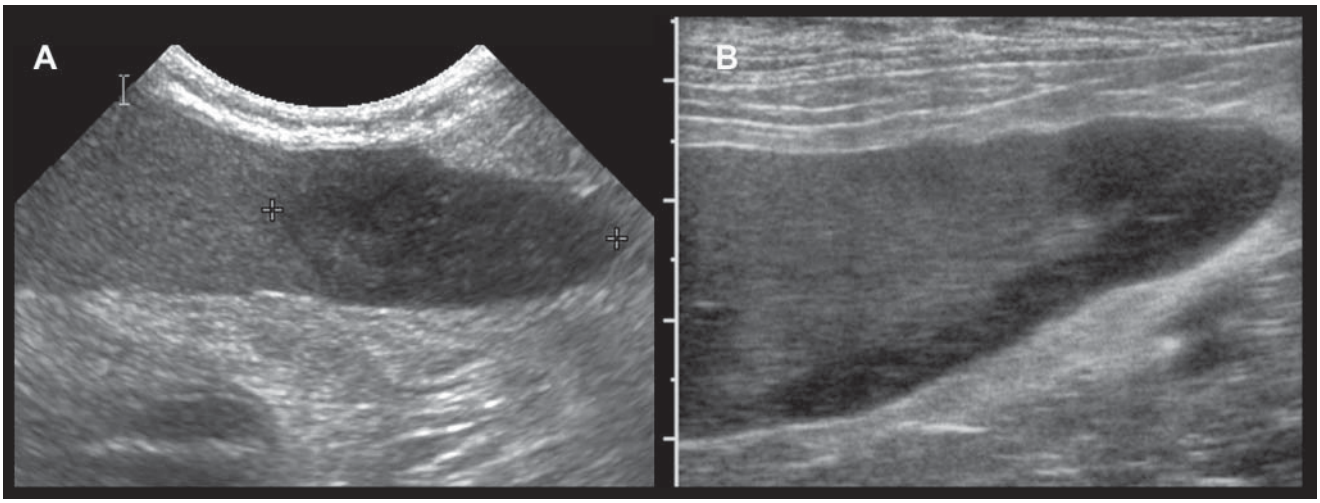


Figure 7.46. Splenic infarcts in two dogs. A: In a 10-year-old Australian Shepherd, a sharply demarcated, lacy hypoechoic area is observed at the caudal extremity of the spleen (between the cursors), which is confined to the normal splenic border without evidence of a mass effect. **B:** In a 9-year-old mixed-breed dog, the infarcted area follows the margins of the caudal extremity of the spleen while sparing the center.

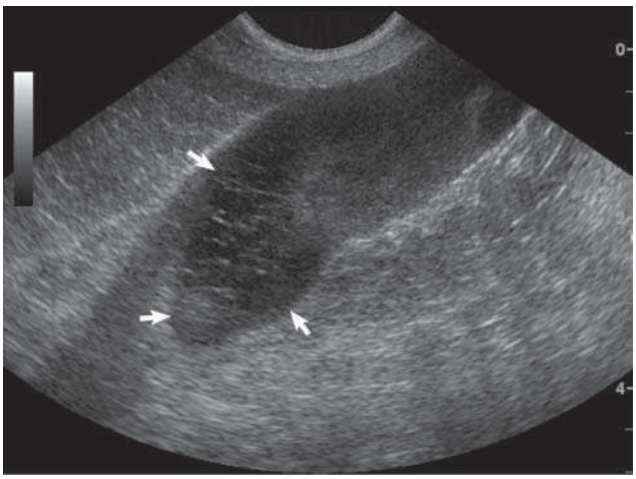


Figure 7.47. Splenic infarct in a 12-year-old male mixed-breed dog. A sharply demarcated hypoechoic area with a lacy pattern is associated with the cranial aspect of the spleen (arrows). On color flow Doppler (not shown), there is no evidence of blood flow in this triangular infarcted region.

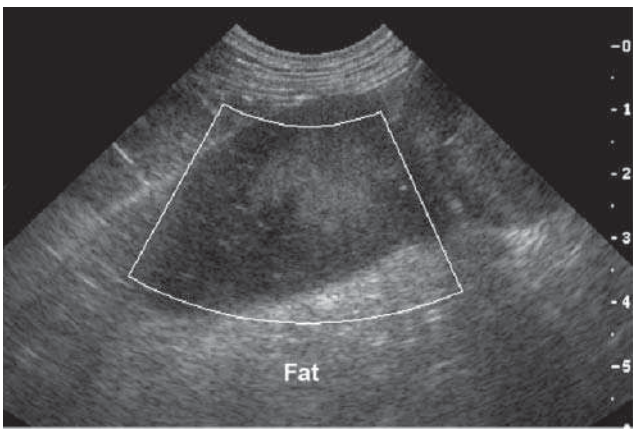


Figure 7.48. Splenic infarct in a 15-year-old Golden Retriever. An inhomogeneous lacy hypoechoic area within the spleen does not show blood flow on color Doppler examination. The fat at the dorsal margin of the spleen is hyperechoic.

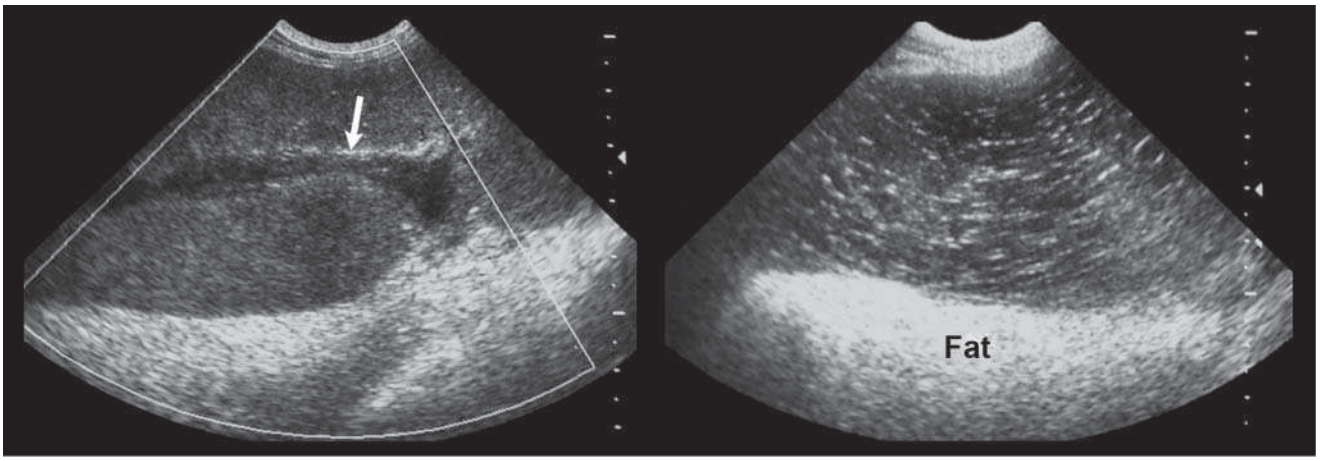


Figure 7.49. **Splenic torsion in a 6-year-old standard Poodle. Left:** Sonographic image of the spleen at the time of presentation. The spleen is homogeneously hypoechoic and within normal limits for size. Upon Doppler examination, no flow was detected in the splenic veins, and a hyperechoic thrombus is seen (arrow). **Right:** Sonographic image of the splenic parenchyma 2 days later. The spleen is enlarged and has a diffuse, lacy hypoechoic echotexture. The adjacent fat is hyperechoic.



Figure 7.50. **Perivenous hyperechoic triangle at the level of the splenic hilus in two dogs. A:** A hyperechoic triangle (arrows) is a common feature observed with splenic torsion. **B:** This feature can also be observed with massive splenic infarction. The second dog **(B)** was suffering from severe necrotic pancreatitis and progressively developed splenic infarction. At surgery, the spleen was not twisted, but was removed because of the complete venous thrombosis. In each case, the adjacent fat was hyperechoic.

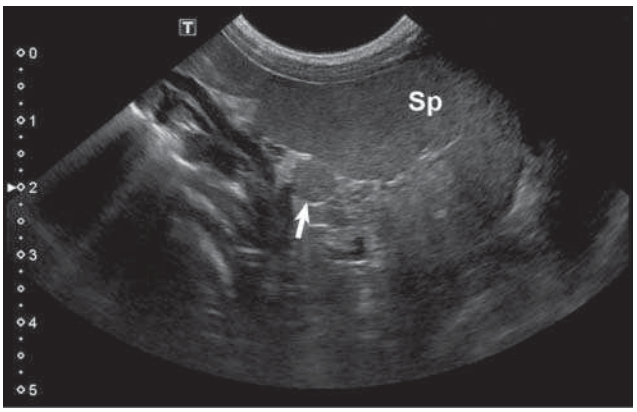


Figure 7.51. **Accessory spleen in a dog.** A small rounded structure (arrow) is present along the mesenteric side of the spleen, near the hilus. It has similar echogenicity as the spleen (Sp).

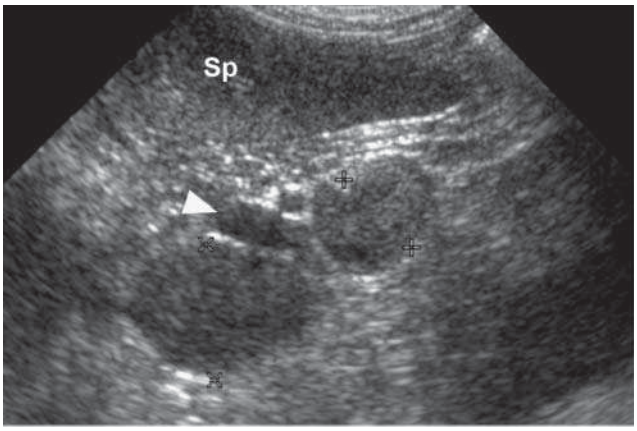


Figure 7.52. Lymphoma in a Shi Tzu. In the far field to the spleen (Sp) there are two enlarged lymph nodes (0.9 and 1.3 cm in diameter, respectively; between the cursors) adjacent to a branch of the splenic vein (arrowhead).

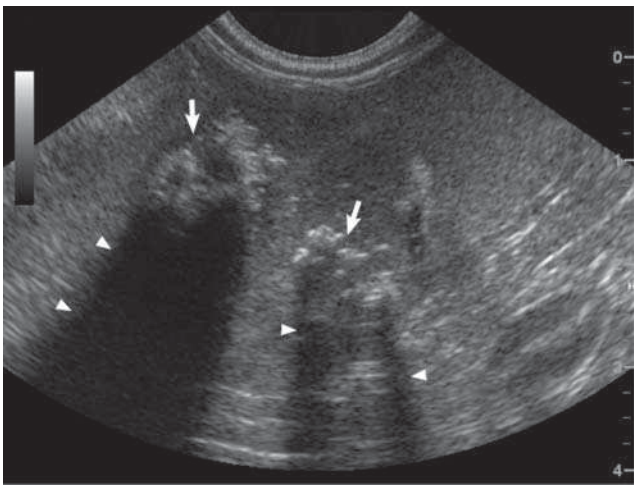


Figure 7.53. Extraskeletal osteosarcoma in a 10-year-old female mixed-breed dog. Irregularly marginated hyperechoic lesions (arrows) associated with the splenic parenchyma show strong distal acoustic shadowing (arrowheads).

nodules along the splenic vessels close to the hilus (Figure 7.52).

Strongly hyperechoic areas with strong distal acoustic shadowing are indicative of dystrophic mineralization or a mineralized neoplasm such as extraskeletal osteosarcoma (Figure 7.53).

Gas inclusions in the spleen, though rarely seen, are indicative of infection with gas-producing bacteria (Gaschen et al. 2003). Gas typically appears as hyperechoic foci with reverberation or dirty shadowing artifacts (Figure 7.54).

At times, a spleen of normal size may appear speckled with numerous small and non-shadowing hyperechoic speckles or stripes (Figure 7.55). These findings are most commonly associated with Cushing's disease, diabetus mellitus, or chronic corticosteroid use (Càceres 2012).

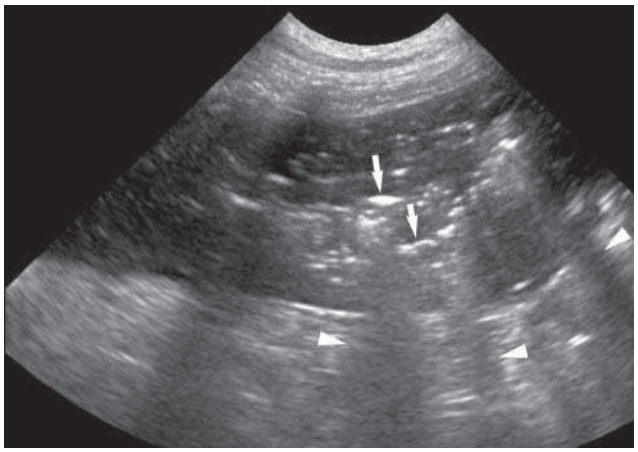


Figure 7.54. Infection with gas-producing bacteria secondary to torsion and necrosis in a 3-year-old Labrador. The enlarged, poorly echogenic and lacy spleen has several hyperechoic foci (arrows) associated with reverberation and shadowing artifacts (arrowheads). A moderate amount of echogenic effusion, and free gas was noted in the abdomen (not shown).



Figure 7.55. Speckled spleen in a 12-year-old Lhasa Apso with Cushing's disease. Numerous small hyperechoic foci are seen throughout the entire organ.

Interventional Procedures

Fine-needle aspiration of the spleen is routinely performed and is particularly useful in the diagnosis of diffuse infiltrative disorders such as lymphoma or mast cell tumor in which the spleen may appear sonographically normal (Crabtree et al. 2010; Book et al. 2011). In most cases, freehand aspiration is possible because of the organ's superficial location. A guide may be useful in cases of deep focal lesions.

Aspiration of fluid-filled splenic mass lesions such as hemangiosarcomas or hematomas frequently remains inconclusive because of blood dilution. Splenic tissue core biopsy is considered safe (Watson et al. 2011), although biopsy of a cavitary mass should be avoided due to the risk of hemorrhage.



Visit our website at **www.SmallAnimalUltrasonography.com** for complementary video clips with annotations and text on:

- Normal spleen anatomy and scanning
- Myelolipomas
- Splenic lymphoma
- Nodular hyperplasia and extramedullary hematopoiesis
- Hemangiosarcoma and peritoneal effusion
- Splenic torsion
- Splenic venous thrombus and infarcts

References

Book AP, Fidel J, Wills T, Bryan J, Sellon R, Mattoon J (2011) Correlation of ultrasound findings, liver and spleen cytology, and prognosis in the clinical staging of high metastatic risk canine mast cell tumors. Vet Radiol Ultrasound 52:548–554.

Càceres AV (2012) Association between hyperechoic splenic speckles and stripes with several medical conditions in 22 dogs [Abstract] Vet Radiol Ultrasound 53: 110.

Crabtree AC, Spangler E, Beard D, Smith A (2010) Diagnostic accuracy of gray-scale ultrasonography for the detection of hepatic and splenic lymphoma In dogs. Vet Radiol Ultrasound 51:661–664.

Crevier FR, Wrigley RH (2000) The sonographic features of splenic lymphoid hyperplasia in 31 dogs: A retrospective study (1980–2000) [Abstract]. Vet Radiol Ultrasound 41:566.

Cuccovillo A, Lamb CR (2002) Cellular features of sonographic target lesions of the liver and spleen in 21 dogs and a cat. Vet Radiol Ultrasound 43:275–278.

Day MJ, Lucke VM, Pearson H (1995) A review of pathological diagnoses made from 87 canine splenic biopsies. J Sm Anim Pract 36:426–433.

Fife WD, Samii VF, Drost WT, Mattoon JS, Hoshaw-Woodard S (2004) Comparison between malignant and nonmalignant splenic masses in dogs using contrast-enhanced computed tomography. Vet Radiol Ultrasound 45:289–297.

Gaschen L, Kircher P, Venzin C, Hurter K, Lang J (2003) Imaging diagnosis: The abdominal air-vasculogram in a dog with splenic torsion and clostridial infection. Vet Radiol Ultrasound 44:553–555.

Hanson JA, Papageorges M, Girard E, Menard M, Hebert P (2001) Ultrasonographic appearance of splenic disease in 101 cats. Vet Radiol Ultrasound 42:441–445.

Hardie EM, Vaden SL, Spaulding K, Malarkey DE (1995) Splenic infarction in 16 dogs: A retrospective study. J Vet Intern Med 9:141–148.

Lamb CR, Hartzband LE, Tidwell AS, Pearson SH (1991) Ultrasonographic findings in hepatic and splenic lymphosarcoma in dogs and cats. Vet Radiol Ultrasound 32:117–120.

Laurenson MP, Hopper K, Herrera MA, Johnson EG (2010) Concurrent diseases and conditions in dogs with splenic vein thrombosis. J Vet Intern Med 24:1298–1304.

Mai W (2006) The hilar perivenous hyperechoic triangle as a sign of acute splenic torsion in dogs. Vet Radiol Ultrasound 47:487–491.

Nyland TG, Mattoon JS, Herrgesell ER, Wisner ER (1995) Spleen. In: Nyland TG, Mattoon JS, eds. Small Animal Diagnostic Ultrasound. Philadelphia: WB Saunders, pp 128–143.

O'Brien RT, Waller KR, Osgood TL (2004) Sonographic features of drug-induced splenic congestion. Vet Radiol Ultrasound 45:225–227.

Ohlerth S, Dennler M, Rüefli E, Hauser B, Poirier V, Siebeck N, Roos M, Kaser-Hotz B (2008) Contrast harmonic imaging characterization of canine splenic lesions. J Vet Intern Med 22:1095–1102.

Ramirez S, Douglass JP, Robertson ID (2002) Ultrasonographic features of canine abdominal malignant histiocytosis. Vet Radiol Ultrasound 43:167–170.

Reese SL, Zekas LJ, Iasbik MC, Lehman A, et al (2013) Effect of evoflurane anesthesia and blood donation on the ultrasonographic appearance of the spleen in 60 healthy cats. Vet Radiol Ultrasound 54:168–175.

Rossi F, Rabra S, Vignoli M, Haers H, Terragni R, Saunders JH (2010) B-mode and contrast-enhanced sonographic assessment of accessory spleen in the dog. Vet Radiol Ultrasound 51:173–177.

Sato AF, Solano M (2004) Ultrasonographic findings in abdominal mast cell disease: A retrospective study of 19 patients. Vet Radiol Ultrasound 45:51–57.

Saunders HM (1998) Ultrasonography of abdominal cavitary parenchymal l esions. Vet Clin North Am Small Anim Pract 28:755–775.

Saunders HM, Neath PJ, Brockman DJ (1998) B-mode and Doppler ultrasound imaging of the spleen with canine splenic torsion: A retrospective evaluation. Vet Radiol Ultrasound 39:349–353.

Schwarz LA, Penninck DG, Gliatto J (2001) Canine splenic myelolipomas. Vet Radiol Ultrasound 42:347–348.

Sharpley JL, Marolf AJ, Reichle JK, Bachand AM, Randall EK (2012) Color and Doppler ultrasonography for characterization of splenic masses in dogs. Vet Radiol Ultrasound 53:586–590.

Watson AT, Penninck D, Knoll JS, Keating JH, Sutherland-Smith J (2011) Safety and correlation of test results of combined ultrasound-guided fine-needle aspiration and needle core biopsy of the canine spleen. Vet Radiol Ultrasound 52:317–322.

Wilson DV, Evans AT, Carpenter RA, Mullineaux DR (2004) The effect of four anaesthetic protocols on splenic size in dogs, Vet Anaesth Analg 31:102–108.

Wrigley RH, Konde LJ, Park RD, Lebel JL (1988) Ultrasonographic features of splenic lymphosarcoma in dogs: 12 cases (1980–1986). J Am Vet Med Assoc 193:1565–1568.

CHAPTER EIGHT

Gastrointestinal Tract

Dominique Penninck[1] and Marc-André d'Anjou[2,3]

[1] *Department of Clinical Sciences, Cummings School of Veterinary Medicine, Tufts University, North Grafton, MA, USA*

[2] *Centre Vétérinaire Rive-Sud, Brossard, Québec, Canada*

[3] *Faculté de médecine vétérinaire de l'Université de Montréal, Saint-Hyacinthe, Québec, Canada*

Preparation and Scanning Procedure

Animals can be scanned while they are in dorsal recumbency, right or left recumbency, or standing position, if needed, to optimize an acoustic window by displacing the intraluminal fluid to the region of interest. Left lateral recumbency helps with the evaluation of the fundus, whereas right lateral recumbency improves the evaluation of the pylorus and duodenum. The standing position can be helpful for evaluating the ventral aspect of the pylorus and the body of the stomach. However, the results of these positional studies also depend on a dog's conformation, the degree of stomach dilation, the nature of gastric contents, and patient cooperation.

A high-frequency (8 MHz and higher) curvilinear or linear transducer is recommended to best evaluate the gastrointestinal (GI) wall layering. Curvilinear probes with a small footprint are useful because they can more easily be placed below the rib cage or between ribs for the assessment of the stomach and proximal duodenum. Transverse and longitudinal/sagittal views of the GI segments are required to fully assess the thickness and the extent of a suspected lesion (Figure 8.1).

Little preparation is needed; a fast of 12 hours can reduce interference with gastric contents and the associated gas, but the results are inconsistent. Gas in the GI tract is the most common cause of reverberation artifacts such as ring-down and comet-tail artifacts (Figure 8.2A,B; see Chapter 1). Gas may also result, alone or in combination with ingesta or fecal material, in variable forms of acoustic shadowing (Figure 8.2C).

Ultrasonographic Anatomy of the Normal Gastrointestinal Tract

The wall thickness and layering, and relative motility of different segments of the GI tract, can be evaluated. The thickness of the GI tract can be measured by placing calipers on the outer aspect of the serosa and on the mucosal inner border.

Table 8.1 lists the mean of normal thickness of the GI wall in dogs and cats. The data are inspired by several publications and are also based on the authors' experience (Penninck et al. 1989; Newell et al. 1999; Goggin et al. 2000; Delaney et al. 2003; Gladwin et al. 2014; Di Donati et al. 2013; Winter et al. 2013). It is important to remember that assessing the thickness of the GI tract is only a small part of diagnosing a GI disorder.

The distal esophagus, which can occasionally be seen on ultrasound in small dogs (Figure 8.3A), is difficult to access because its position is cranial to the diaphragm and because of the interposition of gas in the surrounding lungs.

The stomach is the largest portion of the GI tract and can be identified easily by its rugal folds (Figures 8.1A, 8.3B, 8.4A). The gastric wall is challenging to measure mainly when the stomach is collapsed. There is a significant difference between the wall thickness at the rugal folds and at the interrugal location The thickness varies depending on the degree of distension and the size of the dog. Peristalsis is observed at a rate of four to five contractions/minute in dogs.

The descending duodenum (Figures 8.1B, 8.3C), which is the thickest segment of small bowel in dogs,

Atlas of Small Animal Ultrasonography, Second Edition. Edited by Dominique Penninck and Marc-André d'Anjou.
© 2015 John Wiley & Sons, Inc. Published 2015 by John Wiley & Sons, Inc.
Companion website: www.SmallAnimalUltrasonography.com

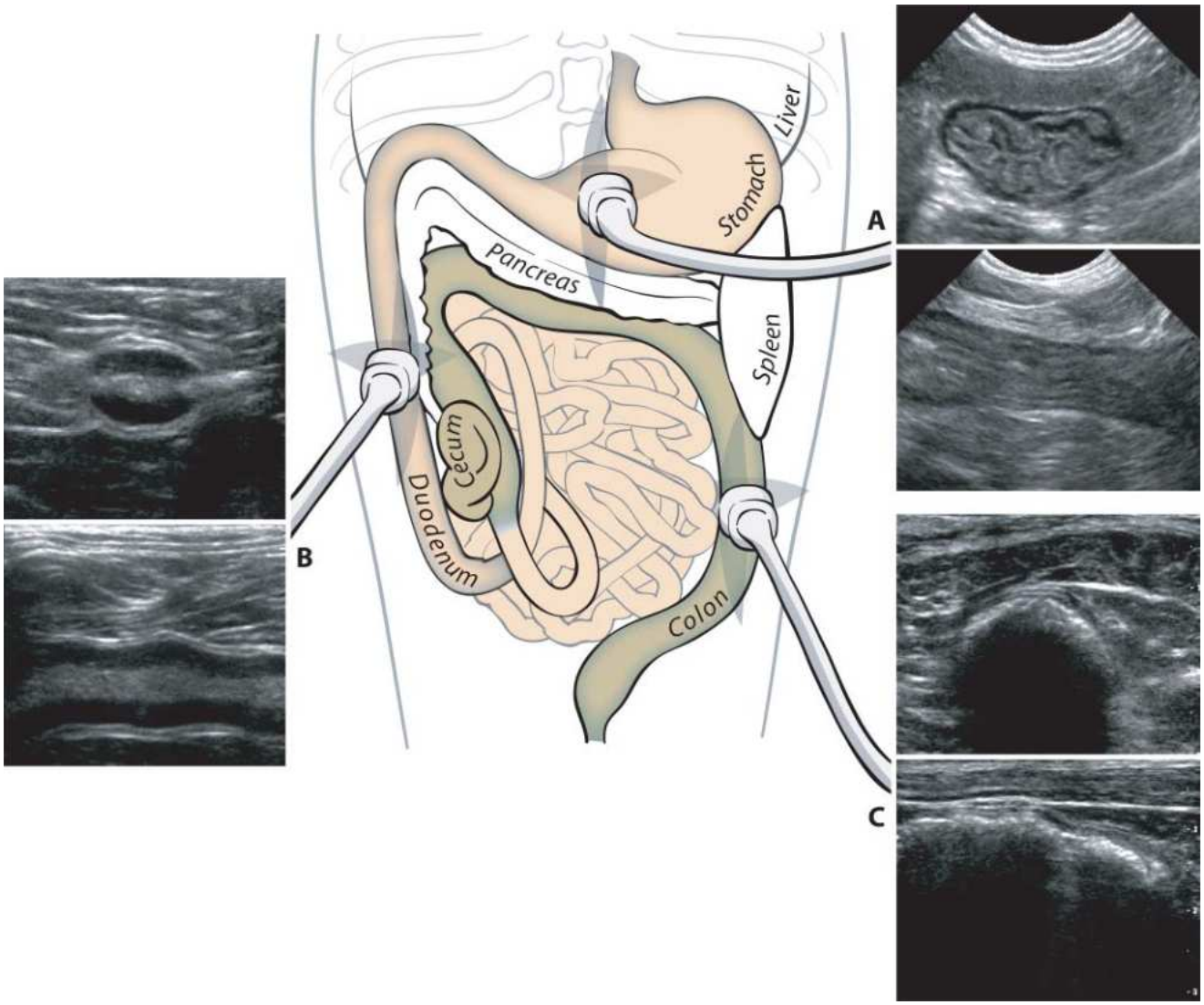


Figure 8.1. Ultrasonographic anatomy of the normal canine gastrointestinal tract in dorsal recumbency. Illustration of the location of the main gastrointestinal segments, with placements of the probe to fully evaluate some of these segments. **Plan A** shows the position of the probe on the stomach. Both transverse (top sonographic image) and longitudinal images (bottom sonographic image) are obtained by sliding the probe along the long axis of the stomach. **Plan B** shows the position of the probe on the descending duodenum. Both transverse (top sonographic image) and longitudinal images (bottom sonographic image) of this bowel segment are displayed. **Plan C** shows the position of the probe on the descending colon. Both transverse (top sonographic image) and longitudinal images (bottom sonographic image) of the colon are displayed.

has a superficial and rectilinear course along the right lateral abdominal wall. At times, Peyer's patches can be seen as small, regularly spaced mucosal depressions that should not be mistaken for ulcers. They can after depressions on one side of the wall be seen in dogs with no clinical signs of active gastrointestinal disease, but as they are not seen in most dogs, it is unclear if they are seen when they are reactive. The duodenum in cats has a thickness similar to the jejunum. On the transverse plane of any small intestinal loop, one can see an extended hyperechoic stripe on each side of the lumen, probably representing altered alignment of villi in collapsed bowel segments (Rault et al. 2004) (Figure 8.3C,D).

The duodenal papilla (Figures 8.3D, 8.4C) is identified easily in the proximal portion of the descending duodenum as a ring-like structure on the transverse view of the duodenum, and as a short tubular structure on the longitudinal plane.

The ileum in cats (Figure 8.4E) is a short intestinal segment with a prominent submucosa and muscularis, resulting in an intestinal segment thicker that the rest

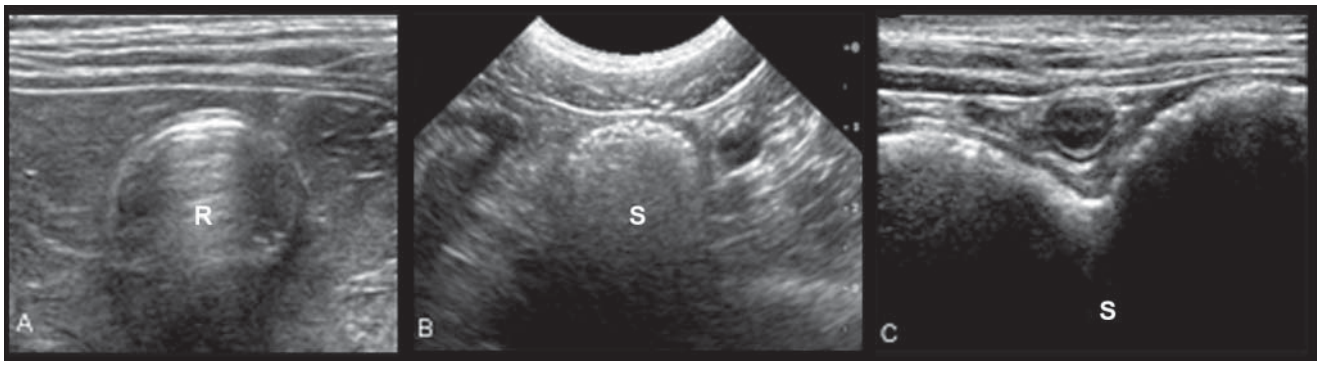


Figure 8.2. Artifacts commonly seen associated with the gastrointestinal tract. A: Gas in the colon of this dog creates a reverberation artifact (R) masking most of the far wall. The sound is entirely reflected back from the gas and then bounces back and forth between the probe and the gas, creating multiple echoes from one ultrasound pulse. **B, C:** The mixture of gas and fecal material in the gastrointestinal tract often creates acoustic shadowing (S) appearing as an area of low-amplitude echoes created by highly attenuating structures. The shadowing can be dirty **(B)** or clean **(C)**, depending on its homogeneity.

Table 8.1
Mean references values for the gastrointestinal (GI) wall. These values are only useful when used in combination with other sonographic features, such as wall layering and distribution of changes, and placed in context of the clinical presentation

	Stomach	Duodenum	Jejunum	Ileum	Cecum/Colon
Dog					
<15 kg	2–5 mm	3.8	3.0	3.0	1.5
15–30 kg	2–5 mm	4.1	3.5	3.5	1.5
>30 kg	2–5 mm	4.4	3.8	3.8	1.5
Cat	2–4 mm	2.2	2.2	2.8	1.5

Stomach: these values are dependent of the gastric distension.
Duodenum/jejunum/colon in dogs, the table summarizes the mean intestinal wall thickness as recently published (Gladwin et al. 2014).
Duodenum/jejunum/ileum in cats, the table summarizes the mean intestinal wall thickness as recently published (Di Donato et al. 2014).
Cecum in cats (Besso et al. 2004); cecum in dogs: based on the authors' experience, granted that the adjacent colon is normal.
Colon in cats (Goggin et al. 2000).

of the intestinal tract. The ileocecocolic junction can be challenging to identify in dogs because the cecum is most commonly gas-filled (Figure 8.3F). In cats, the ileocecocolic junction (Figure 8.4E) can be more easily recognized. The cecum is a flattened conical structure in cats and is a spiral-shaped, gas-filled structure in dogs. The colon has a thin, layered wall and often contains gas and feces (Figures 8.1C, 8.2, 8.3G, 8.4F).

Composite images of the main segments of the GI tract in dogs and cats illustrate their main features (Figures 8.3, 8.4).

Five ultrasonographic layers can be identified throughout the GI tract. From the lumen to the serosal surface, one can identify the hyperechoic mucosal interface in contact with the lumen, the nearly anechoic mucosa, the hyperechoic submucosa, the nearly anechoic muscular layer, and the hyperechoic subserosa and serosa (Figure 8.5). Recent publications (Geyer et al. 2014; Di Donati et al. 2014; Winter et al. 2014) report the relative proportion of each wall layer to the overall thickness of the wall. In dogs, the mucosa represents about 63% of the total wall thickness of the duodenum, and about 60% of the total wall thickness of the jejunum; while the muscular layer represents about 13% (for the duodenum) and 15% (for the jejunum) of the total wall thickness. In the colon, all layers have similar wall contribution (Gladwin et al. 2014).

In cats, the mucosa represents about 58% of the total wall thickness of the duodenum, and about 55% of the total wall thickness of the jejunum; while the muscular layer represents about 13% (duodenum) and 14%

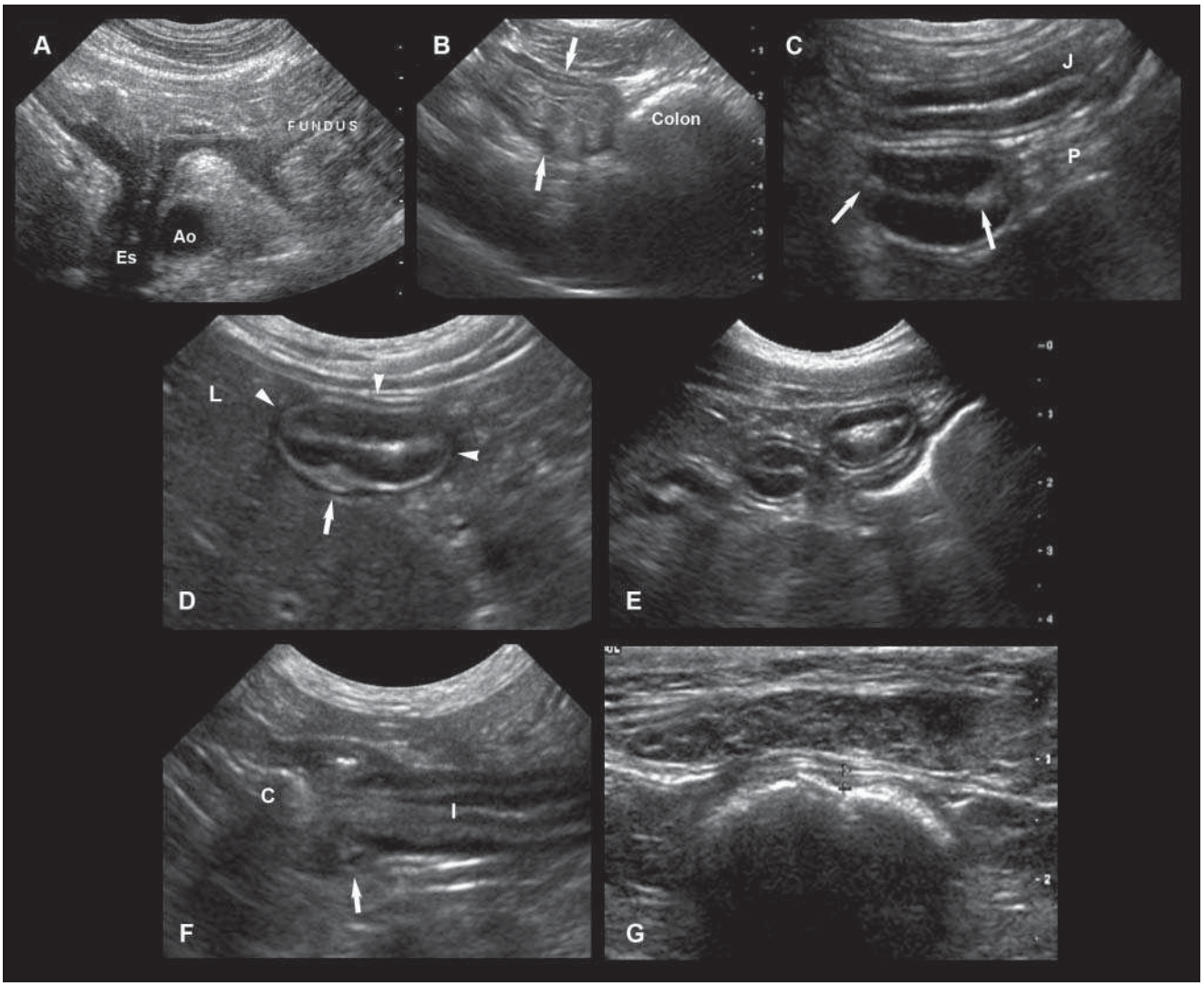


Figure 8.3. **Sonograms of normal gastrointestinal segments in dogs. A:** On transabdominal approach, the esophagus is rarely seen. In this 10-year-old corgi, the most distal portion of the esophagus (E) is visible. In the same image is a transverse view of the aorta (Ao) and the fundus of the stomach. **B:** The stomach (arrows) is easily recognized by its location, the presence of rugal folds, and its peristaltic activity. When the stomach is collapsed, as in this dog, it is difficult to assess the wall thickness accurately. Note the adjacent transverse colon located caudal to the stomach body. **C:** The proximal duodenum is a rectilinear segment coursing along the right lateral abdominal wall. The duodenum has a thicker wall than the remaining small bowel (J, jejunum). On this transverse plane, notice the extended stripe on each side of the lumen (arrows), this is a normal finding. P, pancreas. **D:** In the proximal portion of the descending duodenum (arrowheads), the duodenal papilla, seen on the transverse plane in this image (arrow), can be easily identified. **E:** Jejunal segments are freely looping in the mid-abdomen. The wall layering is visible. **F:** The ileocecocolic junction (arrow) is often difficult to identify because of gas collected at that location. In this dog, the ileum (I) is seen entering the ascending colon (C) on a longitudinal plane. **G:** The colon, often gas- or feces-filled, has a thinner wall than the small bowel. In this dog, the finely layered colonic wall is 1.5 mm thick.

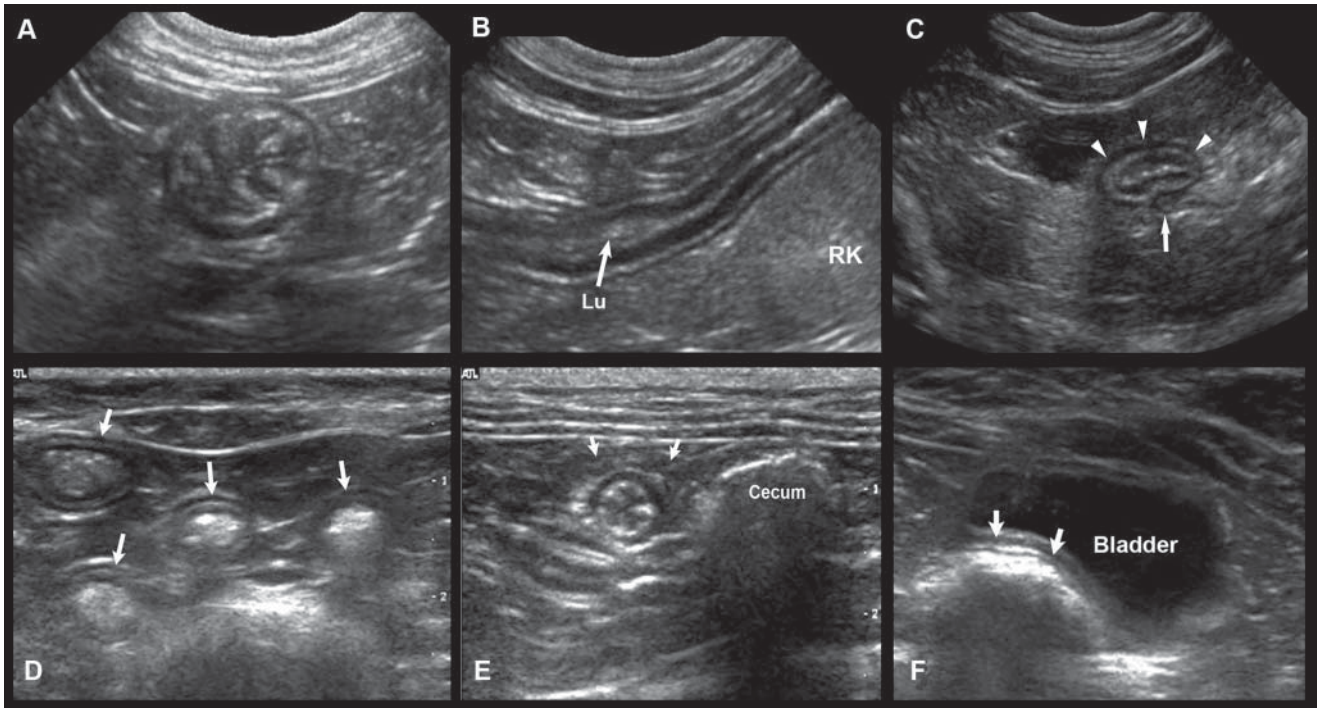


Figure 8.4. **Sonograms of normal gastrointestinal segments in cats. A:** Transverse sonogram of the collapsed gastric fundus in an adult cat. Rugal folds are well seen. **B:** Longitudinal sonogram of the duodenum. The wall layering is visible. RK, right kidney. Lu, lumen. **C:** Transverse sonogram of the descending duodenum (arrowheads). The duodenal papilla is well delineated (arrow). **D:** Several loops of jejunum, containing fluid and gas, are present (arrows). There is no significant difference between the thickness of the duodenum and jejunum in cats. **E:** Transverse sonogram of the ileum. The gas-filled cecum is on the right of the ileum, and the ileum is entering the echogenic fluid-filled ascending colon (arrows). This short segment of bowel has more prominent submucosa and muscularis than the remaining bowel segments in cats. **F:** Transverse sonogram of the feces-filled descending colon in a normal cat. The thin wall and its layering are barely visible (arrows), just ventral to the hyperechoic interface created by the presence of feces and its associated shadow in the far field.

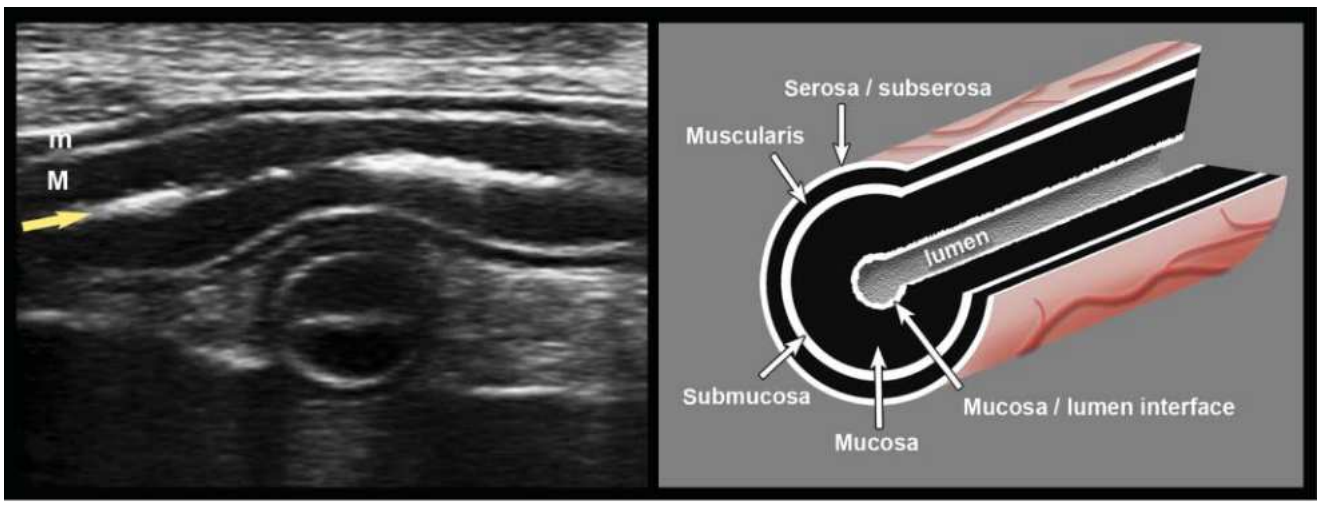


Figure 8.5. **Normal intestinal layers.** Sonogram of two intestinal segments, one sagittal in the near field and the other in the tranversal plane. The yellow arrow points to the lumen. Part of the spleen is seen in the far field. M, mucosa. M, muscular layer. On the right, the five ultrasonographic layers are illustrated. The lumen varies in echogenicity according to its content. It is bordered by a hyperechoic interface that delineates the thick, nearly anechoic mucosal layer. Then the thin hyperechoic submucosa, thin nearly anechoic muscularis, and thin hyperechoic subserosa/serosa can be visualized.

(for the jejunum) of the total wall thickness. For the ileum in cats, the total thickness and relative layer thickness varies depending on the location where the measurements are taken (on the folds vs between folds). In the feline ileum, the submucosa and muscular layers are more prominent than in the rest of the small intestines. These reference values are useful in evaluating disorders affecting only some of the layers of the GI wall.

The normal luminal contents can vary and may consist of food, mucus, fluid, or gas (Figure 8.6). Some food may have an unusual appearance and mimic foreign material (Figure 8.7).

The hepatic, gastric, pancreatico-duodenal, jejunal and colic lymph nodes are involved in the lymphatic drainage of the gastrointestinal tract (see Chapter 15) and should be evaluated when a gastrointestinal disorder is suspected.

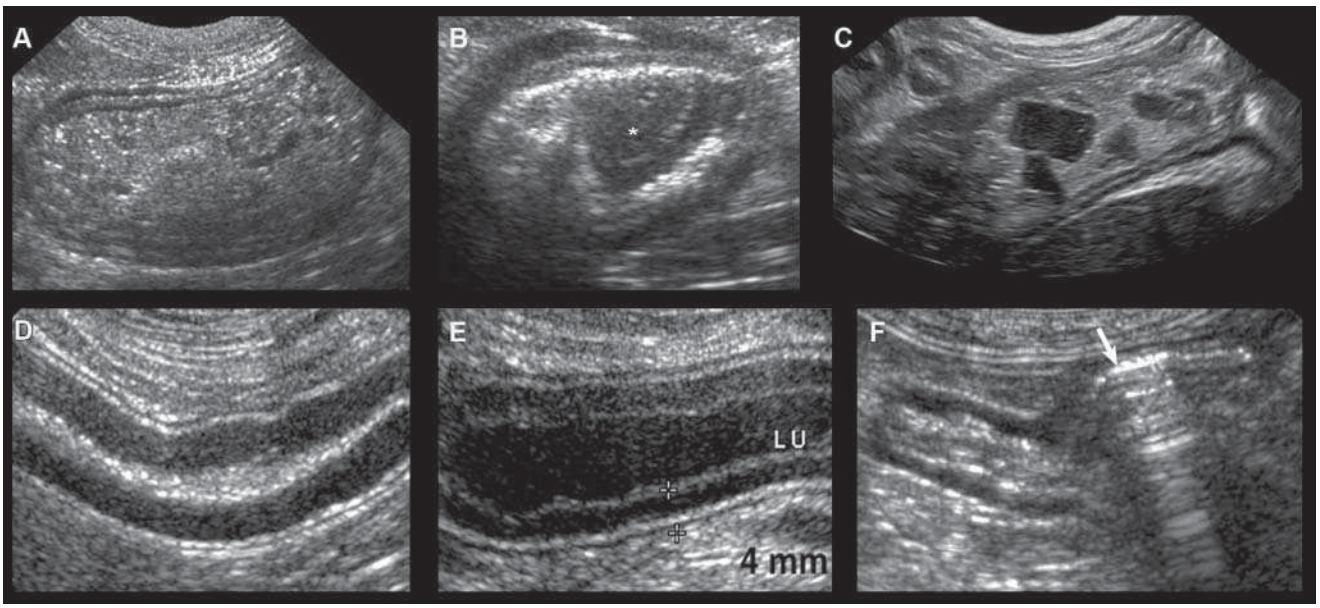


Figure 8.6. Normal luminal contents. A–C: The alimentary pattern consists of food particles of variable size and shape in the gastric lumen. It may or may not be associated with imaging artifacts. In this dog, small, rounded, echogenic balls of food can be identified in the gastric lumen. **B:** A large amount of food or large pieces of food, as in this dog (*), can occasionally mimic a mass or a foreign body in the stomach. **C:** Numerous structures of variable shape and size are seen in the stomach of a dog after a homemade meal. **D:** The mucous pattern appears as a bright interface in the lumen of this jejunal segment. Note the absence of artifact with this pattern. The gastrointestinal wall can be fully evaluated. **E:** The fluid pattern is characterized by anechoic to uniformly echogenic luminal contents. This pattern optimizes the visualization of the wall layers on each side of the lumen. LU, lumen of the bowel. **F:** The gas pattern appears as an intraluminal, hyperechoic, reflective surface. At the ileocolic junction in this cat, a small amount of gas (arrow) is seen in the ascending colon. The gas is associated with a reverberation artifact.

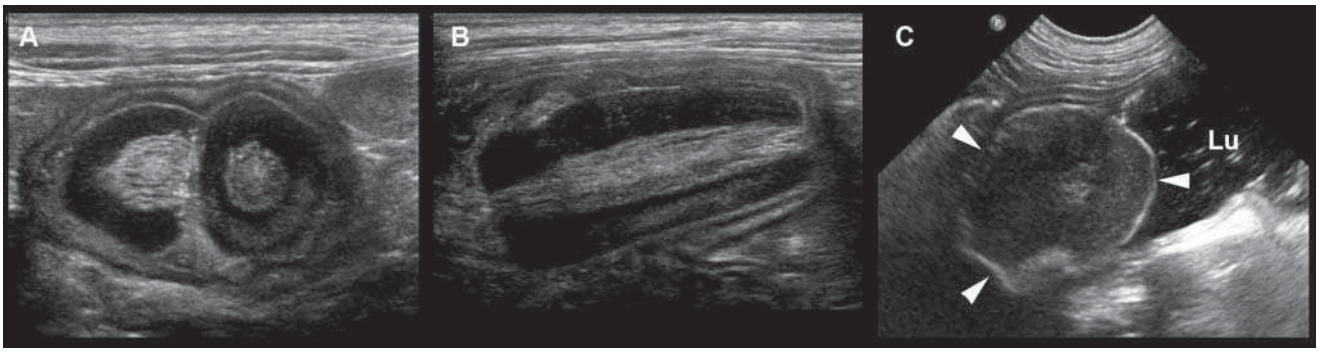


Figure 8.7. Unusual luminal contents. A, B: Baby carrots. Transverse (**A**) sonogram of two layered structures present in the gastric lumen of a 7-months-old Pug. The baby carrot has a distinct appearance in longitudinal plane **(B). C:** An irregularly rounded and echogenic structure (arrowheads) is noted in this 2-year-old Collie presented for acute vomiting, probably resulting from ingestion of raw potatoes, which are toxic in dogs. Lu, fluid-filled lumen of the stomach.

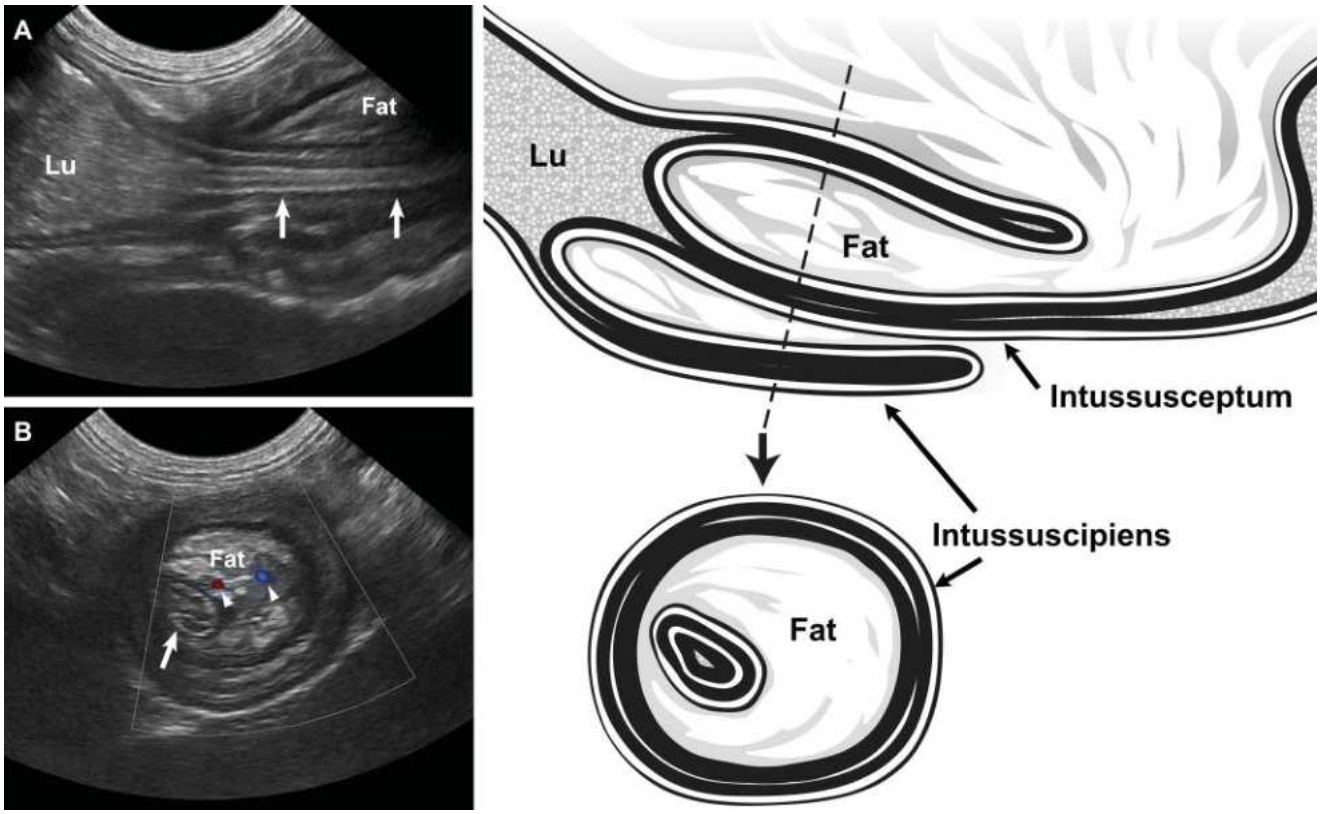


Figure 8.8. **Intussusception in a dog.** Illustrations of the relationship of the intussuscipiens, intussusceptum, and surrounding structures. On the top **(A)** is the longitudinal sonogram of a jejuno-ileal intussusception and its corresponding schematic illustration. On the bottom **(B)** is the transverse sonogram of a jejuno-ileal intussusception and its corresponding schematic illustration. The intestinal lumen (Lu) is dilated with fluid because of mechanical obstruction, and hyperechoic mesenteric fat is invaginated with the intussusceptum within the intussuscipiens. Mesenteric vessels (arrowheads) often follow the mesenteric fat within the intussuscipiens. The arrows point to the invaginated intestine.

Sonographic Features of Gastrointestinal Disorders

Intussusception

The main ultrasonographic feature of an intussusception is the multilayered appearance of the wall (also called **concentric rings** or **ring sign**), representing the superimposed wall layers of the intussusceptum and intussuscipiens (Figure 8.8).

In dogs and cats (Lamb and Mantis 1998; Patsikas et al. 2003), the appearance of intussusception varies somewhat with the location and length of the GI segment involved, the duration of the process, and the orientation of the scan plane relative to the axis of the intussusception. The intussuscipiens (outer bowel segment) is often thickened, edematous, and hypoechoic, whereas the thickness and layering of the intussusceptum may appear normal. The invaginated portion can involve different segments of the GI tract, such as the stomach (Figures 8.9, 8.10), small bowel (Figure 8.11), or colon (Figures 8.12, 8.13).

Gastric intussusception is rare, but when encountered it can be challenging to diagnose ultrasonographically (Hoffman et al. 2003; Lee et al. 2005). It may involve part of the esophagus, segments of stomach or proximal duodenum. Frequently, in jejuno-jejunal or jejuno-ileo-ceco-colic invaginations, mesenteric fat and vessels invaginate within the intussuscipiens. On occasions, inflammatory pseudocysts, enlarged lymph nodes (Figures 8.12, 8.13), foreign bodies (Figure 8.11), or tumoral mass (Figure 8.14) in older patients can be seen within or near the intussusception site.

At times, lesions affecting the GI tract, such as plication associated with linear foreign bodies (Figure 8.15), sacculation, or hyperplastic gastric mucosa protruding into the lumen, can simulate the pattern of intussusception. By evaluating the lesion in several planes, one can avoid such pitfalls.

Figure 8.10. Gastroesophageal intussusception. A: lateral radiograph of the thorax of a gastroesophageal intussusception in a 6-month-old German shepherd. The esophagus is gas-distended (arrowheads) cranially, and an elongated soft tissue mass (arrows) is present in its caudal aspect; this represents part of the invaginated stomach. **B:** the sagittal sonogram shows a partially fluid-filled gastric lumen (*). The thickened and edematous gastric wall (arrows) is located cranial to the diaphragm (arrowheads). L, liver located in the cranial abdomen.

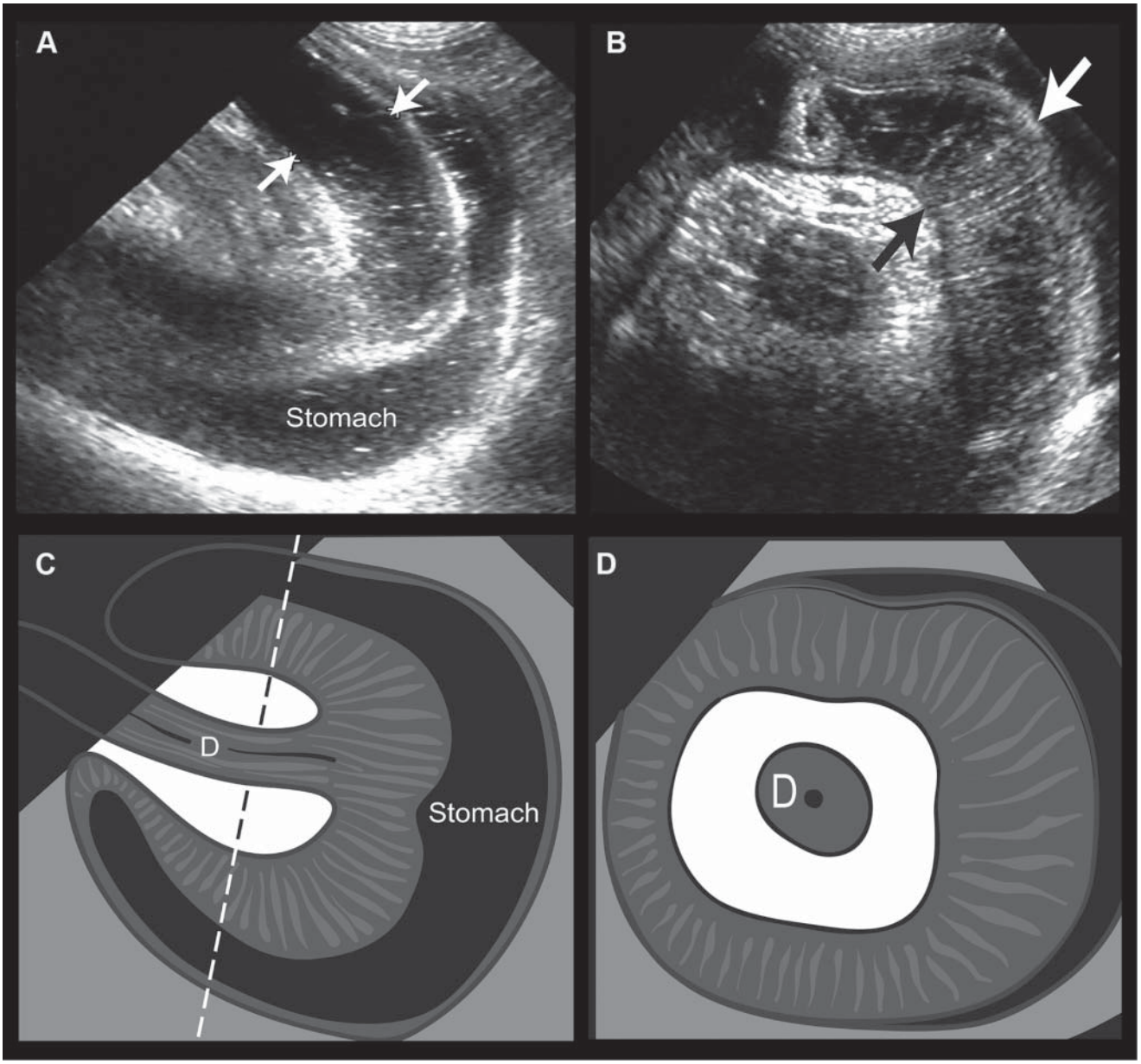


Figure 8.9. Duodenogastric intussusception in a dog. Illustration of a duodenogastric intussusception in a 6-year-old male Labrador Retriever with glomerulonephritis and presented because of severe, acute vomiting. The most proximal portion of the duodenum is invaginated within the pylorus, which protrudes within the fluid-filled gastric body (stomach). The gastric wall was severely thickened and hypoechoic because of severe edema (arrows). This change could be misinterpreted as a mass. D, duodenum.

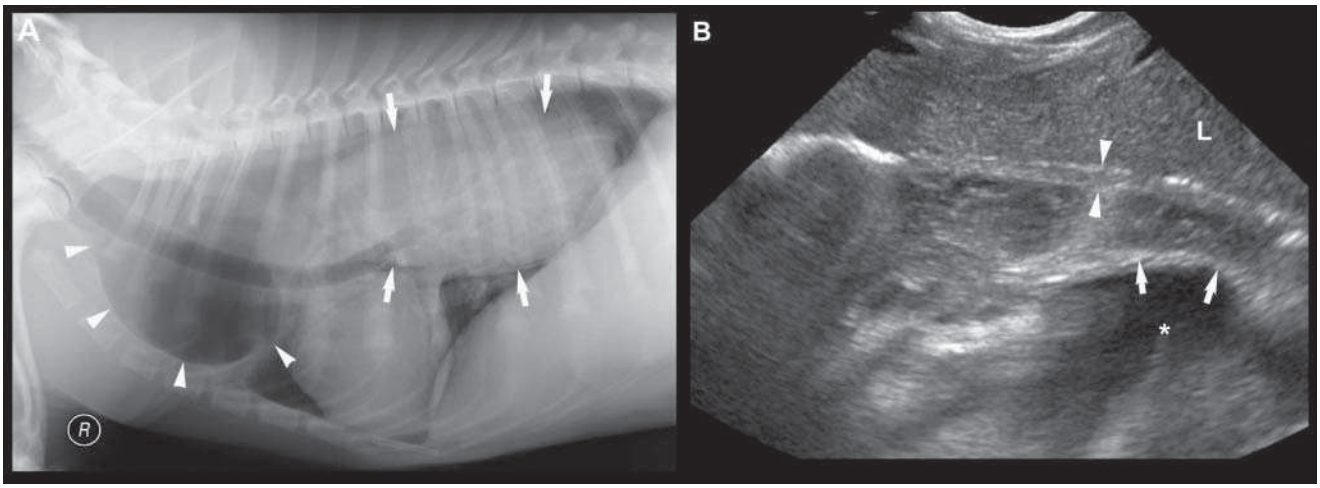


Figure 8.10. **Gastroesophageal intussusception.** (for full caption, see facing page)

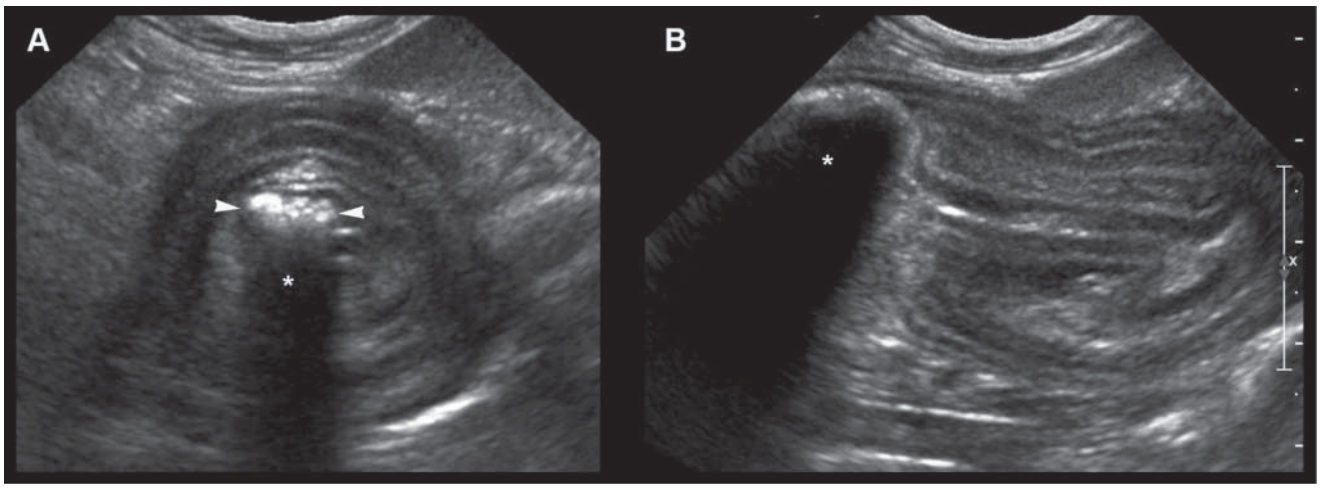


Figure 8.11. **Jejunal intussusception and linear foreign body in a dog.** Transverse **(A)** and longitudinal **(B)** sonograms of a jejunojejunal intussusception identified in a young Labradoodle. The intussuscepted segment contains a linear foreign body (arrowheads) associated with acoustic shadowing (*). Note the numerous wall layers of the intussucepted and intussuscepiens segments on both views.

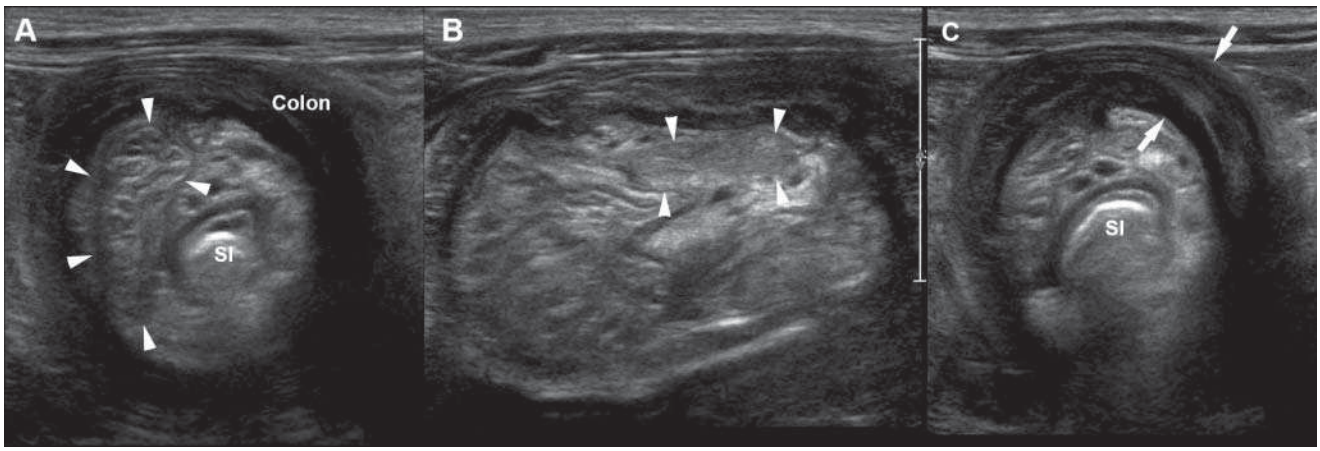


Figure 8.12. **Jejuno-colic intussusception.** Transverse **(A, C)** and longitudinal **(B)** sonograms of a distal jejunocolonic intussusception detected in a 4-month-old Golden Retriever. In **A**, the colon is moderately thickened and edematous. The arrowheads outline the invaginated cecum located next to a small intestinal segment (SI). In **B**, the arrowheads point to one of the invaginated jejunal lymph nodes. In **C**, the colonic wall (arrows) is thickened and layers are barely seen.

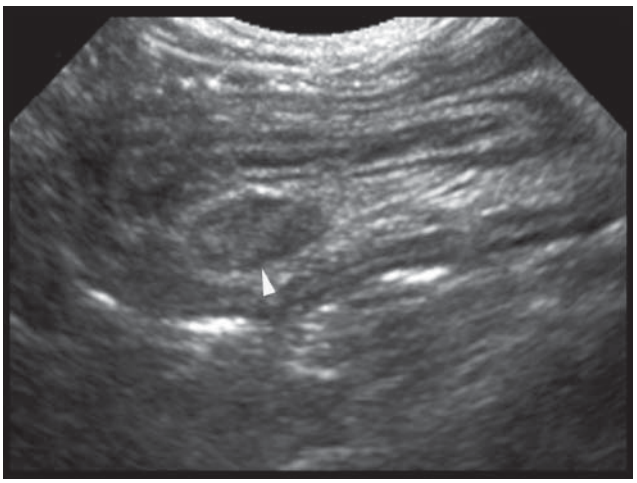


Figure 8.13. Jejuno-jejunal intussusceptions in a Siamese cat. Longitudinal sonogram of the intussusception showing a jejunal lymph node (arrowhead) in the intussusception.



Figure 8.14. Colonic intussusception and adenocarcinoma. Transverse sonographic **(A)** and sagittal **(B)** sonograms of a large nodular echogenic colonic thickening/mass (arrowheads) associated with an intussusception in a 15-year-old cat. The mass was diagnosed as a colonic adenocarcinoma The arrows point to the invaginated segment of colon with a small amount of echogenic fluid in its lumen. F, invaginated fat; and an asterisk is placed on the lumen of intussusceptum in **A**. **C:** Gross specimen of the intussusception associated with an asymmetric transmural adenocarcinoma (arrowheads). F, fat.

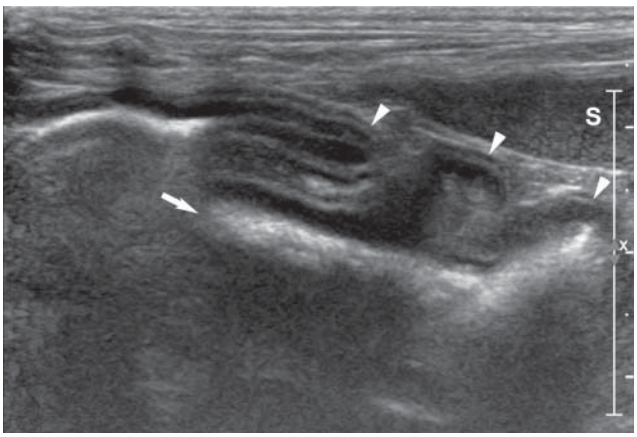


Figure 8.15. Plication mimicking intussusception. Longitudinal sonogram of a long plicated intestinal segment with a linear foreign body (arrow) in the lumen of this 2-year-old Dachshund presented with 4 days of anorexia. The exuberant folds of the plication (arrowheads) can mimic an intussusception.

Foreign Bodies

Gastrointestinal foreign bodies vary greatly in size, shape, and echogenicity. Segmental fluid or gas accumulation within the stomach or part of the intestinal tract is an indicator of mechanical ileus (obstruction). When present, abnormal fluid distension facilitates the detection of foreign material (Figure 8.16).

Balls are easily identified because of their characteristic curvilinear interface. They may vary in echogenicity, depending on the make-up of their material (Figure 8.17). At times, foreign material (such as balls) may be an incidental finding; therefore, it is important to consider the clinical history to appropriately manage the patient's presenting signs.

Independent of the type of foreign body, the presence of bright interface associated with strong shadowing is highly suggestive of a foreign material (Tidwell and Penninck 1992). However, fluid or gas accumulation orad to the foreign material is necessary to confirm the obstructive nature of the obstruction. Feces in the colon can simulate foreign material, as compact fecal material is similarly associated with strong shadowing. It is thus critical to identify accurately the segment of the intestinal tract, especially differentiating small bowel from colon (Figure 8.2). Occasionally, the contour of the interface can enable the identification of the type of foreign body, such as a curved regularly lobulated surface of a peach pit.

Gastric trichobezoars, referred to as **hairballs**, are commonly seen in cats. These compact foreign bodies appear as irregular bright interfaces with a strong, uniform, clean acoustic shadow (Figure 8.18A). In dogs and cats, several foreign bodies can be encountered

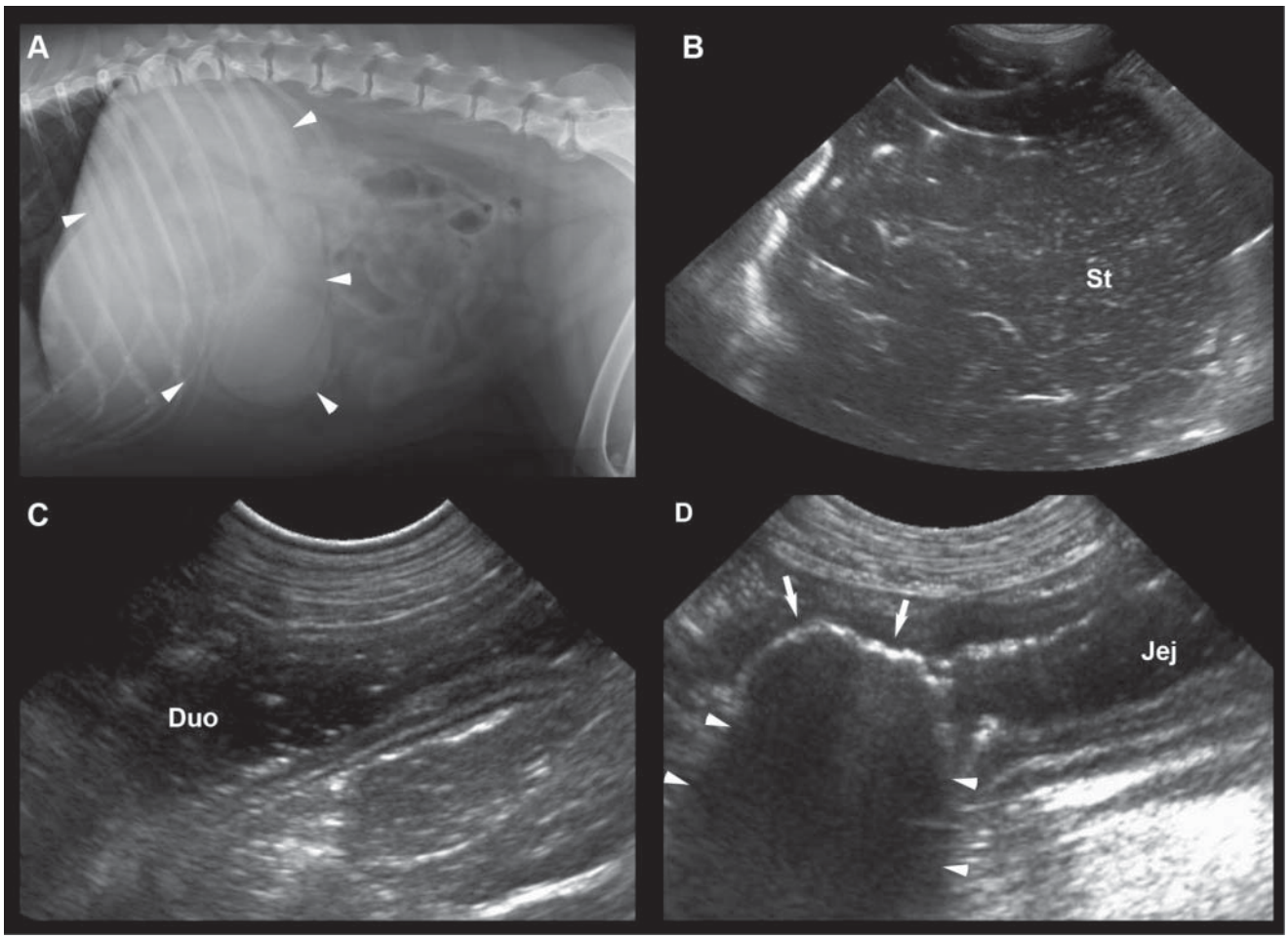


Figure 8.16. Proximal jejunal obstructive foreign body. A: Lateral radiograph of a 13-year-old cocker with 3 days of vomiting and anorexia showing a moderately fluid- and gas-distended stomach (arrowheads). **B:** Transverse sonogram of the fluid-distended stomach. Decreased gastric motility is noted during the examination. **C:** The descending duodenum (Duo) is fluid-distended. **D:** The proximal jejunum (Jej) is also fluid-distended up to the obstructive foreign body (arrows) associated with strong shadowing (arrowheads).

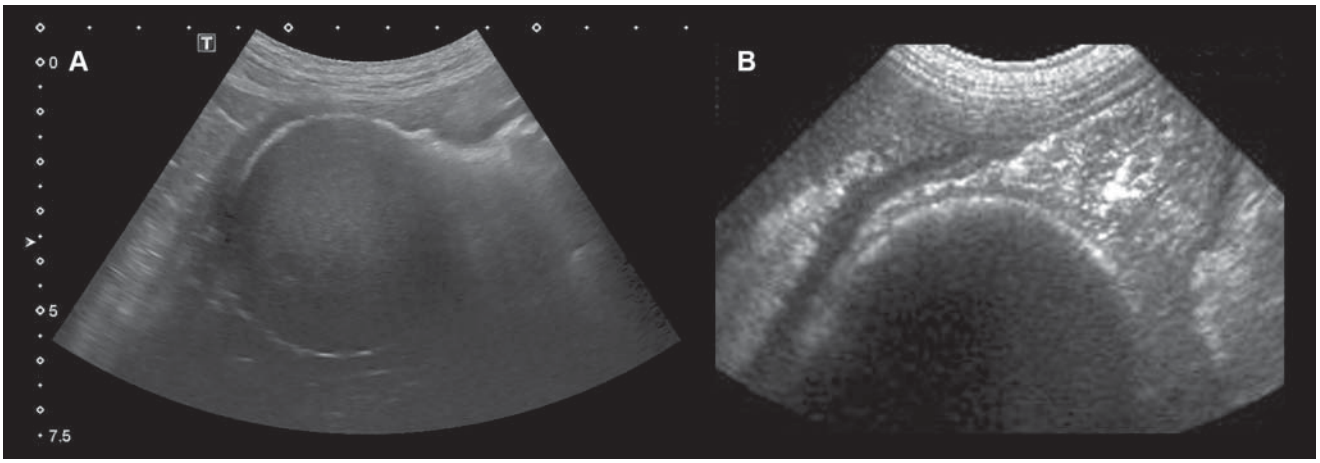


Figure 8.17. **Gastric foreign bodies: play balls. A:** A rubber ball is present in the stomach of this dog over several examinations, without causing clinical signs. The foreign object is spherical and of mild, uniform echogenicity with only partial acoustic shadowing. **B:** In this other dog, the ball appears as a bright curvilinear interface associated with strong acoustic shadowing.

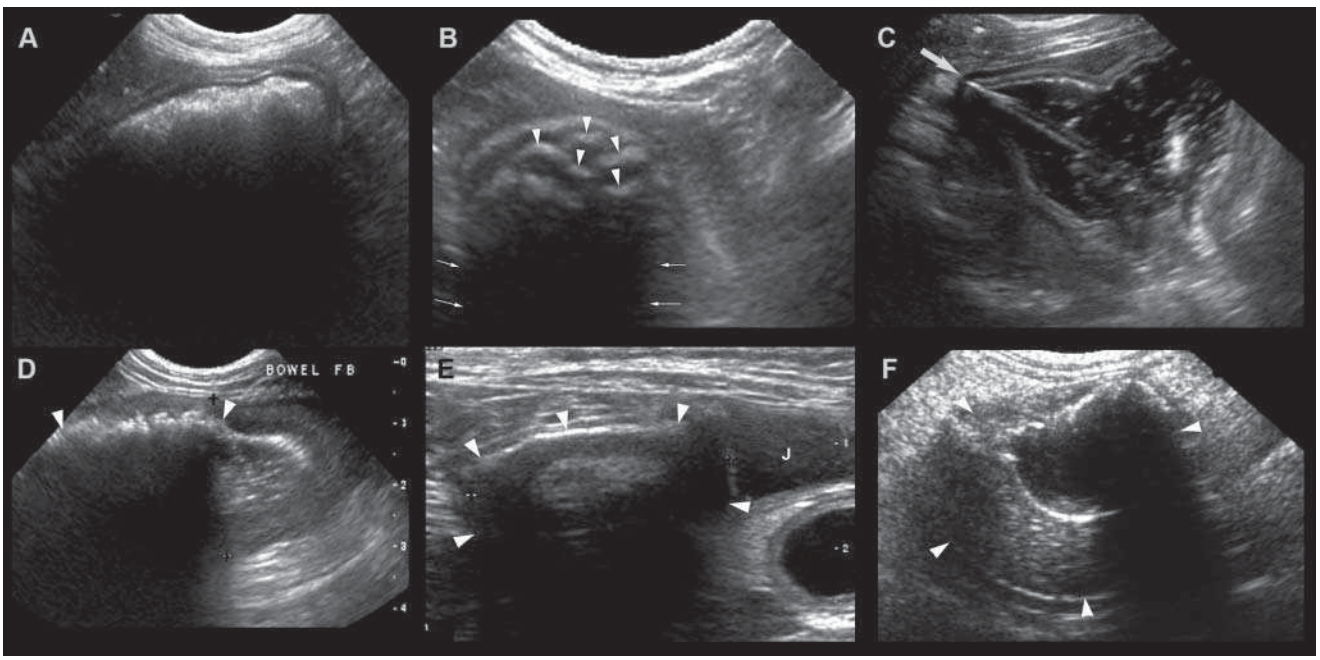


Figure 8.18. **Intestinal foreign bodies.** A wide range of foreign material can be found in the gastrointestinal tract. Most of them are associated with strong acoustic shadowing. **A:** Trichobezoars are compact foreign bodies with a bright interface and a uniform and clean acoustic shadow, as seen in the stomach of this long-haired domestic cat. **B:** Elastic bands in the stomach of a young cat mimic prominent rugal folds (arrowheads). The spacing and the uniform shadowing (arrows) supported the presence of foreign material. **C:** Several sharp pine needles were present in the stomach of a dog. One of them (arrow) penetrates the wall. **D:** A large piece of corncob (arrowheads) is in this dilated and thickened jejunal segment. **E:** A poorly echogenic object with an echogenic center (arrowheads) is noted in the fluid-dilated jejunum (J) of a cat. A piece of a plastic toy was removed surgically. **F:** A rounded and nearly layered structure (arrowheads) is in a dilated segment of small intestine. At first, this appearance was confused for a thickened bowel segment. At surgery, a large fragment of a "Kong" toy was removed.

that have variable size, shape, echogenicity, and acoustic shadowing. The ultrasonographic features depend on the physical properties of the material (Figure 8.18).

Perforating foreign bodies, such as ingested teriyaki sticks, are usually anchored within the stomach and may affect the surrounding soft tissue within and outside the cranial abdominal cavity (Penninck and Mitchell 2003) (Figure 8.19). The perforated wall is locally thickened, and focal loss of layering is common. The adjacent fat is often hyperechoic as the result of regional steatitis.

Linear foreign bodies present as bright linear interfaces, commonly associated with shadowing, and the affected bowel segment often appears plicated (Figure 8.20). The degree of plication varies with duration and severity. Intestinal distension is often less pronounced than is the case with larger obstructive foreign bodies. Linear foreign bodies vary in diameter, contour, and length and part of the foreign material may be stocked in the pyloric antrum or any place along the intestinal tract.

The presence of GI parasites can mimic the appearance of linear foreign bodies. Roundworms (*Ascaris*) appear as smooth, tubular linear hyperechoic structures (Figure 8.21). Shadowing is usually not observed with these adult parasites.

At times, foreign material accumulates at a pathologically narrowed intestinal site. The narrowing can be caused by intussusception, post-traumatic or surgical stricture, or focal neoplastic infiltrate (Figure 8.22).

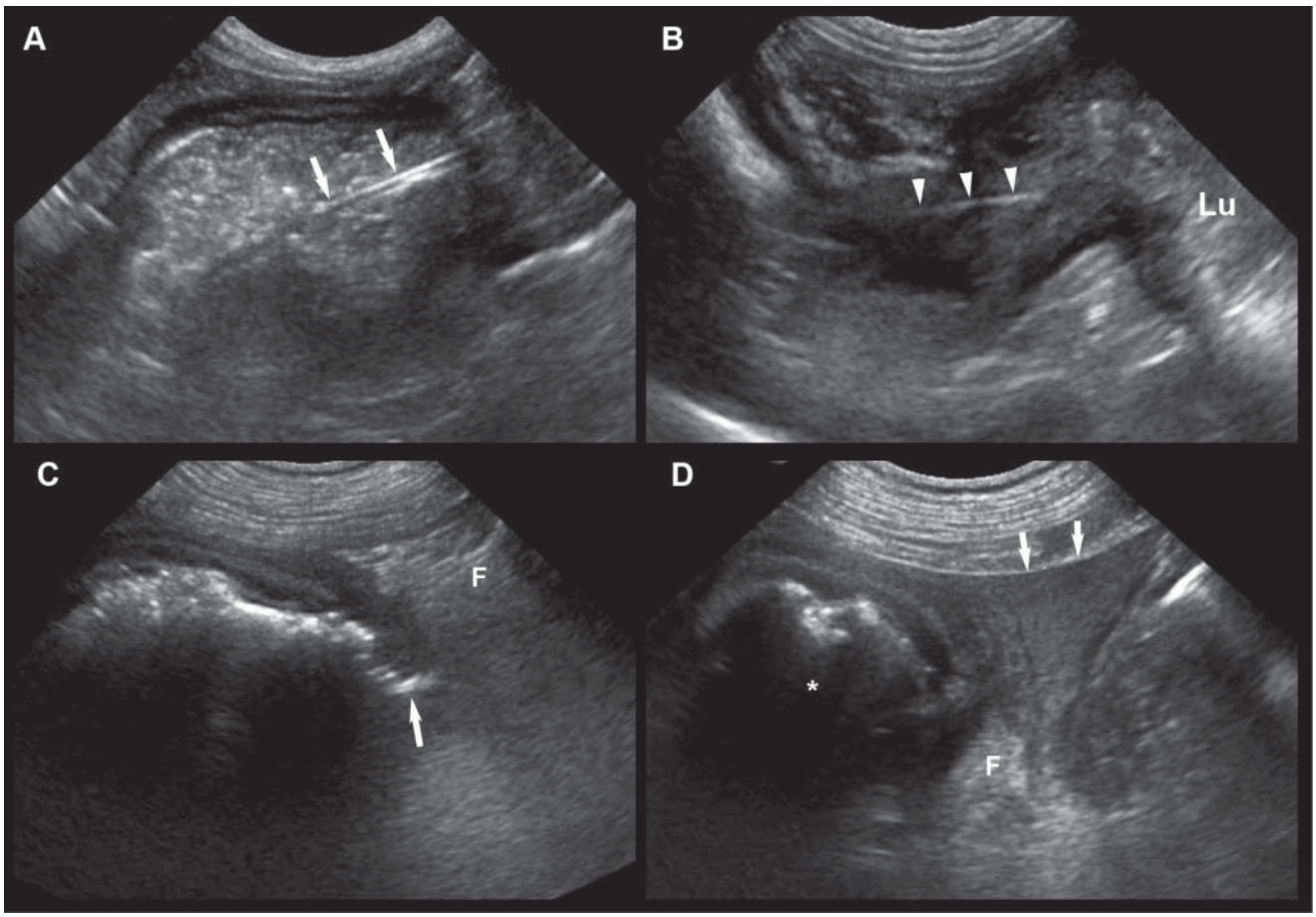


Figure 8.19. **Perforating foreign bodies. A, B:** Part of a hard plastic foreign body (arrows in **A**) appears as a long, linear, bright interface anchored within the pylorus (arrowheads in **B**) of this 4-year-old Boston Terrier. In this dog, there was also hypertrophy of the pyloric canal (not well seen on this image). These findings were confirmed at surgery. Lu, gastric lumen. **C, D:** A plastic cup perforated a jejunal segment in a 6-year-old Bernese Mountain Dog. The adjacent fat is hyperechoic **(F)** and the intraluminal gas is dissecting the wall (arrow). In addition, a moderate amount of markedly echogenic effusion (arrows) is consistent with septic peritonitis.

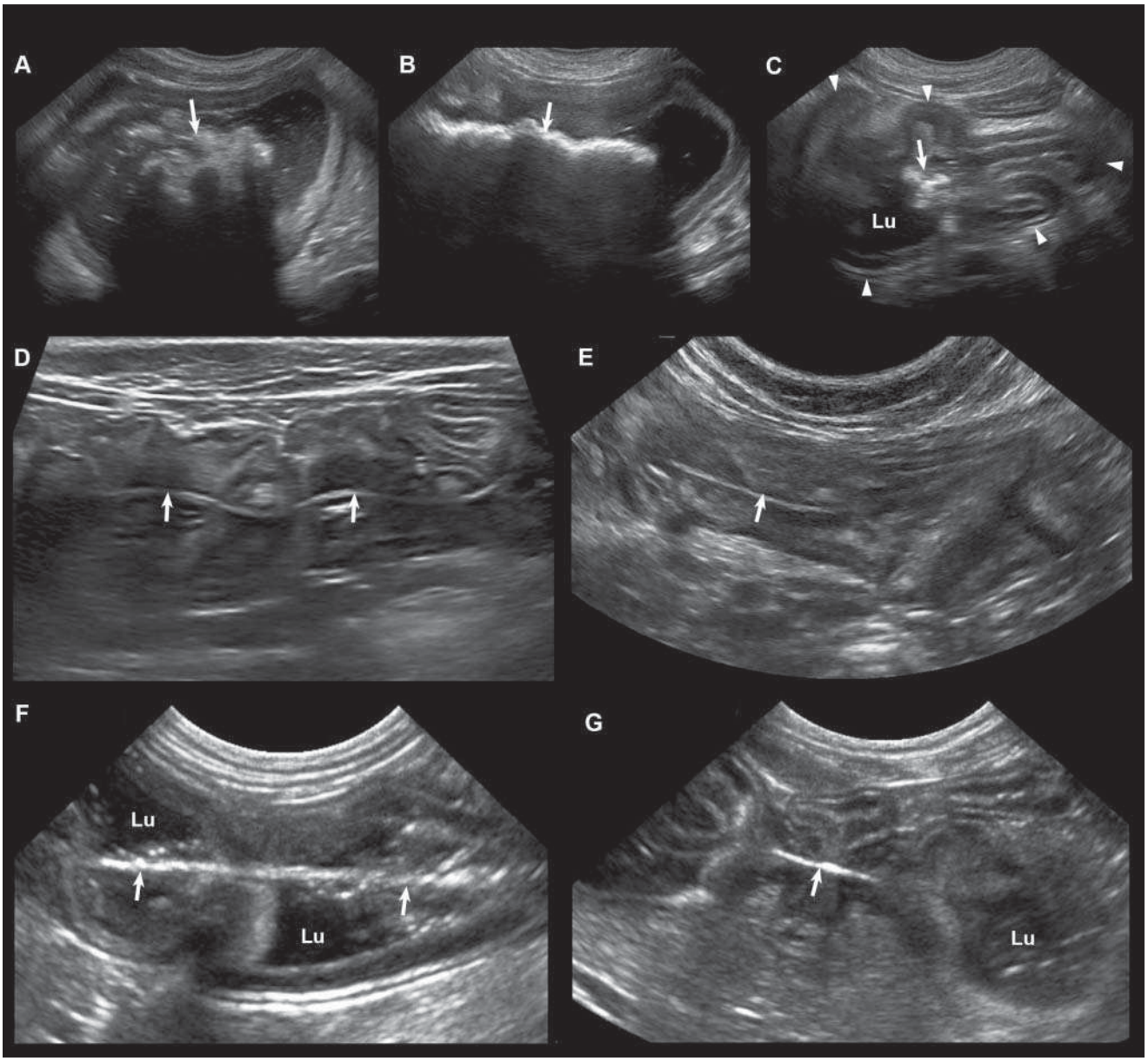


Figure 8.20. **Linear foreign bodies in two dogs and one cat. A–C:** A 3-year-old English Bulldog. Foreign material (arrows) associated with strong shadowing is present in the stomach **(A).** The content extends into the descending duodenum **(B)**. Numerous plicated jejunal loops (arrowheads) are seen on each side of the lumen (Lu) **(C)**. **D, E**: In a cat with a thin linear foreign body (arrows) extending into the small intestine, severely plicated bowel pattern is seen. **F, G:** In an 11-year-old Irish Setter, extensive duodenal and jejunal plication was noted due to a string (arrows). Lu, intestinal lumen.

Hernia and Volvulus

In some instances, the intestines may be displaced and/or trapped in an abnormal location, this can lead to vascular compromise of the incarcerated intestinal segment (Junius et al. 2004). This may happen following a traumatic event or previous surgeries. Displaced intestinal segments can then be seen in the thorax, through the abdominal wall, inguinal ring (Figure 8.23), or perineal region. It is useful to evaluate the affected bowel segments for altered layering, integrity of the wall, and vascular deficit using Doppler mode.

Mesenteric volvulus refers to an abnormal rotation of the mesenteric root resulting in vascular compression and ischemic event of the entrapped intestinal segments. It is important to make the diagnosis quickly as

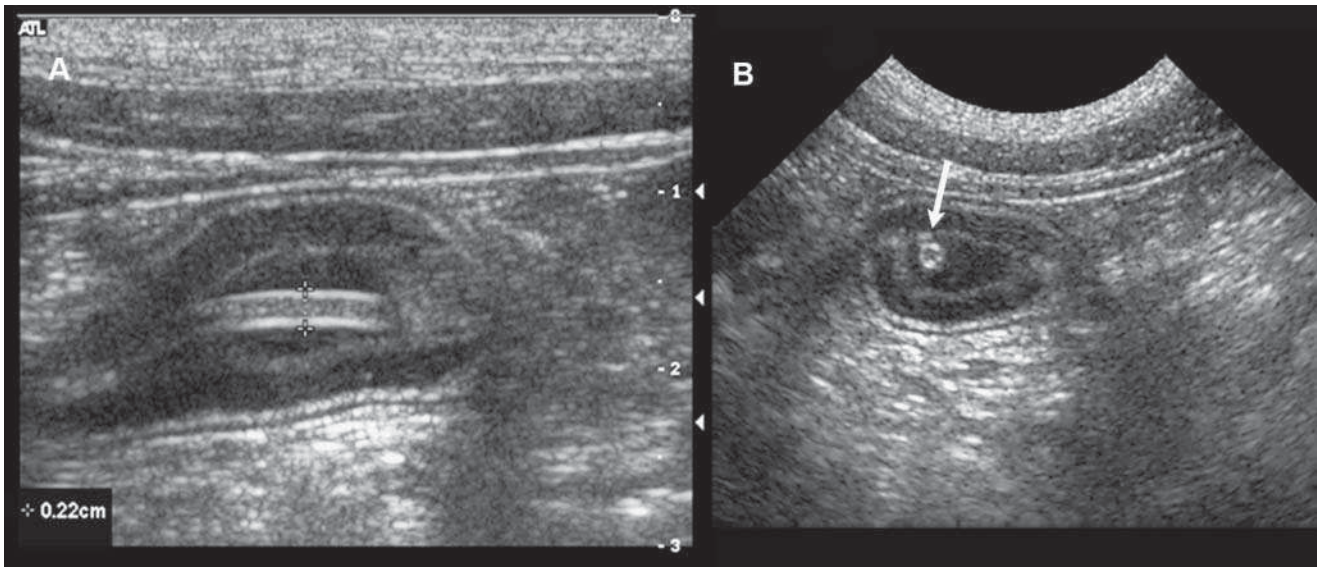


Figure 8.21. Roundworms. Longitudinal **(A)** and transverse **(B)** sonograms of a roundworm in a jejunal segment of a young dog with chronic diarrhea. Several other worms were identified throughout the intestinal tract, in association with fluid accumulation. These worms appear as tubular, double-interfaced, hyperechoic structures (between the cursors and at the arrow) in the lumen of the gastrointestinal tract. During real-time evaluation, the worms can be seen moving if they are alive.

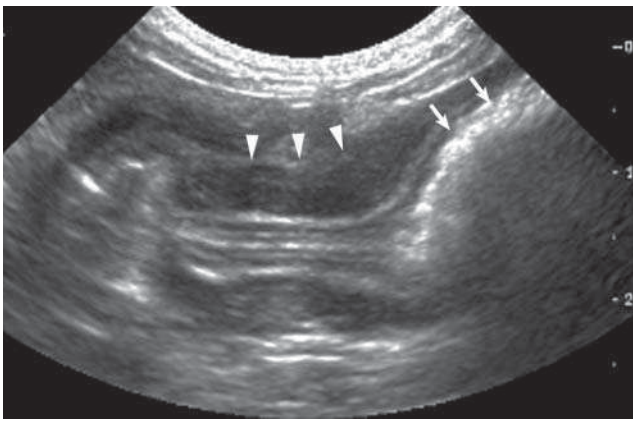


Figure 8.22. Partially obstructive intestinal adenocarcinoma. Foreign material (arrows) accumulated proximal to the focally thickened (arrowheads) jejunal segment. Surgical resection was performed and the histopathological diagnosis was adenocarcinoma.

this represents a surgical emergency. On ultrasound, several intestinal loops may appear moderately distended with gas and fluid and have thickened wall with altered layering. The extent, severity, and length of time of the volvulus can vary, but identifying a mechanical obstruction by observing two populations of bowel diameter is key to expedite the surgical correction. With time, compromised intestinal segments are necrotic and sloughing of the mucosa may lead to thinner intestinal wall and amorphous echogenic contents (Figure 8.24).

Inflammatory Diseases

Wall thickening is a common finding in inflammatory diseases, but this finding is not specific (Rudolf et al. 2005). Symmetry, extent of the wall thickening, and layer identification are useful parameters in distinguishing inflammation from neoplasia (Penninck et al. 2003; Gaschen 2011). Inflammation is usually characterized by extensive and symmetrical wall thickening with visible layering. However, depending on the severity of the inflammation and the presence of wall edema or hemorrhage, layering can be altered, as seen by change in echogenicity or relative thickness of one or more layers.

In **gastritis**, diffuse or localized wall thickening with decreased motility can be identified. Commonly the stomach is collapsed during the ultrasound evaluation, limiting accurate assessment of the wall thickness. In severe gastritis, the wall thickening can be associated with increased echogenicity or decreased visualization of the wall layers (Figure 8.25).

Gastric **ulcers** may be identified as discrete, mucosal defects outlined by hyperechoic microbubbles accumulated at the crater site (Figure 8.26). Hyperechoic speckles representing gas can also be observed in the affected wall. Fluid accumulation and decreased

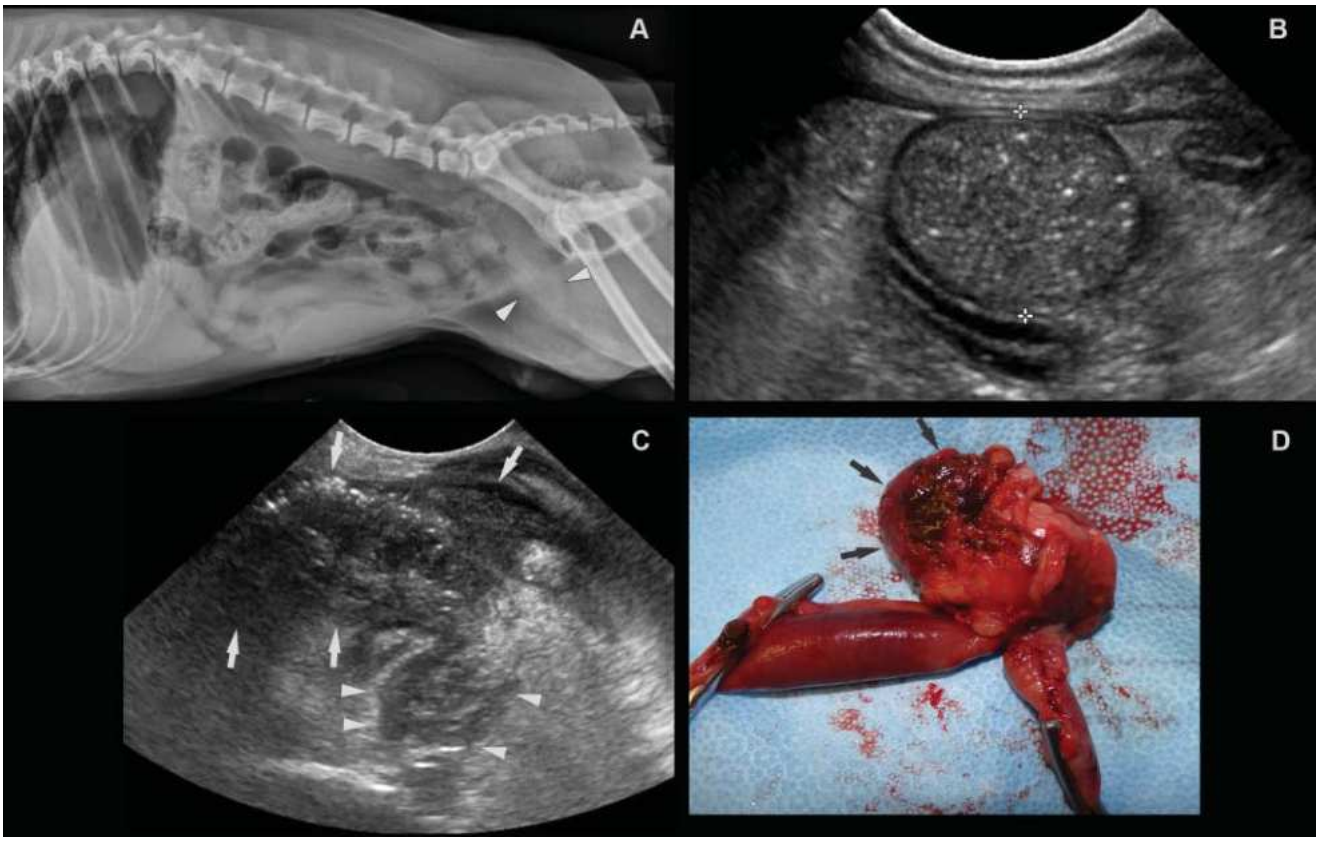


Figure 8.23. **Jejunal segment herniation in an 11-year-old Pomeranian dog with a inguinal swelling. A:** Lateral radiograph showed subtle increased opacity in the caudo-ventral abdomen, with a tubular structure superimposed to the inguinal region (arrowheads). **B:** A dilated jejunal segment (between cursors) compared with an adjacent segment located dorsally to it. **C**: In the inguinal swelling, the dilated jejunal segment (arrowheads) appears to be in continuity with an enlarged structure suspected to represent a necrotic intestinal segment (arrows). The peripheral fat is hyperechoic. **D:** Surgical specimen of the resected jejunal segment found in the inguinal hernia. The wall was confirmed to be necrotic and friable (arrows). Intestinal contents leaked into the hernia.

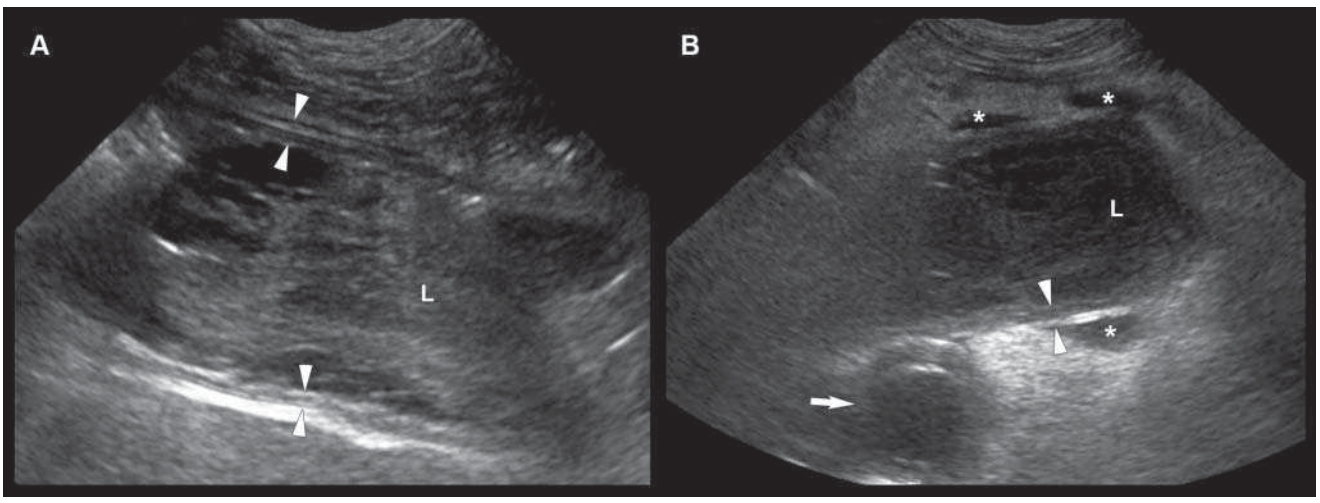


Figure 8.24. **Mesenteric rent and volvulus in a 5-year-old Labrador dog presented for acute vomiting and abdominal pain. A:** Sagittal sonogram of one of several distended jejunal loops. It contains amorphous echogenic fluid in the lumen (L) and the wall (arrowheads) is thin (<2 mm at some locations). **B**: The fat surrounding the bowel loops is hyperechoic, limiting the visualization of the affected intestines. Moderate echogenic effusion (*) is present in the abdomen. A mesenteric volvulus due to a mesenteric rent was diagnosed at surgery and the resected jejunal loops were confirmed to be necrotic and hemorrhagic on histopathological evaluation.

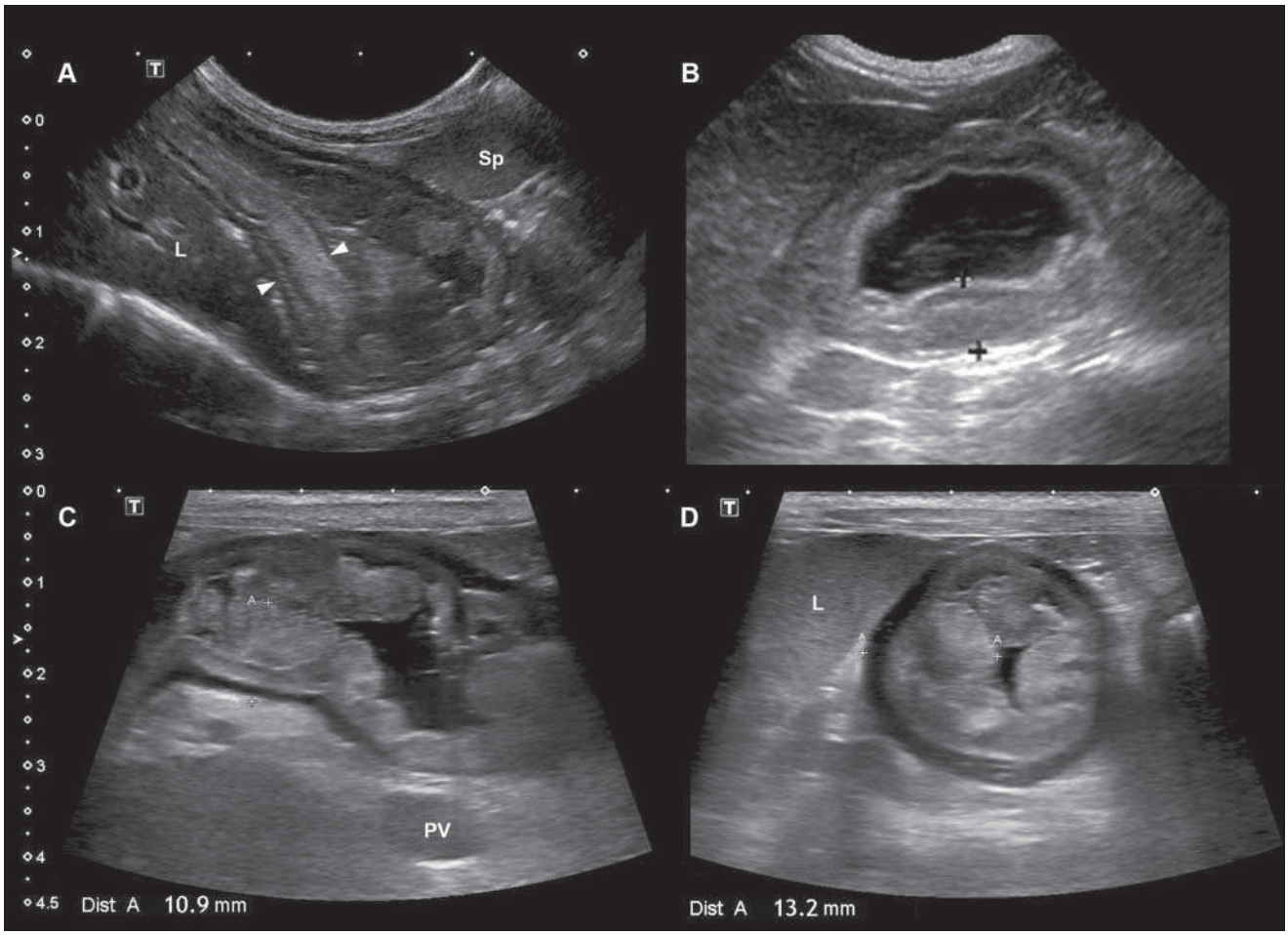


Figure 8.25. **Gastritis. A:** In this 4-year-old Lhasa Apso with acute vomiting, the stomach is mildly dilated with fluid and shows a thickened wall (between cursors) and a hyperechoic mucosa. These signs resolved on follow-up examination 1 week later. L, liver; Sp, spleen. **B:** A moderately thickened (8 mm [cursors]) and hyerechoic wall is noted in this 1-year-old cat with severe chronic ulcerative gastritis. **C, D:** Longitudinal **(C)** and transverse **(D)** images of the gastric body of a 5-year-old, small, mixed-breed dog with chronic vomiting. The wall (between cursors) and more specifically the gastric mucosa are markedly thickened and hyperechoic, forming almost polypoid projections into the gastric lumen. Endoscopic biopsies confirmed severe lymphocytic gastritis with mucosal hyperplasia. L, liver; PV, portal vein.

gastric motility are common findings in ulcerative disease (Penninck et al. 1997). Ulcers can be seen in both inflammatory and neoplastic diseases. As there is often marked focal thickening with loss of layering, the underlying disorder cannot be characterized reliably.

Gastric edema, which is commonly associated with underlying inflammation and ulceration, appears as extensive and moderate thickening with altered layering. The thin inner mucosal hypo- to anechoic layer borders the remaining loosely striated wall (Figure 8.27). Because of the degree of thickening and the disrupted layering, this condition could easily be mistaken for a tumor.

Uremic gastropathy is commonly encountered in patients with chronic uremia. The ultrasonographic features are a moderately thickened gastric wall with prominent rugal folds and a hyperechoic line at the mucosal–luminal interface secondary to mineralization of the mucosa (Grooters et al. 1994) (Figure 8.28).

Common intestinal inflammatory diseases such as lymphocytic-plasmacytic enteritis are associated with mild to moderate wall thickening that most commonly affects several or all intestinal segments with a variable degree of severity. Other intestinal disorders include eosinophilic enteritis, inflammatory bowel disease

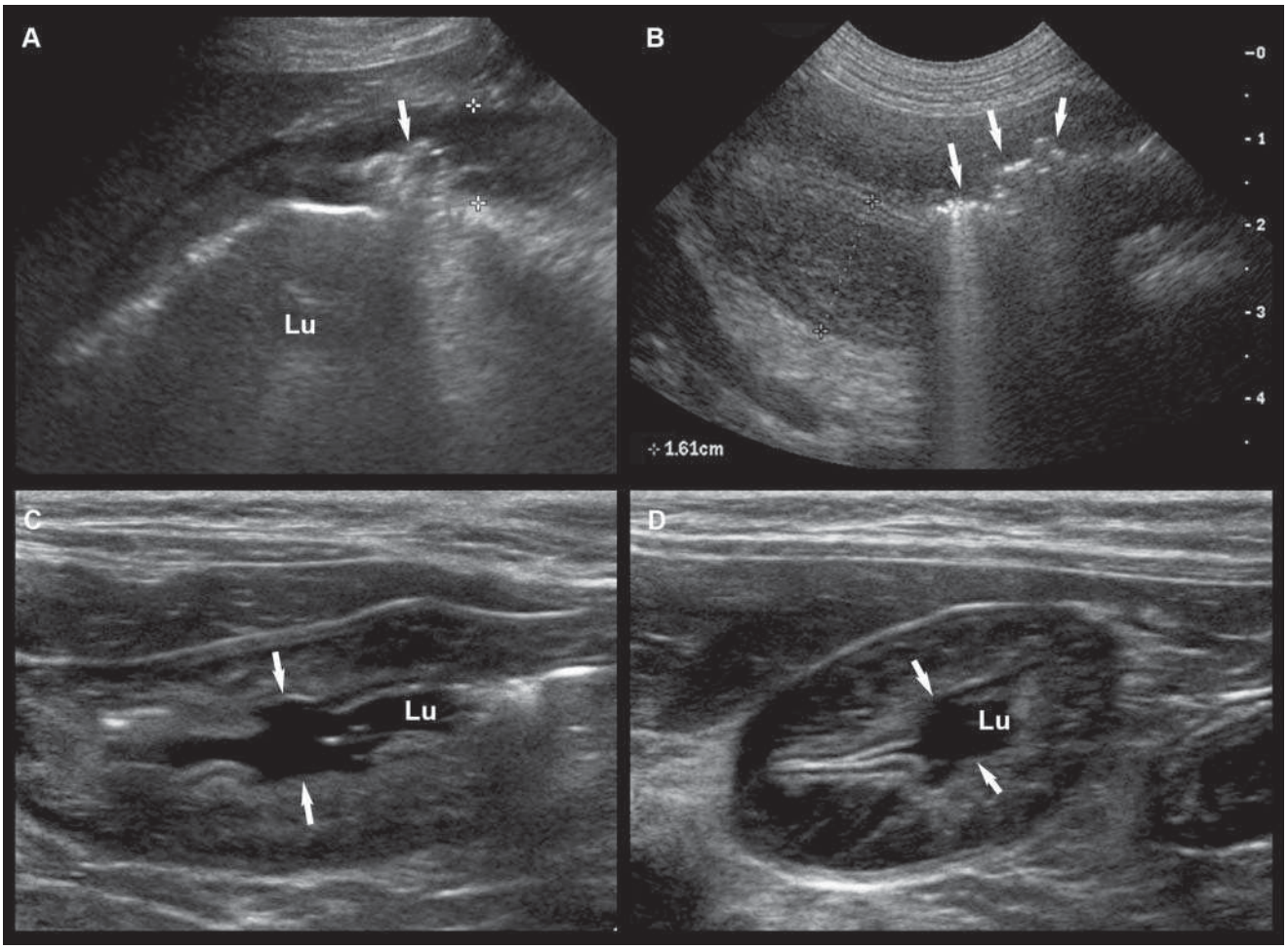


Figure 8.26. **Gastric ulcers.** (for full caption, see facing page)

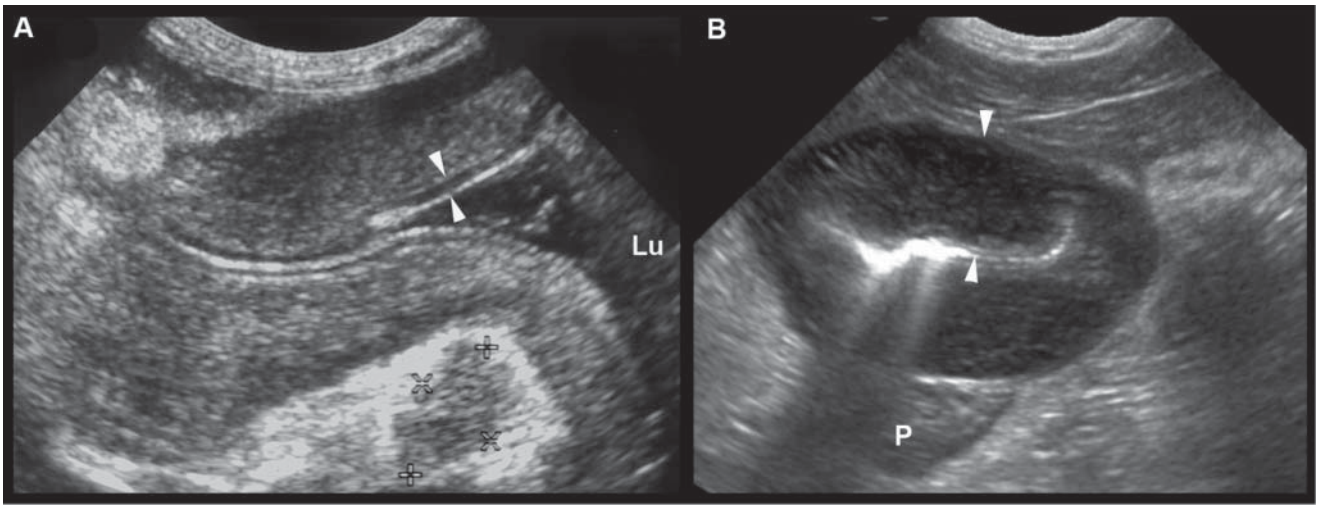


Figure 8.27. **Gastric edema in two dogs. A:** Longitudinal sonogram of the pyloric antrum of a 2-year-old Chihuahua with moderate to severe pyogranulomatous gastritis. Wall edema obliterates the normal wall layering, and only a thin, nearly anechoic band represents the mucosa (arrowheads). A small amount of fluid is in the gastric lumen (Lu). Mild regional lymphadenopathy is noted (cursors). **B:** Transverse sonogram of the moderately thickened and edematous gastric wall (arrowheads) of a 5-year-old cocker with anuric renal failure. Hyperechoic foci associated with a mixture of shadowing and reverberation are present in the lumen. P, pancreas.

Figure 8.26. **Gastric ulcers. A:** Marked focal gastric wall thickening (between cursors) with loss of layering is noted in this 8-year-old Boxer. Within the thickest portion of the wall is a central crater (arrow). The wall measures 1.4 cm. Lu, lumen. **B:** Hyperechoic speckles (arrows), consistent with gas, are found in the thickened wall of this dog with uremic gastritis and ulcerations. The layers are ill-defined. The edematous wall opposite the ulceration reaches 1.6 cm in thickness (between the cursors). **C:** Sagittal sonogram of the stomach of a Siamese cross with extensive gastric ulcer and edema. A small amount of echogenic fluid is seen in the gastric lumen (Lu). The wall is thickened and there is clear interruption of the mucosal layer, on its side of the lumen. The arrows point to the ulcer site. **D:** Transverse sonogram of the stomach of the same cat seen in **C**.

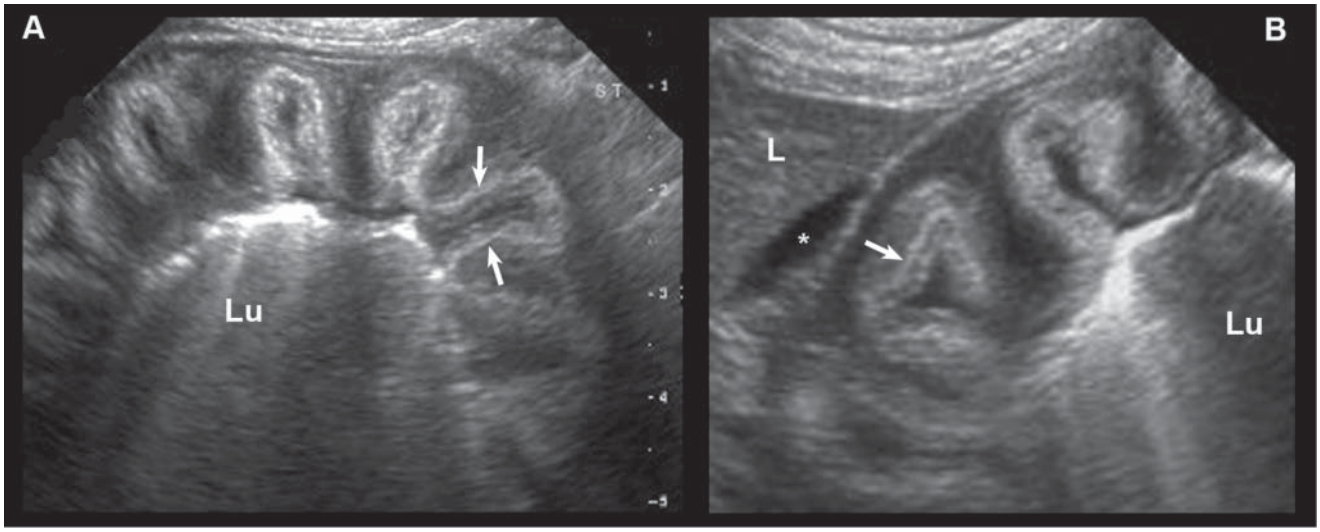


Figure 8.28. **Uremic gastropathy. A:** Uremic gastropathy is seen in dogs or cats suffering from chronic uremia. Thickening of the wall with a hyperechoic line (arrows) along the gastric mucosa and mineralization at the mucosal–luminal interface are common findings. **B:** Enlarged view of the gastric wall changes. A scant amount of effusion (*) is present between the liver and stomach. L, liver; Lu, lumen.

(IBD), granulomatous enteritis, lymphangiectasia, and food allergies. In these disorders, mild to moderate wall thickening can affect primarily the mucosa, the submucosa, and/or the muscular layer. In the mucosa, the changes can be diffuse increased echogenicity of the mucosa, echogenic mucosal speckles, hyperechoic striations, or hyperechoic line paralleling the lumen. Increased mucosal echogenicity and mucosal speckles have been described in lymphocytic-plasmacytic enteritis (Baez et al. 1999; Penninck et al. 2003). However, mucosal speckles can also be encountered in dogs that have been recently fed; in these cases, the speckles disappear at the end of digestion (Figure 8.29). In some cases, a discrete hyperechoic border is noted on the luminal margin of the mucosa; this finding has anecdotally resolved over time in dogs initially presented for acute GI signs (Figure 8.30). Also, Peyer's patches in the descending duodenum may become prominent in dogs with transient GI signs (Figure 8.29C). A hyperechoic line of variable thickness, present within the mucosa, can often be encountered with the newer high-resolution transducers; this line has been reported to represent fibrosis, which may or may not be associated with concurrent inflammatory condition (Penninck et al. 2010) (Figure 8.30A). The possibility of this line representing visible lymphatic vessels has also been presented (Pollard et al. 2013).

Linear hyperechoic lines within the mucosa and aligned perpendicularly to the lumen axis most likely represent dilated lacteols (Figure 8.31). This finding is commonly associated with protein-losing enteropathy and lymphangiectasia, and occasionally this pattern can be associated with diffusely infiltrative tumors such as histiocytic sarcoma (Sutherland-Smith et al. 2007).

Primary submucosal thickening can be seen in various inflammatory disorders, but can be especially pronounced in parasitic infections (Kvitko-White et al. 2011). Parasites such as Heterobilharzia americana can affect dogs but the infestation may be sub-clinical (Figure 8.32).

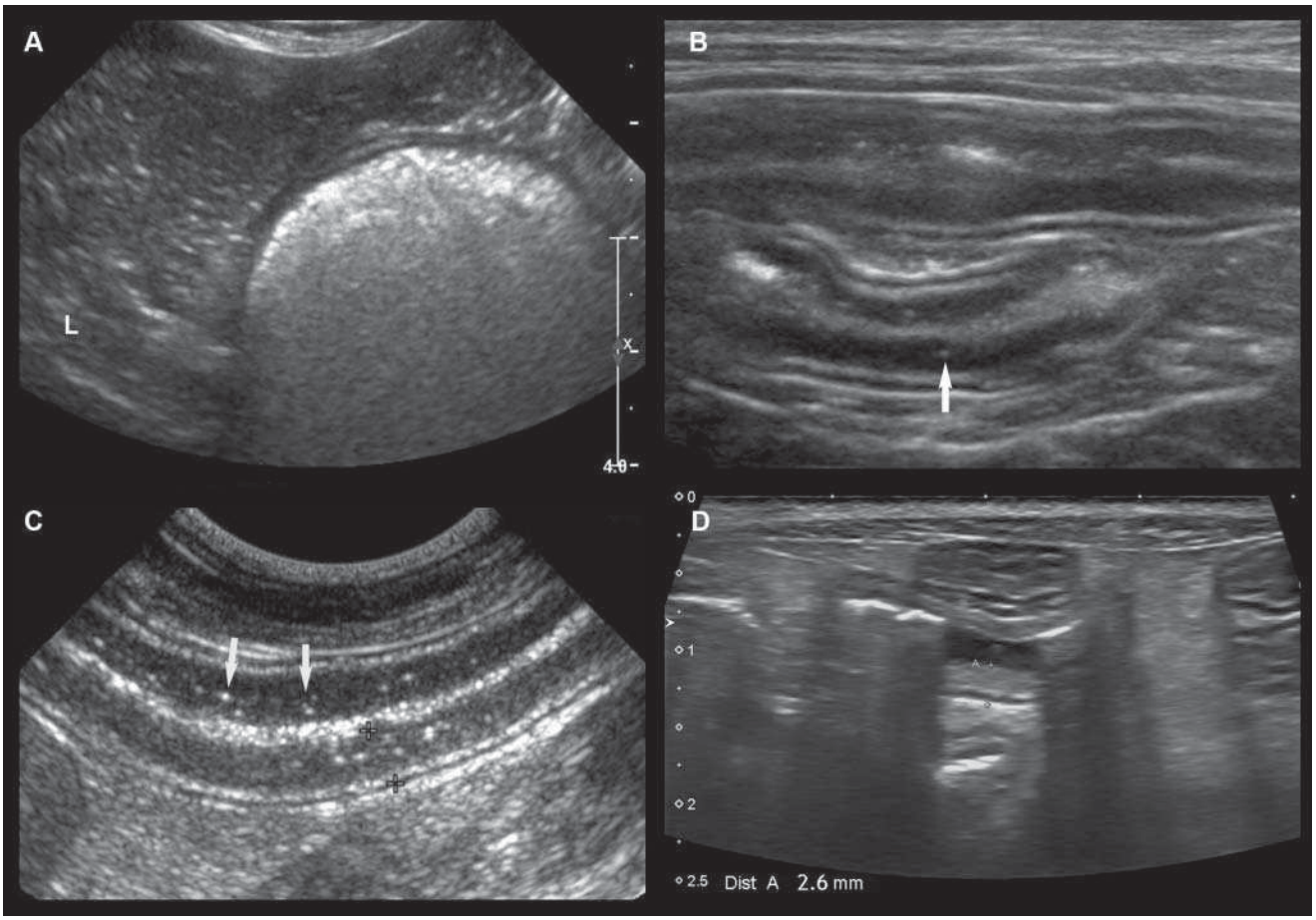


Figure 8.29. **Mucosal changes. A:** Stomach filled with food of a dog after meal ingestion. L, liver. **B:** A couple of hours later, mucosal speckles (arrow) are present in several small intestines while they were absent on the pre-prandial evaluation. **C:** Longitudinal sonogram of a mildly thickened jejunal segment of a dog with lymphocytic-plasmacytic enteritis. Several bright speckles (arrows) are unevenly distributed within the prominent mucosal layer, but the wall layers can still be identified. **D:** In a cat with acute enteritis, several intestinal segments were thickened, hypermotile, and partially fluid-filled. The wall layers were visible, but the mucosa appeared hyperechoic.

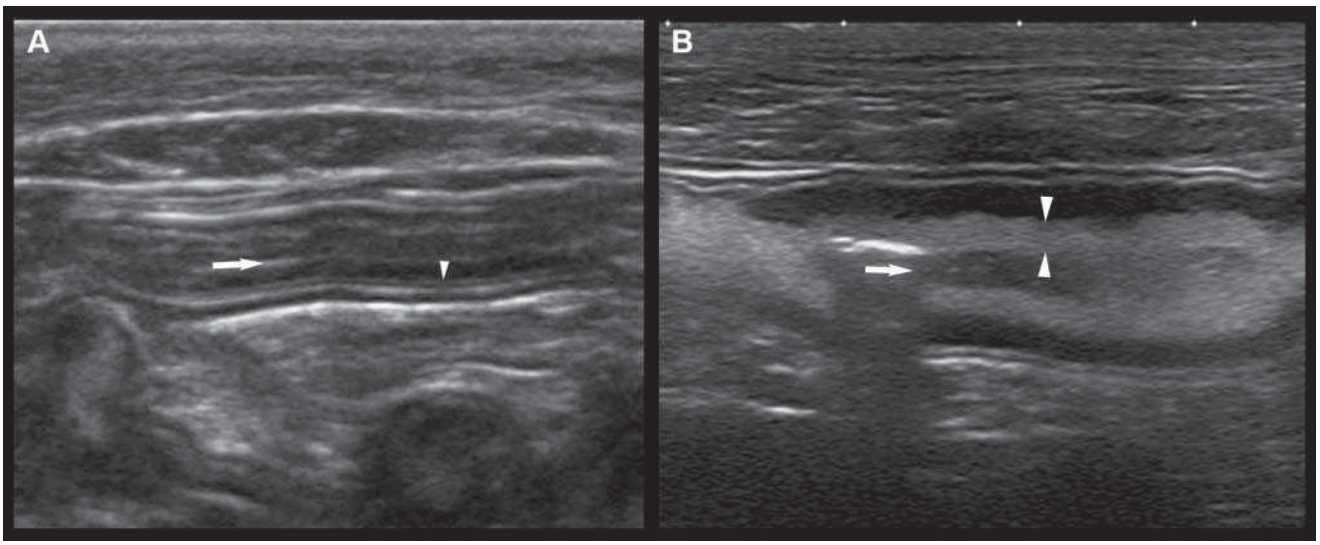


Figure 8.30. **Mucosal line parallel to the lumen.** (for full caption, see facing page)

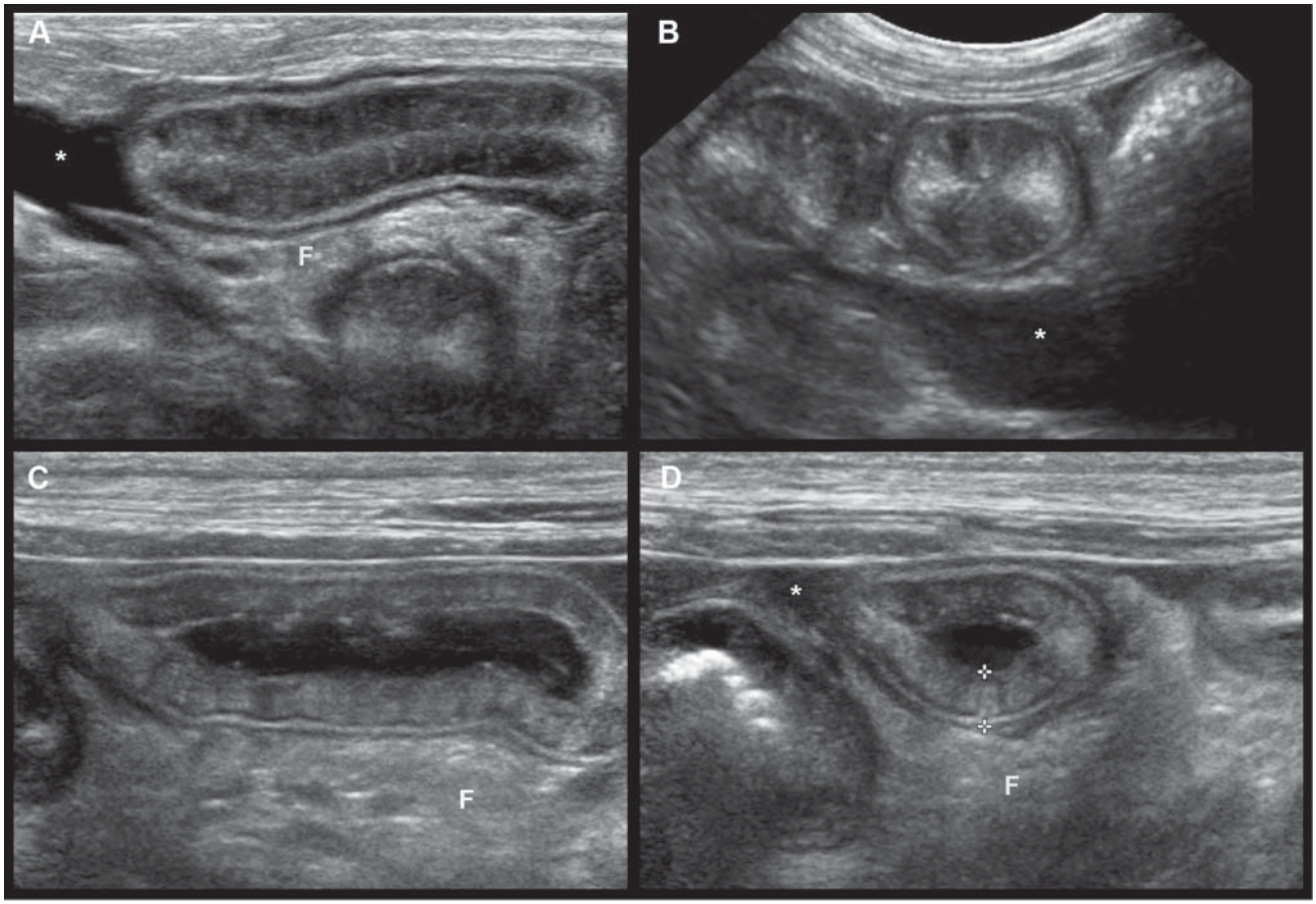


Figure 8.31. **Mucosal hyperechoic striations.** Longitudinal **(A)** and transverse **(B)** sonograms of thickened jejunal segments with hyperechoic linear striations within the mucosal layer of a 5-year-old French Bulldog. The striations represent dilated lacteals. This dog had a long history of irritable bowel syndrome. Peritoneal effusion is present (*). **C, D:** Similar but more severe findings are present in this 9-year-old Jack Russell Terrier presented with protein-losing enteropathy. Note the thickened and hyperechoic adjacent fat (F), often present in these cases.

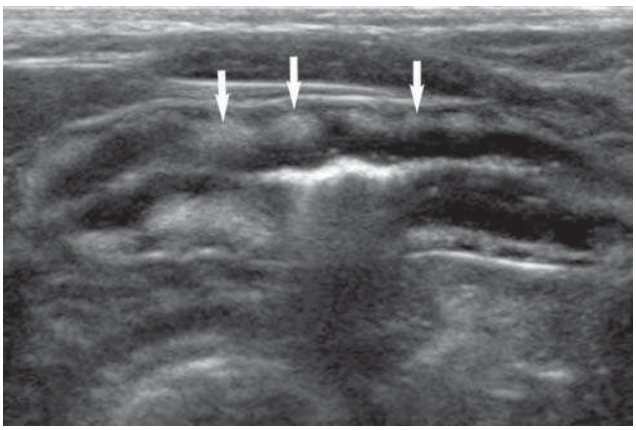


Figure 8.32. **Submucosal change.** There is nodular thickening of the submucosa (arrows) of most intestinal loops in this Dachshund with parasitic infestation (Heterobilharzia americana). The dog had no clinical signs.

Figure 8.30. **Mucosal line parallel to the lumen. A:** A fine hyperechoic line (arrowhead) near the submucosa is paralleling the lumen (arrow) of this jejunal segment in a cat without gastrointestinal sign. This line likely represents fibrosis. **B:** A thick hyperechoic band (arrowheads) is noted on the luminal side of the mucosa of several jejunal segments in this dog presented for acute vomiting and diarrhea. On the ultrasound recheck performed several weeks later, the band was no longer visible. The arrow points to the lumen.

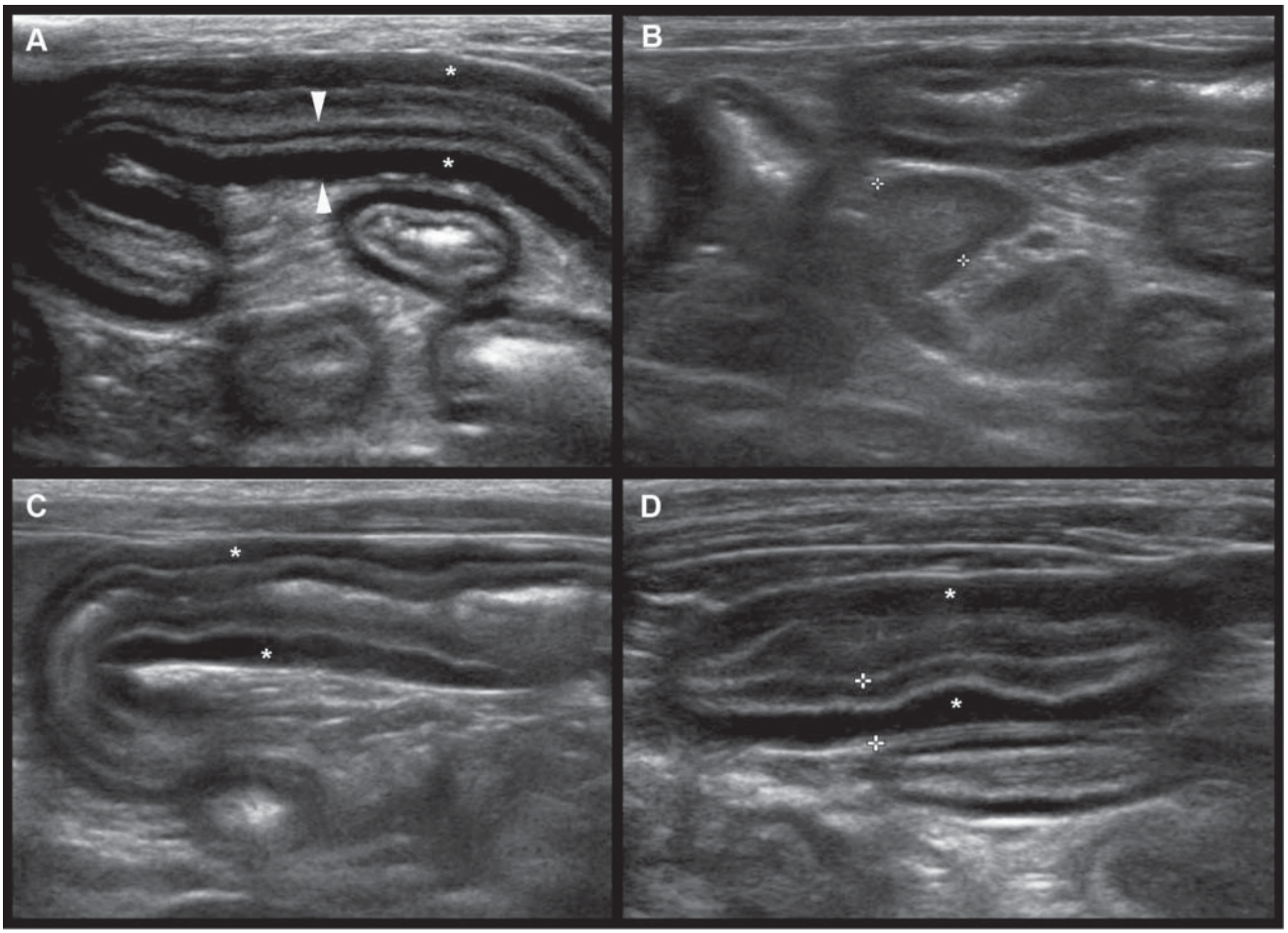


Figure 8.33. **Intestinal wall muscular thickening.** (for full caption, see facing page)

Smooth muscle thickening is reported in eosinophilic enteritis, particularly in cats (Tucker et al. 2014), but this finding is not specific and can also be present in other disorders, such as mechanical obstruction secondary to foreign material, IBD or tumoral infiltration (Penninck 2002; Diana et al. 2003; Zwingenberger et al. 2010; Daniaux et al. 2014) (Figure 8.33).

In hemorrhagic enterocolitis, unlike most of the inflammatory disorders we have just described, there is thinning of the wall, as the combined result of atonic, fluid-filled intestinal segments and sloughing of the mucosa (Figure 8.34). This has been specifically described in young dogs affected with parvoviral enteritis (Standler et al. 2010).

Corrugation of the small bowel appears as regular and symmetrical undulations of the wall, but the serosa remains relatively linear (Figure 8.35). This non-specific finding can be associated with regional inflammation, such as enteritis, pancreatitis, peritonitis, abdominal neoplasia, or bowel ischemia (Moon et al. 2003). This should not be mistaken

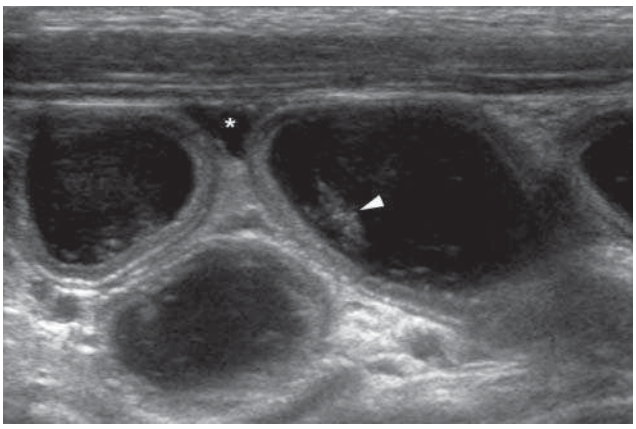


Figure 8.34. **Hemorrhagic enterocolitis in a 8-month-old English Pointer with acute abdominal pain.** The jejunal segments are fluid-filled, atonic and the wall thickness is 1.3 mm. Amorphous echogenic material (arrowhead) representing sloughed mucosa and/or blood clot is present in the lumen. A small amount of effusion (*) is present.

Figure 8.33. **Intestinal wall muscular thickening. A, B:** A 5-year-old cat with marked lymphoplasmacytic enteritis. The intestinal wall is thickened (3.5 mm, arrowheads)), especially the muscular layer (*). The jejunal lymph nodes are mildly enlarged (7 mm, between cursors). **C, D:** An 8-year-old cat with a jejunal mass confirmed to represent feline eosinophilic sclerosing fibroplasia (see Figure 8.68B). Numerous thickened (arrowheads) intestinal segments have hypertrophic muscular layers (*) of variable thickness. Notice the slight variation in appearance of the mucosa and submucosa in jejunal loops.

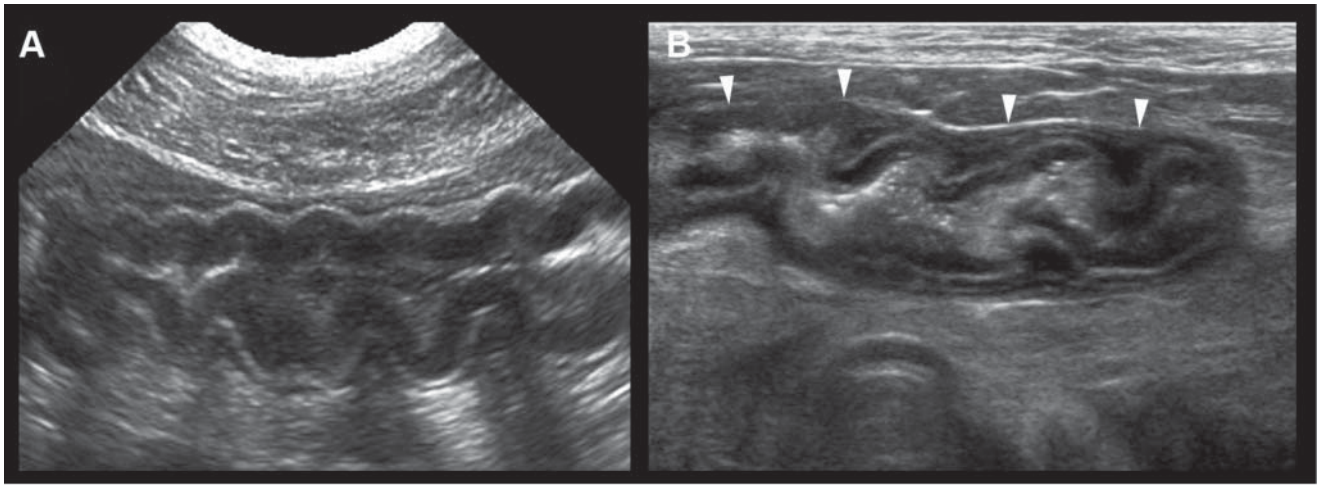


Figure 8.35. **Bowel corrugation. A:** Several corrugated bowel segments are present in this 5-year-old Weimaraner. Chronic peritonitis secondary to multifocal perforation of the jejunum was present at surgery. **B:** Similar corrugation is seen in this jejunal segment of a 10-year-old Yorkie with protein-losing enteropathy. Note the that the serosal contour (arrowheads) is straight relative to the other layers.

for intestinal plication, which causes asymmetrical undulation of bowel walls (see Figure 8.20).

In cases of severe inflammatory changes encountered with lymphoplasmacytic, eosinophilic, or granulomatous enteritis (fungal, parasitic, or post-traumatic), edema, hemorrhage, and fibrosis can severely disrupt the wall layering and be associated with mass lesions suggestive of a tumoral process (see section on non tumoral mass). Inflammation, such as pancreatitis and duodenitis, can also be caused by regional extension of affected adjacent tissue (Figure 8.36).

Cecal inflammation called **typhlitis** appears as poorly echogenic or nodular thickening of the cecal wall (Taeymans et al. 2011) (Figure 8.37). Ultrasound recheck is helpful in assessing response to treatment, especially as these changes may be similar in round-cell infiltrates.

Colonic inflammatory changes may be subtle, such as mild thickening of the wall with the presence of discrete small submucosal hypoechoic nodules, which are speculated to represent intraparietal reactive lymphoid follicles (Citi et al. 2013) (Figure 8.38A). Redundancy of the folds resulting in wall thickening but still visible wall layering may represent wall edema (Figure 8.38C,D). In ulcerative colitis, the luminal mucosal border is irregular because of the numerous small superficial ulcers affecting the mucosa (Figure 8.38 E,F).

Gas dissection within the wall, or pneumatosis, can be seen at any segment of the gastrointestinal tract. This finding is of unclear clinical significance, and in presence of GI clinical signs, the authors recommend following up the changes that usually resolve within 1 month (Figure 8.39).

Parasitic infestations such as peritoneal cestodiasis are rare. Cystic subserosal lesions have been found on the GI tract of affected dogs or cats (Venco et al. 2005) (Figure 8.40).

Postoperative Changes, Perforation and Dehiscence

In postoperative enterotomy or enterectomy, the surgical site can be identified by the regular alignment of sutures, which appear as small bright interfaces along or around the bowel, depending on the choice of surgical procedure (Matthews et al. 2008) (Figure 8.41). Focal thickening of the bowel with loss of layering is

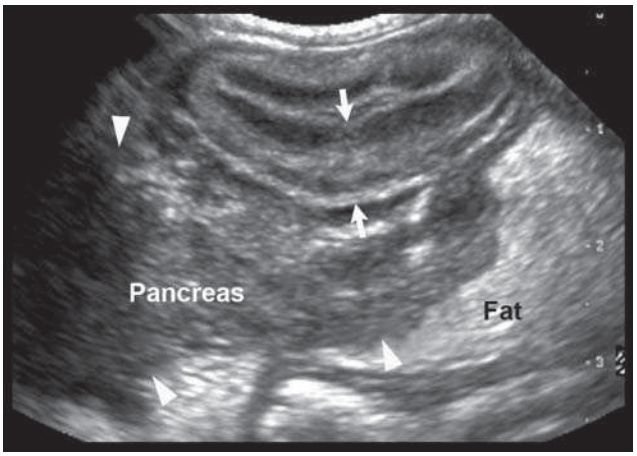


Figure 8.36. Duodenitis and pancreatitis in a dog. The duodenum is thickened, and the wall layering appears affected but still visible (arrows). The adjacent right limb of the pancreas is enlarged and hypoechoic (arrowheads). Hyperechoic mesenteric fat outlines the margins of the inflamed pancreas.

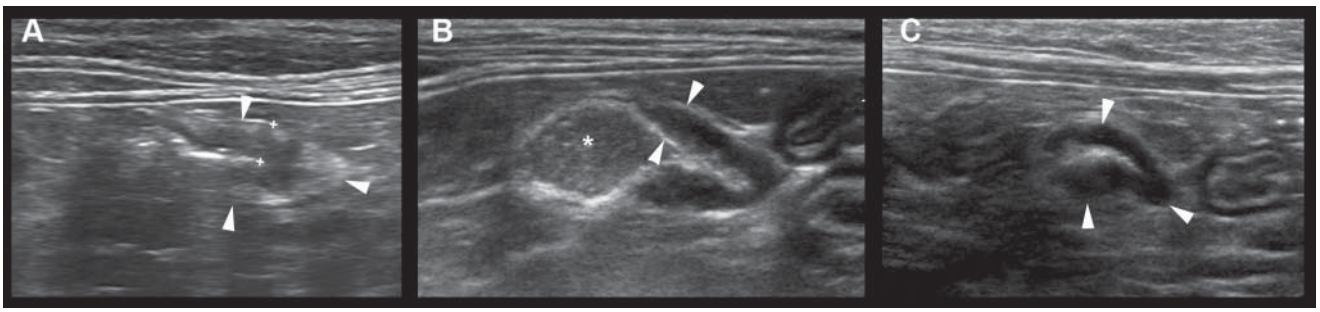


Figure 8.37. Inflammatory cecal changes in cats. A: In this cat presented for vomiting, the thickened (2 mm) cecal wall (between cursors) has a slightly nodular appearance. Arrowheads point to the delimitations of the cecum. No other gastrointestinal (GI) abnormalities were identified. Weeks later, the cecal changes resolved and the cat was asymptomatic. **B:** In this 1-year-old Siamese cross, the cecal wall (arrowheads) is thickened (3 mm) and hypoechoic. Worms were noted in the small intestines. Echogenic fluid is noted in the adjacent colon (*). This change resolved over time. **C:** A 12-year-old cat with 3 days of vomiting has a thickened and hypoechoic cecal wall (arrowheads delineating the cecum). The adjacent (not shown) colic lymph nodes were hypoechoic and rounded. In the absence of any other GI changes, these features support typhlitis and a recheck ultrasound is recommended. Notice that in these three cases of cecal inflammation, the cecum maintains its overall shape.

commonly seen, and can partially resolve over time (Mareschal et al. 2010). Postoperative dehiscence can be challenging to diagnose ultrasonographically, as free fluid and gas are expected to be present and these features are hallmarks of perforation as well. However, the presence of fluid trapped near the enterectomy site and possible thinning of the wall at the site can support dehiscence (Figure 8.42). Sampling the free fluid and the entrapped fluid collection may be useful.

In perforation secondary to foreign-body migration (Figure 8.43), deep ulceration, or postoperative dehiscence, the affected wall is thickened and can be hypoechoic, with focal loss of layering (Boysen et al. 2003). At times, a hyperechoic tract can be seen crossing the wall, and the adjacent mesentery is significantly increased in echogenicity because of focal steatitis or peritonitis (Figures 8.43, 8.44). Fluid accumulation can often be seen near the perforation or dehiscence site, and free peritoneal gas can sometimes be detected as short, bright, linear interfaces in the most upper portion of the abdomen and be associated with comet-tail artifacts (Figures 8.43B, 8.44B). In septic peritonitis, the free abdominal fluid is often echogenic (Figures 8.19D, 8.45).

At times, a stricture can be seen at a previous enterotomy or enterectomy site. Abnormal fluid, gas, or food accumulation is then noted proximal to the stricture site (Figure 8.46B).

A fluid pocket representing a sterile seroma may accumulate near or at a recent surgical or ultrasound-guided biopsy site (Figure 8.47). This is a rare and transient complication of surgical intestinal biopsies.

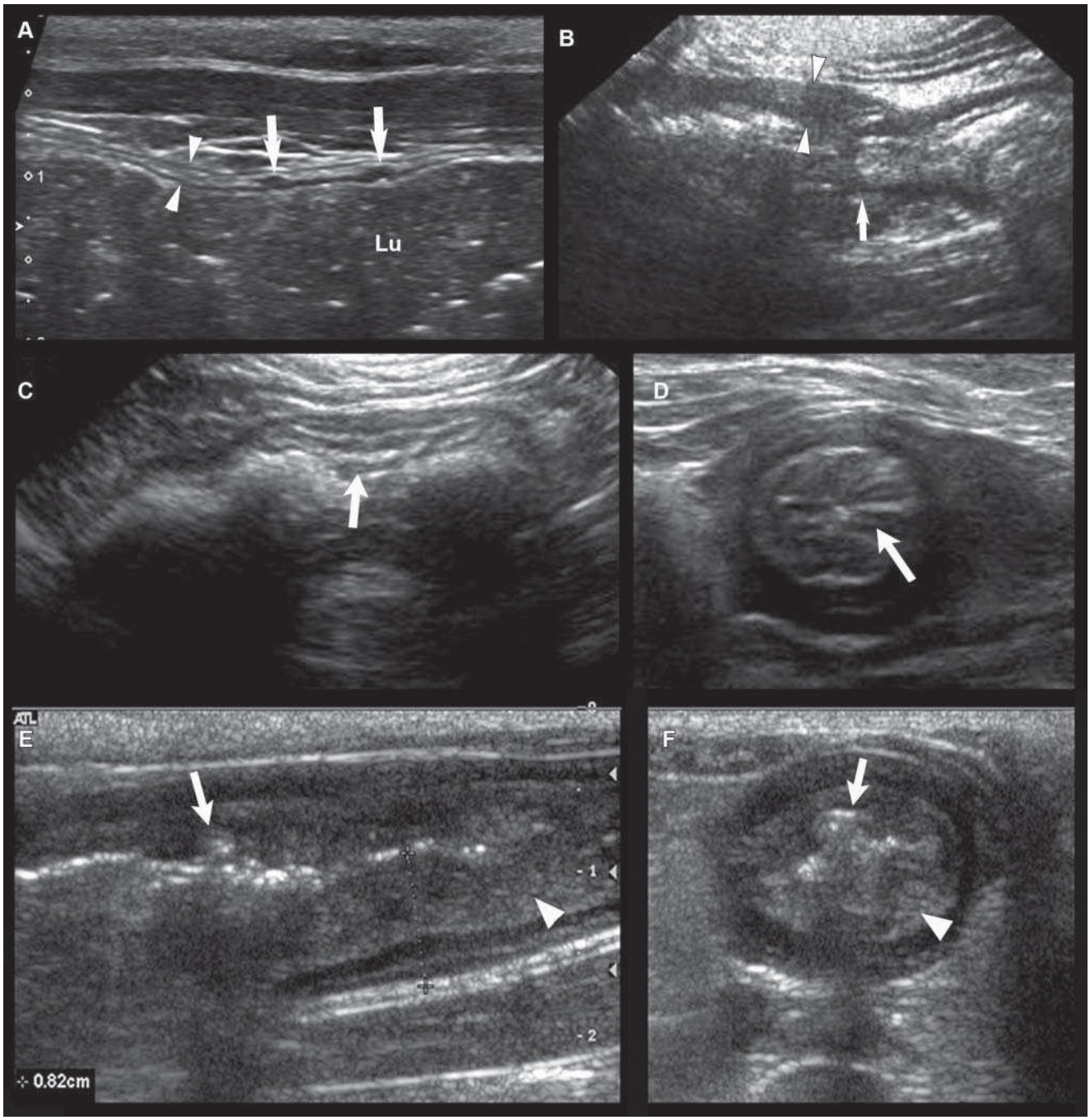


Figure 8.38. **Inflammatory colonic changes. A:** Sagittal sonogram of the colonic wall (between arrowheads) of a cat with diarrhea. Several small hypoechoic nodules (arrows) are present within the submucosa. These changes resolved after medical management. **B:** Sagittal sonogram of the ileocecocolic junction of a dog with parasitic (hookworm) colitis. The wall is circumferentially thickened (arrowheads), and the wall layering is lost at the junction between the ileum and cecum and/or colon (arrow). **C, D:** Colonic wall redundancy can be seen in this cat presented for obstipation. Numerous folds can be identified (arrows) on the longitudinal **(C)** and transverse **(D)** planes. **E, F:** Longitudinal **(E)** and transverse **(F)** sonograms of a segment of the descending colon in a cat with severe ulcerative colitis. The wall is diffusely, severely thickened, especially the mucosa. This mucosa is hyperechoic (arrowheads) and presents irregular, hyperechoic, crater-like lesions consistent with ulceration (arrows). The mucosal surface is irregular in the rest of the segment, also consistent with erosions.

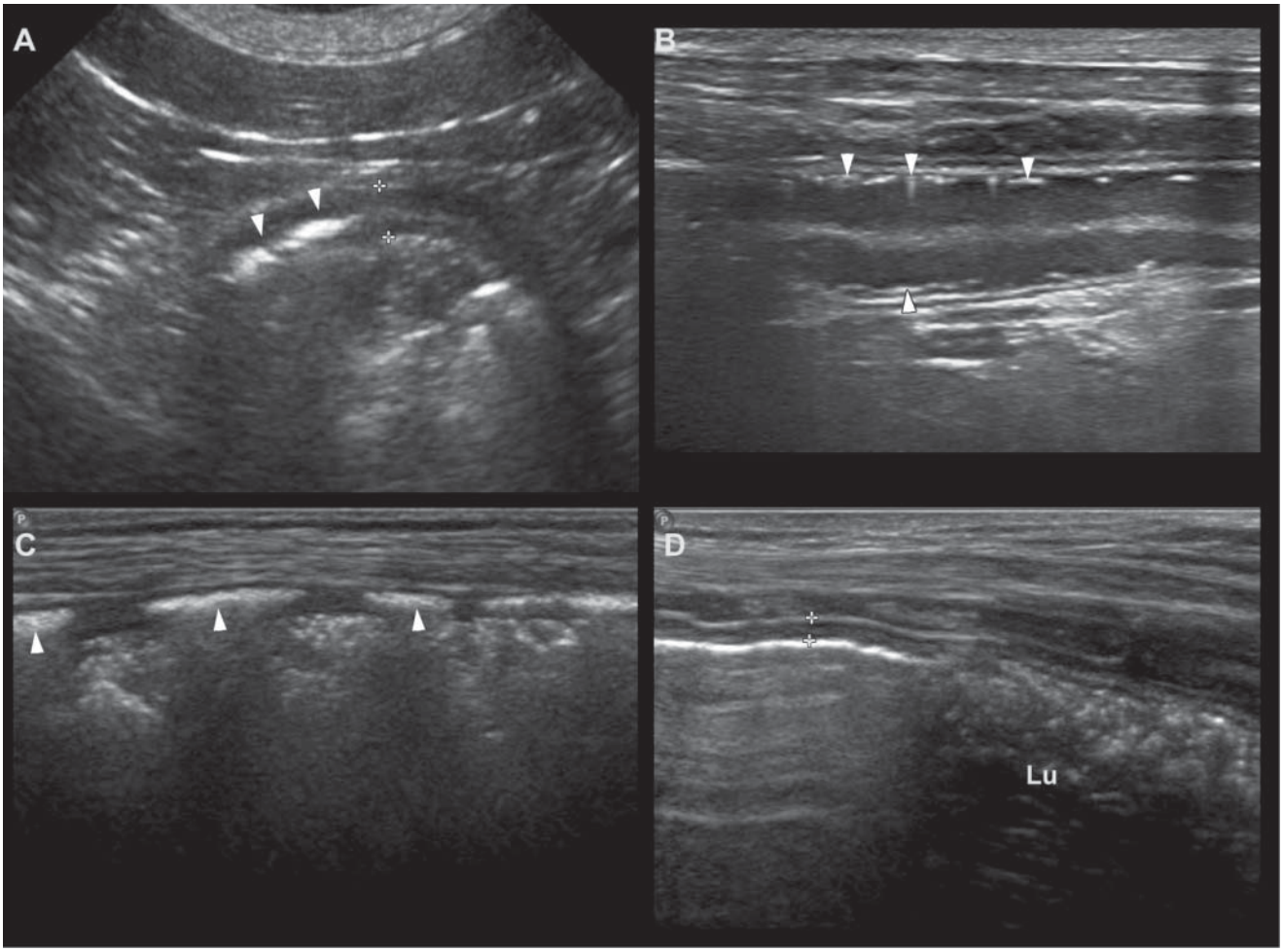


Figure 8.39. **Gastrointestinal pneumatosis.** Gas can be seen dissecting any segment of the gastrointestinal (GI) tract. Examples of gas dissecting (arrowheads) the gastric wall **(A)**, the duodenal wall **(B)**, and the colonic wall **(C). D:** the recheck ultrasound of the colon in the dog presented in **C** showed a normal colonic wall, 3 weeks after the initial pneumatosis coli was detected.

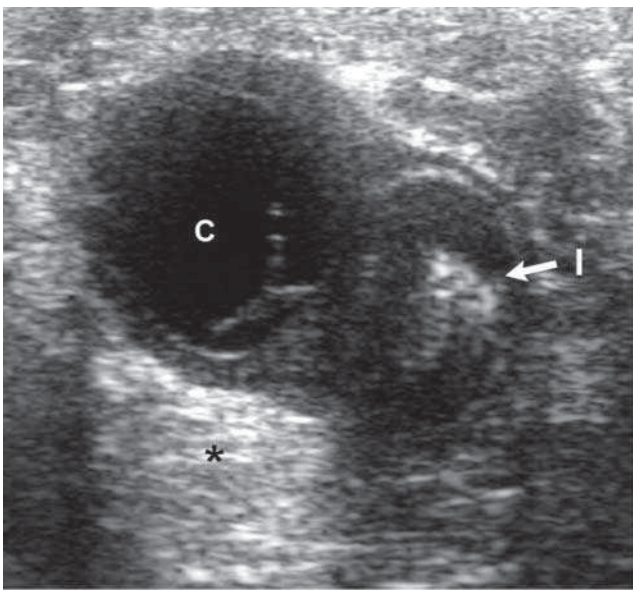


Figure 8.40. **Peritoneal cestodiasis.** Transverse sonogram of an intestinal segment (I) in a 6-year-old mixed-breed dog with a round, anechoic cystic lesion (C) associated with the serosal surface. Far (*) enhancement is noted beyond the hypoattenuating fluid as a hyperechoic band. Image reprinted with permission (Venco et al. 2005).

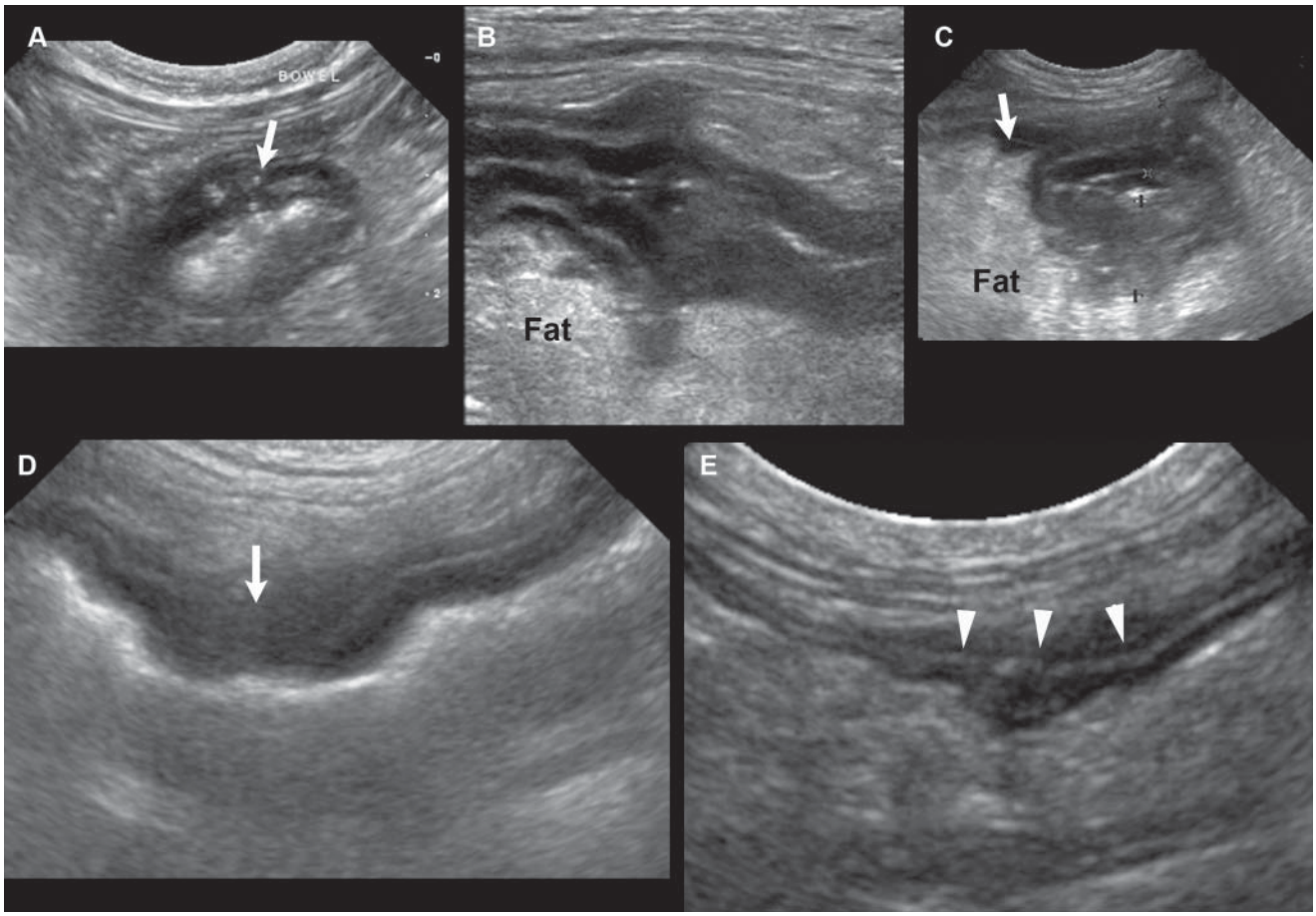


Figure 8.41. **Postoperative enterotomy. A:** Normal immediate postoperative sonogram of an enterotomy site in a dog. The sutures appear as discrete, small, bright interfaces (arrow). **B, C:** Longitudinal **(B)** and transverse **(C)** planes obtained at the site of anastomosis. The wall layering is disrupted, and the wall margins are deformed (between the cursors). Free gas and free fluid (arrow) are commonly encountered. The surrounding fat is hyperechoic. **D:** Several days later, the wall layering remains disrupted (arrow) in this longitudinal sonogram. **E:** Several weeks after surgery, despite a persistent focal thickening, the submucosa layer can be seen crossing the previous surgical site (arrowheads) in this dog with no gastrointestinal signs.

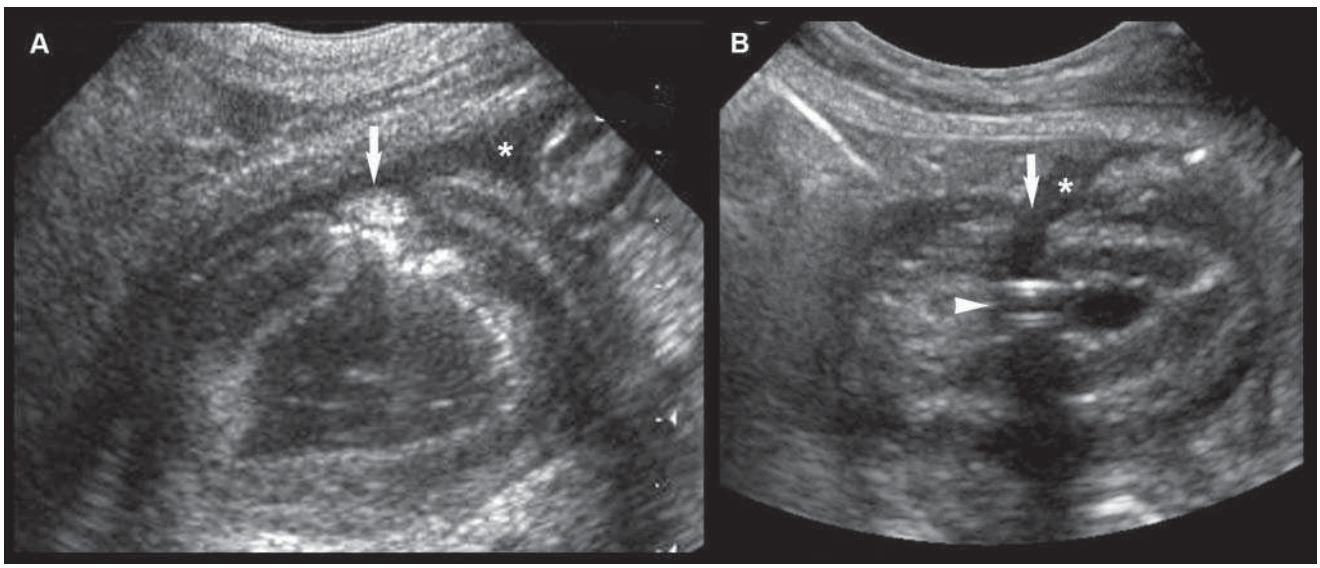


Figure 8.42. **Intestinal dehiscence. A:** There is dehiscence at the duodenal suture site in this 4-year-old Jack Russell Terrier. Fluid accumulation (*) and bright hyperechoic fat are centered at the dehiscence site. Discontinuity of the duodenal wall is identified (arrow). **B:** Transverse sonogram of the proximal descending duodenum of a 9-year-old Poodle with dehiscence as evidenced by the disruption of the wall (arrow). An arrowhead points to a stent (recently placed in the duodenal papilla because of extrahepatic biliary obstruction). Abdominal effusion (*) is also present.

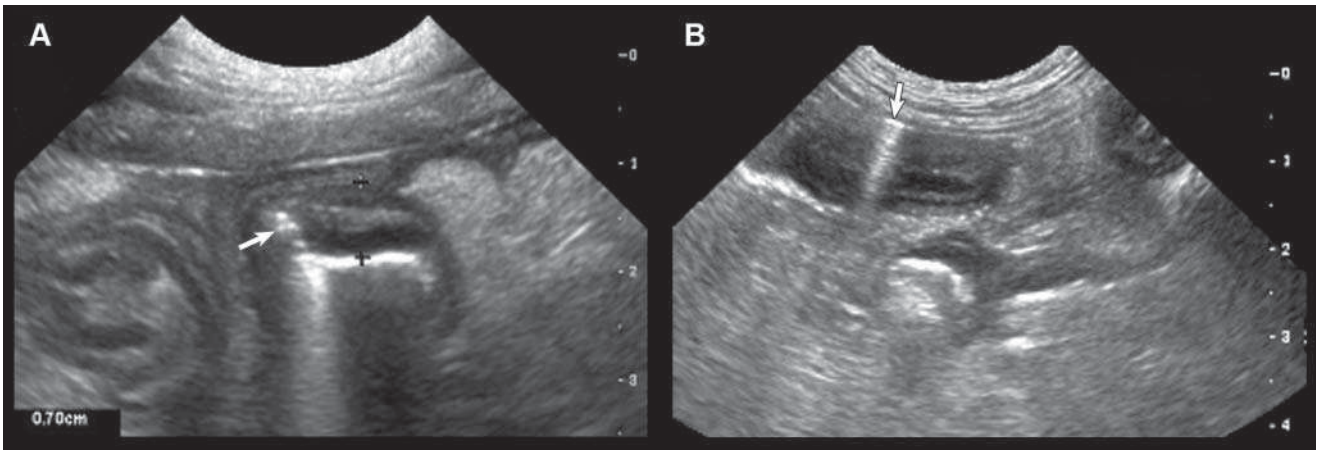


Figure 8.43. **Intestinal perforation. A:** A jejunal perforation secondary to foreign bodies (hairpins) was surgically confirmed in this 5-year-old Weimaraner. A hyperechoic gas tract (arrow) dissects the focally thickened jejunal segment (between the cursors). **B:** Free gas (arrow) and a moderate amount of echogenic fluid (not seen on this image) in the abdomen indicate perforation.

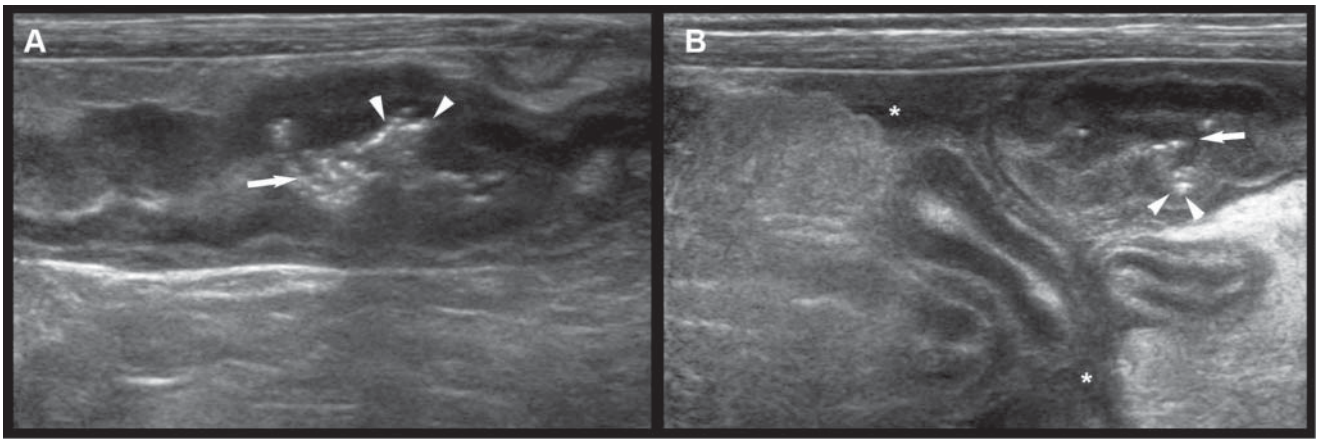


Figure 8.44. **Perforating ulcers.** Numerous enteric ulcerations are present in this 15-year-old Miniature Pinscher. The fat adjacent to the perforation site is hyperechoic, indicative of focal steatitis or peritonitis. Echogenic fluid is present in the abdomen (*). The arrows point to the lumen. On histopathology, there was diffuse histiocytic sarcoma in the small intestines (see also Figure 8.64).

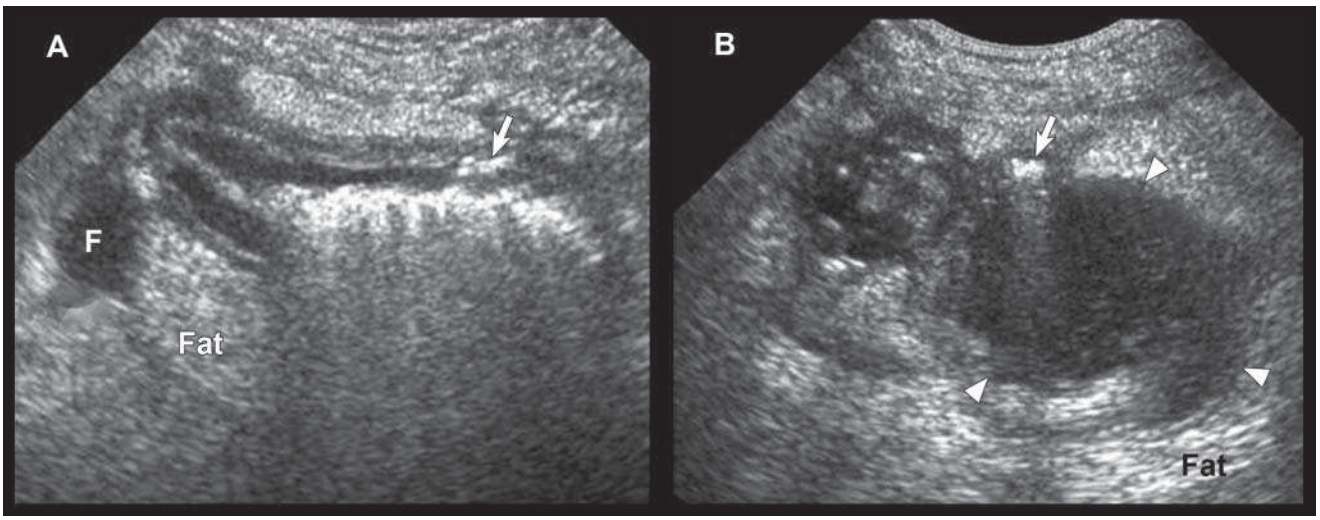


Figure 8.45. **Intestinal perforation and peritoneal abscess.** This 11-year-old English Setter had a septic abdomen. **A:** A hyperechoic tract dissects the bowel wall (arrow). Peritoneal fluid (F) is noted and the mesenteric fat is hyperechoic. Free gas (arrow) is noted. **B:** A localized fluid pocket representing an abscess cavity (arrowheads) is near the perforation site (arrow). At surgery, the perforation, local abscessation, and peritonitis were confirmed.

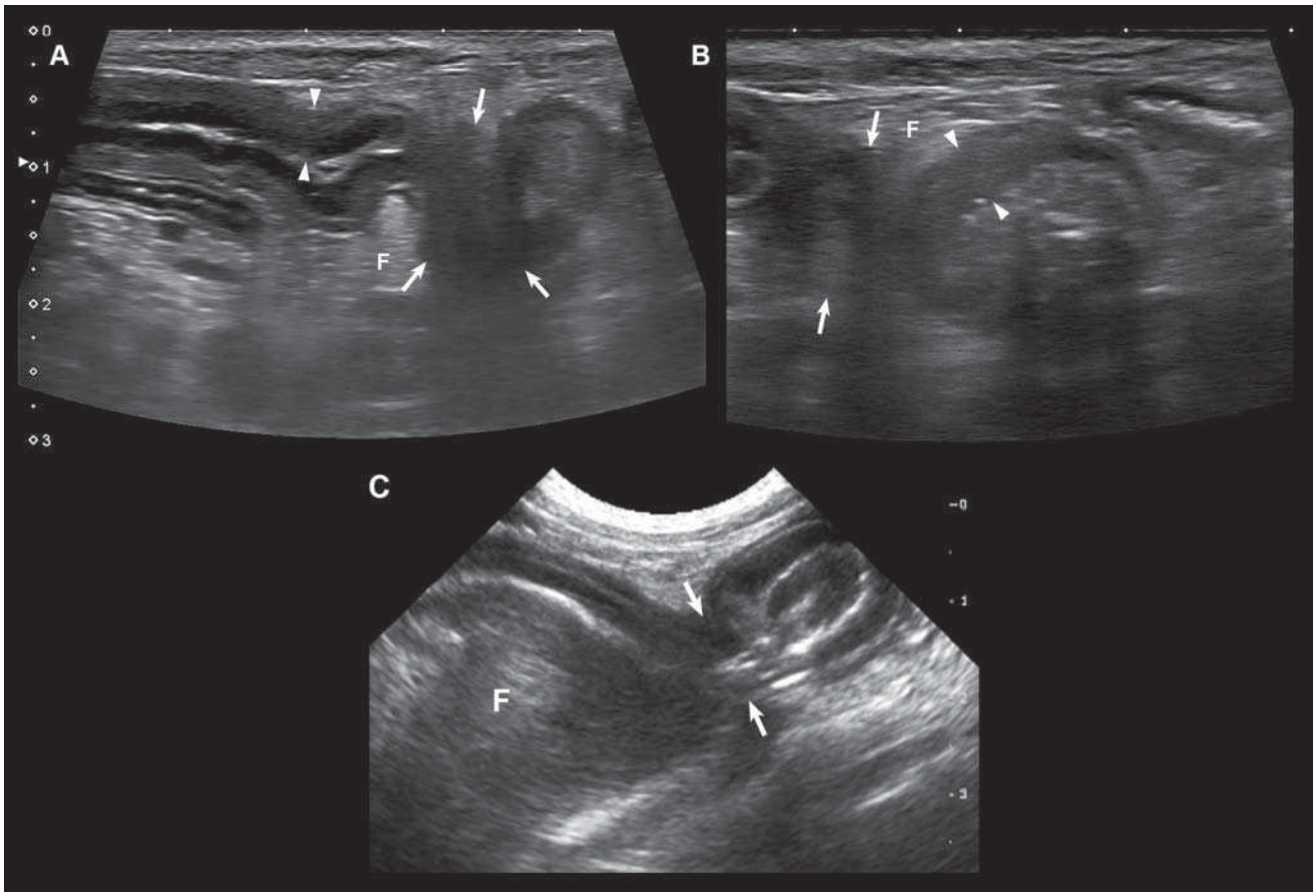


Figure 8.46. **Intestinal strictures in two dogs. A, B:** Intestinal strangulation in a dog with spontaneous mesenteric hernia. **A:** A segment of jejunum is focally deviated, poorly defined and associated with loss of wall layers (arrows). The adjacent fat (F) is hyperechoic. Aborally, the wall is mildly thickened and its layers are partly affected. **B**: Orally, the segment is dilated and associated with moderate wall thickening with loss of layering (arrowheads). Incarceration of a segment of jejunum through a defect in the mesentery was identified in surgery. The wall of the strangulated portion was necrotic and required resection. **C:** Stricture at a previous surgical site in a dog. Severe fluid distension (F) is noted proximal to the stricture site (arrows) in this dog with previous enterectomies for intestinal foreign bodies. Stricture at the previous surgical site was diagnosed surgically.

Gastrointestinal Tumors

Gastrointestinal neoplasia is often associated with motility disturbances that produce luminal fluid or gas accumulation near the affected site; this may optimize the visualization of the lesion (Penninck 1998).

In dogs and cats, the most common ultrasonographic findings in GI lymphoma are transmural thickening associated with the diffuse loss of normal wall layering, reduced wall echogenicity, decreased localized motility, and regional lymphadenopathy (Penninck et al. 1994). These features are similar in the stomach and along the intestinal tract. Gastric masses can have variable size, from extensive infiltration to segmental involvement (Figure 8.48). The thickening of the GI wall can range widely, from 5 mm to over several centimeters (Figures 8.49, 8.50). Jejunal lymphadenopathy is a common finding in intestinal lymphoma and in some instances can be responsible for most of the mid-abdominal mass effect (Figure 8.51B). Occasionally, the omentum and mesentery may be diffusely infiltrated, and be responsible for the large mass effect, detected on palpation, or seen radiographically (Figure 8.52). Ulcerated lymphoma can be encountered as an irregular mucosal surface or as a large defect centered on the affected portion of the GI tract (Figure 8.53). GI lymphoma can display several lesions along the GI tract, and they uncommonly create partial or complete obstruction. In cats, alimentary lymphoma is sometimes affecting the intestinal tract without fully disrupting the wall layering, and in some of these cats, the muscular layer of the intestinal

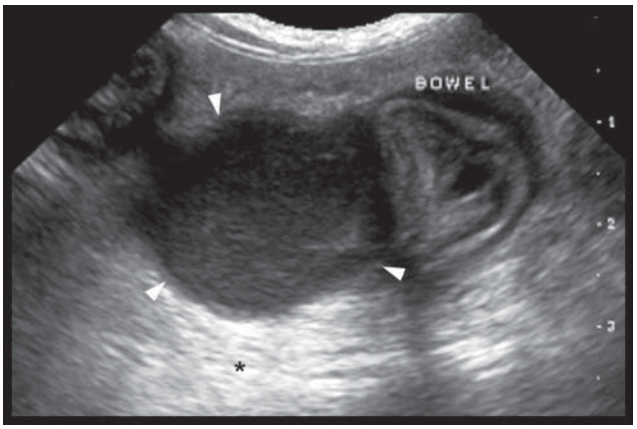


Figure 8.47. Subserosal seroma following surgical biopsy. A discrete, rounded and hypoechoic fluid cavity (arrowheads) associated with acoustic enhancement (*) is deforming the adjacent intestinal wall and lumen. This represents a cystic seroma secondary to a recent surgical intestinal biopsy. The dog had no clinical signs related to this finding.

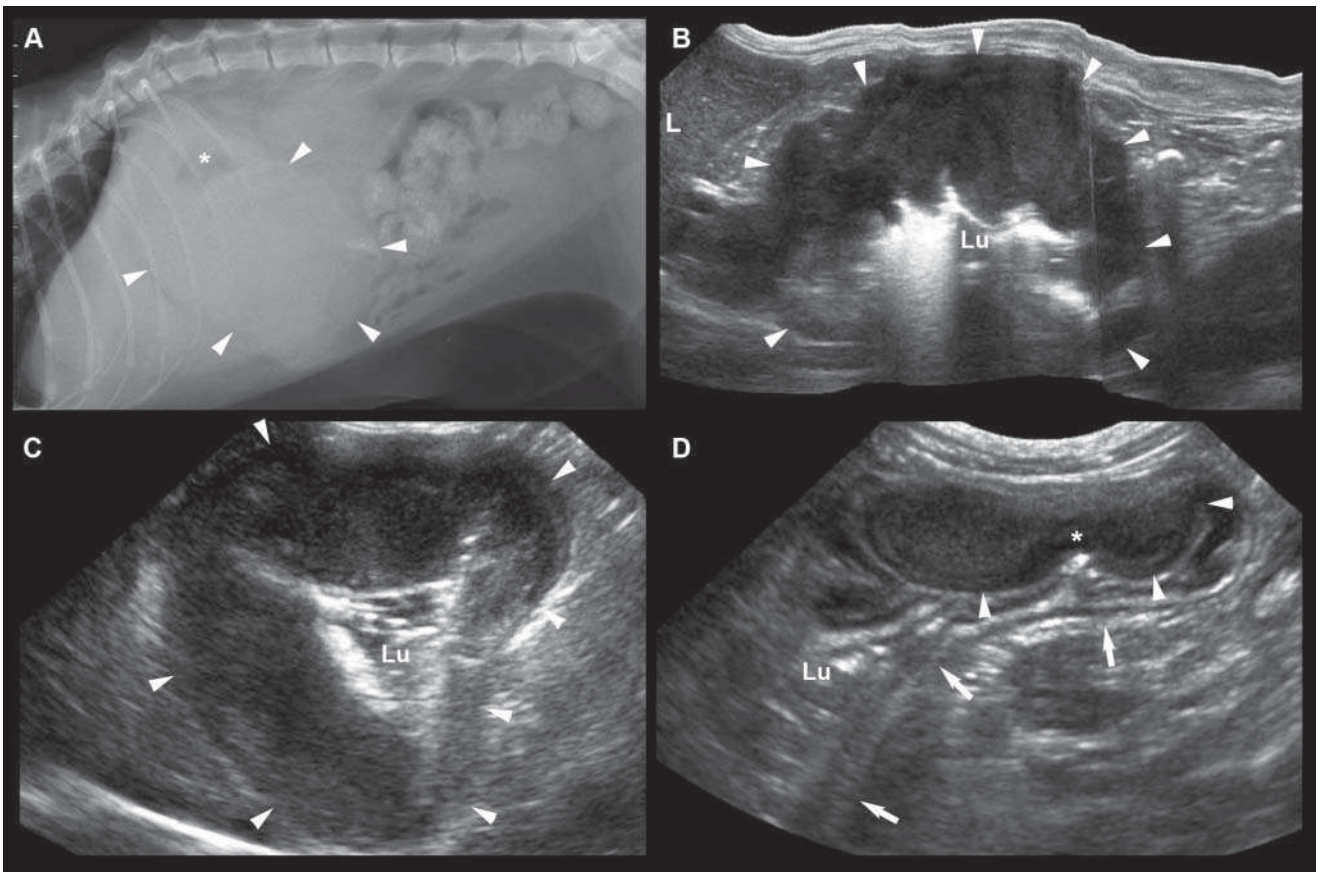


Figure 8.48. Gastric lymphoma in cats. A: Lateral radiograph of an 11-year-old cat with vomiting. A large soft-tissue mass (arrowheads) replaces the stomach containing a small amount of gas (*) in its lumen. **B:** Panoramic sonogram of the same stomach, emphasizing the large size of the mass. The gastric mass (arrowheads) is poorly echogenic and a small amount of gas is noted in the lumen (Lu). L, liver. **C:** Transverse sonogram of the same stomach shows the transmural, circumferential neoplastic infiltrate diagnosed as lymphoma on fine-needle aspirates. **D:** In this 15-year-old cat, only a segment of the gastric wall is thickened with loss of layers (arrowheads). The adjacent and facing gastric walls are still layered (arrows). Just below the asterisk (*) there is evidence of small superficial ulceration of the lesion diagnosed as lymphoma on fine-needle aspirates. Lu, lumen.

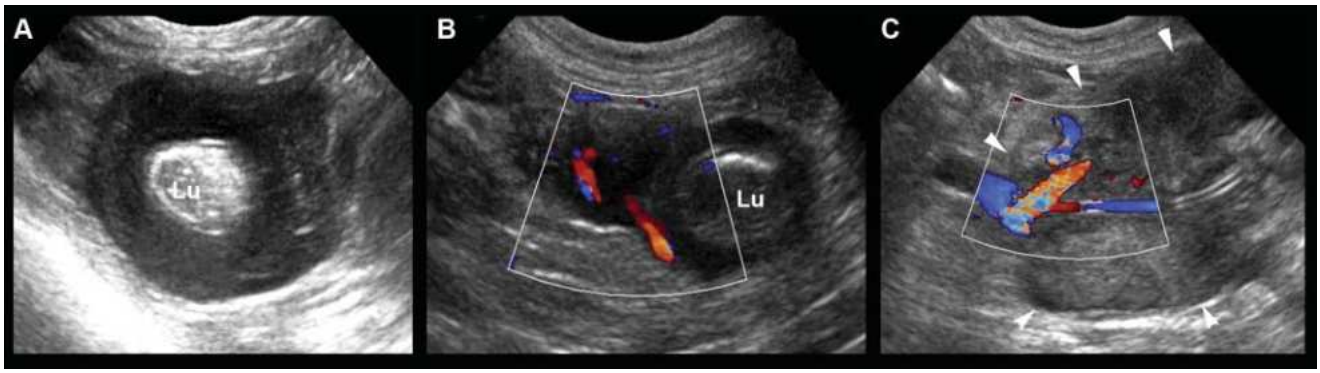


Figure 8.49. **Intestinal lymphoma in a 15-year-old cat with anorexia and weight loss. A:** Transverse sonogram of the duodenum with transmural thickening and loss of wall layering. A small amount of echogenic fluid is noted in the lumen (Lu). **B:** Transverse sonogram of a fluid-filled jejunal segment with loss of wall layering, and asymmetric thickening that seems to invade the adjacent mesentery (see the color flow box). **C:** Sagittal sonogram of the enlarged jejunal lymph nodes (arrowheads) infiltrated by lymphoma. The central jejunal vessels are useful anatomical landmarks to identify these lymph nodes.

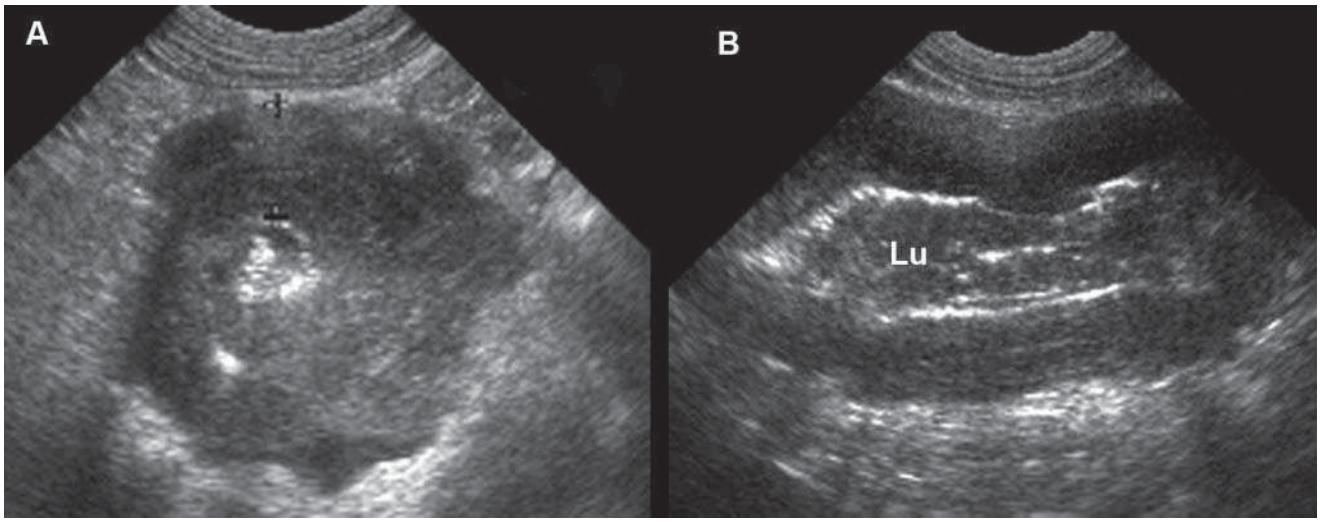


Figure 8.50. **Intestinal lymphoma in a 10-year-old Golden Retriever.** Transverse **(A)** and longitudinal **(B)** sonograms of the thickened jejunum. There is circumferential, irregular thickening (between the cursors: 1.3 cm) with complete loss of wall layering. Fluid is noted in the lumen (Lu).

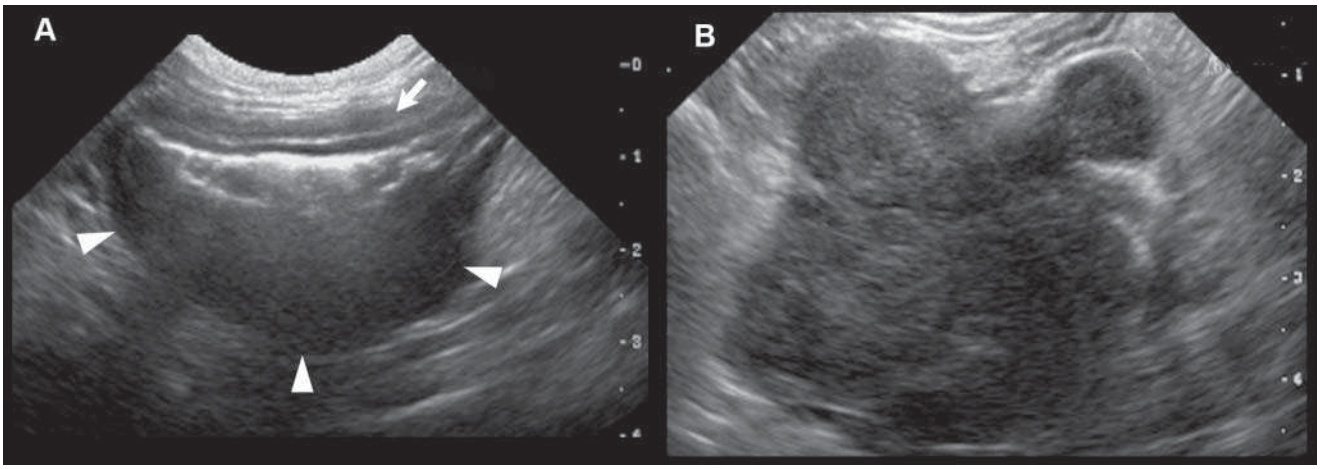


Figure 8.51. **Intestinal lymphoma. A:** Longitudinal sonogram of an asymmetrically thickened (1.5 cm) bowel segment in an 11-year-old cat diagnosed with alimentary lymphoma. The loss of layering involved mostly one side of the wall (arrowheads). The muscular layer appears particularly thickened in the opposite wall (arrow). **B:** The jejunal lymph nodes were markedly enlarged (4.5 cm thick), lobulated, and hypoechoic.

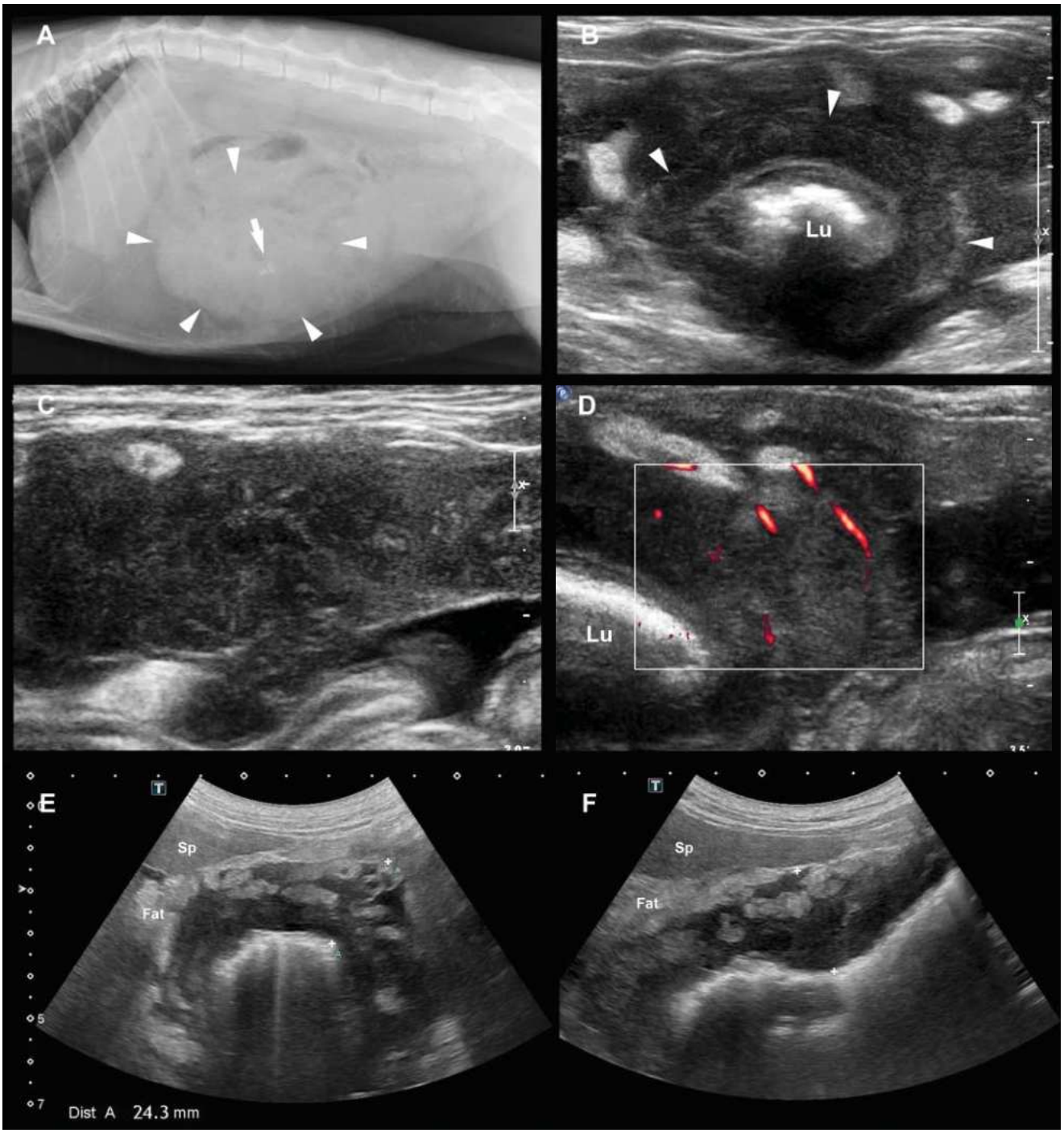


Figure 8.52. **Jejunal and omental lymphoma in a 2-year-old cat (A–D) and a 4-year-old Labrador (E, F). A:** Lateral radiograph showing regional decreased serosal detail of the abdomen (arrowheads) that supports a mass effect with suspected abdominal effusion or infiltration. A small amount of radiopaque debris (arrow) is located in this region, and presumed to be within the gastrointestinal (GI) tract. Notice the wet hair artifacts along the ventral abdominal wall. **B:** Transverse sonogram of a jejunal segment with marked thickening of the wall (outlined by arrowheads) and extensive omental invasion, as also noted in **C** and **D:** Peritoneal effusion is present. The omental thickening, even poorly echogenic, can be distinguished from fluid because of the detection of blood vessels (**D**). Lu, lumen. **E, F:** In this 4-year-old Labrador Retriever with weight loss, abdominal distension and pain, a segment of jejunum is markedly thickened (24 mm) and heterogeneous with indistinct layering. The lymphoma infiltrates the peripheral fat, making it difficult to differentiate wall from fat.

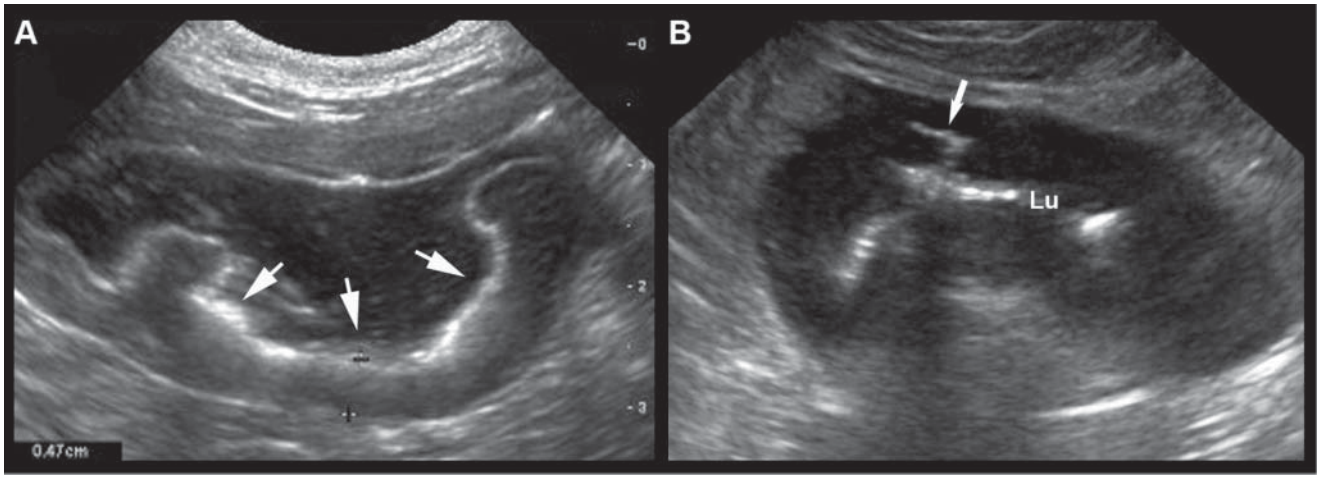


Figure 8.53. **Ulcerated lymphoma. A:** Longitudinal sonogram of an ulcerated lymphoma in a 15-year-old cat with vomiting and depression. Part of the gastric wall is moderately thickened (4.7 mm), with complete loss of layering. The mucosal surface appears irregular, and a layer of hyperechoic microbubbles has accumulated at the site of the extensive ulceration (arrows). The stomach is filled with fluid and was hypomotile during the exam. **B:** Sagittal sonogram of an ulcerated jejunal lymphoma in an 11-year-old cat with decreased appetite. An irregular hyperechoic tract (arrow) is crossing the thickened and poorly echogenic wall. Lu, lumen.

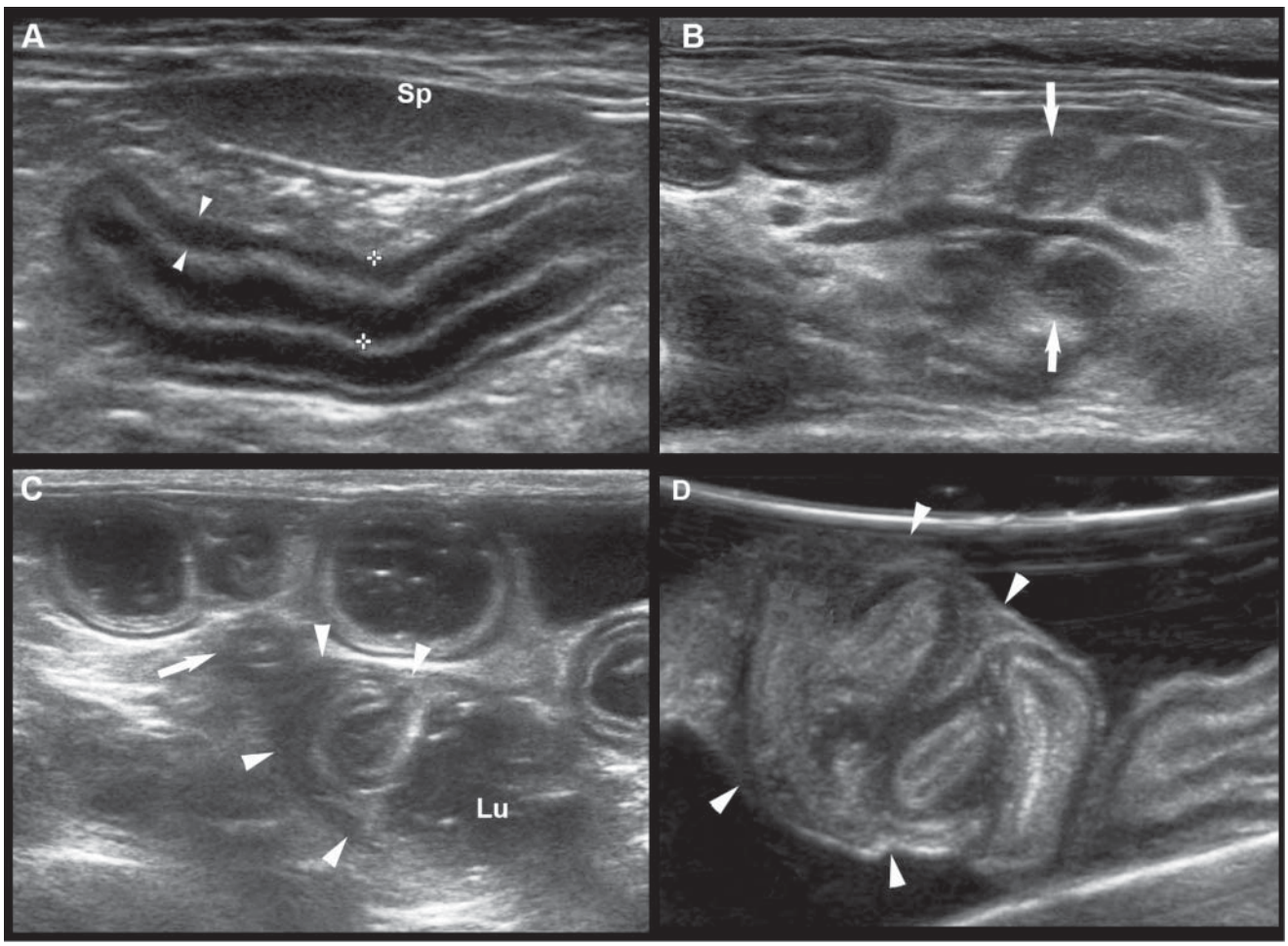


Figure 8.54. **Feline lymphoma without loss of layering. A:** A 13-year-old cat with 3 months of vomiting and weight loss. The intestinal wall of numerous intestinal segments is thickened (3.8 mm), with the muscular layer being particularly prominent and irregular (arrowheads). Sp, spleen. **B:** The jejunal lymph nodes are rounded and enlarged (8 mm) (arrows). **C, D:** A 9-year-old cat with progressive weight loss**. C:** In the near field, several intestines are fluid-dilated and hyperperistaltic. At the junction of maximally dilated jejunum and normal jejunum (arrow), a segment of jejunum folded on itself (arrowheads) is noted. **D:** After surgical resection, the specimen was scanned in a water bath. There is again evidence of a tightly folded segment of jejunum (arrowheads) with visible layers. The histopathological diagnosis was lymphoma primarily confined to the serosa.

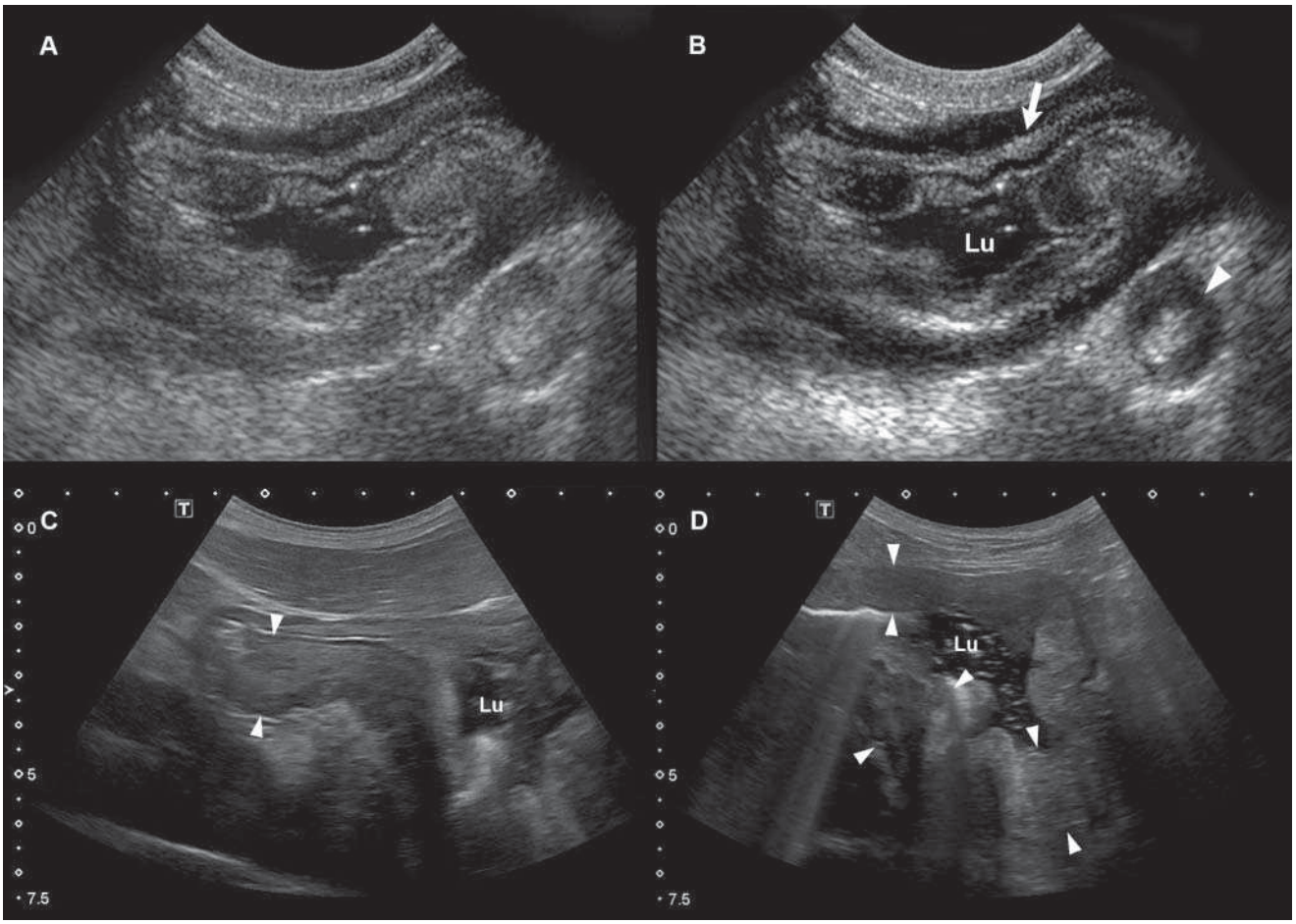


Figure 8.55. Gastric altered layering ("pseudolayering" sign) with adenocarcinoma. Longitudinal sonographic **(A)** and enhanced **(B)** images of the pyloric antrum of a dog with carcinoma. The markedly thickened wall (up to 1.3 cm) displayed a pseudolayering pattern (arrow) suggestive of carcinoma. A mild amount of fluid is noted in the lumen (Lu). The gastric lymph node is enlarged (0.8 × 1.3 cm) (arrowhead) and has a target appearance (a hypoechoic rim around a bright center). **C, D**: In this 12-year-old Chow Chow, the pseudolayering is more evident at the gastric body (arrowheads in C), whereas the wall is more heterogeneous at the fundus (D), presumably due to necrosis, edema or hemorrhage. The stomach is also fluid-filled (Lu, lumen), which can be present because of increased wall rigidity.

wall is thickened (Figure 8.54), making the distinction between inflammatory and neoplastic changes more challenging (Zwingenberger et al. 2010; Tucker et al. 2014). Serosal infiltration is rare, but if it occurs, it may restrict the lumen (Figure 8.54).

The most common ultrasonographic finding in gastric carcinoma is transmural thickening associated with altered wall layering that correlates with the unevenly layered tumor distribution noted histopathologically (Penninck et al. 1998). This altered layering, previously called pseudo-layering, appears as a moderately echogenic zone surrounded by outer and inner, poorly echogenic lines (Figure 8.55). However, other associated mural changes, such as edema, inflammation, fibrosis, or hemorrhage, can mask this hallmark feature (Figure 8.55D). When present, this particular ultrasonographic feature is strongly suggestive of gastric carcinoma.

Intestinal carcinomas have been documented in dogs and cats, although they are encountered less frequently in cats. The most common ultrasonographic findings are transmural thickening with a complete loss of layering, which is often associated with lymphadenopathy (Paoloni et al. 2002) (Figure 8.56). In the majority of these cases, fluid/gas accumulation proximal to the focal intestinal thickening indicates a mechanical ileus. Intestinal carcinoma shares some of the ultrasonographic features seen in intestinal lymphoma, but the length of the lesion tends to be shorter in carcinoma than in lymphoma, and mechanical ileus is more common in carcinoma than in lymphoma (Figures 8.56, 8.57). The behavior of intestinal

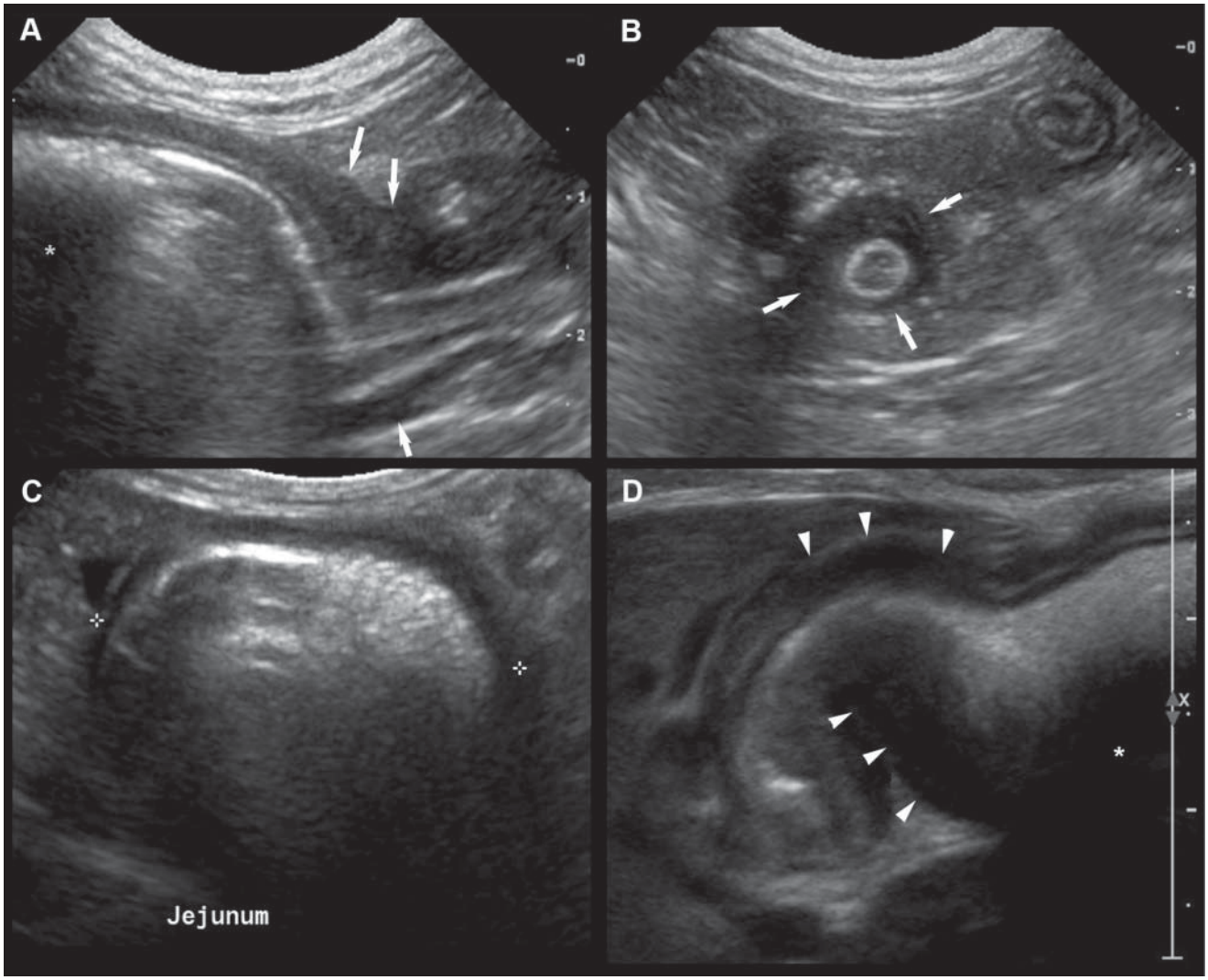


Figure 8.56. **Intestinal adenocarcinomas with obstruction. A:** Longitudinal sonogram of an intestinal adenocarcinoma in a cat with weight loss and anorexia. Proximal to the obstruction site, there is intestinal distension and foreign material accumulation (*). The arrows point to the narrowed and affected bowel segment. **B:** Transverse sonogram of the same lesion. The arrow points to the thickened ileum. **C:** In this 9-year-old cat, there is marked jejunal distension (between cursors, up to 2.5 cm wide), proximal to the obstruction site. **D:** At the tumoral site, there is a short and narrowed segment of jejunum (arrowheads) with loss of layering. The affected portion of intestine is curved on itself. Note the strongly shadowing material (*) accumulated proximal to the obstruction site.

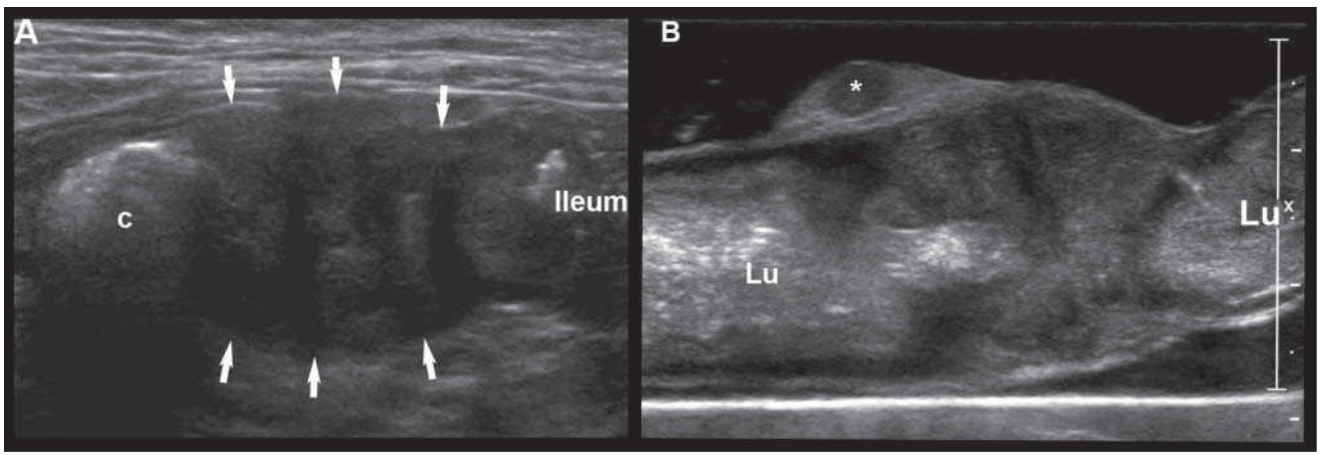


Figure 8.57. **Adenocarcinoma of the ileocecocolic junction of a 12-year-old cat. A**: Longitudinal sonogram of a focally invasive and unevenly circumferential adenocarcinoma invading the ileocecocolic junction of this cat (arrows). c, colon. **B:** After surgical removal, the specimen was placed in a water bath. The extent and echogenicity of the mass can clearly be seen. Lu, lumen A small nodule (*) is present in the adjacent mesentery.

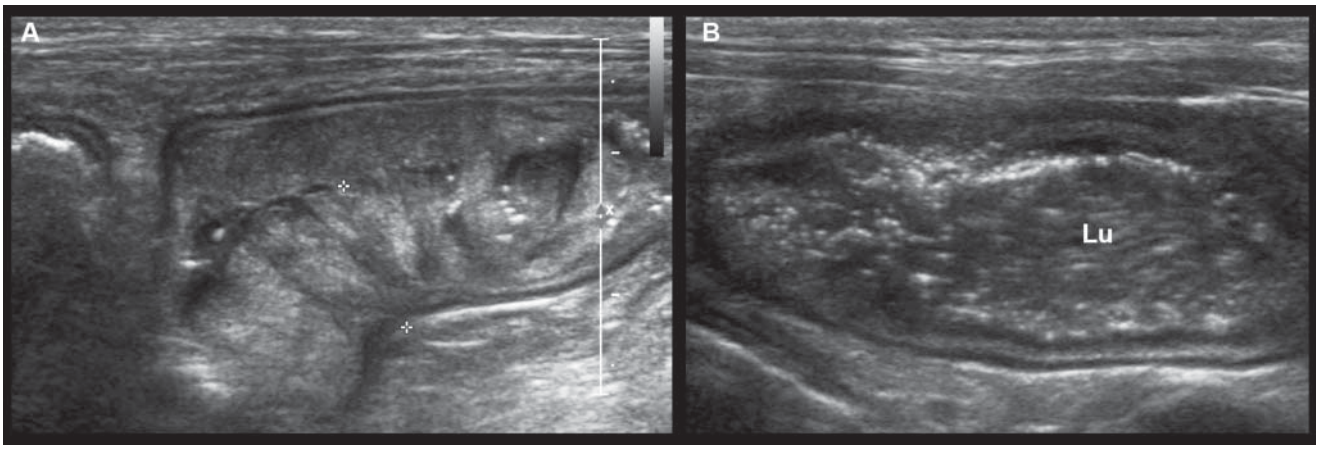


Figure 8.58. Jejunal carcinoma in a 7-year-old Pug with chronic watery diarrhea. A: Longitudinal sonogram of the affected intestine. **A** 1-cm-thick polypoid-like thickening primarily affecting the mucosa is noted **B:** A jejunal segment orad to the lesion is moderately fluid-filled. Lu, lumen. The mass was resected, and the final diagnosis was colonic intramucosal papillary adenocarcinoma. Considering the chronic clinical signs and the marked dysplastic changes, it was speculated that the papillary carcinoma might be a malignant transformation of long-standing adenomatous polyp. Over 2 years later, the dog has no evidence of recurrence of intestinal mass, or gastrointestinal (GI) signs.

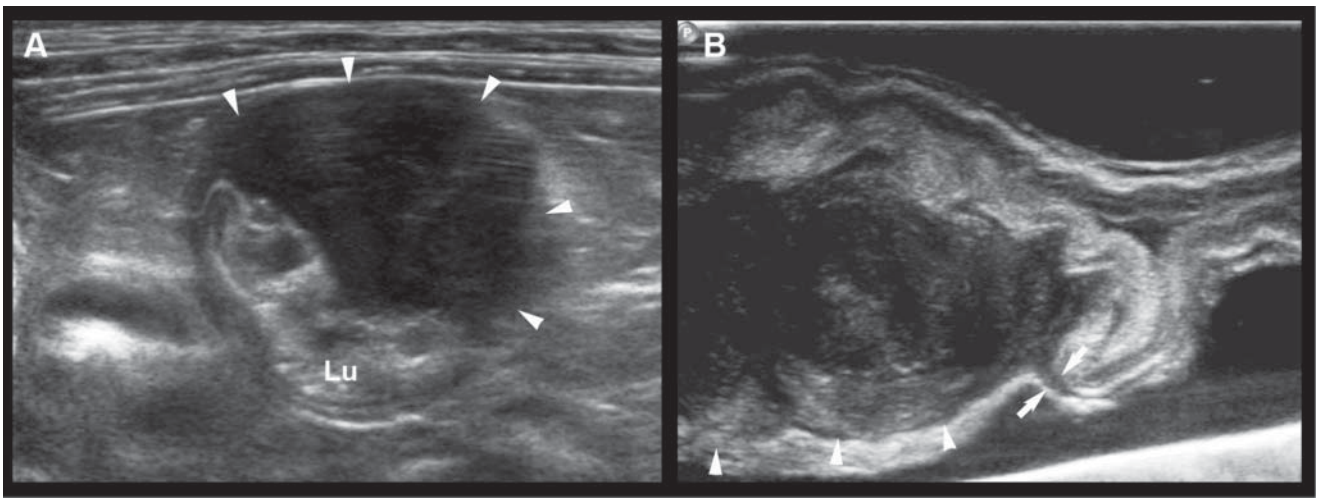


Figure 8.59. Leiomyoma in a 7-year-old Cairn Terrier without any gastrointestinal (GI) signs. Transverse sonogram of the lesion **(A)** and longitudinal sonogram of the surgical specimen placed in a water bath **(B)**. **A:** The mass is nearly anechoic and homogeneous (arrowheads), deforming the outer contour of the jejunum. The layers are focally indistinct. Lu, lumen. **B:** In the water bath specimen, the connection of the mass (arrowheads) to the muscular layer (arrows) is more obvious.

carcinoma may vary accordingly to the histopathological type. Hyperplastic and adenomatous changes may evolve to malignant tumors and the ultrasonographic feautres may therefore be confusing (Figure 8.58).

Smooth muscle tumors (leiomyoma, leiomyosarcoma) have been described as the most common mesenchymal tumors of the GI tract; however, with the advance in histoimmunochemistry, gastrointestinal stromal tumors (GISTs) are being more reliably diagnosed and their prevalence is still unknown. Several ultrasonographic features of GI mesenchymal tumors are helpful in differentiating them from other types of GI neoplasia. Smooth muscle tumors tend to be large (>3 cm) intramural lesions growing out of the serosa as large eccentric or extraluminal masses (Myers and Penninck 1994) (Figures 8.59, 8.60). Because of their common exophytic distribution and their large size, it is difficult to assess the anatomical origin of the mass and even more so to determine the precise layer of tumor origin. During real-time

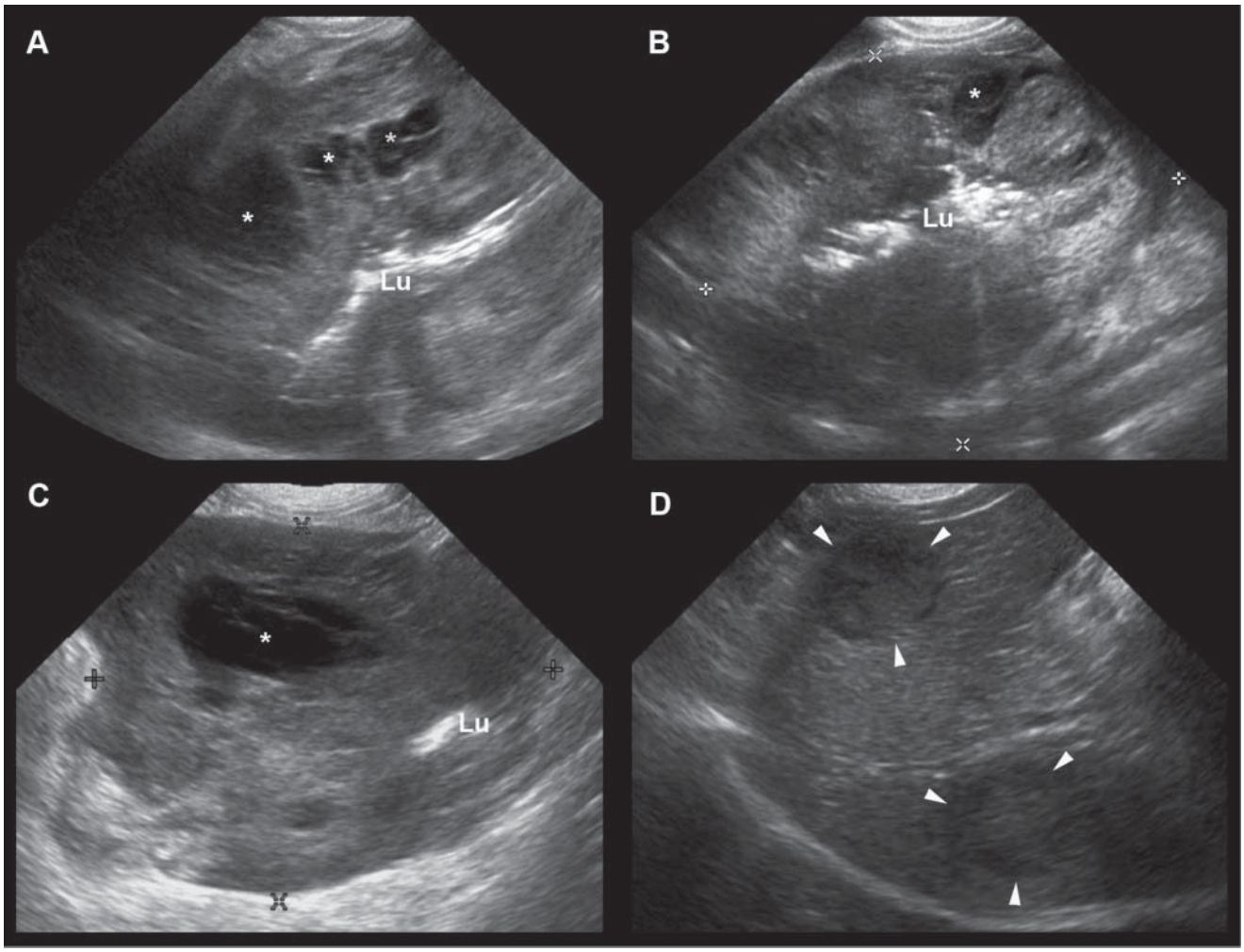


Figure 8.60. **Intestinal leiomyosarcoma in two dogs. A:** Sonogram of a jejunal leiomyosarcoma in a 9-year-old pit bull. The mass is large, inhomogeneous with several cavitary areas (*) which are most likely areas of degeneration and necrosis. **B:** Transverse sonogram of the same mass, displaying similar features, but at the edge of the lesion, the lumen is more centrally located. **C:** In this 8-year-old Golden Retriever, there is also evidence of a large, eccentric and inhomogeneous mass with cavitations (*) Lu = lumen. **D:** Additionally, two hypoechoic masses (arrowheads) were present in the liver. They are hepatic metastases from the colonic leiomyosarcoma.

evaluation, it is important to identify within the mass any gas and/or the small amount of fluid located in the distorted lumen. The presence of a reverberation artifact indicates the presence of gas, and attempts to connect this artifact to an adjacent bowel segment should be made to confirm the GI origin. Large GI mesenchymal tumors tend to be heterogeneous with a mixed echogenic pattern. The presence of anechoic and hypoechoic foci within the mass may correlate with the areas of central degeneration and necrosis frequently found in these large lesions. There is no ultrasonographic feature reliably distinguishing smooth muscle tumors from GISTs (Figures 8.60, 8.61). GISTs might have a higher incidence in cecal location. When gastric in origin, these tumors tend to project into the GI lumen (Figure 8.62).

Other less commonly reported tumors include mast cell tumor (Figure 8.63), histiocytic sarcoma (Figure 8.64), carcinoid, neurilemmoma, nerve-sheath tumor, hemangiosarcoma (Culp et al. 2008), plasmocytoma, extraskeletal osteosarcoma (Stimson et al. 2000), and metastases (Dominguez et al. 2013). Mast cell tumors have been described in cats as often focal hypoechoic, eccentric, and asymmetric nodules/masses (Laurenson et al. 2011). Recently, metastases from a mammary carcinoma have been described as discrete, small, hypoechoic nodules in the jejunal muscular layer (Dominguez et al. 2014).

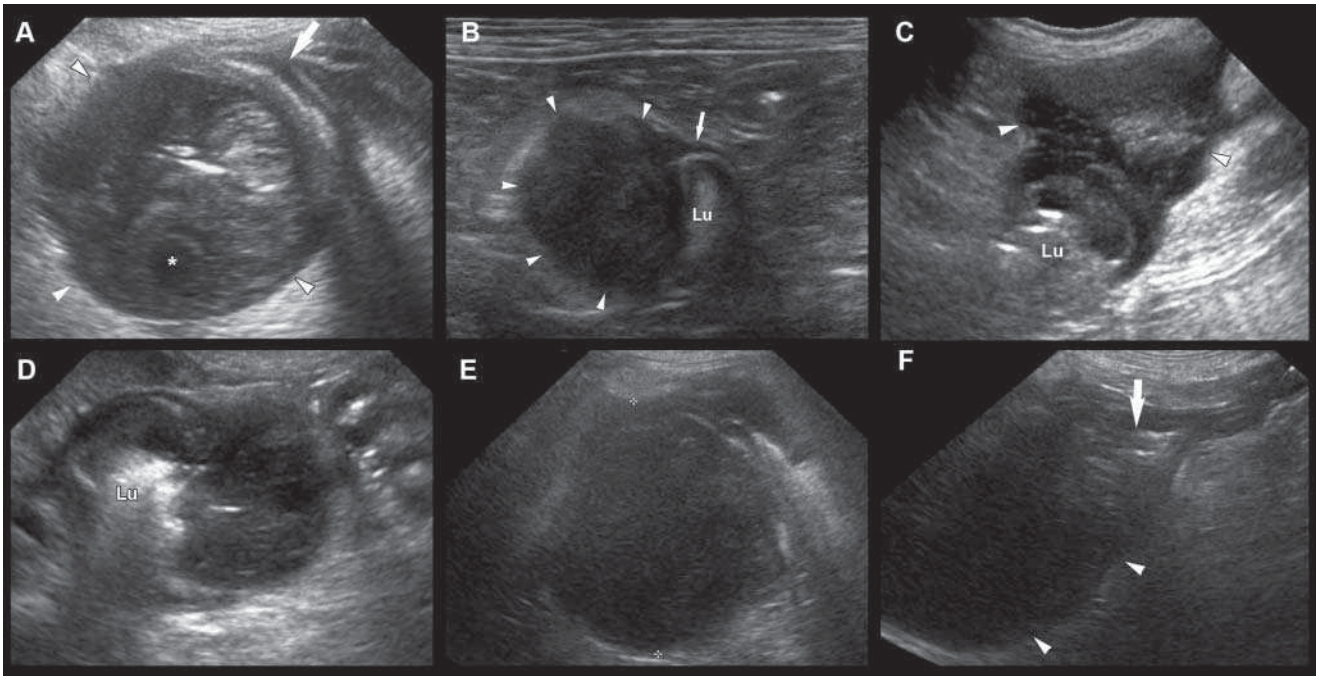


Figure 8.61. **Gastrointestinal stromal tumors (GISTs) in five dogs.** (for full caption, see facing page)

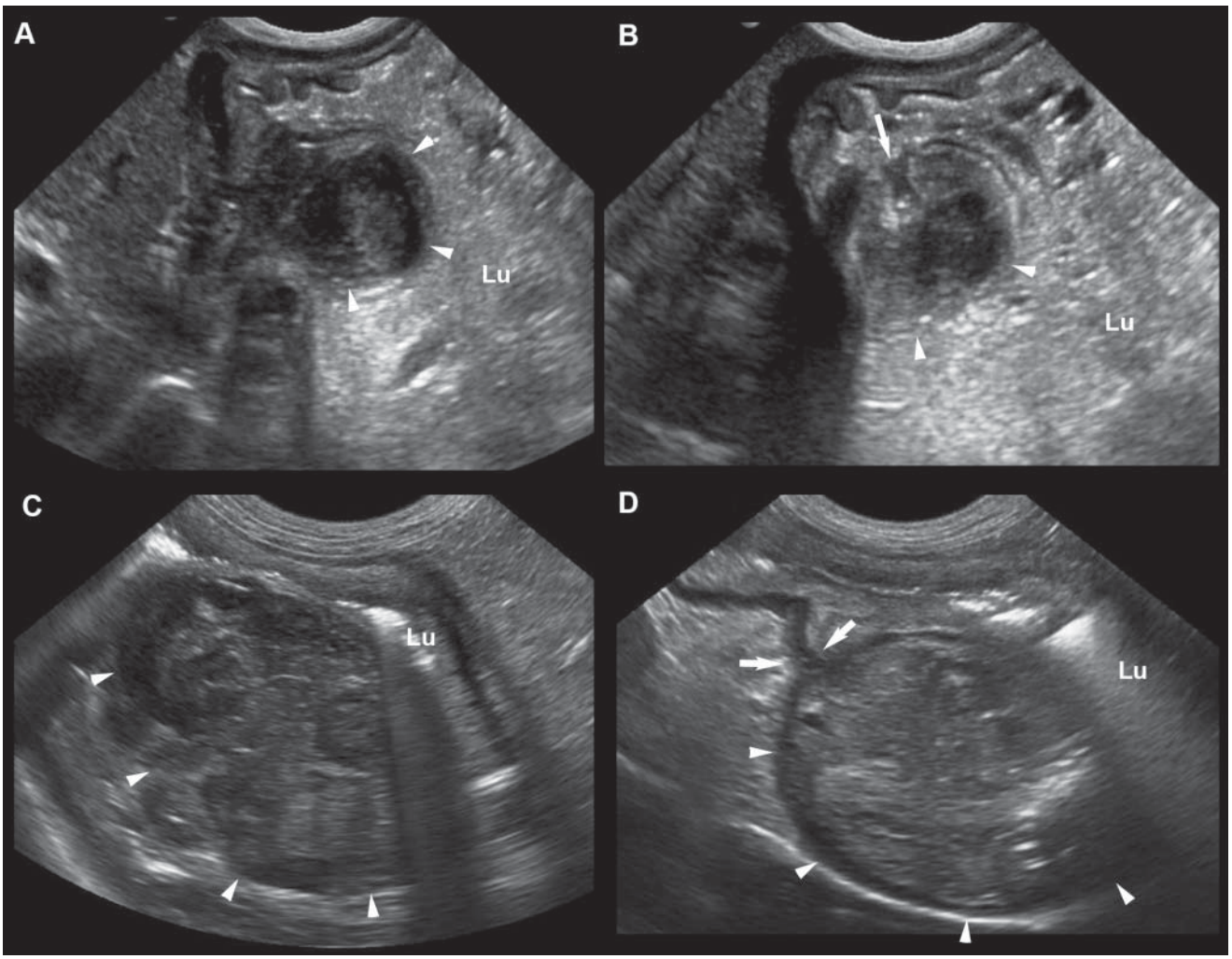


Figure 8.62. **Leiomyoma of the stomach in two dogs.** (for full caption, see facing page)

Figure 8.61. Gastrointestinal stromal tumors (GISTs) in five dogs. A: Transverse sonogram of an inhomogeneous mass in an 8-year-old Labrador Retriever. The connection to the intestine is seen in the near field (arrow). A small hypoechoic area (*) is noted in the mass, which may represent necrosis. **B**: A small poorly echogenic eccentric mass (arrowheads) is asymmetrically disrupting the jejunal wall layering in a 10-year-old Labrador. At the junction with the wall, it appears that the mass arises from the muscular layer of the wall (arrow). Hyperechoic fat is noted near the lesion. **C:** A similar finding of eccentric distribution (arrowheads) is noted in the lesion found in a 14-year-old mixed-breed dog, and in a 5-year-old Boxer. **D, E:** A large (about 10 cm long) poorly echogenic mass (arrowheads) was noted in this 8-year-old Labrador. The intestinal origin is confirmed as the gas on the edge of the mass extends into the intestinal segment in the near field (arrow).

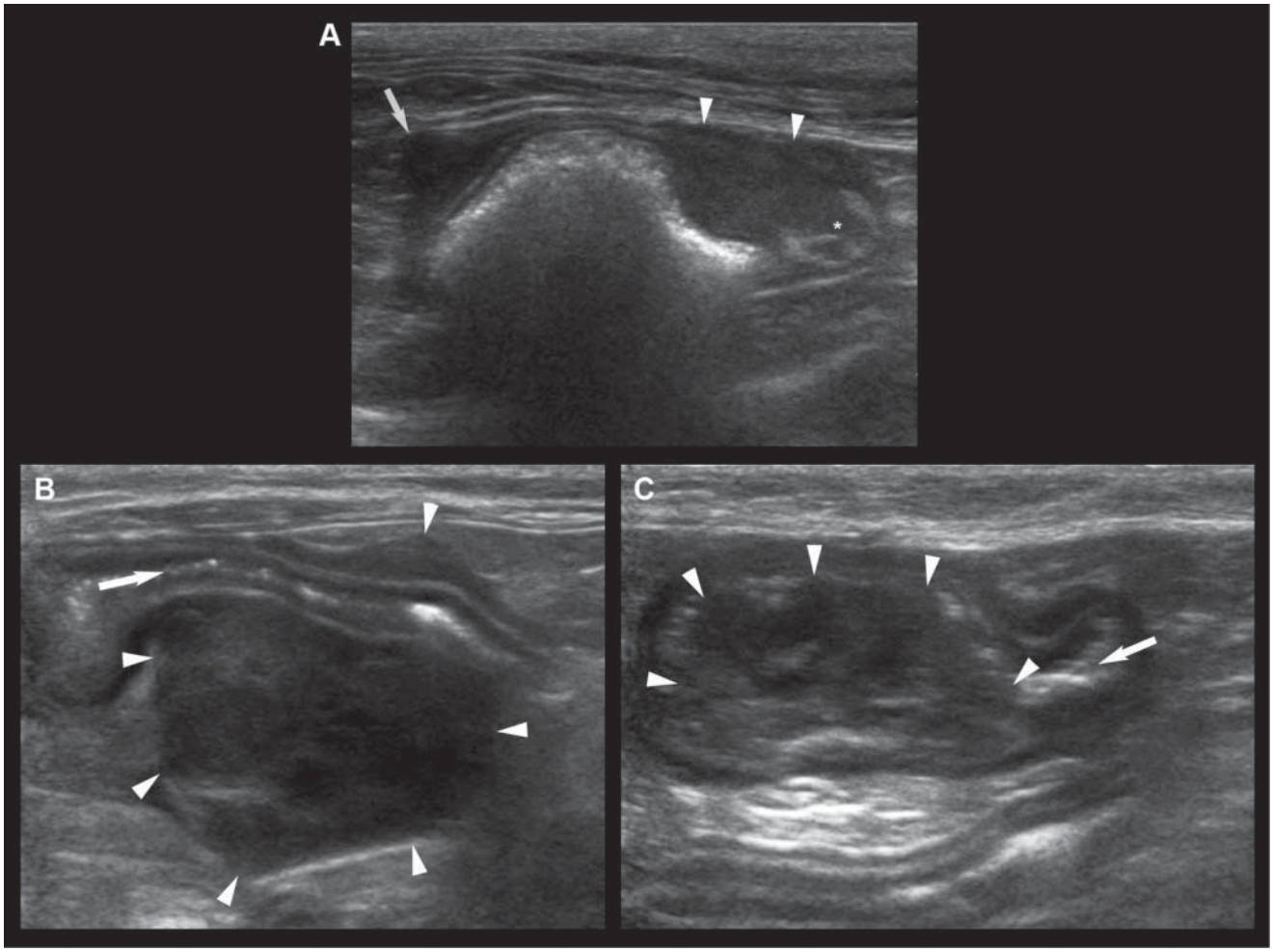


Figure 8.63. Mast cell tumors in cats. A: On this transverse sonogram, lesions are seen in the ileocecocolic junction of a 14-year-old cat. Transmural thickening with loss of layering is noted in the cecum (arrowheads). Altered layering and asymmetric thickening of the proximal ascending colonic wall is also present, creating a bulge on the serosal surface (arrow). An asterisk indicates the ileum. A mast cell tumor was diagnosed on ultrasound-guided fine-needle aspirates. **B, C:** In this 12-year-old cat with chronic weight loss, there are several hypoechoic jejunal masses. **B**: One mass is primarily eccentric (arrowheads) and is not projecting into the intestinal lumen (arrow). **C:** Another large mass is projecting into the lumen (arrow) of the affected jejunal loop (arrowheads). There was no evidence of mechanical ileus.

Figure 8.62. Leiomyoma of the stomach in two dogs. A, B: Sonograms of the small (2.2 cm) poorly echogenic nodule projecting into the lumen of the greatly fluid distended stomach of a 10-year-old Xolo dog presented for vomiting and collapse. The arrowheads outline the lesion. In **B**, the arrow points to the ulcerated portion of the nodule, responsible for the severe bleeding. The lesion was close to the cardia, but was completely and successfully resected. Lu, lumen. **C, D:** Sonograms of a large (>4 cm) and inhomogeneous gastric mass (arrowheads), near the cardia, in a 13-year-old West Highland White Terrier. In **D**, the arrows point to the visible connection with the muscular layer.

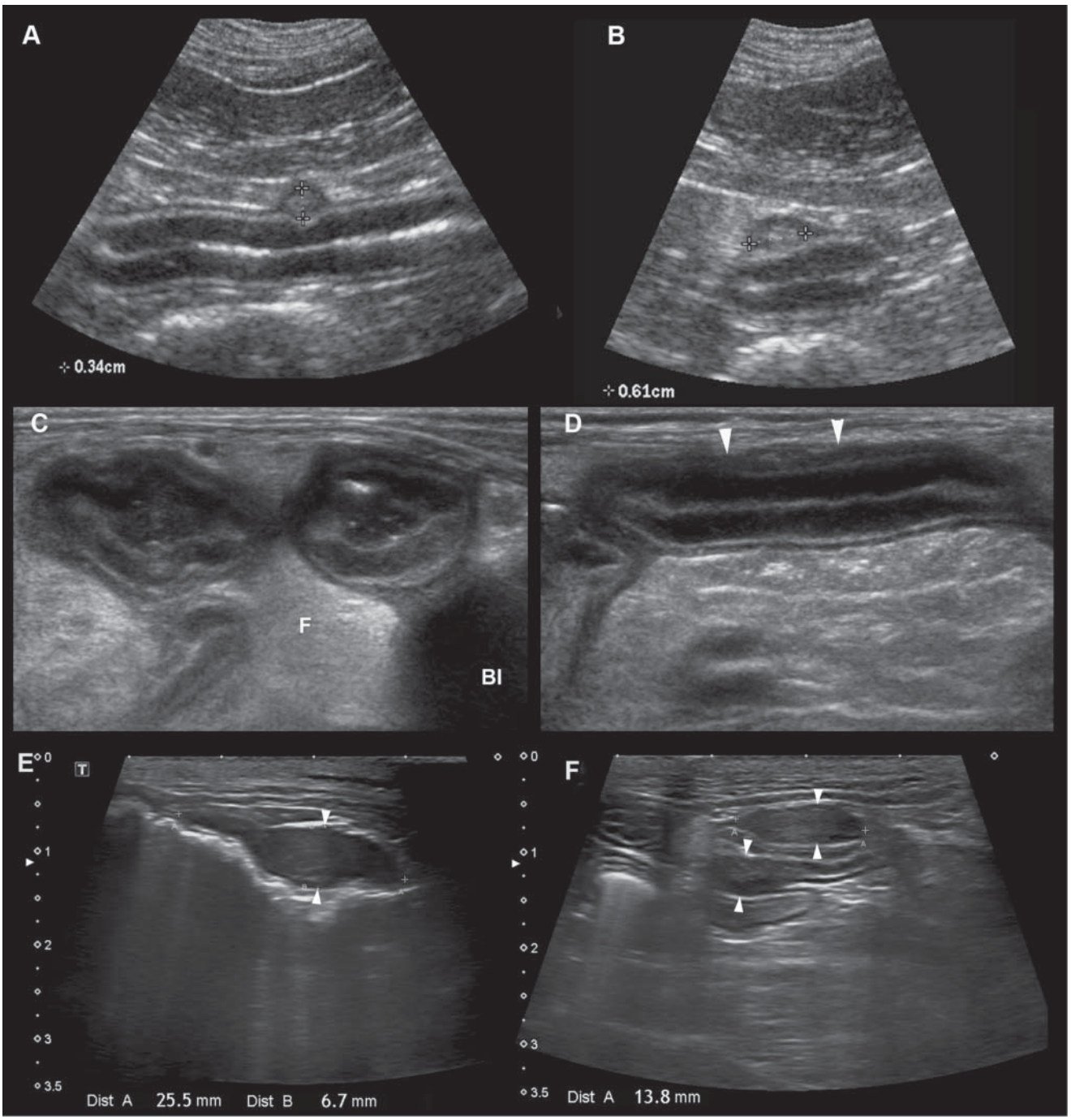


Figure 8.64. **Histocytic sarcoma.** Longitudinal (**A**) and transverse (**B**) sonograms of a segment of jejunum in a Bernese Mountain Dog with disseminated histiocytic sarcoma. A small, well-defined, hyperechoic nodule is present within the muscularis, deforming the contour of the submucosa. Similar lesions were observed in other intestinal segments. All nodules, including those in the liver, were hyperechoic. **C, D**: A 15-year-old Miniature Pinscher with disseminated histiocytic sarcoma throughout the gastrointestinal (GI) tract, liver, and bone marrow. **C:** Most intestinal segments had altered layering (hyperechoic mucosa, mucosal ulceration), hyperechoic fat (F), and echogenic effusion (same case as Figure 8.44). Bl, bladder. **D:** Note the thickened serosa on this jejunal segment (arrowheads). Tumoral infiltrates were reported histopathologically to be more severe on the serosa**. E, F**: In this 6-year-old Bernese Mountain Dog, lesions were identified in the tibia, the kidneys (see Figure 10.29B) and in several intestinal segments. Focal areas of wall thickening primarily affecting the muscular layer are present (arrowheads) in these sonograms. The infiltration is uniform and slightly more echogenic than normal muscular layer.

Gastrointestinal Non-tumoral Nodule or Mass

At times, the hypertrophic mucosal or hyperplastic glandular changes of the gastric wall may appear as a discrete nodule or mass. Exuberant hyperplastic or hypertrophic mucosal or muscular changes cannot be differentiated from benign polyps based on their imaging or gross appearance; however, their overall echogenicity is usually increased in comparison to malignant lesions. Gastric polyps can appear as large, moderately echogenic nodules or masses projecting into the gastric lumen (Figure 8.65). They are often asymptomatic unless located in the pylorus, thus creating a gastric outflow disturbance.

Extensive hyperplastic changes can be found at other locations along the GI tract. If located within the proximal portion of the descending duodenum, these changes may induce outflow obstruction or compromise the bile flow (Figure 8.66).

Duodenal adenomatous polyps have been reported in cats (MacDonald et al. 1993); they are commonly

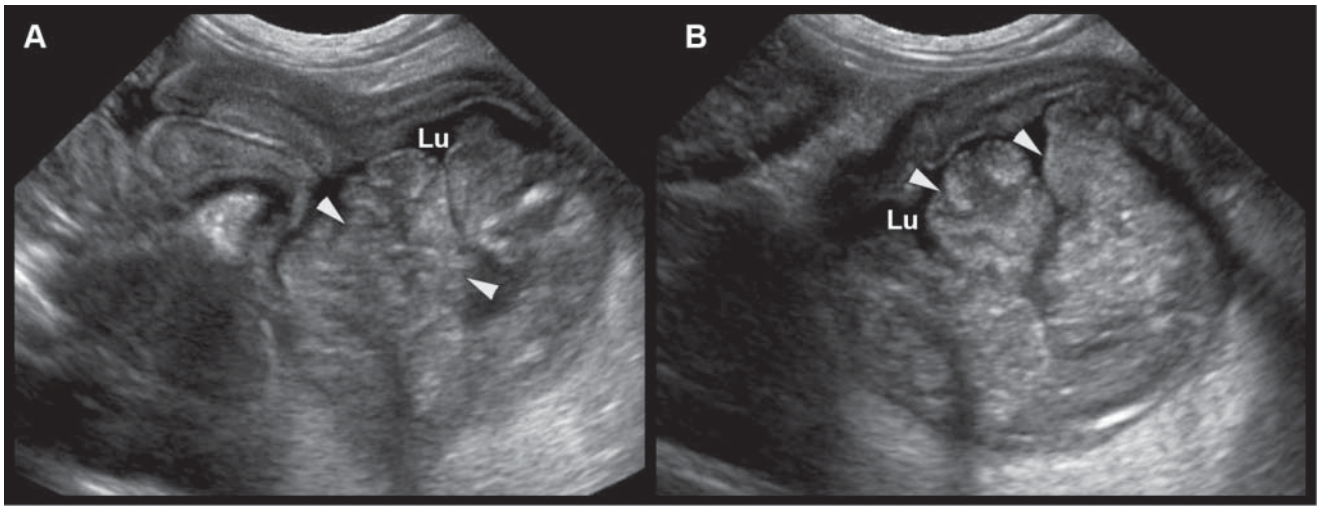


Figure 8.65. Adenomatous polyps in the stomach in an 11-year-old Jack Russell Terrier. Longitudinal (**A**) and transverse (**B**) sonograms show extensive polypoid projections (arrowheads) filling a large portion of the gastric lumen (Lu).

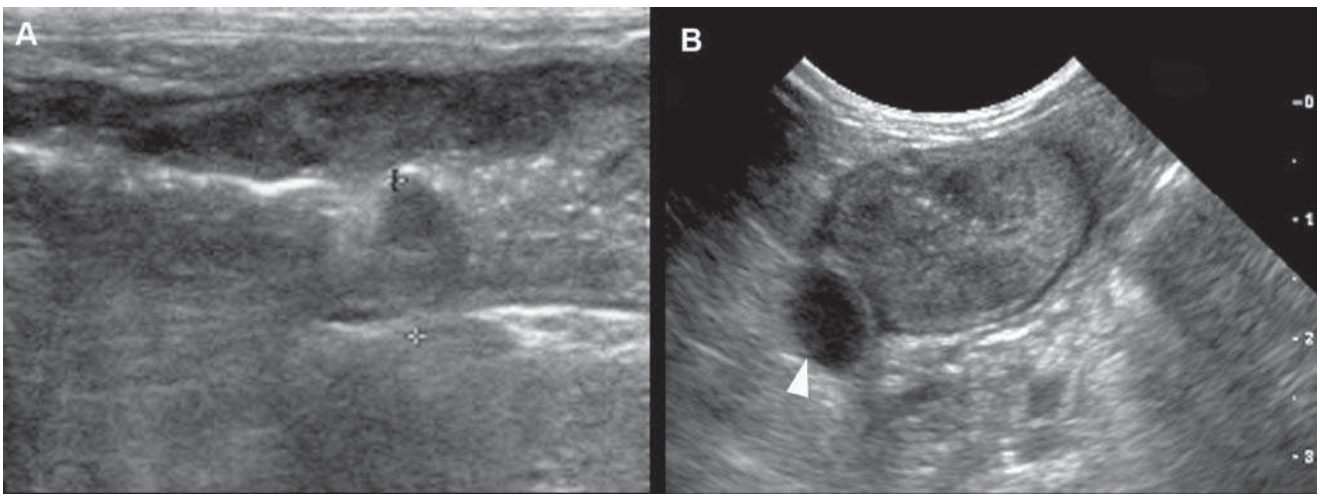


Figure 8.66. Duodenal mucosal hyperplasia evolving into adenocarcinoma. Longitudinal **(A)** and transverse **(B)** images of marked diffuse duodenal thickening (between the cursors) in a 13-year-old cat. The distal common bile duct is fluid-dilated (arrowhead). Initial surgical biopsies were diagnostic of extensive tubulovillous, adenomatous, mucosal hyperplasia. Drastic surgical resection was performed 7 months later, and the final histopathologic diagnosis was duodenal adenocarcinoma. The sonographic features had not progressed during this long period.

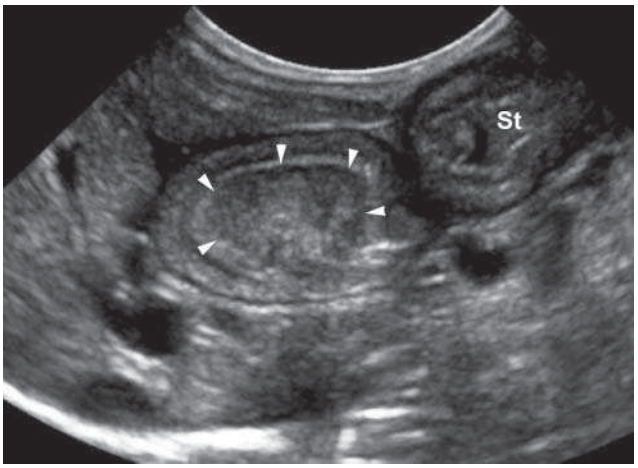


Figure 8.67. Duodenal polyp in an 11-year-old cat. An echogenic nodular lesion (arrowheads) is filling the lumen of the antral/proximal duodenal lumen. St, stomach.

associated with bleeding ulcers. They can easily be missed on ultrasound, as they often are uniformly echogenic and can blend with the surrounding GI contents (Figure 8.67).

Large single or multiple masses of mixed echogenicity, described as eosinophilic fibrosing dysplasia in cats (Weissman et al. 2012), have features similar to neoplasia (e.g., loss of layering, deformity of the wall), but they tend to be associated with hyperechoic areas within the mass, probably corresponding to the fibrosis (Figure 8.68).

Similarly, any granulomatous lesions affecting any segment of the GI tract may have features suggestive of neoplasia. Granulomatous masses may be associated with trauma (healed foreign-body perforation), parasitic, viral (such as feline infectious peritonitis), fungal (such as pythiosis; Graham et al. 2000) or bacterial infections (Figure 8.69). Performing aspirates

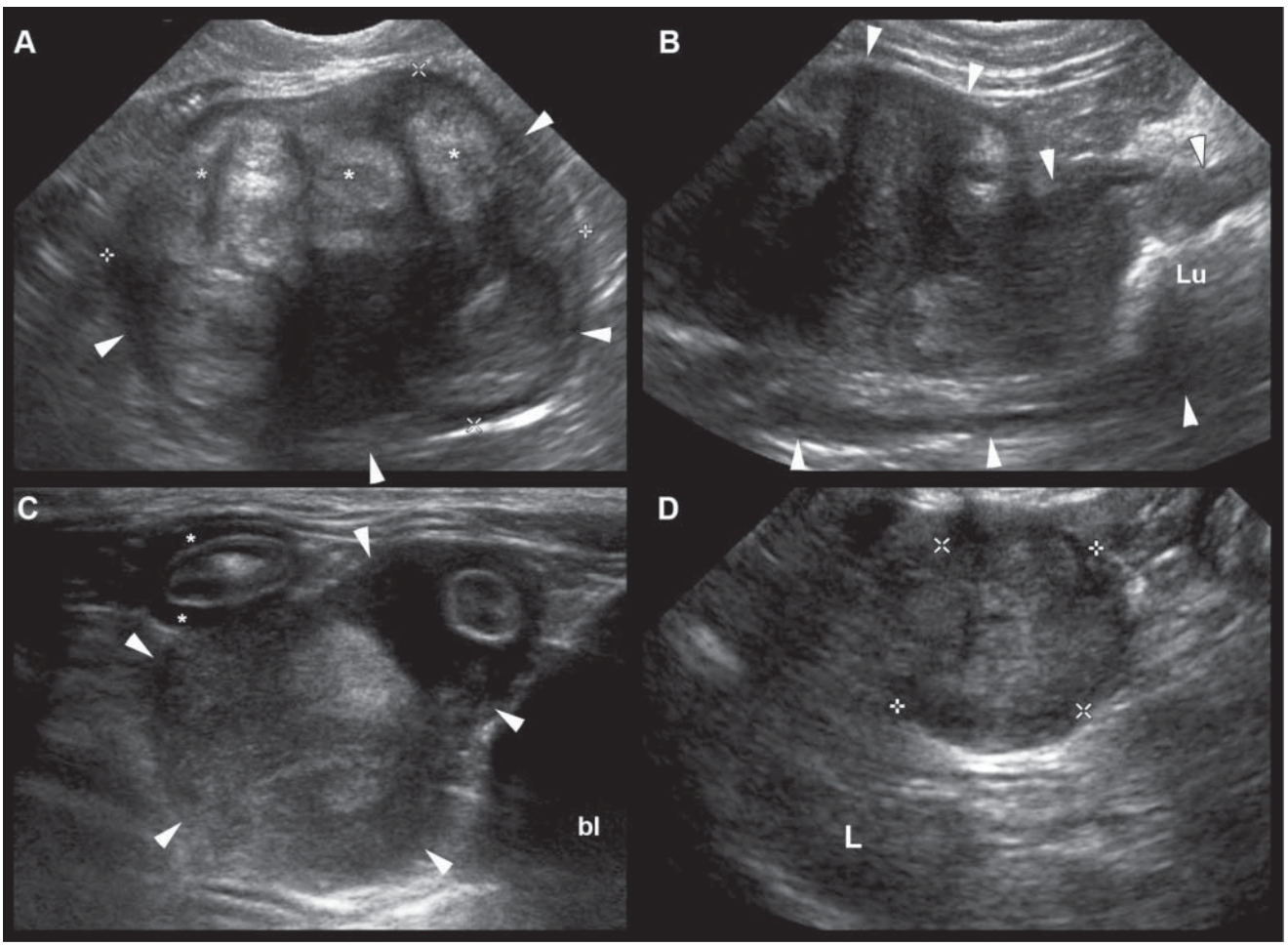


Figure 8.68. Feline eosinophilic sclerosing fibroplasia in two cats. (for full caption, see facing page)

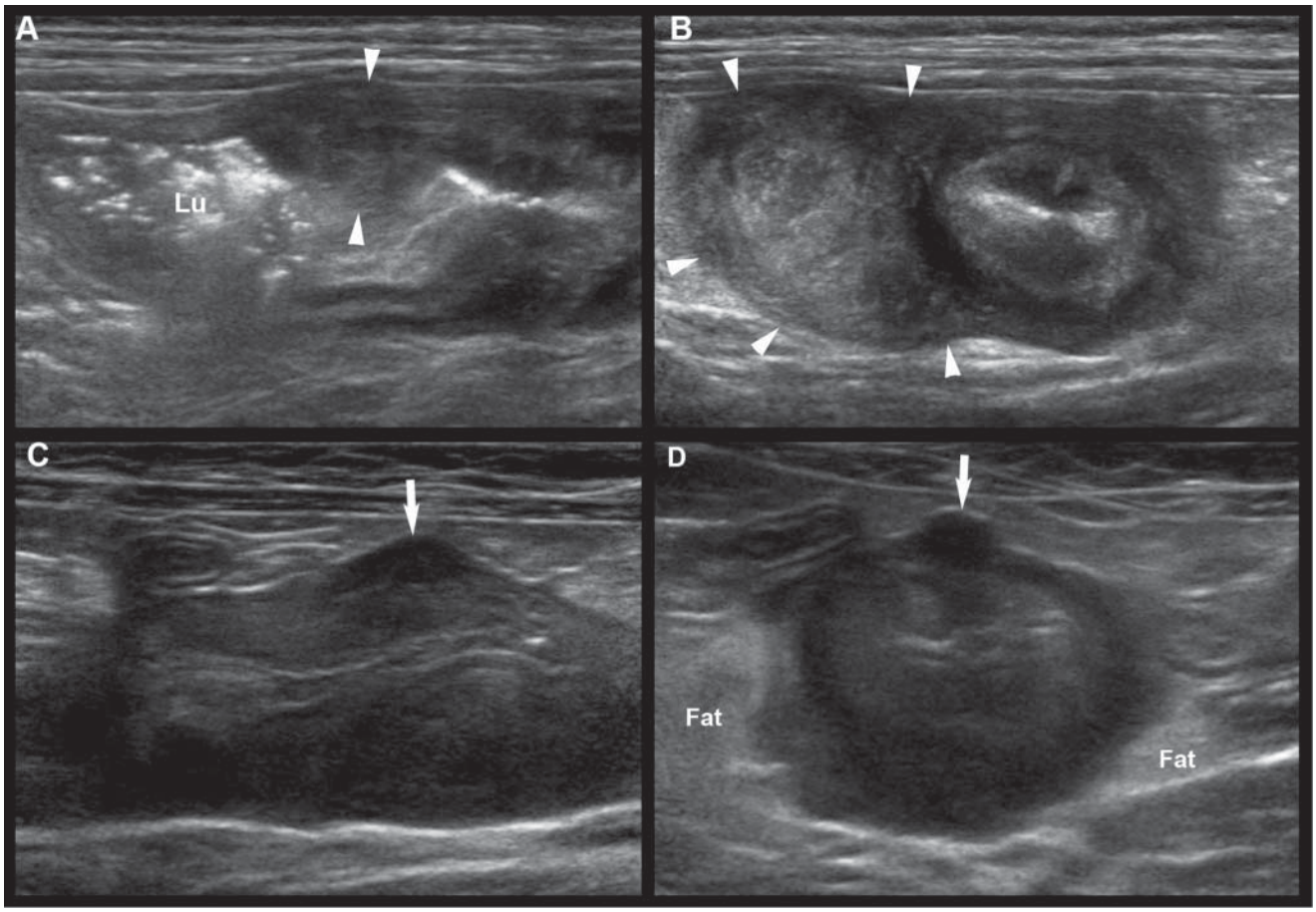


Figure 8.69. Granulomatous enteritis in a dog and a cat. Sagittal (**A**) and transverse (**B**) sonograms of a segment of jejunum in a Portuguese Water Dog. The wall (arrowheads) of this jejunal segment is thickened and associated with loss of layering, and its lumen (Lu) has irregular contours. In the transverse view (**B**), the asymmetric and eccentric distribution is more obvious (arrowheads). Longitudinal **(C)** and transverse **(D)** sonograms of the thickened descending colon in a 1-year-old cat. The serosal contour is irregular (arrow). Marked disruption of the wall layering is noted. The regional fat is also hyperechoic.

or biopsies of these lesions is essential not to misdiagnose them as neoplastic, and to choose the optimal treatment modality.

Congenital Disorders

Congenital GI disorders are rare in small animals. Intestinal duplication has been reported in the literature (Spaulding et al. 1990; Parry-Smith et al. 2008). They can be encountered in any segment of the GI tract, and even though they represent a benign process that may be incidentally detected later in life, they are sometimes associated with pancreatitis (if duodenal in origin) or neoplasia (Figure 8.70)

Congenital pyloric stenosis mostly reported in brachycephalic dogs results in concentric hypertrophy of the circular smooth muscle layer. Gastric hyperplastic polyp associated with obstruction can be seen in French Bulldog puppies (Kuan et al. 2009) (Figure 8.71) and in adults.

In small-breed dogs, chronic hypertrophic pyloric stenosis can be encountered (Figure 8.72). The hypertrophic and/or hyperplastic changes primarily affect the smooth muscle layer of the pylorus

Figure 8.68. Feline eosinophilic sclerosing fibroplasia in two cats. Transverse **(A)** and longitudinal **(B)** sonograms of a large asymmetric and inhomogeneous mass (arrowheads) deforming the contour of the colon in a 10-year-old Rag cat. Lu, lumen. Notice the large hyperechoic areas (*) within the mass, corresponding to the abundant fibrosis. **C:** An eccentric jejunal mass with hyperechoic area is present in an 8-year-old cat. **D:** An inhomogeneous mixed echogenicity nodule (between cursors) is also seen in the liver (L) and was also confirmed as eosinophilic sclerosing fibroplasia. Concurrent muscular hypertrophy (*) is noted in adjacent intestines, as seen in the near field on **C**.

Figure 8.71. Gastric hyperplastic polyp in two French Bulldogs. Sagittal **(A)** and transverse **(B)** sonograms of an exuberant nodular lesion at the pylorus of this 4-month-old French Bulldog with a history of lethargy and regurgitation. In these images there is a multilayered pattern that is suggestive of intussusception. The arrowheads outline the asymmetrical but circumferential lesion protruding into the gastric lumen. **C, D**: Similar lesions are also present in this 2-year-old French Bulldog. In these two dogs, the final diagnosis after surgical resection was chronic mucosal hyperplasia/hyperplastic polyp. GB, gallbladder; L, liver; lu, lumen of pyloric antrum.

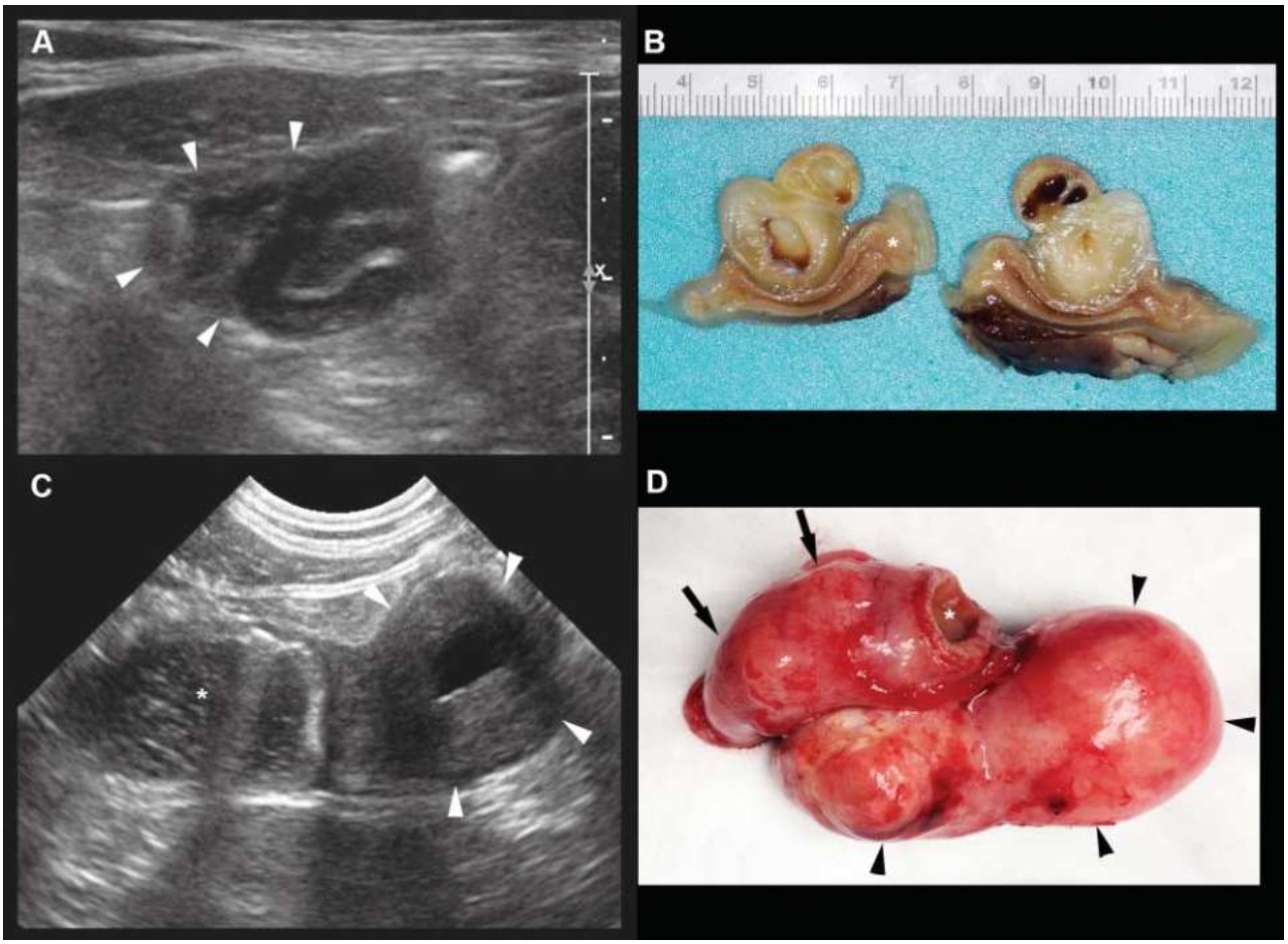


Figure 8.70. Intestinal duplication in two cats. A, B: An 8-year-old cat with decreased appetite. **A**: the mesenteric border of the duodenum (arrowheads) is deformed by a thick-walled cavitated structure. **B:** Corresponding gross sections of the resected duodenum (*) and the duplication (arrowheads), confirmed histopathologically. **C, D:** A 15-year-old cat presented for vomiting. **C:** The fluid-distended duodenum (*) is obstructed by the adjacent thick-walled, cystic mass protruding in the duodenal lumen. **D:** Corresponding gross sections of the resected duodenum (*) and the duplication (arrowheads)**.** The final histopathological diagnosis was duodenal duplication with adenocarcinoma (arrows).

(Biller et al. 1994), but it is common to see concurrent mucosal changes. Because of this chronic condition, the stomach tends to be flaccid, and a moderate amount of fluid or food accumulates in it.

GI Vascular Disorders

Infarction, ischemia or angiodysplasia are uncommon and very challenging to diagnose (Fan et al. 1999; Wallack et al. 2003). Bowel infarction may be difficult to identify with ultrasound initially. The affected segment(s) may become dilated with variable wall thickening and normal layering. Subsequently (72 hours after presentation), wall thickening becomes more obvious and layers become indistinct. The adjacent fat becomes hyperechoic and peritoneal effusion develops (Figure 8.73). Mesenteric vessels should be

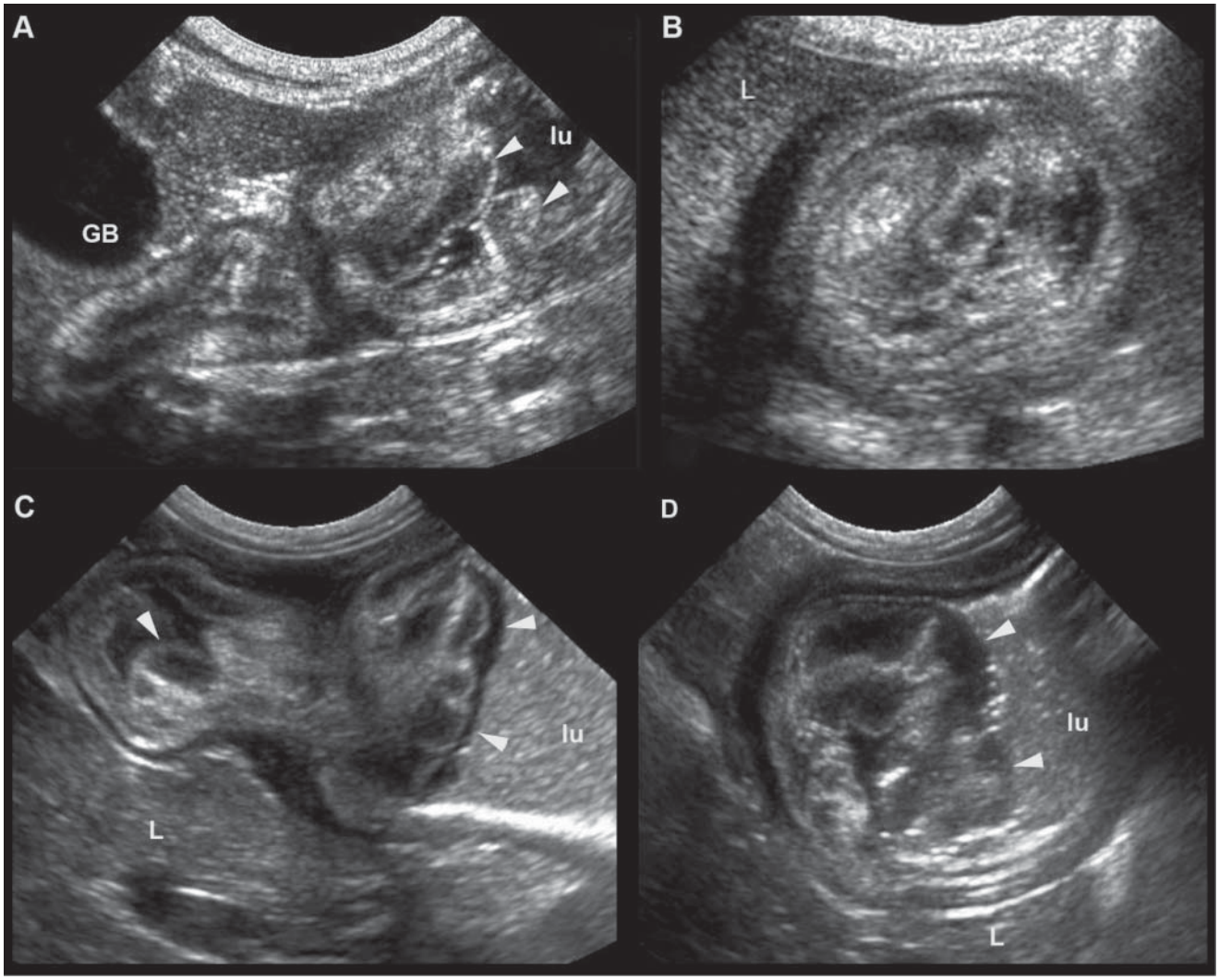


Figure 8.71. **Gastric hyperplastic polyp in two French Bulldogs.** (for full caption, see facing page)

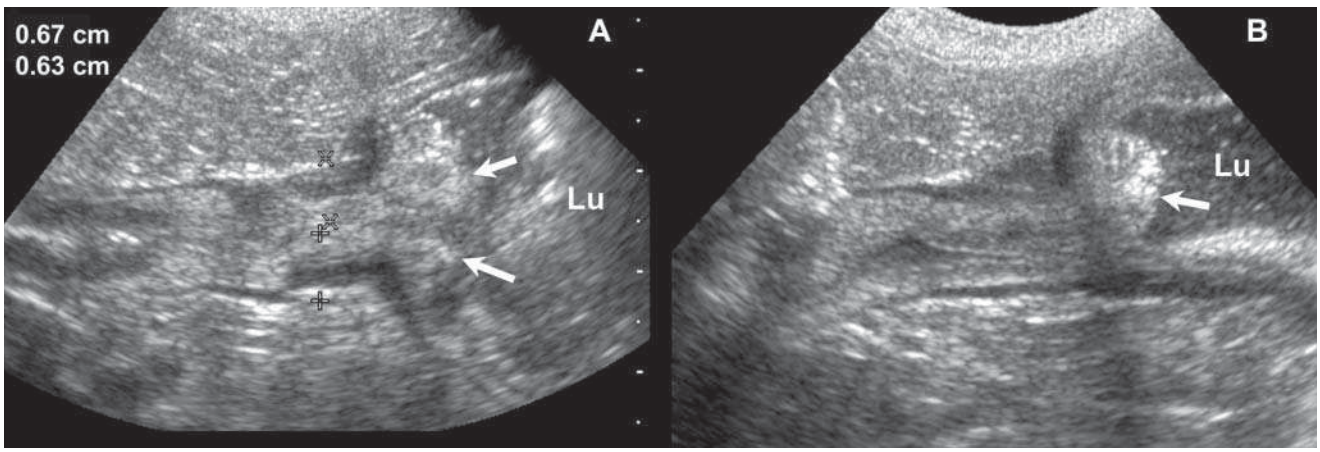


Figure 8.72. **Chronic hypertrophic pyloric stenosis. A, B:** There is moderate thickening at the pyloroduodenal junction in this 9-year-old Shih Tzu. The hypertrophied walls (between the cursors) protrude as two rounded projections (arrows) into the fluid-filled pyloric antrum (Lu). The wall layers are faintly visible.

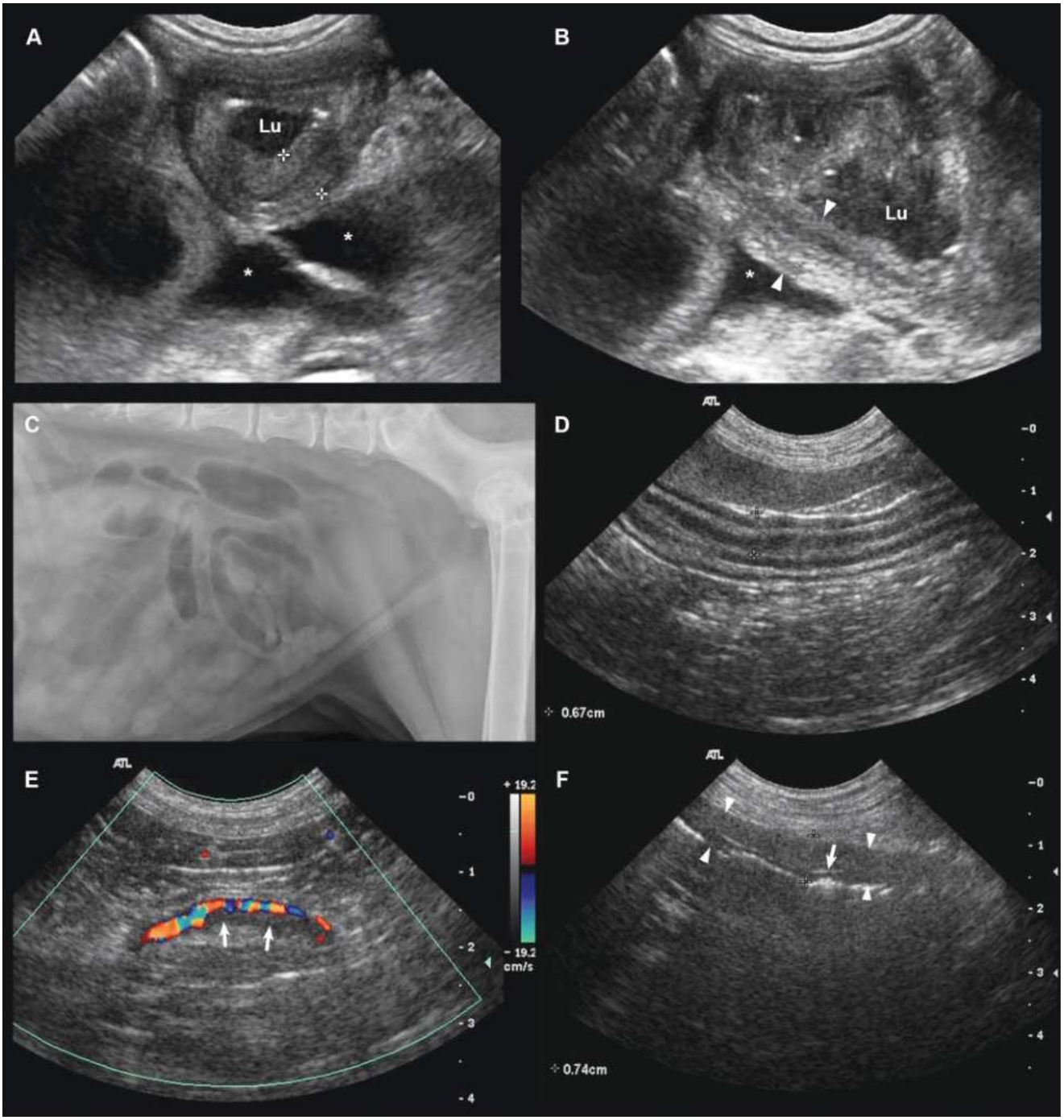


Figure 8.73. **Vascular compromise due to intestinal volvulus in a 3-year-old Poodle presented for acute abdominal pain and vomiting. A:** Most intestinal loops are thickened (6–7 mm), with loss of layering (arrowheads), and hypomotile. Peritoneal effusion (*) is present. **B:** Amorphous echogenic structures floating within the lumen were shown to be blood clots and mucosal sloughing on autopsy. Lu, intestinal lumen. **C–F:** Mesenteric thromboembolism and infarction in a Golden Retriever with glomerulonephritis and hypercoagulability. **C**: Lateral abdominal radiograph obtained at the time of presentation in which several intestinal loops are mildly dilated with gas and fluid. **D, E**: Subsequent ultrasound examination showed moderate thickening of a few segments of jejunum (0.67mm, cursors in **A**) and partial thrombosis (arrows) of a branch of the cranial mesenteric artery. **F:** On follow-up examination after the beginning of thrombolytic therapy (2 days later), jejunal wall thickening progressed (between arrowheads and cursors) and layers became indistinct. Additionally, pneumatosis (arrow) dissecting the wall was present. The abdominal fat was also markedly hyperechoic and hyperattenuating, preventing identification of vessels.

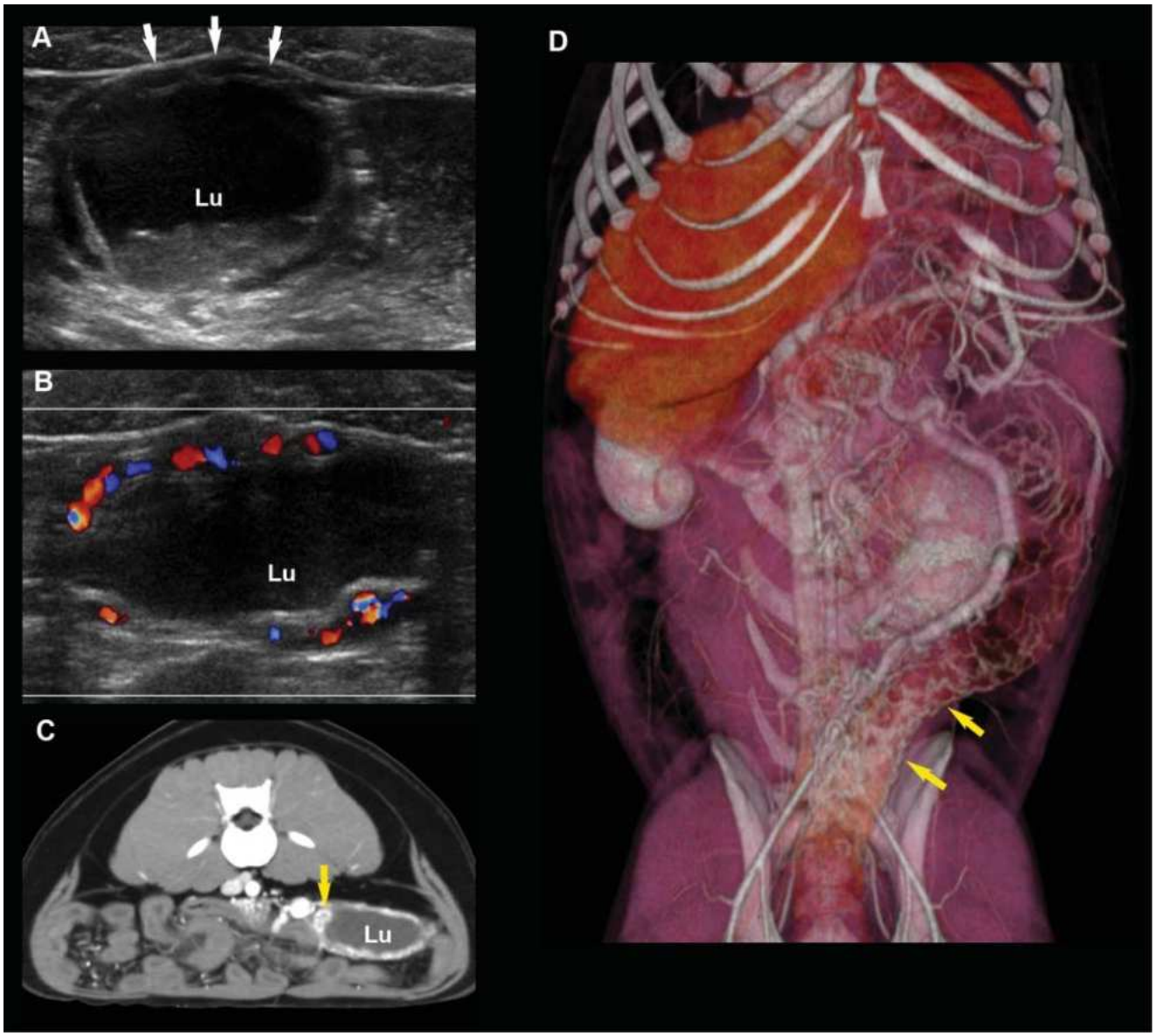


Figure 8.74. Intestinal vascular anomaly in a 9-month-old Labrador dog with vomiting and diarrhea. A, B: Transverse sonograms of one fluid-filled colonic segment with a thickened, nodular-like wall made of intramural enlarged varices (arrows in **A**), as confirmed using color flow Doppler **(B)**. A large network of numerous anomalous small vessels was seen throughout the abdomen, especially in the mesentery and near the main portal vein. **C:** Transverse post-contrast computed tomography (CT) image of the caudal abdomen showing the intramural colonic vessels (arrow). **D:** Reconstructed CT dorsal image illustrating the numerous anomalous enlarged and tortuous vessels (arrows) supportive of portal hypertension and acquired portosystemic shunts. The left side of the liver is nearly absent. Because of the guarded prognosis, the dog was euthanized and the final diagnosis is arteriovenous malformation with marked arteriolar proliferation and hypertrophy, venous ectasia, lobular atrophy, and fibrosis.

assessed for the presence of thrombosis, although this evaluation may be limited by hyperattenuating fat.

In severe congenital or acquired vascular disorders, numerous anomalous vessels (arteriovenous fistulae or varices) may develop as the result of portal hypertension, and also affect the GI tract (Figure 8.74). In these cases, it is recommended to perform a CT angiogram to assess the abdominal vasculature more completely.

Interventional Procedures

Percutaneous ultrasound-guided fine-needle aspiration and automated microcore biopsy of GI lesions are safe, alternative procedures to use instead of endoscopic or surgical biopsy. The guided techniques of fine-needle aspiration using either a 22- or 20-gauge spinal needle, and/or microcore automated biopsy

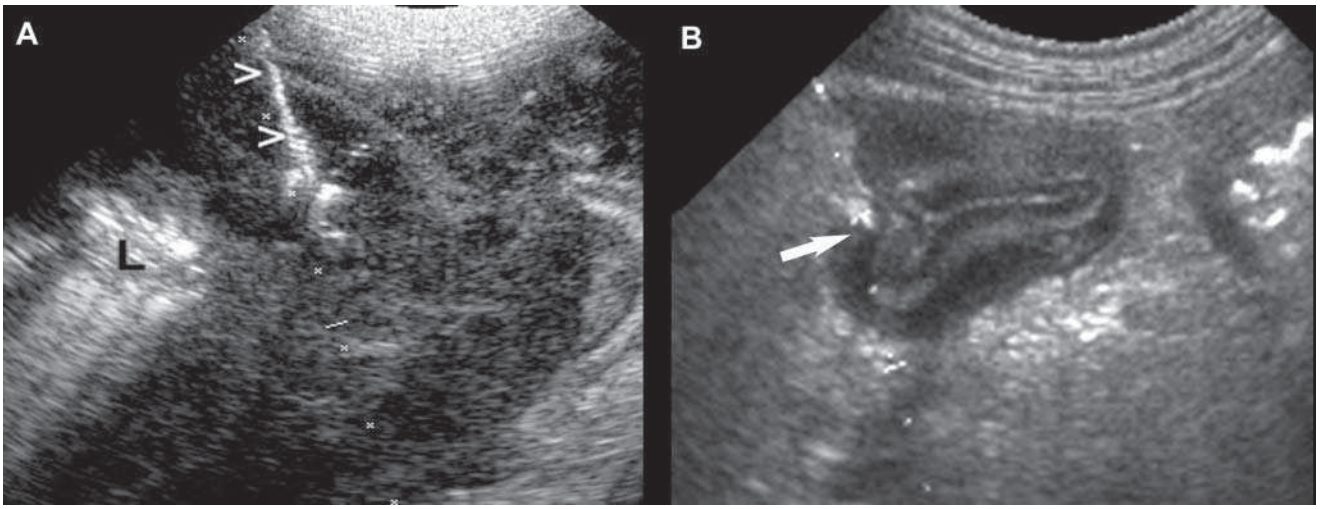


Figure 8.75. Ultrasound-guided biopsy and fine-needle aspiration. A: An ultrasound-guided core biopsy was performed on this markedly thickened and distorted intestinal wall of a dog diagnosed with lymphoma. The visible needle path enables careful placement of the needle (>), far away from the intestinal lumen (L). **B:** Fine-needle aspiration can also be performed safely. Notice the needle tip (black arrow) engaged in this mildly thickened bowel segment.

using an 18-gauge Tru-Cut needle, assisted by an automated biopsy gun, are efficient and safe methods of obtaining a diagnostic sample (Penninck et al. 1993) (Figure 8.75).

They are especially useful when lesions are not accessible endoscopically – because of their location in the GI tract or when involving a deep portion of the wall – and when surgical resection is not a safe option for a compromised patient. One paramount safety rule is to carefully locate and avoid the lumen.

In the presence of a GI lesion associated with regional lymphadenopathy, it is recommended to target both structures in order to increase the chance of obtaining one or more diagnostic samples.

Complications such as local hemorrhage or seroma collection (Figure 8.47) are uncommon. Intestinal content leakage, which can be a serious complication, can be avoided by careful selection of the biopsy site.



Visit our website at **www.SmallAnimalUltrasonography.com** for complementary video clips with annotations and text on:

- Normal GI anatomy and scanning (dog and cat)
- Intussusception
- Foreign bodies
- Enteritis
- Lymphangiectasia
- Ulceration
- Lymphoma
- Carcinoma
- Mesenchymal tumors

References

Baez JB, Hendrick MJ, Walker LM, Washabau RJ (1999) Radiographic, ultrasonographic, and endoscopic findings in cats with inflammatory bowel disease of the stomach and small intestine: 33 cases (1990–1997). J Am Vet Med Assoc 215:349–354.

Besso J, Rault D, Begon (2004). Feline cecum and ileocecocolic junction: normal ultrasonographic features and clinical applications (abstract). Vet Radiol Ultrasound 45:599.

Biller DS, Partington BP, Miyabayashi T, Leveille R (1994) Ultrasonographic appearance of chronic hypertrophic pyloric gastropathy in the dog. Vet Radiol Ultrasound 35:30–33.

Boysen SR, Tidwell AS, Penninck DG (2003) Sonographic findings in dogs and cats with intestinal perforation: A retrospective study (1995–2001). Vet Radiol Ultrasound 44:556–564.

Citi S, Chimenti T, Marchetti V, Millanta F, Mannucci T(2013). Micronodular lesions in the colonic submucosa in 42 dogs and 14 cats. Vet Radiol Ultrasound 54:646–651.

Couturier L, Rault D, Gatel L, Belli P (2012) Ultrasonographic characterization of the feline cardia and pylorus in 34 healthy cats and three abnormal cats. Vet Radiol Ultrasound 53:342–347.

Culp WT, Drobatz KJ, Glassman MM, et al. Feline visceral hemangiosarcoma. J Vet Intern Med 2008;22(1):148–52.

Daniaux LA, Laurenson MP, Marks SL, Moore PF, Taylor SL, Chen RX, Zwingenberger AL (2014) Ultrasonographic thickening of the muscularis propria in feline small intestinal small cell T-cell lymphoma and inflammatory bowel disease. J Feline Med Surg 16(2):89–98.

Delaney F, O'Brien RT, Waller K (2003) Ultrasound evaluation of small bowel thickness compared to weight in normal dogs. Vet Radiol Ultrasound 44:577–580.

Di Donato P, Penninck DG, Pietra M, Cipone M, Diana A (2014) Ultrasonographic measurement of the relative thickness of intestinal wall layers in clinically healthy cats. J Feline Med Surg 16:333–339.

Diana A, Pietra M, Guglielmini C, Boari A, Bettini G, Cipone M (2003) Ultrasonographic and pathologic features of intestinal smooth muscle hypertrophy in four cats. Vet Radiol Ultrasound 44:566–569.

Diana A, Penninck DG, Keating JH (2009) Sonographic findings of gastric polyps in 7 dogs. Vet Radiol Ultrasound 50:201–204.

Dominguez E, Anadon E, Espada Y, Grau-Roma L, Majo N, Novellas R (2014) Imaging diagnosis-ultrasonographic appearance of small bowel metastasis from canine mammary carcinoma. Vet Radiol Ultrasound 55: 208–212.

Fan TM, Simpson KW, Polack E, Dykes N, Harvey J (1999) Intestinal haemorrhage associated with colonic vascular ectasia (angiodysplasia) in a dog. J Small Anim Pract 40:25–30.

Gaschen L (2011). Ultrasonography of small intestinal inflammatory and neoplastic diseses in dogs and cats. Vet Clin Small Anim 41:329–344.

Gaschen L, Kircher P, Stüssi A et al (2008) Comparison of ultrasonographic findings with clinical activity index (CIBDAI) and diagnosis in dogs with chronic enteropathies. Vet Radiol Ultrasound 49:56–64.

Gladwin NE, Penninck D, Webster CRL (2014) Ultrasonographic evaluation of the thickness of wall layers in the intestinal tract of dogs. Am J Vet Res 75:349–353.

Goggin JM, Biller DS, Debey BM, Pickar JG, Mason D (2000) Ultrasonographic measurement of gastrointestinal wall thickness and the ultrasonographic appearance of the ileocolic region in healthy cats. J Am Anim Hosp Assoc 36:224–228.

Graham JP, Newell SM, Gregore GB, Lester NV (2000) Ultrasonographic features of canine intestinal pythiosis. Vet Radiol Ultrasound 41:273–277.

Grooters AM, Miyabayashi T, Biller DS, Merryman J (1994) Sonographic appearance of uremic gastropathy in four dogs. Vet Radiol Ultrasound 35:35–40.

Hoffman KL (2003) Sonographic signs of gastroduodenal linear foreign body in 3 dogs. Vet Radiol Ultrasound 44:466–469.

Junius G, Appeldoorn AM, Schrauwen E (2004) Mesenteric volvulus in the dog: a retrospective study of 12 cases. J Small Anim Pract. 45:104–107.

Kuan S, Hoffman K, Tisdall (2009) Ultrasonogrphic and surgical findings of a gastric hyperplastic polyp resulting in pyloric obstruction in an 11-week-old French Bulldog. Aus Vet J 87:253–255.

Kvitko-White HL, Sayre RS, Corapi WV, Kathy A, Spaulding KA (2011). Imaging diagnosis – Heterobilharzia americana infection in a dog. Vet Radiol Ultrasound 52:538–541.

Lamb CR, Mantis P (1998) Ultrasonographic features of intestinal intussusception in 10 dogs. J Small Anim Pract 39:437–441.

Laurenson MP, Skorupski KA, Moore PF, Zwingenberger AL (2011) Ultrasonography of intestinal mast cell tumors in the cat. Vet Radiol Ultrasound 52:330–334.

Lee H, Yeon S, Lee H, et al. (2005) Ultrasonographic diagnosis: Pylorogastric intussusception in a dog. Vet Radiol Ultrasound 46:317–318.

MacDonald JM, Mullen HS, Moroff SD (1993) Adenomatous polyps of the duodenum in cats: 18 cases (1985–1990). J Am Vet Med Assoc 202(4):647–651.

Mareschal A, Penninck D (2010) Long term ultrasonographic follow-up of intestinal surgical sites in dogs. Vet Radiol Ultrasound 51:652–655.

Moon ML, Biller DS, Armbrust LJ (2003a) Ultrasonographic appearance and etiology of corrugated small intestine. Vet Radiol Ultrasound 44:199–203.

Matthews AR, Penninck DG, Webster CRL (2008) Assessment of post-operative ultrasonographic appearance of uncomplicated enterotomy or enterectomy sites in dogs. Vet Radiol Ultrasound 49: 477–483.

Moon M, Biller D, Armbrust LJ (2003b) Ultrasonographic appearance and etiology of intestinal corrugated small intestines. Vet Radiol Ultrasound 44:199–203.

Myers NC, Penninck DG (1994) Ultrasonographic diagnosis of gastrointestinal smooth muscle tumors in the dog. Vet Radiol Ultrasound 35:391–397.

Newell SM, Graham JP, Roberts GD, Ginn PE, Harrison JM (1999) Sonography of the normal feline gastrointestinal tract. Vet Radiol Ultrasound 40:40–43.

Paoloni MC, Penninck DG, Moore AS (2002) Ultrasonographic and clinicopathologic findings in 21 cases of canine intestinal adenocarcinoma. Vet Radiol Ultrasound 43:562–567.

Patsikas MN, Papazoglou LG, Papaioannou NG, Savvas I, Kazakos GM, Dessiris AK (2003) Ultrasonographic findings of intestinal intussusception in seven cats. J Feline Med Surg 5:335–343.

Parry-Smith P, Czerwinska M, Krudewig C (2008) Duodenal duplication cyst in a young cat. Vet Record 162:826–827.

Penninck DG (1998) Ultrasonographic characterization of gastrointestinal tumors. Vet Clin North Am 28:777–797.

Penninck DG (2002) Gastrointestinal tract. In: Nyland T, Mattoon J, eds. Small Animal Diagnostic Ultrasound, 2nd edition. Philadelphia: WB Saunders, pp 207–230.

Penninck DG, Crystal MA, Matz ME, Pearson SH (1993) The technique of percutaneous ultrasound guided fine-needle aspiration biopsy and automated microcore biopsy in small animal gastrointestinal diseases. Vet Radiol Ultrasound 34:433–436.

Penninck DG, Matz M, Tidwell AS (1997) Ultrasonographic detection of gastric ulceration. Vet Radiol Ultrasound 38:308–312.

Penninck D, Mitchell SL (2003) Ultrasonographic detection of ingested and perforating wooden foreign bodies in four dogs. J Am Vet Med Assoc 223:206–209.

Penninck DG, Moore AS, Gliatto J (1998) Ultrasonography of canine gastric epithelial neoplasia. Vet Radiol Ultrasound 39:342–348.

Penninck DG, Moore AS, Tidwell AS, Matz ME, Freden GO (1994) Ultrasonography of alimentary lymphosarcoma in the cat. Vet Radiol Ultrasound 35:299–304.

Penninck DG, Nyland TG, Fisher PE, Kerr LY (1989) Normal ultrasonography of the canine gastrointestinal tract. Vet Radiol Ultrasound 30:272–276.

Penninck DG, Smyers B, Webster CRL, Rand W, Moore AS (2003) Diagnostic value of ultrasonography in differentiating canine enteritis from intestinal neoplasia. Vet Radiol Ultrasound 44:570–575.

Penninck D, Webster CRL, Keating JH (2010) The sonographic appearance of intestinal mucosal fibrosis in cats. Vet Radiol Ultrasound 51:458–461.

Rudorf H, van SG, O'Brien RT et al. (2005) Ultrasonographic evaluation of the thickness of the small intestinal wall in dogs with inflammatory bowel disease. J Small Anim Pract 46:322–326.

Pollard R, Johnson EG, Pesavento PA, Baker TW, Cannon AB et al. (2013) Effect of corn oil administered orally on conspicuity of ultrasonographic small intestinal lesions in dogs with lymphangiectasia. Vet Radiol Ultrasound 54:390–397.

Rault DN, Besso JG, Boulouha L, Begon D (2004) Significance of a common extended mucosal interface observed in transverse small intestine sonograms. Vet Radiol Ultrasound 45:177–179.

Smith TJ, Baltzer WI, Ruaux CG, Heidel JR, Carney P (2010) Gastric smooth muscle hamartoma in a cat. J Feline Med Surg 12:334–337.

Spaulding KA, Cohn LA, Miller RT, Hardie EM (1990) Enteric duplication in two dogs. Vet Radiol Ultrasound 31:83–88.

Standler N, Wagner W (2010) Ultrasonographic appearance of canine parvoviral enteritis. Vet Radiol Ultrasound 51:69–74.

Stimson EL, Cook WT, Smith MM, Forrester SD, Moon ML, Saunders GK (2000) Extraskeletal osteosarcoma in the duodenum of a cat. J Am Anim Hosp Assoc 36: 332–336.

Sutherland-Smith J, Penninck DJ, Keating JH, Webster CRL (2007) The morphological significance of ultrasonographic intestinal hyperechoic striations in dogs. Vet Radiol Ultrasound 48:51–57.

Taeymans O, Holt N, Penninck D, Webster CR (2011) Ultrasonographic characterization of feline ileocecocolic abnormalities. Vet Radiol Ultrasound 52:335–339.

Tidwell AS, Penninck DG (1992) Ultrasonography of gastrointestinal foreign bodies. Vet Radiol Ultrasound 33:160–169.

Tucker S, Penninck D, Keating JH, Webster CRL (2014) The histopathologic and ultrasonographic features of eosinophilic enteritis in cats: 27 cases (2002–2011). J Feline Med Surg. Online: March 3, 2014.

Venco L, Kramer L, Pagliaro L, Genchi C (2005) Ultrasonographic features of peritoneal cestodiasis caused by Mesocestoides sp. in a dog and in a cat. Vet Radiol Ultrasound 46:417–422.

Wallack ST, Hornof WJ, Herrgesell EJ (2003) Ultrasonographic diagnosis: Small bowel infarction in a cat. Vet Radiol Ultrasound 44:81–85.

Weissman A, Penninck D, Wester C, Hecht S, Keating J, Craig LE (2012) Ultrasonographic and clinicopathological features of feline gastrointestinal eosinophilic sclerosing fibroplasia in 4 cats. J Feline Med Surg 15:148–154.

Winter MD, Londono L, Berry CR, Hernandez JA (2014) Ultrasonographic evaluation of relative gastrointestinal layer thickness in cats without clinical evidence of gastrointestinal tract disease. J Feline Med Surg 16:118–124.

Zwingenberger AL, Marks SL, Baker TW, Moore PF (2010) Ultrasonographic evaluation of the muscularis propria in cats with diffuse small intestinal lymphoma or inflammatory bowel disease. J Vet Int Med 24: 289–292.

CHAPTER NINE

Pancreas

Dominique Penninck[1] and Marc-André d'Anjou[2,3]

[1] *Department of Clinical Sciences, Cummings School of Veterinary Medicine, Tufts University, North Grafton, MA, USA*
[2] *Centre Vétérinaire Rive-Sud, Brossard, Québec, Canada*
[3] *Faculté de médecine vétérinaire de l'Université de Montréal, Saint-Hyacinthe, Québec, Canada*

Preparation and Scanning Procedure

The pancreas is a thin, elongated organ located along the greater curvature of the stomach and the mesenteric border of the descending duodenum. Gas in the gastrointestinal tract often hampers complete evaluation. A 12-hour fast may reduce gas interference.

The anatomical landmarks used to locate the right pancreatic lobe are the right kidney; the descending duodenum, with its straight course along the right abdominal wall; and the pancreaticoduodenal vein paralleling the descending duodenum (Figure 9.1). The right pancreatic lobe can be imaged from a ventral or lateral approach, with a longitudinal scan-plane orientation used to find the descending duodenum and right kidney. Using the ventral approach, the transducer is placed under the last rib of the animal and angled dorsally to image the right kidney. The scan plane is then moved medially until the descending duodenum is imaged medial to the right kidney. Alternatively, the ventral approach can start caudal to the xiphoid process. In a longitudinal scan plane, the stomach is identified and the scan plane is moved laterally toward the right following the pyloric antrum into the descending duodenum. This latter approach is often limited to cats and small dogs.

The lateral approach is preferred to locate the descending duodenum in deep-chested dogs. Once the descending duodenum is located by using the ventral or lateral approach, the right pancreatic lobe and the pancreaticoduodenal vein can be identified. In large and deep-chested dogs, it is often necessary to use an intercostal window to access the most cranial portion of the descending duodenum and the corresponding portion of the pancreas. On occasion, the right pancreatic lobe is best scanned from the right side, with the animal in a right lateral recumbency as gastric fluid moves in the dependent pyloric antrum.

The pancreatic body can be imaged from ventrally or from the right side, with the animal in a dorsal, left, or right lateral recumbent position, by moving the scan plane craniomedially to the proximal descending duodenum and caudally to the pyloric antrum. The portal vein is a useful landmark located just dorsal and to the left of the body of the pancreas (Figure 9.1). A transverse scan just caudal to the porta hepatis and pylorus may be used to locate this vein and the body of the pancreas. The left pancreatic lobe is more difficult to image in dogs because of gas interference in the adjacent stomach and transverse colon. However, in cats, the left limb can usually be more easily identified than the right limb.

High-frequency transducers (≥8 MHz) are recommended to evaluate the pancreas, especially in cats and small to medium-sized dogs. The small contact area of sectorial, narrow curvilinear or microconvex transducers facilitates access to the right cranial abdominal quadrant for imaging under or between the right ribs.

Ultrasonography of the Normal Pancreas

In Dogs

The pancreas is thin, amorphous, and poorly distinct from the adjacent mesenteric fat. The pancreas is divided into three portions: right lobe, left lobe, and body (Figure 9.1). The right lobe lies in the mesoduodenum, dorsomedial to the descending duodenum, ventral to the right kidney, and ventrolateral to the

Atlas of Small Animal Ultrasonography, Second Edition. Edited by Dominique Penninck and Marc-André d'Anjou.
© 2015 John Wiley & Sons, Inc. Published 2015 by John Wiley & Sons, Inc.
Companion website: www.SmallAnimalUltrasonography.com

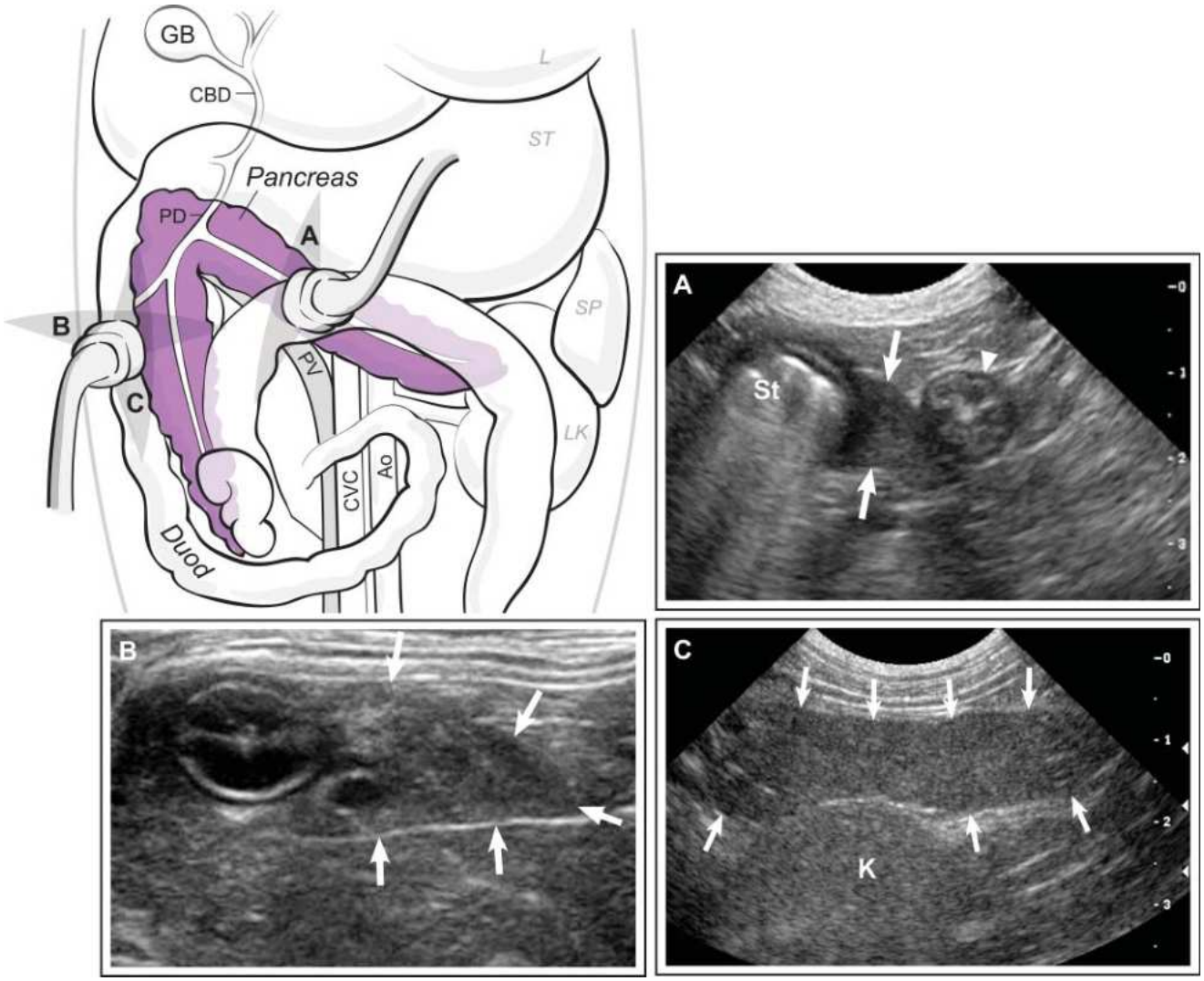


Figure 9.1. **Approach to the normal canine pancreas.** Illustration of the pancreas within the abdominal cavity, with the probe positioned along the left and right lobes of this organ at locations A, B, and C. Ao, aorta; CBD, common bile duct; CVC, caudal vena cava; Duod, duodenum; GB, gallbladder; L, liver; LK, left kidney; PD, pancreatic duct; PV, portal vein; SP, spleen; ST, stomach. **A:** Transverse sonogram of the left lobe (arrows) seen between the stomach (St) and the collapsed transverse colon (arrowhead). **B:** Transverse sonogram of the right lobe of the pancreas (arrows). The layered descending duodenum is lateral to the pancreas. The pancreaticoduodenal vein appears as an anechoic rounded structure within the lobe. **C:** Longitudinal sonogram of the right pancreatic lobe (arrows) near the right kidney (K).

portal vein. Mostly the veins draining the right lobe are seen ultrasonographically. The body lies caudal to the pyloric region, in the right cranial abdomen, and craniomedial to the right kidney and ventral to the portal vein. The left lobe originates at the pancreatic body, lies dorsocaudal to the gastric antrum, and continues across the midline between the stomach and the transverse colon. The normal left lobe is occasionally seen in the triangular region defined by the spleen, stomach, and left kidney. The normal pancreas is homogeneous and is isoechoic or slightly hyperechoic to the liver The pancreaticoduodenal vein is seen clearly in the right lobe and can be followed into the gastroduodenal vein and portal vein. Seldom, a normal pancreas can be diffusely hyperechoic but within normal range for size (Figure 9.2).

The mean measurements of the normal canine pancreas and pancreatic duct are summarized in Table 9.1. A useful reference value for the thickness of a normal pancreas in a medium-sized dog (15–30 kg) is about

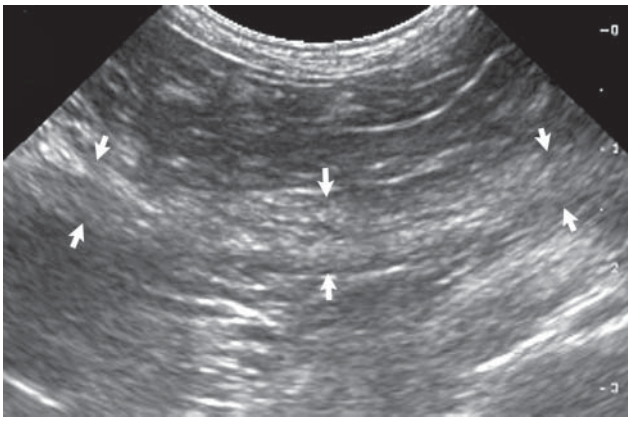


Figure 9.2. Normal pancreas in an old dog. Longitudinal sonogram of the left lobe of the pancreas in this 12-year-old Yorkie. The pancreas (arrows) is diffusely increased in echogenicity but maintains a normal size. The histopathology of the pancreas was unremarkable.

Table 9.1
Guidelines for measurements of the pancreas and pancreatic duct in dogs and cats

	Mean left lobe thickness	Mean body thickness	Mean right lobe thickness	Pancreatic duct diameter
Dogs[a]	6.5 mm	6.3 mm	8.1 mm	0.6 mm
Cats[b]	5.8 mm	6.2 mm	4.4 mm	1 mm[c]

Results are displayed as means according to the references in the notes below.
[a]In dogs without clinical signs of gastrointestinal disease (Penninck et al. 2013). The authors also found that the pancreatic thickness in all lobes and diameter of the pancreatic duct significantly increased with body weight.
[b]The means presented in the table are compiled means obtained from four references (Etue et al. 2001; Moon et al. 2005; Hecht et al. 2006; Hecht and Henry 2007).
[c]Reported to be up to 2.5 mm in older (>10 years old) cats without evidence of pancreatic disease.

1 cm (Penninck et al. 2013). Contrary to previous reports, the pancreatic duct can be seen in normal dogs, especially in the right lobe. Penninck et al. (2013) also found that pancreatic thickness and pancreatic duct diameter correlate with body weight, but not with age.

In Cats

In contrast to dogs, the caudal third of the feline right limb curves cranially, giving it a hook-like appearance (Etue et al. 2001). The pyloroduodenal angle and the pancreatic body are more centrally located, and the angle formed by the left and right lobes with the pancreatic body is narrower. The normal sonographic appearance of the feline pancreas is isoechoic to slightly hyperechoic to the adjacent liver lobes and nearly isoechoic to the surrounding mesenteric fat (Figure 9.3).

The mean thickness measurements for each part of the pancreas and the pancreatic duct in cats are summarized in Table 9.1. The left lobe of the pancreas is often more easily identified than the right lobe. It is also important to know that in older cats (>10 years old), the pancreatic duct diameter can be dilated up to 2.5 mm without concurrent pancreatic disorders (Hecht et al. 2006, 2007).

Ultrasonographic Features of Pancreatic Disorders

Pancreatitis

Pancreatitis has various ultrasonographic appearances, depending on the severity, duration, and extent of pancreatic and peripancreatic tissue inflammation.

In acute pancreatitis, the pancreas is enlarged and diffusely hypoechoic, while the surrounding fat appears moderately hyperechoic and often hyperattenuating as the result of fat saponification (Figure 9.4). In dogs, the right limb of the pancreas tends to be most commonly affected, whereas in cats, the changes tend to be more severe in the body and left limb.

In cats, similar changes can be seen in acute pancreatitis, but pancreatic enlargement and diffuse changes in pancreatic and surrounding fat echogenicity may be less obvious (Figure 9.5). A combination of tests such as feline pancreatic lipase immunoreactivity (fPLI) and abdominal ultrasound can optimize the non-invasive diagnosis of feline pancreatitis (Forman et al. 2004).

Pancreatitis in cats has been reported to be associated with hepatic lipidosis, inflammatory bowel disease, and cholangiohepatitis (Akol et al. 1993). Recheck ultrasound exams can be valuable in assessing progress (Figure 9.5F)

Thickened gastric and/or duodenal wall and regional peritoneal effusion can be seen in association with pancreatitis (Saunders et al. 2002) (Figure 9.6). The thickening of the gastric and duodenal wall is usually not associated with complete loss of layering, although the wall layers can be altered and gastric

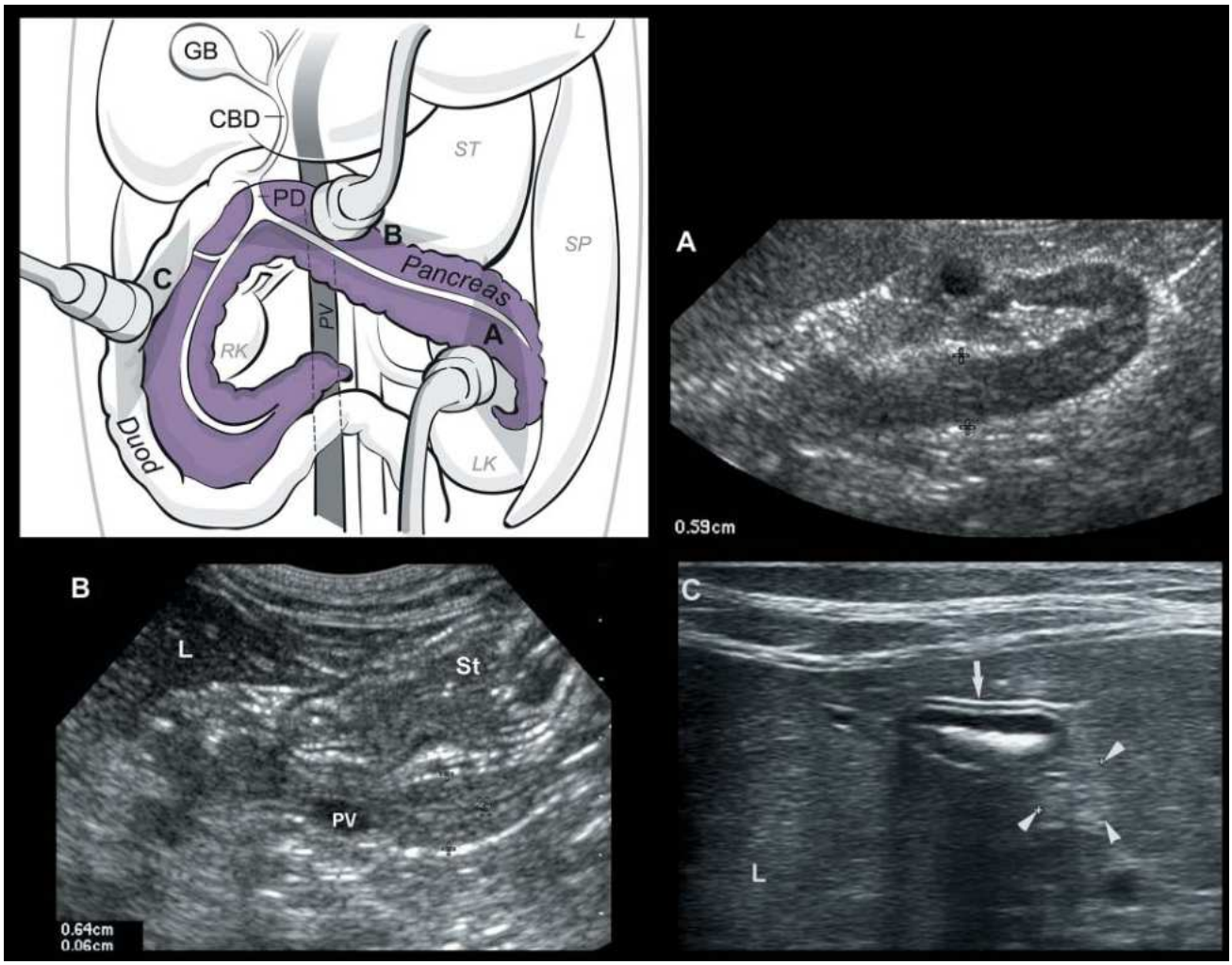


Figure 9.3. Approach to the normal feline pancreas. Illustration of the pancreas within the abdominal cavity with the probe positioned along the left (A) and right lobes (C) and body (B) of this organ. CBD, common bile duct; Duod, duodenum; GB, gallbladder; L, liver; LK, left kidney; PD, pancreatic duct; PV, portal vein; RK, right kidney; SP, spleen; and ST, stomach. **A:** Longitudinal sonogram showing the hook-shaped distal extremity of the left lobe. **B:** Longitudinal sonogram of the body. Notice the PV dorsal to the body (cursors). L, liver; St, stomach. **C:** Transverse sonogram of the right lobe of the pancreas (arrowheads). An arrow points to the duodenum. L: liver.

wall edema may be present (Figure 9.6). Occasionally, the adjacent transverse colon can also be affected (Figure 9.4).

In severe hemorrhagic, necrotizing pancreatitis, irregular hypo- to anechoic area(s) represent necrosis and hemorrhage of part of the pancreas and peripancreatic tissue (Figure 9.7). The pancreatic margins usually become ill-defined. The adjacent mesentery is hyperechoic and hyperattenuating because of regional inflammation and edema. In these cases, contrast enhanced computed tomography can complement ultrasound in better defining the extent of pancreatic necrosis (Jaeger et al. 2003).

Pancreatic edema appears as numerous hypoechoic stripes demarcating pancreatic lobulation and dissecting the enlarged pancreas (Figure 9.8). Pancreatic edema may be associated with pancreatitis (Figure 9.8A,B), although it can also be caused by hypoalbuminemia or portal hypertension (Figure 9.8C) (Lamb 1999).

Focal pancreatic lesions caused by acute pancreatitis contain combined areas of pancreatic necrosis, hemorrhage, and surrounding inflamed mesentery (Edwards et al. 1990). The hypoechoic and anechoic areas corresponding to collections of hemorrhage and necrotic tissue may vary with chronicity, become more organized

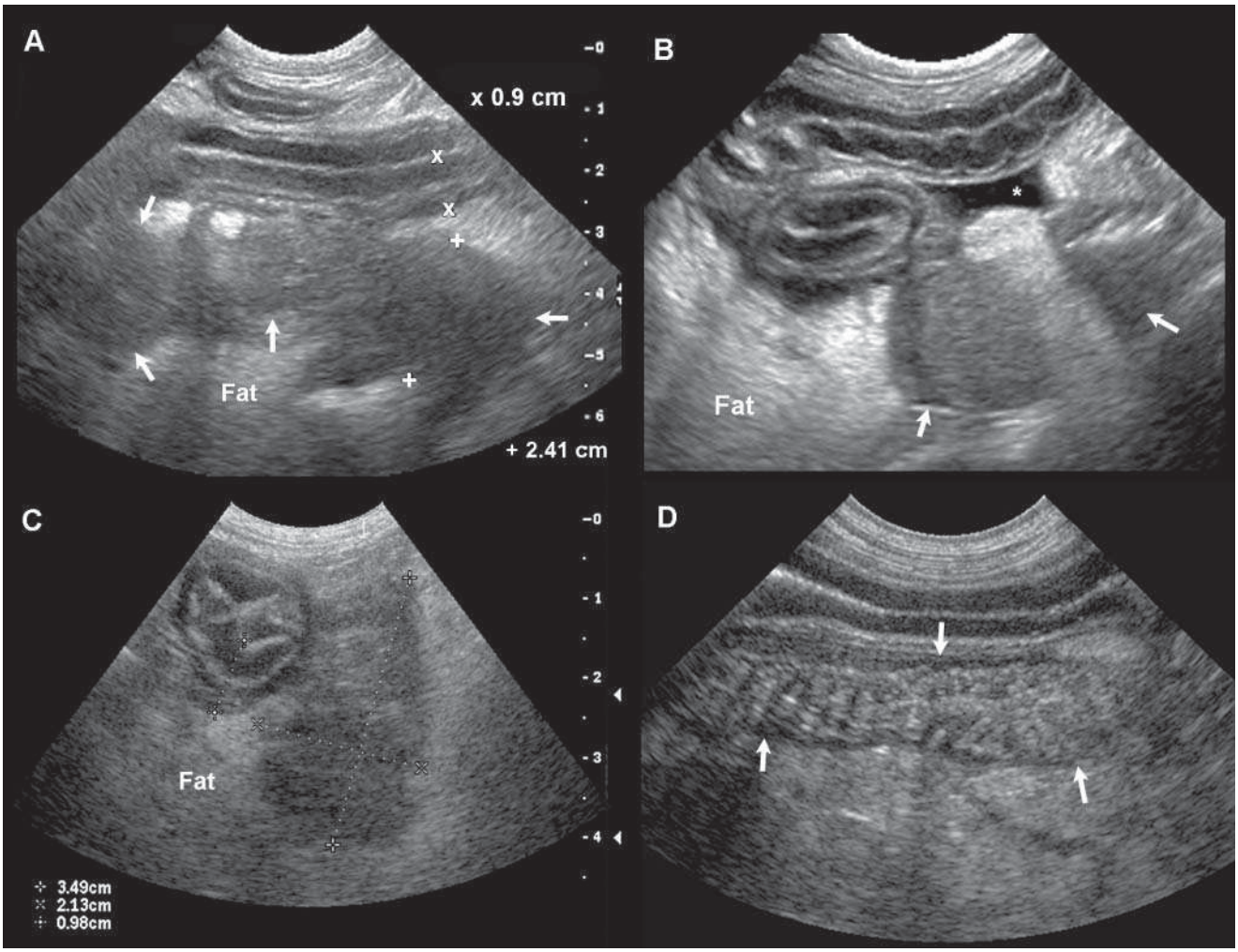


Figure 9.4. **Acute pancreatitis in dogs. A:** Longitudinal sonogram of the thickened (2.4 cm, cursors +), irregular, hypoechoic right lobe of the pancreas (arrows) surrounded by hyperechoic mesenteric fat. The descending duodenum is also thickened (9 mm, cursors ×), but its layers are still visible. **B:** Transverse sonogram of the same lobe (arrows). Notice the extension of the bright fat and the small amount of anechoic effusion (*) between the bowel loops. The bowel segment in the near field is corrugated. **C:** Transverse sonogram of the right limb of the pancreas of a dog with acute abdominal pain and vomiting. The pancreas (cursors) is enlarged, hypoechoic, irregular, and ill-defined. The surrounding fat is hyperechoic and hyperattenuating, hampering the visualization of deeper structures. The wall of the descending duodenum is thickened (1 cm), but layers are still visible. **D:** In the same dog, the colon (arrows) was markedly corrugated. A normal bowel loop is in the near field.

and develop into a pseudocyst or abscess. Pseudocysts are fluid-filled lesions caused by pancreatitis, they are surrounded by a capsule of fibrous tissue. The fluid is composed of pancreatic secretions originating from a ruptured duct. Pancreatic pseudocysts are anechoic to poorly echogenic rounded lesions, occasionally associated with acoustic enhancement in the far field. They are reported in both dogs and cats (Rutgers et al. 1985; Hines et al. 1996; VanEnkevort et al. 1999) (Figure 9.9). On occasions, large pseudocysts may cause extrahepatic biliary obstruction (Marchevsky et al. 2000).

Retention cysts are caused by pancreatic duct blockage and cannot be differentiated from congenital cysts or pseudocysts (Figure 9.10). Pancreatic abscesses are circumscribed collections of pus, usually located within the pancreas or close to it, containing little or no pancreatic necrosis (Salisbury et al. 1988). They are more common in dogs (Figure 9.11) than in cats (Figure 9.12). Ultrasonographic differentiation among these different fluid-filled pancreatic lesions is impossible. Abscesses with echogenic fluid may also mimic masses.

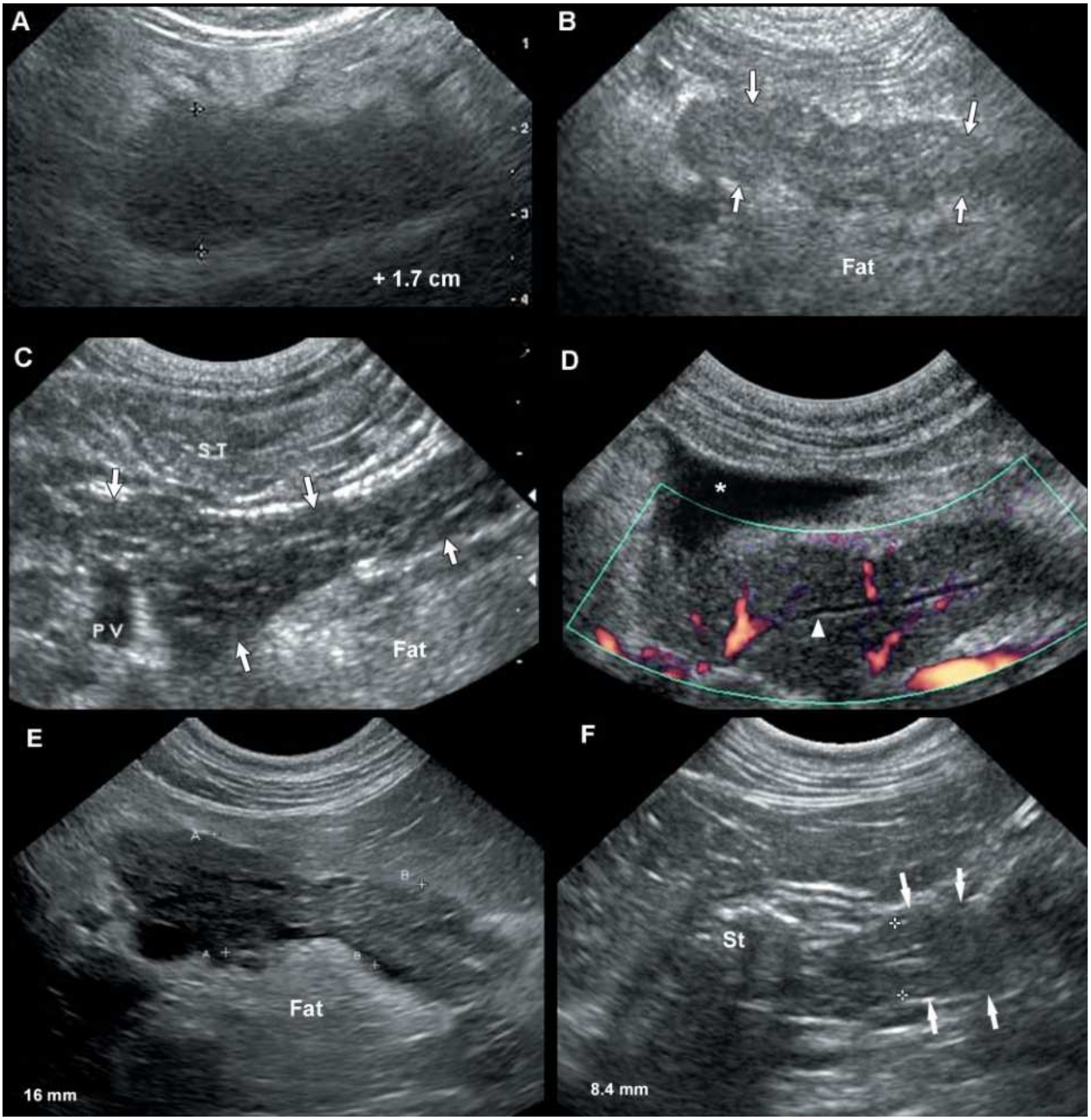


Figure 9.5. **Acute pancreatitis in cats. A:** Longitudinal sonogram of the left lobe of the pancreas. The lobe is markedly thickened, hypoechoic, and surrounded by hyperechoic local fat. **B:** In another cat, the pancreas is only mildly thickened, but the surrounding fat is bright, outlining the irregular pancreatic contours (arrows). **C:** The body and left lobe of the pancreas are within the upper limits of normal for size but appear hypoechoic. PV, portal vein; ST, stomach. **D:** Power Doppler longitudinal image of the left limb of the pancreas in another cat. The pancreas is enlarged, hypoechoic, and surrounded by hyperechoic fat and focal anechoic peritoneal effusion (*). The pancreatic duct is clearly delineated (arrowhead) and not associated with flow, in comparison with nearby vessels. **E, F:** Diffuse and severe acute pancreatitis with follow-up in this 6-year-old cat. The pancreas is markedly thickened (16 mm), hypoechoic, surrounded by hyperechoic fat on initial examination **(E)**. On the 8-day recheck (F), the pancreas (between arrows and calipers) returns to normal for size (8.4 mm) and echogenicity.

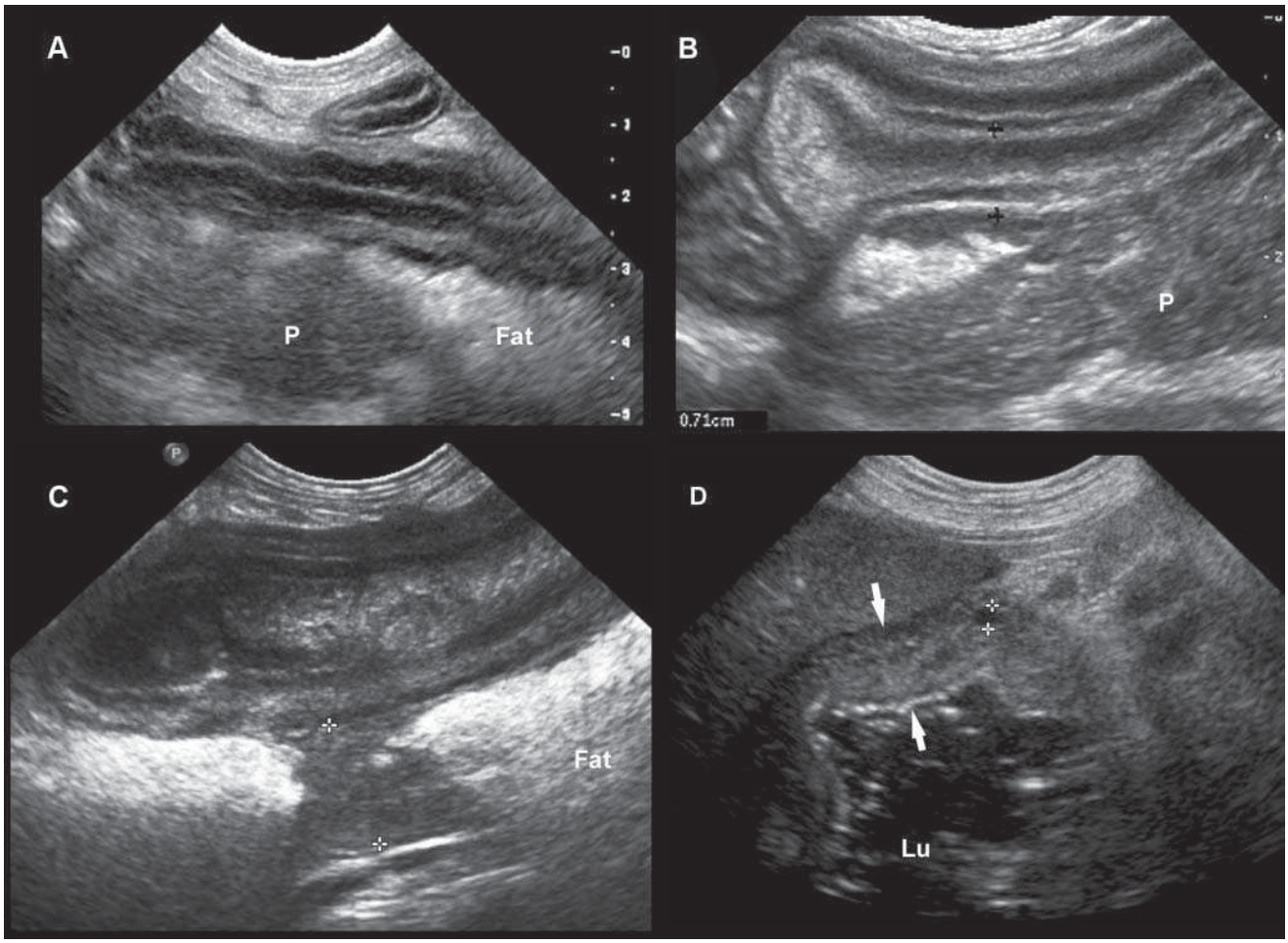


Figure 9.6. **Duodenal and gastric changes associated with pancreatitis in three dogs. A, B:** Longitudinal sonograms of two dogs diagnosed with severe acute pancreatitis. In both, the duodenum is thickened and atonic, and the wall layering is altered. The right pancreatic (P) limb is hypoechoic and the surrounding fat is hyperechoic. **C, D**: In this 6-year-old Sheba dog, the severe pancreatitis (between cursors in C) is associated with duodenitis and gastritis with wall edema (in D, between arrows). A small cyst is present in the gastric wall (between cursors).

Ultrasound-guided fine-needle aspiration is recommended to determine the nature of the collection. Peritoneal effusion secondary to pancreatitis is more common with the severe, hemorrhagic, necrotizing form of pancreatitis. The effusion tends to accumulate in small pockets between the pancreas and adjacent mesentery.

Bile duct obstruction secondary to pancreatic inflammation and subsequent fibrosis can cause gallbladder and bile duct distension. In these cases, the common bile duct (CBD) is dilated and tortuous (Figure 9.13). In dogs, the normal CBD can be challenging to identify and, when seen, it is considered within the normal range if it is up to 3 mm; whereas in cats, the CBD often is visible and considered within normal limits when up to 4 mm in diameter. A CBD exceeding 4 mm in diameter is suggestive of obstruction (Léveillé et al. 1996). Serial ultrasonographic examinations of the biliary tract can be necessary to document progressive mechanical obstruction. Progressive dilation of the biliary tract from the common bile duct to the peripheral intrahepatic ducts occurred 1 week after experimental bile duct ligation (Nyland and Gillette 1982). In some instances, the dilation of extrahepatic bile ducts and gallbladder might not resolve despite re-established patency after obstruction.

The mass effect created by an inflamed hypoechoic pancreas and hyperechoic peripancreatic tissue can displace the descending duodenum. Because the right pancreatic lobe is located dorsomedial to the descending duodenum, this loop of bowel is at times displaced ventrolaterally. In subacute to chronic

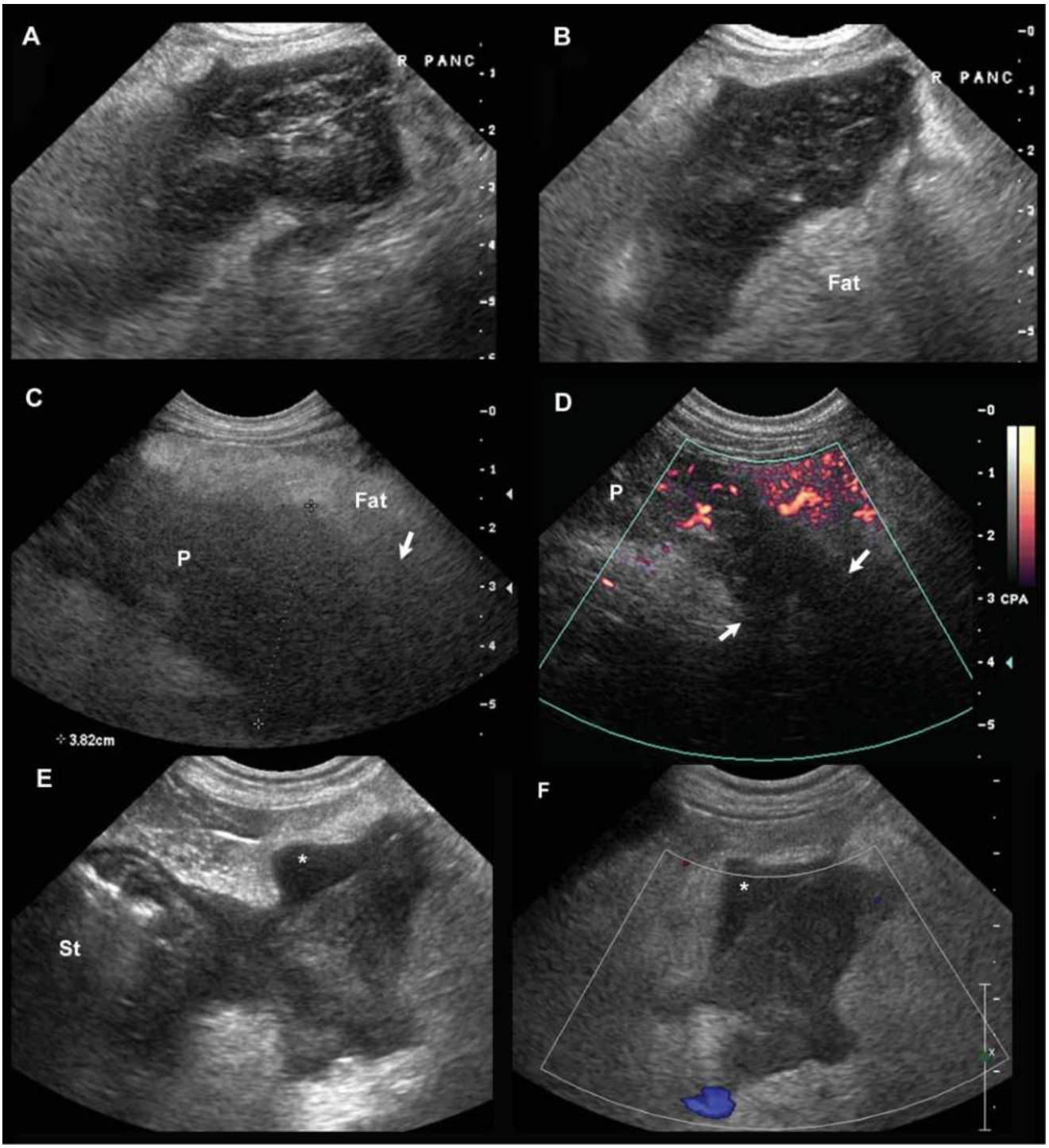


Figure 9.7. **Necrotizing hemorrhagic pancreatitis in two dogs. A, B:** Transverse **(A)** and longitudinal **(B)** sonograms of the thickened pancreas of an 8-year-old Labrador Retriever with active suppurative pancreatitis with areas of hemorrhage and necrosis. The inhomogeneous and hypoechoic pancreas has irregular margins outlined by bright fat. **C, D:** Longitudinal sonograms of the right pancreatic limb in a 10-year-old Golden Retriever with severe necroticohemorrhagic pancreatitis. The pancreatic limb (P) is markedly enlarged, hypoechoic, and ill-defined, particularly in its distal extremity (arrows). Using power Doppler **(D)** in this same region, there is no evidence of vascular flow motion, in comparison with the proximal portion of the limb. The superficial fat shows increased vascularity. **E:** Transverse sonogram of the left limb of the pancreas of a 7-year-old Miniature Schnauzer. The pancreas is enlarged, poorly echogenic and bordered by an anechoic region (*) probably representing a developing pseudocyst. **F:** With color Doppler, no vascularization is present in this segment of affected pancreas. St, stomach.

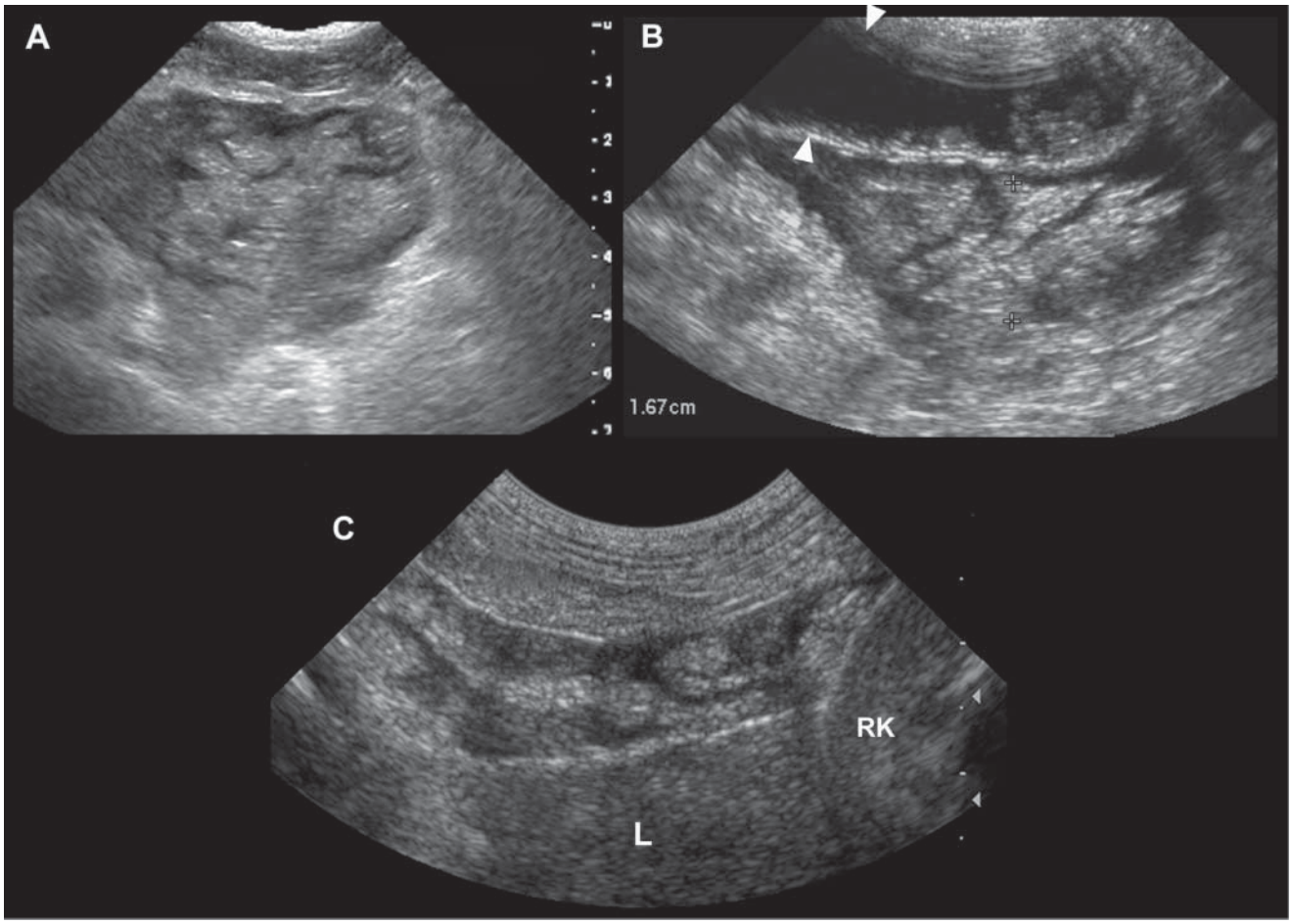


Figure 9.8. **Pancreatic edema in dogs. A:** Transverse sonogram of the edematous thickened pancreas (the same dog as in Figure 9.7A,B). The pancreas is enlarged and has anechoic stripes. The surrounding fat is hyperechoic. **B:** Longitudinal sonogram of the right pancreatic lobe of a 3-year-old Welsh corgi with pancreatitis. Hypoechoic striations are crossing the pancreas, and the contours of the pancreas are outlined by fluid. A dilated, fluid-filled segment of bowel is noted in the near field (arrowheads). **C:** Longitudinal sonographic image of the right pancreatic limb (arrows) in a small dog with acute portal hypertension following surgery for an extrahepatic portosystemic shunt. Characteristic hypoechoic to anechoic stripes noted in the pancreas are consistent with edema. These changes resolved a day later. L, liver; RK, right kidney.

active pancreatitis, the pancreas remains a distinct, well-defined hypoechoic structure that contrasts with the slightly hyperechoic peripancreatic mesentery (Figure 9.14A). At times, irregular margins of the pancreas and foci of mineralization can be seen (Figure 9.14B). Chronic pancreatitis characterized by interstitial fibrosis with acinar atrophy and lymphocytic infiltrates is rarely suspected clinically. Most cases encountered have vague clinical signs and non-specific laboratory values. In these cases, the pancreas can be within normal range for size, and the parenchyma is often inhomogeneous with hyperechoic non-shadowing foci or lines (Figure 9.14C,D). In cats, chronic pancreatitis is twice more frequent than acute pancreatitis. As this condition is often subclinical, it is very difficult to confirm the pancreatic changes histopathologically. On ultrasound, the changes can be similar to those described in dogs or subtle to inexistent (Figure 9.15). Acute necrotizing pancreatitis cannot reliably be differentiated from chronic non-suppurative pancreatitis based on clinicopathologic testing and/or sonographic abnormalities (Ferreri et al. 2003). A tissue core biopsy (ultrasound-guided, laparoscopic, or surgical) can be obtained to confirm the diagnosis.

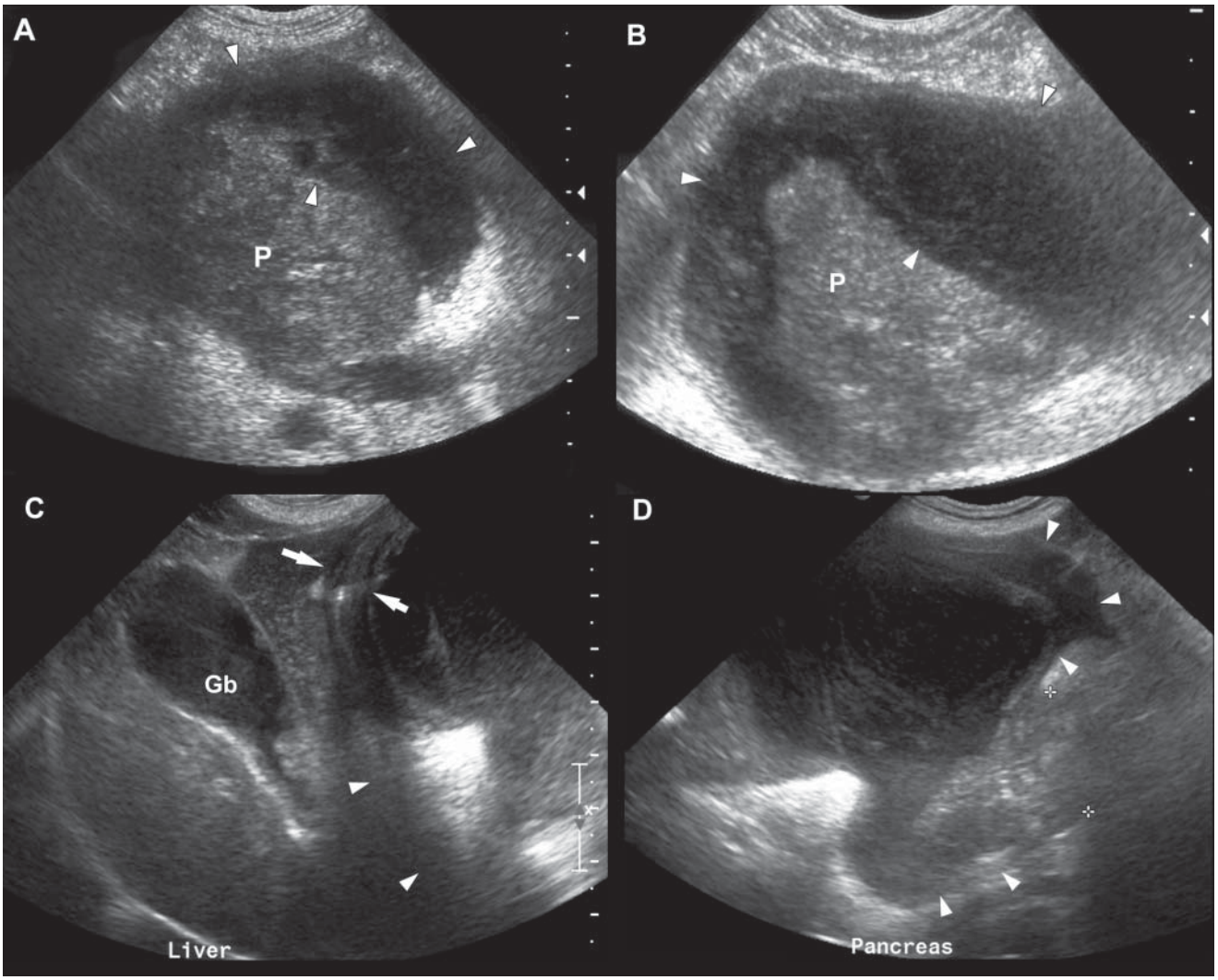


Figure 9.9. Pancreatic pseudocyst in two dogs. Transverse **(A)** and longitudinal **(B)** sonograms of a large pancreatic pseudocyst associated with a severe acute pancreatitis. Part of the thickened and hypoechoic pancreas (P) is in the center of the hypoechoic to nearly anechoic lesion representing the pseudocyst (arrowheads). Ultrasound-guided fine-needle aspiration confirmed the diagnosis. **C, D:** A 6-year-old Beagle with a very large fluid cavity (arrowheads) containing settling echogenic sediments and associated with the left lobe of the pancreas. The lesion is drastically displacing the stomach cranially (arrows) to the point that the mass was initially thought to originate from the stomach.

In cats, the pancreatic duct can appear dilated (up to 2.5 mm), especially in older cats with no clinical evidence of active or chronic pancreatic disease. It can, at times, also be associated with acute pancreatitis (Wall et al. 2001) or chronic pancreatitis.

Exocrine Pancreatic Insufficiency

Exocrine pancreatic insufficiency (EPI) in dogs usually results from pancreatic acinar atrophy and is commonly diagnosed in breeds such as German Shepherd Dogs. In cats, it usually caused by chronic/end-stage pancreatitis, especially in cats but less commonly in dogs (Watson 2003). Only few publications reported the sonographic appearance of EPI. Hyperechogenic and inhomogeneous parenchyma have been reported in cats and dogs (Watson 2003; Hecht 2006). In confirmed cases of EPI, the authors encountered a reduced size of the pancreatic parenchyma, hyperechoic parenchyma, and dilated pancreatic duct with or without calculi (Figure 9.16). It is also interesting that, at times, the intestinal tract is hypermotile and distended with echogenic contents, possibly related to the malabsorption encountered with EPI (Figure 9.16)

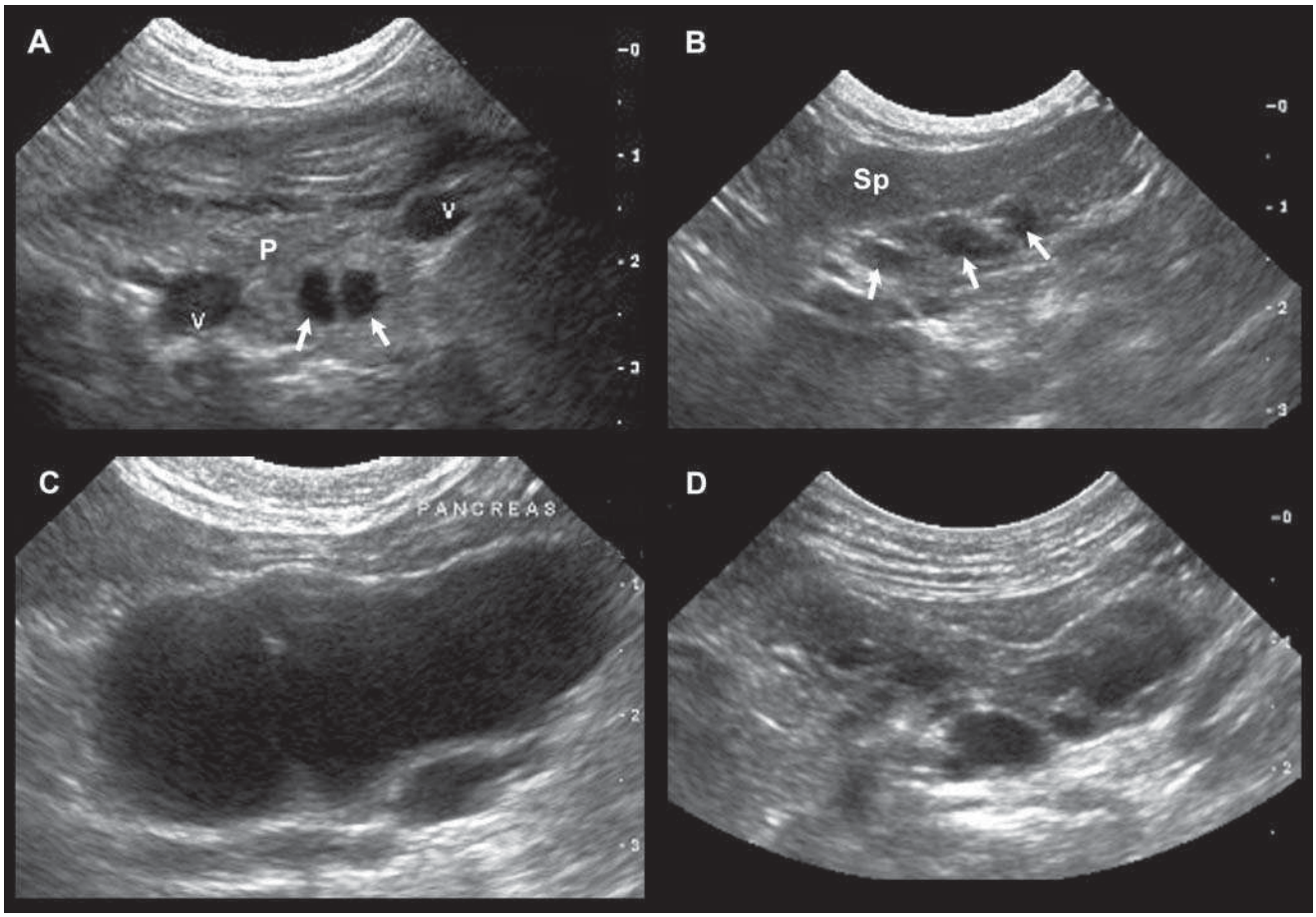


Figure 9.10. **Pancreatic cysts in dogs and cats. A:** Oblique sonogram of two small cystic lesions (arrows) in the left pancreatic lobe (P) of an 11-year-old Miniature Schnauzer. St, stomach; V, adjacent vessels. **B:** Longitudinal sonogram of the distal extremity of the left pancreatic lobe of an 18-year-old cat with several cyst-like changes (arrows). This cat had no clinical history of previous pancreatitis. Sp, spleen. **C:** Large pancreatic cyst on the left lobe and body of the pancreas in a 16-year-old cat. **D:** The same region after ultrasound-guided drainage of the cyst presented in **C**.

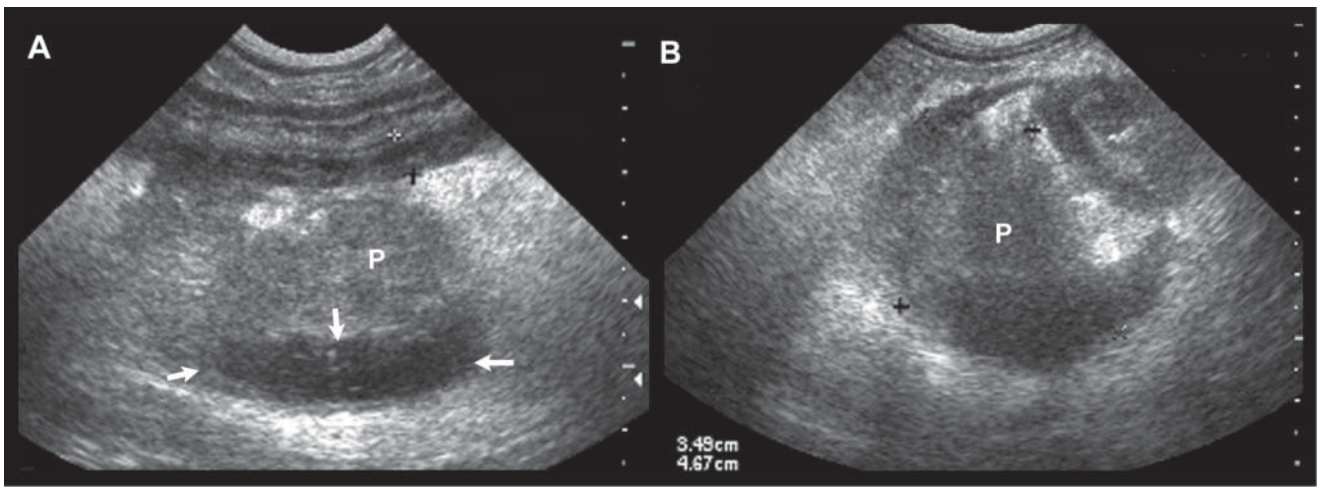


Figure 9.11. **Pancreatic abscess in two dogs. A:** Longitudinal sonogram of an ovoid discrete hypoechoic cavity (arrows) in the right pancreatic lobe (P) of a 6-year-old Cocker Spaniel. Notice the thickened and atonic (fluid-filled) duodenum in the near field (cursors). The muscularis layer of the duodenal wall is especially prominent. Hyperechoic fat is seen around the pancreas. The cavity was confirmed by ultrasound-guided aspiration to be an abscess. **B:** Transverse sonogram of an abscess (arrows) in the right pancreatic lobe (P) of a 10-year-old Labrador crossed. The peripheral fat is hyperechoic, indicating steatitis.

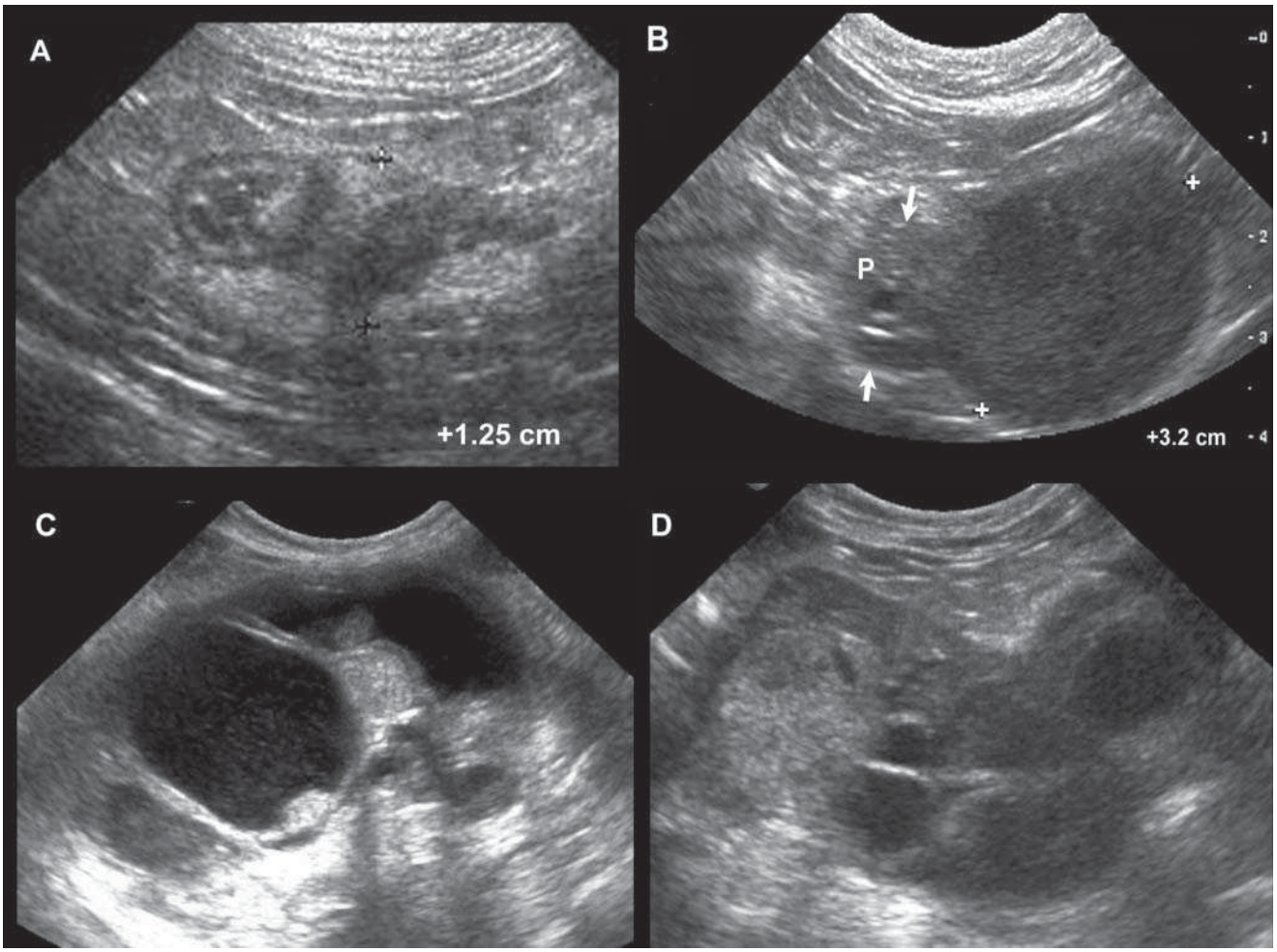


Figure 9.12. **Pancreatic abscess in two cats. A:** Sonogram and corresponding schematic image of a small hypoechoic cavity (arrow) in the cranial part of the right pancreatic lobe (between the cursors). The lesion deforms the contour of the pancreas and is outlined by focally bright fat. **B:** Large cavity containing a mildly echogenic fluid (between the cursors, +) severely deforming the right lobe of the pancreas (P, between the arrows). With gentle pressure, the echogenic fluid moved on real-time examination. **C, D:** Complex cystic changes on the pancreas in a 6-year-old Norwegian forest cat. Several cavities of variable size and echogenicity are present. Fine-needle-aspirations showed abscessation.

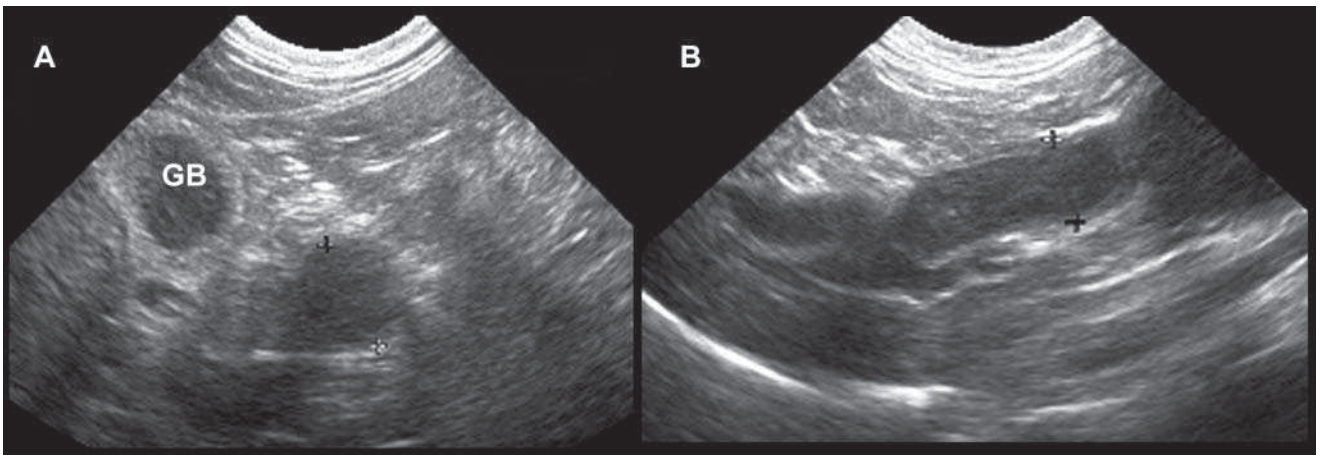


Figure 9.13. **Dilated common bile duct in a cat with pancreatitis.** Transverse **(A)** and longitudinal **(B)** sonograms of the common bile duct (CBD, between the cursors) in a cat with pancreatitis and pancreatic abscess (the same cat as in Figure 9.12B). The CBD is greatly distended, reaching 1.4 cm in diameter proximally **(A)** and 1.2 cm distally **(B)**. Notice that the CBD and gallbladder (GB) walls are thickened.

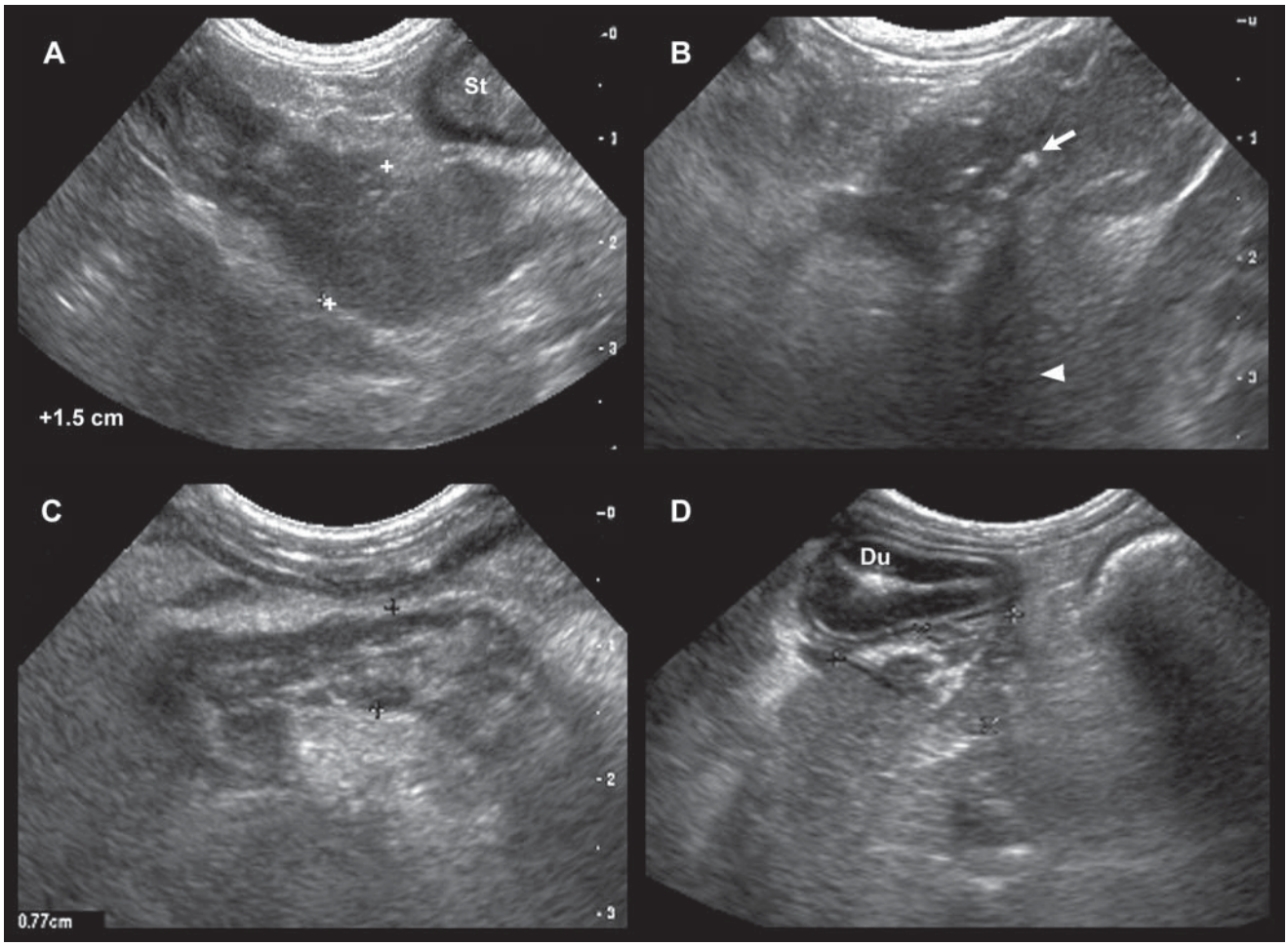


Figure 9.14. **Chronic pancreatitis in three dogs. A:** Diffuse chronic active necrotizing pancreatitis with fibrosis and regeneration in a 14-year-old Shih Tzu. The pancreas (cursors) is markedly irregular and mostly hypoechoic, with a few inhomogeneous areas. It is 1.5 cm thick. St, stomach. **B:** Chronic pancreatitis in an 11-year-old mixed-breed dog. Numerous hyperechoic foci are seen in the pancreas (arrow). Some of these foci are associated with shadowing (arrowhead), suggesting mineralization. The pancreas is hypoechoic, but the surrounding fat is normal. The longitudinal **(C)** and transverse **(D)** sonograms of the right pancreatic lobe (between the cursors) in an 8-year-old Australian Shepherd dog, showing a pancreas that is within normal range for size but very inhomogeneous. Du, duodenum.

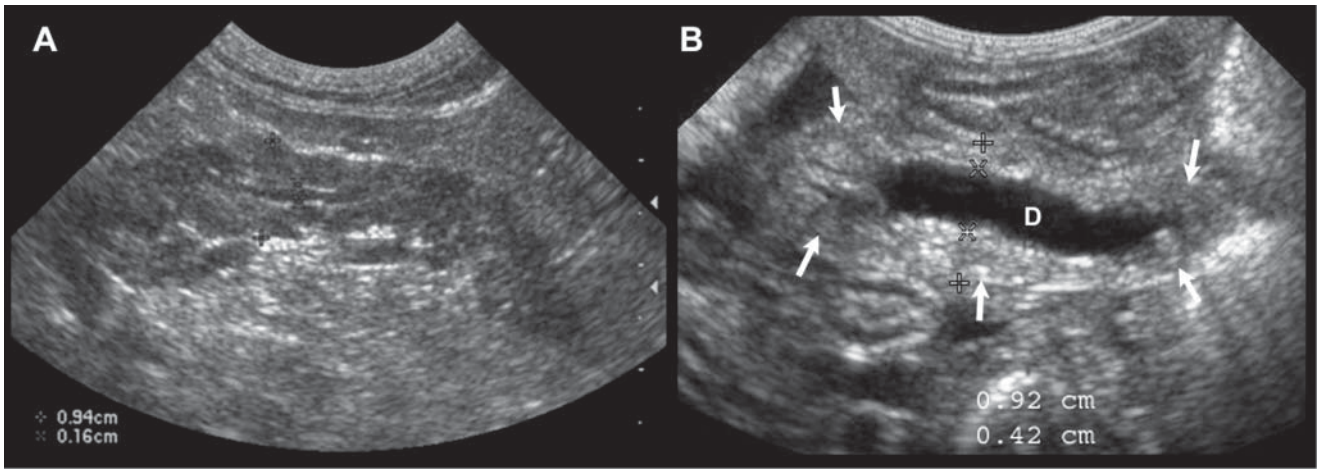


Figure 9.15. **Chronic pancreatitis in two cats. A:** Longitudinal sonographic image of the left pancreatic limb of a cat with diffuse lymphoplasmocytic pancreatitis. The pancreas is irregular and mildly hypoechoic. The central pancreatic duct appears normal. **B:** Chronic pancreatitis with pancreatic atrophy and islet cell fibrosis in another cat. The pancreas (arrows) appears thickened (9.2 mm) and hyperechoic, but the pancreatic duct (D) is dilated (4.2 mm), accounting for nearly half of the overall pancreatic lobe thickness.

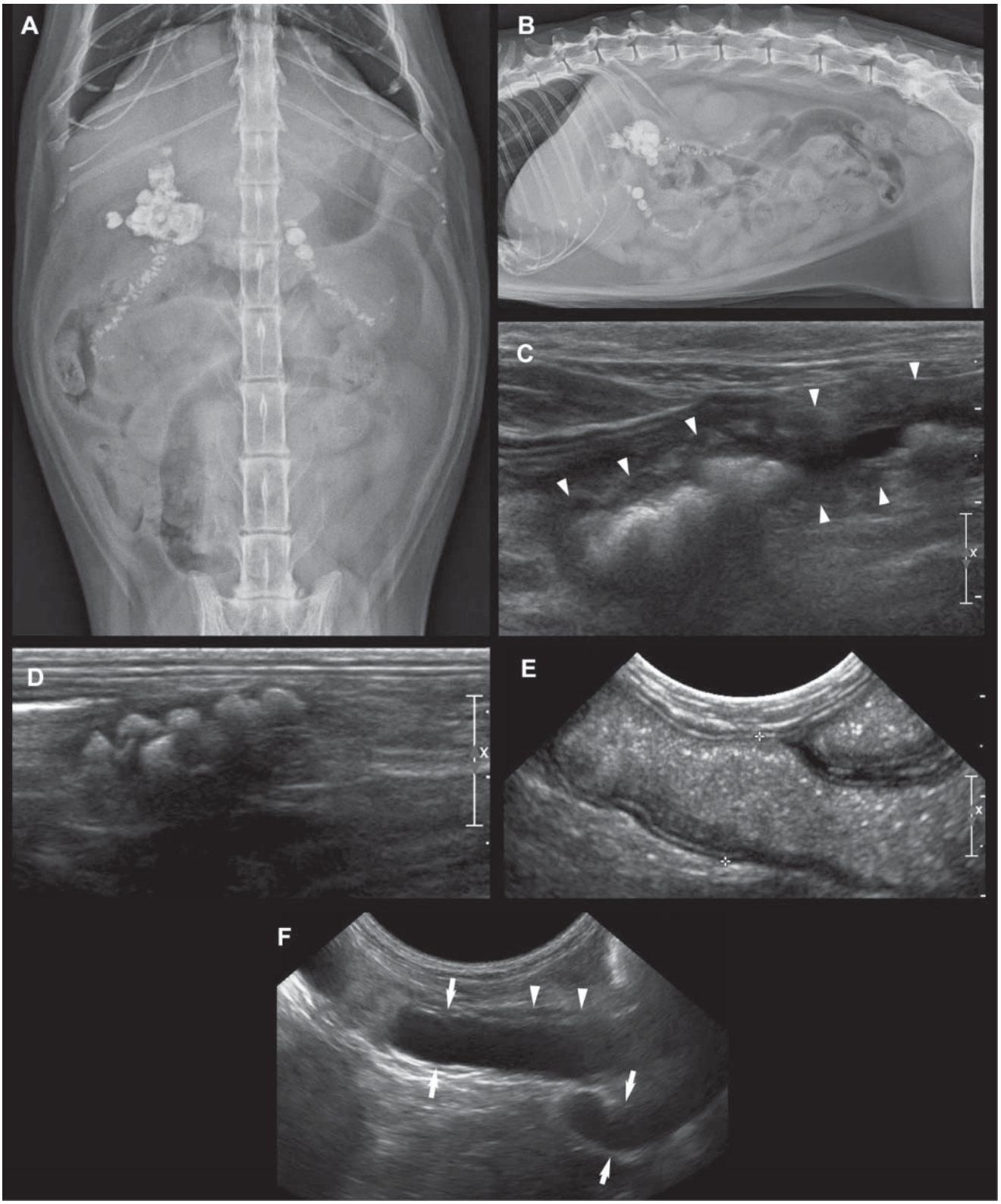


Figure 9.16. **Exocrine pancreatic insufficiency in two cats.** In this 17-year-old domestic shorthair with chronic pancreatitis, the ventrodorsal **(A)** and the right lateral **(B)** radiographs showed this long string of calculi along the trajectory of the entire pancreatic duct and suspected to be also in part of the biliary system. On ultrasound, there are numerous irregular calculi **(C, D)** associated with shadowing. The pancreatic tissue is barely seen in this cat (arrowheads). The intestines of this cat **(E)** are hyperperistaltic and dilated (1.3 cm) with echogenic contents; this may support the malabsorption seen in exocrine pancreatic insufficiency. **F**: In this 14-year-old cat, the pancreatic duct was moderately dilated while the pancreas was nearly inexistent. No calculi were present in the pancreatic ductal system.

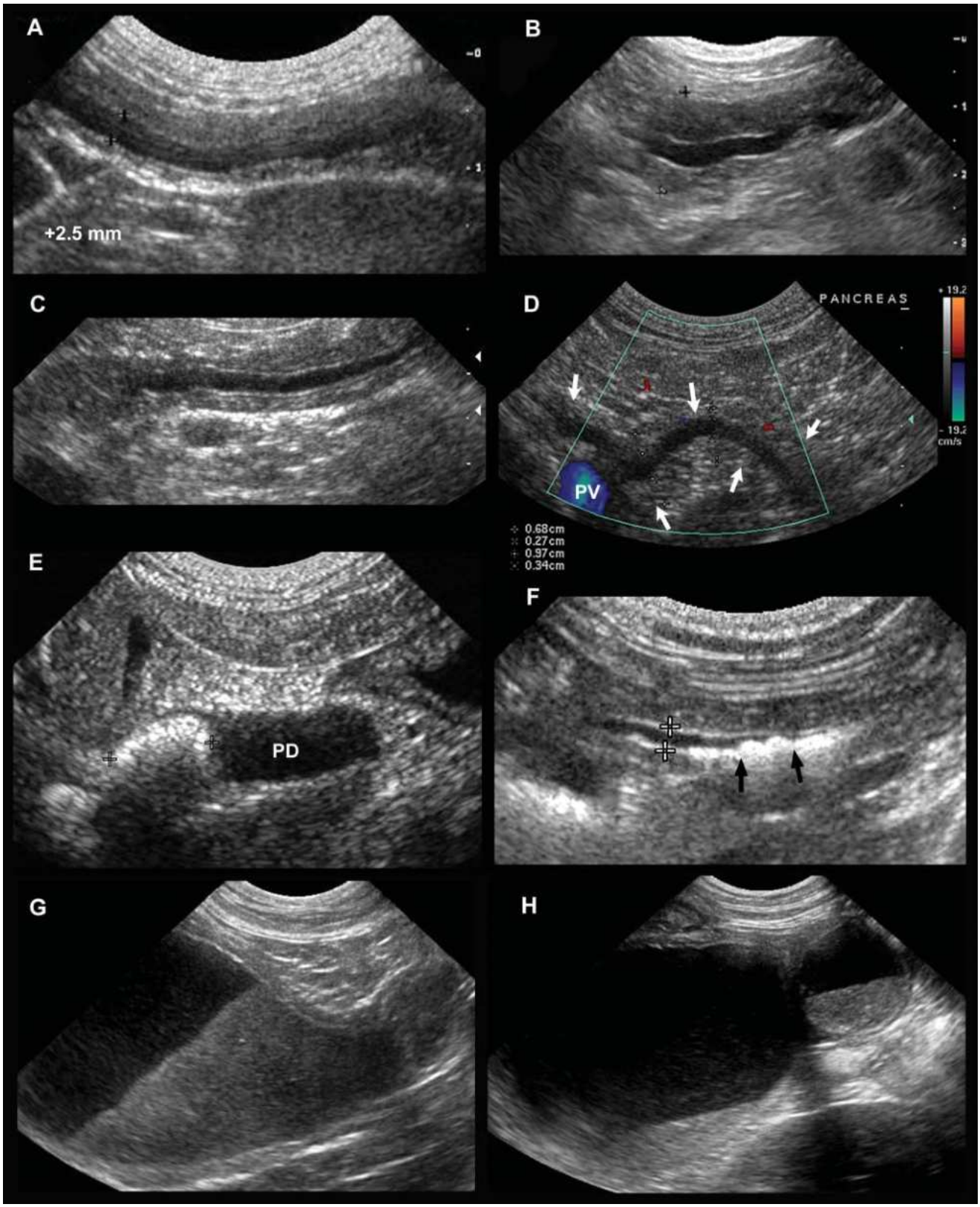


Figure 9.17. Dilated pancreatic duct (PD) in cats. A: A smoothly dilated, 2.5-mm-wide PD (between the cursors) in a 12-year-old cat with two concurrent pancreatic cystic lesions and hepatic disease (not shown). **B:** A dilated, 3-mm-wide PD in a 16-year-old cat with concurrent hepatitis and suspected pancreatitis. The pancreas is delineated by the cursors. **C:** A dilated 3.5-mm-wide PD with a thickened wall in a 14-year-old cat with hepatitis and fibrosing choledochitis. The pancreas appears normal. **D:** A dilated, 3.4-mm-wide PD (between the cursors) in an elderly cat with pancreatic atrophy. The pancreatic tissue around the PD is barely visible (arrows). Color Doppler can be useful in differentiating a PD from vessels. PV, portal vein. **E:** Large calculus (between the cursors) in this dilated, 1-cm-wide PD. **F:** Dilated and thickened PD with small intraluminal calculi and mineralized sediments. **G, H:** Hugely dilated pancreatic duct in a 15-year-old cat presented for progressive inappetence. The markedly dilated PD contains partially settling cellular fluid. No calculi were seen. The pancreas was barely identified in some segments.

Pancreatolithiasis and abnormal pancreatic duct

Pancreatolithiasis refers to the presence of calculi in the pancreatic ductal system or parenchyma. This uncommon occurrence can be diagnosed radiographically or sonographically (Figures 9.16, 9.17). The size and number of calculi can vary widely. Calculi are associated with shadowing. They can also be associated with a variable degree of ductal dilation, or an anomaly such as pseudobladder and underlying chronic pancreatitis (Bailiff 2004). Pseudobladder is described as a dilated segment of the pancreatic duct of unknown etiology; this fluid-filled focal dilation can be confused with a pseudocyst or abscess.

After surgical ligation of pancreatic duct in four dogs, a study showed endoscopic evidence of progressive dilation of the pancreatic ductal system and atrophy of the acinar tissue replaced by fibrosis and fat and resulting in increased echogenicity of the parenchyma (Morita et al. 1998).

In cats, the authors also encountered marked saccular dilation of the pancreatic duct without evidence of obstruction. (Figure 9.17**).** In these uncommon cases, the pancreatic duct wall is mildly thickened, and mixed anechoic to echogenic fluid is noted in the lumen. The exact etiology of this severe distension is unknown.

Pancreatic Nodular Hyperplasia and Neoplasia

Pancreatic nodular hyperplasia is occasionally seen in the pancreas of older dogs and cats. Well-defined

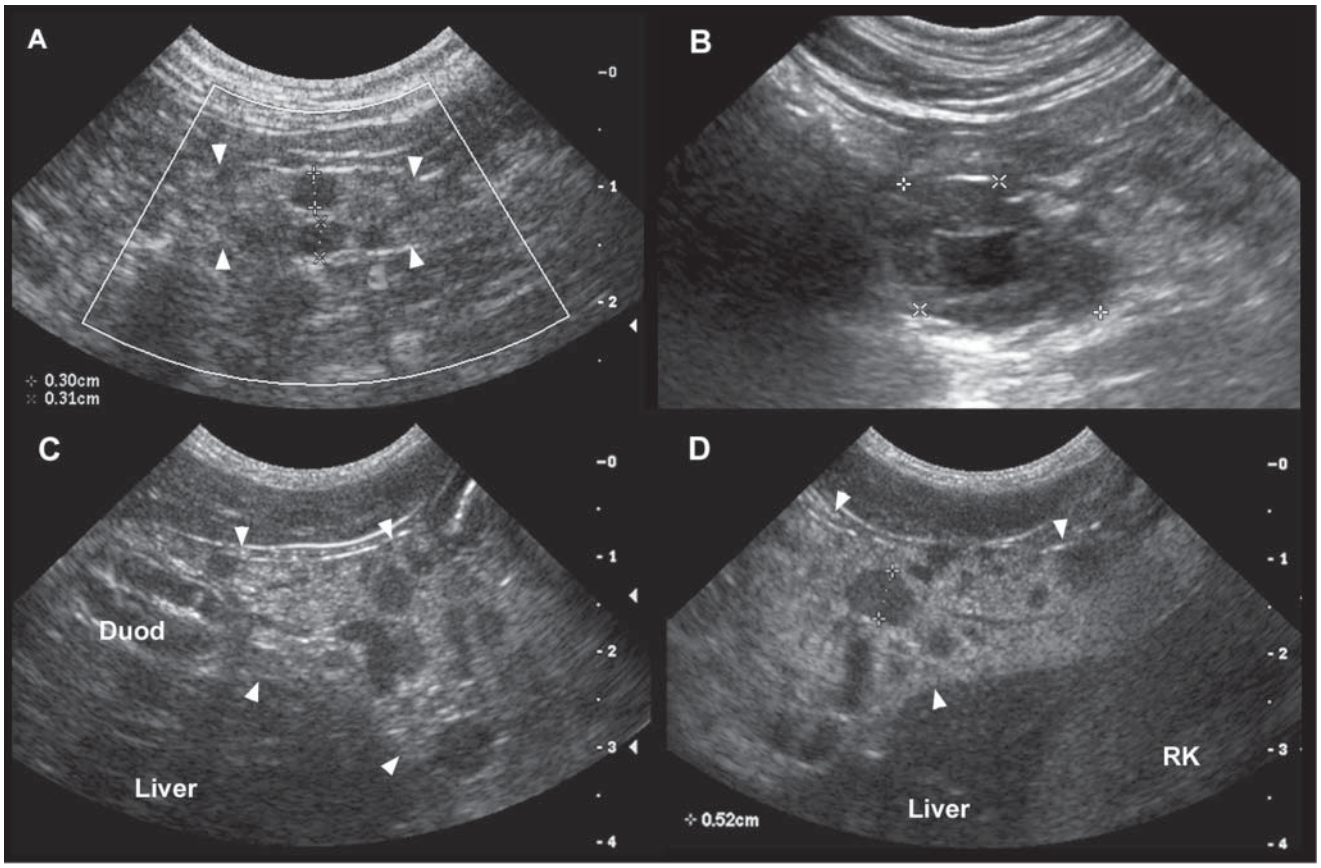


Figure 9.18. Nodular hyperplasia in a cat and a dog. A: Longitudinal sonographic image with color Doppler of the pancreas of a cat with chronic inflammatory bowel disease. Two well-defined 3-mm hypoechoic nodules (between the cursors) are identified in the left pancreatic limb (arrowheads). The rest of the pancreas is mildly heterogeneous. **B:** A 15-year-old cat with a heart murmur had a cavitated nodule in the pancreas that was aspirated under ultrasound guidance. It was interpreted as likely nodular hyperplasia, and did not change in appearance on recheck ultrasound performed 3 months later. **C, D:** Transverse **(B)** and longitudinal **(C)** sonographic images of the right pancreatic limb of a small-breed dog with diabetes mellitus. Several well defined, hypoechoic nodules of variable size and shape are seen throughout the pancreatic tissue (arrowheads), which is otherwise hyperechoic. There was no evidence of changes to the peripheral fat. Fine-needle aspiration of the pancreas revealed the presence of mild, chronic pancreatitis with nodular hyperplasia. Duod, duodenum; RK, right kidney.

hypoechoic to nearly isoechoic nodules that can vary in size are recognized (Hecht et al. 2007) (Figure 9.18). These nodules can be confused for neoplastic disorders, such as insulinomas. They may also look similar to cysts, although far acoustic enhancement is not usually associated with soft-tissue nodules.

Pancreatic exocrine tumors such as adenocarcinomas (Figure 9.19) arise from acinar cells or ductal epithelium. Even though these tumors are rare, they are the most common type of pancreatic neoplasia in small animals. They tend to develop in the central portion of the gland. As they grow, they may compress the CBD, invade the adjacent gastric and duodenal segments, and frequently metastasize to the liver (Figure 9.20) (Lamb et al. 1995). They are often poorly echogenic nodules or masses that can be associated with mineralized foci. Carcinomatosis may appear as a mass centered on the pancreas with numerous poorly echogenic nodules disseminated throughout the abdominal cavity; abdominal effusion is a common finding in this neoplasm (Figure 9.21; see also Figure 15.17).

Other tumors are occasionally encountered in the pancreas of dogs and cats: cystadenoma, adenoma (Figure 9.22), metastatic carcinoma, and lymphoma (Figure 9.23).

Pancreatic endocrine tumors such as glucagonomas, insulinomas, and gastrinomas are uncommon. From that group, insulinomas are the most commonly encountered in dogs. The ultrasound detection rate varies depending on the size and distribution of the lesions, the equipment quality, and the operator's experience. The visibility of these lesions may also be affected by the presence of overlying gastrointestinal

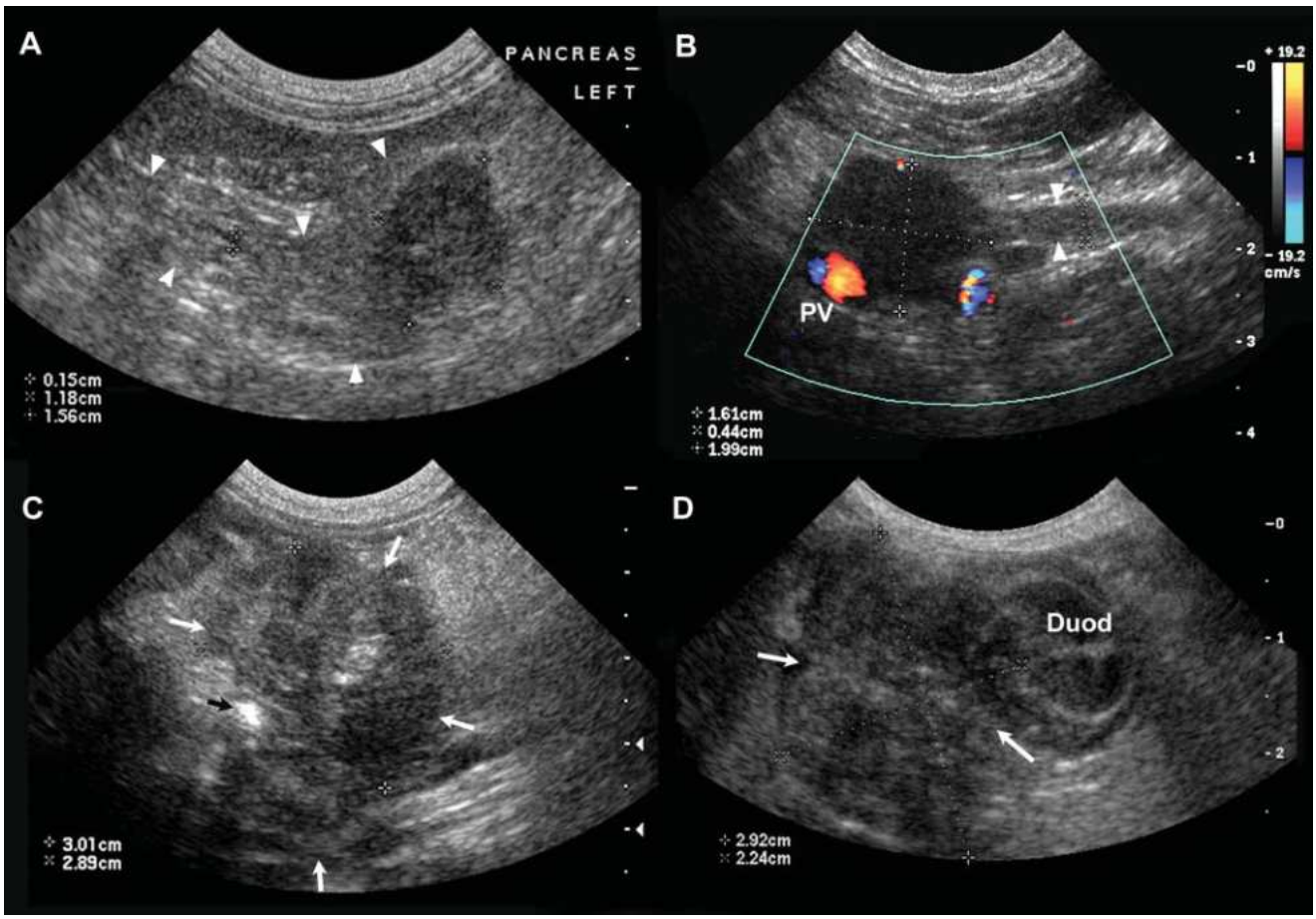


Figure 9.19. **Pancreatic carcinomas A:** Longitudinal sonographic image of the left pancreatic limb (arrowheads) in a cat. A small hypoechoic nodule is present at the tail of this limb indicated pancreatic adenocarcinoma. **B:** Another hypoechoic nodule found in the proximal portion of the left pancreatic limb of a cat. This nodule is adjacent to the portal vein (PV). The rest of the left limb (arrowheads) is normal. Pancreatic adenocarcinoma was confirmed histologically. **C:** A larger mass (white arrows, 3 cm) in another cat is consistent with a poorly differentiated carcinoma. This mass is heterogeneous and has mineral foci (black arrow) associated with acoustic shadowing. **D:** Transverse sonographic view of a pancreatic mass (arrows) invading the wall of the duodenum in a dog. A poorly differentiated carcinoma was diagnosed with cytology after fine-needle aspiration.

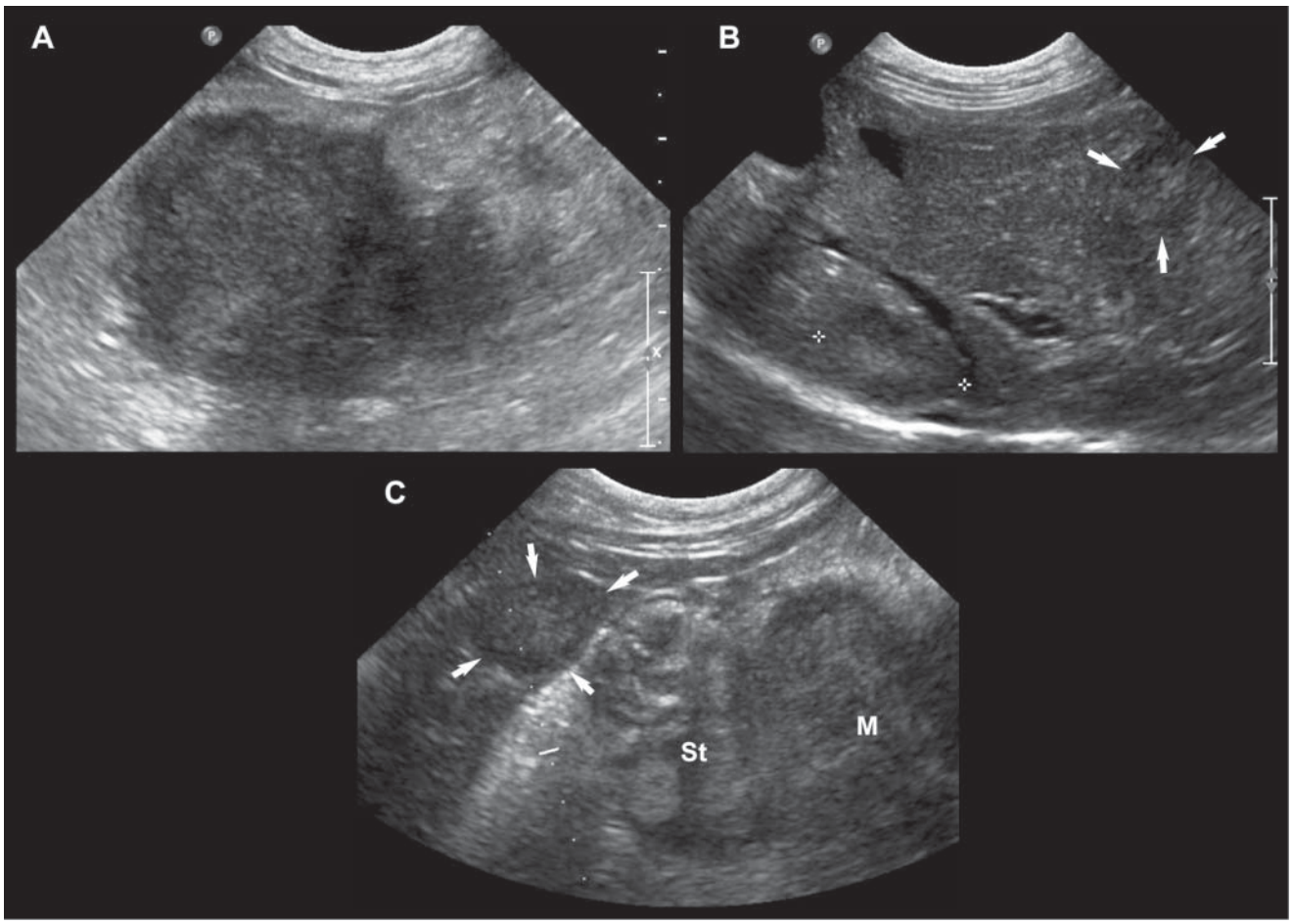


Figure 9.20. **Pancreatic carcinoma with hepatic metastases in an 11-year-old cat. A:** A large (>3 cm thick) hypoechoic pancreatic mass is noted. **B:** Several target-like hepatic nodules (arrows, and cursors) are present in the liver. **C:** One hepatic nodule (arrows) is aligned with the biopsy tract, and carcinoma metastases were confirmed histopathologically. St, stomach; M, pancreatic mass.

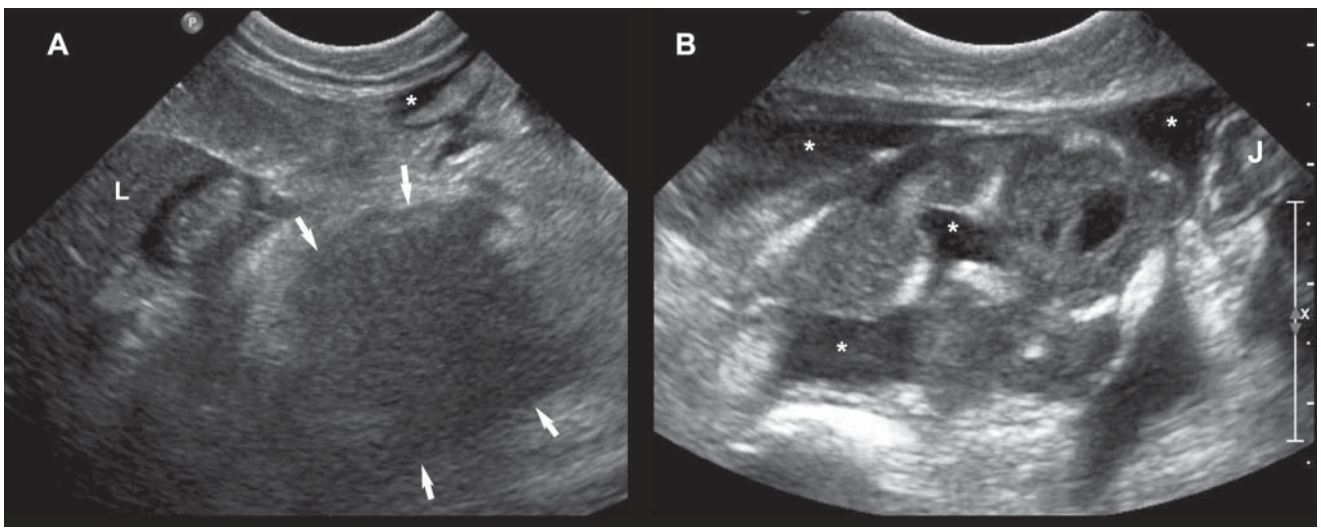


Figure 9.21. **Carcinomatosis with large pancreatic mass in an 11-year-old cat with ascites. A:** A large hypoechoic pancreatic mass (arrows) is outlined by hyperechoic fat. Anechoic peritoneal effusion (*) is present. L, liver. **B:** In the mid-abdomen, the thickened and nodular mesentery is "floating" in the effusion. J, jejunal segment.

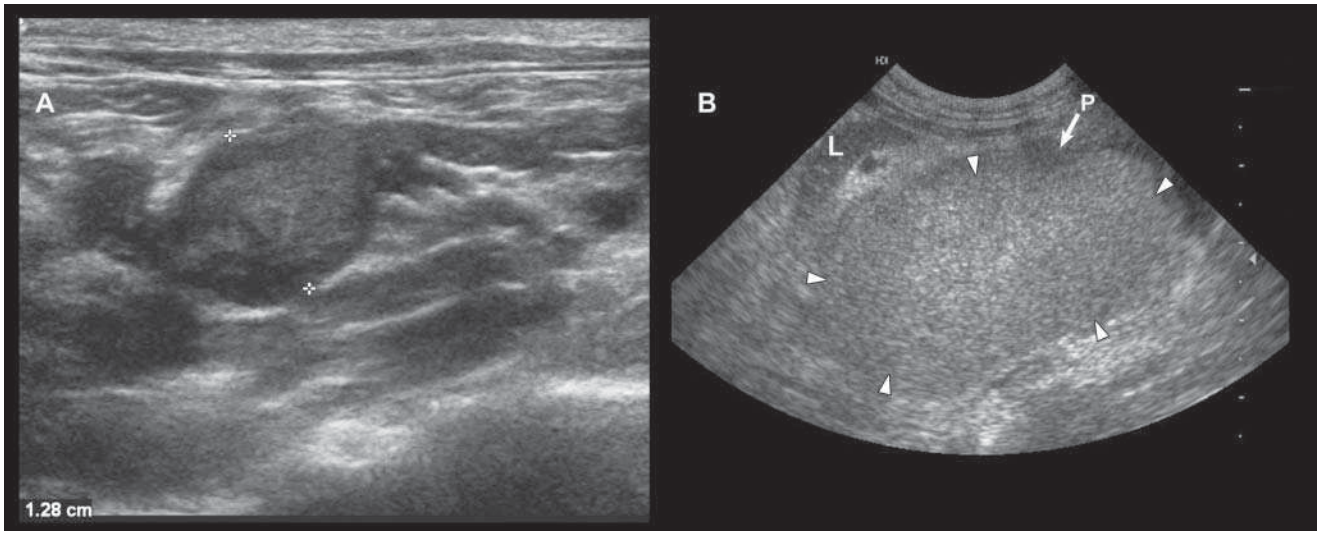


Figure 9.22. **Pancreatic adenoma in two cats. A:** An incidental 1.3 cm nearly isoechoic nodule is deforming the contour of the right limb of the pancreas. An ultrasound-guided fine-needle aspirate diagnosed an adenoma. The nodule is regularly monitored to assess any change in size or echogenicity. **B**: In this other 12-year-old cat presented for inappetence and vomiting, a smooth, uniformly echogenic mass was identified in proximity to the pancreas (P) and the regional fat was hyperechoic. Exploratory surgery and histopathology revealed a pancreatic adenoma with pancreatitis.

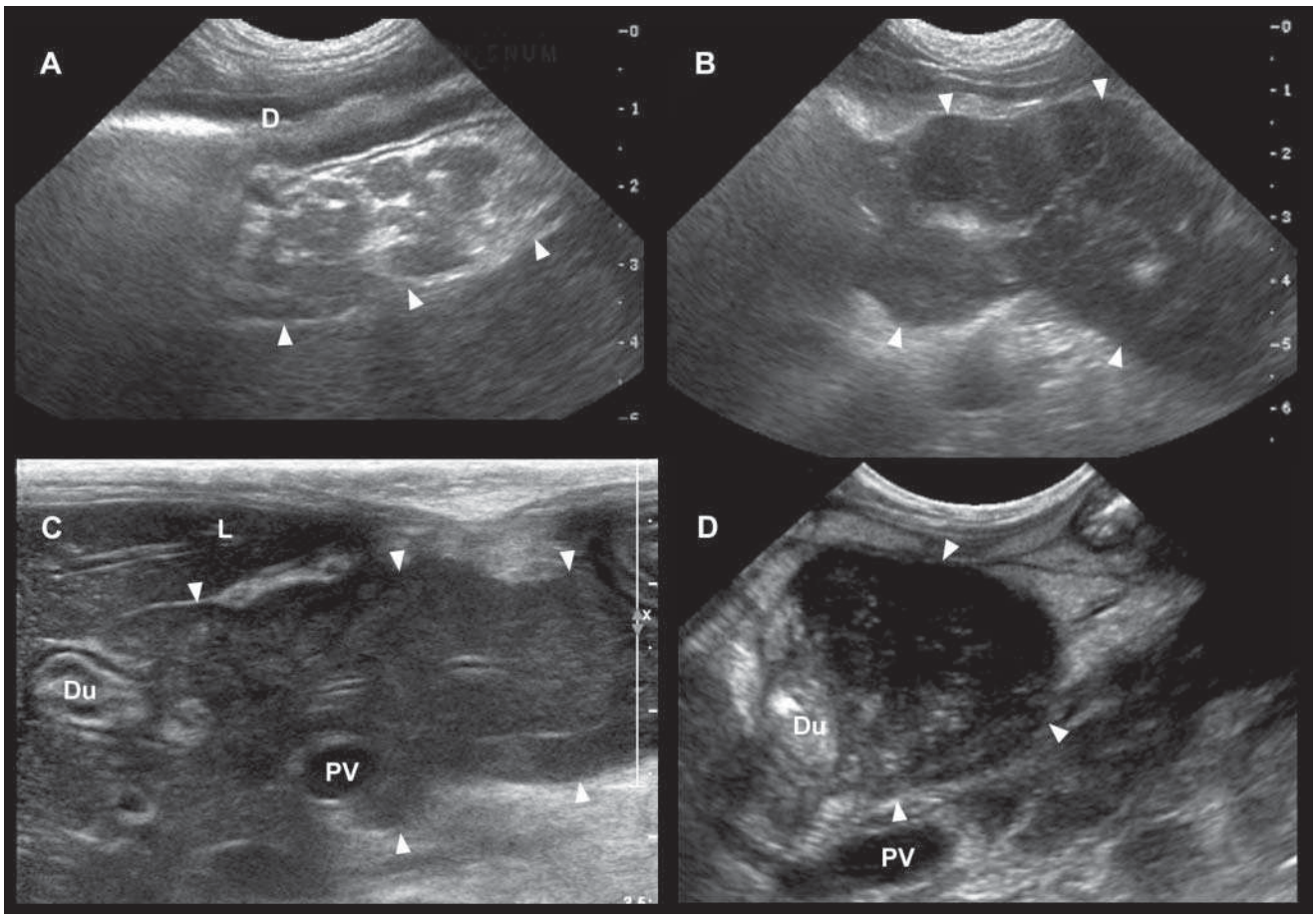


Figure 9.23. **Pancreatic lymphoma. A:** Numerous variably sized hypoechoic nodules replace the normal echotexture of the pancreas (arrowheads) in this 4-year-old mixed-breed dog. The duodenum (D) is seen in the near field. **B:** Diffuse pancreatic enlargement (arrowheads) associated with diffuse hypoechogenicity in a 7-year-old Labrador Retriever. **C, D**: In this cat, lymphoma was diagnosed in the pancreas, mesentery and gastrointestinal tract**.** The pancreas is markedly and diffusely thickened and hypoechoic with irregular margins (arrowheads). Du, duodenum, PV, portal vein. The surrounding fat is hyperechoic and several anechoic stripes are noted in the near field **(D)**.

content and by body conformation (e.g., deep-chested or obese dogs). Insulinomas can present as a solitary nodule, multiple nodules, or an ill-defined area of abnormal echogenicity (Figure 9.24). The size of the pancreatic lesions varies greatly, but a majority of the lesions tend to be ≤2.5 cm and poorly echogenic (Lamb et al. 1995). Cross-sectional imaging modalities such as computed tomography (CT) and magnetic resonance imaging (MRI) can be very useful in identifying insulinomas (Figure 9.24) in cases in which ultrasound failed to detect a lesion despite strong clinical suspicion (Mai and Careres 2008).

Most endocrine tumors are malignant and tend to spread to the regional lymph nodes and liver. Therefore, sonographic screening of the hepatic parenchyma and regional lymph nodes is recommended to detect possible hepatic metastasis (Figure 9.24). Metastatic lymph nodes are often enlarged and hypoechoic. The close anatomical relationship between the hepatic lymph nodes and the body of the pancreas can complicate the distinction between pancreatic nodule from hepatic lymphadenomegaly. Whereas pancreatic tumors usually present as a focal nodule or mass, neoplasia cannot reliably be differentiated from pancreatitis or nodular hyperplasia.

Special Procedures

Fine-needle aspirations or core biopsies of diffuse or focal pancreatic lesions can be performed safely

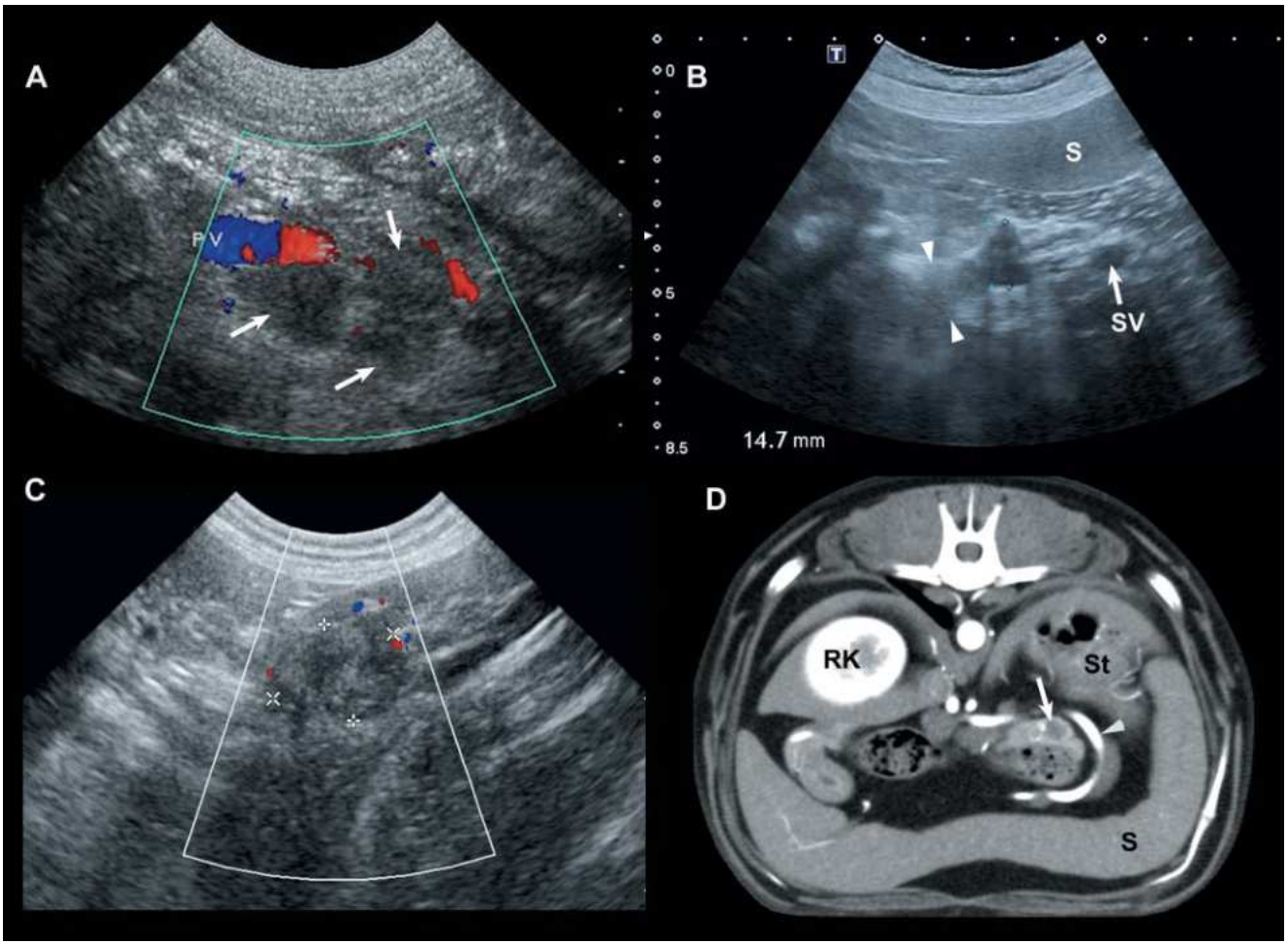


Figure 9.24. Pancreatic insulinoma in dogs. Insulinomas appear as single or multiple hypoechoic nodules in these dogs **(A–C)**. **A:** Color Doppler assessment of the pancreatic region with several small hypoechoic nodules (arrows). The portal vein (PV) is ventral to the body of the pancreas. **B**: In another dog, a 15 mm hypoechoic nodule (cursors) was identified in the left pancreatic limb, in proximity to the splenic vein (SV) and spleen (S). **C**: Discrete hypoechoic nodule is noted in the right pancreatic lobe of this Golden Retriever presented for hypoglycemia. **D**: Commonly, small insulinomas cannot be detected ultrasonographically, as in this dog, and a contrast CT image outlines the small hypoattenuating nodule (arrow) well. The arrowhead points to the splenic artery. St, stomach; RK, right kidney; S, spleen.

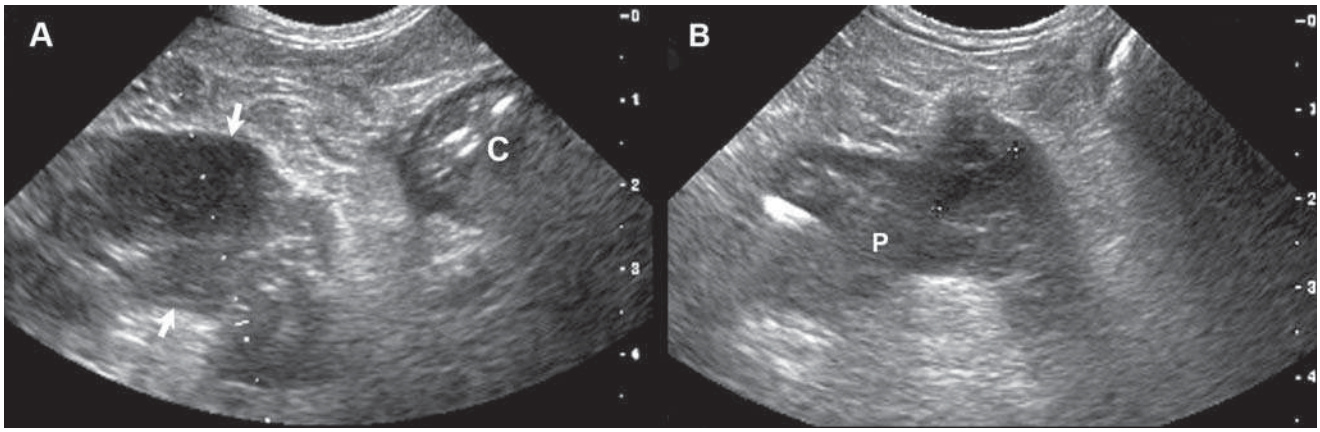


Figure 9.25. Drainage of cavitary lesion in 9-year-old Australian Shepherd. A: A hypoechoic cavity (arrows) is present in the enflamed pancreas of this dog. The needle track guide is centered on the cavity. The cavity was drained, and about 10 ml of bloody purulent fluid was withdrawn. The final diagnosis was sterile abscess. C, colon. **B:** A recheck 1 week later shows a smaller and poorly defined cavity (between the cursors) in the same portion of the pancreas (P), and the dog's condition improved clinically. The peripheral fat remained hyperechoic.

if adequate precautions are taken to avoid laceration of large vessels or pancreatic parenchyma. An experimental study in dogs, evaluating the effects of ultrasound-guided aspirations and surgical pancreatic biopsies showed no serum lipase elevation during the time frame (Cordner et al. 2010).

Fluid-filled lesions, such as pseudocysts and abscesses, can also be sampled and drained safely under ultrasound guidance (Figure 9.25). The presence of anechoic fluid in cavitary lesions can be misleading as to the type of fluid to be aspirated. Even though the fluid may be poorly cellular, its consistency cannot be predicted by its echogenicity. Anechoic fluid might be very viscous and therefore difficult to drain.

Ultrasound-guided cholecystocentesis can be performed to alleviate the clinical signs due to extrahepatic biliary obstruction secondary to severe pancreatitis, as these patients are often poor candidates for surgery (Herman et al. 2005). The procedure can be repeated if clinically indicated.

Serial ultrasound examinations are useful in monitoring resolution or progression of fluid-filled lesions or response to treatment (Figure 9.26).



Visit our website at **www.SmallAnimalUltrasonography.com** for complementary video clips with annotations and text on:

- Normal pancreas (dog and cat)
- Pancreatitis in dogs
- Pancreatitis in cats
- Pseudocyst
- Necrotizing pancreatitis in dogs

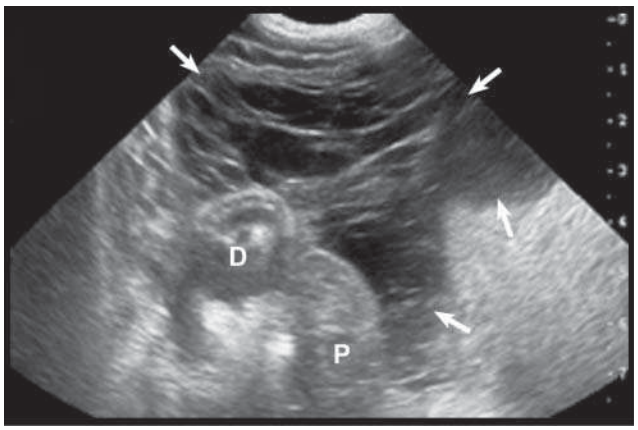


Figure 9.26. Recheck after lidocaine intraperitoneal injection in a Miniature schnauzer with pancreatitis. The injection was performed to control persistent and severe pain. An extensively hypoechoic to anechoic and striated area (arrows) near the pancreas (P) and duodenum (D) most likely represents an iatrogenic hematoma.

- Pancreatic carcinoma
- Insulinoma

References

Akol KG, Washabau RJ, Saunders HM, Hendrick MJ (1993) Acute pancreatitis in cats with hepatic lipidosis. J Vet Intern Med 7:205–209.

Bailiff NL, Norris CR, Seguin B, Griffey SM, Ling GV (2004) Pancreatolithiasis and pancreatic pseudobladder associated with pancreatitis in a cat. J Am Anim Hosp Assoc 40(1):69–74.

Cordner AP, Armstrong PJ, Newman SJ, Novo R, et al (2010) Effect of pancreatic tissue sampling on serum pancreatic enzyme levels in clinically healthy dogs. J Vet Diagn Invest 22_702–707.

Edwards DF, Bauer MS, Walker MA, Pardo AD, McCracken MD, Walker TL (1990) Pancreatic masses in seven dogs following acute pancreatitis. J Am Anim Hosp Assoc 26:189–198.

Etue SM, Penninck DG, Labato MA, Pearson S, Tidwell A (2001) Ultrasonography of the normal feline pancreas and associated anatomical landmarks: A prospective study of 20 cats. Vet Radiol Ultrasound 42:330–336.

Ferreri JA, Hardam E, Kimmel SA et al. (2003) Clinical differentiation of acute necrotizing from chronic nonsuppurative pancreatitis in cats: 63 cases (1996–2001). J Am Vet Med Assoc 223:469–474.

Forman MA, Marks SL, De Cock HEV, Hergesell EJ et al. (2004) Evaluation of serum feline pancreatic lipase immunoreactivity and helical tomography versus conventional testing for the diagnosis of feline pancreatitis. J Vet Intern Med 18:807–815.

Hecht S, Penninck DG, Keating JH (2007) Imaging findings in pancreatic neoplasia and nodular hyperplasia in 19 cats. Vet Radiol Ultrasound 48:45–50.

Hecht S, Penninck DG, Mahony OM, King R, Rand WM (2006) Relationship of pancreatic duct dilation to age and clinical findings in cats. Vet Radiol Ultrasound 47:287–294.

Hecht S, Henry G (2007) Sonographic evaluation of the normal and abnormal pancreas. Clin Tech Small Anim Pract 22:115–121.

Herman BA, Brawer RS, Murtaugh RJ, Hackner SG (2005) Therapeutic percutaneous ultrasound guided cholecystocentesis in three dogs with extrahepatic biliary obstruction and pancreatitis. J Am Vet Med Assoc 227:1782–1786 .

Hines BL, Salisbury SK, Jakovljevic S, De Nicola DB (1996) Pancreatic pseudocyst associated with chronic-active necrotizing pancreatitis in a cat. J Am Anim Hosp Assoc 32:147–152.

Jaeger JQ, Mattoon JS, Bateman SW, Morandi F (2003) Combined use of ultrasonography and contrast enhanced computed tomography to evaluate acute necrotizing pancreatitis in two dogs. Vet Radiol Ultrasound 44:72–79.

Lamb CR (1999) Pancreatic edema in dogs with hypoalbuminemia and portal hypertension. J Vet Intern Med 13:498–500.

Lamb CR, Simpson KW, Boswood A, Matthewman LA (1995) Ultrasonography of pancreatic neoplasia in the dog: A retrospective review of 16 cases. Vet Rec 37:65–68.

Léveillé R, Biller DS, Shiroma JT (1996) Sonographic evaluation of the common bile duct in cats. J Vet Intern Med 10:296–299.

Mai W, Caceres AV (2008). Dual phase computed tomographic angiography in three dogs with pancreatic insulinoma. Vet Radiol Ultrasound 49:141–148.

Marchevsky A, Yovich JC, Wyatt KM (2000) Pancreatic pseudocyst causing extrahepatic biliary obstruction in a dog. Asu Vet 78:99–101.

Moon ML, Panciera DL, Ward DL, Steiner JM, Williams DA (2005) Age-related changes in the ultrasound appearance of the normal feline pancreas. Vet Radiol Ultrasound 46:138–142.

Morita Y, Takiguchi M, Yasuda J, Eom KD et al (1998) Endoscopic ultrasonographic findings of the pancreas after pancreatic duct ligation in the dog. Vet Radiol Ultrasound 39:557–562.

Nyland TG, Gillette NA (1982) Sonographic evaluation of experimental bile duct ligation in the dog. Vet Radiol Ultrasound 23:252–260.

Penninck DG, Zeyen U. Taeymans O, Webster CR (2013) Ultrasonographic measurement of the pancreas and pancreatic duct in clinically normal dogs. Am J Vet Res 74:433–437.

Rutgers C, Herring DS, Orton EC (1985) Pancreatic pseudocyst associated with acute pancreatitis in a dog: Ultrasonographic diagnosis. J Am Anim Hosp Assoc 21:411–416.

Salisbury SK, Lantz GC, Nelson RW, Kazacos EA (1988) Pancreatic abscess in dogs: Six cases (1978–1986). J Am Vet Med Assoc 193:1104–1108.

Saunders HM (1991) Ultrasonography of the pancreas. Probl Vet Med 3:583–603.

Saunders HM, VanWinkle TJ, Drobatz K, Kimmel SE, Washabau RJ (2002) Ultrasonographic findings in cats with clinical, gross pathologic, and histologic evidence of acute pancreatic necrosis: 20 cases (1994–2001) J Am Vet Med Assoc 221:1724–1730.

VanEnkevort BA, O'Brien RT, Young KM (1999) Pancreatic pseudocysts in 4 dogs and 2 cats: Ultrasonographic and clinicopathologic findings. J Vet Intern Med 13:309–313.

Wall M, Biller DS, Schoning P, Olsen D, Moore LE (2001) Pancreatitis in a cat demonstrating pancreatic duct dilatation ultrasonographically. J Am Anim Hosp Assoc 37:49–53.

Watson PJ (2003) Exocrine pancreatic insufficiency as an end stage pancreatitis in four dogs. J Small Anim Pract 44:306–312.

CHAPTER TEN

Kidneys and Ureters

Marc-André d'Anjou[1,2] and Dominique Penninck[3]

[1] *Centre Vétérinaire Rive-Sud, Brossard, Québec, Canada*
[2] *Faculté de médecine vétérinaire de l'Université de Montréal, Saint-Hyacinthe, Québec, Canada*
[3] *Department of Clinical Sciences, Cummings School of Veterinary Medicine, Tufts University, North Grafton, MA, USA*

Preparation and Scanning Technique

Prior to the ultrasonographic examination, the animal's hair must be clipped, and ultrasonic gel must be applied to its skin to optimize images of the kidneys. Animals can be scanned in dorsal, left, or right recumbency. The left kidney can usually be well visualized with a ventrolateral approach, although the presence of gas or feces in the descending colon can sometimes limit its evaluation. The right kidney is typically more difficult to image, especially in deep-chested dogs, because of its deep localization in the craniodorsal abdomen. A right ventrolateral subcostal approach is usually sufficient. However, in certain dogs, a lateral approach through the 11th or 12th intercostal space might be necessary. The visualization of the right kidney can also be affected by the presence of intestinal content, especially in the descending duodenum, ascending colon, or cecum.

Kidneys can markedly vary in depth according to an animal's body conformation. In small dogs and cats, a high-frequency sonographic probe (≥7.5 MHz) is recommended, whereas kidneys of larger dogs usually require a probe with more penetration (≤5 MHz). Convex probes are generally more useful because they enable the entire kidney to be imaged. Microconvex probes have a smaller footprint and can be more easily used intercostally. Linear probes provide higher spatial resolution and are favorably used in animals with superficial kidneys. Spatial compounding allows a wider field of view so that the entire kidney can be included in the image.

Kidneys should be scanned from cranial to caudal and lateral to medial, in several transverse and longitudinal planes, to fully assess all portions, including the cortex, medulla, and collecting system (Figure 10.1).

Ultrasonographic Anatomy of Normal Kidneys

In many dogs, the left kidney can be evaluated through the body of the spleen, which provides a good acoustic window. The right kidney is more cranial and dorsal, particularly in dogs, and is usually in contact or in close proximity with the hepatic parenchyma at the level of the caudate lobe. Both kidneys are symmetrical in size and shape in cats and dogs. Kidneys can be oval, particularly in cats, or bean-shaped, which is more common in dogs.

Kidneys can be measured on all planes, and volumes can be estimated. The renal length in normal cats usually varies between 3.0 and 4.5 cm and is influenced by breed. For instance, ragdoll, British shorthair and Sphinx cats were reported to have length values (in cm) of 3.87 ±0.41, 3.77 ±0.43 and 4.09 ±0.33, respectively. Kidneys are also typically larger in intact cats and often become smaller with advancing age. The right kidney may also be longer than the left (Debruyn et al. 2013).

In dogs, absolute measurements must also take into account total body weight and conformation, because there are great variations (Barr et al. 1990). The renal length can also be compared with the aorta diameter or with the length of L5 or L6 in dogs (Mareschal et al. 2007; Barella et al. 2012) (Figure 10.2), although the range of normal remains relatively large with these ratios, limiting their usefulness in practice.

Renal cortex, medulla, and the collecting system can be visualized with ultrasonography in dogs

Atlas of Small Animal Ultrasonography, Second Edition. Edited by Dominique Penninck and Marc-André d'Anjou.
© 2015 John Wiley & Sons, Inc. Published 2015 by John Wiley & Sons, Inc.
Companion website: www.SmallAnimalUltrasonography.com

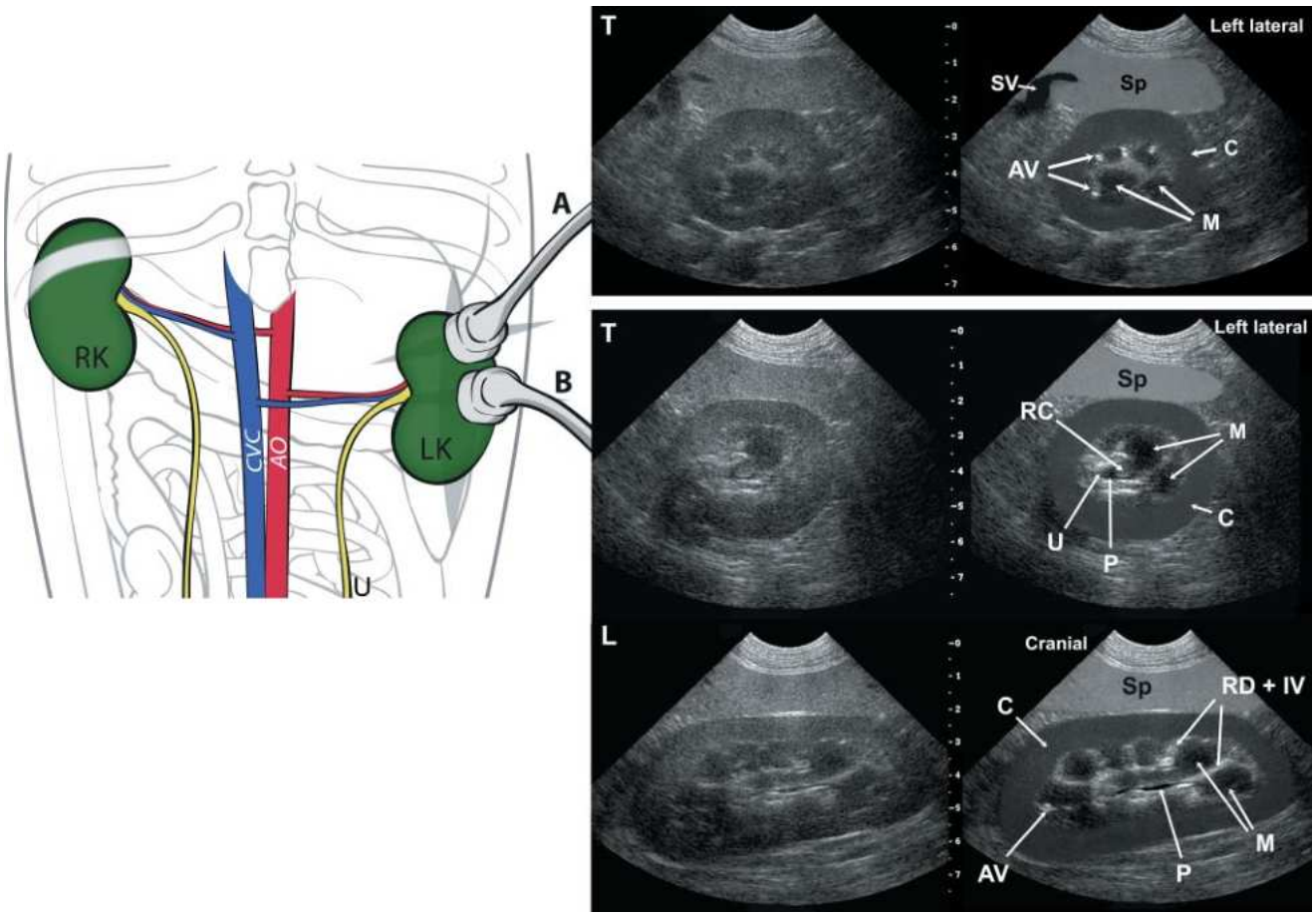


Figure 10.1. Sonographic approach and normal anatomy in the dog. In dorsal recumbency, a ventrolateral approach to the left kidney is used. The probe is moved through the kidney sequentially in transverse and longitudinal planes. AO, aorta; CVC, caudal vena cava; LK, left kidney; and RK, right kidney. **A:** Transverse **(T)** sonogram performed on the cranial pole of the left kidney. **B:** The probe is placed at the hilus region: Transverse **(T)** and longitudinal **(L)** sonograms with corresponding schematic and labeled images. AV, arcuate vessels; C, renal cortex; M, renal medulla; P, pelvis; RC, renal crest; RD + IV, renal diverticuli and interlobar vessels; Sp, spleen; SV, splenic vein; U, ureter.

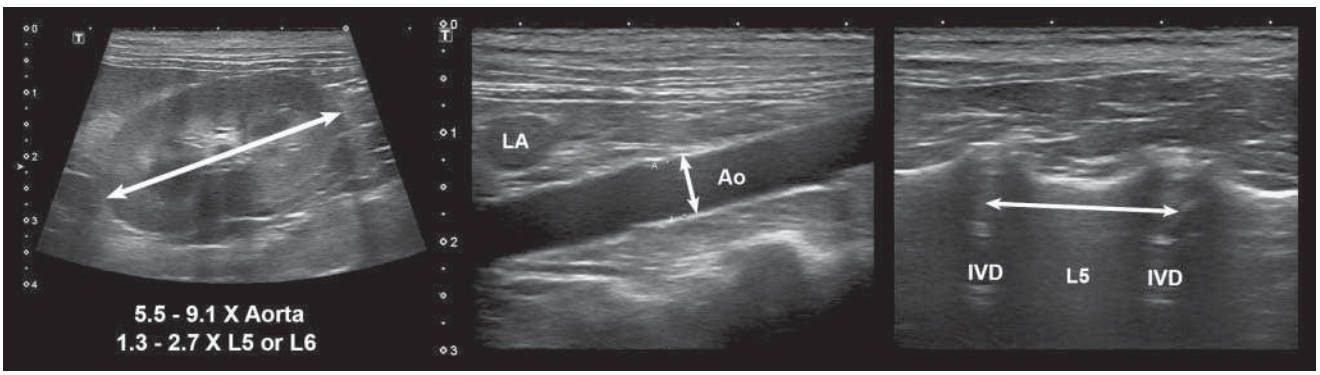


Figure 10.2. Normal ranges for renal-to-aorta and renal-to-L5 (or L6) ratios in dogs. The maximal renal length is compared to the maximal luminal diameter of the aorta (identified after reviewing the cineloop) or to the length of L5 or L6.

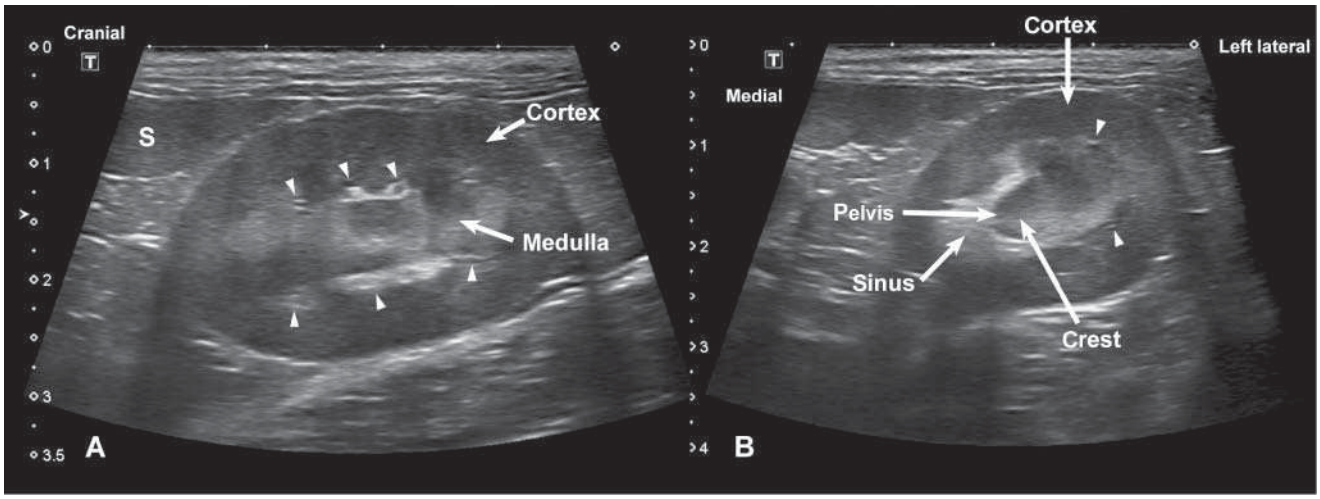


Figure 10.3. Normal feline kidney. Longitudinal **(A)** and transverse **(B)** images of the left kidney in a normal cat. The renal cortex is more echogenic than the medulla, but isoechoic when compared with the superficial spleen (S). The renal crest may be more echoic, as in this cat. The renal pelvis is surrounded by the hyperechoic sinus. Arcuate vessels (arrowheads) appear as short parallel hyperechoic lines at the corticomedullary junction.

and cats (Figures 10.1, 10.3). The renal medulla is hypoechoic when compared with the cortex, which is usually hypoechoic or isoechoic to the liver and typically hypoechoic to the spleen. However, in dogs and cats with normal renal function, renal cortices can be hyperechoic to the liver (Ivancic and Mai 2008). In cats, the accumulation of fatty vacuoles in the renal cortex appears to contribute to its hyperechogenicity (Yeager and Anderson 1989) (Figure 10.4). The angle of insonation may also influence the echogenicity of the cortex. Renal extremities may be more echogenic because of the difference in tubule angulation (i.e., anisotropy), with conventional or spatial compounding imaging (Ruth et al. 2013) (Figure 10.4). Sonographers should be careful when using this area as a landmark for comparing the renal cortex and nearby structures' echogenicities.

The medulla appears separated into several lobulated segments by the presence of linear echogenicities representing borders of the interlobar vessels and diverticuli. The medulla is nearly anechoic in certain animals and with high-contrast image settings, which should not be confused with dilatation of the renal pelvis. The outer medulla, which parallels the cortex below the arcuate arteries, may also be isoechoic to the cortex, giving the impression of cortical thickening, or even hyperechoic to it, forming a hyperechoic band superficial to the arcuate arteries (Figure 10.4). This is more frequent in small breeds and in young dogs (Hart et al. 2013). The renal crest is the prolongation of the renal medulla and is in contact with the pelvis.

The walls of the arcuate arteries can be observed as paired, short, hyperechoic lines at the corticomedullary junction, which can sometimes generate an acoustic shadow and must be differentiated from mineralization (Figures 10.2, 10.4). These vessels, as well as the larger renal and intralobar vessels, can also be evaluated with color Doppler or power Doppler (Figure 10.5). The renal arteries and veins, usually single on each side, can be followed from the hilus to the aorta and caudal vena cava, respectively. These vessels must be differentiated from dilated ureters.

The renal pelvis is often visualized in dogs and cats with normal renal function and particularly when diuresis is triggered by intravenous fluids or diuretics (d'Anjou et al. 2011). The pelvic height in dogs and cats usually measures less than 2 mm when using a transverse plane, although it may sometimes exceed 3 mm (Figure 10.4). Conversely, the renal diverticuli and ureter are not normally seen in dogs and cats. The pelvis is surrounded by the sinus, which contains fat and appears hyperechoic and is particularly prominent in obese cats.

Ultrasonographic Features of Renal Disorders

Congenital and Inherited Renal and Ureteral Malformations

With the exception of polycystic kidney disease and ectopic ureters, congenital malformations of the upper urinary tract are rare in dogs and cats. Renal agenesis

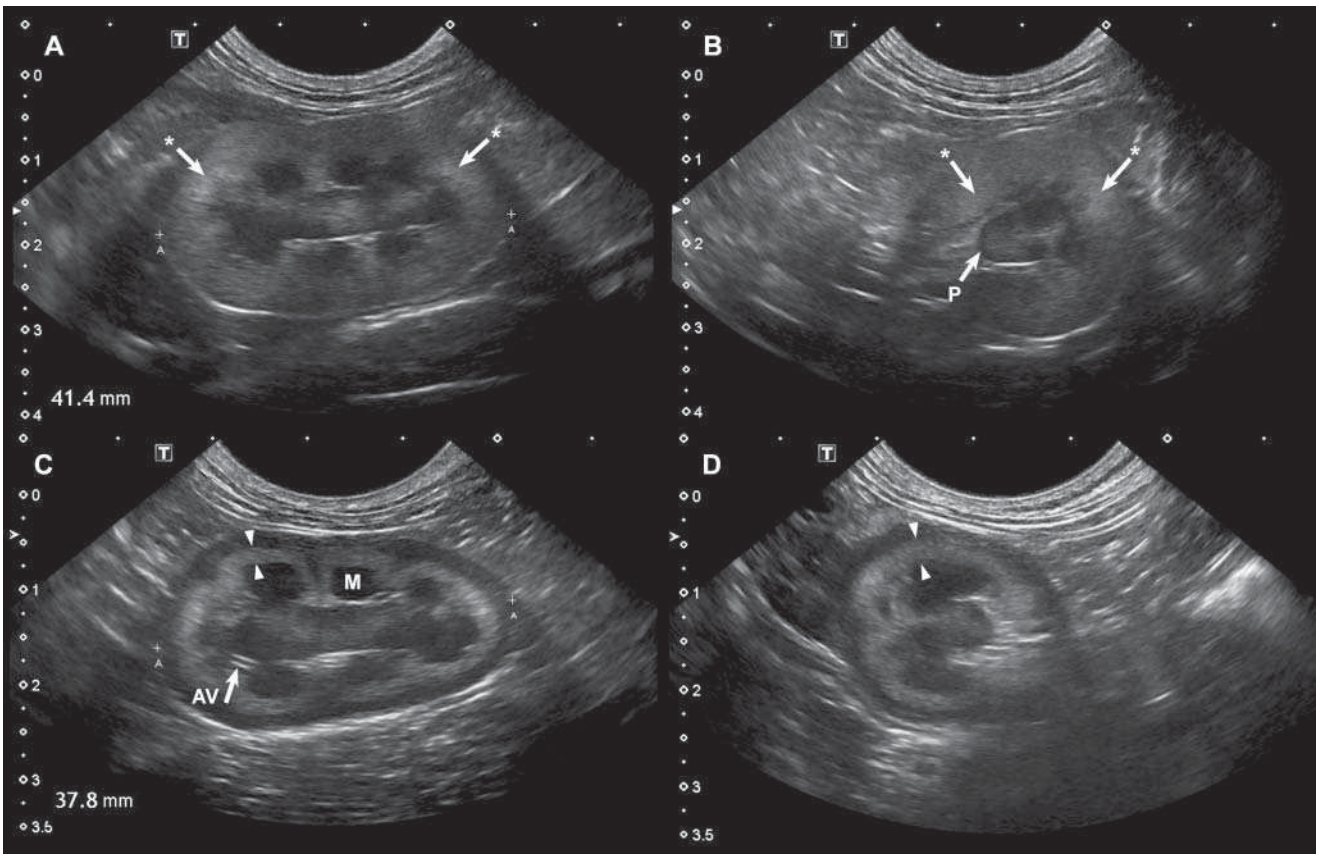


Figure 10.4. **Normal variants in cats and dogs. A**, **B**: The renal cortex is hyperechoic in this cat with normal renal function, presumably due to the accumulation of lipids. Note that some areas of the cortex are more echogenic (*) because of the difference in tubule angulation (i.e., anisotropy). The pelvis is minimally dilated, which is considered normal. **C**, **D**: These longitudinal (**C**) and transverse (**D**) sonographic images of the right kidney were obtained in a clinically normal 1-year-old Lhasa Apso. The outer medulla is hyperechoic, forming a band (between arrowheads) at the periphery of the inner medulla (M). AV, arcuate vessels.

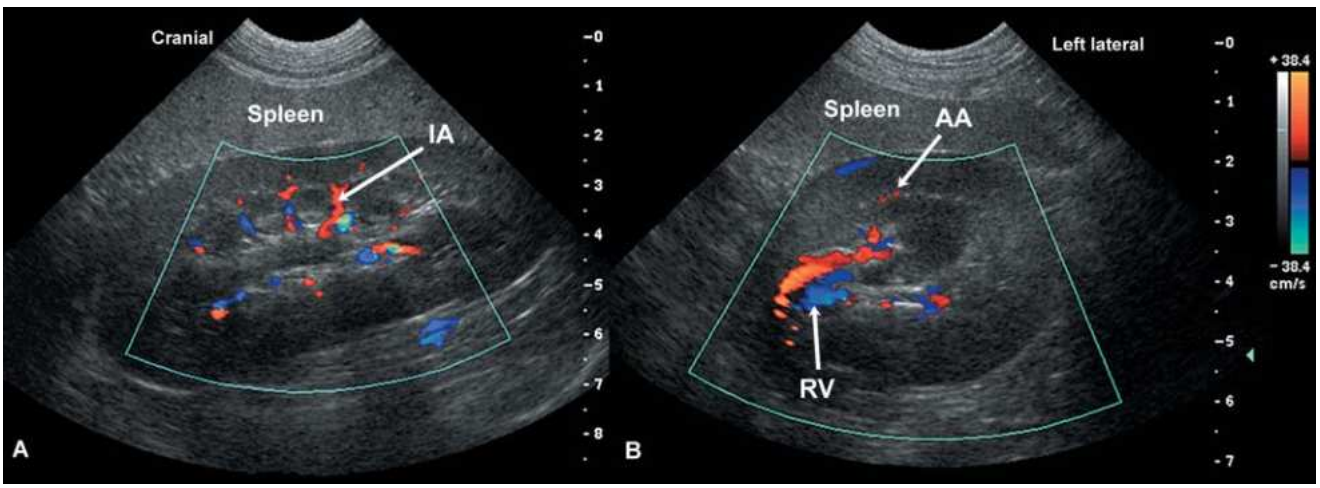


Figure 10.5. **Renal vasculature with color Doppler in a normal dog.** Longitudinal **(A)** and transverse **(B)** images of the left kidney. The vascular flow can be observed with color Doppler through the renal, interlobar, and arcuate vessels. AA, arcuate artery; IA, interlobar artery; RV, renal vein.

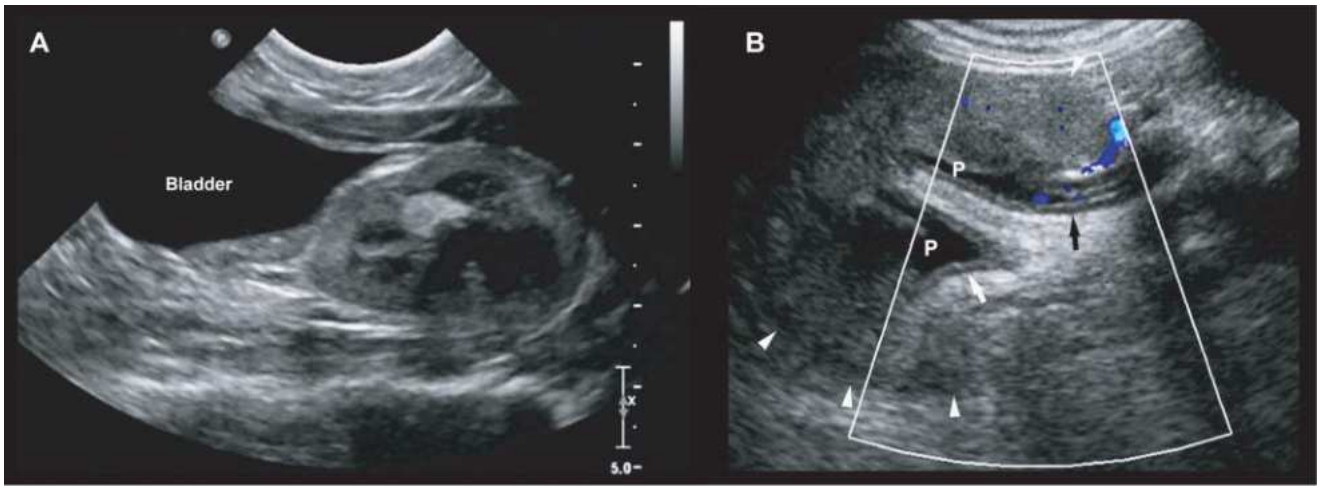


Figure 10.6. **Congenital malformations of kidneys and ureters. A:** Ectopic kidney in a 8-year-old cat presented for acute vestibular signs. The right kidney is located caudodorsally to the urinary bladder. The kidney is 3.3 cm long and deformed. The hyperechoic area near the center represents the renal sinus. **B:** Renal pelvis duplication in an English Bulldog presented for azotemia. The right kidney (arrowheads) of this 3-year-old spayed female dog was associated with two ureters (white and black arrows) connected to two pelvices (P). Both ureters were hyperperistaltic.

(complete absence) or hypoplasia/dysplasia is often associated with compensatory enlargement of the unique kidney. Renal ectopia, fusion and duplication have also been reported (Allworth and Hoffman 1999; Esterline et al. 2005; Hecht et al. 2005) (Figure 10.6). Renal dysplasia is defined as disorganized development of renal parenchyma, focally or globally, because of anomalous differentiation. It may affect several breeds of dogs, with or without a familial basis. The sonographic changes vary according to the severity of the disease. Subclinical renal dysplasia may show a hyperechoic or speckled medulla with loss of corticomedullary distinction (Seiler et al. 2010). Severely affected kidneys tend to become small, irregular, and diffusely hyperechoic, similarly to kidneys with chronic inflammatory disease (Abraham 2003) (Figure 10.7). These young dogs may be predisposed to ascending pyelonephritis, which contributes to the morphological modifications observed on ultrasound (Abraham 2003). Juvenile nephropathy is another form of renal disease affecting young dogs. Boxers are particularly affected and often present concurrent

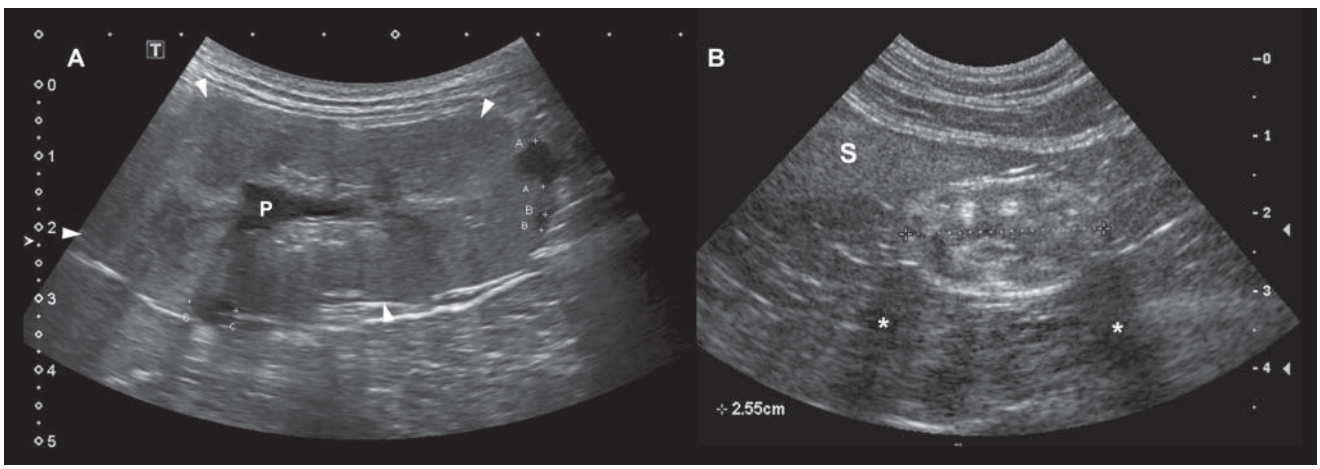


Figure 10.7. **Renal dysplasia in two dogs. A**: Longitudinal images of the left kidney (arrowheads) of a 10-month-old Labrador Retriever with bilateral renal dysplasia. Each kidney was deformed, smaller than normal, and the corticomedullary distinction was greatly reduced. In this one, several spherical anechoic cysts are present (between cursors) and the pelvis (P) is dilated and distorted. **B**: In another adult mixed-breed dog, the left kidney is small and hyperechoic to the spleen. Edge shadowing is also observed (*). The right kidney appeared normal.

urethral sphincter mechanism (Chandler et al. 2007). Although these renal anomalies can be confirmed only with histological analysis, renal dysplasia or juvenile nephropathy should be suspected in a young dog with deformed kidneys and clinical renal insufficiency.

Diffuse Parenchymal Renal Diseases

Increased renal echogenicity is one of the most common findings in dogs and cats with renal insufficiency. Several renal diseases can be associated with increased cortical and/or medullary echogenicity in the acute or chronic phases of the process. Other than renal dysplasia or juvenile nephropathy, interstitial and glomerular nephritis, acute tubular nephrosis or necrosis (caused by ethylene glycol, grapes in dogs, and lily in cats), end-stage renal disease, and nephrocalcinosis can all cause renal hyperechogenicity (Barr et al. 1989; Adams et al. 1991; Forrest et al. 1998; Eubig et al. 2005). In some of these disease processes, the cortical echogenicity can be more specifically increased, enhancing the corticomedullary distinction. This can be dramatic in cases of acute tubular necrosis and calcium oxalate deposition caused by ethylene glycol toxicity (Figure 10.8). In other cases, both medulla and cortex can become hyperechoic, causing reduced corticomedullary border distinction (Figure 10.9). This is particularly evident in dogs and cats with chronic renal disease (Figures 10.10–10.13). The medulla may be more specifically hyperechoic with leptospirosis, diffusely or forming a band as a the result of congestion,

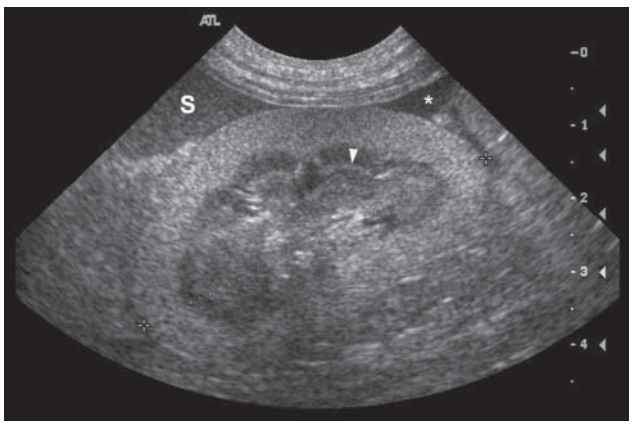


Figure 10.8. Ethylene glycol toxicity in a dog. On this longitudinal image of the right kidney, the cortex is markedly hyperechoic in comparison with the adjacent spleen, because of oxalate crystal deposition and tubular necrosis. The corticomedullary distinction is enhanced and a hyperchoic rim sign is present in the medulla (arrowheads). Mild peritoneal effusion (*) was also present.

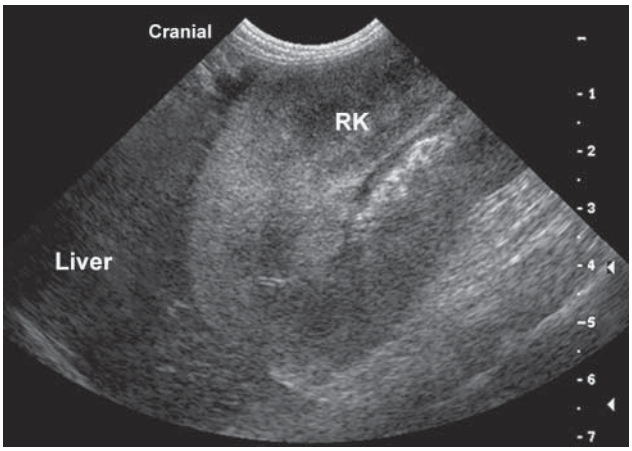


Figure 10.9. Acute interstitial nephritis caused by leptospirosis. Longitudinal image of the right cranial abdomen of a dog with acute renal insufficiency. The right kidney (RK) is enlarged and diffusely hyperechoic. This hyperechogenicity contrasts with the concurrent hypoechogenicity involving the adjacent liver, which was presumably caused by hepatitis. The renal corticomedullary distinction is significantly reduced.

edema, hemorrhage, and necrosis (Figures 10.14, 10.15) (Forrest et al. 2005). A hyperechoic medullary band parallel to the corticomedullary border – also known as the **medullary rim sign** – has also been observed in several other disease processes, such as acute tubular necrosis (ethylene glycol toxicity), nephrocalcinosis, and pyogranulomatous vasculitis caused by feline infectious peritonitis, as well as in normal cats and dogs (Barr et al. 1989; Biller et al. 1992; Forrest et al. 1998; Mantis and Lamb 2000) (Figures 10.8, 10.11, 10.16). This hyperechoic band has been attributed to an insult to the renal tubules in the deepest portion of the medulla, which is most metabolically active and therefore more susceptible to ischemia (Biller et al. 1992). Due to their relatively high prevalence in dogs and cats, renal hyperechogenicity and medullary rim signs should not be considered as accurate indicators of renal disease; however, the possibility remains that these findings could represent sentinel signs of early renal disease or past renal insult (Mantis and Lamb 2000).

Kidneys of older dogs and cats can present several alterations without clinical evidence of renal disease (Figure 10.17). Apart from parenchymal echogenicity, interpretation must also take into consideration parameters such as size, shape, contour, and internal architecture. Small, irregular, and diffusely hyperechoic kidneys are generally indicative of chronic interstitial nephritis (Figures 10.12, 10.13). The remodeling process affecting these kidneys, which involves fibrosis, causes

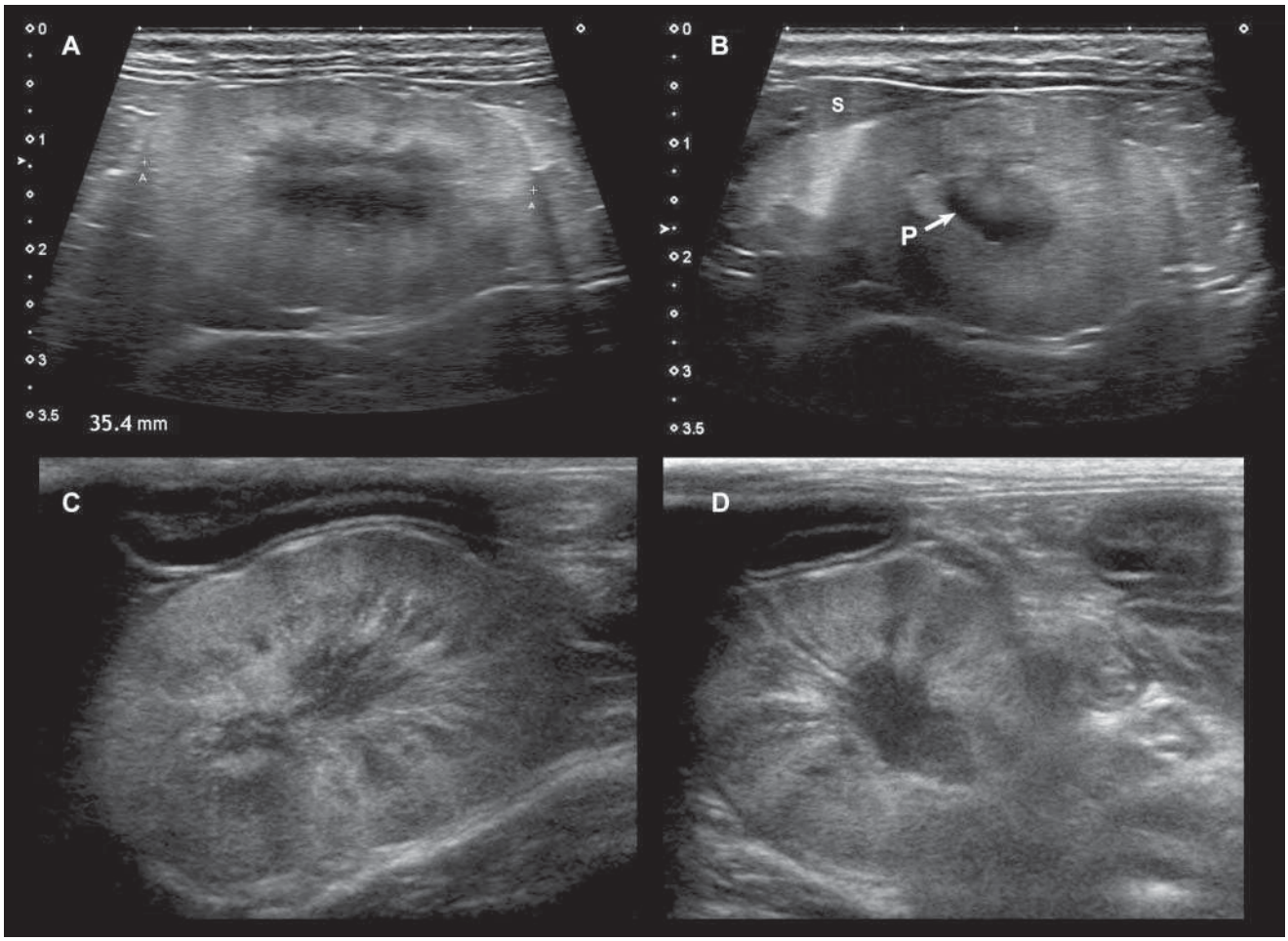


Figure 10.10. Chronic interstitial nephritis in cats. On these longitudinal **(A)** and transverse **(B)** images of the left kidney of 12-year-old domestic shorthair cat, both the cortex and medulla appear hyperechoic and poorly demarcated. The changes are more pronounced in the outer portion of the medulla. The renal contour is irregular, but the kidney remains normal in size. The renal pelvis is mildly dilated due to increased diuresis. S, spleen. **C, D**: Moderate multifocal lymphocytic-plasmacytic interstitial nephritis in a 6-year-old Oriental shorthair cat presented for a 6-month history of azotemia. Longitudinal **(C)** and transverse **(D)** sonograms showed small rounded kidneys with irregular margins. Radiating hyperechoic striations are noted through the cortex and medulla; they probably represent the marked tubular vacuolation (lipid) with multifocal tubular necrosis.

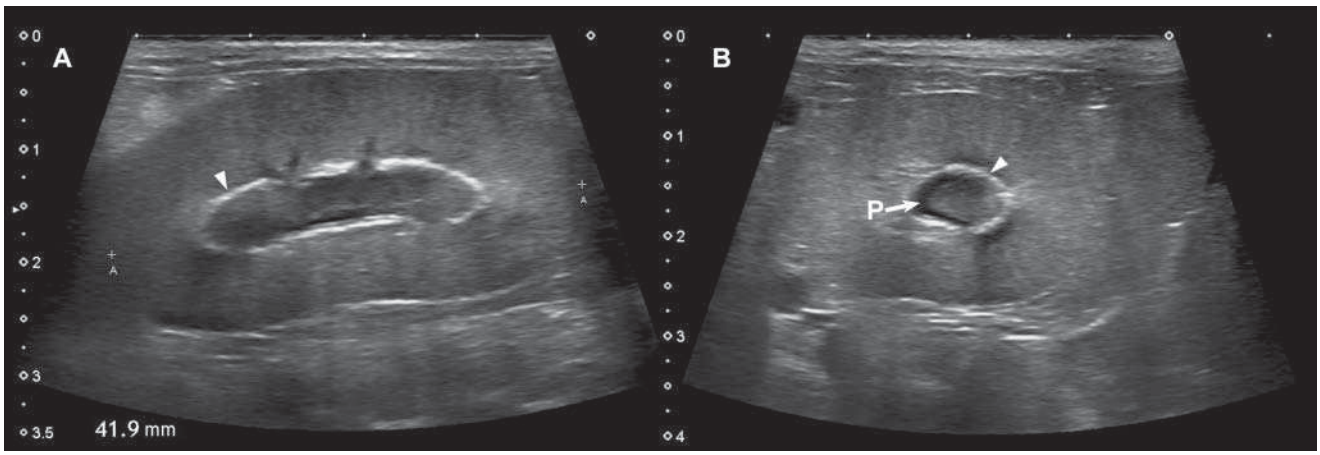


Figure 10.11. Chronic renal disease in an 11-year-old small-breed dog with creatinemia and proteinuria. On these longitudinal **(A)** and transverse **(B)** images of the left kidney, the cortex is hyperechoic and thickened. A prominent hyperechoic rim sign is present in the outer medulla (arrowheads). The pelvis (P) is mildly dilated. Glomerulonephritis and amyloidosis should first be considered based on the clinical and sonographic findings.

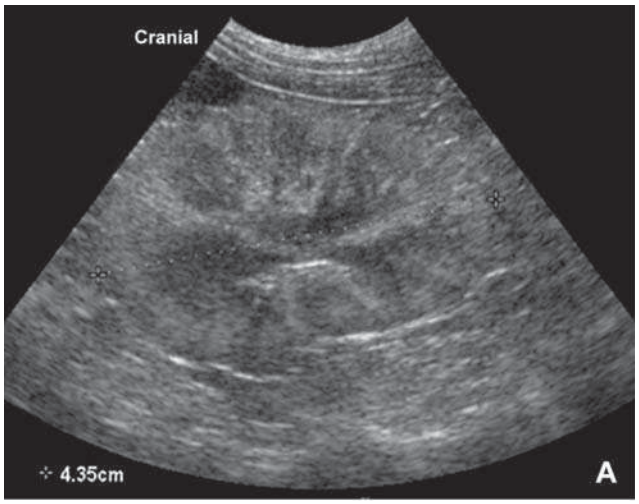


Figure 10.12. Nephrosclerosis. Longitudinal image of the left kidney of a 5-year-old shar-pei with chronic renal insufficiency and proteinuria. The cortex is markedly hyperechoic, granular in echotexture, and appears thinned when compared with the medulla. The kidney is also small and mildly irregular. Nephrosclerosis was the histological diagnosis based on ultrasound-guided biopsies. Sp, spleen.

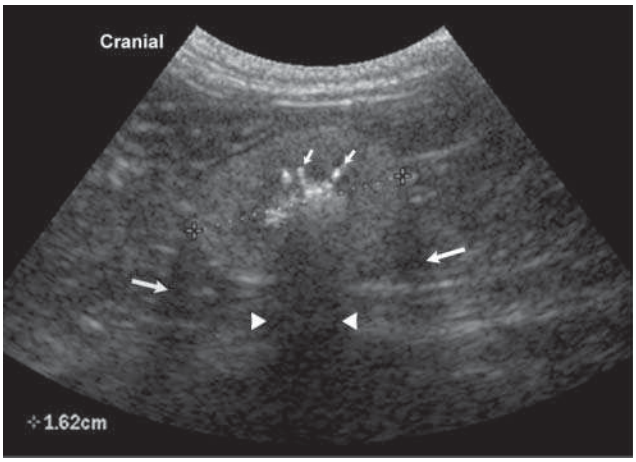


Figure 10.13. Chronic interstitial nephritis with dystrophic mineralization. Longitudinal image of the left kidney in a cat with chronic renal insufficiency. This kidney is small and hyperechoic. The corticomedullary distinction is reduced, and several linear and irregular hyperechoic foci noted in the region of the pelvis and diverticuli (short arrows) are associated with acoustic shadowing (arrowheads). These foci indicated dystrophic mineralization. Edge shadowing is also observed (long arrows).

architectural distortions. Linear or patchy dystrophic mineralization can also be observed in these kidneys, especially in the region of the collecting system, where the mineralization appears as poor or well-defined hyperechoic foci that cause acoustic shadowing (Figure 10.13). These mineral foci are usually difficult to differentiate from true nephroliths, which can also accompany chronic renal diseases. Kidneys affected with acute processes, such as infectious pyelonephritis, interstitial nephritis (e.g., caused by leptospirosis), or acute tubular necrosis (e.g., caused by ethylene glycol), can become enlarged and hyperechoic, with a contour that usually remains smooth (Figures 10.8, 10.9, 10.16). Perinephric effusion can also be observed in patients with acute renal failure (Figure 10.8) (Forrest et al. 1998; Holloway and O'Brien 2007).

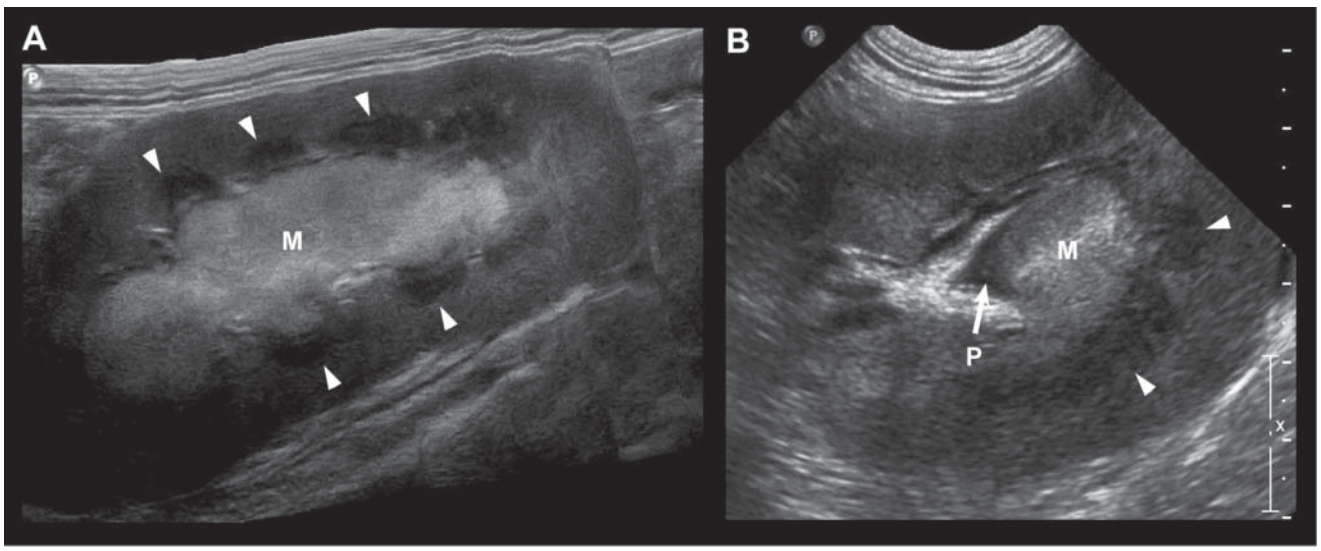


Figure 10.14. Leptospirosis in a 2-year-old German shepherd with acute renal insufficiency. Longitudinal **(A)** and transverse **(B)** images of the right kidney on which the inner medulla (M) is markedly hyperechoic, while the outer medulla (arrowheads) and cortex appear normal. Moderate pyelectasia (P) is also present.

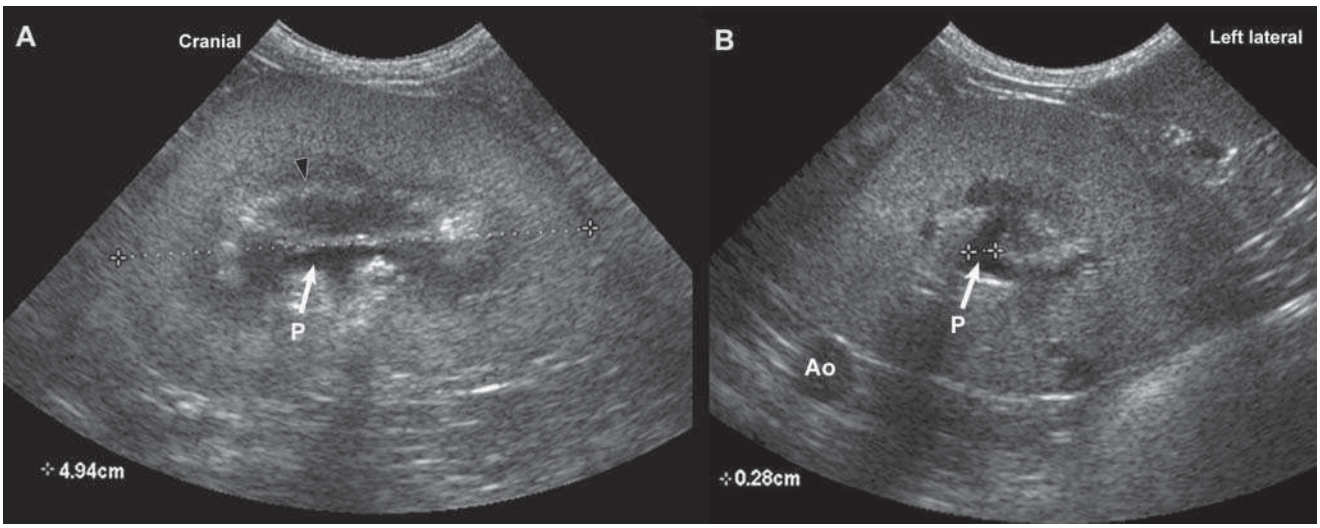


Figure 10.15. **Acute leptospirosis.** Longitudinal **(A)** and transverse **(B)** images of the left kidney (arrowheads) in a small-breed dog diagnosed with leptospirosis. The kidney is smoothly enlarged and hyperechoic, and the corticomedullary distinction is reduced. The renal pelvis (long arrow) is also dilated. Additionally, a medullary rim sign is present (arrowhead). Ao, aorta.

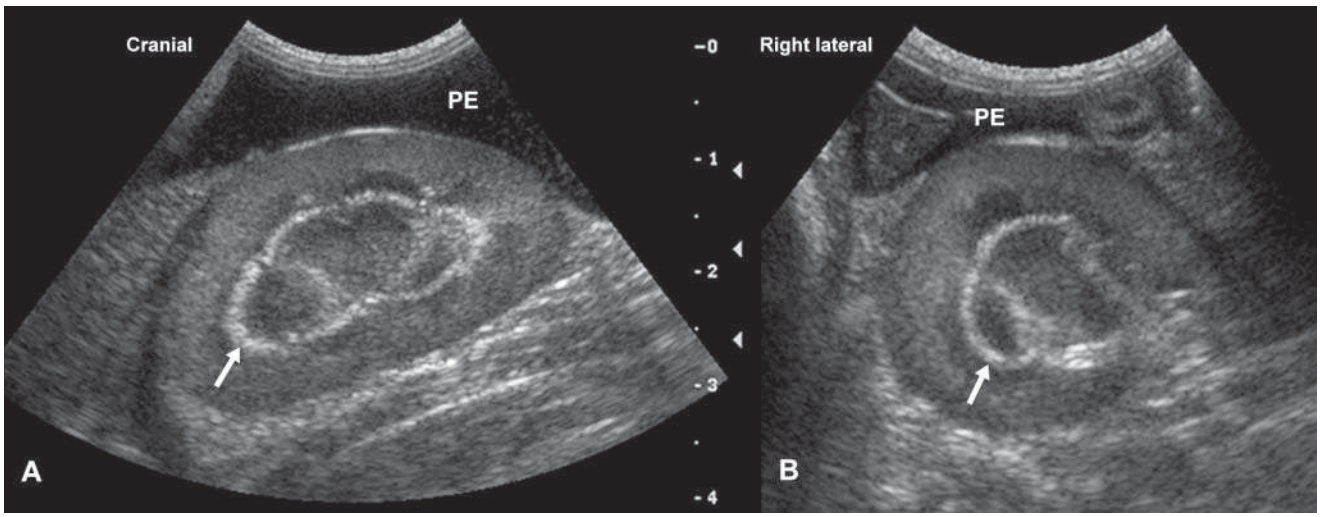


Figure 10.16. **Pyogranulomatous vasculitis.** Longitudinal **(A)** and transverse **(B)** images of the right kidney in a cat diagnosed with feline infectious peritonitis. A prominent hyperechoic band is in the medulla (arrow), parallel to the cortical margin, consistent with a medullary rim sign. Pronounced peritoneal effusion (PE) is also present.

Protein-losing glomerular diseases, such as glomerulonephritis and renal amyloidosis, cannot be distinguished from other types of diffuse renal disorders. Affected kidneys are commonly hyperechoic and can vary in size according to the chronicity of the disease (Figure 10.18).

Renal parenchymal mineralization (nephrocalcinosis) in dogs and cats with or without hypercalcemia can cause renal diffuse cortical and/or medullary hyperechogenicity, a medullary rim sign, and/or dispersed hyperechoic foci (Figure 10.19).

Neoplastic processes typically cause focal or multifocal renal changes, with the exception of lymphoma in cats. With lymphoma in cats, the kidneys typically become enlarged, irregular, and hyperechoic and often present characteristic hypoechoic subcapsular thickening (Valdès-Martinez et al. 2007) (Figure 10.20). Other findings can include hyperechoic foci or striations throughout the medulla, pyelectasia, and hypoechoic medullary or cortical nodules or masses. Other tumors, such as squamous cell carcinoma and nephroblastoma, may diffusely infiltrate the

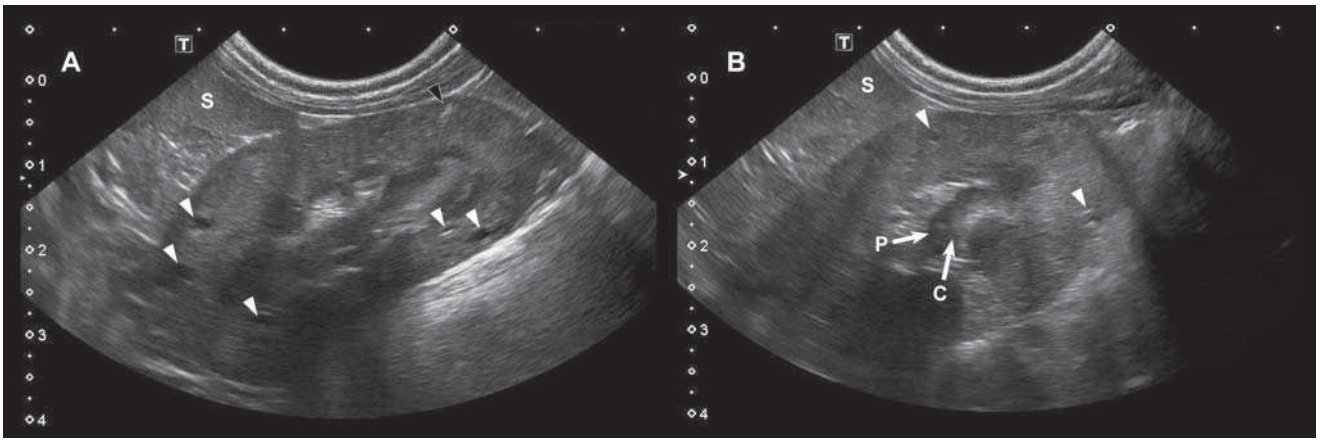


Figure 10.17. Renal degeneration in a 12-year-old mixed-breed dog with normal creatinine seric concentration. In these longitudinal **(A)** and transverse **(B)** images of the left kidney, the renal cortex is isoechoic to the adjacent spleen (S) and filled with small anechocic cysts (white arrowheads) and hyperechoic lines (black arrowhead). The renal crest (C) is hyperechoic and the pelvis is mildly dilated.

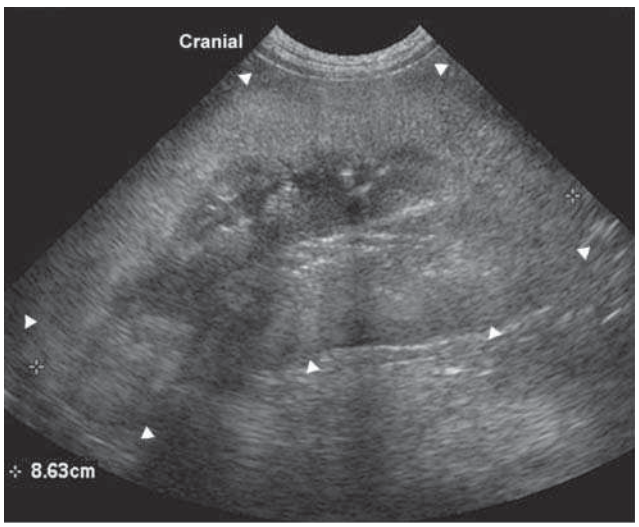


Figure 10.18. Glomerulonephritis. Longitudinal image of the left kidney (arrowheads) of a German shepherd diagnosed with bilateral glomerulonephritis. The kidney appears smoothly enlarged and hyperechoic, particularly at the level of the cortex, which also appears subjectively thickened.

kidney and markedly distort the renal architecture (Figure 10.21).

Focal Parenchymal Renal Disorders

In comparison with diffuse parenchymal lesions for which ultrasound lacks sensitivity and specificity, several types of focal lesions can be identified with superior accuracy. Renal cysts, nephroliths or dystrophic mineralization, and cortical infarcts are more common than primary or metastatic neoplasia, granulomas, and abscesses.

Renal Cavitary Lesions

Benign renal cysts typically appear as round to oval, anechoic structures with a thin, well demarcated, hyperechoic rim and may show distal acoustic enhancement (Reichle et al. 2002) (Figure 10.22A,B). Cysts can be solitary or multifocal and vary in size. In some patients, internal echoes can be observed in association with hemorrhage or necrotic debris.

Autosomal-dominant polycystic kidney disease (PKD) mainly affect Cairn Terriers and Persian and Persian-related cats. PKD can be variable in severity, can sometimes be associated with chronic interstitial nephritis, and may cause significant renal distortion (Figure 10.22C,D). Most of these cysts are in the cortex or at the corticomedullary junction (Reichle et al. 2002). Ultrasound scanning by an experienced sonographer at 10 months of age appears reliable for PKD diagnosis (Wills et al. 2009). With recent ultrasound units and higher frequency (10–14 MHz) probes, PKD may even be diagnosed with 96% sensitivity and 91% specificity as early as 3 months of age (Bonazzi et al. 2009).

Renal cysts can also be secondary to chronic renal diseases in dogs and cats (Figure 10.17).

Solitary cysts, which can sometimes become relatively large and present a complex architecture with

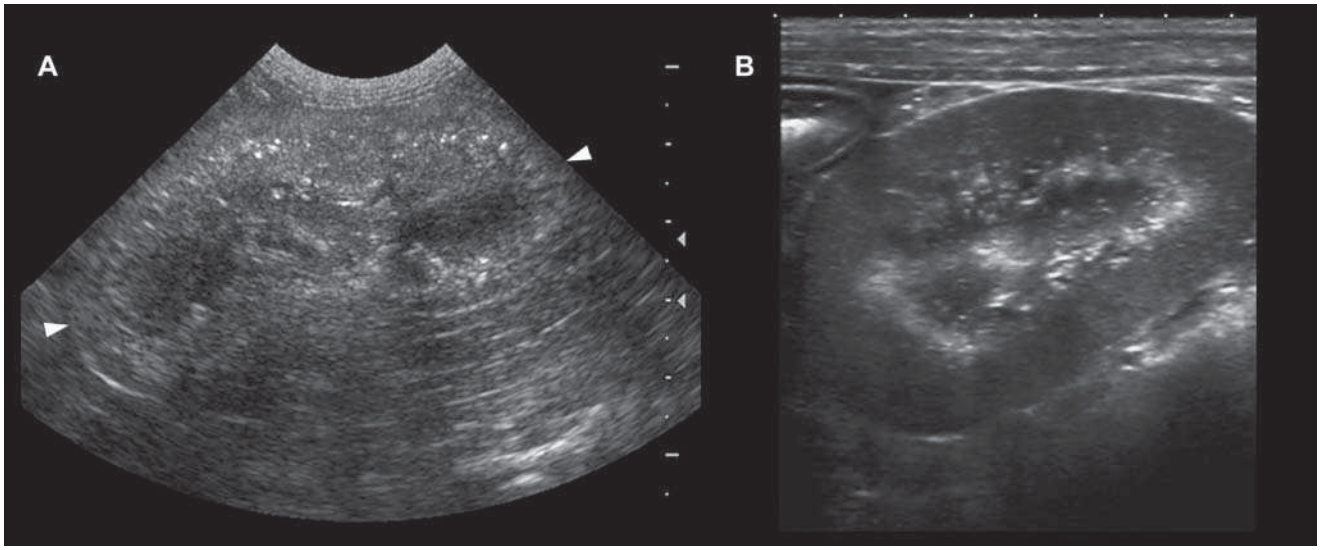


Figure 10.19. **Nephrocalcinosis in two dogs with hypercalcemia. A**: On this longitudinal image, small hyperechoic foci (arrows) are seen throughout the left kidney, particularly involving the cortex, consistent with extensive renal calcification. **B**: In another dog, hyperechoic dots are seen in the medulla, while the cortex is relatively normal.

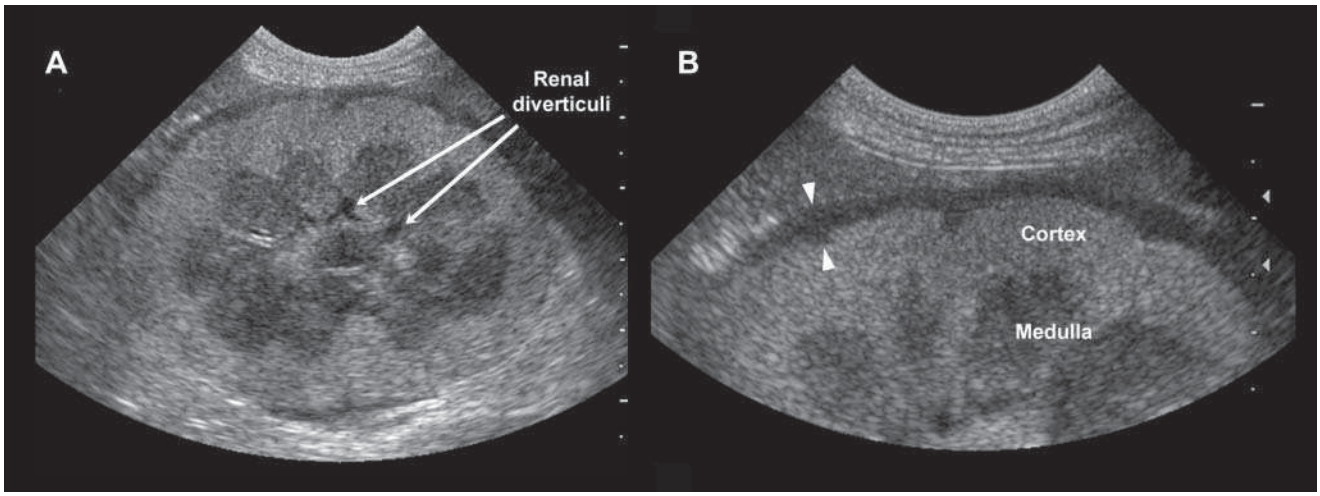


Figure 10.20. **Renal lymphoma in cats. A, B**: On these longitudinal images, the left kidney is enlarged, reaching more than 6 cm in length, and moderately hyperechoic. The lobulated sections of the medulla appear prominent, and a hypoechoic halo is present at the periphery of the cortex (between the short arrows). Mild dilatation of the renal diverticuli is also apparent (long arrows). These features are commonly seen with renal lymphoma in cats. **C, D**: In another cat, the peripheral subcapsular hypoechoic layer (between arrowheads) is more pronounced and traversed by vessels (arrow in **D**). The renal parenchyma is deformed, heterogeneous and associated with poor corticomedullary distinction. **E**: In this other cat, the right kidney is also deformed and shows poor corticomedullary distinction, but the subcapsular halo sign is less evident (arrowhead). **F:** Longitudinal ultrasonographic image of the right kidney in another cat. The kidney is enlarged, reaching more than 8 cm in length, and markedly heterogeneous. Several ill-defined hypoechoic nodules and masses are in the parenchyma, distorting its architecture. This pattern is another manifestation of lymphoma in cats. (*continued overleaf*)

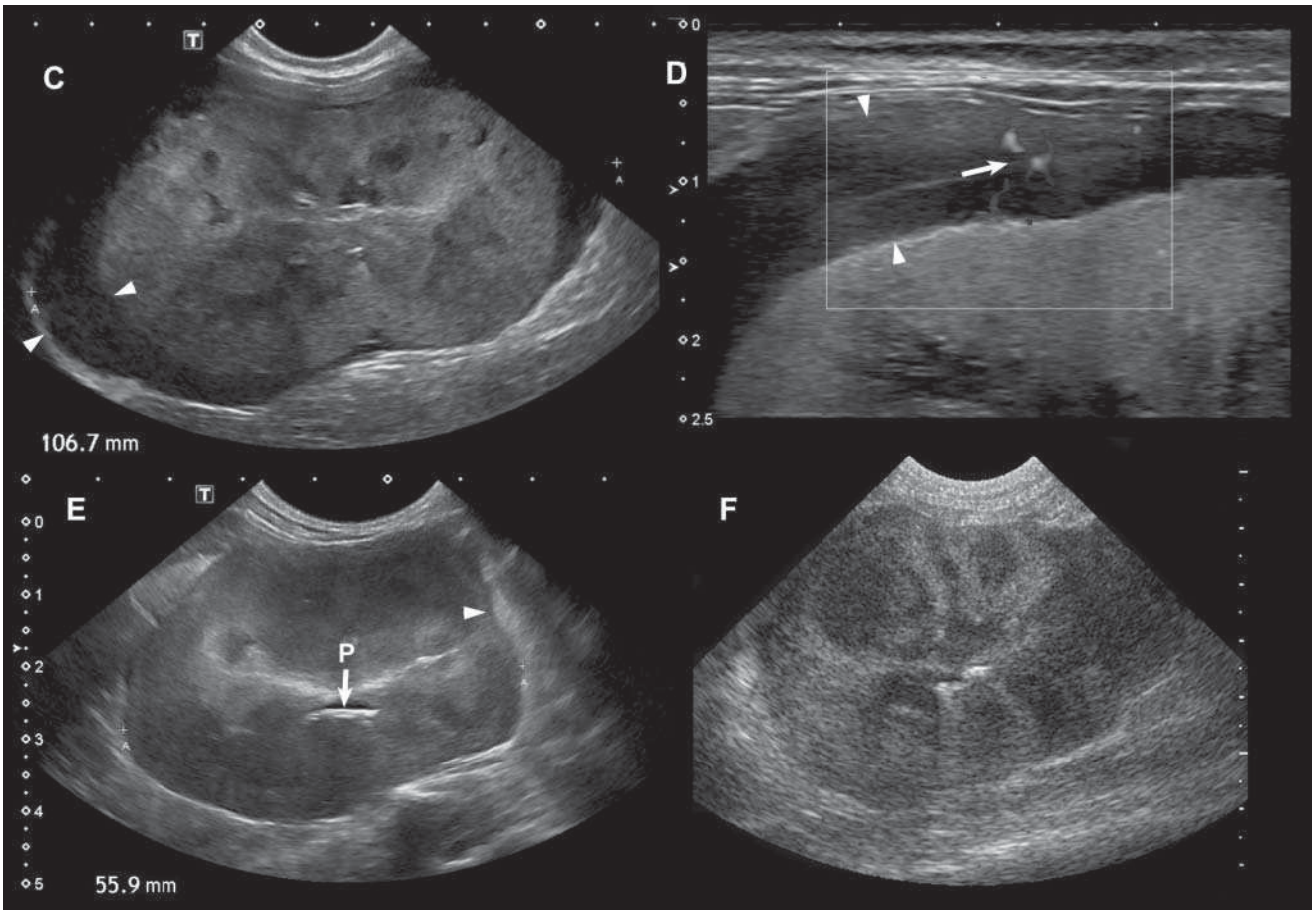


Figure 10.20. *Continued*

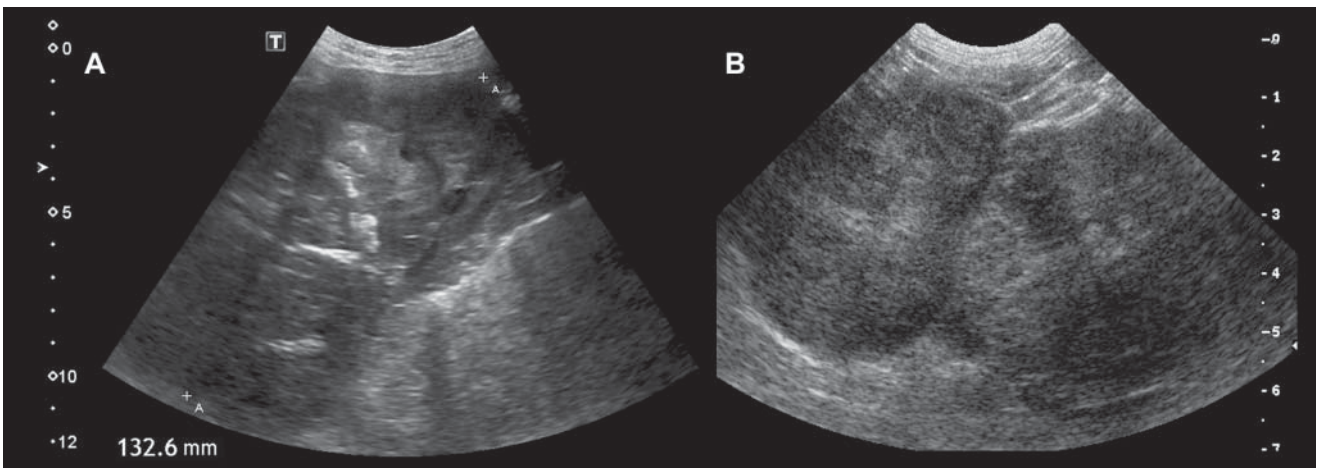


Figure 10.21. **Diffuse neoplastic infiltration in the kidney of a dog and a cat. A:** Longitudinal sonogram of the right kidney of a 12-year-old German Shepherd Dog with hematuria. The kidney has been replaced by a large, mostly hyperchoic mass, with heterogeneous hyperechoic areas, some of which are consistent with calcification. A cytological sample revealed the presence of carcinoma. **B:** A large neuroblastoma deforms the contours of the kidney of this cat and is heterogeneous with hypoechoic and hyperchoic areas intermingled. Only a small portion of the kidney was recognizable as renal tissue (not shown).

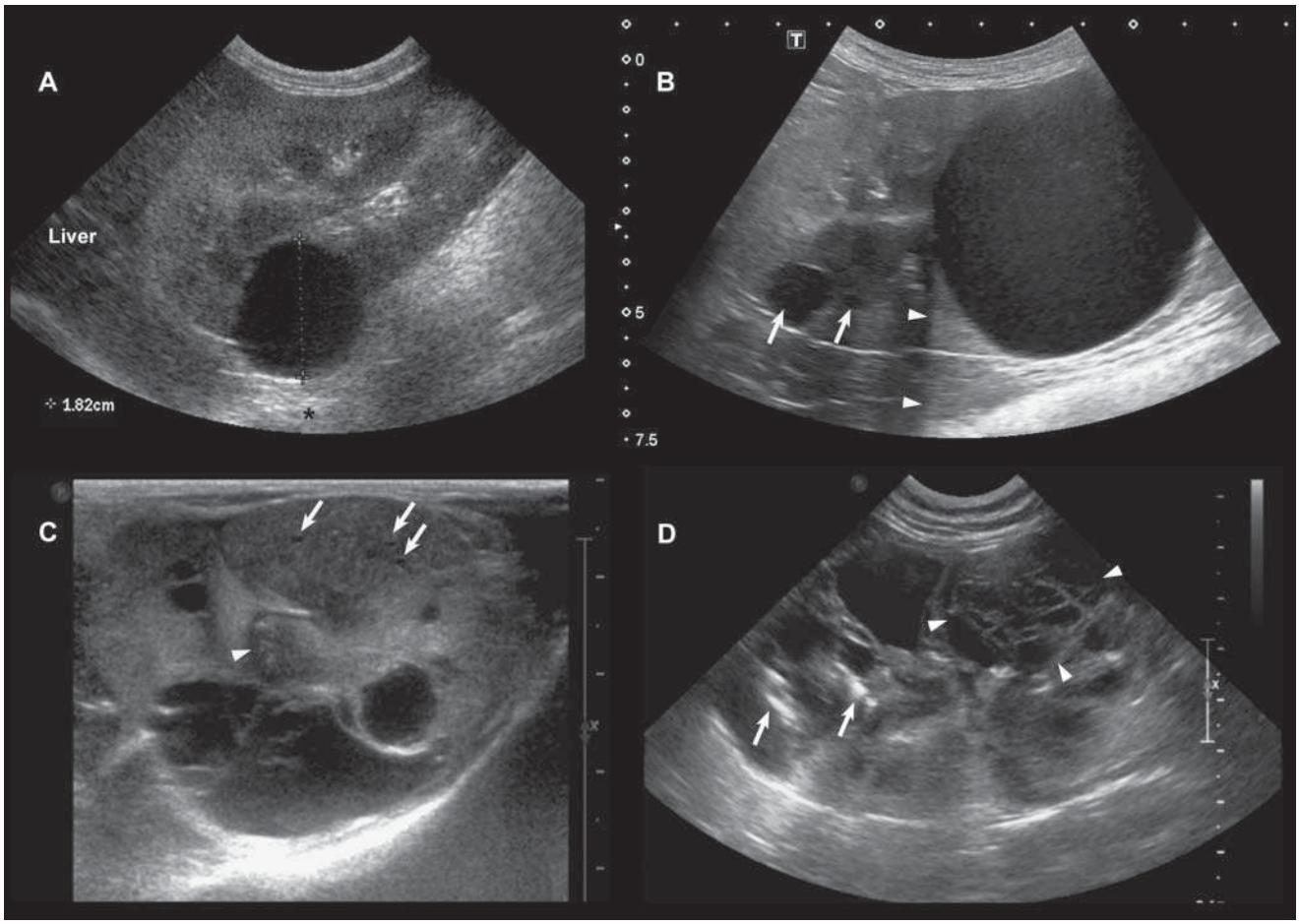


Figure 10.22. **Renal cysts and polycystic kidney disease in dogs and cats. A**: Longitudinal image of the right kidney in a dog with an incidental cortical cyst, which appears as a 1.8-cm, round, well-defined, anechoic structure, associated with distal acoustic enhancement (*). The renal cortex (delineated by arrowheads) is hyperechoic to the adjacent liver, although there was no clinical evidence of renal failure. **B**: In another dog, a 6-cm-wide cyst with smooth borders deforms the caudal pole of the left kidney, while small cysts (arrows) are also present cranially. Note the far acoustic enhancement artifact dorsal to the larger cyst (arrowheads). **C, D:** Transverse (**C**) and longitudinal (**D**) images of kidneys in two different cats with polycystic kidney disease. A large cyst **(C)** deforms the dorsal portion of the left kidney, while smaller cysts are present more ventrally (arrows). The arrowhead points to the pelvis. The renal parenchyma **(D)** is completely replaced by cysts of variable size and shape. Some of the cysts show a complex architecture (between arrowheads). Calcifications are also present (arrows).

debris or septas (Figure 10.22D), may mimic solitary solid or cavitary masses, abscesses, and hematomas (Figure 10.23). Renal abscesses can usually be differentiated from true cysts by the presence of echoes and sedimentation within the cavitary lesion and especially by a rather poorly demarcated and irregular contour. Distal enhancement may still be present if the cellular count remains relatively small. Infected renal cysts may resemble cysts with cellular debris or hemorrhage, requiring fine-needle aspiration for diagnosis (Figure 10.23A).

Solid masses or nodules are typically associated with static internal echoes that can be affected by gain settings and that are usually not associated with distal acoustic enhancement. Large solid masses can also appear cavitated because of necrosis. Renal cystadenocarcinomas have been reported in German shepherds and are usually associated with dermatofibrosis (Moe and Lium 1997). With ultrasonography, a fluid-filled cavity (or cavities) typically predominates, infiltrating the kidney, with a solid-tissue component that can protrude inside the cyst(s). Similar features can be encountered with renal cystadenoma, which was reported in a domestic shorthair cat as a large complex cystic structure occupying most of the renal parenchyma (Mosenco et al. 2008) (Figure 10.24).

Renal telangiectasia has been reported in Welsh corgis, and consists of cavernous masses filled with blood

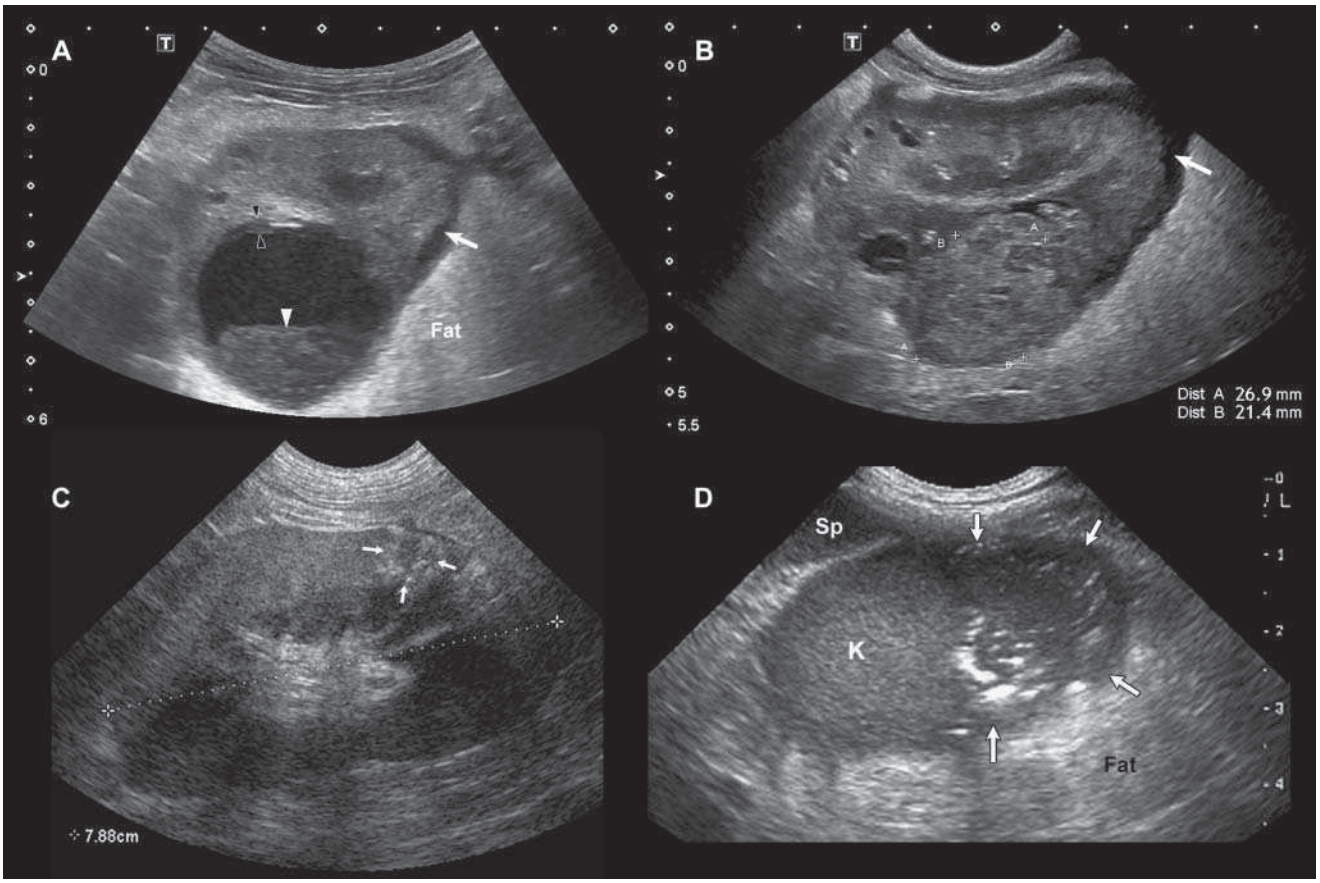


Figure 10.23. **Renal abscesses in three dogs. A, B:** Abscess in associated with chronic nephropathy. On initial examination **(A)**, a cavitary lesion with a hypoechoic wall (between black arrowheads) was identified in the craniodorsal portion of the left kidney. The lesion contained nearly anechoic fluid on top and cellular sediment on the bottom (white arrowhead). The retroperitoneal fat was hyperechoic, and subcapsular and perirenal effusion (arrow) was present. Following fine-needle aspiration under ultrasound guidance **(B)**, the abscess was drained, but hemorrhage developed, forming a clot that filled the cavity. Subcapsular and perirenal effusion was again present (arrow), and the kidney showed numerous cysts and reduced corticomedullary distinction. Presumably, one of the cysts became infected. Culture revealed *Escherichia coli*. **C:** Septic embolus and abscess formation. Longitudinal image of the left kidney in a Golden Retriever diagnosed with bacterial septicemia. An ill-defined hyperechoic rim-like focus (arrows), with a hypoechoic center, is at the level of the renal cortex. A septic exudate was aspirated with ultrasound guidance. **D:** Renal abscess caused by a wooden foreign-body perforation. A poorly echogenic cavity (arrows) with a few bright echoes (mixture of debris and gas) involves the caudal pole of the left kidney (K). The retroperitoneal fat is hyperechoic, and a small amount of fluid is noted in the near field, adjacent to the abscess, which was confirmed at surgery. S, spleen.

(Moore and Thornton 1983) that can mimic neoplasia (Figure 10.25).

Renal Solid-Mass Lesions

Solid-tissue proliferative diseases can appear as homogeneous or heterogeneous, hypoechoic, isoechoic or hyperechoic, regular or irregular lesions, with variably well-defined margins (Figures 10.21, 10.26–10.30). This variable ultrasonographic appearance is reflected by the cell type, as well as by the variable presence and distribution of vessels, tissue necrosis, fibrosis, mineralization, and hemorrhage. The renal internal architecture is variably altered depending on the size and invasiveness of the process. Nearby vascular invasion or thrombosis may also be present (Figure 10.31). Because of their variable characteristics, renal primary or metastatic neoplastic processes cannot be easily distinguished with ultrasonography. However, lymphoma and malignant histiocytosis (histiocytic sarcoma) tend to appear as hypoechoic nodules or masses (Figures 10.28, 10.29).

Other types of solitary neoplastic masses include adenocarcinomas, hemangiomas, nephroblastomas,

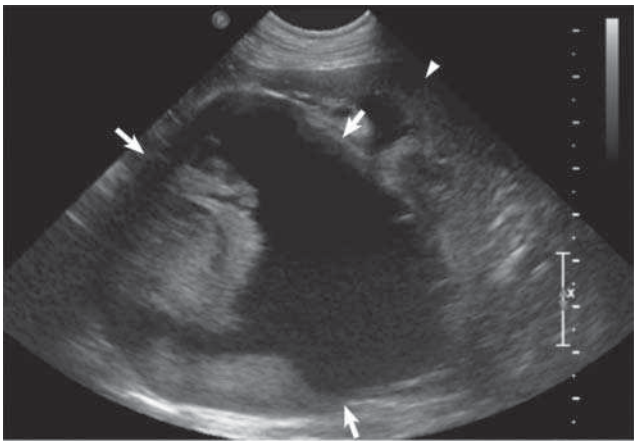


Figure 10.24. Cystadenoma in an 11-year-old Golden Retriever with no abdominal clinical signs. A very large, primarily cystic mass is deforming most of the cranial and central portions of the left kidney. The mass was surgically removed and was diagnosed as a cystadenoma.

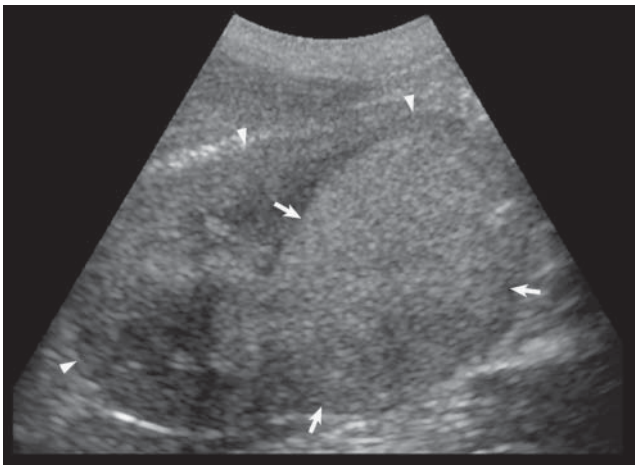


Figure 10.26. Renal adenocarcinoma. Longitudinal image of the left kidney (arrowheads) of a 6-year-old dog with chronic weight loss and anorexia. A relatively well-circumscribed hyperechoic mass (arrows) found in the caudal pole was confirmed to be a renal primary adenocarcinoma.

and several types of sarcomas, including hemangiosarcoma, as well as metastases (Gasser et al. 2003). These neoplastic processes can be well defined or ill-defined and can be associated with retroperitoneal hemorrhage or completely replace normal parenchymal architecture. The absence of an identifiable kidney in the region lateral to the origin of the renal vessels might be the only sign that can help in confidently suspecting a renal mass. Other imaging tests (excretory urography, computed tomography [CT], or magnetic resonance imaging [MRI]) can be required to confirm the origin of the mass and determine its extent for surgical planning.

Other less common solid processes, such as granulomas (fungal diseases), pyogranulomas (feline infectious peritonitis), or solid abscesses can appear similar to neoplastic processes (Figure 10.32). Hence, fine-needle aspiration or biopsy is required in most cases to achieve a precise diagnosis.

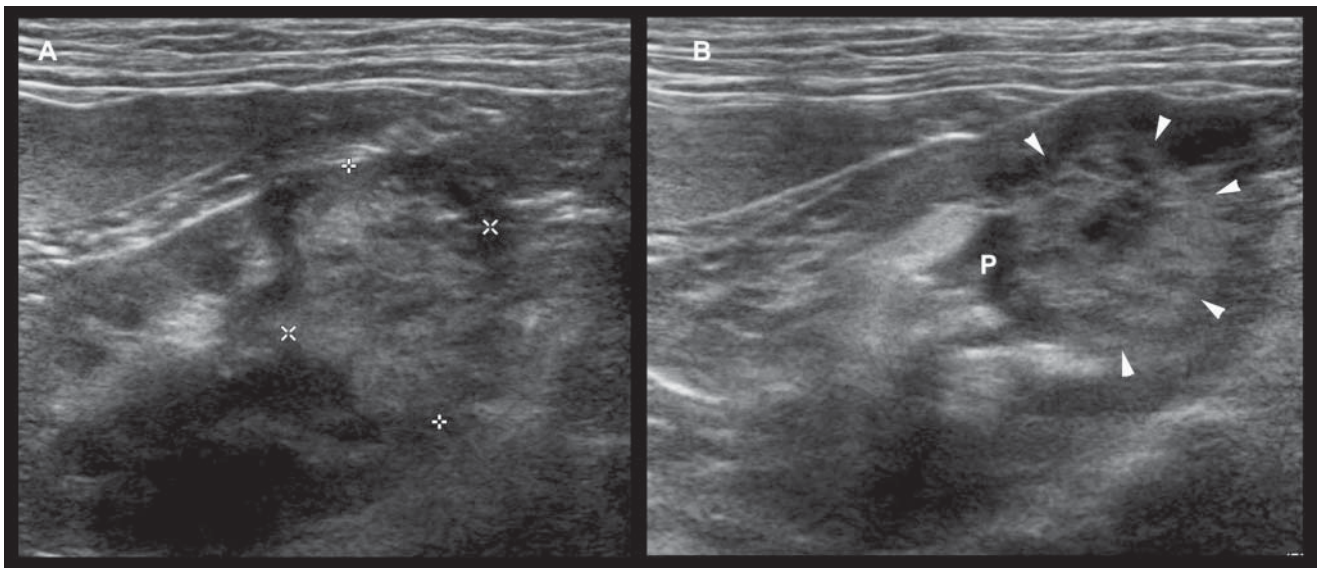


Figure 10.25. Telangiectasia in a 11-year-old Welsh Corgi presented for hematuria. An ill-defined primarily hyperechoic mass (2.1 × 1.8 cm, cursors) with numerous cystic changes is present in the central and caudal region of the left kidney. The kidney was removed surgically and the diagnosis was multifocal, coalescing telangiectasia.

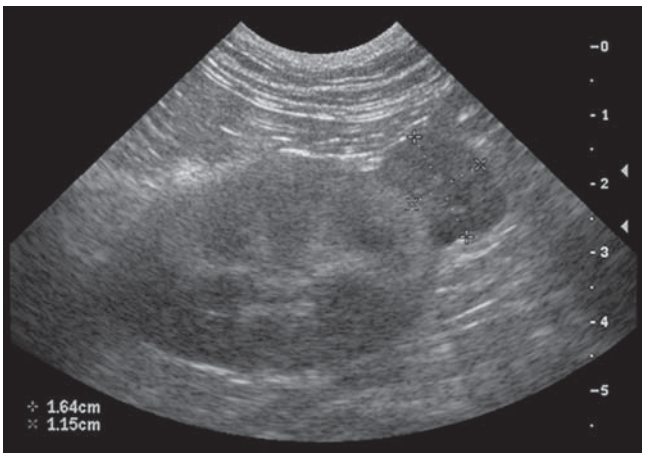


Figure 10.27. **Metastatic carcinoma.** Longitudinal image of the left kidney of a cat in which a pulmonary mass was identified on radiographs. Tumor staging revealed a paracortical hypoechoic nodule at the caudal renal pole. A metastatic focus of bronchoalveolar carcinoma was suspected on cytological examination.

Other Focal Lesions

Mineral foci are commonly identified in kidneys of older dogs and cats because of soft-tissue mineralization or urolithiasis (Figures 10.13, 10.33). The appearance of these hyperechoic foci and associated acoustic shadows depends on their size and differs between conventional and spatial compound imaging (Heng et al. 2012). With spatial compounding, the mineral foci are typically more echogenic and thus more conspicuous. However, the multi-angle compound image reduces the strength of acoustic shadowing, which may even disappear.

Renal infarcts can be identified as linear or wedged-shaped, well-defined hyperechoic lesions in the cortex, perpendicular to the capsule. Although their appearance can vary, chronic infarcts are typically hyperechoic and cause focal cortical depression or atrophy (Figure 10.34). These chronic infarcts may also be hyperattenuating, generating an acoustic shadow. Benign renal infarcts can also look similar to septic emboli, although these tend to be more heterogeneous in appearance (Figures 10.24A, 10.34D). Although extremely rare, gas foci can also be present within kidneys because of hematogenous or ascending infection (Figure 10.24B).

Disorders of the Collecting System

The renal pelvis and diverticuli are usually not distended in normal dogs and cats. Dilatation of the pelvis, also termed pyelectasia, is more easily recognized and more reliably measured on a transverse plane at the level of the renal hilus (Figure 10.35). It appears as an anechoic crescent at the medial margin of the renal crest (the deep portion of the medulla) (Figures 10.4B, 10.14, 10.15). Mild dilatation of the pelvic diverticuli can sometimes be difficult to differentiate from adjacent interlobar vessels without the use of color or power Doppler (Figure 10.35).

Pyelectasia can be observed in normal animals and those with increased diuresis (e.g., diuretic therapy or chronic renal insufficiency), congenital malformation (e.g., ureteral ectopia), pyelonephritis, lower urinary obstruction and neoplasia (d'Anjou et al. 2011) (Figures 10.4, 10.7, 10.10, 10.11, 10.14, 10.15, 10.36–10.38). The ureter can also be seen in some

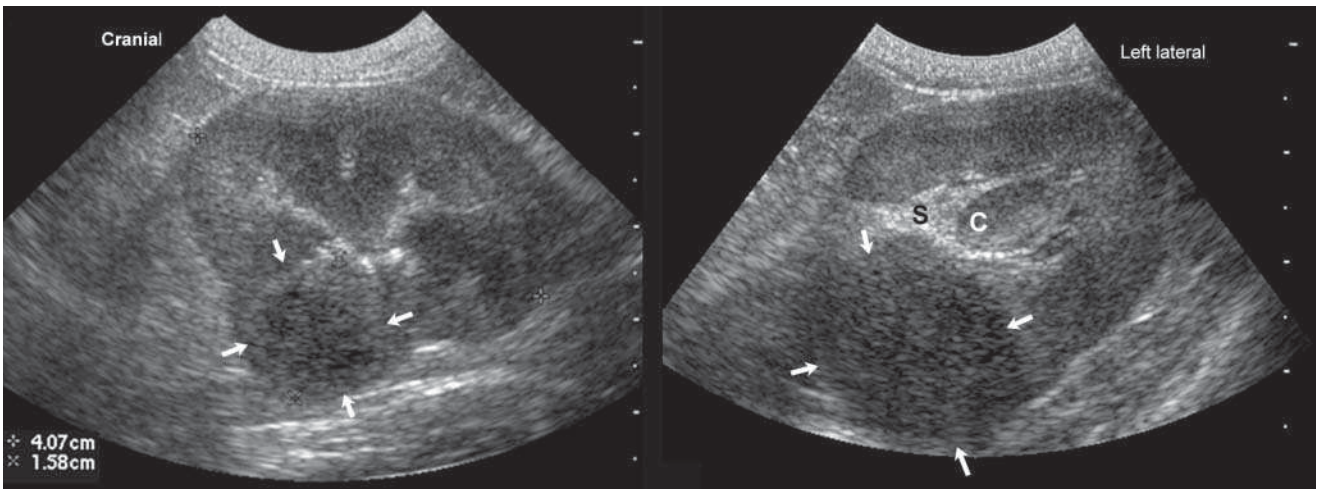


Figure 10.28. **Solitary nodule.** Longitudinal **(left)** and transverse **(right)** images of the left kidney in a Lhasa Apso with multicentric lymphoma. A hypoechoic nodule (arrows) is in the renal cortex, adjacent to the renal sinus (S) and crest (C).

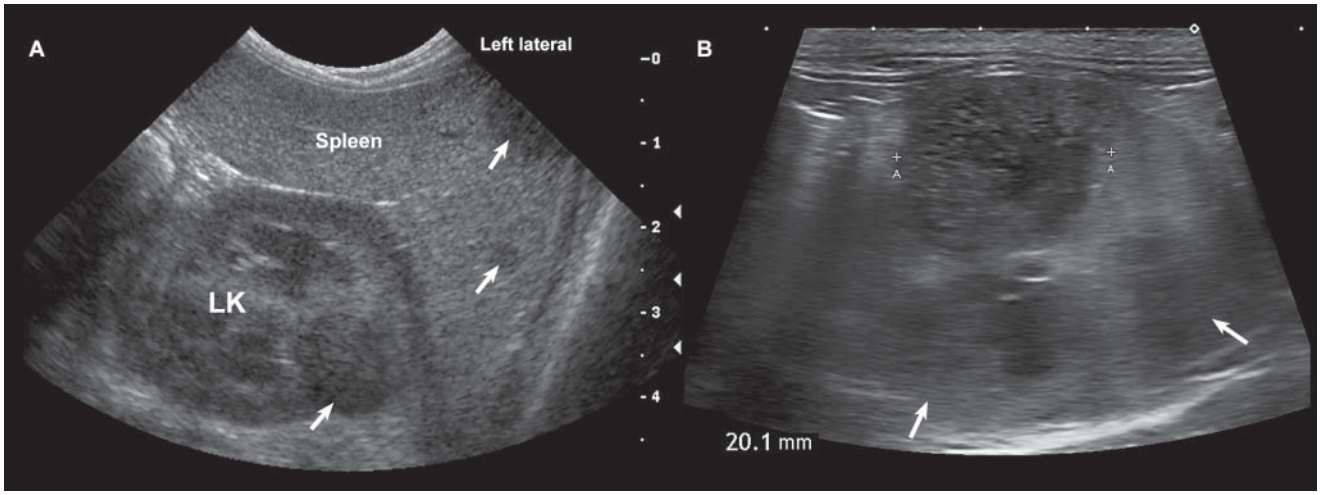


Figure 10.29. **Disseminated histiocytic sarcoma. A**: Transverse image of the left kidney (LK) in a medium-sized dog. A hypoechoic nodule (arrows) involves the renal cortex, deforming its contour. This nodule was not associated with far acoustic enhancement. Similar nodules of variable size were also detected in the liver and spleen (other arrows). **B**: In this Bernese Mountain Dog, both kidneys were filled with hypoechoic nodules of variable size. This image of the left kidney shows a 2-cm well-defined hypoechoic nodule with small hyperechoic dots (between cursors) and ill-defined hypoechoic foci (arrows). Tumors of round-cell origin should be considered when these lesions are found. Disseminated histiocytic sarcoma (malignant histiocytosis) was identified in both dogs.

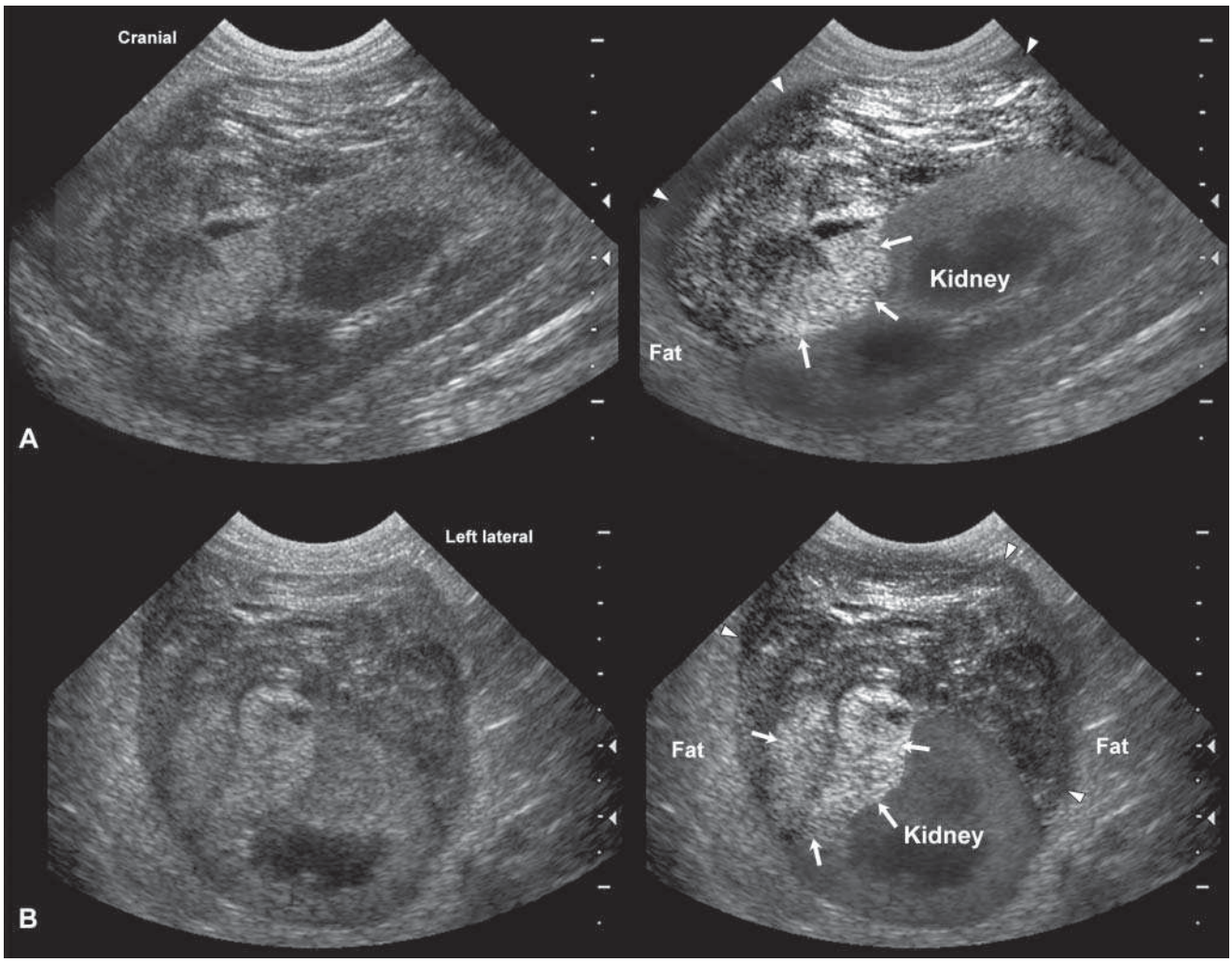


Figure 10.30. **Renal hemangiosarcoma and retroperitoneal hemorrhage.** Longitudinal **(A)** and transverse **(B)** ultrasonographic and enhanced images of the left kidney in a large dog with suspected intra-abdominal hemorrhage. A large, ill-defined and heterogeneous mass encircles the ventral aspect of the left kidney (arrowheads). The most ventral component of this mass appears lamellate, consistent with hemorrhage. A smaller portion of this retroperitoneal mass appears more solid, uniform and hyperechoic (arrows), and appears to invade the renal cortex, consistent with a primary renal hemangiosarcoma.

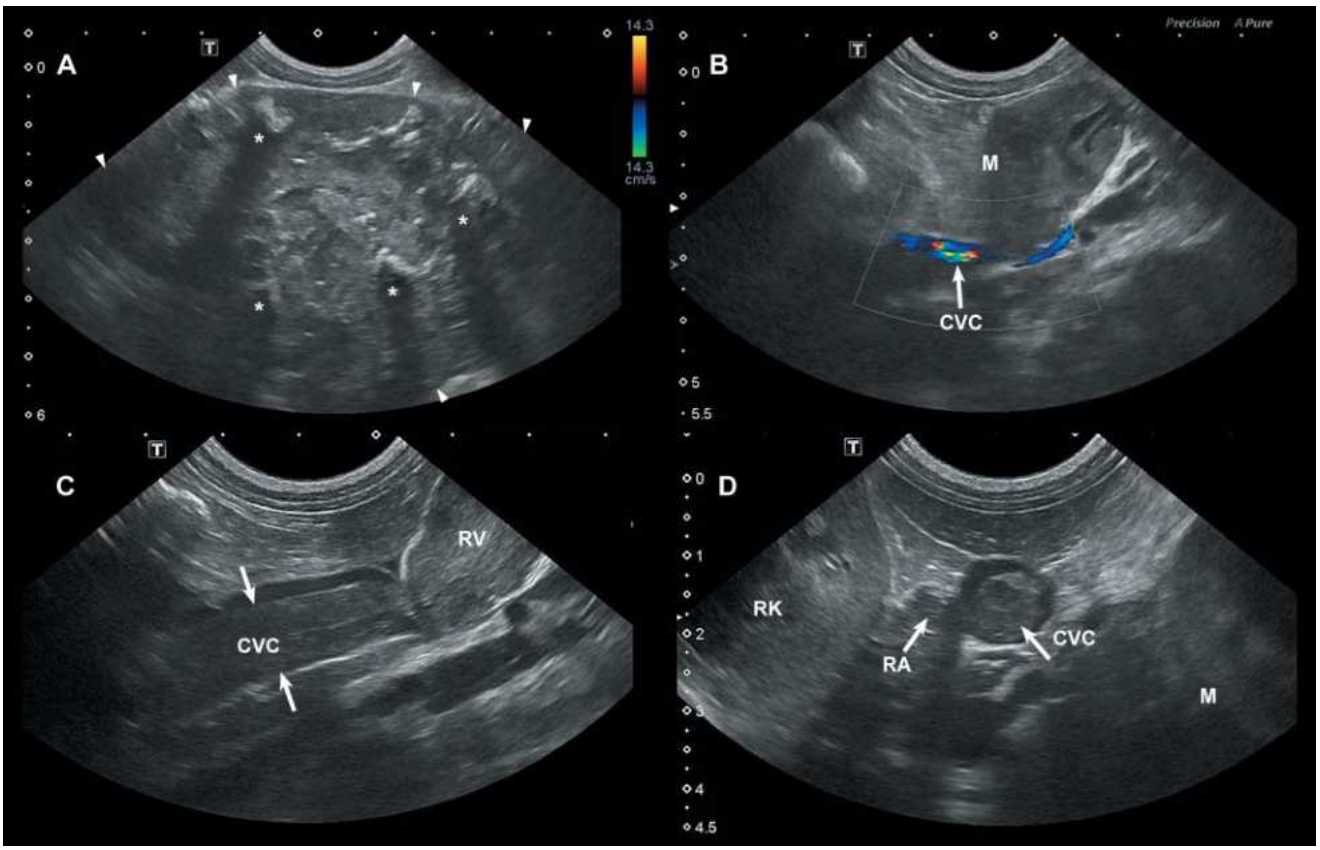


Figure 10.31. **Undifferentiated sarcoma invading the left kidney with venous thrombosis in a dog. A**: The large mass (arrowheads) is moderately echogenic and heterogeneous and shows several mineral foci casting shadows (*). It compresses the caudal vena cava (CVC in **B**) and is associated with massive thrombosis that begins in the left renal vein (RV) to extend into the CVC cranially (in **C**). The thrombus fills more than 75% of the CVC lumen (in **D**). Mild peritoneal and retroperitoneal effusions were also present. M, mass; RA, right adrenal gland; RK, right kidney.

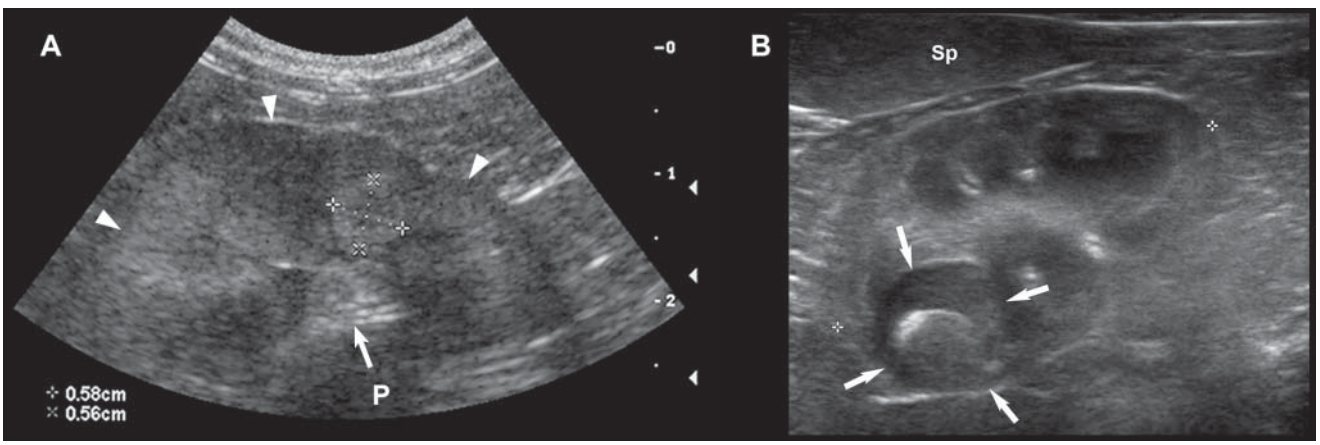


Figure 10.32. **Non-neoplastic solid lesions. A**: Longitudinal image of the left kidney of a cat with clinically suspected infectious peritonitis. The renal architecture and contour (arrowheads) are markedly deformed, and the renal parenchyma is heterogeneous. A 0.6-cm hyperechoic nodule (cursors) is in the medulla, adjacent to the renal pelvis (P). Pyogranulomatous nephritis was diagnosed by fine-needle aspiration. **B**: Longitudinal sonogram of the left kidney of a 9-year-old Pekinese cross presented for vomiting and heart murmur. A 1.35-cm inhomogeneous non-vascularized nodular lesion is present in the cranial pole of the kidney. Fine-needle aspiration was performed and only necrotic tissue was seen. Follow-up examinations (more than 6 months) showed partial regression of the lesion and a remodeled echogenicity (not shown). It was assumed that this lesion represented an old hematoma or granuloma.

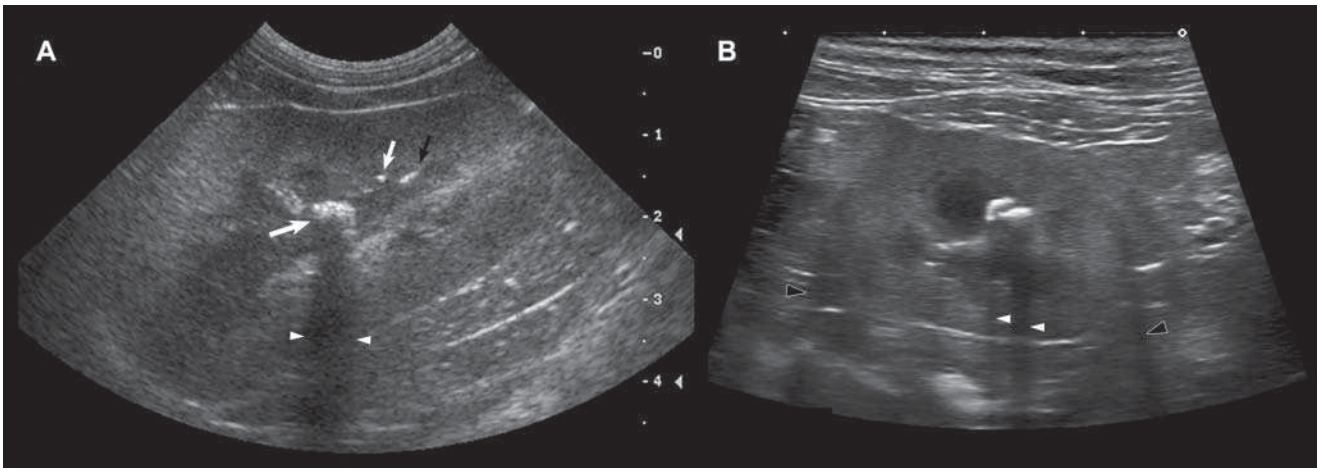


Figure 10.33. **Renal mineralization. A**: Longitudinal image of the left kidney of a clinically normal dog. Several foci of mineralization (arrows) are in the region of the collecting system, the largest being associated with acoustic shadowing (arrowheads). These mineral foci may represent nephroliths and/or dystrophic mineralization. **B:** In this spatial compounding sonographic image, two prominent mineral foci are detected in the kidney of this cat. Note the acoustic shadows distal to the mineralization (white arrowheads) and distal to the edges of the kidney (black arrowheads), which is otherwise normal. There was no evidence of pyelectasia.

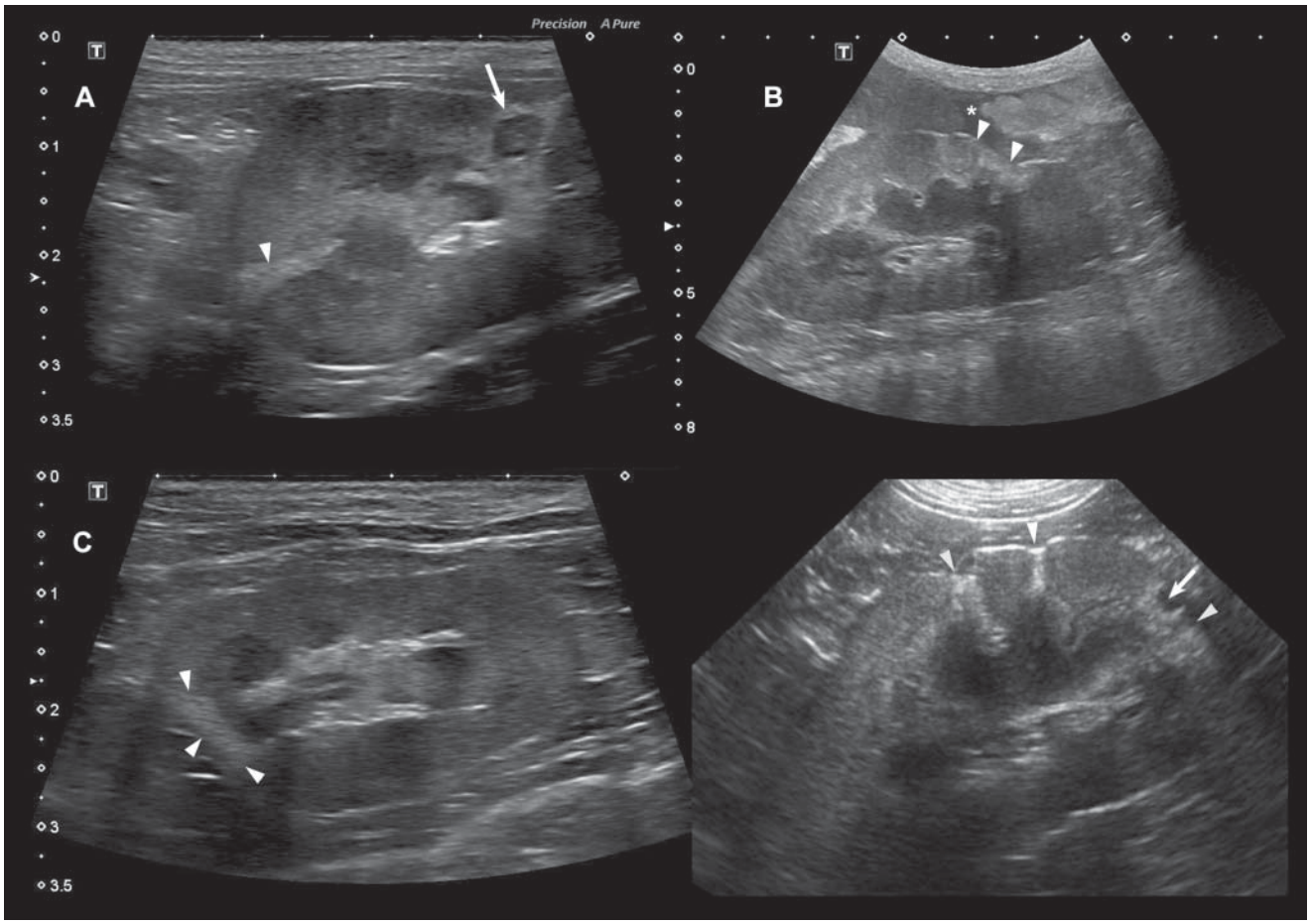


Figure 10.34. **Cortical infarction. A**: In this longitudinal sonographic image centered on the cranial pole of the left kidney of a cat with renal insufficiency, there is evidence of a triangular-shaped hyperechoic focus in the cortex of the cranial pole (arrowhead), consistent with an infarct. A small cavitary focus was also present in the central portion of another infarct (arrow), for which fine-needle aspiration revealed necrotic tissue without inflammation, evidence of renal dysfunction. **B**: In this dog with hemoabdomen (*), a hyperechoic depression (arrowheads), indicating chronic infarction, is present at the caudal margin of the left renal cortex. **C:** In another 8-year-old cat with normal renal function, the infarcted cortex is hyperechoic and reduced in size (arrowheads), resulting in flattening of the cranial renal pole. **D**: Extensive embolic infarction in a 11-year-old Labrador presented for lethargy and thrombocytopenia. Hyperechoic, triangular areas associated with cortical indentation are present (arrowheads) some of which with a hypoechoic focus (arrow) consistent with septic embolism.

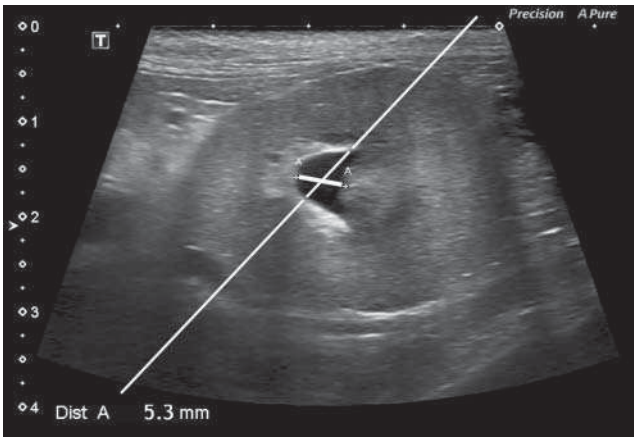


Figure 10.35. Renal pelvis measurement. The renal pelvis can be more accurately detected and measured in the transverse plane, ensuring that the height of the pelvis is measured perpendicularly (between cursors). Measurements obtained in the longitudinal plane may overestimate its size, depending on the angle of the transducer relative to the kidney (such as along the white line).

Table 10.1
Differential diagnosis of pyelectasia and hydronephrosis in small animals

Pyelectasia	Hydronephrosis
Intravenous fluid therapy	Pelvic or ureteral obstruction caused by calculus, infiltrative mass at bladder trigone, ureter or renal pelvis, stricture, cellular debris (e.g., blood clot), or retroperitoneal mass
Diuretic therapy	
Increased diuresis caused by renal insufficiency or other condition	
Pyelonephritis and ureteritis	
Distended bladder	
Ectopic ureter or another congenital malformation	Lower urinary tract obstruction
	Congenital malformation

of these patients and be most easily identified on transverse planes at the level of the hilus, central to the renal vessels. Table 10.1 lists causes of pyelectasia and hydronephrosis in dogs and cats.

When pyelectasia is more pronounced or if hydronephrosis develops because of urinary flow obstruction, renal diverticuli appear as rounded, anechoic finger-like projections that connect with the renal pelvis (Figures 10.39, 10.41, 10.43–10.45). Markedly dilated diverticuli and pelvis must be differentiated from renal cysts or sections of the medulla. The presence of protein or cells (pus or hemorrhage) may increase the urine echogenicity and even be associated with sedimentation, such as is sometimes seen in cases of pyelonephritis (Figures 10.37).

Pyelonephritis is generally associated with pyelectasia (Figures 10.36–10.40), although the renal pelvis

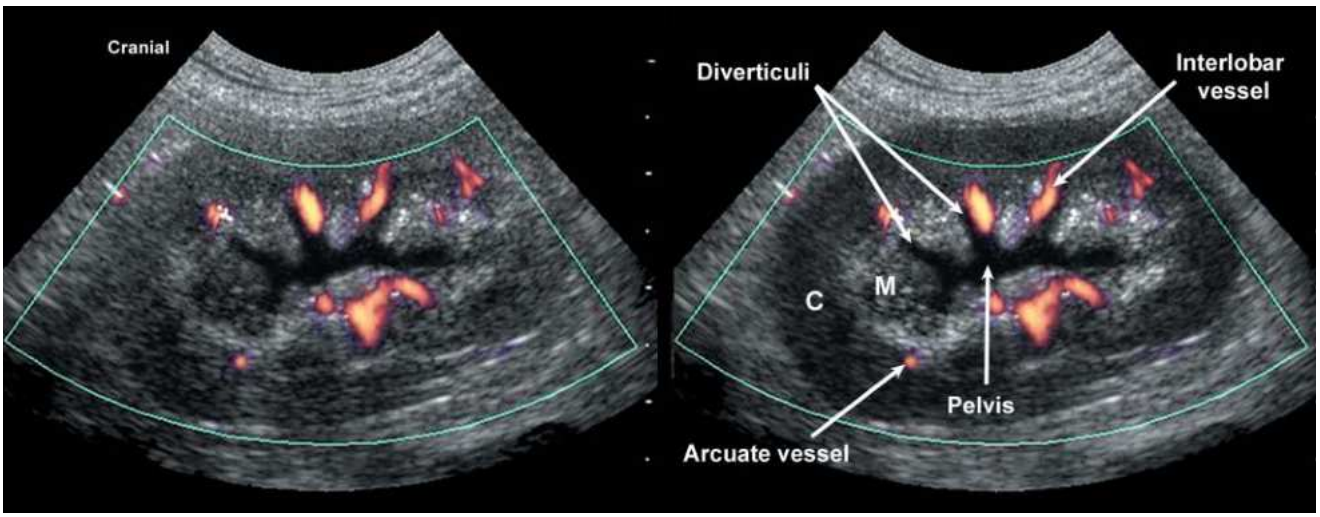


Figure 10.36. Dilated diverticuli in a cat with chronic pyelonephritis. Sagittal ultrasonographic and schematic images of the left kidney. The renal pelvis is distended, as well as the diverticuli, which appear distinct from the interlobar vessels on power Doppler. The medulla (M) is hyperechoic to the cortex (C) because of nephrocalcinosis.

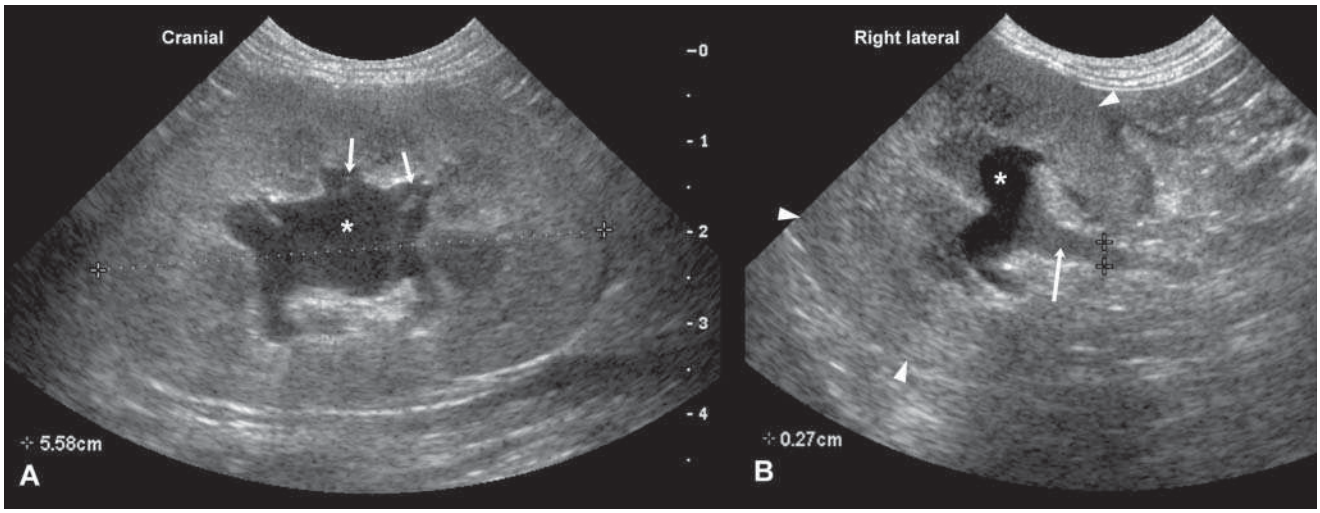


Figure 10.37. Dilated pelvis and ureter in a cat with pyelonephritis. Longitudinal **(A)** and transverse **(B)** ultrasonographic images of the right kidney of a small-breed dog with acute renal failure and abdominal pain. The kidney (arrowheads) is enlarged and hyperechoic, and the corticomedullary distinction is attenuated. The renal pelvis (*) and diverticuli (short arrows) are moderately dilated. The proximal ureter is also mildly dilated and contains highly echogenic urine (long arrow), consistent with pus. These signs were caused by ascending urinary infection that probably resulted in some level of obstruction increasing the size of the pelvis. Note the sharp, oblique line of cellular sediment in the pelvis on the transverse view, which was parallel to the exam table.

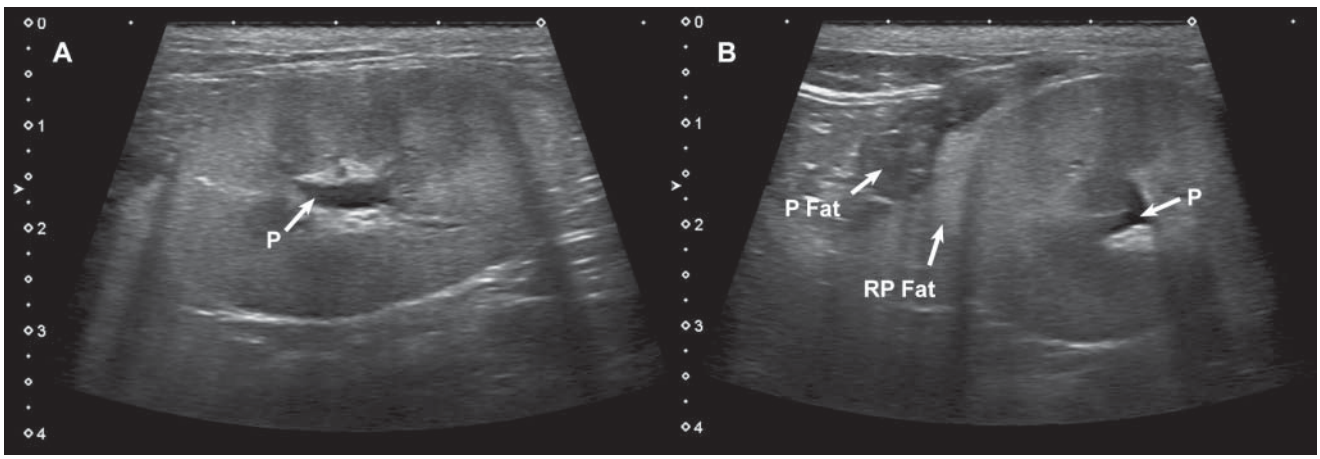


Figure 10.38. Acute pyelonephritis in a cat. Longitudinal **(A)** and transverse **(B)** sonographic images of the right kidney of a domestic shorthair cat with acute renal failure and abdominal pain. The renal pelvis (P) is mildly dilated (2 mm in height) and the retroperitoneal (RP) fat is hyperechoic when compared with the adjacent peritonal (P) fat.

may remain normal in mild or early pyelonephriti (Neuwirth et al. 1993).With chronic pyelonephritis, in addition to parenchymal changes, the pelvis and diverticuli can become distorted and show a hyperechoic rim because of fibrous tissue remodeling (Figures 10.39, 10.40).

As opposed to pyelectasia, the term hydronephrosis is used when obstruction is present, such as that caused by the migration of a nephrolith or by an infiltrating process involving the pelvis, the ureter, or, more commonly, the ureterovesicular junction. A pelvic height ≥13mm measured on a transverse image is predictive of outflow obstruction caused by one of these conditions (d'Anjou et al. 2011). However, pelvic dilatation is not a sensitive sign of obstruction, as pelvic height can remain at ≤2 mm with partial obstruction (Figure 10.42). In cases of chronic obstruction, progressive distension of the renal pelvis and diverticuli can cause marked parenchymal atrophy (Figures 10.43–10.45). The presence of moderately echogenic content dispersed or filling the pelvis, or generating a fluid-debris level responding

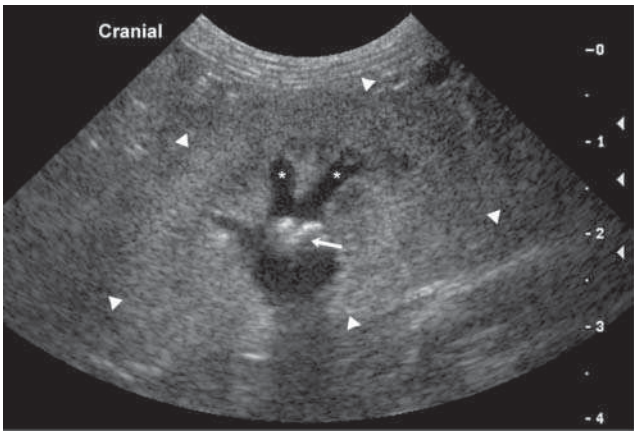


Figure 10.39. Chronic pyelonephritis and nephroliths. Longitudinal image of the left kidney of a cat with renal failure and abdominal pain. The kidney (outlined by arrowheads) is hyperechoic and irregular, and its pelvis anddiverticuli (*) are distended and deformed, appearing as hypoechoic finger-like projections. Irregular hyperechoic and hyperattenuating foci (arrow) are in the center of the pelvis, consistent with small nephroliths. The corticomedullary junction is indistinct. These signs were caused by chronic pyelonephritis in association with urolithiasis.

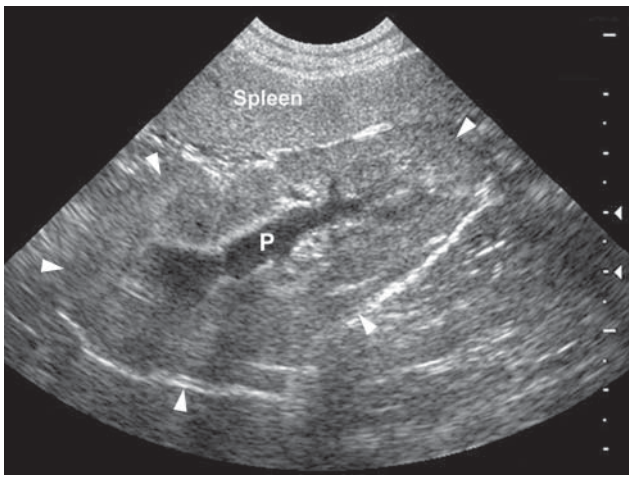


Figure 10.40. Severe chronic pyelonephritis. Longitudinal image of the left kidney in a large-breed dog with chronic renal insufficiency and recurrent cystitis. The kidney is markedly irregular (arrowheads) and diffusely hyperechoic, appearing isoechoic to the spleen. The hypoechoic pelvis (P) is moderately distended and irregular, and its contour is hyperechoic.

to gravity, should be considered as a strong indicator of pyonephrosis (Choi et al. 2010). Pyonephrosis represents a consequence of obstructive pyelonephritis, or outflow obstruction with secondary ascending infection (Figure 10.46).

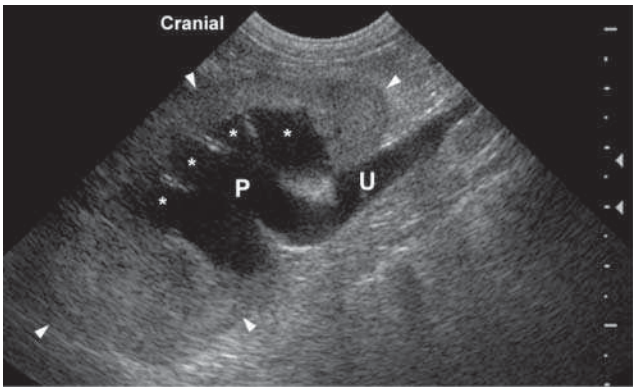


Figure 10.41. Obstructive hydronephrosis. Longitudinal image of the right kidney (arrowheads) in a dog with ureteral obstruction caused by a ureterolith. The distended pelvic diverticuli (*) are rounded and partially separated by hyperechoic septa that contain interlobar arteries and veins. The distended proximal ureter (U) is also apparent, communicating with the pelvis (P).

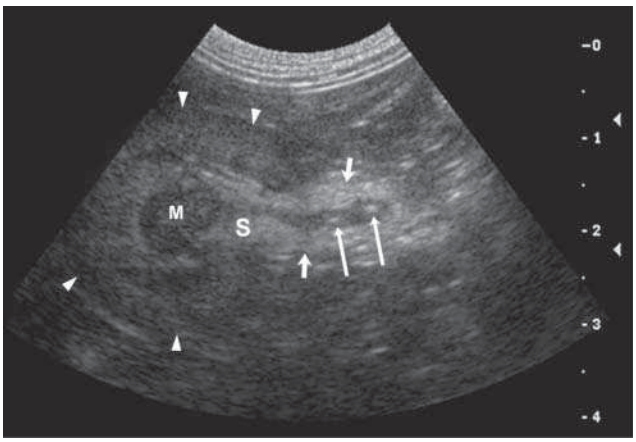


Figure 10.42. Non-obstructive uroliths in a cat. Transverse image obtained at the level of the right renal hilus of a cat with abdominal pain. Two small hyperechoic foci in the center of the ureter (long arrows) are associated with peripheral fat hyperechogenicity (short arrows), suggesting ureteritis. There is no evidence of ureteral outflow obstruction. On the follow-up exam, these small uroliths were found in the urinary bladder. M, medulla; S, sinus.

Ureteral distension, also termed hydroureter, is usually observed in combination with hydronephrosis in cases of urine outflow obstruction. Distended ureters, which can become markedly enlarged and tortuous with long-standing obstructions, can usually be followed caudally to the level of the obstruction. Color or Power Doppler can be useful in differentiating an abdominal vessel from a distended ureter (Figure 10.47). Migrated uroliths appear as hyperechoic structures that are usually associated with

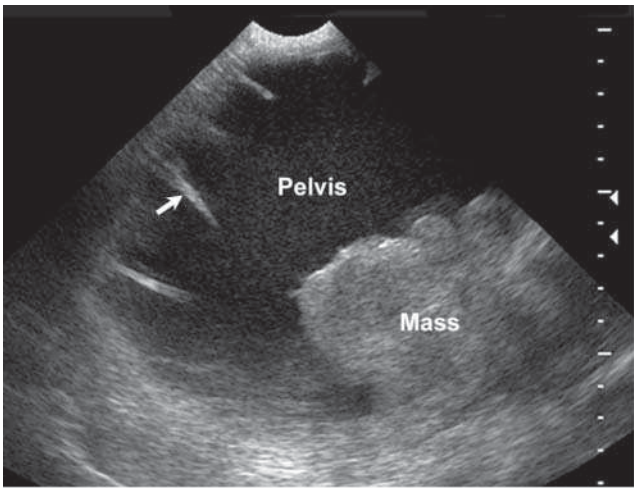


Figure 10.43. **Severe hydronephrosis.** Longitudinal image of the left kidney in a dog with severe renomegaly diagnosed on radiographs. The kidney appears as a fluid-filled cavity with peripheral hyperechoic bands consistent with interdiverticular septa (arrow). A large, irregular, hyperechoic mass at the level of the renal hilus is invading the renal pelvis and ureter and causing the hydronephrosis. Surgical resection confirmed the presence of a soft-tissue sarcoma.

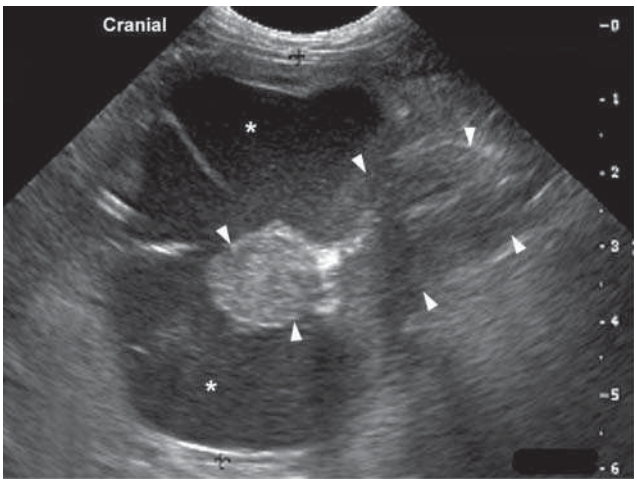


Figure 10.44. **Hemangiosarcoma in a Dachshund.** The mass (arrowheads) is centered on the pelvis and is responsible for the severe hydronephrosis affecting the right kidney. The renal diverticuli are markedly dilated (*) and contain echogenic fluid, particularly in the dependent portion, consistent with hemorrhage.

acoustic shadowing (Figure 10.48). With complete obstruction, the ureter appears dilated cranially and abruptly blunted caudally at the level of the urolith. Several migrating uroliths may be present, justifying a detailed examination of the entire region of each ureter, up to the level of the bladder. The identification

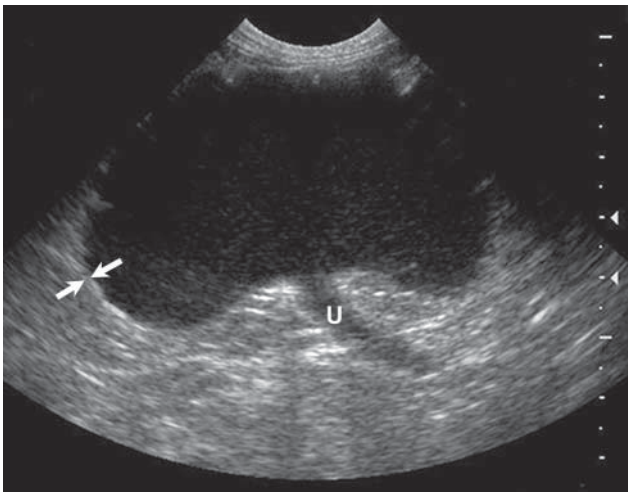


Figure 10.45. **Severe hydronephrosis.** Longitudinal image of the left kidney in a cat with severe renomegaly. The kidney is completely replaced by hypoechoic fluid, with a rim of parenchyma remaining that is only a few millimeters thick (arrows). Hydroureter is also identified (U). Inadvertent ligation of the distal ureter, secondary to a previous ovariohysterectomy, was identified during exploratory surgery.

of small uroliths can be limited by the presence of overlying gastrointestinal structures, such as the descending colon, or by the lack of significant ureteral distension (Kyles et al. 2005) (Figure 10.49). Color or power Doppler may also confirm the presence or absence of a ureteral jet (Figure 10.50). When combining radiography and ultrasonography, the sensitivity to detect urolithiasis in cats has been reported to reach 90% (Kyles et al. 2005).

Although transitional cell carcinomas infiltrating the bladder trigone and/or ureter are more commonly responsible for ureteral obstruction (Figure 10.51), especially in dogs, other processes such as lymphoma, retroperitoneal soft-tissue sarcomas, abscesses, or granulomas can also compress and/or infiltrate the ureter (Figure 10.52). Ureteral fibroepithelial polyps have also been reported in dogs as intraluminal, pedunculated masses causing ureteral obstruction and hydronephrosis (Reichle et al. 2003) (Figure 10.53).

Ureteral obstruction can also be caused by a blood clot or an inflammatory stricture, which can be more challenging to diagnose and differentiate. Other imaging tests, such as excretory urography, which can be combined with CT, can be required in patients in which a clear diagnosis cannot be made by using ultrasonography.

Unilateral or bilateral congenital ectopic ureters, which are more common in female dogs, can sometimes be identified and followed to their termination

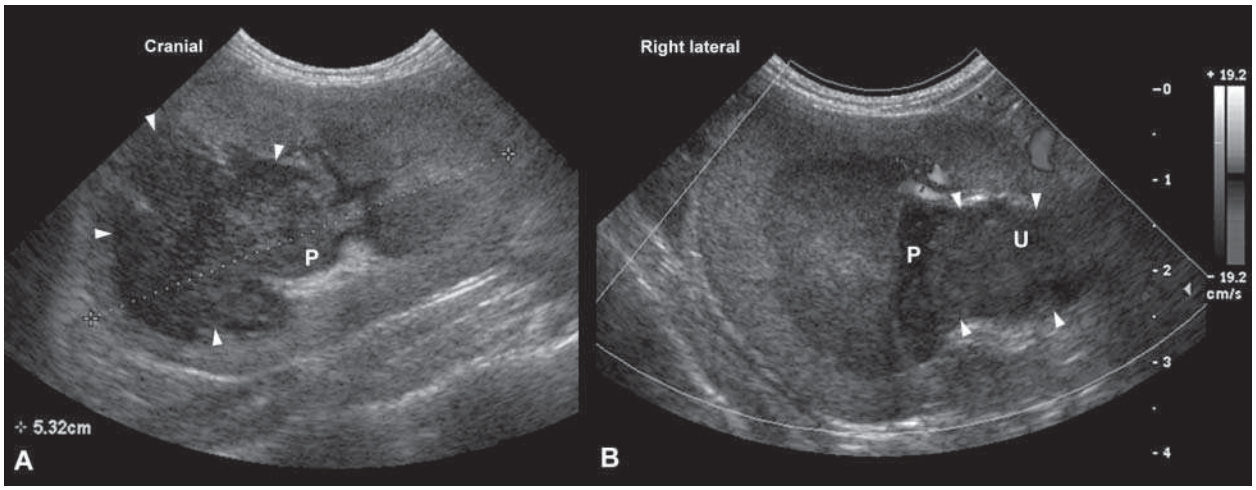


Figure 10.46. **Pyonephrosis and ureteral abscess.** Longitudinal **(A)** and transverse **(B)** images of the right kidney of a dog with fever and abdominal pain. The renal pelvis (P) and diverticuli are asymmetrically dilated in the cranial pole of the kidney (arrows). The proximal portion of the ureter (U) is also distended. These portions of the collecting system contain echogenic material diagnosed as pus by means of ultrasound-guided pyelocentesis.

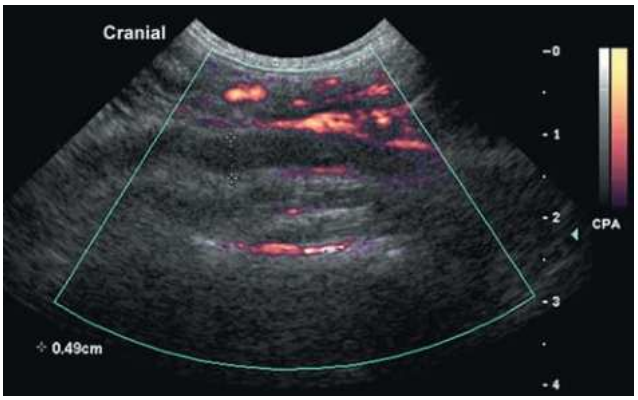


Figure 10.47. **Hydroureter.** Longitudinal image obtained with power Doppler in the left mid-abdomen of a young female dog with urinary incontinence. A 0.5-cm-wide hypoechoic tubular structure can be seen coursing from the renal pelvis to the caudal abdomen, consistent with a dilated ureter. No flow is present. This ureter terminated in the vagina rather than in the urinary bladder, indicating ectopia.

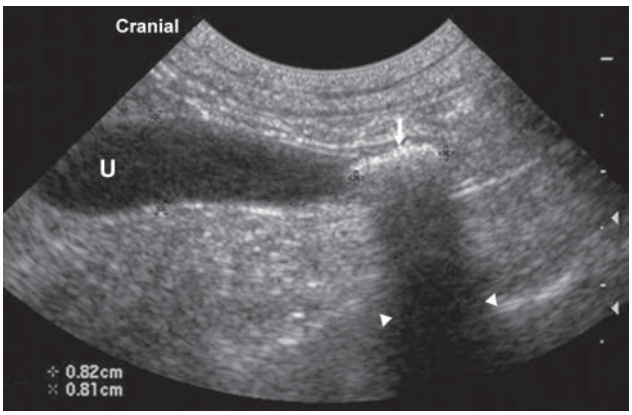


Figure 10.48. **Hydroureter.** Longitudinal image obtained along the mid-portion of the right ureter (U) in a dog with hydronephrosis. An ovoid 0.8-cm-wide hyperechoic structure (arrow) found in the lumen of the ureter is associated with a strong acoustic shadow (arrowheads), with proximal luminal dilatation, indicating an obstructive urolith.

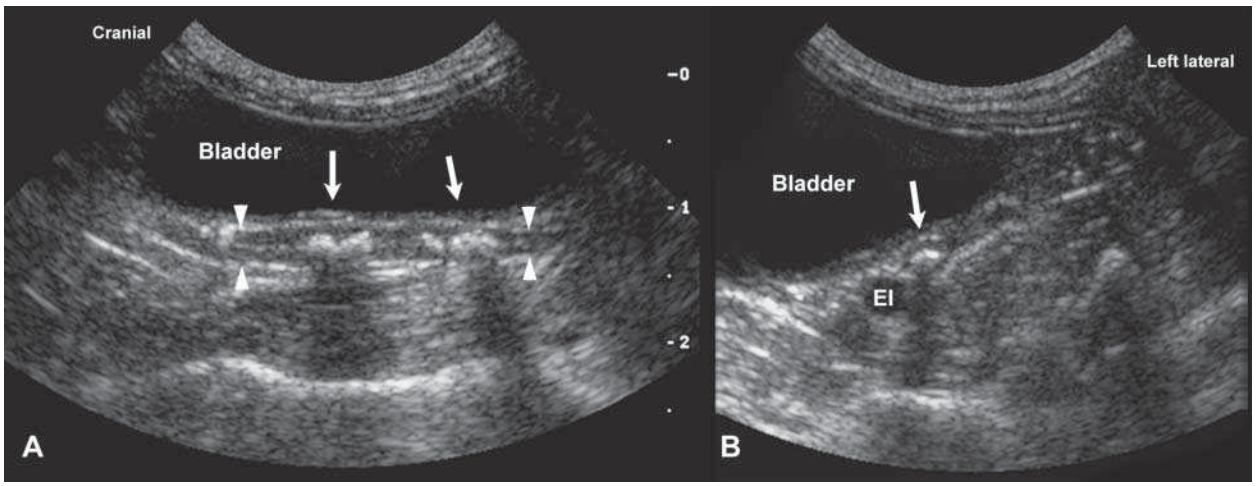


Figure 10.49. **Non-obstructive uroliths in a cat.** Longitudinal **(A)** and transverse **(B)** images of the distal right ureter of a cat with a chronic history of urolithiasis. Several hyperechoic foci (arrows) are found in the ureter (arrowheads) of this cat without evidence of hydroureter or hydronephrosis. Acoustic shadows are noted in the far field. Some of these calculi were eventually found in the bladder. The ureteral wall is mildly thickened due to edema and/or inflammation. EI, external iliac vessel.

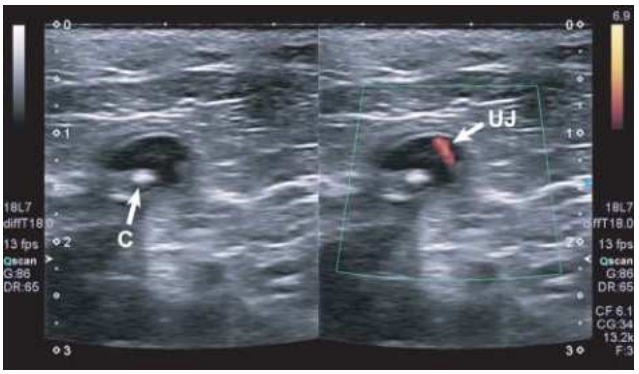


Figure 10.50. **Urolith in distal ureter.** Transverse B-mode (**left**) and power Doppler (**right**) sonographic images obtained at the bladder trigone of a cat with right-sided hydronephrosis. A hyperechoic structure consistent with a calculus (C) is lodged in the distal portion of the right ureter. Urine jet (UJ) is only visible from the left ureter.

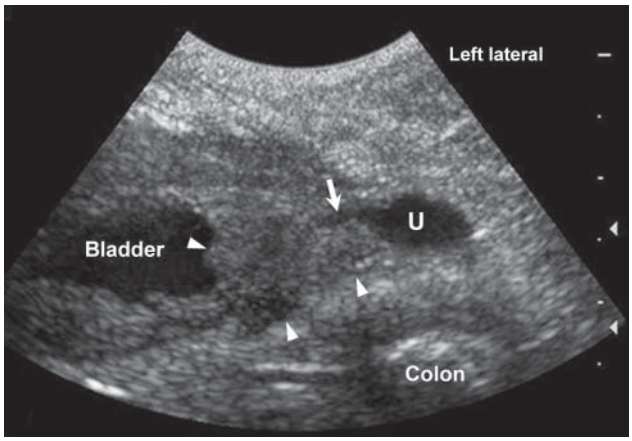


Figure 10.51. **Infiltrative bladder mass and hydroureter.** Transverse image obtained at the level of the neck of the urinary bladder in a female dog with chronic hematuria. An irregular and poorly defined transmural mass involves the region of the right ureterovesicular junction (arrowheads). The distal portion of the right ureter is dilated (U) by the stenosis (arrow).

site (the urethra, most commonly, or the vagina or the colon) (Figure 10.54). These ureters are often distended because of partial obstruction at the site of termination or intramural tunneling, ileus, and/or ascending infection (Figure 10.55). Hydronephrosis can also be present, especially when there is marked hydroureter. With B-mode or with color or power Doppler ultrasonography, an intravesical urine jet can sometimes be observed adjacent to the ureterovesical junction (Lamb and Gregory 1998). The visualization of this ureteral jet can be facilitated by administering a diuretic after withholding water for several hours. A jet of diluted urine can be more easily observed within a bladder

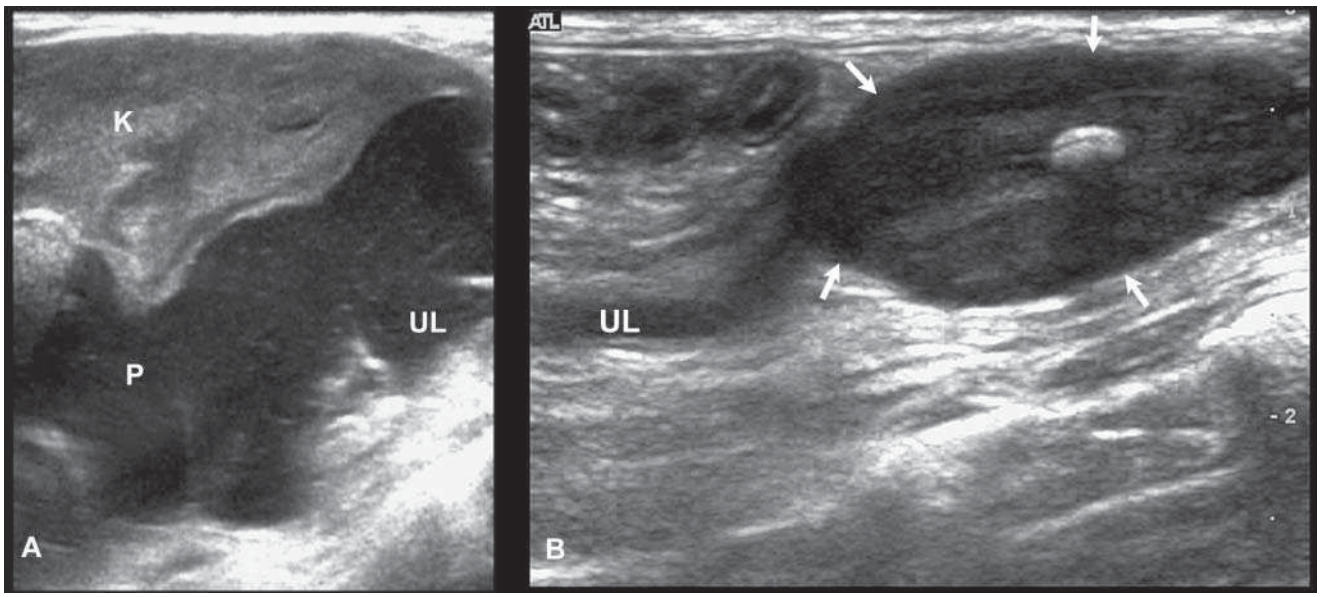


Figure 10.52. **Infiltrative ureteral lymphoma.** Longitudinal images obtained at the level of the right kidney **(A)** and mid-right ureter **(B)** in a cat. The kidney (K) is deformed, and the corticomedullary distinction is significantly reduced. The renal pelvis (P) and proximal ureter (UL) are dilated. An oval, hypoechoic, uniform mass (arrows) is found at the level of the right ureter. The ureteral lumen (UL) is dilated cranially. Incidentally, a 3-mm hyperechoic urolith was lodged in the lumen of the infiltrated ureter. Histopathology revealed the presence of an unusual lymphoma infiltrating the kidney and ureter.

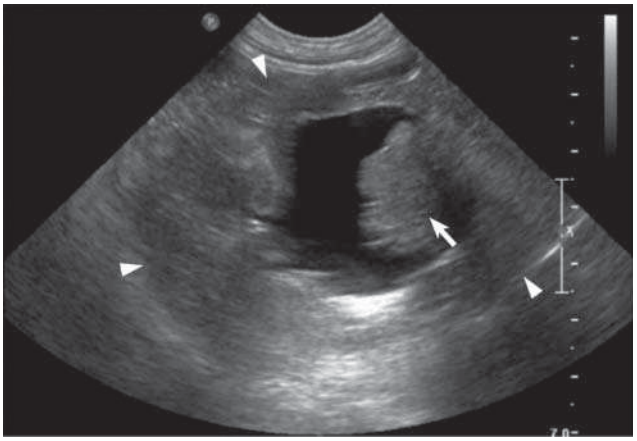


Figure 10.53. Fibroepithelial polyp in a dog. Longitudinal image of the right kidney of a Scottish Terrier presented for vomiting (jejunal obstruction). The right kidney is deformed by a lobulated mass associated with marked pelvic dilation. The right kidney was surgically removed and diagnosed as fibroepithelial polyp with hydronephrosis.

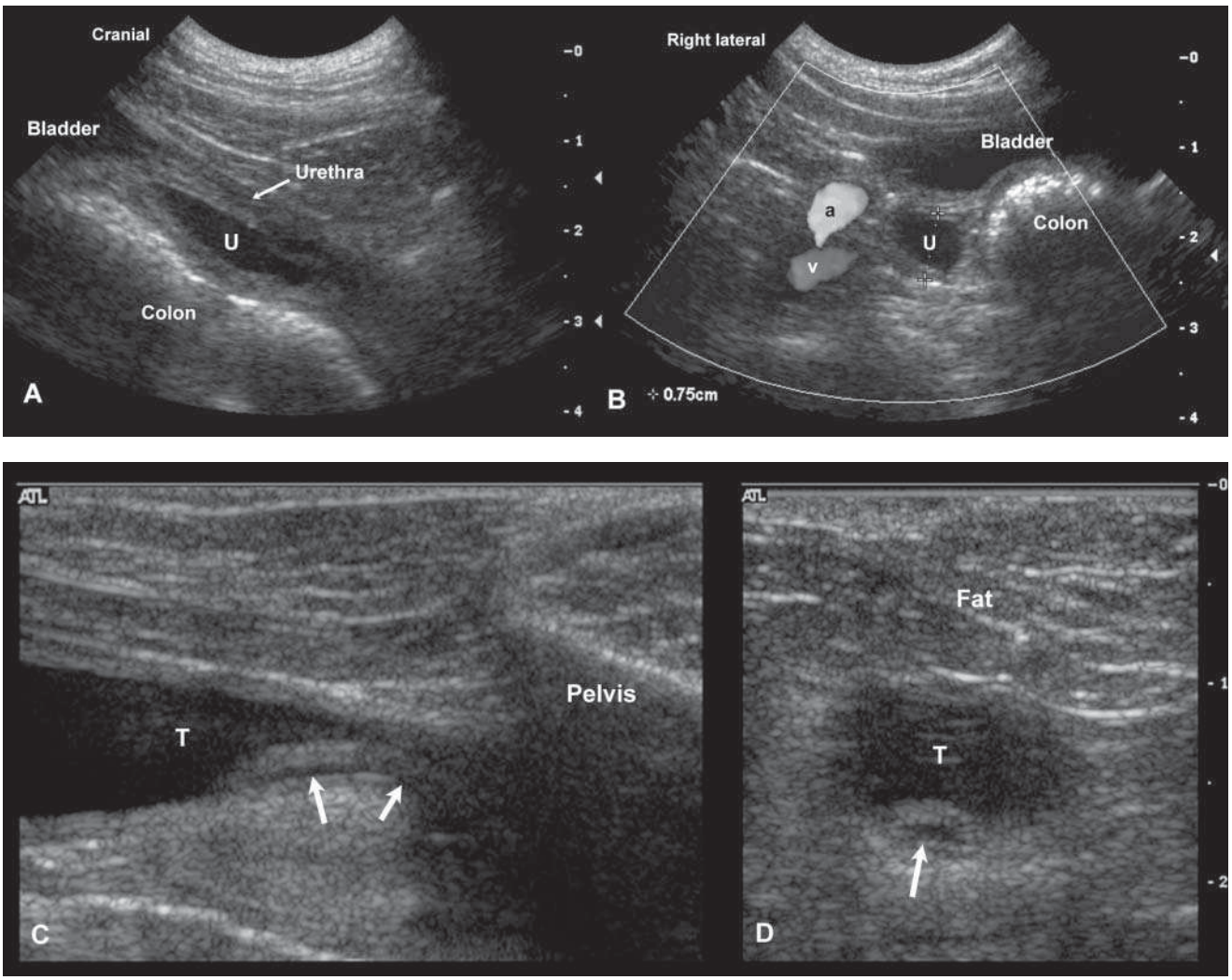


Figure 10.54. Ectopic ureters. A, B: Longitudinal **(A)** and transverse **(B)** images obtained in the region of the bladder trigone, in which a tubular structure filled with an anechoic fluid (U) extends beyond the ureterovesicular junction, along the distal colon. There is no flow on color Doppler, as opposed to the external iliac artery (a) and vein (v), which supports a diagnosis of ureteral ectopia. Excretory urography confirmed a termination into the distal portion of the urethra. **C, D:** Longitudinal **(C)** and transverse **(D)** images of the bladder trigone (T) in a young female dog with urinary incontinence. A fluid-filled tubular structure (arrows) consistent with a distal ureter extends through the wall of the bladder, on the dorsal midline, beyond the ureteral papilla. Because of the shadow created by the pelvis, the termination of this ureter could not be determined with ultrasonography. An intramural (tunneling) ectopic ureter terminating into the urethra was confirmed at surgery.

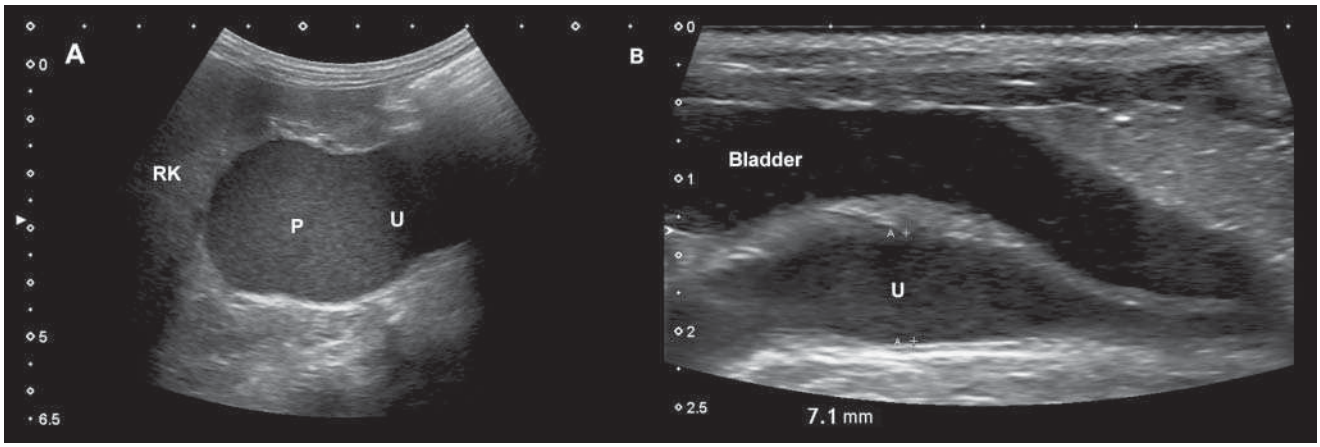


Figure 10.55. Ectopic ureter with ascending infection. Longitudinal sonographic images of the proximal **(A)** and distal **(B)** portions of the right ectopic ureter in a young dog with chronic incontinence and recent onset of lethargy. The right renal pelvis (P) and ureter (U) are severely distended with echogenic urine, consistent with pus. The ureter (7.1 mm in diameter in **B**) extends beyond the bladder to terminate into the pelvic urethra. RK, right kidney.

filled with more concentrated urine. However, the visualization of a urine jet into the bladder lumen cannot exclude the possibility of tunneling ectopic ureters with multiple fenestrations.

Ureterocele is another congenital ureteral malformation, which can sometimes be associated with ectopia (Stiffler et al. 2002). An intravesical ureterocele is characterized by a focal cystic dilatation of the distal submucosal portion of the ureter that protrudes into the bladder lumen (see Figure 11.31). A thin-walled, round structure containing anechoic fluid can be observed within the neck of the bladder by means of ultrasonography (Stiffler et al. 2002). Ectopic ureterocele involves the distal portion of an ectopic ureter.

Disorders of the Perinephric Retroperitoneal Space

Several types of fluid can accumulate in the retroperitoneal space at the periphery of one or both kidneys. Acute renal failure caused by nephrotoxicity, leptospirosis, or interstitial nephritis predisposes to bilateral perirenal effusion, whereas unilateral effusion may be more indicative of pelvic or ureteral obstruction or rupture (Holloway and O'Brien 2007). Retroperitoneal transudate appears as linear or triangular to oval-shaped, anechoic to hypoechoic foci at the periphery of the renal cortex. It may also present a "marble-like" pattern due to alternating bands of retroperitoneal fat and fluid pockets (Figure 10.56).

These changes can also be found with the accumulation of urine or blood, usually following trauma to the kidney and/or ureter, or from spontaneous ureteral rupture due to severe infection of the collecting system (Figures 10.57, 10.58). Although the effusion can be confirmed and characterized with ultrasonography and fine-needle aspiration, the rupture cannot be easily localized and usually requires other imaging tools, such as excretory urography or ultrasound-guided pyelography (Specchi et al. 2012).

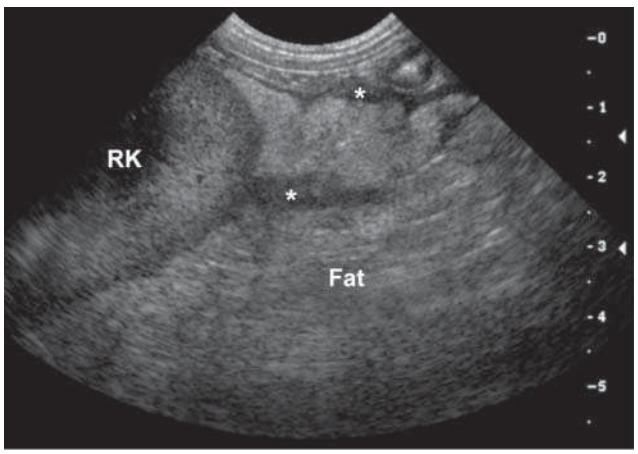


Figure 10.56. Retroperitoneal effusion. Longitudinal image obtained in the region just caudal to the right kidney (RK) of a dog with acute renal insufficiency caused by leptospirosis. Irregular linear hypoechoic regions (*) are within the retroperitoneal space, caudal to the renal cortex, consistent with transudation. The fat appears mildly hyperechoic, which was attributed to edema.

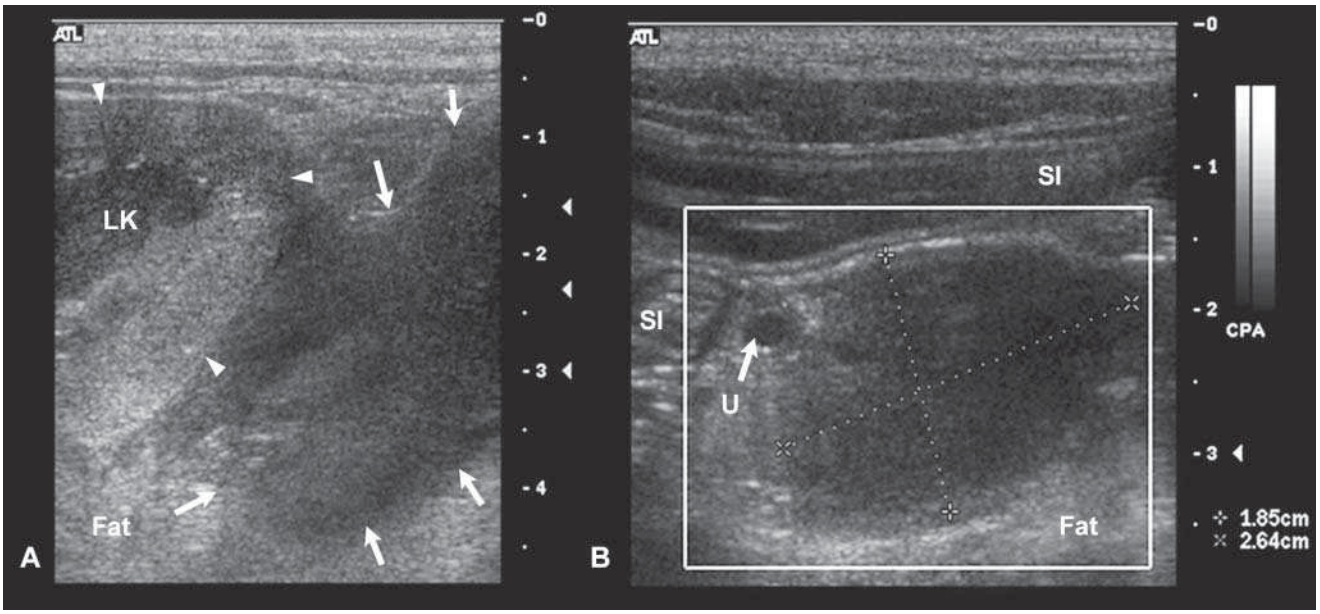


Figure 10.57. Ureteral rupture, retroperitoneal urinoma, and abscess. Longitudinal **(A)** and transverse **(B)** ultrasound images obtained with a linear transducer at the caudal aspect of the left kidney (LK, arrowheads). A poorly defined accumulation of hypoechoic fluid (arrows) is in the retroperitoneal space, caudal to the kidney **(A)** and lateral to the left ureter (U) **(B)**. The retroperitoneal fat is hyperechoic. In **B**, power Doppler is used to differentiate the mildly dilated ureter from an abdominal vessel. The paraureteral fluid collection was sampled with ultrasound guidance, and urine and pus were identified. SI, small intestine.

Retroperitoneal inflammatory processes result in hyperechoic and hyperattenuating fat. These changes are common with acute pyelonephritis and ureteritis, and renal abscess (Figures 10.23, 10.24, 10.40). Exudates and acute hemorrhage tend to be more echogenic because of their higher cell count.

Perinephric pseudocysts, which have been more commonly reported in cats, appear as an accumulation of fluid, usually anechoic, around one or both kidneys, and most commonly between the capsule and the renal cortex (Ochoa et al. 1999; Beck et al. 2000) (Figure 10.59). These pseudocysts typically encircle the kidneys, although they can be focal (Miles and Jergens 1992). According to a report on 26 cats, subcapsular perirenal pseudocysts are formed by accumulation of a transudate between the capsule and parenchyma of the kidney, because of underlying parenchymal disease, and may contribute to abdominal discomfort (Beck et al. 2000). Urine may also be contained in these pseudocysts (Ochoa et al. 1999).

Urinomas, described as an encapsulated accumulation of urine caused by traumatic extravasation (Figure 10.57), can appear similar to pseudocysts. Fine-needle aspiration can be helpful in confirming the nature of the perirenal fluid.

Interventional Procedures

Ultrasound-guided fine-needle aspiration and biopsy have become routine procedures complementing renal ultrasonography. The choice of needle size (gauge) and length depends on the size, vascularity, and depth of the targeted tissue. Usually, 20- to 22-gauge needles are used for fine-needle aspiration, and 14- to 20-gauge needles are used for automated core biopsy (Figures 10.60, 10.61). Fine-needle aspiration can usually be performed with the animal under minimal sedation, whereas biopsy usually requires general anesthesia. Neoplastic processes, such as lymphoma, are usually diagnosed on a cytological specimen obtained with fine-needle aspiration, although a more confident diagnosis can sometimes require a biopsy. When inflammatory processes are suspected, biopsy is generally recommended because it enables a better discrimination between processes. Complications associated with ultrasound-guided biopsy have been reported to vary between 9% in dogs and 15% in cats, and most commonly have included hemorrhage (Vaden et al. 2005). Older dogs and severely azotemic dogs were at higher risk for complications (Vaden et al. 2005). Larger-gauge needles (14- or 16-gauge) are

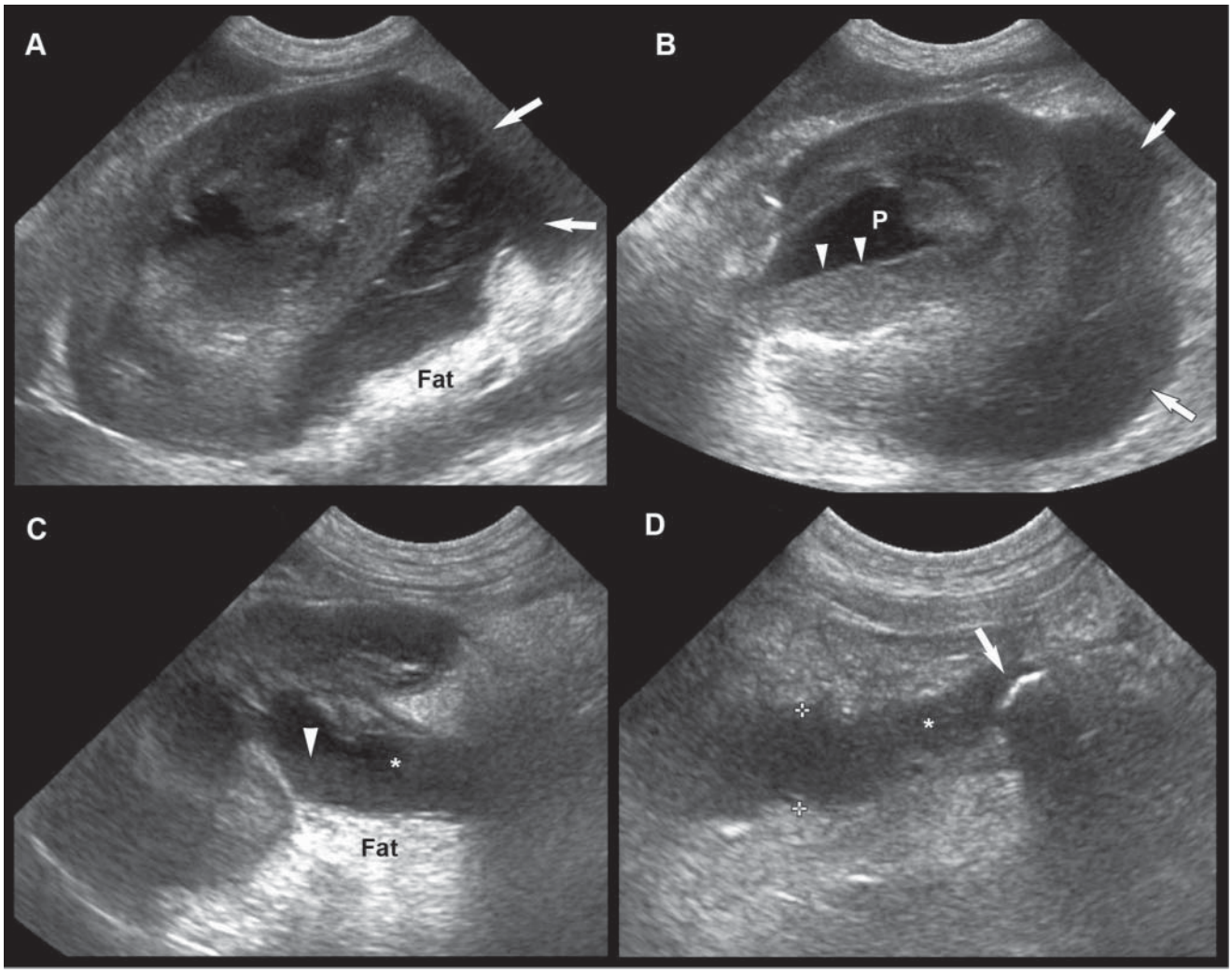


Figure 10.58. **Ureteral calculi and rupture in a 11-year-old Lhaso/Poodle mix. A:** Faintly striated fluid is noted in the subcapsular space of the left kidney (arrows), which was confirmed to be a subcapsular hematoma at surgery. The adjacent fat is hyperechoic. **B:** The kidney presents a distended pelvis (P) with settled echogenic sediment (arrowheads). Subcapsular and retroperitoneal fluid (arrows)) is present and the fat is hyperechoic. **C**: At the hilus of the kidney, the dilated pelvis and proximal ureter (*) contain echogenic urine (pus, arrowhead). **D:** This image was obtained along the proximal dilated ureter (between cursors, and *) and one of the two obstructing calculi (arrows) is seen associated with acoustic shadowing.

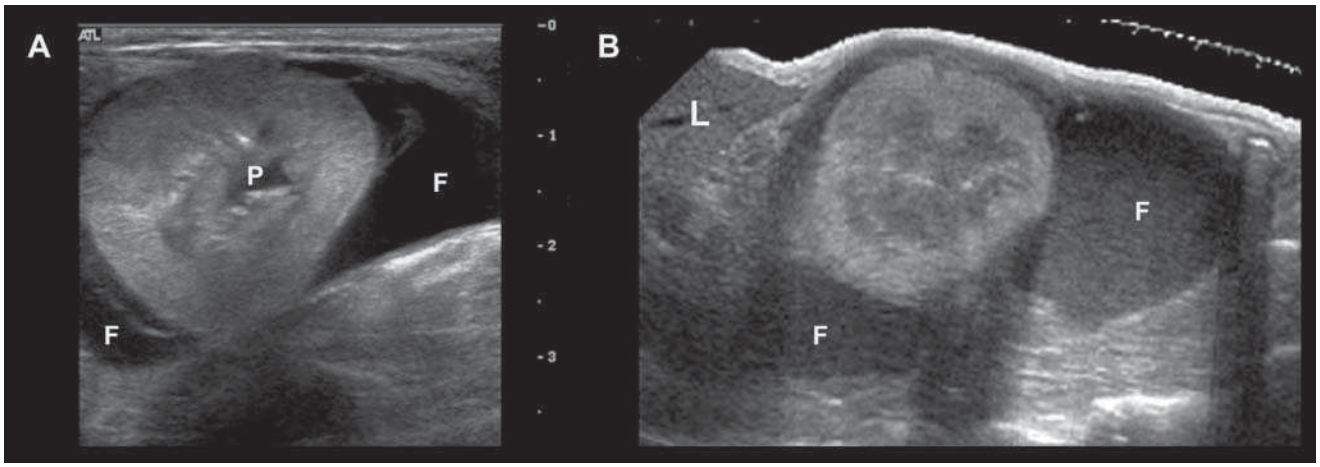


Figure 10.59. **Perinephric pseudocyst associated with different types of renal disease in two cats. A**: Chronic interstitial nephritis. Longitudinal image of the left kidney (LK) of a cat with chronic renal insufficiency. The kidney is small (2.54 cm), deformed, irregular, and diffusely hyperechoic because of chronic interstitial nephritis. The kidney is contained in a large anechoic fluid-filled cavity (F), consistent with a perinephric pseudocyst. **B**: Diffuse squamous cell carcinoma in another cat. Panoramic longitudinal view of the right kidney showing the subcapsular echogenic fluid distension (F). The kidney was distorted and hyperechoic.

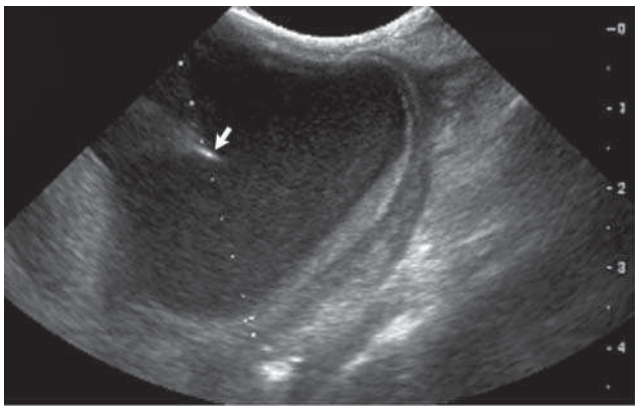


Figure 10.60. Ultrasound-guided aspiration. A fine-needle aspiration is performed on a perirenal pseudocyst (the same cat as in Figure 10.22). The needle tip (arrow) is in the fluid-filled cavity.

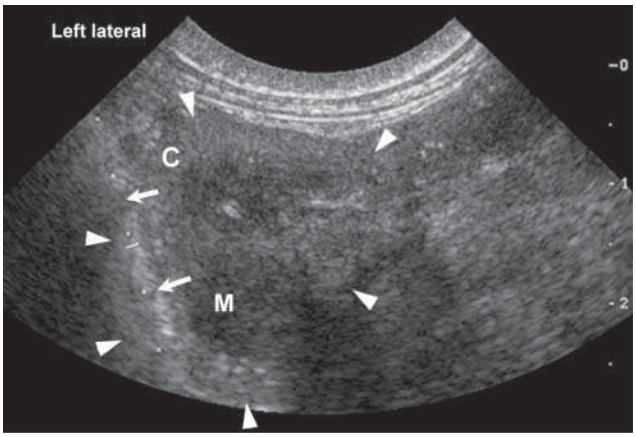


Figure 10.61. Ultrasound-guided renal biopsy. A biopsy is performed through the lateral cortex (C) of the left kidney (arrowheads) of a shar-pei (the same as in Figure 10.11B). The hyperechoic needle (arrows) is seen along the biopsy-guided tract (dotted line), avoiding the medulla (M).

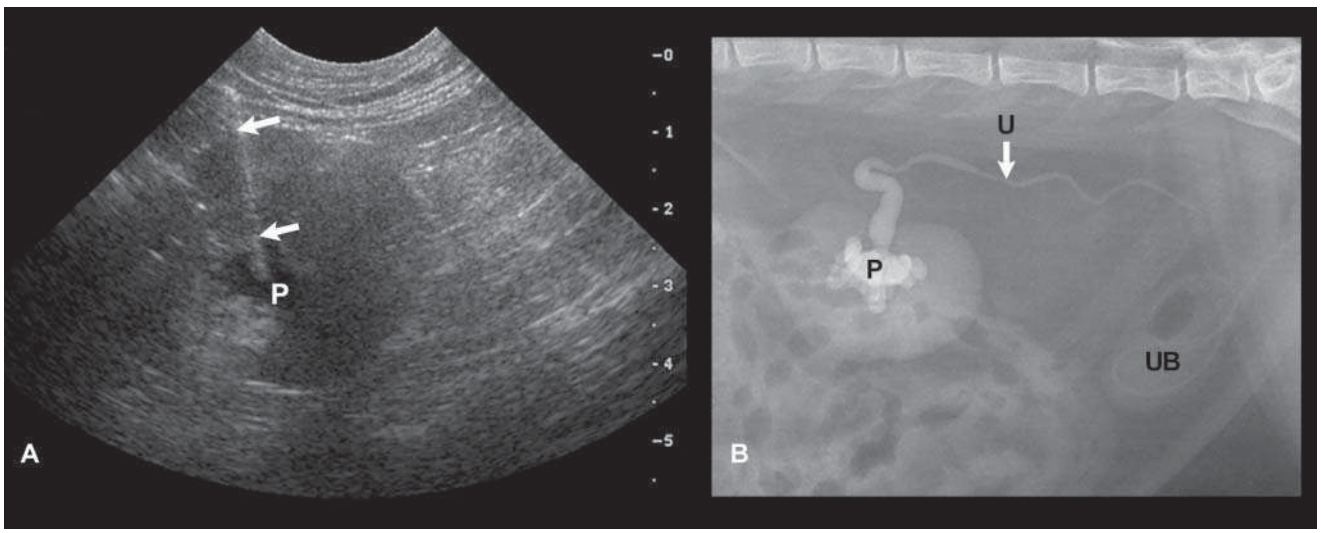


Figure 10.62. Ultrasound-guided pyelocentesis and pyelography. A: Transverse ultrasound image of the left kidney in cat with acute renal failure and anuria. The right kidney was previously removed for a suspected tumor. A 21-gauge 38-mm -long needle (arrows) was inserted into the renal pelvis (P) for urine collection. This was followed by the injection of 5 mL of iopamidol (300 mg iodine/mL). **B:** On a lateral radiograph of the caudal abdomen obtained 10 minutes later, opacification of the pelvis and ureter (U) is observed. A urinary catheter and an oval gas bubble are visible in the bladder. Ureteral obstruction is indicated by the lack of contrast medium reaching the distal ureter and urinary bladder (UB). An obstructive clot was identified in the distal ureter at surgery.

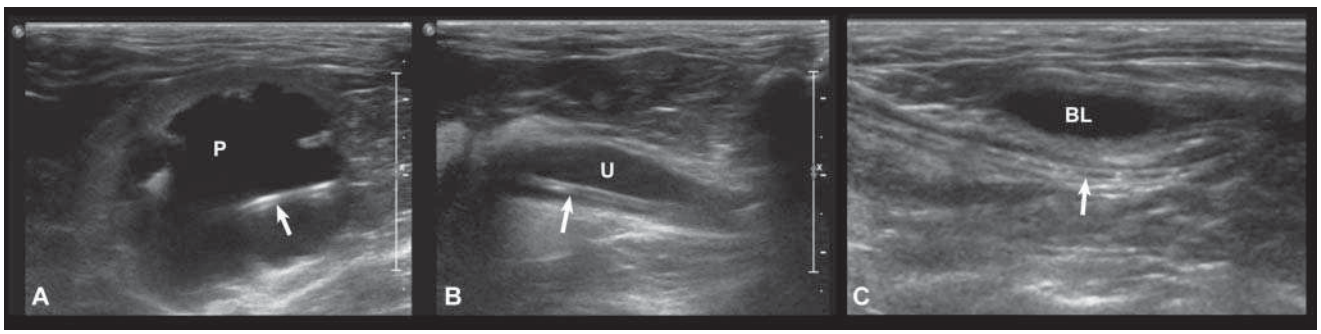


Figure 10.63. Ultrasound monitoring of renal stenting in a cat with chronic obstruction. Ultrasound can be used to confirm the placement and location of stent extremities and follow ureteral patency. The stent appears as a hyperechoic tubular structure (arrows). P, pelvis; BL, bladder.

associated with higher-quality specimens (i.e., with larger number of glomeruli), but also with greater likelihood of hemorrhage (Rawlings et al. 2003).

Fine-needle drainage of cavitary lesions, such as cysts or abscesses, can also be performed as a diagnostic and/or therapeutic procedure (Figure 10.57).

In place of excretory urography, fine-needle aspiration of a distended pelvis (pyelocenthesis) can be performed and followed by intrapelvic injection of iodine-based contrast medium (Rivers et al. 1997) (Figure 10.62). After a 22-gauge spinal needle with a 45° angle is inserted through the great curvature of the kidney, a volume of contrast medium equal to one-half of the aspirated volume of urine is injected with ultrasound guidance prior to radiographic exposure. By allowing a higher concentration of contrast medium to reach the pelvis and ureter in cases of renal failure, their shape and content can be better defined. Additionally, the risk of contrast medium-induced nephropathy can be lowered in animals with compromised renal function. Antegrade pyelography can be a useful alternative in the diagnosis and localization of ureteral obstructions in azotemic cats (Adin et al. 2003). Complications are considered rare. As with renal aspiration or biopsy, hematuria can occur.

Some dogs and cats can benefit from drainage of large renal cysts or pseudocysts (Ochoa et al. 1999). Therapeutic drainage and lavage of the renal pelvis can also help to remove obstructive pus in dogs with pyonephrosis (Szatmari et al. 2001).

Ultrasound may also help in placing or monitoring ureteral or intrarenal stents in animals with ureteral obstruction or rupture (Figure 10.63).



Visit our website at **www.SmallAnimalUltrasonography.com** for complementary video clips with annotations and text on:

- Normal kidneys
- Chronic interstitial nephritis
- Acute nephritis
- Pyelonephritis
- Renal lymphoma
- Renal primary neoplasia
- Polycystic renal disease
- Perirenal pseudocyst
- Obstructive nephrolithiasis and hydronephrosis
- Ectopic ureters

References

Abraham LA, Beck C, Slocombe RF (2003) Renal dysplasia and urinary tract infection in a bull mastiff puppy. Aust Vet J 81:336–339.

Adams WH, Toal RL, Breider MA (1991) Ultrasonographic findings in dogs and cats with oxalate nephrosis attributable to ethylene glycol intoxication: 15 cases (1984–1988). J Am Vet Med Assoc 199:492–496.

Adin CA, Herrgesell EJ, Nyland TG, et al. (2003) Antegrade pyelography for suspected ureteral obstruction in cats: 11 cats (1995–2001). J Am Vet Med Assoc 222:1576–1581.

Allworth MS, Hoffman KL (1999) Crossed renal ectopia with fusion in a cat. Vet Radiol Ultrasound 40:357–360.

Barella G, Lodi M, Sabbadin LA, Faverzani S (2012) A new method for ultrasonographic measurement of kidney size in healthy dogs J Ultrasound 15:186–191.

Barr FJ, Holt PE, Gibbs C (1990) Ultrasonographic measurements of normal renal parameters. J Small Anim Pract 31:180–184.

Barr FJ, Petteson MW, Lucke VM, Gibbs C (1989) Hypercalcemic nephropathy in three dogs: Sonographic appearance. Vet Radiol Ultrasound 30:169–173.

Beck JA, Bellenger CR, Lamb WA, et al. (2000) Perirenal pseudocysts in 26 cats. Aust Vet J 78:166–171.

Bonazzi M, Volta A, Gnudi G, Cozzi MC, Strillacci MG et al. (2009) Comparison between ultrasound and genetic testing for the early diagnosis of polycystic kidney disease in Persian and exotic shorthair cats. J Feline Med Surg 11:430–434.

Biller DS, Bradley GA, Partington BP (1992) Renal medullary rim sign: Ultrasonographic evidence of renal disease. Vet Radiol Ultrasound 33:286–290.

Chandler ML, Elwood C, Murphy KF, Gajanayake I, Syme HM (2007) Juvenile nephropathy in 37 boxer dogs. J Small Anim Pract 48:690–694.

Choi J, Jang J, Choi H, Kim H, Yoon J (2010) Ultrasonographic features of pyonephrosis in dogs. Vet Radiol Ultrasound 51:548–553.

Debruyn K, Paepe D, Daminet S, Haers, Combes A, Duchateau L et al. (2013) Comparison of renal ultrasonographic measurements between healthy cats and three cat breeds: Ragdoll, British Shorthair and Sphynx. J Feline Med Surg 15:478–482.

Esterline ML, Biller DS, Sicard GK (2005) Ureteral duplication in a dog. Vet Radiol Ultrasound 46:485–489.

Eubig PA, Brady MS, Gwaltney-Brant SM, Khan SA, Mazzaferro EM, Morrow CM (2005) Acute renal failure in dogs after the ingestion of grapes or raisins: A retrospective evaluation of 43 dogs (1992–2002). J Vet Intern Med 19:663–674.

Forrest LJ, O'Brien RT, Tremelling MS, Steinberg H, Cooley AJ, Kerlin RL (1998) Sonographic renal findings in 20 dogs with leptospirosis. Vet Radiol Ultrasound 39:337–340.

Gasser AM, Bush WW, Smith SS, Walton R (2003) Extradural spinal, bone marrow, and renal nephroblastoma. J Am Anim Hosp Assoc 39:80–85.

Hart DV, Winter MD, Conway J, Berry CR (2013) Ultrasound appearance of the outer medulla in dogs without renal dysfunction. Vet Radiol Ultrasound 54:653–658.

Hecht S, McCarthy RJ, Tidwell AS (2005) What is your diagnosis? Ectopic kidney. J Am Vet Med Assoc 227: 223–224.

Holloway A, O'Brien R (2007) Perirenal effusion in dogs and cats with acute renal failure. Vet Radiol Ultrasound 48:574–579.

Ivancic M, Mai W (2008) Qualitative and quantitative comparison of renal vs. hepatic ultrasonographic intensity in healthy dogs. Vet Radiol Ultrasound 49:368–373.

Kyles AE, Hardie EM, Wooden BG, et al. (2005) Clinical, clinicopathologic, radiographic, and ultrasonographic abnormalities in cats with ureteral calculi: 163 cases (1984–2002). J Am Vet Med Assoc 226:932–936.

Lamb CR, Gregory SP (1998) Ultrasonographic findings in 14 dogs with ectopic ureter. Vet Radiol Ultrasound 39:218–223.

Mantis P, Lamb CR (2000) Most dogs with medullary rim sign on ultrasonography have no demonstrable renal dysfunction. Vet Radiol Ultrasound 41:164–166.

Mareschal A, d'Anjou MA, Moreau M, Alexander K, Beauregard G (2007) Utrasonographic measurement of kidney-to-aorta ratio as a method os estimating renal size in dogs. Vet Radiol Ultrasound 48(5):434–438.

Miles KG, Jergens AE (1992) Unilateral perinephric pseudocyst of undetermined origin in a dog. Vet Radiol Ultrasound 33:277–281.

Moe L, Lium B (1997) Hereditary multifocal renal cystadenocarcinomas and nodular dermatofibrosis in 51 German shepherd dogs. J Small Anim Pract 38:498–505.

Moore FM, Thornton GW (1983) Telangiectasia of Pembroke Welsh corgi dogs. Vet Pathol 20:203–208.

Mosenco AS, Culp WTN, Johnson V, french A, Mehler SJ (2008) Renal Cystadenoma in a domestic shorthair. J Feline Med Surg 10:102–105.

Neuwirth L, Mahaffey M, Crowell W, et al. (1993) Comparison of excretory urography and ultrasonography for detection of experimentally induced pyelonephritis in dogs. Am J Vet Res 54:660–669.

Ochoa VB, DiBartola SP, Chew DJ, Westropp J, Carothers M, Biller D (1999) Perinephric pseudocysts in the cat: A retrospective study and review of the literature. J Vet Intern Med 13:47–55.

Rawlings CA, Diamond H, Howerth EW, Neuwirth L, Canalis C (2003) Diagnostic quality of percutaneous kidney biopsy specimens obtained with laparoscopy versus ultrasound guidance in dogs. J Am Vet Med Assoc 223:317–321.

Reichle JK, DiBartola SP, Léveillé R (2002) Renal ultrasonographic and computed tomographic appearance, volume, and function of cats with autosomal dominant polycystic kidney disease. Vet Radiol Ultrasound 43:368–373.

Reichle JK, Peterson II RA, Mahaffey MB, Schelling CG, Bartez PY (2003) Ureteral fibroepithelial polyps in four dogs Vet Radiol Ultrasound 44:433–437.

Rivers BJ, Walter PA, Polzin DJ (1997) Ultrasonographic-guided, percutaneous antegrade pyelography: Technique and clinical application in the dog and cat. J Am Anim Hosp Assoc 33:61–68.

Ruth JD, Heng HG, Miller MA (2013) Effect of anisotropy and spatial compound imaging on renal cortical echogenicity in dogs. Vet Radiol Ultrasound 54:659–665.

Seiler GS, Rhodes J, Cianciolo R, Casal ML (2010) Ultrasonographic fingings in cairn terriers with preclinical renal dysplasia. Vet Radiol Ultrasound 51:453–457.

Specchi S, Lacava G, d'Anjou MA, Zini E, Auriemme E (2012) Ultrasound-guided percutaneous antegrade pyelography with computed tomography for the diagnosis of spontaneous partial ureteral rupture in a dog. Can Vet J 53:1187–1190.

Stiffler KS, Stevenson MAM, Mahaffey MB, Howerth EW, Barsanti JA (2002) Intravesical ureterocele with concurrent renal dysfunction in a dog: A case report and proposed classification system. J Am Anim Hosp Assoc 38:33–39.

Szatmari V, Osi Z, Manczur F (2001) Ultrasound-guided percutaneous drainage for treatment of pyonephrosis in two dogs. J Am Vet Med Assoc 218:1796–1799.

Vaden SL, Levine JF, Lees GE, Groman RP, Grauer GF, Forrester SD (2005) Renal biopsy: A retrospective study of methods and complications in 283 dogs and 65 cats. J Vet Intern Med 19:794–801.

Valdès-Martinez A, Cianciolo R, Mai W (2007) Association between renal hyopechoic subcapsular thickening and lymphosarcoma in cats. Vet Radiol Ultrasound 48:357–360.

Wills SJ, Barrett EL, Barr FJ, Bradley KJ, Helps CR, Gruffydd-Jones TJ (2009) Evaluation of repeatability of ultrasound scanning for detection of feline polycystic kidney disease. J Feline Med Surg 11:993–996.

Yeager AE, Anderson WI (1989) Study of association between histologic features and echogenicity of architecturally normal cat kidneys. Am J Vet Res 50:860–863.

CHAPTER ELEVEN

Bladder and Urethra

James Sutherland-Smith and Dominique Penninck

Department of Clinical Sciences, Cummings School of Veterinary Medicine, Tufts University, North Grafton, MA, USA

Preparation and Scanning Technique

After clipping of ventral abdominal hair, ultrasonic gel is applied to the skin. A transabdominal approach with the animal in dorsal recumbency is preferred, but left or right lateral recumbency or a standing position may be used in confirming the presence of intraluminal sediment or calculi, which will fall toward the gravity-dependent wall. If the penile urethra is to be imaged, then hair may need to be clipped from the perineum and the region cranial to the scrotum.

A medium- to high-frequency (5–8 MHz or higher) convex, linear, or sector transducer is recommended. A microconvex transducer with a small contact area has the advantage of being easier to point toward the intrapelvic structures. Two complementary transverse and longitudinal planes are used to fully assess the bladder and urethra (Figure 11.1).

The best ultrasound images of the bladder are obtained when it is moderately distended. If the bladder is empty and pathology is suspected, it is advisable to rescan the bladder after waiting for it to refill naturally, place a urinary catheter and fill the bladder with sterile isotonic (0.9%) saline, or to administer intravenous furosemide.

Ultrasonographic Anatomy of the Normal Urinary Bladder and Urethra

The bladder is within the caudoventral abdomen, and the urethra extends into the pelvic canal. The descending colon, aorta, and caudal vena cava are dorsal to the urinary bladder. These vessels can be identified by their location and by using color Doppler (Figure 11.2).

Air within the colon, combined with the curvilinear interface of the bladder wall, may cause a mirror-image artifact of the urinary bladder (Figure 11.3). In intact females, the uterine body is between the urinary bladder and the colon.

The four histological bladder wall layers are the mucosa (hypoechoic), submucosa (hyperechoic), muscularis (hypoechoic), and serosa (hyperechoic). However, these layers are difficult to define sonographically compared with the gastrointestinal tract. The bladder wall thickness decreases as the urinary bladder volume increases (Figure 11.4). In addition, the normal bladder wall thickness increases up to 1 mm with increasing body weight in dogs (Geisse et al. 1997) (Table 11.1). The normal range of bladder wall thickness in cats has been reported to be up to 1.7 mm (Finn-Bodner 1995).

The trigone of the bladder is not clearly delineated from the remainder of the bladder wall. The ureteral entry to the urinary bladder is not commonly seen unless there is dilation. Ureteral papillae may be seen extending from the mucosal surface of the dorsal wall and should not be confused with other causes of focal wall thickening (Figure 11.5).

Jets of urine may be seen emerging from the dorsal bladder wall at the trigone. These ureteral jets appear as a burst of hyperechoic speckles on B-mode ultrasound or a pulse of positive (red) signal on color flow Doppler (Figure 11.6). The visualization of ureteral jets is variable because it requires a difference in the specific gravity between the urine in the bladder and the urine exiting the ureter. Intravenous furosemide (1 mg/kg) can be utilized to enhance the visualization of ureteral jets within the urinary bladder.

The normal urine within the urinary bladder is most commonly anechoic. However, echogenic urine is not

Atlas of Small Animal Ultrasonography, Second Edition. Edited by Dominique Penninck and Marc-André d'Anjou.
© 2015 John Wiley & Sons, Inc. Published 2015 by John Wiley & Sons, Inc.
Companion website: www.SmallAnimalUltrasonography.com

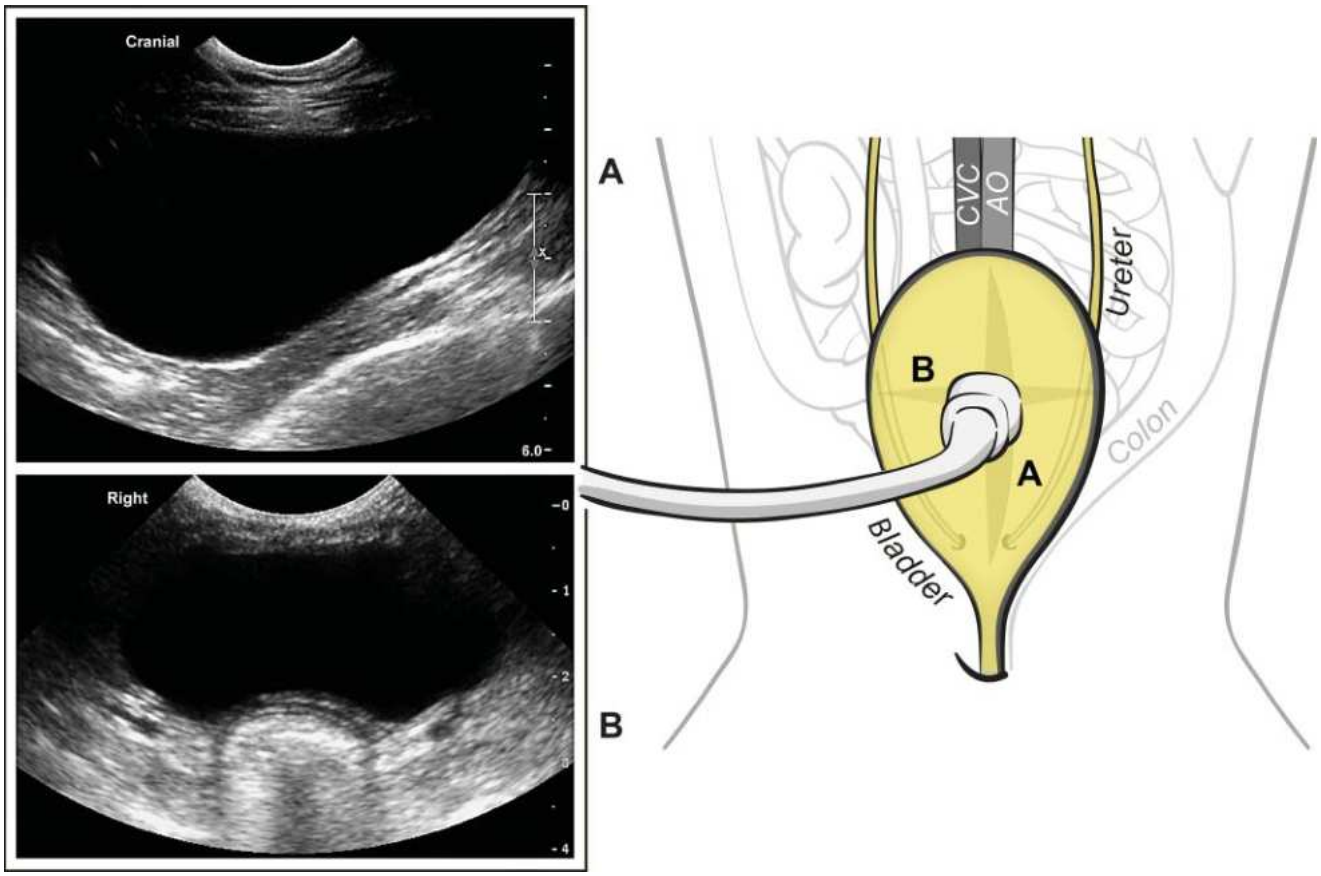


Figure 11.1. Composite image of the urinary bladder and adjacent anatomical structures in a dog. The schematic diagram on the right shows the position of the urinary bladder, the dorsally located colon, aorta, and caudal vena cava, as well as transducer positions for the standard longitudinal and transverse imaging planes. **A:** A longitudinal sonogram of the urinary bladder filled with normal anechoic urine. **B:** A transverse sonogram of the urinary bladder. The colon is located dorsally in the far field and is causing mild indentation of the dorsal bladder wall. AO, aorta; CVC, caudal vena cava.

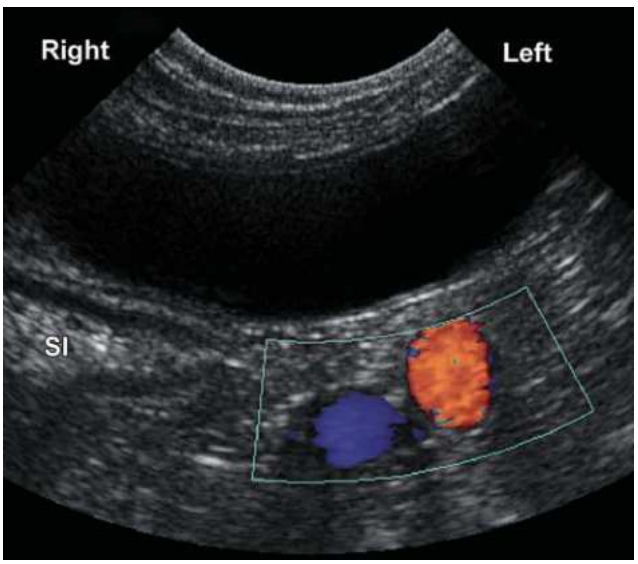


Figure 11.2. Normal bladder and main vessels in a dog. Color flow Doppler transverse sonogram of the urinary bladder and the dorsally located aorta (red) and caudal vena cava (blue), to the left of an intestinal loop (SI).

Table 11.1
Variation in bladder wall thickness with changes in intraluminal volume in dogs

Degree of Bladder Distension	Mean Thickness (mm)	Standard Deviation (mm)
Minimal (0.5 mL/kg)	2.3	0.43
Mild (2 mL/kg)	1.6	0.29
Moderate (4 mL/kg)	1.4	0.28

Adapted from Geisse et al. (1997).

necessarily indicative of urinary tract disease, and may be seen especially in normal cats; therefore, a urinalysis can assist in determining its significance. Additionally, images of the urinary bladder are prone to side-lobe and grating-lobe artifacts that can create the appearance of pseudosludge (Figure 11.7). Adjustment of the gain and use of spatial compounding and

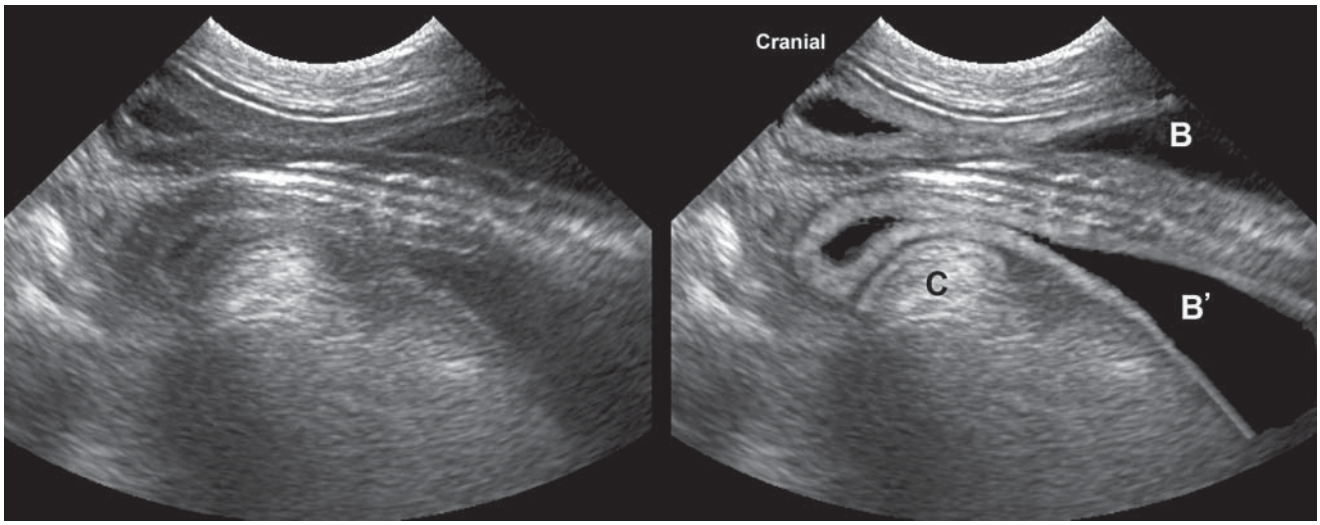


Figure 11.3. **Mirror-image artifact in a dog. Left:** Longitudinal sonogram of the urinary bladder with a mirror-image artifact caused by errors in position of echoes reflected from the ventral colon wall–colon luminal gas interface. **Right:** The corresponding labeled schematic representation. B, bladder; B′, mirror image of the bladder; C, colon.

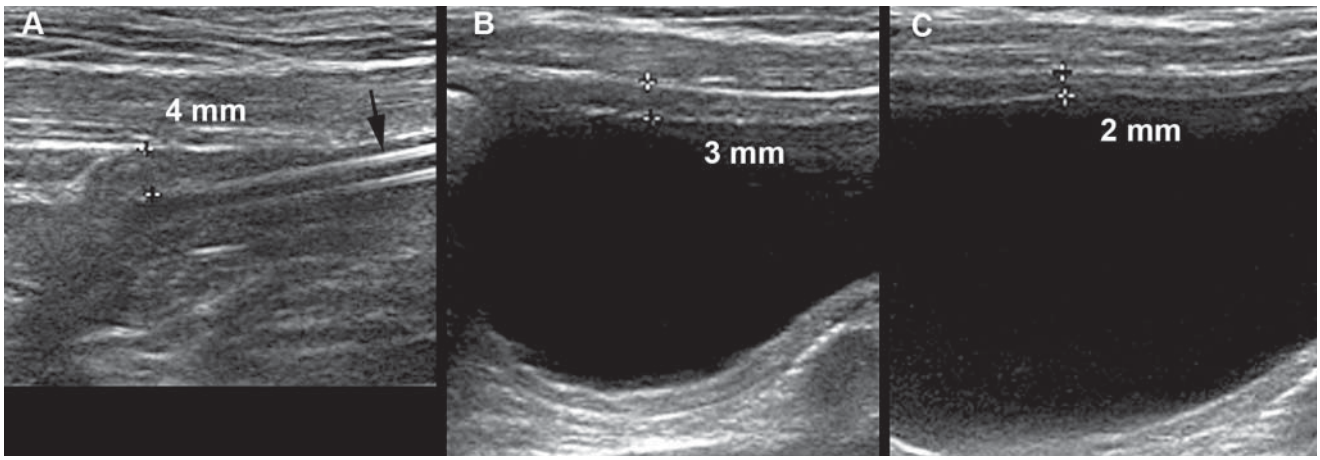


Figure 11.4. **Normal bladder thickness and distension in a 30-kg dog.** A series of longitudinal ultrasound images of the urinary bladder with different volumes of sterile saline infused into the bladder lumen. **A:** Longitudinal sonogram of an empty urinary bladder with an indwelling red-rubber urinary catheter (arrow). The urinary bladder wall thickness is 4 mm. **B:** A total of 60 ml (2 ml/kg) of saline is infused, and the bladder wall thickness now is 3 mm. **C:** With a total volume of 120 ml (4 ml/kg), the bladder wall thickness is 2 mm.

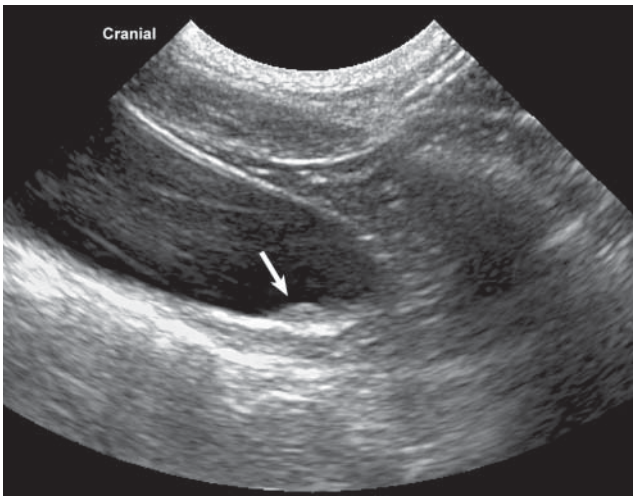


Figure 11.5. **Normal ureteral papillae in a dog.** Longitudinal sonogram of the trigone of the urinary bladder. There is a smooth, broad-based echogenic protuberance (arrow) at the dorsocaudal aspect of the urinary bladder consistent with a normal ureterovesicular junction.

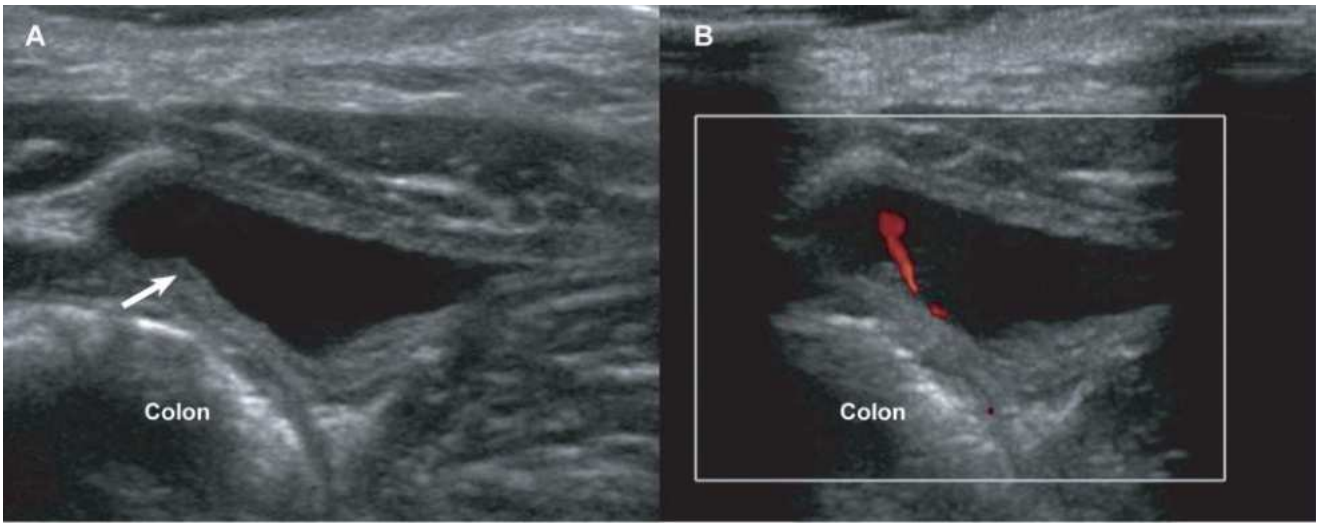


Figure 11.6. **Ureteral jet in a dog. A:** Transverse sonogram of a bladder in the trigone region using B-mode ultrasound. No ureteral jets are visible in proximity to the right ureterovesicular junction (arrow). **B:** Transverse color flow Doppler sonogram of a ureteral jet. The use of color flow Doppler can aid the detection of ureteral jets. The red indicates flow toward the transducer.

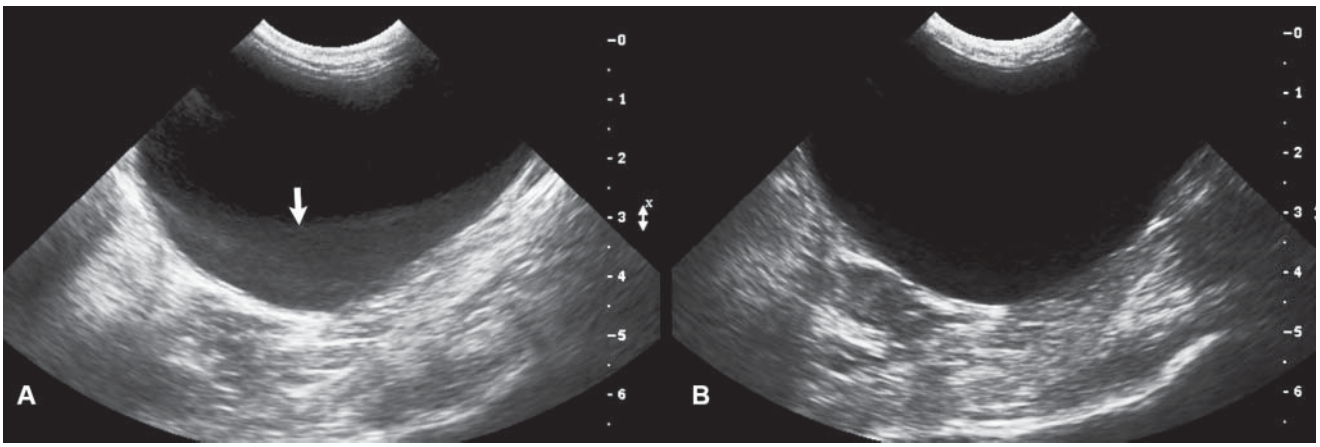


Figure 11.7. **Pseudosludge and side-lobe artifacts. A:** Longitudinal sonogram of the urinary bladder illustrating pseudosludge (arrow) caused by side-lobe and grating-lobe artifacts. These echoes are caused by reflections at the margins of the bladder wall. Scanning with the animal standing may help in confirming this artifact. True sediment should fall to the dependent wall and typically shows a straight linear border (see Figure 11.26). **B:** Longitudinal sonogram of the same urinary bladder. The time gain compensation has been adjusted to reduce the appearance of the pseudosludge artifact. The use of spatial compounding will also help to reduce this artifact.

harmonic ultrasound (Figure 11.8) help to reduce the formation of these sometimes confusing echoes.

Retrograde positive-contrast urethrography remains the preferred modality for assessing the entire urethra. Ultrasound is a useful and complementary modality for part of the accessible urethra. The urethra extends caudally from the bladder into the pelvic canal (Figure 11.9).

In male dogs, the prostate surrounds the proximal urethra. Shadowing from the pubis obscures the caudal intrapelvic portion of the urethra. The proximal penile urethra is located within the corpus spongiosum between the corpus cavernosum dorsally and the bulbospongiosus and retractor penis muscles ventrally (Figure 11.10A). The distal penile urethra is located within the urethral groove of the os penis dorsally and the bulbus glandis ventrally (Figure 11.10B). The urethral lumen is not normally seen unless there is urinary bladder distension, in which case urethral obstruction should be considered. The urethral wall

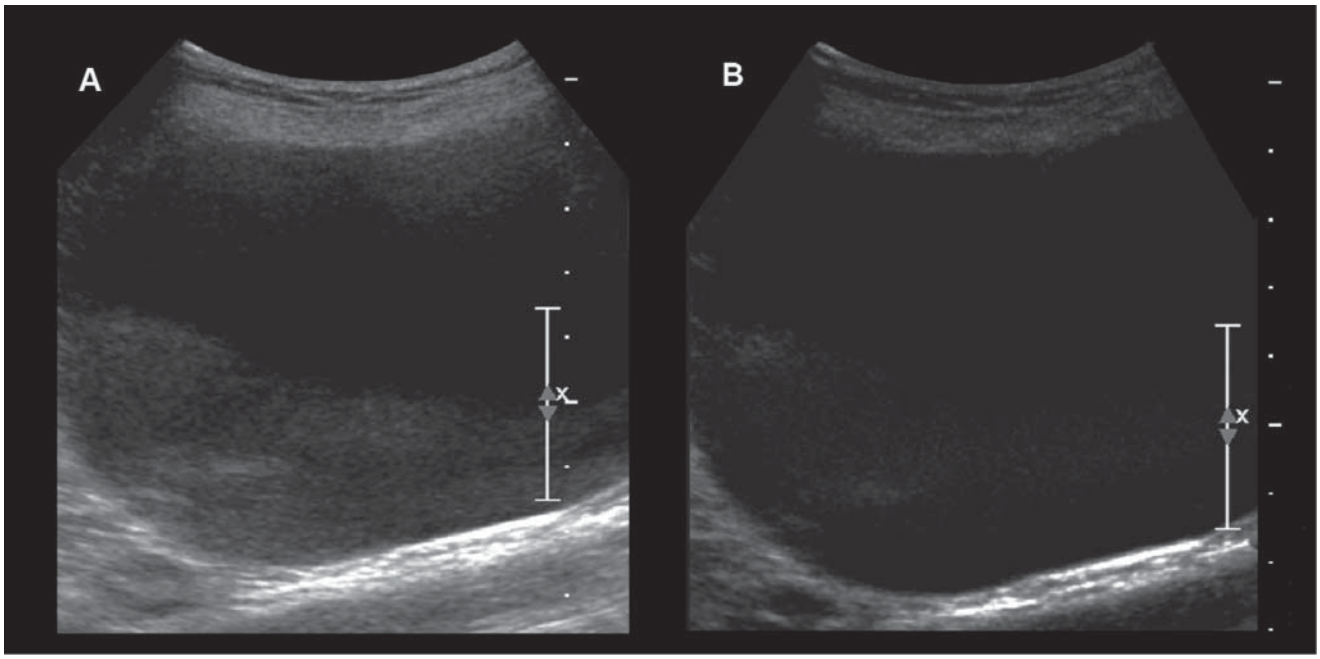


Figure 11.8. B-mode (A) and harmonic (B) longitudinal sonogram of a urinary bladder and pseudosludge in a dog. Harmonic ultrasound **(B)** reduces both the near-field and the far-field artifacts.

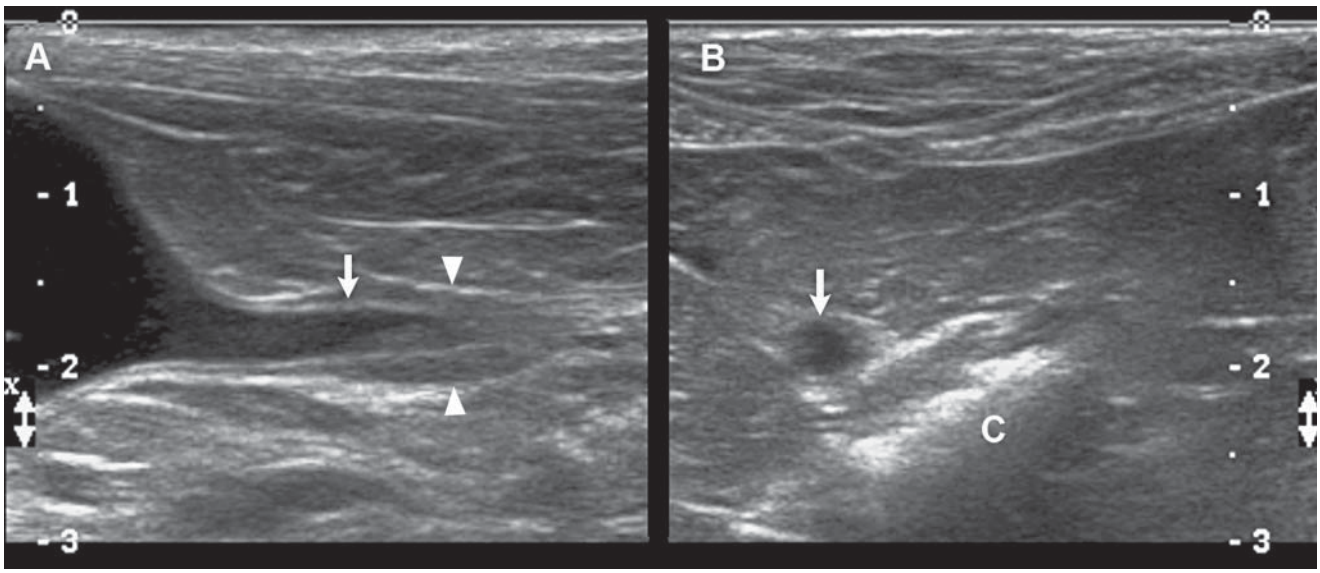


Figure 11.9. Normal urethra in a male dog. Duplex sonogram of the proximal urethra (arrow) in longitudinal **(A)** and transverse **(B)** planes. Distal to the prostate (arrowheads), the urethral lumen is not visible. The descending colon (C) is seen in the far field in **B**.

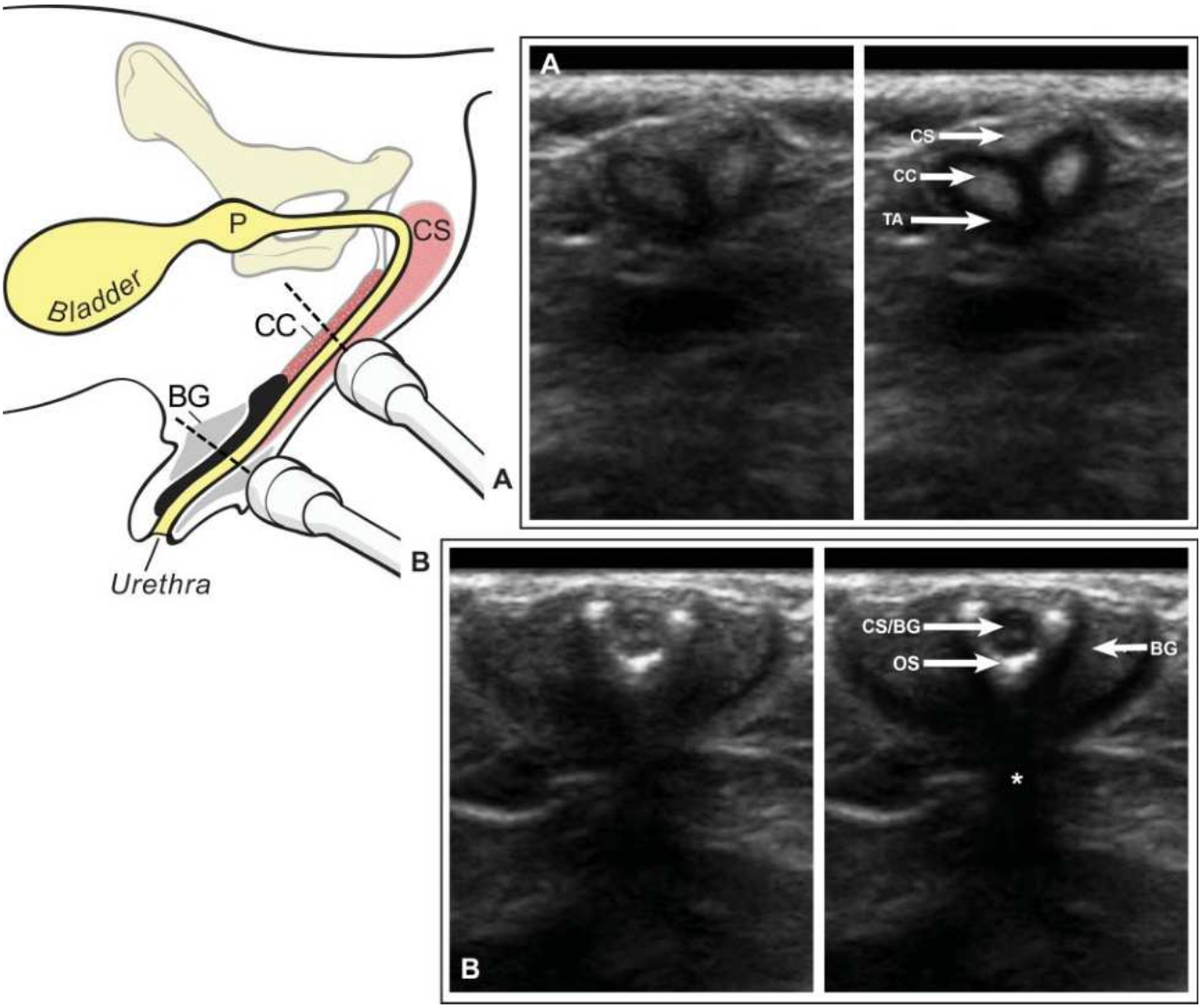


Figure 11.10. **Normal penile urethra in a dog.** On the left, an illustration of the anatomical structures near the urethra is presented. The dotted lines **(A, B)** correspond to the transverse planes seen on the sonograms on the right. P, prostate**. A:** Transverse sonogram (with and without labels) of the mid-penile urethra at a level just cranial to the scrotum. The urethra cannot be delineated but is located within the corpus spongiosum (CS). CC, corpus cavernosum; TA, tunica albuginea. **B:** Transverse sonogram (with and without labels) of the distal penile urethra at the level of the os penis (OS), which is seen as a hyperechoic U-shaped structure with distal shadow. The urethra is located within the anastomosing tissue of the CS and bulbus glandis (CS/BG). The BG forms the bulk of the tissue surrounding the os penis.

Figure 11.11. **Cystitis in dogs and cats. A:** Longitudinal sonogram of the urinary bladder showing moderate cranioventral thickening of the bladder wall. The urine from the dog cultured positive for *Escherichia coli* on multiple occasions. **B:** Longitudinal sonogram of the urinary bladder showing moderate, diffuse, hypoechoic, thickening of the bladder wall in this cat. Notice the presence of a large amount of sediment and calculi in the dependent portion of the bladder. **C:** Longitudinal sonogram of a severe cystitis in a Chow Chow with concurrent prostatitis. Notice the marked thickening (1.3 cm) affecting most of the bladder wall. **D:** Transverse sonogram of the same dog as in **C**.

is composed of the same histological layers as the urinary bladder. These layers are not readily resolved when normal.

Ultrasonographic Features of Bladder and Urethral Disorders

Cystitis

Cystitis most commonly causes extensive irregular hypoechoic thickening of the urinary bladder wall. This thickening is usually greatest at the cranioventral aspect of the urinary bladder (Figure 11.11).

Etiologies are typically inflammatory or bacterial. The thickened hypoechoic/hyperechoic or layered bladder wall typical of cystitis can be associated with other findings, such as calculi, necrotic debris, or blood clots. Less common infectious causes of cystitis with similar or worsened ultrasound features include parasite infestation and fungal infection. Granulomatous fungal cystitis (*Histoplasma capsulatum*) has been reported in one cat to cause marked diffuse, uniformly hyperechoic urinary bladder wall thickening (Taylor et al. 2012). Other fungal agents such as candida can also be encountered, especially in immune compromised animals.

Pseudomembranous cystitis in dogs and cats is associated with severe diffuse ulceration, necrosis, and hemorrhage of the bladder wall, as well as intraluminal necrotic, fibrinous and hemorrhagic tags and debris. These detached tags and debris can predispose to urinary bladder outflow obstruction. The ultrasound features include urinary bladder wall thickening as well as multiple hyperechoic luminal septations (Le Boedec et al. 2011) (Figure 11.12).

Emphysematous cystitis is characterized by gas-forming bacteria such as *Escherichia coli*, *Aerobacter*

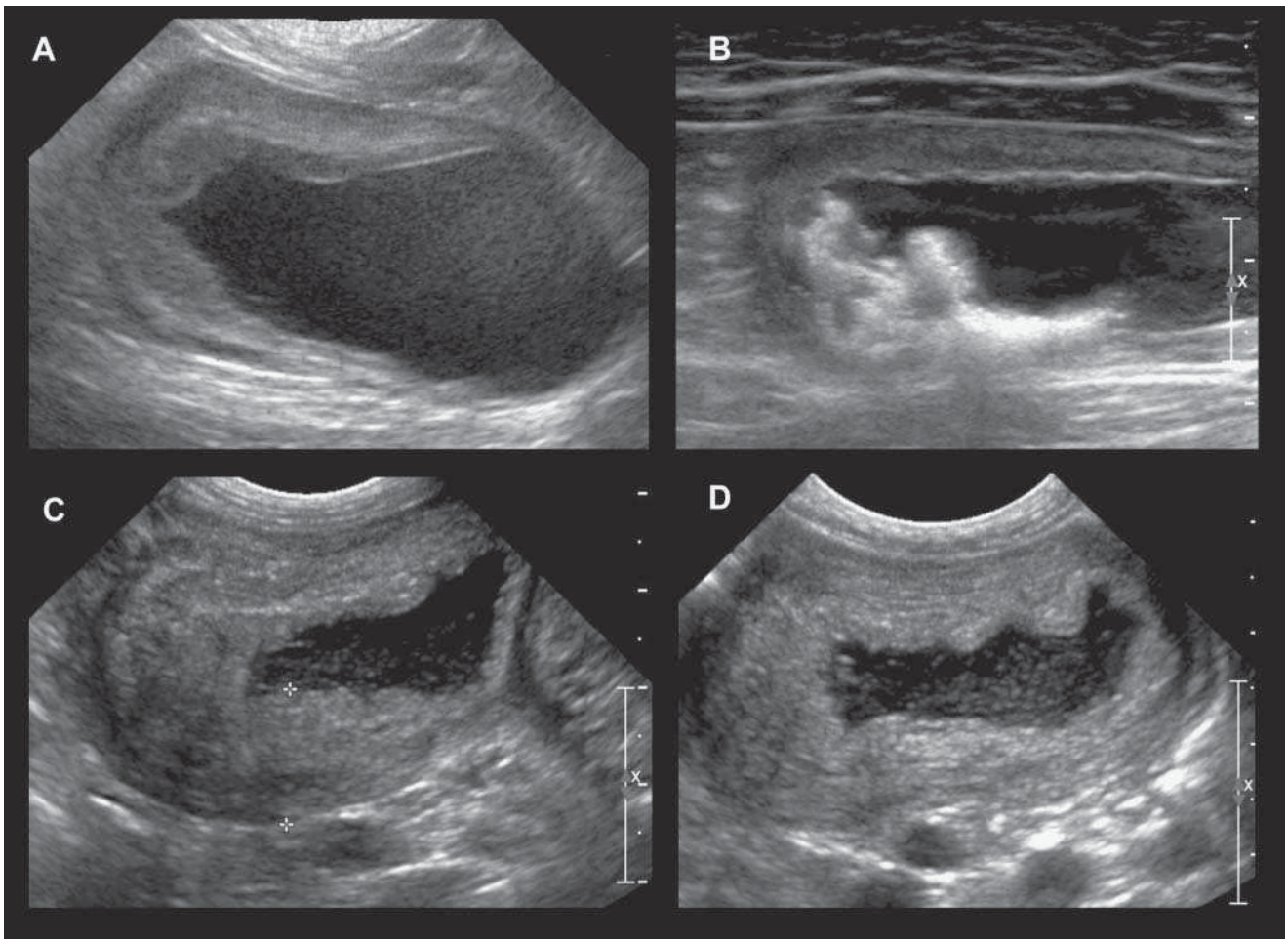


Figure 11.11. Cystitis in dogs and cats. (for full caption, see facing page)

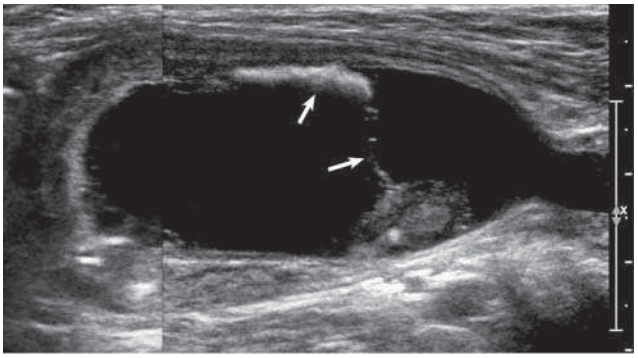


Figure 11.12. Pseudomembranous and mycoplasma cystitis in a 2-year-old Chihuahua with hematuria and urinary obstruction. Composite of two longitudinal sonograms of the bladder. Moderate thickening of the wall with uneven mucosal surface is noted. In addition, the ventral wall displays a hyperechoic band (arrows) that represents the sloughing mucosa with fibrin strands extending dorsally (as the dog is in dorsal recumbency). Mycoplasma and other bacteria were confirmed in this patient.

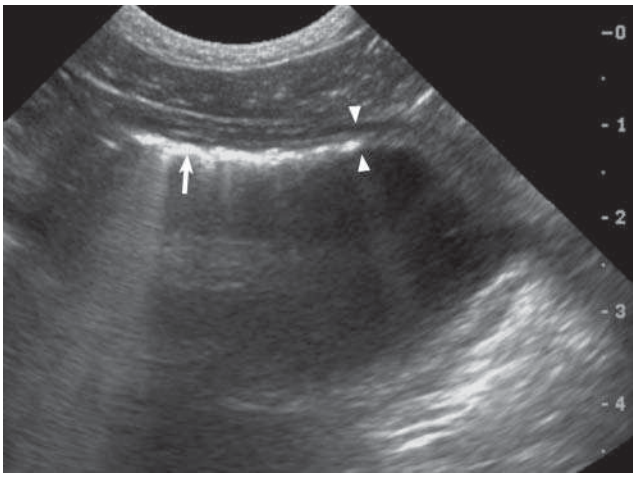


Figure 11.13. Emphysematous cystitis in an 8-year-old Greyhound with chronic cystitis. Longitudinal sonogram of the urinary bladder showing a hyperechoic interface (arrow) in the ventral bladder wall (between arrowheads) with multiple reverberation artifacts, consistent with emphysematous cystitis. The urine cultured positive for *Escherichia coli*.

aerogenes, *Proteus mirabilis*, and *Clostridium* sp. within the bladder wall and is seen most commonly in diabetic animals with glucosuria. The sonographic appearance is multifocal, irregular, hyperechoic interfaces with distal reverberation artifact (Petite et al. 2006) (Figure 11.13). By using alternative patient positions, free luminal gas (often seen in catheterized patients) can be distinguished from emphysematous cystitis. The free luminal gas will move with patient position, whereas the bladder wall gas will remain in the same location.

Polypoid cystitis is an uncommon form of cystitis reported in dogs. It can present as a hyperechoic polypoid to pedunculated mass or masses projecting into the lumen, as well as diffuse bladder wall thickening in some cases (Martinez et al. 2003) (Figure 11.14A,B). These masses occur most commonly in the cranioventral aspect of the urinary bladder (Martinez et al. 2003). Polypoid cystitis with mass-like mucosal proliferations and severe diffuse bladder wall thickening from severe suppurative or granulomatous cystitis can overlap the

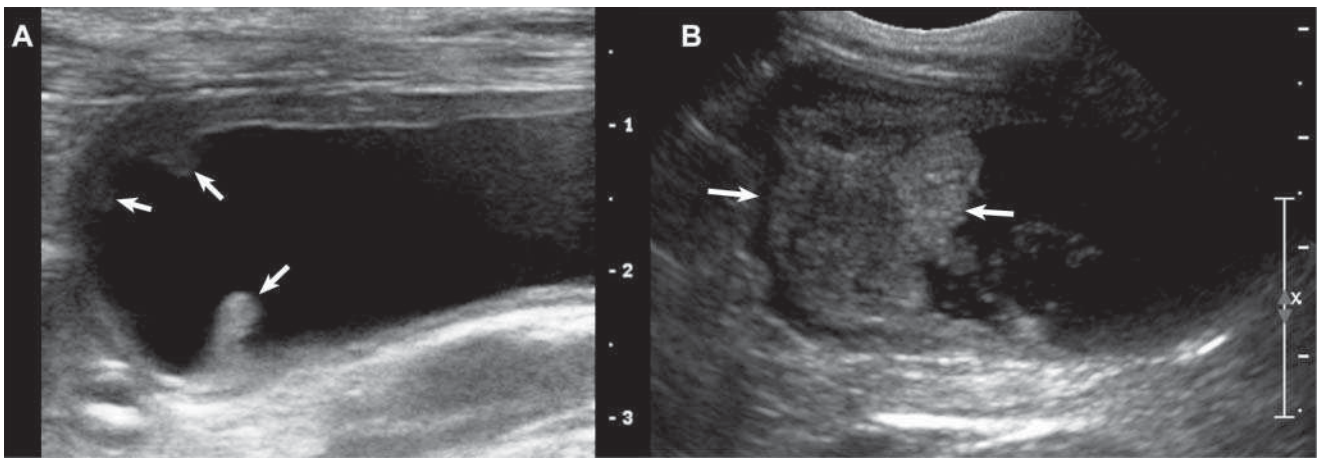


Figure 11.14. Polypoid cystitis in two dogs. A: Longitudinal sonogram of the urinary bladder of an 8-year-old fox terrier with three small pedunculated lesions (arrows) extending from the right bladder wall into the bladder lumen, confirmed to be polypoid cystitis. The bladder wall thickness is otherwise within normal limits. **B:** Longitudinal sonogram of an 8-year-old Cocker Spaniel with a broad-based thickening/mass of the cranial bladder wall (between arrows). Histopathology following surgical excisional biopsy revealed a mucosal polyp.

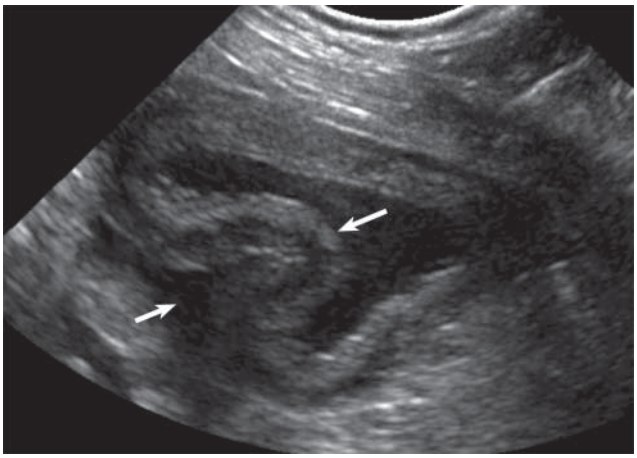


Figure 11.15. Bladder wall inversion in a 13-year-old Labrador cross. The unusual apical "mass" (arrows) represents a fold of the wall projecting into the lumen. This dog had chronic cystitis with numerous successive catheter placements. The fold disappeared over time.

ultrasound features associated with neoplasia, and suction biopsies are recommended in these cases.

Bladder wall inversion is a rare condition that is speculated to be associated with cystitis in dogs and cats. It has ultrasound features of an apical mass-like tissue thickening with the folded bladder wall protruding into the lumen. The inversion results in an indented apical serosal margin of the bladder. The thickened and inverted bladder wall has preserved wall layering, resulting in characteristic multiple hyperechoic and hypoechoic interfaces (Adin et al. 2011) (Figure 11.15). This condition may also be encountered as a temporary event after long-term catheter placement.

Neoplasia

Transitional cell carcinoma (TCC) is the most common neoplasm of the urinary bladder. TCC is typically an irregular bladder wall mass with a broad-based attachment projecting into the urinary bladder lumen. The echogenicity is often mixed and has an overall appearance that can be poorly to moderately echogenic. It may also be partly mineralized, which can be confused for calculi. The masses are described most commonly in the bladder neck (trigone) region and dorsal bladder wall (Leveille et al. 1992); however, they can be seen at any location in the bladder (Figure 11.16). Because of the location of the ureteral papilla in the trigone region, unilateral or bilateral hydroureter may be encountered. It is common for the mass to extend into the proximal urethra. Dogs with TCC may have concurrent cystitis, urethritis, calculi, and/or blood clots.

A wide variety of other bladder tumor types are possible, including epithelial (squamous cell carcinoma) and mesenchymal tumors (botryoid rhabdomyosarcoma, chemodectoma, peripheral nerve sheath tumor, leiomyosarcoma, leiomyoma, fibroma, fibrosarcoma, hemangioma, hemangiosarcoma, lymphoma [Benigni et al. 2006], and mast cell tumor) (Figures 11.17–11.22). Ultrasonographic differentiation of tumor type and differentiation from non-neoplastic disease are often impossible without a biopsy. However, a mass with a smooth luminal surface and serosal extension is more likely to have a mesenchymal origin. Uncommonly, bladder tumors can diffusely invade the bladder wall (Figure 11.21B).

The most common urethral neoplasms in dogs include TCC, squamous cell carcinoma, and adenocarcinoma. Proximal urethral neoplasms are often caused by local spread of bladder or prostatic neoplasms. Urethral TCC has a markedly hyperechoic non-shadowing mucosal line and may be associated with hypoechoic thickening of the urethral wall (Figures 11.16B, 11.17) (Hanson and Tidwell 1996). Squamous cell carcinoma is most commonly associated with the distal urethra. Other types of neoplastic processes can compress or invade the urethra along its path (Figure 11.23).

Enlargement of the medial iliac, hypogastric, sacral, or superficial inguinal lymph nodes is not specific to bladder or urethral disease, but they should be located and measured to aid the staging of a suspected neoplastic disease. Due to dynamic changes within the urinary bladder wall with different volumes of urine and the variation between operators, the response of bladder wall to therapy can be difficult to assess accurately with ultrasound (Hume et al. 2010).

Calculi

High-frequency bladder ultrasound may have a similar accuracy as radiographic contrast procedures in calculi detection (Weichselbaum et al. 1999). However, ultrasound has a tendency to overestimate true cystolith size by several millimeters compared with other imaging modalities (Byl et al. 2010). Cystic or urethral calculi are usually mobile and collect in the dependent portion of the lumen. They are usually spherical, with a hyperechoic curvilinear interface. However, they can vary in number, size, and shape. A distal shadow is only variably present and is more likely seen with a higher transducer frequency and with calculi of a greater thickness and width and/or with

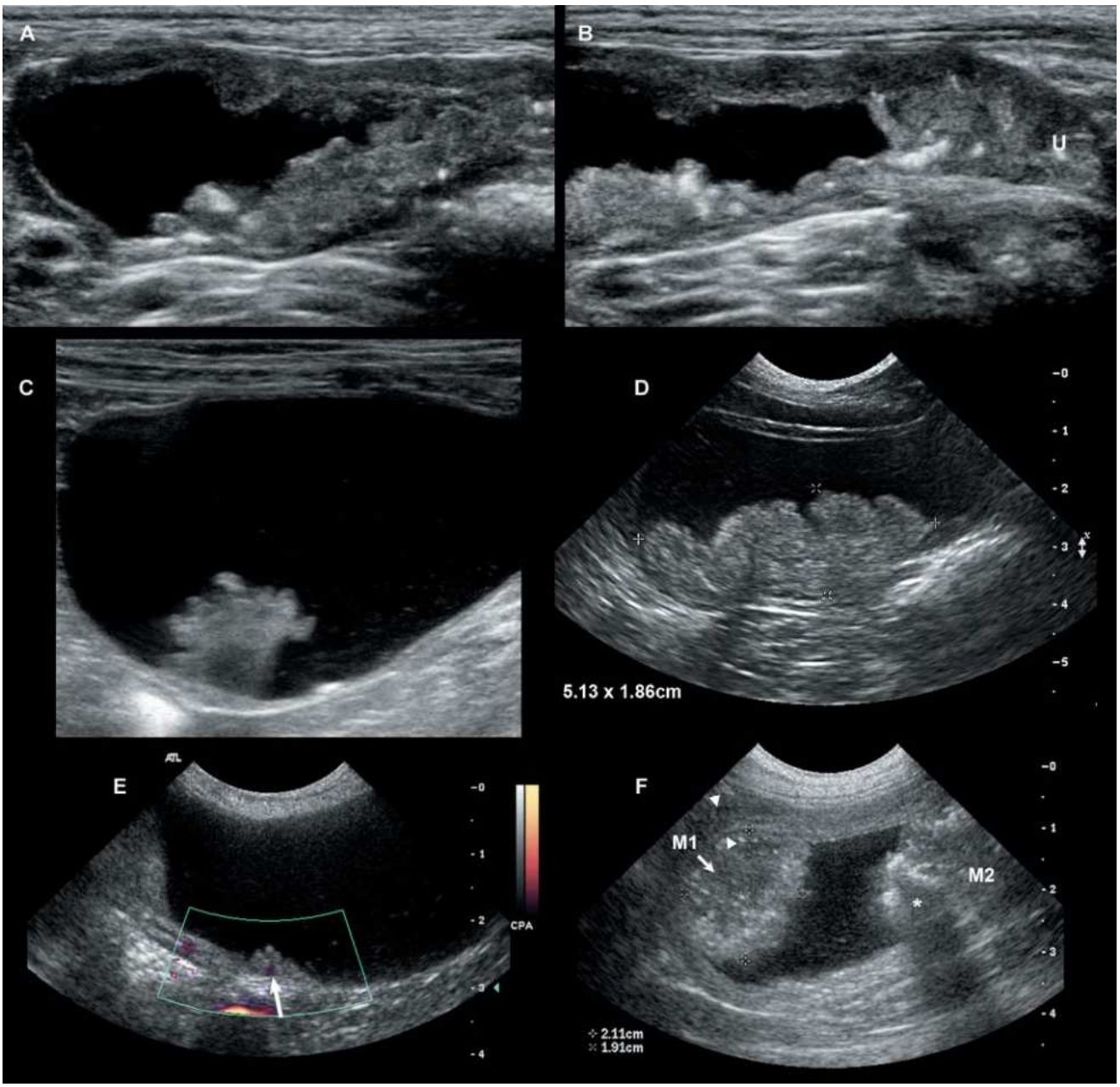


Figure 11.16. **Transitional cell carcinoma (TCC) in dogs. A:** Longitudinal sonogram of an extensive TCC affecting the ventral and dorsal bladder wall in a 10-year-old Lhasa Apso. **B:** In the same dog, the TCC extends caudally into the bladder neck and urethra (U). **C:** A cauliflower-shaped nodule arising from the craniodorsal wall was found incidentally in a dog presented for urinary obstruction secondary to a urethral calculus. It was confirmed as papillary non-infiltrating TCC after surgical removal. **D**: Longitudinal sonogram of a broad-based hyperechoic mass associated with the craniodorsal bladder wall, consistent with TCC. **E**: Longitudinal sonogram in another dog without urinary clinical signs in which focal irregular thickening of the dorsal bladder wall was detected incidentally. Color Doppler signal (arrow) confirmed that this lesion was attached to the bladder wall, as opposed to a blood clot. **F:** Two separate TCC masses (M1 and M2) in another dog with mineralization causing acoustic shadowing (*). The arrowheads delineate the apical bladder wall.

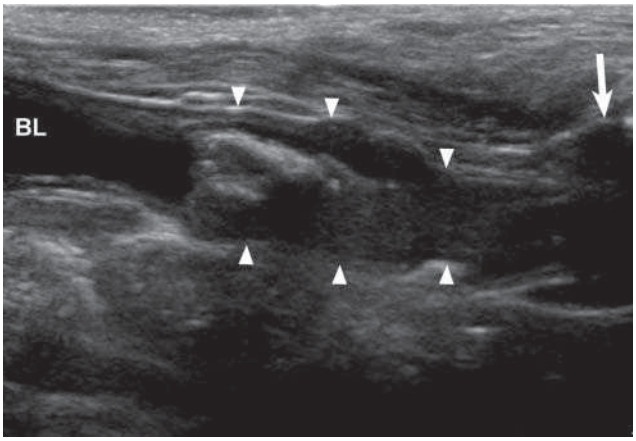


Figure 11.17. Urethral transitional cell carcinoma in a 14-year-old Cairn Terrier female. Longitudinal sonogram of the bladder neck (BL) and proximal urethra. The proximal urethra is thickened (arrowheads), and mineralized areas are present. The pubic bone (arrow) and its associated shadowing prevented a complete assessment of the lesion. A suction biopsy confirmed transitional cell carcinoma.

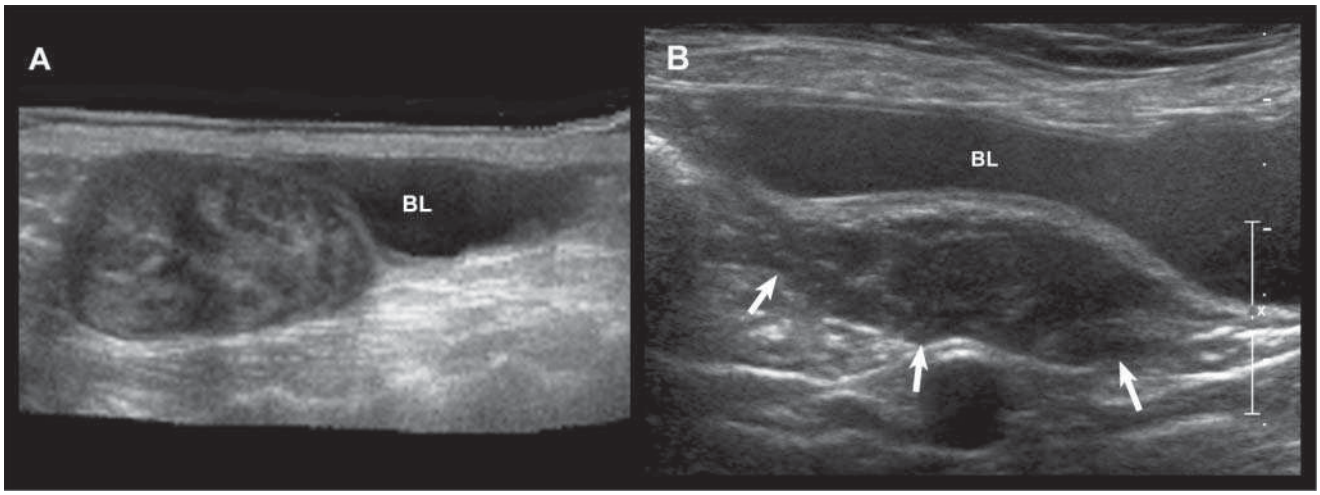


Figure 11.18. Bladder smooth muscle tumors in dogs. A: Longitudinal panoramic sonogram of a large echogenic mass deforming the contour of the bladder (BL). The mass was diagnosed as low-grade leiomyosarcoma**. B**: Longitudinal sonogram of the bladder of a large fusiform mass (arrows) deforming the craniodorsal wall of the bladder (BL). The mass was diagnosed as a leiomyoma.

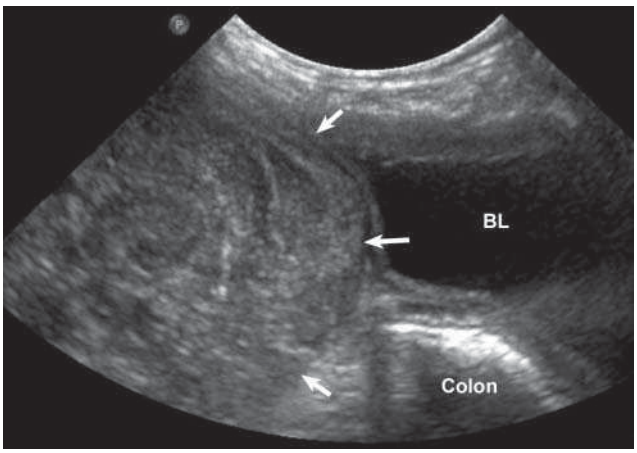


Figure 11.19. Bladder hemangiosarcoma in a dog. Longitudinal sonogram of a large (over 7 cm long) inhomogeneous mass (arrows) associated with the cranial bladder (BL) wall. The mass was removed surgically and the histopathologic diagnosis was hemangiosarcoma.

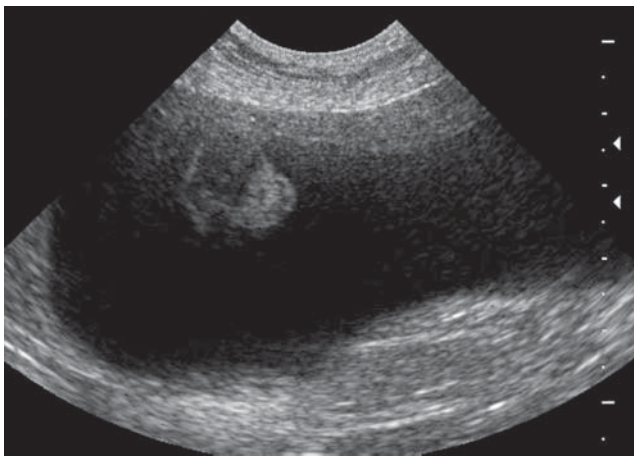


Figure 11.20. Bladder mast cell tumor in a dog. Longitudinal sonogram of a urinary bladder with a highly vascular, pedunculated, mixed-echogenicity mass originating from the cranioventral bladder wall. Cytology of the mass with special stains was consistent with a mast cell neoplasm.

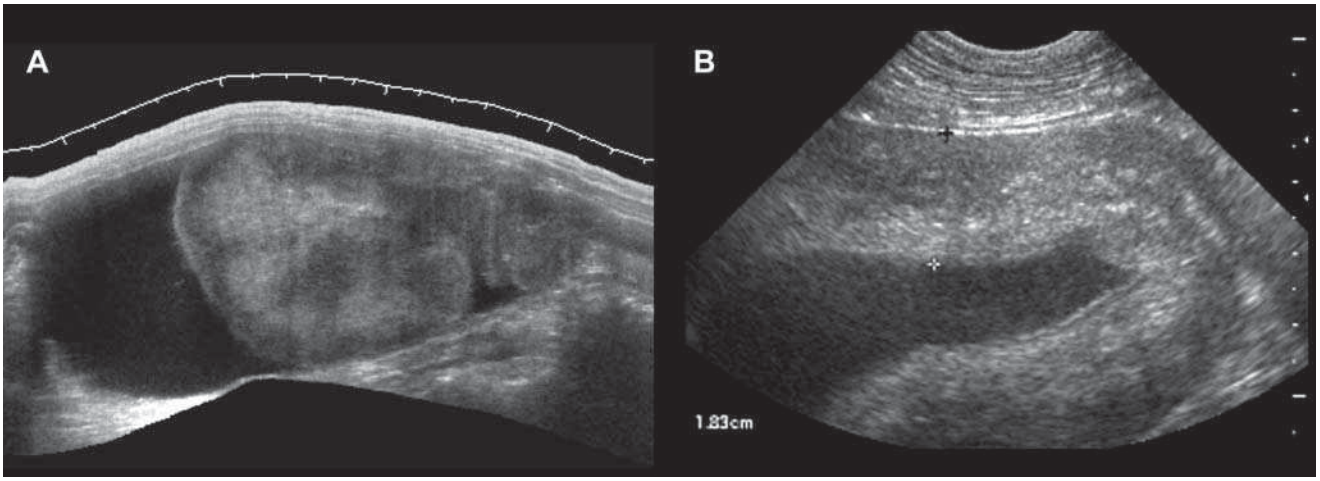


Figure 11.21. **Extensive bladder tumors in two dogs. A:** Panoramic longitudinal sonogram of a large caudal bladder mass involving the trigone of a dog. The histopathology obtained at necropsy revealed a poorly differentiated carcinoma. **B:** Longitudinal sonogram of the bladder of a 6-year-old Labrador Retriever with diffuse carcinomatous infiltration of the wall.

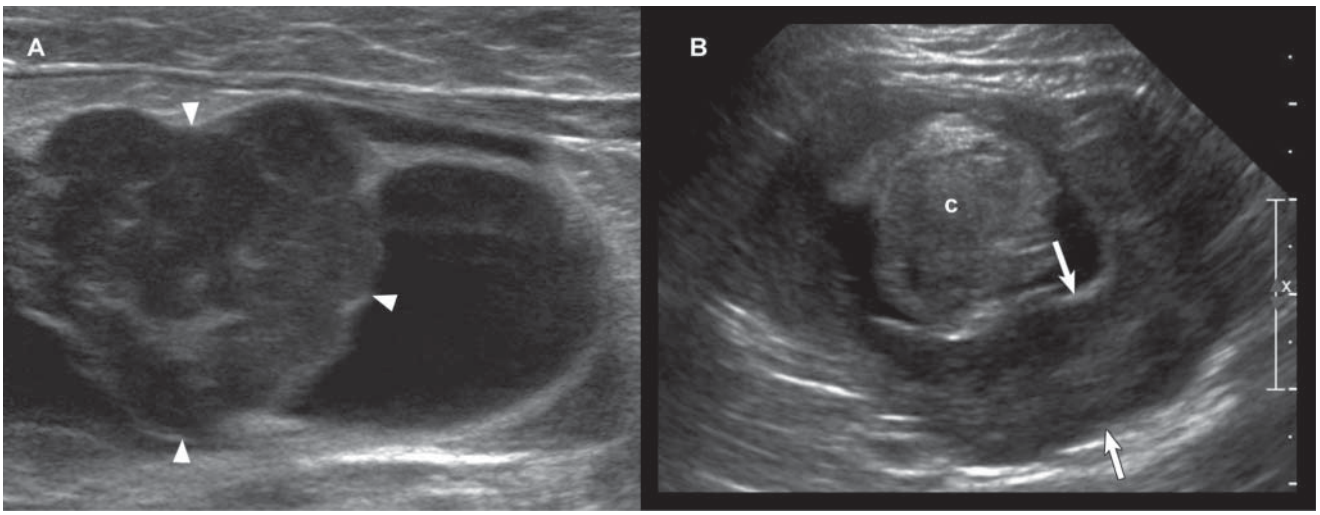


Figure 11.22. **Lymphoma in two cats. A:** A multilobulated, poorly echogenic mass (arrowheads) is deforming the cranial aspect of the bladder in this 11-year-old cat with multicentric lymphoma. **B:** In this 3-year-old cat with hematuria and straining to urinate, the bladder is unevenly but diffusely thickened (arrows) and an echogenic amorphous structure is filling most of the lumen; this represents a blood clot (c).

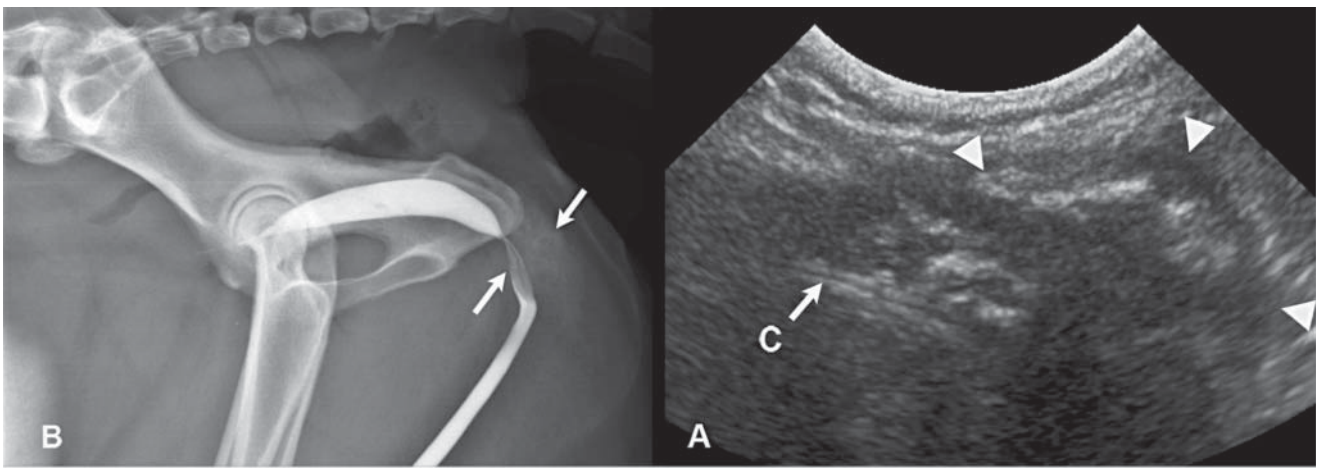


Figure 11.23. **Urethral osteosarcoma in a dog. A:** Positive-contrast retrograde urethrogram showing a mineral opacity mass (arrows) causing marked attenuation of the urethral contrast. **B:** Longitudinal sonogram of the caudal membranous urethra, which contains an indwelling catheter (arrow C). A hyperechoic shadowing mass (arrowheads) is caudodorsal to the urethra. The histopathologic diagnosis from an ultrasound-guided microcore biopsy was osteosarcoma.

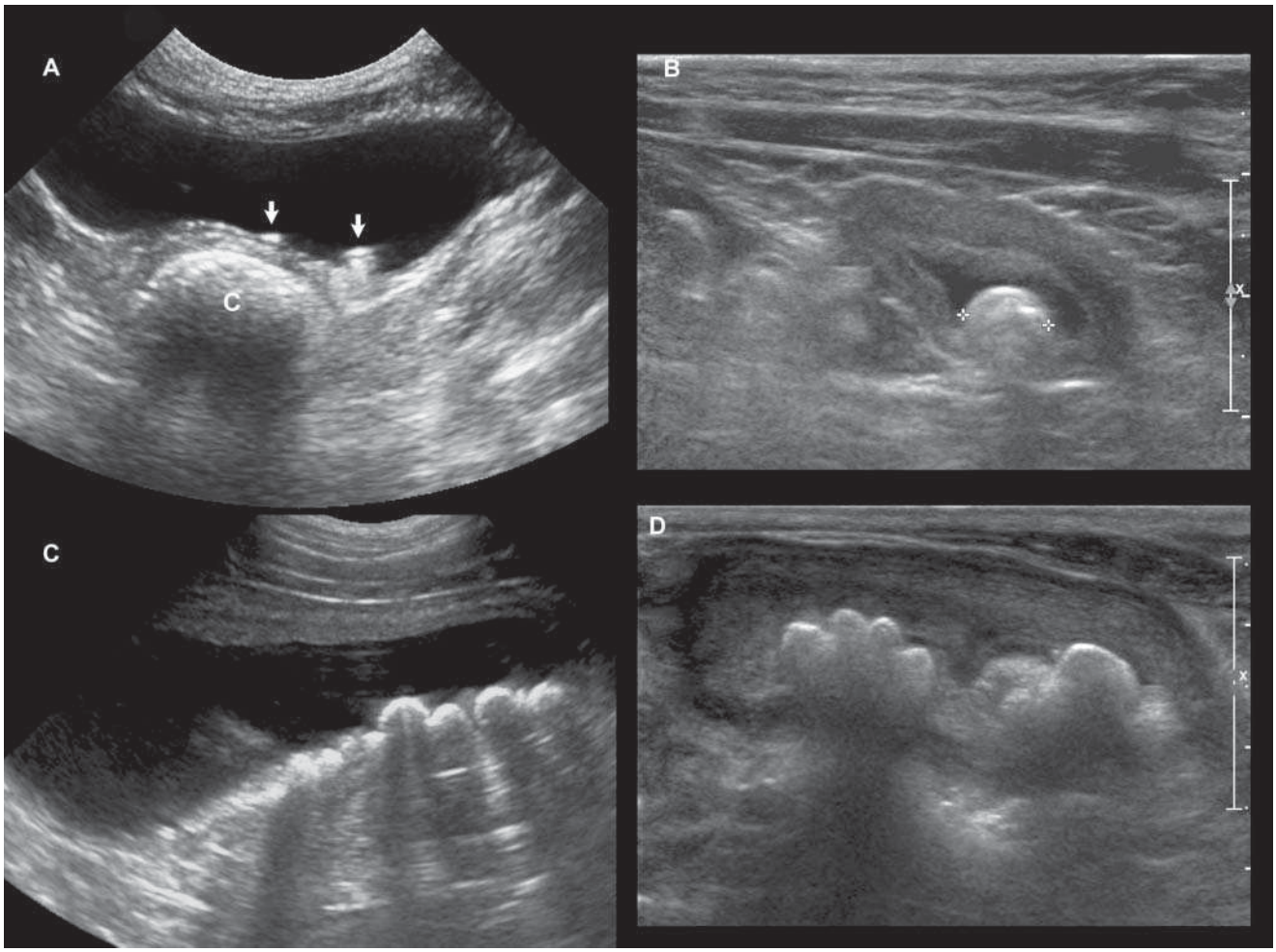


Figure 11.24. **Cystic calculi in dogs and cats. A:** Transverse sonogram of the urinary bladder showing two small hyperechoic structures associated with the dependent bladder wall (arrows) that are thought to represent small cystic calculi, even if acoustic shadowing is not present. Urinalysis revealed calcium oxalate crystalluria. The colon (C) is associated with acoustic shadowing. **B:** Longitudinal sonogram in a 3-year-old Ragdoll cat with a nearly collapsed and thickened bladder containing a spherical calculus (between calipers) associated with faint shadowing. **C:** Numerous, variable-size calculi are present in the bladder of a 3-year-old Australian Shepherd cross. **D:** Longitudinal sonogram of a collapsed and thickened bladder filled with numerous rounded calculi associated with shadowing.

an irregular surface (Figure 11.24). A reverberation artifact may also occur distal to cystic calculi. The presence or absence of these artifacts does not correlate with the composition of the calculus (Weichselbaum et al. 2000). Although the appearance is non-specific, crystalluria may be seen as a collection of swirling moderate-intensity intraluminal echoes. A collection of small calculi or mineralized sediment may generate a linear interface (Figure 11.25). This sediment usually suspends with gentle agitation of the urinary bladder, or with a change in position of the animal. Although generally less echogenic, pyuria may share similar features, appearing as an echogenic collection settling on the depending portion of the bladder (Figure 11.26).

When color flow Doppler is applied on the suspected calculus, a twinkle artefact can be observed (Andrulli et al. 2010). This useful artifact appears as a zone of rapidly flashing red and blue color signals (mimicking vascular turbulence), distal to a highly reflective structure, and helps to support the etiology as mineral calculi or sediment. (Figure 11.27)

Although the urethra cannot be evaluated completely with ultrasound, urethral calculi may be identified, particularly in the penile portion of the urethra in male dogs (Figure 11.28). Enlargement of the urinary bladder with dilation of the urethral lumen can be supportive of urethral obstruction (Figure 11.29).

The descending colon can indent and appear confluent with the dorsal wall of the urinary bladder.

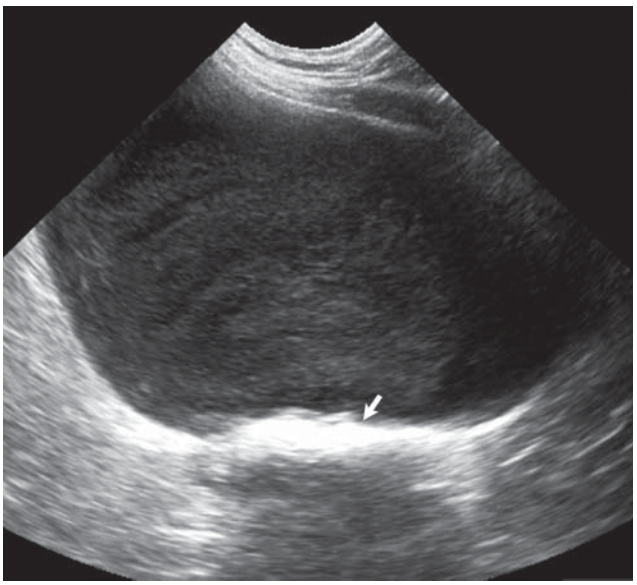


Figure 11.25. Bladder sediment in a dog. Transverse sonogram of diffusely echogenic urine and a collection of hyperechoic material (arrow) on the dependent bladder wall with distal shadowing. The urinalysis showed 3+ amorphous crystalluria.

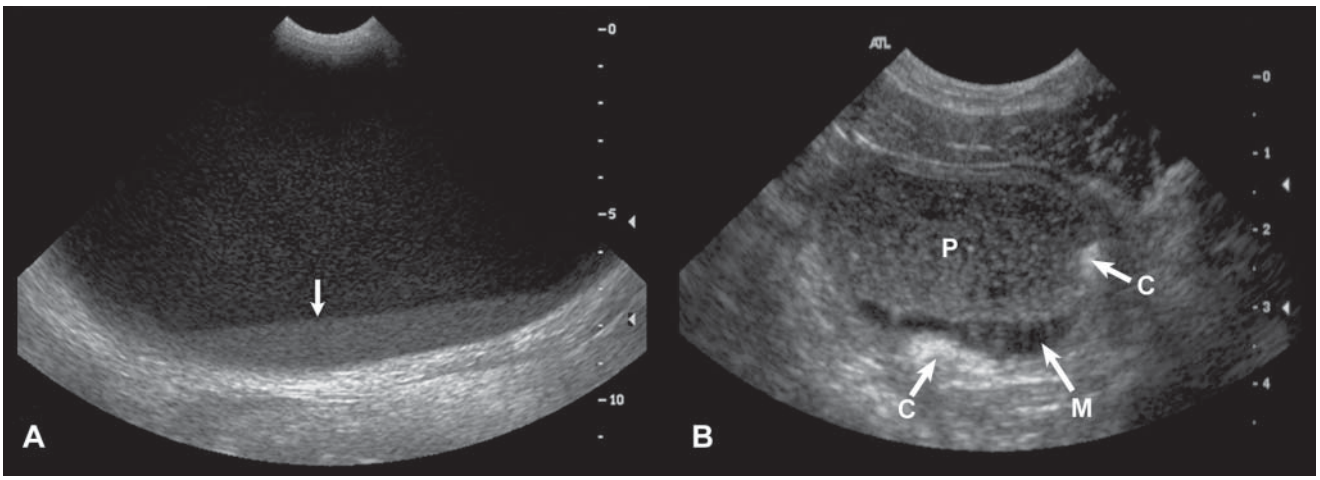


Figure 11.26. Pyuria in two dogs. A: Pyuria appears as non-shadowing, moderately echogenic sludge that progressively sediments during the exam. A straight horizontal border is seen (arrow). It should not be confused with a side-lobe artifact. **B:** In another dog with pyuria, a layer of hypoechoic mucus (M) with hyperechoic striations is found between the pus in suspension (P) and calculi (C) and the dorsal bladder wall.

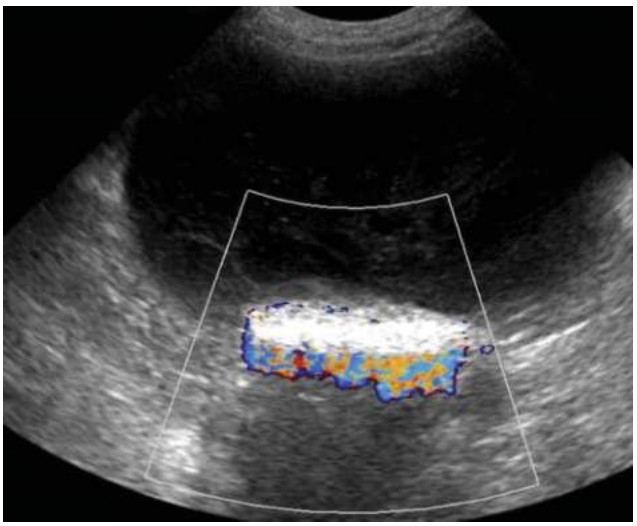


Figure 11.27. Twinkle artifact with calculi. Using color flow Doppler, an area of rapidly flashing colored signals is displayed when encountering mineralized structures. In this 5-year-old Beagle cross, the twinkle artifact is present distal to the small calculi and mineralized sediment seen in the bladder. This may be useful in detecting small calculi or mineralized sediments, especially in absence of shadowing artifact.

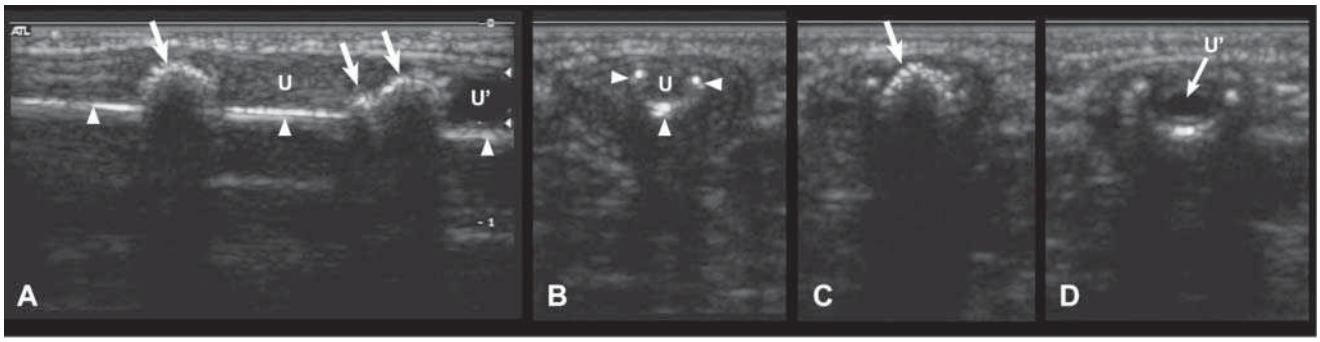


Figure 11.28. Urethral calculi in a dog. Longitudinal (**A**) and contiguous transverse (**B–D**) sonograms of the distal penile urethra in dog presented for urinary obstruction. Two larger, mildly irregular, hyperechoic calculi (arrows) with distal shadowing are lodged in the urethra (U), which is distended proximally (U′). Transverse image **B** was obtained distal to the most proximal (or caudal) calculus **(C)**, whereas image **D** was obtained just proximal (or caudal). The ventral portion of the os penis appears as a linear hyperechoic interface in the longitudinal plane (**A**, arrowheads) and is U-shaped in the transverse plane (B, arrowheads). On analysis, the calculi were made of calcium oxalates.

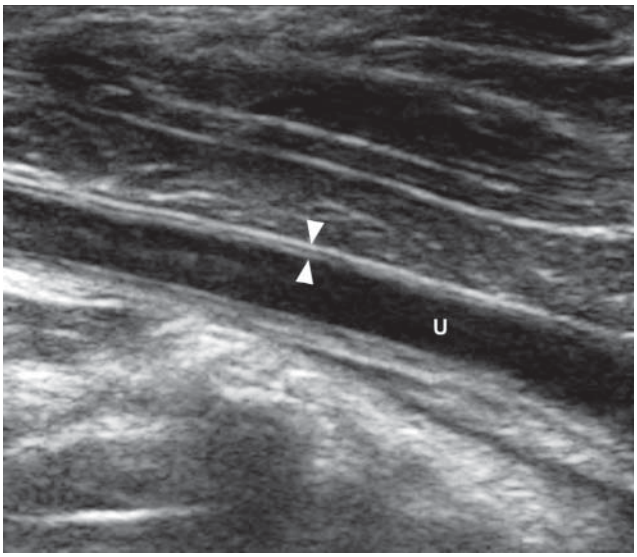


Figure 11.29. Urethral distension in a blocked cat. Longitudinal sonogram of the dilated urethra. The lumen (not normally visualized) contains nearly anechoic urine (U). Urethral wall layers can be visualized (arrowheads).

The hyperechoic interface and shadowing artifact generated by the colon can mimic a large cystic calculi (Figure 11.24A). Rotation of the transducer into the longitudinal plane will reveal the colon as a linear interface running the length of the image, whereas the calculi should remain approximately spherical. Additionally, repositioning the animal into a standing or lateral position should cause any calculi to fall to the dependent wall, whereas the colon remains in a dorsal location.

Intraluminal Blood Clots and Mural Hemorrhage

Blood clots and mural hemorrhage may be caused by bladder trauma, cystitis, a generalized bleeding disorder, or neoplasia. Blood within the urinary bladder lumen or wall can have a variable appearance and can mimic exuberant inflammatory disease or neoplasia. Intraluminal clots vary in echogenicity and range from thin linear structures to large round masses (Figure 11.30).

Mural hemorrhage may cause diffuse uniform wall thickening. Recheck examinations will help to differentiate neoplastic or inflammatory mural disease as bladder wall thickening secondary to systemic bleeding disorders resolves rapidly at the approximate rate of 1 mm/day once the underlying abnormalities are corrected (O'Brien and Wood 1998). Intraluminal blood clots can be differentiated from a neoplastic mass by their absence of color flow Doppler signal. In addition, the mobility of these intraluminal structures may also be demonstrated with repositioning of the patient.

Congenital Anomalies

Although rare, a variety of congenital urinary bladder abnormalities may be identified sonographically. They may predispose patients to incontinence or urinary tract infections, or may be incidental findings. Anomalous conditions include urachal diverticulum, patent urachus, urachal cysts, ureteroceles, and ectopic ureters.

Ureteroceles are cystic dilations of the terminal ureter within the urinary bladder. They can be subdivided

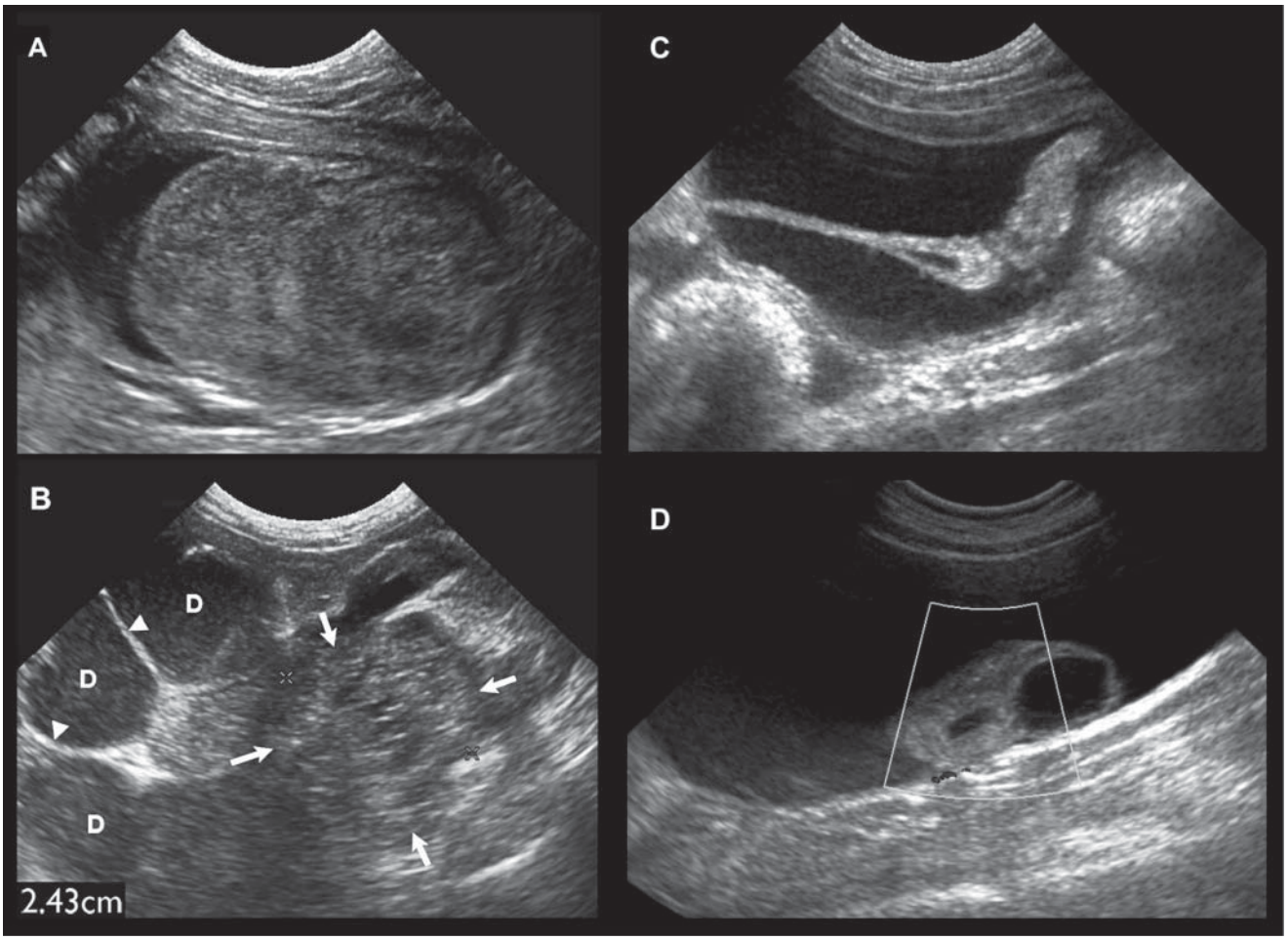


Figure 11.30. **Bladder blood clots dogs. A:** Longitudinal sonogram of the urinary bladder, which contains a smooth, ovoid, inhomogeneous, echogenicity mass. Differential diagnoses included a bladder neoplasm or a hematoma. **B:** A transverse sonogram of the right kidney of the same dog as in **A** with a 2.43-cm-diameter right hilar renal mass (arrows). The hyperechoic bands of tissue (arrowheads) radiating from the hilus to the periphery are characteristic of hydronephrosis. Echogenic urine is found in the dilated diverticuli (D), consistent with hemorrhage. At necropsy, the urinary bladder mass was a hematoma secondary to renal hemangiosarcoma. **C:** Longitudinal sonogram of the urinary bladder, which contains a floating linear hyperechoic structure of variable thickness. A urinalysis revealed numerous red blood cells highly suggestive of a suspended blood clot. **D:** A longitudinal sonogram of the bladder containing an amorphous structure with an echogenic periphery and an anechoic center. The mass had no identifiable color flow Doppler signal. This 5-year-old Golden Retriever passed a blood clot shortly after the examination.

as orthotopic or ectopic, depending on whether the ureters enter the bladder at a normal location. Ureteroceles are thin-walled, smooth, spherical, and cyst-like structures that protrude into the bladder lumen and are filled with anechoic fluid (Figure 11.31). Ectopic ureters may be identified ultrasonographically either by dilated ureters coursing beyond the dorsal bladder neck caudally or by an absence of ureteral jets in the trigone region (Figure 11.32; see Chapter 10).

A vesicourachal diverticulum is a fluid-filled structure that extends as a convex out-pouching of the bladder lumen, usually with a thin wall, although it can become thick and irregular in cases of chronic cystitis. These diverticuli can vary in size and are typically in cranioventral aspect of the urinary bladder wall (Figure 11.33). Diverticulum may also occur at other locations because of trauma or cystitis.

Trauma and foreign bodies

A positive-contrast retrograde cystourethrogram is the preferred method of diagnosing rupture of the

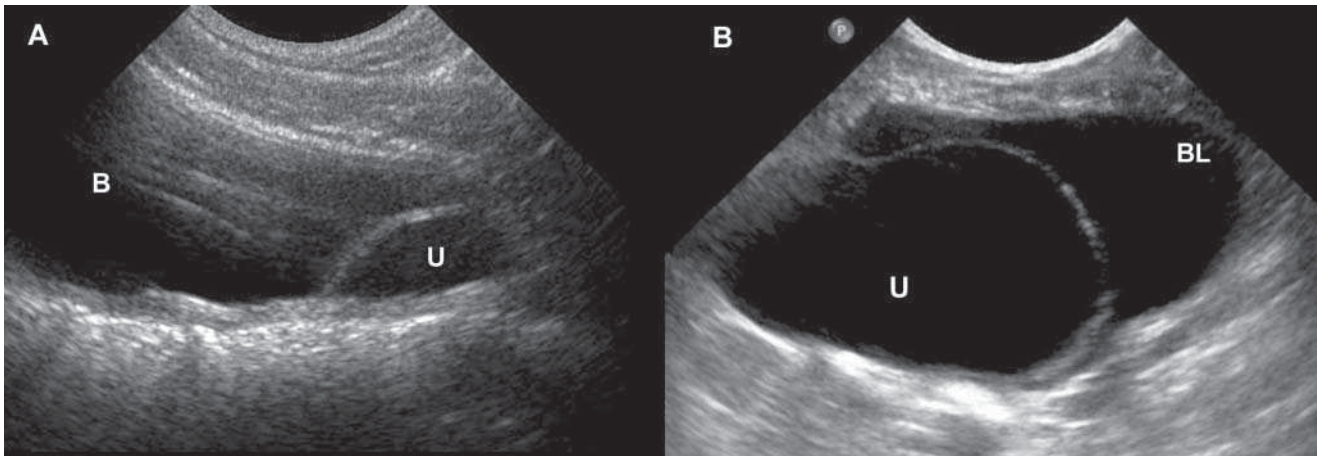


Figure 11.31. **Ureterocele in two dogs. A**: Longitudinal sonogram of the urinary bladder (B) with a thin-walled cystic outpouching of the left ureter (U). The cystic structure contains anechoic fluid and is consistent with a ureterocele. Image courtesy of C. Warman, Veterinary Specialist Group, Auckland, New Zealand. **B:** Transverse sonogram of the bladder with the markedly dilated ureterocele (U) protruding into the bladder lumen (BL). Notice the thin wall of the ureterocele. This 2-year-old Dachshund also had severe right hydroureter and hydronephrosis.

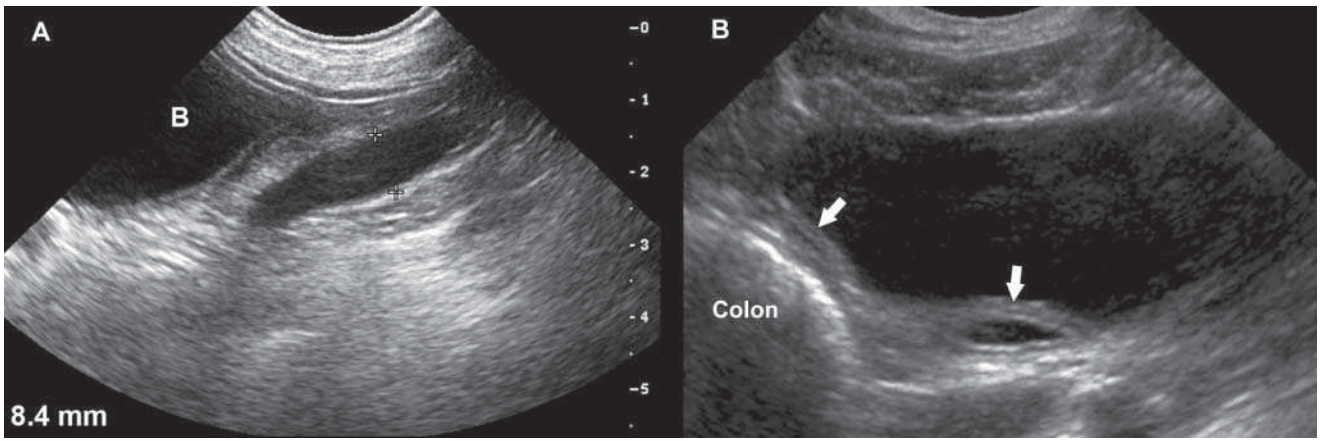


Figure 11.32. **Ectopic ureter. A:** Longitudinal sonogram of a dilated ureter (8.4-mm cursors), which was followed from the left kidney and courses caudal to bladder neck (B), consistent with an ectopic ureter**. B:** Transverse sonogram of the bladder, showing the intramural trajectory of both mildly dilated ureters (arrows) in this 1-year-old Labrador with long-standing incontinence. The bilateral intramural ectopia was confirmed on cystoscopy.

urethra or urinary bladder. On ultrasound, the ruptured urinary bladder wall is thickened (Figure 11.34), and there is abdominal effusion of echogenicity that depends on urine cellularity. Calculi or other debris can also accumulate in the peritoneal cavity. A hypoechoic bladder wall defect or tract may be seen occasionally.

This should be distinguished from a refraction artifact associated with the cranial aspect of the urinary bladder when abdominal effusion is present. The interpretation of the artifact is aided by a concurrent edge shadow and absence of bladder wall thickening (Figure 11.35).

Iatrogenic wall trauma during cystocentesis is very uncommon, but may be encountered, especially if the wall is abnormal (Figure 11.36).

At times, surgical sites may appear abnormally thickened as the result of suture reaction. In these instances, the wall remains excessively thickened and a suture pattern can be seen (Figure 11.37).

On rare occasions, foreign bodies can be found in the bladder lumen, they can include grass

Figure 11.34. **Sonogram and contrast radiographic study of a ruptured urinary bladder in a dog. A:** Longitudinal sonogram. The indwelling, saline-filled Foley catheter can be seen caudally (arrow). There is marked thickening of the bladder wall (arrowheads) and a loss of visualization of the bladder lumen. Abdominal effusion is also noted. Because of the suspicion of bladder rupture, a positive-contrast cystogram was performed. Hyperechoic foci are noted in the dorsally displaced bladder lumen, associated with acoustic shadowing (*), consistent with calculi. **B:** Lateral radiograph of the caudal abdomen following a retrograde positive-contrast cystogram. Contrast is free within the peritoneal space. At surgery, the bladder rupture and hematoma were identified.

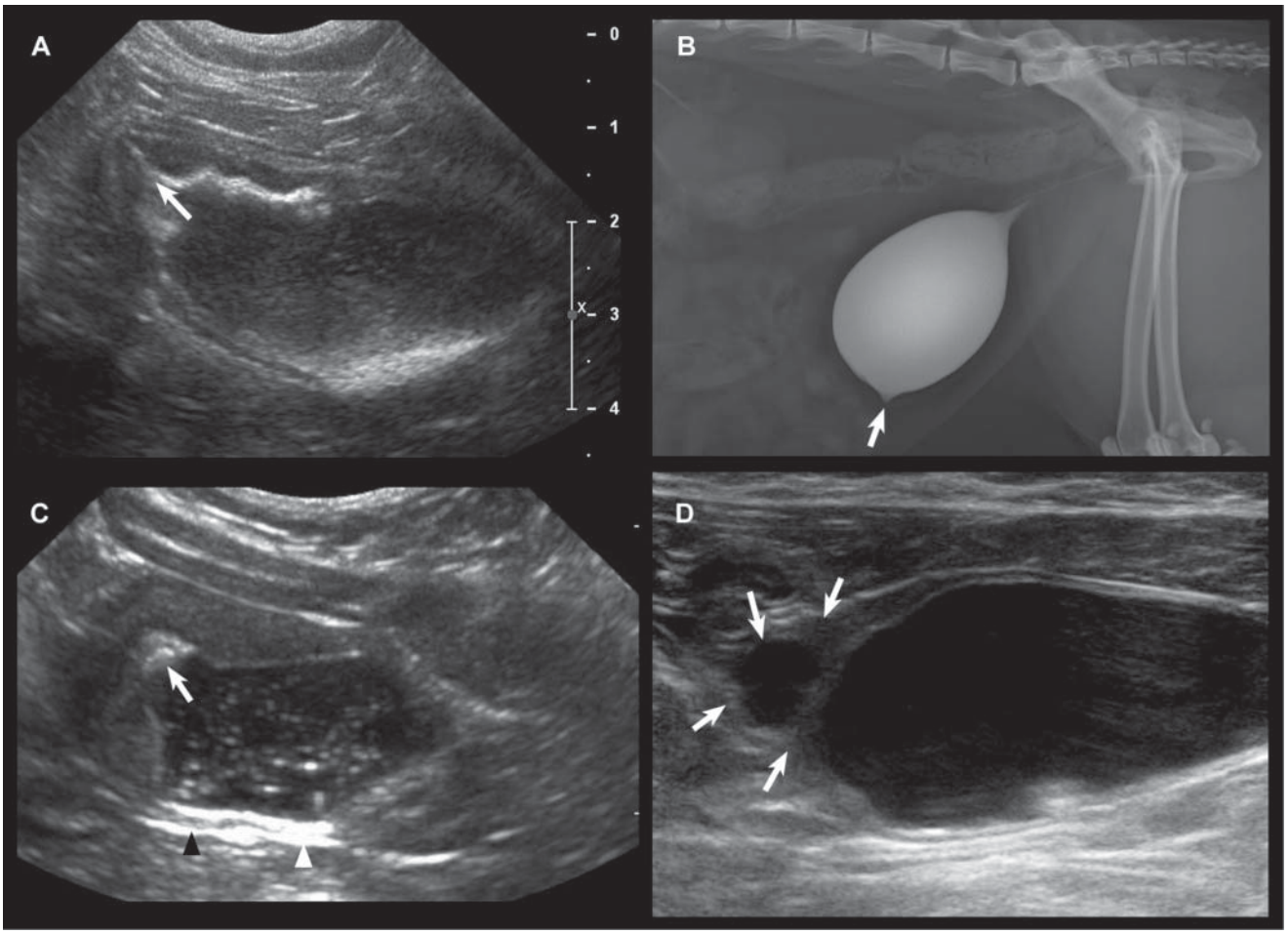


Figure 11.33. **Vesicourachal diverticulum in two cats. A:** Longitudinal sonogram of the bladder in a 6-year-old castrated male cat presented for pollakiuria and recurrent episodes of urethral obstruction. A focal depression (arrow) is present in the cranioventral aspect of the bladder, which is otherwise thickened and irregular. A moderate amount of echogenic sediment is present in the lumen. **B:** The lateral radiograph of the positive-contrast cystogram displays the urachal diverticulum (arrow). **C:** Longitudinal sonogram of the bladder of a 5-year-old cat with chronic cystitis. A similar depression is noted in the cranioventral aspect of the bladder and a small amount of hyperechoic sediment is collected at this level. **D:** Three months later, a well defined sacculation is visible in the cranioventral bladder wall. On sequential exams, calculi were seen lodged in the diverticulum. Images A and B courtesy of C. Warman, Veterinary Specialist Group, Auckland, New Zealand.

Figure 11.36. **Traumatic cystocentesis.** A blind cystocentesis was performed in this 11-year-old cat. **A:** On this longitudinal sonogram, there is thickening of the cranioventral bladder wall, supportive of cystitis, and small calculi were seen on the dependent portion of the bladder. In addition, a hyperechoic line (arrow) is crossing the wall, representing the tract of the recent cystocentesis. **B:** A small amount of fluid (arrowheads) is present near the bladder neck and the regional fat is hyperechoic. Two weeks later, these features had resolved.

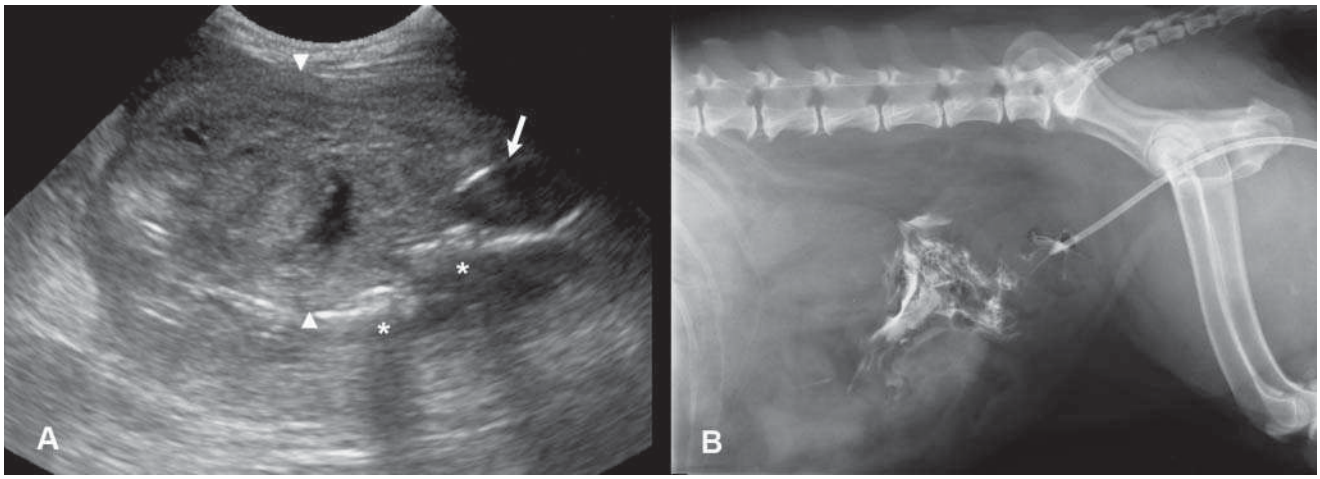


Figure 11.34. Sonogram and contrast radiographic study of a ruptured urinary bladder in a dog. (for full caption, see facing page)

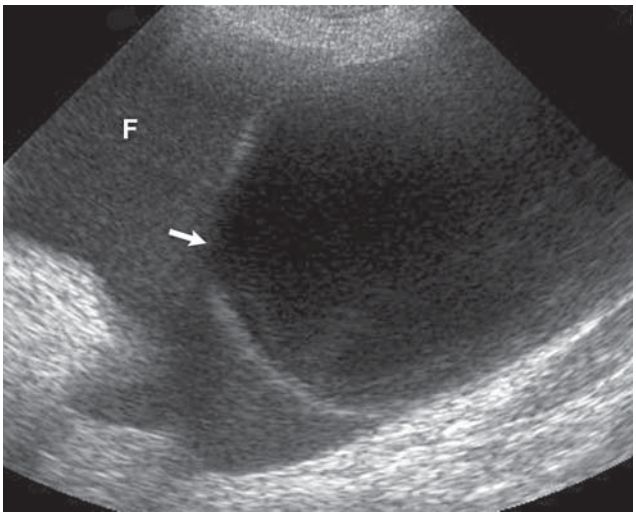


Figure 11.35. Refraction artifact versus bladder rupture in a dog. Longitudinal sonogram of the bladder containing anechoic urine surrounded by echogenic abdominal effusion (F). The refraction artifact at the cranial aspect of the bladder mimics bladder wall rupture (arrow), but no bladder wall rupture is present.

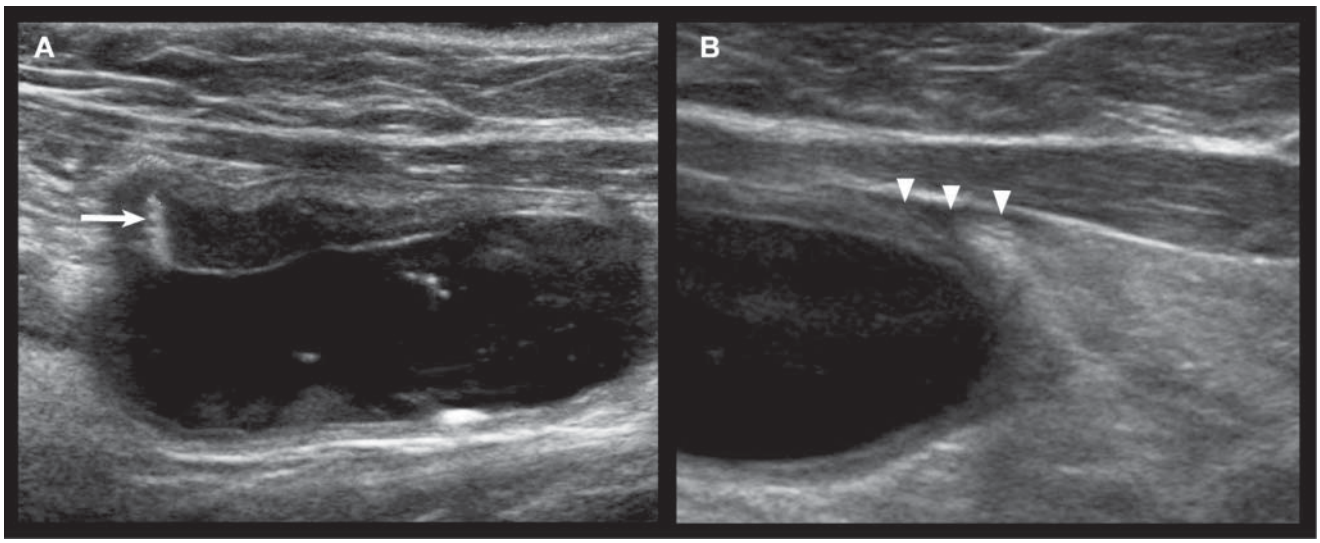


Figure 11.36. Traumatic cystocentesis. (for full caption, see facing page)

Figure 11.38. **Luminal foreign bodies. A:** Longitudinal sonogram of the bladder of a 13-year-old cat recently catheterized. At removal, the tip of the catheter was missing. A small, linear structure (arrow) with faint double line was seen on the dependent portion of the bladder. The catheter tip was then removed via cystoscopy. **B:** Longitudinal sonogram of the bladder of a 6-year-old corgi with severe cystitis, mucosal hyperplasia (not shown), mineralized sediment (not shown), and fibrin strands (arrowhead). A rounded anechoic structure (between cursors) with a central double line was seen floating in the bladder. This is presumed to represent a broken off Foley catheter balloon. **C:** Longitudinal sonogram of the prostatic urethra (arrowheads) in a dog with a grass awn (arrow) lodged in the lumen. Image courtesy of Dr Ulrich Zeyen, Centro Veterinario Specialisito, Rome, Italy.

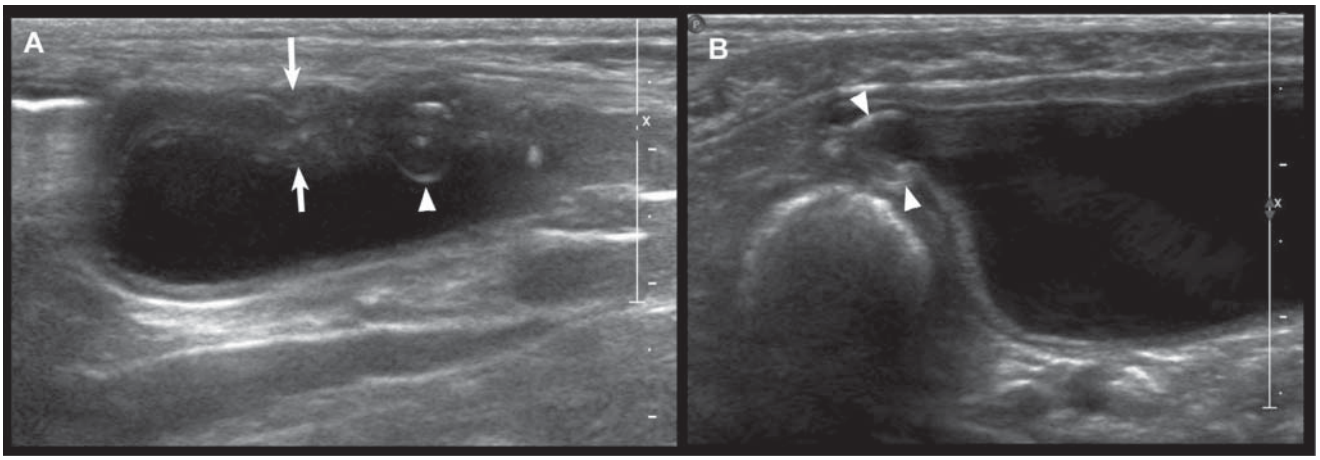


Figure 11.37. **Post-surgical incision recheck. A:** An 11-year-old corgi had a cystotomy performed 11 weeks earlier for ureteral calculi. The bladder wall is thickened, irregular (arrows) and a curvilinear structure (arrowhead) can be seen within the wall, probably representing suture material. This reactive incision was removed and was diagnosed as marked submucosal edema with neutrophilic and lymphocytic inflammation. **B:** On this longitudinal sonogram of a dog with surgery performed 3 months earlier (same dog as on Figure 11.16C), there is a focal thickening of the cystotomy site, and a curvilinear structure (arrowheads) is noted within the incision, probably representing suture material. The cranioventral wall is also mildly thickened (not shown) and a small amount of mineralized sediment is seen (not shown) in the dependent portion of the bladder. This likely represents cystitis, but the presence of suture visible in the lumen may contribute to a focal inflammation.

awn (Cherbinsky et al. 2010), or parts of catheters (Figure 11.38A,B).

Special Procedures

Cystocentesis

Once sufficient bladder distension is determined by ultrasonography, a guided cystocentesis can be safely performed. The skin can be prepared with an alcohol-soaked swab. A 22-gauge, 1- or 1.5-inch needle attached to a 5-ml syringe is used. Starting with a longitudinal image of the urinary bladder, the needle is placed just cranial to the transducer while trying to keep the needle aligned with the plane of the ultrasound beam. The needle appears as a fine linear hyperechoic interface that often causes distal reverberation or shadowing artifacts (Figure 11.39).

Suction Biopsy

Cystoscopic biopsy and ultrasound-guided suction biopsy are the preferred methods of confirming bladder or urethral neoplasia. Percutaneous fine-needle aspiration of suspected TCC in the bladder is not recommended because the technique can lead to regional spread of the tumor along the needle tract.

The suction biopsy is performed under heavy sedation or general anesthesia. An appropriately sized red-rubber catheter with side holes is connected to a 20-ml syringe and is placed aseptically into the urinary bladder. The urinary bladder (if empty) is filled with a small volume of sterile saline to provide an acoustic window and better delineate the abnormal tissue to sample. Only a small volume is required because the bladder wall collapsing around the catheter aids the aspiration of the targeted tissue

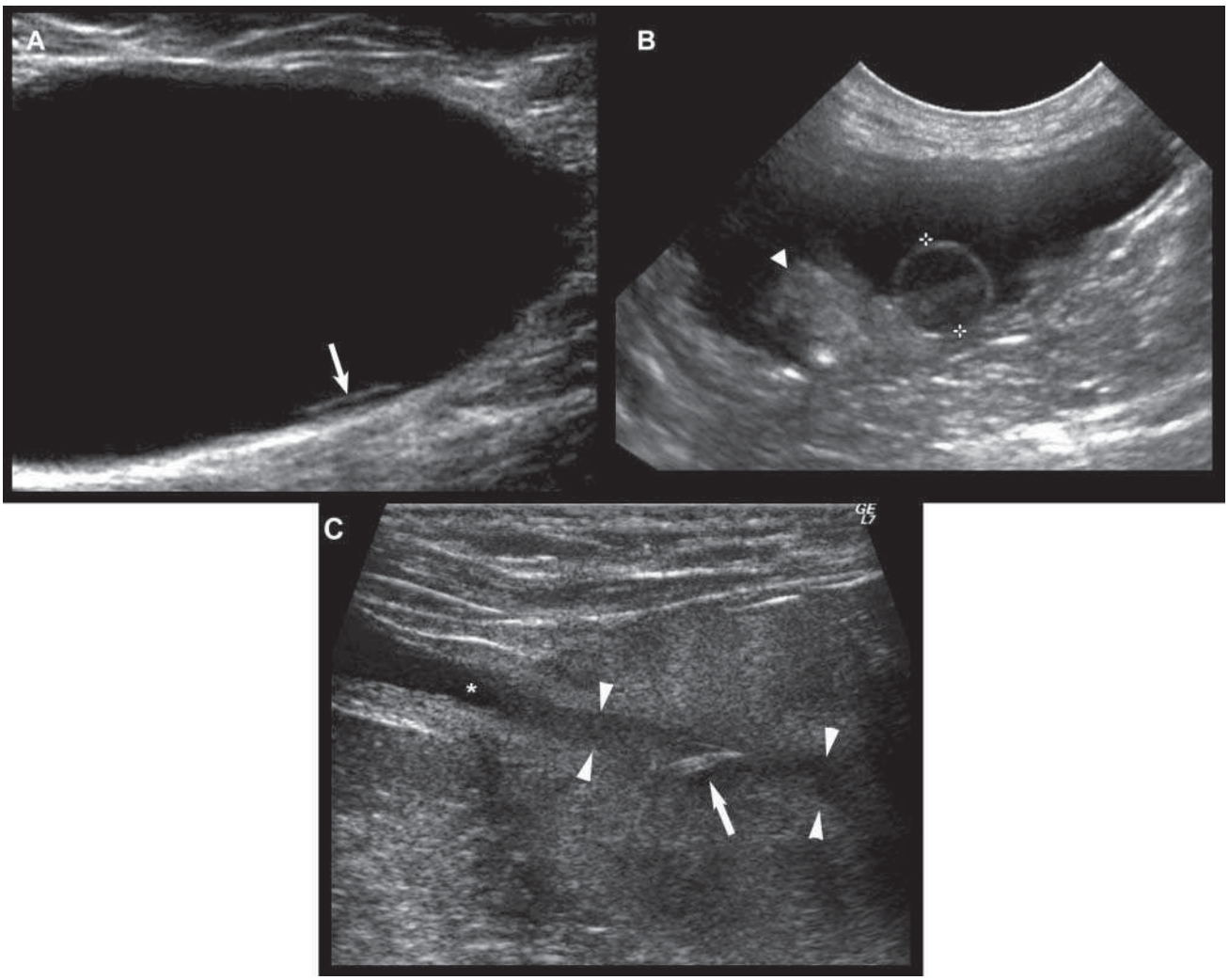


Figure 11.38. Luminal foreign bodies. (for full caption, see facing page)

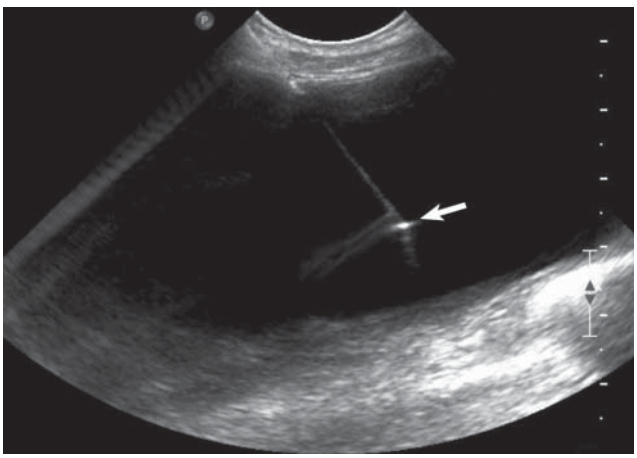


Figure 11.39. Cystocentesis in a dog. Longitudinal sonogram of the urinary bladder during cystocentesis. The fine hyperechoic line created by the needle and the hyperechoic needle tip (arrow) within the lumen are visualized.

rather than urine. The catheter tip is visualized within the urinary bladder as a pair of parallel hyperechoic lines with a hypoechoic lumen, and the side holes of the catheter can also be identified as discrete hypoechoic defects (Figure 11.40). The catheter tip can then be positioned adjacent to the bladder mass or wall thickening to be biopsied. High-frequency ultrasound may enable more specific placement by visualization of the catheter holes.

The syringe plunger is pulled back. If urine is obtained, then the catheter is rotated to reposition the side hole adjacent to the tissue of interest. Once negative pressure can be maintained, the pressure is applied and released three to four times, collecting tissue from the adjacent mucosa. Suction is applied and held, with the aim being to adhere the catheter to the mass. The urinary catheter is abruptly withdrawn 4–6 cm from the bladder while the suction is held,

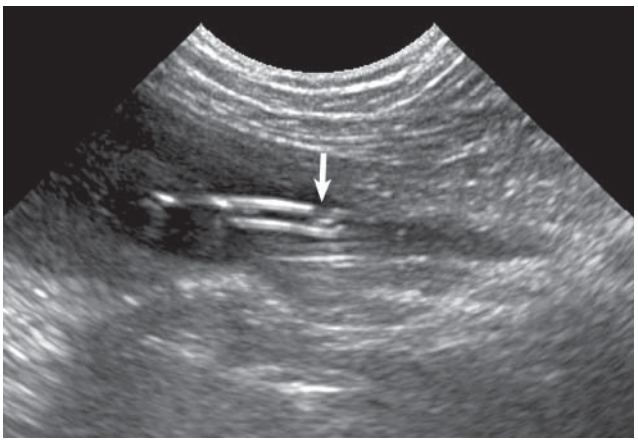


Figure 11.40. Suction biopsy in a dog. Longitudinal sonogram of the urinary bladder and an indwelling red-rubber catheter during a suction biopsy. The catheter walls are hyperechoic and the lumen is hypoechoic. A small defect in the catheter wall (arrow) corresponds to one of the side holes in the catheter, which can be guided into the desired location of the biopsy.

with the aim of pulling a larger fragment of tissue from the mass. The contents of the catheter are then emptied into formalin or smeared on a slide for cytology. If the procedure is repeated, a new red-rubber catheter is used. Intravesicular hemorrhage is a potential complication of this procedure (Lamb et al. 1996).

Interventional Guidance and Monitoring

Ultrasound has a role to play in the implementation and monitoring of interventional lower urinary tract procedures. The monitoring of treatment response, especially in cancer patients, is useful. On rare occasions, seeding of TCC can be seen in adjacent tissues following previous cystocentesis or post-surgically (Figure 11.41). Although limited to the cranial aspect of the urethra, the non-invasive nature of ultrasound allows more frequent monitoring of urethral stent lumen patency (Figure 11.42). Ultrasound has also been advocated to help guide and monitor the palliative cystoscopic laser ablation of transitional cell tumors (Cerf et al. 2012), or can assist the flushing procedure to distinguish amorphous mucus accumulation from soft-tissue mass (Figure 11.43).

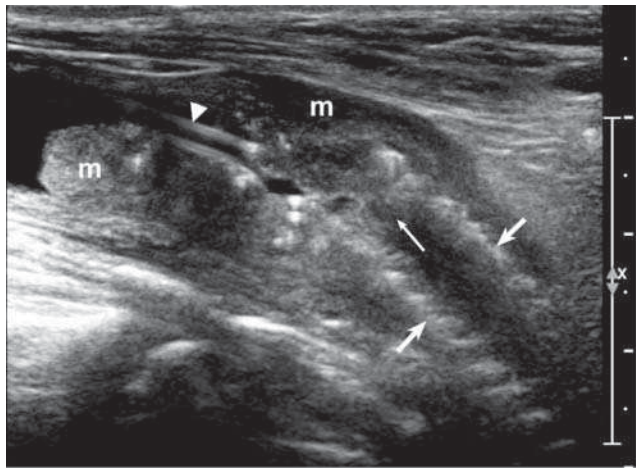


Figure 11.42. Urethral stent in a dog. Longitudinal sonogram of a dog with progressive transitional cell carcinoma (TCC) mass (m) at the bladder neck and urethra. After a few months of placement of a urethral stent (large arrows), the stent patency is compromised (small arrow) by echogenic structure obliterating its lumen. Part of a ureteral catheter is seen (arrowhead).



Visit our website at **www.SmallAnimalUltrasonography.com** for complementary video clips with annotations:

- Normal bladder/urethra
- Cystitis
- Polypoid cystitis
- Calculi
- Blood clot
- Ureteral jet
- Bladder tumors

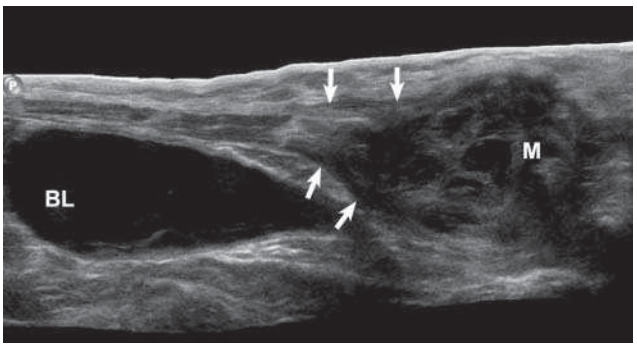


Figure 11.41. Transitional cell carcinoma (TCC) seeded in the rectus abdominis of a 10-year-old Maine Coon cat. Longitudinal panoramic sonogram of the caudal abdomen, including the bladder (BL) and the irregular mass (M), invading part of the rectus abdominis (arrowheads). This cat had a TCC mass previously removed surgically. There is no evidence of tumor recurrence at the bladder site.

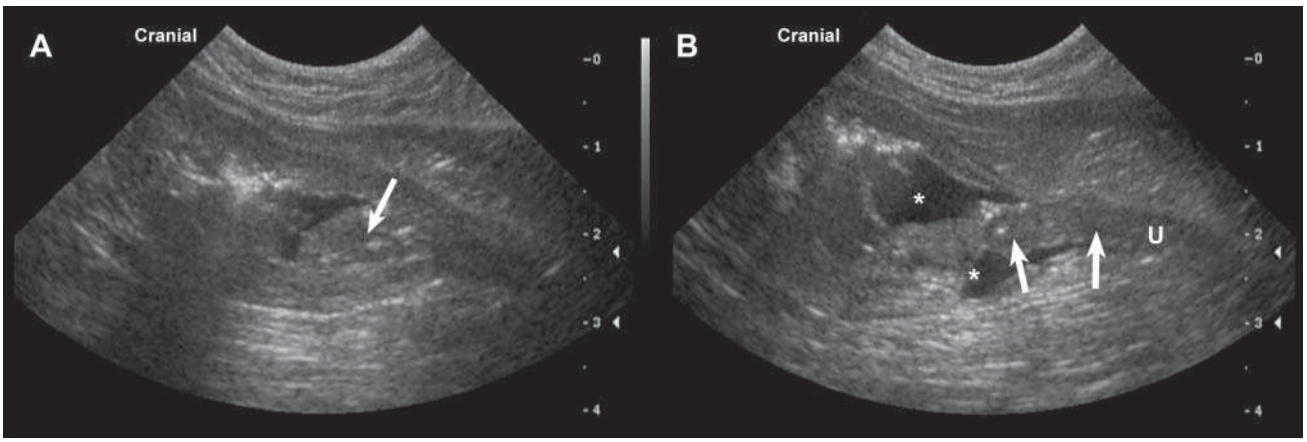


Figure 11.43. Mucus plug in an obstructed cat. A: Initial longitudinal sonographic images showed a hyperechoic mass (arrow) silhouetting with the dorsal bladder wall at the trigone. **B**: Once saline was injected through a urinary catheter, the mass detached from the wall, forming a tubular structure delineated by anechoic urine mixed with saline (*). This plug extended into the urethra (U). It was removed surgically and confirmed to represent mucus mixed with cellular debris and crystals.

References

Adin CA, Chew DJ, Heng HG, Townsend KL, Karnik K (2011) Bladder inversion and secondary hematuria in a 6-month-old domestic shorthair cat. J Am Vet Med Assoc 239:370–373.

Andrulli S, Turin A, Bigi MC, Ravani P, Trunchieri A, Locatelli F (2010). Colour Doppler twinkling in kidney stones: artifact or sign? NDT Plus 3:151–154.

Benigni L, Lamb CR, Corzo-Menendez N, Holloway A, Eastwood JM (2006) Lymphoma affecting the urinary bladder in three dogs and a cat. Vet Radiol Ultrasound 47: 592–596.

Byl KM, Kruger JM, Kinns J, Nelson NC, Hauptman JG, Johnson CA. (2010) In vitro comparison of plain radiography, double-contrast cystography, ultrasonography, and computed tomography for estimation of cystolith size. Am J Vet Res 71:374–380.

Cerf DJ, Lindquist EC (2012) Palliative ultrasound-guided endoscopic diode laser ablation of transitional cell carcinomas of the lower urinary tract in dogs. J Am Vet Med Assoc 240:51–60.

Cherbinsky O, Westropp J, Tinga S, jones B, Pollard R (2010). Ultrasonographic features of grass awns in the urinary bladder. Vet Radiol Ultrasound 51:462–465.

Finn-Bodner ST (1995) The urinary bladder. In: Cartee RE, Selcer BA, Hudson JA et al., eds. Practical Veterinary Ultrasound. Philadelphia: Lea and Febiger, pp 210–235.

Geisse AL, Lowry JE, Schaeffer DJ, Smith CW (1997) Sonographic evaluation of urinary bladder wall thickness in normal dogs. Vet Radiol Ultrasound 38:132–137.

Hanson JA, Tidwell AS (1996) Ultrasonographic appearance of urethral transitional cell carcinoma in ten dogs. Vet Radiol Ultrasound 37:293–299.

Hume C, Seiler G, Porat-Mosenco Y, Caceres A, Shofer F, Sorenmo K (2010) Cystosonographic measurements of canine bladder tumours. Veterinary and Comparative Oncology 8:122–126.

Lamb CR, Trower ND, Gregory SP (1996) Ultrasound-guided catheter biopsy of the lower urinary tract: Technique and results in 12 dogs. J Small Anim Pract 37:413–416.

Le Boedec K, Pastor ML, Lavoué R, Reynolds BS (2011) Pseudomembranous cystitis, an unusual condition associated with feline urine outflow obstruction: Four cases. J Feline Med Surg 13:588–593.

Leveille R, Biller DS, Partington BP, Miyabayashi T (1992) Sonographic investigation of transitional cell carcinoma of the urinary bladder in small animals. Vet Radiol Ultrasound 33:103–107.

Martinez I, Mattoon JS, Eaton KA, Chew DJ, DiBartola SP (2003) Polypoid cystitis in 17 dogs (1978–2001). J Vet Intern Med 17:499–509.

O'Brien RT, Wood EF (1998) Urinary bladder mural hemorrhage associated with systemic bleeding disorders in three dogs. Vet Radiol Ultrasound 39:354–356.

Petite A, Busoni V, Heinen MP, Billen F, Snaps F (2006) Radiographic and ultrasonographic findings of emphysematous cystitis in four nondiabetic female dogs. Vet Radiol Ultrasound 47:90–93.

Taylor, AR, Barr JW, Hokamp JA, Johnson MC, Young BD (2012) Cytologic diagnosis of disseminated histoplasmosis in the wall of the urinary bladder of a cat. J Am Anim Hosp Assoc 48:203–208.

Weichselbaum RC, Feeney DA, Jessen CR, Osborne CA, Dreytser V, Holte J (1999) Urocystolith detection: Comparison of survey, contrast radiographic and ultrasonographic techniques in an in vitro bladder phantom. Vet Radiol Ultrasound 40:386–400.

Weichselbaum RC, Feeney DA, Jessen CR, Osborne CA, Dreytser V, Holte J (2000) Relevance of sonographic artifacts observed during in vitro characterization of urocystolith mineral composition. Vet Radiol Ultrasound 41:438–446.

CHAPTER TWELVE

Adrenal Glands

Marc-André d'Anjou[1,2] and Dominique Penninck[3]

[1] *Centre Vétérinaire Rive-Sud, Brossard, Québec, Canada*
[2] *Faculté de médecine vétérinaire de l'Université de Montréal, Saint-Hyacinthe, Québec, Canada*
[3] *Department of Clinical Sciences, Cummings School of Veterinary Medicine, Tufts University, North Grafton, MA, USA*

Preparation and Scanning Technique

The adrenal glands are small, paired structures located in the craniodorsal abdomen, medial and often cranial to the ipsilateral kidney, and adjacent to the aorta (left) and caudal vena cava (right) (Figure 12.1) in the retroperitoneal space. The cells of the adrenal cortex produce cortisol and other corticoids, aldosterone, androgens, estrogens, and progestins, whereas the chromaffin cells of the medulla produce catecholamines (Feldman and Nelson 2004). The adrenal glands are a key component of the endocrine system, and their deranged function can produce a wide range of clinical signs, which may be vague or non-specific. The ultrasonographic evaluation of the adrenal glands may be technically challenging, particularly in large dogs, but their assessment is considered part of a complete abdominal scan in both dogs and cats. Although the glands are small, a competent sonographer using good-quality equipment can identify both glands in most patients. For a ventral or lateral approach, the mid-abdominal hair coat should be clipped caudal to the costal arch and extend laterally to the level of the lumbar musculature and over the last few intercostal spaces on the right. Evaluation of the adrenal glands requires a sound knowledge of the regional anatomy and is facilitated by the use of convex probes with small footprints, as these can be more easily manipulated. In small patients, high-frequency linear probes are recommended for both adrenals as they produce images of higher spatial resolution and diagnostic quality. Due to its location, the right adrenal gland may more difficult to assess with these probes, because of their larger footprint and narrow field of view. Sedation may be helpful in evaluating agitated, aggressive, or painful patients, and in obese patients, because it relaxes the abdomen and allows the operator to apply pressure with less patient discomfort.

Sonography of the Normal Adrenal Glands

In Dogs

Normal ultrasound features are illustrated in Figure 12.1. The normal adrenal glands are hypoechoic to the surrounding fat and well defined. They may also exhibit a thin hyperechoic rim running parallel to the capsule, representing the junction between cortex and medulla, or a more uniformly hyperechoic medulla. The presence of well-demarcated cortex and medulla is considered by the authors to be supportive of normality. The left gland has an elongated bilobed shape, frequently described as resembling a peanut. The right adrenal gland has a more complex shape. Its cranial pole is often folded or V-shaped, and is therefore more difficult to clearly visualize. Its caudal pole is elongated and more consistently identified.

The adrenal glands are accessible from a ventral or lateral approach, in dorsal or lateral recumbency, respectively. Gas, ingesta, and feces in the gastrointestinal tract can limit their access. When scanning patients in dorsal recumbency, it may be helpful to tilt them to enable placement of the probe further dorsally. Gentle pressure may be necessary to move an overlying segment of bowel. When scanning patients in lateral recumbency, the probe is placed on the upper side of the abdomen as far dorsal as possible, just ventral to the lumbar transverse processes, to minimize interference from interposed gas in the small intestine and colon.

Atlas of Small Animal Ultrasonography, Second Edition. Edited by Dominique Penninck and Marc-André d'Anjou.
© 2015 John Wiley & Sons, Inc. Published 2015 by John Wiley & Sons, Inc.
Companion website: www.SmallAnimalUltrasonography.com

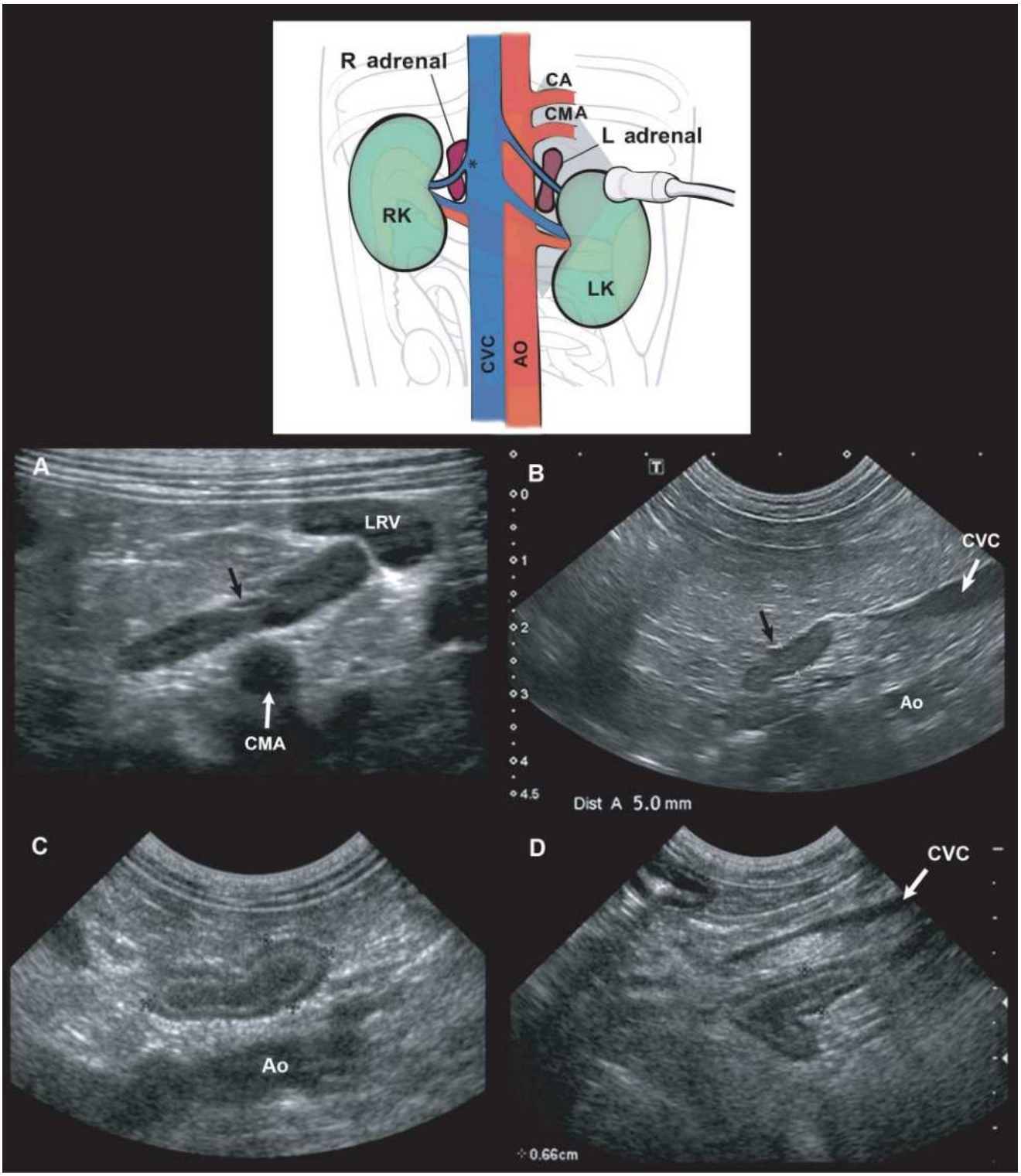


Figure 12.1. Normal adrenal glands in dogs. The schematic drawing illustrates the localization of the adrenal glands in a dog in dorsal recumbency (ventral approach). Note the phrenicoabdominal vein (*) extending ventral to mid-portion of each adrenal gland. AO, aorta; CA, celiac artery; CMA, cranial mesenteric; CVC, caudal vena cava; LK, left kidney; RK, right kidney. **A:** Dorsal oblique plane image of a normal canine left adrenal gland. Note the elongated bilobed shape with a portion of a phrenicoabdominal vessel in cross-section within the ventral groove (black arrow). The anechoic structure caudal and lateral to the gland is the left renal vein (LRV), whereas the cranial mesenteric artery (CM) lies deep to the mid-body of the adrenal gland. **B:** Sagittal oblique plane image of a normal right adrenal gland in a Golden Retriever. The gland is fusiform and is parallel to the aorta (Ao) in the far field. It is also closely apposed to the caudal vena cava (CVC), which is compressed by the transducer. Hyperechoic borders of the phrenicoabdominal vein are noted at the mid-ventromedial aspect of the gland (black arrow) **C, D:** Sagittal plane images of normal left **(C)** and right **(D)** adrenal glands in a clinically normal toy Poodle. A well-defined hyperechoic rim is at the corticomedullary junction. The left gland is slightly oblique in regard to the aorta (Ao), located dorsally, and has a characteristic peanut shape, and the right gland appears as an arrowhead cranially. The CVC is compressed in the near field.

To identify the **left adrenal gland**, the probe is placed on the left abdominal wall, slightly caudal to the last rib, more ventrally if the patient is placed in dorsal recumbency, or laterally if in right lateral recumbency. The probe is smoothly fanned using a sagittal to dorsal plane depending on the conformation of the patient, the presence of overlying intestinal content and patient recumbency. The left kidney is initially imaged in the longitudinal plane, before the probe is moved medially to find the aorta. The probe is then rotated until a longitudinal image of the aorta is obtained. The gland is located at the left ventral aspect of the aorta, just cranial to the origin of the left renal artery, and ventral or caudal to the origin of the cranial mesenteric and celiac arteries (Figures 12.1, 12.2). Alternatively, the probe can follow the left renal vein in its transverse plane from a longitudinal view of the kidney, to identify the adrenal gland just cranial as the vein crosses the aorta. In thin animals, the gland is closely apposed to the aorta. As the quantity of body fat increases, it is laid down around the adrenal gland, increasing separation from the aorta, but also providing contrast and making the gland more prominent. The long axis of the left adrenal gland may be slightly tilted in comparison with the long axis of the aorta, and the probe may need to be rotated until the length of the left adrenal gland is maximized. The phrenicoabdominal vein may be seen as two fine, hyperechoic parallel lines obliquely crossing the mid-body of the adrenal gland (Figure 12.1A). The phrenicoabdominal vessels may be quite small and not seen on B-mode images, but blood flow can usually be seen with color Doppler examination (Figure 12.2B).

To identify the **right adrenal gland**, the probe is placed on the ventrolateral aspect of the right abdominal wall, just caudal to the last rib and oriented craniodorsally. Using an oblique longitudinal plane, the probe is fanned dorsal and ventral from the right kidney until the caudal vena cava is identified. A common error is to apply too much pressure to the abdominal wall, which collapses the caudal vena cava and prevents its identification. The caudal vena cava may appear to pulse because of referred motion from the adjacent aorta, but may be distinguished from the aorta by applying mild or moderate pressure, which will cause the vessel to collapse (Figures 12.1D, 12.3). Alternatively, Doppler interrogation reveals craniad, low-velocity venous flow within the vena cava that appears blue in standard color flow Doppler, whereas the aorta shows a pulsatile, high-velocity red color signal. The vena cava and aorta are close together in the mid-abdomen, and in some dogs both vessels can be seen in the same scan plane, and become separate more cranially. Once the vena cava is imaged in longitudinal plane, the probe is gently moved laterally to identify the right adrenal gland that often partly impinges on the lumen of that vein. Its caudal pole is flatter and more easily identified, whereas its cranial pole if often folded. It may be necessary to place the probe in one of the last two or three intercostal spaces if the gland cannot be imaged by angling the probe cranially from a position caudal to the last rib (Brinkman et al. 2007)

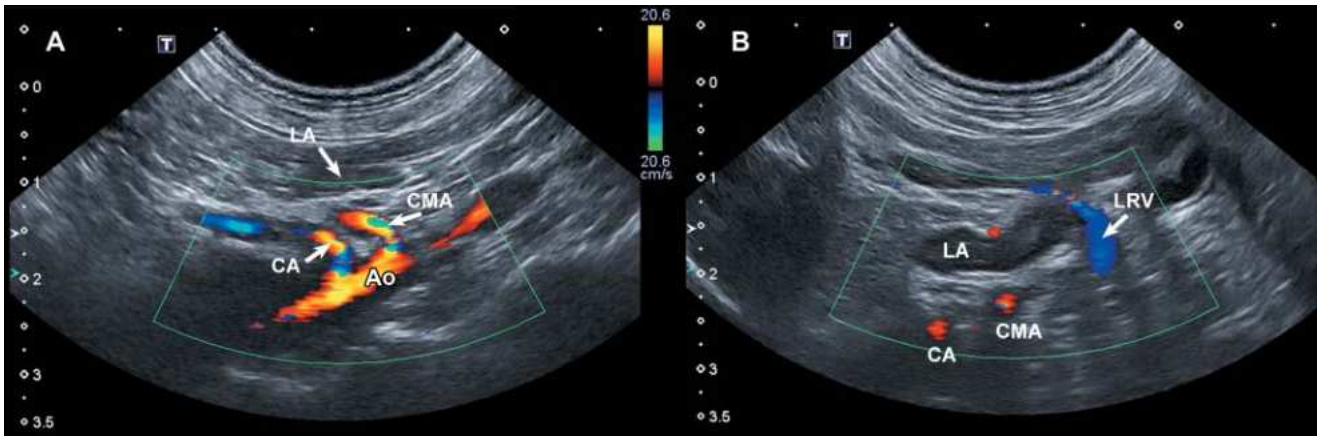


Figure 12.2. Vascular landmarks for the left adrenal gland in dogs. A, B: Sagittal sonographic images of a normal left adrenal gland and nearby vascular landmarks in a small-breed dog in dorsal recumbency. The left adrenal (LA) lies ventrolateral and somewhat caudal to the celiac artery (CA) and cranial mesenteric artery (CMA), as they exit the aorta (Ao). The gland is also located just cranial to the left renal vein (LRV) that crosses the ventral border of the aorta to reach the caudal vena cava. Note the color pattern of these vessels on color Doppler that depends on the direction of blood flow. Color flow aliasing is recognized as a layered pattern of colors in the central portion of the celiac and cranial mesenteric arteries due to high velocity (see Chapter 1 for more information on this artifact).

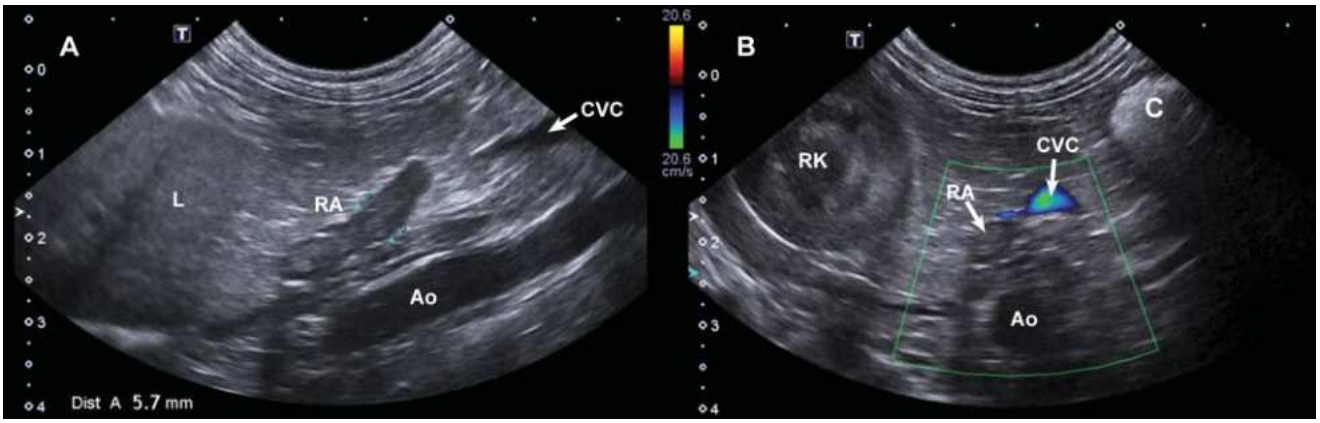


Figure 12.3. Normal right adrenal gland in a Labrador Retriever. Sagittal **(A)** and transverse **(B)** sonographic images in which the right adrenal gland (RA) is seen in proximity to important vascular landmarks. It lies between the caudal vena cava (CVC) and the aorta (Ao), caudal to the liver (L) and dorsomedial to the right kidney (RK). The CVC is collapsed as pressure is applied by the sonographer to get closer to the gland in this large dog. Note the distinction between the hyperechoic medulla and hypoechoic cortex, which is used by the authors as a sign of normality. C, colon.

(Figure 12.1). This approach works better in small dogs because pressure cannot be used to bring the gland closer to the probe.

A wide range of normal adrenal sizes has been reported in dogs of different breeds (see Table 12.1 for practical reference). The left adrenal gland is 3–16 mm in maximum diameter and 10–50 mm long. The right adrenal gland is up to 3–14 mm in maximum diameter and 10–39 mm long (Barthez et al. 1995; Grooters et al. 1995; Hoerauf and Reusch 1996; Douglass et al. 1997). The broad range of reported sizes reflects that patients selected for inclusion were described as normal, young, old, healthy, or not showing signs of any endocrine disease, and these studies may have included dogs with subclinical or non-functional adrenal lesions. The maximum diameter of the adrenal gland at the caudal pole is most representative of adrenal size and is generally used for discriminating normal dogs from those with adrenal hyperplasia or neoplasia. Studies have shown that adrenal measurements vary in dogs of different sizes and may vary from left to right (Choi et al. 2011; de Chalus et al. 2012). It must, however, be pointed out that patient positioning and probe angulation may affect this measurement, which is also limited by the spatial resolution of the system used. Given the potential for measuring errors, particularly for deep glands in large dogs, this reference number should be combined with other features, such as the shape and echogenicity of the gland.

Table 12.1
Range of measurements in longitudinal plane for normal adrenal glands in dogs and cats based on the literature and used by the authors

	Thickness or width (mm)[a]	Length (mm)[b]
Dogs	6–8	10–50
Cats	3.5–4.5	10–11

[a]Normal range assuming the shape and demarcation of the gland is normal.
[b]Length measurement considered less relevant since glands are often not fully linear.

In Cats

The adrenal glands in cats are found by using a similar approach to that employed in dogs. In most cats, scanning the area medial to the kidney and adjacent to the aorta or caudal vena cava is sufficient to identify the adrenal glands. The same vascular landmarks as used in dogs can also be used to find the feline adrenal glands. The feline adrenal gland is ovoid and uniformly hypoechoic (Figure 12.4). With high-frequency transducers, one can sometimes distinguish between cortex and medulla. In normal cats, both adrenal glands are typically 10–11 mm long and 3.5–4.5 mm in maximum thickness (Cartee et al. 1993; Zimmer et al. 2000; Zatelli et al. 2007; Combes et al. 2012). Small hyperechoic foci may be found in otherwise normal adrenal glands of older cats (Combes et al. 2012) (Figure 12.5). These are believed to indicate microscopic calcification and may be associated with acoustic shadowing depending on their size and the type of transducer used.

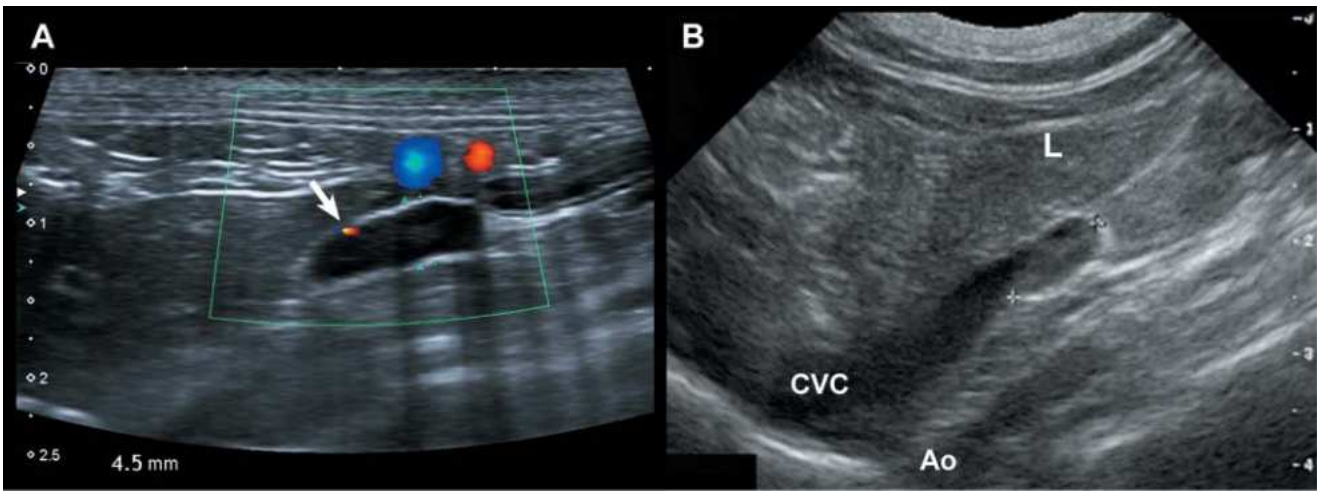


Figure 12.4. **Normal adrenal glands in cats. A:** Sagittal sonographic image of a normal feline left adrenal gland. The gland is ovoid (between the cursors, 4.5 mm in thickness), lying dorsal to the left renal vein and artery, with blue and red color Doppler signals, respectively. The left kidney being more mobile in cats, these vessels change in position in regard to the gland. Note the small phrenicoabdominal artery (arrow) at its ventral border. **B:** Sagittal image of a normal right adrenal gland in another cat. The gland appears as an ovoid hypoechoic structure (between the cursors, 1 cm in length), and the medulla is slightly more echogenic than the cortex. The caudal vena cava (CVC) and aorta (Ao) are in the same plane. L, liver.

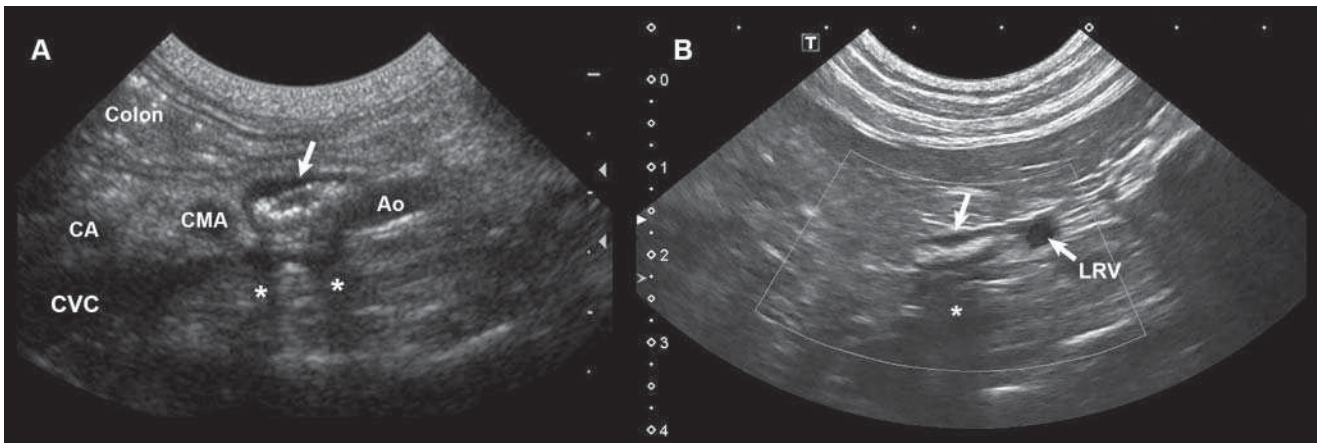


Figure 12.5. **Incidental adrenal mineralization in two old cats.** Sagittal oblique sonographic images of variably mineralized left adrenal glands (arrows) in two cats. The mineralization results in acoustic shadowing (*) in each case, but without evidence of adrenomegaly. Similar changes were apparent on the right side. Vascular landmarks are noted. Ao, aorta; CA, celiac artery; CMA, cranial mesenteric artery; CVC, caudal vena cava; LRV, left renal vein.

Sonographic Findings in Adrenal Disorders

Cushing's Syndrome

Cushing's syndrome or hyperadrenocorticism is one of the most common endocrinopathies in dogs. Ultrasound is frequently used as part of the medical database in these dogs (Behrend et al. 2002). However, it must be remembered that, although ultrasound may provide useful data, it cannot be used alone in diagnosing hyperadrenocorticism. Pituitary-dependent hyperadrenocorticism (PDH) accounts for approximately 80% of dogs with hyperadrenocorticism. If a patient's history, clinical signs, and laboratory test results support a diagnosis of hyperadrenocorticism, PDH should be suspected if both adrenal glands appear symmetrically enlarged (Barthez et al. 1998; Feldman and Nelson 2004) (Figure 12.6).

Unfortunately, the adrenal glands may measure within the normal range in some cases of PDH or may demonstrate unilateral or asymmetrical

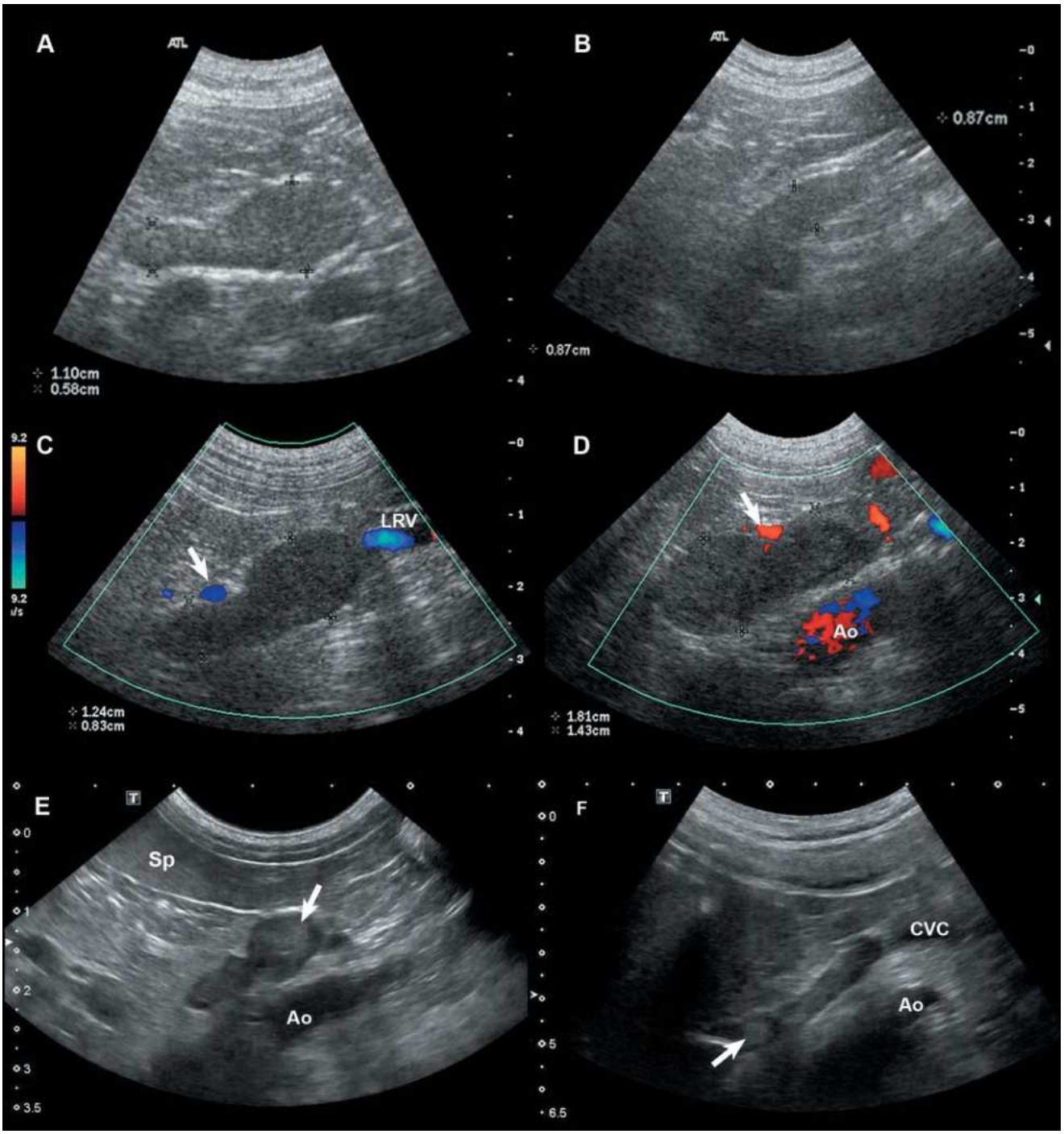


Figure 12.6. **Pituitary-dependent adrenal hyperplasia in three dogs. A, B:** In this medium-sized dog, the left adrenal gland is asymmetrically enlarged, with its caudal pole reaching 11 mm in thickness, while the right gland is more uniformly enlarged (caudal pole reaching 8.7 mm in thickness). **C, D**: Color Doppler images obtained in another dog with a pituitary tumor and signs of hyperadrenocorticism. Both adrenals are enlarged, which is more evident on the right side **(D)**. The caudal pole of the left gland **(B)** is thicker than the cranial pole. The right adrenal gland **(C)** is mildly inhomogeneous. Phrenicoabdominal vessels are seen at the ventromedial aspect of each gland (arrows). Other vascular landmarks, such as the aorta (Ao) and the caudal vena cava (CVC), are also in the scanned field. **D, E**: In another dog with hyperadrenocorticism, hyperechoic nodules are present in both glands, the largest in the caudal pole on the left and cranial pole on the right (arrows). Sp, spleen; Ao, aorta; CVC, caudal vena cava.

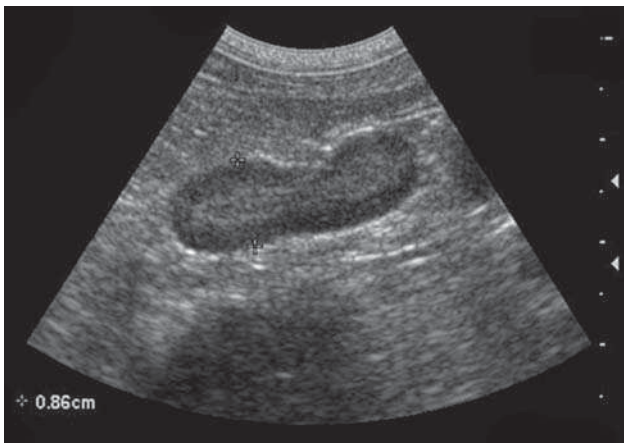


Figure 12.7. Rounded adrenal gland in a dog with a chronic, non-endocrinian disorder. Dorsal oblique image of the left adrenal gland in a small-breed dog with a chronic disease, but without evidence of hyperadrenocorticism. The gland is rounded. Note the hyperechoic medulla in comparison to the cortex.

enlargement (Barthez et al. 1995; Benchekroun et al. 2010). As already mentioned, some healthy dogs have adrenal glands that exceed 8 mm in maximal diameter. Some dogs with chronic non-endocrine disease may also exhibit mild symmetrical adrenal enlargement (Figure 12.7).

Adrenal tumor hyperadrenocorticism (ATH) caused by functional adrenocortical tumors accounts for approximately 20% of dogs with naturally occurring hyperadrenocorticism. In dogs with compatible clinical signs and clinicopathologic findings, ATH should be considered if one adrenal gland is enlarged, contains a nodule, or has been effaced by a mass, while the contralateral gland is small (≤5.0 mm) or not seen, suggesting that it has been suppressed (Benchekrounet al. 2010) (Figure 12.8). However, in some cases, the functional tumor may be small and is not detected by ultrasonography. Further confounding the diagnosis, there are reports of dogs with tumors of both the pituitary gland and the adrenal cortex, as well as bilateral primary adrenal neoplasia (Greco et al. 1999).

In dogs with hyperadrenocorticism caused by exogenous steroid administration, the adrenal glands may appear small or may not be seen. These changes are reversible within one month after the end of therapy (Pey et al. 2012).

In contrast to dogs, adrenal disease is uncommon in cats. Feline Cushing's syndrome is uncommon, but ultrasonography may be helpful in determining whether the disease is pituitary-dependent or caused by a functional adrenal cortical tumor. The criteria are similar to those in dogs (Watson and Herrtage 1998; Feldman and Nelson 2004).

Addison's Disease

A diagnosis of Addison's disease cannot be made based on ultrasonographic findings alone. However, in a dog with consistent clinical and laboratory findings, the detection of adrenal glands measuring 3.4 mm or less, or failure to detect the glands, despite a technically adequate study, can be considered circumstantial evidence supporting a diagnosis of hypoadrenocorticism (Hoerauf and Reusch 1999; Wenger et al. 2010) (Figure 12.9).

Adrenal Nodules and Masses

The sonographic appearance of adrenal nodules and masses is non-specific (Figure 12.10). The differential diagnosis for solid lesions includes cortical adenoma, cortical adenocarcinoma, pheochromocytoma, myelolipoma, metastasis, and hyperplasia. Cortical tumors may or may not be functional.

Adrenal tumors can produce excessive cortisol, causing clinical signs of hyperadrenocorticism, excessive aldosterone, or several types of sex hormones (Hill et al. 2005; Briscoe et al. 2009; Millard et al. 2009). Pheochromocytomas commonly result in hypertension, but may also produce vague, non-specific, or intermittent clinical signs (Feldman and Nelson 2004). Their sonographic features are also non-specific (Figures 12.10D, 12.11, 12.13).

Adrenal nodules and masses vary in size and echogenicity. Solid lesions exceeding 2 cm generally predict benign or malignant neoplasia rather than hyperplasia, whereas lesions exceeding 4 cm usually indicate malignant neoplasia (Besso et al. 1997). Yet, both benign neoplasms and hyperplasia may produce quite large lesions. The most reliable sign of malignancy is evidence of invasion of local tissues and vessels, which can occur with adrenocortical carcinomas and pheochromocytomas (Platt et al. 1998). These tumors may invade the adjacent kidney or musculature and extend to involve the vertebrae and cause neurological signs. Locally invasive lesions may be recognized sonographically, especially if they distort the

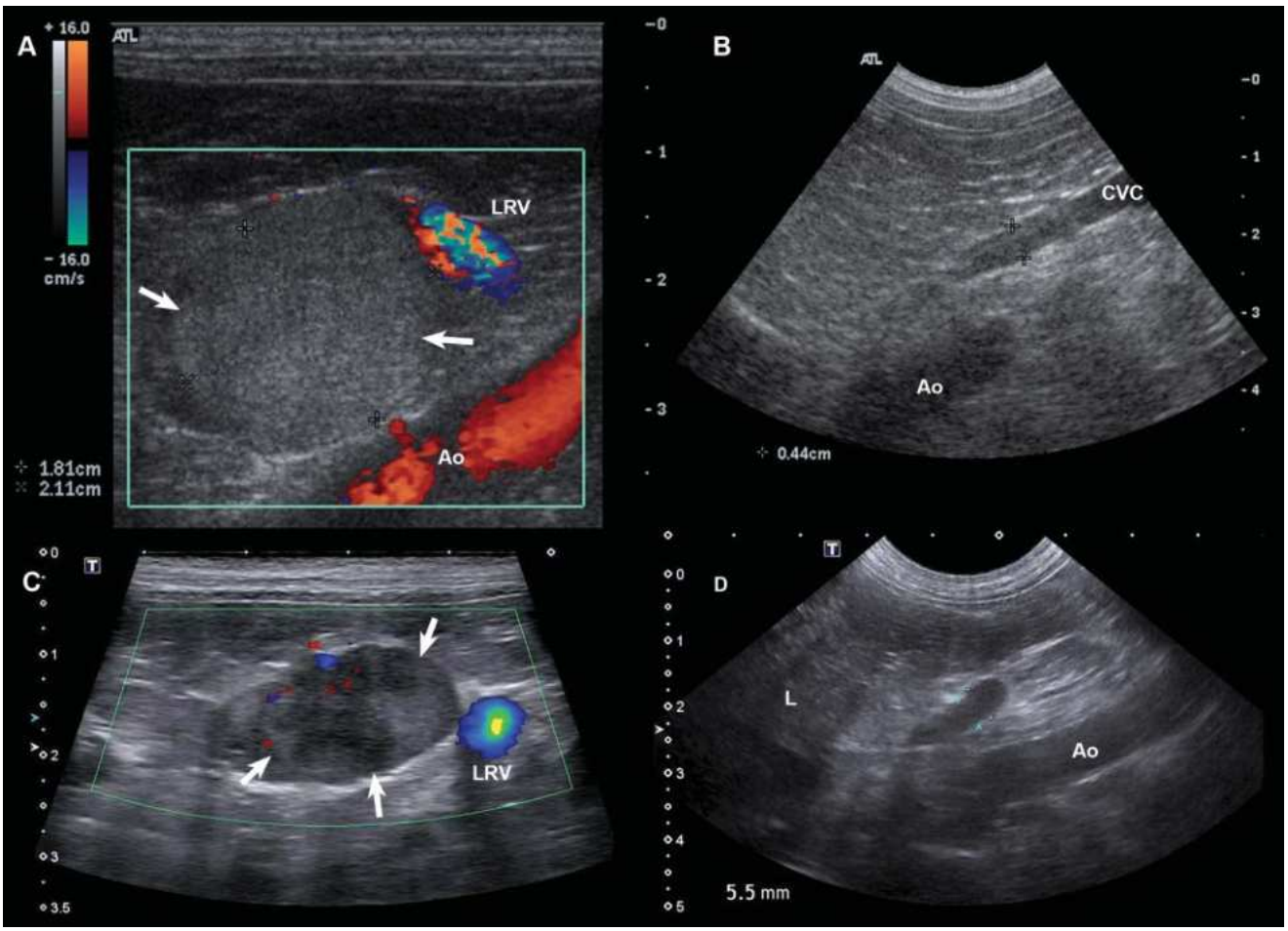


Figure 12.8. **Primary adrenal hyperadrenocorticism in two dogs.** Sagittal oblique sonographic images of the left **(A)** and right **(B)** adrenal glands in a large dog with Cushing's disease. A 2-cm, uniform and moderately echogenic cortical adenoma (arrows) invades the left adrenal gland, in contact with the left renal vein (LRV). The contralateral gland is at the lower range of normal in thickness, probably due to suppression. **C, D**: In this other dog, the left adrenal gland is invaded by a 13 × 17 mm mass (arrows) that is more inhomogeneous, consistent with a carcinoma. The right adrenal is normal in thickness (5.5 mm). LRV, left renal vein; Ao, aorta; L, liver.

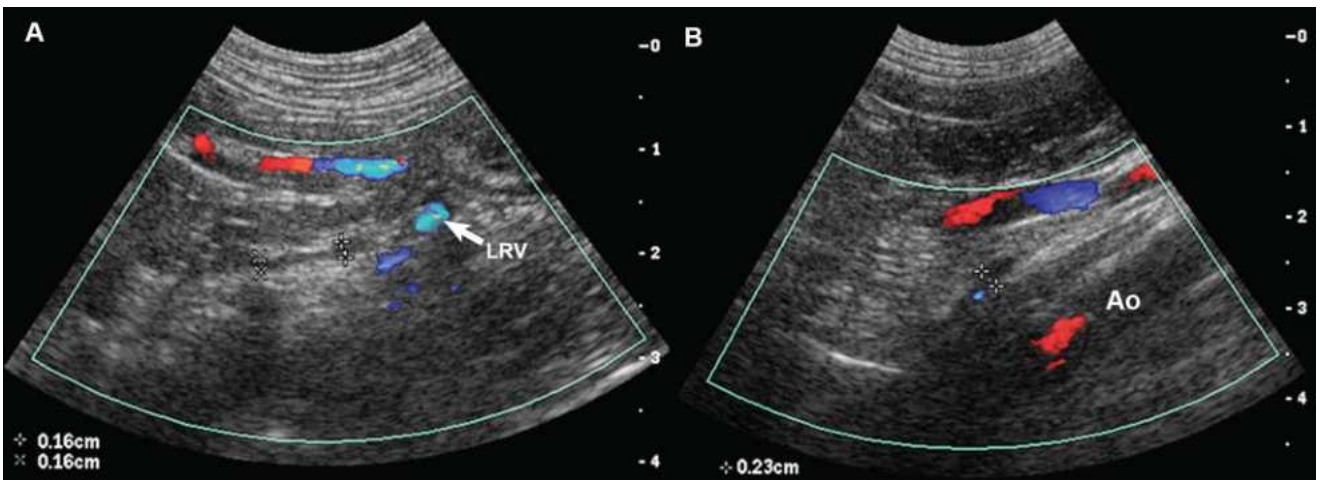


Figure 12.9. **Addison's disease in a dog.** Sagittal ultrasound images of the left **(A)** and right **(B)** adrenal glands in a dog with hypoadrenocorticism. Both glands are significantly reduced in diameter (between the cursors). Ao, aorta; RV, left renal vein.

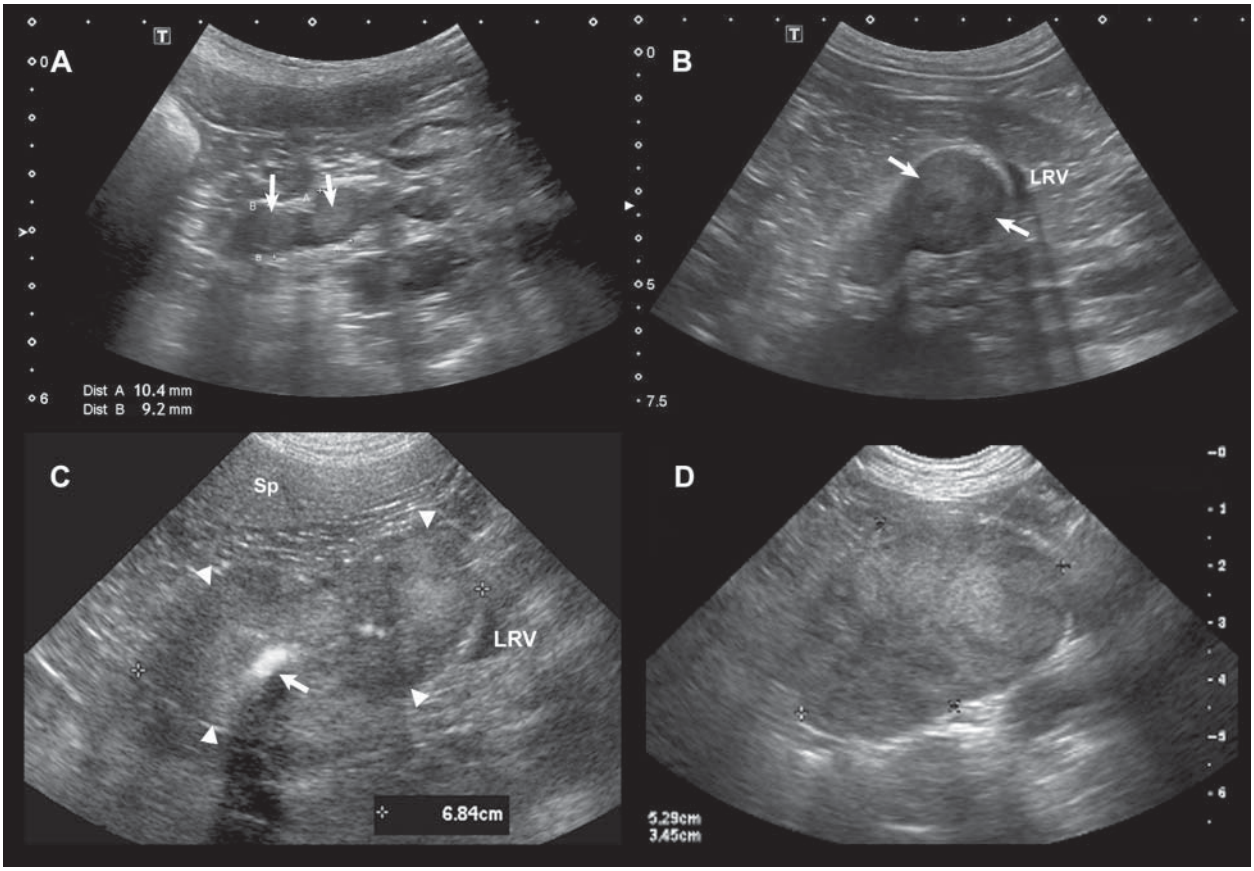


Figure 12.10. **Adrenal nodules and masses in four dogs. A:** Sagittal sonogram of the left adrenal gland of a toy Poodle with pituitary-dependent hyperadrenocorticism. Note the hyperechoic nodules in each pole of the gland, which is thickened (up to 10.4 mm). **B**: Sagittal sonogram of the left adrenal gland of a mountain Bernese dog with histiocytic sarcoma. A 2-cm nodule is identified in the caudal pole of the adrenal gland, deforming the adjacent left renal vein (LRV). Fine-needle aspiration of the nodule confirmed metastasis. **C:** Transverse sonogram of an adenocarcinoma of the left adrenal gland in an 11-year-old large-breed dog. A large, irregular, inhomogeneous mass (arrowheads) has replaced the left adrenal gland. This mass contains amorphous mineralization, as seen as shadowing hyperechoic foci (arrow). There was no sonographic evidence of vascular invasion, although caudal displacement and compression of the left renal vein (LRV) are seen. Sp, spleen. **D**: Sagittal sonogram of a pheochromocytoma in an 8-year-old Boxer crossed. A large inhomogeneous mass is identified medial to the left kidney, but not invading the adjacent vessels.

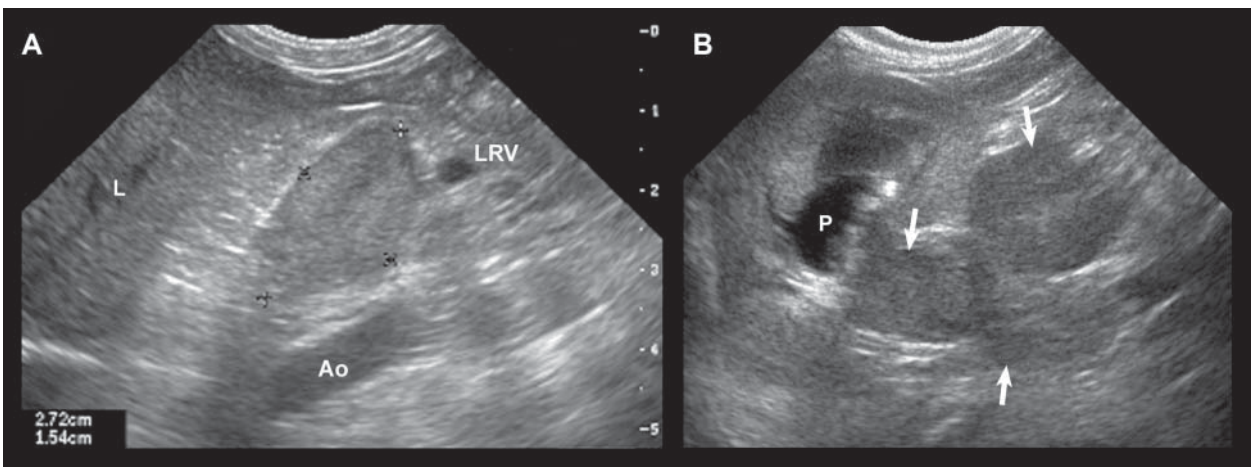


Figure 12.11. **Adrenal pheochromocytomas in two dogs. A:** Sagittal sonogram of a pheochromocytoma of the right adrenal gland in a 9-year-old Chihuahua cross. The mass is homogeneously echogenic and appears ventral to the aorta (Ao) and just cranial to the left renal vein (LRV). L, liver. **B:** Sagittal sonogram of a pheochromocytoma in the 15-year-old Golden Retriever. The mass is adjacent to right renal vein (RV) and caudal vena cava (CVC), but not invading them, as confirmed during surgery. **B**: Invasive pheochromocytoma in another dog. Dorsal plane image obtained in the right craniodorsal abdomen. The right kidney is in the near field (arrowheads), and the renal pelvis (P) is moderately dilated. A bilobed, hypoechoic mass (arrows) extends into the hilus of the kidney. The pelvic dilation suggests partial obstruction of the ureter by invasion or encasement by the mass.

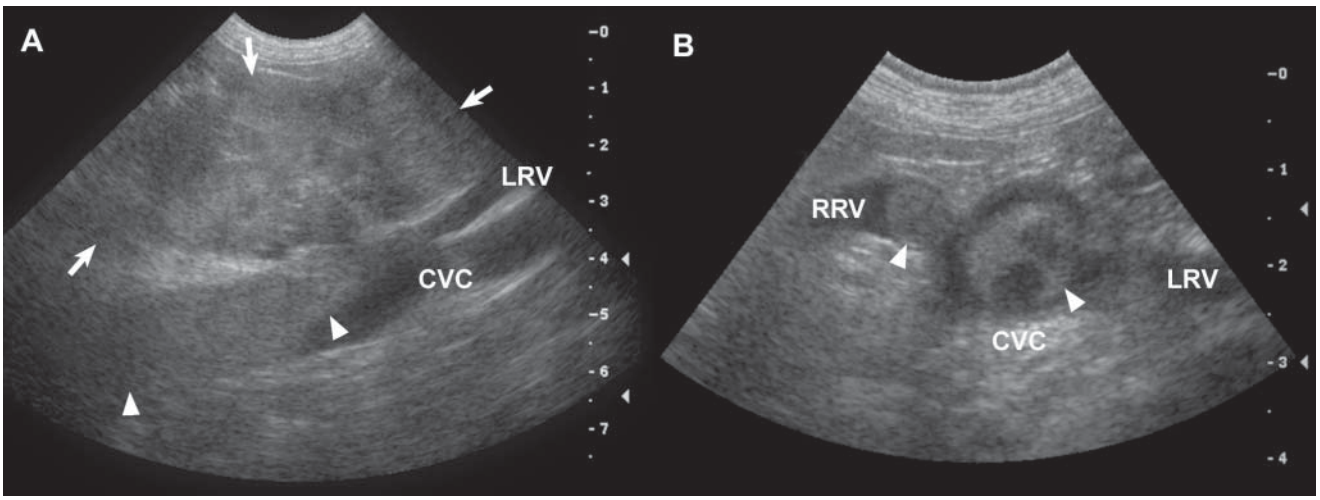


Figure 12.12. **Adrenocortical carcinoma and venous thrombosis in a dog.** Sagittal **(A)** and transverse **(B)** plane images obtained in the left mid-abdomen of a dog with peritoneal effusion and pelvic limb swelling. A large, irregular, inhomogeneous mass (arrowheads) is ventral to the caudal vena cava (CVC), displacing the left renal vein caudally (LRV). A moderately echogenic structure, with hypoechoic portions **(B)**, is found in the lumen of the CVC, protruding into the right renal vein (RRV), consistent with thrombosis (arrows). At surgery, there was no evidence of vascular invasion by the mass, although this was initially suspected.

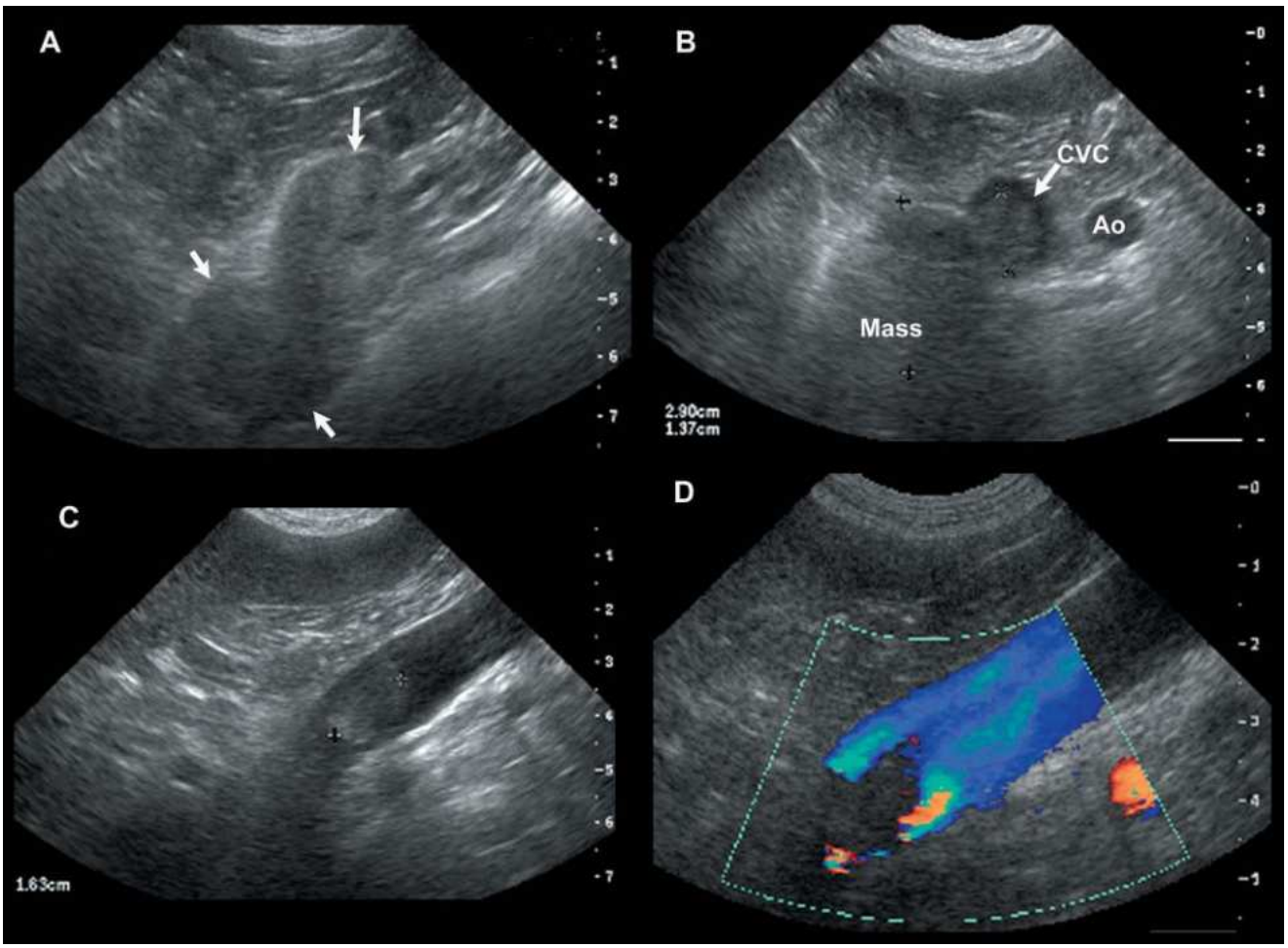


Figure 12.13. **Large pheochromocytoma and venous thrombosis in a 12-year-old mixed-breed dog. A:** Sagittal sonogram of a large pheochromocytoma (arrows) of the right adrenal gland. **B:** A transverse sonogram of the mass and the invaded caudal vena cava (CVC), which appears significantly larger than the adjacent aorta (Ao). **C:** The echogenic thrombus is well seen in the lumen of the vessel. **D:** The color Doppler assessment outlines the caudal margin of the thrombus. The vascular invasion was confirmed at surgery.

kidney (Figure 12.11B). However, the adrenal origin of a mass may be difficult to establish with ultrasound when extensive and poorly marginated. Non-adrenal retroperitoneal malignancies, such as hemangiosarcomas (see Figure 15.18) and renal carcinomas, may be confused for adrenal tumors, requiring computed tomography (CT) or magnetic resonance imaging (MRI) for better distinction.

Ultrasound represents a good screening tool for identifying invasion of the caudal vena cava and thrombus formations that may occur with adrenal malignancies (Davis et al. 2010) (Figures 12.12–12.14). Other local vessels may also be invaded, such as the renal veins, adrenal veins, and phrenicoabdominal vessels. The presence of a venous thrombus adjacent to an adrenal mass is highly suggestive of malignancy. Hyperadrenocorticism may cause a hypercoagulable state and, in this condition, aortic thrombus can also be detected.

Hyperechoic foci with distal acoustic shadowing, representing mineralization, are not specific of malignancy. Both benign and malignant lesions can become mineralized (Figures 12.10, 12.15). The shape of the adrenal lesion may offer some circumstantial evidence as to type. If the gland retains a normal shape, hyperplasia is considered more likely. Discrete, well-defined hyperechoic nodules suggest benign neoplasia, whereas amorphous, irregularly shaped and inhomogeneous masses suggest malignancy.

Adrenal tumors are rare in cats and result in variable clinical signs (Figure 12.16). An adrenal gland tumor should be considered in neutered cats with newly developed physical and sex related behavioral changes (Millard et al. 2007).

Adrenal nodules and small masses have become more common incidental findings as operator experience has increased and machine quality has improved.

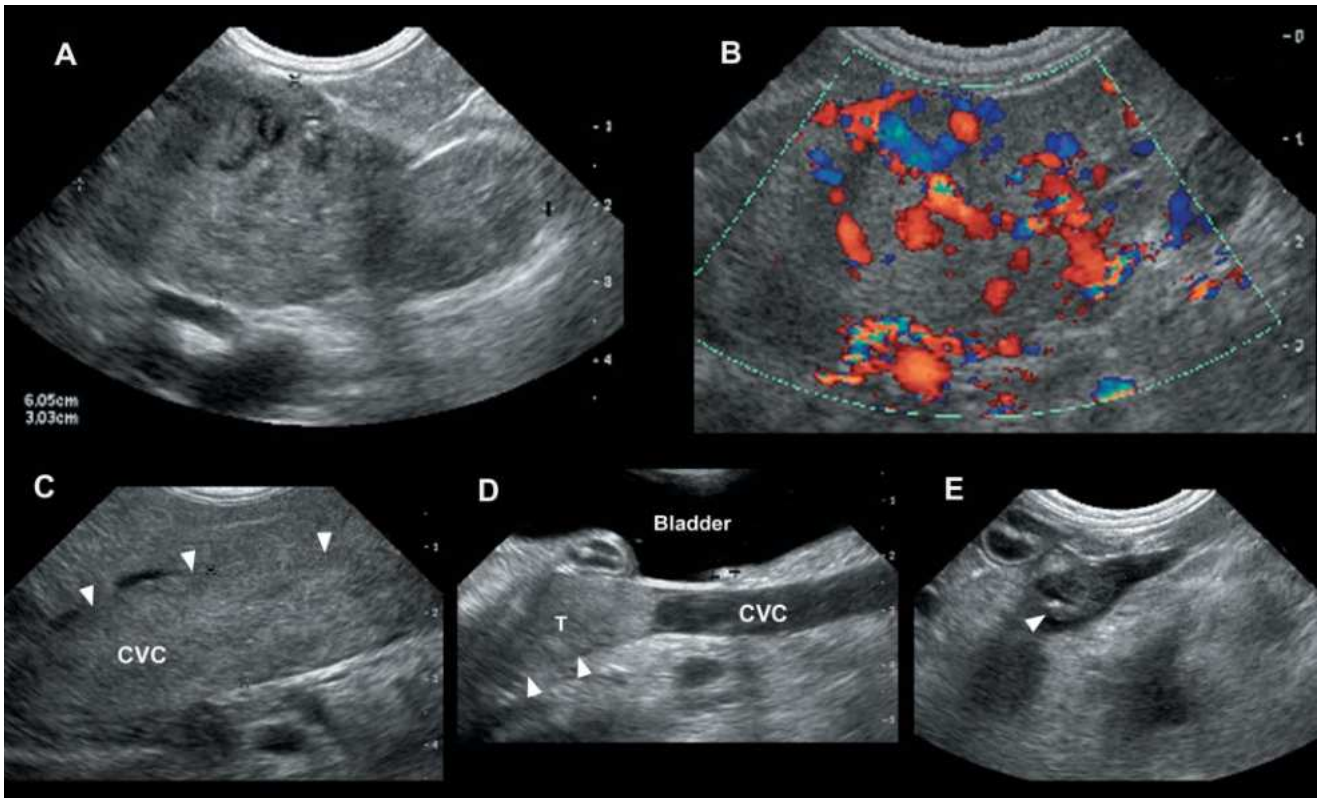


Figure 12.14. **Invasive adrenal tumor in an 11-year-old schnauzer. A:** Sagittal sonogram of a large invasive tumor of the left adrenal gland. **B:** On color Doppler evaluation, the mass appears highly vascular. **C:** An extensive thrombus is within the caudal vena cava (CVC) outlined by white arrowheads. **D:** The thrombus (T) extends caudally up to the level of the bladder. **E:** Inhomogeneous, echogenic thrombus (arrow) is also seen invading the renal vein. The small bright focus within the thrombus most likely represents mineralization. The highly vascular mass and dependent thrombus could not be successfully resected at surgery.

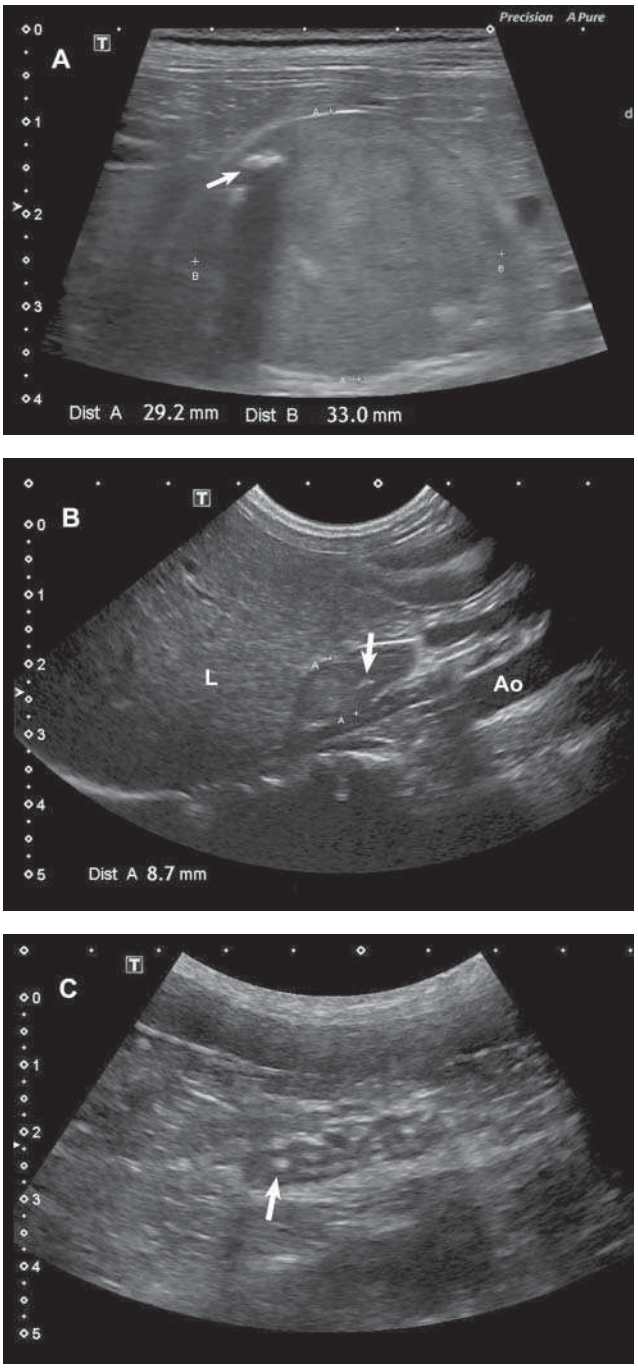


Figure 12.15. Mineralization of benign adrenal lesions. **A**: Adrenal adenoma with mineralization (arrow) casting a shadow in a medium-sized dog with primary hyperadrenocorticism. **B**: Hyperechoic focus (arrow) suggesting mineralization in the right adrenal gland of a Lhasa Apso with biocheminal evidence of pituitary-dependent hyperadrenocorticism (PDH). L, liver; Ao, aorta. **C:** Sagittal sonographic image of the left adrenal gland of another dog treated over 2 years for PDH. Note the contour irregularity of the gland and the numerous hyperechoic foci (arrow), most of which are near the corticomedullary junction. These foci may have indicated fibrosis, which may mimic mineralization with ultrasound.

These are sometimes referred to as "incidentalomas" (Figure 12.17) and leave clinicians with the dilemma of how far the diagnosis should be pursued. Many of these lesions cause no clinical signs, and a diagnosis is never confirmed. Reported diagnoses include normal tissue, nonfunctional cortical tumors, granulomas, adrenal cysts, myelolipoma, hemorrhage, metastatic tumor, and pheochromocytoma (Feldman and Nelson 2004; Morandi et al. 2007). The medical history and clinical signs should be reviewed for evidence of endocrine disease. Clinicopathologic tests are indicated if any such signs are identified. Larger masses or nodules (>2 cm) are more likely to be neoplastic, so surgical removal should be considered. However, many of these patients have serious concurrent illnesses and may be old, so such an invasive approach may not be indicated or acceptable to the owner. If there is no evidence of endocrine disease or sonographic evidence of invasiveness, serial ultrasound examinations at 1- to 3-month intervals can be used to monitor for enlargement or progression of the lesion. If there is evidence of progression, surgical excision may be prudent.

Adrenal changes with other diseases

Chronic illness and stress influence the hypophyseal–adrenals axis and may alter adrenal size in dogs and cats. Adrenals may be normal (Ramspott et al. 2012) or enlarged in cats with hyperthyroidism, and hyperechoic foci may be more prevalent (Combes et al. 2012). Adrenomegaly may also be associated with hyperaldosteronism and hyperprogesteronism in cats (Brisco et al. 2009).

Interventional Procedures

Fine-needle aspiration or biopsy of adrenal nodules or masses may be attempted (Figure 12.18). However, in dogs these tests are of equivocal value and are not without risk. It may be difficult to distinguish hyperplasia and benign and malignant adrenocortical tumors based on cytologic criteria. Attempted fine-needle aspiration or biopsy of a pheochromocytoma may cause uncontrollable hemorrhage or paroxysmal hypertension.



Visit our website at **www.SmallAnimalUltrasonography.com** for complementary video clips with annotations and text on:

- Normal adrenal glands
- Adrenal hyperplasia
- Adrenal adenoma and adenocarcinoma
- Adrenal pheochromocytoma

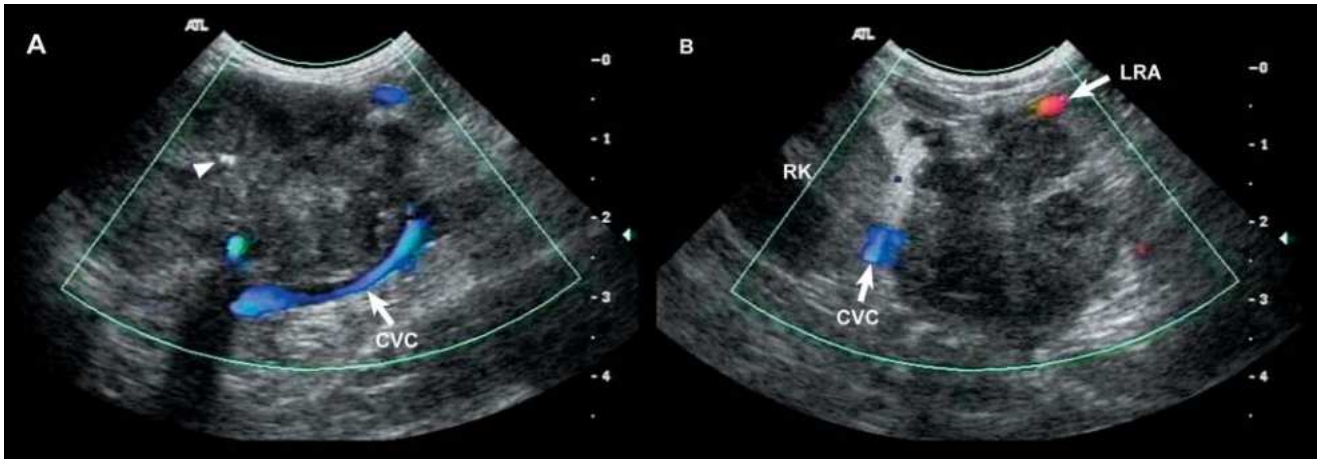


Figure 12.16. **Adrenocortical carcinoma in a 12-year-old domestic short hair cat.** Sagittal **(A)** and transverse **(B)** sonographic images of a large, irregular, inhomogeneous and mostly hypoechoic mass with discrete mineralization (arrowhead) identified in the region of the right adrenal gland in a cat presented for lethargy. The caudal vena cava (CVC) is deviated and compressed. The mass could not be resected due to local invasion of several structures including the aorta and surgical evidence of retroperitoneal carcinomatosis. LRA, left renal artery; RK, right kidney.

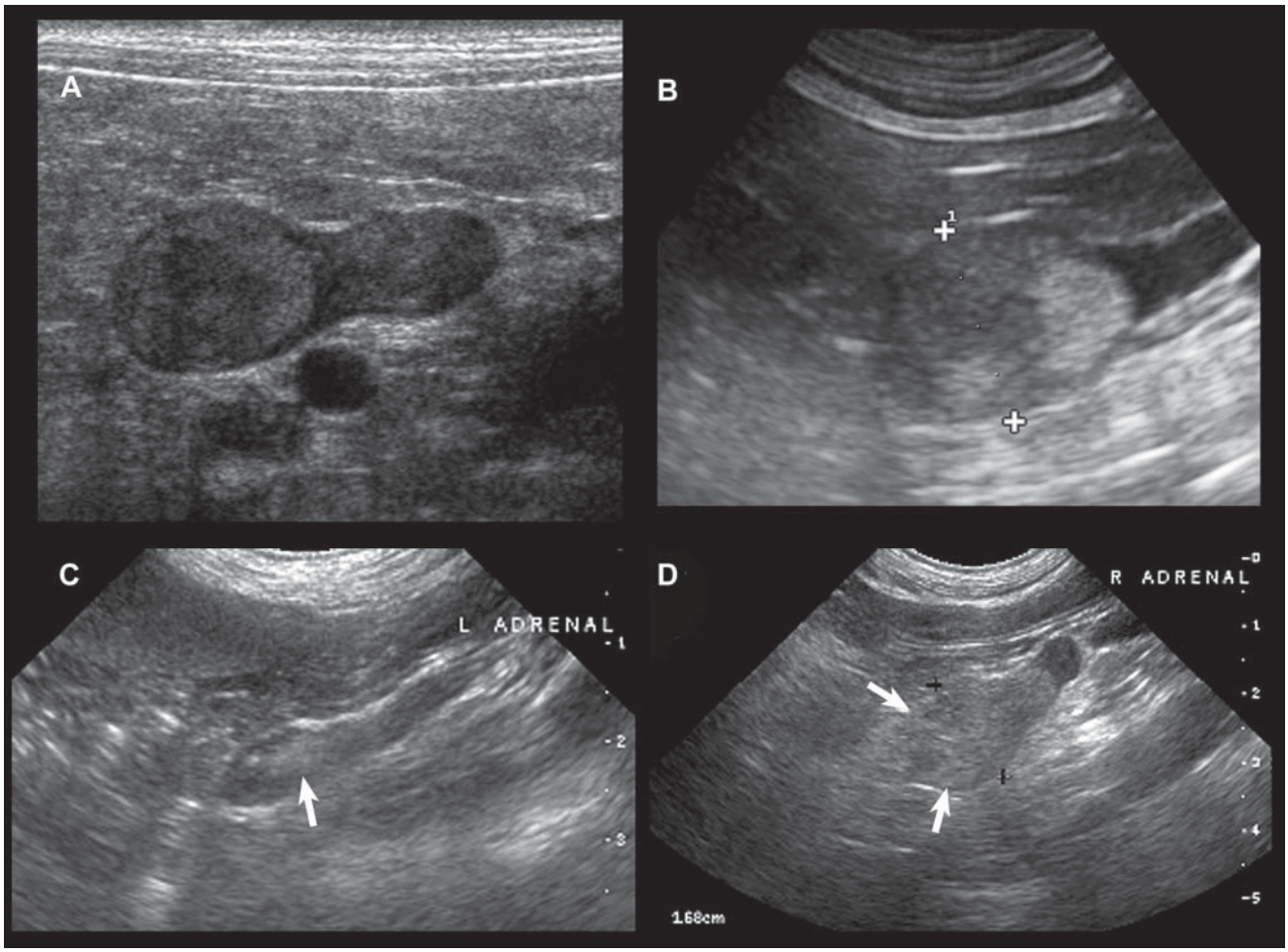


Figure 12.17. **Incidental adrenal lesions in dogs. A:** Dorsal plane image of a left adrenal gland. A well-defined, inhomogeneous, hyperechoic nodule is in the cranial pole of the adrenal gland. The nodule was an incidental finding and remained unchanged on serial examinations. Anechoic cross-sections of the celiac and cranial mesenteric arteries are seen dorsally. **B:** Primarily hyperechoic but slightly inhomogeneous nodule in the left adrenal gland of a dog confirmed to represent a myelolipoma in the center of an adenoma. **C, D:** Sagittal sonogram of both adrenal glands of a 15-year-old Siberian Husky with incidental bilateral changes in echogenicity and shape (arrows). These changes remained unchanged on serial examinations.

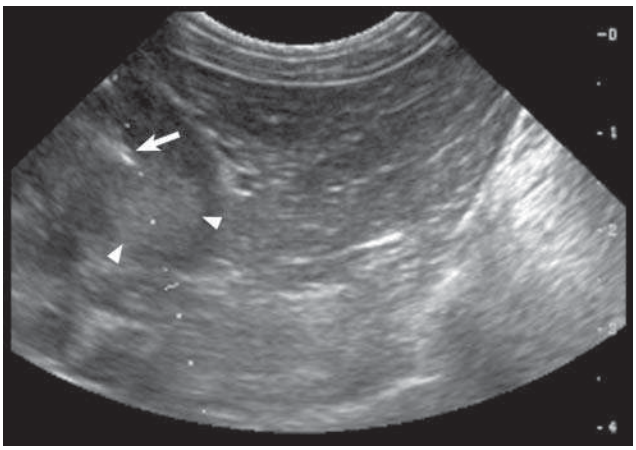


Figure 12.18. Fine-needle aspiration using a 22-gauge spinal needle (arrow) was performed on this adrenal mass (arrowheads) in a dog. No complication was encountered during the procedure. The final diagnosis was adrenocortical adenocarcinoma.

References

Barthez PY, Nyland TG, Feldman EC (1995) Ultrasonographic evaluation of adrenal glands in dogs. J Am Vet Med Assoc 207:1180–1183.

Barthez PY, Nyland TG, Feldman EC (1998) Ultrasonography of the adrenal glands in the dog, cat, and ferret. Vet Clin North Am Small Anim Pract 28:869–885.

Behrend EN, Kemppainen RJ, Clark TP, Salman MD, Peterson ME (2002) Diagnosis of hyperadrenocorticism in dogs: A survey of internists and dermatologists. J Am Vet Med Assoc 220:1643–1649.

Benchekroun G, de Fornel-Thibaud P, Rodríguez Piñeiro MI, Rault D, Besso J, et al. (2010) Ultrasonography criteria for differentiating ACTH dependency from ACTH independency in 47 dogs with hyperadrenocorticism and equivocal adrenal asymmetry. J Vet Intern Med 24:1077–1085.

Besso JG, Penninck DG, Gliatto JM (1997) Retrospective ultrasonographic evaluation of adrenal lesions in 26 dogs. Vet Radiol Ultrasound 38:448–455.

Brinkman EL, Biller DS, Armbrust LJ, O'Brien RT (2007) The clinical utility of the right lateral intercostal ultrasound scan technique in dogs. J Am Anim Hosp Assoc 43:179–186.

Briscoe K, Barrs VR, Foster DF, Beatty JA (2009) Hyperaldosteronism and hyperprogesteronism in a cat. J Feline Med Surg. 11:758–762.

Cartee RE, Finn-Bodner ST, Gray BW (1993) Ultrasound examination of the feline adrenal gland. J Diagn Med Sonogr 9:327–330.

Choi J, Kim H, Yoon J (2011) Ultrasonographic adrenal gland measurements in clinically normal small breed dogs and comparison with pituitary-dependent hyperadrenocorticism. J Vet Med Sci 73:985–989.

Combes A, Vandermeulen E, Duchateau L, Peremans K, Daminet S, Saunders J (2012) Ultrasonographic measurements of adrenal glands in cats with hyperthyroidism. Vet Radiol Ultrasound 53:210–216.

Davis MK, Schochet RA, Wrigley R (2012) Ultrasonographic identification of vascular invasion by adrenal tumors in dogs. Vet Radiol Ultrasound 53:442–445.

De Chalus T, Combes A, Bedu A, Pey P, Daminer S, Duchateau L, Saunders J (2013) Ultrasonographis adrenal gland measurements in healthy Yorshire terriers and Labrador Retrievers. Anatomica Histologia Embryologia 42:57–64.

Douglass JP, Berry CR, James S (1997) Ultrasonographic adrenal gland measurements in dogs without evidence of adrenal disease. Vet Radiol Ultrasound 38:124–130.

Feldman EC, Nelson RW (2004) The adrenal gland. In: Feldman EC, Nelson RW, eds. Canine and Feline Endocrinology and Reproduction, 3rd edition. St Louis: WB Saunders, pp 394–439.

Greco DS, Peterson ME, Davidson AP, Feldman EC, Komurek K (1999) Concurrent pituitary and adrenal tumors in dogs with hyperadrenocorticism: 17 cases (1978–1995). J Am Vet Med Assoc 214:1349–1353.

Grooters AM, Biller DS, Merryman J (1995) Ultrasonographic parameters of normal canine adrenal glands: Comparison to necropsy findings. Vet Radiol Ultrasound 36:126–130.

Hill KE, Scott-Moncrieff JC, Koshko MA, Glickman LT, Glickman NW, Nelson RW, Blevins WE, Oliver JW (2005) Secretion of sex hormones in dogs with adrenal dysfunction. J Am Vet Med Assoc 226:556–61.

Hoerauf A, Reusch C (1996) Ultrasonographic evaluation of the adrenal glands in healthy dogs, dogs with Cushing's disease due to functional adrenal tumors and dogs with Addison's disease [Abstract]. Vet Radiol Ultrasound 37:488.

Hoerauf A, Reusch C (1999) Ultrasonographic evaluation of the adrenal glands in six dogs with hypoadrenocorticism. J Am Anim Hosp Assoc 35:214–218.

Millard RP, Pickens EH, Wells KL (2009) Excessive production of sex hormones in a cat with an adrenocortical tumor. J Am Vet Med Assoc 234:505–508.

Morandi F, Mays JL, Newman SJ, Adams WH (2007) Imaging diagnosis – bilateral adrenal adenomas and myelolipomas in a dog. Vet Radiol Ultrasound 48(3):246–249.

Pey P, Daminet S, Smets PM, Duchateau L, Travetti O, Saunders JH (2012) Effect of glucorticoid administration on adrenal gland size and sonographic appearance in beagle dogs. Vet Radiol Ultrasound 53:204–209.

Platt SR, Sheppard BJ, Graham J, Uhl EW, Meeks J, Clemmons RM (1998) Pheochromocytoma in the vertebral canal of two dogs. J Am Anim Hosp Assoc 34:365–371.

Ramspott S, Hartmann K, Sauter-Louis C, Weber K, Wehner A (2012) Adrenal function in cats with hyperthyroidism. J Feline Med Surg 14:262–266.

Watson PJ, Herrtage ME (1998) Hyperadrenocorticism in six cats. J Small Anim Pract 39:175–184.

Wenger M, Mueller C, Kook PH, Reusch CE (2010) Ultrasonographic evaluation of adrenal glands in dogs with primary hypoadrenocorticism or mimicking diseases. Vet Rec 167:207–210.

Zatelli A, D'Ippolito , Fiore I, Zini E (2007) Ultrasonographic evaluation of the size of the adrenal glands in 24 diseased cats without endocrinopathies. Vet Rec 160: 658–660.

Zimmer C, Horauf A, Reusch C (2000) Ultrasonographic examination of the adrenal gland and evaluation of the hypophyseal-adrenal axis in 20 cats. J Small Anim Pract 41:156–160.

CHAPTER THIRTEEN

Female Reproductive Tract

Rachel Pollard[1] and Silke Hecht[2]

[1] *University of California, Davis, School of Veterinary Medicine, Department of Surgical and Radiological Sciences, Davis, CA, USA*

[2] *Department of Small Animal Clinical Sciences, University of Tennessee College of Veterinary Medicine, Knoxville, TN, USA*

Examination Technique

The ovaries and the uterus are the only female reproductive organs routinely visualized by means of ultrasonography. The normal oviducts are usually too small to be seen, and the vulva and vagina are difficult to image transabdominally because of their intrapelvic location. Mammary glands are infrequently examined.

Indications for ultrasonographic examination of the female reproductive tract include pregnancy identification, assessment of normal fetal development and viability, vaginal discharge, clinical signs compatible with hormonal imbalances suggesting ovarian dysfunction, and abdominal mass lesions in intact queens and bitches. Indications for ultrasonographic examination of the mammary glands include abnormal findings on palpation (swelling, pain, and heat) and a need to assess the extent of mammary gland neoplasia.

The examination is performed with the animal in dorsal recumbency (Figure 13.1). An approach in lateral recumbency may prove useful in the examination of the ovaries. A 5-MHz transducer is usually sufficient to visualize an enlarged, fluid-filled uterus, fetal structures, or abdominal mass lesions; however, a 7.5- or 10-MHz transducer provides better detail in the examination of smaller structures and is recommended for most indications. For the examination of the mammary glands, a high-resolution transducer (7.5 MHz or higher) is recommended.

Ovaries

Normal Sonographic Anatomy

The ovaries are oval structures located caudal, and often lateral, to the caudal pole of the kidneys, which are used as landmarks for their identification. Depending on the phase of the cycle, they measure approximately 1–2 cm long in dogs and less than 1 cm in cats. As previously reported (Yeager et al. 1995), the appearance of the ovary varies during the estrus cycle (Figures 13.2–13.5). During anestrus and early proestrous, the ovary is small (~1.2 cm in length), oval, and uniform in echogenicity. During proestrus, the ovary enlarges and becomes more spherical. Follicles begin to appear as anechoic oval fluid cavities up to 11 mm in diameter ranging in number from zero to 10 per ovary. On the day of ovulation, the follicle number decreases to zero to two per ovary and the remaining follicles reduce in size. The contour of the ovary may be bumpy and a scant amount of fluid may be seen surrounding it. During estrus, the maximum ovarian size is reached, equaling a 300–400% increase over size during anestrus. The contour of the ovary remains bumpy, and fluid-filled corpora lutea may be seen (mean of three per ovary). Corpora lutea are 5–9 mm diameter and tend to be thicker-walled and more variable in shape compared with preovulatory follicles. During diestrus, the ovarian contour remains bumpy and size reduces. The corpora lutea gradually decrease in size while increasing in echogenicity. Around 10–14 days

Atlas of Small Animal Ultrasonography, Second Edition. Edited by Dominique Penninck and Marc-André d'Anjou.
© 2015 John Wiley & Sons, Inc. Published 2015 by John Wiley & Sons, Inc.
Companion website: www.SmallAnimalUltrasonography.com

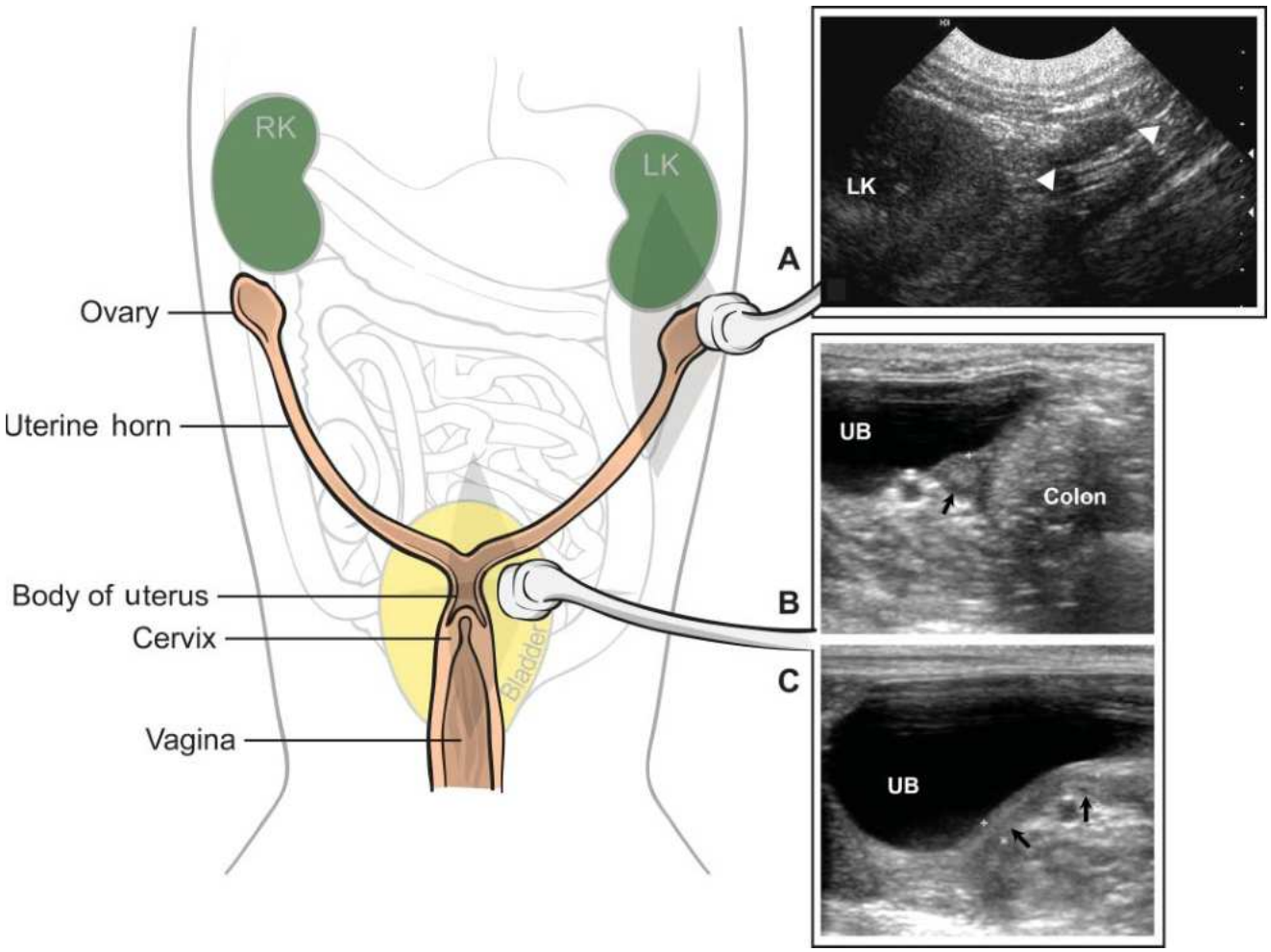


Figure 13.1. **Normal female reproductive tract.** On the left is a schematic representation of the anatomy of the female reproductive tract. The ovaries are located caudal and often lateral to the kidneys. The cervix and body of the uterus are located dorsal to the urinary bladder. The uterine horns extend craniolaterally from the uterine body and are infrequently visible during anestrus. **A:** Sagittal image of a normal left canine ovary (arrowheads). The left kidney (LK) is used as a landmark, and the ovary is identified as an ovoid soft-tissue structure of medium echogenicity caudal to the caudal pole of the kidney. **B, C:** Transverse **(B)** and sagittal **(C)** images of the normal canine uterus during anestrus. On the transverse image, the uterus (black arrow) is identified as a circular structure between the urinary bladder (UB) and colon, which are used as landmarks. On the sagittal image, the uterus (black arrows) is seen as a tubular structure of medium echogenicity dorsal to the UB.

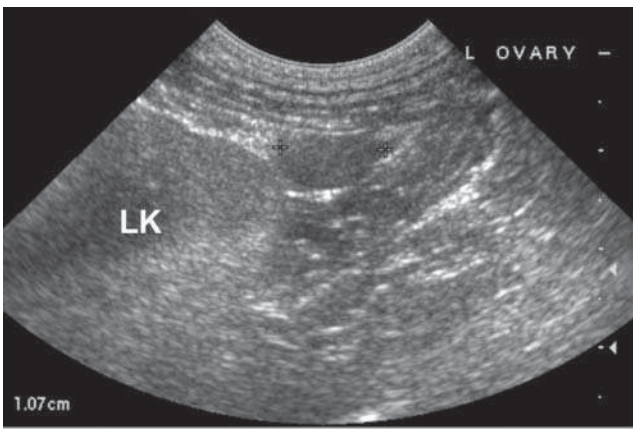


Figure 13.2. **Normal ovary during anestrus.** Sagittal image of the left ovary (between the cursors) in a 6-year-old Labrador Retriever during anestrus. The ovary is smoothly marginated, and slightly hypoechoic to the adjacent left renal cortex (LK), without evidence of follicles or corpora lutea.

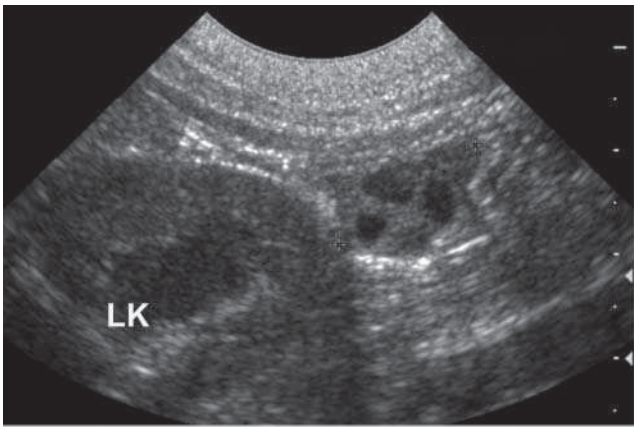


Figure 13.3. Normal ovary during proestrus or early estrus. Sagittal image of the left ovary (between the cursors) in a 6-year-old Labrador Retriever during late proestrus or early estrus. The three circular anechoic follicles within the ovary are associated with far enhancement. LK, left kidney.

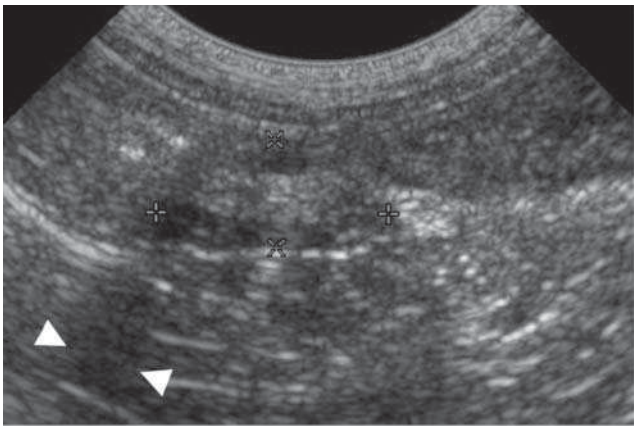


Figure 13.4. Normal ovary during diestrus. Sagittal image of the left ovary (between the cursors) in an 8-year-old Shih Tzu during diestrus. Several small circular hypoechoic corpora lutea are associated with the ovary. A hypoechoic linear band extending distally from the cranial pole of the ovary is consistent with edge shadowing artifact (arrowheads).

after ovulation, the corpora lutea appear solid and remain as such for the duration of diestrus. Although ultrasonographic changes during the ovarian cycle have been well studied in dogs, the exact time of ovulation cannot be predicted (Yeager et al. 1995; Silva et al. 1996).

Ovarian Disorders

Ovarian diseases are uncommon in dogs and very rare in cats. In many cases, a presumptive diagnosis of an ovarian abnormality is made based on clinical findings, and ultrasonography is used to confirm the suspicion rather than serving as the primary means of diagnosis (England et al. 2003).

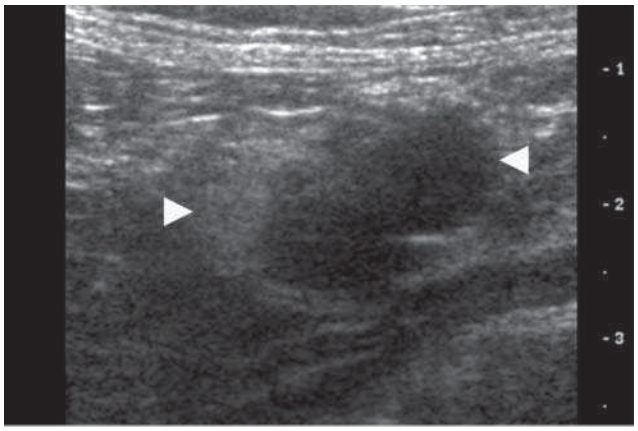


Figure 13.5. Normal ovary during pregnancy. Sagittal image of the left ovary (between the arrowheads) in a pregnant 4-year-old Pointer. Two large hypoechoic corpora lutea cause a lumpy gland contour.

Ovarian cysts appear as anechoic, well-circumscribed, and thin-walled structures with distal enhancement (Figures 13.6, 13.7). Hormonally inactive cysts arising from the ovarian bursa and hormone-producing follicular and luteinizing cysts cannot be differentiated through ultrasonography. Large follicles and corpora lutea may be confused with ovarian cysts and can only be ultrasonographically differentiated by serial ultrasound examinations. Follicles should not persist longer than 30 days and corpora lutea for no more than 60 days. The finding of fluid-filled structures associated with the ovary has to be interpreted in light of the clinical presentation when serial examinations are not being performed.

Ovarian tumors (epithelial tumors, sex-cord stromal tumors, and germ-cell tumors), which appear as nodules or masses of variable size and echogenicity, may have a cystic or mineral component (Figures 13.8, 13.9). Tumor types cannot be differentiated ultrasonographically, although teratomas and teratocarcinomas have the tendency to become very large and contain bone or mineral. The origin of an ovarian mass can be difficult to determine when the enlarging organ changes position and moves ventrally from its original location (Diez-Bru et al. 1998). Common concurrent findings include ascites, pyometra, and cystic endometrial hyperplasia.

On occasion, ovarian tissue will be left behind during ovariohysterectomy (Figure 13.10). Animals usually present with clinical signs of estrus. Alternatively,

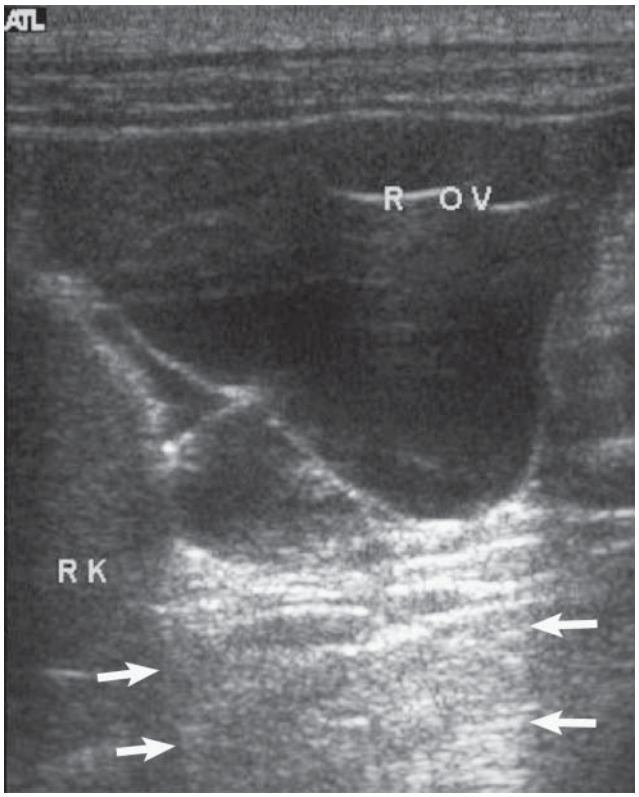


Figure 13.6. Ovarian cysts in a dog. The right ovary (R OV) has been replaced by several large, thin-walled anechoic structures. The cysts are characterized by distal enhancement (arrows). RK, right kidney.

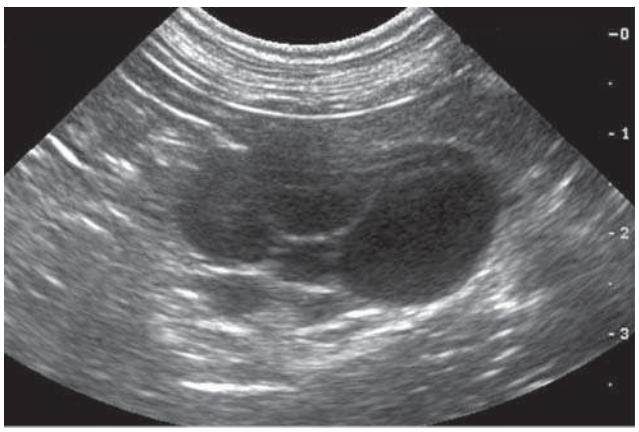


Figure 13.7. Cystic ovary in a 15-year-old Vizsla. Multiple thin-walled anechoic structures are associated with the left ovary. Normal ovarian parenchyma cannot be identified.

animals with ovarian remnants can develop stump pyometra. In these instances, ultrasound can be used to search for residual ovarian tissue. In most circumstances, residual ovarian tissue is located in the normal anatomic location for an ovary. However, the entire area from the caudal poles of the kidneys to the level

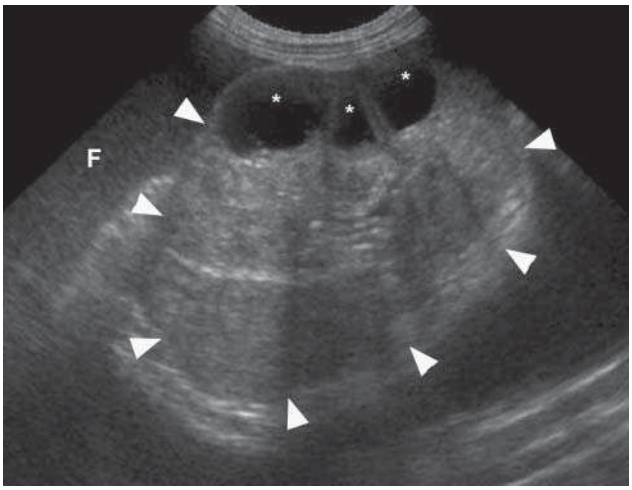


Figure 13.8. Ovarian carcinoma in a 7-year-old German Shepherd Dog. A large mixed echogenic mass (arrowheads) with cystic regions (*) is located caudal to the left kidney and surrounded by echogenic ascites (F).

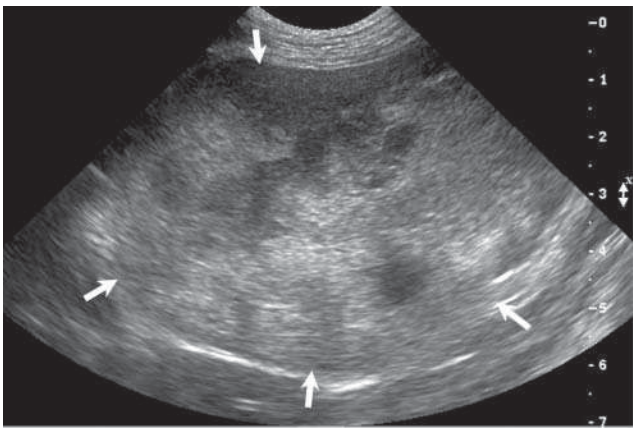


Figure 13.9. Sex-cord stromal tumor arising from residual ovarian tissue in a spayed 9-year-old Labrador Retriever. A large inhomogeneous and mixed echogenic mass (arrows) is associated with the mid-abdomen.

of the bladder should be searched for abnormal tissue (Davidson and Baker 2009).

Uterus

Normal Sonographic Anatomy

The normal non-gravid uterus is inconspicuous, often difficult to identify in dogs, and usually not seen in cats. It is best identified in the caudal abdomen, where it appears as a tubular structure between the urinary bladder (ventral) and the descending colon (dorsal) (Figure 13.1). Its size and appearance depend on the size of the animal, previous pregnancies, and stage of

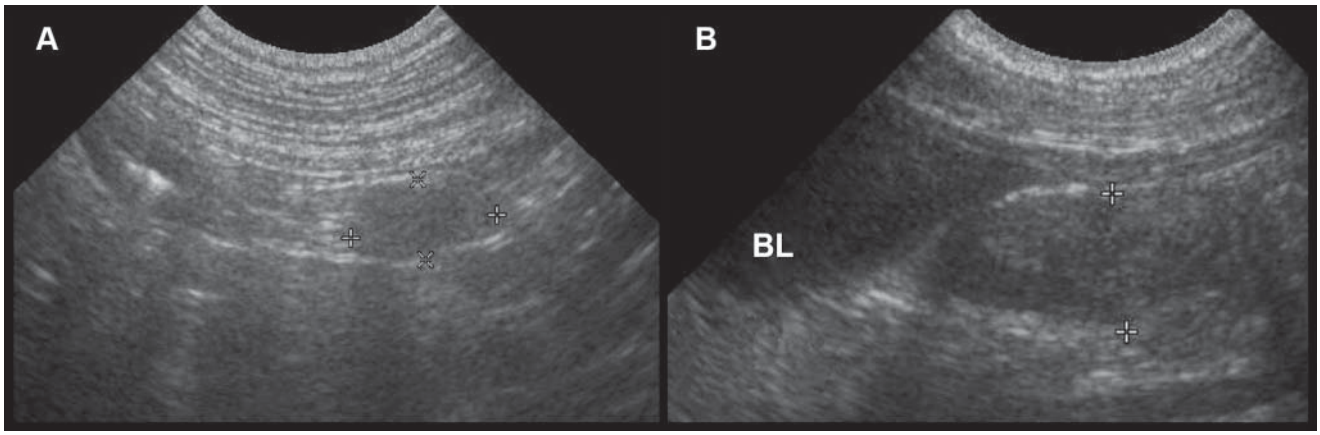


Figure 13.10. Ovarian remnant in a 9-year-old Bull Mastiff. A: Tissue resembling an ovary (cursors) is visible caudal to the right kidney (not shown). **B:** The uterine stump (cursors) is enlarged and easily visible residing lateral and dorsal to the urinary bladder (BL).

Table 13.1
Ultrasonographic appearance of the canine uterus during the estrus cycle

Time	Appearance of the Uterus
Late diestrus and anestrus	Uniformly hypoechoic Neither layered wall nor luminal echo 3–8 mm in diameter Difficult to detect Vagina and cervix difficult to distinguish from the uterine body
Proestrus, estrus, metestrus, and early diestrus	1-mm hyperechoic luminal echo and hypoechoic inner layer of uterine wall variably present Relatively easy to detect 1–3 mm larger in diameter in comparison with anestrus Focal enlargement of cervix with "bull's eye" appearance in cross section because of multiple layers

Data from Yeager and Concannon (1995).

the estrus cycle (Table 13.1, Figures 13.11, 13.12). After identification of the cervix or the uterine body, the uterus is traced cranially to the level of the bifurcation and the uterine horns. An alternative approach is the identification of the uterine horns close to the ovaries; however, their small diameter at this location hinders identification. Even if the uterine body and the cervix are seen in a non-gravid animal, the uterine horns may not be visible because of their small size and surrounding intestinal segments. The lack of identifiable wall layers helps in differentiating uterine horns from intestinal loops.

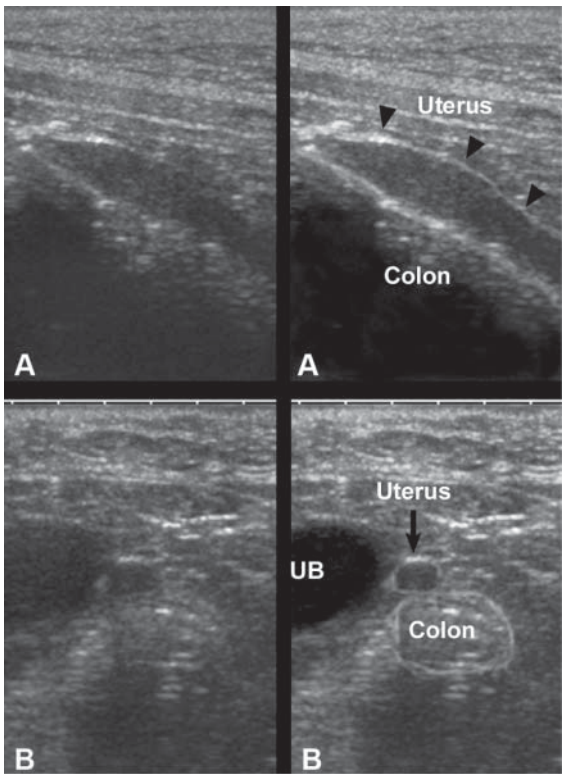


Figure 13.11. Normal anestrus uterus in a 6-year-old Scottish Terrier. A (and corresponding enhanced image A'): On the sagittal image, the uterus (arrowheads) is a tubular, homogeneous structure of medium echogenicity dorsal to the colon, which is characterized by a hyperechoic interface and distal dirty shadowing. The transition between the cervix and the uterine body is inconspicuous. The urinary bladder is not visible on this image. **B** (and corresponding enhanced image B'): On the transverse image, the uterus (arrow) appears as a round, homogeneous structure dorsal to the colon and to the left of the urinary bladder (UB).

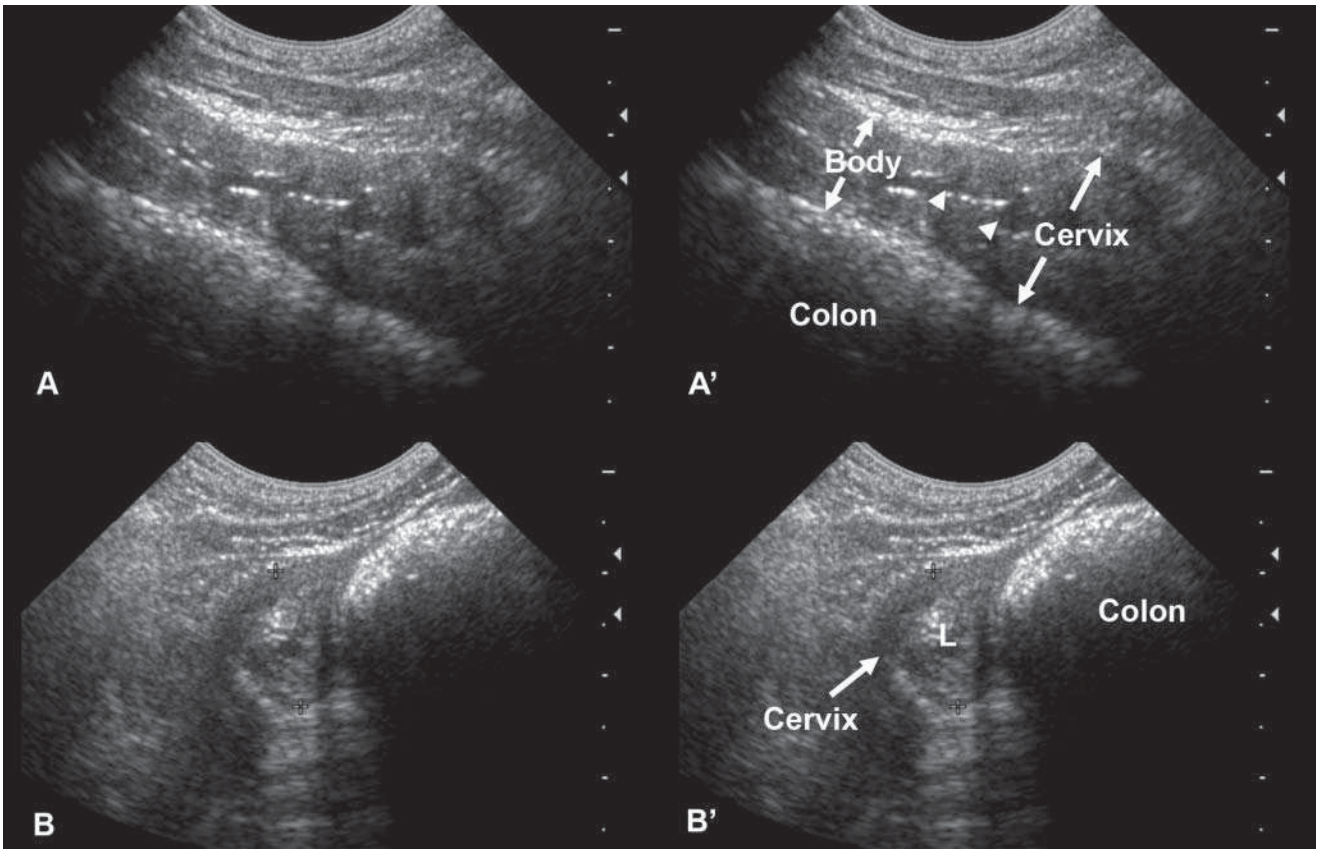


Figure 13.12. Normal late-proestrus or early-estrus uterus in a 6-year-old Labrador Retriever (the same dog as in Figure 13.3). **A, A′:** Sagittal sonographic and enhanced images of cervix and body of the uterus. The uterine wall is thicker than during anestrus. Hyperechoic luminal echoes and a small volume of intraluminal fluid are present (arrowheads). The diameter of the cervix is larger than the diameter of the uterine body. **B, B′:** Transverse sonographic and enhanced images of the cervix (between the cursors). The cervix is thick-walled, with hyperechoic and hypoechoic echoes within the lumen (L). The uterus is located lateral to the descending colon.

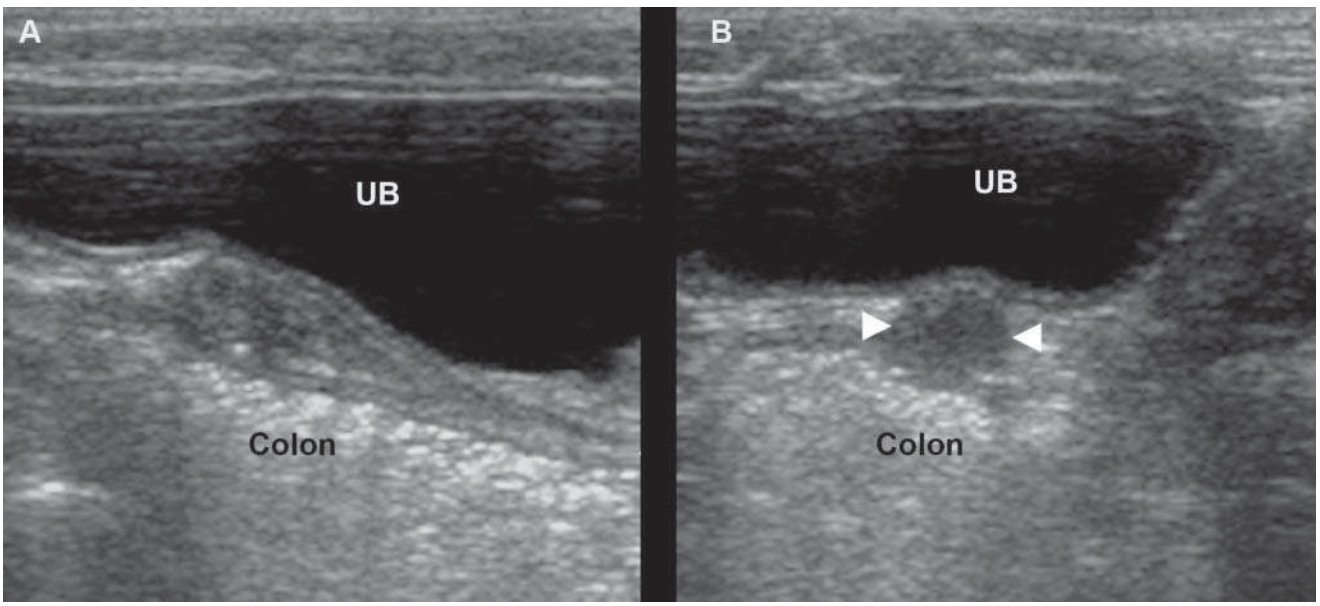


Figure 13.13. Uterine stump in a healthy 12-year-old mixed-breed dog. A: Sagittal image. The uterine stump appears as a tubular structure between the urinary bladder (UB) and the colon. **B:** Transverse image. The uterine stump (between the arrowheads) appears as a circular hypoechoic structure between the UB and the colon.

In spayed dogs, the uterine stump is usually inconspicuous and may be visible as a blind-ended tubular structure between urinary bladder and colon (Figure 13.13).

Pregnancy

Normal Pregnancy

Ultrasonography is a reliable method for diagnosing pregnancy in dogs and cats. Inconsistency exists in the literature regarding the time of the earliest definitive diagnosis, partially because it is difficult to determine the time of conception in dogs. The improved image detail provided by more recent ultrasound systems could contribute to earlier diagnosis.

The most commonly used definition of gestational age is the number of days after luteinizing hormone (LH) peaks in dogs and the number of days after breeding in cats (Mattoon and Nyland 1995). According to these definitions, the length of normal pregnancy is 65 ± 1 day for dogs and 61 days for cats. A practical problem is that information on hormone assays is often unavailable to animal owners and ultrasonographers. If the time of breeding is known, pregnancy can usually be ruled out 30–33 days after the last breeding in dogs and 15–20 days after the last breeding in cats, based on a negative ultrasonographic examination.

Ultrasonography is useful in monitoring normal embryonic and fetal development (Yeager et al. 1992; Zambelli et al. 2002) (Figures 13.14–13.19).

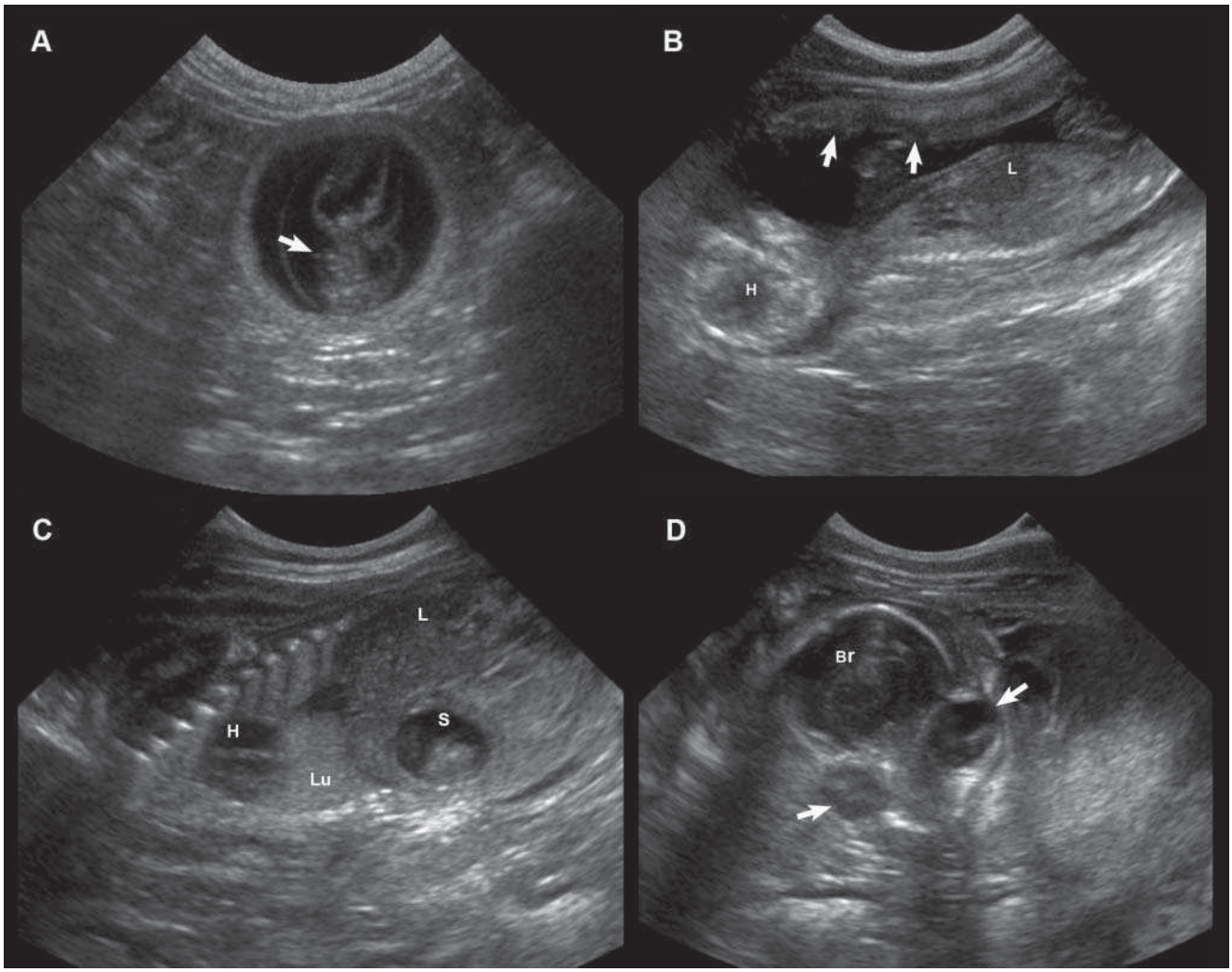


Figure 13.14. Progression of normal pregnancy in a domestic shorthair cat. A (day 24)**:** The embryo (arrow) is visible within the gestational chamber surrounded by copious fluid. **B** (day 39)**:** Sagittal image of the fetus with the head (H) to the left. Liver parenchyma (L) is visible. The placenta is in the near field (arrows). **C** (day 60): Sagittal image of the fetus. The heart (H), fluid-filled stomach (S) and liver (L) are easily visualized. The lung (Lu) is hyperechoic. **D** (day 60)**:** A dorsal view of the skull shows the brain (Br) and eyes (arrows).

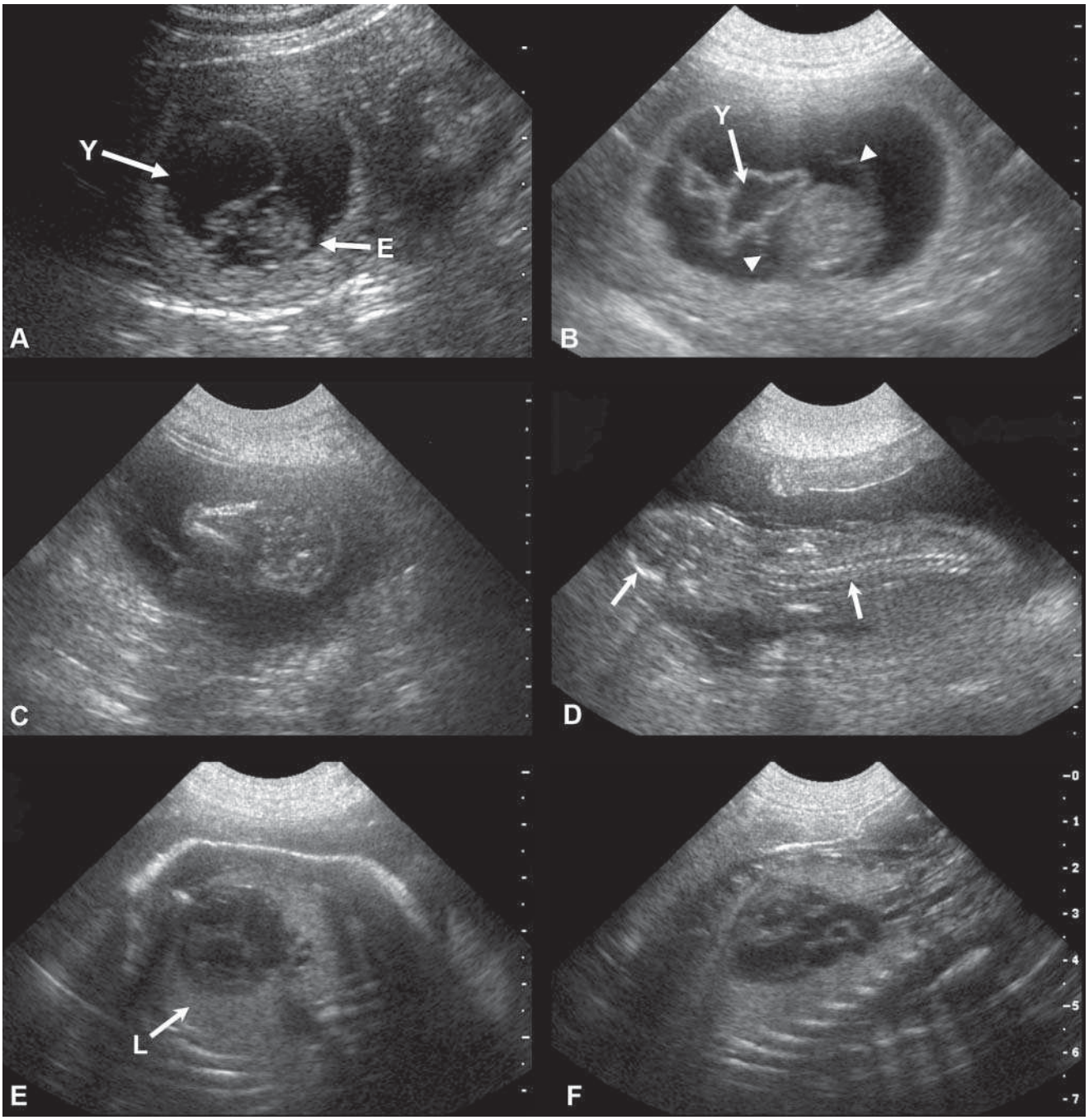


Figure 13.15. Progression of normal pregnancy in a 4-year-old Labrador Retriever. The dog was bred twice during the last estrus. The results of hormone assays are not available. **A:** Day 28 after last breeding. An embryo (E) is visible in the fluid-filled gestational sac. A flickering heartbeat was observed on real-time examination. The yolk sac (Y) is the fluid-filled structure adjacent to the fetus. **B:** Day 35. Transverse image of the fetus. The surrounding allantoic membrane is indicated by arrowheads. The yolk sac (Y) is the folded fluid-filled structure adjacent to the fetus. **C:** Day 42. Dorsal plane image of the fetal head. The mandible is to the left on the image, and the cranium and brain are to the right. **D:** Day 42. Dorsal plane image of the fetal body. Skull (to the left of the image) and vertebral column are clearly visible (arrows). **E:** Day 60. Transverse image of the fetal thorax. The heart is clearly visible and is surrounded by hyperechoic lung (L). **F:** Day 60. Sagittal image of the fetal thorax. Cardiac chambers and large vessels are clearly visible. The surrounding lung is hyperechoic.

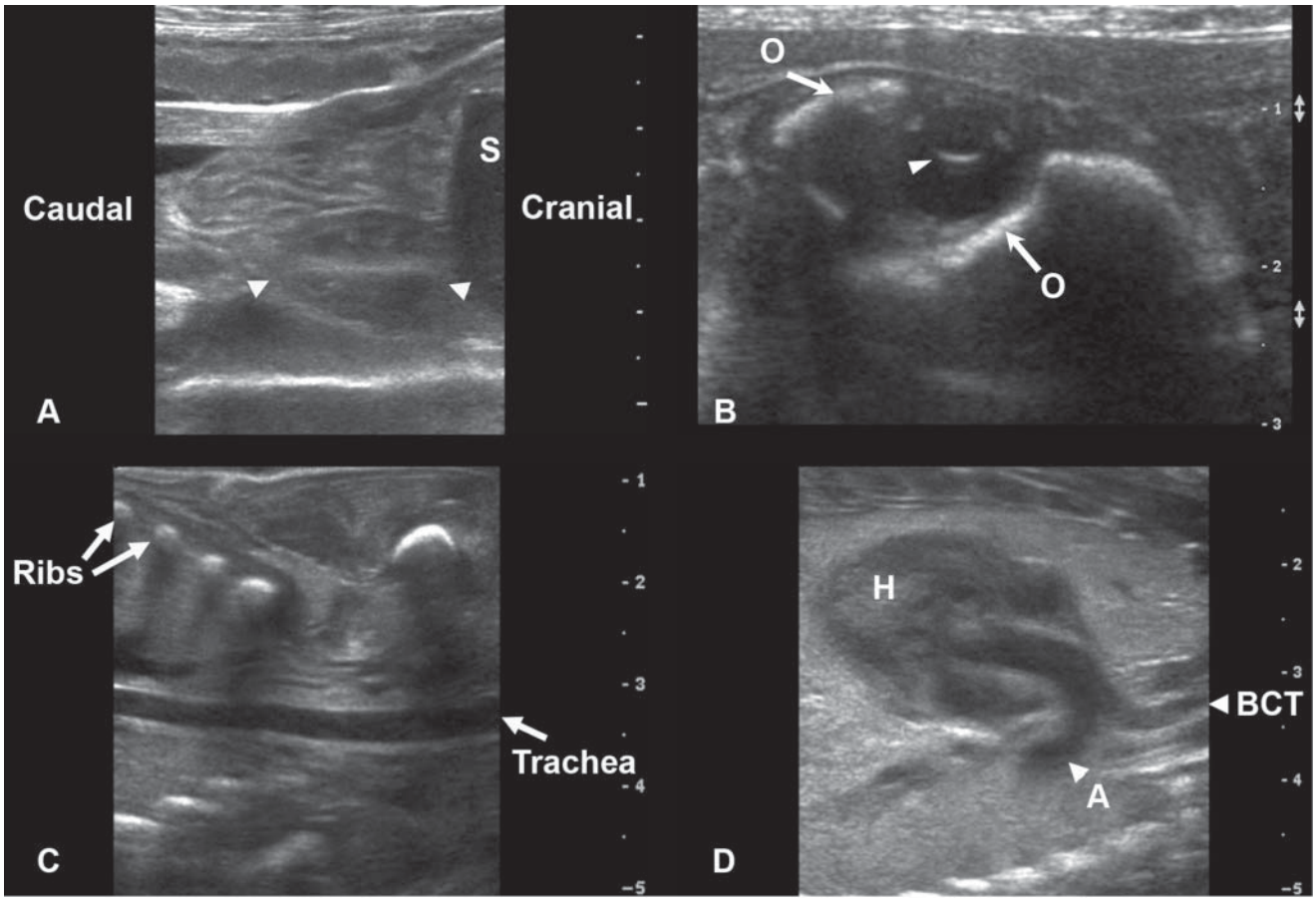


Figure 13.16. Normal late-term pregnancy in a 4-year-old Pointer. Ultrasonographic examination was performed 2 months after last breeding. The dog had four healthy puppies delivered by Cesarean section 2 days after the ultrasonographic examination. **A:** Sagittal image of the fetal abdomen. The left kidney (arrowheads), with distinct cortex and medulla, is caudal to the fluid-filled stomach (S). Tubular intestinal segments are in the near field. **B:** Sagittal image of the fetal eye, which appears as a circular anechoic structure within a hyperechoic osseous orbit (O). The posterior capsule of the lens is clearly seen (arrowhead). **C:** Dorsal image of fetal caudal neck and cranial thorax. The trachea is tubular and fluid-filled. The ribs are characterized by small curvilinear bright interfaces associated with strong shadows. **D:** Sagittal image of the thorax. The aortic arch and proximal aorta (A) are well visualized, originating from the heart (H) in the near field. The aortic arch gives rise to the brachiocephalic trunk (BCT).

The first reliable ultrasonographic indicator of pregnancy is the detection of gestational chambers, which appear as small, thin-walled anechoic structures within the uterus. Embryos can be discerned at days 23–25 in dogs and at days 16–18 in cats. The fetus develops rapidly after day 30, enabling the identification of internal organs. A summary of ultrasonographic findings at different stages of pregnancy is presented in Table 13.2. Formulas have been developed and published to determine gestational age and predict time of parturition based on measurements of fetal dimensions (Beck et al. 1990; England et al. 1990; Yeager et al. 1992; Mattoon and Nyland 1995) (Table 13.3). Using these parameters, time of parturition can be predicted with an accuracy of ± 1–3 days (England et al. 2003; Lenard et al. 2007). Ultrasonographic determination of litter size is not reliable (Toal et al. 1986; Lenard et al. 2007).

Normal Postpartum Uterus

Ultrasonographic changes during normal involution of the postpartum uterus have been described. Uterine wall thickness and volume of intraluminal fluid decrease, and the uterus becomes less conspicuous over time. Uterine involution usually takes 3–4 weeks in dogs and 24 days in cats (Pharr and Post 1992; Ferretti et al. 2000).

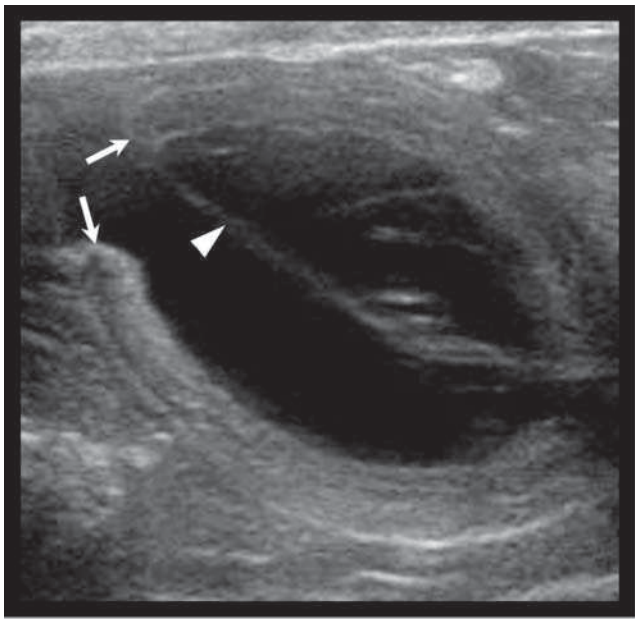


Figure 13.17. Sonogram of a 25-day-old canine fetus. The zonular placenta is distinctly identified (arrows). The arrowhead points to a thin membrane probably representing either part of the allantoic membrane or the yolk sac.

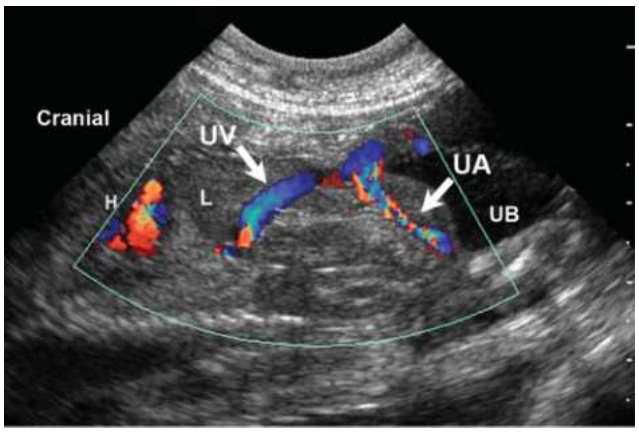


Figure 13.18. Normal fetal circulation. The head of the fetus is to the left of the image. The umbilical vein (UV) and umbilical artery (UA) extend cranially to the liver (L) and caudally to the cranial aspect of the fluid-filled urinary bladder (UB), respectively. The heart (H) is visible cranial to the diaphragm. The heterogeneous color pattern observed in the umbilical artery is caused by aliasing, a Doppler artifact that results when pulse-repetition frequency is too low in regard to a high-velocity blood flow.

Sonography of Abnormal Pregnancy

The most common abnormalities of pregnancy in dogs and cats are resorption (embryonic death before 25 days) and abortion (fetal death after 35 days). Embryonic resorption manifests as loss of the normal anechoic gestational chamber, with accumulation of echogenic material within the lumen, loss of embryonic heartbeat, embryonic disintegration, and ultimately collapse of the gestational chamber with thickening of the uterine wall (England 1998) (Figures 13.20, 13.21).

Signs of fetal death include absence of heartbeat and fetal movement, abnormal fetal posture, reduced volume and increased echogenicity of fluid in the gestational sack, accumulation of gas within fetus or uterus, and fetal disintegration (England et al. 2003) (Figure 13.22). Failure of implantation of the conceptus, small size or underdevelopment of the conceptus for true gestational age, and abnormal location of the conceptus within the uterus usually cannot be diagnosed

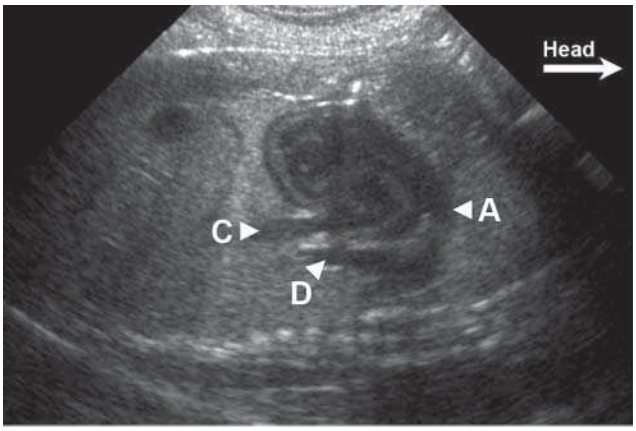


Figure 13.19. Normal fetal circulation. The head of the fetus is to the right of the image. The caudal vena cava (C) and the aorta (A) enter and leave the right and left heart, respectively. The aorta gives off the ductus arteriosus (D).

Table 13.2
Ultrasonographic diagnosis of pregnancy

Ultrasonographic Findings	Dog (Days After LH[a] Surge)	Cat (Days After Breeding)
Gestational chamber	20	10
Placental layers of uterine wall	22–24	15–17
Embryo and heartbeat	23–25	16–18
Fetal movement	34–36	30–34
Skeleton	33–39	30–33
Bladder and stomach	35–39	29–32
Liver (hypoechoic) and lung (hyperechoic)	38–42	29–32

[a]LH, luteinizing hormone.
Data from Yeager et al. (1992) and Zambelli et al. (2002).

Table 13.3
Formulas to predict gestational age and days before parturition in dogs and cats[a]

Gestational age in dogs (±3 days)
Less than 40 days
GA = (6 · GSD) + 20
GA = (3 · CRL) + 27
More than 40 days
GA = (15· HD) + 20
GA = (7 · BD) + 29
GA = (6 · HD) + (3 · BD) + 30
Days before parturition in dogs
DBP = 65 – GA
Gestational age in cats (±2 days)
Greater than 40 days
GA = 25 · HD + 3
GA = 11 · BD + 21
Days before parturition in cats
DBP = 61 – GA

[a]Gestational age (GA) is based on days after luteinizing hormone (LH) surge in dogs and days after breeding in cats. Gestational sac diameter (GSD), crown-rump length (CRL), head diameter (HD), and body diameter (BD) measurements are in centimeters. Days before parturition (DBP) is based on 65 ± 1 days after LH surge in dogs and 61 days after breeding in cats.
Data modified and adapted from England et al. (1990), Yeager et al. (1992), and Beck et al. 1990.
Reprinted from Mattoon and Nyland (1995), with permission from Elsevier.

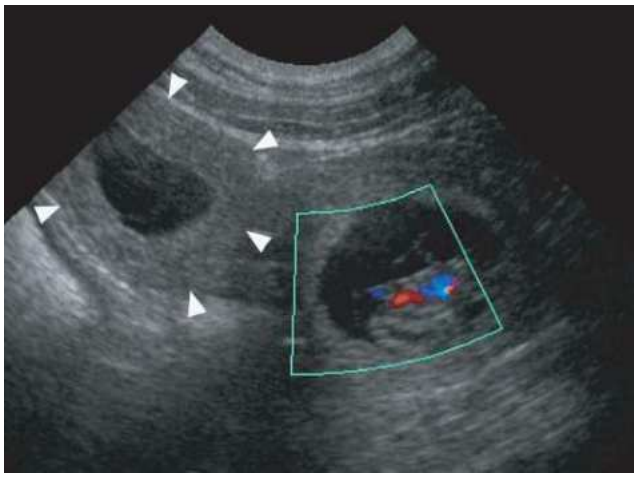


Figure 13.20. Embryonic resorption in a 2-year-old Mastiff 28 days after last breeding. Transverse image of a viable fetus (on the right) and a collapsed thick-walled gestational chamber (arrowheads), which contains a small amount of anechoic fluid. The embryo is no longer identified.

(England 1998). Ultrasonography is of particular value in assessing fetal viability and distress. Normal fetal heart rate has been reported to be twice that of maternal heart rate and is a reliable indicator of fetal viability. Bradycardia is the normal response of a fetus to hypoxia and is an important parameter to identify in dystocia.

Although a large number of congenital defects can occur in dogs and cats, these defects are very rarely diagnosed in utero. Examples of fetal abnormalities

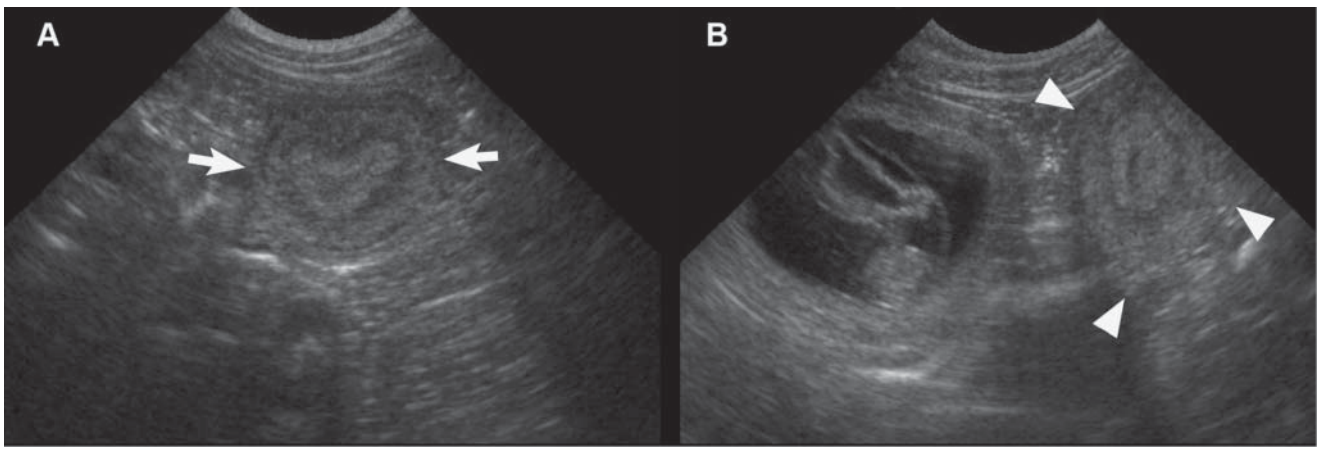


Figure 13.21. Embryonic resorption in a 7-year-old Vizsla A: Ultrasonographic examination 35 days after the last breeding. A thick-walled gestational chamber (arrows) is filled with echogenic material and fluid. Embryonic structures are not visible. **B:** Transverse image of a viable fetus on the left and a collapsed gestational chamber (arrowheads).

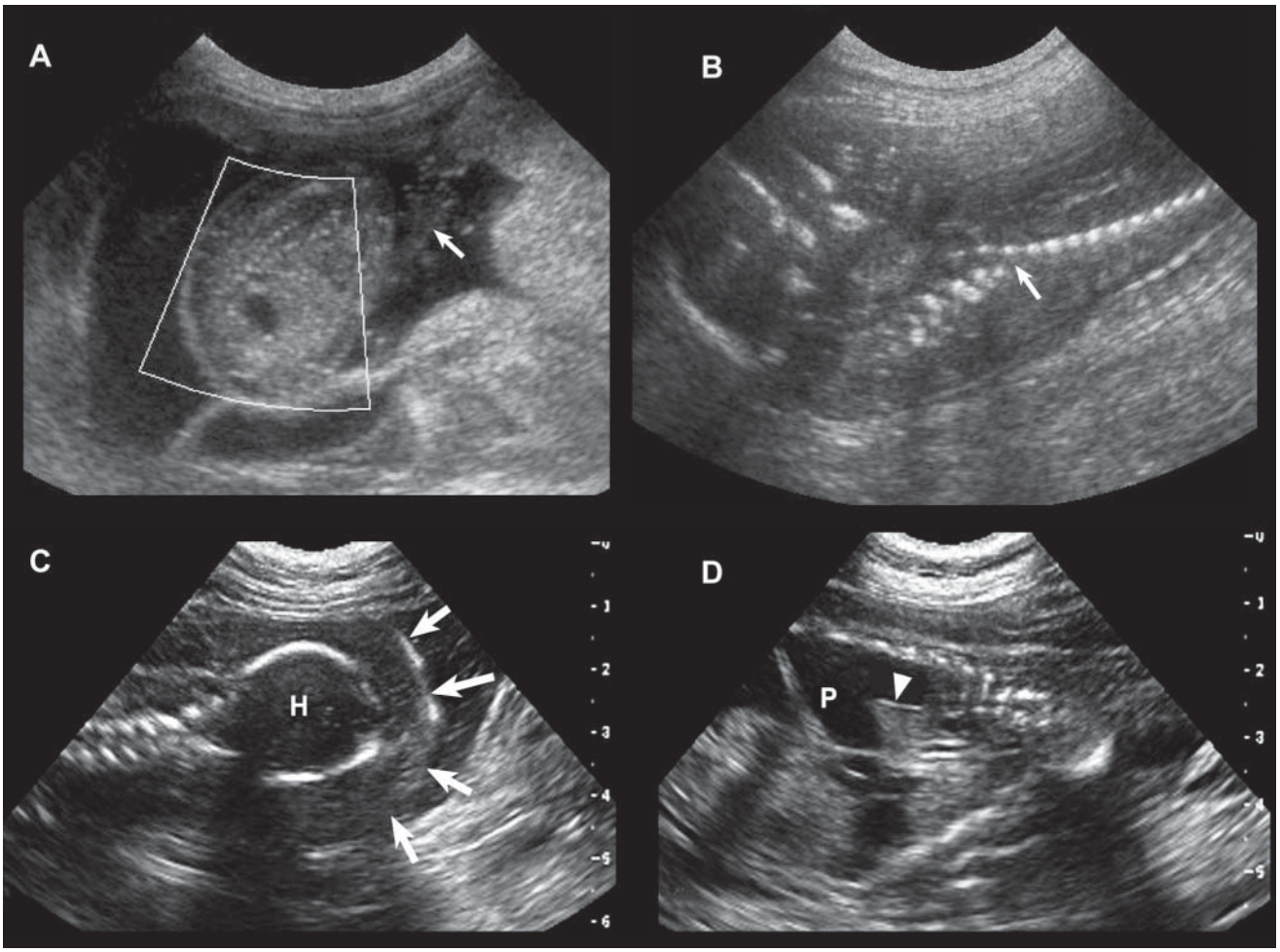


Figure 13.22. **Fetal abnormalities. A:** 1-year-old Chihuahua bred 30 days before presenting for acute hemorrhagic vulvar discharge. Doppler interrogation confirms a lack of fetal circulation. Echogenic material in the uterus is concerning for hematoma formation (arrow)**. B**. This sagittal image taken of a fetus in a 5-year-old Chesapeake Bay Retriever 50 days after breeding shows malalignment of the axial skeleton (arrow) and disruption of the skull. **C, D:** Anasarca in a Chinook dog. The affected fetus was surrounded by contained fluid (arrows in **C**), best seen here around the head (H) and neck. A moderate pleural effusion (P) associated with retracted echogenic lungs (arrowheads) is noted in **D**.

that can be detected by means of ultrasonography include hydrocephalus, fetal pleural effusion, and hydrops fetalis or anasarca (Allen et al. 1989). Only a few other pregnancy disorders have been reported in small animals. Uterine torsion is a potentially life-threatening condition that is characterized by infarction of the affected uterine segment, with subsequent wall thickening, increased echogenicity of the uterine wall and fetal fluids, and fetal death (Figure 13.23).

Uterine Diseases

Fluid within the uterus is easily visualized, and the echogenicity of the luminal contents is variable. Although hydrometra and mucometra are usually characterized by anechoic luminal fluid, and pyometra and hemometra tend to show echogenic luminal contents, ultrasonographic differentiation of these entities is often not possible (Figures 13.24–13.27).

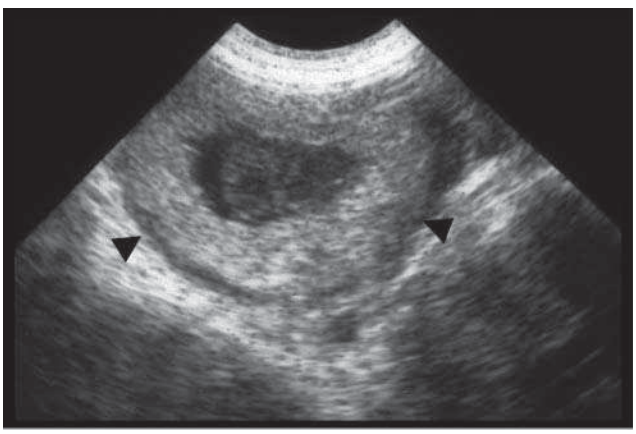


Figure 13.23. **Uterine torsion in a pregnant cat.** This transverse sonogram shows a uterine horn (arrowheads) that is thickened, hyperechoic, and contains material of soft-tissue echogenicity. A small volume of peritoneal fluid is noted around it. Fetal structures cannot be discerned.

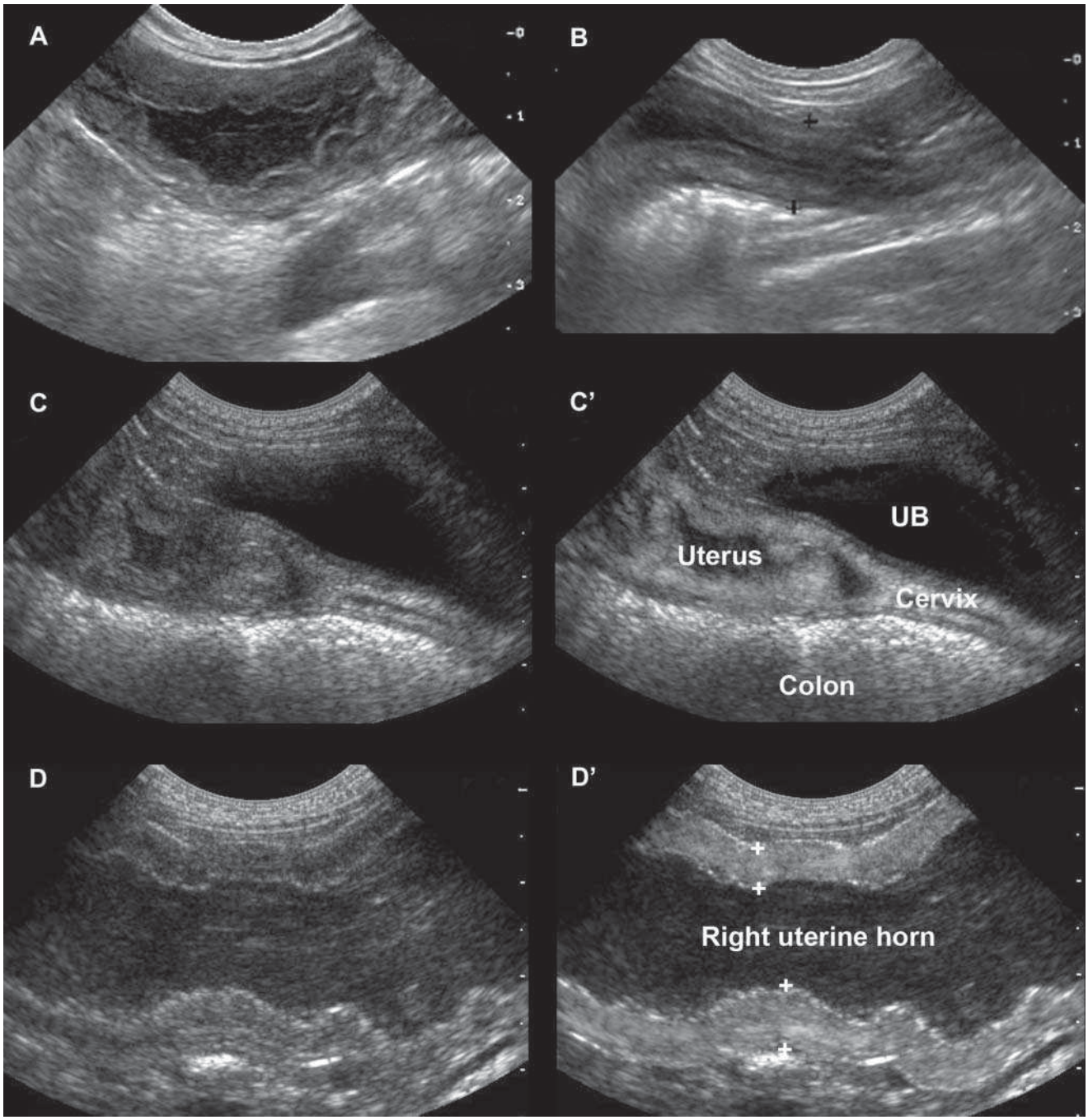


Figure 13.24. **Endometritis and pyometra in two dogs. A, B:** Endometritis in a 1-year-old German shepherd. Sagittal sonograms of a thickened uterine horn **(A)** and body **(B)** containing a small amount of anechoic fluid are shown. Notice the irregular margins of the uterus. **C,D:** Pyometra in an 8-year-old Shih Tzu. Ultrasonographic **(C)** and enhanced and labeled **(C′)** images of the cervix and body of the uterus. The cervix is closed. The uterus is thick-walled and distended with echogenic material. The uterus appears between the descending colon containing gas dorsally, and the urinary bladder (UB) ventrally. Ultrasonographic **(D)** and enhanced and labeled **(D′)** images of the right uterine horn showing a thickened wall (between the cursors, 0.5–0.8 cm). The lumen of the uterus contains echogenic fluid.

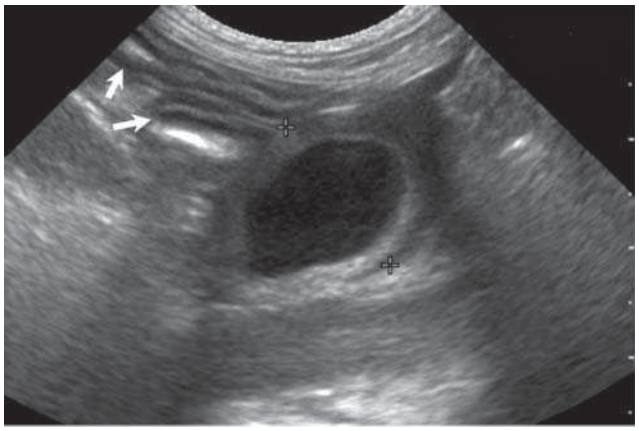


Figure 13.25. Pyometra in an 11-year-old Whippet. On this transverse image, the left uterine horn (between the cursors) is thick-walled (approximately 3 mm) and contains anechoic fluid. The uterine wall does not show wall layers, enabling differentiation from adjacent small intestinal segments (arrows).

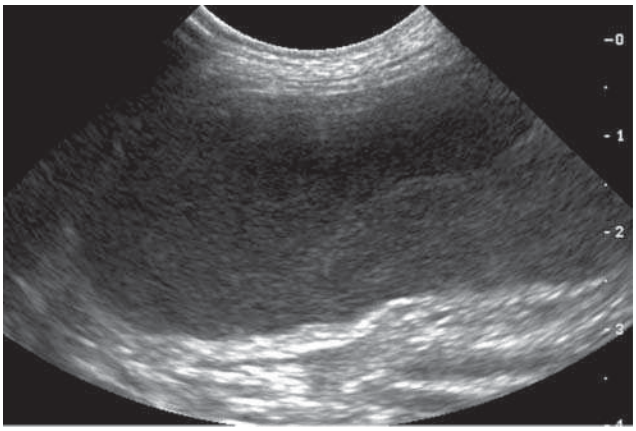


Figure 13.26. Pyometra in an 11-year-old Shiba Inu. The uterus is distended with fluid. The echogenicity of the fluid in the far field is higher than in the near field, indicating settling of particles (cells) in the dependent portion of the uterus.

Concurrent uterine wall thickening, endometrial cysts, and polyps are common. Uterine stump pyometra manifests as a fluid-filled, blind-ended pouch between the urinary bladder and descending colon (Figure 13.28).

Cystic endometrial hyperplasia causes thickening of the endometrium, with cystic lesions embedded in the uterine wall because of proliferation of endometrial glands (Voges and Neuwirth 1996) (Figure 13.29). The hyperplasia is commonly associated with fluid accumulation within the uterine lumen and may precede the development of mucometra or pyometra (Figure 13.30), or be associated with endometritis.

Neoplasms of the uterus or the uterine stump, such as polyps, leiomyomas, leiomyosarcomas, or adenocarcinomas, are rare (Klein 1996). They appear as nodules or masses of variable shape, size, and echogenicity and may be associated with fluid accumulation within the uterine lumen (Figures 13.31, 13.32). Vaginal masses can be visualized when they become large enough to extend from the pelvic canal into the abdomen (Figure 13.33). Uterine stump granulomas manifest as mass lesions of variable echogenicity between the bladder and colon (Figure 13.34). Hematoma formation

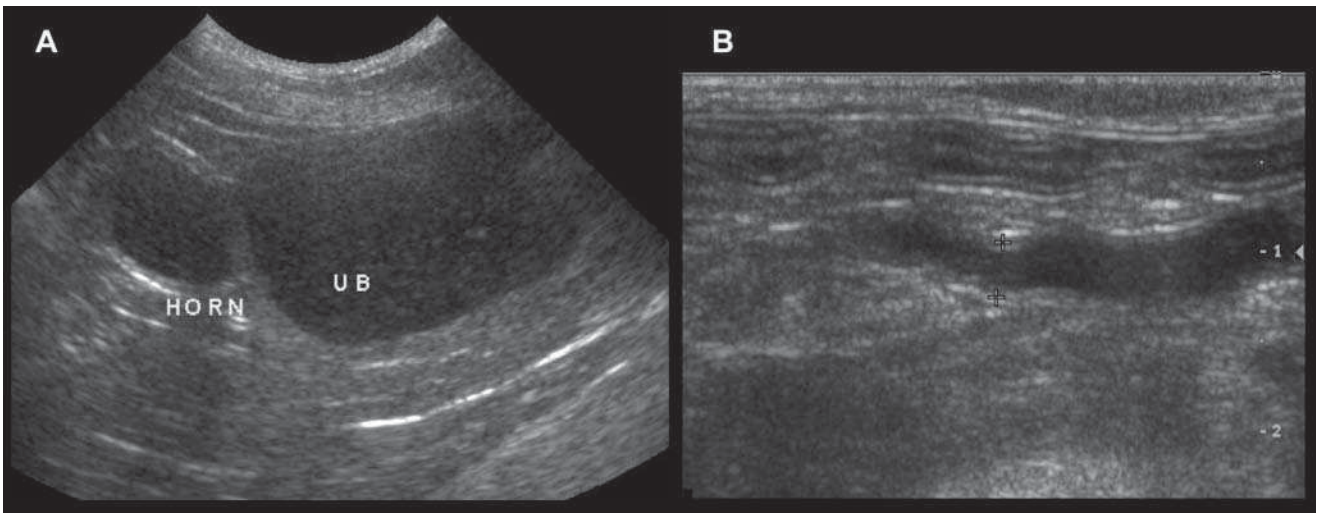


Figure 13.27. Hydrometra in two dogs. A: A sagittal image of the urinary bladder (UB) and left uterine horn is shown obtained from a 9-year-old Collie. The fluid within the uterus is similar in echogenicity to urine. **B:** Sagittal image of the right uterine horn (calipers) of a 3-year-old Chihuahua. The uterine horn is mildly distended with anechoic fluid.

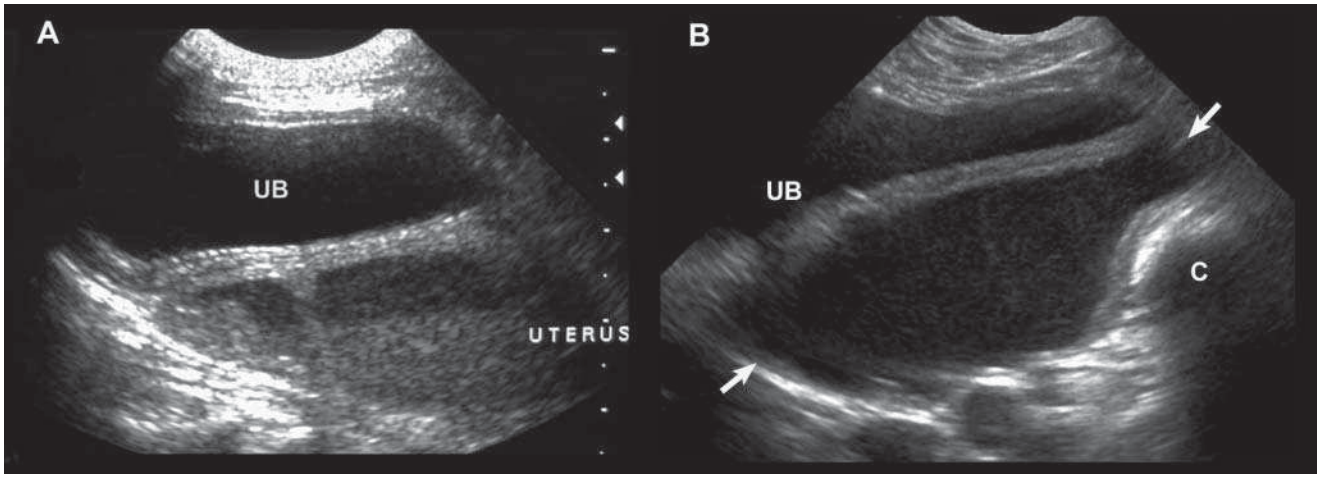


Figure 13.28. **Uterine stump pyometra in two dogs.** Sagittal **(A)** image of the uterus of a dog that previously had a hysterectomy. The uterine stump appears as a blind-ended pouch dorsal to the urinary bladder (UB). The luminal fluid in the far field is more echogenic than in the near field, consistent with settling of solid particles (cells) in the dependent portion. **B:** The markedly fluid-distended stump (arrows) seen dorsal to the bladder (UB) and the colon (C) was removed surgically and found to contain about 250 ml of pus. Residual ovary tissue was removed as well (not seen on ultrasound).

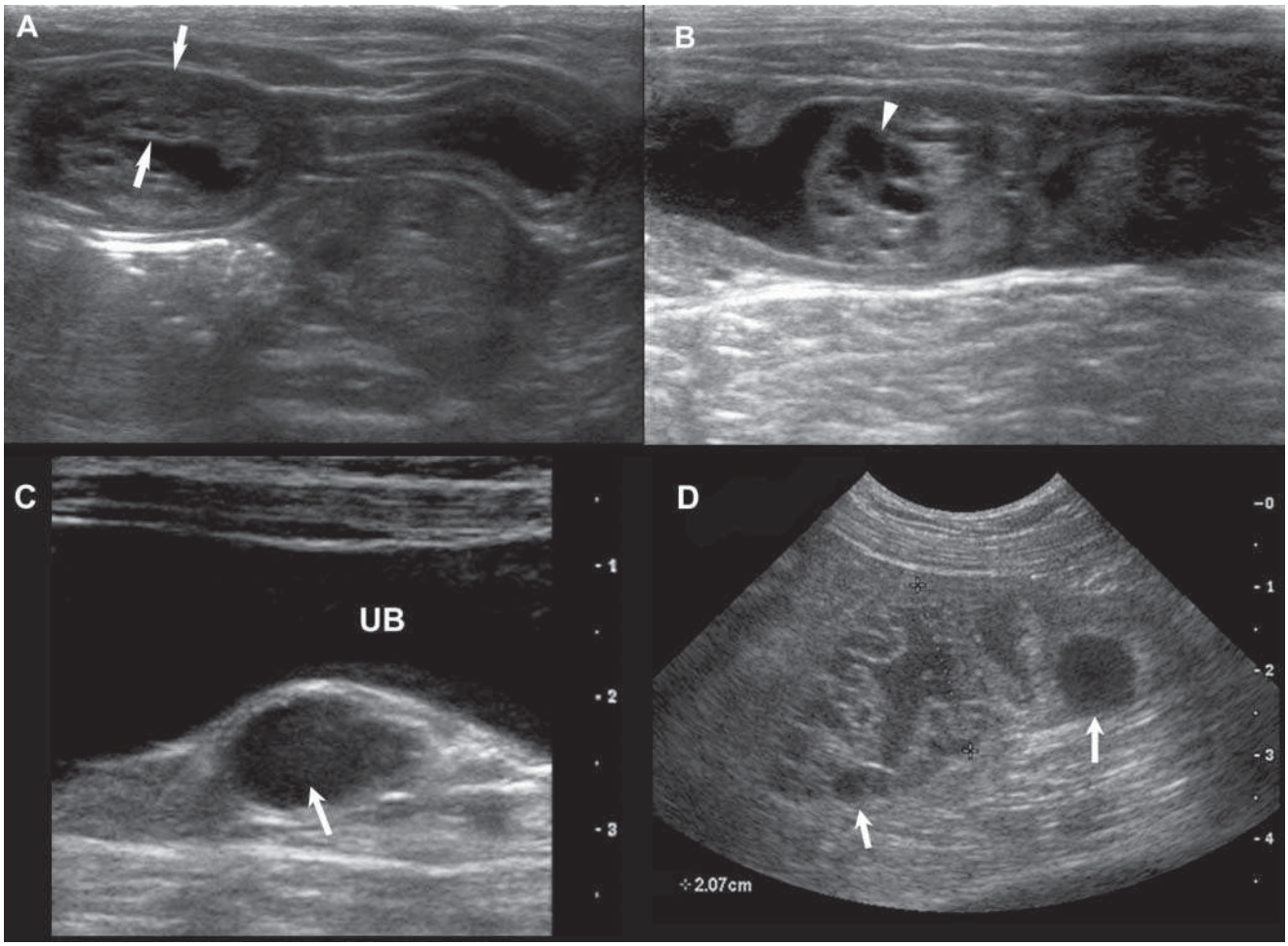


Figure 13.29. **Cystic endometrial hyperplasia in a cat and in two dogs. A, B:** Sagittal images of the uterine horns of an 8-year-old domestic shorthair cat with severe cystic endometrial hyperplasia (confirmed histopathologically). The uterine wall is thick, irregular (arrows), and multiple hypo- and anechoic structures (arrowhead) are visible within the wall. Both ovaries of this cat were multicystic. **C:** Cystic endometrial hyperplasia in a 1-year-old spayed Sheltie with residual ovarian tissue. A lobulated cystic structure (arrow) confined to the uterine stump is present dorsal to the urinary bladder (UB) **D:** Ultrasound image of a segment of an enlarged uterine horn (between the cursors) in an intact female dog with a history of chronic vulvar discharge. The uterine wall is thickened and irregular, and several anechoic to hypoechoic cysts (arrows) are identified.

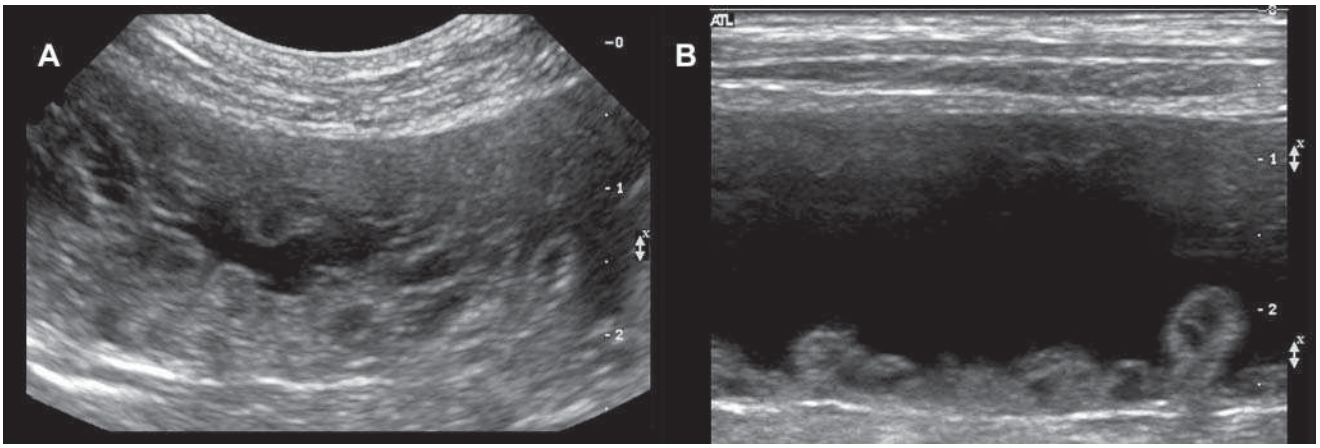


Figure 13.30. Presumptive cystic endometrial hyperplasia and mucometra in a 5-year-old Briard. Sagittal images of different areas of the left uterine horn obtained with a curvilinear **(A)** and a linear **(B)** transducer. The uterus is filled with anechoic fluid and thick-walled, with multiple anechoic cysts embedded in the uterine wall.



Figure 13.31. Uterine stump carcinoma in a 5-year-old Boxer. This sagittal image shows a mixed echogenicity mass (cursors) of more than 5-cm diameter identified in the caudal abdomen.



Figure 13.32. Uterine leiomyoma in an 8-year-old Rottweiler. A mixed echogenicity mass (between the cursors) is identified in the caudal abdomen, which measures 8.3 × 5.2 cm in maximum diameter and contains small mineralized foci with distal shadowing.

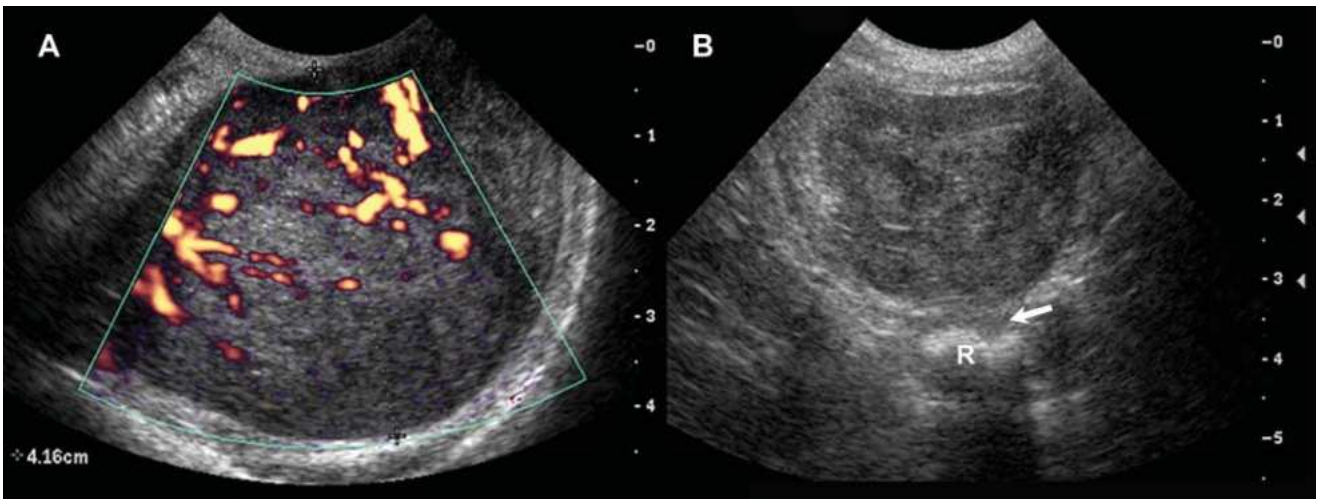


Figure 13.33. Vaginal leiomyoma. Power Doppler **(A)** and B-mode **(B)** ultrasound images of a prolapsing mass in the vagina of a 10-year-old American Eskimo Dog. A prominent vascular pattern is seen throughout the mass, which is also heterogeneous. This mass causes dorsal displacement of the rectum (R), but does not show evidence of wall invasion (arrow).

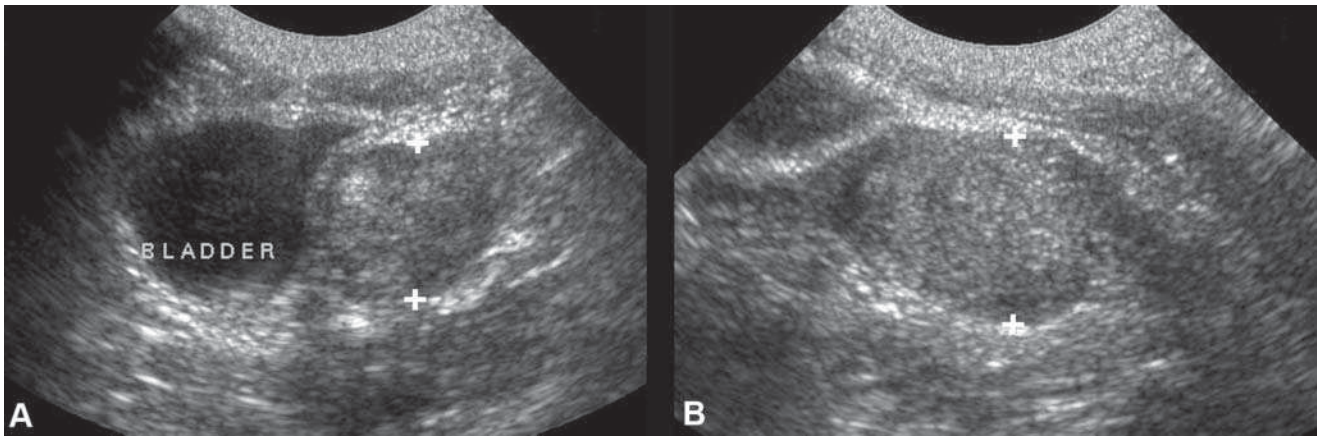


Figure 13.34. Uterine granuloma in a 13-year-old cat. Transverse **(A)** and sagittal **(B)** images show a 1.5-cm homogeneous mass lesion of medium echogenicity (between the cursors) dorsal and to the left of the urinary bladder.

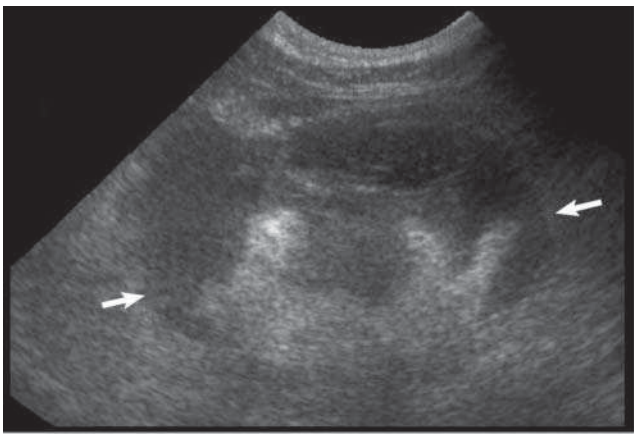


Figure 13.35. Uterine stump hematoma and abscess in a 2-year-old Australian Shepherd 1 week after ovariohysterectomy. A mixed echogenic mass (arrows) is present at the cranial aspect of the uterine stump with marked reactivity to the surrounding mesentery.

with or without abscessation can occur at the uterine stump following ovariohysterectomy and appear mass-like when ligatures loosen (Figure 13.35). Differentiation of neoplastic from non-neoplastic uterine or vaginal mass lesions and ultrasonographic distinction among different tumor types is not possible.

Mammary Glands

Sonography of Normal Mammary Glands

The appearance of the mammary glands changes under hormonal influences (late-term pregnancy and lactation). Normal mammary tissue in non-lactating dogs is coarse and hypoechoic (Figure 13.36). In lactating bitches, mammary tissue is more prominent, large vessels enter the glands, and milk-filled ducts are encountered (Figure 13.37).

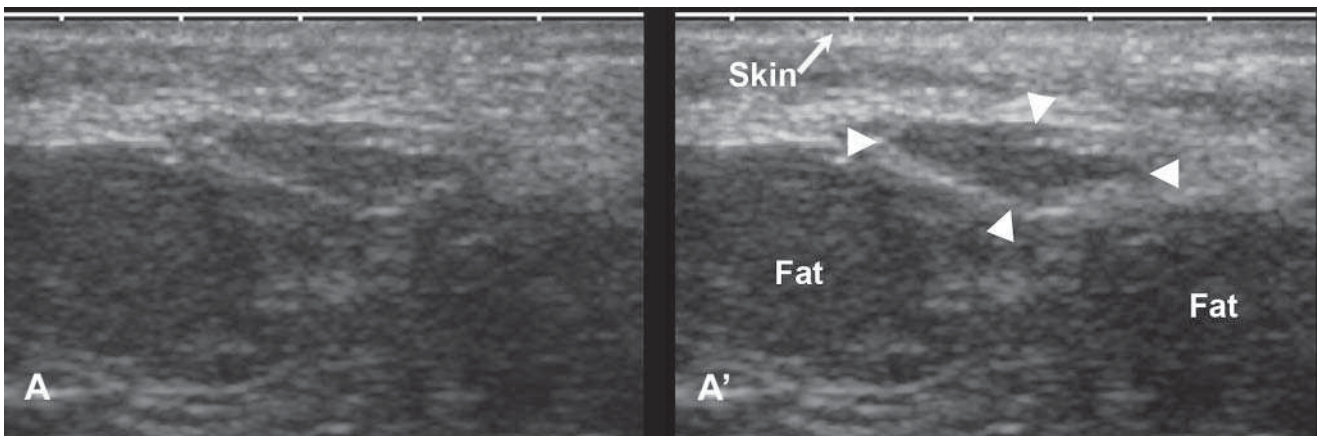


Figure 13.36. Inactive mammary tissue in an anestrus 7-year-old nulliparous Beagle. Ultrasonographic **(A)** and labeled **(A')** images in which the mammary gland (arrowheads) is inconspicuous, small (1.0 × 0.5 cm), and of similar echogenicity and texture as adjacent subcutaneous fat.

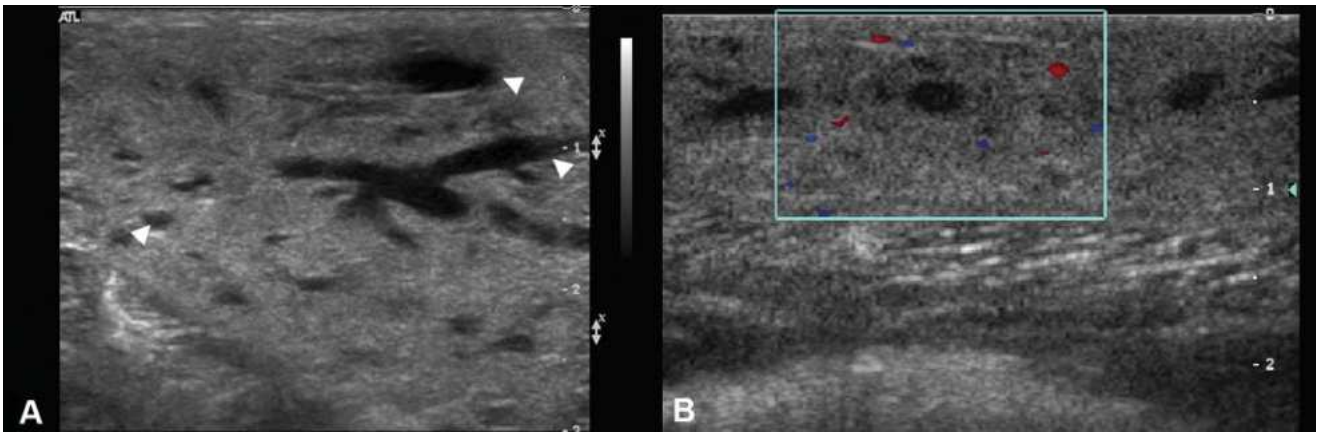


Figure 13.37. Active mammary tissue in a 4-year-old dog 2 days prior to parturition. A: The mammary tissue measures up to 3 cm in thickness, is of medium echogenicity, and contains numerous tubular milk-filled ducts (arrowheads). **B:** On color Doppler examination, there is no color signal detected in the ducts.

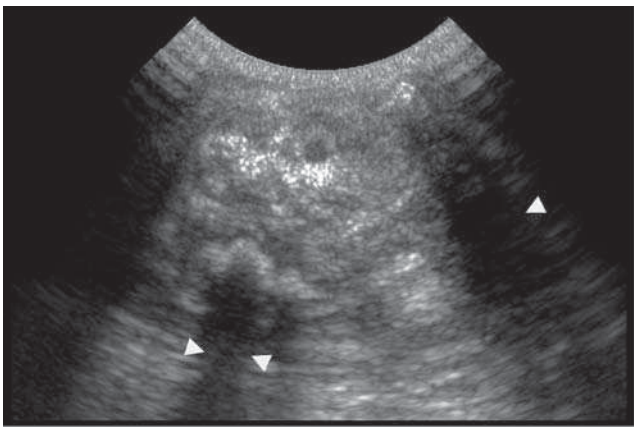


Figure 13.38. Mixed mammary tumor in a 6-year-old Rottweiler. An approximately 3-cm heterogeneous mass is associated with a mammary gland. Strong distal acoustic shadowing (arrowheads) indicates mineralization.

Sonography of Abnormal Mammary Glands

Abnormalities of the mammary glands include neoplasia, cysts, and inflammation. Mammary tumors appear ultrasonographically as irregular, mixed echogenic mass lesions of variable size (Figures 13.38, 13.39). Benign and malignant mammary tumors cannot be differentiated based on their appearance using conventional or color-flow Doppler ultrasound; however, malignant tumors are characterized by a significantly higher blood flow velocity compared with benign tumors when using Triplex Doppler ultrasound (Feliciano et al. 2012). As metastases are common in malignant tumors, the axillary and/or inguinal lymph nodes should be examined for enlargement and abnormal echotexture. Mastitis manifests as swelling

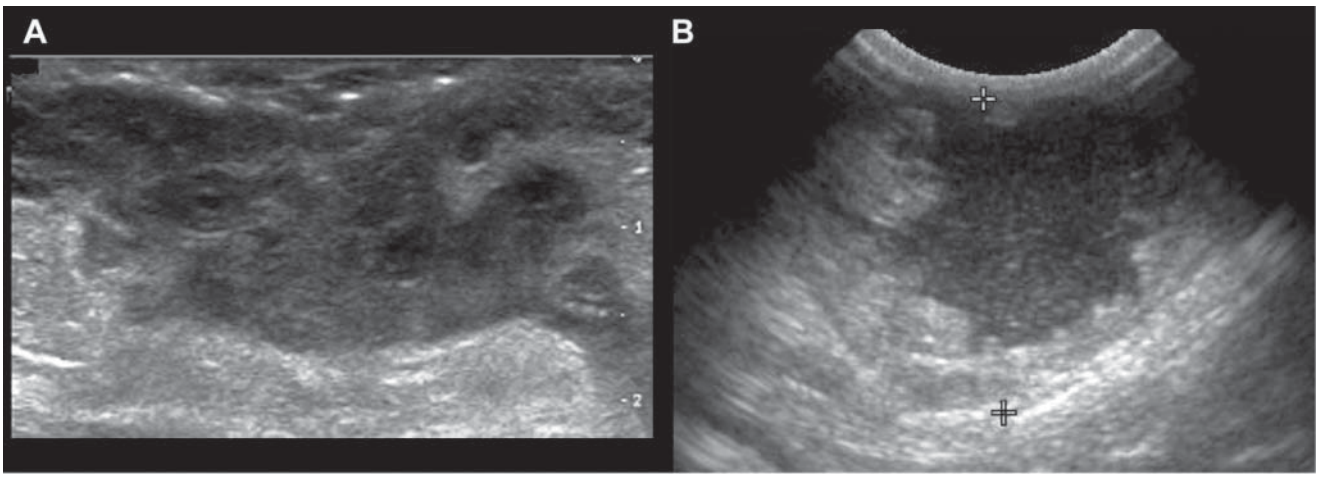


Figure 13.39. Complicated mammary carcinoma in a cat and in a dog. A: The ulcerated and extensive mass invades most of the right middle to caudal mammary chain in a 14-year-old cat. The mass is poorly echogenic, highly vascularized on color flow Doppler (not shown) and has irregular margins. **B**: This is an abscessed mammary carcinoma in a 12-year-old long-haired Dachshund. A thick-walled mass is shown (cursors) with an accumulation of echogenic fluid centrally. The mass arose from the right caudal mammary gland.

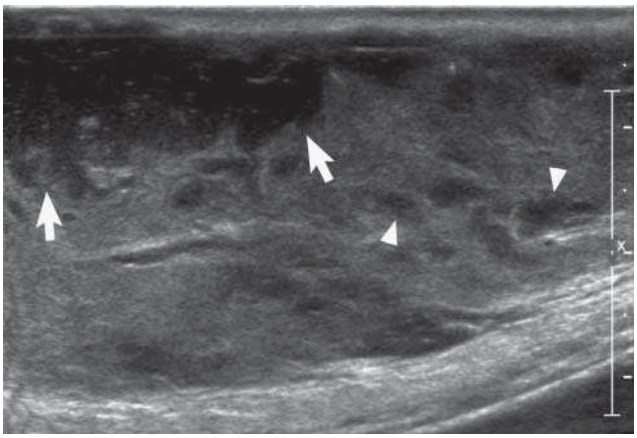


Figure 13.40. Mastitis and abscess in an 11-year-old intact Afghan dog with recurrent pseudo-gestation. The mammary gland is diffusely enlarged and inhomogeneous with several small echogenic cavities (arrowheads). A larger superficial collection of fluid (arrows) is present and pus was collected.

and hypoechogenicity of the mammary tissue, with abscessation in severe cases (Figure 13.40).

Interventional Procedures

Depending on size and location, fine-needle aspiration or biopsy of mass lesions associated with the ovary or the uterus can be performed under ultrasound guidance following the same principles and precautions as in other organ systems. Because of the risk of leakage into the peritoneal cavity, uterine fluid is usually not aspirated. Amniocentesis is not a routine procedure in the assessment of pregnant dogs or cats.

Visit our website at **www.SmallAnimalUltrasonography.com** for complementary video clips with annotations and text on:

- Normal ovaries and uterus
- Normal pregnancy
- Pyometra
- Cystic endometrial hyperplasia

References

Allen WE, England GCW, White KB (1989) Hydrops foetalis diagnosed by real time ultrasonography in a bichon frisé bitch. J Small Anim Pract 30:465–467.

Beck KA, Baldwin CJ, Bosu WTK (1990) Ultrasound prediction of parturition in the queen. Vet Radiol Ultrasound 31:32–35.

Davidson AP, Baker TW (2009) Reproductive ultrasound of the Bitch and Queen. Topics Companion Anim Med 24 (2):55–63.

Diez-Bru N, Garcia-Real I, Martinez EM, Rollan E, Mayenco A, Llorens P (1998) Ultrasonographic appearance of ovarian tumors in 10 dogs. Vet Radiol Ultrasound 39:226–233.

England GCW (1998) Ultrasonographic assessment of abnormal pregnancy. Vet Clin North Am Small Anim Pract 28:849–868.

England GCW, Allen WE, Porter DJ (1990) Studies on canine pregnancy using B-mode ultrasound: Development of the conceptus and determination of gestational age. J Small Anim Pract 31:324–329.

England GCW, Yeager AE, Concannon PW (2003) Ultrasound imaging of the reproductive tract of the bitch. In: Concannon PW, England GCW, Verstegen JP, Linde-Forsberg C, eds. Recent Advances in Small Animal Reproduction. Ithaca, NY: International Veterinary Information Service.

Feliciano MAR, Vicente WRR, Silva MAM (2012) Conventional and Doppler ultrasound for the differentiation of benign and malignant canine mammary tumours. J Small Anim Pract 53:332–337.

Ferretti LM, Newell SM, Graham JP, Roberts GD (2000) Radiographic and ultrasonographic evaluation of the normal feline postpartum uterus. Vet Radiol Ultrasound 41:287–291.

Klein MK (1996) Tumors of the female reproductive system. In: Withrow SJ, MacEwen EG, eds. Small Animal Clinical Oncology. Philadelphia: WB Saunders, pp 347–355.

Lenard ZM, Hopper BJ, Lester NV, Richardson JL, Robertson ID (2007) Accuracy of prediction of canine litter size and gestational age with ultrasound. Aust Vet J 85: 222–225.

Mattoon JS, Nyland TG (1995) Ovaries and uterus. In: Nyland TG, Mattoon JS, eds. Small Animal Diagnostic Ultrasound. Philadelphia: WB Saunders, pp 231–249.

Pharr JW, Post K (1992) Ultrasonography and radiography of the canine postpartum uterus. Vet Radiol Ultrasound 33:35–40.

Silva LDM, Onclin K, Verstegen JP (1996) Assessment of ovarian changes around ovulation in bitches by ultrasonography, laparoscopy and hormonal assays. Vet Radiol Ultrasound 37:313–320.

Toal RL, Walker MA, Henry GA (1986) A comparison of real-time ultrasound, palpation and radiography in pregnancy detection and litter size determination in the bitch. Vet Radiol Ultrasound 27:102–108.

Voges AK, Neuwirth L (1996) Ultrasound diagnosis: Cystic uterine hyperplasia. Vet Radiol Ultrasound 37:131–132.

Yeager AE, Concannon PW (1995) Ultrasonography of the reproductive tract of the female dog and cat. In: Bonagura JD, ed. Kirk's Current Veterinary Therapy XII. Philadelphia: WB Saunders, pp. 1040–1052.

Yeager AE, Mohammed HO, Meyers-Wallen V, Vannerson L, Concannon PW (1992) Ultrasonographic appearance of the uterus, placenta, fetus, and fetal membranes throughout accurately timed pregnancy in beagles. Am J Vet Res 53:342–351.

Zambelli D, Caneppele B, Bassi S, Paladini C (2002) Ultrasound aspects of fetal and extrafetal structures in pregnant cats. J Feline Med Surg 4:95–106.

CHAPTER FOURTEEN

Male Reproductive Tract

Silke Hecht[1] and Rachel Pollard[2]

[1] *Department of Small Animal Clinical Sciences, University of Tennessee College of Veterinary Medicine, Knoxville, TN, USA*

[2] *University of California, Davis, School of Veterinary Medicine, Department of Surgical and Radiological Sciences, Davis, CA, USA*

Preparation and Scanning Procedure

Ultrasonographic examination of male reproductive organs is commonly performed in dogs but rarely in cats. Examination technique, normal findings, and disorders of the male reproductive tract described in this chapter pertain to dogs unless indicated otherwise.

Indications for examination of the male reproductive tract include andrologic evaluation of breeding dogs; identification of retained testicles; difficulties or abnormalities in urination or defecation; abdominal, scrotal, and penile pain or discomfort; caudal abdominal mass lesions; perineal hernia; clinical signs compatible with hormonal imbalances (hyperestrogenism); scrotal or penile trauma; abnormalities noted on rectal examination; and palpable scrotal abnormalities.

The prostate is examined transabdominally after routine clipping and application of contact gel. The dog is usually positioned in dorsal recumbency. A rectal examination technique has been described (Zohil and Castellano 1995), but is not used routinely. A 5.0-MHz transducer may be sufficient to identify gross prostatic abnormalities such as paraprostatic cysts or prostatic abscesses; however, a 7.5- or 10-MHz transducer provides better detail and is recommended for most indications. The prostate is located in the caudal abdomen or cranial pelvic canal. It is identified caudal to the urinary bladder and ventral to the distal descending colon and rectum. Examination is performed in transverse and sagittal planes (Figure 14.1). Instillation of saline into the urinary bladder may improve the acoustic window (Feeney et al. 1989; Johnston et al. 1991b). In some dogs, especially in neutered dogs with an empty or intrapelvic bladder, ultrasonographic identification of the prostate may be challenging. In these cases, a concurrent digital rectal examination can be performed to identify the prostate and push it toward the ultrasound transducer. The use of contrast-enhanced ultrasound for examination of the prostate has been described in dogs (Bigliardi and Ferrari 2011; Vignoli et al. 2011) but is at this point not widely used.

The testicles should be examined with a high-frequency transducer (at least 7.5 MHz). A linear transducer with broad contact area and good resolution in the near field is preferable over a sector or curvilinear transducer. Use of a standoff pad is recommended by some examiners. Clipping of the scrotum is usually unnecessary. Ultrasound gel is preferred as a contact medium over alcohol because of the risk of scrotal irritation. The testicles are scanned in at least two planes (sagittal and transverse) (Figure 14.2).

The penis is occasionally examined to identify urethral abnormalities or to assess integrity of the os penis. Dependent on the examiner's preference, a linear or curvilinear high-frequency transducer (7.5 MHz or higher) may be used. The examination is started at the level of the os penis and is continued proximally to the level of the ischium. Evaluation of the penile urethra may be enhanced by instillation of saline using a balloon-type catheter inserted into the distal penile urethra.

Prostate

Normal Sonographic Anatomy of the Prostate

The location, size, and appearance of the prostate varies with age, previous disease, and status

Atlas of Small Animal Ultrasonography, Second Edition. Edited by Dominique Penninck and Marc-André d'Anjou.
© 2015 John Wiley & Sons, Inc. Published 2015 by John Wiley & Sons, Inc.
Companion website: www.SmallAnimalUltrasonography.com

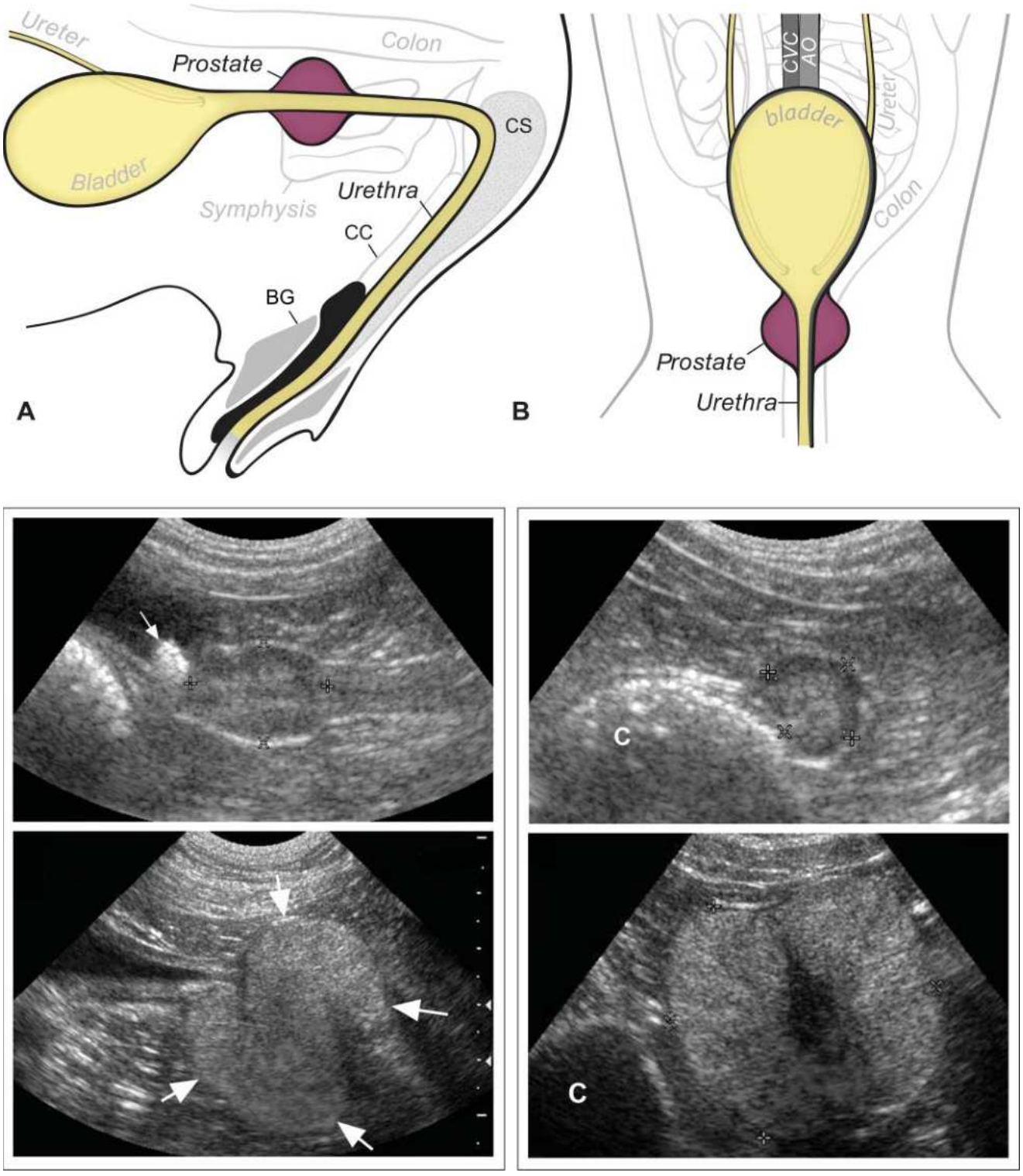


Figure 14.1. **Normal anatomy of the canine prostate.** Sagittal (**A**) and ventral (**B**) illustrations of the prostate and the surrounding structures in an adult male dog. BG, bulbus glandis; CC, corpus cavernosum; CS, corpus spongiosum. **Sonograms:** The sonograms on the top are sagittal (left) and transverse (right) images of a castrated dog. On the top left sonogram, the arrow points to a small cystic calculus in the bladder neck. The sonograms at the bottom are sagittal (left) and transverse (right) images of a 5-year-old Golden Retriever. **C**, colon. On the bottom left image, the arrows delineate the prostate.

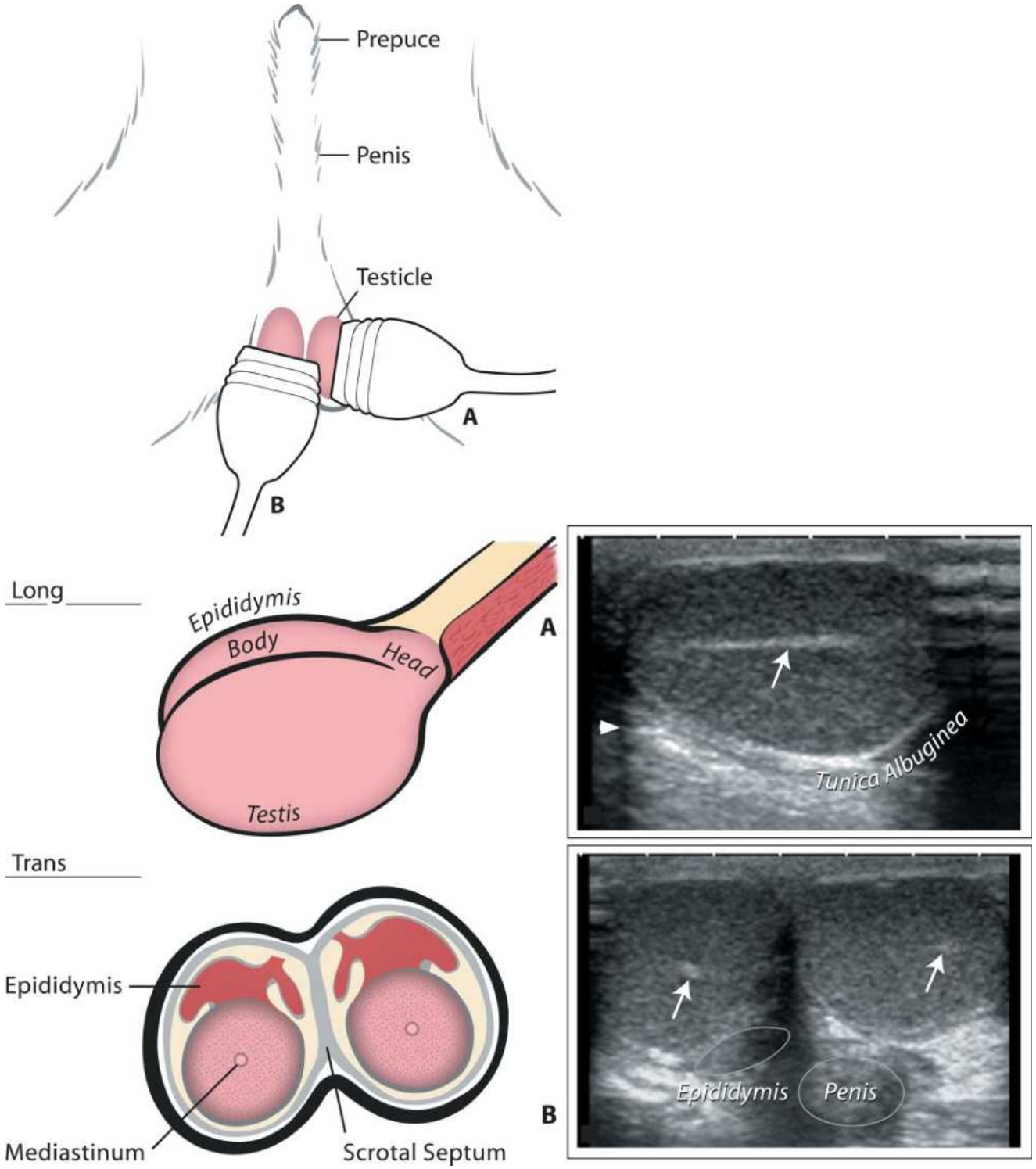


Figure 14.2. Scanning technique and normal sonographic anatomy of the testicle in an adult dog. On the top of the figure, there is a schematic representation of the position of the probe on the testicles (A and B correspond to the images below). **A:** Sagittal image of the right testicle. The testicle is oval, of medium echogenicity, and of fine and homogeneous echotexture. The tunica albuginea is smooth, thin, and hyperechoic. The mediastinum testis is seen as a central linear hyperechoic band. The epididymis is not visualized. Edge shadowing occurs at the cranial pole of the testicle (arrowhead). **B:** Transverse image of the testicles. The testicles are round and of medium echogenicity. The mediastinum testis is seen as a central or slightly eccentric hyperechoic focus in the right and left testicles, respectively. Portions of epididymal bodies are visualized dorsal to the testicles. The ovoid structure dorsal to the testicles represents part of the penis.

(intact vs neutered) (Feeney et al. 1989; Johnston et al. 1991b). In intact dogs, the prostate is of medium echogenicity and homogeneous, with a fine to medium coarse echotexture and smooth margins (Mattoon and Nyland 2002). On sagittal images, the shape is rounded to ovoid. On transverse images, the two prostatic lobes are symmetrical. The vertical raphe and prostatic urethra with surrounding urethralis muscle are generally visible as a hypoechoic area between both lobes (Figures 14.1, 14.3). The urethral structures may be associated with edge shadowing on transverse images, which should not be misinterpreted as a lesion. In intact males, age-related changes in ultrasonographic appearance of the prostate include an increase in size and echogenicity (Figures 14.1, 14.4). Prostatic cysts are a common incidental finding in older dogs (Ruel et al. 1998; Mattoon and Nyland 2002). Prostatic size in intact dogs is significantly correlated with age and body weight (Ruel et al. 1998; Atalan et al. 1999) (Table 14.1). In neutered dogs, the prostate is small, inconspicuous, hypoechoic, and homogeneous. The two lobes usually cannot be distinguished (Figure 14.5). Incidental parenchymal inhomogeneities may occasionally be observed in the prostate of older castrated dogs (Figure 14.6).

Sonographic Findings in Prostatic Abnormalities

Benign prostatic hyperplasia (BPH), bacterial prostatitis, paraprostatic cysts, and prostatic neoplasia are the

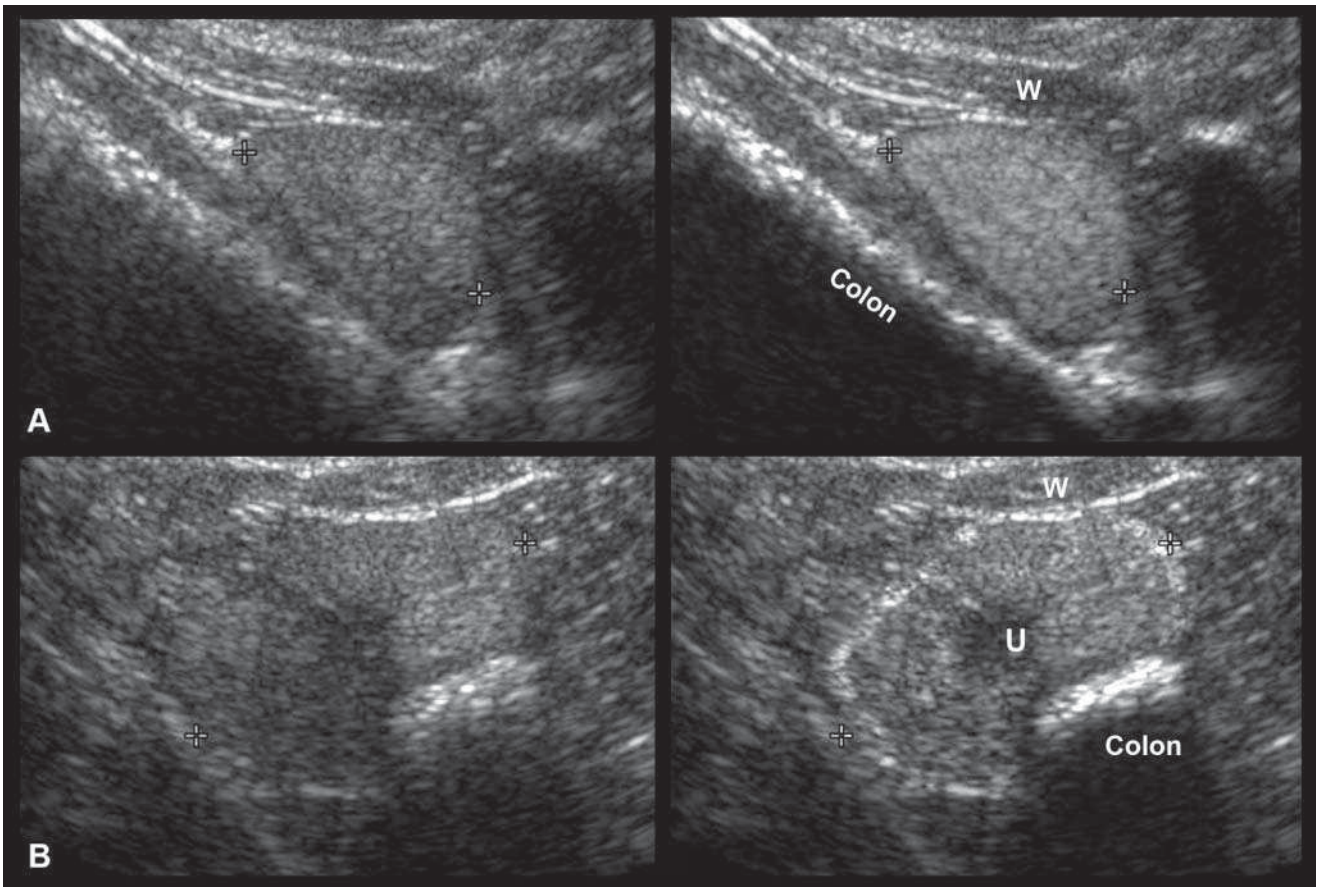


Figure 14.3. **Normal prostate in a 1-year-old intact Boston Terrier. A:** Sagittal image. The prostate appears as an ovoid, homogeneous structure of medium echogenicity dorsal to the abdominal wall (W) and ventral to the colon. The irregular, hyperechoic interface that casts a strong shadow in the colon is caused by the presence of feces. The urinary bladder is not visible in this image. Caudal and ventral to the prostate, the hyperechoic interface of the pubis marks the pelvic inlet. The shadow caused by the pubis represents a limiting factor when assessing the structures contained in the pelvis canal. **B:** Transverse image. The prostate is bilobed and appears oblique because of the angulation of the probe. The lobes are symmetrical and homogeneous. The central prostatic urethra and urethralis muscle (U) are hypoechoic. The colon is dorsal to the prostate. W, abdominal wall. The images on the right are enhanced and labeled.

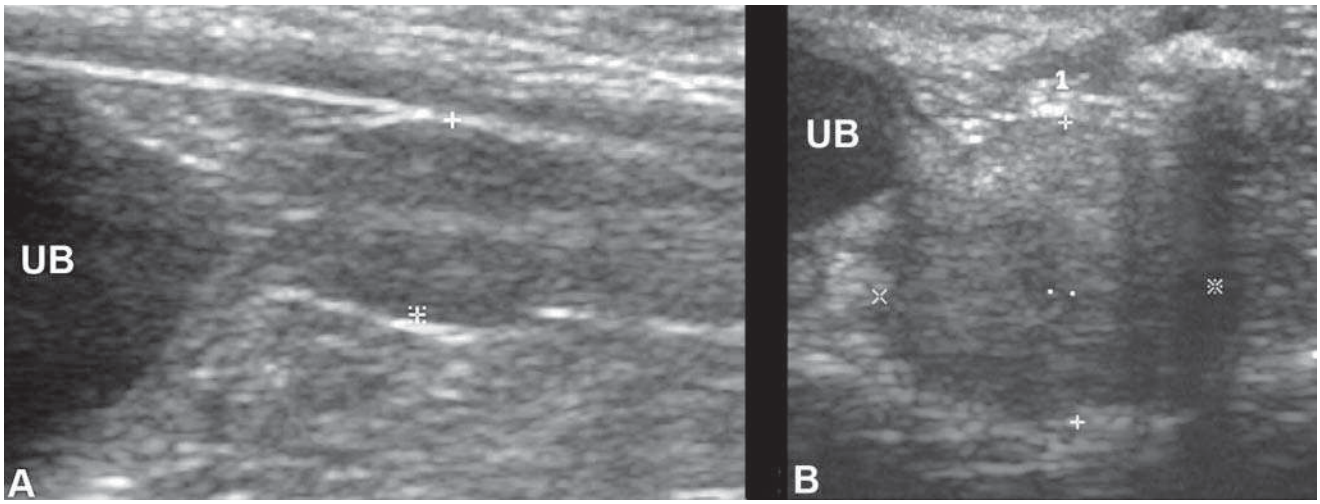


Figure 14.4. Comparison of the appearance of the normal prostate in a juvenile and an adult intact small breed dog. **A:** Sagittal image of the prostate in a 3-month-old Shih Tzu. The prostate (between the cursors) is ovoid, hypoechoic, and small (5 mm high). The urinary bladder (UB) is noted cranial to the prostate. **B:** Sagittal image of the prostate in a 9-year-old toy Poodle. The prostate (between the cursors) is rounded, of medium echogenicity, and 1.8 cm high. UB, urinary bladder.

Table 14.1
Prostatic dimensions in healthy intact dogs and correlation to age and body weight

	Ruel et al. 1998	Atalan et al. 1999
Length (cm)	1.7–6.9	1.8–5.0
Height (on transverse image) (cm)	1.3–4.7	1.4–3.6
Width (cm)	1.8–6.9	1.4–4.3
Volume (cm^3)	2.3–80.0	8.1–28.2
Correlation between prostatic length (L [cm]), age (A [years]), and body weight (BW [kg])	$L = (0.055 \times BW) + (0.143 \times A) + 3.31$	
Correlation between prostatic height (H [cm]), age (A [years]), and body weight (BW [kg])	$H = (0.044 \times BW) + (0.083 \times A) + 2.25$	
Correlation between prostatic width (W [cm]), age (A [years]), and body weight (BW [kg])	$W = (0.047 \times BW) + (0.089 \times A) + 3.45$	
Correlation between prostatic volume (V [cm^3]), age (A [years]), and body weight (BW [kg])	$V = (0.867 \times BW) + (1.885 \times A) + 15.88$	$V = 8.48 + (0.238 \times BW)$ $V = 9.79 + (0.871 \times A$

Adapted from Ruel et al. (1998) and Atalan et al. (1999).

most common prostatic disorders in dogs. Prostatic cysts are a common incidental finding or may be seen in association with BPH and other prostatic diseases. Prostatic abscesses may develop as a complication of bacterial prostatitis and/or infected cysts.

Benign prostatic hyperplasia is a spontaneous condition in older dogs and is a common incidental finding. The prostate is enlarged, of normal to increased echogenicity, and of homogeneous or inhomogeneous echotexture (Figure 14.7). On transverse images, the two lobes are usually symmetrical, although asymmetrical enlargement may occur. Intraprostatic cysts are common and manifest as circular to irregularly shaped anechoic areas of variable size (Figures 14.8, 14.9).

Acute and chronic infections occur in the canine prostate, usually secondary to ascent of urethral bacteria into a gland with BPH (Johnston et al. 2000). The prostate may be of normal size or enlarged. Echogenicity and echotexture of the prostatic parenchyma are variable, ranging from normal to heterogeneous. Although changes in echogenicity and echotexture tend to be more severe than those seen with BPH, ultrasonographic differentiation of these conditions is often not possible, and prostatitis in many cases

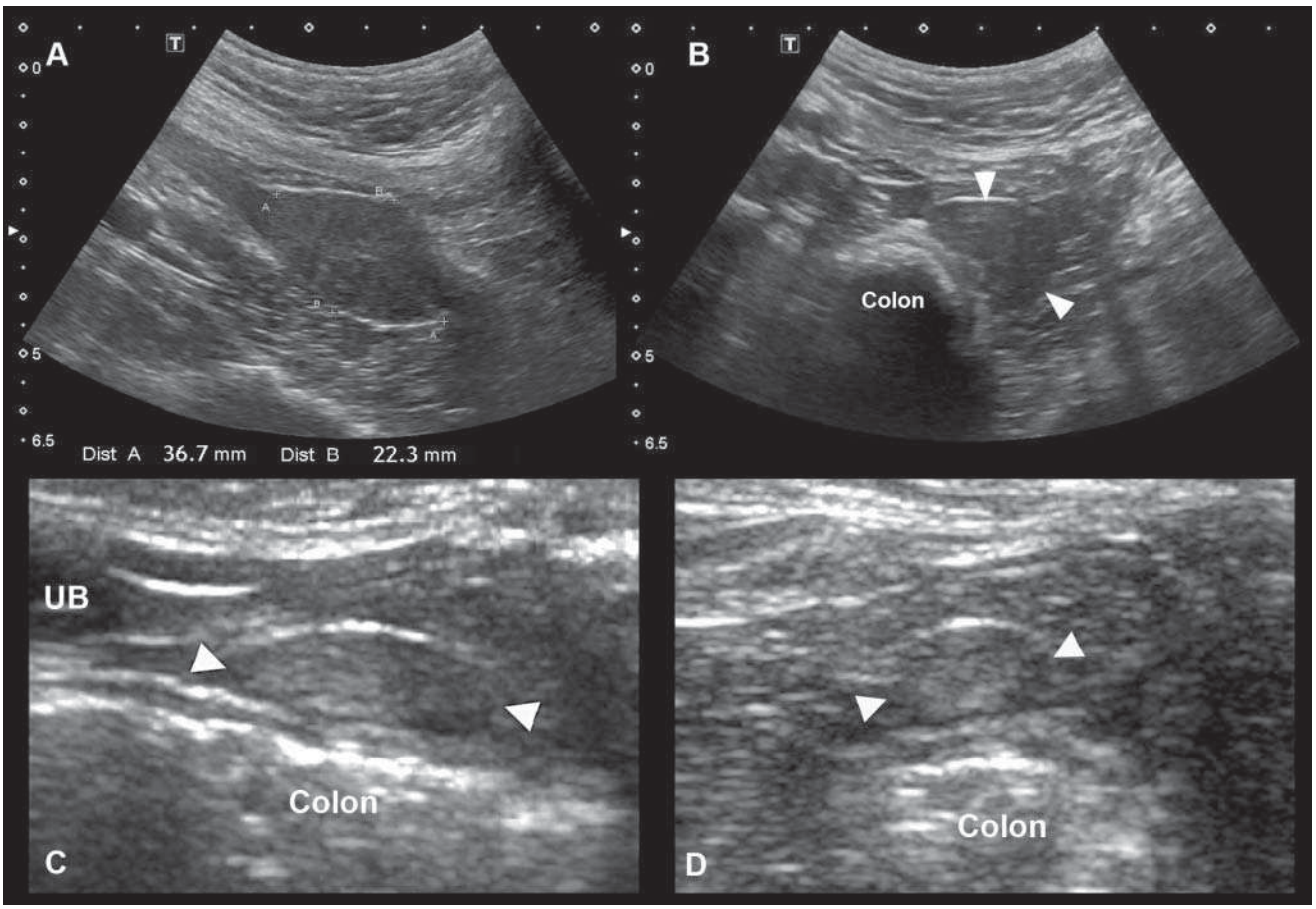


Figure 14.5. **Normal prostate in two neutered dogs. A, B:** Sagittal **(A)** and transverse **(B)** images of a normal prostate in a 5-year-old Dalmatian dog that was neutered at the age of 2 years. The prostate (between the cursors and arrowheads) is ovoid and ventral and to the left of the colon. Its two lobes, which are well seen in the transverse view, are homogeneously hypoechoic. **C, D:** Sagittal **(C)** and transverse **(D)** images of a normal prostate in an 8-year-old neutered Pomeranian. The prostate (arrowheads) is small, elongated in the sagittal view, oval in the transverse view, and of medium echogenicity.

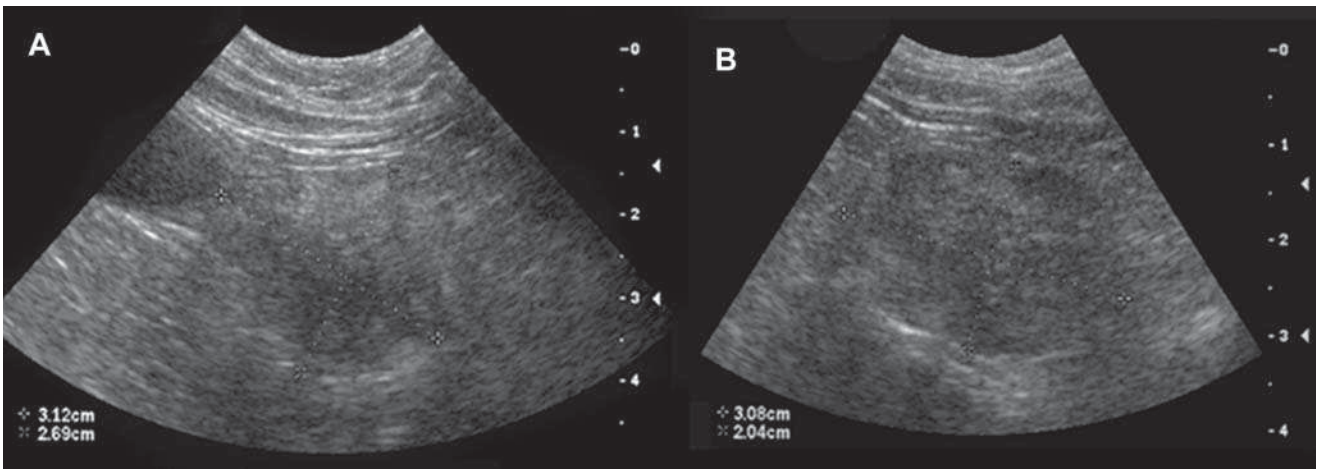


Figure 14.6. **Prostatic remodeling in an old dog with late neutering.** Sagittal **(A)** and transverse **(B)** images of the prostate of a 10-year-old dog neutered at the age of 8 years. The prostate (between the cursors) is larger than seen in dogs neutered at a younger age (Figure 14.5) and appears heterogeneous. Biopsies revealed the presence of normal prostatic tissue with fibrosis and small residual cysts. Some of these changes may be attributed to previous prostatitis. The appearance of the prostate did not significantly change on follow-up examinations.

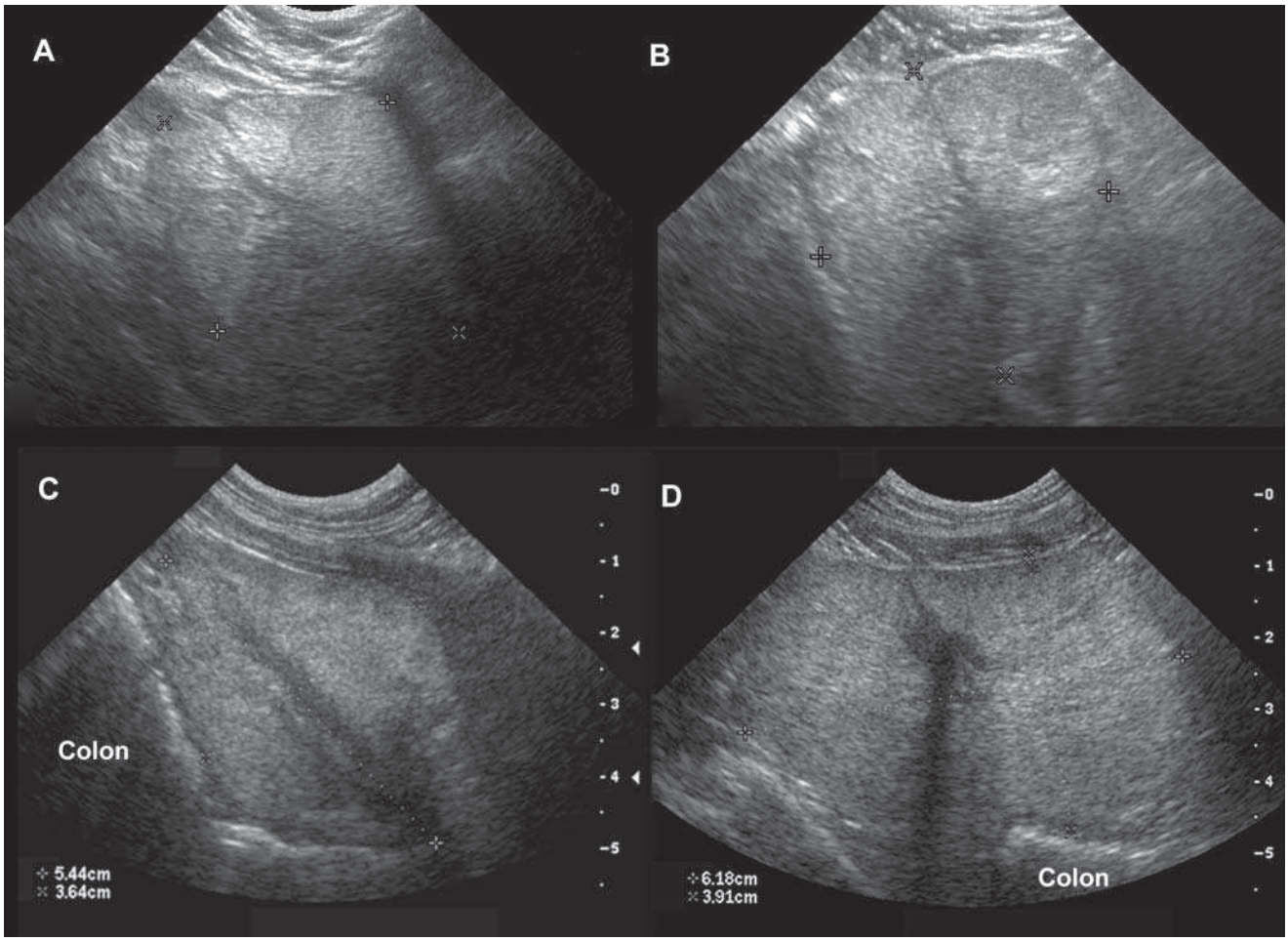


Figure 14.7. **Benign prostatic hyperplasia in two dogs. A, B:** Sagittal **(A)** and transverse **(B)** images of the prostate in a 9-year-old German Shorthair Pointer. The prostate (between the cursors) is enlarged (5.8 × 4.6 × 4.0 cm). The prostatic parenchyma is mostly hyperechoic and slightly inhomogeneous. The prostatic lobes are symmetrical on the transverse view. **C, D:** Sagittal **(C)** and transverse **(D)** images of the prostate of a 6-year-old Rottweiler in which similar signs are observed. An edge shadow noted on the transverse image is caused by the presence of the round, central urethra.

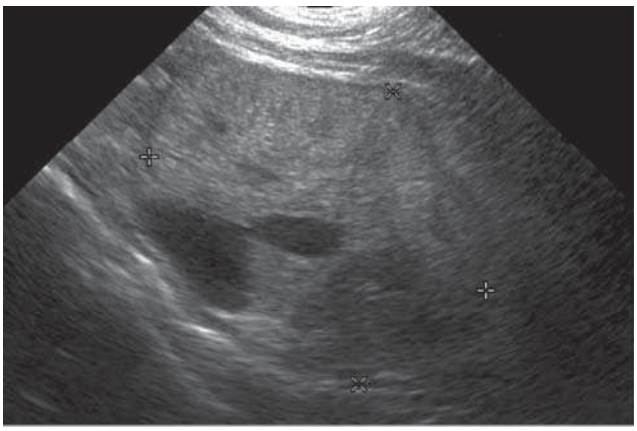


Figure 14.8. **Benign prostatic hyperplasia and intraprostatic cysts in a 10-year-old husky.** A sagittal image of the prostate shows prostatic enlargement (5.3 × 4.4 cm), inhomogeneity of the parenchyma, and multiple anechoic areas consistent with prostatic cysts.

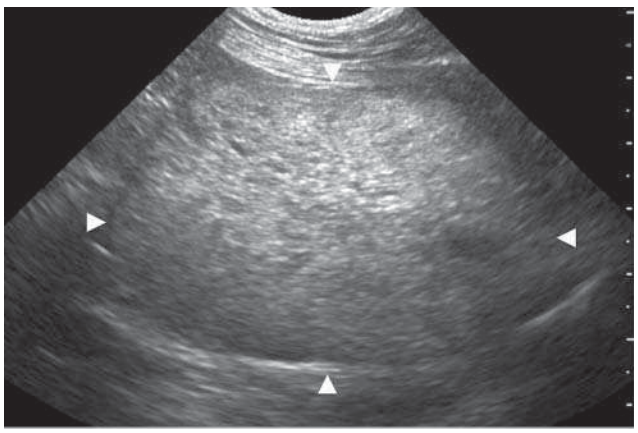


Figure 14.9. **Benign cystic prostatic hyperplasia in a 10-year-old Golden Retriever.** This parasagittal image shows prostatic enlargement (between arrowheads; 7.2 × 4.2 cm) and generalized hyperechogenicity of the parenchyma, with numerous interspersed hypoechoic foci consistent with small cysts.

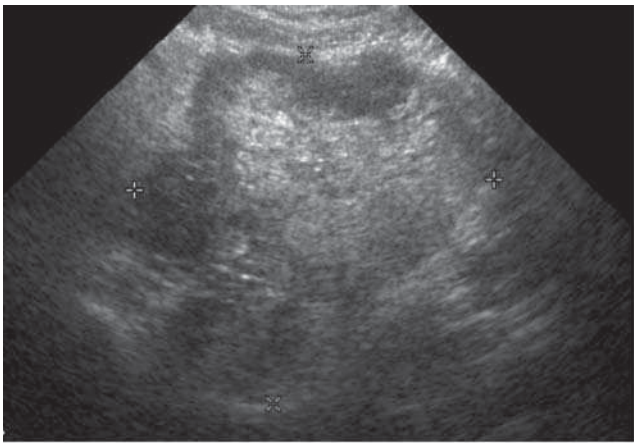


Figure 14.10. Benign prostatic hyperplasia and chronic lymphoplasmacytic prostatitis in an 11-year-old mixed-breed dog. A sagittal image of the prostate (between the cursors), shows that it is enlarged (5.9 × 5.7 cm), inhomogeneous, and has an irregular contour and mixed echogenicity.

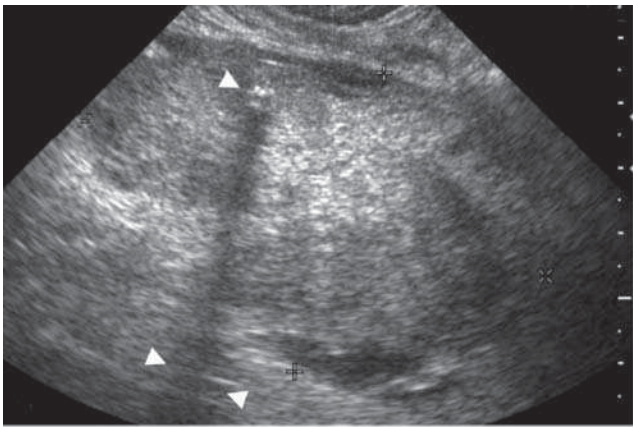


Figure 14.12. Severe, diffuse chronic-active, suppurative prostatitis with multifocal necrosis, abscessation, and interstitial hemorrhage in a 9-year-old mixed-breed dog. Sagittal sonogram of the prostate (between the cursors) shows that it is enlarged (7.5 × 4.8 cm), irregular in contour, and mixed in echogenicity, with multiple irregularly marginated anechoic areas consistent with abscesses. Parenchymal mineralization is seen as a strongly hyperechoic focus with distal shadowing (arrowheads).

complicates pre-existing BPH (Figure 14.10). In some cases of acute prostatitis, hyperechoic fat or a scant volume of effusion may be detected adjacent to the prostate (Figure 14.11). Prostatic abscesses can develop subsequent to prostatitis and may appear similar to prostatic cysts (Figures 14.12, 14.13). Other ultrasonographic findings in prostatic abscessation include development of a thick wall around the abscess cavity, intracavitary accumulation of echogenic fluid, gas inclusions in the case of infection with gas-producing bacteria, and septation (Figure 14.14). Dystrophic mineralization may be encountered in chronic prostatitis (Bradbury et al. 2009) (Figure 14.12).

Fungal prostatitis is rare, causes variable ultrasonographic changes, and may mimic prostatic neoplasia (Figure 14.15).

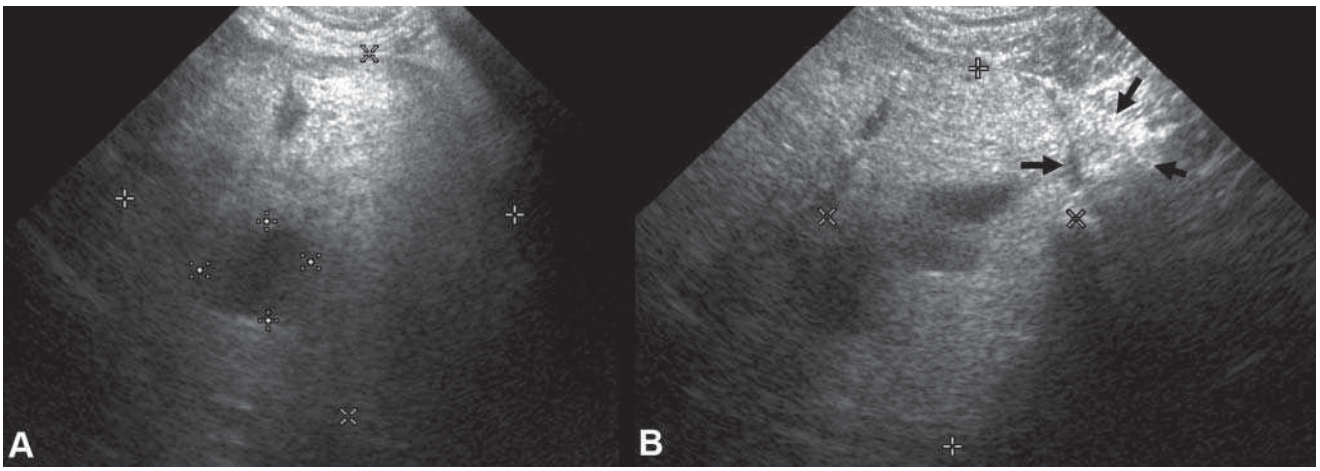


Figure 14.11. Acute prostatitis, benign prostatic hyperplasia, and intraprostatic cysts in an 8-year-old German Shepherd Dog. The diagnosis of prostatitis was based on clinical and ultrasonographic findings. No infectious organisms were seen on aspirates of one of the prostatic cysts. **A:** Sagittal image of the prostate. The prostate (between the cursors) is enlarged (6.4 × 6.0 cm), hyperechoic, and has multiple round to oval, hypoechoic to anechoic cavitations of up to 1.8 cm diameter. **B:** Transverse image of the left lobe of the prostate (between the cursors) and the paraprostatic tissues. The right lobe of the prostate is not completely included in the field of view. A small volume of abdominal effusion and strongly hyperechoic fat is adjacent to the prostate (arrows), suggesting prostatic inflammation with secondary steatitis.

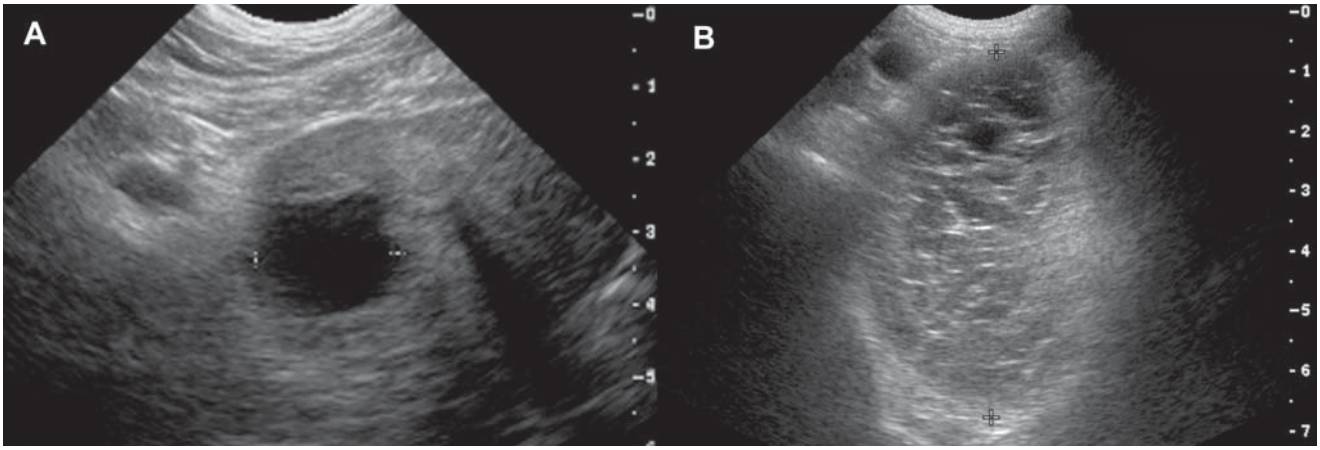


Figure 14.13. **Prostatic abscesses in two dogs. A:** Septic abscess. This transverse sonogram centered on the right lobe of the prostate of a 3-year-old Border Collie shows a well-defined anechoic cavity (between the cursors). The volume of the lesion is estimated at 3.9 mL. **B:** Sterile prostatic abscess in an 8-year-old Boxer. This transverse image shows a lacy hypoechoic to anechoic septated lesion of more than 6 cm maximum diameter associated with the right lobe (between the cursors).

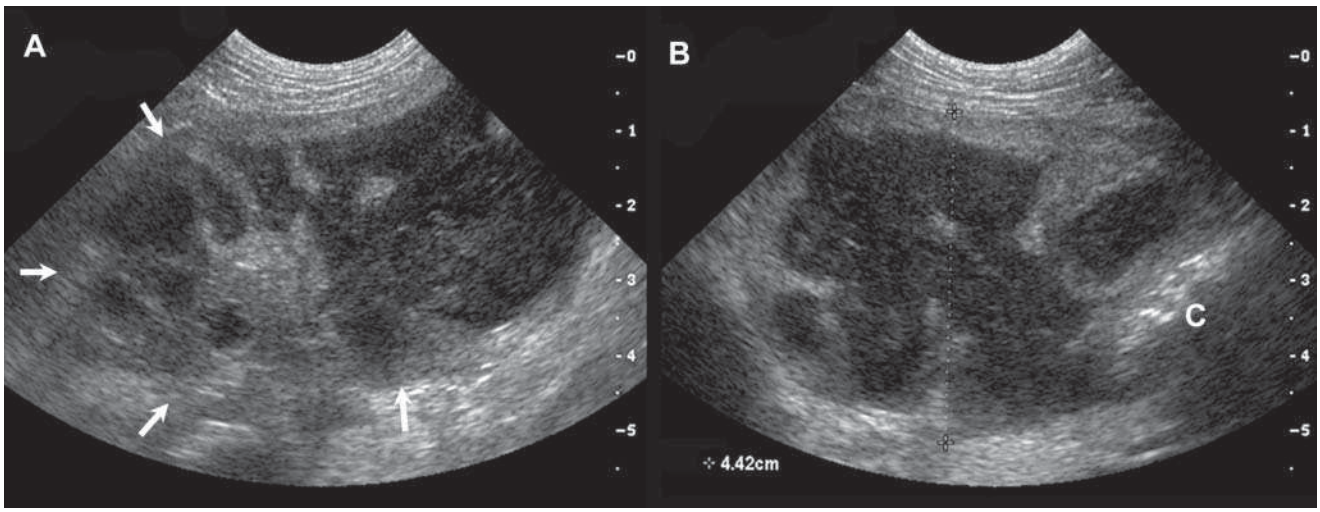


Figure 14.14. **Septic prostatitis in a dog.** Sagittal **(A)** and transverse **(B)** images of the prostate of an intact male dog with signs of abdominal pain and fever. The prostate is markedly enlarged and deformed (arrows) because of multiple hypoechoic cavitary lesions, the largest reaching 4.4 cm in diameter. Ultrasound-guided aspiration of these cavitations revealed the presence of neutrophils with bacteria. C, descending colon.

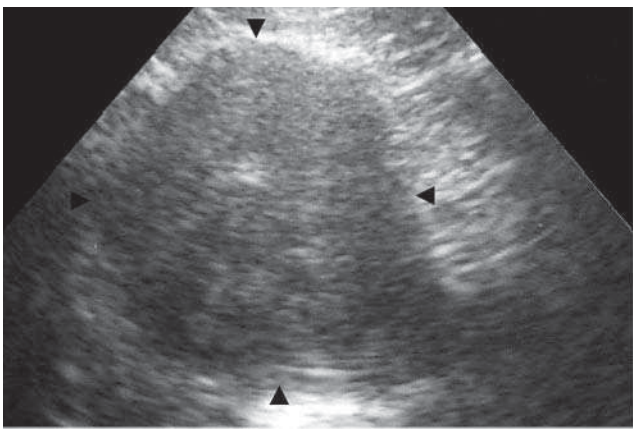


Figure 14.15. **Fungal prostatitis (blastomycosis) in an 8-year-old Cocker Spaniel.** The transverse image shows an enlarged, irregularly marginated, inhomogeneously hypoechoic prostate (arrowheads) with surrounding hyperechoic fat. Enlarged medial iliac lymph nodes were also seen (not shown).

Paraprostatic cysts are fluid-filled remnants of the Müllerian duct system that occur predominantly in older large-breed dogs (Stowater and Lamb 1989) (see also below under "Disorders of sexual development"). Unlike true intraprostatic cysts, paraprostatic cysts are located in the vicinity of the prostate, but may communicate with intraprostatic cavitations. The cyst wall is of variable thickness (Figures 14.16, 14.17). Paraprostatic cysts contain anechoic to echogenic fluid, can become very large, may contain internal septa, and may be mineralized (Figure 14.18). Sometimes it is difficult to differentiate paraprostatic cysts from the urinary bladder. In these cases, catheterization of the urinary bladder with evacuation of urine or infusion of saline is useful in differentiating the urinary bladder from paraprostatic cysts.

Ultrasonographic findings in prostatic neoplasia are variable. Adenocarcinoma is considered the most common tumor type. Other tumor types include undifferentiated carcinoma, squamous cell carcinoma, transitional cell carcinoma, lymphoma, and hemangiosarcoma (Winter et al. 2006). Bladder or urethral

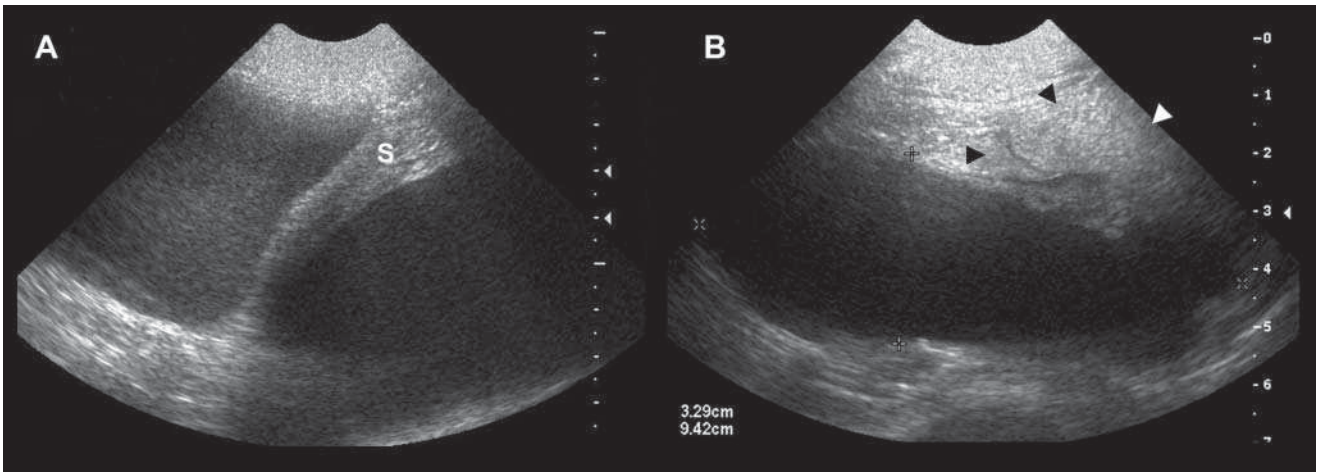


Figure 14.16. **Paraprostatic cyst in a 4-year-old cryptorchid Labrador Retriever (A) and a middle-aged dog (B). A:** The transverse image was acquired at the level of the mid-abdomen. The fluid-filled structures were separate from the urinary bladder (not shown). A thick echogenic septum (S) separates a compartment filled with very echogenic fluid (left) from one with less echogenic fluid (right). **B:** The cyst (between the cursors) is seen as a tubular anechoic structure without a discernible wall extending cranially from the dorsal aspect of the hyperechoic prostate (arrowheads).

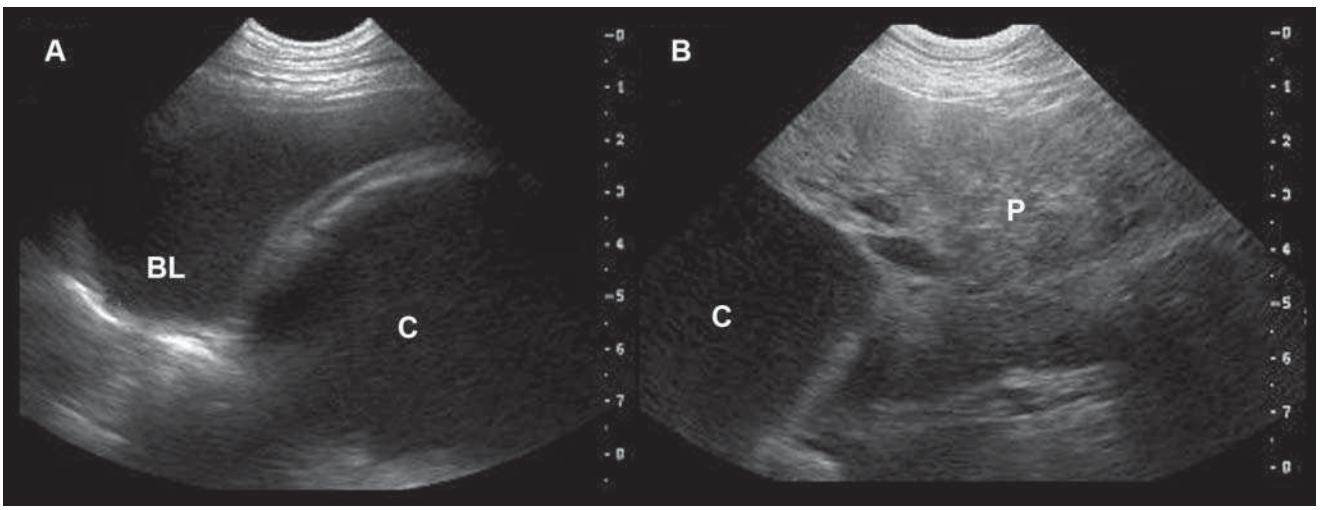


Figure 14.17. **Paraprostatic cysts and acute prostatitis in an 8-year-old Boxer. A:** The main cyst (C) is dorsal to the bladder (BL). **B:** The prostate (P) is moderately enlarged and contains several smaller parenchymal cysts. The main large cyst (C) appears to originate from the right lobe.

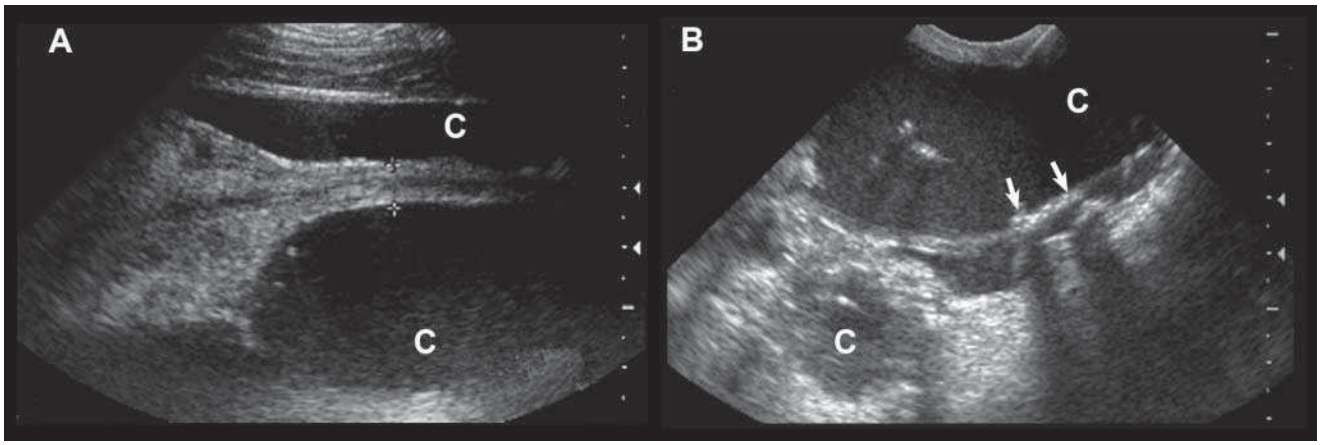


Figure 14.18. Complex paraprostatic cysts and suppurative prostatitis in a German Shepherd Dog. Numerous cysts (C) are in the mid-abdomen and caudal abdomen. **A:** The cyst walls measure up to 6 mm thick (between the cursors). The echogenicity of cystic fluid ranges from anechoic to echogenic. **B**: Mineralized foci are associated with the wall (arrows) and lumen of some of the cysts.

transitional cell carcinoma can extend into the prostatic parenchyma. In contrast to other prostatic disorders neutered dogs are commonly affected by prostatic neoplasia and may even be predisposed (Teske et al. 2002). Typically, the prostate is enlarged and irregular, with a hypoechoic to heterogeneous echotexture (Figures 14.19, 14.20). On transverse images, the prostatic lobes are usually asymmetrical (Figures 14.19, 14.21). Mineralization of the prostatic parenchyma is often seen (Bradbury et al. 2009), and metastases to medial iliac or hypogastric lymph nodes are common (Figures 14.20, 14.22). The surrounding fat may also become hyperechoic, and irregular bony proliferation of the ventral margin of the vertebral bodies of the caudal lumbar vertebrae may be seen, consistent with bone metastases. Other occasional findings in prostatic neoplasia are urethral obstruction, bladder wall thickening, or ureteral obstruction with hydroureter and hydronephrosis if the mass extends to the trigone of the urinary bladder.

Testicles

Normal Sonographic Anatomy of the Testicles

Normal testicles are of medium echogenicity and have a fine, homogeneous echotexture (Pugh et al. 1990). The testicular border is characterized by a thin, smooth and hyperechoic tunica albuginea. On sagittal images, a central hyperechoic line is visible that represents the mediastinum testis (Figure 14.2A). On transverse images, the mediastinum testis appears as a centrally located hyperechoic focus (Figure 14.2B). In very young dogs, the testicles are small but homogeneous, and the mediastinum can be identified (Figure 14.23). In older dogs, small hyperechoic foci representing testicular septa are occasionally visible. Testicular size is directly related to body weight (Hecht 2001; Hecht et al. 2003) (Table 14.2).

The head and tail of the epididymis are located at the cranial and caudal poles of the testicle, respectively,

Table 14.2
Testicular dimensions in healthy intact dogs and correlation to body weight

Body Weight (kg)	Length (cm)	Width (cm)	Height (cm)	Mediastinal Width (cm)
1–10	1.5–3.3	1.0–2.2	0.8–1.6	0.1–0.2
11–20	2.0–3.9	1.4–3.2	1.3–2.2	0.1–0.2
21–30	3.0–4.0	1.5–3.6	1.5–2.4	0.1–0.3
31–40	2.6 to >4.0[a]	1.7–3.7	1.6–3.2	0.1–0.3
>40	3.4 to >4.0[a]	2.6–3.8	1.6–3.0	0.1–0.3

[a]The transducer field of view was limited to 4 cm, and accurate measurements were not possible beyond that point.
Adapted from Hecht (2001).

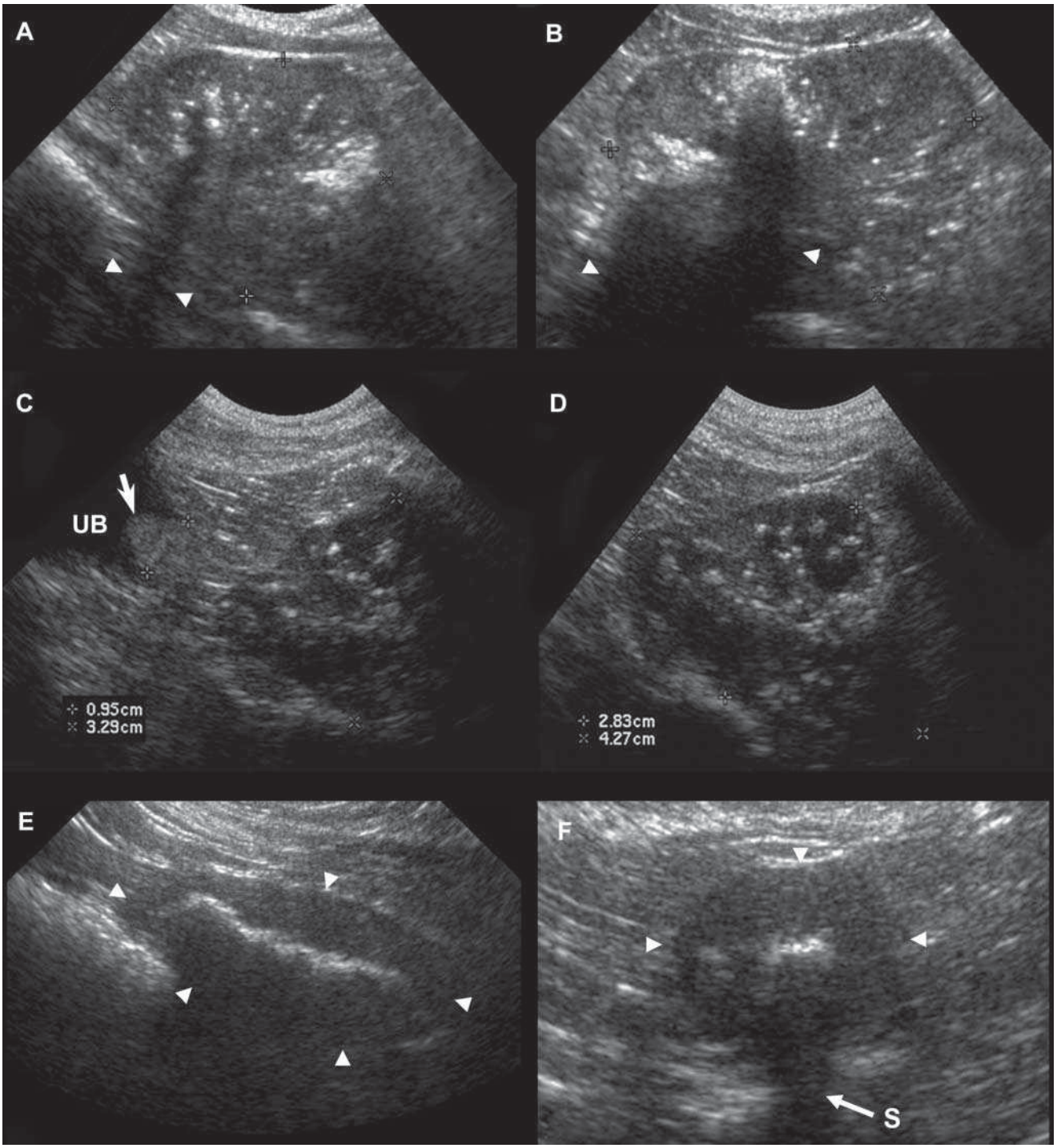


Figure 14.19. **Prostatic adenocarcinoma and transitional cell carcinoma in three dogs. A, B:** Sagittal **(A)** and transverse **(B)** images of a prostatic adenocarcinoma in an older, neutered, mixed-breed dog. The prostate (between the cursors) is large for a neutered dog, inhomogeneous, and has irregular margins. Prostatic parenchyma is of mixed echogenicity. Multiple strongly hyperechoic areas with distal shadowing (arrowheads) are consistent with mineralization. **C, D:** Sagittal **(C)** and transverse **(D)** images of a prostatic adenocarcinoma in an older, neutered, large-breed dog. The prostate is enlarged, irregular, and relatively hypoechoic, with several small hyperechoic foci. A protuberance (arrow) is also seen projecting into the urinary bladder (UB) secondary to tumor invasion. **E, F:** Sagittal **(E)** and transverse **(F)** images of transitional cell carcinoma, probably originating from the prostatic urethra, in a 12-year-old, neutered Labrador Retriever. The prostate (arrowheads) has retained a normal shape, but is large for a neutered dog. Prostatic parenchyma is hypoechoic. The centrally located, strongly hyperechoic line with distal acoustic shadowing (arrow, S) is consistent with urethral mineralization.

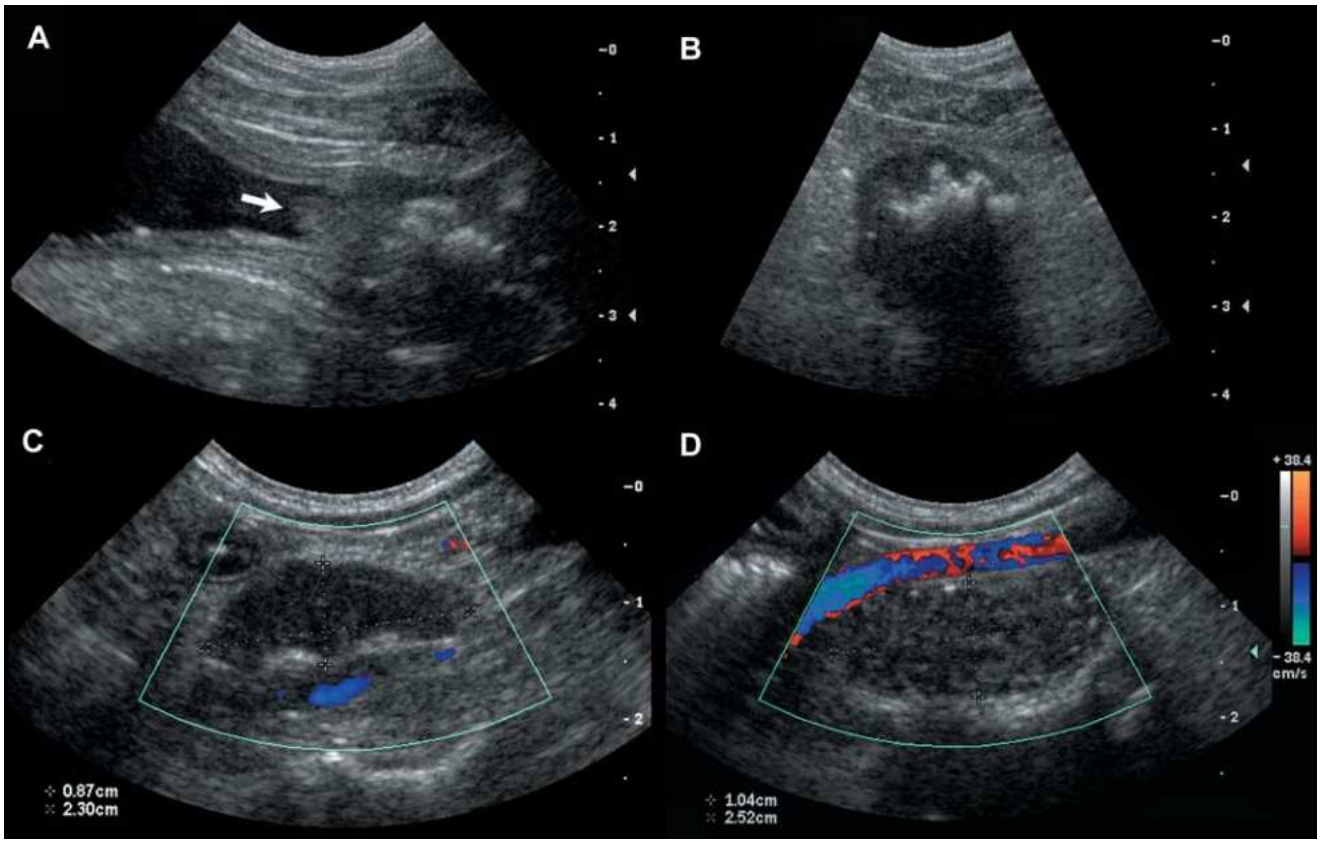


Figure 14.20. Transitional cell carcinoma and regional lymphadenopathy in an old, neutered dog with hematuria and dysuria. Sagittal **(A)** and transverse **(B)** images of the bladder neck and prostate. Strongly shadowing hyperechoic foci are noted in the prostate, and a soft-tissue projection extends into the bladder lumen (arrow). Sagittal images of right medial iliac **(C)** and hypogastric **(D)** lymph nodes, which appear enlarged and irregular. The medial iliac node **(C)** is relatively uniform and nearly anechoic in comparison with the hypogastric **(D)** node that is heterogeneous and coarse in echotexture. These lymph nodes are adjacent to the external and internal iliac vessels, respectively.

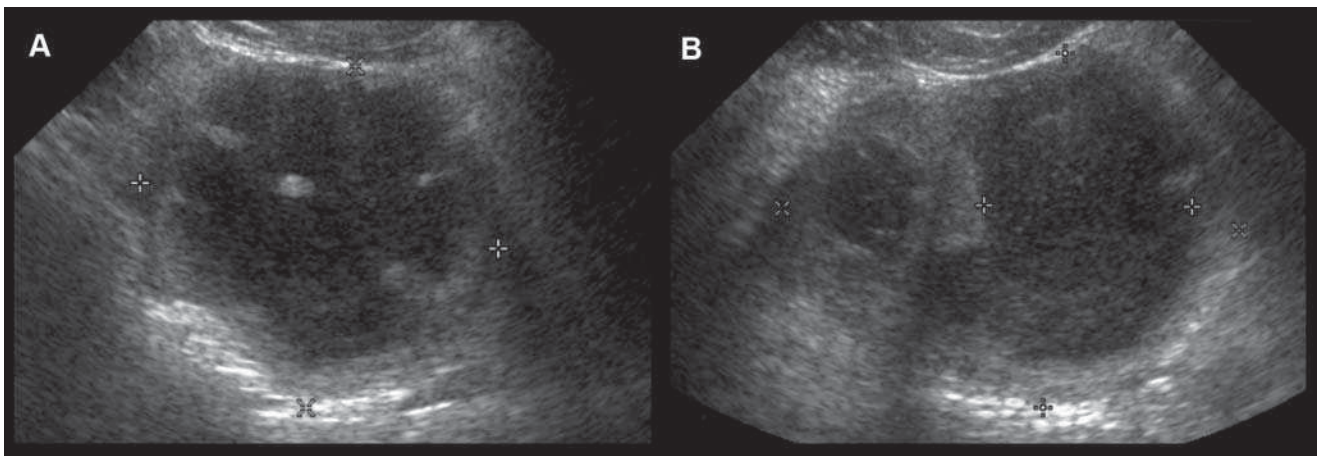


Figure 14.21. Prostatic hemangiosarcoma in a 10-year-old, neutered Greyhound. A: Sagittal image. The prostate (between the cursors) is enlarged with echogenic margins and a central hypoechoic to anechoic area. **B:** Transverse image. There is asymmetry and inhomogeneity of the prostatic lobes. The prostate (between the cursors) is of mixed echogenicity, with hypoechoic to anechoic cavitary areas.

Figure 14.24. **Normal epididymis and pampiniform plexus in a 9-year-old mixed-breed dog. A:** Sagittal image of the epididymal tail (arrowheads). It is caudal to the testicle (T), hypoechoic, and of coarse echotexture. **B:** Parasagittal image of the testicle demonstrating the tubular body of the epididymis (arrowheads) dorsolateral to the testicle (T). **C:** Sagittal image of the epididymal head and adjacent part of the spermatic cord (arrowheads), which appear hypoechoic and coarse in comparison with the cranial pole of the testicle (T). **D:** Sagittal color Doppler image of part of the spermatic cord. Tortuous vessels of the pampiniform plexus are recognized by the color flow signal.

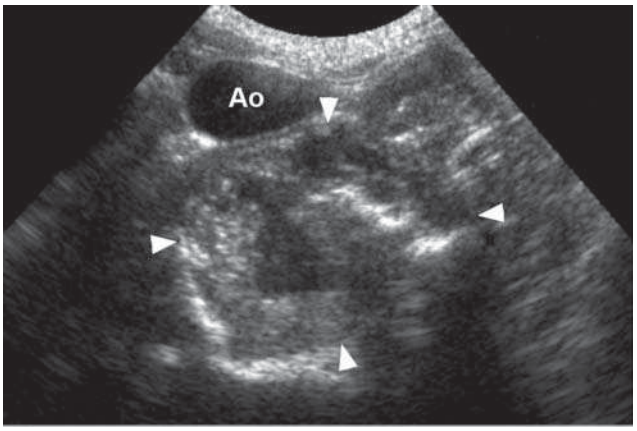


Figure 14.22. **Metastatic lymphadenopathy secondary to prostatic adenocarcinoma in an older, neutered, mixed-breed dog** (the same dog as in Figure 14.19A,B). On this transverse image, the right medial iliac lymph node (arrowheads) is enlarged and irregular in shape and margination. Multiple hypoechoic to anechoic areas indicate cavitation, and multifocal strongly hyperechoic foci with acoustic shadowing are compatible with mineralization. The aorta (Ao) is visualized as an anechoic circular structure in the near field.

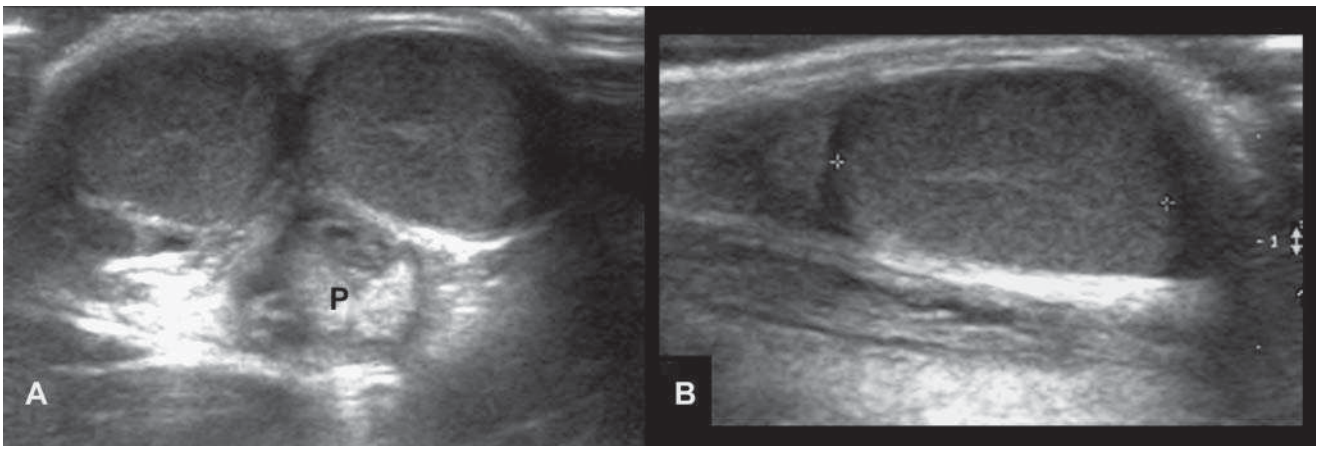


Figure 14.23. **Testicles in a 3-month-old Pointer.** The testicles (between the cursors) are small (less than 2 cm long), ovoid, and homogeneous. **A:** Transverse sonogram of both testicles. Part of the penis (P) is dorsal to the testicles. **B:** Sagittal sonogram of the left testis (between the cursors). The mediastinum testis is seen. The head of the epididymis is visible on the left of the image.

and the body is found dorsal to the testicle. In comparison with testicular parenchyma, epididymal parts are hypoechoic and have coarse echotexture (Figure 14.24A–C). Examination of the entire epididymis in one plane is usually not possible because of its location and course, and requires repositioning of the ultrasound probe with examination in at least two planes. The spermatic cord can be followed from the head of the epididymis to the inguinal ring and is characterized by the large tortuous anechoic venous structures of the pampiniform plexus. This plexus presents a prominent and complex flow pattern on color or power Doppler (Figure 14.24D).

Sonographic Findings in Testicular Abnormalities

Testicular disorders include developmental disorders (cryptorchidism), testicular neoplasia, inflammatory disorders (orchitis and epididymitis), testicular or epididymal cysts, duct ectasia of the epididymis, torsion, infarction, atrophy, and trauma. Other disease

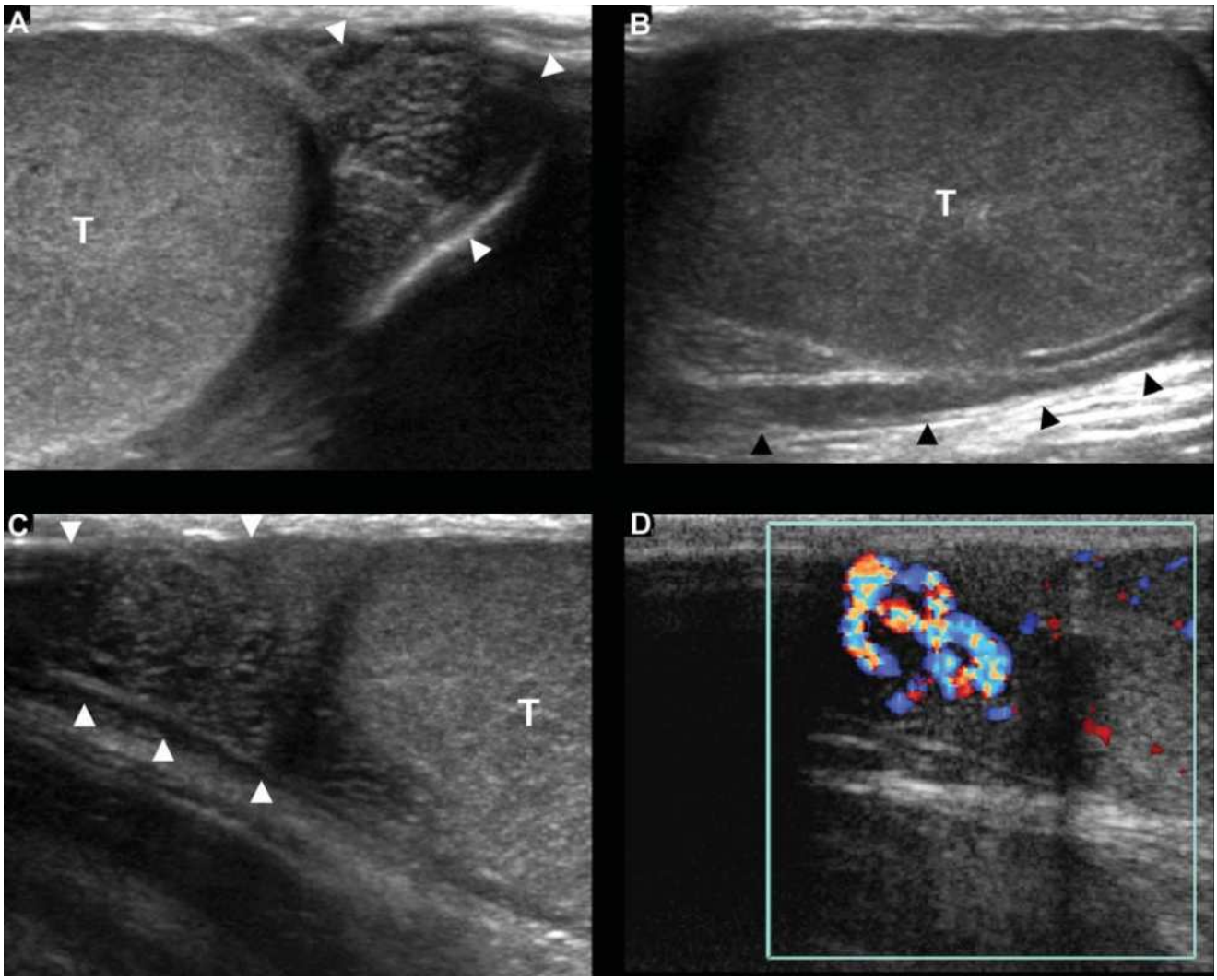


Figure 14.24. Normal epididymis and pampiniform plexus in a 9-year-old mixed-breed dog. (for full caption, see facing page)

processes that affect the scrotum include accumulation of fluid (hydrocele or hematocele) and scrotal hernia. Ultrasound has a high accuracy in diagnosis of testicular and/or scrotal disorders in dogs (Hecht 2001; Hecht et al. 2003).

While cryptorchidism is relatively common, other disorders of sexual development are poorly documented in dogs and cats (see page 448). Cryptorchid testicles are usually small and hypoechoic, but have normal architecture with a central hyperechoic mediastinum (Figures 14.25, 14.26). They can be found anywhere between the caudal pole of the kidneys to the inguinal area. If the mediastinum testis is not developed, identification of an undescended testicle may be difficult (Figure 14.27). The sensitivity of ultrasound for the identification of inguinal or abdominal cryptorchid testicles in dogs and cats is high (Hecht 2001; Felumlee et al. 2012). Occasionally,

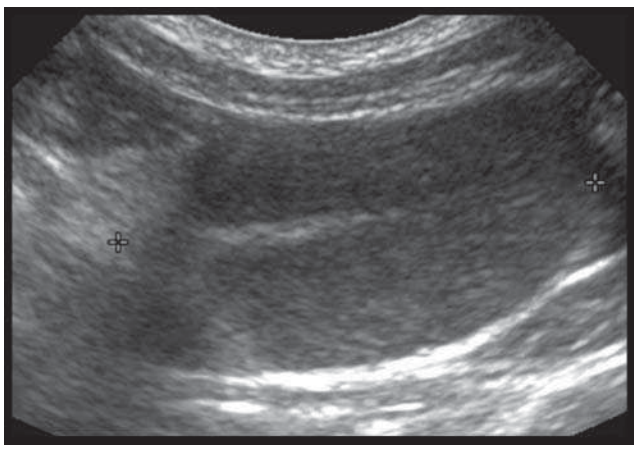


Figure 14.25. Abdominal cryptorchidism in a 1-year-old Golden Retriever. The left testicle (between the cursors) is intra-abdominal, small (3.1 cm long), hypoechoic, and of normal architecture.

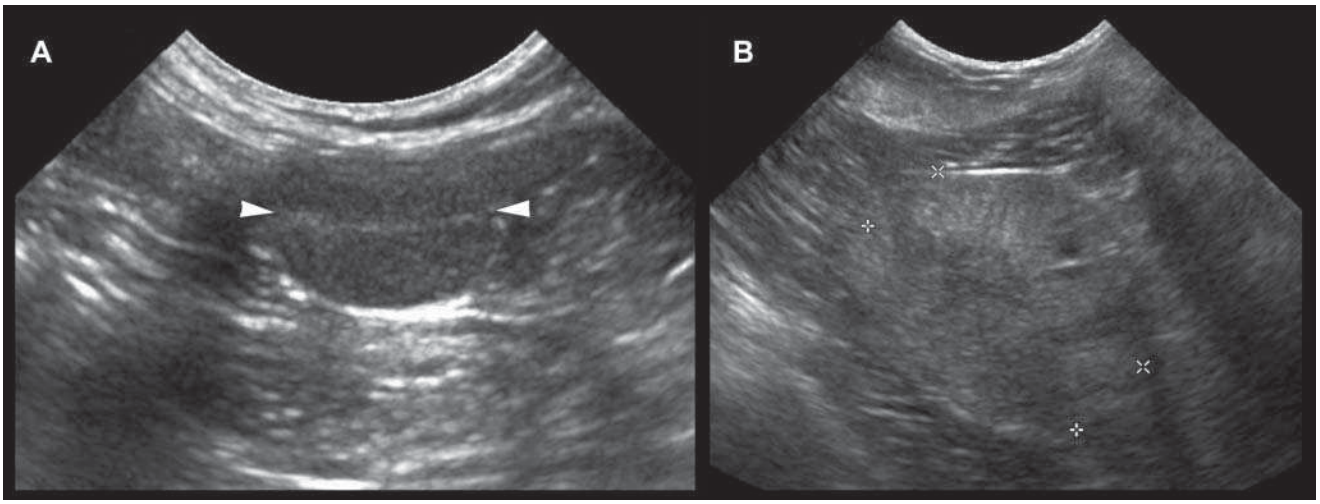


Figure 14.26. Abdominal cryptorchidism in a 9-year-old Dachshund. (A) The left testicle (between the cursors) is intra-abdominal, small (14 mm long), and of normal architecture. **(B)** The prostate is mildly enlarged (3.5 cm long), symmetrical and mostly homogeneous with a few small cysts. These findings support benign cystic prostatic hyperplasia.

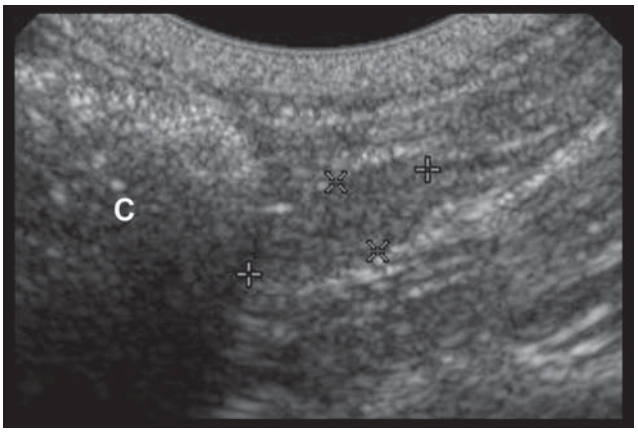


Figure 14.27. Abdominal cryptorchidism in a 7-month-old Boston Terrier. The testicle (between the cursors) is adjacent to the descending colon (C). It is inconspicuous, homogeneous, and measures 1.0 × 0.4 cm. The mediastinum testis is not visible.

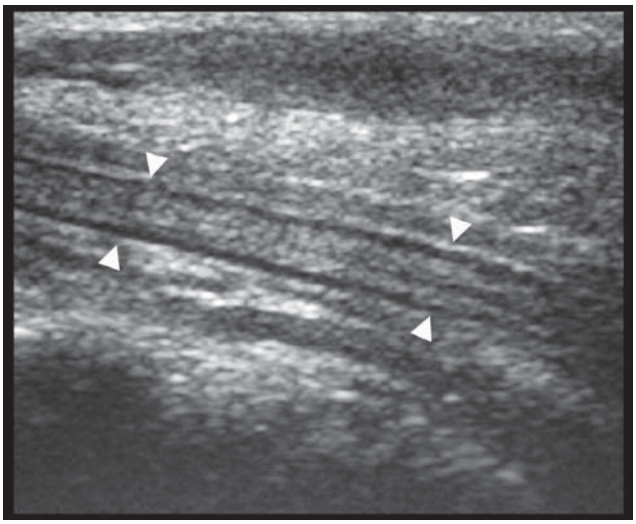


Figure 14.28. Prominent gubernaculum testis in a cryptorchid 5-month old Mastiff. The gubernaculum (arrowheads) appears as tubular structure of 3 mm diameter and was seen extending from the caudal pole of the intra-abdominal right testicle to the inguinal ring.

the gubernaculum testis is visualized. It appears as a tubular structure extending from the caudal pole of the retained testicle to the inguinal ring (Figure 14.28). Abdominally and inguinally located testicles are predisposed to neoplastic transformation and can reach considerable size in this instance.

Testicular tumors are common. Leydig (interstitial) cell tumors are frequent incidental findings in descended testicles in older dogs and may occur bilaterally. They are usually benign. Seminomas and Sertoli cell tumors can affect cryptorchid and descended testicles. These tumors have the potential for hormone production and metastases. Other tumor types are extremely rare. Testicular tumors in cryptorchid testicles tend to exhibit more malignant behavior than in descended testicles and occur in younger animals (Hecht 2001).

Ultrasonographic findings in testicular tumors range from circumscribed small nodules to large complex masses with disruption of normal testicular anatomy (Johnston et al. 1991a) (Figures 14.29–14.32).

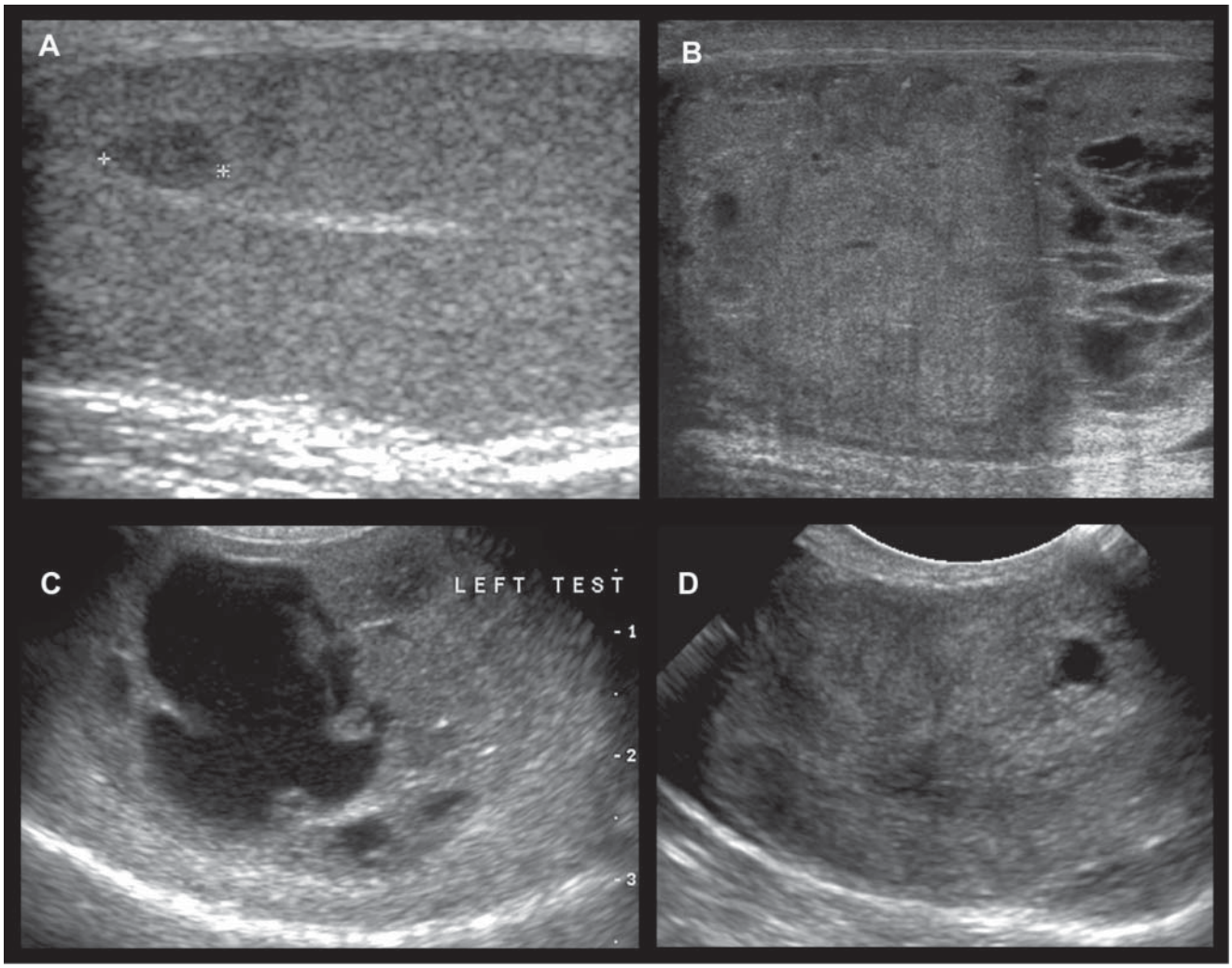


Figure 14.29. **Leydig cell tumors in four dogs. A:** Sagittal image of the left testicle in a 15-year-old Labrador Retriever. A hypoechoic nodule of 5 mm diameter (between the cursors) is associated with the testicular parenchyma adjacent to the linear hyperechoic mediastinum testis. **B:** Sagittal image of the left testicle in a 10-year-old Boxer. The testicle is enlarged and of heterogeneous echotexture with complete obliteration of normal testicular parenchyma and large cavitations in the caudal part. **C:** Sagittal image of the left testicle in a 10-year-old Golden Retriever. The testicular parenchyma has been largely replaced by an approximately 3-cm, mixed echogenic and cavitary mass. **D:** Sagittal image of the left testicle in a 13-year-old sheltie. The testicular parenchyma is of mixed echogenicity, the testicle has an irregular margin, and the mediastinum testis is not visible.

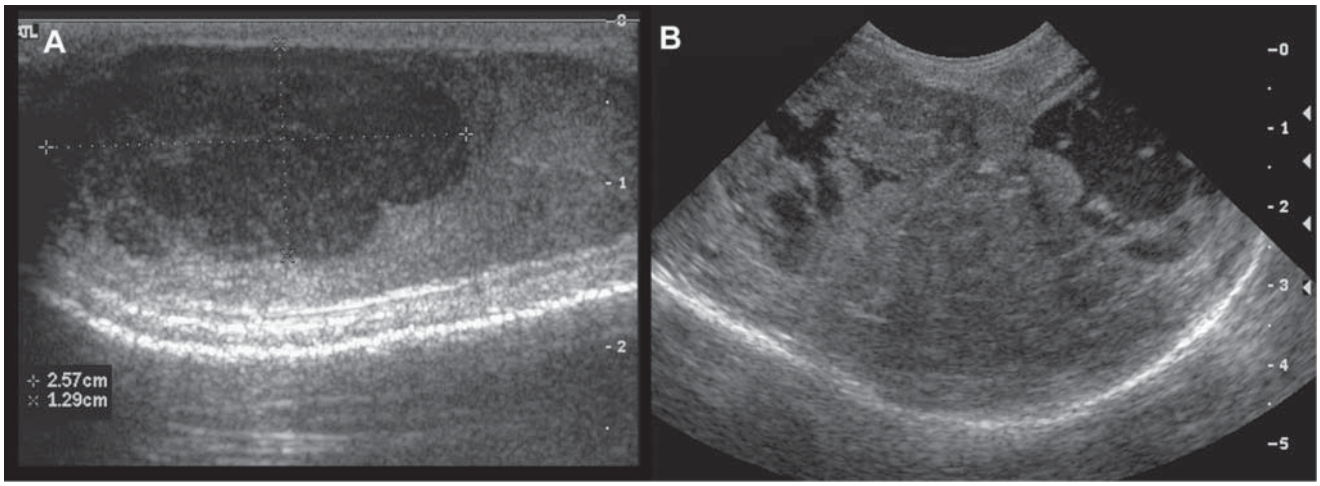


Figure 14.30. **Seminomas in two dogs. A:** Sagittal image of the left testicle in an 8-year-old large-breed dog. An irregular, but well-defined, hypoechoic nodule measuring 2.6 × 1.3 cm is in the testicle (between the cursors). **B:** Sagittal image of the left testicle in a 10-year-old Labrador Retriever with an enlarged, endured scrotum. The testicular parenchyma is completely replaced by an inhomogeneous mass with several irregular cavitations containing anechoic to echogenic fluid.

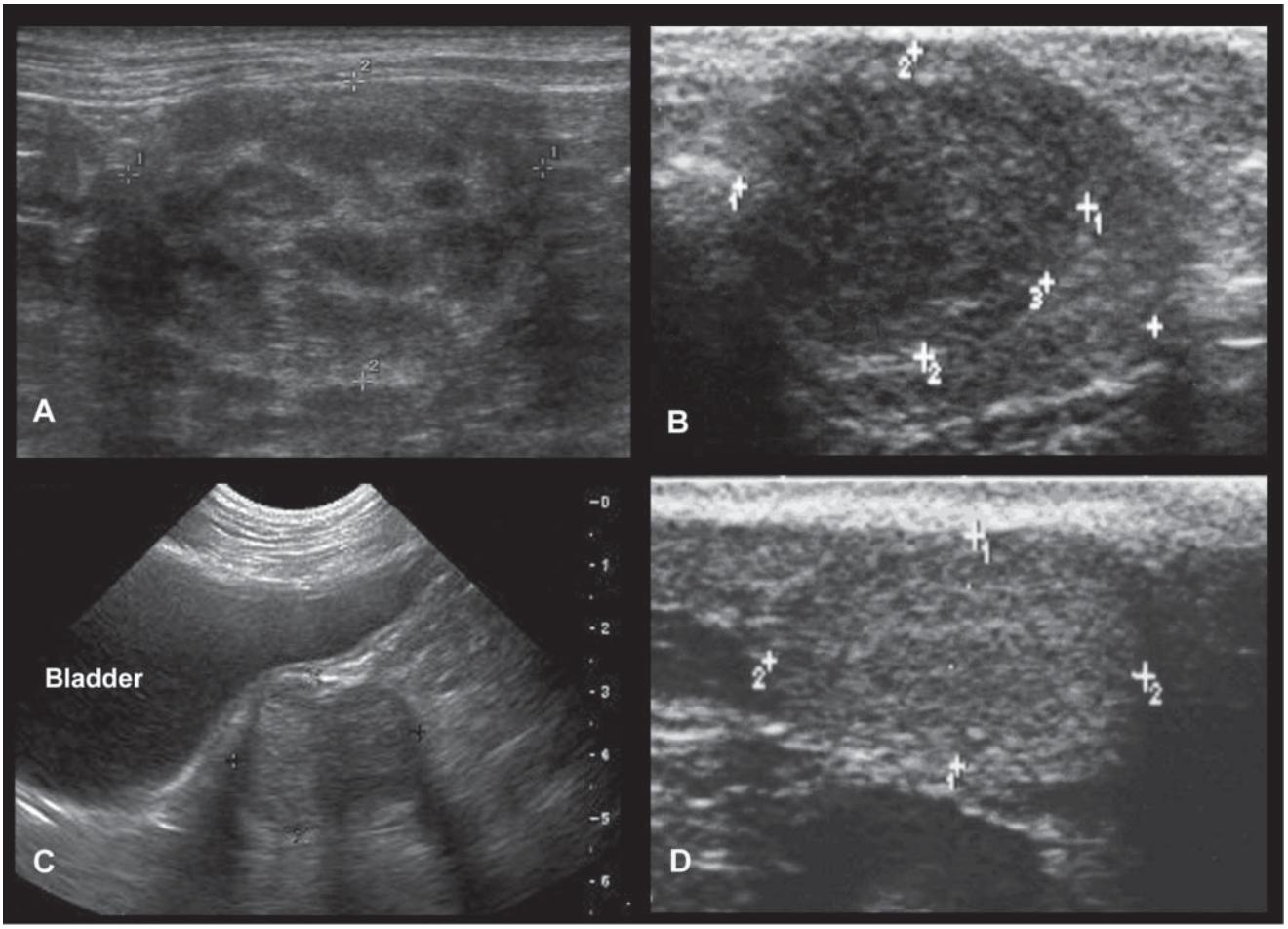


Figure 14.31. **Sertoli cell tumors in four dogs. A:** Sagittal image of the left abdominal cryptorchid testicle (between the cursors) in a 6-year-old Jack Russell Terrier. The testicle is enlarged (3.4 × 2.6 cm) and heterogeneous. **B:** Transverse image of the right inguinal cryptorchid testicle in an 8-year-old mixed-breed dog. A 1.9 × 1.8 cm hypoechoic nodule (between the cursors) is associated with the testicle. **C:** Sertoli cell tumor of a retained right testicle in an 8-year-old Boxer. An echogenic mass of approximately 2.5 cm diameter dorsal to the bladder is associated with strong edge shadows. **D:** Sagittal image of the left testicle in a 12-year-old West Highland White Terrier. The testicle is within the scrotum and of normal size and shape. The testicular parenchyma is of mixed echogenicity, and the mediastinum testis is not visible.

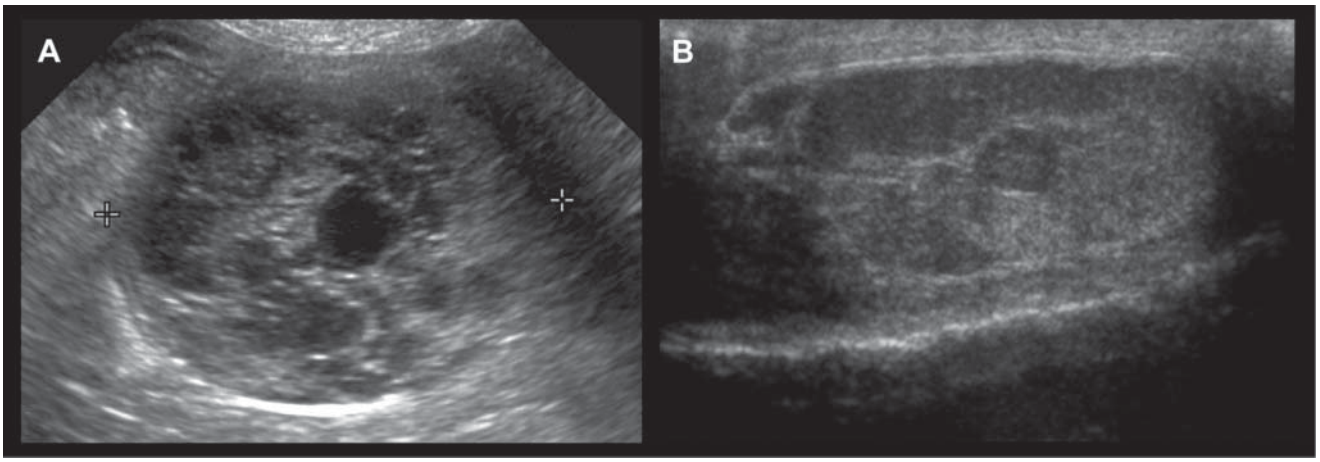


Figure 14.32. **Mixed testicular tumors in two dogs. (A)** Mixed tumor (seminoma and Sertoli cell tumor) of an abdominal cryptorchid testicle in a 13-year-old sheltie. The enlarged (4.5 cm), mixed echogenic testicle (between the cursors) has multiple anechoic areas. **(B)** Mixed tumor (Leydig cell tumor and seminoma) of a scrotal testicle in an 8-year-old Golden Retriever. The testicle is relatively small, heterogenous, and a mediastinum testis is not identified.

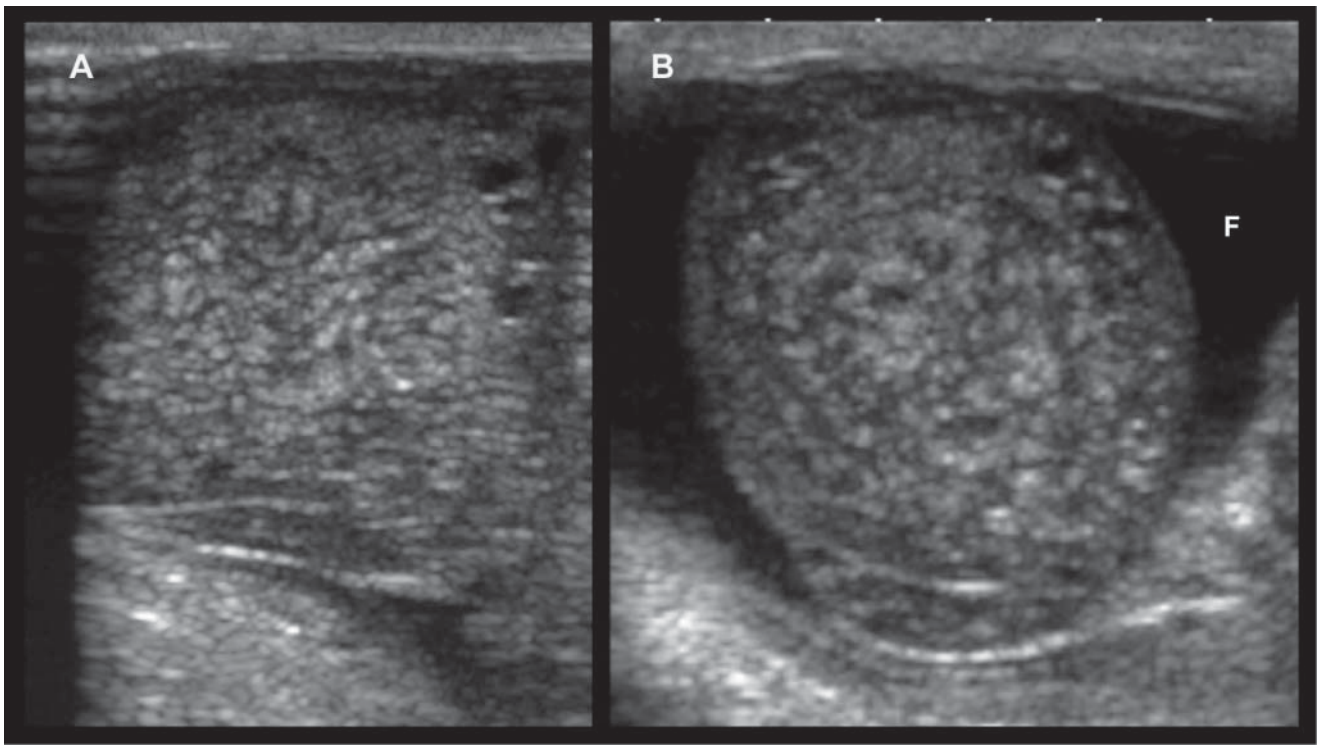


Figure 14.33. Tumor of the epididymis in a 5-year-old Rottweiler. Sagittal **(A)** and transverse **(B)** images of the head of the right epididymis show marked enlargement and a coarse echotexture. A small volume of fluid (F) is adjacent to the epididymis, consistent with a mild hydrocele **(B).** Ultrasound guided fine needle aspiration of the epididymis yielded a diagnosis of lymphoma.

Different tumor types cannot be distinguished ultrasonographically (Pugh and Konde 1991; Hecht et al. 2003). Concurrent prostatic changes such as benign prostatic hyperplasia or squamous metaplasia are common, especially in hormone-producing tumors. In case of metastatic neoplasia, enlarged medial iliac lymph nodes may be seen.

Tumors of the epididymis are rare and result in generalized epididymal enlargement or mass lesions (Figure 14.33).

Orchitis and epididymitis may occur subsequent to hematogenous spread of infectious organisms, may result from urinary tract or prostatic inflammation, or may be caused by scrotal trauma. Inflammatory scrotal disorders exhibit variable ultrasonographic characteristics, ranging from diffuse echogenicity changes of the testicle and/or epididymis to complex masses and anechoic areas subsequent to abscess formation (Pugh and Konde 1991; Hecht et al. 2003; Ober et al. 2004) (Figures 14.34–14.37). Fluid may accumulate within the scrotum or the scrotum may thicken. Whereas testicular and epididymal size increase in acute inflammation, they decrease in chronic cases.

Testicular or epididymal cysts are occasional incidental findings. They appear as anechoic, well-circumscribed, rounded areas, often with distal acoustic enhancement (Figures 14.38, 14.39). Abnormal focal or generalized enlargement (ectasia) of epididymal ducts is occasionally noted and is of uncertain etiology and significance (Figure 14.40).

Testicular torsion most commonly affects retained neoplastic testicles. In this instance, the ultrasonographic examination shows an abdominal mass of variable size and echogenicity, with decreased or absent blood flow on color Doppler examination (Miyabashi et al. 1990; Hecht 2001) (Figure 14.41). Intra-abdominal and intrascrotal torsion of non-neoplastic testicles and vascular compromise of other etiology (infarction or space-occupying lesions within the inguinal ring) are rare (Hecht et al. 2004) (Figures 14.42, 14.43). Depending on the degree and duration of vascular occlusion, the affected testicle may appear hyperechoic or hypoechoic, increased, normal or decreased

Figure 14.37. Severe orchitis in a 9-year-old Glen of Imaal Terrier. A: The sagittal image of the right testicle shows an enlarged and hyperechoic testis with a stellar pattern, corresponding to the severe parenchymal edema histologically reported. **B:** The transverse image of both testicles shows the size and echogenicity discrepancy. A moderate amount of fluid (arrowhead) is present around the affected testis and epididymis. No infectious organisms were found.

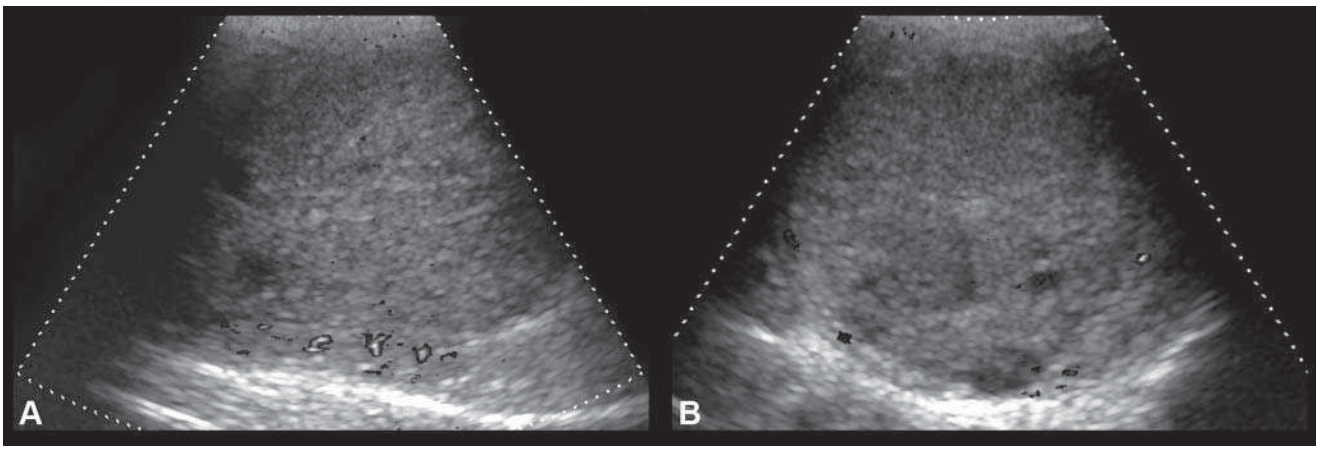


Figure 14.34. Severe, subacute, necrotizing and suppurative orchitis and epididymitis of undetermined etiology in a 3-year-old Golden Retriever. Sagittal **(A)** and transverse **(B)** images of the left testicle show that the testicle is enlarged and heterogeneous, with disruption of normal architecture. On color Doppler examination, blood flow was reduced compared with the normal right testicle (not shown).

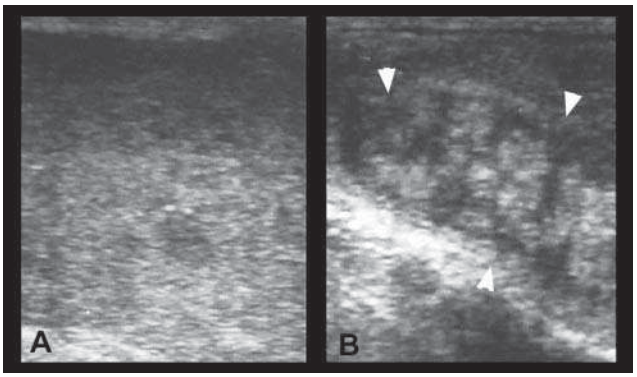


Figure 14.35. Fungal orchitis and epididymitis (blastomycosis) in a 3-year-old Walker hound. Sagittal images of the right testicle **(A)** and head of the epididymis **(B)** show testicular and epididymal (arrowheads) enlargement and inhomogeneity.

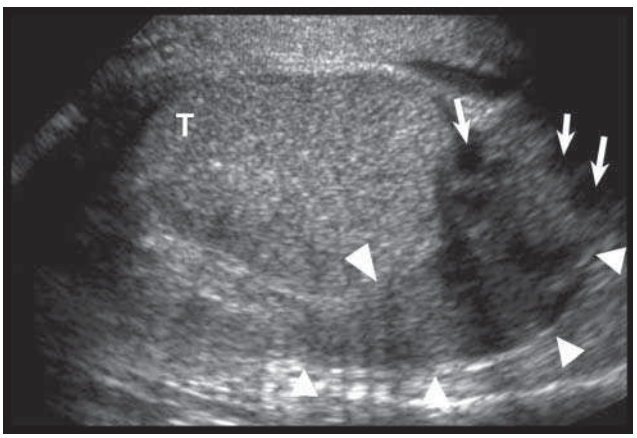


Figure 14.36. Epididymitis in a 9-year-old Labrador Retriever. On the parasagittal image of the left testicle, the epididymis (arrowheads) is larger than usual and of mixed echogenicity. Several anechoic areas are noted in the tail of the epididymis (arrows) which may represent cysts, small abscesses, or dilated ducts. The testicle (T) is within normal limits for size and echotexture.

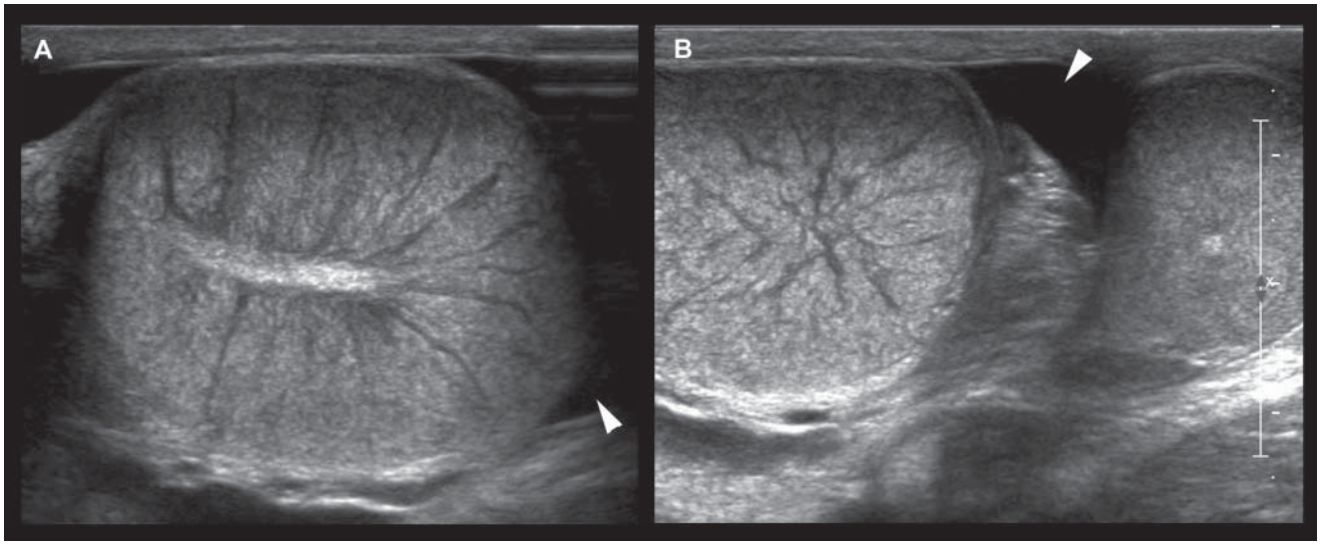


Figure 14.37. Severe orchitis in a 9-year-old Glen of Imaal Terrier. (for full caption, see facing page)

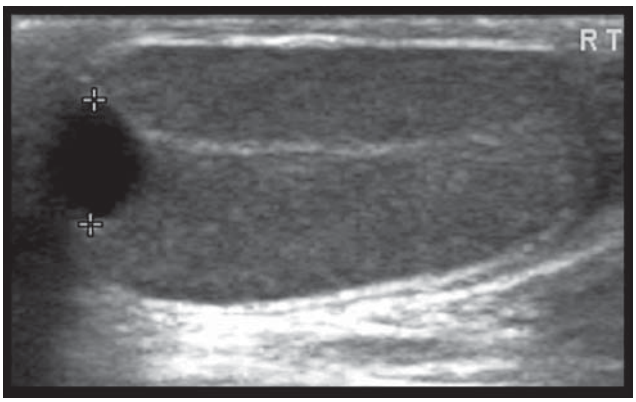


Figure 14.38. Cyst associated with the cranial pole of the right testicle in a 7-year-old Yorkshire Terrier. A round anechoic structure of 5 mm diameter (between the cursors) is associated with the testicular parenchyma.

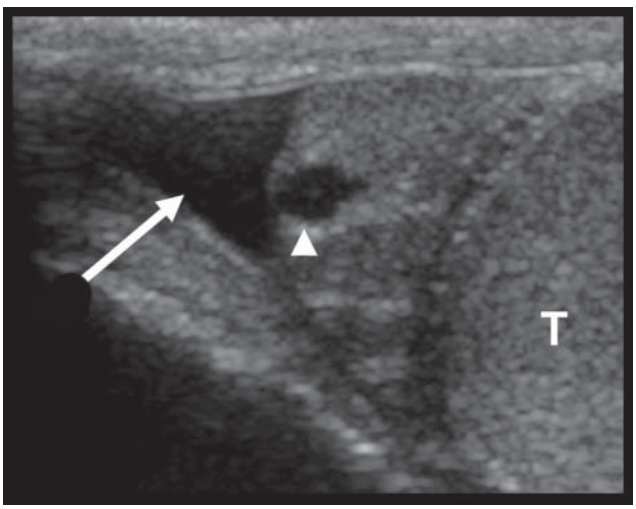


Figure 14.39. Epididymal cyst and mild hydrocele in a 7-year-old mixed-breed dog. An anechoic structure of approximately 3 mm diameter is associated with the head of the epididymis (arrowhead), just cranial to the testicle (T). The triangular anechoic area cranial to the head of the epididymis is consistent with a small volume of intrascrotal fluid (arrow).

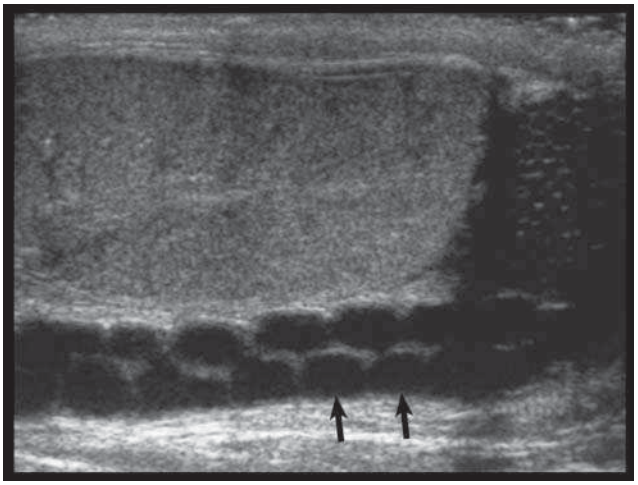


Figure 14.40. Marked diffuse duct ectasia of the epididymis in a 9-year-old Weimaraner. The sagittal image of the right testicle shows distinct tubular structures (arrows) filled with anechoic fluid throughout the tail and body of the epididymis.

in size, with initially normal architecture. Concurrent abdominal or scrotal effusion is common, especially in acute cases.

Testicular atrophy may have a number of causes, such as thermal insult (e.g., in cryptorchid testicles), previous orchitis, hormonal influences, or vascular compromise. Atrophic testicles are small and hypoechoic, but maintain their normal architecture (Figures 14.44, 14.45; see also Figures 14.26, 14.27).

Whereas ultrasonography plays a major role in assessing human patients with scrotal trauma, it is rarely performed for this indication in dogs. Findings include scrotal hematoma, hematocele, scrotal contusion, intratesticular hematoma, and testicular rupture. Scrotal hematomas with accumulation of blood within scrotal soft tissues manifest as space-occupying lesions of variable echogenicity that displace the testicle and epididymis (Figures 14.46, 14.47). With hematocele formation, there is intrascrotal fluid accumulation of variable echogenicity. Testicular contusions and hematomas appear as diffuse echogenicity changes to the testicular parenchyma or mass lesions of variable echogenicity. Differentiation from testicular lesions of inflammatory or neoplastic etiology is mainly based on medical history rather than ultrasonographic characteristics. Inhomogeneous echotexture of the testicular parenchyma with loss of contour definition indicates testicular rupture.

Hydrocele manifests as anechoic to echogenic material adjacent to the testicles. The condition is rare in dogs. It may be an occasional incidental finding, but is more commonly found secondary to scrotal disorders (e.g., orchitis and testicular torsion). It may also occur secondary to ascites when abdominal fluid descends through the inguinal ring (Figure 14.48).

With inguinal or scrotal hernia, abnormal contents (e.g., bowel loops or mesenteric fat) may be found within the inguinal ring or scrotum. Concurrent findings include hydrocele, testicular congestion or infarction.

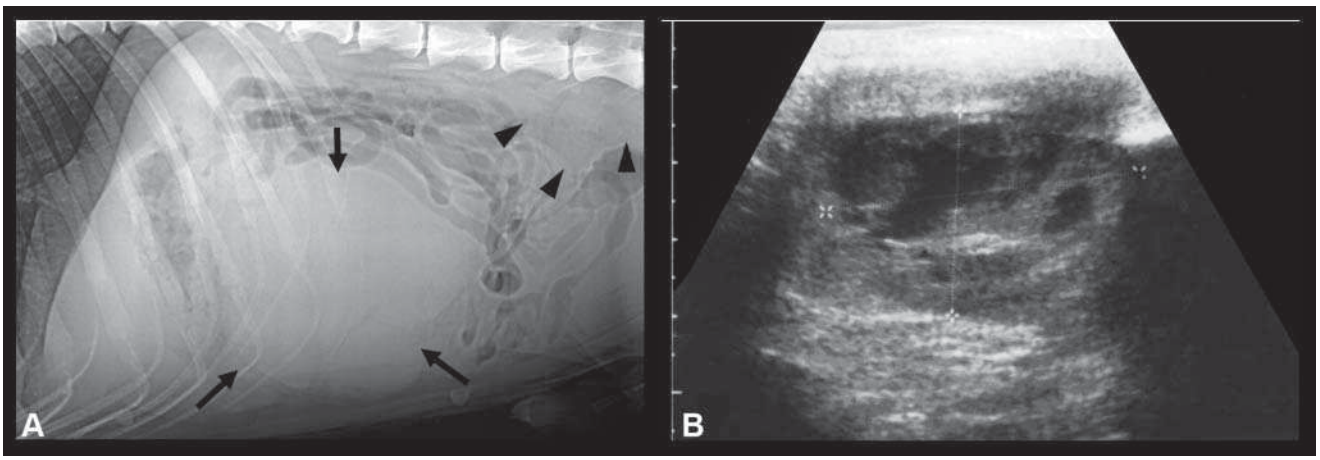


Figure 14.41. Intra-abdominal torsion of a retained neoplastic testicle (Sertoli cell tumor) in a 9-year-old German Shepherd Dog. A: The lateral abdominal radiograph shows a lobulated soft-tissue mass >20 cm in diameter associated with the cranial ventral abdomen (arrows). Enlarged sublumbar lymph nodes (arrowheads) are consistent with metastatic disease. Prominent mammillae are noted, consistent with feminization caused by the hormone-producing tumor. **B:** The ultrasonographic image shows a mixed echogenic mass (only shown in part).

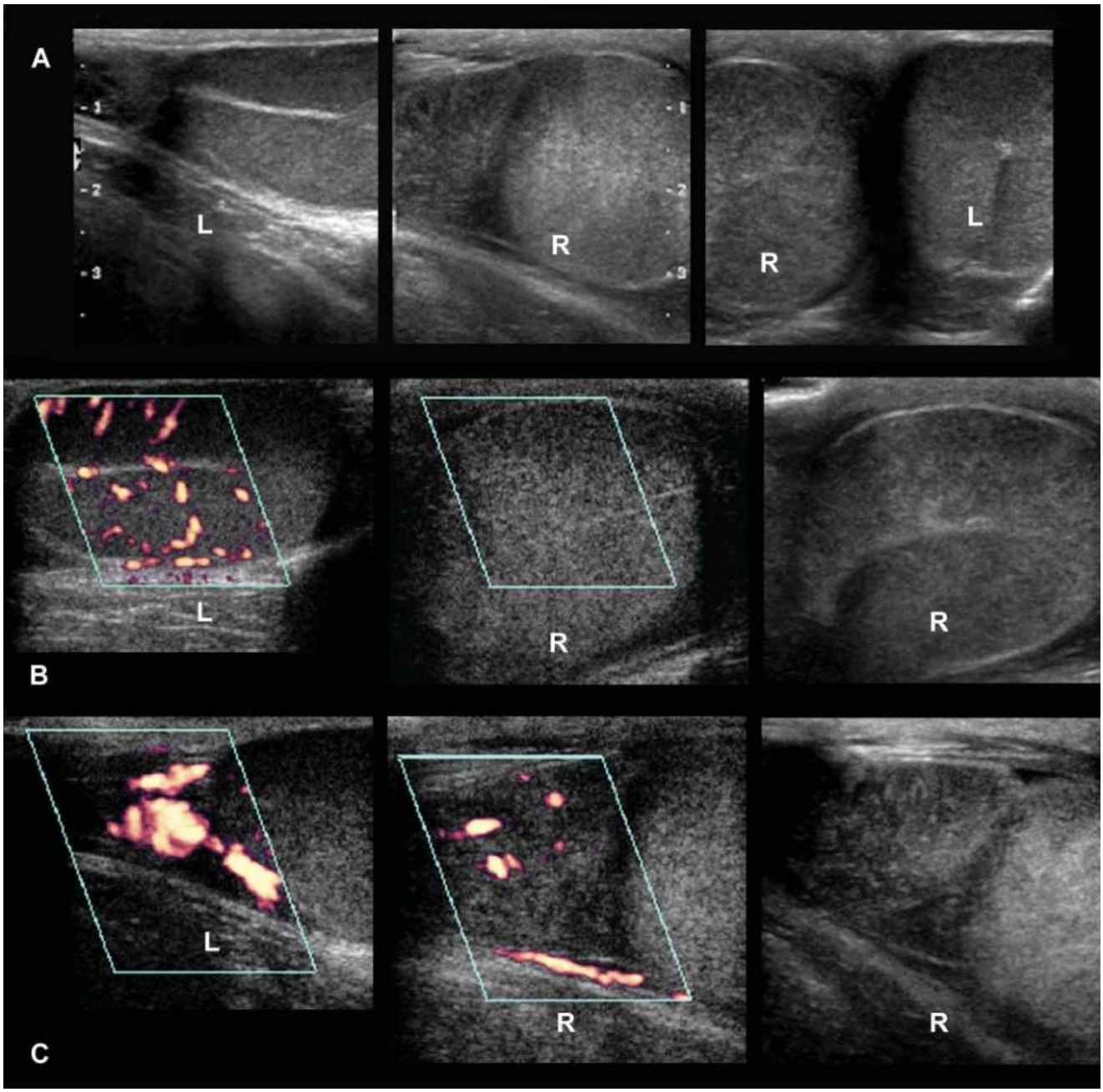


Figure 14.42. **Scrotal testicular torsion in a 1-year-old Border Collie.** The left testis (L) is normal, whereas the right testicle (R) has hemorrhage and numerous thrombi, compatible with torsion and underlying orchitis and epididymitis. **A:** The left and right testicles are imaged side by side. The right testicle and epididymis are significantly larger than the left. **B:** Comparative color Doppler signal between the left (normal) and the right testis (no flow). **C:** Comparative color Doppler signal between the left (normal) and the right epididymis (poor flow).

Penis

Normal Sonographic Anatomy of the Penis

At the level of the distal penis, the smooth, hyperechoic interface of the os penis is surrounded by penile soft tissues (glans penis) and the prepuce. The urethra is located within a V-shaped ventral groove in the os penis and is usually not visible unless distended (Figure 14.49). Proximal to the osseous part, penile soft tissues (corpus cavernosum, corpus spongiosum, and muscles of the penis) are of medium echogenicity and inconspicuous.

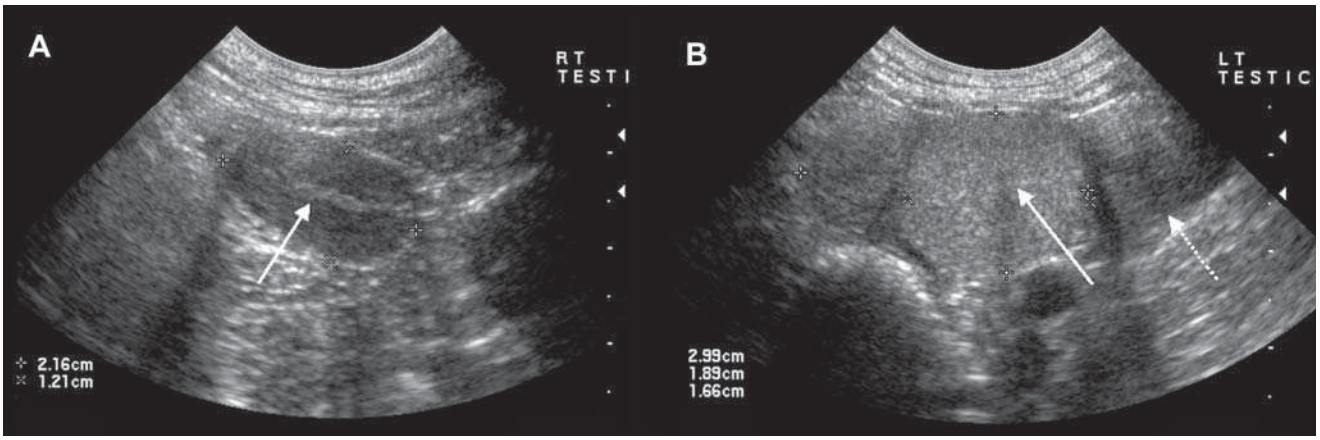


Figure 14.43. **Intra-abdominal torsion of a non-neoplastic testicle in a 6-month-old, bilaterally cryptorchid Boxer. A:** Sagittal ultrasonographic image of the right intra-abdominal atrophic testicle (between the cursors). The mediastinum testis (arrow) is clearly visible within the hypoechoic testicle. **B:** Sagittal ultrasonographic image of the left intra-abdominal testicle. The testicle appears globoid rather than oval and hyperechoic compared with the right. The mediastinum testis (solid arrow) is barely recognizable. Two additional round structures are seen adjacent to the testicle and are relatively hypoechoic. They represent the enlarged head and tail (broken arrow) of the epididymis. Reprinted with permission from Hecht et al. (2004).

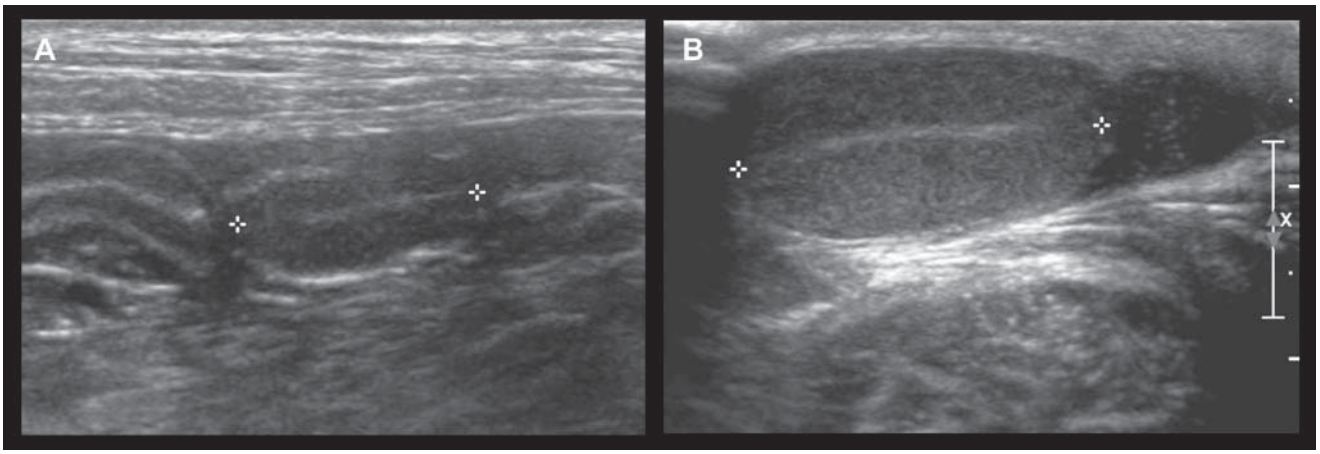


Figure 14.44. **Testicular atrophy in a 1.5-year-old, right-sided cryptorchid Shi Tzu.** On the sagittal image, the right testicle (**A,** between cursors) is small (1.4 cm long) while the left scrotal testicle (**B**, between cursors**)** is normal in size (2.2 cm long).

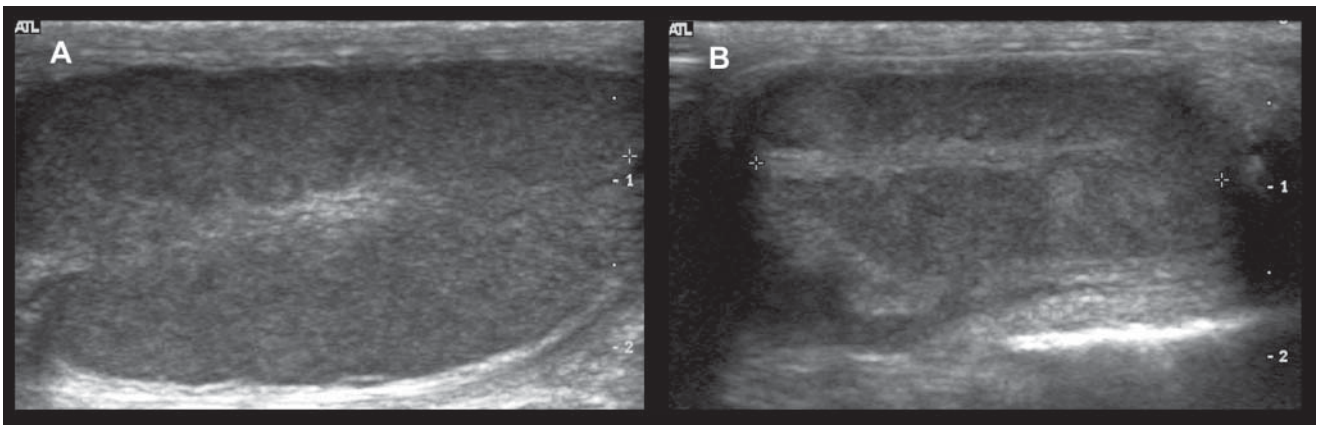


Figure 14.45. **Testicular atrophy of unknown etiology in a 12-year-old Doberman. A:** Sagittal image of normal right testicle. The testicle measures 3.8 cm long (between the cursors), is of normal medium echogenicity, homogeneous, and with centrally located linear hyperechoic mediastinum testis. **B:** Sagittal image of the atrophic left testicle. The testicle is smaller than the right (2.7 cm long [between the cursors]), hypoechoic, and slightly inhomogeneous. The centrally located mediastinum testis is visible.

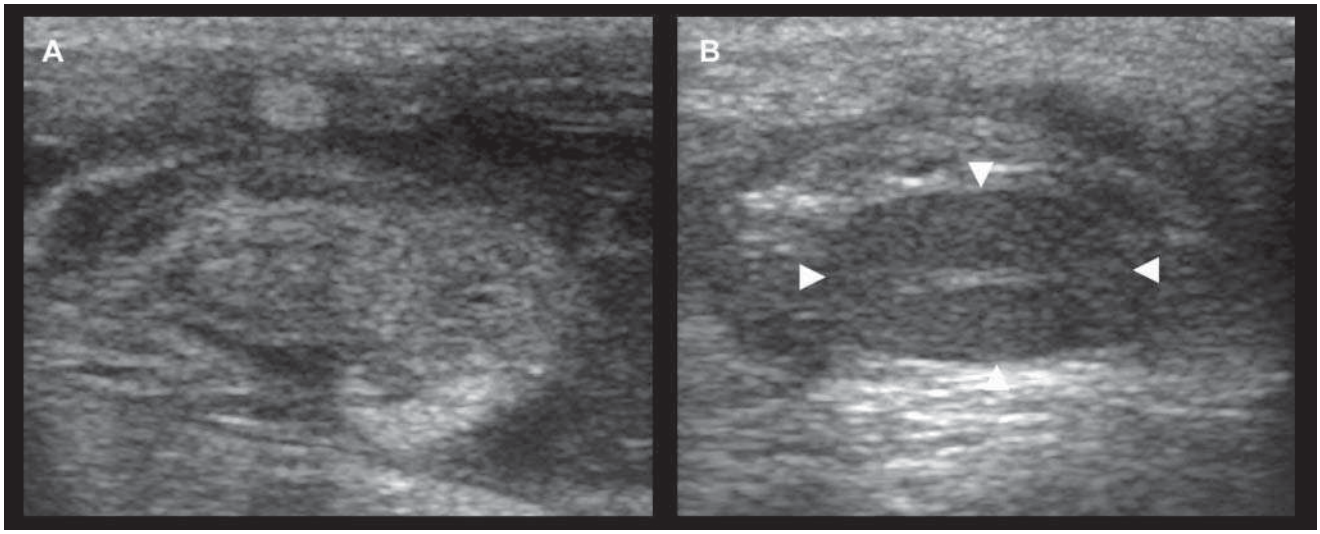


Figure 14.46. **Blunt scrotal trauma in a 5-month-old dog. A:** The scrotum is enlarged and filled with material of mixed echogenicity, representing a hematoma at varying stages of organization. **B:** The left testicle (arrowheads) is displaced and surrounded by material of mixed echogenicity.

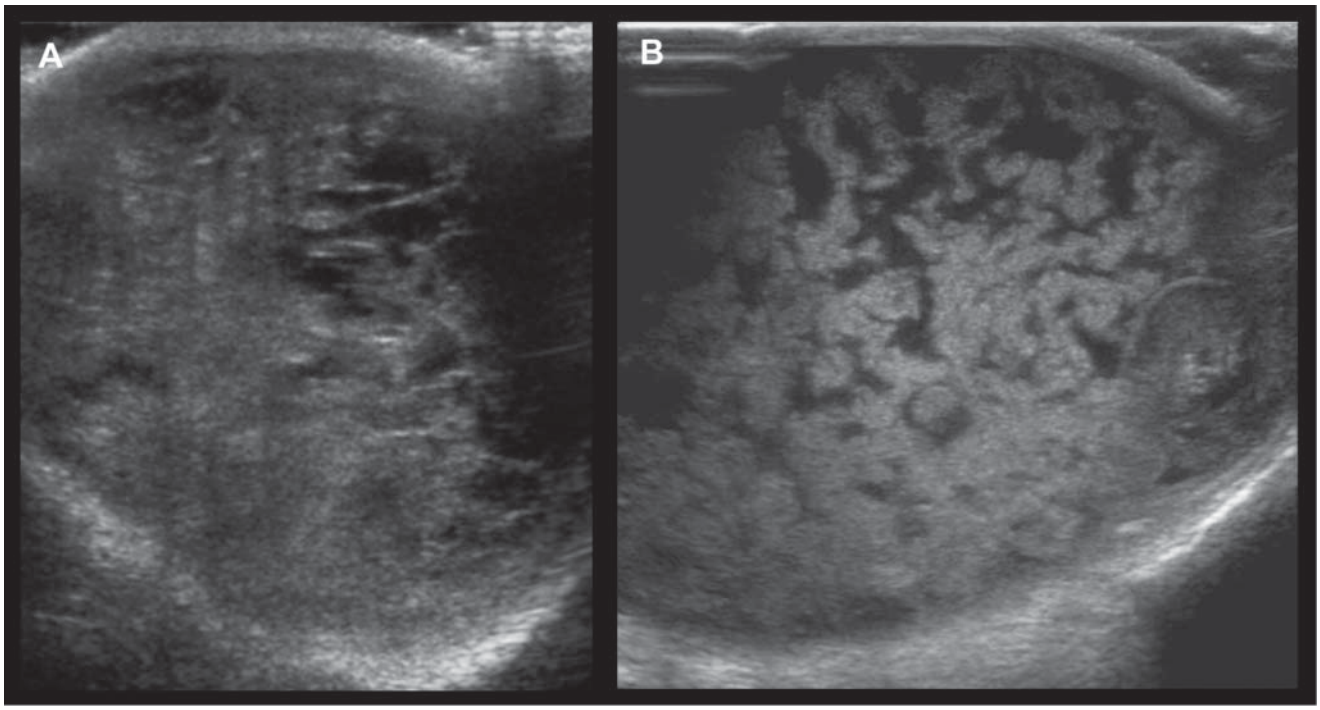


Figure 14.47. **Scrotal hematomas following surgical trauma (castration) in two dogs. A:** In a 1-year-old Weimaraner, the scrotum contains a large (>6 cm diameter) mixed echogenic mass. **B:** An old organized hematoma is noted in the scrotum of this 2-year-old Golden Retriever, castrated several months ago. It was confirmed at surgery.

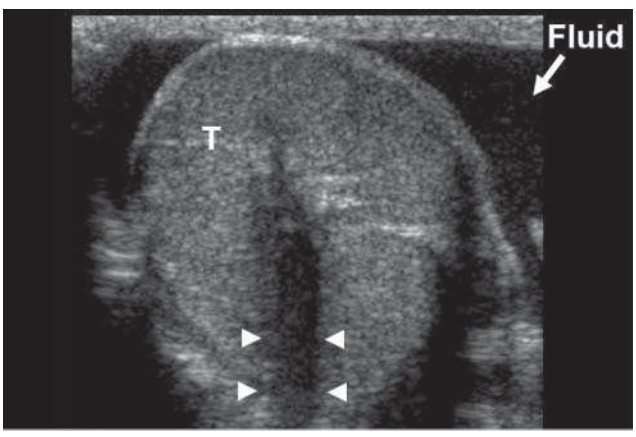


Figure 14.48. **Transverse image of the right hemiscrotum in a 9-year-old dog with ascites and subsequent hydrocele.** The testicle (T) is surrounded by anechoic fluid. Acoustic shadowing (arrowheads) is observed distal to the centrally located mediastinum testis.

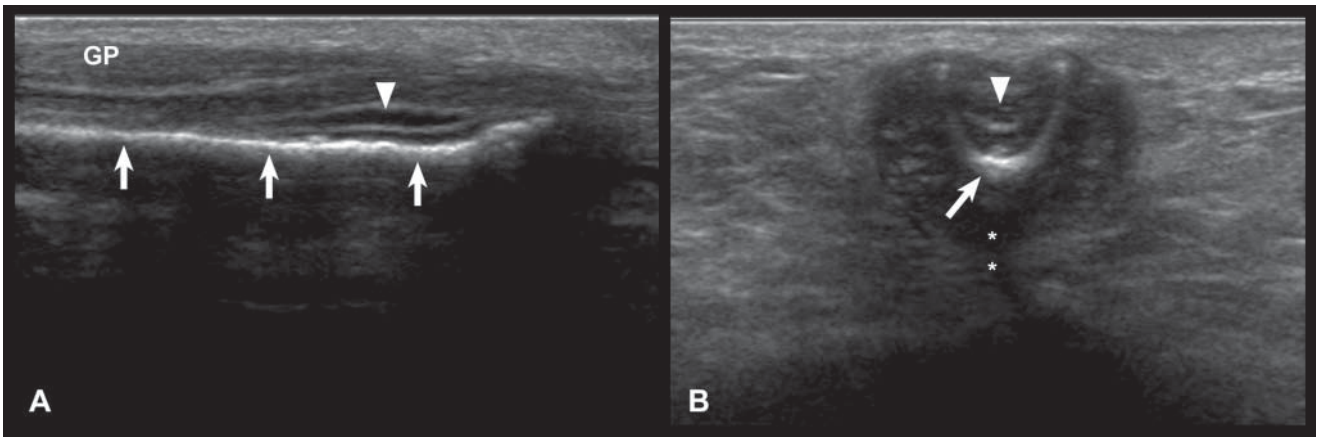


Figure 14.49. **Normal canine penis.** Sagittal **(A)** and transverse **(B)** sonographic of the penis in an adult intact dog. On sagittal image **(A)**, the prepuce and part of the glans penis (GP) are in the near field ventral to the linear strongly hyperechoic interface of the os penis (outlined by arrows). On transverse image **(B)**, the hyperechoic groove of the os penis (arrow) is characterized by distal shadowing (*). The urethra is visible (arrowhead). Surrounding penile soft tissues are symmetrical.

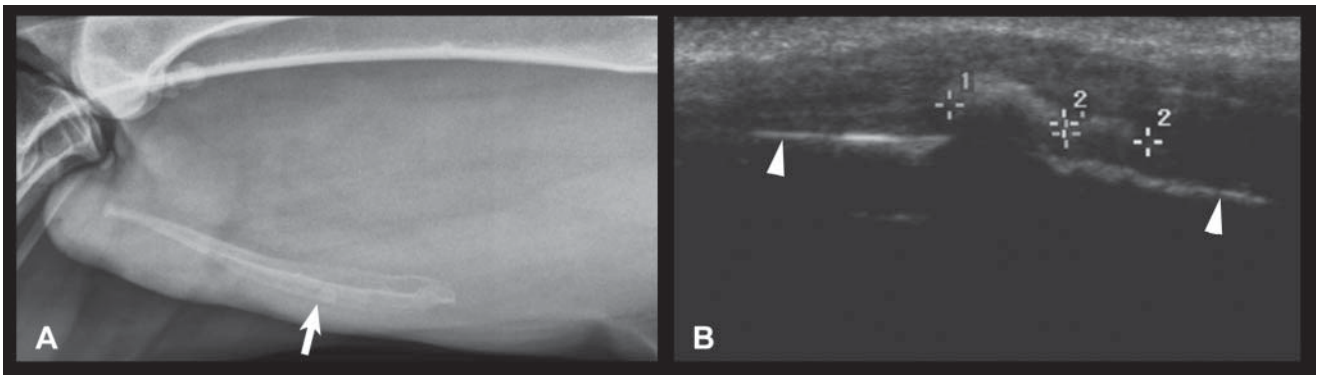


Figure 14.50. **Urethral calculi (urate stones) in a 1-year-old Dalmatian.** A lateral radiograph of the caudoventral abdomen with the legs flexed forward **(A)** shows a faint round focal opacity superimposed over the ventral aspect of the os penis (arrow). On the sagittal ultrasonographic image of the penis **(B)** two hyperechoic urethral calculi (between cursors) measuring 5 and 7 mm in diameter, respectively, are clearly recognized in the near field immediately ventral to the linear hyperechoic os penis (arrowheads).

Sonographic Findings in Penile Abnormalities

Common abnormalities of the penis that warrant ultrasonographic examination include urethral calculi (Figure 14.50), fracture or neoplasia of the os penis, or urethral lesions such as tumor or stricture. Lesions of the os penis cause discontinuity of its osseous contour (Figure 14.51). Concurrent soft-tissue changes may be encountered, particularly in acute trauma (Figure 14.52). Penile tumors are rare and are unlikely to have a specific pattern (Figure 14.53). Urethrography remains the imaging modality of choice for assessing urethral patency and integrity.

Other Findings

Disorders of Sexual Development

These can be subdivided into three categories: chromosomal abnormalities, gonadal abnormalities and phenotypic abnormalities (Meyers-Wallen 2008; Christensen 2012). A diagnosis is typically achieved by means other than ultrasonography. Testicular hypoplasia or testicular tumors may be found in animals affected with XXY trisomy. XX male hermaphrodites are typically bilaterally cryptorchid. Male pseudohermaphrodites with persistent Müllerian duct syndrome have Müllerian duct derivatives (oviducts, uterus, cervix) along with bilateral

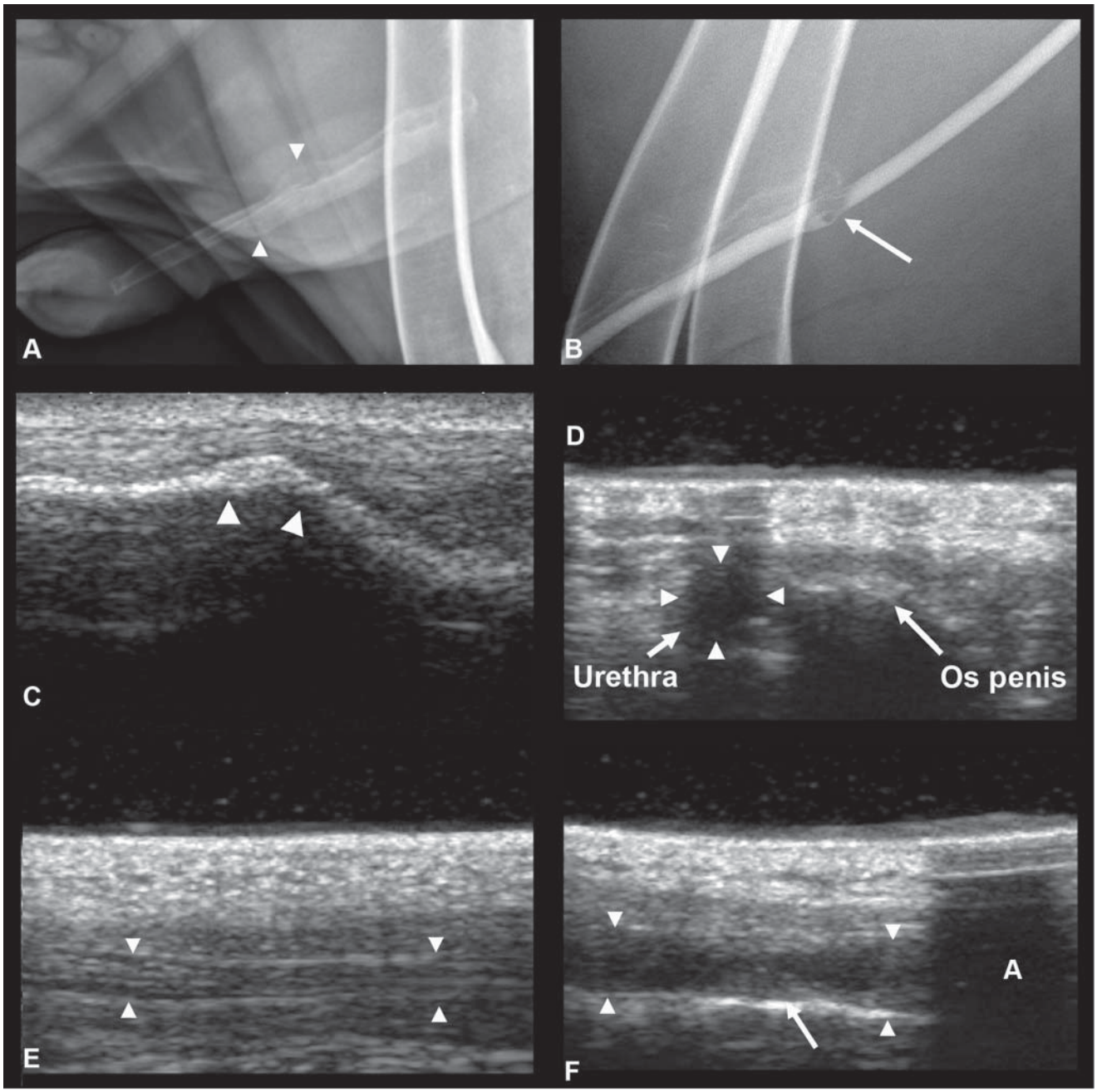


Figure 14.51. Healed fracture of the os penis and mural urethral lesion (urethritis) in a 6-year-old Mastiff with dysuria. **A:** The lateral radiograph shows irregularity of penile contour at the mid-body of the os penis (arrowheads), consistent with previous fracture. **B:** The urethrogram demonstrates a filling defect associated with the prostatic urethra at the most caudal level of the os penis (arrow). **C:** Sagittal ultrasonographic image of the mid-body of the os penis. There is an irregular contour to the hyperechoic interface of the os penis at the previous fracture site (arrowheads). **D:** Transverse image of the penis during instillation of saline to facilitate urethral identification. The os penis is characterized by its irregular hyperechoic surface and distal shadowing. The fluid-distended urethra is visible as an anechoic circular structure (arrowheads) lateral to the os penis. The unusual urethral position was attributed to previous trauma. **E:** Sagittal image of the urethra, which appears as an inconspicuous tubular structure (arrowheads). **F:** Sagittal image of the urethra during instillation of saline. The urethra (arrowheads) is fluid-filled. The filling defect identified during the urethrogram manifests as urethral wall thickening and irregularity (arrow). The hypoechoic area around the letter A is artifactual because of poor transducer-to-skin contact. **D–F:** The anechoic area in the near field represents part of the standoff pad.

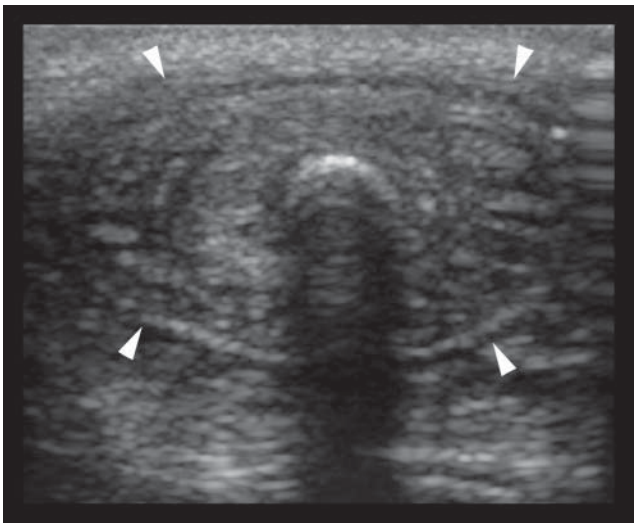


Figure 14.52. Penile trauma in a 4-year-old Belgian Malinois. The transverse image at the level of the os penis (recognized as the central hyperechoic structure with distal acoustic shadowing) shows diffuse edematous swelling of the prepucial and penile soft tissues (arrowheads) without evidence of an underlying bone lesion.

testes (commonly cryptorchid) and normal internal male genitalia. Affected males may present for cryptorchidism or clinical signs of pyometra, urinary tract infection or prostatic disease with associated imaging findings. Animals with failure of androgen-dependent masculinization possess two testicles, but internal and external male genitalia fail to develop, and the external phenotype may be female.

Perineal Hernia

Perineal hernias are caused by separation of perineal muscles and occur almost exclusively in male intact dogs. The hernial sac is accessible for direct ultrasonographic examination via a perineal approach and may contain pelvic and retroperitoneal fat, serous fluid, rectum, prostate, urinary bladder or small intestine (Hedlund and Welch Fossum 2007; Figure 14.54)

Neuticles

Testicular prostheses may be implanted in neutered dogs and appear as well circumscribed structures within the scrotum. Their echogenicity is variable, and concurrent artifacts (distal shadowing, edge shadowing, or reverberation) may be noted (Figure 14.55).

Interventional Procedures

Percutaneous fine-needle aspiration or biopsy of the prostate is easily performed. The same principles and precautions used in other interventional procedures apply. To avoid urethral injury during the procedure, a urinary catheter should be placed to facilitate identification of the prostatic urethra. In cases of suspected prostatic neoplasia, sampling by means of traumatic catheterization or prostatic massage should be given preference because of the risk of implantation of tumor cells along the needle tract after percutaneous aspiration (Nyland et al. 2002).

Percutaneous drainage of prostatic abscesses and in situ injection of antibiotics is a valid alternative method

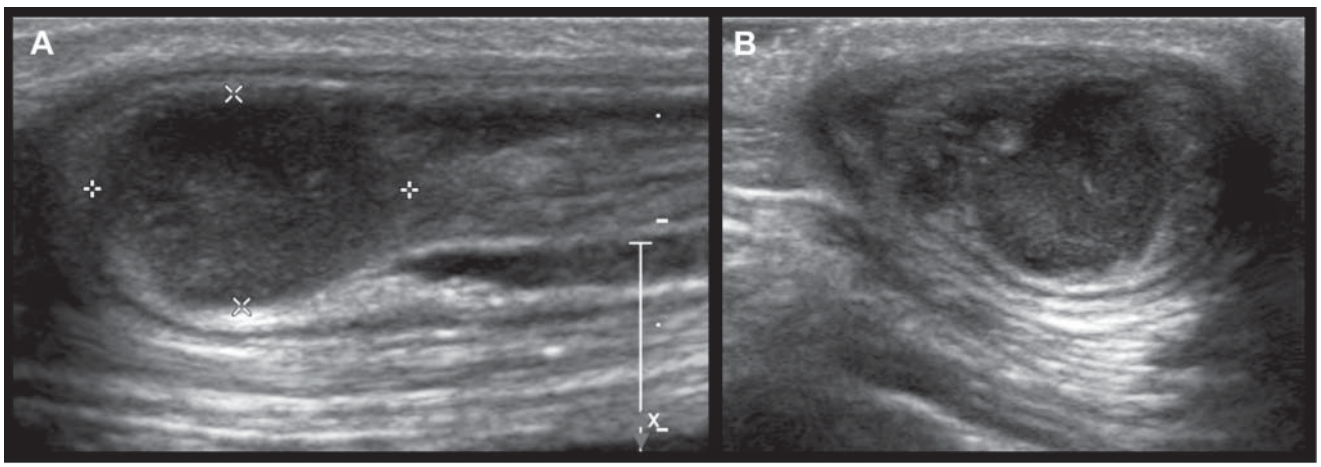


Figure 14.53. Penile tumor in a 7-year-old Beagle. The sagittal **(A)** and transverse **(B)** images show a discrete, poorly echogenic nodule associated with the tip of the penis. The biopsies were diagnostic of a soft-tissue sarcoma, suspected to be hemangiosarcoma.

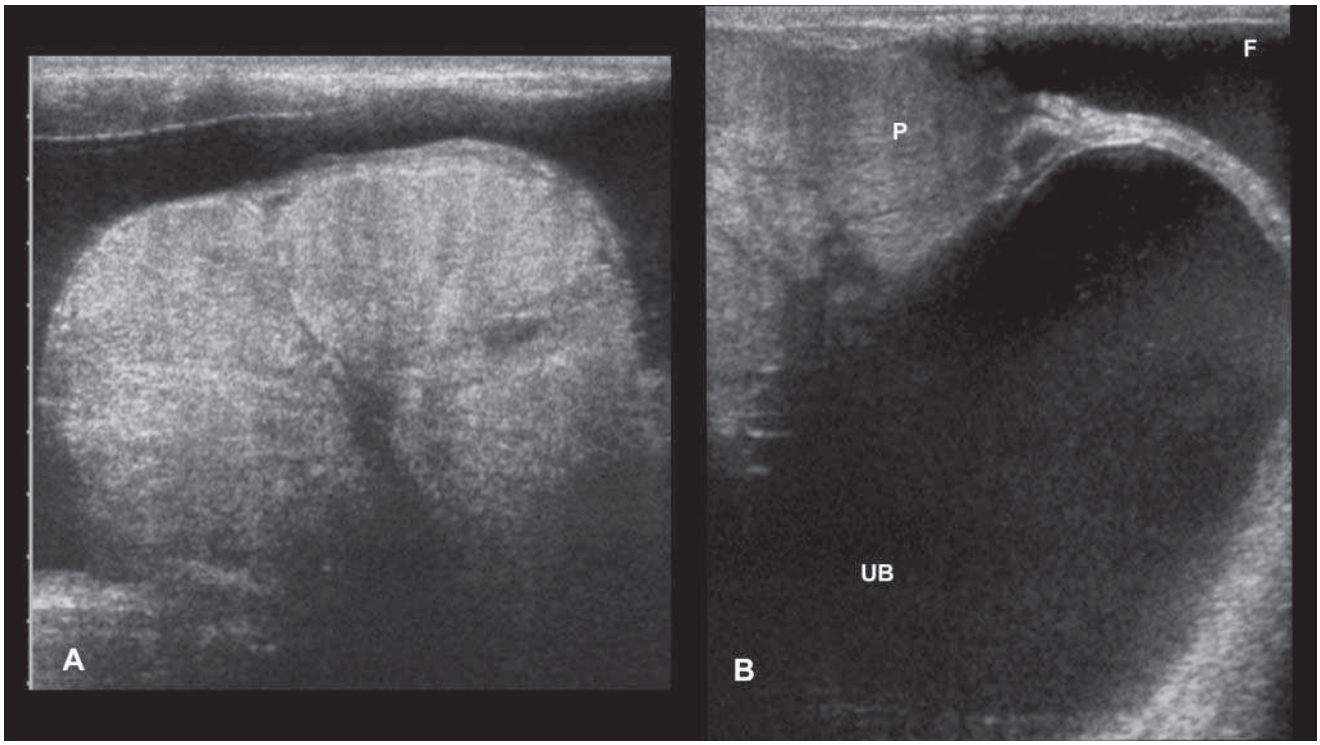


Figure 14.54. **Perineal hernia in a 9-year-old mixed-breed dog. A:** The transverse image shows the entire prostate being located within the hernia sac. The prostate is diffusely hyperechoic and contains a small hypoechoic lesion in the left lobe, consistent with benign prostatic hyperplasia and a small prostatic cyst. **B:** The sagittal image demonstrates herniation of the urinary bladder (UB) along with the prostate (P). Fluid (F) surrounds prostate and bladder on both images.

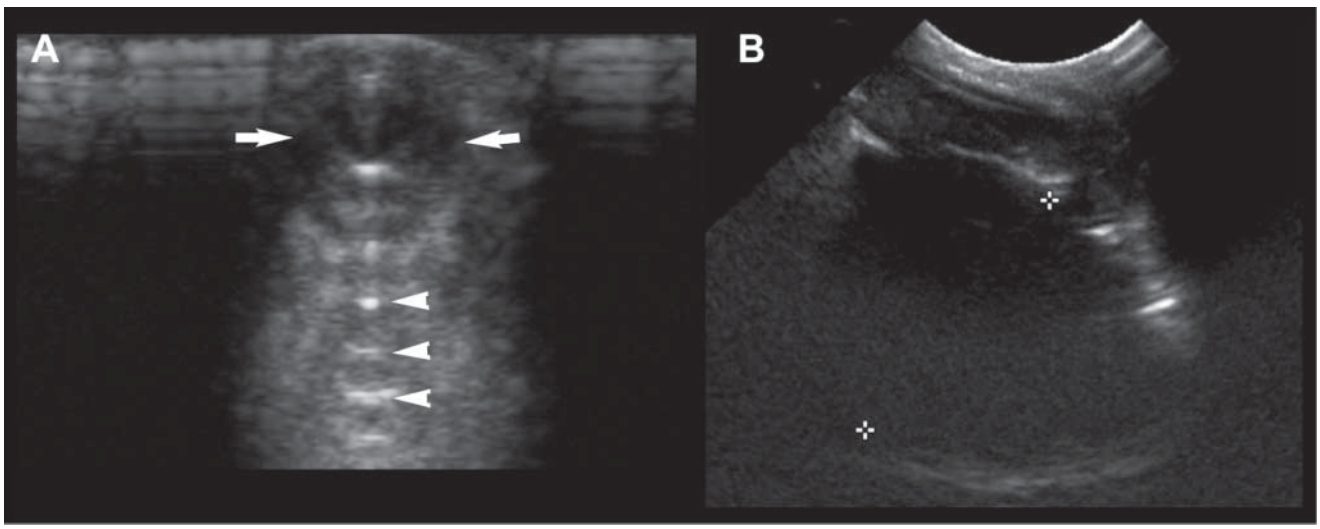


Figure 14.55. **Neuticles in two dogs. A:** The sagittal image of the scrotum in this 10-year-old mixed-breed dog demonstrates a round and mostly hypoechoic, approximately 8-mm-diameter structure with distal reverberation artifacts. **B:** In this Great Dane, the neuticle is about 3 cm long and anechoic.

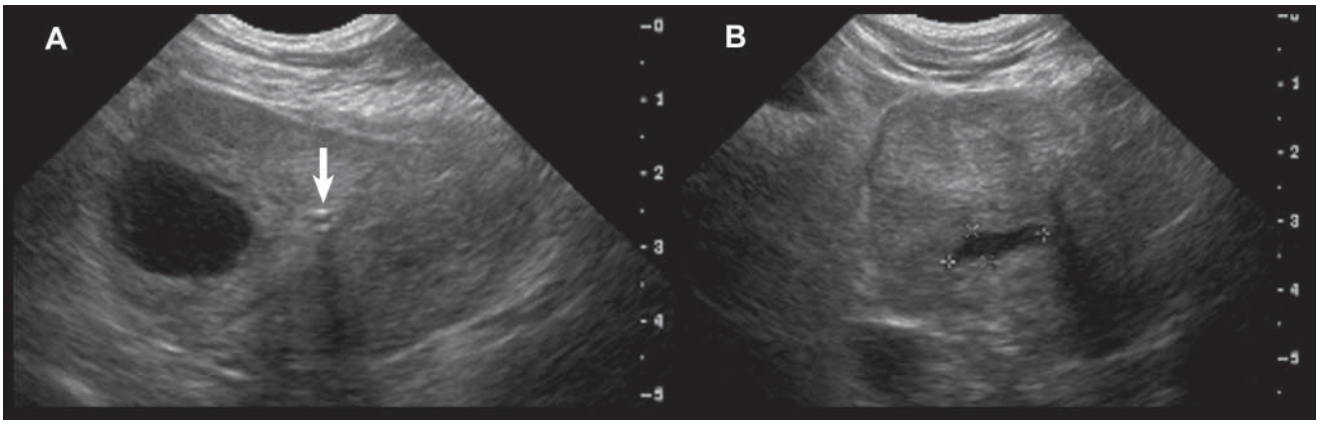


Figure 14.56. Drainage of a prostatic abscess in a 3-year-old Border Collie. A: Transverse sonogram of the prostate with right lobe abscess. The arrow points to the urethral catheter that has been placed to better identify and avoid the urethra during the procedure. **B:** Transverse sonogram of the prostate after drainage. The abscess cavity is nearly collapsed.

to surgical intervention, especially in immunocompromised patients (Boland et al. 2003) (Figure 14.56). Percutaneous drainage of paraprostatic cysts can be performed to temporarily relieve patient discomfort. However, recurrent filling usually warrants surgery at a later stage.

Fine-needle aspiration or biopsy of intra-abdominal testicular tumors is commonly performed, following the same principles and precautions as in biopsies of other abdominal organs. Fine-needle aspiration of intrascrotal testicles is infrequently performed in veterinary medicine. However, the procedure has a high accuracy in the diagnosis of testicular neoplasms, with a low risk of adverse effects (Dorsch et al. 2006; Gouletsou et al. 2011).



Visit our website at **www.SmallAnimalUltrasonography.com** for complementary video clips with annotations and text on:

- Normal prostate/testes
- Benign prostatic hyperplasia
- Prostatic tumor
- Prostatic abscess
- Testicular tumor

References

Atalan G, Holt PE, Barr FJ (1999) Ultrasonographic estimation of prostate size in normal dogs and relationship to body-weight and age. J Small Anim Pract 40:119–122.

Bigliardi E, Ferrari L (2011) Contrast-enhanced ultrasound of the normal canine prostate gland. Vet Radiol Ultrasound 52:107–110.

Boland LE, Hardie RJ, Gregory SP, Lamb CR (2003) Ultrasound-guided percutaneous drainage as the primary treatment for prostatic abscesses and cysts in dogs. J Am Anim Hosp Assoc 39:151–159.

Bradbury CA, Westropp JL, Pollard RE (2009) Relationship between prostatomegaly, prostatic mineralization, and cytologic diagnosis. Vet Radiol Ultrasound 50:167–171.

Christensen BW (2012) Disorders of sexual development in dogs and cats. Vet Clin North Am Small Anim Pract 42:515–526.

Dorsch R, Majzoub M, Hecht S, Hartmann K, Hirschberger J (2006) Diagnostische Wertigkeit der Hodenzytologie beim Hund. Tieraerztl Prax 34:91–98.

Feeney DA, Johnston GR, Klausner JS, Bell FJ (1989) Canine prostatic ultrasonography: 1989. Semin Vet Med Surg (Small Anim) 4:44–57.

Felumlee AE, Reichle JK, Hecht S, et al (2012) Use of ultrasound to locate retained testes in dogs and cats. Vet Radiol Ultrasound epub ahead of print.

Gouletsou PG, Galatos AD, Leontides LS, Sideri AI (2011) Impact of fine- or large-needle aspiration on canine testes: clinical, in vivo ultrasonographic and seminological assessment. Reprod Domest Anim 46:712–719.

Hecht S (2001) Sonographische Diagnostik des Skrotalinhaltes beim Hund unter besonderer Beruecksichtigung testikulaerer Neoplasien [Doctoral thesis]. Munich: Chirurgische Tierklinik, Ludwig-Maximilians University.

Hecht S, King R, Tidwell AS, Gorman SC (2004) Ultrasound diagnosis: Intra-abdominal torsion of a non-neoplastic testicle in a cryptorchid dog. Vet Radiol Ultrasound 45:58–61.

Hecht S, Matiasek K, Koestlin R (2003) Die sonographische Untersuchung des Skrotalinhaltes beim Hund unter besonderer Beruecksichtigung testikulaerer Neoplasien. Tieraerztl Prax 31:199–210.

Hedlund CS, Welch Fossum T (2007) Surgery of the digestive system. In: Welch Fossum T, ed. Small Animal Surgery, 3rd edition. St Louis: Mosby Elsevier, pp 339–530.

Johnston GR, Feeney DA, Johnston SD, O'Brien TD (1991a) Ultrasonographic features of testicular neoplasia in dogs: 16 cases (1980–1988). J Am Vet Med Assoc 198:1779–1784.

Johnston GR, Feeney DA, Rivers B, Walter PA (1991b) Diagnostic imaging of the male canine reproductive organs: Methods and limitations. Vet Clin North Am Small Anim Pract 21:553–589.

Johnston SD, Kamolpatana K, Root-Kustritz MV, Johnston GR (2000) Prostatic disorders in the dog. Anim Reprod Sci 60–61:405–415.

Mattoon JS, Nyland TG (2002) Prostate and testes. In: Nyland TG, Mattoon JS, eds. Small Animal Diagnostic Ultrasound. Philadelphia: WB Saunders, pp. 250–266.

Meyers-Wallen VN (2008) Inherited disorders of the reproductive tract in dogs and cats. In: Bonagura J, ed. Kirk's Current Veterinary Therapy. Philadelphia: WB Saunders, pp. 1034–1039.

Miyabashi T, Biller DS, Cooley AJ (1990) Ultrasonographic appearance of torsion of a testicular seminoma in a cryptorchid dog. J Small Anim Pract 31:401–403.

Nyland TG, Wallack ST, Wisner ER (2002) Needle-tract implantation following US-guided fine-needle aspiration biopsy of transitional cell carcinoma of the bladder, urethra, and prostate. Vet Radiol Ultrasound 43:50–53.

Ober CP, Spaulding K, Breitschwerdt EB, Malarkey DE, Hegarty BC (2004) Orchitis in two dogs with Rocky Mountain spotted fever. Vet Radiol Ultrasound 45: 458–465.

Pugh CR, Konde LJ (1991) Sonographic evaluation of canine testicular and scrotal abnormalities: A review of 26 case histories. Vet Radiol Ultrasound 32:243–250.

Pugh CR, Konde LJ, Park RD (1990) Testicular ultrasound in the normal dog. Vet Radiol Ultrasound 31:195–199.

Ruel Y, Barthez PY, Mailles A, Begon D (1998) Ultrasonographic evaluation of the prostate in healthy intact dogs. Vet Radiol Ultrasound 39:212–216.

Stowater JL, Lamb CR (1989) Ultrasonographic features of paraprostatic cysts in nine dogs. Vet Radiol Ultrasound 30:232–239.

Teske E, Naan EC, van Dijk EM, Van Garderen E, Schalken JA (2002) Canine prostate carcinoma: epidemiological evidence of an increased risk in castrated dogs. Mol Cell Endocrinol 29:251–5.

Vignoli M, Russo M, Catone G et al. (2011). Assessment of vascular perfusion kinetics using contrast-enhanced ultrasound for the diagnosis of prostatic disease in dogs. Reprod Domest Anim 46:209–213.

Winter MD, Locke JE, Penninck DG (2006) Imaging diagnosis: Urinary obstruction secondary to prostatic lymphoma in a young dog. Vet Radiol Ultrasound 47:597–601.

Zohil AM, Castellano C (1995) Prepubic and transrectal ultrasonography of the canine prostate: A comparative study. Vet Radiol Ultrasound 36:393–396.

CHAPTER FIFTEEN

Abdominal Cavity, Lymph Nodes, and Great Vessels

Marc-André d'Anjou[1,2] and Éric Norman Carmel[2,3]

[1] *Centre Vétérinaire Rive-Sud, Brossard, Québec, Canada*
[2] *Faculté de médecine vétérinaire de l'Université de Montréal, Saint-Hyacinthe, Québec, Canada*
[3] *Centre Vétérinaire Laval, Laval, Québec, Canada*

Preparation and Scanning Technique

To have access to all portions of the abdominal cavity of dogs and cats, hair must be clipped ventrally and laterally between the costal arch and caudal margin of the abdomen. Clipping may be extended more cranially in deep-chested dogs to better visualize the subcostal region. After the application of acoustic gel, the animal can be scanned in dorsal, left, or right recumbency. Some disorders of the peritoneal space, such as effusion or free air, respond to gravity and may require repositioning the animal to reach a diagnosis.

Ultrasonographic probes must be selected according to the size of the animal and the depth of the evaluated region(s). A high-frequency probe (7.5 MHz and higher) is recommended in cats and in small dogs or if superficial structures are examined, whereas probes with more penetration (5.0–7.5 MHz and lower) are useful when assessing deep portions of larger dogs. Disorders affecting the attenuation of the ultrasound beam may also influence the probe selection. For example, peritoneal transudation is associated with reduced sound attenuation, as opposed to inflammatory or neoplastic processes involving the omentum, which typically produce increased ultrasound attenuation. In these instances, probes with a higher or lower frequency, respectively, may improve image quality. Sectorial or convex probes are preferred because they can reach all portions of the abdomen, including the subcostal region, as opposed to linear probes, which have a larger footprint. Tissue harmonic imaging and spatial compounding may help in assessing superficial peritoneal lesions or reduce rib acoustic shadow for the subcostal space. Doppler evaluation of abdominal vascular structures requires the use of dedicated probes and software.

Ultrasonographic Anatomy of the Normal Peritoneal and Retroperitoneal Cavity, Fat, Vessels, and Lymph Nodes

The peritoneum is composed of a thin serous membrane that is divided into parietal and visceral components. The peritoneal cavity is a potential space located between these two layers that contain only a scant volume of fluid that serves as a lubricant. However, this amount of fluid is usually not detectable with ultrasound, except in very young patients where a minute amount of physiological peritoneal fluid may be identified (Stander 2010). The peritoneum appears as a smooth hyperechoic interface that is better appreciated when a moderate volume of ascites is present. A variable amount of fat is present, mainly in the falciform ligament, omentum, mesentery, and retroperitoneum. The fat appears coarse in echotexture and of low to moderate echogenicity with hyperechoic speckles. The mesentery and omentum cannot be easily distinguished, although the mesentery may be

Atlas of Small Animal Ultrasonography, Second Edition. Edited by Dominique Penninck and Marc-André d'Anjou.
© 2015 John Wiley & Sons, Inc. Published 2015 by John Wiley & Sons, Inc.
Companion website: www.SmallAnimalUltrasonography.com

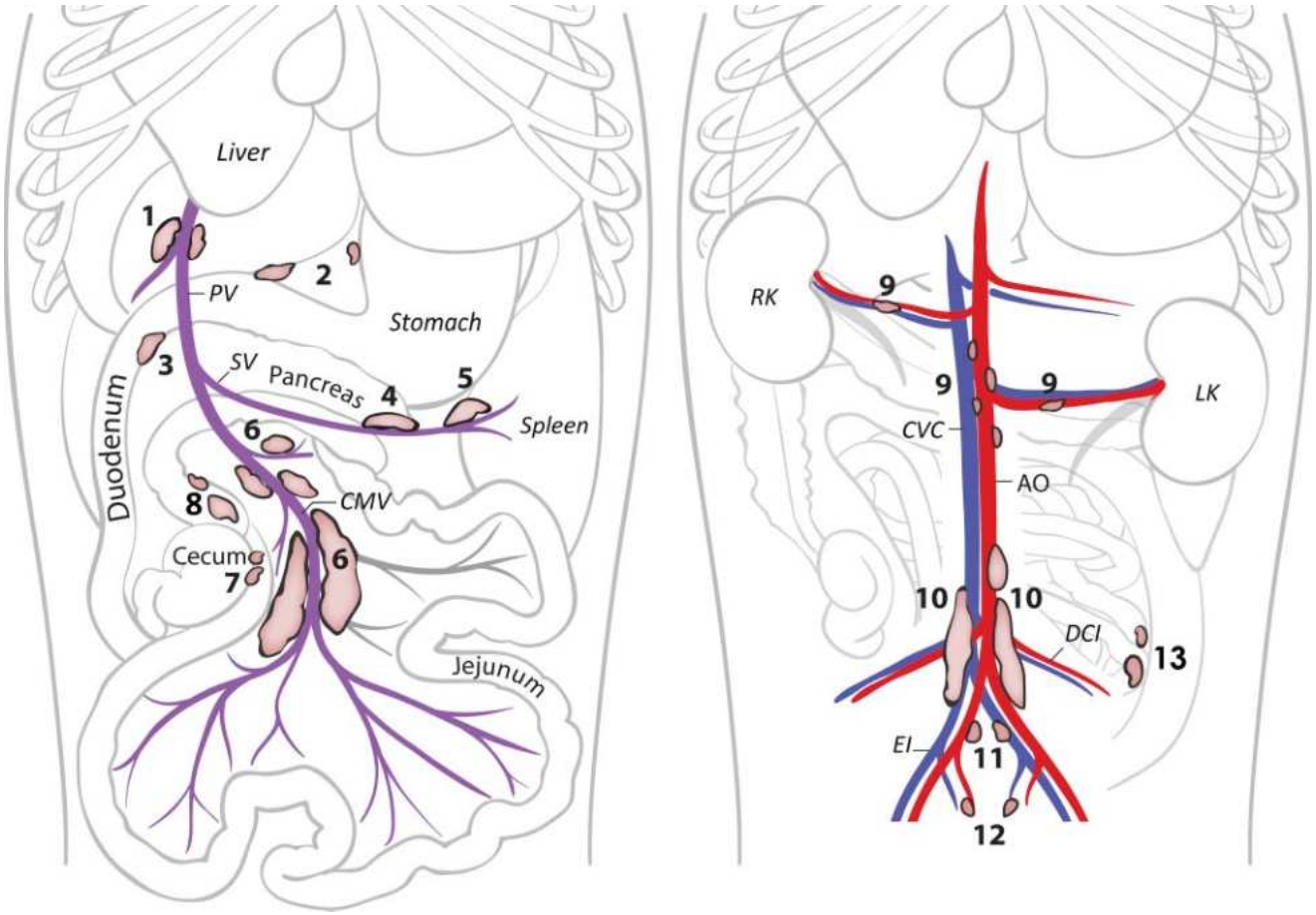


Figure 15.1. Schematic illustration of abdominal lymph nodes and major vessels. Note the intimate anatomical relationship between lymph nodes and vessels. Lymph nodes: 1, hepatic; 2, gastric; 3, pancreaticoduodenal; 4 and 5, splenic; 6, jejunal; 7, ileocecal; 8, colic; 9, renal and lumbar aortic; 10, medial iliac; 11, internal iliac; 12, sacral, and 13, caudal colic. Vessels: AO, aorta; CMV, cranial mesenteric vein; CVC, caudal vena cava; DCI, deep circumflex iliac vessels; EI, external iliac vessels; PV, portal vein; SV, splenic vein. Other landmarks: LK, left kidney; RK, right kidney.

recognized as it contains vessels and lymph nodes that can be visualized in most patients.

A thorough knowledge of vascular anatomy and hemodynamics is necessary to facilitate the identification and assessment of abdominal vessels (Spaulding 1997; Finnn-Bodner and Hudson 1998; Szatmari et al. 2001; Schreurs et al. 2008; Bezuidenhout 2013a,b). A schematic illustration of the principal vessels in the abdomen, as well as major lymph nodes, of dogs and cats is presented in Figure 15.1. While the abdominal aorta supplies the arterial flow for all structures, the venous flow is separated between the portal system and the systemic circulation (see the section on "Extrahepatic Portal Vasculature" in Chapter 6). In comparison with the portal system, a limited number of abdominal veins drain directly into the caudal vena cava (CVC). The CVC crosses the abdomen from caudal to cranial, remaining on the right of the midline. Visible veins with B-mode ultrasonography include, from caudal to cranial, the convergence of iliac veins (external, internal, common, and deep circumflex), renal veins, phrenicoabdominal veins, and hepatic veins The aorta is more dorsal than the CVC in the cranial abdomen and remains on the left side, and then it lies next to it caudally. Major abdominal branches of the aorta that can be localized ultrasonographically include, from cranial to caudal, celiac artery (left gastric, hepatic, and splenic arteries), cranial mesenteric artery, renal arteries, and aortic trifurcation where external iliac arteries arise. These vessels are useful landmarks for identifying abdominal lymph nodes.

Abdominal lymph nodes are routinely evaluated in small animal patients, because the nodes drain several organs and structures. Table 15.1 lists the location and drainage of the abdominal lymph nodes in dogs and cats (Pugh 1994; Schreurs et al. 2008; Bezuidenhout 2013c).

Several lymph nodes are easily identified in dogs and cats, especially for more superficial nodes, in young and smaller patients, and when using more recent

Table 15.1
Location and drainage of abdominal lymph nodes

Lymph Nodes	Location	Drainage Areas
Hepatic	Along the portal vein, caudal to the *porta hepatis*	Liver, stomach, duodenum, and pancreas
Splenic	Along the splenic veins and the left pancreatic lobe	Liver, spleen, esophagus, stomach, pancreas, and omentum
Gastric	Near the pylorus, close to lesser curvature	Diaphragm, liver, esophagus, stomach, duodenum, pancreas, and peritoneum
Pancreaticoduodenal	Near the cranial duodenal flexure, between the pylorus and the right pancreatic limb	Duodenum, pancreas, and omentum
Jejunal	Along the mesenteric vascular tree (cranial mesenteric artery and vein)	Jejunum, ileum, and pancreas
Colic	Near the ileocolic junction (right colic), mesocolon (middle colic), and the caudal descending colon (left colic)	Ileum, cecum, and colon
Lumbar aortic and renal	Along aorta and near the kidneys	Spinal structures, ribs, peritoneum, kidneys, adrenals, bladder, uterus, prostate, and gonads
Medial iliac, internal iliac, and sacral	At the caudal aortic trifurcation, between the deep circumflex and the external iliac arteries (medial iliac), medial to the internal iliac arteries (internal iliac) and along the median sacral artery (sacral)	Ureters, bladder, uterus, prostate, gonads, peripelvic and pubic areas, abdominal skin, caudal vertebrae, pelvis, hindlimb muscles, and bones

ultrasound units. These lymph nodes are generally uniformly isoechoic to slightly hypoechoic to the adjacent fatty tissues, with fine echotexture, smooth in contour, and fusiform to oval (Llabrés-Diaz 2004; Nyman and O'Brien 2007; Mayer 2010) (Figure 15.2). A thin hyperechoic capsule is often identified, and occasionally normal hyperechoic central lines corresponding to vascular walls and fat can be seen crossing these nodes in the region of the nodal hilus. Blood flow may, however, not be apparent with color Doppler examination. For jejunal nodes, such flow can be detected in only 33% of dogs, particularly when younger than 2 years of age (Agthe 2009).

Reference values for lymph node dimensions have been reported, but not for all groups of nodes. As for the adrenals, measuring maximal thickness (i.e., smallest axial dimension) or width (i.e., largest axial dimension) is more reliable than length when estimating lymph node size in dogs and cats. Reference ranges reported in dogs and cats are summarized in Table 15.2. Jejunal lymph nodes tend to be relatively larger in young healthy puppies (mean diameter of 6–7mm), often irregular, and hypoechoic or with a hypoechoic rim (Stander 2010; Krol and O'Brien 2012). This enlargement and reduced cortical echogenicity are probably explained by the fact that the intestinal tract of young animals is continuously exposed to new antigens (Agthe 2009).

Due to the great variation in lymph node dimensions among dogs and cats, the shape of these nodes may actually represent a more useful landmark than absolute measurements. A ratio comparing the short and long axes measuring less than 0.5 is generally considered normal (Llabrés-Diaz 2004; Nyman et al. 2004). This has been validated for medial iliac and superficial inguinal nodes in dogs (Mayer 2010). However, this ratio has limited usefulness for other lymph nodes, such as jejunal nodes, that tend to be much longer and may exceed the field of view or present a curved shape (Agthe 2009).

Lymph nodes routinely identified include the jejunal (or mesenteric) and medial iliac lymph nodes. Jejunal nodes appear as a group of fusiform nodes aligned with the cranial mesenteric artery and vein and their branches within the omentum. Some of these nodes can be relatively long. The iliosacral lymphocenter is the group formed by the sublumbar lymph nodes, which are located along the caudal aortic trifurcation. The medial iliac lymph nodes, which are typically larger than the other nodes, may be more easily identified from a lateral flank approach rather than from the ventral abdomen, because the former allows the

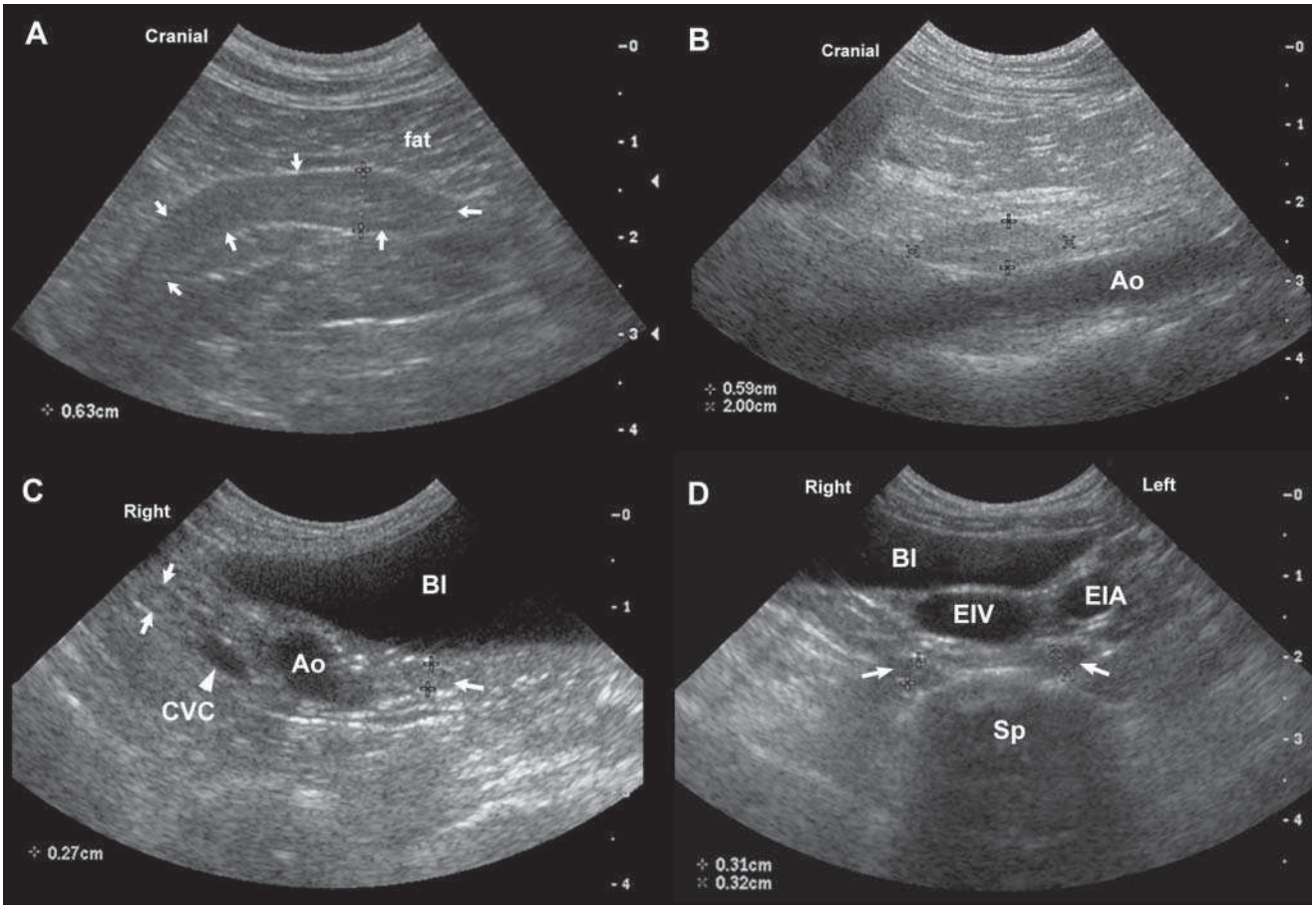


Figure 15.2. **Normal lymph nodes.** (for full caption, see facing page)

Table 15.2
Lymph node dimensions in normal dogs and cats

	Maximal thickness or height (mm)	Maximal width (mm)	Maximal thickness used by the authors
Adult dog			
Jejunal[a]	3.9 (1.6-8.2)	7.5 (2.6–14.7)	5–8 mm*
Medial iliac[b]	4.6–4.8 (±0.18–0.20)	5.9–6.1 (±0.19–0.25)	
Superficial iliac[b]	3.1 (±0.12)	6.1–6.8 (±0.34–0.36)	
Pediatric dog			
Jejunal[c]	7.1 ± 2.2 (1.5–12.5)		10 mm
Medial iliac[d]		4.4 (1.9–8.2)	10 mm
Cat			
Pancreaticoduodenal[e]	4.6 (3.6–6.2)		4–5 mm
Hepatic[e]	2.9 (2.5–3.6)		4 mm
Jejunal[e]	5 (2.8–7.2)		4–6 mm
Ileocecal[e]	4.1 (2.7–4.8)		5 mm
Medial iliac[e]	4.5 (1.3–14)		5–6 mm

Results are displayed as median (range) or mean (standard deviation).
[a]In dogs without clinical signs of GI disease (Agthe 2009). Authors suspected that some of these nodes might have been reactive, especially in dogs less than 2 years of age.
[b]In clinically healthy adult dogs (Mayer 2010). Right and left medial lymph nodes were not different in size.
[c]In 7- to 12-week-old healthy Beagle puppies (Stander 2010).
[d]In 53 clinically normal puppies between 4 and 6 week-old (Krol and O'Brien 2012).
[e]In 10 adult cats without clinical evidence of abdominal disease (Schreurs 2008). These nodes were identified in more than 50% of the cats.
*Depending on dog size.

Figure 15.2. **Normal lymph nodes. A, B:** Longitudinal ultrasonographic images of normal jejunal (**A**, arrows) and medial iliac (**B**, cursors) lymph nodes in two dogs. The nodes are fusiform, well defined, uniform, and mildly hypoechoic compared with the peripheral fat. The short-to-long axis ratio is less than 0.5. Ao, aorta. **C, D:** Transverse images of normal medial iliac (**C**, arrows) and internal iliac (**D**, arrows) lymph nodes in another dog. Note the proximity of these nodes to the urinary bladder (Bl) and to the caudal vena cava (CVC) and aorta (Ao), as well as their branches (EIA and EIV: left external iliac artery and vein). The spine (Sp) is located just dorsal to the internal iliac nodes and appears as a strongly shadowing interface.

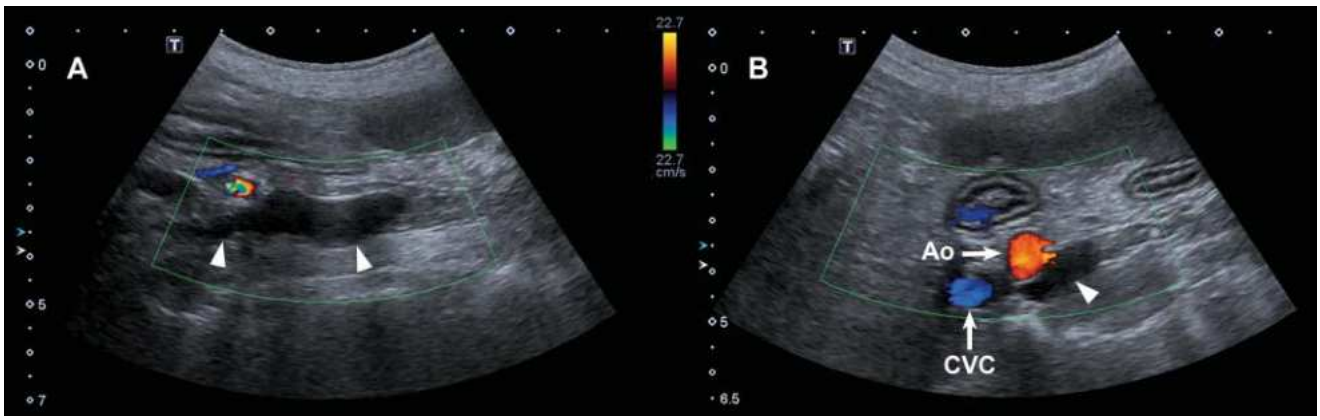


Figure 15.3. **Cysterna chyli in a 10-year-old Labrador dog with gastroenteritis.** There was no peritoneal effusion or other signs of lymphatic congestion. The cysterna (arrowheads) appears as a well-defined cystic structure partly encircling the mid-abdominal aorta on its dorsal left border. It appears fusiform in the longitudinal plane (**A**) and oval to semicircular in the transverse plane (**B**).

probe to be placed closer to the node, thus avoiding the descending colon (Llabrés-Diaz 2004). These nodes can vary in number, but, commonly, a node reaching 7–8 mm in thickness in large dogs is often recognized on the left and right sides of the aorta and CVC, respectively, and usually just cranial to the circumflex iliac arteries and veins. Smaller hypogastric nodes are sometimes recognized more caudally, medial to the internal iliac arteries and veins, although these nodes are often inaccessible with ultrasound.

An oval to semicircular tubular anechoic structure a few millimeters in size, corresponding to the cisterna chyli, may be found in the mid-dorsal retroperitoneal space in dogs and cats, partly encircling the abdominal aorta in the area of the cranial mesenteric artery (Etienne et al. 2013). The cisterna when visible may reach in maximal thickness of 7 mm in dogs and 3 mm in cats without chylous effusion (Figure 15.3).

Peritoneal Effusion

Peritoneal effusion can be detected with ultrasonography if the volume of free fluid exceeds approximately 2 mL/kg, which is half of what is needed for a radiographic diagnosis (Henley et al. 1989). Even smaller amounts of effusion are probably identified with more recent ultrasound systems. Peritoneal fluid distribution depends on its nature and on gravity. Free fluid moves with gravity, between abdominal organs, and locates itself according to the position of the animal. Free fluid is more likely to be detected when scanning the dependent portion of a dog that is in lateral recumbency (Boysen et al. 2004). Small volumes of free fluid often appear as triangular collections that are anechoic or hypoechoic to the surrounding tissues and are better identified at the left lateral margin of the spleen, between hepatic lobes or intestinal loops, or cranial to the apex of the bladder (Spaulding 1993). However, trapped or loculated fluids can remain in the non-dependent portion of the abdomen. Trapped fluids are more commonly associated with chronic exudates. Figure 15.4 illustrates the variable appearance of peritoneal effusion depending on its localization and magnitude. Care must be taken not to confuse free or trapped peritoneal fluid with fluid-filled structures, such as severe hydronephrosis, hydroureter, dilated bowel loops, or cysts (Figure 15.5). Structures such as bowel loops or mesenteric folds are usually observed moving within the fluid,

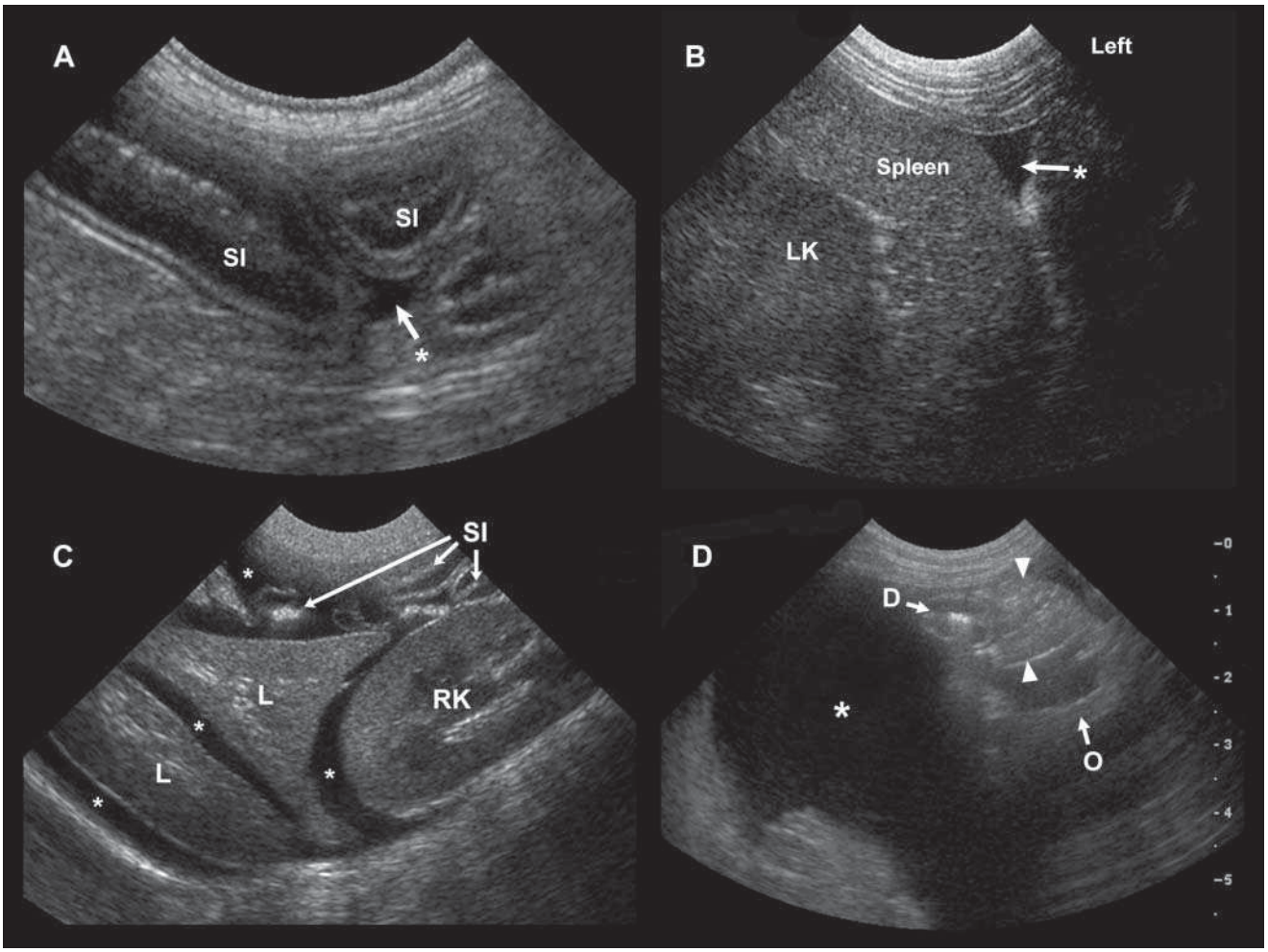


Figure 15.4. **Pure or modified transudates in dogs.** (for full caption, see facing page)

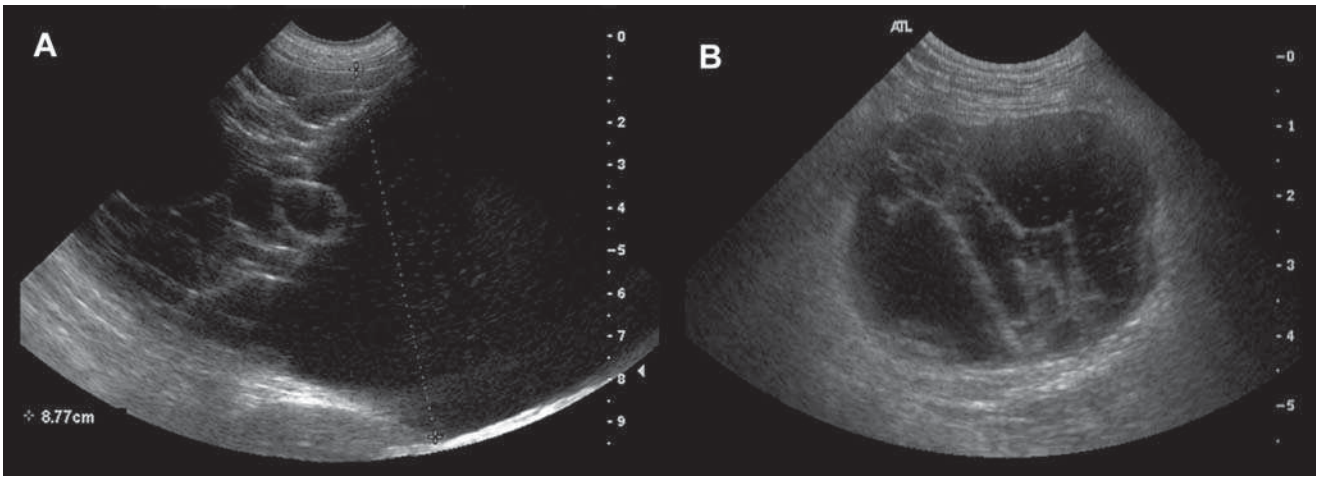


Figure 15.5. **Loculated fluid. A:** Longitudinal image obtained in the right abdominal quadrant of a cat with a chronically distended abdomen. A large fluid-filled multiloculated cyst is identified, displacing all surrounding structures. Several septae are seen throughout this benign cavitary structure that originated from the omentum. **B:** Omental seroma in a dog following intestinal surgery. The cavitary area is filled with anechoic fluid and septae. This cystic mass was confirmed not to be an abscess, via fine-needle aspiration.

Figure 15.4. Pure or modified transudates in dogs. Longitudinal **(A)** and transverse **(B)** images obtained in a dog with hypoproteinemia in the mid-ventral and left-lateral portions of the abdomen, respectively. Small triangular anechoic foci (*) are between small intestinal loops (SI) and lateral to the spleen, consistent with a low cellular fluid. A pure transudate was aspirated under ultrasound guidance. LK, left kidney. **C**: Longitudinal image obtained in the right cranial abdomen of another dog with peritoneal effusion. Several structures, such as liver lobes (L), right kidney (RK), and small intestinal loops (SI), are separated by anechoic areas (*). **D**: Transverse image obtained in the right cranial abdomen of a dog with cardiac tamponade. The peritoneal space is distended by a large volume of anechoic effusion (PE). The descending duodenum (D), pancreas (arrowheads), and omentum (O) are distinctly visualized within the contrasting anechoic fluid. The appearance of the effusion in all these dogs is suggestive of a pure or modified transudate rather than an exudate.

particularly if a large volume of peritoneal fluid is present (Figure 15.4D).

The echogenicity of the peritoneal fluid is usually proportional to its content in cells and other debris, which act as ultrasound reflectors. Low cellular fluids, such as transudates, are typically anechoic to hypoechoic (Figure 15.4), in comparison with exudates, which are typically moderately echogenic (Figure 15.6A). Highly cellular and homogeneous purulent exudates can actually appear isoechoic to soft-tissue organs, such as the spleen, and sometimes be recognized only because of their visible motion and lack of vascularity. Exudates can also be septated because of fibrin strands that commonly develop with this type of effusion, particularly with purulent peritonitis (Spaulding 1993). Carcinomatosis may also result in hyperechoic fluid (Figure 15.6B). Chylous effusion tends to be associated with echogenic effusion (Figure 15.6C).

Peritoneal hemorrhage varies in appearance according to the interval between the onset of bleeding and the time of the ultrasonographic examination. Fresh peritoneal blood may appear anechoic or echogenic, with swirling of particles within the fluid (Pintar et al. 2003) (Figure 15.6D). Hematomas can develop and initially appear as amorphous masses of homogeneous echogenicity. Lysis of the hematoma produces a more heterogeneous appearance, with the formation of cystic areas and septa (Figure 15.7). In a previous study of 39 dogs with non-traumatic hemoabdomen, a malignancy was identified in 80% of cases and hemangiosarcoma in 70% (Pintar et al. 2003).

However, it must be pointed out that some overlap exists with regard to the echogenic appearance of different types of fluids. Hence, modified transudates may look similar to exudates. Other ultrasonographic findings, such as the presence of nodules on the surface of the peritoneum in cases of carcinomatosis, or in the presence of a large splenic mass, should be used to orient the diagnosis.

Table 15.3 describes the typical appearance of variable types of peritoneal effusion in dogs and cats.

Table 15.3
Typical ultrasonographic appearance of peritoneal effusions

Ultrasonographic Appearance	Diagnostic Differential
Anechoic or hypoechoic fluid	Pure or modified transudate Serohemorrhagic fluid Urine leak Chylous effusion
Echogenic with mobile particles	Fresh hemorrhage Modified transudate Purulent exudate or loculated abscess Serosanguinous exudate Carcinomatosis Chylous effusion
Highly echogenic with fibrous strands	Purulent exudate
Mobile echogenic masses	Blood clots Masses or nodules attached to the mesentery, omentum or visceral serosa (carcinomatosis)

Peritonitis, Steatitis, and Pneumoperitoneum

A variable amount of effusion is observed with peritonitis in dogs and cats, usually with moderate to high echogenicity because of the high cellular content (Boysen et al. 2003) (Figure 15.6A). The peritoneum, omentum, and mesentery may also appear thickened, hyperechoic, and hyperattenuating, focally or diffusely (Figure 15.8A–C). These features can significantly limit the penetration of the ultrasound beam and consequently the ability to visualize and

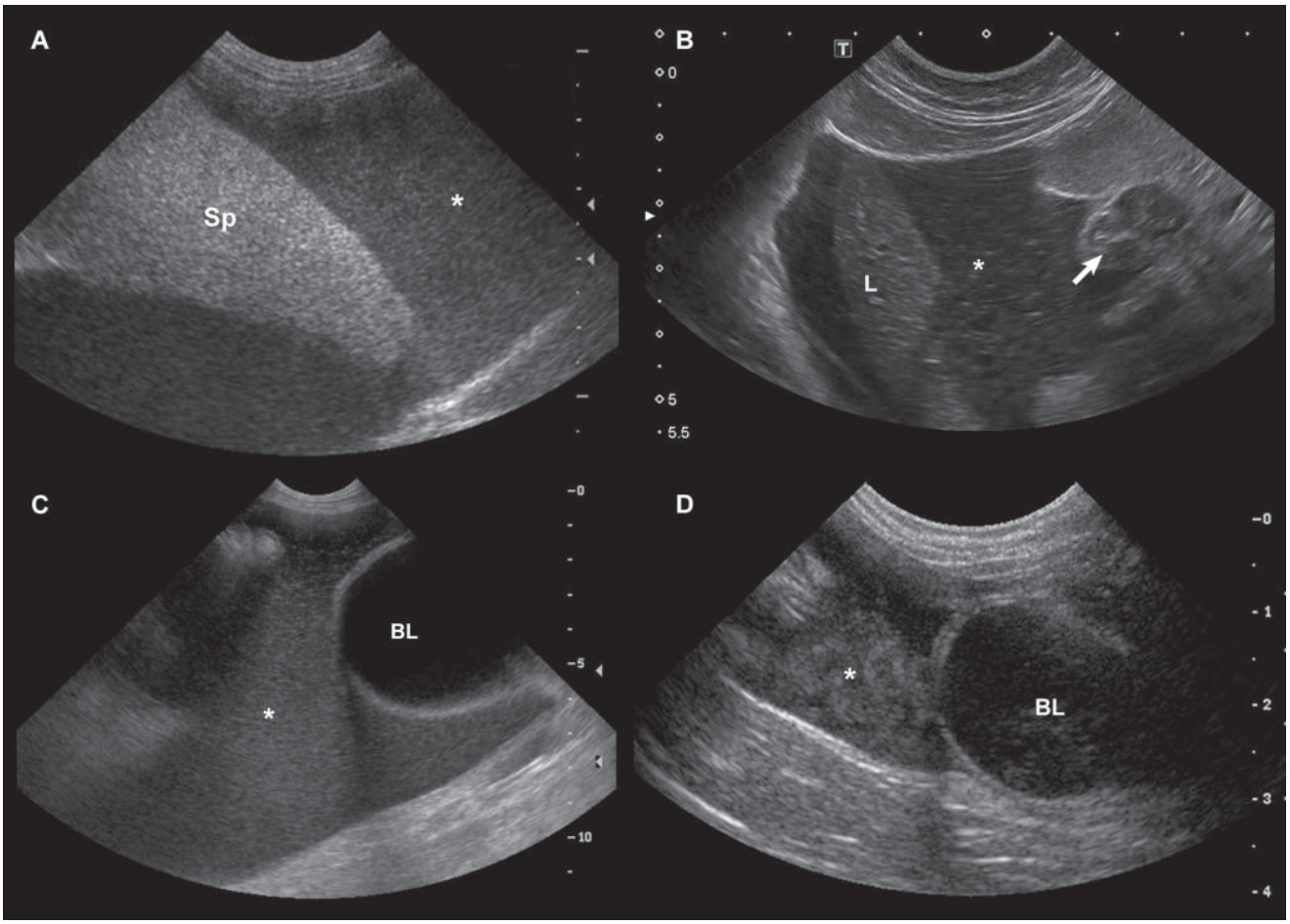


Figure 15.6. **Echogenic peritoneal effusions in dogs and cats. A**: Longitudinal image of a dog with abdominal distension and pain. A large volume of particulate, echogenic, peritoneal effusion (*) is seen around the spleen (Sp). These features are suggestive of a cellular effusion, such as exudate or hemorrhage. A diagnosis of septic peritonitis was made based on fluid aspiration. **B**: In this cat with pancreatic adenocarcinoma and carcinomatosis, there is marked peritoneal effusion (*), which presents hyperechoic speckles. A hypoechoic nodule (arrow) is detected in the omentum **C**: Chylous effusion (*) is typically of moderate to high echogenicity, as in this dog. BL, bladder. **D**: Longitudinal image of the caudal abdomen of a cat diagnosed with multifocal biliary carcinomas. Floating, echogenic structures (*), not attached to any structure and consistent with blood clots, were identified cranial to the bladder (BL).

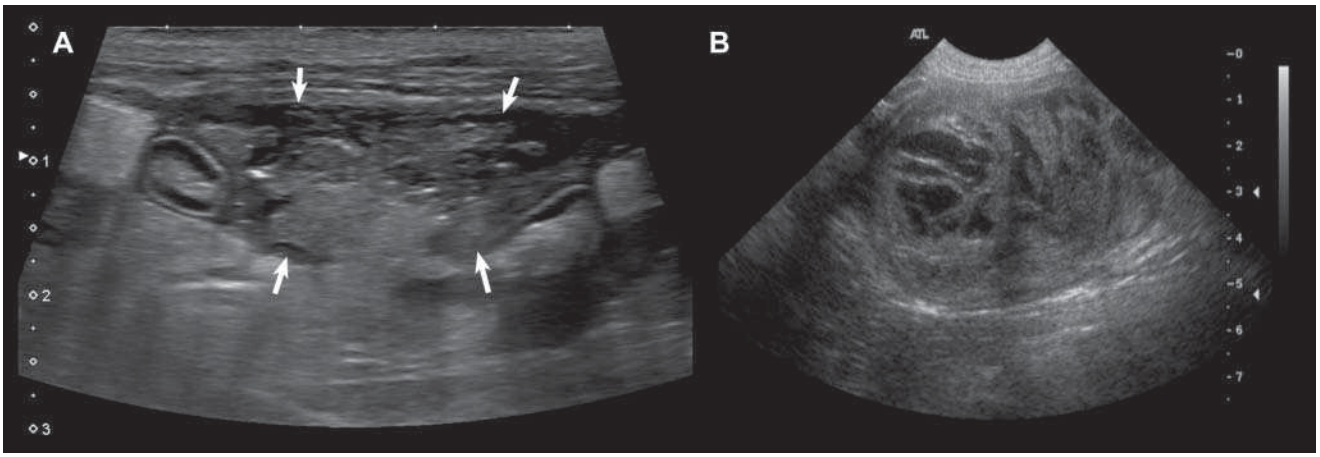


Figure 15.7. **Peritoneal hematomas. A:** Longitudinal image of the mid-ventral abdomen of a dog that had previous intestinal surgery for removing a foreign body. Postoperative dehiscence resulted in peritonitis and a large hematoma formed between intestinal loops. This hematoma appears as a large mass (between arrows) of heterogeneous echogenicity, with a few hyperechoic speckles presumably indicating trapped air bubbles. **B:** This mass of mixed echogenicity was found in the peritoneal cavity of another dog with splenic hemangiosarcoma. While the appearance of this mass suggested metastasis, it was confirmed to represent a large hematoma.

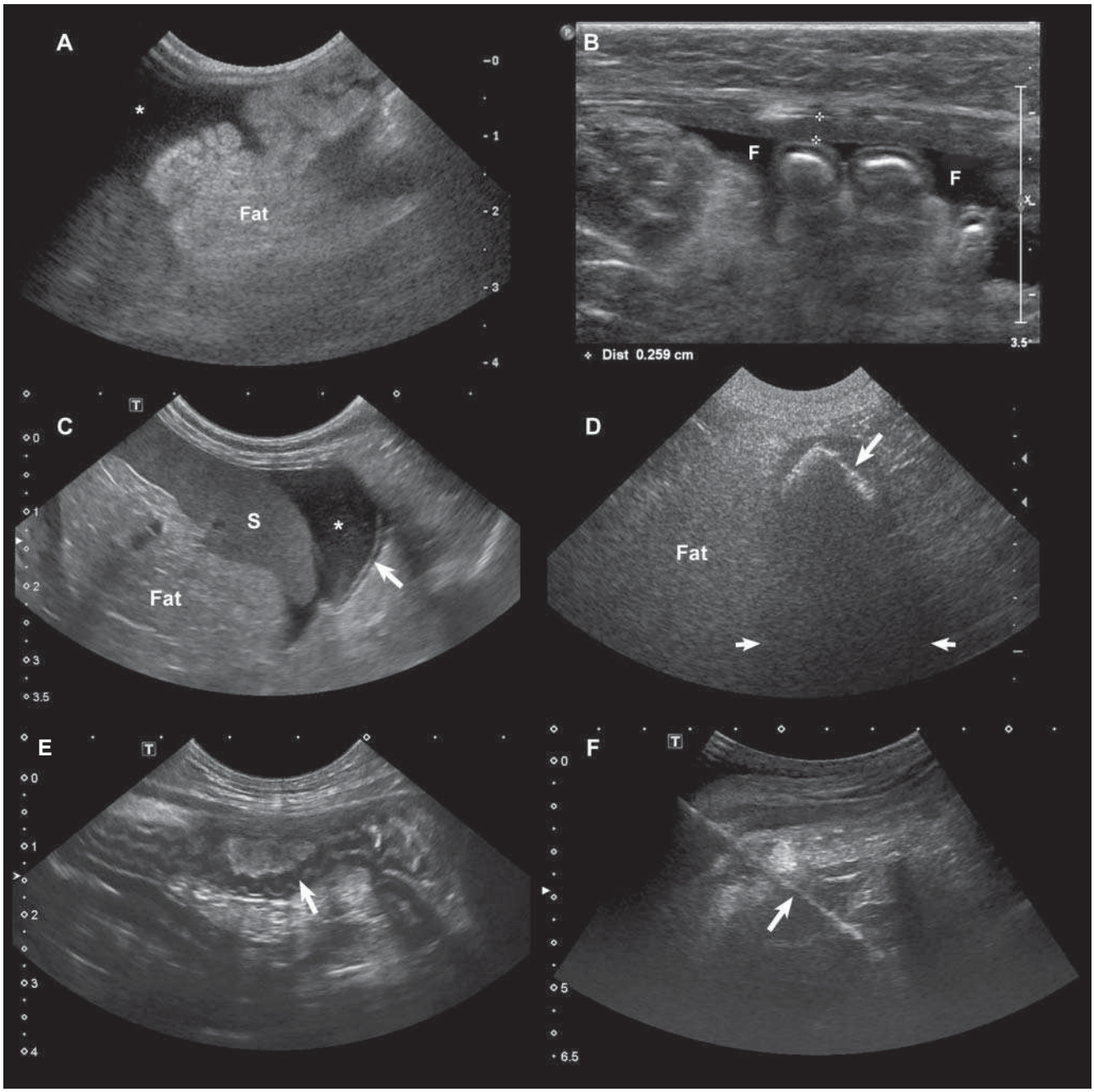


Figure 15.8. **Peritonitis and steatitis. A:** Feline infectious peritonitis. A large volume of hypoechoic peritoneal effusion (*) is seen around a markedly thickened, irregular, hyperechoic mesentery (Fat). The changes to the mesentery were caused by pyogranulomatous vasculitis and steatitis (the same cat as in Figure 10.16). **B:** In another 13-year-old cat with feline infectious peritonitis, the abdominal wall serosa is thickened (2.6 mm), delineated with anechoic peritoneal fluid (F). **C:** Surgical dehiscence following cystotomy in a small dog. Echogenic peritoneal effusion (*) is detected between the spleen (S) and the thickened peritoneum (arrow). **D:** Intestinal perforating foreign body. Transverse image obtained in the right mid-abdomen of a dog with a history of acute vomiting and severe abdominal pain. A triangular hyperechoic interface (long arrow) is in a small intestinal loop, associated with far acoustic shadowing (short arrows), consistent with a foreign body. The peripheral mesenteric and omental fat is hyperechoic and hyperattenuating, and a mass effect was observed on other peripheral structures. These features are typical of steatitis caused by intestinal perforation. **E:** Intestinal corrugation (arrow) secondary to septic peritonitis in a dog with gastric ulcer perforation. The corrugated bowel is surrounded with hyperechoic fat. **F:** Migrating wooden stick in a dog. In this dog that presented for recurrent craniolateral abdominal pain and swelling, a hyperechoic linear foreign body (arrow) casting partial acoustic shadowing was detected originating from the stomach and reaching the subcutaneous tissues.

assess deep organs. In these instances, the abdominal structures appear ill-defined, and their inner architecture cannot be well recognized. An area of mesenteric fat hyperechogenicity is suggestive of inflammation (steatitis/vasculitis) in dogs and cats, and should be thoroughly investigated for a possible nearby source of inflammation, such as intestinal perforation or pancreatitis (Boysen et al. 2003). A ruptured biliary tract with secondary bile peritonitis must also be considered when focal effusion associated with hyperechoic fat is present in the cranial abdomen at the liver hilus (see Chapter 6). Bladder rupture is also typically associated with variable amount of effusion and hyperechoic fat in the caudal abdomen (see Chapters 6 and 11).

Leakage or rupture of the gastrointestinal (GI) tract is one of the most common causes of septic peritonitis in dogs and cats. GI leakage may be caused by post-surgical intestinal dehiscence, GI perforation caused by a penetrating foreign body, GI ulcer (benign or malignant), gastric dilatation and volvulus, intestinal intussusception, intestinal infarction, penetrating abdominal trauma, or iatrogenic cause (Figures 15.7A, 15.8B,D) (Boysen et al. 2003). Inflamed perienteric fat often appears as a mass effect, displacing adjacent structures such as intestinal loops. In addition to the other aforementioned ultrasonographic changes, GI ileus with fluid accumulation is commonly observed. Primary bacterial peritonitis with no identifiable intra-abdominal source of infection or penetrating injury is also described in dogs and cats, generally producing an exudative effusion and similar inflammatory changes (Culp et al. 2009). GI contents such as foreign material or free gas can sometimes be recognized in the peritoneal space. Free gas appears as echogenic foci or lines that are associated with reverberation artifacts, such as comet tails. These lines collect between the non-dependent abdominal wall and intra-abdominal structures, such as the liver, omentum, stomach, or intestine, but they may also be contained in tissues surrounding the GI tract, such as the mesentery (Figure 15.9). When peritoneal effusion is present, gas bubbles can appear as floating echogenic foci. Free gas tends to shift in position with bowel or patient movement.

Pneumoperitoneum can also be caused by abdominal wall trauma, bladder rupture, an extension of pneumothorax, splenic necrosis, and clostridial peritonitis, or it can be idiopathic (Saunders and Tobias 2003). If a large volume of free air is in the peritoneal cavity, ultrasonographic visualization of deep structures may be significantly hampered by reverberation artifacts or shadowing. Because free air can persist for a few weeks after celiotomy, the significance of free air found in dogs or cats after surgery must be interpreted with caution, particularly if other signs of intestinal dehiscence are not present. Similarly, in these post-surgical cases, a small amount of effusion of low echogenicity and mildly hyperechoic fat are often recognized, usually resolving between 3 and

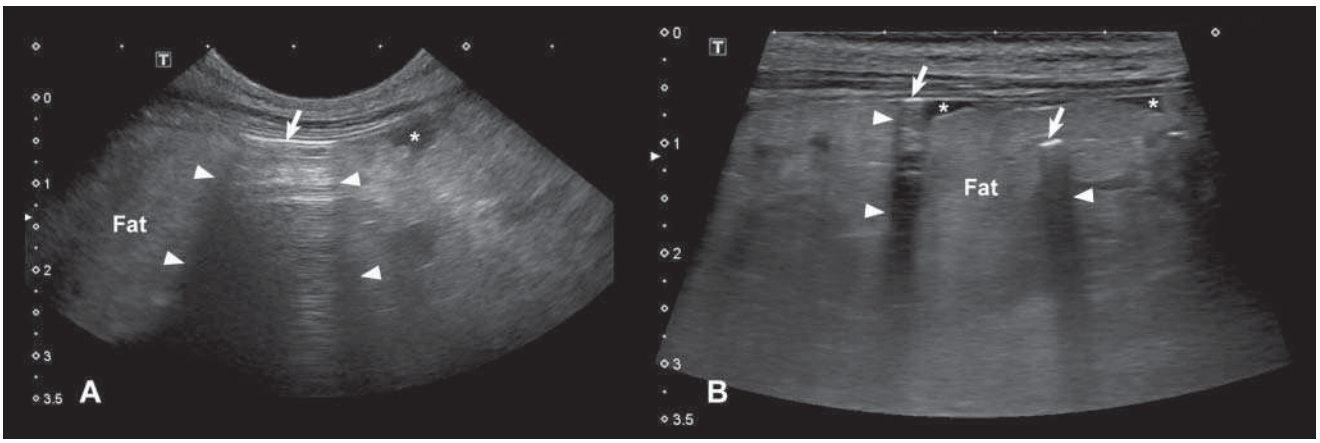


Figure 15.9. Free air in the peritoneal space and mesentery in a dog with intestinal perforation. A: In the cranioventral abdomen, hyperechoic lines are detected between the abdominal wall and omental fat, which correspond with the upper side abdomen of this dog in dorsal recumbency. A combination of distal shadowing and reverberation artifacts, including "comet tails", are present (between arrowheads). These artifacts move during the exam along the inner surface of the abdominal wall, indicating free air. **B:** More caudally, shorter hyperechoic lines consistent with air bubbles (arrows) are seen between the abdominal wall and the mesenteric fat, as well as within the mesentery. A combination of distal shadowing and reverberation artifacts are also present (between arrowheads). A small volume of peritoneal effusion (*) is also detected.

10 days (Matthews et al. 2008). Peritoneocentesis and follow-up examinations may be required to rule out dehiscence.

Omental and mesenteric sterile steatitis has also been recognized in dogs and cats (Komori et al. 2002; Zini et al. 2007; Adamama-Moraitou et al. 2008). Although the etiology of this condition is unknown, predisposing factors could include recent surgery, retained surgical material, prior abdominal trauma, ulcerative disease, autoimmune disease, hypocalcemia, or drugs. Sonographic features include a well-defined hyperechoic mass in the root of the mesentery, displacing intestinal loops (Figure 15.10). Infectious or non-infectious sclerosing encapsulating peritonitis is a rare condition characterized by hyperechoic thickening of the serosal surface and parietal peritoneum with numerous string-like adherences between organs (Adamama-Moraitou et al. 2004).

Peritoneal Abscesses, Granulomas, and Pyogranulomas

Abscess formation can precede or follow the onset of peritonitis. Ultrasonographically, peritoneal abscesses often present as fluid pockets with particles, surrounded by an ill-defined hyperechoic wall and sometimes internal septa or gas foci (Campbell 2009) (Figure 15.11A). The cavitary portion of the abscess is often hypoechoic, and far acoustic enhancement may

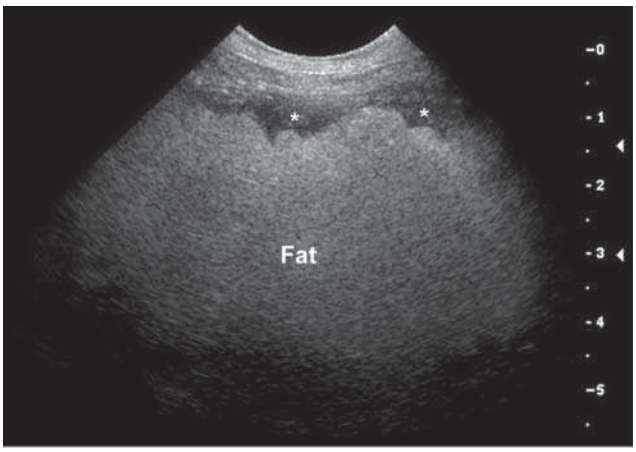


Figure 15.10. Omental or mesenteric steatitis. Longitudinal image of the right abdomen of a dog that had recent surgery for splenic torsion. An irregular, hyperechoic, hyperattenuating mass occupies a large portion of the right abdomen and is surrounded by hypoechoic peritoneal effusion (*). These changes were attributed to omental or mesenteric steatitis, possibly secondary to surgical manipulation. They eventually resolved. The ultrasonographic changes to the fat prevented any visualization of deep abdominal structures.

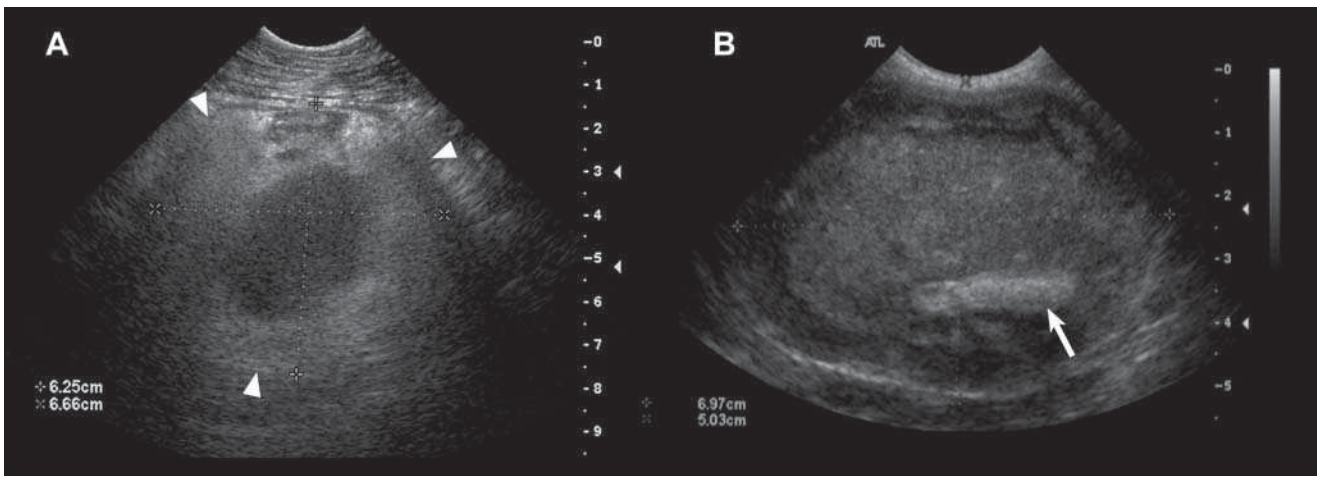


Figure 15.11. Peritoneal abscesses in two dogs. A: Transverse image of the left caudal abdomen of a dog with abdominal pain. An ill-defined hypoechoic area, surrounded by an ill-defined hyperechoic rim (arrows), is present without evidence of organ involvement. A sterile abscess, attached to the omentum and mesentery, was confirmed at surgery. **B**: In another dog with a history of chronic abdominal pain, a 7-cm-long oval mass of mixed echogenicity was detected and confirmed to represent a caseous abscess with vegetal fragments. The abscess presents a hypoechoic wall containing pus and debris of moderate echogenicity, and a hyperechoic structure (arrow) presumably consistent with the caseous portion.

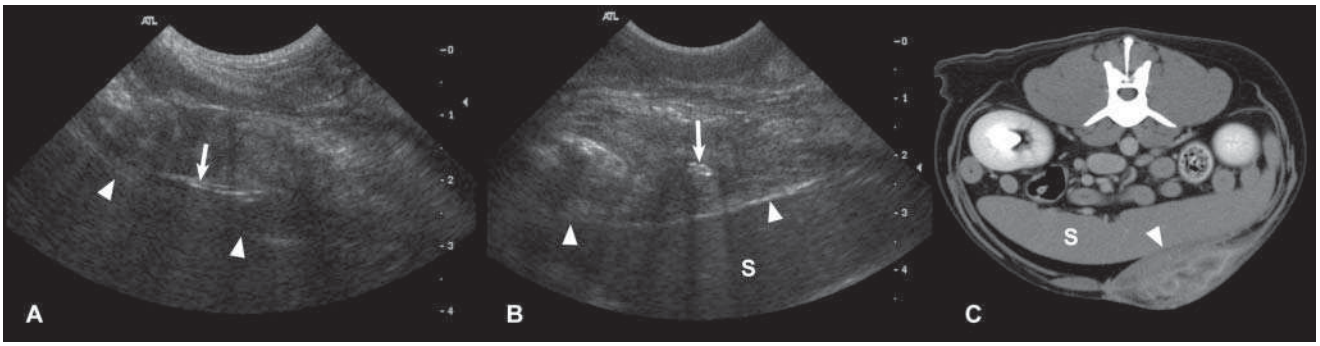


Figure 15.12. Grass awn migration in a dog. Sagittal (**A**) and transverse (**B**) sonographic images of a dog presented for recurrent ventral abdominal swelling. Heterogeneous tissue thickening is seen ventral to the peritoneal surface (arrowheads). In the sagittal plane (**A**), a 3-cm-long, fusiform structure composed of nearly parallel, sharply demarcated hyperechoic lines is detected (arrow). This structure is tubular in the transverse plane (**B**). **C**: This mass of tissue delineated by the peritoneum (arrowhead) was initially interpreted as probable neoplasia with contrast-enhanced computed tomography. Retrospective assessment did not help in identifying the grass awn. Ultrasound was also used to locate the foreign object during surgery.

be recognized unless the cell count is too high, or there is gas with reverberating artifact when gas is present. Conversely, caseous abscesses may be associated with some acoustic shadowing (Figure 15.11B).

Peritoneal granulomas or pyogranulomas are rare in small animals. They can be found with feline infectious peritonitis, mycobacterial or fungal diseases, or caused by foreign bodies, such as retained surgical sponges (Merlo and Lamb 2000; Share and Utroska 2002). Foreign bodies can produce a suppurative granulomatous or pyogranulomatous response of variable size (Figure 15.12). Some foreign bodies, such as wooden sticks or grass awns, can migrate through the abdominal wall or GI and create a sinus tract that can be recognized by their tubular, often tortuous shape and their marked hypoechogenicity in comparison with the surrounding tissues, which appear hyperechoic because of the inflammatory reaction and/or scar tissue (Stander and Kirberger 2011; Penninck and Mitchell 2003). The foreign body itself is not always ultrasonographically visible or associated with signs of peritonitis. Wooden sticks usually appear as linear hyperechoic interfaces, with acoustic shadowing in most cases (Figure 15.8D). However, plant materials chronically embedded in tissues can undergo a degradation that can render these objects less attenuating and therefore less likely to be associated with acoustic shadowing (Staudte et al. 2004). Grass awns appear as spindle-shaped, linear, hyperechoic interfaces measuring 3–4 cm long, with acoustic shadowing less commonly observed than with wood (Staudte et al. 2004; Gnudi et al. 2005) (Figure 15.12). Retained surgical sponges typically appear as a hypoechoic mass with central hyperechoic foci or bands and are associated with other variable signs of peritonitis (Merlo and Lamb 2000) (Figure 15.13), although the sonographic appearance may vary depending on the type of sponge or the presence of a concurrent abscess (Mai et al. 2001).

Nodular Fat Necrosis

Nodular fat necrosis, also referred as Bates body, is a benign and incidental finding in dogs and cats,

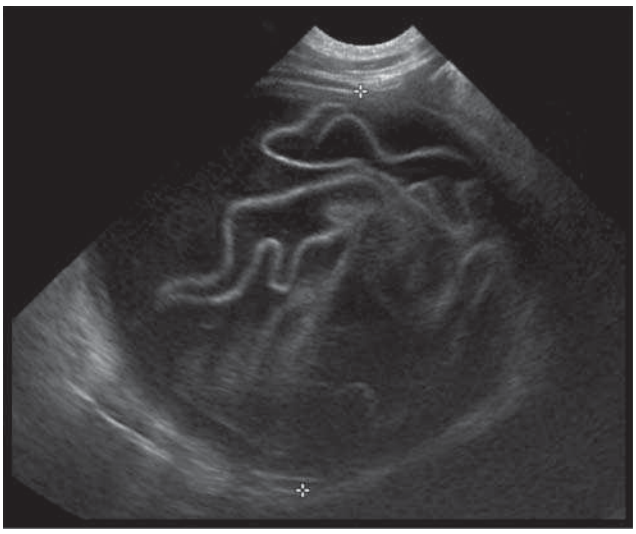


Figure 15.13. Retained surgical sponge in a 7-month-old Mastiff. A rounded mass with an unusual internal pattern made of well demarcated, folded layers is noted. At surgery, this was confirmed to be a gossypiboma.

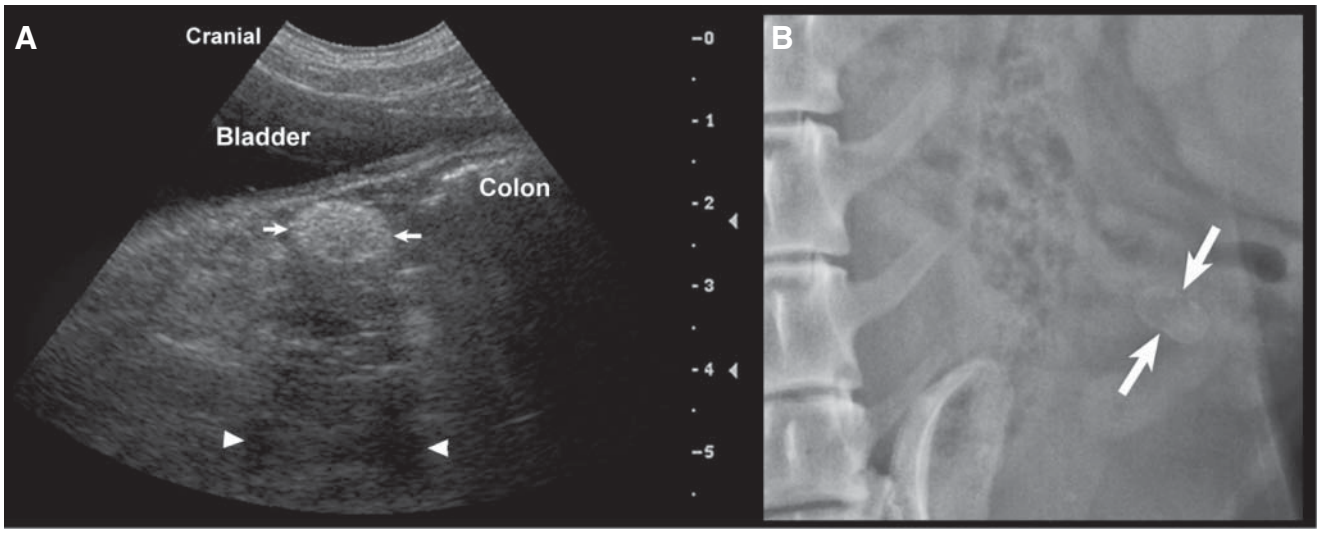


Figure 15.14. **Fat nodular necrosis. A**: Longitudinal image obtained in the caudal abdomen of a dog with chronic renal disease. A well-defined, oval, hyperechoic nodule (arrows) is dorsal to the bladder trigone. Partial acoustic shadowing is noted in the far field (arrowheads), indicating ultrasound-beam hyperattenuation in comparison with adjacent fat. These features are consistent with incidental fat nodular necrosis. **B:** Corresponding radiographic appearance of nodular necrosis (Bates body).

appearing as partially mineralized circular to oval soft-tissue masses in the abdominal fat. With ultrasound, these foci can be recognized as well-defined hyperechoic and hyperattenuating (acoustic shadow) nodules or masses in the abdominal fat, which can be multiple in the same patient (Schwarz et al. 2000) (Figure 15.14). A hypoechoic center may also be observed.

Peritoneal and Retroperitoneal Neoplasia

Peritoneal soft-tissue masses seen with ultrasonography are most often related to abdominal organs, such as the spleen, liver, pancreas, or intestine. Lipomas, infiltrative or not, may also be found within the omentum, mesentery, or other portions of the abdomen (Figure 15.15). These fatty masses are typically hyperechoic and can be hyperattenuating, some with a necrotic center mimicking an abscess (Mayhew and Brockman 2002). Other neoplastic processes, such as lymphoma or mesotheliomas, may infiltrate the omentum or mesentery, which can appear markedly heterogeneous (Figure 15.16).

Widespread dissemination of neoplasia throughout the peritoneum, a condition referred to as carcinomatosis, is more common than primary peritoneal tumors. The term carcinomatosis is used in veterinary medicine to include peritoneal invasion by epithelial, mesenchymal, or hematopoietic tumors (Monteiro and O'Brien 2004), although sarcomatosis and lymphomatosis are often used for peritoneal dissemination sarcomas and lymphomas, respectively. In cats, the most common sites of primary carcinomas associated with carcinomatosis are the liver, pancreas, and intestine (Monteiro and O'Brien 2004). In dogs, peritoneal spread by ruptured hemangiosarcoma probably represents the most common type of carcinomatosis or sarcomatosis (Monteiro and O'Brien 2004). Free peritoneal effusion is expected in most cases of carcinomatosis. The volume and echogenicity of the fluid can vary and may be influenced by a high protein content, concurrent presence of sterile or septic peritonitis, or hemorrhage. Peritoneal effusion contributes to the visibility of nodules attached to the peritoneal surfaces or within the floating omentum or mesentery. Metastatic nodules tend to appear isoechoic to the abdominal wall or hypoechoic to adjacent fat (Monteiro and O'Brien 2004), although their echogenicity, as well as their size and shape, can vary (Figures 15.17). Infiltrated omentum or mesentery can appear focally or diffusely thickened, sometimes described as "omental or mesenteric cakes", or show large masses (Figure 15.17D). Additionally, mineral foci may be observed as hyperechoic foci casting an acoustic shadow.

Soft-tissue sarcomas, especially hemangiosarcoma, can be found in the retroperitoneal space, particularly in dogs (Liptak et al. 2004) (Figure 15.18).

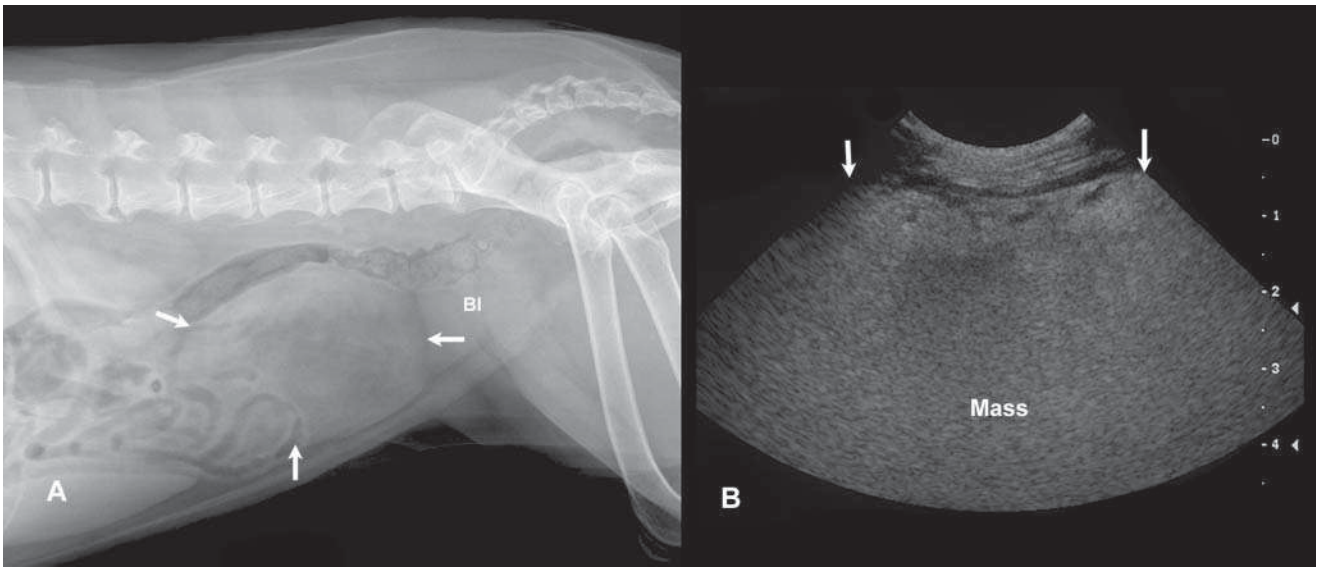


Figure 15.15. **Mesenteric lipoma. A:** Lateral abdominal radiograph of the abdomen of a large-breed dog with a palpable abdominal mass. A mildly inhomogeneous mass (arrows) in the caudal abdomen is deforming the descending colon and bladder (Bl). The mass is of intermediate opacity between fat and soft tissue. **B:** Longitudinal sonographic image of a portion of this mass that contacts the ventral abdominal wall (arrows) and extends beyond the limits of the scanned field of view. This mass is hyperechoic, hyperattenuating, and relatively uniform. A mesenteric lipoma was surgically confirmed.

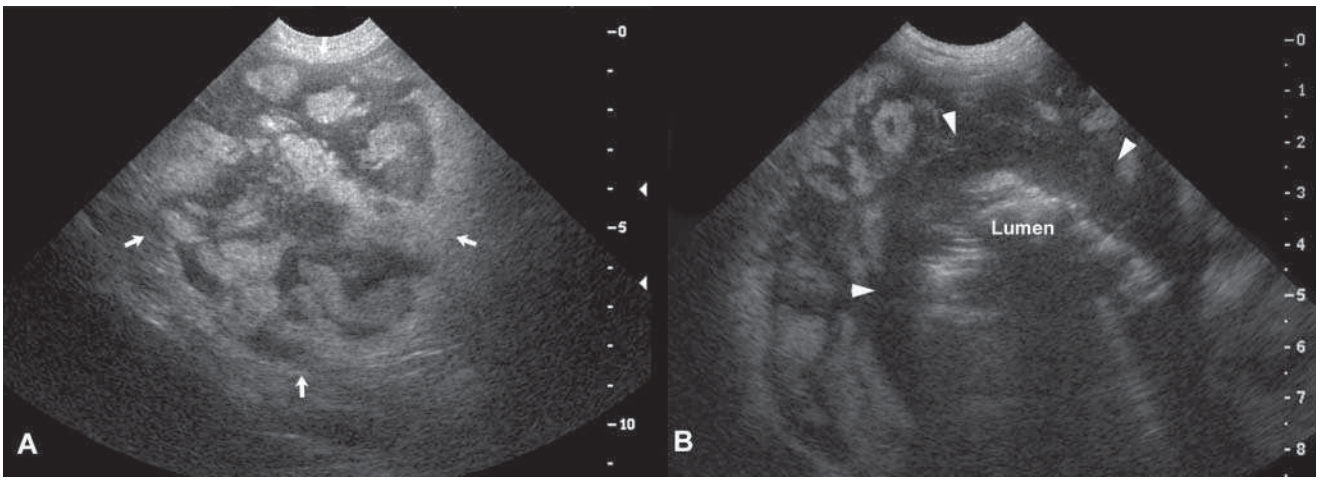


Figure 15.16. **Mesenteric infiltrative mass.** Transverse images obtained in the right caudal abdomen of a dog with intestinal lymphoma. **A:** A large ill-defined mass with mixed echogenicity is observed (arrows), surrounded by hyperechoic fat. **B:** In the central portion of this mass, a segment of small intestine is found with thickened and irregular hypoechoic walls (arrowheads). Mesenteric infiltration by the intestinal lymphoma was confirmed.

Ultrasonography can be useful in differentiating a retroperitoneal mass from retroperitoneal effusion, renomegaly, or renal mass suspected on radiographs. Retroperitoneal soft-tissue masses are often heterogeneous and ill-defined, and may invade major vessels such as the CVC, aorta, or renal vessels. However, it can be difficult to differentiate true large retroperitoneal masses from masses originating from the adrenal glands or urinary system. Alternate imaging such as computed tomography and magnetic resonance imaging may also help in better defining the origin and extent of retroperitoneal masses.

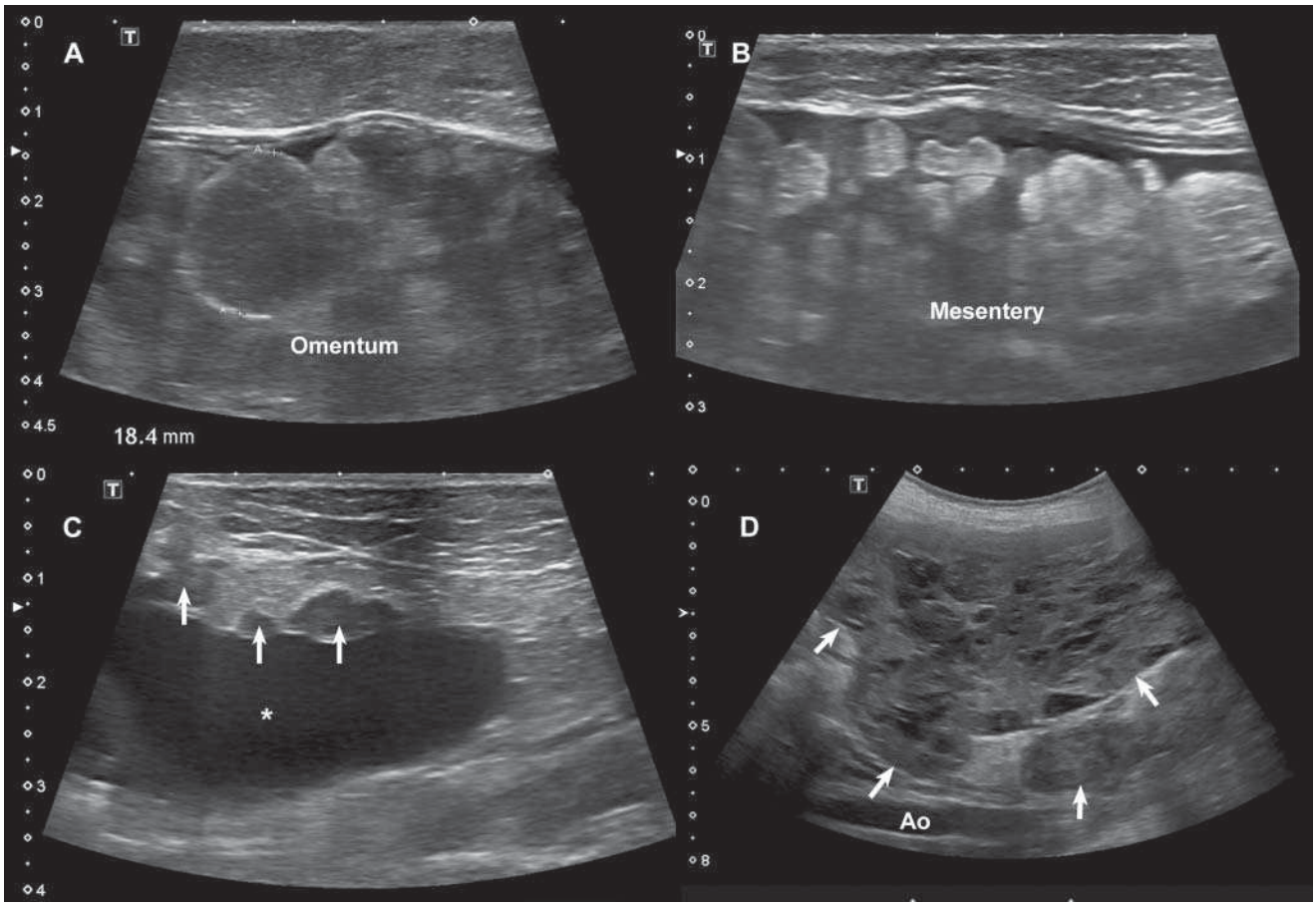


Figure 15.17. Carcinomatosis and sarcomatosis. A, B: In these two cats with pancreatic adenocarcinoma, nodules of variable echogenicity are disseminated in the omentum and mesentery. **C**: In one of these cats (the same one as in **A**), hypoechoic nodules also invade the peritoneal lining and adjacent abdominal wall, delineated dorsally by the peritoneal fluid (*). **D**: In this dog with undifferentiated soft-tissue sarcoma, masses (arrows) were found throughout the abdominal cavity, consistent with sarcomatosis.

Lymphadenopathy

Changes in size, shape, contour, and internal echogenicity and echotexture are important criteria that help to detect lymphadenopathies and differentiate benign from malignant processes.

Enlarged lymph nodes typically become more rounded. Ratios comparing their short (S) and long (L) axes increase more significantly with neoplastic infiltration (Llabrés-Diaz 2004; Nyman et al. 2004). S/L axis ratios > 0.7 are usually predictive of neoplasia (Figure 15.19), as opposed to ratios < 0.7, which more consistently indicate normal or reactive lymph nodes (Figure 15.20) (Nyman and O'Brien 2007). However, this ratio must be used with caution for certain nodes, such as jejunal nodes, which are much longer and therefore associated with a lower S/L axis ratio, even when malignant.

Internal nodal architecture tends to be more affected by neoplastic infiltration (Llabrés-Diaz 2004; Nyman et al. 2004). Reactive lymph nodes tend to present a normal hyperechoic hilus unlike with neoplastic infiltrations (Figure 15.20B). Primary or metastatic neoplastic lymph nodes are commonly hypoechoic (Figures 15.19, 15.21, 15.22), facilitating their identification, although areas of hyperechogenicity may be present if coagulative necrosis, hemorrhage, or mineralization is also present (Figure 15.21). Lymph node heterogeneity has also been significantly associated with malignancy in dogs, but not in cats (Kinns and Mai 2007).

Massively infiltrated lymph nodes can become markedly enlarged and distorted (Figure 15.23). Hypoechoic or anechoic areas may also be seen as the result of liquefaction necrosis or cyst formation (Llabrés-Diaz 2004) (Figures 15.24A, B). Cysts may also

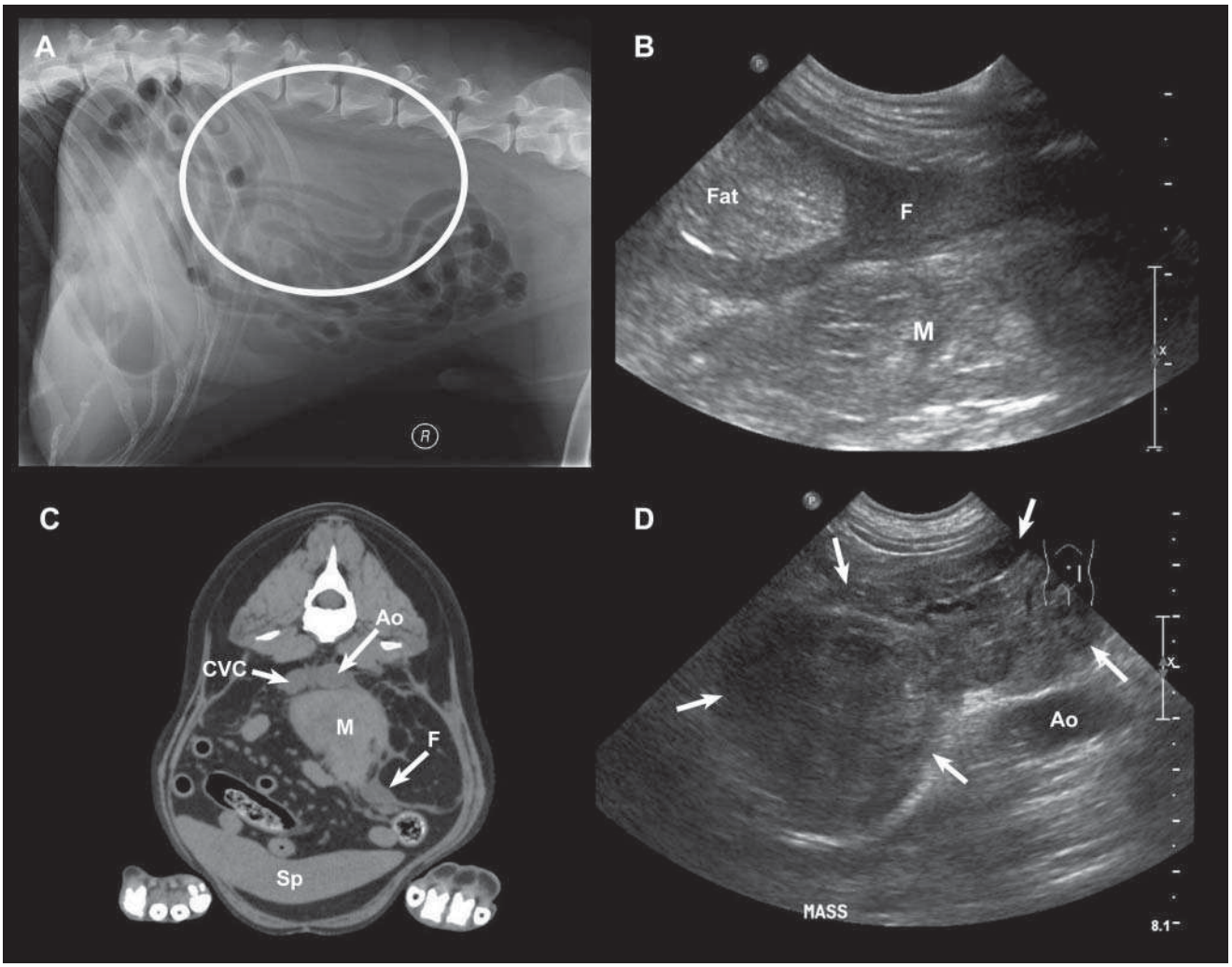


Figure 15.18. **Retroperitoneal hemangiosarcoma in an 11-year-old Labrador cross.** A: On the lateral abdominal radiograph, there is an increased opacity in the retroperitoneal space, and the kidneys are not clearly identified. B: A mild amount of echogenic fluid (F) is present in the retroperitoneal space and represents hemorrhage. M, mass. **C:** On this transverse computed tomography image, the retroperitoneal mass (M) and the adjacent retroperitoneal fluid (F) are seen. Sp, spleen; Ao, aorta; CVC, caudal vena cava. **D:** Longitudinal sonogram of part of the inhomogeneous mass (arrows) invading most of the retroperitoneal space, ventral to the aorta (Ao).

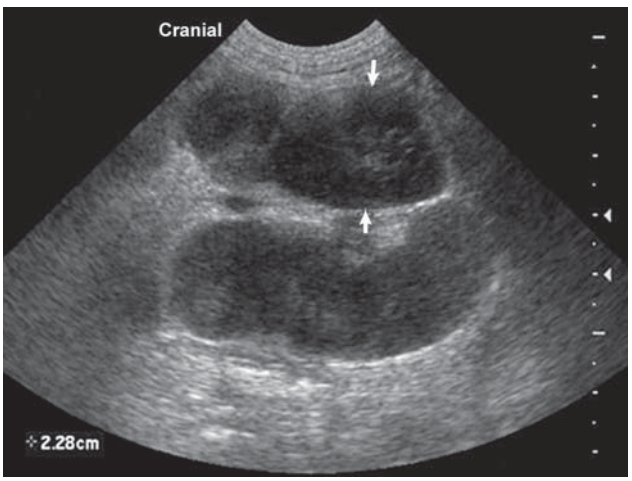


Figure 15.19. **Malignant lymph nodes.** Longitudinal image obtained in the mid-abdomen of a dog with peripheral lymphadenomegaly. Multiple oval to rounded, well-defined, hypoechoic masses are in the root of the mesentery, consistent with enlarged mesenteric lymph nodes (arrows). The ultrasonographic features of these nodes are highly suggestive of malignancy, particularly lymphoma.

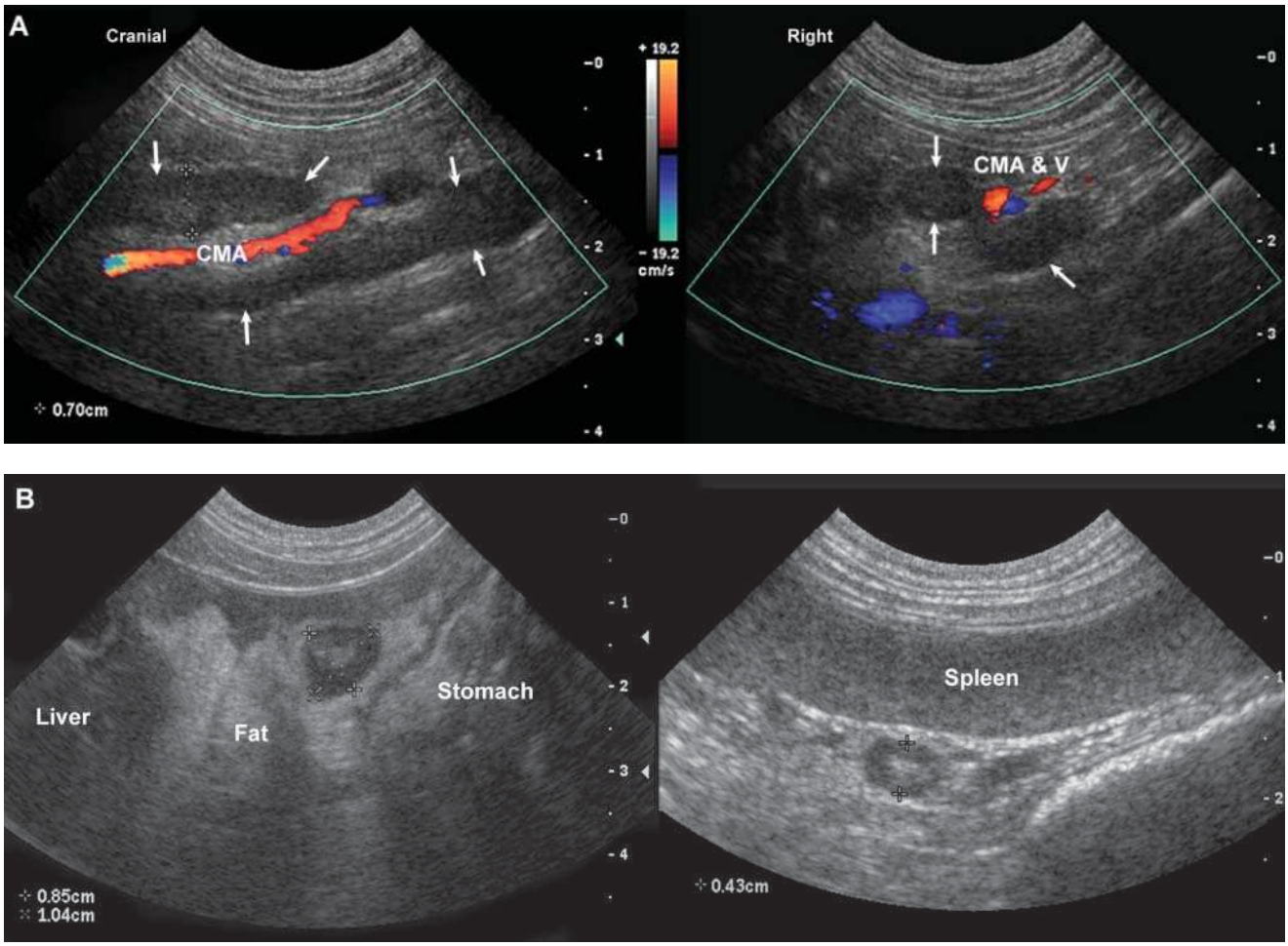


Figure 15.20. **Reactive lymphadenopathy. A:** Longitudinal and transverse sonographic images of the mid-abdomen of a dog with a history of inflammatory bowel disease. The mesenteric lymph nodes (arrows) are more prominent because of reduced echogenicity, particularly peripherally, as well as mild mesenteric fat hyperechogenicity. The cranial mesenteric artery and vein (CMA & V) are noted between these nodes, serving as a useful landmark for their identification. The orientation of the flow in the artery, which is directed toward the probe, is displayed as a red signal on color Doppler. **B:** Ultrasound images of mildly enlarged gastric (left) and splenic (right) lymph nodes in a cat with septic peritonitis. The fat around the gastric lymph node is hyperechoic, contrasting with the hypoechoic lymph node. The hilar portion of these nodes remains hyperechoic.

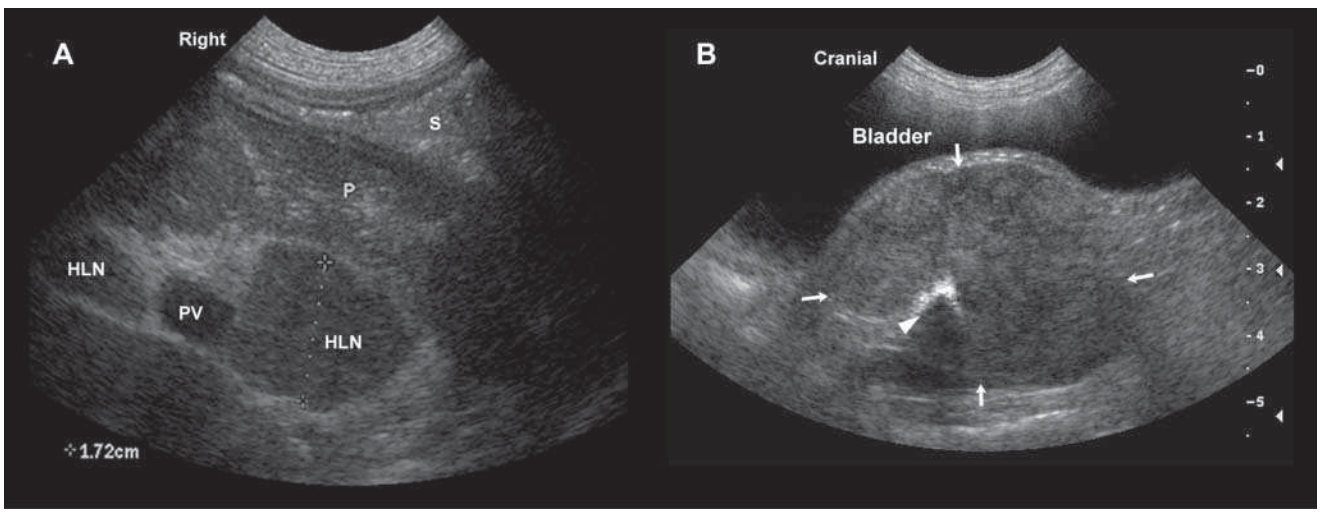


Figure 15.21. **Neoplastic hepatic and sublumbar lymph nodes in two dogs. A**: Transverse sonographic image obtained at the porta hepatis in a dog with pulmonary histiocytic sarcoma. The hepatic lymph nodes (HLNs) are identified adjacent to the portal vein (PV) and dorsal to the body of the pancreas (P) and stomach (S). These nodes are enlarged, irregular, and less echogenic than normal. They remain relatively uniform. Disseminated histiocytic sarcoma was identified in the liver and several abdominal lymph nodes. **B:** Anal sac gland lymphatic metastases. Longitudinal image obtained in the caudal abdomen of a dog with a perianal mass. A large heterogeneous mass (arrows) with well-defined contours is dorsal to the urinary bladder, in the region of the medial iliac lymph nodes. A hyperechoic focus (arrowhead) associated with acoustic shadowing, consistent with mineralization, is in the cranial portion of the mass. Metastatic anal sac carcinoma was diagnosed with cytology on fine-needle aspiration.

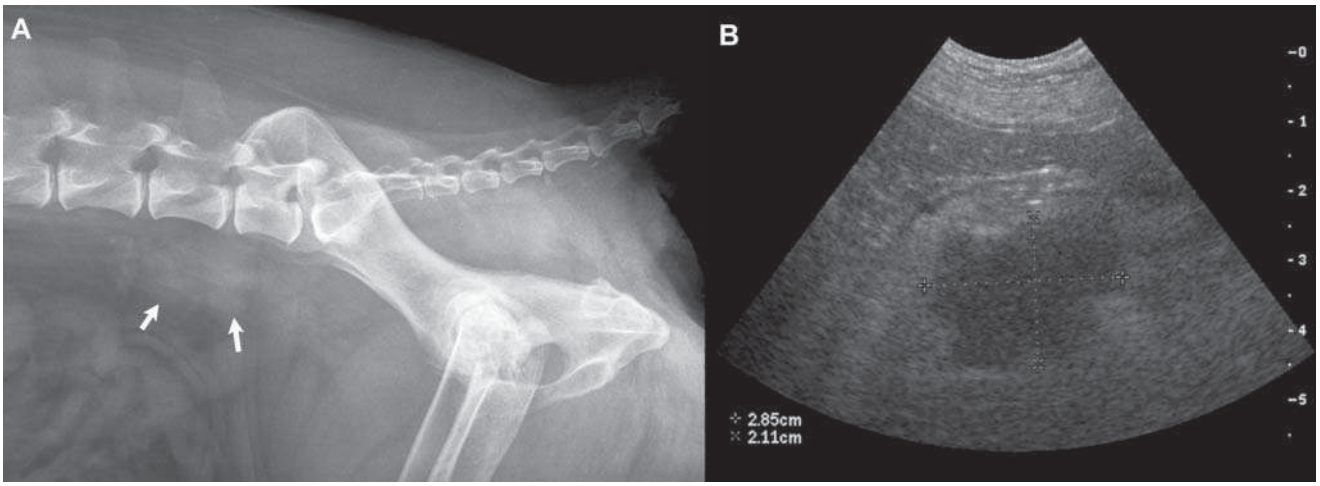


Figure 15.22. Sublumbar lymphadenopathy caused by metastatic carcinoma. A: Lateral abdominal radiograph of a medium-sized breed dog with metastatic carcinoma. An ill-defined, lobulated, soft-tissue opacity (arrows) is ventral to the sixth and seventh lumbar vertebrae. **B:** Longitudinal sonographic image obtained in the same region, lateral to the right iliac artery and vein (not shown). An irregular, hypoechoic mass with surrounding mildly hyperechoic fat, consistent with metastatic disease, is at the location of a medial iliac lymph node.

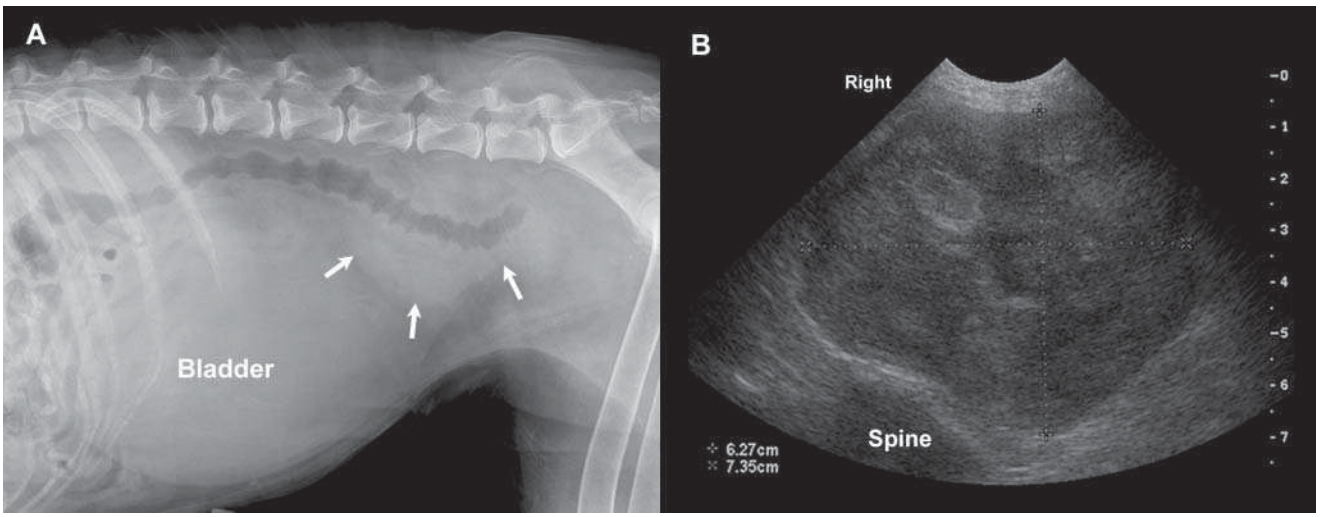


Figure 15.23. Sublumbar lymphadenopathy caused by metastatic sarcoma. A: Lateral abdominal radiograph of a large-breed dog with partial urinary obstruction and signs suggestive of colitis. A somewhat lobulated soft-tissue opacity is in the caudodorsal abdomen and displacing the descending colon ventrally and associated with marked bladder distension. The colon is corrugated. **B:** Transverse sonographic image obtained in the caudal abdomen. The mass suspected on radiographs is large and heterogeneous (between the cursors). Metastatic soft-tissue sarcoma to lymph nodes was highly suspected based on fine-needle aspiration.

form due to the loss of lymphoid tissue in ageing, atrophying lymph nodes (Figure 15.24C) (Elmore 2006). Malignant nodes may also be inflamed or abscessed and can therefore become markedly heterogeneous (Figure 15.24D).

Inflammatory lymph nodes also tend to be ill-defined (Nyman et al. 2004). Non-inflamed malignant nodes are usually sharper in contour and may be associated with acoustic far enhancement. However, some overlap exists in the ultrasonographic appearance of benign and malignant lymph node pathologies. For example, granulomatous diseases, such as pythiosis, histoplasmosis, or feline infectious peritonitis, can mimic neoplasia by producing severe abdominal

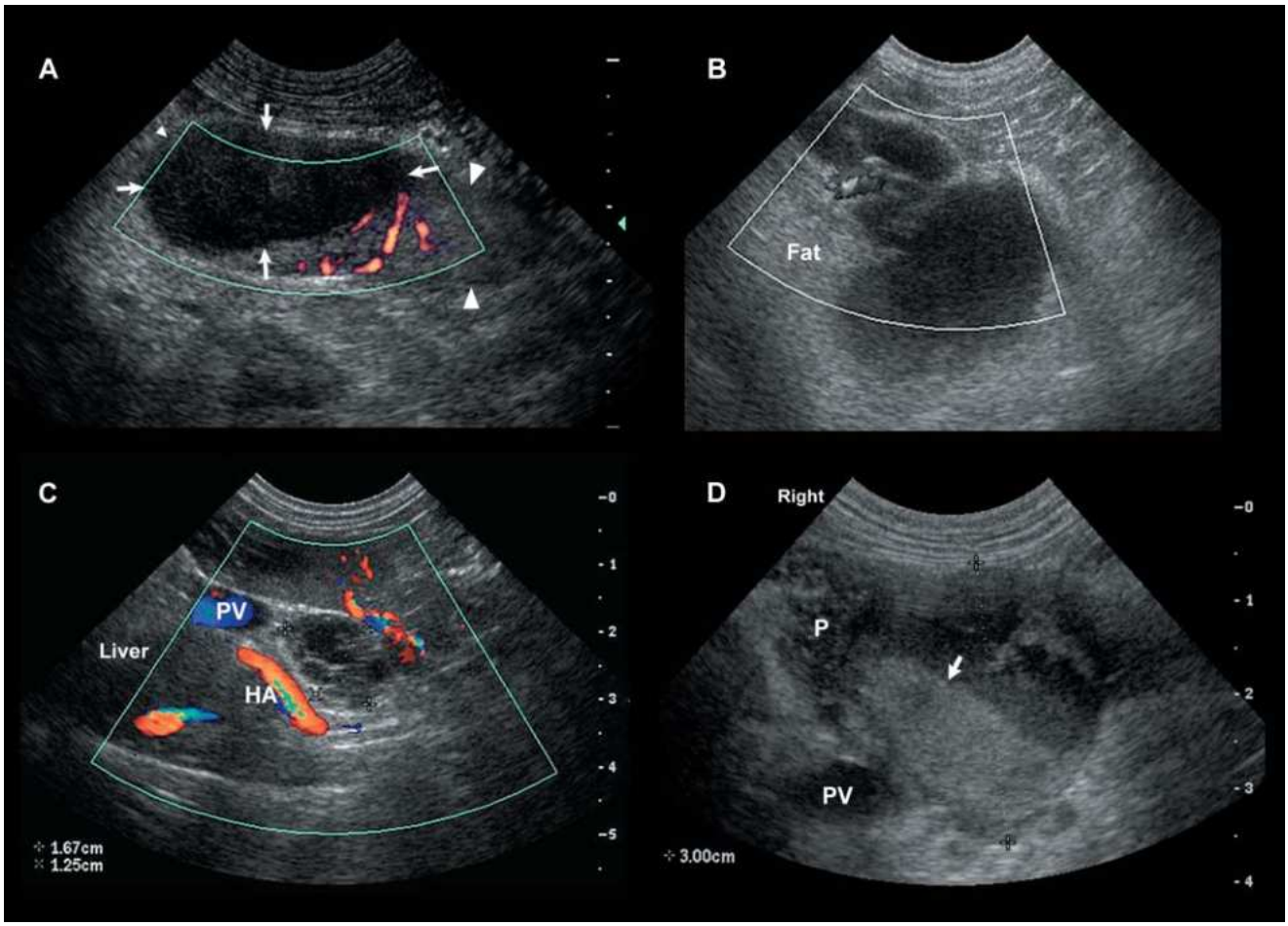


Figure 15.24. **Cavitary lymph nodes. A:** Cystic node with lymphoma. Longitudinal image of a jejunal lymph node in a dog with multicentric lymphoma. A large, oval, anechoic, avascular area (arrows) is in the cranial region of the enlarged lymph node (arrowheads). Fine-needle aspiration confirmed the presence of a fluid-filled cavity or cyst within this portion of the node, and lymphoma was confirmed in the caudal solid portion. **B:** Necrosis. On this ultrasound image, two adjacent jejunal lymph nodes are severely enlarged, nearly anechoic, and ill-defined. The surrounding fat is markedly hyperechoic. Fine-needle aspiration revealed the presence of metastatic carcinoma associated with necrosis and inflammation. **C:** Benign cystic node. Multiple, irregular, well-defined anechoic cysts are incidentally found in the hepatic node of this dog with urinary calculi. HA, hepatic artery; PV, portal vein. **D:** Abscessed malignant node. Transverse image of a severely enlarged hepatic lymph node in a dog with multicentric lymphoma and suspected pancreatitis. Echogenic fluid is in the affected node, with a cellular sediment forming a line (arrow) parallel to the horizontal plane (probe placed obliquely). The adjacent pancreas (P) is hypoechoic and the peripheral fat is mildly hyperechoic.

lymphadenomegaly or even masses (Graham et al. 2000; Lewis and O'Brien 2010) (Figure 15.25).

Color or spectral Doppler, power Doppler, or contrast ultrasonography may increase the accuracy in differentiating benign from malignant nodes (Nyman et al. 2004; Nyman and O'Brien 2007), although Doppler evaluation may be difficult to achieve in some deep lymph nodes (de Swarte et al. 2011). In benign nodes, the blood flow distribution is primarily hilar, whereas it tends to be more peripheral or mixed with malignancies. Resistive and pulsative indices (RI, PI) are also higher in malignant nodes. Cut-off values for discriminating these groups of nodes have not been clearly established in dogs and cats, and vary among types of nodes. For superficial lymph nodes in dogs, RI > 0.65 and PI > 1.45 are reported to indicate malignancy (Nyman et al. 2005), whereas values of 0.67 and 0.76 for RI, and 1.02 and 1.23 for PI, are associated with malignant jejunal and medial iliac lymph nodes, respectively (Prieto et al. 2009).

Because of the overlap of results for each ultrasound criterion, these parameters should be considered

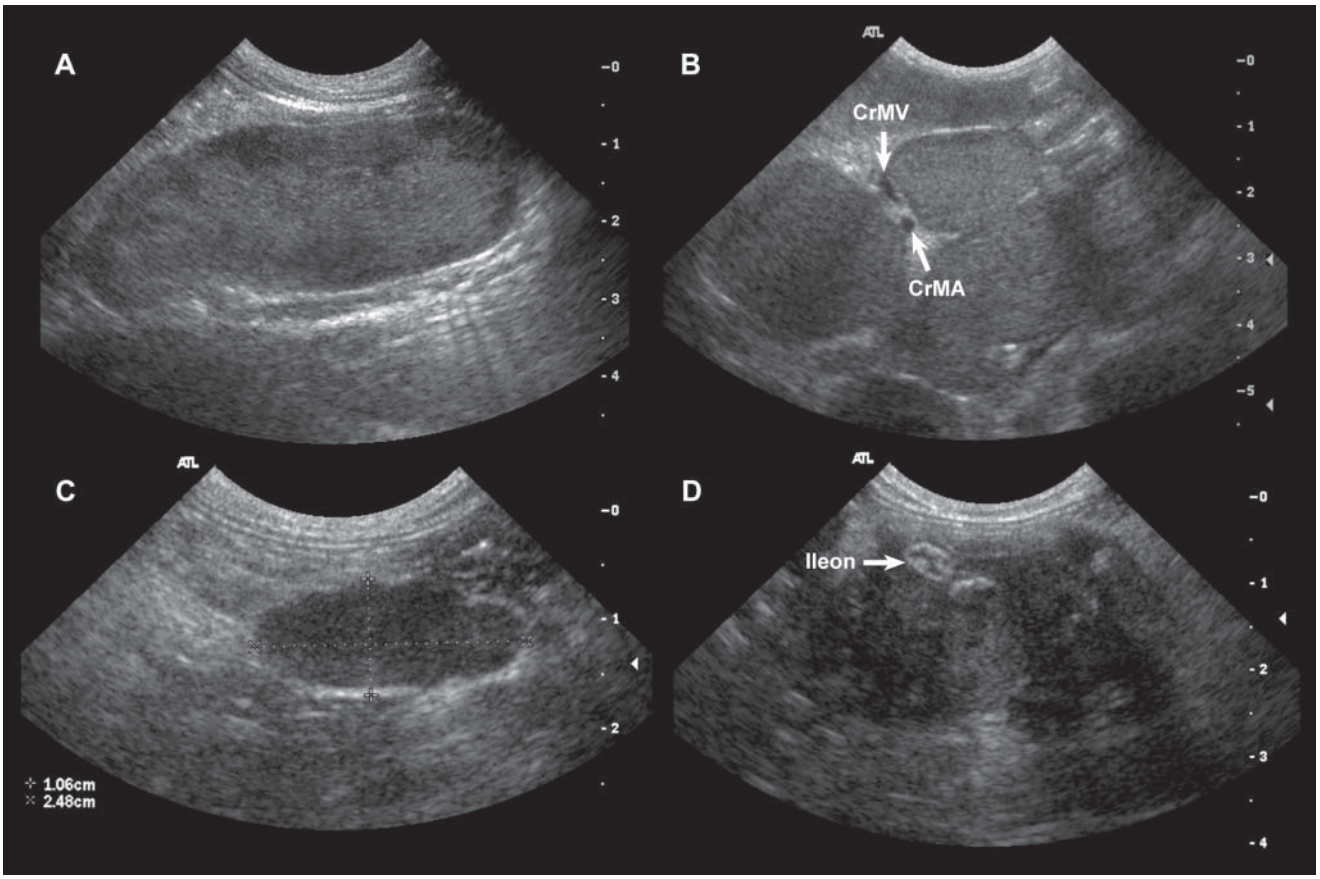


Figure 15.25. Granulomatous lymphadenopathy. A: Longitudinal image obtained in a dog diagnosed with an intestinal mass and a jejunal lymph node that appears moderately enlarged (2 cm thick × 6 cm long). This lymph node is not as hypoechoic as typically seen with lymphoma. Surgery confirmed the presence of severe granulomatous enteritis caused by pythiosis. **B**: Transverse image of the mid-abdomen of another dog with mycobacterosis. The jejunal lymph nodes are markedly enlarged and uniformly hyperechoic, surrounding the cranial mesenteric vein (CrMV) and artery (CrMA). **C, D**: In this cat, one of the jejunal lymph nodes is enlarged and hypoechoic (between cursors in **C**). An irregular and ill-defined hypoechoic mass is seen surrounding the ileocecal junction, infiltrating the intestinal walls and adjacent lymph nodes. These features were initially suspected to indicate neoplasia, but a granulomatous infiltration due to histoplasmosis was confirmed.

conjointly for increased accuracy in the differentiation of malignant and benign lymph nodes. For instance, the combination of irregular contour and perinodal hyperechoic fat is predictive of malignancy in dogs (de Swarte et al. 2011). These studies also highlight the fact that malignant nodes cannot be reliably differentiated from benign nodes with ultrasound, justifying cytologic or histopathologic sampling.

Vascular Thrombosis and Other Vascular Anomalies

In addition to the portal system, thrombi and emboli involving the CVC, aorta, or iliac vessels can be detected with ultrasonography in dogs or cats. A thorough evaluation of all vascular branches, including femoral veins and arteries, is required when pelvic thromboembolic disease is suspected.

The appearance of thrombosis can vary in the acute and chronic phases. Initially, the thrombus may be poorly echogenic and more difficult to identify using standard B-mode. The lack of flow as evaluated with spectral Doppler, color Doppler, or power Doppler, as well as the lack of compressibility (applicable to distal CVC and peripheral veins), are useful signs in the identification of acute thrombosis (Linkins et al. 2006). With time, an echogenic area, usually attached to a portion of the vessel wall, is observed filling a portion of the vascular lumen. The thrombus can appear uniform or heterogeneous because of blood clot lysis and recanalization.

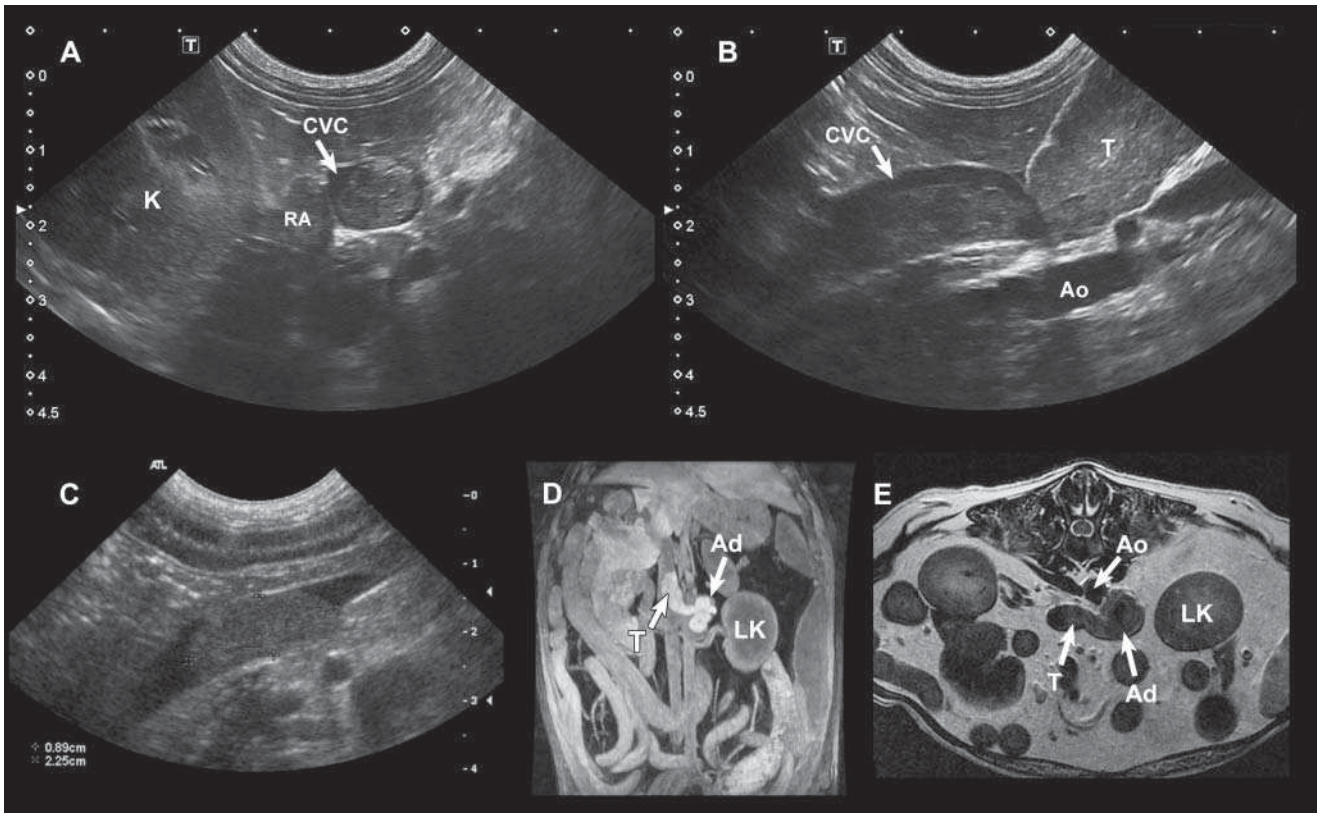


Figure 15.26. **Thrombosis of the caudal vena cava (CVC). A, B:** In this dog with renal adenocarcinoma, there is an echogenic thrombus filling most of the venous (CVC) lumen in transverse **(A)** and longitudinal **(B)** planes. More caudally, it extends into the right renal vein that is markedly distorted by the malignant thrombus (T). K, left kidney; RA, right adrenal gland; Ao, aorta. **C–E:** In another dog with adrenal adenocarcinoma, a thrombus (between cursors) is detected in the CVC. This thrombus is associated with contrast enhancement in the dorsal spoiled gradient recalled echo (SPGR) magnetic resonance (MR) image **(D)** and extends into an abnormal left adrenal (Ad). The transverse T2-weighted MR image (E) shows the connection between the malignant thrombus (T) and the left adrenal (Ad) through the phrenicoabdominal vein, just ventral to the aorta (Ao).

Its differentiation with a proliferative mass may be difficult.

Caudal vena cava thrombosis can be caused by the cranial extension of spontaneous femoral or iliac vein thrombosis, by the invasion of malignant tumors involving adjacent organs, such as the liver, kidneys and adrenal glands, which produces endothelial damage (Figure 15.26) (Finn-Bodner and Hudson 1998; Davis et al. 2012), or by a predisposing hypercoagulable state. External compression of the CVC may cause flow congestion, which represents a predisposing factor for thrombus formation. Chronic obstructions or increases in blood flow resistance in the CVC can lead to peritoneal effusion and collaterals formation (Figure 15.27).

Distal aortic and iliac thromboembolism represents an important complication associated with cardiomyopathies in cats. In dogs, aortic and iliac thromboembolism is usually present because of a disorder associated with a hypercoagulable state, cardiac disease, or neoplasia (Boswood et al. 2000) (Figure 15.28).

Vascular wall mineralization, particularly involving the aorta, can sometimes be observed in dogs and is usually considered an incidental finding. However, aortoiliac thrombosis secondary to severe mineralized arteriosclerosis has been reported in one dog (Drost et al. 1999). Hyperechoic plaque-like lesions can be observed at the inner margin of the wall, with acoustic shadowing if they are large enough (Figure 15.29).

Abdominal vascular malformations other than portosystemic shunts are extremely rare in dogs and cats. The use of ultrasonography in the identification of segmental aplasia of the CVC with azygos continuation has been reported in dogs (Fischetti and Kovak 2008). Acquired abdominal aortic aneurysm/pseudoaneurysm has been described in dogs in association with blood stasis due to fungal infection or migrating grass awn (Llabrés-Diaz et al. 2010; Gerhenson et al. 2011).

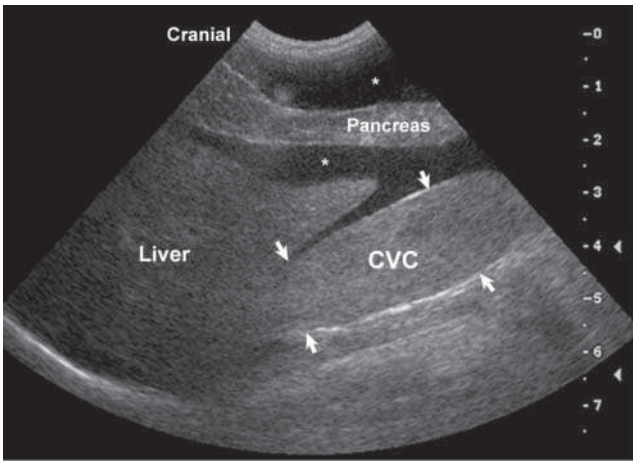


Figure 15.27. Massive caudal vena cava (CVC) thrombosis. Longitudinal image obtained in the right cranial abdomen of a dog with severe ascites (*). The CVC is enlarged, and its lumen is diffusely and uniformly echogenic, consistent with thrombosis. There was no evidence of flow on color or power Doppler. A hepatic mass infiltrating the CVC was suspected.

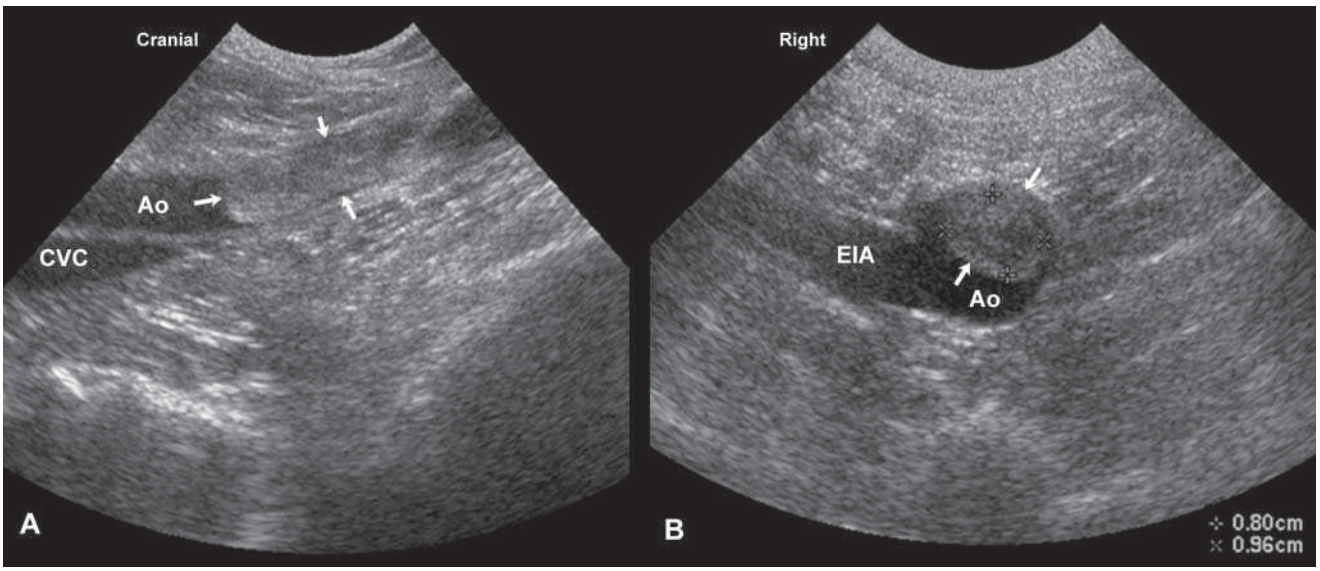


Figure 15.28. Aortic thromboembolism. Longitudinal **(A)** and transverse **(B)** images of the caudal portion of the abdominal aorta (Ao) in a dog with pelvic weakness. An echogenic, relatively well-defined, tubular structure in the aorta is occluding most of its lumen, consistent with a thromboembolus (arrows). The dog had hyperadrenocorticism, which was considered as the probable predisposing factor for thrombus formation. CVC, caudal vena cava; EIA, external iliac artery.

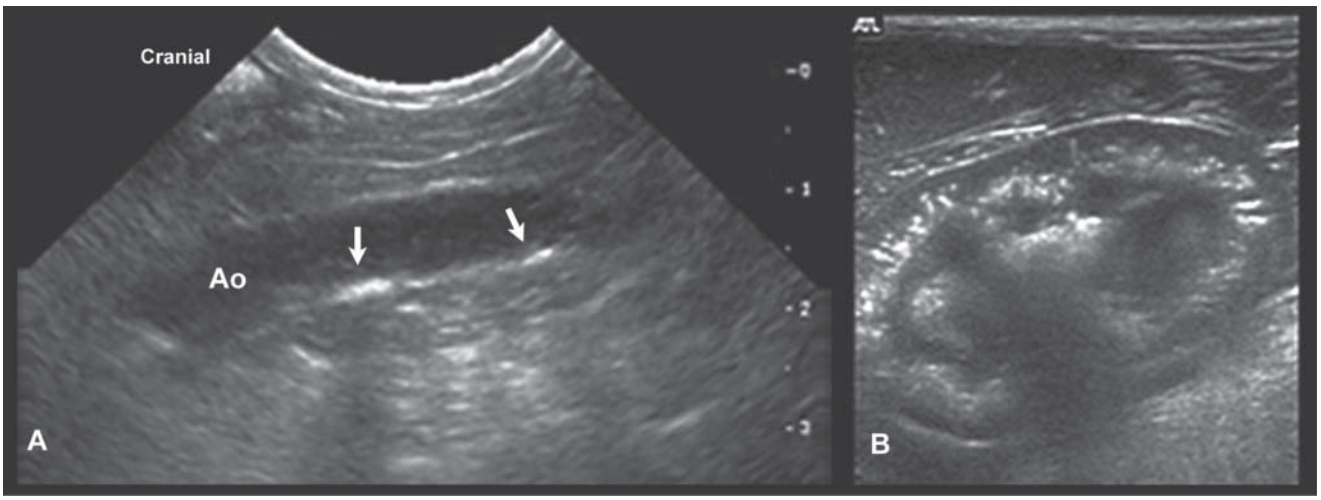


Figure 15.29. Aortic wall mineralization. A: Longitudinal sonographic image of the caudal abdominal aorta of a dog with chronic Cushing's disease. Linear hyperechoic foci (arrows) with acoustic shadowing are along the inner margin of the dorsal aortic (Ao) wall. **B:** Extensively distributed hyperechoic striations and dots are also found in the left kidney, particularly in the cortex, of this dog, which is consistent with nephrocalcinosis. Similar changes were present in the other kidney.

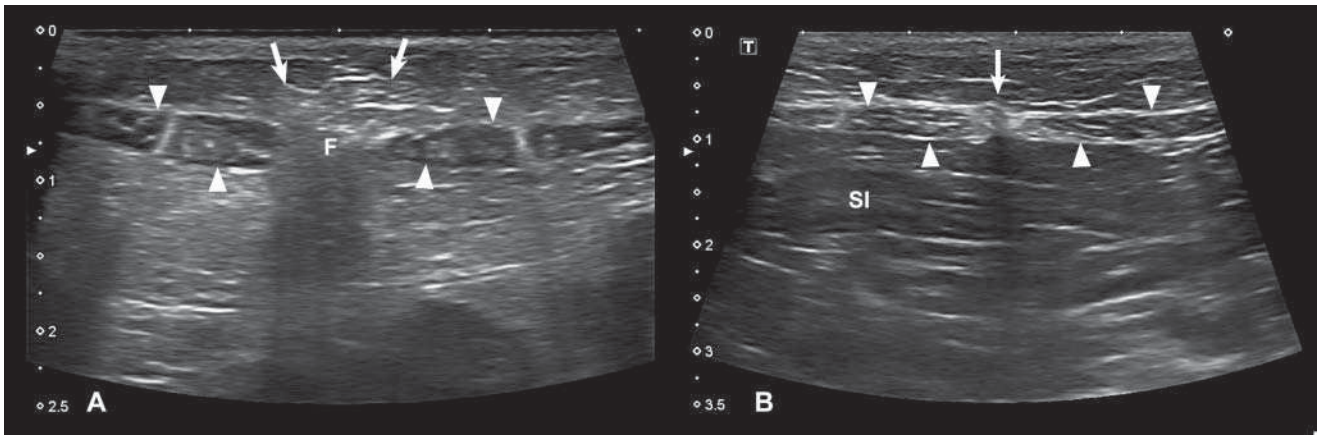


Figure 15.30. **Abdominal wall hernia. A**: In this cat with palpable and reducible mid-abdominal hernia, there is a wall defect on the midline filled with an amorphous tissue of mild echogenicity consistent with fat (F). There is no evidence of bowel loops or other organs in the subcutaneous tissues. The muscular wall on each side (arrowheads) is thicker than normally seen **(B)**, because of reduced tension. **B**: The normal linea alba (white line, arrow) in another cat is associated with distal shadowing. Note the appearance of the abdominal wall musculature (between arrowheads). SI, small intestine.

Abdominal Wall Hernia

Hernias of the abdominal wall may be congenital or traumatic in origin. Congenital hernias are typically located on the midline, with variable amounts of fat herniating through the defect (Figure 15.30). Larger defects can be associated with herniation of visceral structures such as intestines, spleen or bladder. Ultrasound is useful in determining the nature of the herniated tissues.

Interventional Procedures

Fine-needle aspiration of peritoneal fluids is used routinely with ultrasonography in dogs and cats. With minimal practice, even a small amount of fluids can be securely aspirated. Abdominal masses and lymph nodes can also be aspirated or biopsied. Cavitated masses, abscesses, or cysts can also be drained with ultrasound guidance.

Visit our website at **www.SmallAnimalUltrasonography.com** for complementary video clips with annotations and text on:

- Normal abdominal cavity (fat tissues, abdominal wall, peritoneum, vessels and lymph nodes)
- Peritoneal effusions
- Mesenteric mass
- Peritonitis
- Carcinomatosis
- Vascular thrombosis
- Lymphadenopathy
- Abdominal wall hernia

References

Adamama-Moraitou KK, Prassinos NN, Galatos AD, Tontis DK, Rallis TS (2008) Isolated abdominal fat tissue inflammation and necrosis in a cat. J Feline Med Surg 10:192–197.

Adamama-Moraitou KK, Prassinos NN, Patsikas MN, Psychas V, Tsioli B, Rallis TS (2004) Sclerosing encapsulating peritonitis in a dog with leishmaniasis. J Small Anim Pract 45:117–121.

Agthe P, Caine AR, Posch B, Herrtage ME (2009) Ultrasonographic appearance of jejunal lymph nodes in dogs without clinical signs of gastrointestinal disease. Vet Radiol Ultrasound 50:195–200.

Bezuidenhout AJ (2013a) The heart and arteries. In: Evans HE, de Lahunta A, ed. Miller's Anatomy of the Dog, 4th edition. Philadelphia: WB Saunders, pp 428–504.

Bezuidenhout AJ (2013b) Veins. In: Evans HE, de Lahunta A, ed. Miller's Anatomy of the Dog, 4th edition. Philadelphia: WB Saunders, pp. 505–534.

Bezuidenhout AJ (2013c) The lymphatic system. In: Evans HE, de Lahunta A, ed. Miller's Anatomy of the Dog, 4th edition. Philadelphia: WB Saunders, pp. 535–562.

Boswood A, Lamb CR, White RN (2000) Aortic and iliac thrombosis in six dogs. J Small Anim Pract 41:109–114.

Boysen SR, Rozanski EA, Tidwell AS, Holm JL, Shaw, SP, Rush JE (2004) Evaluation of a focused assessment with sonography for trauma protocol to detect free abdominal fluid in dogs involved in motor vehicle accidents. J Am Vet Med Assoc 225:1198–1204.

Boysen SR, Tidwell AS, Penninck D (2003) Ultrasonographic findings in dogs and cats with gastrointestinal perforation. Vet Radiol Ultrasound 44:556–564.

Campbell BG (2009) Primary omental abscessation or omental infarction in four dogs. J Am Anim Hosp Assoc 45:168–175.

Culp WTN, Zeldis TE, Reese MS, Drobatz KJ (2009). Primary bacterial peritonitis in dogs and cats: 24 cases (1990–2006). J Am Vet Med Assoc 234:906–913.

Davis MK, Schochet RA, Wrigley R (2012) Ultrasonographic identification of vascular invasion by adrenal tumors in dogs. Vet Radiol Ultrasound 53: 442–445.

De Swarte M, Alexander K, Rannou B, et al. (2011) Comparison of sonographic features of benign and neoplastic deep lymph nodes in dogs. Vet Radiol Ultrasound 52:451–456.

Drost TW, Bahr RJ, Henry GA, Campbell GA (1999) Aortoiliac thrombus secondary to a mineralized arteriosclerotic lesion. Vet Radiol Ultrasound 40:262–266.

Elmore SA (2006) Histopathology of the lymph nodes. Toxicol Pathol 34:425–454.

Etienne AL, Cavrenne R, Gomeren K, Bolen G, Busoni V (2013) Ultrasonographic characteristics of the cisterna chyli in eight dogs and four cats. Vet Radiol Ultrasound 54(4):398–402.

Finn-Bodner ST, Hudson JA (1998) Abdominal vascular sonography. Vet Clin North Am Small Anim Pract 28:887–943.

Fischetti AJ, Kovak J (2008) Azygous continuation of the caudal vena cava with and without portocaval shunting. Vet Radiol Ultrasound 49:573–576.

Gnudi G, Volta A, Bonazzi M, Gazzola M, Bertoni G (2005) Ultrasonographic features of grass awn migration in the dog. Vet Radiol Ultrasound 46:423–426.

Gershenson RT, Melidone R, Sutherland-Smith J, et al. (2011) Abdominal aortic aneurysm associated with systemic fungal infection in a German shepherd dog. J Am Anim Hosp Assoc 47:45–49.

Graham JP, Newell SM, Roberts GM, Lester NV (2000) Ultrasonographic features of canine gastrointestinal pythiosis, Vet Radiol Ultrasound 41:273–277.

Henley RK, Hager DA, Ackerman N (1989) A comparison of two-dimensional ultrasonography and radiography for the detection of small amounts of free peritoneal fluid in the dog. Vet Radiol Ultrasound 30:121–124.

Kinns J, Mai W (2007) Association between malignancy and sonographic heterogeneity in canine and feline abdominal lymph nodes. Vet Radiol Ultrasound 48:565–569.

Komori S, Nakagaki K, Koyama H, Yamagami T (2002) Idiopathic mesenteric and omental steatitis in a dog. J Am Vet Med Assoc 221:1591–1593.

Krol L, O'Brien R (2012) Ultrasonographic assessment of abdominal lymph nodes in puppies. Vet Radiol Ultrasound 53:455–458.

Lewis KM, O'Brien RT (2010) Abdominal ultrasonographic findings associated with feline infectious peritonitis: A retrospective review of 16 cases. J Am Anim Hosp Assoc 46:152–160.

Linkins LA, Stretton R, Probyn L, Kearon C (2006) Interobserver agreement on ultrasound measurements of residual vein diameter, thrombus echogenicity and Doppler venous flow in patients with previous venous thrombosis. Thromb Res 117:241–247.

Llabrés-Diaz FJ (2004) Ultrasonography of the medial lymph nodes in the dog. Vet Radiol Ultrasound 45:156–165.

Llabrés-Diaz FJ, Brissot H, Ibarrola P (2010) Imaging diagnosis – Celiac artery pseudoaneurysm associated with a migrating grass awn. Vet Radiol Ultrasound 51:508–511.

Mai W, Ledieu D, Venturini L, Fournel C, Fau D, Palazzi X, Magnol JP (2001) Ultrasonographic appearance of intra-abdominal granuloma secondary to retained surgical sponge. Vet Radiol Ultrasound 42:157–160.

Matthews AR, Penninck DG, Webster CR (2008) Postoperative ultrasonographic appearance of uncomplicated enterotomy or enterectomy sites in dogs. Vet Radiol Ultrasound 49:477–83.

Mayer MN, Lawson JA, Silver TI (2010) Sonographic characteristics of presumptively normal canine medial iliac and superficial inguinal lymph nodes. Vet Radiol Ultrasound 51:638–641.

Mayhew PD, Brockman DJ (2002) Body cavity lipomas in six dogs. J Small Anim Pract 43:177–181.

Merlo M, Lamb CR (2000) Radiographic and ultrasonographic features of retained surgical sponge in eight dogs. Vet Radiol Ultrasound 41:279–283.

Monteiro CB, O'Brien RT (2004) A retrospective study on the sonographic findings of abdominal carcinomatosis in 14 cats. Vet Radiol Ultrasound 45:559–564.

Nyman HT, Kristensen AT, Flagstad A, McEvoy FJ (2004) A review of the sonographic assessment of tumor metastases in liver and superficial lymph nodes. Vet Radiol Ultrasound 45:438–448.

Nyman HT, Kristensen AT, Skovgaard IM, et al (2005) Characterization of normal and abnormal canine superficial lymph nodes using gray-scale B-mode, color flow mapping, power, and spectral Doppler ultrasonography: a multivariate study. Vet Radiol Ultrasound 46: 404–410.

Nyman HT, O'Brien RT (2007) The sonographic evaluation of lymph nodes. Clin Tech Small Anim Pract 22:128–137.

Penninck D, Mitchell S (2003) Ultrasonographic detection of ingested and perforating wooden foreign bodies in four dogs. J Am Vet Med Assoc 223:206–209.

Pintar J, Breitschwerdt EB, Hardie EM, Spaulding KA (2003) Acute nontraumatic hemoabdomen in the dog: A retrospective analysis of 39 cases (1987–2001). J Am Anim Hosp Assoc 39:518–522.

Prieto S, Gomez-Ochoa P, de Blas I, et al. (2009) Pathologic correlation of resistive and pulsatility indices in canine abdominal lymph nodes. Vet Radiol Ultrasound 50:525–529.

Pugh CR (1994) Ultrasonographic examination of abdominal lymph nodes in the dog. Vet Radiol Ultrasound 35:110–115.

Saunders WB, Tobias KM (2003) Pneumoperitoneum in dogs and cats: 39 cases (1983–2002). J Am Vet Med Assoc 223:462–468.

Schwarz T, Morandi F, Gnudi G, et al. (2000) Nodular fat necrosis in the feline and canine abdomen. Vet Radiol Ultrasound 41:335–339.

Schreurs E, Vermote K, Barberet V, et al. (2008) Ultrasonographic anatomy of abdominal lymph nodes in the normal cat. Vet Radiol Ultrasound 39:68–72.

Share B, Utroska B (2002) Intra-abdominal botryomycosis in a dog. J Am Vet Med Assoc 220:1025–1027.

Spaulding KA (1993) Sonographic evaluation of peritoneal effusion in small animals. Vet Radiol Ultrasound 34:427–431.

Spaulding KA (1997) A review of sonographic identification of abdominal blood vessels and juxtavascular organs. Vet Radiol Ultrasound 38:4–23.

Stander N, Wagner WM, Goddard A, et al. (2010) Normal canine pediatric gastrointestinal ultrasonography. Vet Radiol Ultrasound 51:75–78.

Stander N, Kirberger RM (2011) Diagnostic imaging of migrating kebab (sosatie) sticks – a review of 8 cases. J S Afr Vet Assoc 82:160–165.

Staudte KL, Hopper BJ, Gibson NR, Read RA (2004) Use of ultrasonography to facilitate surgical removal of non-enteric foreign bodies in 17 dogs. J Small Anim Pract 45:395–400.

Szatmari V, Sotonyi P, Voros K (2001) Normal duplex Doppler waveforms of major abdominal blood vessels in dogs: A review. Vet Radiol Ultrasound 42:93–107.

Zini E, Hauser B, Ossent P, et al. (2007) Pansteatitis and severe hypocalcaemia in a cat. J Feline Med Surg 9: 168–171.

CHAPTER SIXTEEN

Clinical Applications of Contrast Ultrasound

Robert O'Brien[1] and Gabriela Seiler[2]

[1] *College of Veterinary Medicine, Section of Radiology, University of Illinois, Urbana, IL, USA*
[2] *College of Veterinary Medicine, North Carolina State University, Raleigh, NC, USA*

Procedure and Scanning Technique

In preparation of a contrast-enhanced ultrasound (CEUS) examination, intravenous access should be provided for contrast medium injections. As several injections are often necessary, an indwelling catheter is advantageous. A T-port or three-way stopcock allows for easy contrast medium injection immediately followed by a saline flush (Figure 16.1). All contrast media should be administered as close to the vein as possible to minimize destruction within a non-biological environment and adherence of the bubbles to the tubing walls. Sedation is usually not necessary, but may be advised if the patient is fractious or panting excessively, as motion will hinder thorough examination of the vascular dynamic of contrast medium inflow.

Once the patient and contrast agent are prepared, the organ or lesion of interest is identified using grayscale ultrasound imaging. The settings of the ultrasound system are then changed to CEUS imaging. Prior to contrast medium injection the image is essentially devoid of signal as the grayscale image is subtracted. Most systems will allow for a dual screen where the grayscale image is simultaneously presented for anatomic reference (Figure 16.2).

Contrast medium is injected as a bolus, followed by a saline flush. If available on the ultrasound system, a counter can be started at the time of injection for future reference about timing of contrast material inflow and peak enhancement. The contrast study should always be recorded on video clips rather than still images, as the timing and dynamics of contrast medium inflow provide essential information, and it can be available for review later on.

Dosages are quite small, depending on the medium used, ranging from 0.1 to 1.0 mL. Therefore, all contrast administration should also be immediately followed by sterile saline, to push any contrast within the port or catheter into the patient. Inconsistently, the first injection results in disappointing signal strength, whilst subsequent injections, using the same dose, have much better contrast enhancement. Although the exact cause is indeterminate, it is assumed that the first injection "loads" adherence sites in the port, catheter or vessel walls throughout the body (bubbles are a bit sticky), allowing the bulk of the subsequent injections to arrive at the imaged areas of interest.

Perfusion imaging is the mainstay of contrast ultrasound imaging. The "perfusion pattern" is often used to differentiate normal from lesion, or malignant from benign. Different organs require different techniques and will be explained in subsequent sections. Recent research has indicated that prolonged infusion of contrast may provide diagnostic benefits and, at least one manufacturer (Bracco Diagnostics, Cranbury, NJ), makes an infusion pump specific for contrast medium injection.

Contrast Media and Software

The most commonly available ultrasound contrast media include Definity (Lantheus Medical Imaging,

Atlas of Small Animal Ultrasonography, Second Edition. Edited by Dominique Penninck and Marc-André d'Anjou.
© 2015 John Wiley & Sons, Inc. Published 2015 by John Wiley & Sons, Inc.
Companion website: www.SmallAnimalUltrasonography.com



Figure 16.1. Patient prepared for contrast-enhanced ultrasound imaging with an indwelling catheter and attached T-port. A saline flush is already attached to the extension set. The contrast medium is ready to be injected as close as possible to the patient's vein.

North Billerica, MA), Sonovue (Bracco Imaging, Monroe Township, NJ) and Sonozoid (Daiichi-Sankyo, Tokyo, Japan). Each has particular preparation and administration guidelines established by the manufacturer that should be tightly followed. Definity should be "shaken" with the specific vial mix unit provided by the manufacturer. Sonovue and Sonozoid are prepared by addition of sterile saline into the ported vial and hand-shaken. All these media can be subsequently hand-shaken to redistribute the bubbles within the saline carrier. Definity should not be agitated in the vial mix unit after initial preparation. All contrast media are listed in the package insert as single-use vials. Unpublished data by the authors indicate that prepared Definity can be stored for at least 1 month with little degradation of bubble integrity. Sonovue is composed of more fragile bubbles and can be stored for up to 2 weeks. Both media should be refrigerated during storage and hand-shaken immediately prior to administration.

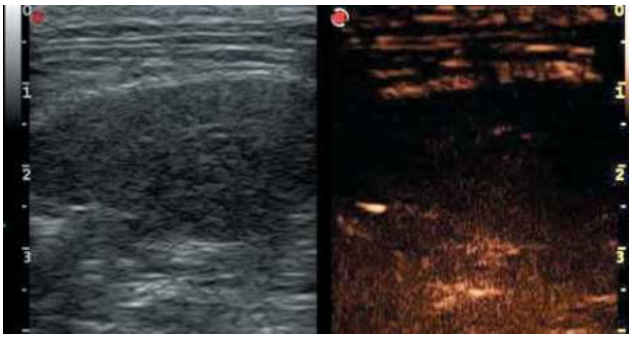


Figure 16.2. Grayscale (left) and contrast ultrasound (right) images of the liver of a dog prior to contrast medium injection. The grayscale information is removed on the contrast ultrasound image; side-by-side comparison with the grayscale image available on most ultrasound systems can help the ultrasonographer to keep an area of interested within the scan field.

Ultrasound contrast media are essentially "bubbles" composed of two components: an inert fluorocarbon gas surrounded by a lipoprotein shell (Ohlerth and O'Brien 2007). These bubbles are easily distortable and destroyable. The distortability feature allows the compression and rarefaction components of incident sound waves to decrease and increase the diameter of the bubbles. With very low-energy incident sound, the bubbles change size in a linear fashion, the bubbles increasing and decreasing in size in a sinusoidal pattern directly proportional to the ambient pressure. However, with increased incident sound energy, the bubbles act in a non-linear fashion, spending more time in expansion than in compression. A frequency analysis of the signal being transmitted by bubbles at this energy level reveals the incident sound frequency (e.g., 3 MHz, first harmonic) and additional sound signals at multiples of the incident (e.g., 6 MHz, second harmonic). With incident sound of even higher-energy, bubbles are destroyed ("popped"), releasing a large amount of incident and harmonic frequency sound energies. Additionally, the use of contrast medium enhances color or power Doppler signals, although the inflow rate must be quite high to maintain this improved Doppler signal with continuous imaging. This usually results in characterization of at least one generation of smaller vessels or seeing a vessel not seen without contrast-enhanced Doppler.

Although all ultrasound contrast media are composed of a spectrum of bubble sizes, the predominant size is of a diameter that allows maximum signal when used with a relatively low-frequency transducer. This is convenient when imaging large breed dogs, especially for liver nodules, but less optimal for smaller

patients or more superficial organs where the spatial resolution of a higher-frequency transducer would be desired. As there are fewer bubbles to resonate at higher frequency, the signal-to-noise ratio decreases as the incident sound frequency increases. This will be a technological challenge until new contrast media with higher resonating frequencies become commercially available.

Ultrasound contrast media, unlike iodinated and gadolinium agents, are strictly vascular agents, without any interstitial component. Contrast effects are the visualization of these bubbles against a black background, generally indicating both large and small vessels. Unlike Doppler, contrast ultrasound is the assessment of perfusion – essentially to the level of the smallest capillaries in an organ or lesion. Sonozoid also has the property of being imaged after incorporation into tissue macrophages. This allows delayed tissue imaging of the liver and spleen, after the blood pool of contrast media has been eliminated from the body. Normal elimination of the inert gas is in the lungs, and the lipoprotein shell is excreted in the bile. Duration of the contrast enhancement is dependent on the medium used and the imaging characteristics being applied. Typically, contrast ultrasound scans last up to 2 minutes. Multiple injections are often necessary to image multiple lesions or organs. Multiple injections are not associated with increased risk of side effects (Seiler et al. 2013).

Unlike most forms of imaging contrast media, ultrasound contrast media are inherently fragile, whereas barium, iodinated compounds and gadolinium are stable chemical compounds. Microbubbles are easily destroyed by high-energy sound, including typical gray-scale energies and all Doppler signals. Contrast medium can also be destroyed through mishandling, such as an overly fast an injection through small-gauge needles, improper compliance with manufacturer preparation guidelines, or too high an incident energy (usually indicated by the mechanical index on the ultrasound machine) during contrast imaging. Imagers should always be cognizant of the fragile nature of contrast media and strive to maintain integrity of these bubbles throughout all storage, preparation and administrations phases.

Safety

The risk of adverse effects with commercial ultrasound contrast media is quite low. In a study evaluating the risk in dogs and cats administered either Sonovue or Definity, the incidence was 1% in dogs and 0% in cats (Seiler et al. 2013). The observed effects in dogs were vomiting and collapse (one dog each), and the exact causality of the effect was loosely coincidental in each case. These data suggest a very high safety margin of these two agents in dogs and cats. Contrast ultrasound had no significant effect on renal function in normal cats (Leinonen et al. 2011). Anaphylactoid reactions have been reported in two dogs administered a commercial product containing human albumin (Optison, Mallinckrodt, Inc., CA, USA) (Yamaya et al. 2004). This product should be avoided in veterinary medicine, especially given the availability of safer products (O'Brien and Holmes 2007). Known contraindications of all contrast media in human patients are pulmonary hypertension, ventricular cardiac arrhythmias, and congestive heart failure (Claudon et al. 2008). These may also be clinical contraindications in veterinary medicine, although this has not been investigated.

Clinical Applications in Small Animals

Liver

In the liver, contrast medium inflow will first be observed in the hepatic arteries, typically about 10 seconds after peripheral venous contrast medium injection. Peak enhancement is reached after about 20–30 seconds, after contrast medium has distributed throughout the portal venous system (Figure 16.3). This is followed by uniform perfusion in dogs (Ziegler et al. 2003) and cats (Leinonen et al. 2010a).

Benign liver lesions typically enhance to a similar degree as the surrounding liver parenchyma at peak enhancement, whereas neoplastic lesions lack the portal venous blood supply and remain hypoperfused at peak enhancement (Figure 16.4).

The most relevant data for the use of contrast ultrasound in a clinical setting has been from studies on liver nodules. Of particular note is the accuracy of contrast ultrasound to differentiate malignant from benign nodules. In a study of 32 dogs with liver nodules, contrast ultrasound had 97% accuracy in predicting which nodules would be malignant (O'Brien et al. 2004). The only false positive was a large (>3 cm) benign hepatoma. Contrast ultrasound also may improve sensitivity for smaller nodules, as indicated by a study in which contrast ultrasound detected small (3–5 mm diameter) hemangiosarcoma nodules in the liver of dogs that were unrecognized on grayscale imaging (O'Brien 2007). In a study evaluating primary splenic masses and concurrent liver nodules, contrast ultrasound was 100% accurate in

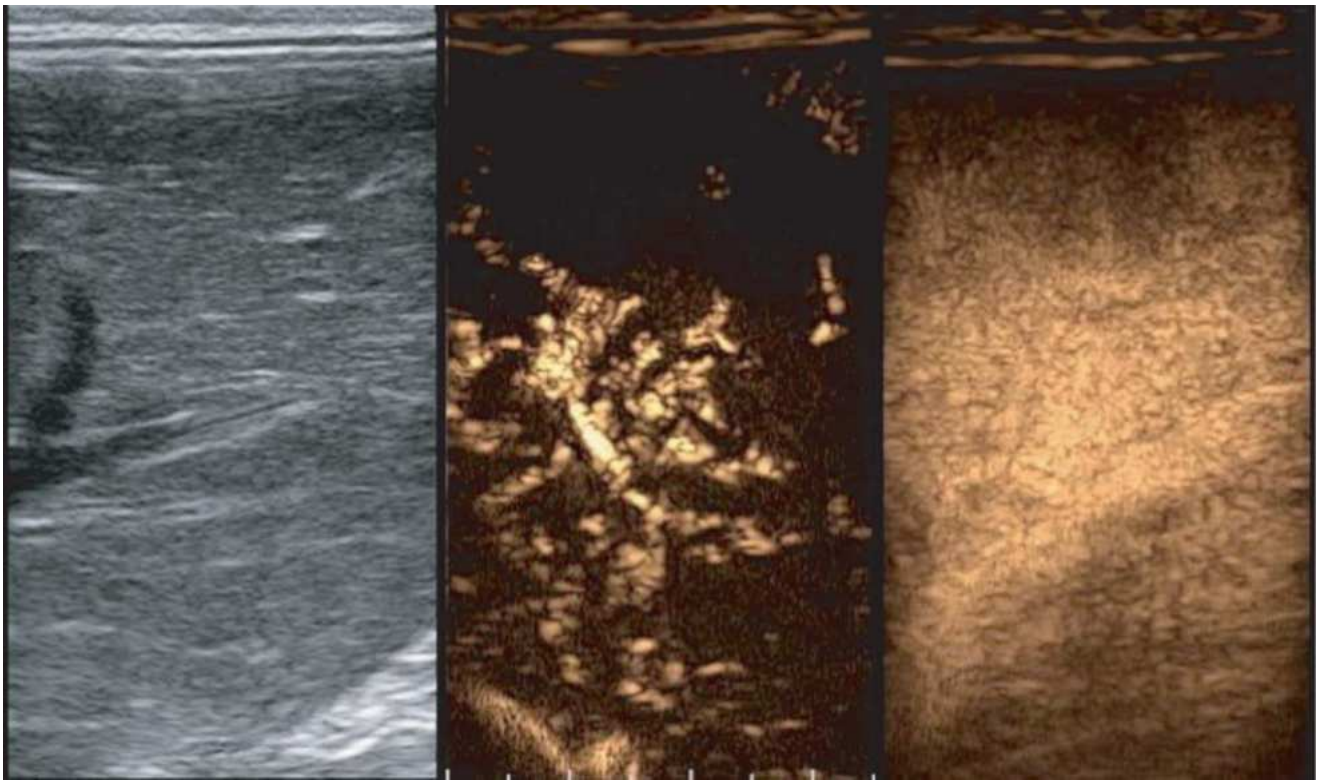


Figure 16.3. Grayscale image (left), arterial phase (middle) and portal venous phase (right) contrast-enhanced images of the liver of a normal dog. The contrast medium is displayed in yellow and outlines the architecture of the hepatic arterial vasculature in the arterial phase. In the portal venous phase, the liver parenchyma uniformly enhances.

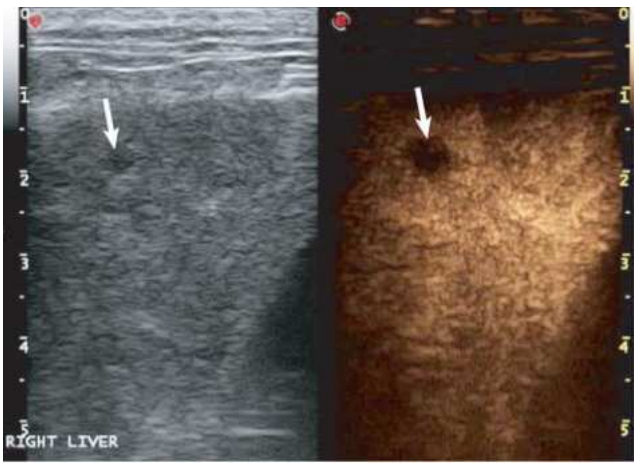


Figure 16.4. Grayscale (left) and contrast-enhanced ultrasound (right) images of the liver of a 10-year-old Golden Retriever with a splenic mass and hemoabdomen. A hypoechoic nodule (arrow) is faintly visible in the periphery of the liver on the grayscale image. During peak enhancement of the liver parenchyma, this nodule (arrow) remains hypoechoic, indicating hypoperfusion, and is consistent with a malignant lesion. Metastatic hemangiosarcoma was confirmed with histopathology.

differentiating between malignant and benign nodules (Ivancic et al. 2009).

A second aspect of contrast ultrasound imaging in both liver and spleen is referred to as "delayed," "late," "parenchymal," or "Kupffer" imaging. This form of imaging makes use of the reticuloendothelial system's ability to attach or phagocytize foreign intravascular lesions. Sonozoid is a contrast medium able to make use of this aspect of the normal liver and spleen (Kanemoto et al. 2008; Nakamura et al. 2009). The assumption is that benign nodules share the same reticuloendothelial cells, whereas malignant nodules would not have this tissue macrophage population. Delayed imaging with Sonozoid was also highly accurate in differentiating between benign and malignant nodules in 25 and 27 dogs, respectively, imaged in delayed phase imaging. In these studies, a hypoperfused pattern in the nodule, as compared with the hyperperfused surrounding normal liver, was associated with malignancy (Kanemoto et al. 2009; Nakamura et al. 2010). However, delayed imaging, whilst of possible imaging convenience, did not improve accuracy beyond the perfusion phase results in the same dogs.

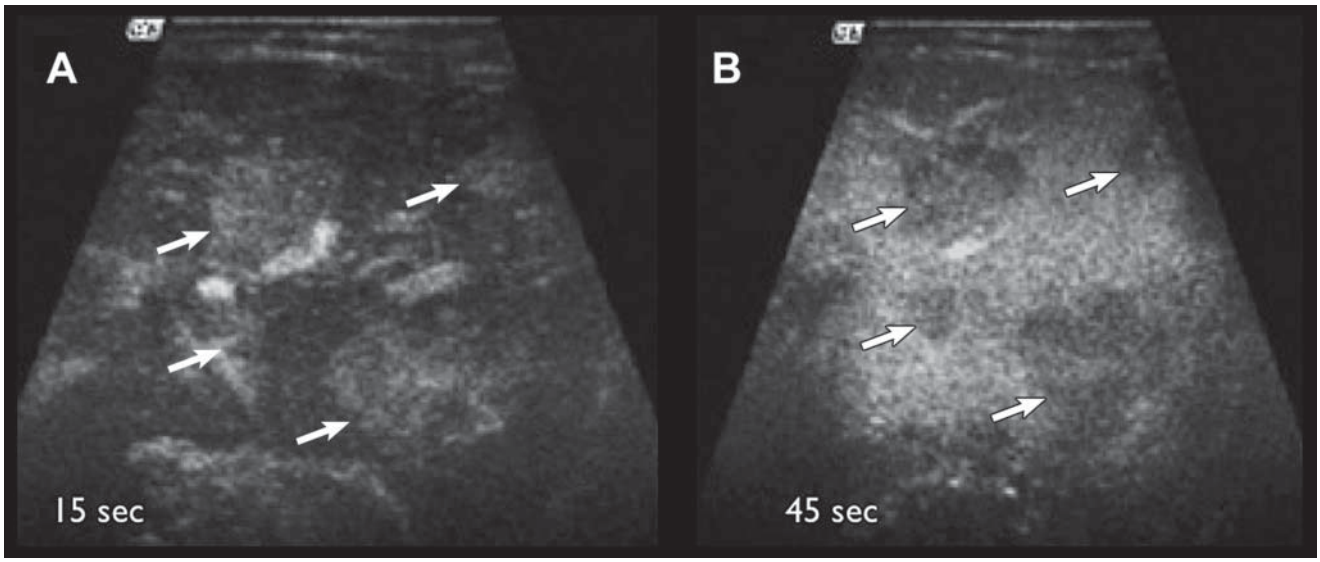


Figure 16.5. Contrast enhancement of malignant lymphoma nodules in the liver of a dog. Note the "early-in, early-out wash in" pattern seen with most carcinoma and round-cell metastatic nodules in the liver. There is hyperperfusion of the nodules (arrows) at 15 sec (**A**) and relative hypoperfusion of the nodule compared with the normal surrounding liver at peak normal liver perfusion (45 sec, **B**).

Two patterns may be seen with malignancy, depending on cell type. The first and most common pattern in human metastatic carcinoma, and seen with most carcinoma, round-cell neoplasia and a few sarcoma nodules in dogs, is the "early in, early out pattern" (Figure 16.5). With this pattern, the lesion's enhancement is the same as the normal liver in the initial vascular phase, but it becomes hypoechoic to the rest of the liver during the normal peak liver enhancement. In human patients, the contrast pattern correlates with histological grade. However, differing patterns are reported for hepatocellular carcinoma in dogs in late-stage imaging (Kanemoto et al. 2009; Nakamura et al. 2010).

The second pattern is seen with hemangiosarcoma nodules and, less frequently, other carcinomas and sarcomas. With this pattern, the nodule never completely enhances, remaining hypoechoic throughout the imaging, and tortuous fringe vessels are seen on the periphery of the nodule (Figure 16.6). These tortuous feeder vessels are also important in characterizing splenic nodules and, possibly, other organs. This pattern has been noted in the liver of a cat with metastatic hemangiosarcoma (Webster et al. 2008). There is a combination of documented and anecdotal information that metastatic hemangiosarcoma has a similar perfusion pattern regardless of organ, including liver (O'Brien et al. 2004), spleen (Rossi et al. 2008), peritoneum, and lymph nodes.

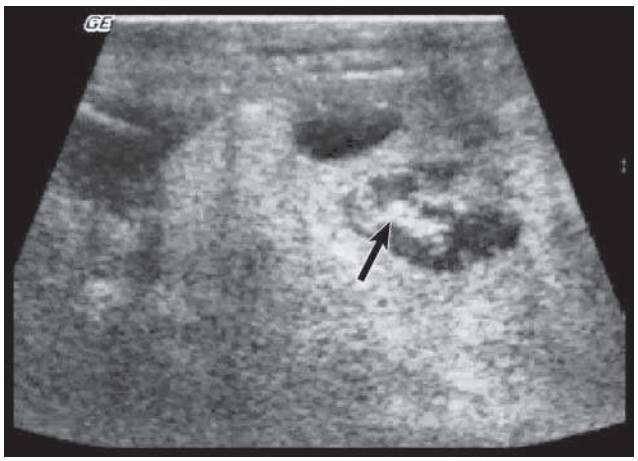


Figure 16.6. Contrast ultrasound image of hemangiosarcoma in the liver of a dog. Note the tortuous feeder vessel penetrating the mass (arrow).

Scan protocols for nodules depend on the grayscale visualization of these nodules. If nodules are noted on grayscale imaging, then contrast ultrasound is performed on those nodules for detailed characterization. If nodules are not detected initially, than the entire liver should be scanned within the 30 seconds of peak liver perfusion. Often multiple injections are necessary to completely evaluate all liver lobes. Obvious, the two protocols can be combined to maximize detection and characterization of metastatic lesions.

Larger masses may not be as dependably characterized. If a uniform enhancement is seen, the mass is benign, but a mixed pattern has been reported in both large malignant masses and larger benign masses with necrotic portions (O'Brien et al. 2004).

Initial data indicate that the peak perfusion of the liver in dogs with portosystemic shunts is sooner than in normal control dogs, presumably because of increased hepatic arterial flow (Salwei et al. 2003). However, the control dogs were not the same age or breed, and more recent personal evidence indicates that younger and smaller dogs have faster liver perfusion than older and larger dogs. Additional studies seem to be indicated, as assessment of time-to-peak would be a simple method to assess the arterial component of liver blood flow.

Spleen

Unlike the liver, the normal spleen in normal dogs may have a heterogeneous early parenchymal phase (Ohlerth et al. 2007). Large areas of the normal spleen may be hypoperfused compared with surrounding regions. Eventually, the entire spleen becomes homogeneously enhanced in normal cats and dogs (Figure 16.7). This regional heterogeneity is more common in cats than in dogs, and is more severe in anesthetized cats than in awake cats (Leinonen et al. 2010b).

After the initial success of contrast ultrasound in the liver, the spleen seemed an equally likely subject for characterization of nodules. Early reports were mixed as to the accuracy of contrast ultrasound for detecting malignant nodules. The initial study indicated that malignant nodules were most commonly hypoenhancing (compared with normal surrounding spleen) at peak and in early washout phases (Rossi et al. 2008). However, a subsequent study demonstrated that lymphomatous nodules were uniformly isoenhancing at peak and the majority were isoenhancing in washout (Ohlerth et al. 2008). In a study evaluating primary splenic masses, the perfusion pattern did not assist in the characterization of benign versus malignant (Ivancic et al. 2009). These initial results justify additional

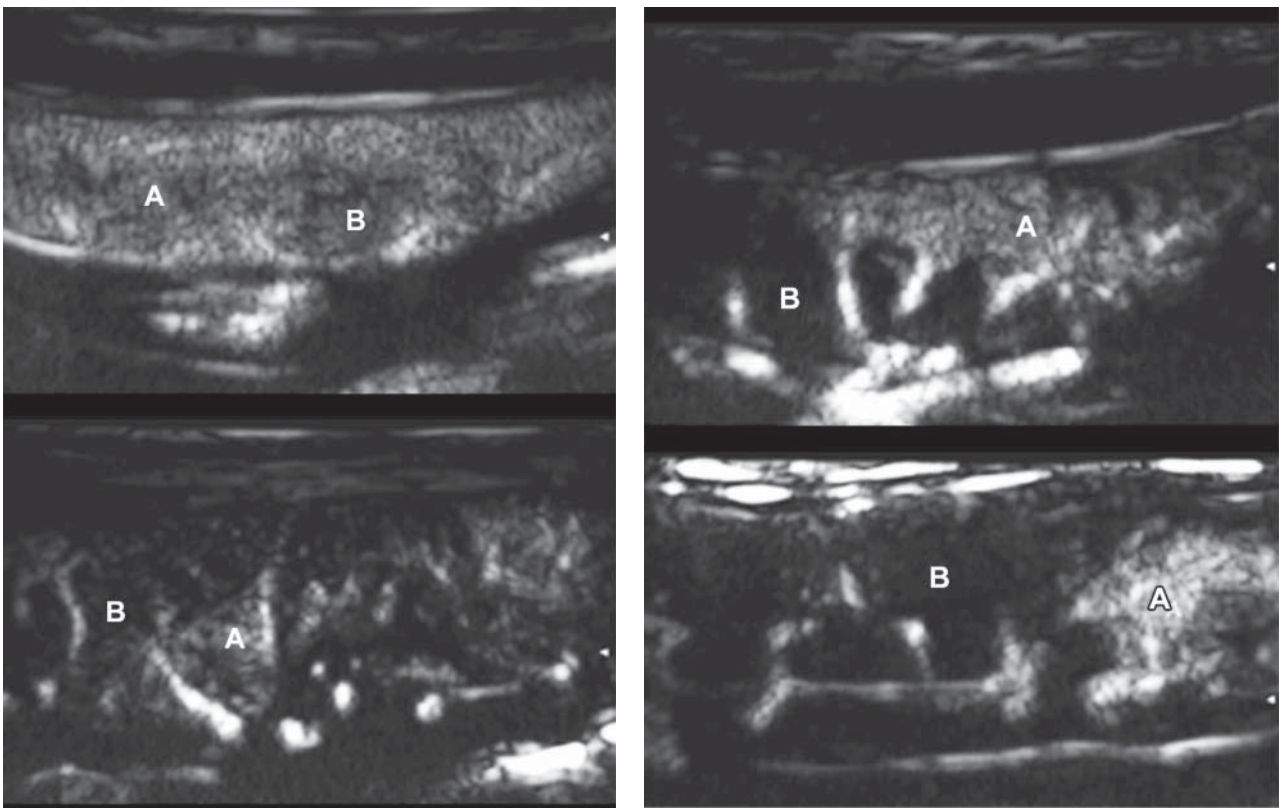


Figure 16.7. Contrast ultrasound of the spleen in four normal anesthetized cats. In the early perfusion phase, the splenic parenchyma is typically heterogeneous. Variably sized areas are hyperenhancing (**A**) compared with other areas that are hypoenhancing (**B**). The spleen eventually becomes uniformly enhancing in all normal cats and dogs.

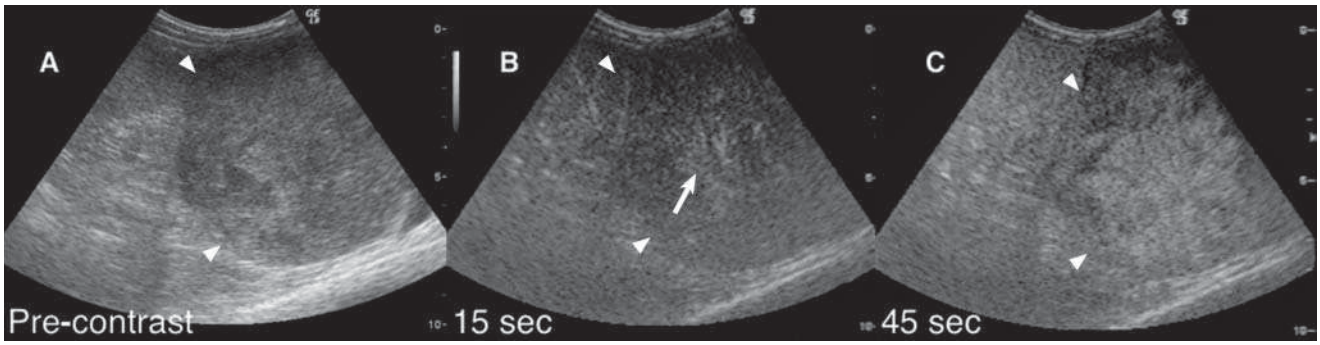


Figure 16.8. Grayscale (A) and contrast-enhanced (B, C) ultrasound images of a dog presented with hemoabdomen. A large, mostly hypoechoic mass (arrowheads) was identified in the spleen (A). Multiple blood vessels (arrow) are seen entering the center of the mass during the arterial phase (B), while a large portion of the mass contrast enhances during peak enhancement (C). The histopathologic diagnosis was lymphoid hyperplasia with hematoma formation.

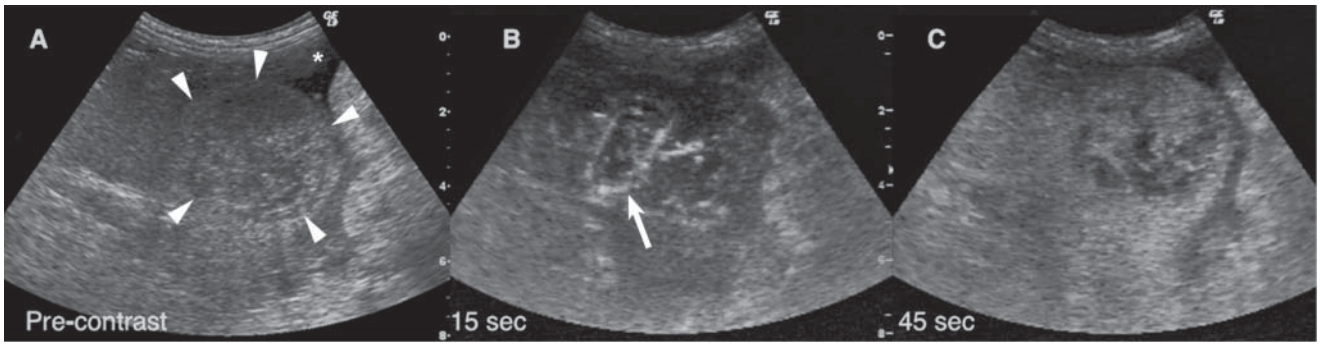


Figure 16.9. Grayscale (A) and contrast-enhanced (B, C) ultrasound images of a dog presented with hemoabdomen. A cavitated mass is seen in the body of the spleen (A). A cluster of slightly tortuous vessels is visible during the arterial phase **(B)** and most of the mass is perfused at peak enhancement **(C)**. The histopathologic diagnosis was hemangiosarcoma.

studies using larger populations for determining the clinical utility of CEUS for characterizing splenic nodules and masses in dogs.

As described for hemangiosarcoma nodules in the liver (Figure 16.6), malignant splenic nodules, including but not limited to metastatic hemangiosarcoma, often have tortuous feeding vessels entering the nodules from the periphery. Tortuous feeder vessels may, in fact, be exclusively seen in malignant focal lesions (Rossi et al. 2008; Taeymans et al. 2011) (Figures 16.8–16.10).

Kidney

The normal renal vasculature is composed of a solitary large afferent artery branching into interlobar arteries that radiate from the renal hilus through the medulla to the level of the corticomedullary (CM) junction. The arcuate arteries extend perpendicular to the interlobar arteries, parallel to and at the level of the CM junction. These branch into radially oriented interlobular arteries, parallel to the interlobar arteries, which extend to the glomeruli within the cortex. Efferent vessels from the glomeruli supply proximal and distal convoluted tubules and the loops of Henle. The perfusion pattern in a normal kidney is therefore dependably and symmetrically biphasic with the cortex perfusing before the medulla (Waller et al. 2007) (Figure 16.11). This pattern is reported in cats (Kinns et al. 2010; Leinonen et al. 2011).

Several renal lesions such as infarction (Figure 16.12), nephritis (Figure 16.13) or neoplasia (Figure 16.14) can result in regional hypoperfusion (Haers et al. 2010). This non-specificity precludes accurate characterization, but may provide a useful mechanism for better defining the margins of lesions.

Lymph Nodes

The blood flow in normal lymph nodes enters at the apex of the ellipse and has a large central vessel in the lymph node hilus with symmetrical radiating vessels.

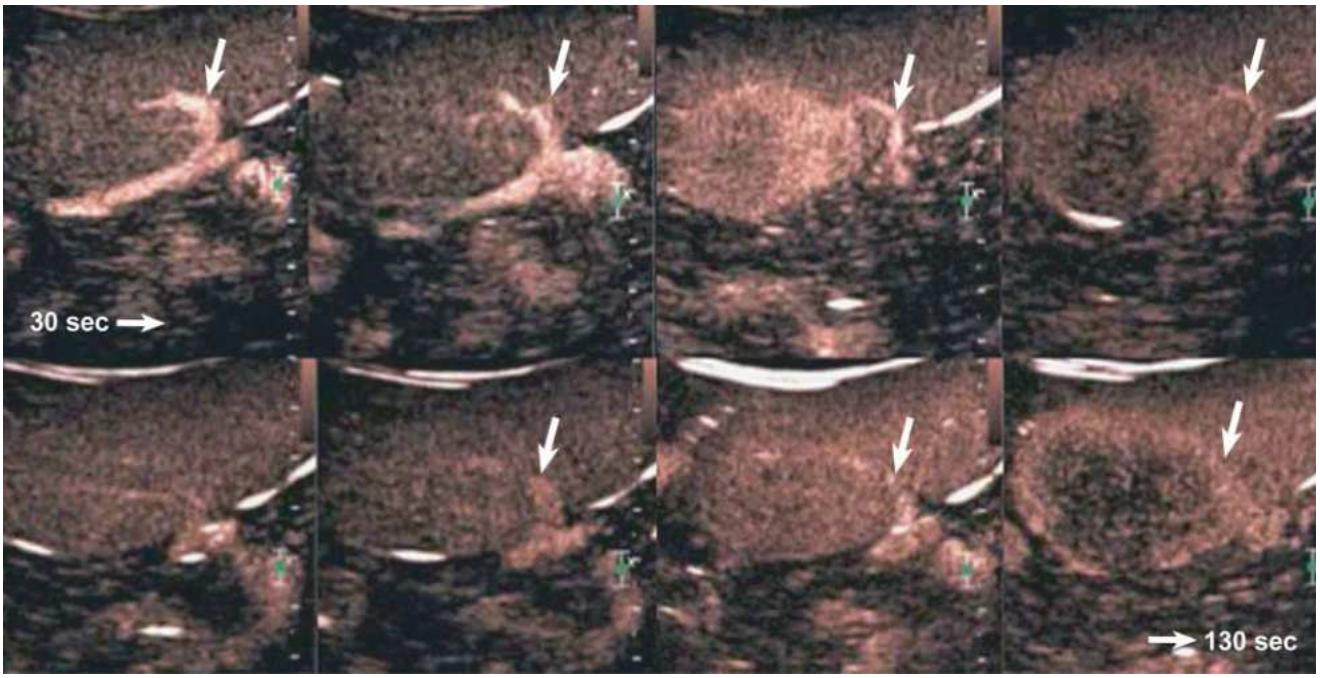


Figure 16.10. **Tortuous feeding vessel coursing toward a focal malignant histiocytosis lesion in the cranial aspect of the spleen of a dog.** (for full caption, see facing page)

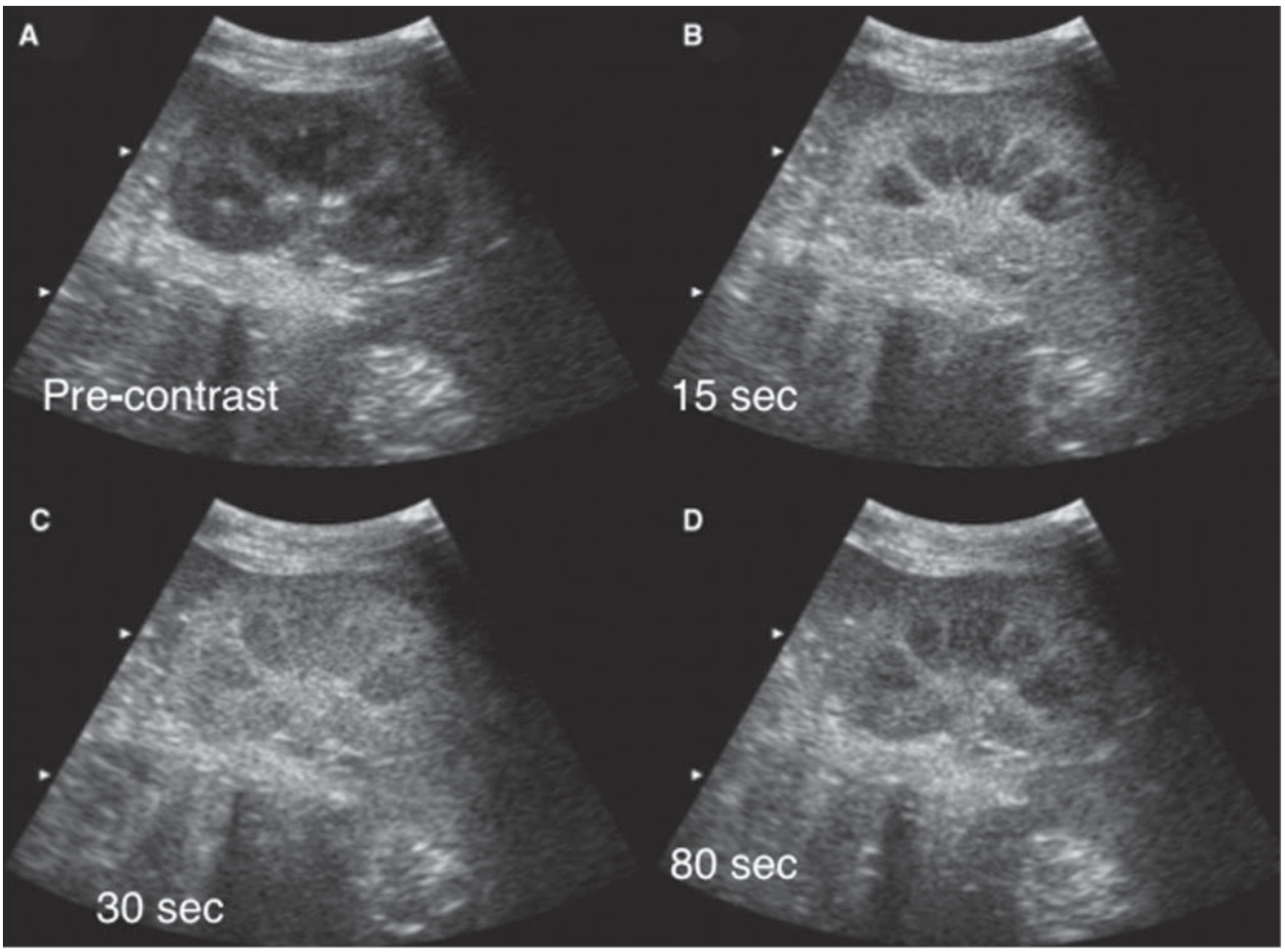


Figure 16.11. **Grayscale (A) and contrast ultrasound (B, C) scans in a normal dog.** Note the uniform intense contrast enhancement of the cortex at 15 seconds (**B**) followed by gradual decrease in contrast enhancement of the medulla by 45 seconds (**C**). The contrast eventually washes out by 80 seconds (**D**).

Figure 16.10. Tortuous feeding vessel coursing toward a focal malignant histiocytosis lesion in the cranial aspect of the spleen of a dog. These images were acquired from 30 seconds after the start of the injection (upper left image), to 130 seconds after the start of the injection (lower right image). The large feeding vessel is arising outside the splenic parenchyma, has a tortuous course, and closer to the lesion gives off smaller branches that surround the nodule. The nodule varies in echogenicity over time. Image courtesy of Dr Olivier Taeymans.

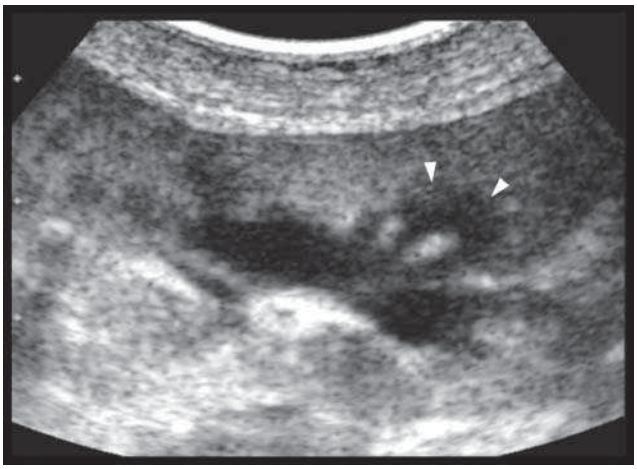


Figure 16.12. Contrast ultrasound of a dog with renal infarction. There is focal lack of contrast enhancement in the caudal cortex (arrowheads) consistent with lack of perfusion peripheral to the interlobar arteries.

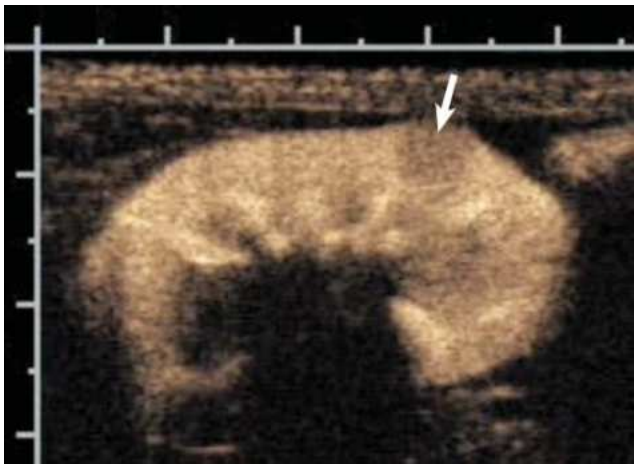


Figure 16.14. Malignant histiocytosis nodule in the left kidney of a dog. There is a nodular area deforming the renal contour showing reduced contrast enhancement (arrow).

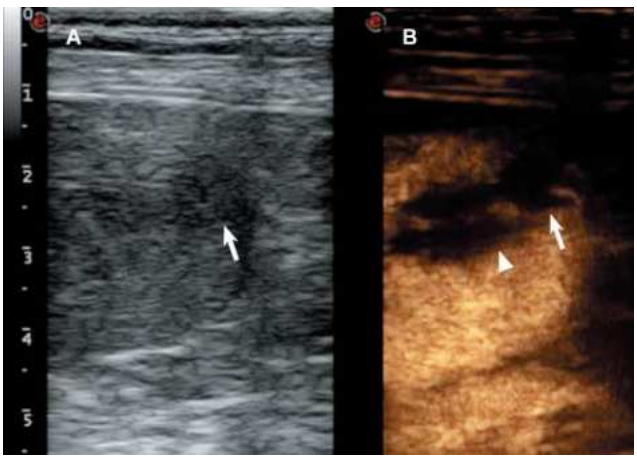


Figure 16.13. Contrast ultrasound of a dog with suppurative nephritis. Note the ill-defined hypoechoic lesion involving the caudal renal cortex on grayscale ultrasound **(A)** (arrow). The lesion is associated with hypoperfusion on contrast ultrasound (**B**) and also involves the medulla (arrowhead).

Normal lymph nodes perfuse symmetrically and uniformly (Gaschen et al. 2010; Salwei et al. 2005). Perfusion of malignant lymph nodes is reported to be similar to normal lymph nodes (Salwei et al. 2005).

Aberrancy of that pattern has been documented using contrast ultrasound imaging (Salwei et al. 2005). Aberrant vessels in the pericapsular or subcapsular regions, somewhat analogous to tortuous feeder vessels in malignant liver and splenic nodules, are commonly seen in lymphomatous malignant lymph nodes (Figure 16.15). Asymmetry of the hilar vessels or branches thereof can also be seen. These finding may also be noted with Doppler sonography, although sensitivity may be improved with contrast-enhanced Doppler imaging (Figure 16.16).

Pancreas

The normal pancreas has a very intense, uniform, but brief perfusion pattern in cats and dogs (Figure 16.17). Contrast enhancement in the right pancreatic limb is seen initially in the pancreaticoduodenal artery, followed by uniform parenchymal enhancement. Contrast medium is then recognized in the pancreaticoduodenal vein. The parenchymal enhancement occurs coincidental to duodenal wall perfusion in dogs (Johnson-Neitman et al. 2012) and cats (Leinonen et al. 2010a).

With pancreatitis in dogs, most of the parenchyma has persistent normal hyperperfusion, but regional

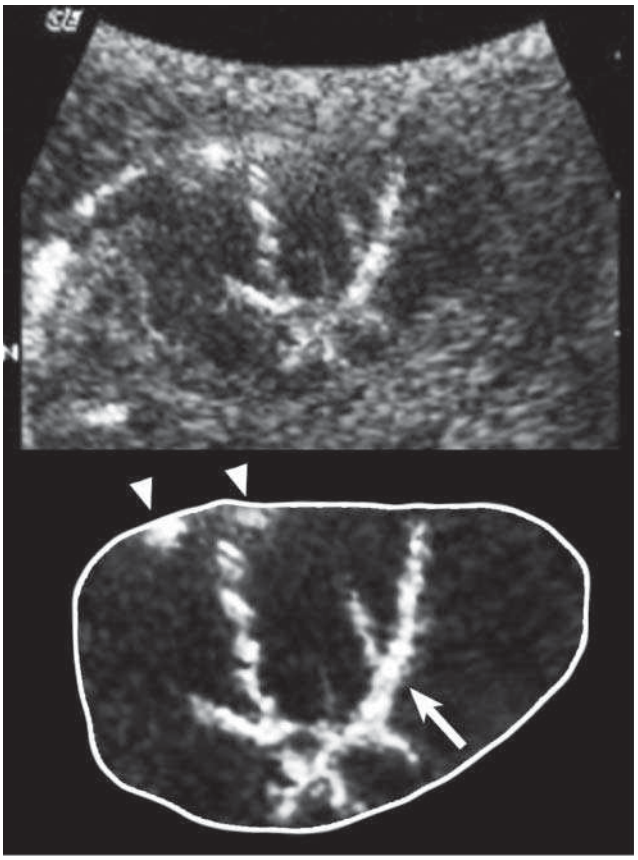


Figure 16.15. Contrast ultrasound image (A) and diagram of vascular features (B) of a dog with lymphomatous lymph node. Note the aberrant subcapsular (arrowhead) and asymmetrical vessels not originating from the central hilus (arrow).

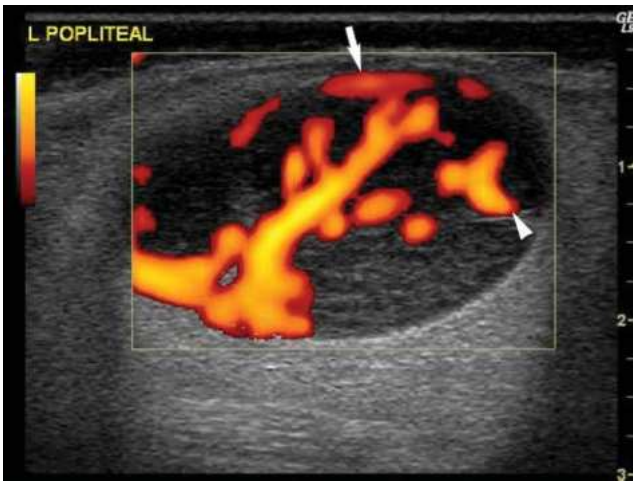


Figure 16.16. Contrast-enhanced power Doppler ultrasound of the enlarged and hypoechoic popliteal lymph node of a dog with lymphoma. The vasculature is distorted and abnormal, with large subcapsular (arrow) and aberrant (arrowhead) vessels.

hypoperfused lesions are consistently noted (Figures 16.18, 16.19) (Shanaman et al. 2012). These lesions may represent areas of temporary ischemia or more permanent necrosis. The cytological/histological diagnosis, size and number of these regions may relate to severity of the pancreatitis, although this has not been investigated.

Contrast enhanced ultrasound can be helpful for characterization of pancreatic nodules. Similar to the perfusion patterns used in computed tomography (CT) imaging (Mai and Cáceres 2008), strong enhancement during the arterial phase may be typical for insulinomas compared with other pancreatic lesions such as carcinomas that tend to be poorly perfused initially (Figure 16.20).

Gastrointestinal Tract

All regions of the gastrointestinal tract in cats (Leinonen et al. 2010a) and dogs (Johnson-Neitman et al. 2012) show brief and intense contrast enhancement. This was also seen intraoperatively in

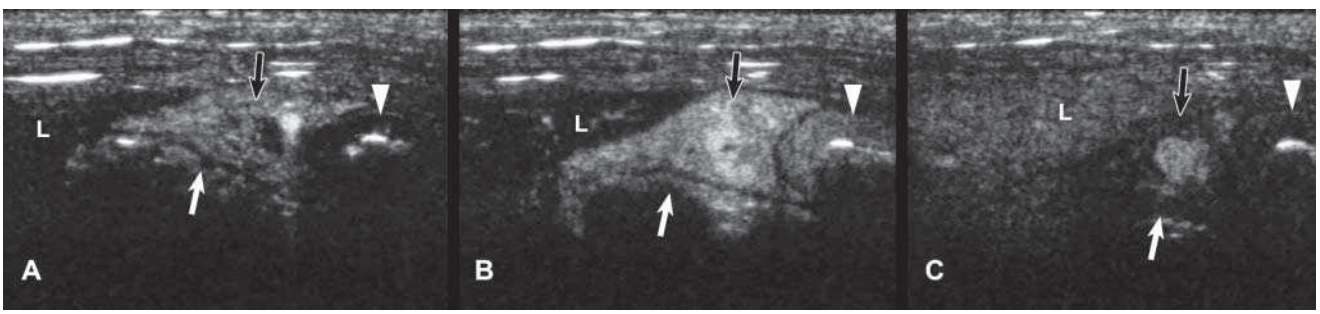


Figure 16.17. Contrast ultrasound of a normal pancreas in a dog with arterial (A), perfusion (B) and venous (C) phases. The colonic (white arrow) and duodenal (white arrowhead) walls contrast enhance concurrently with the pancreas (black arrow) **(B)**. In **C**, the liver (L) enters its early perfusion state concurrent with pancreas washout and late venous phase.

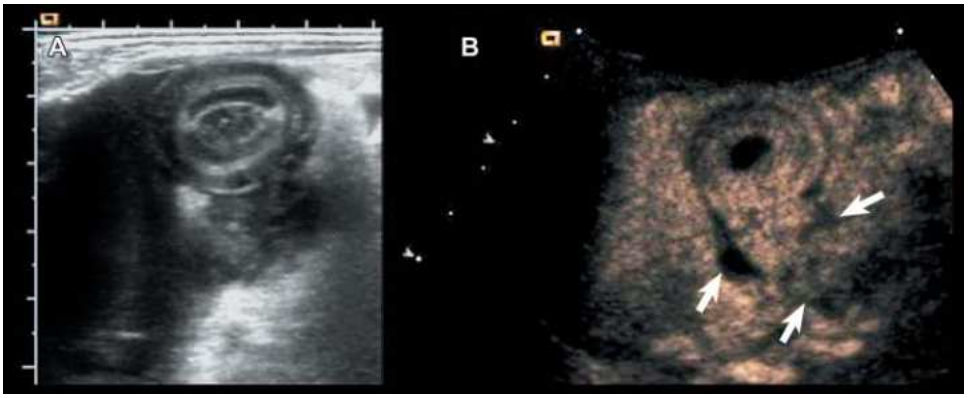


Figure 16.18. Grayscale (A) and contrast ultrasound (B) of a dog with pancreatitis that clinically resolved in 48 hours. Note the small regional perfusion deficits that could correspond to edema, ischemia or necrosis (arrows).

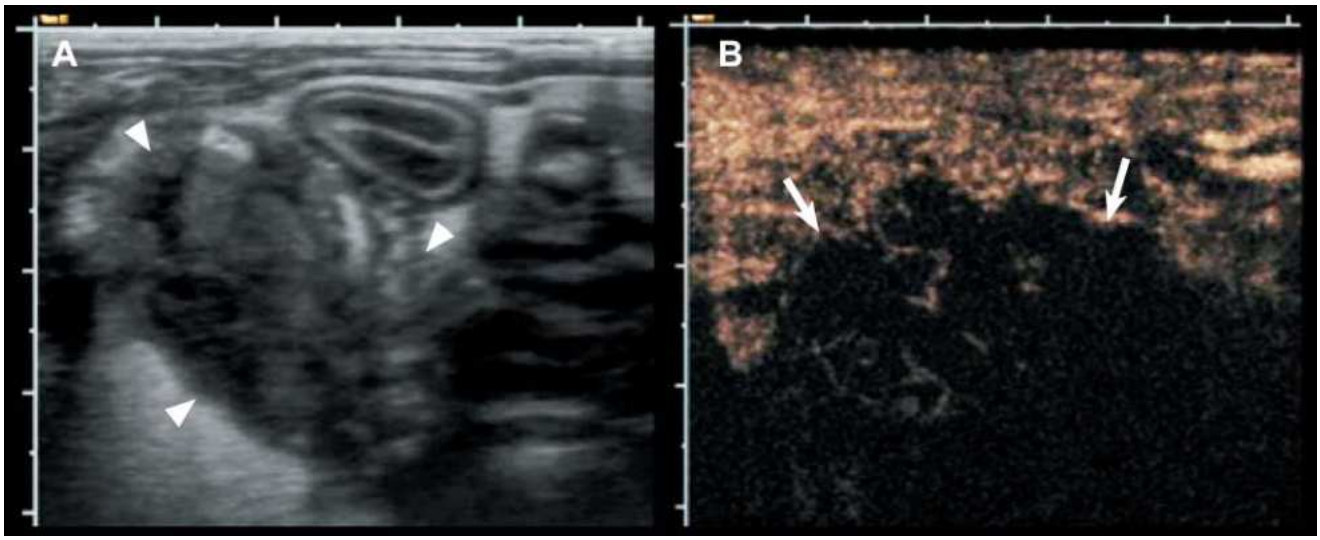


Figure 16.19. Transverse grayscale (A) and longitudinal contrast ultrasound (B) images of dog with severe pancreatitis. In this dog, clinical signs progressed and the patient succumbed to multiple organ failure 72 hours after presentation. The pancreas is enlarged and hypoechoic (arrowheads) in the pre-contrast image **(A)**. Note the large area of hypoperfusion (arrows) after contrast injection.

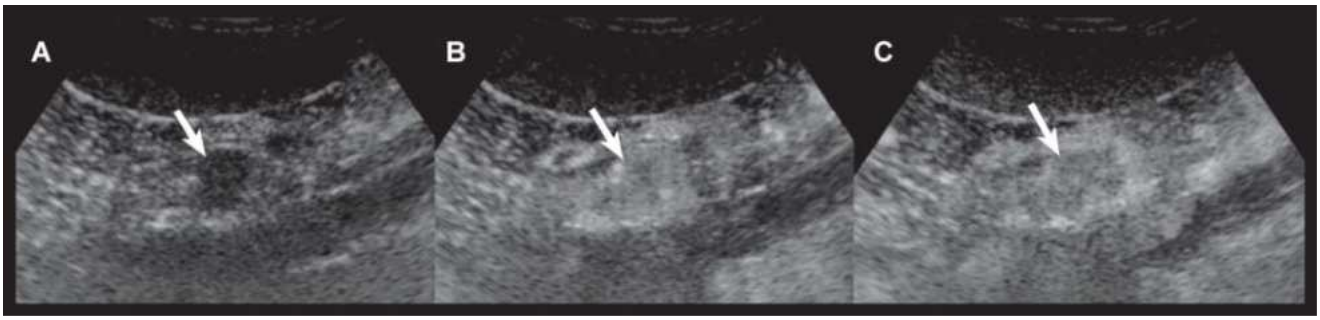


Figure 16.20. An 8-year-old female spayed Boxer with suspected insulinoma. A: A hypoechoic nodule was detected in the pancreas (arrow). **B:** During the arterial phase, there is strong enhancement of the nodule (arrow) whereas the surrounding pancreas enhances only mildly and heterogeneously. **C:** During peak pancreatic enhancement, contrast enhancement of the nodule (arrow) is already reduced due to rapid washout of the lesion.

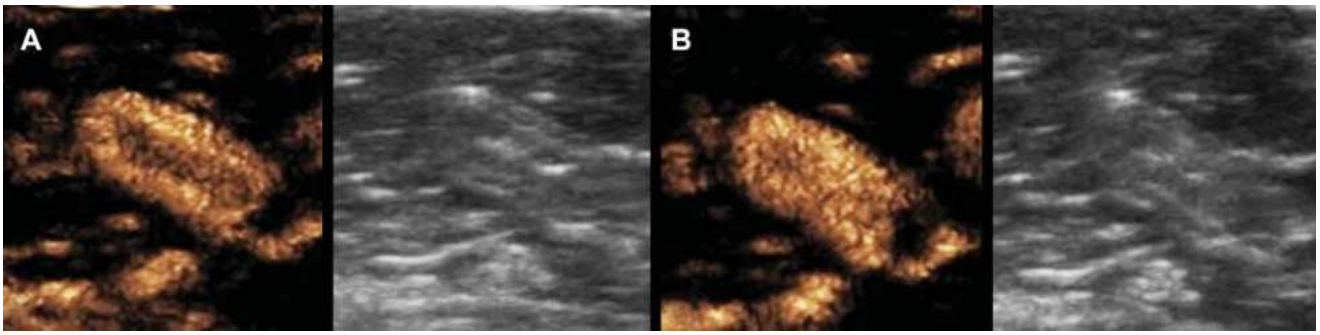


Figure 16.21. Contrast (left) and grayscale (right) ultrasound images of the normal jejunum in a cat. Note the initial subjective enhancement of the serosal and submucosa region (**A**) and subsequent uniform mural enhancement (**B**). Image courtesy of Dr Alessia Diana, University of Bologna, Italy.

anesthetized dogs (Jiménez et al. 2011). In cats, rapid intense enhancement of the serosal and submucosal layers is followed by gradual enhancement of the entire wall (Figure 16.21). In the late phase, the washout of the submucosal layer occurs last (Diana et al. 2011). Although not investigated for utility in discriminating between benign and malignant tumors or between tumor types, contrast ultrasound may play a role in prognostication. In a study investigating CT and CEUS in dogs with signs of acute abdomen, perfusion defects were identified more accurately with CEUS than with multi-slice contrast CT. Defects were noted in the wall of two dogs with necropsy-proven gastric lymphoma (Figure 16.22) and concurrent pneumoperitoneum, and a dog with a linear foreign body with jejunal wall necrosis noted at surgery (Figure 16.23) (Shanaman et al. 2012). Assessment of viability of the gastrointestinal tract may be a clinically useful indication of CEUS both pre- and intra-operatively.

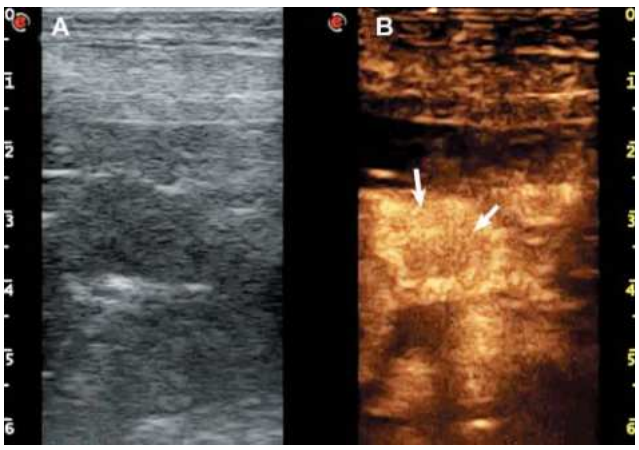


Figure 16.22. Grayscale (A) and contrast (B) ultrasound images of a dog with gastric lymphoma. Note the regional perfusion deficit in the gastric wall (arrows). The lumen is the hypoechoic region deep to the thickened wall.

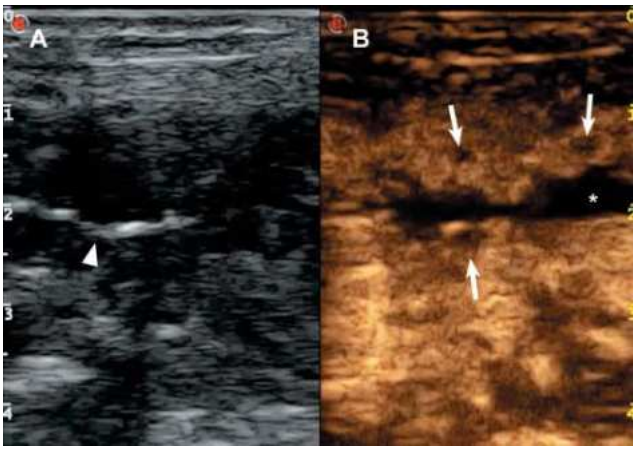


Figure 16.23. Contrast ultrasound of dog with a linear foreign body in the duodenum and jejunum. Note the small perfusion deficits in the walls of the duodenum (arrows), consistent with the surgically observed wall necrosis. The lumen shows the linear foreign body (arrowhead) on the grayscale image and is filled with hypoechoic fluid (*) that becomes conspicuous after contrast injection.

Adrenal Gland

Normal adrenal glands enhance rapidly and uniformly in a centrifugal way from the medulla to the cortex followed by a gradual homogeneous decrease in enhancement (Bargellini et al. 2013; Pey et al. 2013). In dogs with pituitary-dependent hyperadrenocorticism, the perfusion characteristics of the adrenal glands differs significantly from that of healthy dogs (Bargellini et al. 2013; Pey et al. 2013). Contrast medium inflow progresses rapidly in both cortex and medulla at the same time, with a chaotic enhancement pattern (Figure 16.24). This enhancement pattern is in accordance with histologic findings in hyperplastic adrenal glands that are characterized by hyperplasia of the

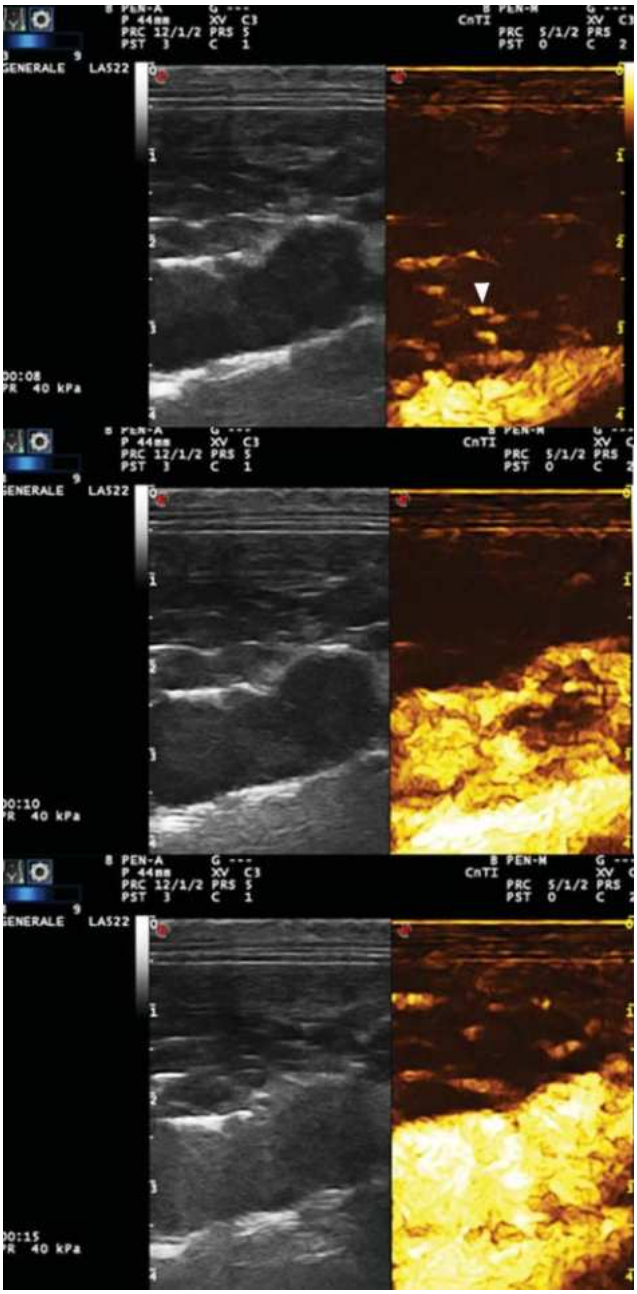


Figure 16.24. Grayscale (left) and contrast (right) ultrasound images of an enlarged left adrenal in a dog with pituitary-dependent hyperadrenocorticism. A: Note the central longitudinal vessel (arrowhead) during the wash-in phase (8 seconds) **B:** Chaotic wash-in of cortex and medulla (10 seconds) followed by eventual homogeneous enhancement (**C**) (15 seconds). Images courtesy of Drs Paolo Bargellini, Paolo Fonti and Giuseppe Rubini, Italy.

zona fasciculata and proliferation of irregular blood vessels. Characterization of adrenal gland nodules and masses has not been investigated in veterinary medicine.

Prostate Gland

The utility of contrast ultrasound for characterizing malignant versus benign prostate gland diseases has not been investigated.

Vascular Diseases

Diseases with a primarily vascular basis would seem ripe for investigation with contrast ultrasound imaging. While we can hypothesize that contrast-enhanced Doppler or perfusion ultrasound should help diagnose splenic torsion and infarction, gastric dilation volvulus, aortic and portal thrombosis and lung lobe torsion, it has not been investigated in veterinary medicine.

Summary

Contrast ultrasound requires four components beyond typical grayscale imaging:

- contrast medium
- contrast software
- contrast-capable transducer
- intravenous access.

Skill and experience with this modality aid implementation in a clinical setting. Characterization of malignant versus benign nodules has been validated for the liver and needs more investigation for the spleen. Larger masses seem more problematic because of the prevalence of avascular regions regardless of the underlying pathology. Aberrant feeder vessels appear to be a useful attribute seen only with malignant splenic masses and nodules, liver nodules and malignant lymph nodes. More investigation is required to determine the clinical utility of contrast ultrasound in the kidney, gastrointestinal tract, pancreas, and other organs. However, there seems to be great potential to take advantage of this relative quick, minimally invasive and very safe modality for any disease that has an abnormal vascular or perfusion aspect.



Visit our website at **www.SmallAnimalUltrasonography.com** for complementary video clips with annotations and text on:

- Contrast-enhanced ultrasound: technique and principles of interpretation

References

Bargellini P, Orlandi R, Paloni C, et al. (2013) Contrast-enhanced ultrasonographic characteristics of adrenal glands in dogs with pituitary-dependent hyperadrenocorticism. Vet Radiol Ultrasound 54:283–292.

Claudon M, Cosgrove D, Albrecht T et al. (2008) Guidelines and good clinical practice recommendations for contrast enhanced ultrasound (CEUS) - Update 2008. Ultraschall Med - Eur. J Ultrasound 29:28–44.

Diana A, Specchi S, Baron Toaldo M, et al. (2011) Contrast-enhanced ultrasonography of the small bowel in healthy cats. Vet Radiol Ultrasound 52:555–559.

Gaschen L, Angelette N, Stout R (2010) Contrast-enhanced harmonic ultrasonography of medial iliac lymph nodes in healthy dogs. Vet Radiol Ultrasound 51: 634–637.

Haers H, Vignoli M, Paes G, et al. (2010) Contrast harmonic ultrasonographic appearance of focal space-occupying renal lesions. Vet Radiol Ultrasound 51:516–522.

Ivancic M, Long F, Seiler GS (2009) Contrast harmonic ultrasonography of splenic masses and associated liver nodules in dogs. J Am. Vet Med Assoc. 234:88–94.

Jiménez DA, O'Brien RT, Wallace JD, et al. (2011) Intraoperative contrast-enhanced ultrasonography of normal canine jejunum. Vet Radiol Ultrasound 52:196–200.

Johnson-Neitman JL, O'Brien RT, Wallace JD (2012) Quantitative perfusion analysis of the pancreas and duodenum in healthy dogs by use of contrast-enhanced ultrasonography. Am J Vet Res 73:385–392.

Kanemoto H, Ohno K, Nakashima K, et al. (2008) Vascular and Kupffer imaging of canine liver and spleen using the new contrast agent Sonazoid. J Vet Med Sci Jpn Soc Vet Sci 70:1265–1268.

Kanemoto H, Ohno K, Nakashima K, et al. (2009) Characterization of canine focal liver lesions with contrast-enhanced ultrasound using a novel contrast agent – Sonazoid. Vet Radiol Ultrasound 50:188–194.

Kinns J, Aronson L, Hauptman J, Seiler G. (2010) Contrast-enhanced ultrasound of the feline kidney. Vet Radiol Ultrasound 51:168–172.

Leinonen MR, Raekallio MR, Vainio OM, et al. (2010a) Quantitative contrast-enhanced ultrasonographic analysis of perfusion in the kidneys, liver, pancreas, small intestine, and mesenteric lymph nodes in healthy cats. Am J Vet Res 71:1305–1311.

Leinonen MR, Raekallio MR, Vainio OM, et al. (2010b) Effect of anaesthesia on contrast-enhanced ultrasound of the feline spleen. Vet J 190: 273–277.

Leinonen MR, Raekallio MR, Vainio OM, et al. (2011) The effect of contrast-enhanced ultrasound on the kidneys in eight cats. Vet J Lond. Engl. 1997 190:109–112.

Mai W, Cáceres AV (2008) Dual-phase computed tomographic angiography in three dogs with pancreatic insulinoma. Vet Radiol Ultrasound 49:141–148.

Nakamura K, Sasaki N, Yoshikawa M, et al. (2009) Quantitative contrast-enhanced ultrasonography of canine spleen. Vet Radiol Ultrasound 50:104–108.

Nakamura K, Takagi S, Sasaki N, et al. (2010) Contrast-enhanced ultrasonography for characterization of canine focal liver lesions. Vet Radiol Ultrasound 51: 79–85.

O'Brien RT (2007) Improved detection of metastatic hepatic hemangiosarcoma nodules with contrast ultrasound in three dogs. Vet Radiol Ultrasound 48:146–148.

O'Brien RT, Holmes SP (2007) Recent advances in ultrasound technology. Clin Tech Small Anim Pract 22:93–103.

O'Brien RT, Iani M, Matheson J, et al. (2004) Contrast harmonic ultrasound of spontaneous liver nodules in 32 dogs. Vet Radiol Ultrasound 45:547–553.

Ohlerth S, Dennler M, Rüefli E, et al. (2008) Contrast harmonic imaging characterization of canine splenic lesions. J Vet Intern Med 22:1095–1102.

Ohlerth S, O'Brien RT (2007) Contrast ultrasound: General principles and veterinary clinical applications. Vet J 174:501–512.

Ohlerth S, Rüefli E, Poirier V, et al. (2007) Contrast harmonic imaging of the normal canine spleen. Vet Radiol Ultrasound 48:451–456.

Pey P, Daminet S, Smets, PMY, et al. (2013) Contrast-enhanced ultrasonographic evaluation of adrenal glands in dogs with pituitary-dependent hyperadrenocorticism. Am J Vet Res 74:417–425.

Rossi F, Leone VF, Vignoli M, et al. (2008) Use of contrast-enhanced ultrasound for characterization of focal splenic lesions. Vet Radiol Ultrasound 49:154–164.

Salwei RM, O'Brien RT, Matheson JS (2003) Use of contrast harmonic ultrasound for the diagnosis of congenital portosystemic shunts in three dogs. Vet Radiol Ultrasound 44:301–305.

Salwei RM, O'Brien RT, Matheson JS (2005) Characterization of lymphomatous lymph nodes in dogs using contrast harmonic and power Doppler ultrasound. Vet Radiol Ultrasound 46:411–416.

Seiler GS, Brown JC, Reetz JA, et al. (2013) Safety of contrast-enhanced ultrasonography in dogs and cats: 488 cases (2002–2011). J Am Vet Med Assoc 242:1255–1259.

Shanaman MM, Schwarz T, Gal A, et al. (2012) Comparison between survey radiography, b-mode ultrasonography, contrast-enhanced muliti-detector computed tomography findings in dogs with acute abdominal signs. Vet Radiol Ultrasound 2013. 54: 591–604.

Taeymans O, Penninck D (2011) Contrast enhanced sonographic assessment of feeding vessels as a discriminator between malignant vs. benign focal splenic lesions. Vet Radiol Ultrasound 52:457–461.

Waller KR, O'Brien RT, Zagzebski JA (2007) Quantitative contrast ultrasound analysis of renal perfusion in normal dogs. Vet Radiol Ultrasound 48:373–377.

Webster N, Holloway A (2008) Use of contrast ultrasonography in the diagnosis of metastatic feline visceral haemangiosarcoma. J Feline Med Surg 10:388–394.

Yamaya Y, Niizeki K, Kim J, et al. (2004) Anaphylactoid response to Optison (R) and its effects on pulmonary function in two dogs. J Vet Med Sci Jpn Soc Vet Sci 66:1429.

Ziegler LE, O'Brien RT, Waller KR, et al. (2003) Quantitative contrast harmonic ultrasound imaging of normal canine liver. Vet Radiol Ultrasound 44:451–454.

CHAPTER SEVENTEEN

Musculoskeletal System

Marc-André d'Anjou[1,2] and Laurent Blond[3]

[1] *Centre Vétérinaire Rive-Sud, Brossard, Québec, Canada*
[2] *Faculté de médecine vétérinaire de l'Université de Montréal, Saint-Hyacinthe, Québec, Canada*
[3] *Clinique Vétérinaire Languedocia, Montpellier, France*

Preparation and scanning procedure

While magnetic resonance imaging (MRI) and computed tomography (CT) have gained in popularity for the assessment of the musculoskeletal system in dogs and cats, ultrasonography represents a complementary and cost-effective alternative, particularly for soft tissues when combined with radiography. It also enables dynamic assessment of joints, ligaments, and tendons, as well as guidance for fine-needle aspirations or biopsies, and even foreign body removals. Structures are typically scanned in both longitudinal and transverse planes, probe positioning being particularly critical to correctly assess fiber alignment in muscles or tendons. A high-frequency linear transducer is preferred, but may not always be optimal due to the small and/or curved surface of some structures. Curvilinear probes may be useful for areas with a curved surface or deeper portions that require lower transducer frequency. A standoff pad may also facilitate assessment of curved structures with a small surface, for instance when using a large linear probe (Caine et al. 2009).

Musculoskeletal ultrasonography can be performed without sedation or anesthesia most of the time, although dynamic assessment of joints and tendons may be limited in painful patients. The size of some structures, particularly in smaller (<15 kg) dogs and cats, the system performance, and the complex anatomy represent limiting factors in ultrasonography for musculoskeletal disorders. Yet, numerous musculoskeletal conditions can be readily identified with this modality and their healing process can be monitored cost-effectively.

Shoulder

Scanning Technique

Ultrasonography of the shoulder joint and the surrounding tissues is best performed with a linear transducer using frequencies greater than 10 MHz. Curvilinear probes may be used to facilitate the approach to deeper portions or areas with a curved surface, such as the axillary area. The hair around the joint is clipped. All tendons and muscles are scanned longitudinally and transversely.

The sonogram of the shoulder joint starts by scanning the supraspinatus and infraspinatus muscles down to their attachment sites on the greater tubercle (Figures 17.1A, 17.2). Then the biceps tendon/muscle is examined, after external rotation (supination) of the shoulder joint (Figures 17.1B). Abducting the limb may also allow better access to the region. The scan can begin at the muscle belly, along the craniomedial aspect of the humeral diaphysis. The probe is then gradually moved proximally along its proximal tendon, which lies within the bicipital groove and is at that level surrounded by its sheath, at the medial aspect of the shoulder joint and just medial to the greater tubercle. The biceps tendon is then followed proximally to its origin on the supraglenoid tubercle of the scapula. The tendon and its sheath are contained in the bicipital groove by a transverse ligament between the greater and lesser tubercles, but these are not clearly seen with ultrasound (Figure 17.2).

The intra-articular structures of the shoulder are imaged by positioning the transducer laterally in a caudocranial orientation immediately caudal to the acromion, which serves as a landmark (Figure 17.3).

Atlas of Small Animal Ultrasonography, Second Edition. Edited by Dominique Penninck and Marc-André d'Anjou.
© 2015 John Wiley & Sons, Inc. Published 2015 by John Wiley & Sons, Inc.
Companion website: www.SmallAnimalUltrasonography.com

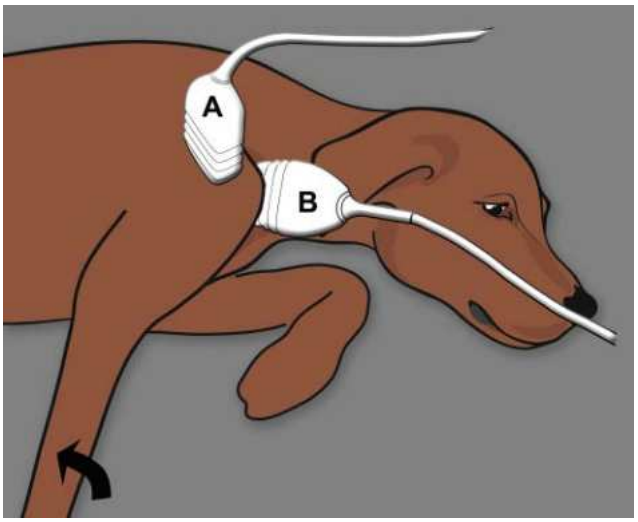


Figure 17.1. Scanning technique for the shoulder. Illustration showing the position of the dog and ultrasound probe for obtaining longitudinal images of the supraspinatus and infraspinatus muscles **(A)** and biceps tendon **(B)**. For the assessment of the biceps tendon, the leg must be pulled and supinated (curved arrow), facilitating the approach to the bicipital groove, which is located medial to the shoulder.

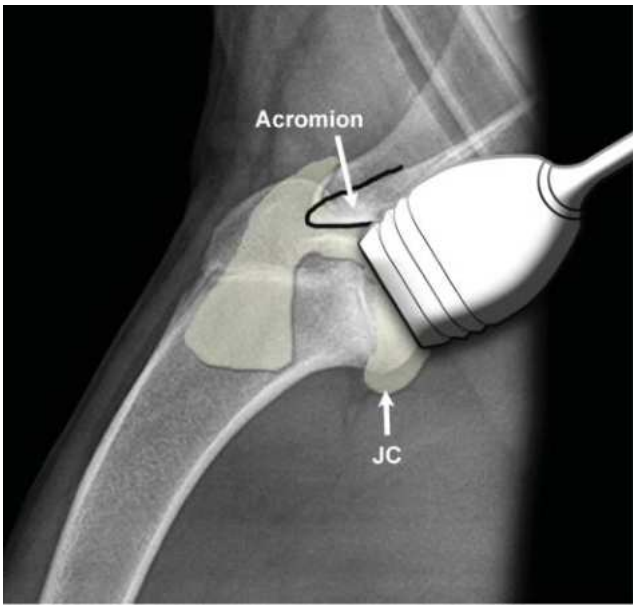


Figure 17.3. Sonographic approach to the shoulder joint. The caudolateral portion of the shoulder joint can be evaluated after placing the probe just caudal to the acromion, which can be easily palpated. The caudal extent of the joint space and capsule (JC) can be assessed.

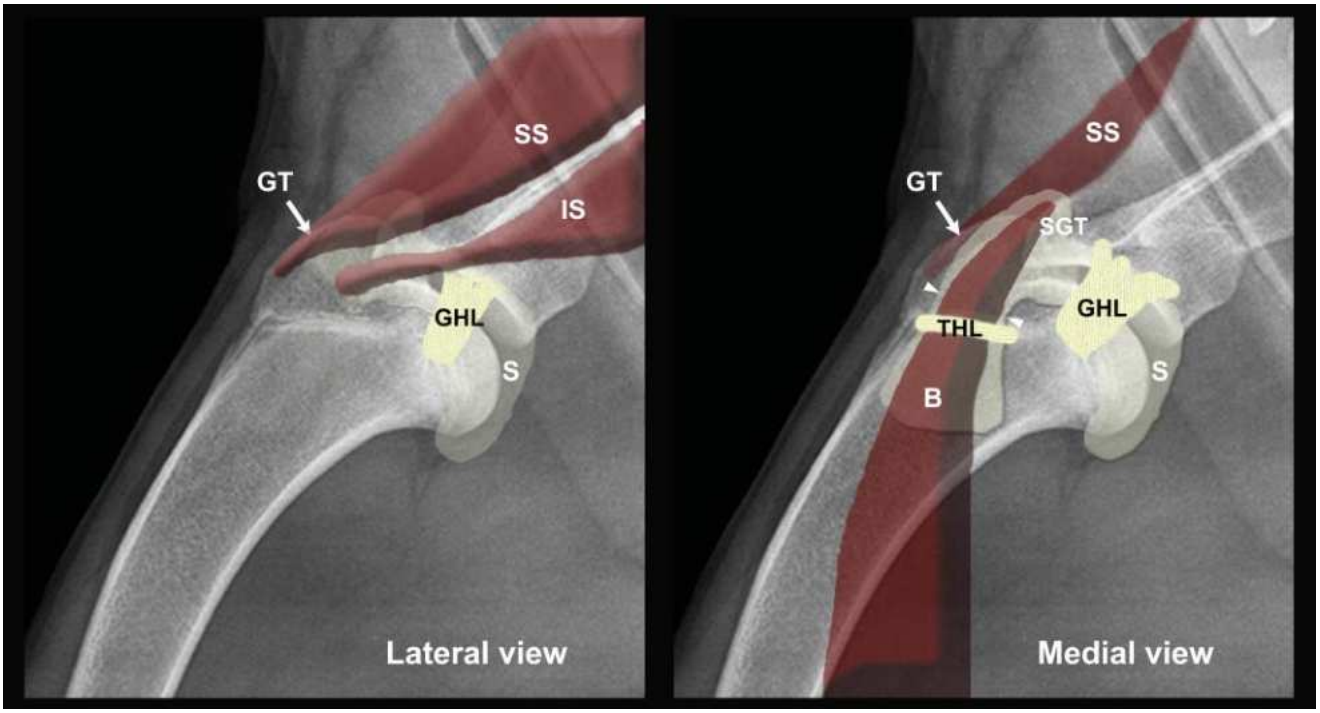


Figure 17.2. Schematic views of the normal shoulder anatomy in dogs. In the lateral view, the supraspinatus (SS) and infraspinatus (IS) muscles and tendons are cranial and caudal to the scapular spine, respectively. The SS tendon inserts on the greater tubercle (MT), just lateral to the bicipital groove. The IS inserts on the lateral aspect of the greater tubercle. The lateral glenohumeral ligament (GHL) is lateral to the joint capsule and synovial space (S). In the medial view, the biceps (B) muscle and tendon course along the medial aspect of the humerus. The tendon of origin is in the bicipital groove, just medial to the greater tubercle (GT). It extends within a tendon sheath (arrowheads) that connects with the shoulder joint synovium (S) and is contained by the transverse humeral ligament (THL). The biceps tendon courses along the insertion site of the supraspinatus (SS) tendon, located craniolaterally, and originates on the supraglenoid tubercle (SGT). The medial GHL is fan-shaped proximally.

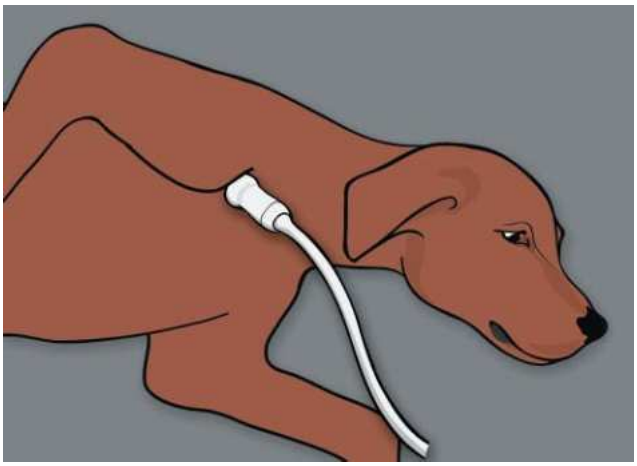


Figure 17.4. Scanning technique for the medial aspect of the shoulder joint. Illustration showing the position of the dog and ultrasound probe when scanning the medial aspect of the shoulder and axillary area. The leg must be abducted. The approach can also be facilitated by pulling (as shown) or extending the leg.

The transducer placed laterally, the joint is scanned by slowly adducting and simultaneously rotating the limb while the probe remains in the same position, in both longitudinal and transverse planes. Scanning the cranial aspect of the shoulder joint is difficult because of the presence of the greater tubercle, which allows only a small surface of probe contact. Imaging of the medial aspect of the shoulder joint may be facilitated by the use of a microconvex transducer, because of the intimate relationship between the thoracic limb and the thoracic wall (Figure 17.4).

Normal Sonographic Anatomy of the Shoulder

Supraspinatus and Infraspinatus Muscles and Tendons

The supraspinatus muscle originates on the supraspinatus fossa of the scapula and extends distally before spreading focally over the greater tubercle on which it inserts (Figures 17.2, 17.5). Proximally over the scapula, the muscle is hypoechoic, loosely striated, and smoothly marginated, before crossing over the craniomedial aspect of the shoulder joint. The greater tubercle appears as a convex, irregular, hyperechoic interface, with acoustic shadowing, on which the supraspinatus muscles inserts (Figure 17.5). At that level, because of the orientation of the tendon fibers, this portion remains similar in appearance to the muscle belly, in comparison to the adjacent biceps tendon.

The infraspinatus muscle is scanned in longitudinal and transverse planes from its origin on the infraspinatous fossa of the scapula to its short tendon at the caudolateral margin of the greater tubercle. The muscle belly is striated with thin hyperechoic bands that run obliquely, connecting a central line to the periphery, giving a characteristic fishbone pattern (Figure 17.6A). The muscle belly becomes narrower distally, merging into a tendon beyond the joint. The tendinous tissue displays typical hyperechoic fibrils arranged in parallel lines, with a peripheral hyperechoic outline (peritendineum). The greater tubercle appears as a hyperechoic convex structure on which the tendon ends, laterally, while curving and tapering when scanned longitudinally (like a bird's beak) (Figure 17.6B). The infraspinatus muscle is covered by the deltoid muscle, which displays typical muscle echotexture (Figure 17.6A).

Biceps Brachii Muscle and Tendon

In the longitudinal plane, the biceps muscle appears hypoechoic, with a hyperechoic line in the center representing the border between the two fused muscle bellies. Hyperechoic lines extend from this central line and run at a slightly oblique angle to the longitudinal axis (fish-bone pattern). The transducer is then positioned proximal to the muscle–tendon interface, which is not well defined (Figure 17.7A,B). The proximal tendon runs within the bicipital groove, which lies medial to the greater tubercle, deep in the medial groove of the shoulder. At that level, transverse scans are preferred for assessing the tendinous texture, the tendon sheath, and the bicipital groove surface. On a transverse plane, the tendon appears as an oval, uniformly hyperechoic structure measuring approximately 3 mm thick in medium-sized to large dogs (Figure 17.7C). The transducer must be placed carefully perpendicular to the tendon fiber to avoid a drop in tendon echogenicity (anisotropy) that could be confused for a lesion. The tendon is surrounded by a thin hypoechoic halo, consistent with a minute amount of fluid within the tendon sheath, which is typically fusiform to oval on cross-section (Figure 17.7C). Thin, linear, hyperechoic interfaces can be seen at the superficial and deep margins of the sheath at the interface level of the tendon sheath wall and humeral surface, respectively. The greater tubercle appears as a hyperechoic convex line at the lateral aspect of the bicipital groove and tendon. It is more distinct than

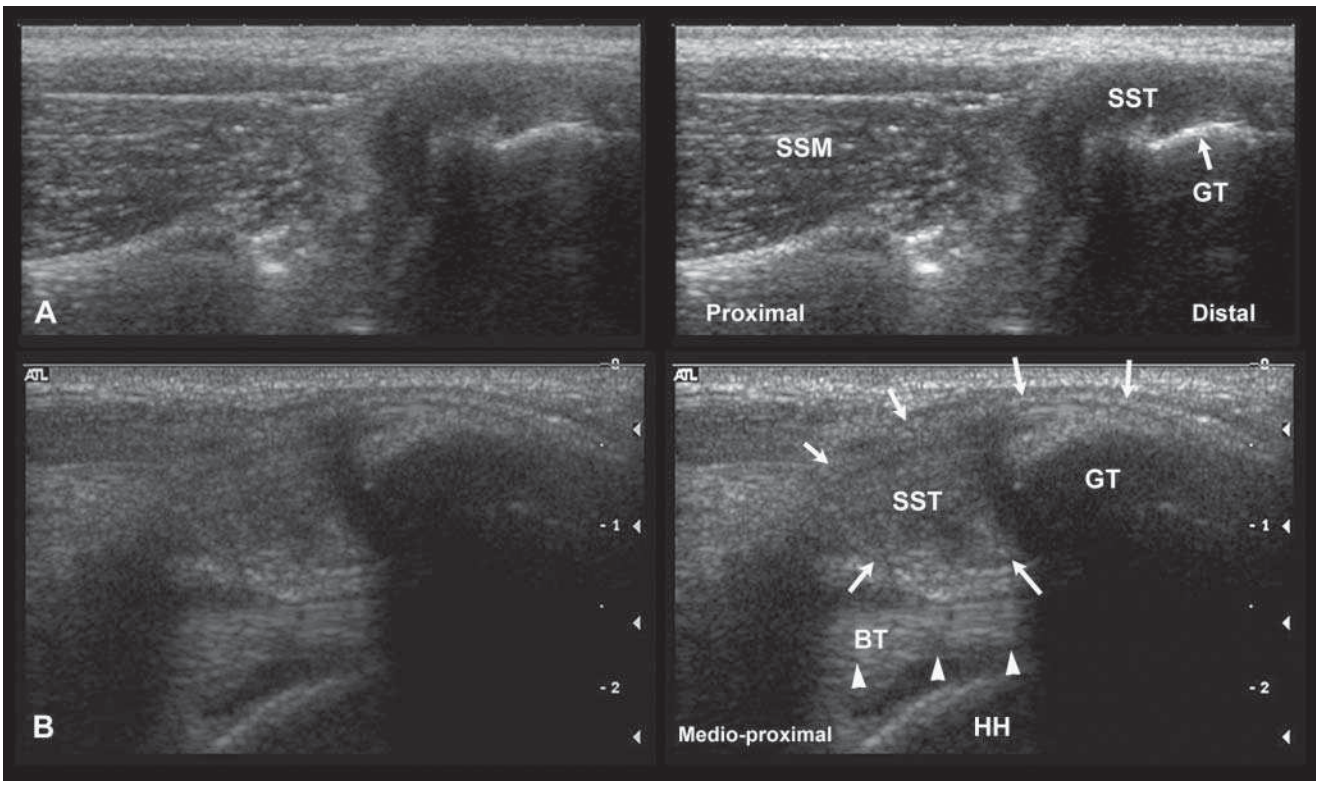


Figure 17.5. Normal sonographic anatomy of the supraspinatus muscle and tendon. Longitudinal **(A)** and transverse **(B)** sonographic and schematic images of the normal supraspinatus muscle (SSM) and supraspinatus tendon (SST) in a large-breed dog. The characteristic hypoechoic echotexture with small hyperechoic dots and lines of the supraspinatus muscle is seen. Because of the orientation and distribution of the tendon fibers, this portion also appears hypoechoic. It fans (arrows) around the humeral greater tubercle (GT) on which it inserts. The greater tubercle and the surface of the humeral head (HH) appear as thin, hyperechoic interfaces casting acoustic shadow. The biceps tendon (BT, arrowheads) and its sheath course caudally and medially, in proximity to the SST.

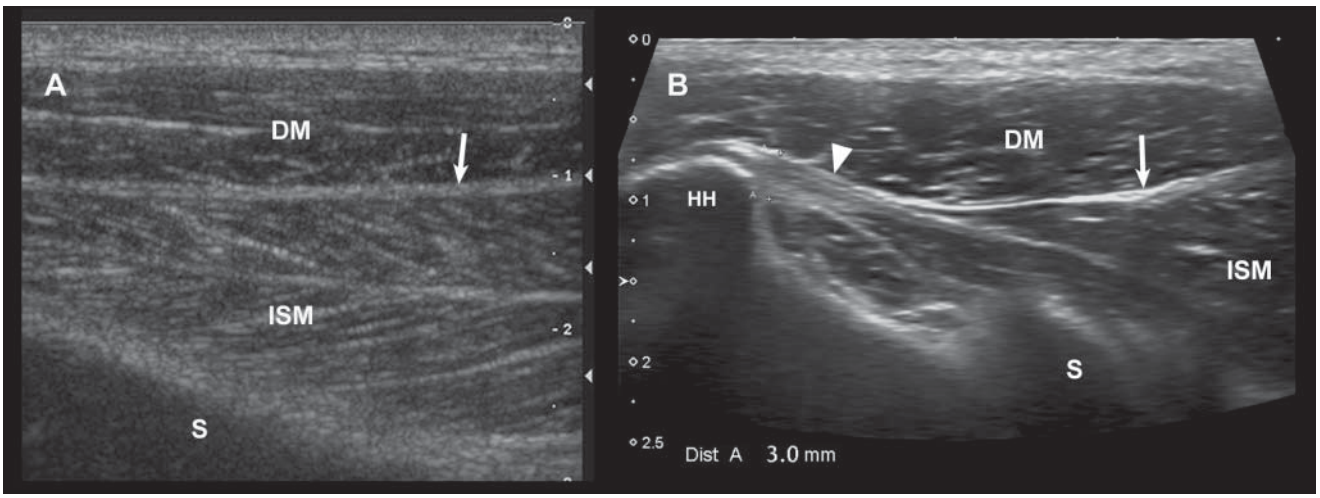


Figure 17.6. Normal sonographic anatomy of the infraspinatus muscle and tendon. A, B: Longitudinal sonographic images of the normal infraspinatus muscle (ISM) and tendon obtained at two different levels. The characteristic fishbone echotexture of the muscle is present. The deltoid muscle (DM) is in the near field, separated by a thin hyperechoic interface (arrow) that represents the intermuscular fascia (arrow). The shadowing hyperechoic surface of the scapula (S) is seen in the far field in **A** and **B**. The infraspinatus tendon (arrowhead and between the cursors) inserts on the lateral surface of the humeral head (HH), just caudal to the greater tubercle and insertion site of the supraspinatus tendon.

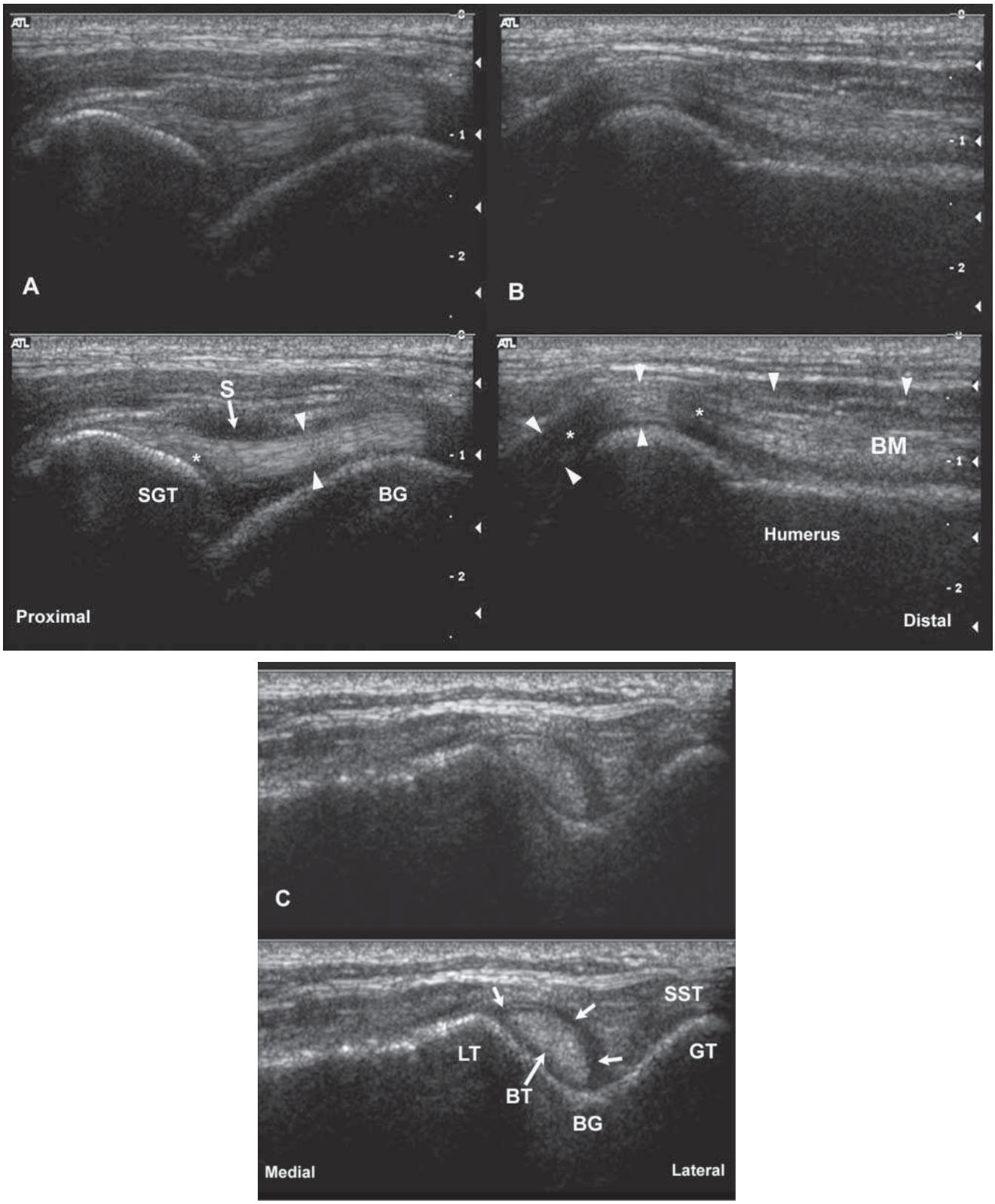


Figure 17.7. Normal sonographic anatomy of the biceps tendon in dogs. A, B: In these longitudinal sonographic and enhanced images of the normal biceps tendon, the most proximal **(A)** and distal **(B)** portions of this tendon are seen (between the arrowheads) (see probe B in Figure 17.1). The characteristic hyperechoic echotexture of the tendon is well visualized when imaged perpendicularly. This tendon is hypoechoic (*) at the level of origin on the supraglenoid tubercle (SGT), as well as in curved portions more distally. Deep to the tendon, the bicipital groove (BG) appears as a curved, hyperechoic interface. The proximal portion of the biceps muscle (BM) is seen distal to the humeral head. **C:** Transverse sonographic and enhanced images obtained at the level of the BG. When imaged perpendicularly, the biceps tendon (BT) appears as a uniformly hyperechoic oval to flat structure surrounded by a thin hypoechoic rim (arrows), representing the tendon sheath with some fluid. The biceps tendon slides along the lateral aspect of the lesser tubercle (LT), medial to the greater tubercle (GT) and supraspinatus tendon of insertion (SST).

the lesser tubercle medially, which is seen only as a small elevation of the reflective line on the surface of the bone. The bicipital groove appears as a smoothly marginated concave hyperechoic line between these tubercles (Figure 17.7C). The intertubercular ligament cannot be distinguished from the surrounding soft tissue. Distally, the distal outpouch of the synovial sheath can appear lobulated in some dogs.

The longitudinal examination is then performed by following the tendon across the joint to its origin on the supraglenoid tubercle of the scapula. More deeply, the hyperechoic convex line of the humeral head bony surface becomes visible. Proximal to this point of orientation, the hypoechoic to anechoic area of the joint space and, dorsally, the supraglenoid tubercle can be distinguished. The latter structure is visible as a slightly convex, hyperechoic interface associated with acoustic shadowing. Because of its curvature along the bicipital groove, the tendon hyperechoic echotexture can be evaluated only when perpendicular to the probe (Figure 17.7B). At the level of the supraglenoid tubercle, the tendinous fibers curve and become hypoechoic as they enter the bone (Figure 17.7A), mimicking a lesion.

Finally, by flexing, extending, abducting, and adducting the shoulder joint, the tendon can be dynamically examined, helping identifying potential adhesions and joint fragments. When the joint is flexed, the hypoechoic joint space enlarges to approximately twice its original size (Kramer et al. 2001b).

Shoulder Joint Space and Medial Glenohumeral Ligament

Positioning of the transducer perpendicular to the joint space enables visualization of the surface of the humeral head as a semicircular, convex, hyperechoic line with distal acoustic shadowing. This hyperechoic subchondral interface should appear smooth and continuous, and covered with a thin anechoic band that represents the articular cartilage. Because of the semi-circular anatomy of the head, only a small section of the surface can be assessed at one time. The articular cartilage is covered by the hypoechoic synovium. The outer, curved line above the cartilage represents the joint capsule (Figure 17.8). This merges with the echotexture of the covering musculature. On the medial side of the joint, the medial glenohumeral ligament, although relatively thin, may sometimes be recognized (Cogar et al. 2008).

Sonographic Features of Specific Shoulder Disorders

Supraspinatus Muscle

Supraspinatus Calcifying Tendinopathy Inflamed or degenerated supraspinatus tendons can be thickened and inhomogeneous because of fibrous disruption, hemorrhage, and/or fibrosis. Mineralization can also be found in the region of insertion on the greater tubercle in the distal part of the tendon. These mineral foci appear as small, hyperechoic, irregularly defined structures, with or without distal acoustic shadowing and with or without a surrounding hypoechoic to anechoic area (reaction tissue) (Long and Nyland 1999) (Figures 17.9, 17.10). While such mineralization may be associated with lameness in dogs and even impinge on the adjacent bicipital tendon and sheath, it may be found in clinically normal dogs, unilaterally or bilaterally (Lafluente et al. 2009).

Infraspinatus Muscle

Contracture of the Infraspinatus Muscle Distinct abnormalities in both echogenicity and echotexture are seen in the affected muscle. The transition from muscle to tendon, and the tendon itself, are usually affected and the affected portions are inhomogeneous

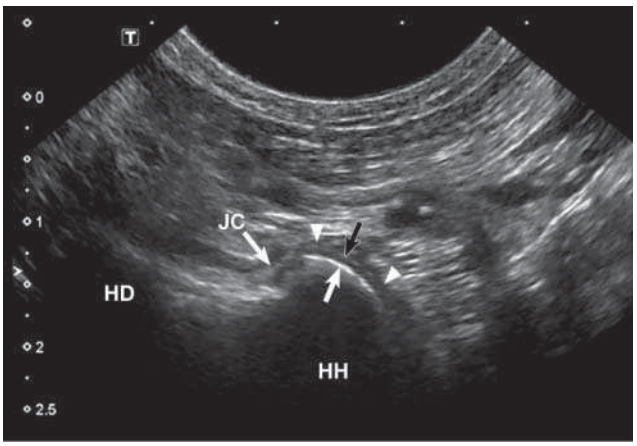


Figure 17.8. Normal sonographic anatomy of the shoulder joint. Longitudinal sonographic image obtained at the caudolateral aspect of the shoulder, showing a portion of the humeral diaphysis (HD) and head (HH). The subchondral bone plate appears as a shadowing, hyperechoic, convex interface (white arrow), covered with a thin anechoic layer representing the articular cartilage (black arrow), and a small volume of hypoechoic synovial fluid and hypoechoic synovium, which are often confluent (arrowheads). The joint capsule (JC) may be visualized, in part, as an outer hyperechoic layer, or confluent with the extra-articular tissues.

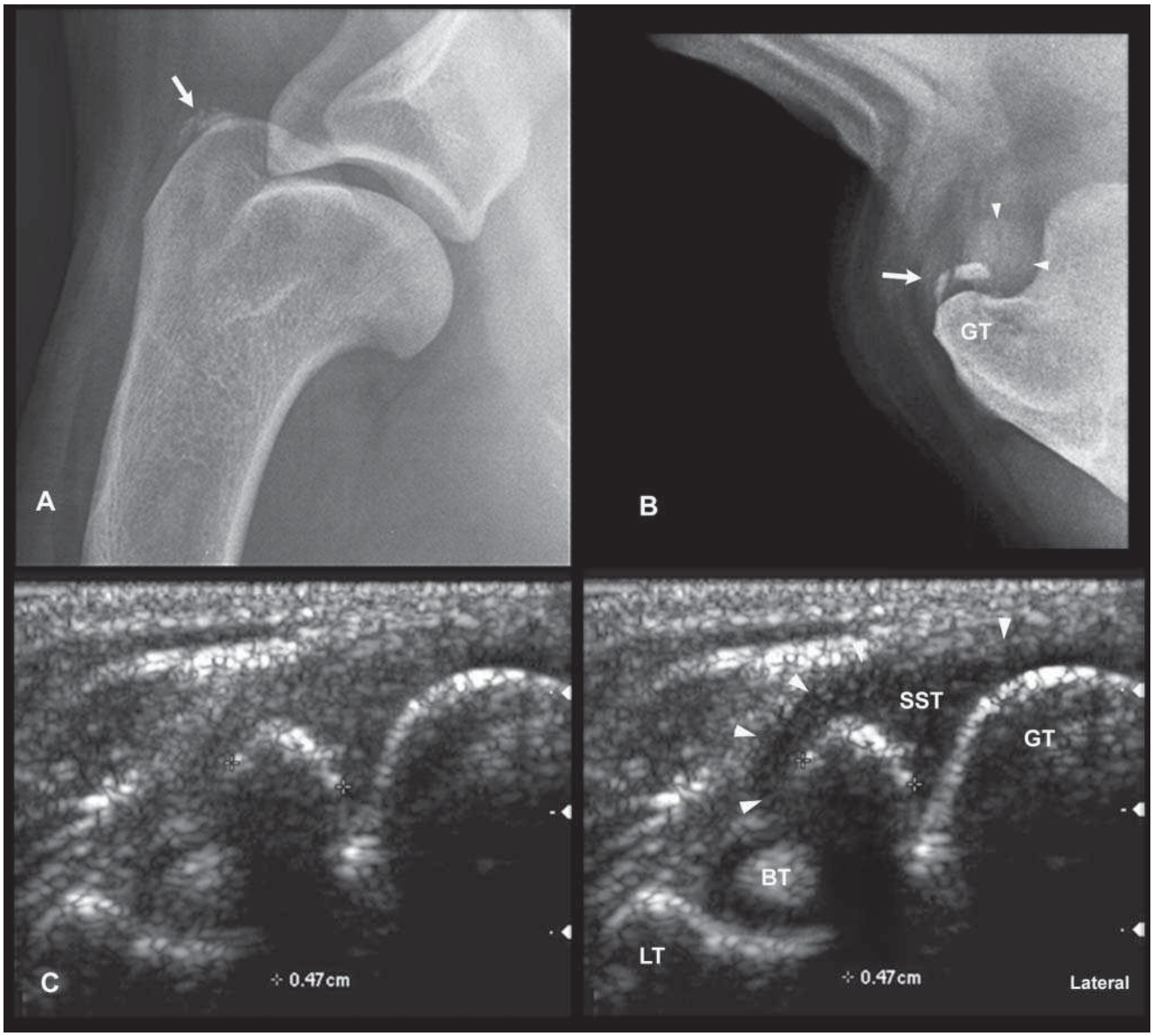


Figure 17.9. **Calcifying supraspinatus tendinopathy. A, B:** Mediolateral and tangential radiographs of the bicipital groove in a large-breed dog with shoulder pain. Small mineral opacities (arrows) are observed in the region of insertion of the supraspinatus tendon, located just lateral to the bicipital groove and biceps tendon (arrowheads). **C:** Transverse sonographic and enhanced images of the bicipital groove in the same dog. An irregular, hyperechoic, shadowing focus is in the distal supraspinatus tendon (SST), consistent with mineralization. This mineralization, as seen in the tangential radiographic projection, is adjacent to the biceps tendon (BT). Moderate distension of the BT sheath is observed, as the result of tenosynovitis, which was suspected to be secondary to the supraspinatus tendon lesion. GT, greater tubercle; LT, lesser tubercle.

with hypoechoic and/or hyperechoic zones, with loss of the normal echotexture (Figure 17.11) (Siems et al. 1998; Franch et al. 2009).

Biceps Tendon

Tenosynovitis The bicipital tendon appears mildly to severely thickened, losing its normal flat to oval shape to become rounded (Figures 17.12–17.14). Its normal fibrillar pattern can also be affected and hypoechoic areas caused by partial tears and/or hemorrhage can be seen. The affected tendon may also appear significantly inhomogeneous. Tendon sheath effusion, which is often observed, appears as an enlarged hypoechoic to anechoic halo surrounding the affected tendon. The effusion can range from mild

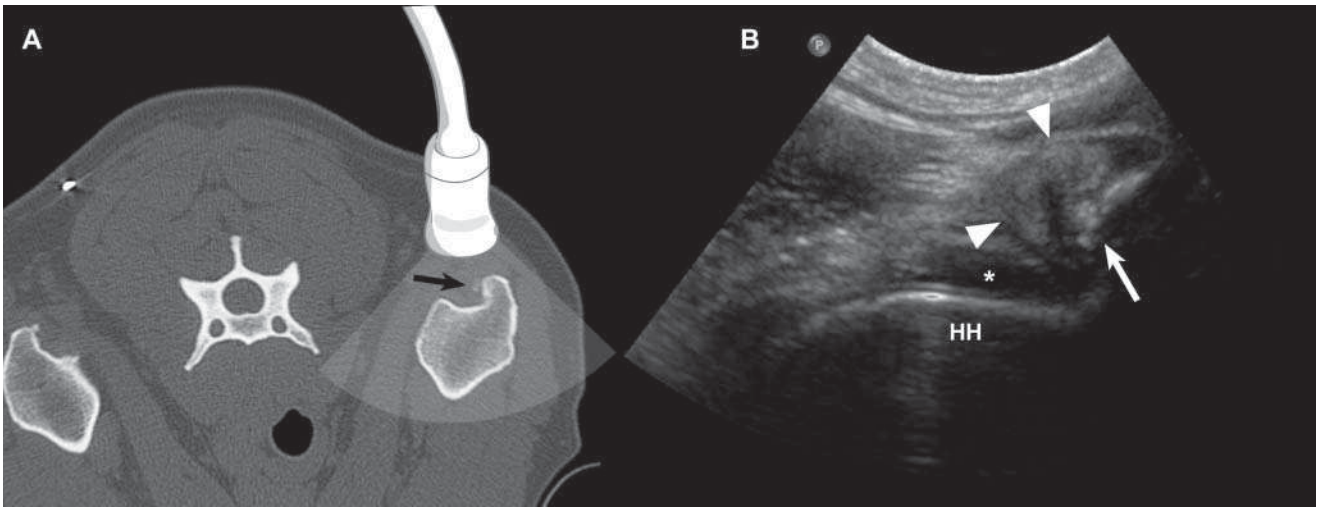


Figure 17.10. Chronic supraspinatus tendinopathy. Transverse computed tomographic **(A)** and sonographic **(B)** images of the insertion site of the supraspinatus tendon (arrowheads) in a large-breed dog with shoulder pain. The supraspinatus tendon is inhomogeneous and mostly hyperechoic, with small hyperechoic foci consistent with mineralization (arrows) next to the greater tubercle. The adjacent bicipital tendon sheath is distended (*). HH, humeral head.

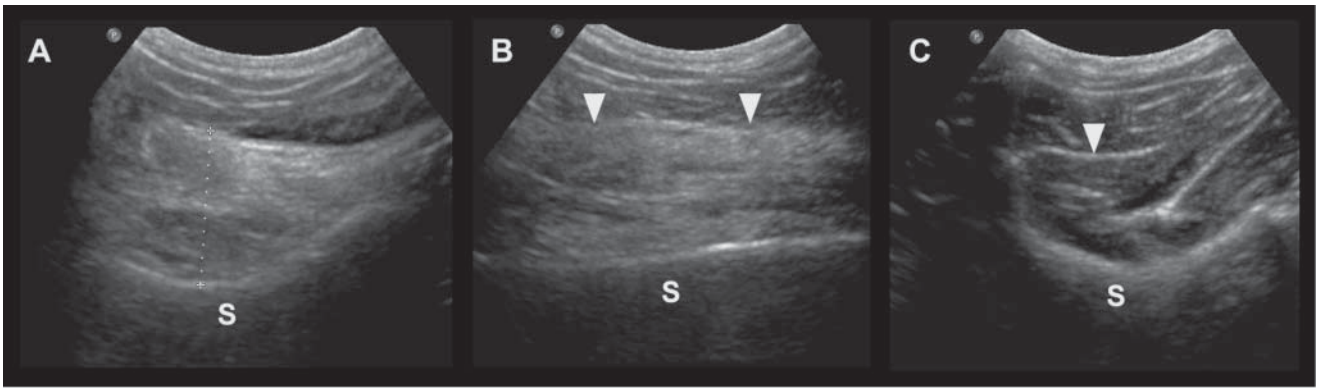


Figure 17.11. Contracture of the infraspinatus muscle. Transverse **(A)** and longitudinal **(B)** sonographic images obtained with the probe placed over the caudal portion of the scapula (S) of a dog with chronic lameness. The infraspinatus muscle (between calipers, arrowheads) is enlarged and hyperechoic. **C:** The contralateral muscle is normal in size and echogenicity.

to severe and is well visualized on transverse images over the bicipital groove. In most cases, the thickened synovium cannot be easily distinguished from the synovial fluid, although irregular synovial thickening or flocculent synovial fluid can be observed in some dogs (Long and Nyland 1999). Fibrous adhesions with the tendon, particularly within the bicipital groove, can also be seen dynamically. In severe cases, the tendon sheath develops a bulge in the direction of the lesser tubercle (Rivers et al. 1992; Kramer et al. 2001b; Esterline et al. 2005).

Osteophytes can form within the bicipital groove as a result of chronic degenerative joint disease and/or bicipital tenosynovitis. They are attached to the tendon sheath and appear as irregular hyperechoic structures that cast shadows when larger than 2–3 mm (Figures 17.13, 17.14). In severe cases, this mineralization may form a tunnel around the tendon, significantly hampering its visualization. Mineralization of the bicipital tendon sheath can also occur and cannot easily be distinguished from migrating calcified bodies, such as those related to osteochondritis dissecans.

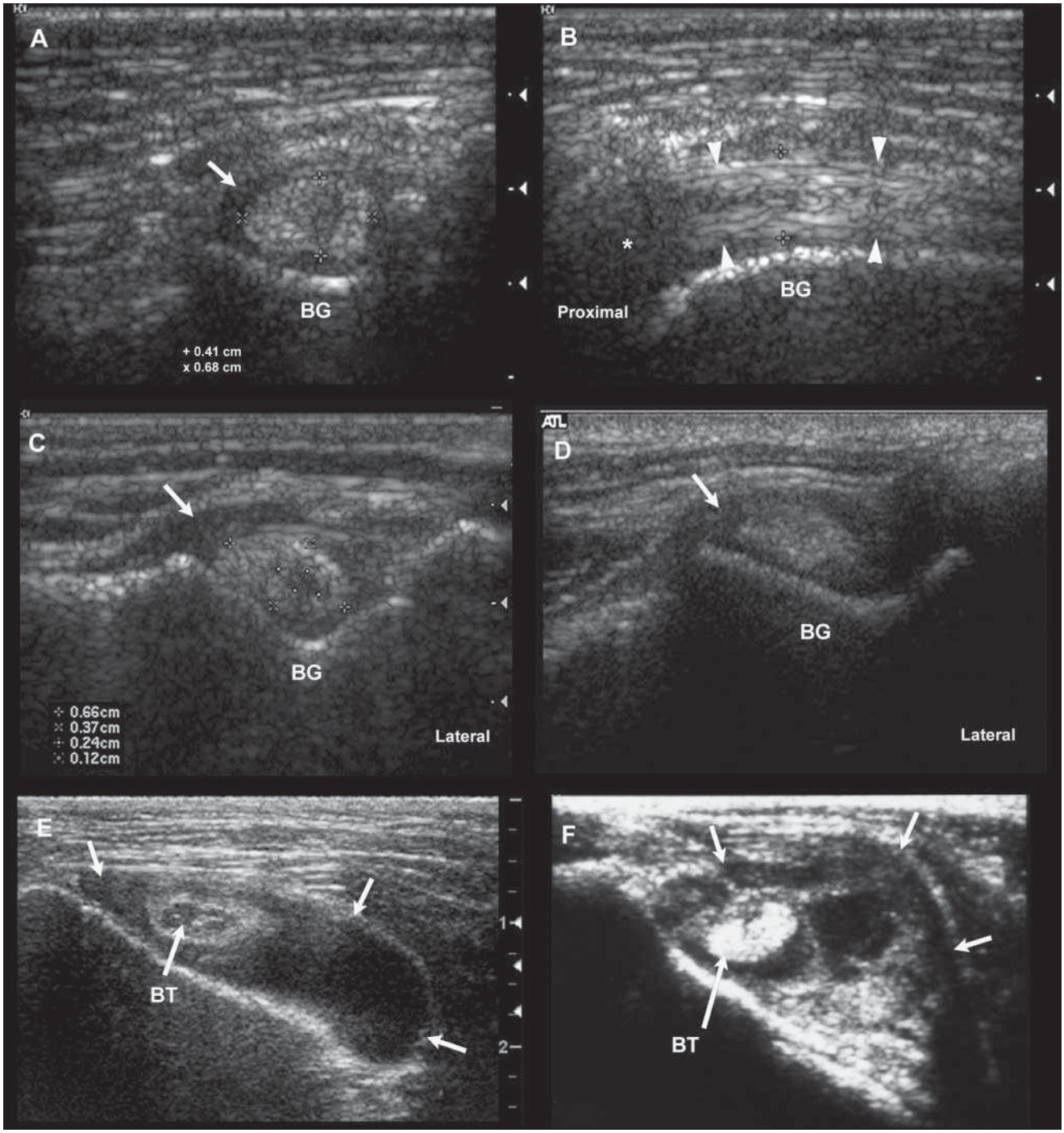


Figure 17.12. **Bicipital tenosynovitis. A, B:** Transverse **(A)** and longitudinal **(B)** sonograms of the biceps tendon (calipers and arrowheads) of a Labrador Retriever scanned at the level of the bicipital groove (BG). The tendon is enlarged and rounded. A hypoechoic core lesion is in the center of the tendon, consistent with central fibrous rupture and hematoma. The tendon sheath (arrow) is mildly distended. **C–E:** Variable levels of tendon sheath distension (arrows) in several dogs with tenosynovitis. Hypoechoic core lesions are in the central portion of the biceps tendon (BT) **(E)**. **F:** Distension of the tendon sheath in another dog with bicipital rupture and hemorrhage. The tendon sheath (arrows) is filled with an inhomogeneously echogenic hematoma that encircle the BT.

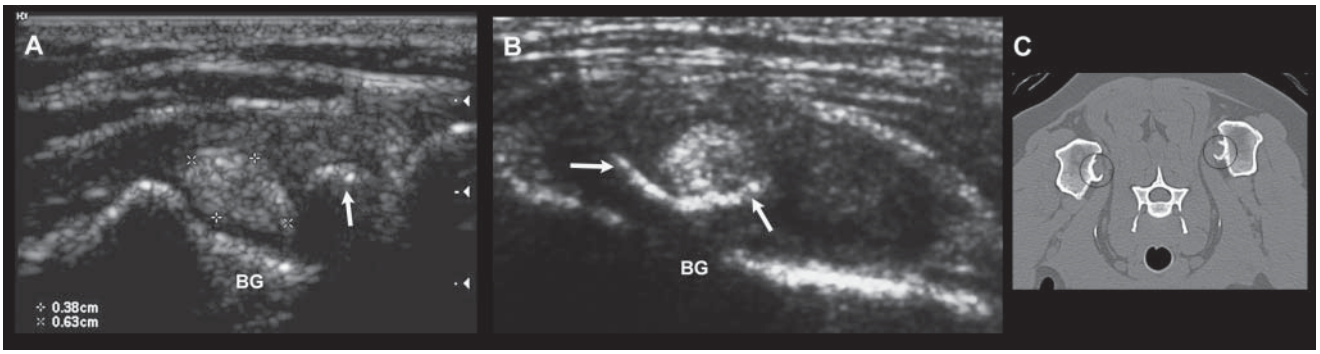


Figure 17.13. Chronic bicipital tenosynovitis with mineralization. Transverse sonographic **(A and B)** and computed tomographic (CT) **(C)** images obtained in three dogs at the level of the bicipital groove (BG). **A:** A hyperechoic, shadowing mineral focus (arrow) is present at the lateral aspect of the bicipital tendon sheath. The adjacent tendon (between the cursors) is mildly thickened. **B:** Tendon sheath wall mineralization can appear as a hyperechoic semicircular groove (arrows) that may partially or completely encircle the biceps tendon**. C:** The mineralization is well appreciated on this CT image as it partially encircles the biceps tendon.

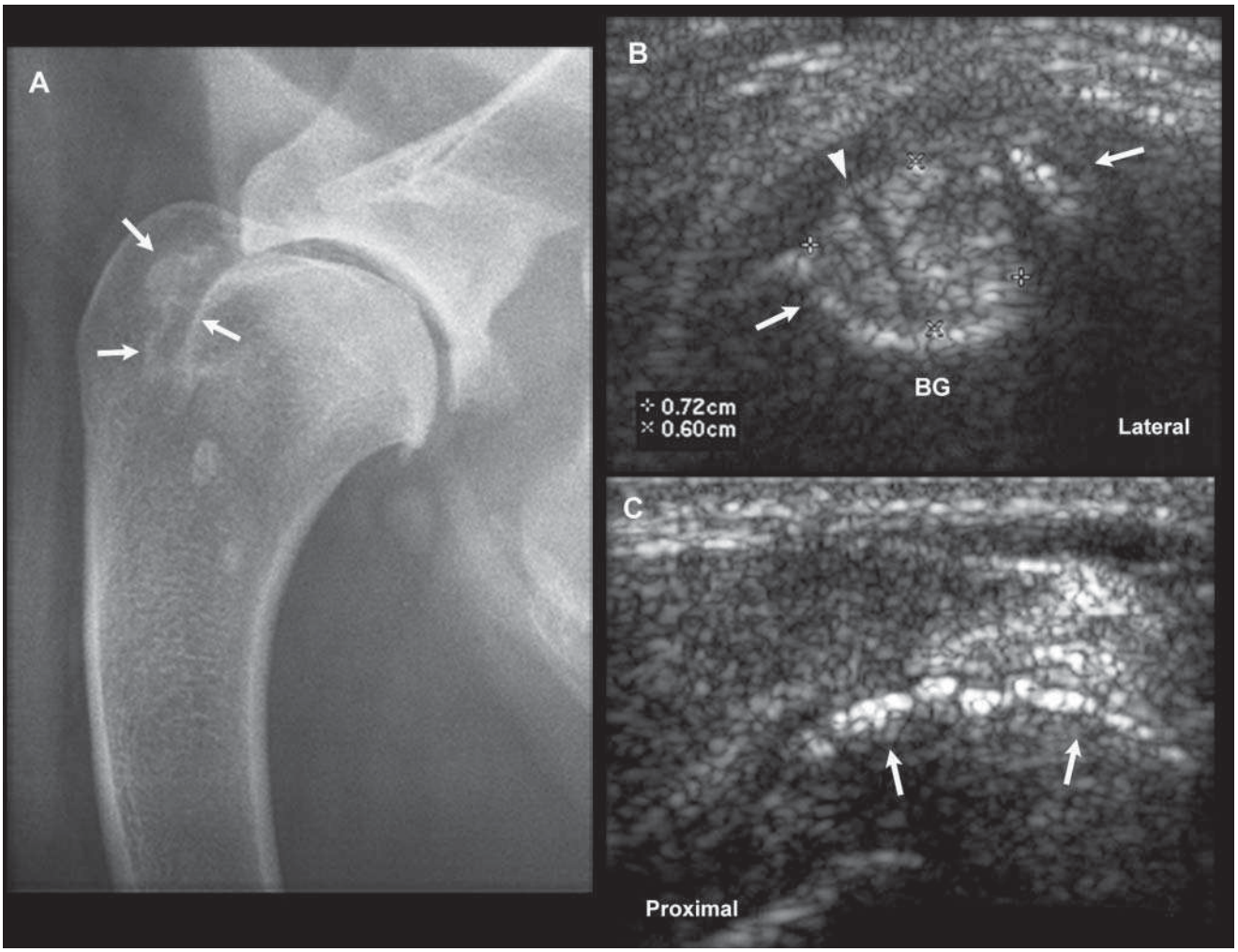


Figure 17.14. Chronic bicipital tenosynovitis with mineralization. A: Mediolateral radiographic view of the shoulder of a 4-year-old Rottweiler with chronic shoulder pain and lameness. Mineralization is found along the bicipital groove (arrows), as well as in the distal region of the tendon sheath. Periarticular new bone formation is also present at the caudal aspect of the shoulder, consistent with degenerative joint disease. **B, C:** Transverse **(B)** and longitudinal **(C)** sonographic images of the bicipital groove (BG) on which an irregular and hyperechoic mineral cast partially encircles the biceps tendon (arrows). The tendon (between the cursors) is enlarged and presents a hypoechoic line (arrowhead) consistent with a tear.

Complete and Partial Tendon Ruptures With complete rupture, the fibrillar structure of the tendon is disrupted. The gap between retracted tendon stumps is usually anechoic or hypoechoic, and moderate to severe tendon sheath effusion can be observed as the result of hemorrhage (Figure 17.15). The distal stump, which is attached to the muscle, is typically more retracted and often of mixed echogenicity and echotexture.

Most partial ruptures occur in the area of the supraglenoid tubercle. At this site, multiple, small, hyperechoic bone fragments with acoustic shadowing can be visible (Figure 17.16A). The proximal part of the tendon tissue appears hypoechoic and mildly to moderately inhomogeneous. In contrast to a complete rupture, areas of tendon tissue displaying a normal fibrillar echotexture can be found in a transverse image. A hypoechoic to anechoic region, can be found in the central portion of the affected tendon **(core lesion)**, at the level of fibrillar disruption and hematoma formation, associated with tendon enlargement (Figures 17.12, 17.16B). A cleft can also be observed in some partially ruptured tendons (Figure 17.14B). Tendon sheath effusion develops around the tendon (Kramer et al. 2001b).

Fractures of the Supraglenoid Tubercle The fractured supraglenoid tubercle is visualized at the proximal extent of the biceps tendon as a hyperechoic, more or less convex structure with smooth margins and acoustic shadowing. The fragment can be seen moving with the tendon during dynamic flexion and extension of the shoulder, in association with moderate tendon sheath effusion. The surface of the tubercle appears irregular, and a bone defect is often observed. In cases of partial avulsion fracture, small bone fragments can be identified adjacent to the supraglenoid tubercle. Hyperechoic foci are observed in the

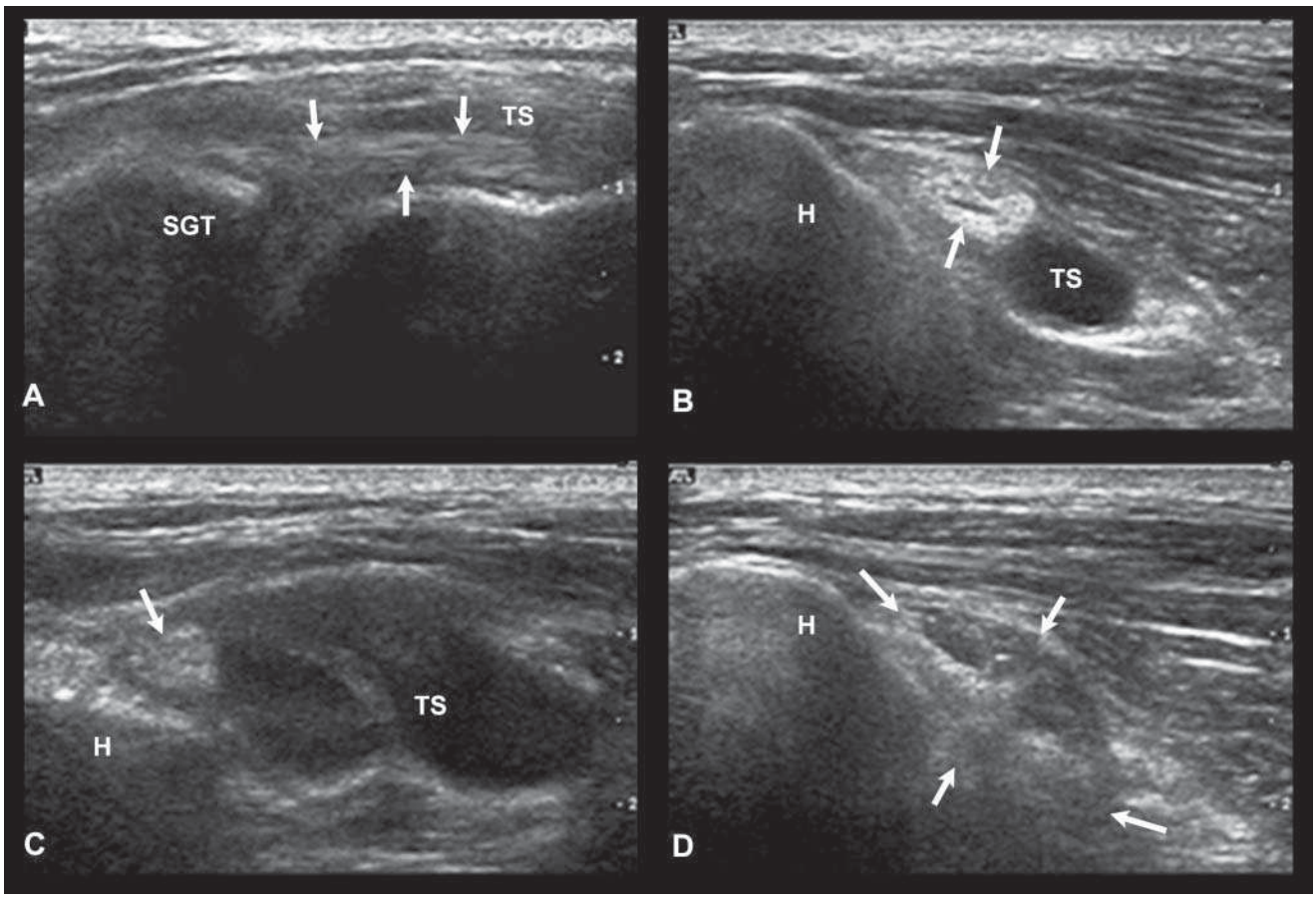


Figure 17.15. Complete bicipital tendon rupture. Longitudinal **(A)** and transverse **(B–D)** sonographic images of the biceps tendon and muscle in a dog with non-weight-bearing lameness. Significant distension of the tendon sheath (TS) is recognized. Hyperechoic and inhomogeneous retracted ends of the biceps tendon (arrows in **B** and **C**) are noted. Mildly echogenic regions, consistent with hemorrhage, are in the synovial sheath **(C)**. The proximal portion of the biceps tendon (**A**, arrows) and muscle (**D**, arrows) is inhomogeneous. Chronic bicipital tenosynovitis with rupture was diagnosed. H, humerus; SGT, supraglenoid tubercle.

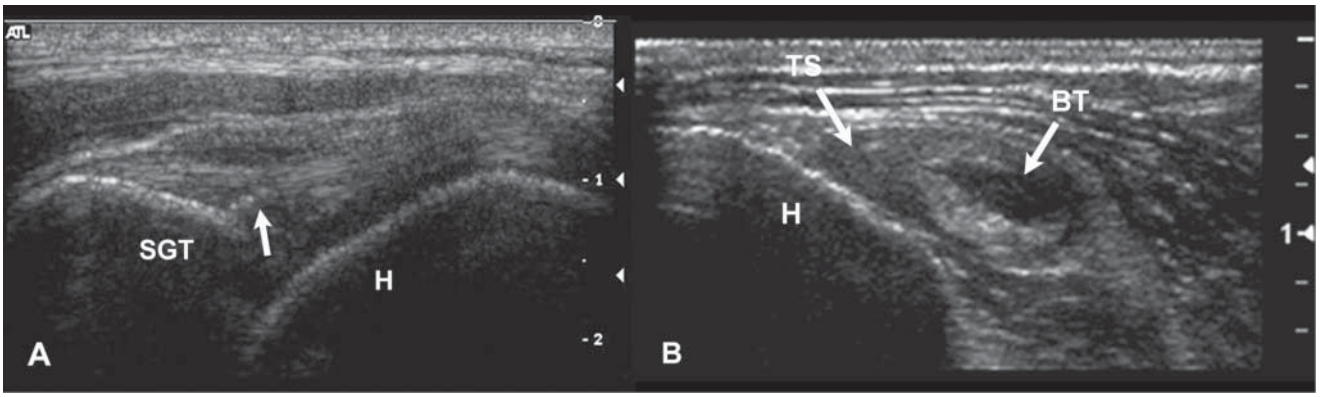


Figure 17.16. **Partial bicipital tendon rupture. A:** Longitudinal sonogram of the proximal portion of the biceps tendon in a dog with partial biceps tendon avulsion. An inhomogeneous, hypoechoic area (arrow) with small hyperechoic dots consistent with mineral fragments is just distal to the region of insertion on the supraglenoid tubercle (SGT). H, humerus. **B:** Transverse sonogram in another dog with partial tendon rupture. An oval anechoic area is in the central portion of the biceps tendon (BT), which is also enlarged. The tendon sheath (TS) has excessive fluid accumulation.

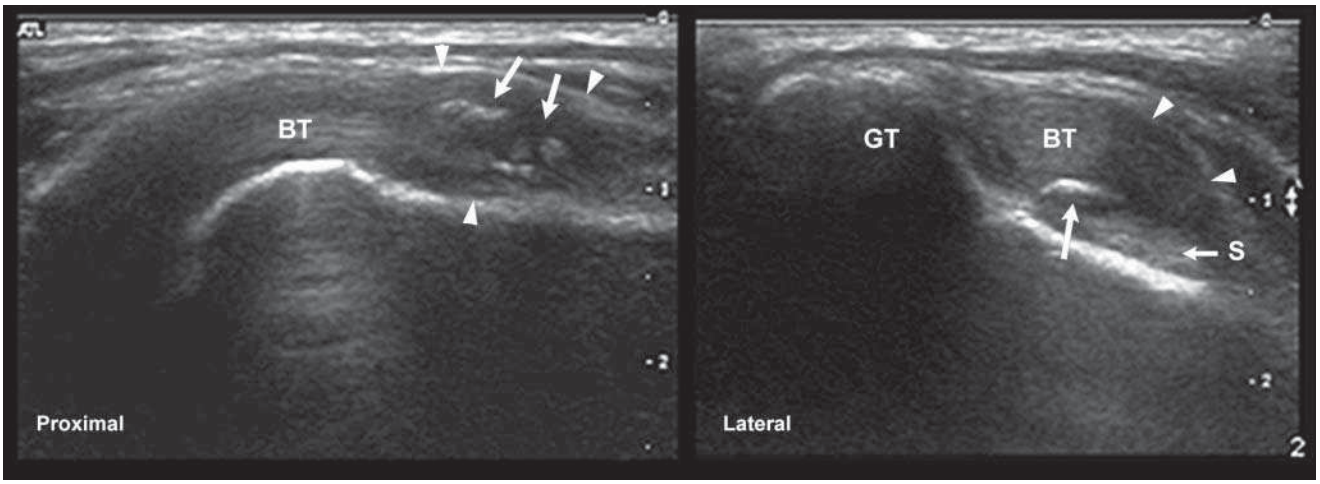


Figure 17.17. **Migrating osteochondral fragments.** Longitudinal and transverse sonograms of the distal tendon sheath in a dog with osteochondritis dissecans of the humeral head. Numerous hyperechoic foci (arrows) are in the distended tendon sheath (arrowheads), around the bicipital tendon (BT). Thickening of the synovial lining (S), consistent with synovitis, is also apparent on the surface of the humerus. GT, greater tubercle.

proximal tendon and may be associated with acoustic shadowing (Kramer et al. 2001b) (Figure 17.16A).

Calcified Bodies in the Tendon Sheath Free bodies in the tendon sheath and caudal to the humeral head are usually caused by osteochondritis dissecans (OCD). Depending on their size, these are chips (>2 mm), microchips (1–2 mm), or stipples (<1 mm). Ultrasonographically, these bodies appear as hyperechoic, rounded or flat structures of different sizes that may cast acoustic shadows. They can be located anywhere around the tendon within the synovial sheath, which is usually distended (Kramer et al. 2001b) (Figure 17.17). These migrated bodies may adhere to the synovium and be difficult to differentiate from osteophytic formations or osteochondromas.

Tendon Luxation Rupture of the transverse ligament causes medial luxation of the tendon over the lesser tubercle. This should be suspected when the tendon is not found in the bicipital groove, but replaced with moderate effusion. The oval tendon with its typical fibrillar echotexture may be found in the region of the lesser tubercle (Figure 17.18). During dynamic examination, the tendon slides back into the groove intermittently (Kramer et al. 2001b).

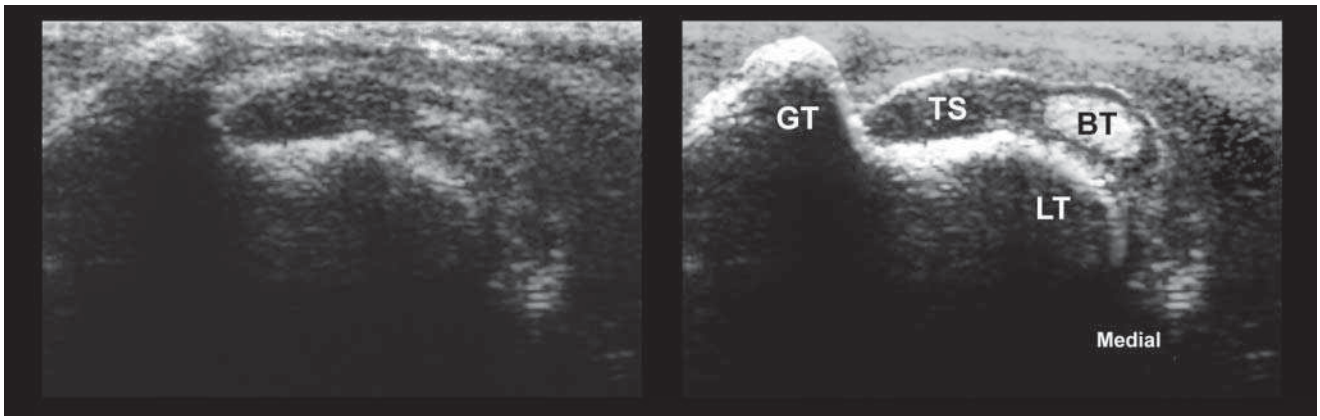


Figure 17.18. Biceps tendon luxation. In these transverse sonographic and enhanced images of the bicipital groove of a dog, the biceps tendon (BT) appears displaced medially over the lesser tubercle (LT). The tendon sheath is filled with fluid at the level of the bicipital groove. GT, greater tubercle; and TS, tendon sheath.

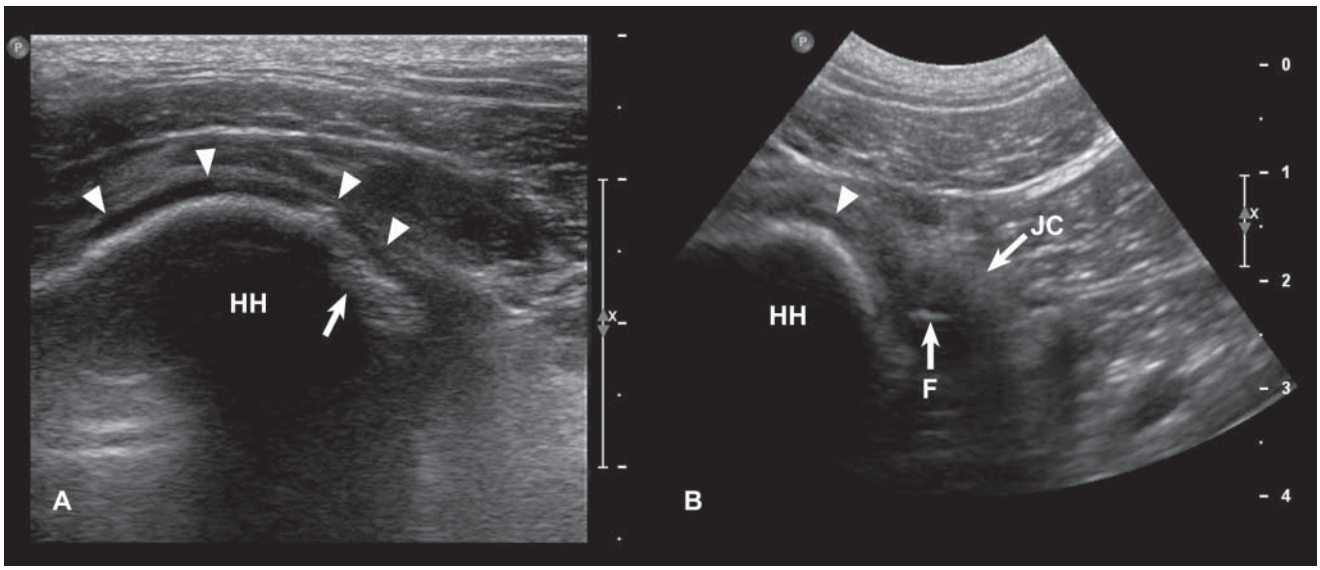


Figure 17.19. Humeral head osteochondritis dissecans. Longitudinal sonographic images of the caudal portion of the humeral head (HH) **(A)** and the caudal joint recess **(B)** in a dog with osteochondritis dissecans (OCD). **A:** The humeral cartilage (arrowheads) is irregular and hyperechoic in its centrocaudal portion, at the level of incomplete subchondral mineralization (arrow). **B:** A mineralized osteochondral fragment (F) has migrated in the caudal joint recess. The joint capsule (JC) is thickened and hyperechoic. The arrowheads point to the intact humeral head (HH) cartilage.

Scapulohumeral Joint

Osteochondritis Dissecans The subchondral defect on the caudal part of the humeral head can be visualized as an irregularity in the hyperechoic convex bone surface. The defect appears hypoechoic, with or without hyperechoic dots or lines, because of disturbed endochondral ossification and osteochondral fissures or fragments (Figure 17.19). "Joint mice" may be found in the caudal synovial recess of the joint, which is typically distended, or may migrate craniodistally into the bicipital tendon sheath (Vandevelde et al. 2006) (Figure 17.17).

Instability Shoulder joint instabilities represent an important source of thoracic limb lameness in dogs that remains difficult to diagnose. Abnormal gliding of the humeral head may be assessed dynamically, but this evaluation is subjective and requires a comparison with the contralateral shoulder. Thickening of the medial glenohumeral ligament may appear thickened and hyperechoic with surrounding effusion. However,

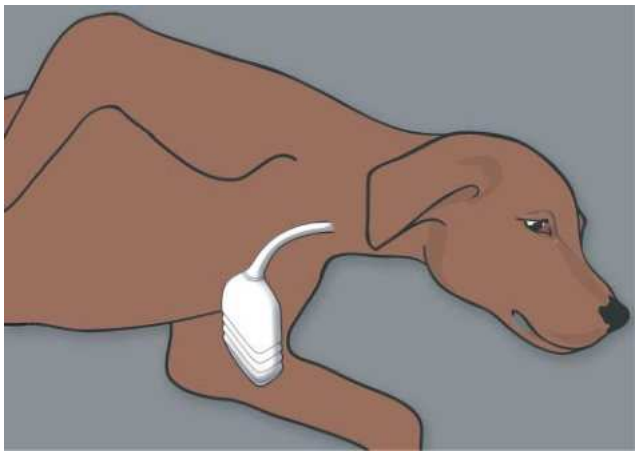


Figure 17.20. Scanning technique for the medial aspect of the elbow. Illustration showing the position of the dog and ultrasound probe when scanning the medial aspect of the elbow.

the accuracy of this modality for detecting shoulder instability remains low (Cogar et al. 2009).

Elbow

Although radiography, CT, and MRI are most commonly used to image the elbow, ultrasonography represents a complementary tool in practice, particularly in the assessment of soft-tissue structures and identifying joint effusion and fragments. The approach to the normal canine elbow has been well described (Knox et al. 2003; Lamb and Wong 2005).

Scanning Technique and Normal Ultrasonographic Anatomy

A linear, high-frequency (>10 MHz) ultrasound transducer is preferred for assessing the small superficial portions of the elbow. This joint can usually be examined without sedation. The hair around the elbow is clipped, and the patient is initially placed in lateral recumbency with the elbow of interest up. After the lateral aspect of the joint has been evaluated, the patient is turned over to assess the medial structures more easily (Figure 17.20).

Lateral Aspect: Muscles and Lateral Collateral Ligament

The humerus and the brachialis muscle on the proximal craniolateral aspect of the joint are examined. During flexion and extension of the elbow, the hypoechoic brachialis muscle can be shown to slide against the smooth, linear, hyperechoic interface of the humerus. The distal portion of the triceps muscle can be seen caudolaterally inserting onto the olecranon.

Distally, the lateral region of the elbow is initially scanned in cross-section to better identify all muscles and tendons. Each muscle and tendon is then scanned longitudinally. The most conspicuous muscle is the extensor carpi radialis located on the craniolateral aspect of the antebrachium. Caudal to this region, the common and lateral digital extensor tendons, as well as the ulnaris lateralis and flexor carpi radialis, are visualized.

The lateral collateral ligament is very thin and more easily assessed proximally, because it displays multiple, fine, hyperechoic parallel lines that attach to the lateral humeral epicondyle. The distal aspect of the ligament may be imaged by sliding the transducer distally along the lateral aspect of the radius. It appears hypoechoic if the ultrasound beam is not directed perpendicular to its long axis.

Caudal Aspect: Triceps, Olecranon, and Anconeal Process

The elbow joint is flexed, and the ultrasound probe is initially placed on the cranial aspect of the olecranon. When a sagittal, perpendicular plane is used, the distal portion of the triceps muscle appears as a hyperechoic structure with multiple fine parallel lines, representing the collagen fibers, which insert onto the olecranon. Two distinct protuberances are recognized on the proximal aspect of the olecranon – the craniolateral and craniomedial tuberosities – which are located proximal to the anconeal process. The transducer is then slightly rotated laterally, enabling visualization of the outline of the anconeal process. This process is examined as the transducer is moved medially from the most lateral edge of the olecranon. The normal anconeal process appears as a curved, hyperechoic interface. Artifactual pseudo-indentations are a common finding on the surface of the bone. The caudal joint capsule is usually not visible.

Cranial Aspect: Joint Space, Muscles, Vessels, and Nerves

This region is examined after the elbow joint has been extended. Proximally, both the brachialis and biceps brachii muscles (Figure 17.21A) can be distinguished; distally, the extensor carpi radialis muscle is visible. In addition, vessels and nerves embedded within the adipose tissue can be visualized. The cranial portion of the humeroradial joint space appears as a thin, hypoechoic cleft between the smooth, hyperechoic

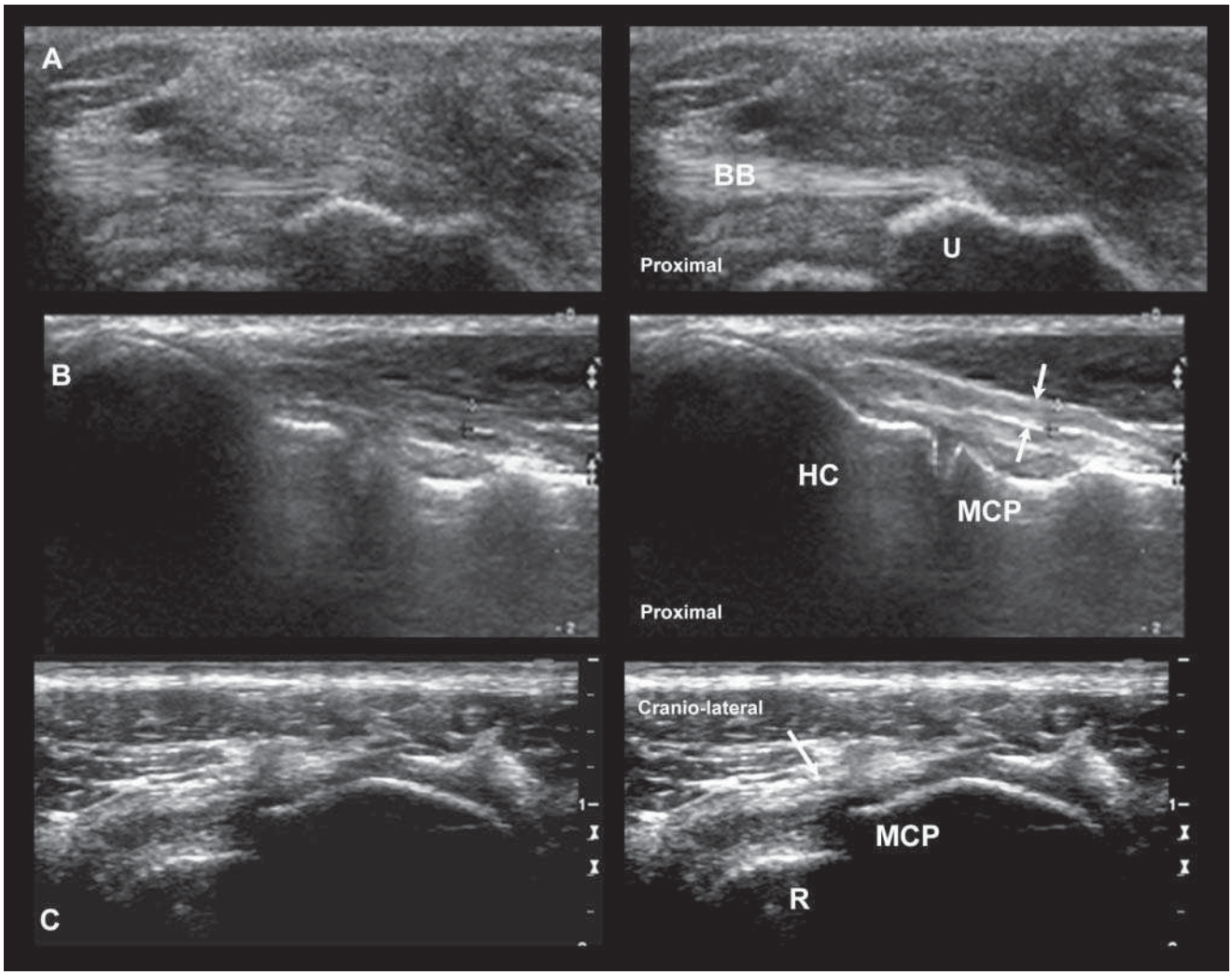


Figure 17.21. **Normal sonographic anatomy of the canine elbow. A:** Longitudinal sonographic and enhanced images of the craniomedial aspect of the elbow. A portion of the distal biceps brachii (BB) appears as a hyperechoic fusiform structure with dense hyperechoic lines inserting on the craniomedioproximal surface of the ulna (U). **B:** Longitudinal sonographic and enhanced images obtained just medial to **A**. The medial collateral ligament (arrows) is just medial to the medial coronoid process (MCP) and humeral condyle (HC). **C:** Transverse-oblique sonographic and enhanced images of the craniomedial aspect of the elbow. The hyperechoic interface of the MCP is well visualized adjacent to the head of the radius (R). The joint capsule is a hyperechoic band (arrow) that cannot be consistently distinguished from collateral ligaments.

contours of the humeral condyle and radial head. The normal joint capsule and synovium cannot be differentiated.

Medial Aspect: Medial Collateral Ligament and Medial Coronoid Process

In the proximal caudomedial region of the elbow, the two heads of the triceps brachii muscle can be differentiated. The medial epicondyle is initially assessed in a longitudinal plane and appears as a curved, slightly irregular, hyperechoic interface on the distomedial aspect of the humerus. The medial collateral ligament, which merges from the medial epicondyle, appears proximally as a thin, linear, hyperechoic structure that is densely packed with fine, parallel echoic lines (Figure 17.21B). The ligament fibers spread caudally to the ulna and become slightly thicker near the radius. Because of the oblique course of the medial collateral ligament, it is often not possible to identify the fibrillar pattern in the distal portion (Lamb and Wong 2005). The biceps brachii tendon can be visualized on the cranial aspect of the distal humerus and followed to its insertion sites on the ulnar and radial tuberosities, just

Figure 17.23. Fragmentation of the medial coronoid process. A: Medial view of the elbow of a 12-month-old Labrador Retriever dog produced with computed tomographic (CT) volume-rendering, on which the fragmentation of the medial coronoid process (FMCP) is well visualized. **B:** This longitudinal sonographic image was obtained with the probe placed medially on the joint, and the marker oriented proximally. The joint capsule is distended (arrowhead) and a gap (arrow) is present at the distal aspect of the medial coronoid process (MCP). The humeral condyle (HC) is mildly irregular. **C, D:** Corresponding transverse CT **(C)** and sonographic **(D)** images in which a fissure (arrows) extends through the MCP. The joint capsule is distended (arrowhead). R, radial head; U, ulna.

adjacent to the medial coronoid process (MCP; Lamb and Wong 2005) (Figure 17.21A). This tendon shows a typical echotexture with hyperechoic lines. When the probe is moved proximally during a transverse scan, the surface of the MCP comes into view as an angular process on the medial aspect of the ulna (Figure 17.21). The MCP is located deep to the medial collateral ligament and biceps tendon (Lamb and Wong 2005). A 90° flexion of the elbow and rotation of the forearm around its longitudinal axis may facilitate the identification of this structure.

Sonographic Features of Specific Elbow Disorders

Osteoarthritis

Even minor effusions of the elbow joint can be visualized. Anechoic fluid in a recess of the joint is considered abnormal and is most commonly associated with elbow dysplasia. With chronic degenerative joint disease (DJD), the joint capsule is visible as a hyperechoic, thick line between the synovium and synovial fluid, and the surrounding musculature. Periarticular new bone formations, caused by osteoarthritis, appear as irregularly circumscribed protuberances on the bony surfaces (Figure 17.22).

Fragmented Medial Coronoid Process (FMCP)

Sonographic detection of the FMCP in dogs is limited, for several reasons (Seyrek-Intas et al. 2009). Fissures and non-displaced or deep fragments are difficult to visualize, and displaced fragments may be confused for an abnormally shaped MCP due to DJD. A completely detached coronoid bone fragment can sometimes be identified as an angular hyperechoic structure with acoustic shadowing, cranial or medial to its anatomically correct position (Figure 17.23). Performing a dynamic examination with mild flexion, extension, pronation and supination of the joint may help in identifying the fragment, which should move independently to the underlying bone (Seyrek-Intas et al. 2009).

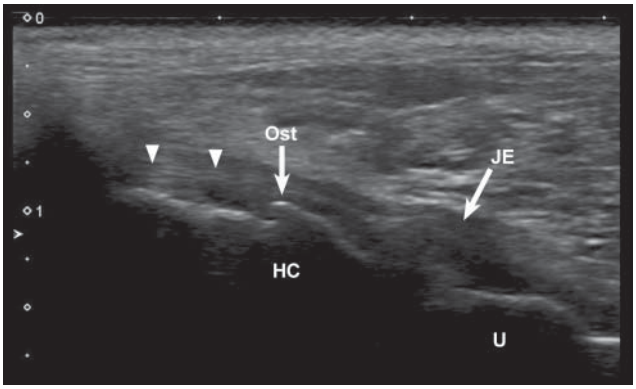


Figure 17.22. Elbow osteoarthritis. Longitudinal sonogram of the medial aspect of the elbow of a 16-month-old dog with elbow pain. An osteophyte (Ost) projects on the medial aspect of the humeral condyle (HC) and moderate joint effusion (JE) are present. Fragmentation of the coronoid process was confirmed arthroscopically. U, ulna.

Ununited Anconeal Process (UNAP)

Ununited anconeal process is recognized as an interruption of the hyperechoic outline of the protuberance (Figure 17.24). In some cases, movement of the fragment can be demonstrated with a dynamic sonogram.

Osteochondritis Dissecans

Osteochondrosis or OCD, which typically affects the medial articular portion of the humeral condyle, is difficult to assess sonographically because of the localization of the defect, but displaced fragments may become visible.

Medical Humeral Epicondyle affection: Fragmentation or Avulsion of the Deep Digital Flexor Muscle and primary flexor enthesopathy

Mineralization associated with the carpal and digital flexor muscles, which originate on the medial humeral epicondyle, is sometimes seen in dogs and is commonly associated with elbow dysplasia. It may relate to avulsion fractures, fragmentation, and/or dystrophic

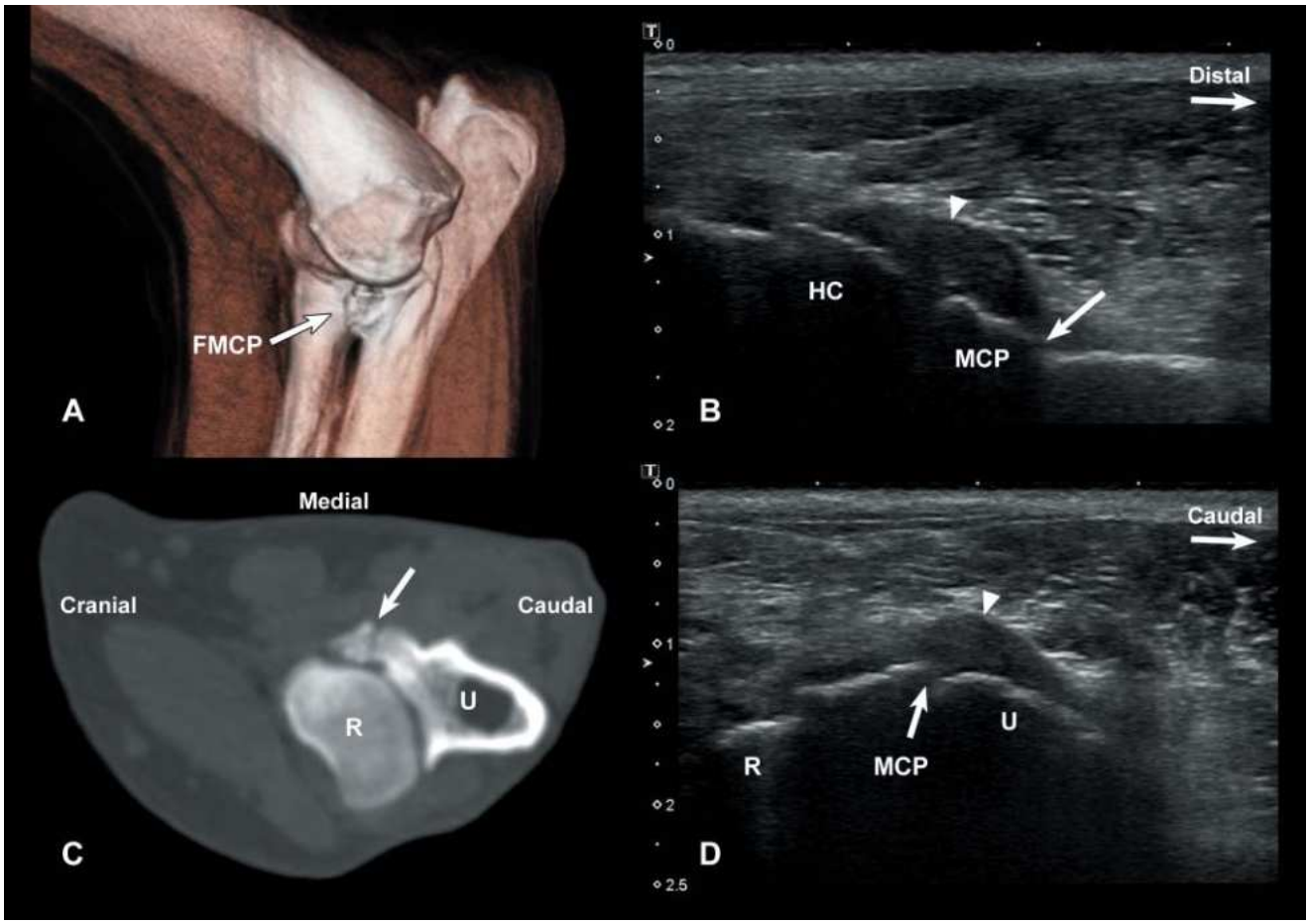


Figure 17.23. **Fragmentation of the medial coronoid process.** (for full caption, see facing page)

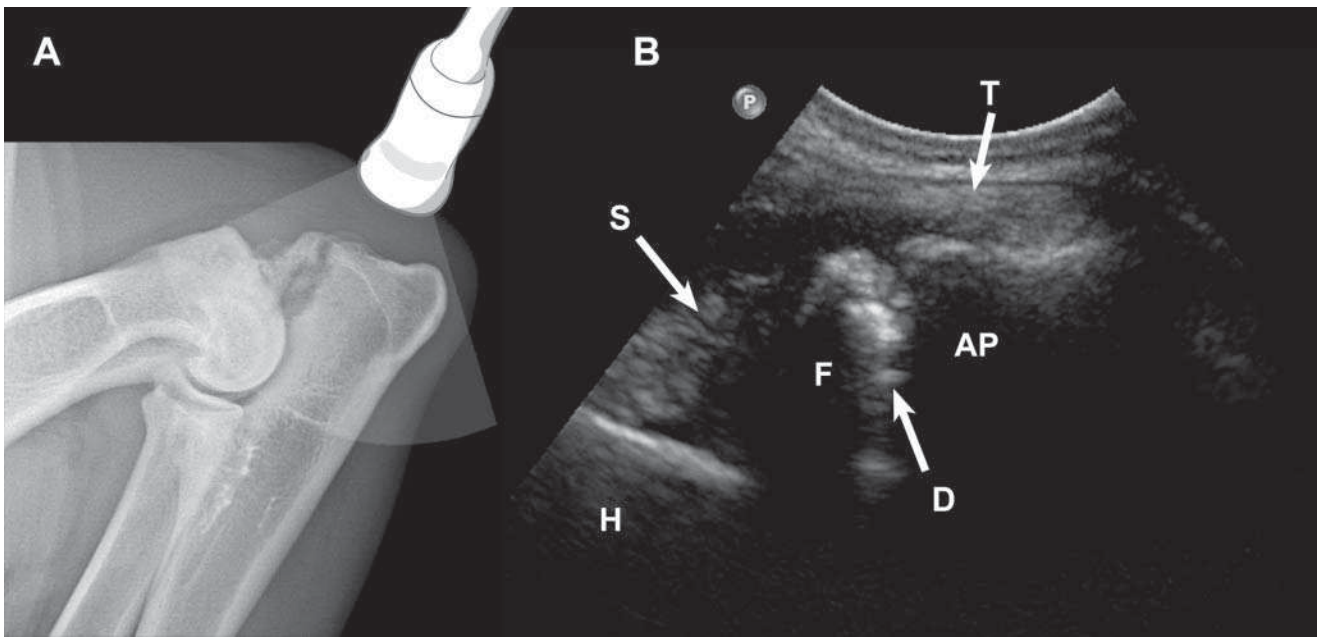


Figure 17.24. **Ununited anconeal process.** Lateral radiograph **(A)** and the corresponding sonographic image **(B)** that was obtained with the probe placed longitudinally on the triceps tendon (T). A defect is present in the anconeal process (AP), leaving a fragment (F) that is displaced cranially. Synovial proliferation (S) consistent with synovitis is present cranially.

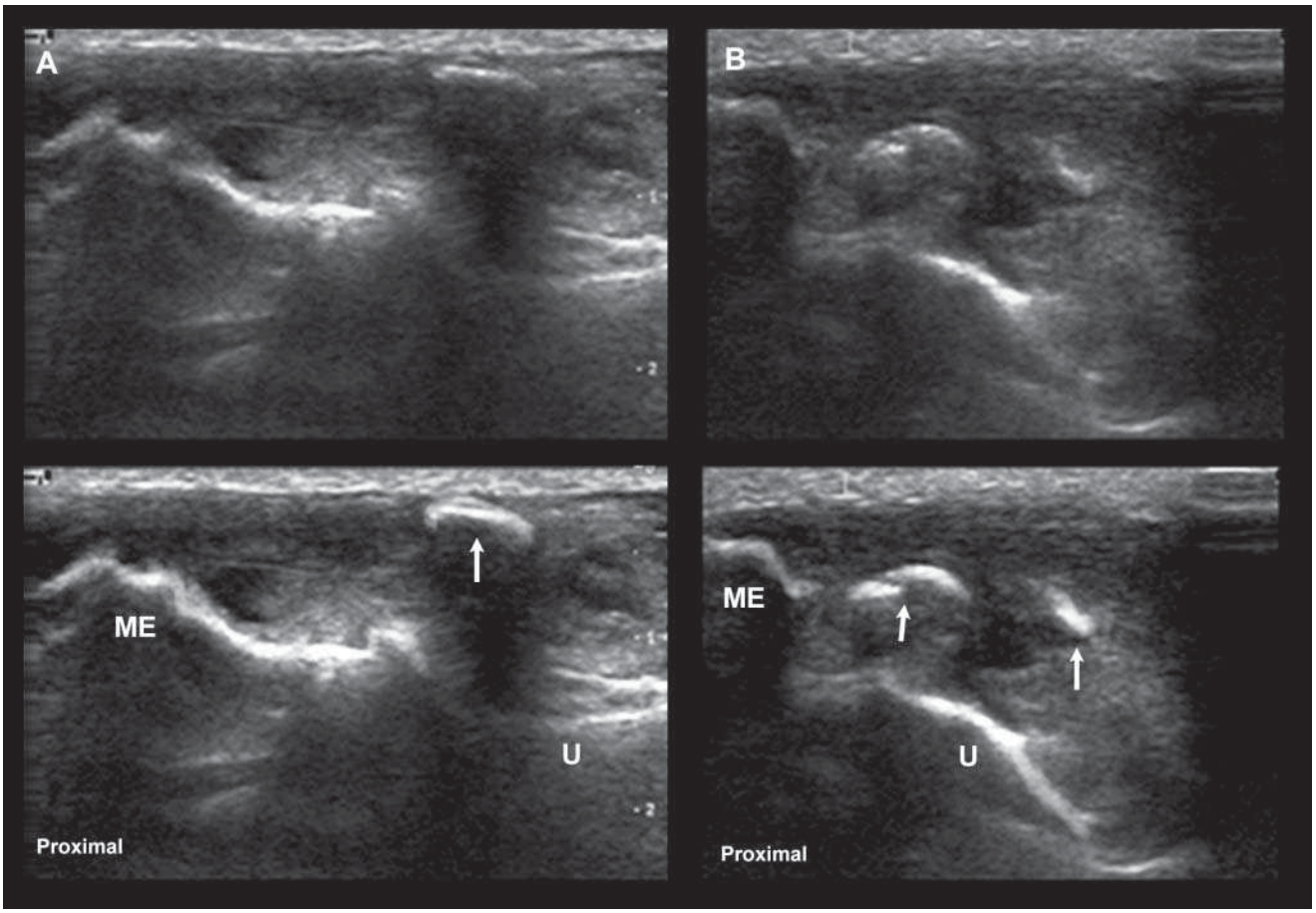


Figure 17.25. Fragmentation of the medial humeral epicondyle. A, B: Longitudinal sonographic and enhanced images obtained at the caudomedial aspect of the medial humeral epicondyle (ME) in a dog. Numerous oval hyperechoic structures (arrows), consistent with calcified bodies, are present at the medial aspect of the cubital joint and proximal ulna (U). The adjacent soft tissues are inhomogeneous and enlarged. The medial epicondyle surface is also irregular.

mineralization (Figure 17.25). These may also relate to primary muscular degeneration and metaplasia, a condition now referred to as primary flexor enthesopathy (Van Ryssen et al. 2012) (Figure 17.26). In affected dogs, irregular margination of the medial humeral epicondyle, with thickening and decreased echogenicity of the tendon of the flexor muscles and presence of fluid around and within the muscle, can be observed with ultrasound (Van Ryssen et al. 2012). Outward bowing of the flexor muscles is another common finding.

Hygroma

In large, heavy dogs, the olecranian bursa, which is located under the insertion of the triceps muscle, can become distended and/or inflamed. The bursa can be filled with variable fluid (blood, pus, or some other) of variable echogenicity. The capsule is hyperechoic and can be thickened (Figure 17.27).

Stifle

Scanning Technique and Normal Sonographic Anatomy

A high-frequency linear transducer (>10 MHz) is usually preferred for assessing all structures of the knee. The hair must be clipped from the distal third of the femur to just below the tibial tuberosity. Initially, the dog is placed in lateral recumbency with the affected limb up (Figure 17.28A,B). The final dynamic examination requires flexion and extension of the joint, as well as inward and outward rotation of the knee in the area of the menisci (Kramer et al. 1999).

The stifle joint is examined from proximally to distally. After scanning the cranial, caudal, and lateral aspects of the joint, the dog is turned over so that the affected limb faces downward, allowing assessment of the medial region (Figure 17.28C). The stifle can be divided into five regions: suprapatellar, infrapatellar,

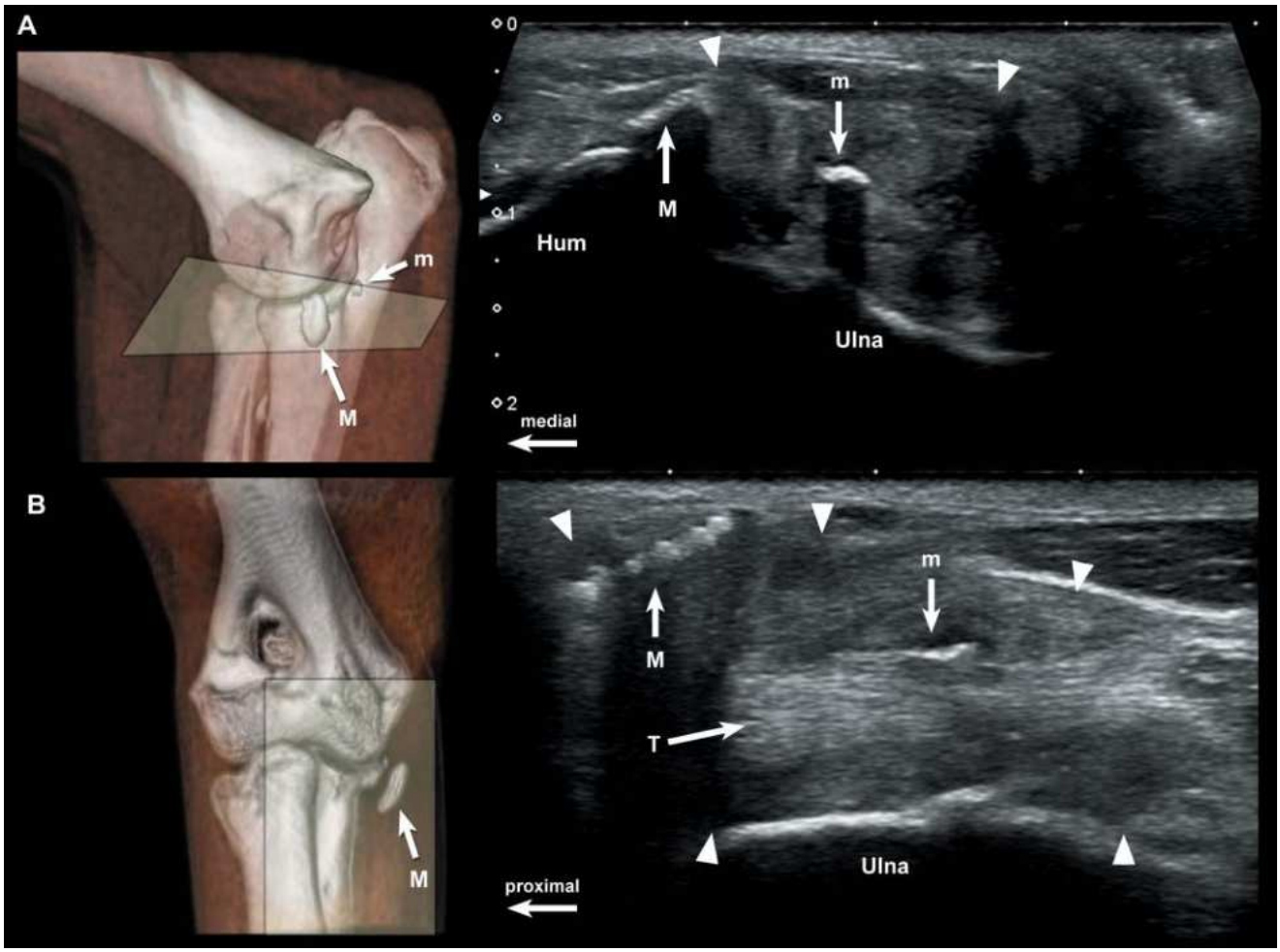


Figure 17.26. **Primary flexor enthesopathy.** Medial **(A)** and dorsal **(B)** views of the elbow of a 14-month-old Golden Retriever dog produced with computed tomographic (CT) volume-rendering, with the overlying transverse and longitudinal planes used to produce the sonographic images on the right (respectively). Large (M) and small (m) mineral fragments are depicted in all images. These mineral bodies are embedded in a heterogeneous mass of moderate echogenicity (arrowheads), consistent with fibrous and metaplastic soft tissue, in part confluent with some of the flexor tendons (T). Note the stronger acoustic enhancement associated with the larger mineral bodies. Hum, humerus.

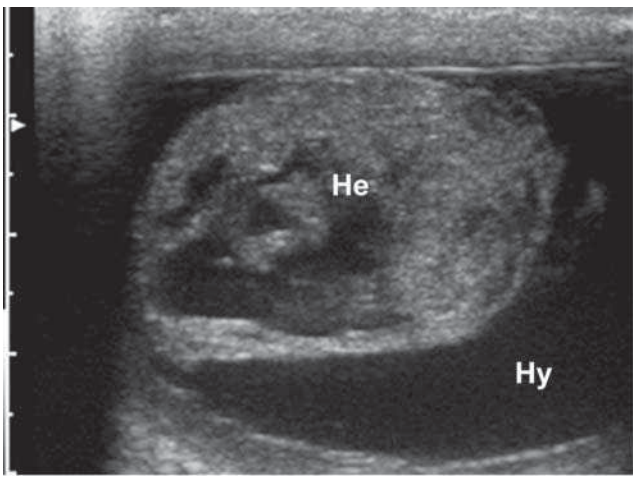


Figure 17.27. **Hemorrhagic hygroma.** The olecranon bursa is markedly distended and filled with an anechoic fluid consistent with hygroma (Hy). Additionally, a large inhomogeneous structure is found in the distended bursa, which is indicative of a chronic hematoma (He).

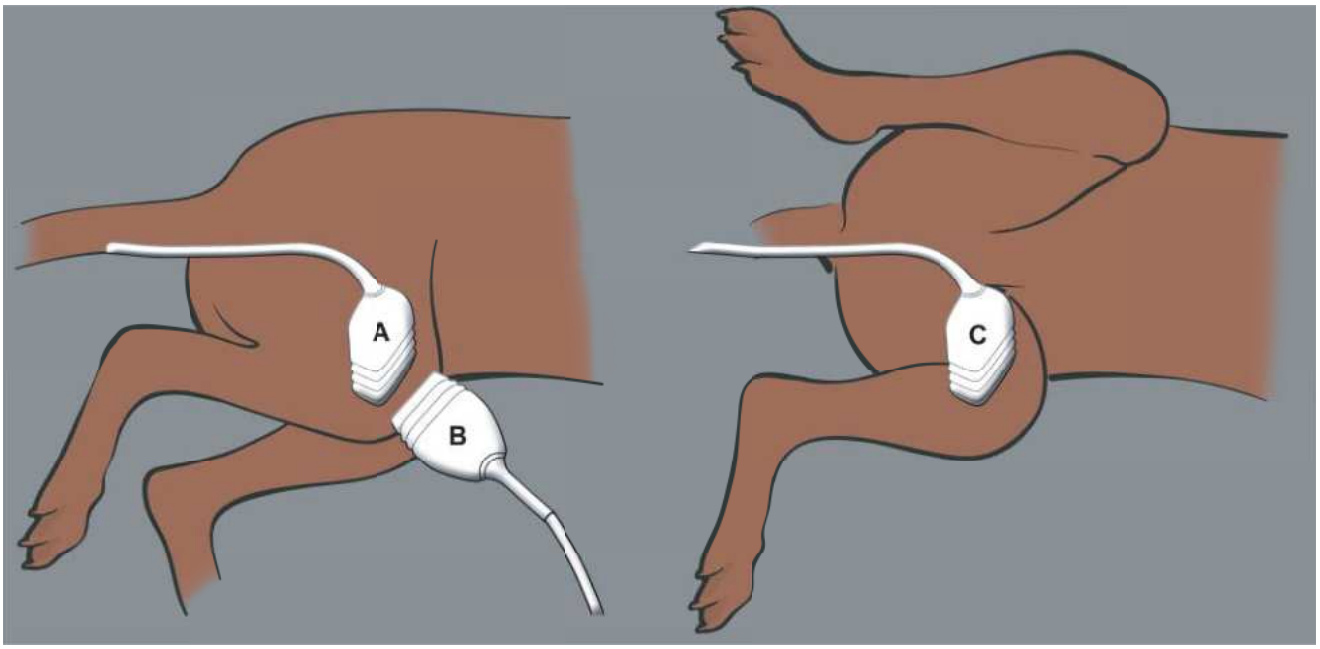


Figure 17.28. Scanning technique for the stifle. The positions of the dog and ultrasound probe when using longitudinal planes to scan the lateral **(A)**, cranial **(B)** and medial **(C)** aspects of the stifle. Longitudinal and transverse planes must be used in all regions.

lateral, caudal, and medial (Kramer et al. 1999). As opposed to human knees, the caudal approach provides low visibility of intra-articular structures in dogs and is therefore not used routinely.

Suprapatellar Region: Quadriceps Tendon, Femoral Trochlea, and Proximal Joint Recess

The suprapatellar region, as its name indicates, includes the region proximal to the patella. The stifle flexed to 45°, longitudinal and transverse scans are used to focus on the distal femur, the patella, the joint capsule, the suprapatellar recess, as well as the quadriceps femoris muscle and tendon (Figure 17.28B). The hyperechoic convex surface of the patella can be used as a landmark. The suprapatellar indentation of the femoropatellar joint sac directly proximal to the patella is of particular interest. In a normal stifle, the suprapatellar recess is a 1- to 2-mm-thick (or smaller), anechoic, more or less inhomogeneous structure located on the cranial border of the hyperechoic distal femoral cortex (Figure 17.29A). The distal tendon of the quadriceps femoris muscle and the femoral trochlea, and covering cartilage, become clearly visible by means of a dynamic scan. The articular cartilage is a 1- to 2-mm-thick anechoic band located directly above the curvilinear, hyperechoic subchondral surface of the femoral trochlea. The depth and surface continuity of this cartilage can be partially examined (Figure 17.29B). The area above the patella can be easily evaluated in a transverse scan with the stifle maximally flexed. This position enables the assessment of the cartilage, as well as the shape and depth of the femoral trochlea. At this point, a dynamic examination (subsequent flexion and extension) enables the assessment of the sliding movement of the patella into the trochlear groove.

Infrapatellar Region: Patella and Patellar Ligament, Femoral Condyles, Infrapatellar Fat Body, and Cruciate Ligaments

Because of the convexity of the femoral condyles, only a few areas of the joint surface can be assessed. Multiple imaging planes of each condyle are necessary. When the stifle is extended, the patella slides proximally on the trochlea, and the medial and lateral femoral condyles can be more fully examined. The joint cartilage is anechoic and smoothly marginated (Figure 17.29B,C), measuring 0.6–1.1 mm thick (Reed et al. 1995).

As the stifle is 90° flexed, the transducer is moved over the patellar ligament and patella (Figure 17.28B). The patella, which appears as a hyperechoic, convex line with strong acoustic shadowing, is partially embedded in the patellar ligament, which presents a characteristic hyperechoic band with a fibrillar echotexture (Figure 17.29C,D). A thin, echogenic, periligamentous sheath is also seen (Mattern et al. 2006). The distal margin of the patellar ligament appears

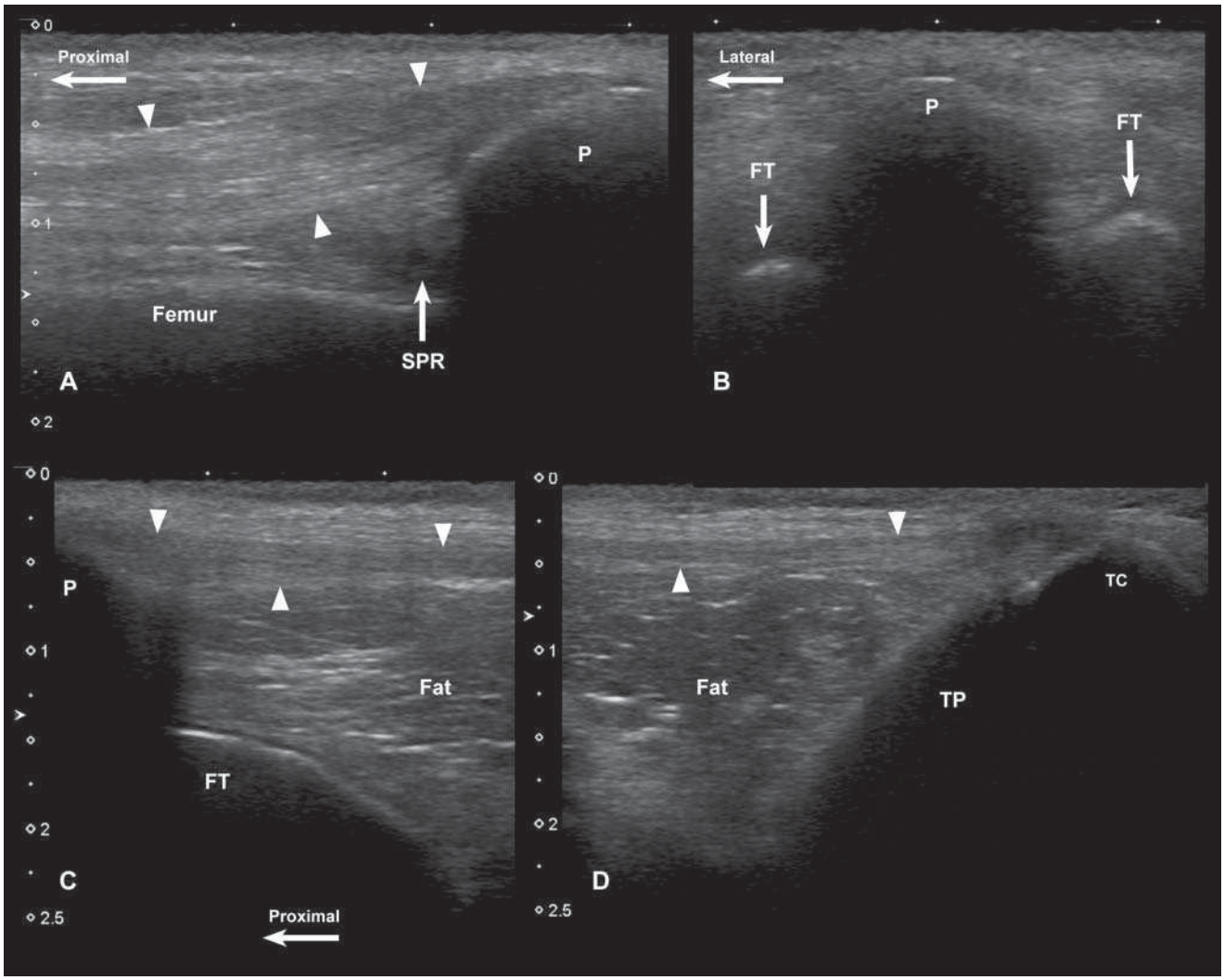


Figure 17.29. Sonographic evaluation of the cranial aspect of the canine stifle A: Normal suprapatellar region. Longitudinal sonogram of the suprapatellar region. The suprapatellar recess (SPR) is seen as a small hypoechoic focus at the proximal aspect of the femoral trochlea, just proximal to the patella (P) and underneath the tendon of insertion of the quadriceps muscle (arrowheads). Only the convex, hyperechoic surface of the patella can be seen. This structure limits the visualization of the femoral trochlea. **B: Normal femoral trochlea and patella.** Transverse sonogram of the patella (P) and of the medial and lateral ridges of femoral trochlea (FT) in a normal dog. The osseous portion of the ridge appears as a smooth, convex, hyperechoic line and is covered by a thin hypoechoic band that represents the cartilage and synovial fluid. These latter components cannot be distinguished. **C, D: Normal infrapatellar region.** Longitudinal sonographic images obtained of the proximal **(C)** and distal **(D)** portions of the infrapatellar region of a normal dog. The patellar ligament (arrowheads) appears as a moderately echogenic, linear band connecting the patella (P) and the tibial crest (TC). The infrapatellar fat pad located caudal to the patellar ligament is relatively hypoechoic and granular in echotexture. Small vessels located within this fat body appear as hyperechoic dots and lines. A thin hypoechoic band (arrowheads) consistent with cartilage and synovial fluid is noted on the surface of the femoral trochlea (FT). It is too thin to be visualized on the tibial plateau (TP) of this dog.

slightly thicker and the insertion site is less echogenic than the rest of the structure. When viewed transversely, the curved margins of the ligament are not visible because of edge-shadowing artifacts.

Beneath the patellar ligament, the infrapatellar fat body is a triangular, poorly demarcated structure of moderate echogenicity and granular echotexture, located cranial to the joint space (Figure 17.29C,D). Within this infrapatellar fat body, vessels are often visible as hyperechoic thin, double-lined, tubular structures with an anechoic center. With the stifle still flexed, lateral rotation of the transducer by 20° enables visualization of the hypoechoic to anechoic cranial cruciate ligament, which extends from the cranial

margin of the tibia to the region between the femoral condyles. The caudal cruciate ligament is difficult to visualize because of its orientation and limited space between the condyles (Arnault et al. 2009). It may be observed as a more or less ovoid hypoechoic structure when using a small footprint convex transducer on a maximally extended stifle. Differentiation between the infrapatellar fat body and the meniscus is usually not possible from a cranial approach (Reed et al. 1995; Kramer et al. 1999).

Lateral and Medial Aspects: Collateral Ligaments, Menisci, Joint Capsule, Synovium, and other structures

Each fabella appears as a convex hyperechoic structure caudoproximal to the stifle joint. When a longitudinal plane is used, the lateral and medial heads of the gastrocnemius muscle come into view next to the caudolateral and caudomedial outline of the condyle and the fabella, respectively. The muscle is identified by the presence of the fabella (or lateral sesamoid bone) within its tendon. The transverse parts of the biceps femoris muscle and the superficial digital extensor tendon run across the tibia on the lateral side.

By means of a longitudinal plane centered on the lateral joint space (Figure 17.30A), the lateral femoral and tibial condyles are visualized proximally and distally, respectively. Static and dynamic sonograms are obtained with stifle flexion and extension, as well as internal and external rotations. The joint capsule, the collateral ligaments, and the lateral meniscus can all be assessed on a longitudinal plane (Figure 17.30B). The same assessment is repeated on the medial side of the joint (Figure 17.30C).

Each meniscus appears as a triangle structure of uniform, medium echogenicity located between the femoral condyle and the tibial plateau. The abaxial

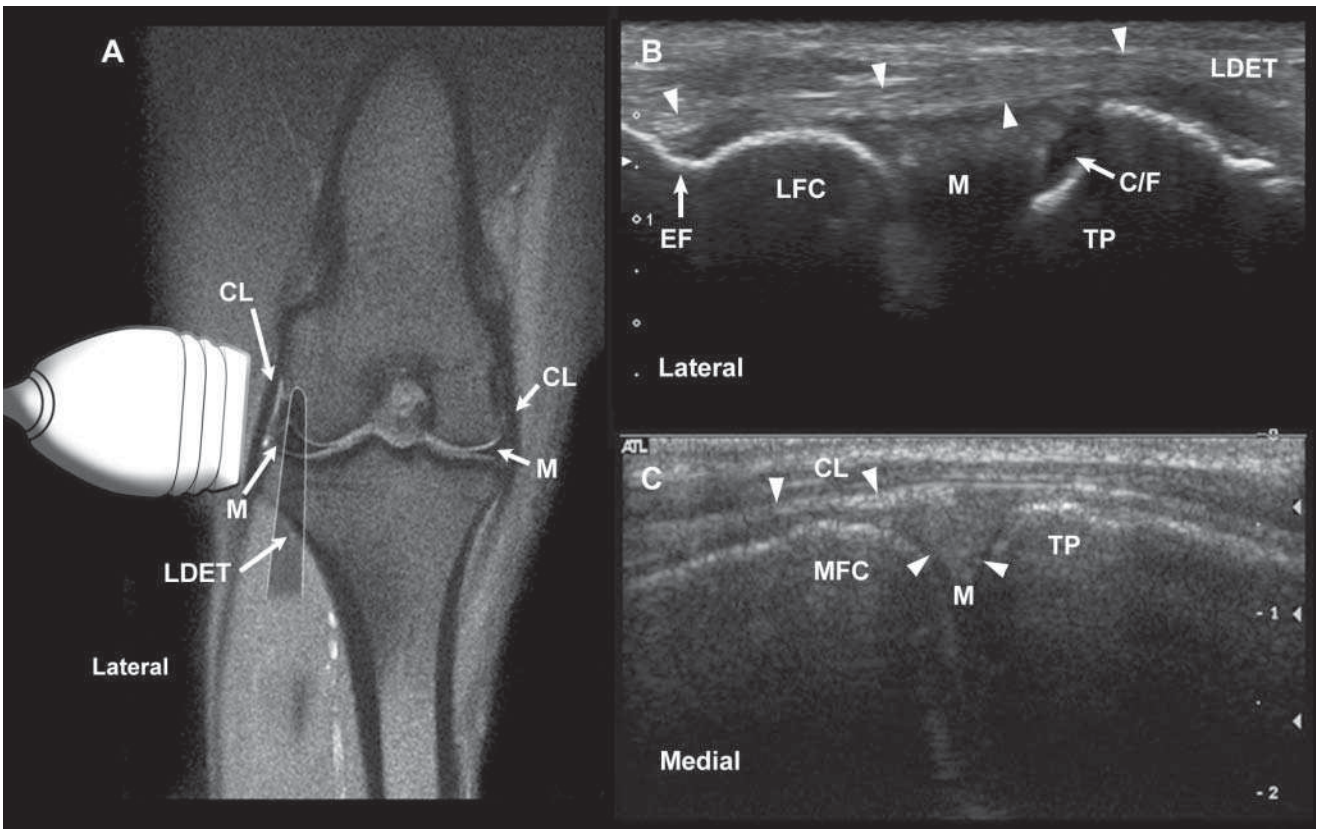


Figure 17.30. Lateral and medial aspects of the stifle: sonographic approach and normal anatomy. When scanned using a longitudinal plane **(A)**, the menisci appear as moderately echogenic, triangular structures (M) located between each femoral condyle and the opposite tibial plateau (TP). Thin hypoechoic layers consistent with articular cartilage and fluid (C/F) are observed on each side of the menisci. On the lateral side **(B)**, the long digital extensor tendon (LDET, arrowheads) can be identified just craniolateral to the lateral meniscus, as it inserts on its extensor fossa (EF). Collateral ligaments (CL) can also be seen crossing the medial and lateral aspects of the joint. The lateral CL is located just caudal to the LDET. Image **B** was obtained in a 5-month-old Boxer and image **C** in an adult Labrador Retriever. LFC, lateral femoral condyle; MFC, medial femoral condyle.

surface of the meniscus should be linear and perfectly aligned with the surface of the adjacent femoral and tibial condyles. Additionally, a fine hypoechoic line may be seen on the femoral and tibial surfaces of the meniscus, consistent with articular cartilage and synovial fluid (Mahn et al. 2005) (Figure 17.30). When the collateral ligament is used as a landmark, three different regions can be examined: the cranial horn, the middle portion, and the caudal horn (Mahn et al. 2005). Only the peripheral portion of the meniscus can be seen due to the convexity of the femoral condyle.

With the probe placed in the longitudinal plane on the lateral side of the joint, the long digital extensor tendon can be identified. It demonstrates a typical fibrillar echotexture and runs between the lateral meniscus and the joint capsule, cranial to the collateral ligament. The origin of the tendon can be traced across the joint to the extensor fossa, a focal depression in the craniolateral margin of the lateral femoral condyle (Figure 17.30B). The tendon runs through the tibialis cranialis muscle and is surrounded by its sheath, formed by an indentation of the joint sac, but is not identified unless it is distended.

Sonographic Features of Specific Stifle Disorders

Cranial Cruciate Ligament Rupture (CCLR)

The sensitivity of ultrasound to detect CCLR is limited, approaching 15% in a recent study on 13 dogs using a high-frequency linear probe (Arnault et al. 2009). While the ruptured ligament is difficult to recognize, especially in the acute phase, several signs may be present. First, joint effusion is typically observed and often extends proximally into the suprapatellar recess, forming an anechoic, tube-like structure surrounded by a hyperechoic line (joint capsule) (Figure 17.31A). Joint effusion also causes cranial displacement and compression of the infrapatellar fat body, which becomes outlined by the anechoic to hypoechoic fluid. This fat body often appears inhomogeneous and more echogenic (Figure 17.31B). Occasionally, small fluid-filled areas (cysts) can be seen within it (Kramer et al. 1999). Distally, the distended synovial sheath that wraps around the tendon of the long digital extensor becomes clearly visible as an anechoic to hypoechoic tubular structure displacing the tibialis cranialis. CCLR is also typically associated with osteoarthritic periarticular new bone formations that develop at the contours of the patella, femoral trochlea ridges, condyles, and epicondyles, as well as the tibial plateau (Arnault et al. 2009) (Figure 17.31C). In addition, the joint capsule appears as a thickened hyperechoic band, and redundant synovial thickening can be visualized, particularly if associated with significant joint effusion.

For direct assessment of the damaged cranial cruciate ligament, a cranial, longitudinal approach is used, and the stifle must be completely flexed, which may be difficult to accomplish in painful, unsedated dogs. In the region of the cranial cruciate ligament, an irregular, anechoic area (hematoma) can sometimes be identified (Kramer et al. 1999; Gnudi and Bertoni 2001). If the rupture has been present for a longer period (chronic rupture), the irregularly demarcated and hyperechoic stumps of the ligament may become evident, particularly at its insertion on the tibial plateau (Figure 17.32) (Kramer et al. 1999). The visibility of the cranial cruciate ligament is limited if a large volume of effusion is present, because this structure appears hypoechoic when scanned at an angle (Kramer et al. 1999; Gnudi and Bertoni 2001). Avulsion fragments may also be recognized as more or less shadowing hyperechoic foci in the central portion of the joint. Chronic ruptures are commonly associated with fibrous tissue proliferation in the region just cranial to the intercondylar groove, which appears as an irregular, hyperechoic structure (Gnudi and Bertoni 2001) (Figure 17.31B).

Meniscal Tears and Degeneration

Meniscal tears and degenerative changes are more commonly observed medially and secondary to stifle instability caused by cranial cruciate rupture. The sensitivity and specificity of ultrasound for detecting meniscal lesions accompanying CCLR reach 82% and 93%, respectively (Arnault et al. 2009). Isolated meniscal damage is rare in dogs and may more commonly affect the lateral meniscus (Mahn et al. 2005). Most tears appear to present a bucket-handle configuration. However, because of the difficulty in visualizing the axial (internal) portion of the menisci, partial and complete tears can be difficult to visualize.

Affected menisci are typically inhomogeneous with hyperechoic and hypoechoic areas and show some abaxial displacement or bulging of their abaxial surface (Arnault et al. 2009) (Figure 17.33). A decrease in the visibility of a meniscus may indicate abnormal displacement due to rupture. A caudally or medially displaced medial meniscus is also usually indicative of rupture, although this phenomenon may be dynamic and not necessarily present during

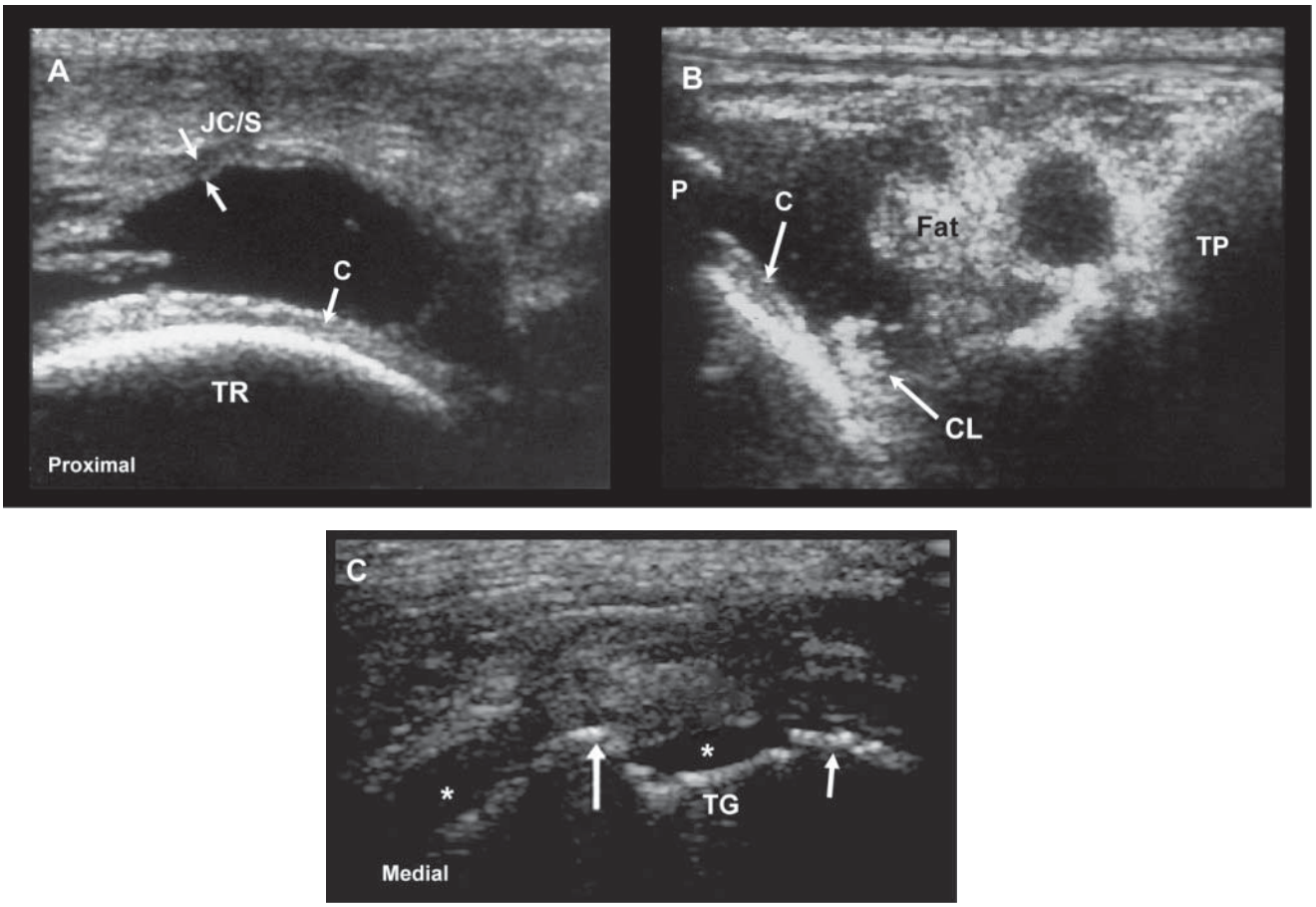


Figure 17.31. **Stifle osteoarthritis. A, B:** Longitudinal sonograms of the proximal joint recess **(A)** and infrapatellar region **(B)** in a dog with chronic stifle degenerative joint disease. Anechoic joint effusion is present, and the joint capsule and synovium (JC/S, arrows) are thickened. The cartilage (C) along the trochlea is hyperechoic and heterogeneous. The infrapatellar fat body is heterogeneous, and an irregular, hyperechoic structure is in the mid-portion of the joint, consistent with a degenerated and ruptured cranial cruciate ligament (CL). P, patella; TP, tibial plateau; TR, trochlear ridge. **C:** Transverse sonographic image of the femoral trochlea in another dog with degenerative joint disease. The cranial surfaces of the trochlear ridges (arrows) are irregular because of osteophytosis. The proximal joint recesses at the medial aspect of the trochlea and over the trochlear groove (TG) are filled with anechoic fluid (*).

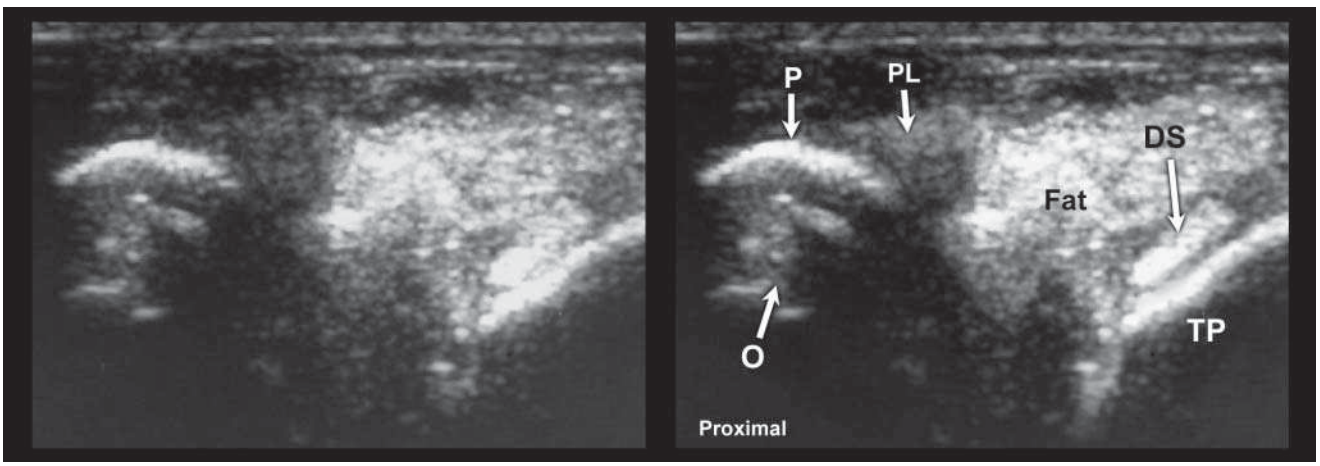


Figure 17.32. **Cranial cruciate ligament rupture.** Longitudinal sonographic and enhanced images of the infrapatellar region in which the distal stump (DS) of the ruptured ligament appears as a hyperechoic band proximal to the tibial plateau (TP). O, osteophytosis over the femoral trochlea; P, patella; PL, patellar ligament.

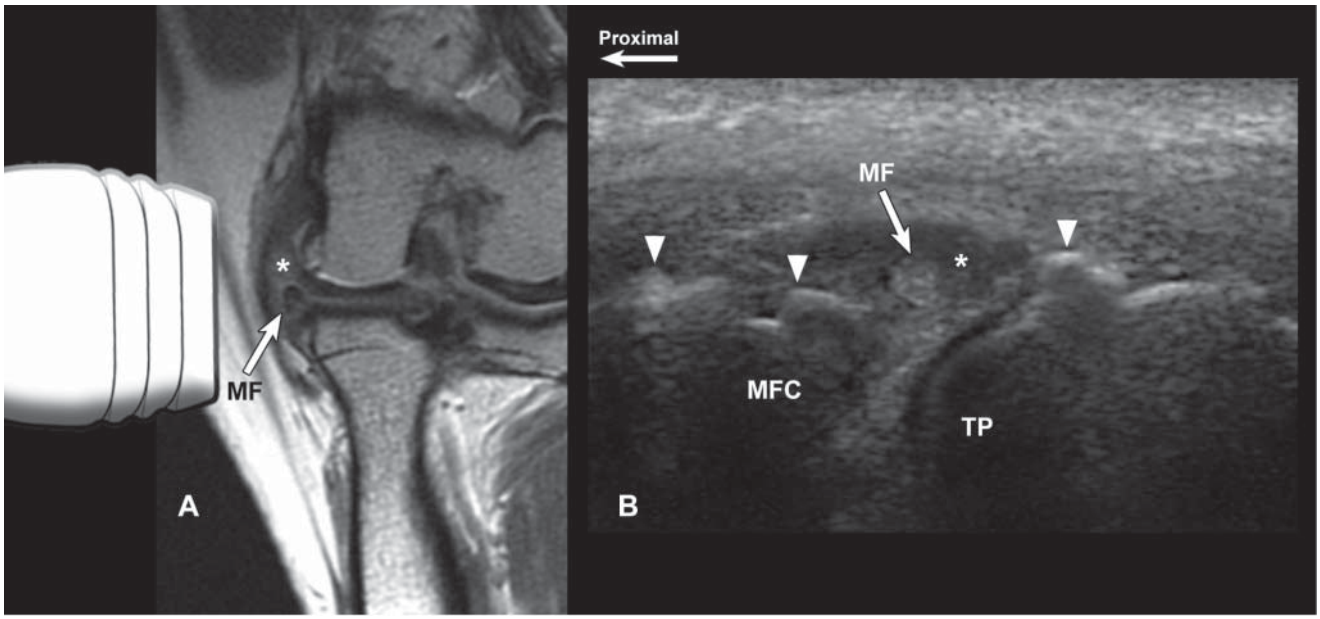


Figure 17.33. **Meniscal tear and displacement. A:** In this dorsal magnetic resonance image of the stifle of a dog with cranial cruciate rupture, there is a meniscal fragment (MF) displaced medially and surrounded with synovial effusion and proliferation (*). **B**: Placement of the ultrasound probe on the medial aspect of the joint (as in Figure 17.28C) allows good visualization of the meniscal fragment (MF), adjacent effusion and synovitis (*), and nearby osteophytosis (arrowheads). MFC, medial femoral condyle; TP, tibial plateau.

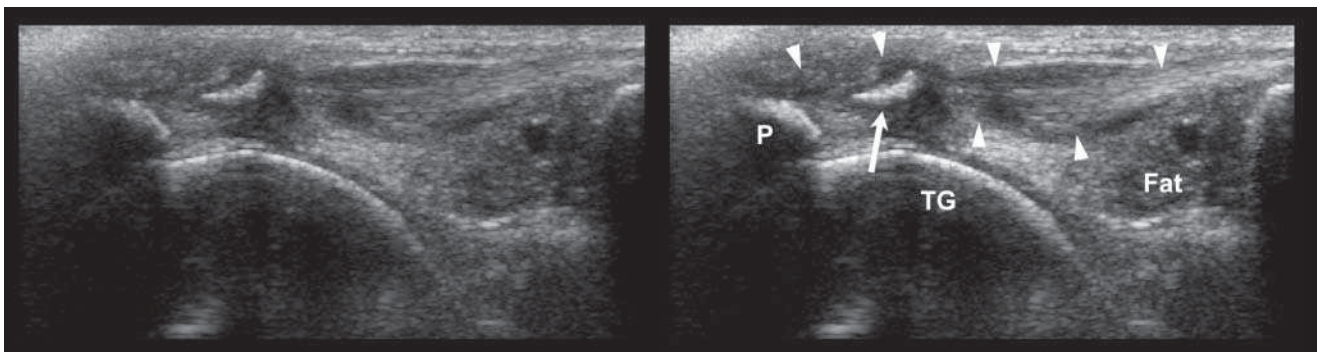


Figure 17.34. **Avulsion fracture of the patella.** Longitudinal sonographic and enhanced images of the infrapatellar region in a dog with acute stifle pain and swelling. The patellar ligament (arrowheads) is irregularly thickened and heterogeneous. A hyperechoic, partially shadowing bony fragment (arrow) is just distal to the patella (P), consistent with fracture of the apex. The distal margin of the patella is abnormally flat, and the patella is displaced proximally. TG, trochlear groove.

examination (Arnault et al. 2009). Joint effusion can be observed at the periphery of the affected meniscus. Ultrasonographic assessment of the menisci can be limited by several factors, including severe fibrosis of the soft tissues along the medial aspect of the joint, marked osteophytosis caused by severe DJD, and previous surgery (Mahn et al. 2005). The size of the dog may also represent a limiting factor because thinner menisci (small patients) or deeper menisci (very large or obese dogs) can be more difficult to visualize well. Joint effusion can be observed at the periphery of the affected meniscus.

Patellar Fractures and Desmopathies

A fracture of the patella is seen as an interruption of the outline of the smooth bone surface (Kramer et al. 1999) and is often associated with damage to the quadriceps tendon (proximally) or patellar ligament (distally).

Ruptures of the patellar ligament can be partial or complete. In both cases, the ligament appears hypoechoic to hyperechoic, with irregular margins at the site of rupture. With avulsion fracture, small hyperechoic bone fragments are visible at the extremity of the ligament and are associated with acoustic shadowing if they are more than 2–3 mm wide (Figure 17.34).

When a longitudinal plane is used, a separation of the ruptured ends can be observed as the stifle is flexed.

Patellar ligament thickening is also recognized following tibial plateau-leveling osteotomy (TPLO), particularly in large dogs and particularly in its distal portion (Mattern et al. 2006). Postoperative changes noted at 1 month also include hypoechoic to anechoic central lesions with partially disrupted ligaments. These changes have been significantly linked to the degree of tibial plateau rotation during the procedure, supporting a role for increased stress in the development of patellar ligament desmitis (Mattern et al. 2006). Tibial tuberosity advancement (TTA) is also associated with ultrasonographically measurable thickening of the patellar ligament 6 weeks postoperatively (Kühn et al. 2011). However, these changes may be clinically insignificant in most dogs.

Avulsion fracture of the tibial tuberosity can also be visualized in the infrapatellar region. During a dynamic ultrasound exam, the acutely avulsed bony structure can move during flexion of the stifle, confirming the diagnosis. However, this motion can be limited, particularly if a fibrous callous is already present.

Collateral Ligament Rupture

In cases of severe and acute rupture of the medial or lateral collateral ligaments, a discontinuity of the affected ligament may be identified. Typically, hematomas are found at the level of the tear, seen as hypoechoic to anechoic, homogeneous to mildly inhomogeneous areas. When a longitudinal medial or lateral approach is used, a dynamic examination of the joint space while stressing its opening medially and laterally may confirm joint instability. Joint effusion rapidly develops and appears as bulging medial and/or lateral synovial recesses. Capsular tear may also be present, and fluid may have accumulated in the periarticular soft tissues.

Osteochondritis Dissecans

Osteochondritis dissecans appears as an irregular defect on the contour of the subchondral bone, typically at the lateral condyle. The abnormal cartilage can vary in thickness and echogenicity but often appears hyperechoic and heterogeneous. Detached pieces of cartilage are seen as hyperechoic structures of variable size. Other free bodies may also be visible, and their location can be determined (Kramer et al. 1999) (Figure 17.35). Joint effusion is typically observed in association with OCD, and periarticular osteophytes develop in the chronic phase.

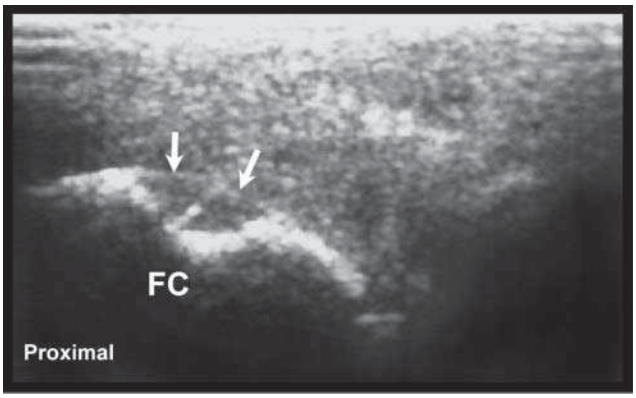


Figure 17.35. Osteochondritis dissecans. Longitudinal sonographic image of the lateral femoral condyle (FC) in a young dog. A concave defect (arrows) is filled with mildly echogenic and partially mineralized cartilage.

Avulsion of the Long Digital Extensor Tendon

In cases of avulsion fracture of the origin of the long digital extensor tendon, shadowing hyperechoic foci consistent with bone fragments can be found just distal to the level of the extensor fossa at the lateral femoral condyle (Kramer et al. 1999).

Hips and Iliopsoas Muscles

Scanning Technique and Normal Sonographic Anatomy

Animals are placed in lateral or dorsal recumbency depending of the region of interest. Although it can be useful in some patients, sedation or anesthesia is usually unnecessary. A high-resolution (>8–10 MHz) linear transducer is recommended.

The lateral and medial portions of the coxofemoral joint are assessed with the dog in lateral recumbency and its affected limb on top, and in dorsal recumbency with the affected hip placed in a frog position, respectively. The femoral head appears as a convex hyperechoic interface with acoustic shadowing. The shadowing caused by the femoral head represents a significant limiting factor in assessing the coxofemoral joint space and acetabulum (Greshake and Ackerman 1992). The articular cartilage appears a smooth hypoechoic layer around the femoral head (Figure 17.36). The joint capsule appears as a hyperechoic line at the periphery of the head and connected to the acetabular margins. Hips can be evaluated in puppies that are up to 7–8 weeks of age (Greshake and Ackerman 1992). The cartilage is thick at that time, and the subchondral bone is partially mineralized and irregular. In mature dogs, the

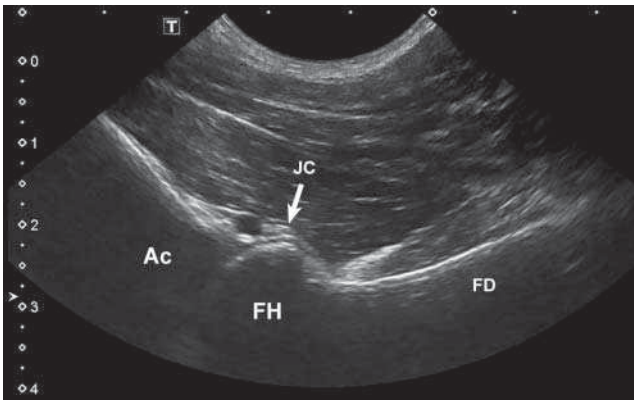


Figure 17.36. **Normal hip.** Ventral sonographic approach to the coxofemoral joint with the dog placed in dorsal recumbency. The joint capsule (JC) is hyperechoic and covers the synovial fluid and cartilage, which form a thin hypoechoic layer covering the femoral head (FH) in this normal Boxer. Ac, acetabulum; FD, femoral diaphysis.

shadowing bony structures hamper complete assessment of these joints.

Iliopsoas muscles and tendons are examined in dorsal recumbency using longitudinal and transverse planes (Cannon et al. 2008). The psoas major muscle originates from the transverse process of L3 and is visualized in longitudinal planes extending caudally as hypoechoic muscle interspersed with obliquely oriented hyperechoic, linear fibers (Figure 17.37A). The mid-body is then identified in longitudinal orientation using the vertebral bodies of L4–L7 as landmarks, which lie dorsal to this large hypoechoic muscle that shows linear hyperechoic fibers oriented parallel to its long axis. Joining by the iliacus muscle, the formed iliopsoas tendon inserts on the lesser trochanter, which is recognized as a small, focal protrusion from the medial surface of the proximal femur (Figure 17.37B). The inserting tendon appears as a fusiform structure with concentric hyperechoic linear fibers.

Iliopsoas Myopathies

Iliopsoas myopathies may be under-diagnosed in practice. Strain injuries typically lead to muscle swelling associated with hypoechoic areas in the acute phase. Fibrosing and calcifying iliopsoas myopathies, which may or may not be traumatic in origin, are occasionally seen in lame or clinically normal dogs, also modifying the muscle and tendon normal size, echotexture and echogenicity (Figure 17.37C,D). Mineralization appears as hyperechoic, irregular structures displaying acoustic shadowing.

Hip Dysplasia and Osteoarthritis

The use of ultrasound in the diagnosis of hip dysplasia has been investigated in young puppies. Although dynamic measurements may predict the onset of osteoarthritis in some dogs, such as Labrador Retriever–Golden Retriever mix puppies (Adams et al. 2000), it appears unreliable for early detection of hip dysplasia in puppies that are 16–49 days old (Fisher et al. 2010). Joint effusion and capsular thickening related to secondary osteoarthritis have the same sonographic appearance as described for other joints (Figure 17.38).

Tarsus

Scanning Technique and Normal Sonographic Anatomy

Several tarsal and periarticular soft-tissue structures can be assessed with ultrasound, especially in large dogs (Caine 2009). Of these, the calcaneal (Achilles) tendon, plantar and collateral ligaments, and the long and lateral digital extensor, tibialis cranialis, and deep digital flexor muscles and tendons are of clinical interest.

The calcaneal tendon consists of all structures that attach to the calcaneal tuberosity. The gastrocnemius and the superficial digital flexor (SDF) tendons represent the two main components. Tendons of the biceps femoris, semitendinosus, and gracilis muscles form another conjoined component, also called the common calcaneal (CC) tendon. The medial and lateral gastrocnemius muscles fuse at their distal aspect, becoming one tendon that runs within the calcaneal tendon, lateral to the SDF tendon, and inserts on the calcaneal tuberosity. Distally, the SDF tendon becomes superficial to form a cap-like structure that contains the rest of the CC tendon and that inserts both laterally and medially on the tuberosity. This tendon is relatively thin at that level and may not be identified in small dogs (Caine et al. 2009). The CC tendon is the deepest portion of the calcaneal tendon and inserts on the dorsal aspect of the calcaneal tuberosity (Hermanson and Evans 1993). Ultrasonography of the calcaneal tendon is performed in a standardized fashion: the tarsocrural joint is slightly flexed, stretching the tendon that can be more easily imaged (Figure 17.39). Initially, a longitudinal scan is performed by placing the probe over the calcaneal tuberosity at the tendon insertion. The transducer is then moved proximally to examine the whole structure, as well as the musculotendinous junctions and muscles. Transverse views are then used

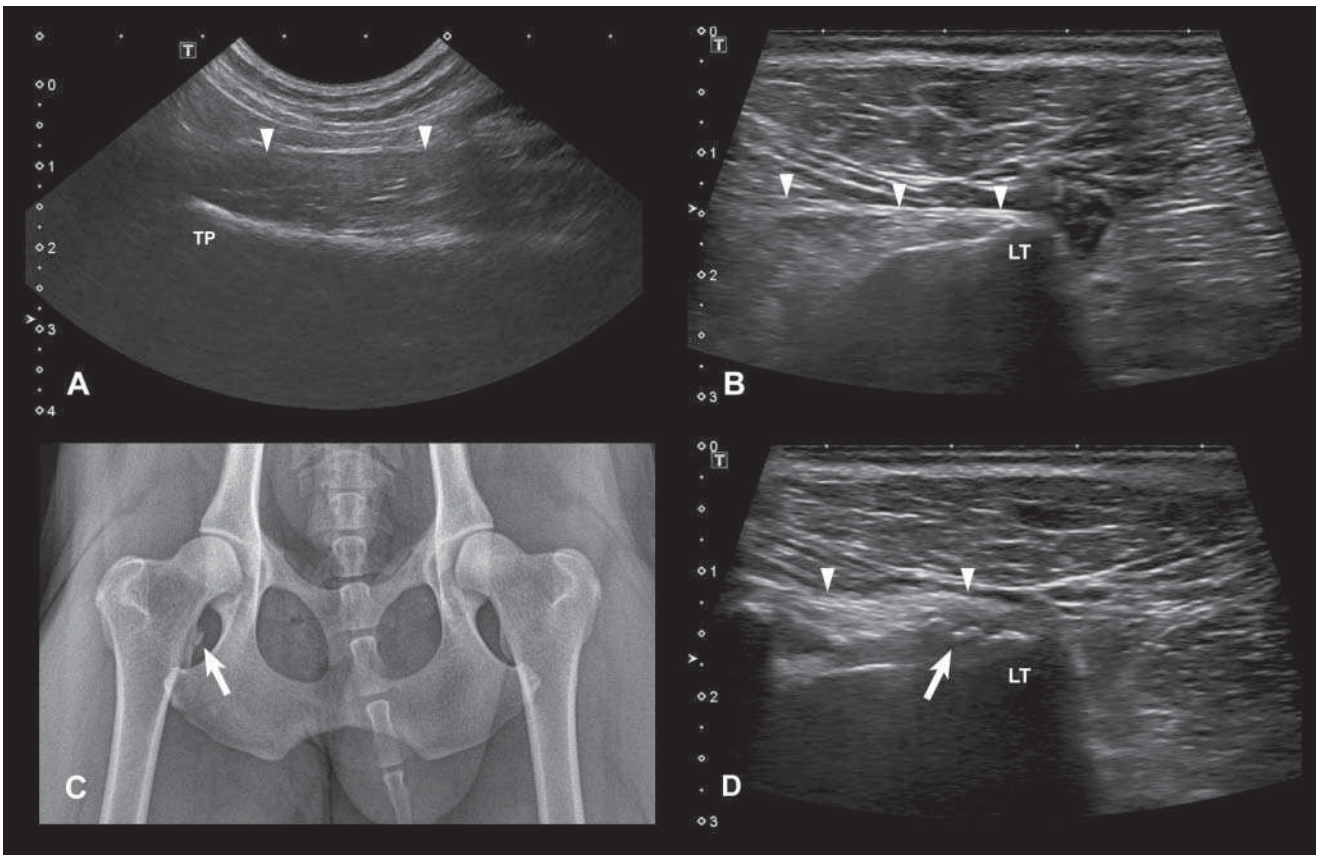


Figure 17.37. Normal and pathologic iliopsoas tendons. Longitudinal sonograms of the origin **(A)** and insertion **(B)** portions of the iliopsoas muscle and tendon in a normal Labrador Retriever dog. The muscular portion (arrowheads in **A**) is more hypoechoic, whereas the insertion tendon (arrowheads in B) has a characteristic hyperechoic fibrillar pattern as it inserts on the lesser trochanter (LT). **C, D**: Ventrodorsal radiograph **(C)** and longitudinal sonogram **(D)** of another dog with partial avulsion of the iliopsoas tendon from the lesser trochanter (LT). Note the mineral fragments (arrows) and the change in shape and echotexture of the tendon (arrowheads) when compared to **B**.

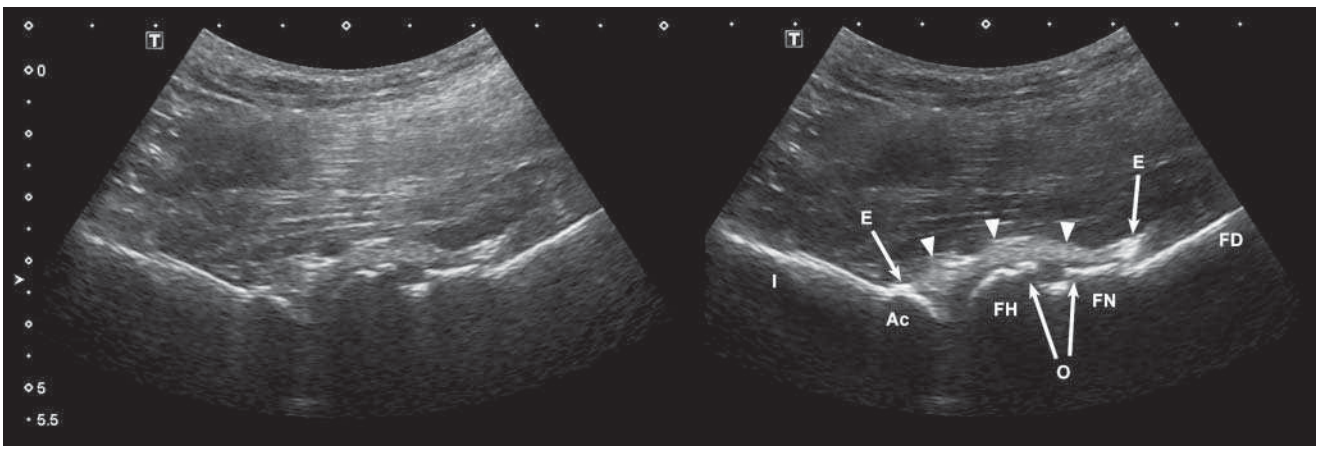


Figure 17.38. Hip joint osteoarthritis. In these sonographic and enhanced images obtained from a ventral parasagittal approach, the coxofemoral joint capsule is thickened and hyperechoic (arrowheads) and associated with enthesophytes (E) at its insertion sites on the acetabular rim (Ac) and femoral neck (FN). The femoral head (FH) and neck are deformed by osteophytes (O). FD, femoral diaphysis; I, ilium.

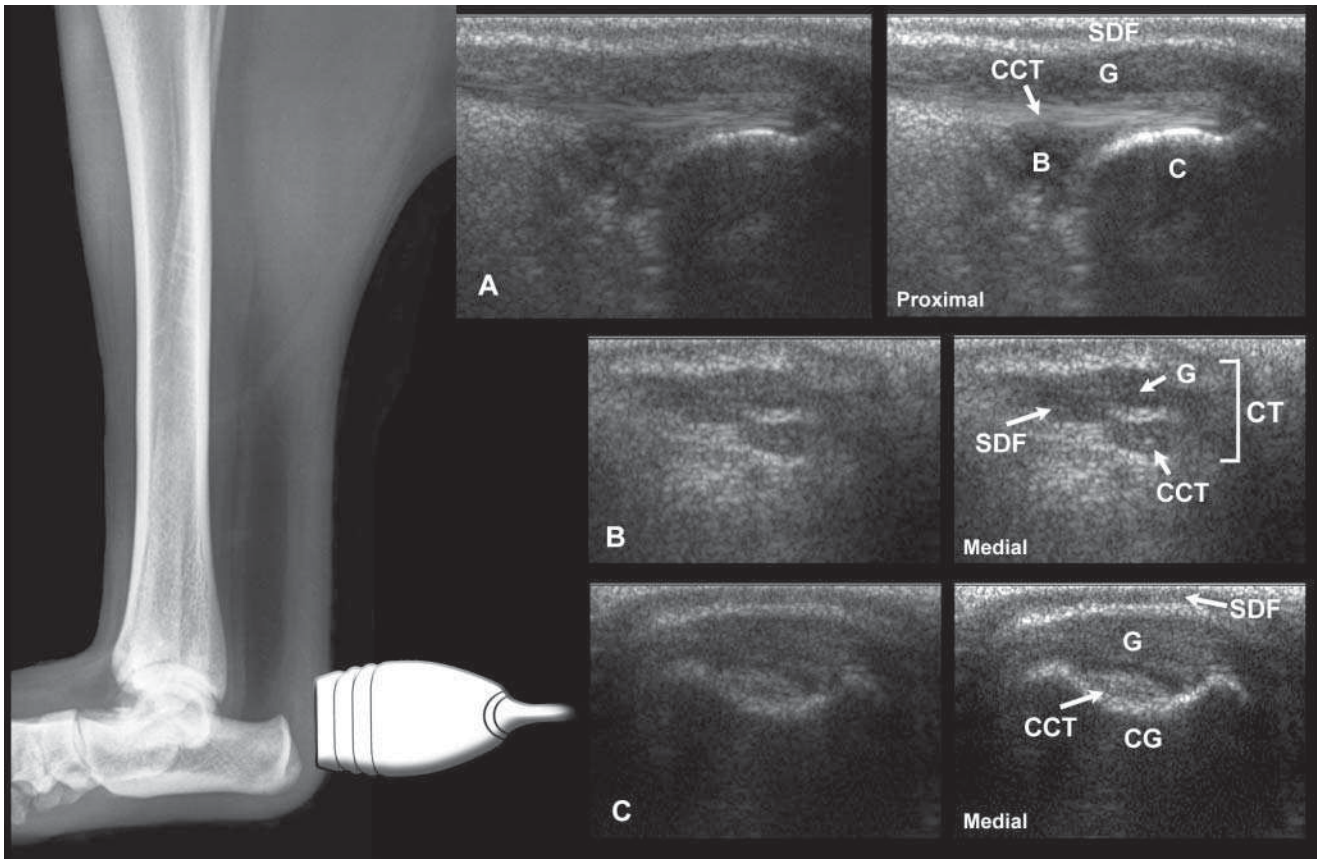


Figure 17.39. Normal sonographic anatomy of the calcaneal (Achilles) tendon. Sonographic and enhanced images. A: Longitudinal sonogram. The common calcaneal tendon (CCT), which is the deepest component of the calcaneal tendon, has a characteristic hyperechoic, linear echotexture when scanned perpendicularly. The other components of the calcaneal tendon, i.e., the gastrocnemius (G) and superficial digital flexor (SDF) tendons, are seen more superficially. The calcaneal bursa (B) appears as a small, triangular anechoic area just proximal to the calcaneal tuberosity **(C)**. **B, C:** Transverse sonograms. These images are obtained at the mid-level **(B)** and distal level **(C)** of the calcaneal tendon (CT). The superficial digital flexor (SDF) lies medial to the gastrocnemius (G) through most of the calcaneal tendon, and caudal to the common calcaneal tendon (CCT). Distally, it becomes a cap-like structure around the calcaneal tuberosity and contains the gastrocnemius and common calcaneal tendons over the calcaneal groove (CG).

to visualize individual portions of the tendon, from the level of their muscular origin to the level of the calcaneal tuberosity. Finally, a dynamic examination is performed (flexion and extension of the hock) (Kramer et al. 2001a; Lamb and Duvernois 2005). A longitudinal image directly above the tuber calcanei shows the surface of the calcaneus as a convex hyperechoic line with distal acoustic shadowing (Figure 17.39A). Immediately proximal to this bony protuberance, which serves as an important landmark, is a 5 × 5-mm, hypoechoic, ill-defined area representing the calcaneal bursa with its surrounding connective tissue (Figure 17.39A). The CC tendon is a moderately echogenic, homogeneous structure with parallel hyperechoic lines (fibrillar echotexture) inserting on the tuberosity (Figure 17.39A). The peritendineum is a smooth hyperechoic band at the periphery of the tendon. Further proximally, the muscles display their typical echotexture (see the section on musculature). On transverse images, the CC tendon is a moderately echogenic, round structure with multiple small hyperechoic dots, that inserts deeply on the dorsoproximal margin of the calcaneal tuberosity (Figure 17.39B,C). The peritendineum surrounding the tendon is visible as a hyperechoic line. However, the presence of edge shadowing prevents a clear visualization of its curved axial and abaxial borders (Rivers et al. 1997; Kramer et al. 2001a; Lamb and Duvernois 2005).

On the plantaromedial side of the tarsus, the deep digital flexor (DDF) tendon may also be recognized as it courses over the sustentaculum tali. It appears oval in transverse scan at the level of that bone, with typical fibrillar echotexture, before deviating centrally, on the medial aspect of the plantar ligament, which

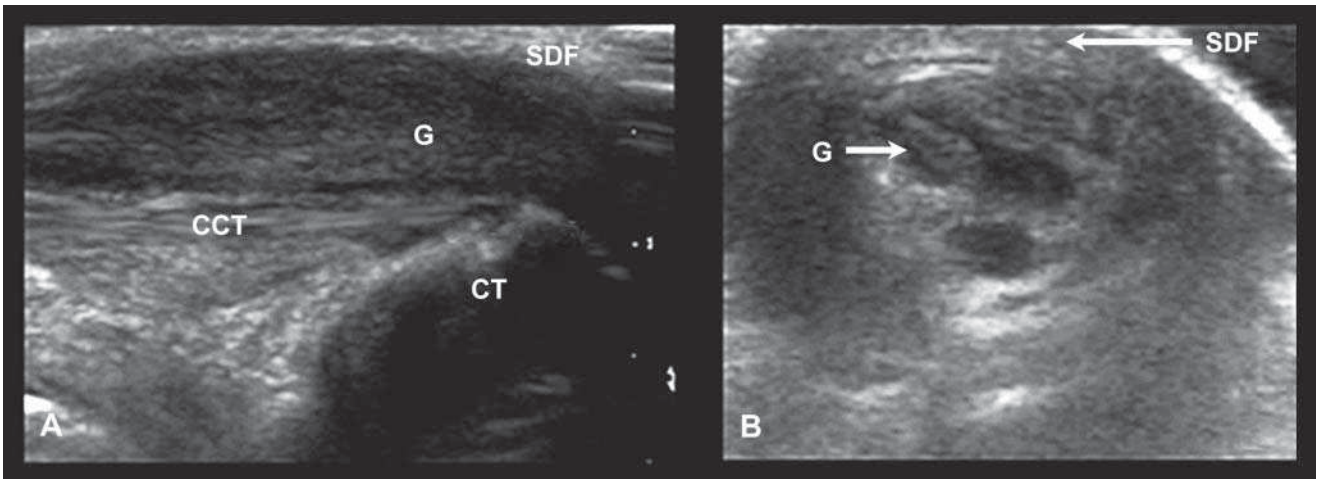


Figure 17.40. Partial rupture of the gastrocnemius tendon. Longitudinal **(A)** and transverse **(B)** sonograms of the calcaneal tendon in a dog with acute trauma. The gastrocnemius tendon (G) is markedly enlarged and the superficial digital flexor tendon (SDF) is displaced caudally but appears intact. The common calcaneal tendon (CCT) is mildly inhomogeneous, which may also be because of partial rupture.

is larger and more echogenic than the DDF tendon, which becomes hypoechoic due to anisotropy artifact (Caine et al. 2009). Dorsal to the tarsus, the long digital extensor tendon can be found before it divides into four smaller tendons distally. It is closely associated with the tibialis cranialis tendon, which deviates medially at the distal tibia (Caine et al. 2009). Laterally, the closely associated lateral digital extensor tendon and peroneus longus tendons can be seen in large dogs, in part attached to the lateral tibial malleolus, and adjacent to the lateral collateral ligaments, which may not be distinctly visible (Caine et al. 2009). The medial collateral ligament may be identified in nearly half of large dogs (Caine et al. 2009).

Disorders of the Calcaneal Tendon

Partial and Complete Rupture and Healing Process

Injuries to the calcaneal tendon (Achilles tendon) are uncommon in small animals and are usually produced by direct trauma (Lamb and Duvernois 2005). In complete rupture, the echotexture of the CC tendon is completely interrupted, and a hypoechoic and inhomogeneous area (hematoma) is observed between the retracted ends of the tendon. The proximal and distal stumps of the tendon appear drumstick-like and inhomogeneous with a mixed echotexture. During dynamic examination, the movement of the ruptured ends is clearly visible.

With partial tendon rupture, the affected portion (deep or superficial) appears inhomogeneous and hypoechoic to anechoic with poorly demarcated areas (Figure 17.40). In contrast, the part of the tendon that is intact displays a normal fibrillar echotexture. Occasionally, a small anechoic fluid borderline is visible between the tendon and the peritendineum. In chronic partial ruptures, images of the affected part of the tendon can vary from highly inhomogeneous to homogeneous and from hypoechoic to moderately hyperechoic (Figure 17.41). The surface of the calcaneal tuberosity may become irregular because of new bone formation. Avulsed fragments and/or dystrophic mineralization can be recognized within the affected tendon as dispersed hyperechoic foci, which can exhibit acoustic shadowing if their size exceeds 2–3 mm (Figure 17.41A) (Rivers et al. 1997; Swiderski et al. 2005; Caine et al. 2009).

By using ultrasonography, the healing process of the CC tendon with or without surgical intervention can be evaluated (Kramer et al. 2001a). Within the first day after trauma, the hematoma between the ends of the tendon stumps appears hypoechoic to anechoic. Organization of the hematoma during the first and second week leads to a more inhomogeneous image with echogenic areas. From weeks 2–6, the diameter and the inhomogeneity of the injured area increase. After 8 weeks, replacement tissue begins to grow in a longitudinal direction, and both diameter and inhomogeneity decrease. The decrease in diameter is accompanied by the reappearance of the characteristic tendinous fibrillar echotexture. This healing process is completed by 10–12 weeks after trauma. However, the

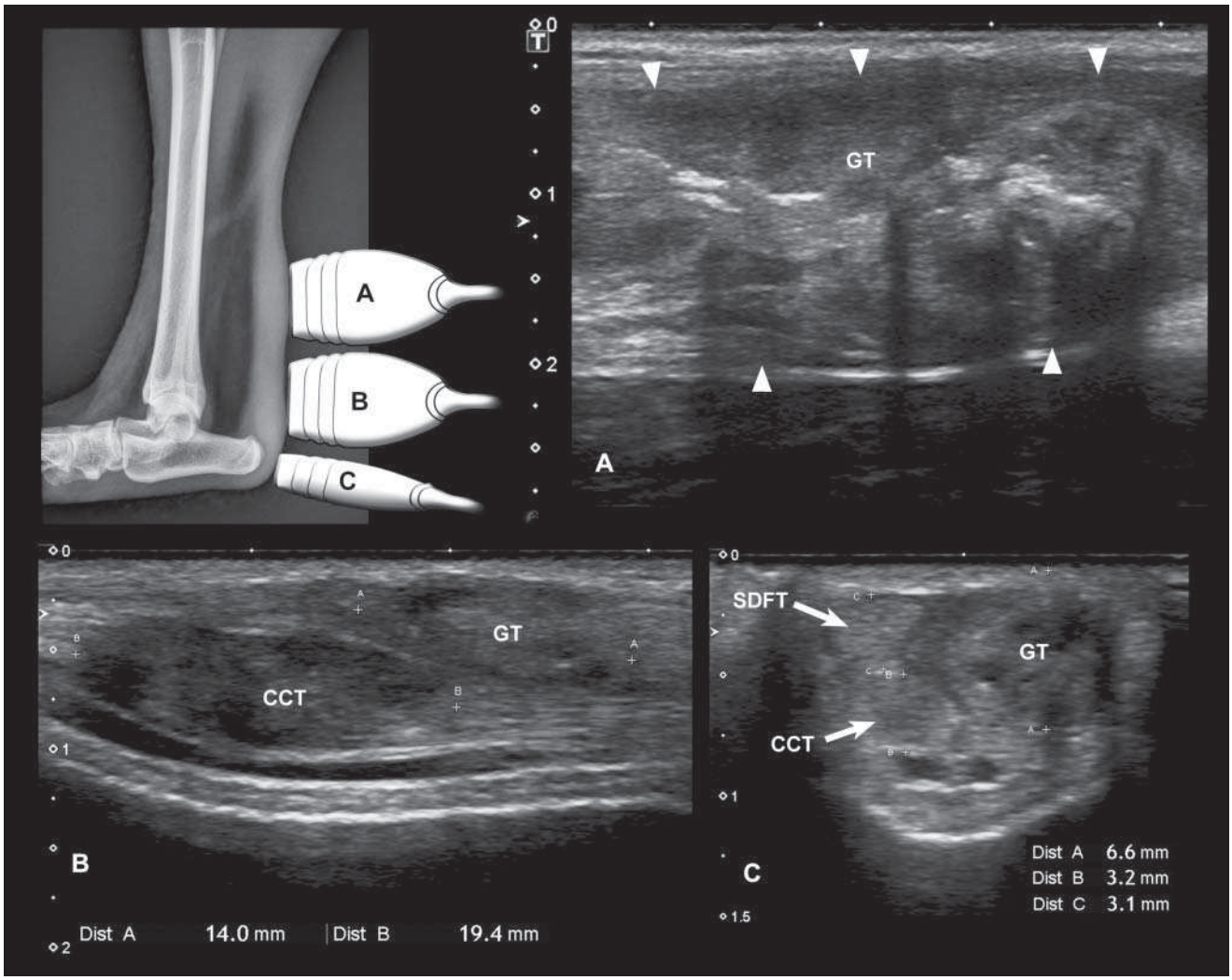


Figure 17.41. Chronic partial rupture of the calcaneal tendon. Longitudinal sonograms obtained at the mid- **(A)** and distal **(B)** calcaneal tendon on which the gastrocnemius tendon (GT) is markedly enlarged, irregular, and heterogeneous in echogenicity at two separate locations, consistent with chronic hemorrhage and fibrous tissue remodeling. Hyperechoic, shadowing foci consistent with dystrophic mineralization are also present proximally **(A)**. The common calcaneal tendon (CCT) is also enlarged and there is loss of its normal fibrillar pattern, also consistent with partial rupture. **C**: In a transverse plane obtained just proximal to the calcaneus, the CCT and superficial digital flexor tendon (SDFT) are enlarged, but with a normal fibrillar pattern.

injured CC tendon remains much less homogeneous in comparison to the unaffected tendon for a long period (up to years). Non-resorbable suture material remains visible as hyperechoic dots.

Luxation of the SDF Tendon Medial or lateral luxation of the SDF tendon can be visualized by obtaining a transverse image above the calcaneal tuberosity. Adjacent to this convex, hyperechoic, shadowing structure, the medially or laterally displaced crescent-shaped to oval tendon comes into view. The luxated tendon can be enlarged and inhomogeneous, and a heterogeneous hematoma can also be observed at the level of fibrous avulsion on the medial or lateral aspect of the calcaneum (Figure 17.42).

Tarsal Joint Instability Damage to the medial or lateral collateral ligaments results in articular swelling that is typically more severe in the area of injury. While hematomas and fibrous tissue can be detected with ultrasound on the affected side(s), clear distinction of the collateral ligaments is limited by their size (Caine et al. 2009) and transducer resolution.

Tarsal Osteochondritis Dissecans While the utility of ultrasound to detect tarsal osteochondral fragments

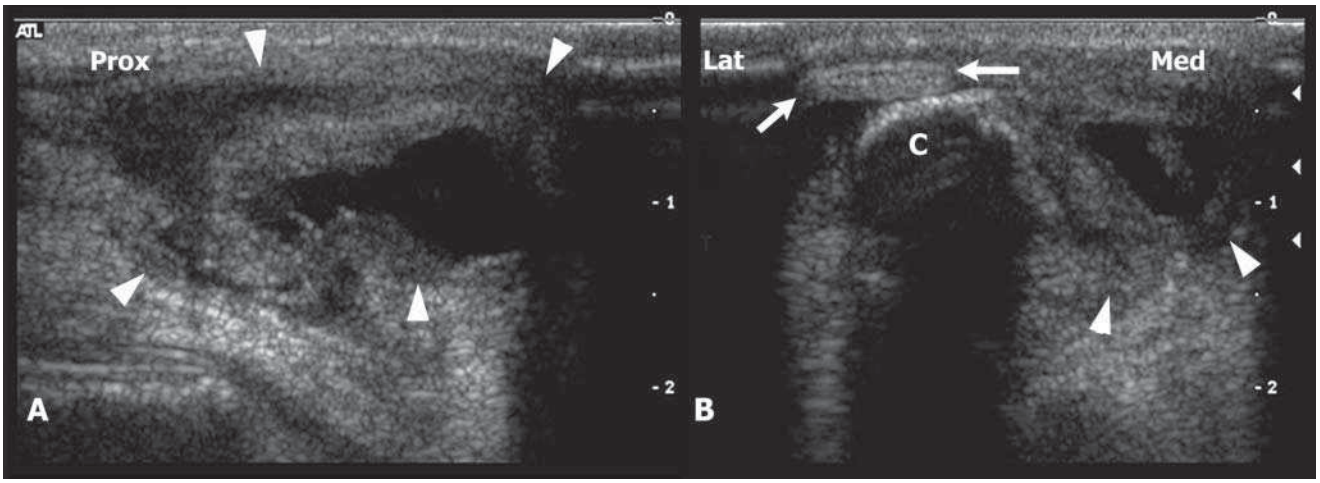


Figure 17.42. Chronic luxation of the superficial digital flexor tendon in large dog. A: In this longitudinal sonogram obtained medial to the calcaneum, an inhomogeneous mass (arrowheads) with anechoic fluid cavities is noted, which is consistent with chronic hematoma and fibrous tissue. Prox, proximal. **B:** Transverse sonogram obtained at the plantaromedial aspect of the calcaneum (C), distal to the calcaneal tuberosity. The superficial digital flexor tendon (arrows) is displaced laterally. The changes caused by chronic hematoma and fibrous tissue thickening are noted medially (arrowheads) in the region of avulsion of tendon insertion. Lat, lateral; Med, medial.

in dogs has not been established, it was found that with this modality, 75% of the trochlear ridges of the talus can be seen, including the most commonly affected sites (Liuti et al. 2007).

Miscellaneous Musculoskeletal Disorders

Musculature

Scanning Technique

Muscles that are located laterally, cranially, or caudally are examined by placing the patient in lateral recumbency with the limb of interest up. Medially located muscles are assessed with the affected limb facing down while abducting the upper limb. Individual muscles are scanned between their origin and insertion by using both longitudinal and transverse planes.

On longitudinal images, the structure of normal muscles appears hypoechoic with fine, oblique, hyperechoic striations. The fascias appear as smooth, continuous, hyperechoic lines, particularly when scanned perpendicularly (Figures 17.6, 17.43). On transverse views, the background is hypoechoic, with echoic dots representing the muscle septa, giving a coarse

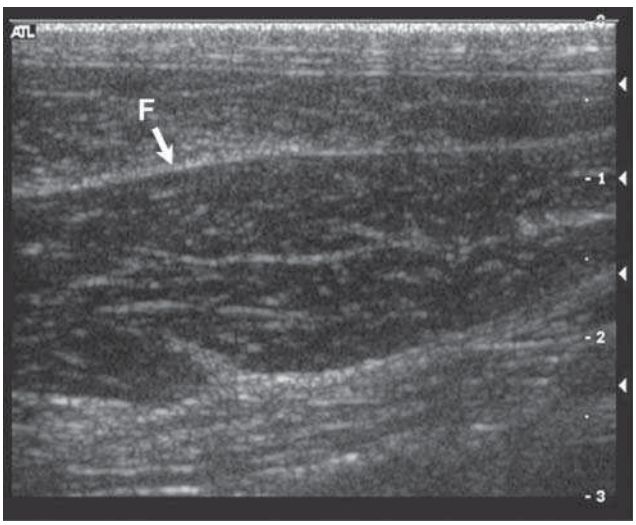


Figure 17.43. Normal muscle sonographic anatomy in a dog. Longitudinal sonographic image of a normal semimembranous muscle showing the characteristic hypoechoic echotexture with fine hyperechoic dots and lines. Intermuscular fascias (F) appear as thin, hyperechoic planes between muscle bellies.

echotexture to the muscle belly. Tangential muscle boundaries are more difficult to image because of edge shadowing (Kramer et al. 1997). Subcutaneous and intramuscular fat planes are usually slightly hyperechoic to muscle bellies, although their appearance can vary.

Miscellaneous Disorders of Muscles and Tendons

Muscle and Tendon Trauma The appearance of muscular trauma varies with the severity and onset of the injury. **Strain injuries**, which may or may not be secondary to a known traumatic event, probably represent an underestimated source of hind lameness in dogs (Breur and Blevins 1997; Nielsen and Pluhar 2004). Hip adductor, pectineus, and particularly iliopsoas muscles appear predisposed to strain injuries. In the acute phase, muscle swelling associated with hypoechoic areas is typically observed (Breur and Pluhar 1997) (Figure 17.44A–C). If the muscle is partially ruptured, the normal muscular echotexture is partially lost and the accompanying hematomas are visible as inhomogeneous, hypoechoic to anechoic, and poorly demarcated areas at the site of injury (Kramer et al. 1997; Swiderski et al. 2005).

Following muscular trauma, the healing process can be evaluated sonographically. In the chronic phase, a hyperechoic and variably inhomogeneous area (with or without acoustic shadowing) at the level of the previous trauma is indicative of scar formation (Breur and Pluhar 1997). The diameter of the muscle may be normal or smaller in the traumatized region.

A **fascial tear** appears as an interruption of the hyperechoic line enrobing the muscle belly, with protrusion of this muscle through the defect. In **complete muscle rupture**, the typical echotexture of the muscle structure at the site of trauma is no longer visible, but is replaced with an anechoic or hypoechoic area representing hemorrhage (Figure 17.44B). In chronic rupture, the region appears highly inhomogeneous with mixed echotexture and echogenicity (organization of the hematoma). The muscle stump can be described as a cob-like, thickened, inhomogeneous structure that is more echogenic than the surrounding tissue. During a dynamic examination with flexion and extension of the limb, the separation of the muscle ends becomes evident (Kramer et al. 1997).

Traumatic avulsion of tendons can also be confirmed with ultrasound. Avulsed tendons are retracted according to the extent of the rupture and level of muscular contraction. Fragments are typically found at the extremity of the stump, appearing as hyperechoic foci with distal acoustic shadowing. In case of acute injury, these fragments are angular and well defined, whereas they tend to become rounded and ill-defined with chronicity. The site of avulsion is typically irregular and a bone defect consistent with the fracture bed can be observed (Figure 17.45). The retracted tendon is thickened and often heterogeneous with loss of normal echotexture.

Fibrosing and Calcifying Myopathies and Tendinopathies Fibrosing and calcifying myopathies and tendinopathies, which may or may not be traumatic in origin, are occasionally seen in lame or clinically normal dogs. The muscular and/or tendinous part of the supraspinatus, iliopsoas, gluteal, and biceps brachii are more commonly affected (Figures 17.9, 17.10, 17.46, 17.47). Gracilis and semitendinous myopathy is a well-described entity in dogs resulting in characteristic clinical signs (Figure 17.48). The affected tendon or muscle may become enlarged, with an altered, inhomogeneous echotexture that varies in echogenicity. Mineral deposits may become visible as hyperechoic, irregular structures that display acoustic shadowing.

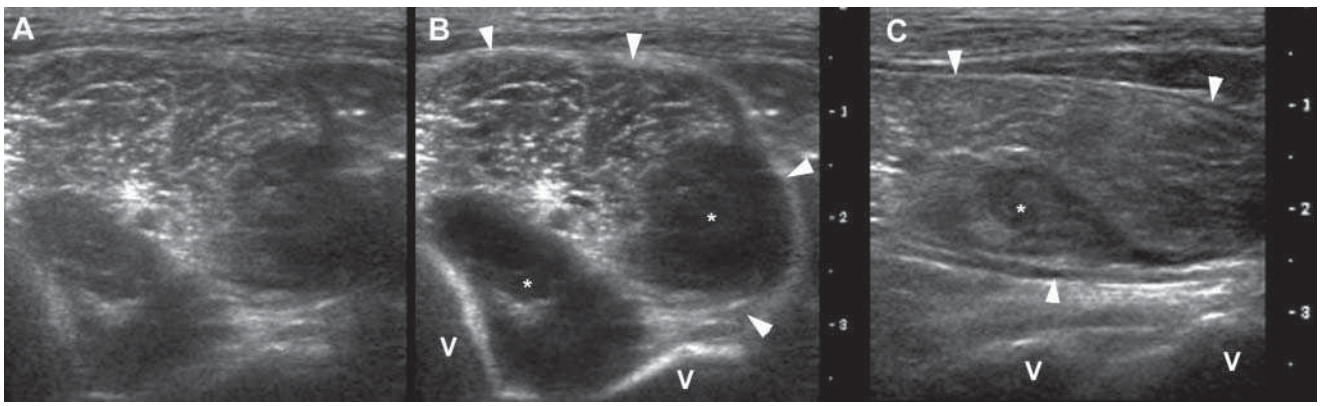


Figure 17.44. **Acute muscle tear. A–C:** Iliopsoas strain in an 8-year-old Boxer that became lame after a strenuous hike. Transverse sonographic **(A)** and enhanced **(B)** images, as well as a longitudinal sonogram **(C)**, of the right iliopsoas muscle obtained at the lateral aspect of the caudal lumbar spine. The muscle (arrowheads) is diffusely enlarged, and two large hypoechoic lesions (*) within the muscle are disrupting its architecture. These areas most likely represent tears associated with hemorrhage and edema. This process was bilateral. V, caudal lumbar vertebra.

Figure 17.46. **Bicipital calcifying myopathy. A:** Mediolateral radiograph of the shoulder region of a 2-year-old large-breed dog with chronic front leg lameness. An irregular mineral opacity is noted superimposed over the proximal humeral metaphysis in the region of the biceps muscle. **B, C:** Longitudinal sonograms obtained at the proximal aspect of the biceps muscle. This portion of the muscle is enlarged (arrows), heterogeneous, and contains irregular hyperechoic areas with acoustic shadowing, consistent with mineralization (M). BT, bicipital tendon. H, humerus. **D, E:** Transverse sonograms. The biceps tendon (cursors) is also mildly enlarged on this transverse image **(D)** obtained at the level of the bicipital groove (BG) (plane D′ in **A**). Just distal to the bicipital groove (plane E′), the biceps muscle (between the cursors in **E**) is thickened and presents hyperechoic foci, some of which are associated with acoustic shadowing, consistent with mineralization and fibrosis. H, humerus.

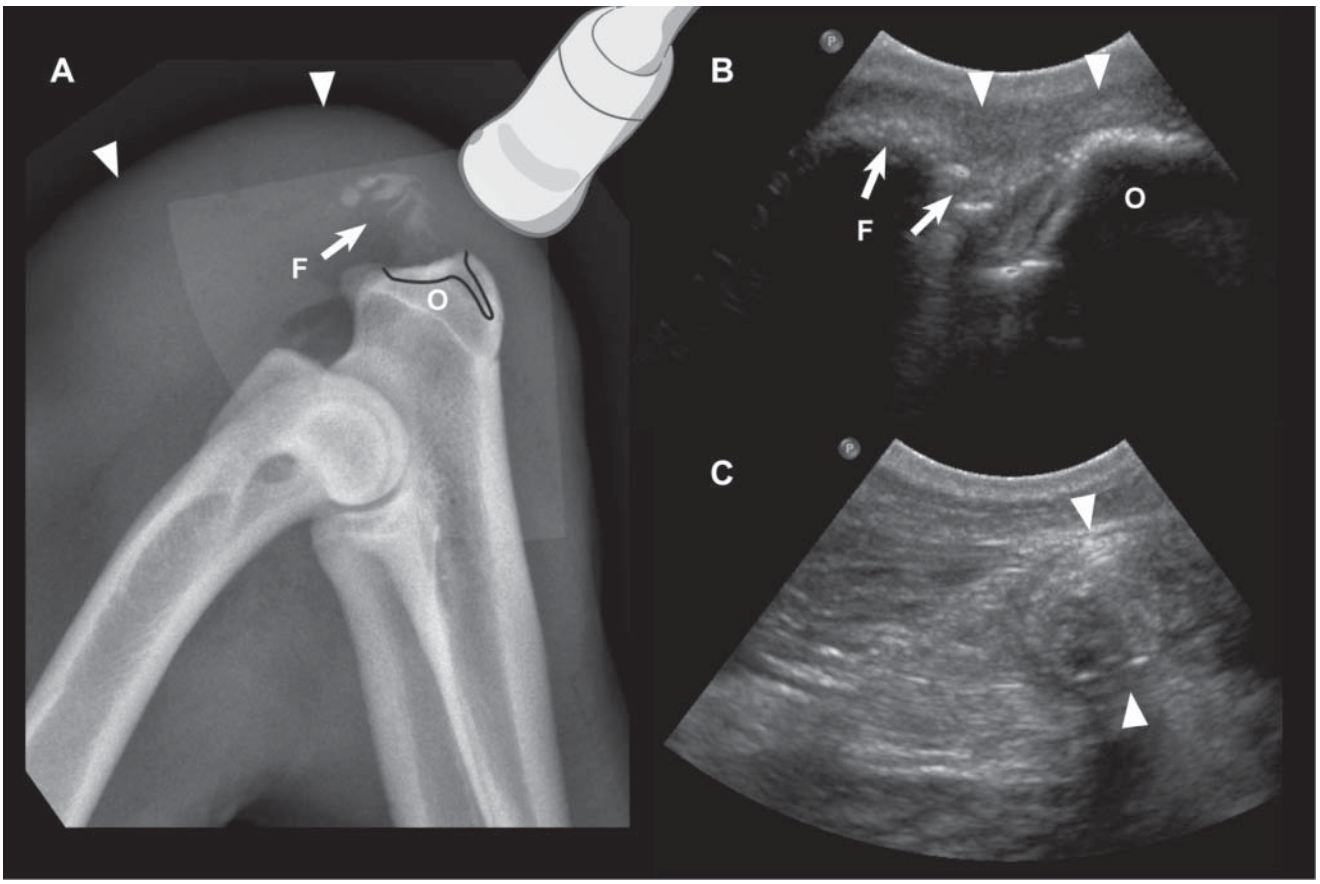


Figure 17.45. **Triceps tendon avulsion fracture. A:** Flexed lateral radiograph of the elbow of a dog with severe thoracic lameness. Note the severe soft-tissue swelling (arrowheads) and the mineral fragments (F) proximal and dorsal to the olecranon (O). The insertion site (black curved line) of the triceps tendon on this bone is mildly irregular. **B:** Sagittal sonographic image obtained at the level of the olecranon (O) showing the mineral fragments (F) casting complete acoustic shadow, distal to the tensor fasciae antebrachii (arrowheads). **C:** Longitudinal sonographic image obtained proximal to the fragments. The triceps tendon is focally enlarged and heterogeneous, with loss of the normal fiber pattern.

Figure 17.47. **Gluteal calcifying myopathy.** Longitudinal sonographic and enhanced images of the distal portion of the middle gluteal (MG) and deep gluteal (DG) muscles. The DG muscle (arrowheads) is heterogeneous and presents hyperechoic foci near its insertion site on the greater trochanter (GT), consistent with mineralization.

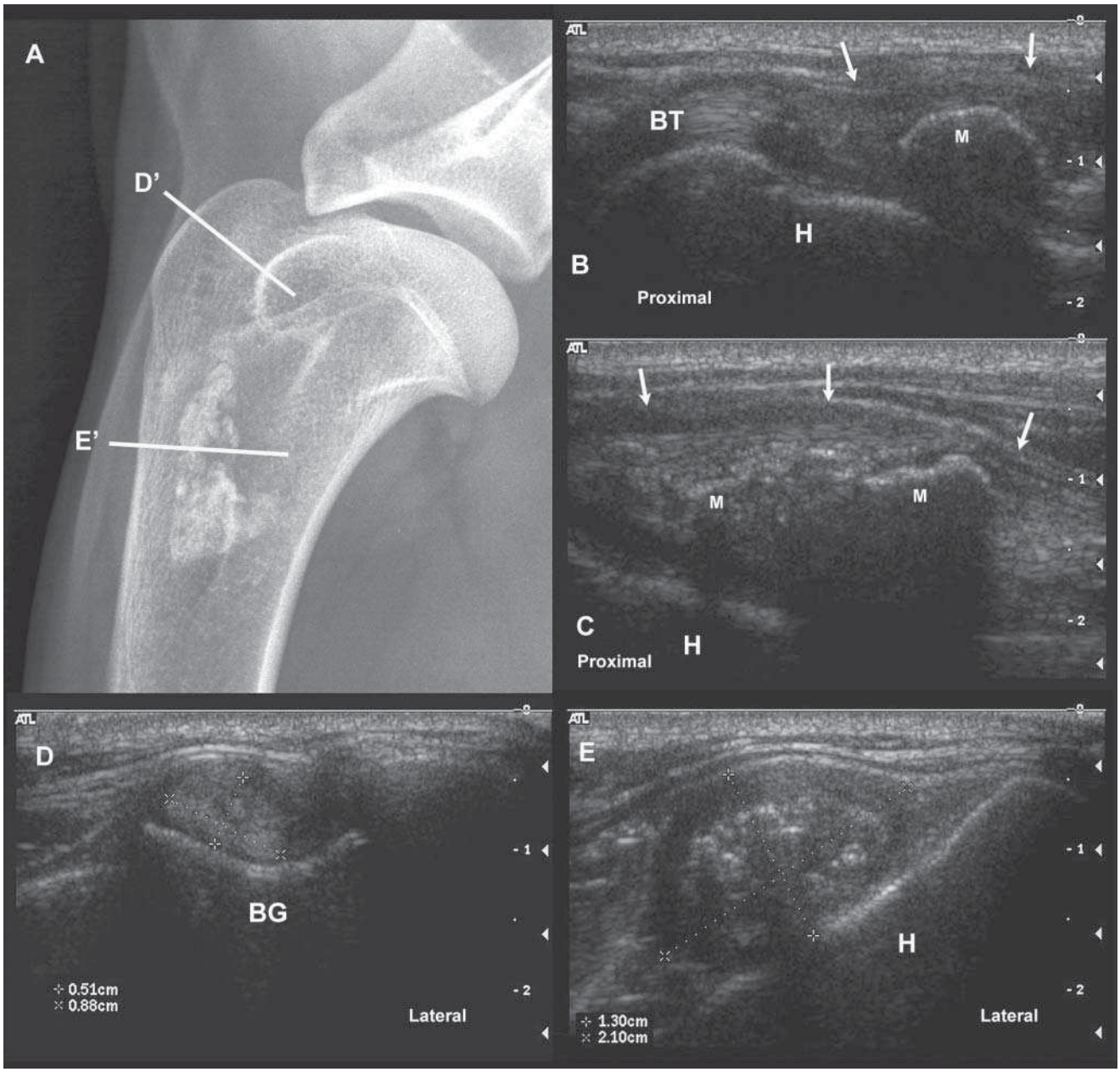


Figure 17.46. **Bicipital calcifying myopathy.** (for full caption, see facing page)

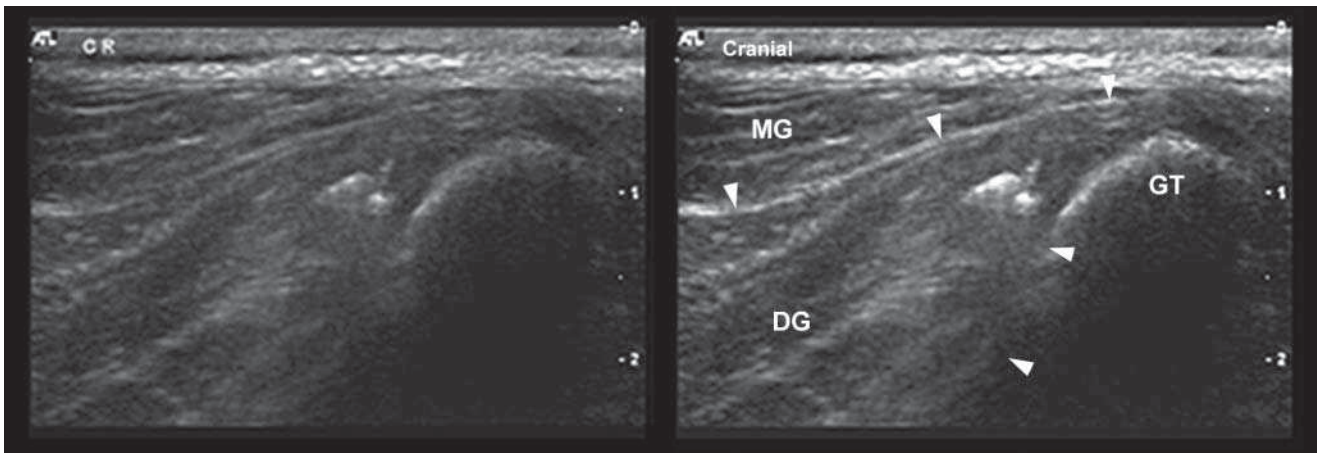


Figure 17.47. **Gluteal calcifying myopathy.** (for full caption, see facing page)

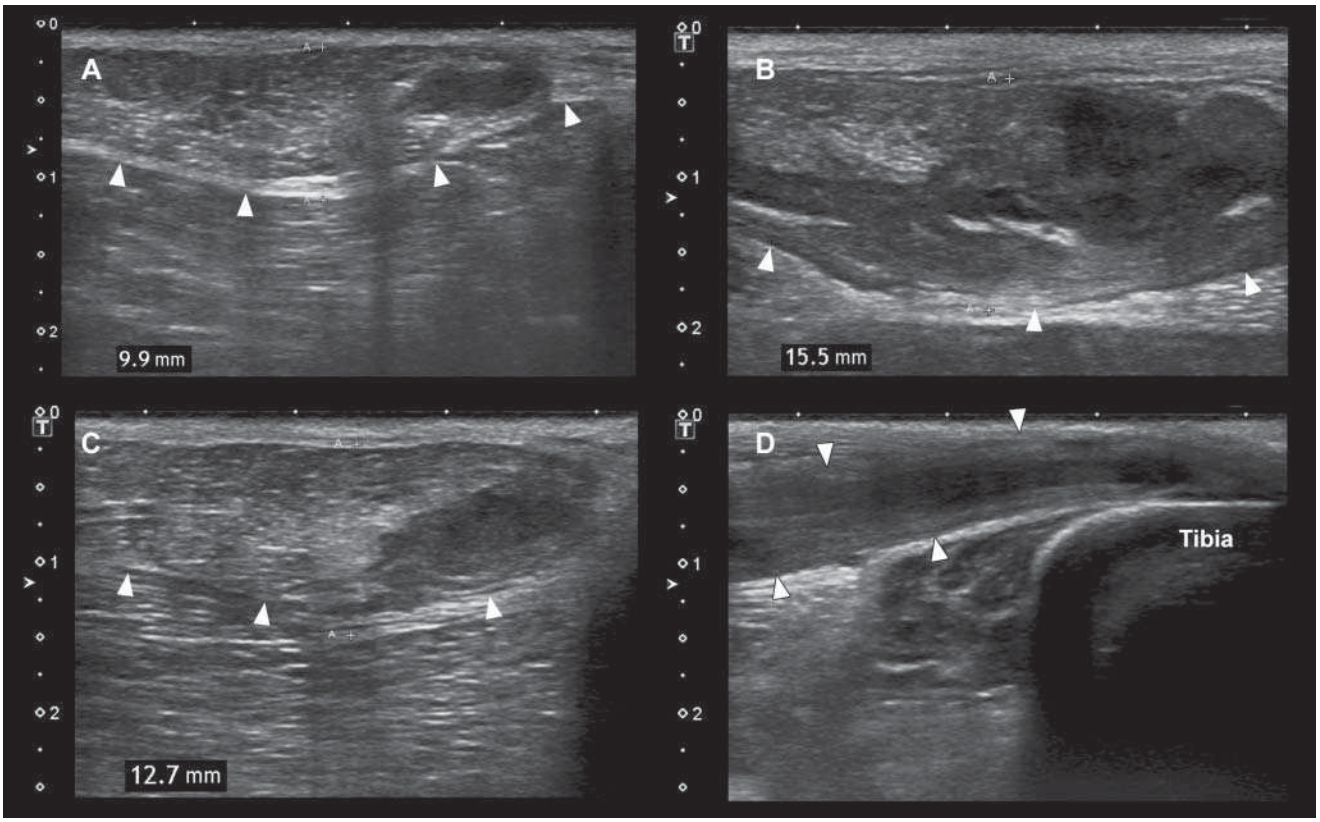


Figure 17.48. **Gracilis fibrosing myopathy. A-C:** Transverse sonographic images obtained at the proximal, mid- and distal thirds of the thigh of a 5-year-old German Shepherd Dog with gradual onset of hind lameness, weakness, and pain. The gracilis muscle (arrowheads) is severely enlarged and mixed in echogenicity. Its echotexture is modified with several hyperechoic areas. Its tendinous portion (seen longitudinally in **D**) is also enlarged and hypoechoic, with its fibrillar pattern being partly lost.

Ligaments

Scanning Technique and Normal Sonographic Anatomy

The ligaments of dogs and cats are usually very small and frequently close to uneven bony surfaces, making sonographic assessment difficult. The use of high-frequency (ideally > 12 MHz) linear transducers directed perfectly perpendicular to the ligament is essential.

In longitudinal scans, linear ligaments appear as hyperechoic structures with a fibrillar echotexture (Figure 17.21). Most ligaments are too small to be consistently identified, particularly in cross-sectional planes, and they cannot be distinguished from the surrounding structures (capsule and muscle fascia). Ligaments with fanning fibers are oriented obliquely (e.g., cruciate ligaments) and are usually hypoechoic.

Sonographic Features of Ligament Disorders

Because of their small size, acutely ruptured ligaments cannot be easily visualized with ultrasound. A small anechoic or hypoechoic hematoma in the area of rupture may be seen in the initial phase. If the injury is associated with a bone avulsion fracture, the fragment is visible as a hyperechoic structure with acoustic shadowing within the reactive tissue (Figure 17.49). The corresponding fragment bed may be recognized as a small concavity on the surface of the adjacent bone. Ruptured ligament stumps can become hyperechoic and thickened, particularly in the chronic phase. Ligament rupture may cause joint instability, which may be evidenced with a dynamic examination. Synovial and capsular thickening develop.

Luxations

Ultrasound may help identifying joint or ligament luxation when physical examination and radiographs are not sufficient. Coxofemoral joint luxation typically causes craniodorsal displacement of the femoral head. Ultrasound may help to confirm the luxation from a lateral approach with the dog in lateral recumbency and the affected hip on top.

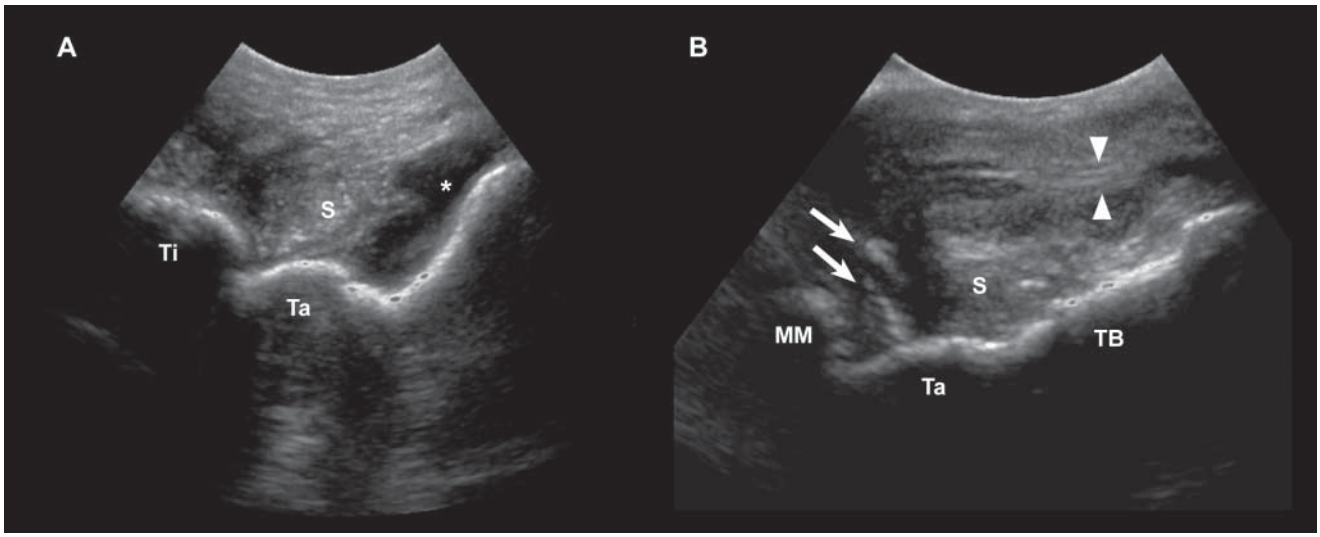


Figure 17.49. Talocrural medial collateral ligament rupture in a dog. Sagittal dorsal **(A)** and sagittal medial **(B)** sonographic images of the talocrural joint of a traumatized dog. The joint synovium (S) is thickened and associated with effusion (*) dorsal to the talus (Ta). Medially, several hyperechoic foci (arrows) are present distal to the tibial medial malleolus (MM), consistent with small bone and/or ligament fragments. The distal stump of the medial collateral ligament is visible more superficially and distally (arrowheads). Ti, tibia; TB, tarsal bone.

Cellulitis, Abscesses, and Foreign Bodies (FBs)

Cellulitis is an inflammatory process involving the connective tissue and typically appears as alternating anechoic and hyperechoic bands in the subcutaneous planes, often resulting in increased ultrasound-beam attenuation, which limits the assessment of deep structures (Figure 17.50). Inflamed tissue can become swollen. **Phlegmon** is a suppurative inflammation of the connective tissue that typically leads to accumulation of hypoechoic fluid pockets in the subcutaneous tissues (Figures 17.50, 17.51). **Necrotizing fasciitis**, which has been described in two puppies affected by *Streptococcus canis*, can also be associated with similar fluid pockets (Kulendra et al. 2008). More confined **abscesses** may also develop and appear as cavitary lesions containing particulate fluid. A hyperechoic wall of variable thickness is often recognized in the chronic phase (Figure 17.50). Internal septa may also form. Thus, abscesses can be complex in ultrasonographic appearance and resemble neoplastic processes. An abscess can be identified as either intramuscular or intermuscular, subfascial, or subcutaneous. Ultrasound-guided fine-needle aspiration or drainage may assist in the diagnosis and treatment of the suppurative process (Figure 17.51B).

Inflammatory processes may be secondary to the presence of **FBs**, such as wooden sticks (Figure 17.52), porcupine quills (Figure 17.53), grass awns (Figure 15.12), glass, or plastic or metal objects. The accuracy of ultrasonography in detecting FBs, particularly if superficial, in people is high (Boyse et al. 2001; Brisson et al. 2004). Although most FBs are hyperechoic to normal soft tissues, their echogenicity can vary, depending on their physical and acoustic characteristics (Boyse et al. 2001; Armbrust et al. 2003). Acoustic shadowing is expected; however, it may only be partial or it may be masked by the presence of a bony structure in the far field or by the ultrasonographic complexity of the associated soft-tissue reaction. Wooden FBs are hyperechoic and cast a shadow when inserted in cadaveric canine manus (Ober et al. 2008), but these may lose their echogenicity and become confounded by the surrounding tissue changes in chronically affected animals (Staudte et al. 2004). A hypoechoic rim, consistent with an inflammatory cast or fistular tract, commonly develops around an FB, helping its identification (Shah et al. 1992; Kramer et al. 1997; Gnudi et al. 2005) (Figure 17.52). A fistular tract that may contain gas may also be recognized (Figure 17.53). Also, in some instances, the artifacts associated with the FBs are more clearly visible than the FB itself. The characteristics of the

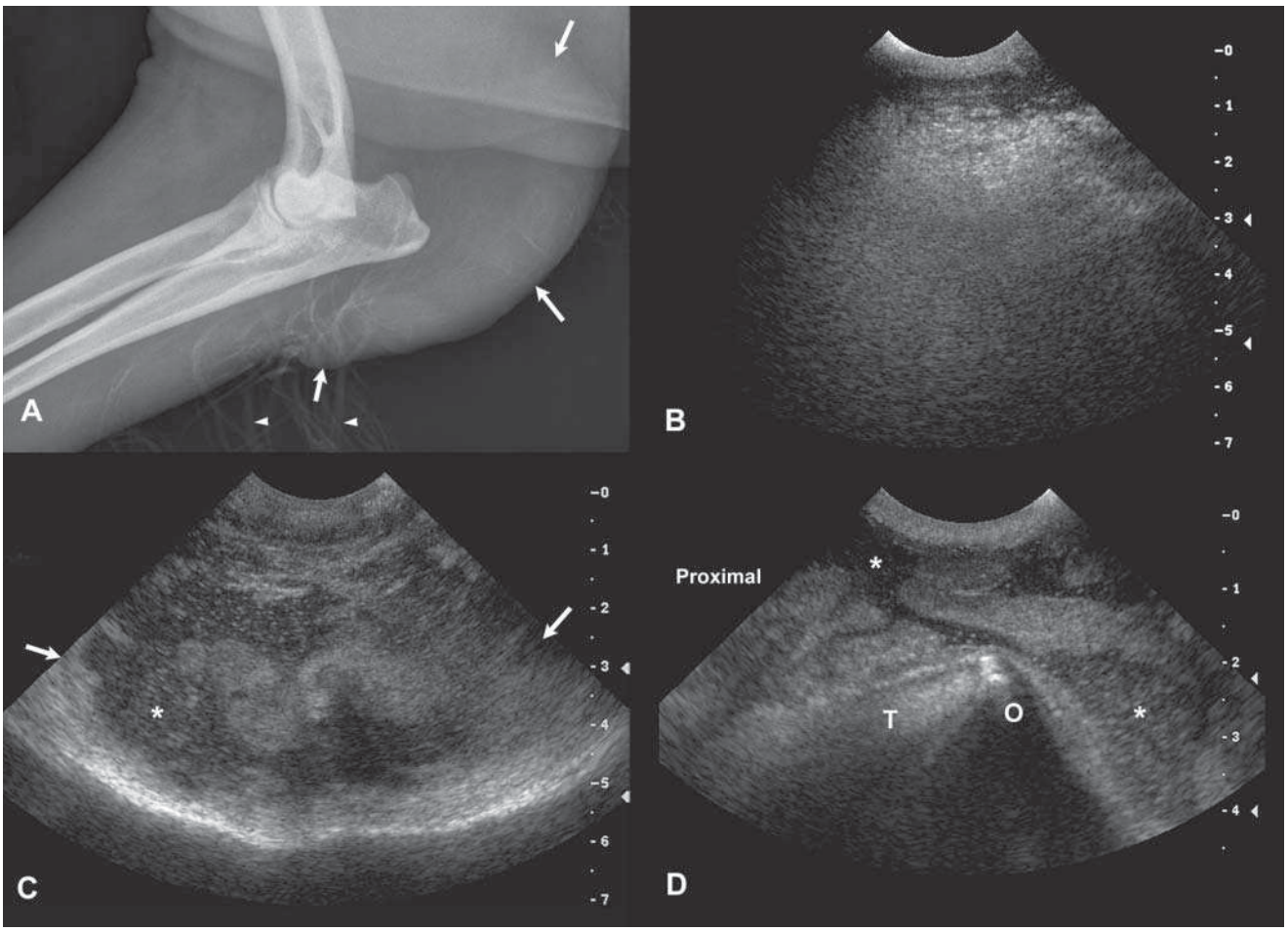


Figure 17.50. **Septic abscess in the elbow region of a dog. A:** Mediolateral radiograph of the elbow region of a 5-year-old large-breed dog with progressive, painful swelling caudal to the elbow. Soft-tissue swelling (arrows) is present without evidence of bone involvement or a radiopaque foreign body. This radiograph was obtained after the ultrasound exam, which explains the presence of artifacts caused by wet hair (arrowheads) caused by the presence of acoustic gel. **B:** In the proximal region of the limb, the subcutaneous tissue appears hyperechoic and hyperattenuating as the result of cellulitis. **C, D:** A large cavitary mass lesion (arrows) containing echogenic fluid (*) and mobile echogenic septa is caudal to the olecranon (O) and triceps tendon (T). An irregular, moderately echogenic capsule is noted proximally (arrow to the left in **C**).

Figure 17.51. **Paramuscular abscess and myositis in a cat.** Transverse **(A)** and longitudinal **(C)** sonographic images obtained at the caudal aspect of the femur (F) in a cat with pelvic limb swelling and fever. An irregular accumulation of echogenic fluid is found between one of the muscles (M) and the femur. **B:** This cavitary lesion was aspirated using ultrasound guidance, which led to a diagnosis of a septic abscess. The arrowheads point to the needle. **D:** A nearby inhomogeneous mass (arrows) was found adjacent to large vessels. Fine-needle aspiration confirmed the presence of septic and necrotic myositis.

Figure 17.52. **Wooden fragment foreign bodies in two dogs. A–C**: The wood fragment presents as a well-defined hyperechoic interface with strong acoustic shadowing, in longitudinal (**A**) and transverse (**B**) sonographic planes. **D**: Transverse sonographic image obtained at the dorsal aspect of the metacarpal bones (MC) of another dog. A thin, straight, hyperechoic foreign body (FB) is surrounded by mildly echogenic inflammatory tissue (arrows). A wooden stick was identified at surgery. Images A–C courtesy of Laurent Couturier, Azurvet, France.

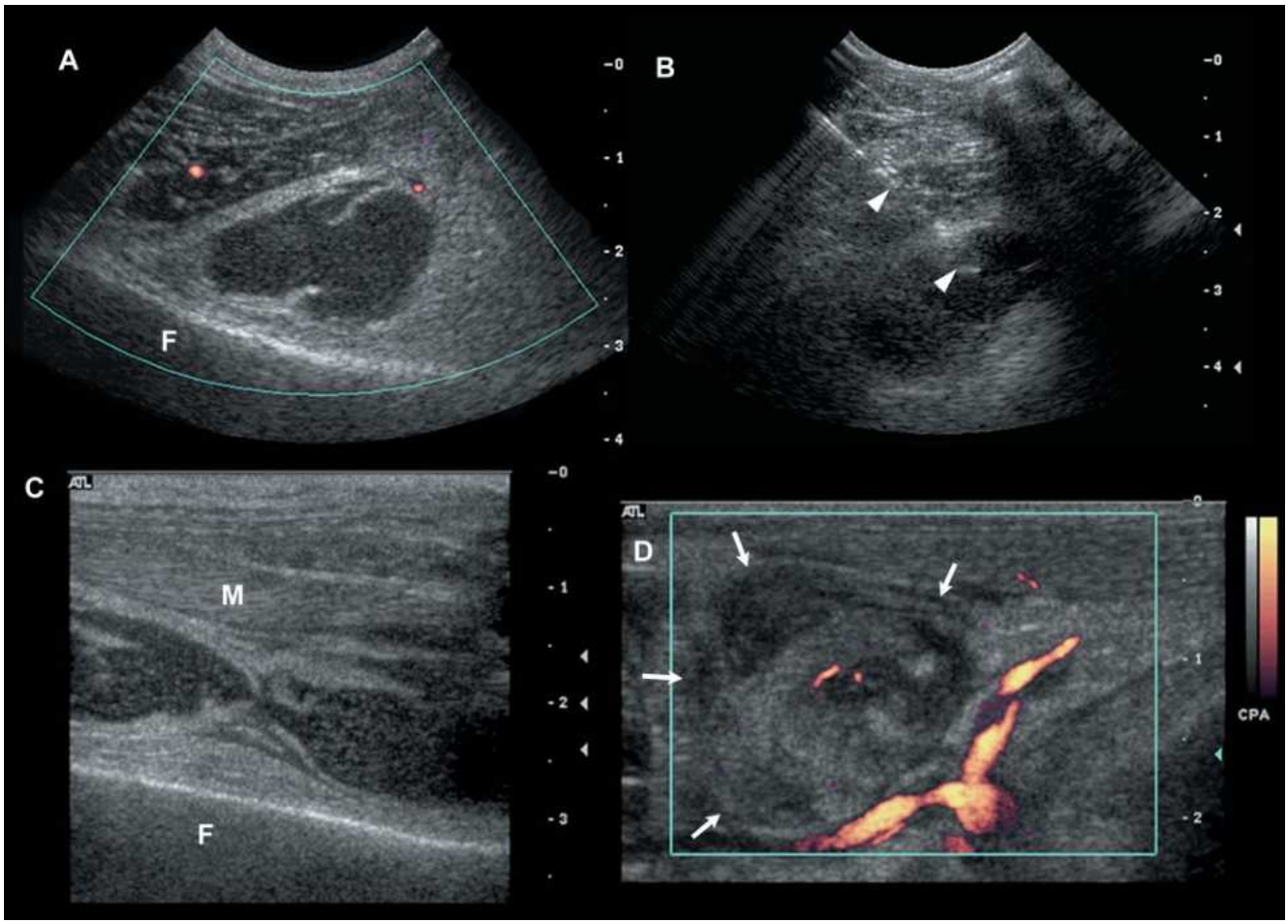


Figure 17.51. **Paramuscular abscess and myositis in a cat.** (for full caption, see facing page)

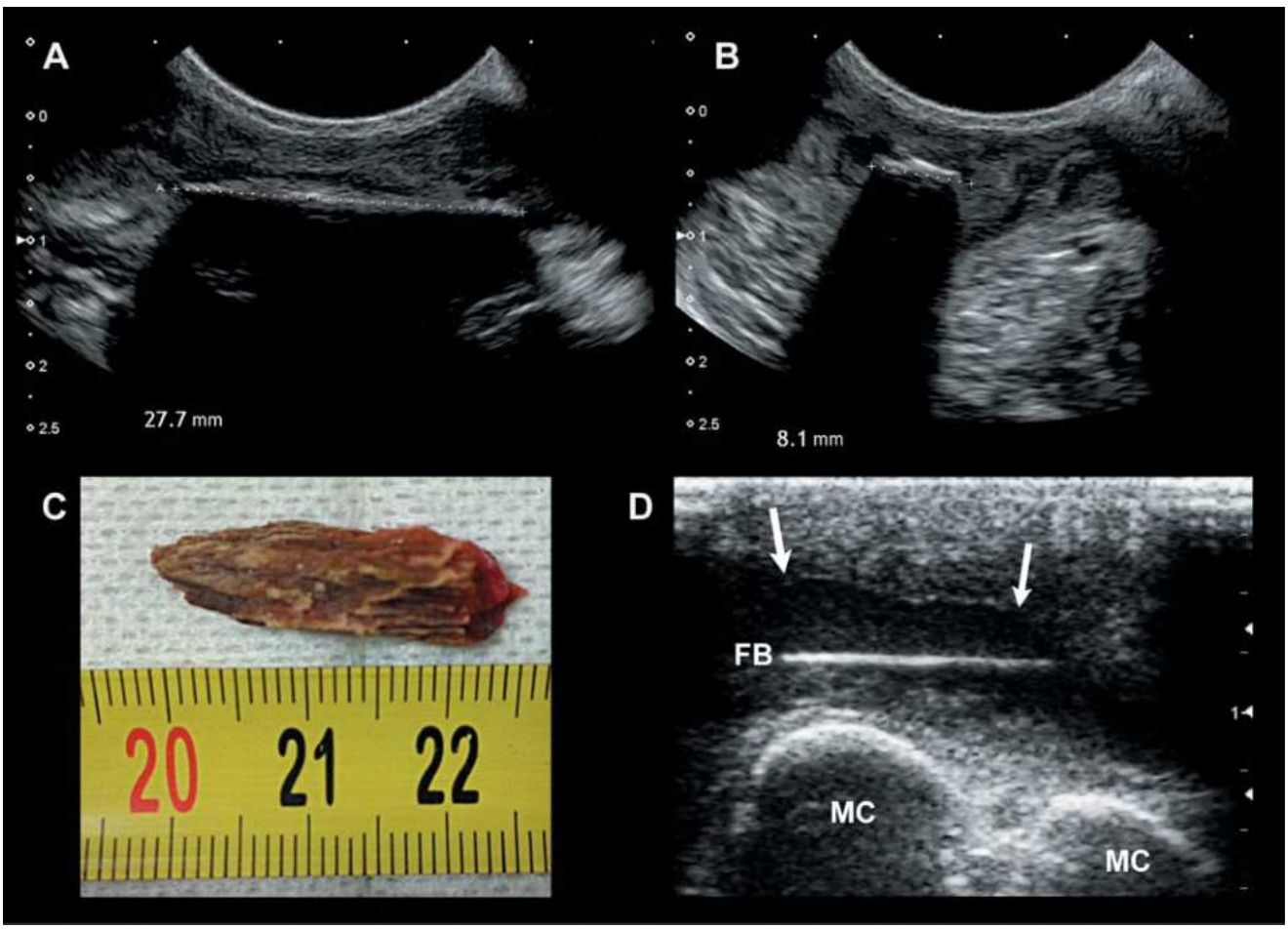


Figure 17.52. **Wooden fragment foreign bodies in two dogs.** (for full caption, see facing page)

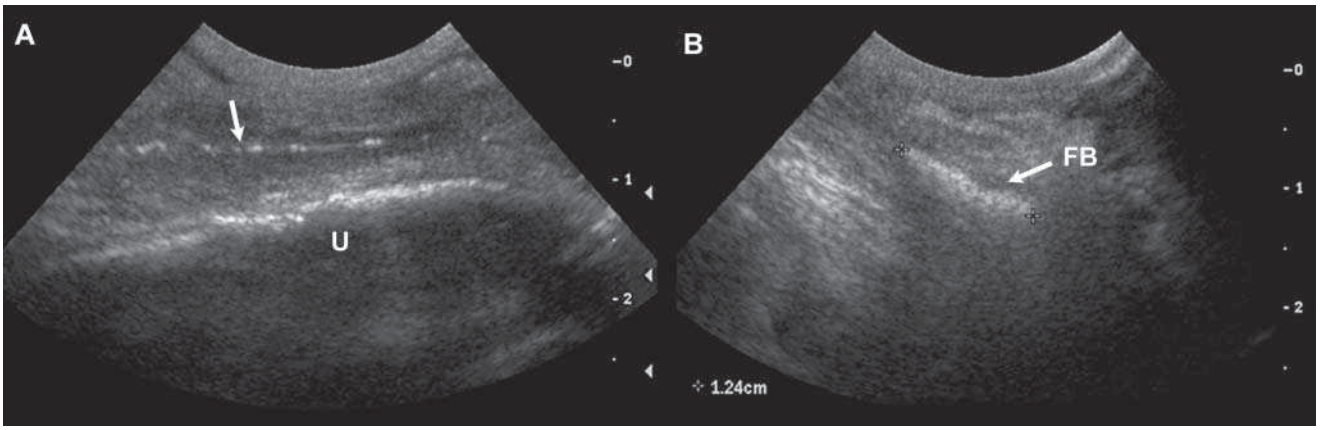


Figure 17.53. Fistular tract and foreign body. A: Longitudinal image of the region caudal to the proximal ulna (U) in a dog with a chronic draining tract. An interrupted hyperechoic line (arrow), consistent with gas, is seen within a hypoechoic cast of fibrous tissue. The caudal surface of the ulna is irregular because of periostitis. **B:** More distally, a 1.2-cm-long hyperechoic interface with dirty shadowing is found, which indicated a foreign body (FB).

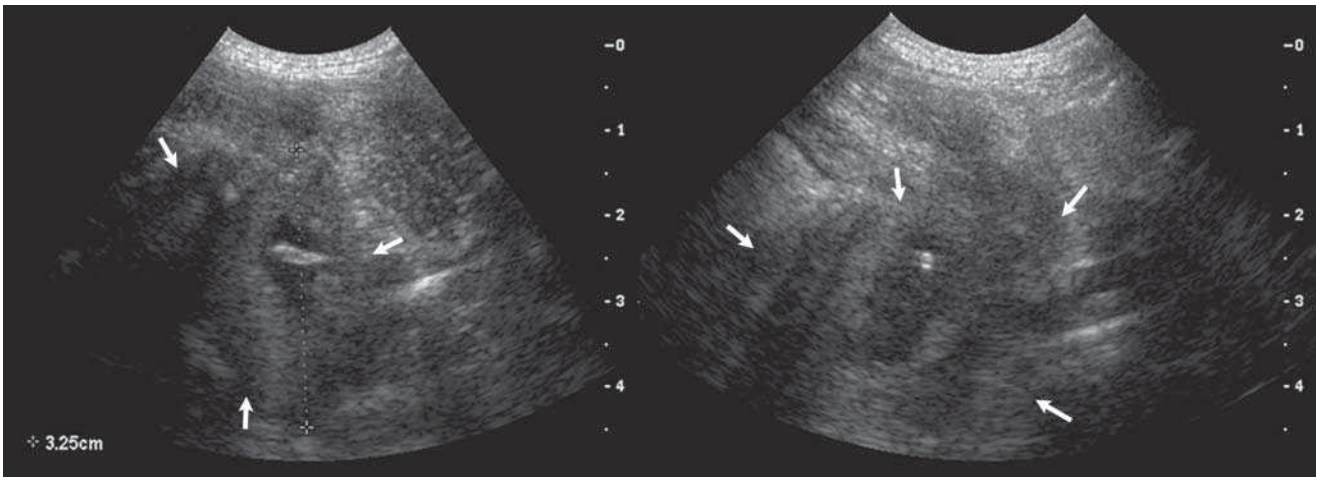


Figure 17.54. Porcupine quill migration and abscess. A 3.25-cm, moderately echogenic mass (arrows) is shown with a central fluid-filled cavity as well as a short, fusiform, double-lined hyperechoic structure when seen longitudinally and circular when seen transversely.

artifacts present deeper to the objects appear to be related to the surface shape of the FBs rather than to its composition (Boyse et al. 2001). Metal objects such as BB pellets are typically associated with reverberation artifacts (comet tails), which may be confused with air bubbles. Metal objects of any size can easily be identifiable on standard radiographs. Glass is typically hyperechoic and may be recognized on radiographs. Porcupine quills, which are usually not visible on radiographs, appear as double-banded, fusiform, hyperechoic structures (Figure 17.54). Grass awns typically appear as a double/triple spindle-shaped echogenic interface, often with acoustic shadowing (Gnudi et al. 2005).

Small FBs may remain undetected if smaller than 2–3 mm or if deeply embedded in tissues. Furthermore, the presence of nearby mineral or aerated structures, such as in the region of the distal extremities (e.g., sesamoid bones) or the larynx and hyoid apparatus, may be confused for FBs or limit their identification.

Ultrasound may also be useful in the surgical localization or removal of the FB (see the section on interventional procedures).

Benign and Malignant Tumors

Soft-tissue tumors can usually be identified using ultrasonography and are classified as solid, cystic,

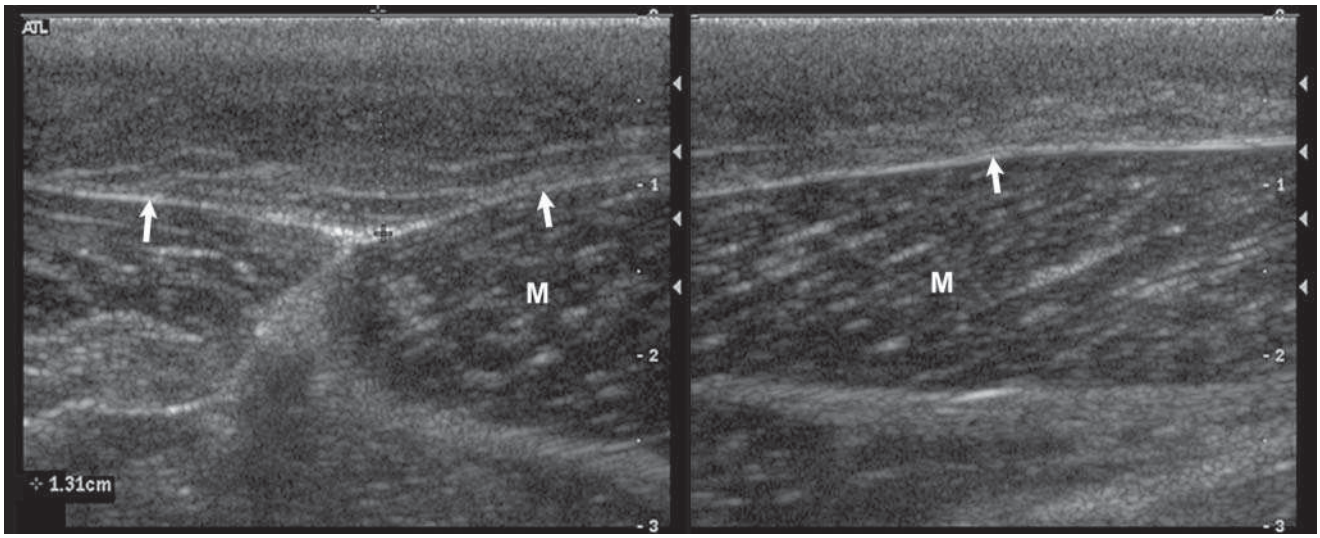


Figure 17.55. Subcutaneous lymphoma in a cat. In these sonographic images obtained at the lateral aspect of the pelvic limb, a moderately echogenic band in the near field is silhouetting with the dermis. Muscle bellies (M) are displaced, but not invaded by the neoplastic process. The muscle fascias (arrows) remain well defined.

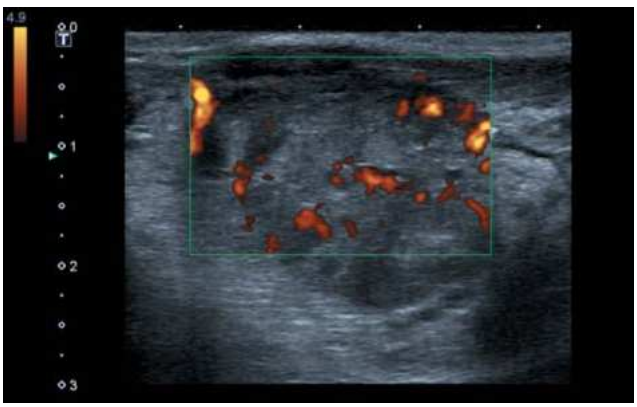


Figure 17.56. Muscular sarcoma in a dog. Sonographic image a 2.5-cm-wide soft-tissue mass involving the gastrocnemius muscle of a dog. The mass is mildly echogenic and heterogeneous, and well vascularized, as evidenced by using color Doppler in the deep portion of the mass.

or mixed lesions. Tumors may range from homogeneous to highly inhomogeneous in echotexture, and from anechoic to highly hyperechoic, sometimes with mineralization (Figures 17.55–17.58). The tumor margins may or may not be clearly visible. When color Doppler is used, malignant tumors can appear hypervascular with tortuous and randomly distributed vessels (Figure 17.56). However, malignant tumors may also be poorly perfused and/or necrotic (Figure 17.57). Ultrasonography cannot accurately differentiate malignant and benign diseases such as hemorrhage (Figure 17.59). Ultrasound-guided or surgical aspiration or biopsy is required in all cases.

Lipomas appear as mildly echogenic masses with diffuse hyperechoic dots and striations (Volta et al. 2006) (Figure 17.60). Lipomas can be located in the subcutaneous or intermuscular planes or within muscles (intramuscular). They typically show a thin, well-defined hyperechoic capsule, although they can be ill-defined when invasive. Yet accurate distinction between invasive or non-invasive lipomas cannot be made by means of ultrasonography.

Ultrasound can also be very useful in the identification of **joint soft-tissue tumors**, such as synovial cell sarcoma or histiocytic sarcoma. These tumors can vary in echotexture and echogenicity but typically appear as an irregular soft-tissue thickening that crosses the joint space, invades the osteochondral junctions, and protrudes into the synovial space (Figure 17.61). The bone surface at the periphery of the joint becomes irregular, and soft-tissue nodules or masses can be seen to extend within the metaphyseal cortex and medulla. These changes may also resemble severe DJD or other arthropathies, which justifies fine-needle aspiration or biopsy that can be safely done under ultrasound guidance.

Joint Effusions

Joint effusion in OCD or osteoarthritis is typically anechoic. In comparison, septic effusions appear more echogenic, and floating particles are often observed

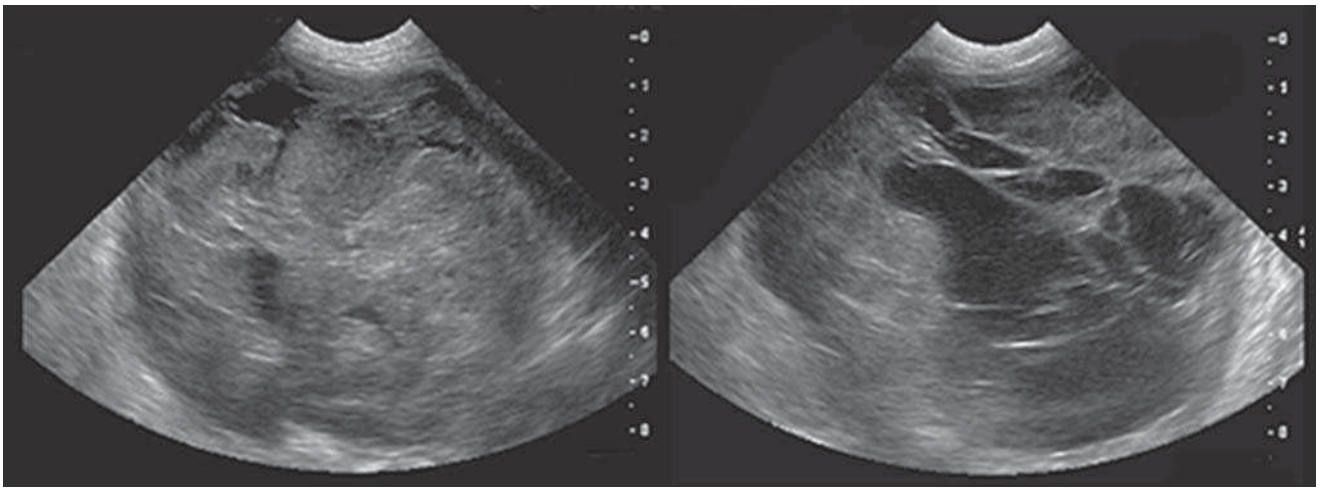


Figure 17.57. **Fibrosarcoma.** Sonographic images of a large soft-tissue mass involving the pelvic limb of a dog. This mass is solid and moderately echogenic in most areas, but also presents anechoic, fluid-filled necrotic and hemorrhagic cavities.

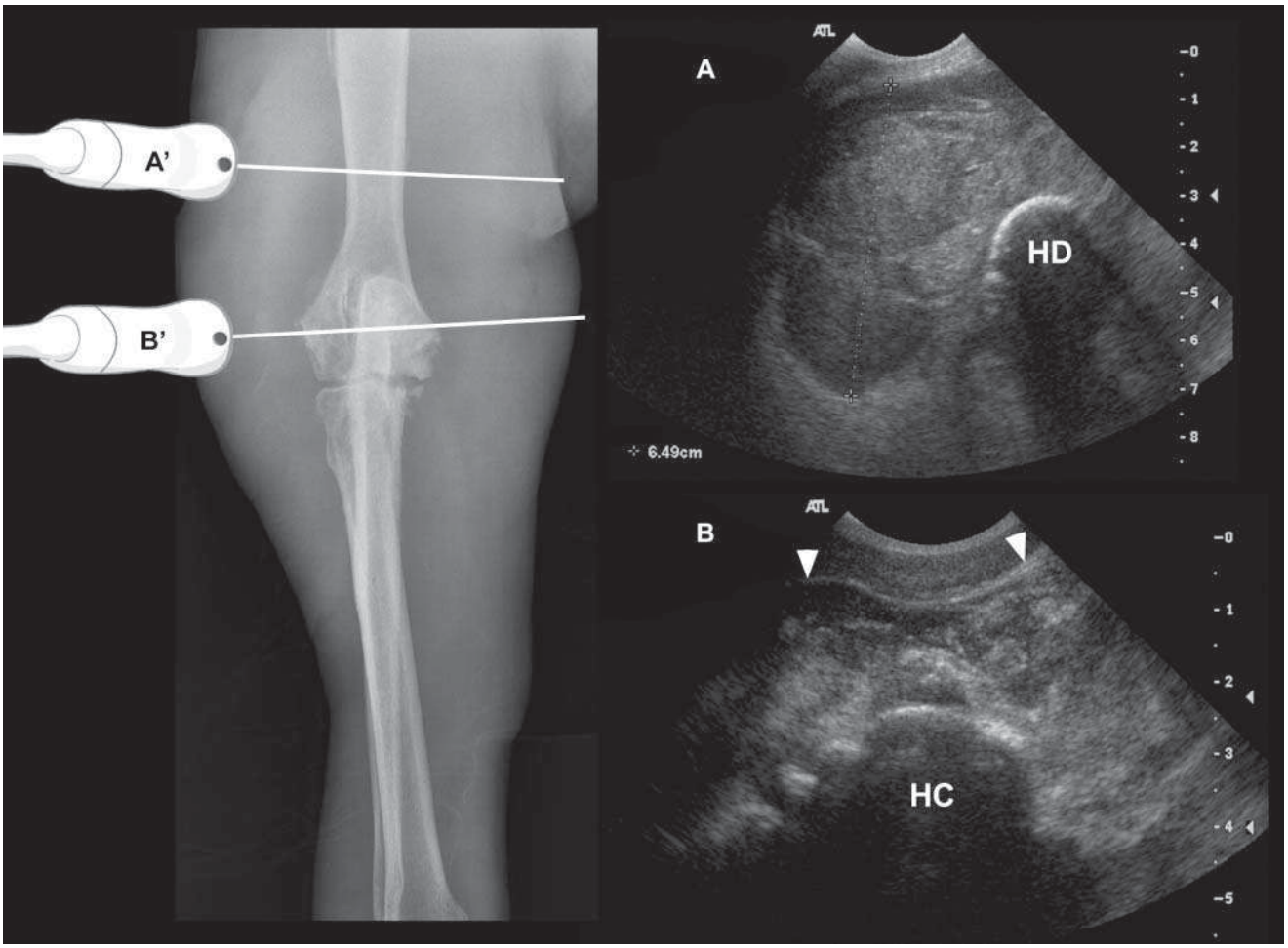


Figure 17.58. **Large soft-tissue sarcoma in a 10-year-old mixed breed dog.** The craniocaudal radiograph of the elbow of this dog shows severe soft-tissue swelling and an irregular new bone formation involving the humeral condyle and proximal radius and ulna. The convex sonographic probe was placed in transverse plane to obtain images **A′** and **B′**, at the level of the humeral diaphysis (HD) and humeral condyle (HC), respectively. Note the heterogeneous mass (arrowheads and between calipers) partly encircling the humerus of this dog.

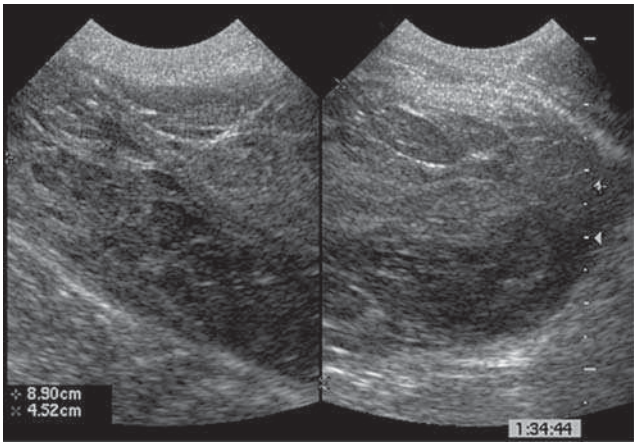


Figure 17.59. Muscular hemorrhage. Sonographic images of the pelvic limb of a dog with rapidly progressive swelling. A hypoechoic, inhomogeneous mass measuring more than 9 cm is noted involving the musculature. Hemorrhage was found on fine-needle aspiration. This mass resolved with time and was presumed to represent a benign spontaneous hematoma of uncertain origin.

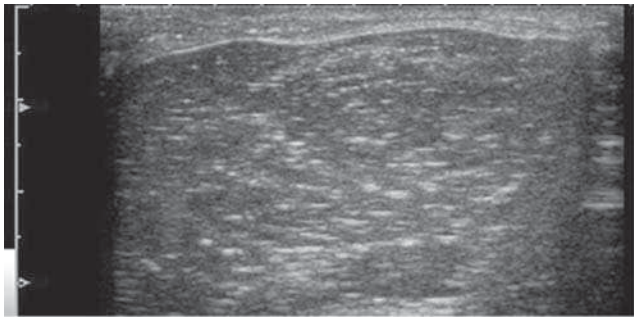


Figure 17.60. Lipoma. Sonographic image of a pelvic limb subcutaneous mass with features characteristic of a lipoma. The mass is moderately echogenic and has uniformly distributed hyperechoic dots and short lines.

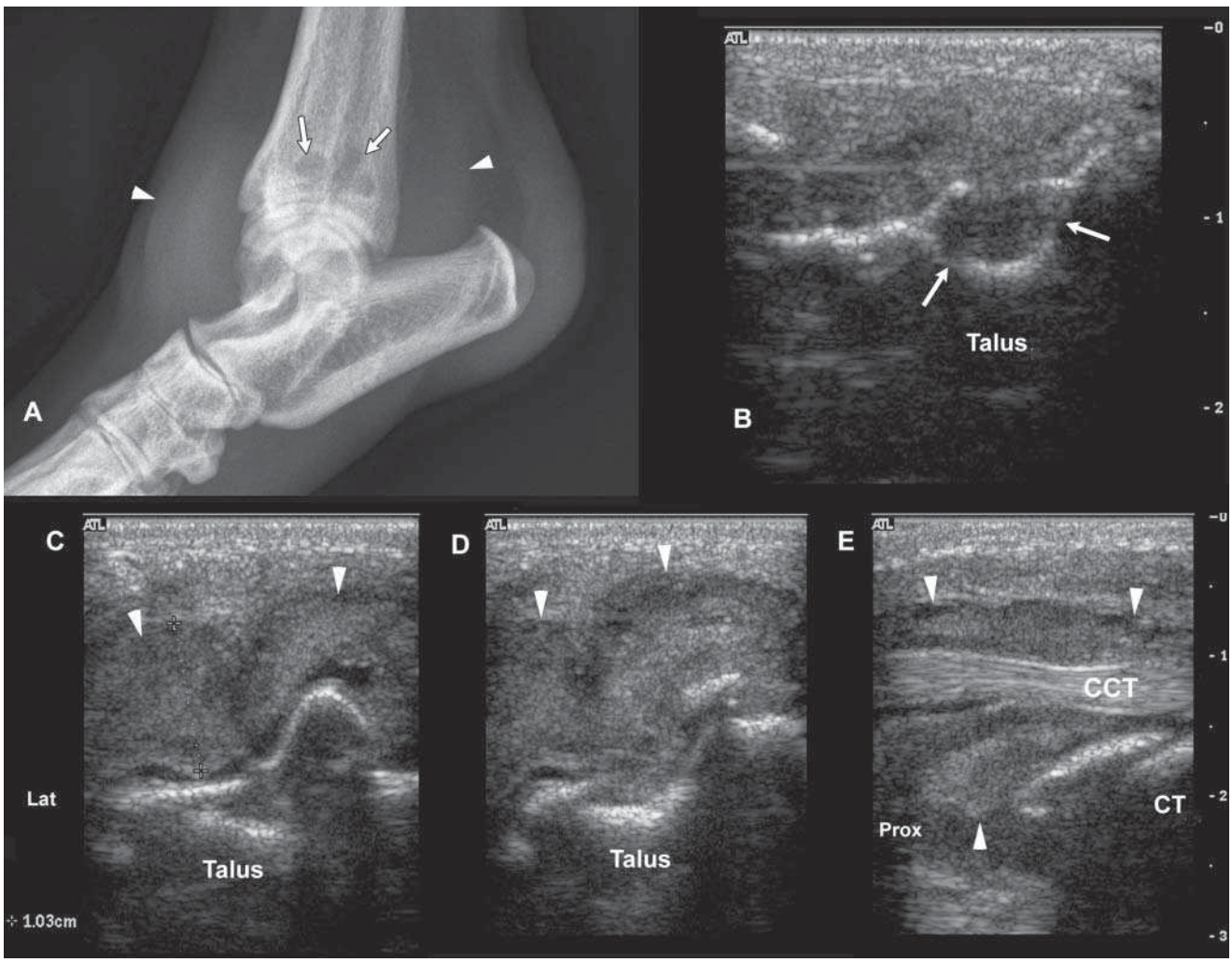


Figure 17.61. Synovial cell sarcoma. A: Mediolateral radiograph of the tarsus of a 6-year-old large-breed dog with chronic lameness. Soft-tissue swelling (arrowheads) is noted at the periphery of the tarsus, as well as lytic foci in the distal tibial metaphysis (arrows) and an irregular periosteal reaction along the caudal aspect of the tibia. **B–D:** Longitudinal **(B)** and transverse **(C, D)** sonograms of the dorsal aspect of the talus that show an irregular layer of echogenic tissue in the near field (arrowheads), as well as irregular bone defects (arrows). Lat, lateral. **E:** Longitudinal sonogram obtained at the plantar aspect. The soft-tissue thickening (arrowheads) is noted at the periphery of the common calcaneal tendon (CCT), reaching the level of the calcaneal tuberosity (CT). These features are supportive of synovial cell sarcoma or synovial histiocytic sarcoma. Prox, proximal.

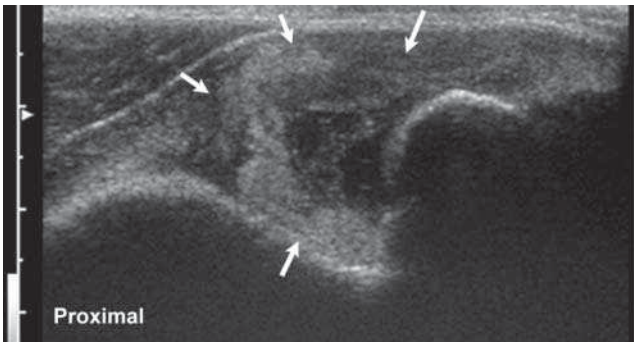


Figure 17.62. Septic arthritis. Longitudinal sonogram of the caudolateral aspect of the elbow of a dog with septic arthritis. A focal accumulation of inhomogeneous, echogenic fluid (arrows) is present, consistent with pus.

(Figure 17.62). Hemorrhagic effusions can range in echogenicity, depending on their chronicity.

Bones

Scanning Technique and Sonographic Anatomy

Although radiography remains the principal modality in the investigation of bone diseases, ultrasonography provide additional information, particularly with regard to the soft-tissue component of these processes. Linear transducers are preferred for superior resolution, although microconvex probes may be preferred when a smaller foot print is necessary. The exam is performed similarly as for muscles and tendons, with the patient in lateral recumbency.

The surface of a long bone is examined by slowly moving the probe along the long axis of the bone, usually in a longitudinal plane, which enables visualization of a larger portion of the bone surface (Risselada et al. 2003). This way, the area of interest can be compared with adjacent normal portions of the bone (e.g., tumor or fracture).

Because of the reflection and absorption of the sound waves, the bone surface appears as a smooth, hyperechoic, continuous line with strong acoustic shadowing. This surface is more irregular at the sites of origin and insertion of tendons and ligaments.

Sonographic Features of Bone Disorders

Osteomyelitis and Bone Tumors Osteomyelitis can vary in ultrasonographic appearance. An ill-defined, irregular hyperechoic interface can be seen superficial to the bone cortex when periosteal new bone formation develops. Peripheral, inflamed soft tissues appear swollen, hypoechoic, and inhomogeneous (Figure 17.63). The lytic cortical surface can be uneven, with multiple indentations (Kramer et al. 1997).

Primary and metastatic bone tumors associated with cortical lysis can be assessed sonographically, particularly if they extend into the surrounding soft tissue. They can vary in echogenicity and uniformity (Figures 17.64–17.66). Occasionally, periosteal elevation (Codman's triangle) is seen. If sufficient cortical lysis is present, the deeper bone tissue can be visualized. Ultrasound is primarily performed in these instances to assist in fine-needle aspiration or biopsy of bone lesions, avoiding the need for surgical biopsy in some patients (Samii et al. 1999).

Fractures Fractures of long bones and their healing process, as well as the associated soft-tissue damage (muscle rupture and hematoma), can be assessed ultrasonographically. Because there are no points of orientation, the exact relationship between the fractured ends is difficult to determine. To standardize the documentation of fracture healing of long bones, multiple and repeatable images must be obtained. The recommended transducer positions for the assessment of long bones are craniolateral (distal humerus, radius, ulna, and tibia) and caudolateral (proximal humerus cranial, femur medial, and fibula) (Risselada et al. 2003).

Ultrasonography can be used to evaluate secondary fracture healing in biologically treated fractures (Risselada et al. 2005). In comparison to radiography, the completion of fracture healing can be determined earlier. Secondary fracture healing can be divided into five stages (Figure 17.67).

During normal fracture healing, the newly developing tissues require more nutrients and have a higher metabolic rate. This requires the development of new vessels (neovascularization) at the fracture site and can be visualized using power Doppler ultrasound. A Doppler signal can be obtained as of day 10 after trauma, reaching a maximum between days 11 and 30, before gradually decreasing. Signals can be detected in and close to the callus (Risselada et al. 2006). Doppler assessment may thus help in investigating cases of delayed bone union.

Vascular anomalies

Arteriovenous fistulas are rare, but when encountered, they typically result in limb soft-tissue swelling. A tortuous network of vessels is identified in proximity to a dilated vein showing a pulsatile flow pattern with Color or pulsed-wave Doppler (Figure 17.68). The connection may sometimes be recognized.

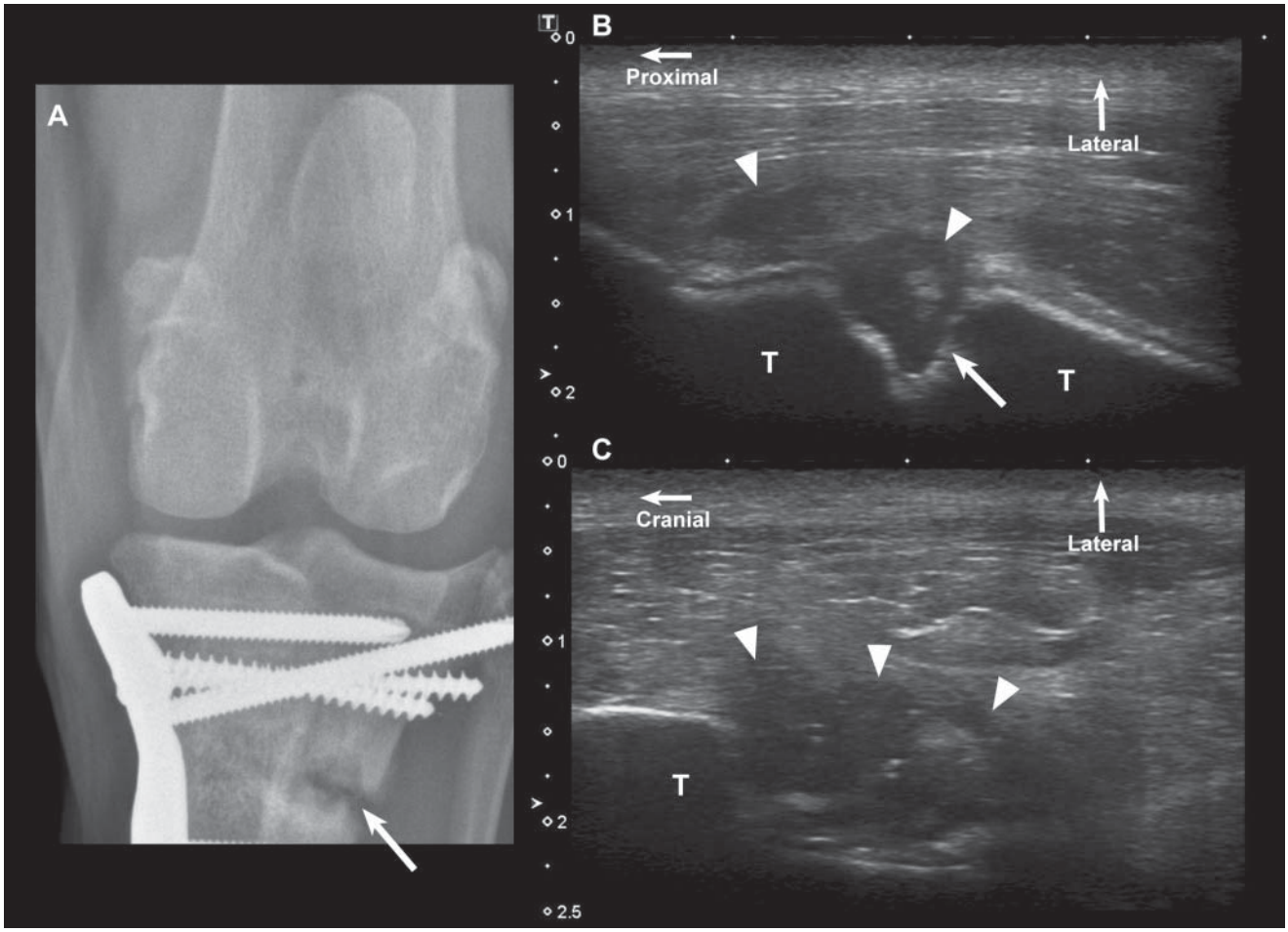


Figure 17.63. **Post-surgical osteomyelitis. A**: Craniocaudal radiograph centered on the stifle of a dog 3 weeks following a tibial plateau leveling osteotomy. The osteotomy line is enlarged, irregular and ill-defined on the medial side, with surrounding sclerosis. Longitudinal **(B)** and transverse **(C)** sonograms were acquired at the site of the osteotomy (arrow in **B**). The hypoechoic area (arrrowheads) was fine-needle-aspirated with ultrasound guidance, revealing a septic fluid. T, tibia.

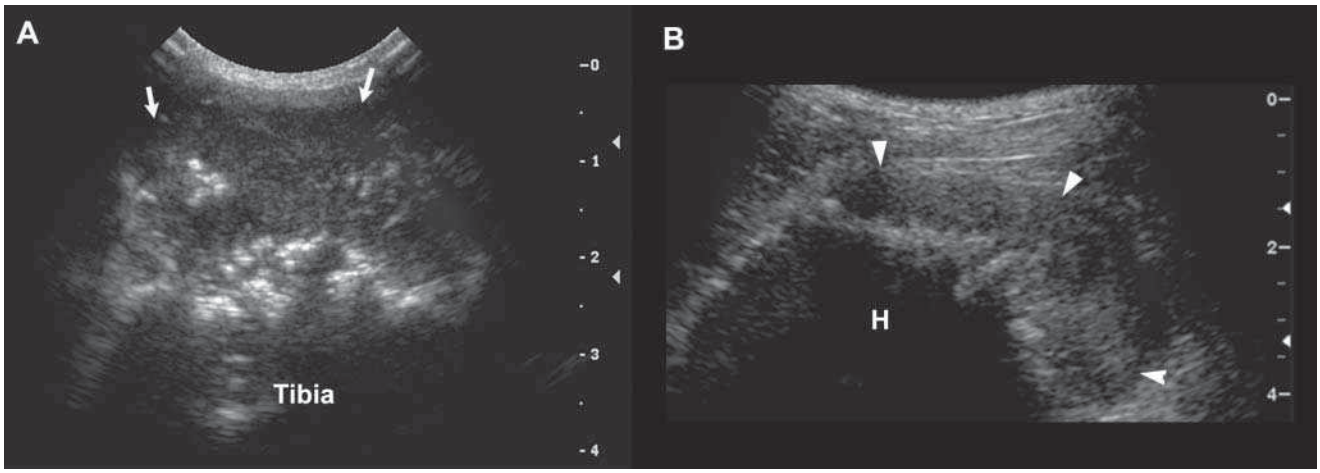


Figure 17.64. **Osteosarcoma.** Sonographic images of aggressive tibial **(A)** and humeral **(B)** mass lesions in two dogs. **A:** An ill-defined, hypoechoic mass (arrows) has hyperechoic foci, some of which are associated with acoustic shadowing, consistent with mineralization. The underlying bone cortex is no longer visible because of the extensive lysis. **B:** A well-defined, mildly echogenic mass (arrowheads) involves the humerus (H). The surface of the humerus is markedly irregular because of aggressive new bone formation and lysis.

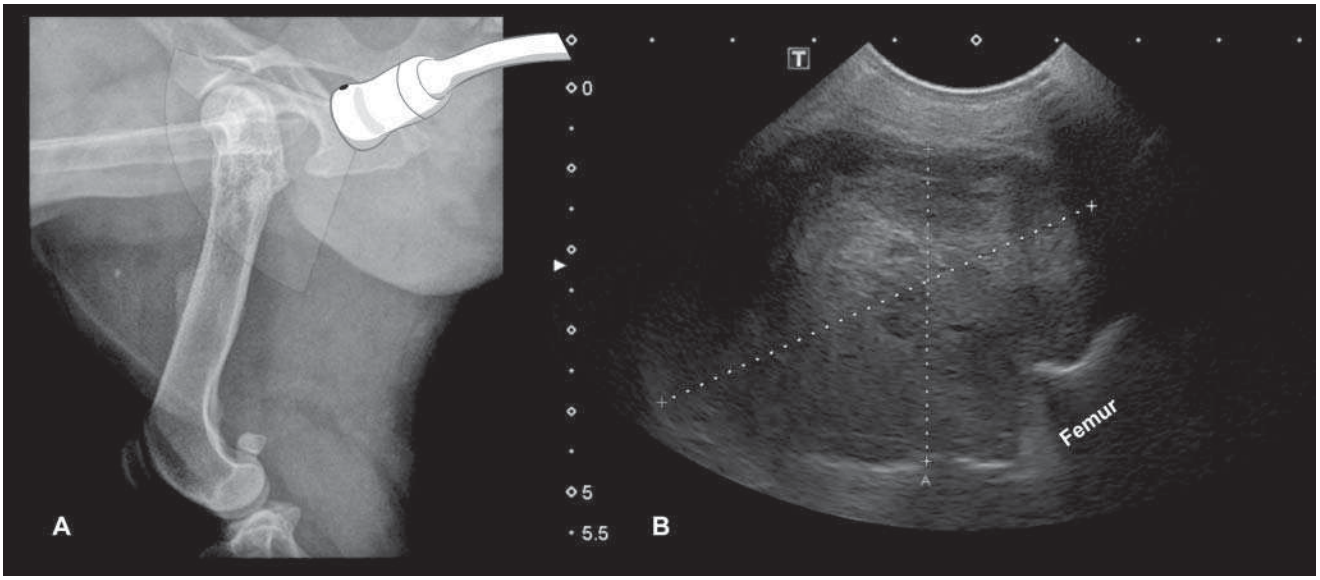


Figure 17.65. **Femoral osteosarcoma in a 10-year-old Scottish Terrier. A:** Lateral radiograph of the femur on which moth-eaten lysis of the proximal diaphysis and metaphysis is detected, as well as a periosteal new bone formation on the cranial surface of the mid-femur. **B:** The sonographic probe was placed laterally over the proximal thigh to obtain this image. The soft-tissue component of this primary bone tumor is exuberant. The mass is globally hypoechoic with hyperechoic ill-defined areas. Images courtesy of Laurent Couturier, Azurvet, France.

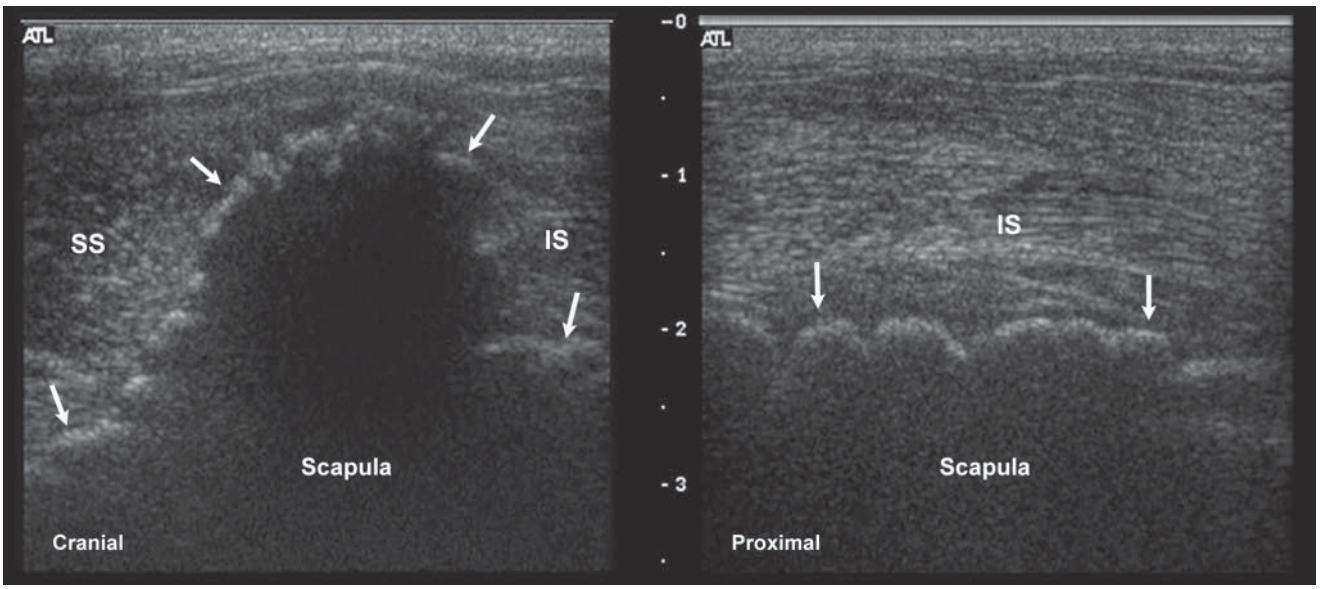
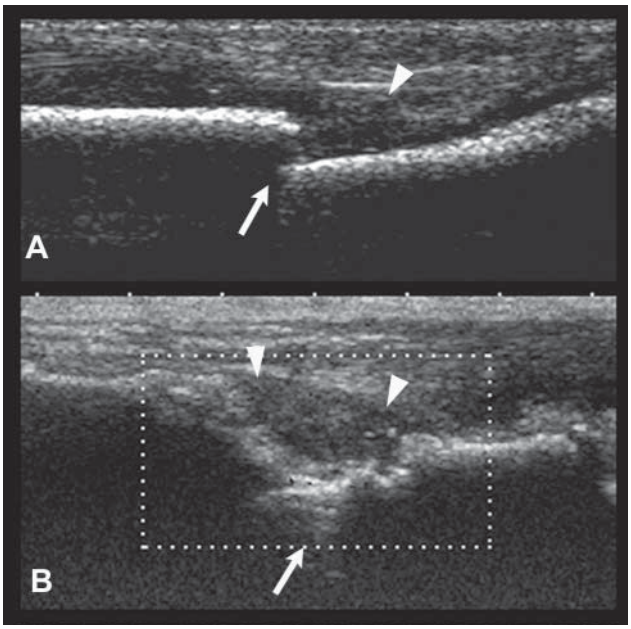


Figure 17.66. **Metastatic carcinoma to the scapula.** Transverse **(left)** and longitudinal **(right)** sonograms of the scapular spine in a dog with a transitional cell carcinoma and metastatic disease. Irregular new bone formation (arrows) is present at the level of the scapula. Adjacent supraspinatus (SS) and infraspinatus (IS) muscles are reduced in thickness and hyperechoic because of atrophy. Several similar lesions were identified in other bones, and metastatic carcinoma was confirmed histologically.



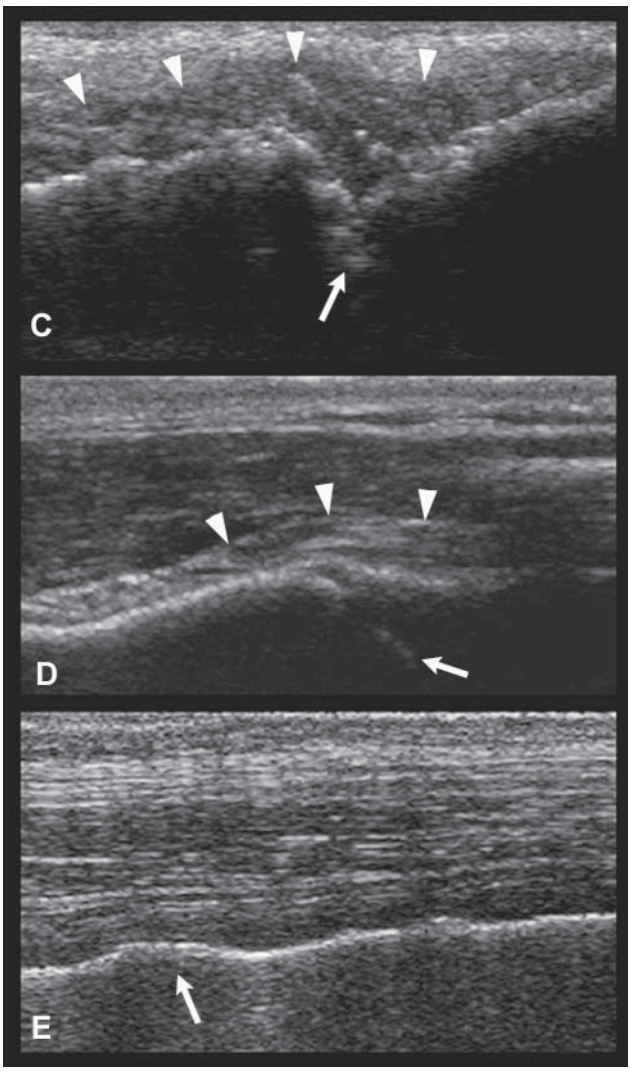


Figure 17.67. Bone fracture: healing process. Sequential sonograms showing progressive bone healing. **A:** Stage I (days 0–7). A discontinuity of the bone cortex is identified that is associated with sharp ends (arrow). Hypoechoic soft-tissue swelling is noted at the fracture site (arrowhead). **B:** Stage II–III (days 7–21). The bone defect (arrow) is progressively remodeled. A non-ossified callus (arrowheads) is present. **C:** Stage IV (days 22–28). The non-ossified callus is progressively more echogenic (arrowheads), and the fracture gap (arrow) is progressively narrower. **D:** Stage V (days 29–42). The fracture gap is nearly completely filled with new bone and poorly seen (arrow). The peripheral callus is reduced in volume (arrowheads). **E:** Stage VI (more than 43 days). The fracture is healed. The surface of the bone remains mildly irregular (arrow).

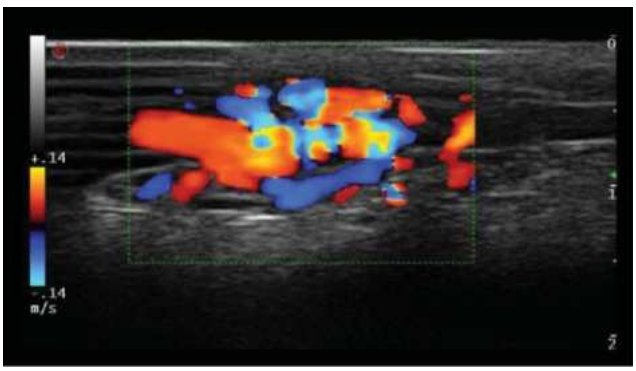


Figure 17.68. Arteriovenous fistula in the thoracic limb of a cat. A tortuous plexus of vessels with pulsatile flow was detected. Image courtesy of Guy Beauregard, Centre Veterinaire Rive-Sud, Canada.

Interventional Procedures

Ultrasound may not always replace CT or MRI for diagnostic purposes, but it allows interventional procedures to be performed in real time, often in awake or minimally sedated patients.

Ultrasound can be used to guide biopsy or aspiration needles into soft-tissue lesions that may not be detected or well characterized with radiography. Ultrasound may also serve to place needles into bone lesions through cortical defects, or into extraosseous soft-tissue extensions or fluid collections that may not be detected on radiographs. This may be particularly useful for suspected bone neoplastic lesions (Samii et al. 1999).

Ultrasound may also serve to guide intra-articular or intra- or paratendinous injections, for diagnostic or therapeutic purposes.

Ultrasound is useful for intraoperative identification of FBs, guiding surgeons in their surgical approach and confirming that all fragments have been successfully removed. This may be particularly valuable for porcupine quills, which are often difficult to localize by palpation only (Figure 17.69). FBs may then be removed by a surgical clamp under ultrasound guidance, or using small, flexible endoscopic forceps through fistular tracts, or surgical incisions (Staudte et al. 2004; Segalen and Durieux 2010) (Figure 17.70). Injection of sterile saline solution into the fistular tract may facilitate identification of the FB fragment(s). Larger foreign objects or those embedded in fibrous tissue may require more extensive surgical exploration.

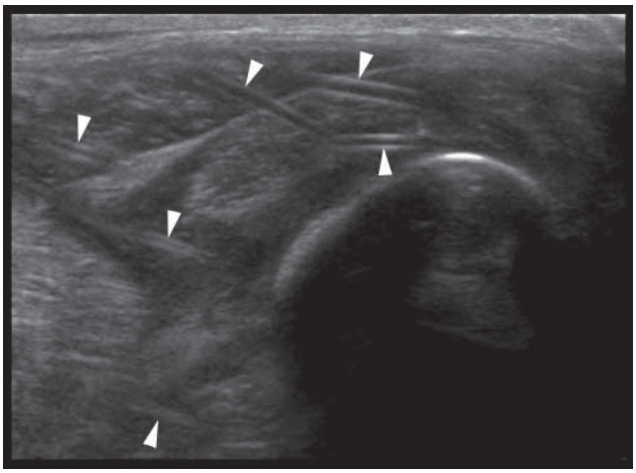


Figure 17.69. Intraoperative identification of residual porcupine quills in a dog. Ultrasound was used in this dog after four porcupine quills were surgically removed. While nothing was felt on palpation, several additional quills (arrowheads) were detected.



Visit our website at **www.SmallAnimalUltrasonography.com** for complementary video clips with annotations and text on:

- Normal shoulder
- Normal common calcaneal tendon
- Bicipital tenosynovitis
- Supraspinatus tendinopathy
- Common calcaneal tendinopathy
- Gracilis myopathy
- Myositis and abscess
- Osteomyelitis
- Joint neoplasia



Figure 17.70. Use of small flexible endoscopic forceps for removal of a grass awn foreign body in a dog. The endoscopic forceps was inserted into the fistular tract and guided to the grass awn foreign body with ultrasound guidance. The endoscopic wire (W) and alligator forceps (F) appear as strongly echogenic interfaces with reverberation, while the grass awn foreign body (FB) is not shadowing. Images courtesy of Franck Durieux, Aquivet, France.

References

Adams WM, Dueland RT, Daniels R, Fialkowski JP, Nordheim EV (2000) Comparison of two palpation, four radiographic and three ultrasound methods for early detection of mild to moderate canine hip dysplasia. Vet Radiol Ultrasound 41:484–490.

Armbrust LJ, Biller DS, Radlinsky MG, Hoskinsons JJ (2003) Ultrasonographic diagnosis of foreign bodies associated with chronic draining tracts and abscesses in dogs. Vet Radiol Ultrasound 44:66–70.

Boyse TD, Fessell DP, Jacobson JA, Lin J, van Holsbeeck MT, Hayes CW (2001) US of soft-tissue foreign bodies and associated complications with surgical correlation. Radiographics 12:1251–1256.

Breur GJ, Blevins WE (1997) Traumatic injury of the iliopsoas muscle in three dogs. J Am Vet Med Assoc 210:1631–1634.

Brisson BA, Bersenas A, Etue SM (2004) Ultrasonographic diagnosis of septic arthritis secondary to porcupine quill migration in a dog. J Am Vet Med Assoc 9:1467–1470.

Cogar S, Cook C, Curry S, Grandis A, Cook J (2008) Prospective evaluation of Techniques for differentiating shoulder pathology as a source of forelimb lamenesss in medium and large breed dogs. Vet Surg 37:132–141.

Esterline ML, Armbrust L, Roush JK (2005) A comparison of palpation guided and ultrasound guided percutaneous biceps brachii tenotomy in dogs. Vet Comp Orthop Traumatol 18:135–139.

Fischer A, Flöck A, Tellhelm B, Failing K, Kramer M, Thiel C (2010) Static and dynamic ultrasonography for the early diagnosis of canine hip dysplasia. J Small Anim Pract 51:582–588.

Franch J, Bertran, Remolins G, Fontecha P, Diaz-Bertraba, Durall I (2009) Simultaneous bilateral contracture of the infraspinatus muscle – Clinical case in a five-year-old Berlgian Shepherd Dog. Vet Comp Orthop Traumatol 22:249–252.

Gnudi G, Bertoni G (2001) Echographic examination of the stifle joint affected by cranial cruciate ligament rupture in the dog. Vet Radiol Ultrasound 42:266–270.

Gnudi G, Volta A, Bonazzi M, Gazzola M, Bretoni G (2005) Ultrasonographic features of grass awn migration in the dog. Vet Radiol Ultrasound 46:423–426.

Greshake RJ, Ackerman N (1992) Ultrasound of the coxofemoral joints of the canine neonate. Vet Radiol Ultrasound 33:99–104.

Hermanson JW, Evans HE (1993) The muscoloskeletal system. In: Evans HE, Christensen GC, eds. Miller's Anatomy of the Dog, 3rd edition. Philadelphia: WB Saunders, pp. 258–384.

Knox VW IV, Sehgal CM, Wood AK (2003) Correlation of ultrasonographic observations with anatomic features and radiography of the elbow joint in dogs. Am J Vet Res 64:721–726.

Kramer M, Gerwing M, Hach V, Schimke E (1997) Sonography of the musculoskeletal system in dogs and cats. Vet Radiol Ultrasound 38:139–149.

Kramer M, Gerwing M, Michele U, Schimke E, Kindler S (2001a) Ultrasonographic examination of injuries to the Achilles tendon in dogs and cats. J Small Anim Pract 42:531–535.

Kramer M, Gerwing M, Sheppard C, Schimke E (2001b) Ultrasonography for the diagnosis of diseases of the tendon and tendon sheath of the biceps brachii muscle. Vet Surg 30:64–71.

Kramer M, Stengel H, Gerwing M, Schimke E, Sheppard C (1999) Sonography of the canine stifle. Vet Radiol Ultrasound 40:282–293.

Kühn K, Ohlerth S, Makara M, Hassig M, Guerrero TG (2011) Radiographic and ultrasonographic evaluation of the patellar ligament following tibial tuberosity advancement. Vet Radiol Ultrasound 52:466–471.

Kulendra E, Coor S (2008) Necrotising fasciitis with sub-periosteal Streptoccocus canis infection in two puppies. Vet Comp Orthop Traumatol 21:474–477.

Lafuente M, Fransson B, Lincoln J, Martinez S, Gavin P, Lahmers K, Gay J (2009) Surgical treatment of mineralized and nonmineralized supraspinatus tendinopathy in twenty-four dogs. Vet Surg 38:380–387.

Lamb C, Duvernois A (2005) Ultrasonographic anatomy of the normal canine calcaneal tendon. Vet Radiol Ultrasound 46:326–330.

Lamb C, Wong K (2005) Ultrasonographic anatomy of the canine elbow. Vet Radiol Ultrasound 46:319–325.

Liuti T, Saunders J, Gielen I, Rycke L, Coopman F, van Bree H (2007) Ultrasound approach to the canine distal tibia and trochlear ridges of the talus. Vet Radiol Ultrasound 48:361–367.

Long C, Nyland TG (1999) Ultrasonographic evaluation of the canine shoulder. Vet Radiol Ultrasound 40:372–379.

Mahn MM, Cook JL, Cook CR, Balke MT (2005) Arthroscopic verification of ultrasonographic diagnosis of meniscal pathology in dogs. Vet Surg 34:318–323.

Mattern KL, Berry RB, Peck JN, de Haan JJ (2006) Radiographic and ultrasonographic evaluation of the patellar ligament following tibial plateau leveling osteotomy. Vet Radiol Ultrasound 47:185–191.

Nielsen C, Pluhar GE (2004) Diagnosis and treatment of hind limb muscle strain injuries in 22 dogs. Vet Comp Orthop Traumatol 18:247–253.

Ober C, Jones J, Larson M, Lanz O, Were S (2008) Comparison of ultrasound, computed tomography, and magnetic resonance imaging in detection of acute wooden foreign bodies in the canine manus. Vet Radiol Ultrasound 49: 411–418.

Reed AL, Payne JT, Constaninescu GM (1995) Ultrasonographic anatomy of the normal canine stifle. Vet Radiol Ultrasound 36:315–321.

Risselada M, Kramer M, de Rooster H, Taeymans O, Verleyen P, van Bree H (2005) Ultrasonographic and radiographic assessment of uncomplicated secondary fracture healing of long bones in dogs and cats. Vet Surg 34:99–107.

Risselada M, Kramer M, van Bree H (2003) Approaches for ultrasonographic evaluation of long bones in the dog. Vet Radiol Ultrasound 44:214–220.

Risselada M, Kramer M, van Bree H, Taeymans O, Verleyen P (2006) Power Doppler assessment of the neovascularization during uncomplicated fracture healing of long bones in dogs and cats. Vet Radiol Ultrasound 47:301–306.

Rivers B, Wallace L, Johnston GR (1992) Biceps tenosynovitis in the dog: Radiographic and sonographic findings. Vet Comp Orthop Traumatol 5:51–57.

Rivers BJ, Walter PA, Kramek B, Wallace L (1997) Sonographic findings in canine common calcaneal tendon injury. Vet Comp Orthop Traumatol 10:45–53.

Samii VF, Nyland TG, Werner LL, Baker TW (1999) Ultrasound-guided fine-needle aspiration biopsy of bone lesions: A preliminary report. Vet Radiol Ultrasound 40:82–86.

Segalen M, Durieux F (2010) Superficial foreign body ultrasonography: diagnosis and mini-Invasive treatment [Échographie des corps étrangers superficiels: diagnostic et traitement mini-invasif] Pratique médicale et chirurgicale de l'animal de compagnie 45:127–134.

Seyrek-Intas D, Michele U, Tacke S, Kramer M, Gerwing M (2009) Accuracy of ultrasonography in detecting fragmentation of the medial coronoid process in dogs. J Am Vet Med Assoc 234:480–485.

Shah ZR, Crass JR, Dubravka CO, Bellon EM (1992) Ultrasonographic detection of foreign bodies in soft tissues using turkey muscle as a model. Vet Radiol Ultrasound 33:94–100.

Siems JJ, Breur GJ, Blevins WE, Cornell KK (1998) Use of two-dimensional real-time ultrasonography for diagnosing contracture and strain of the infraspinatus muscle in a dog. J Am Vet Medic Assoc 212:77–80.

Staudte KL, Hopper BJ, Gibson NR, Read RA (2004) Use of ultrasonography to facilitate surgical removal of non enteric foreign bodies in 17 dogs. J Small Anim Pract 45:395–400.

Swiderski J, Fitch RB, Staatz A, Lowery J (2005) Sonographic assisted diagnosis and treatment of bilateral gastrocnemius tendon rupture in a Labrador retriever repaired with fascia lata and polypropylene mesh. Vet Comp Orthop Traumatol 18:258–263.

Van RysIen B, de Bakker E, Beaumlin Y, Samoy YCA, Van Vynckt D, Gielen I, Ducatelle R, van Bree H (2012) Primary flexor enthesopathy of the canine elbow: imaging and arthroscopic findings in eight dogs with discrete radiographic changes. Vet Compt Orthop Traumatol 25:239–245.

Vandevelde B, Saunders JH, Kramer M, Van Ryssen B, van Bree H (2006) Comparison of the ultrasonographic appearance of osteochondrosis lesions in the canine shoulder with radiography, arthrography and arthroscopy. Vet Radiol Ultrasound 47:174–184.

Volta A, Bonazzi M, Gnudi G, Gazzola M, Bertoni G (2006) Ultrasonographic features of canine lipomas. Vet Radiol Ultrasound 47:589–591.

CHAPTER EIGHTEEN

Spine and Peripheral Nerves

Judith Hudson[1] and Marc-André d'Anjou[2,3]

[1] *Department of Clinical Sciences, College of Veterinary Medicine, Auburn University, Auburn, AL, USA*
[2] *Centre Vétérinaire Rive-Sud, Brossard, Québec, Canada*
[3] *Faculté de médecine vétérinaire de l'Université de Montréal, Saint-Hyacinthe, Québec, Canada*

Scanning Technique for the Spine

A portion of the cervical spinal cord can be imaged in both cats and dogs through the foramen magnum and between the atlas and axis while the neck is fully flexed (Figure 18.1). In addition, windows through ventral slot surgery or surgical sites involving the caudal portion of the brain enable partial evaluation of the cranial cervical spine (Figure 18.2).

Similarly, limited visualization of the lumbar spinal cord is possible through the intervertebral disc space either with a dorsolateral approach through the lumbar musculature or from the ventral aspect when performing abdominal ultrasonography (Figure 18.3). Intervertebral disc calcification and bridging spondylosis deformans can significantly limit the visibility of the spinal cord when imaged at the disc space using the ventral transabdominal approach.

Because of absorption of sound by bone and the resulting acoustic shadowing, ultrasonography of other segments of the spinal cord can usually be performed only during or following surgical laminectomy, corpectomy, or foraminotomy (Nakayama 1993; Gallagher et al. 1995) (Figure 18.4). Postoperatively, the spinal cord can be monitored if a remaining defect in the vertebra provides a sonographic window. Vertebral bone lysis as a result of neoplasia or infection can also provide an acoustic window for the spinal cord. Additionally, the spinal cord may be visible perinatally because of incomplete vertebral ossification.

The spinal cord is small and superficial, making a high-frequency transducer (usually 7–12 MHz) the optimal choice. Transducers with a small footprint are preferred to better fit the narrow surgical sites. The most common use of spinal cord ultrasonography is intraoperatively to evaluate whether all disc material has been removed from the spinal canal during a laminectomy or cervical ventral slot surgery. Other intraoperative applications include evaluation of the cord because of trauma, suspected neoplasia, developmental abnormalities, and infection. For intraoperative applications, the probe must be placed in a long, sterile, plastic cover, and sterile acoustic gel must be used. The surgical site is then filled with sterile saline for optimal ultrasound coupling.

Normal Sonographic Anatomy of the Spine

The spinal cord is poorly echogenic, the meninges are hyperechoic, and the cerebrospinal fluid (CSF) is anechoic (Figure 18.1). When imaged from the dorsal aspect, the most superficial hyperechoic line represents the dura mater and arachnoid together, whereas the deeper line represents the pia mater (Finn-Bodner et al. 1995). Anechoic CSF separates these two hyperechoic lines. Centrally, one or two lines are present at the location of the central canal. Deep to the central canal, two more hyperechoic lines represent the meninges. The surface of the vertebra deep to the spinal cord and meninges appears as a thick hyperechoic line. Absorption of sound prevents imaging of structures deep to the bone surface. Between the vertebrae the intervertebral disc is seen as a hypoechoic structure that slightly displaces the dura dorsally (Nanai et al. 2007).

Atlas of Small Animal Ultrasonography, Second Edition. Edited by Dominique Penninck and Marc-André d'Anjou.
© 2015 John Wiley & Sons, Inc. Published 2015 by John Wiley & Sons, Inc.
Companion website: www.SmallAnimalUltrasonography.com

Figure 18.2. Sonograms of a Boston Terrier undergoing brain surgery. A brain mass caused herniation of the cerebellum (CB). A craniotomy has been performed and an incision made through the dura mater. **A:** Longitudinal sonogram showing the fourth ventricle (4) and spinal cord. F, floor of the cranium. **B:** Longitudinal sonogram made with the transducer moved slightly to the midline, making the central canal (CC) more visible. F, floor of the cranium; MO, medulla oblongata. **C:** Sagittal magnetic resonance image of the brain and the spinal cord. The arrowhead points to the brain-stem mass. CB, cerebellum; LV, lateral ventricle.

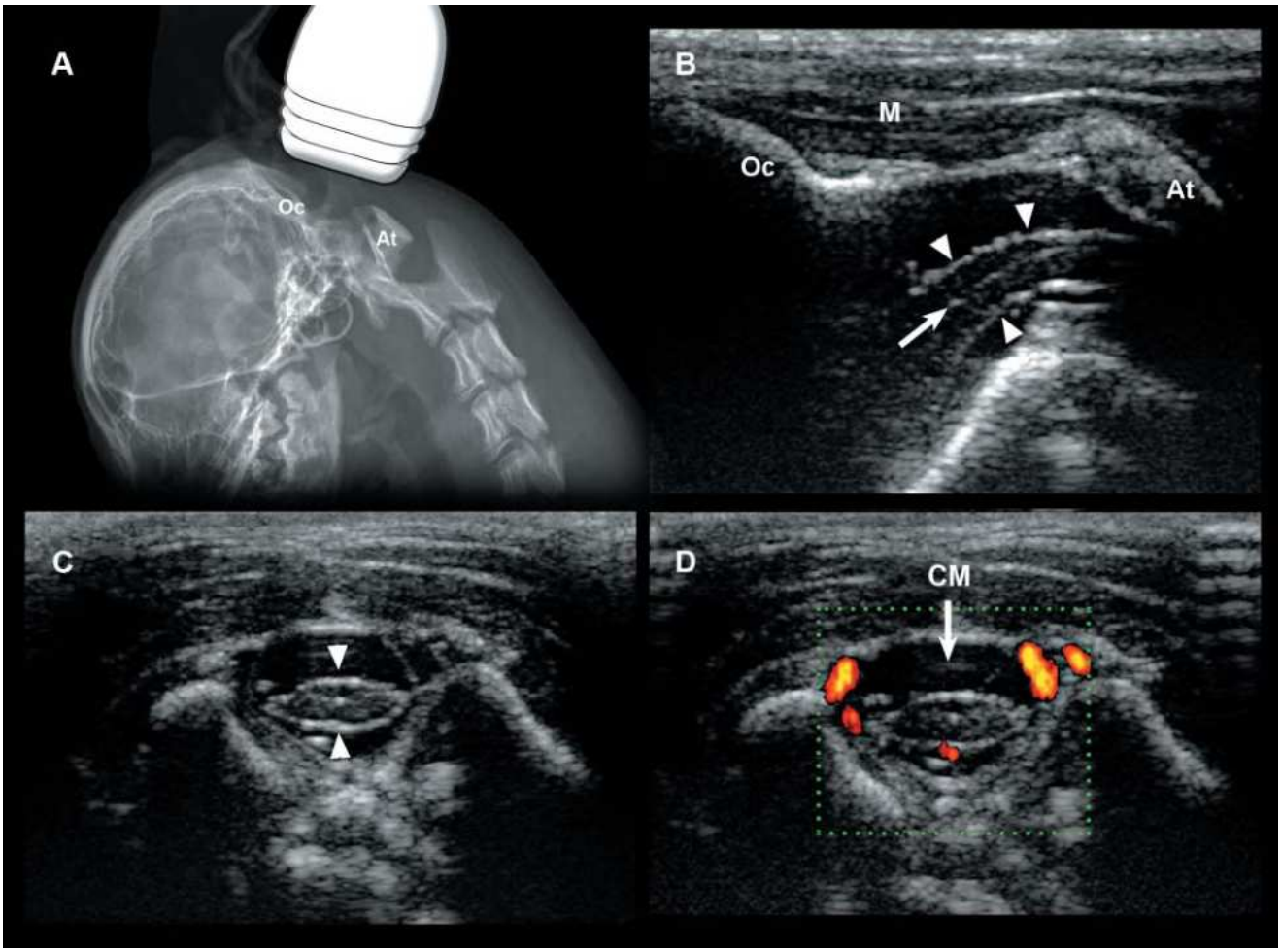


Figure 18.1. Sonographic approach and anatomy of the normal cranial canine cervical spinal cord. A: Probe placement for longitudinal assessment of the cranial cervical spine cord, medulla oblongata and caudal cerebellum through the foramen magnum of the occipital bone (Oc) or atlanto-occipital junction. Neck flexion may facilitate access to this region, although this should be done with caution, particularly if atlanto-axial instability is suspected. Longitudinal **(B)** and transverse **(C)** sonograms obtained at the atlanto-occipital junction using the approach illustrated in **A**. The arrow points to the spinal cord central canal. At, lamina of the atlas. **D:** Power Doppler mode of the neighboring vessels at the same location. Arrowheads outline the cranial portion of the cervical spine, which appears ventral to the cisterna magna (CM), which is filled with anechoic cerebrospinal fluid, and muscles (M).

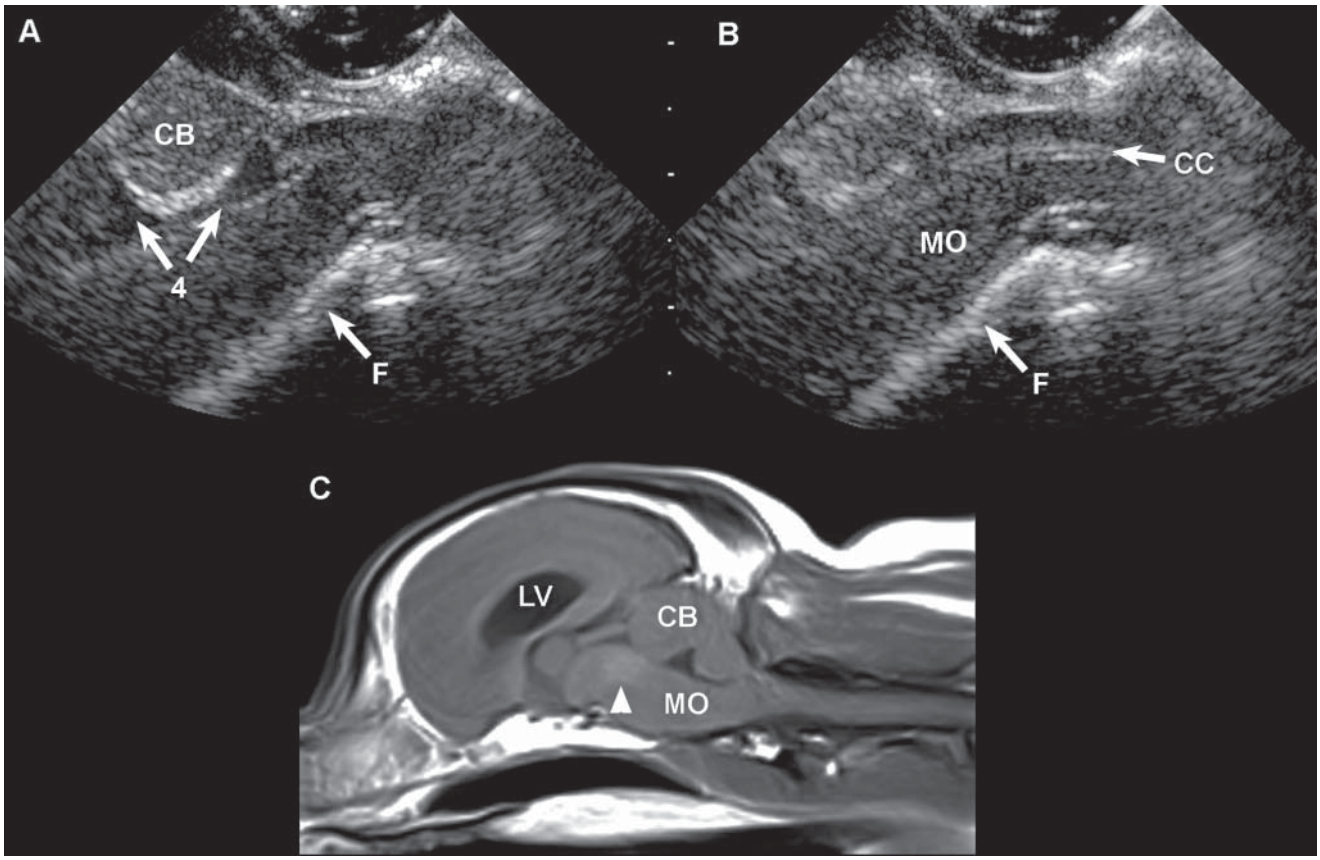


Figure 18.2. **Sonograms of a Boston Terrier undergoing brain surgery.** (for full caption, see facing page)

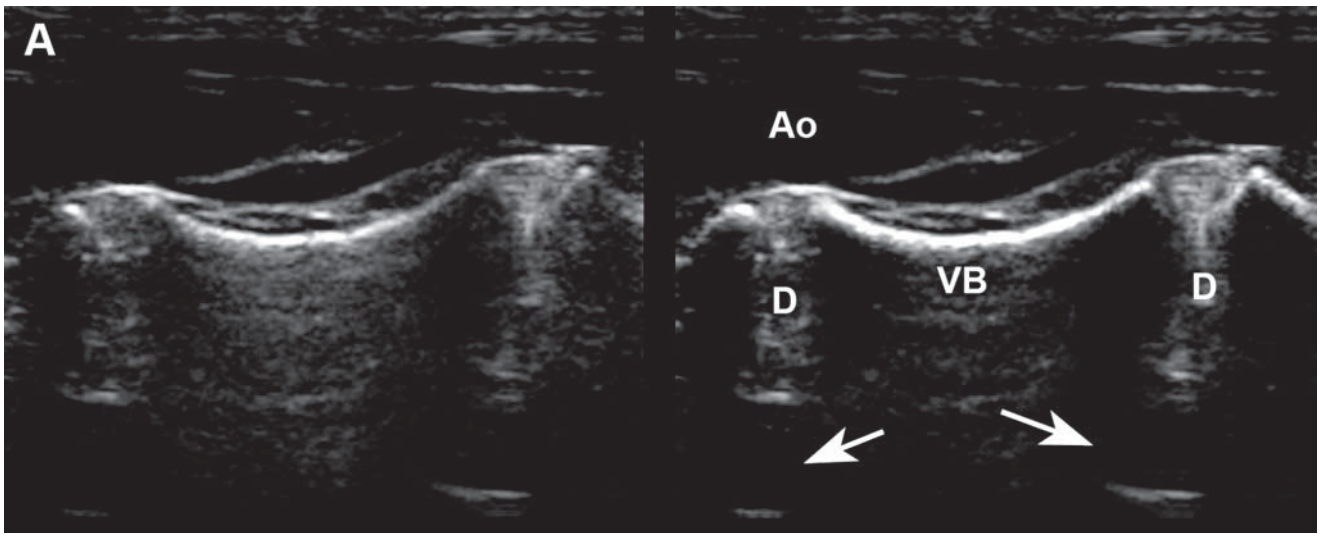


Figure 18.3. **Ventral sonographic anatomy of the lumbar spine. A:** Longitudinal sonogram and corresponding labeled schematic image, obtained via a transabdominal approach, of the caudal lumbar spine of an adult Beagle. The vertebral body (VB) has a distinct curvilinear shape. In normal dogs, the intact disc (D) can be an acoustic window to see part of the cord (arrows). **B:** Transverse sonogram and corresponding labeled schematic image at the level of a disc. The spinal cord is observed dorsally (arrow). **C:** Transverse sonogram and corresponding labeled schematic image at the level of the caudal aspect of the VB. The arrowheads point to the shadowing associated with the vertebral body. AO, aorta; CVC, caudal vena cava. (*continued overleaf*)

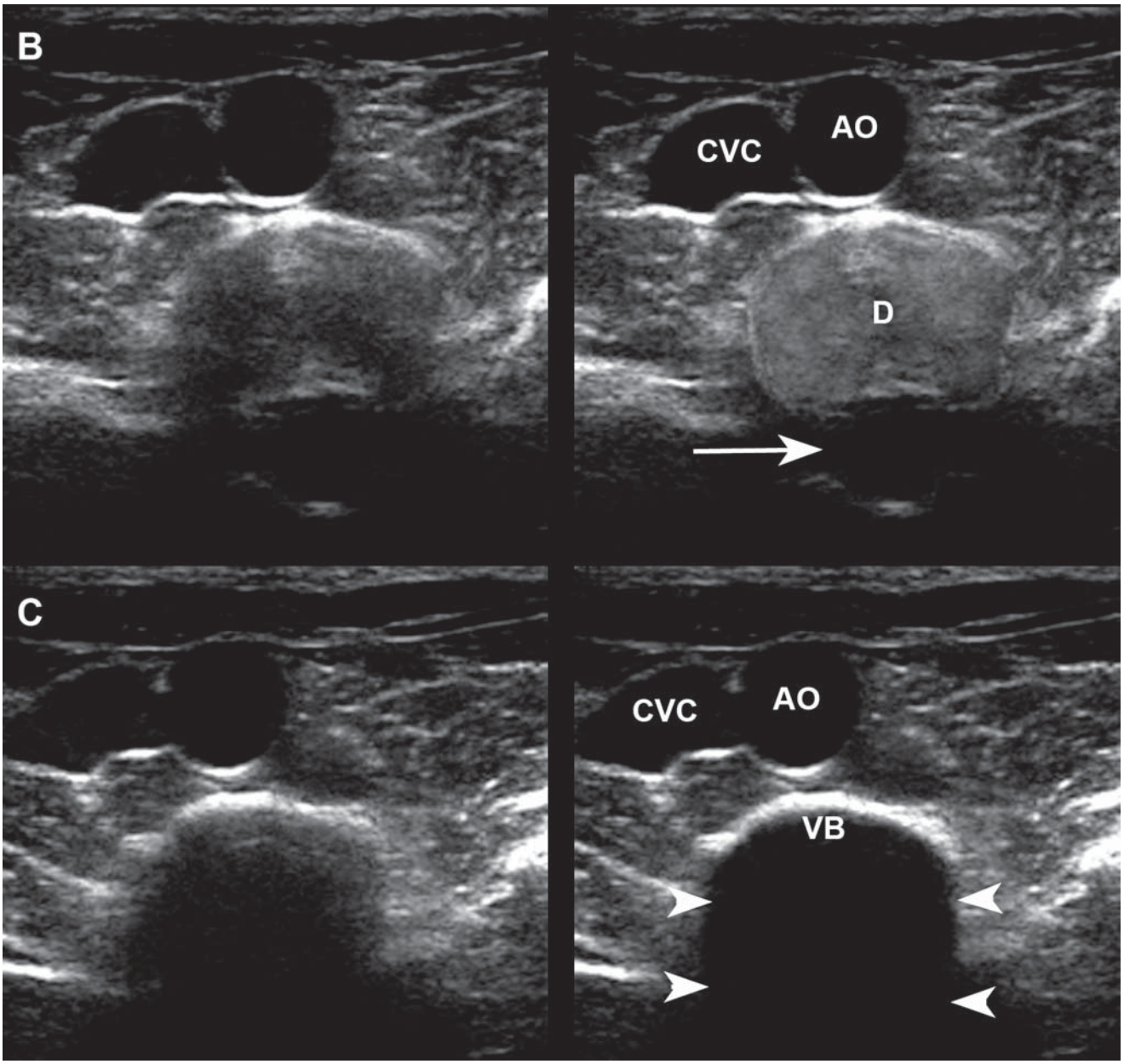


Figure 18.3. *Continued*

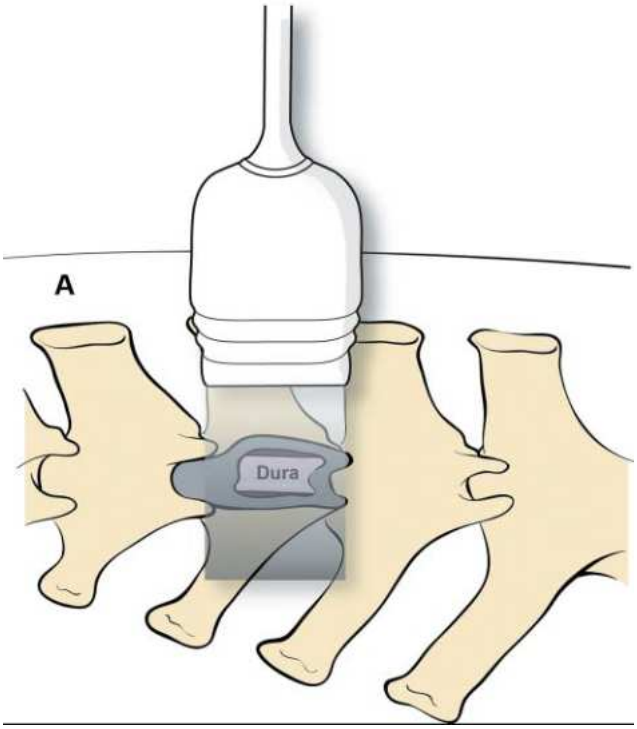
Transverse images can be obtained with a small footprint probe. In these images, the spinal cord is hypoechoic with a circular or oval shape, whereas the central canal appears as a central hyperechoic dot (Finn-Bodner et al. 1995).

The spinal cord is supplied by ventral and dorsal branches of spinal arteries that originate from vertebral, thoracic vertebral, and lumbar arteries. Examination of intraparenchymal branches with Doppler ultrasound has been described (Hudson et al. 1995).

Sonography of Spinal Disorders

Disc Herniation

Disc material is hyperechoic to the spinal cord parenchyma and therefore easily identified (Hudson et al. 1998). Mild disc protrusion shows as a line of hyperechoic echoes whereas herniated disc material may appear as amorphous, hyperechoic material with irregular margins (Figures 18.5). Acute compressive



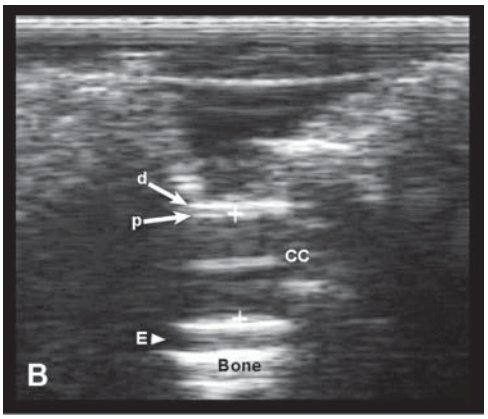


Figure 18.4. **Probe placement and corresponding sonographic image of the canine spinal cord during surgery.** **A**. A high-frequency probe is most appropriate. The view of the spinal cord is limited to the surgical window. **B**. The spinal cord (between the cursors) is relatively hypoechoic, and the meninges are hyperechoic and outline the anechoic cerebrospinal fluid. The bone interface is hyperechoic and hyperattenuating, limiting evaluation of any structure deeper to it. CC, central canal; d, dura mater and arachnoid mater; E, epidural space; p, pia mater.

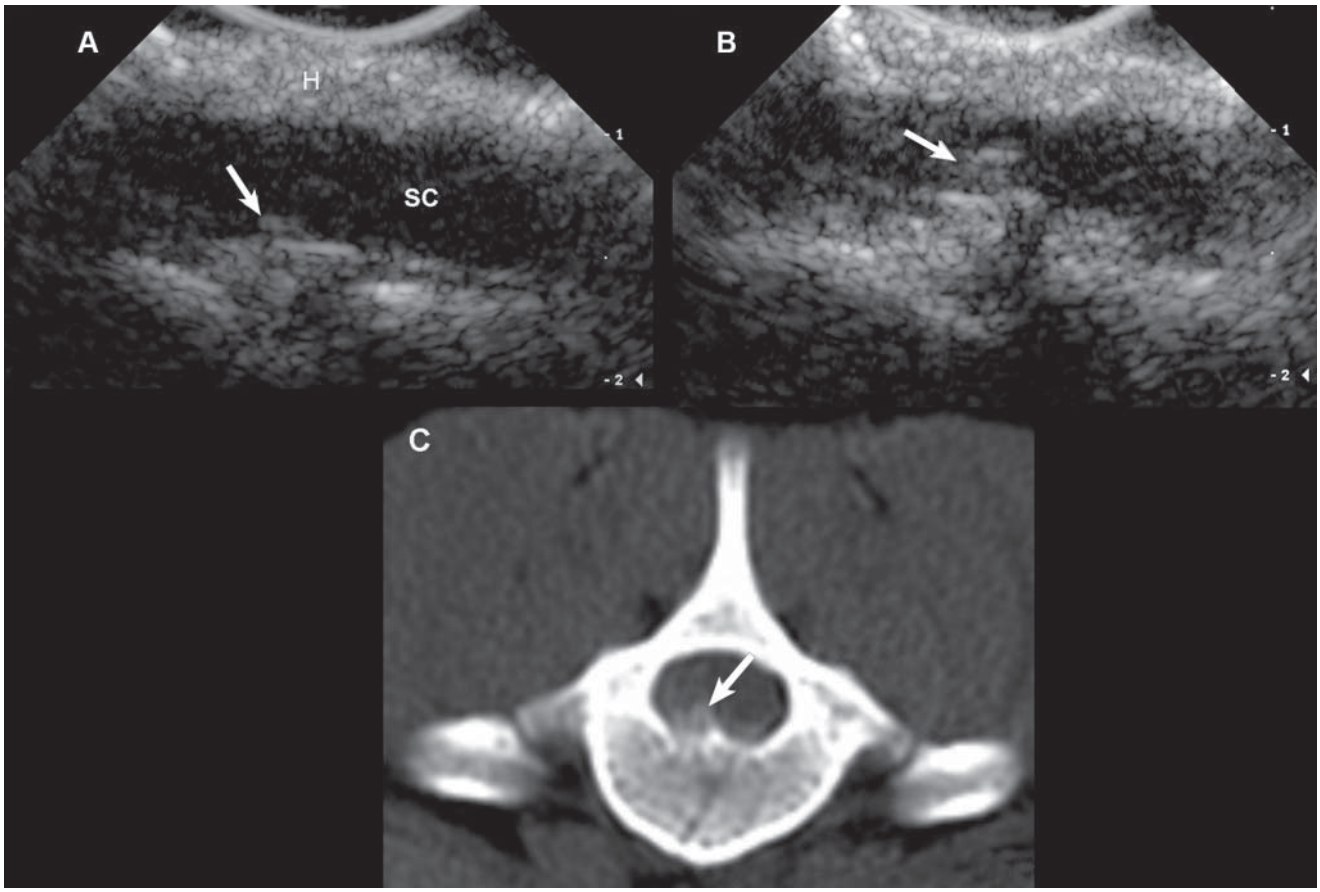


Figure 18.5. **Intraoperative images of a dog with intervertebral disc herniation. A:** Longitudinal sonogram made near the midline. A small amount of hyperechoic disc material (arrow) is seen deep to the hypoechoic spinal cord (SC). Some hemorrhage (H) shows as a hyperechoic region superficial to the spinal cord. **B:** A larger amount of disc material (arrow) is apparent in this longitudinal sonogram made more laterally. **C:** Computed tomographic image of the spinal cord of the same dog showing the hyperattenuating disc material (arrow) on the right side of the midline.

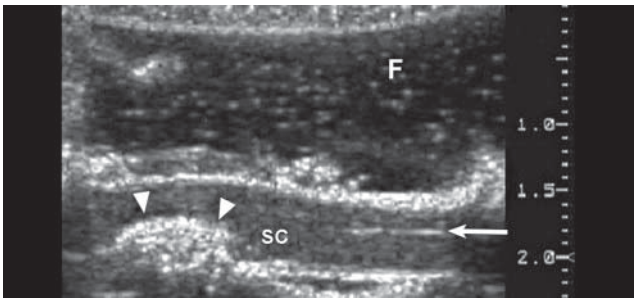


Figure 18.6. Compressive herniated disc material in the vertebral canal of a dog. Longitudinal sonogram of the surgical site filled with saline fluid (F). The hyperechoic disc material (arrowheads) has irregular margins and compresses the spinal cord (SC). Part of the visible central canal (arrow) is seen away from the lesion.

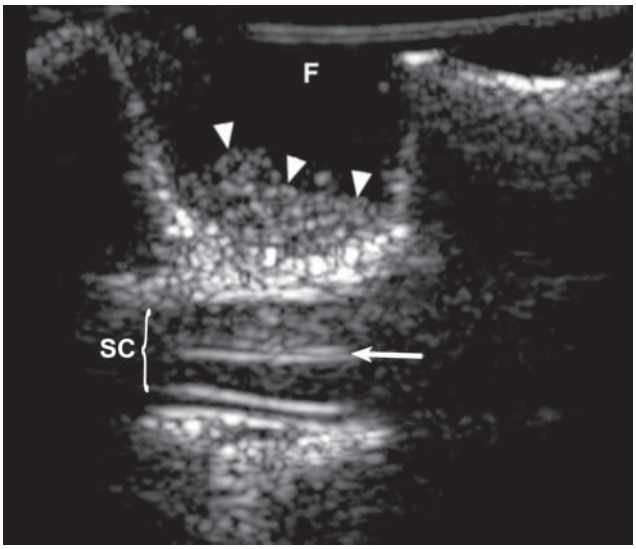


Figure 18.7. Successfully removed disc material in a dog. Compressive disc material was removed at the C4–5 intervertebral disc space. The central canal (arrow) is well visualized; there is no evidence of spinal cord (SC) compression. The echogenic structure (arrowheads) seen dorsal to the spinal cord represents hemostatic foam in situ and should not be confused with disc material. F, fluid at surgery site.

lesions tend to decrease focally the diameter of the spinal cord and compress the central canal so that it is no longer visible (Figure 18.6) (Hudson et al. 1998; Nanai et al. 2007). During surgery, sonography may assist the surgeon in assessing complete removal of disc fragments. There should be restoration of the normal diameter of the spinal cord, visualization of an anechoic central canal, and a gap should be seen between the spinal cord and ligaments on the floor of the neural canal (Nanai et al. 2007). In situ hemostatic gel or foam can mimic the presence of disc material (Figure 18.7).

Hemorrhage

Hemorrhage appears as a hyperechoic region that obscures visualization of the linear echoes normally associated with the spinal cord (Finn-Bodner et al. 1995) (Figure 18.8). Traumatic hematomas in the vertebral canal are amorphous, inhomogeneous, and irregularly marginated (Jones et al. 1996; Rault et al. 2004; Tanaka et al. 2006).

Neoplasia

The appearance of neoplasia varies in echogenicity and uniformity (McConnell et al. 2003; Tanaka et al. 2006). Tumors may arise from the vertebrae (Figure 18.9), as primary tumors or metastases involving the vertebrae are visible as irregular and inhomogeneous areas disrupting the hyperechoic bony interface (Figure 18.9). The involved soft tissue usually appears more hypoechoic than normal, with irregular borders. Neoplasia may also primarily involve soft tissues of the spinal canal, such as the meninges or spinal cord

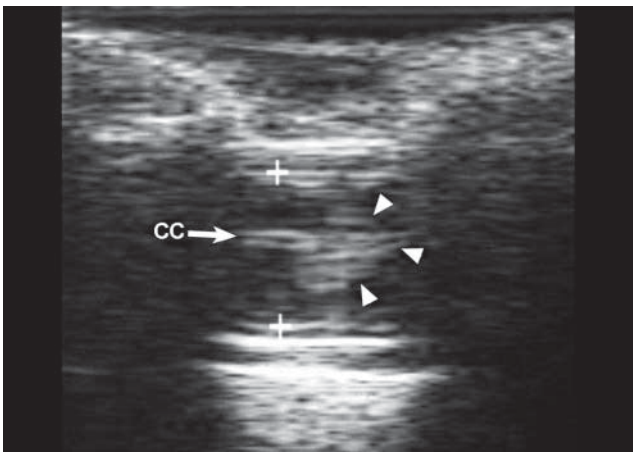


Figure 18.8. Sonogram of a traumatized spinal cord in a dog. Spinal cord hemorrhage appears as a hyperechoic region (arrowheads) obscuring the faint linear echoes normally seen in the spinal cord (between cursors), as well as the hyperechoic interfaces of the central canal (CC).

(Figure 18.10). The exact location or origin and nature of the lesion cannot be diagnosed solely on the ultrasonographic appearance. In one study (Nanai et al. 2007), an anaplastic glioblastoma was described as a clearly demarcated, hyperechoic, oval intramedullary mass. Conversely, an astrocytoma was hypoechoic

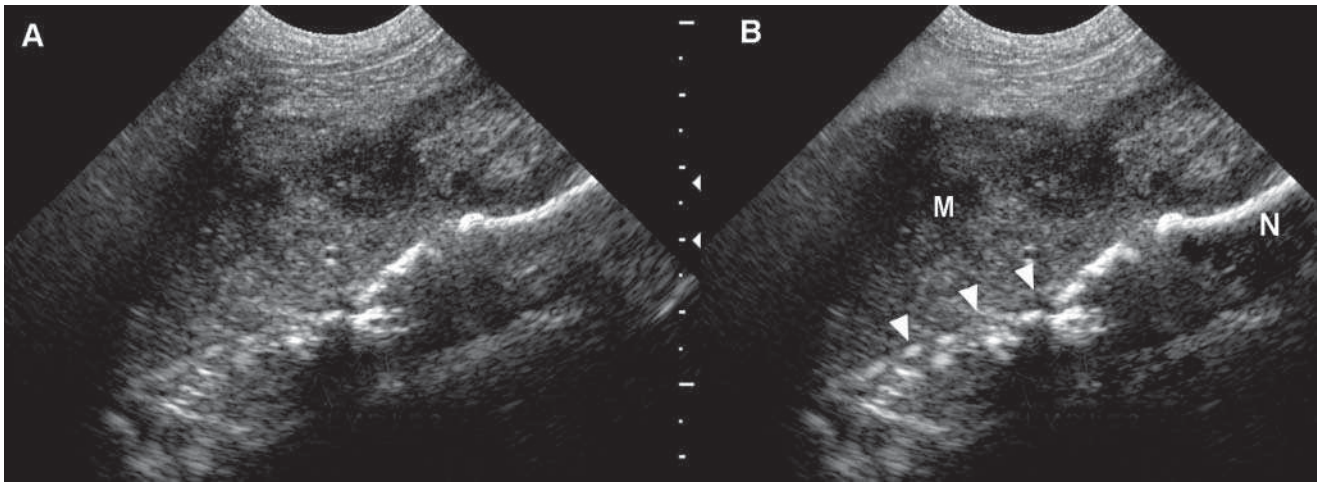


Figure 18.9. Vertebral osteosarcoma in a dog. Sagittal sonogram **(A)** and enhanced labeled image **(B)**. The ventral cortical surface of this lumbar vertebral body is moderately irregular and interrupted (arrowheads). An inhomogeneous and mostly hypoechoic soft-tissue mass (M) extends along the ventral aspect of the vertebra. N, normal adjacent vertebra.

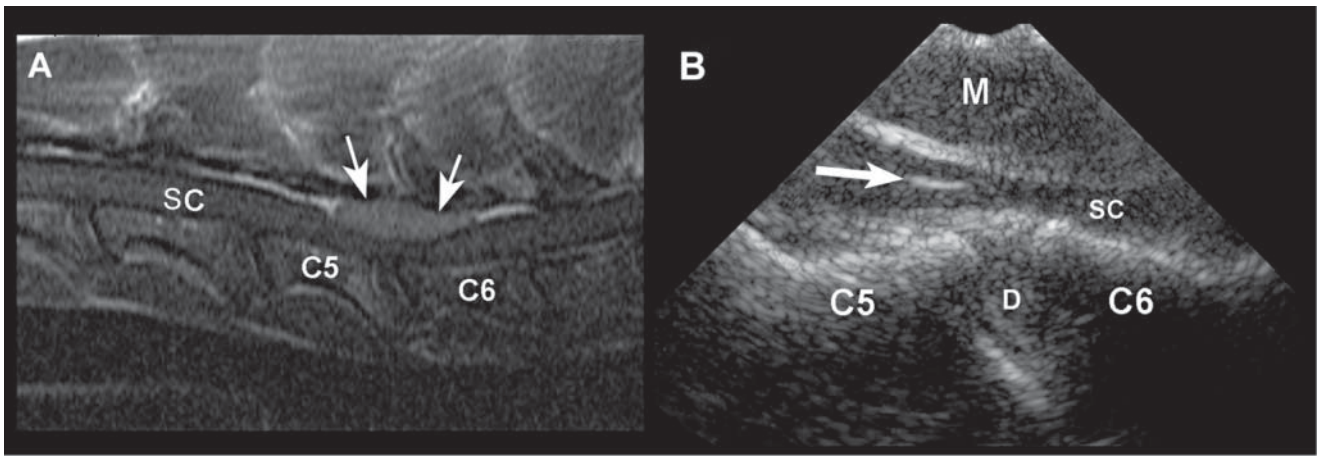


Figure 18.10. Intradural extramedullary mass (M) in an American Foxhound with a 2-month history of chronic progressive tetraparesis. A dorsal laminectomy was performed at C5–6. **A:** Sagittal magnetic resonance image showing the mass (arrows) dorsal to the spinal cord (SC) at C5–6. C5, body of the fifth cervical vertebra; C6, body of the sixth cervical vertebra **B:** Longitudinal sonogram at the laminectomy site showing a hypoechoic mass (M) compressing the spinal cord (SC). The central canal (arrow) cannot be visualized where compression is greatest on this plane. D, intervertebral disc at C5–6.

with anechoic cystic structures and irregular margins. It was difficult to determine whether the mass originated from the spinal cord or dural structures. A myeloma in a third dog had an extradural location and was hypoechoic and clearly marginated. Tumors arising from neurological tissue may appear in unexpected locations such as the kidney (Figure 10.21B).

Serial ultrasound examinations may also help to evaluate progression of neoplastic disease or response to chemotherapy.

Cystic Lesions

Spinal arachnoid or intradural cysts have been reported as cyst-like lesions in the subarachnoid space of dogs and cats (Galloway et al. 1999). These are not lined with a secreting epithelium and are therefore not considered as true cysts.

The fluid contents may be anechoic to isoechoic to the spinal cord (Galloway et al. 1999). The lesions can appear septated with irregular hyperechoic lines. An irregular and thickened dura may be present.

The central canal may or may not be recognized, and the compressed spinal cord may be increased in echogenicity. The line thought to represent the pia in normal animals is not always visible (Galloway et al. 1999). After drainage of arachnoid or intradural cysts, the spinal cord can be monitored for recurrence by using the surgical site as an acoustic window (Hudson et al. 1998).

Syringomyelia

Dilation of the central canal with an ependymal lining (**hydromyelia**) and cavitation within the spinal cord lacking an ependymal lining (**syrinx**), a combined condition known as **syringomyelia**, can occur secondary to numerous conditions, including trauma, neoplasia, intracranial epidermoid cysts, and arachnoiditis (Kirberger et al. 1997; MacKillop et al. 2006; Rusbridge et al. 2006). Syringomyelia has been mainly described in relation to Chiari type I-like malformation syndrome in Cavalier King Charles Spaniels and other small breeds of dogs (Figure 18.11). In these dogs, ultrasononography is useful to evaluate for this condition and cerebellar herniation (Figure 18.12).

In all cases, syringomyelia is thought to occur as a consequence of altered CSF dynamics (Rusbridge et al. 2006). Concurrent myelomalacia might also be found, with a tendency to increase the spinal cord echogenicity with an obliteration of the central canal (Figure 18.13).

Vertebral and Perivertebral Changes

Ventral spondylosis bridges two vertebral bodies along the ventral longitudinal ligament and appears

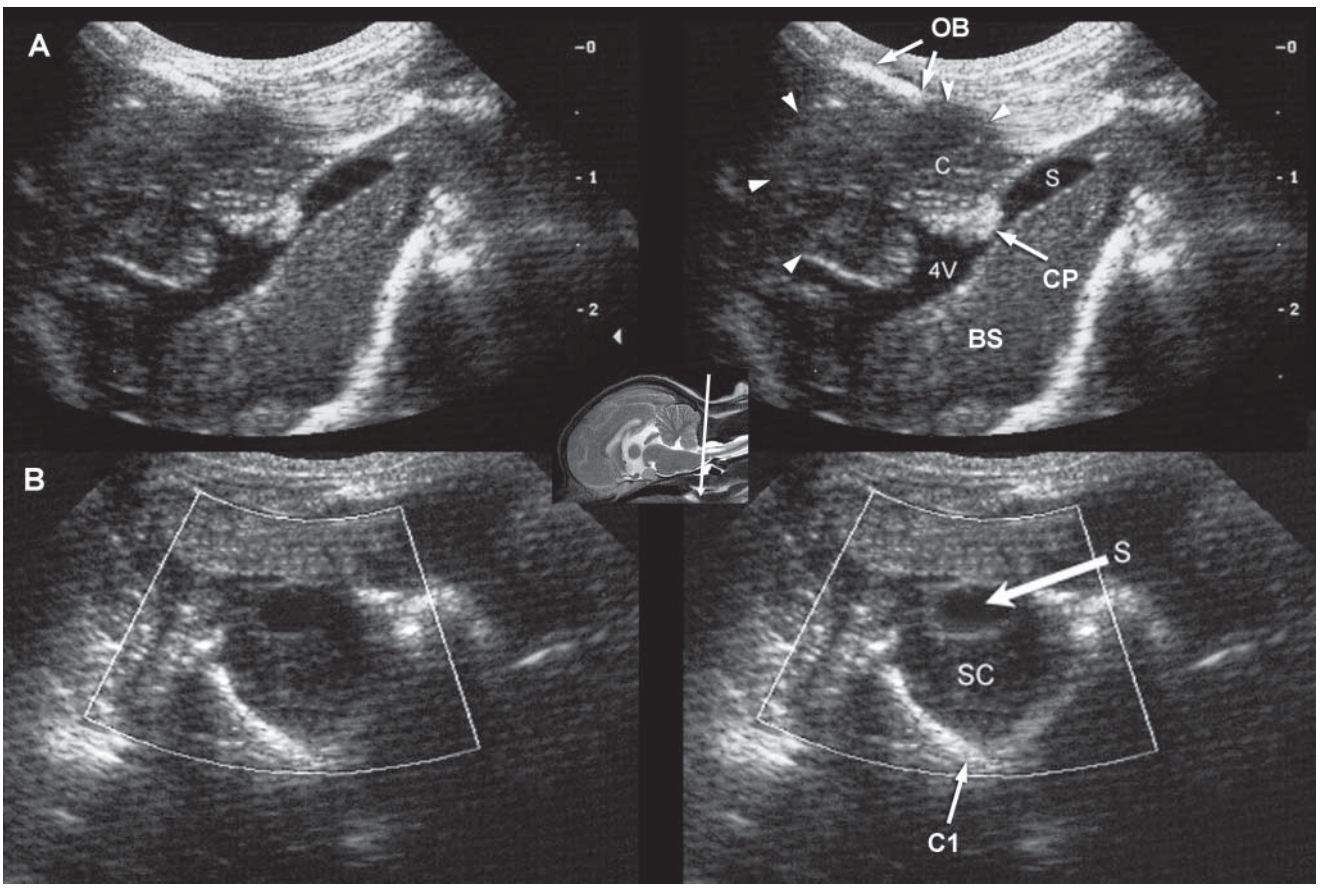


Figure 18.11. Chiari-like malformation with syringomyelia. Sagittal **(A)** and transverse **(B)** sonographic images obtained through a large foramen magnum in a dog with occipital dysplasia. The cerebellum (C, arrowheads) protrudes into the foramen, below the occipital bone (OB). A tubular anechoic fluid collection is observed along the mid-dorsal portion of the cranial cervical spinal cord (SC), consistent with syringomyelia (S). The fourth ventricle (4V) is also dilated. BS, brain stem; CP, choroid plexus of the fourth ventricle.

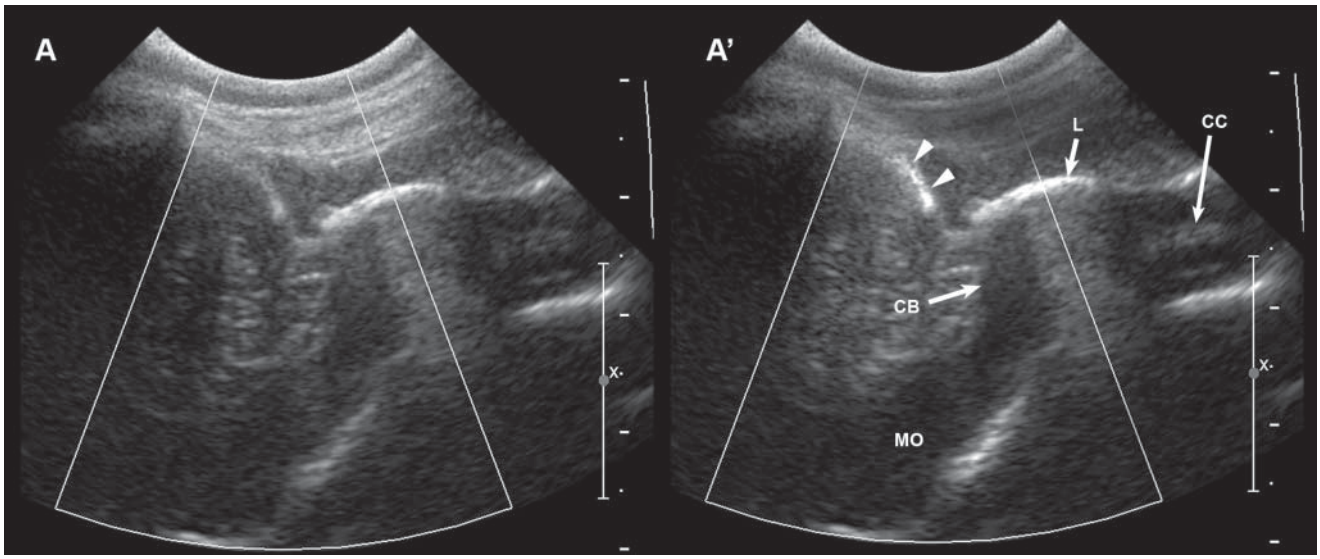


Figure 18.12. Chiari-like malformation without syringomyelia. Sagittal sonogram (**A**) and (**A'**) enhanced image with annotations of a Cavalier King Charles Spaniel with occipital dysplasia. The cerebellum (CB) protrudes caudally to the occipital bone (arrowheads) but the central canal (CC) is normal at the level of C2. L, lamina of C1; MO, medulla oblongata.

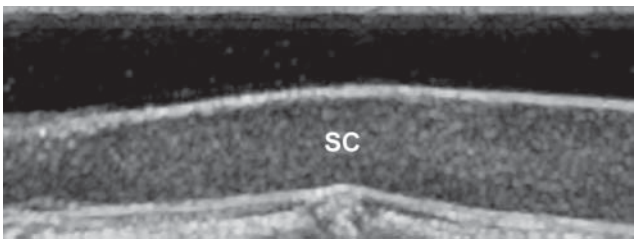


Figure 18.13. Myelomalacia in a dog. Sagittal sonogram of a segment of spinal cord (SC) after laminectomy and durotomy. The cord is uniformly mildly echogenic, and the central canal is not visible. Anechoic fluid is noted in the near field, placed to serve as an acoustic window.

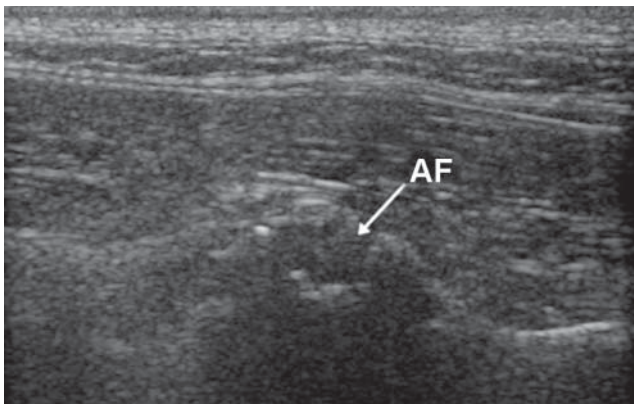


Figure 18.14. Articular facet osteoarthrosis in a dog. Sagittal sonogram of a segment of spine with an irregular hyperechoic surface at the level of the articular facets (AF).

as a hyperechoic bridge associated with acoustic shadowing. The disc at that space cannot be visualized.

Spondylarthrosis or articular facet osteoarthrosis is visible as hyperechoic, irregularly lined surfaces over the joint space and is associated with acoustic shadowing (Figure 18.14).

In discospondylitis (Figure 18.15), a ventral approach to the affected disc enables visualization of a partial or complete loss of the fiber organization of the discs. The vertebral hyperechoic contours become irregular and may be interrupted by the presence of hypoechoic or anechoic lytic foci. Areas of tissue swelling of variable echogenicity are often seen laterally and ventrally to the disc space. The surrounding fat or muscles may also be affected. Ultrasound-guided fine-needle aspirates of the affected discs can be carried out (Rault et al. 2004; Packer et al. 2005).

A sublumbar or paralumbar abscess appears as a hypoechoic to anechoic, inhomogeneous to homogeneous area with irregular and ill-defined margins. In some cases, a foreign body can be identified within the abscess. Foreign material often appears hyperechoic with or without acoustic shadowing (Figure 18.16) (Packer et al. 2005). Affected muscles are typically heterogeneous and adjacent vertebral surfaces associated with irregular new bone formation (Frendin et al. 1999).

Fractures of the vertebral bodies can be visualized as interruptions of the continuous hyperechoic line of the surface of the bone. In acute cases, an inhomogeneous, mixed echotexture hematoma can be seen at the fracture site.

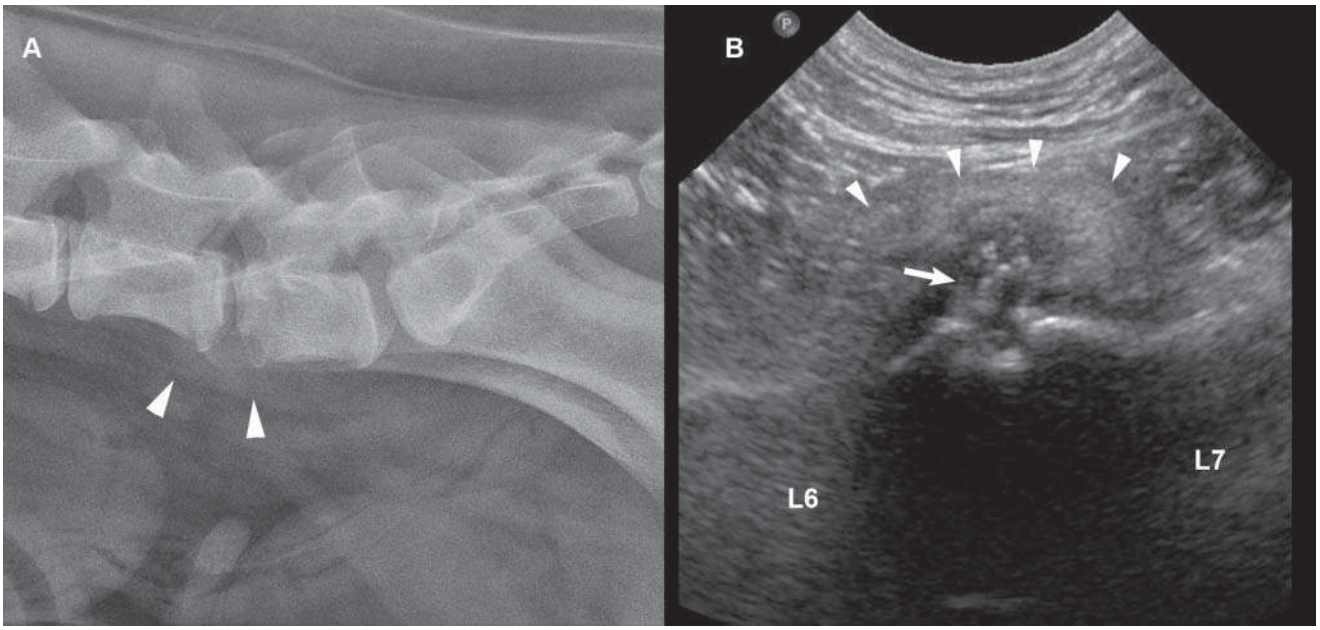


Figure 18.15. **Discospondylitis in a puppy. A:** Lateral radiograph of the lumbosacral region showing lysis and osseous remodeling at the endplates of L6 and L7. Note the soft tissue swelling ventral to the spine (arrowheads). **B**: Longitudinal sonogram with the probe placed at the ventrolateral aspect of L6–L7 showing hyperechoic foci indicating mineralization (arrow) ventral to the intervertebral disc space (D), with ventral hyperechoic soft-tissue thickening (arrowheads) consistent with inflammatory tissue and fibrosis.

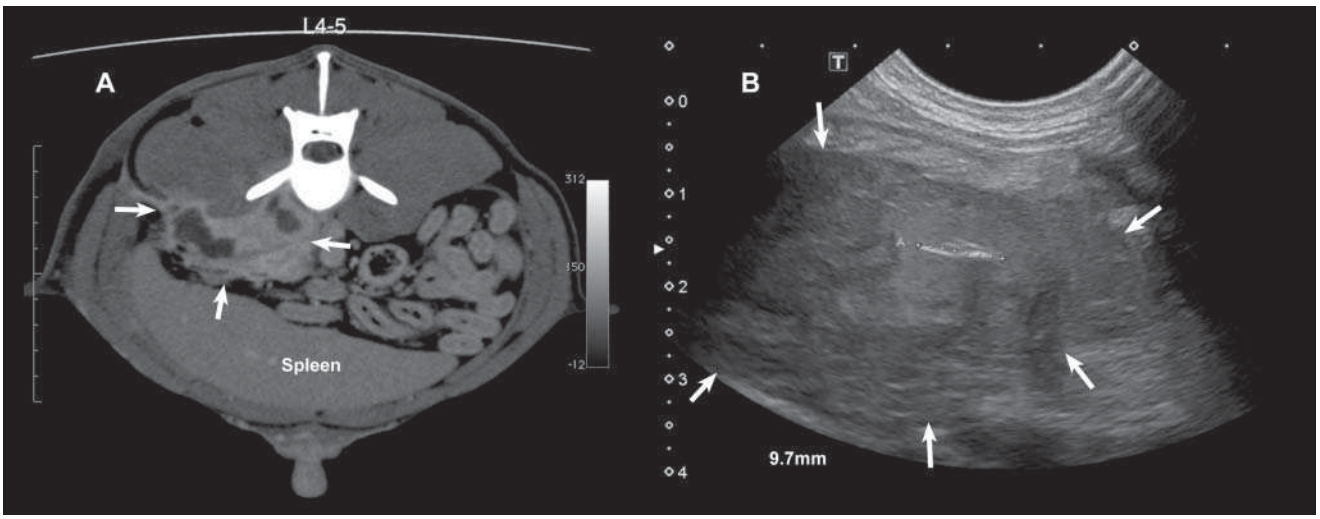


Figure 18.16. **Sublumbar abscess due to grass awn migration in a dog. A**: Computed tomographic (CT) transverse image at the level of L4 on which a 4×5 cm mass with heterogeneous contrast enhancement is present in the right ventral sublumbar muscles (arrows). Using ultrasound with a ventrolateral approach **(B)**, a nearly 1-cm-long fusiform hyperechoic structure consistent with a grass awn (between cursors) is detected within a soft-tissue mass of moderate echogenicity (arrows). This type of foreign body is typically not detected with CT. Images courtesy of Laurent Couturier, Azurvet, France.

Interventional Procedures

Intraoperative ultrasonography can be useful in determining whether herniated disc material remains in the vertebral canal or foramina (Nakayama 1993; Gallagher et al. 1995). The use of spinal ultrasonography has also been described during dorsal laminectomy in dogs with caudal cervical vertebral instability and malformation to ensure that the spinal cord has been adequately decompressed (Nanai et al. 2006). As in other locations, ultrasound-guided aspirates or tissue-core biopsies of focal lesions can be performed if a satisfactory acoustic window is available.

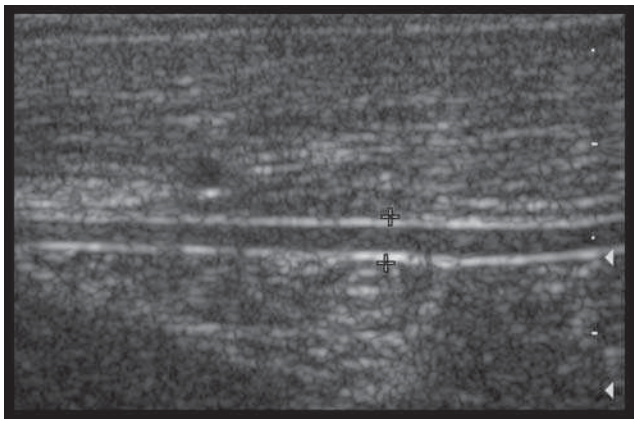


Figure 18.17. Sonographic appearance of a normal canine nerve. The central portion of the nerve is hypoechoic with speckles and surrounded with hyperechoic boundaries.

Scanning Technique and Normal Sonographic Anatomy of Spinal and Peripheral Nerves

Because of their small size and superficial location in extremities, peripheral nerves are preferably scanned with high-frequency (10 MHz and above) linear transducers. If needed, a stand-off pad can be used to place the nerve into the focal zone. Color flow Doppler imaging is useful in differentiating adjacent vessels from nerves. In addition, nerves are not compliant to pressure, unlike vessels, and moving a limb can help in differentiating a tendon from a nerve. Sedation may be required in incompliant or painful patients, allowing limbs to be pulled or abducted more easily. Examination of controlateral nerves may help in confirming suspected abnormalities.

In longitudinal section, nerves of dogs and cats appear as 0.5- to 3-mm-wide, linear hypoechoic structures surrounded by a hyperechoic rim (Figures 18.17) (Hudson et al. 1996; Guilherme and Benigni 2008; Haro et al. 2011; Anson et al. 2013). The walls of nerves are brighter and better defined than vessel walls; vascular walls are less distinct. In transverse section, nerves are circular or oval hypoechoic uniform structures, or show individual components.

The scanning technique and sonographic anatomy of the brachial plexus has been described in both dogs (Hudson et al. 1998; Guilherme and Benigni 2008) and cats (Anson et al. 2013). Beginning with the dog placed in left lateral recumbency facilitates identification of the proximal portion of the right spinal nerves, using the C5–T1 transverse processes and intervertebral disc spaces as landmarks (Guilherme and Benigni 2008). Once the intervertebral disc space and foramen are located in the longitudinal plane, the probe is rotated approximately 90° to be transverse to the spine, with mild craniodorsal–caudoventral inclination to obtain longitudinal images of the origin of each spinal nerve (Figure 18.18). Each nerve appears dorsal to the corresponding vertebral artery and vein. The nerves are then imaged in the transverse plane and followed distally, as they gradually transform into clusters of 1- to 1.5-mm-wide round components (Figure 18.19). Clustered nerve components can also be well visualized by placing the probe cranial to the first rib, pulling the limb caudally. Branches of the brachial plexus are further examined in the axilla, with the animal remaining in the same position but with the upper limb abducted, or in opposite lateral recumbency for a medial approach (Anson et al. 2003). The probe is placed in a parasagittal plane between the shoulder and sternum to identify the plexus in a transverse plane, close to the origin of the axillary artery and vein. These vessels are much larger than the nerves, and particularly the vein that is easily compressible. Because of the sinusoidal orientation of these vessels, color Doppler signal may not be apparent. The median and ulnar nerves are caudal to the brachial artery, whereas the musculocutaneous nerve is located cranially. The probe can then be rotated to image the nerves in longitudinal section and can be slid distally to image the nerves in the mid-humeral region (Figure 18.20). Transverse and longitudinal images of the musculocutaneous, median, and ulnar nerves are obtained from the medial aspect of the mid-humeral regions by aligning the probe perpendicular or parallel to the limb, respectively. Similarly, the radial nerve can be evaluated at the caudomedial and distal lateral aspects of the antebrachium. This nerve appears at that level as a cluster of 0.5-to 1-mm components in both

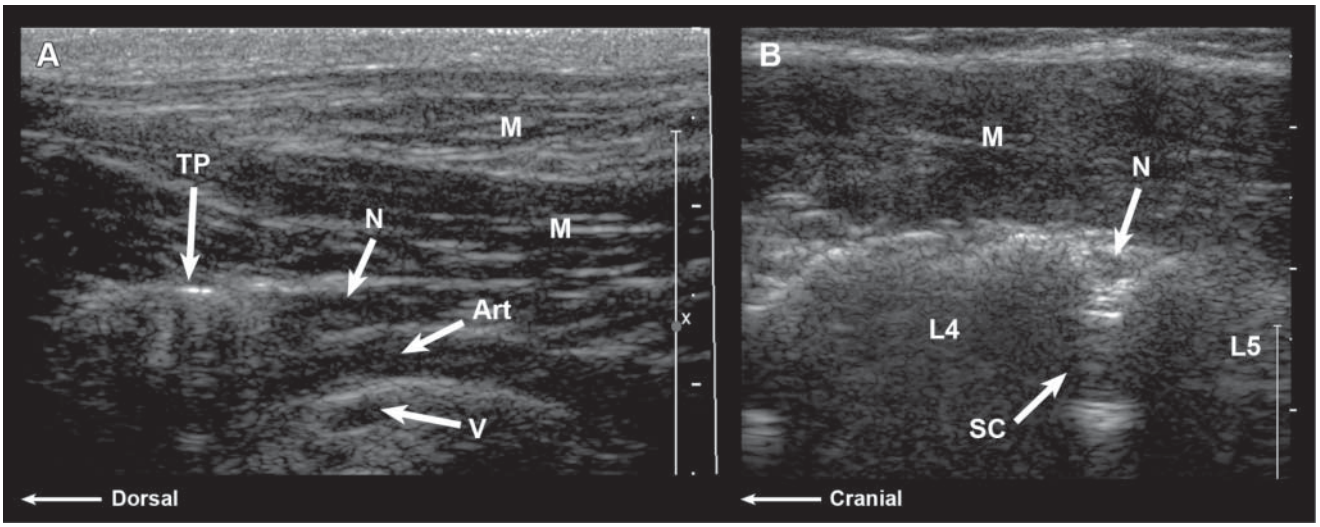


Figure 18.18. **Spinal nerve as it exits its intervertebral foramen. A:** The spinal nerve (N) is identified in the longitudinal plane as it exits the intervertebral foramen, dorsal to the intervertebral artery (Art) and vein (V), ventral to the adjacent vertebral transverse process (TP). **A:** This sonographic image was obtained with the probe held parallel to the lumbar vertebral column slightly lateral to the midline so that the beam passed through the intervertebral foramen in a dorsal oblique plane. The nerve (N) is seen in cross-section as it exits the intervertebral foramen. The spinal cord (SC) can be seen deep to the foramen, between the shadowing fourth and fifth lumbar vertebrae (L4 and L5, respectively). M, paravertebral muscles.

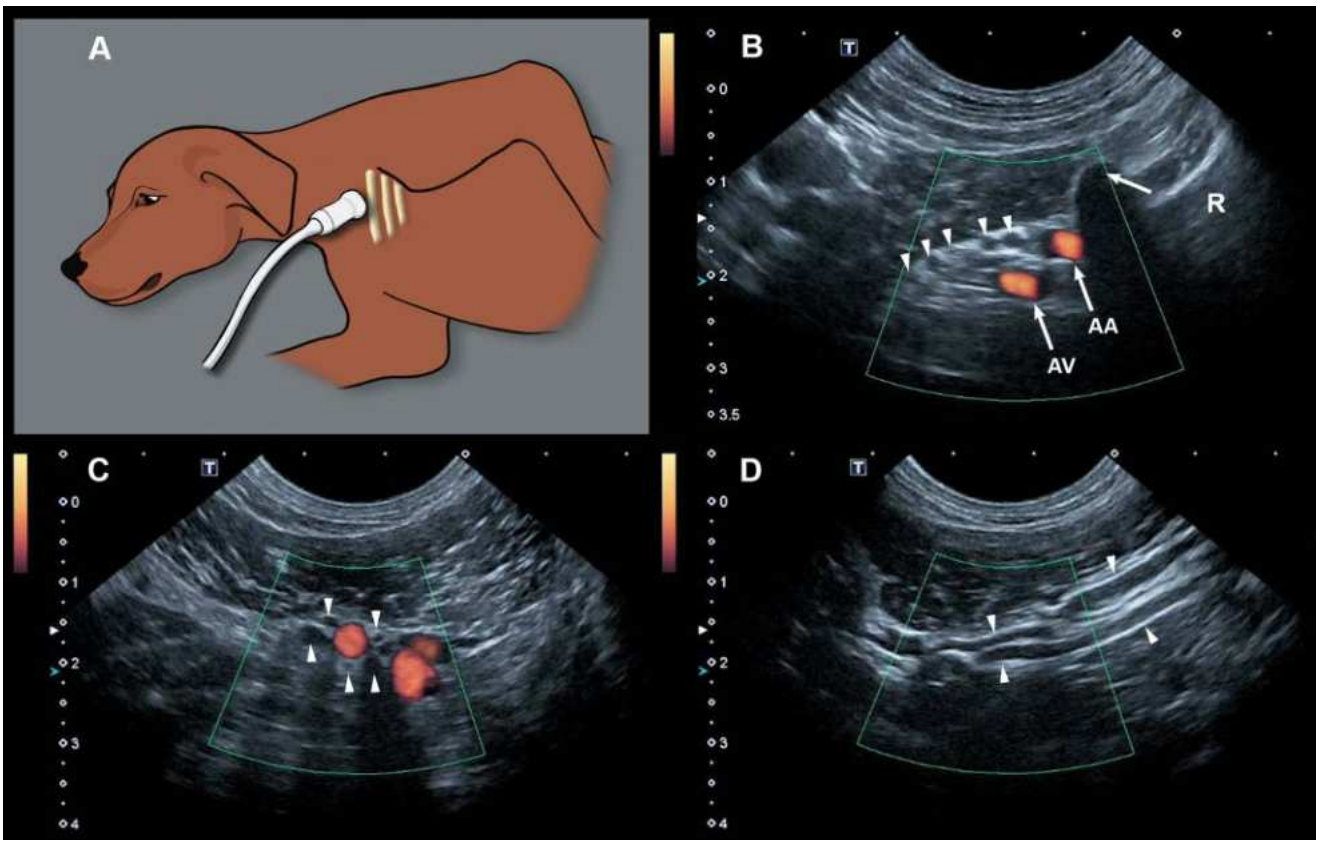


Figure 18.19. **Approach to the left brachial plexus in a dog and normal sonographic appearance. A:** The dog is placed in right lateral recumbency and its left thoracic limb is pulled caudally. The probe is initially placed craniolateral to the first rib. The axilla is then examined, gently moving the probe in the transverse and parasagittal planes. **B**: Components of the brachial plexus (arrowheads) are seen adjacent to the first rib (R) as round hypoechoic structures surrounded with hyperechoic tissue. The nerves measure between 0.5 and 2.5 mm. The axillary vein (AV) and artery (AA) are nearby with power Doppler orange signal. **C, D:** Transverse **(C)** and longitudinal **(D)** sonographic images of the plexus nerves (arrowheads) obtained in the axilla. Note the prominence of their hyperechoic boundaries.

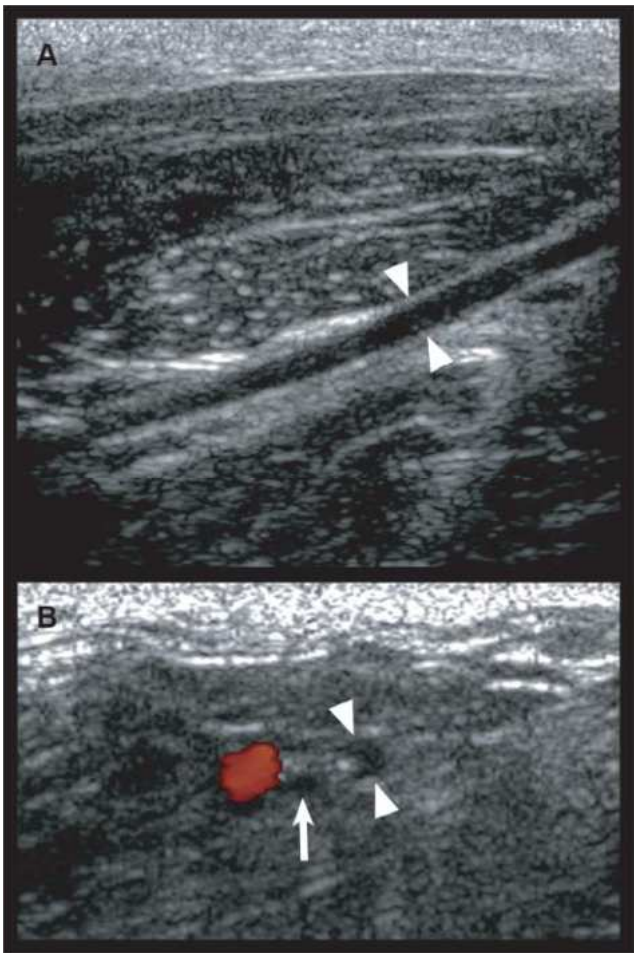


Figure 18.20. Normal ulnar nerve in a dog at the mid-humerus in longitudinal (A) and transverse (B) images. The ulnar nerve (arrowheads) is caudal to the brachial artery (red color Doppler signal in **B**) and median nerve (arrow).

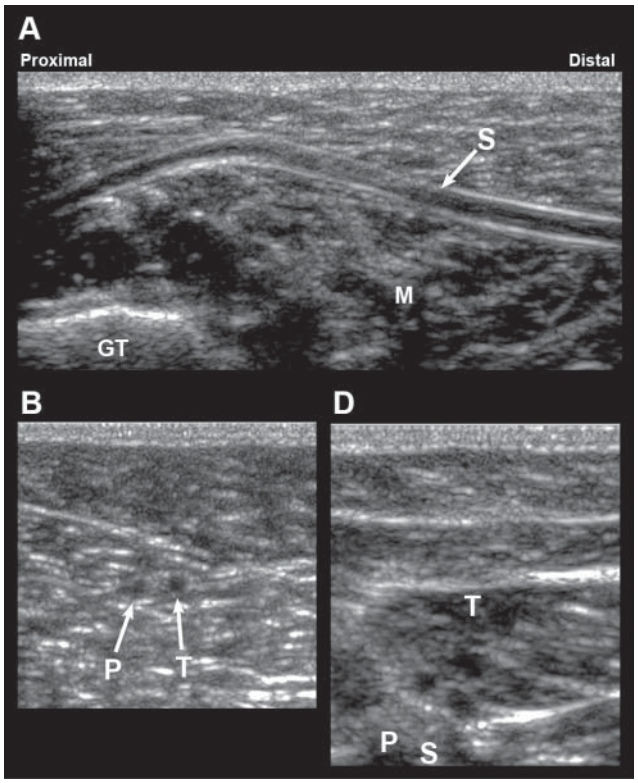


Figure 18.21. Normal sciatic nerve in a cat. The feline sciatic nerve is similar to that of the dog. **A**: Proximal portion of the sciatic nerve (S) near the greater trochanter (GT). **B**: Transverse image of the sciatic nerve in the mid-thigh showing the individual components representing the common peroneal nerve (P) and the larger tibial nerve (T). **C**: Transverse image of the sciatic nerve obtained more distally. Three components are now apparent, representing the common peroneal nerve (P), the tibial nerve (T), and the caudal cutaneous sural nerve branch from the tibial nerve (S).

dogs and cats (Guilherme and Benigni 2008; Anson et al. 2013).

The sciatic nerve and its branches can also be examined in dogs and cats (Benigni et al. 2007; Haro et al. 2011). The caudal part of the lumbosacral trunk and the proximal portion of the sciatic nerves are recognized through the greater ischiatic foramen, using a parasagittal plane just medial to the shaft of the ilium. The sciatic nerve can be followed as it courses dorsolaterally over the acetabulum, bending toward the caudal aspect of the femur. Positioning the probe caudal to the greater trochanter enables a longitudinal image of the nerve that becomes parallel to the femoral neck (Figure 18.21). The nerve then becomes close to the caudal gluteal artery and vein, before extending distally, parallel and caudal to the femoral shaft, between the muscles of the thigh. In the transverse plane, two components of the sciatic nerve are distinguished, the common peroneal nerve, cranially, and the tibial nerve, just caudally.

Sonographic Features of Peripheral Nerve Disorders

Rupture and Demyelination

Rupture or transection of nerves can occur associated with fractures, sharp-object penetration, or other injuries. After injury, loss of visualization of the distal segment strongly suggests rupture.

Serial examination can be useful to determine if there is any evidence of repair after injury. In some animals, a neuroma may form at the site of transection, often appearing as a hypoechoic bulb. Regeneration has been described as irregular regrowth with or without neuroma formation.

Demyelination also can occur after trauma, compression by a mass, or inflammation that is not severe enough to cause transection. In such cases, the nerve is

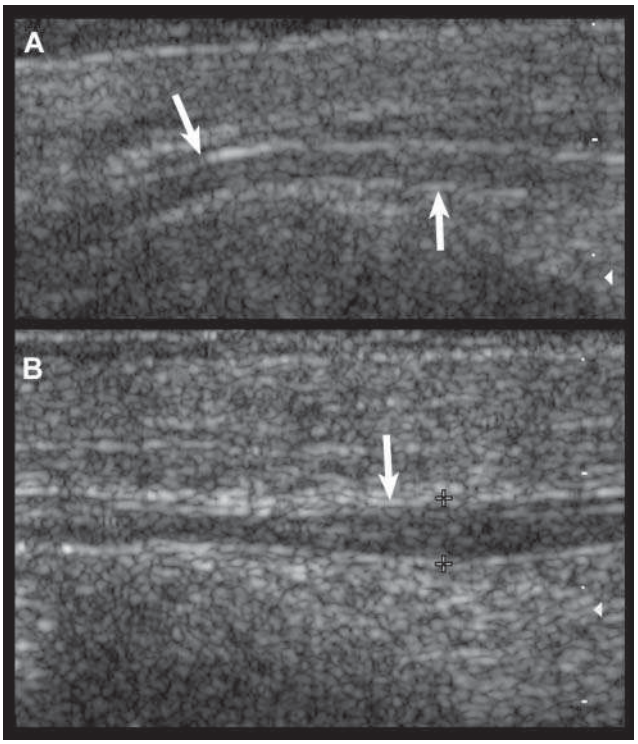


Figure 18.22. Longitudinal sonogram of the right sciatic nerve in a dog with neurological deficits. Compare these images with those of a normal sciatic nerve in Figure 18.21. **A:** The sciatic nerve (arrows) near the greater trochanter. **B:** The sciatic nerve near the mid-femoral region (arrows). The nerve has a variable diameter and irregular interrupted walls. The nerve is swollen in the mid-femoral region and measures 2.9 mm.

poorly visualized distal to the site of injury. Comparison with the nerve on the healthy contralateral side is helpful (Figure 18.22).

Neoplasia

While computed tomography (CT) and magnetic resonance imaging (MRI) are generally considered more useful for detecting peripheral nerve sheath tumors (PNSTs), ultrasound can be useful as initial diagnostic tool or to guide fine-needle aspiration or biopsy. Tumors of the spinal or peripheral nerves can usually be visualized by ultrasonography if they exceed 5 mm. PNSTs in the brachial plexus of dogs have been described as hypoechoic tubular structures (Rose et al. 2005) or as fusiform masses exhibiting mixed echogenicity (Platt et al. 1999) (Figure 18.23). These tumors may also form very oval or spherical masses (Figures 18.23, 18.24). When tubular or fusiform in shape, Color or Power Doppler is useful for discriminating these from adjacent blood vessels (Figure 18.25). Peripheral nerve tumors can occur in

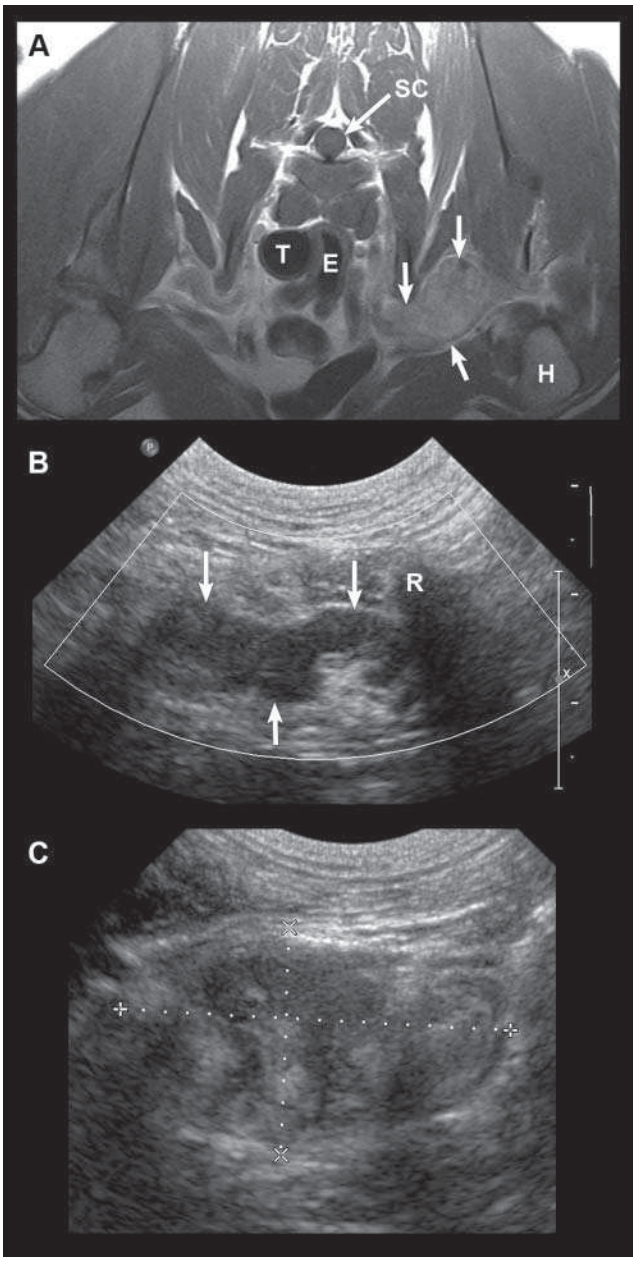


Figure 18.23. Peripheral nerve sheath tumor involving the radial nerve in the brachial plexus of an American Cocker Spaniel with moderate left thoracic limb lameness. A: Contrast T1-weighted transverse magnetic resonance image showing an oblong, lobular mass (arrows) as it exits the spinal canal. Portions of the mass show contrast enhancement, although some areas remained hypointense. SC, spinal cord; T, trachea; E, esophagus; H, humerus. **B:** On ultrasonography, the radial nerve was enlarged, irregular and hypoechoic. R, rib. **C:** The nerve became incorporated in a large heterogeneous mass (calipers) immediately cranial to the first rib. Histopathology following surgical biopsy revealed a peripheral nerve sheath tumor.

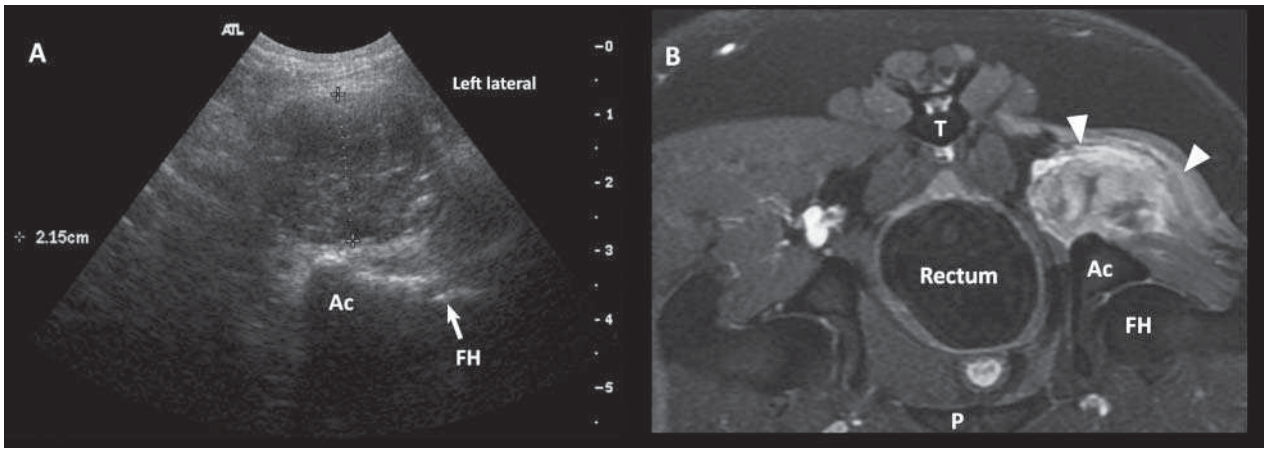


Figure 18.24. **Sciatic nerve sheath fibrosarcoma in a dog. A:** Transverse sonographic image of a 2.15-cm-thick mildly echogenic mass located dorsal to the acetabular bone (Ac) and femoral head (FH). **B:** Transverse post-contrast T1-weighted magnetic resonance sequence with fat saturation, highlighting the contrast-enhancing mass (arrowheads). The adjacent muscles are atrophied and hyperintense. T, tail; P, pubis.

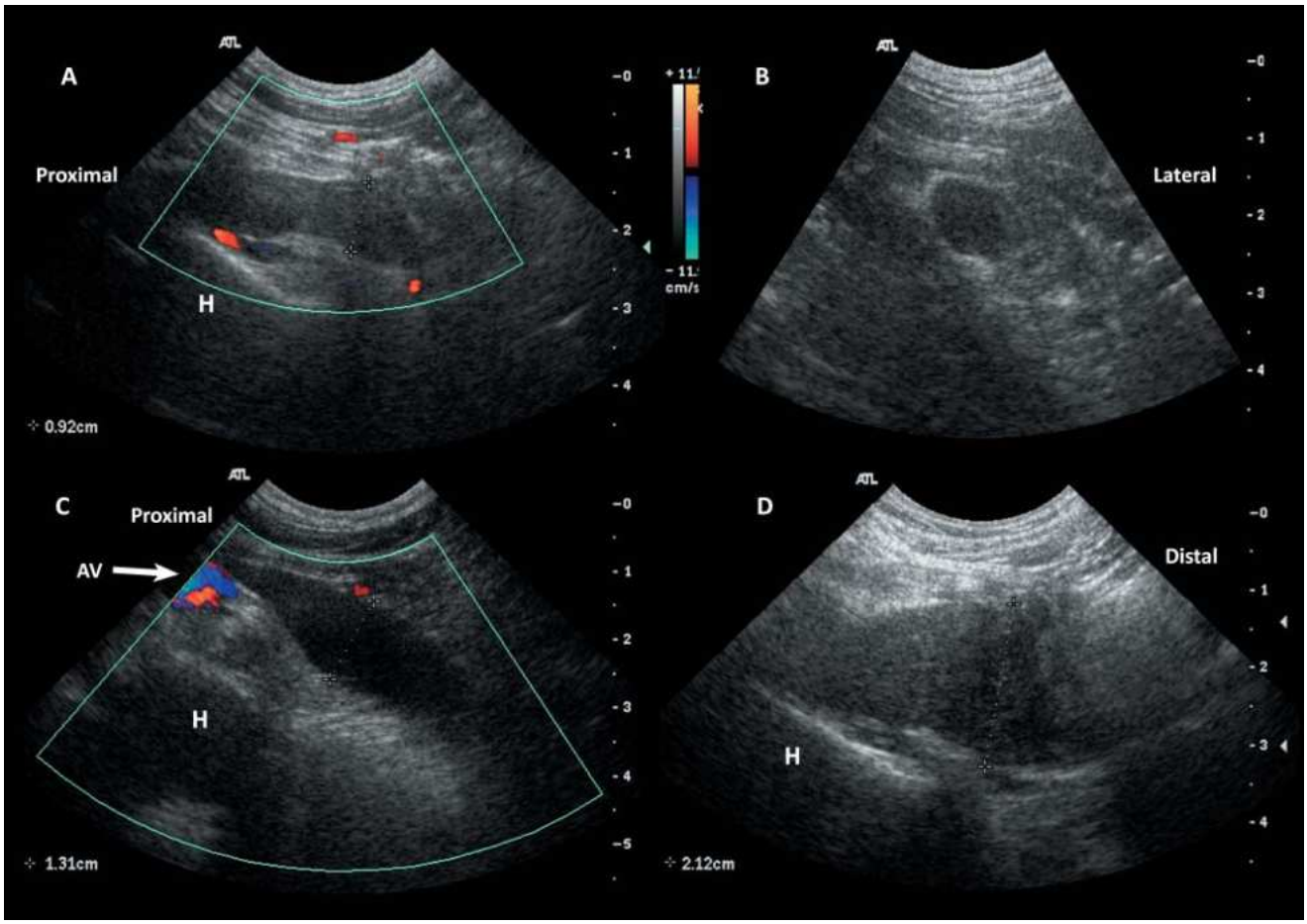


Figure 18.25. **Brachial plexus nerve sheath tumor in a dog.** Color Doppler can be useful in distinguishing enlarged nerves of the brachial plexus from nearby vessels. A well-defined hypoechogenic tubular structure without flow is identified next to the humerus (H) in this longitudinal color Doppler **(A)** and transverse B-mode **(B)** sonographic images. **C:** This structure is followed distally, next to the axillary vein (AV) and (**D**) the humerus, becoming a larger mass approximating 2 cm in diameter.

unusual locations such as the thorax (Essman et al. 2002), urinary bladder wall (Pavia et al. 2012) and other organs.

Other neoplasms involving peripheral nerves are less common (Montoliu et al. 2008). They may originate from nerve components, invade them, or cause compression. These are typically hypoechoic, although they may also present mixed echogenicity and fluid-filled cavities.

Other Disorders of the Peripheral Nerves and Adjacent tissues

Inflammatory neuropathies may be detected in some animals with ultrasound. Chronic lymphocytic – or hypertrophic – neuritis or ganglioneuritis is a rare condition that has been reported involving C2 spinal nerve in a dog (Rodenas et al. 2012). Affected nerves are thickened and hypoechoic, mimicking neoplasia.

In acute partial or complete avulsions of the brachial plexus, a hypoechoic to anechoic, inhomogeneous, and irregularly demarcated area is seen in the axillary region. This area represents the hematoma. Torn nerve tissue can usually not be seen sonographically.

Metastases to the axillary lymph nodes in the area of the brachial plexus can also be identified. Affected lymph nodes are typically rounded, moderately to severely enlarged, and mildly to moderately inhomogeneous. The hilar fat usually disappears. A definitive diagnosis can be obtained by ultrasound-guided needle biopsy.

Interventional Procedures

Ultrasonography can be used to guide fine-needle aspirations or biopsies of spinal, paraspinal or peripheral nerve lesions. Often, these are performed on lesions previously identified with MRI or CT (Figure 18.26). One suggested technique is to insert a 22 gauge spinal needle into the mass and after removing the stylet, to repeatedly push the tip back and forth within the mass (Da Costa et al. 2008). However, in the case of rigid masses that don't exfoliate well, aspiration may be necessary. Sonography could also be useful in guiding the resection of masses associated with nerves.

Ultrasonography can be useful in guiding administration of regional anesthesia. Lidocaine can be injected around the sciatic nerve at the lateral aspect of the canine thigh caudal to the femur and medial to the biceps femoris. The injected lidocaine can appear as a hypoechoic halo, which was termed a "donut sign" by the authors of one study (Echeverry et al. 2010).

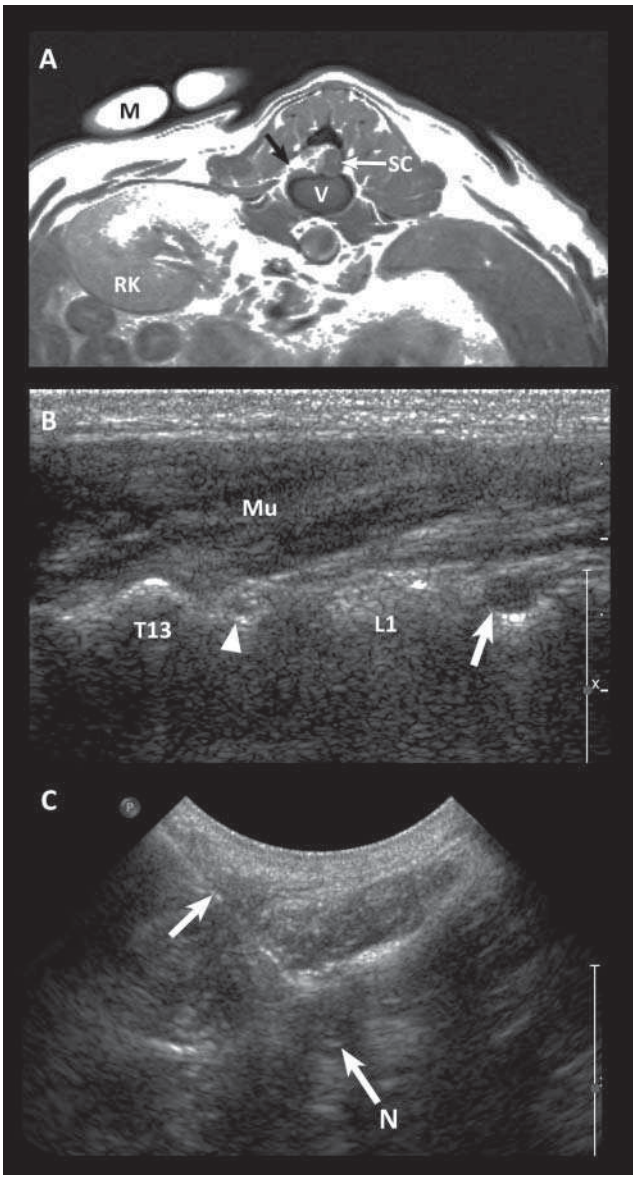


Figure 18.26. Fine-needle aspiration of a nerve sheath tumor involving the dorsal root at L1-L2 in a Jack Russell Terrier with hind limb ataxia for 3 weeks. A: Transverse T1-weighted magnetic resonance images (MRIs) showed marked contrast enhancement of the thickened nerve (black arrow) involving the right nerve root. A vitamin E marker (M) was placed to guide surgical excision following MRI. RK, right kidney; V, vertebral body; SC, spinal cord. **B:** Longitudinal sonogram of the normal T13 nerve (arrowhead) and the enlarged hypoechoic L1 nerve (arrow). Mu, epaxial muscle. **C:** The probe was rotated obliquely to allow ultrasound-guided aspiration (arrow) of the affected nerve root (N). Cells consistent with sarcoma were obtained. Following a dorsal hemilaminectomy and surgical resection, histopathology confirmed a benign nerve sheath tumor.

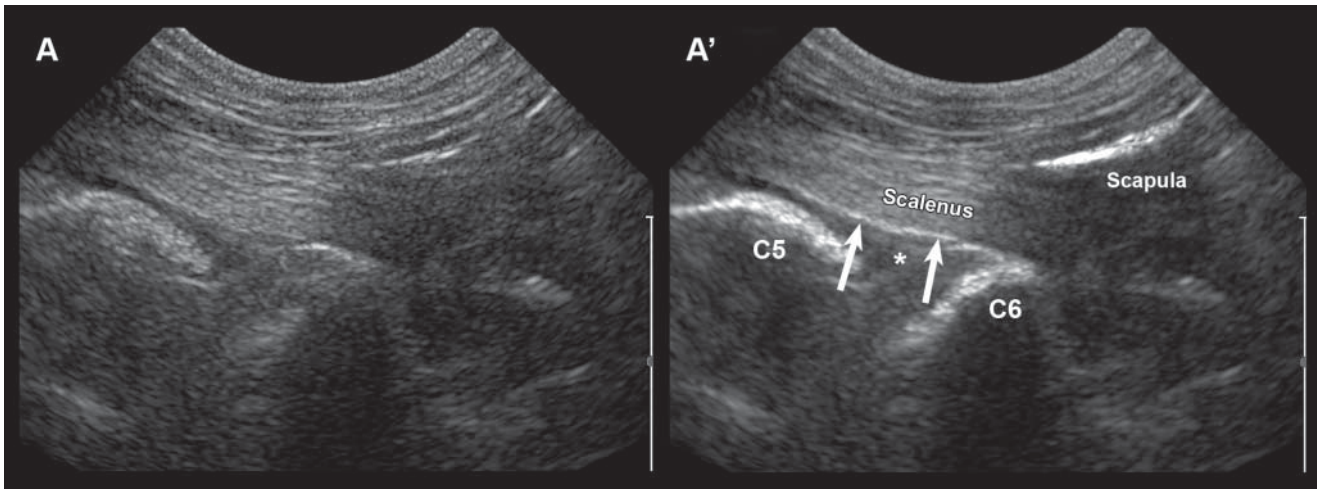


Figure 18.27. Landmarks for blocking the nerve roots of the brachial plexus in dogs. A, A′: The probe is held in a dorsal plane parallel to the long axis of the neck, allowing identification of the C5 and C6 transverse processes. The cranial part of the spine is on the left side of the image. The scapula makes visualization of the C7 transverse process more difficult. Injections are made deep (*) to the fascial plane of the scalenus muscle (arrows), allowing the aliquot to be contained in the vicinity of the exiting spinal nerves (Bagshaw et al. 2009).

Injections can be made around the C6, C7, and C8 cervical spinal nerve roots with a 22-gauge spinal needle using the transverse processes and scalenus muscle as landmarks (Bagshaw et al. 2009) (Figure 18.27). Similarly, ultrasonography can be useful for guiding injections of local anesthetic agents to block the brachial plexus and origin of the femoral nerve in cats (Alvarez et al. 2011). For blocking the feline brachial plexus, the preferred approach included placement of the cat in dorsal recumbency and abduction of the limb to be blocked, while the opposite forelimb was pulled caudally (Anson et al. 2011). A dorsal approach was suggested for blocking the femoral nerve (Alverez et al. 2011). Injection was made into the iliopsoas complex between the L6 and L7 transverse processes with the cats placed in lateral recumbency and the probe held perpendicular to the spine. The dorsal processes of the L6 and L7 lumbar vertebrae and the cranial margin of the proximal ilium can be useful landmarks for the procedure.

Additionally, ultrasonography can aid in locating transected nerve endings prior to surgical repair. Following anastomosis, ultrasonography can be used to monitor the nerves and determine whether healing is occurring (Hudson et al. 1996).



Visit our website at **www.SmallAnimalUltrasonography.com** for complementary video clips with annotations and text on:

- Peripheral nerve sheath tumor
- Vertebral mass invading the spinal canal

References

Alvarez PH, Gil F, Laredo FG, Ayala MD, Belda E, Soler M, Agut A (2011) Abstracts from the 2011 EVDI Annual Meeting (London, England). Ultrasound guidance for the femoral nerve block in cats: An imaging study. Vet Radiol Ultrasound 52:682.

Anson A, Gil F, Laredo FG, Soler M, Ayala MD, Belda E, Agut A (2011) Abstracts from the 2011 EVDI Annual Meeting (London, England). A comparison of two techniques for ultrasound-guided brachial plexus block in cats. Vet Radiol Ultrasound 52:695.

Anson A, Gil F. Lardo F, Soler M, Belda E, Ayala MD, Agut A (2013) Correlative ultrasound anatomy of the feline brachial plexus and major nerves of the thoracic limb. Vet Radiol Ultrasound 54:185–193.

Bagshaw HS, Larenza MP, Seiler GS (2009) A technique for ultrasound-guided paravertebral brachial plexus injections in dogs. Vet Radiol Ultrasound 50:649–654.

Benigni L, Corr SA, Lamb CR (2007) Ultrasonographic assessment of the canine sciatic nerve. Vet Radiol Ultrasound 48:428–433.

Da Costa RC, Parent JM, Dobson H, Ruotsalo K, Holmberg D, Duque MC, Poma R (2008) Ultrasound-guided fine needle aspiration in the diagnosis of peripheral nerve sheath tumors in 4 dogs. Can Vet J 49: 77–81.

Echeverry DF, Gil F, Laredo F, Ayala MD, Belda E, Soler M, Agut A (2010) Ultrasound-guided block of the sciatic and femoral nerves in dogs: A descriptive study. The Vet J 186:210–215.

Essman SC, Hoover JP, Bahr RJ, Ritchey JW, Watson C (2002) An intrathoracic malignant peripheral nerve sheath tumor in a dog. Vet Radiol Ultrasound 43:255–259.

Finn-Bodner ST, Hudson JA, Coates JR, et al. (1995) Ultrasonographic anatomy of the normal canine spinal cord and correlation with histopathology after induced spinal cord trauma. Vet Radiol Ultrasound 36:39–48.

Frendin J, Funkquist B, Hansson K, Lönnemark M, Carlsten J (1999) Diagnostic imaging of foreign body reactions in dogs with diffuse back pain. J Small Anim Pract 40:278–285.

Gallagher JG, Penninck D, Boudriaux RJ, Schelling SH (1995) Ultrasonography of the brain and vertebral canal in dogs and cats: 15 cases (1988–1993). J Am Vet Med Assoc 207:1320–1324.

Galloway AM, Curtis NC, Sommerlad SF, Watt PR (1999) Correlative imaging findings in seven dogs and one cat with spinal arachnoid cysts. Vet Radiol Ultrasound 40:445–452.

Guilherme S, Benigni I (2008) Ultrasonographic anatomy of the brachial plexus and major nerves of the canine thoracic limb. Vet Radiol Ultrasound 49(6):577–583.

Haro P, Gil F, Laredo F, Ayala MD, Belda E, Soler M, Agut A (2011) Ultrasonographic study of the feline sciatic nerve. Journal of Feline Medicine & Surgery 13(4):259–265.

Hudson JA, Finn-Bodner ST, Coates JR, et al. (1995) Color Doppler imaging and Doppler spectral analysis in the spinal cord of normal dogs. Vet Radiol Ultrasound 36:542–547.

Hudson JA, Finn-Bodner ST, Steiss JE (1998) Neurosonography. Vet Clin North Am Small Animal Pract 28:943–971.

Hudson JA, Steiss JE, Braund KG, Toivio-Kinnucan M (1996) Ultrasonography of peripheral nerves during wallerian degeneration and regeneration following transection. Vet Radiol Ultrasound 37:302–312.

Jones JC, Hudson JA, Sorjonen DC, et al. (1996) Effects of experimental nerve root compression on arterial blood flow velocity in the seventh lumbar spinal ganglion of the dog: Measurement using intraoperative Doppler ultrasonography. Vet Radiol Ultrasound 37:133–140.

Kirberger RM, Jacobson LS, Davies JV, Engela J (1997) Hydromyelia in the dog. Vet Radiol Ultrasound 38:30–38.

MacKillop E, Schatzberg SJ, de Lahunta A (2006) Intracranial epidermoid cyst and syringohydromyelia in a dog. Vet Radiol Ultrasound 47:339–344.

McConnell JF, Garosi LS, Dennis R, Smith KC (2003) Imaging of spinal nephroblastoma in a dog. Vet Radiol Ultrasound 44:537–541.

Nakayama M (1993) Intraoperative spinal ultrasonography in dogs: Normal findings and case-history reports. Vet Radiol Ultrasound 34:264–268.

Nanai B, Lyman R, Bichsel P (2006) Intraoperative use of ultrasonography during continuous dorsal laminectomy in two dogs with caudal cervical vertebral instability and malformation ("Wobbler syndrome"). Vet Surg 35:465–469.

Nanai B, Lyman R, Bichsel PS (2007) Use of intraoperative ultrasonography in canine spinal cord lesions. Vet Radiol Ultrasound 48(3):254–261.

Packer RA, Coates JR, Cook CR, Lattimer JC, O'Brien DP (2005) Sublumbar abscess and discospondylitis in a cat. Vet Radiol Ultrasound 46:396–399.

Pavia PR, Havig ME, Donovan TA, Craft D (2012) Malignant peripheral nerve sheath tumour of the urinary bladder in a cat. J Small Anim Pract 53:245–248.

Platt SR, Graham J, Chrisman CL, et al. (1999) Magnetic resonance imaging and ultrasonography in the diagnosis of a malignant peripheral nerve sheath tumor in a dog. Vet Radiol Ultrasound 40:367–371.

Plummer SB, Bunch SE, Khoo LH, Spaulding KA, Kornegay JN (1993) Tethered spinal cord and an intradural lipoma associated with a meningocele in a Manx-type cat. J Am Vet Med Assoc 203:1159–1161.

Rault DN, Besso JG, Ruel Y, et al. (2004) Ultrasonography of discospondylitis: Seven dogs and three cats. In: Annual Scientific Conference of the European Association of Veterinary Diagnostic Imaging, September 8–11, Ghent, Belgium, p 151.

Ródenas S, Summers BA, Saveraid T, Denning A, Marioni-Henry K (2013) Chronic hypertrophic ganglioneuritis mimicking spinal nerve neoplasia: clinical, imaging, pathologic findings, and outcome after surgical treatment. Vet Surg 42: 91–98. 7.

Rose S, Long C, Knipe M, Hornof B (2005) Ultrasonographic evaluation of brachial plexus tumors in five dogs. Vet Radiol Ultrasound 46:514–517.

Rusbridge C, Greitz D, Iskandar BJ (2006) Syringomyelia: Current concepts in pathogenesis, diagnosis, and treatment. J Vet Intern Med 20:469–479.

Tanaka H, Nakayama M, Takase K (2006) Intraoperative spinal ultrasonography in two dogs with spinal disease. Vet Radiol Ultrasound 47:99–102.

Index

Note: Page numbers followed by 'f' indicate figures; and those followed by 't' indicate tables

A
Abscess
  cardiac para-annular, 159f
  cervical, 68–9f
  hepatic, 208, 210f
  pancreatic, 313, 320f
  peritoneal, 465–6, 465f
  prostatic, 430, 431f
  pulmonary, 103, 105f
  renal, 343, 344f
  retrobulbar, 39f
  retroperitoneal, 553, 554f
  subcutaneous, 531, 532–3f
  sublumbar, 553, 554f
  thoracic wall, 84
Acoustic impedance, 1, 2t
Addison's disease, 393, 394f
Adenocarcinoma. *See also* Carcinoma; Tumor(s)
  adrenal, 393, 396f
  gastric, 292, 292f
  intestinal, 292, 293f, 294, 294f
  nasal, 49f
  pancreatic, 325, 325f, 326f
  renal, 344, 345f
  uterine, 416
Adenoma
  adrenal, 393, 394f
  lacrymal gland, 50f
Adrenal glands
  appearance of the normal, 387–90, 388–91f, 390t
  disorders of the, 391–8, 391–400f
  examination of the, 387–90, 388–91f, 390t
  tumor(s) of, 393–8, 394–9f
Agenesis
  gallbladder, 213, 216f
  renal, 333
Aliasing, color Doppler, 16, 17f
Amyloidosis
  hepatic, 193t, 198–200
  renal, 337f, 339
Anisotropy, 13, 16f. *See also* Artifact
Anterior chamber, 26f, 27
Aorta
  abdominal, 456, 456f
  caudal trifurcation of the, 456, 456f
Arterioportal fistula, 230, 233f
Arteriovenous fistula, 65, 541f
Artery(ies)
  arcuate, 333, 334f
  brachiocephalic, 82, 83, 83f
  celiac, 388f, 389, 389f, 456, 456f
  common, carotid, 56f, 57f, 58
  cranial mesenteric, 388f, 389, 389f, 456, 456f
  external and internal maxillary, 56f, 57f, 58
  external carotid, 56f, 57f, 58
  hepatic, 187, 229f, 456, 456f
  hyaloid, 26, 27f
  internal carotid, 55, 56f, 57f, 58
  main pulmonary, 112t, 114, 114f
  renal, 389
Arthritis, septic, 535, 538f
Artifact, 10–18
  aliasing, Doppler, 16, 17f
  anisotropy, 13, 16f
  comet tail, 12f, 13
  electronic interference, 13, 16f
  enhancement, distal or far, 11–12, 12f
  flash, Doppler, 17, 18f
  mirror image, 13, 14f
  partial volume averaging, 13, 15f
  range ambiguity, 13
  reverberation, 12–13, 12f
  shadowing, clean, edge or dirty, 10–11, 10–11f
  side-lobe and grating lobe, 13, 15f
  speed error, 13, 15f
  twinkling, 16, 16f
Ascites, portal hypertension and, 227
Aspiration. *See* Fine-needle aspiration
Atelectasis or lung collapse, 98, 99f
Atrial septal defect, 144, 149, 150f

B
Biliary ducts, dilatation of, 213–17
Biliary ectasia, 213–17, 215f
Biliary obstruction, 213–17, 217–19f
Biliary sludge, 186–8f
Biliary system
  disorders of the, 213–23
  examination of the normal, 186–7, 187–9f
Biopsy
  bladder and urethral, suction, 382, 384f
  gastrointestinal tract, 305, 306, 306f
  kidney, 358, 360f
  liver, 235, 236f
  neck lesion, 75, 78
  pancreas, 328, 329
  prostate, 450, 452
  spleen, 257, 258
  thorax, 106, 107, 110, 110f
  thyroid, 75, 78
Bladder
  blood clot in the, 278f, 377
  disorders of the, 369–81
  examination of the normal, 363–9
  neoplasia of the, 371, 372f, 373f, 374f
  rupture of the, 379, 380f
Bowel. *See* Intestine
Brachial plexus, 555, 556f, 558
Bronchiectasis, 106f

Atlas of Small Animal Ultrasonography, Second Edition. Edited by Dominique Penninck and Marc-André d'Anjou.

© 2015 John Wiley & Sons, Inc.

Published 2015 by John Wiley & Sons, Inc.
Companion website: www.SmallAnimalUltrasonography.com

Bronchogram
air, 100
fluid, 101f
Bursa, calcaneal, 523, 523f

C
Calcification. *See* Mineralization
Calcified bodies, 506–7, 506–7f
Calculus, or calculi
cystic, 375f
renal, 340, 352f
ureteral, 352, 354–5f, 360f
urethral, 371, 377f
Carcinoma. *See also* Adenocarcinoma
adrenal, 393, 395–7f, 397
biliary, 203f, 209f, 219f, 462f
hepatocellular, 200f, 201, 202–3f
laryngeal, 68
pancreatic, 325, 325f
pulmonary, 103f
renal, 344, 345–6f
thyroid, 71, 74f, 75f
transitional cell, 371, 372f
Carcinomatosis
peritoneal, 467, 468f
pleural, 87
Cardiac linear dimensions, 124, 125t, 131f
Cardiac ratio indices, normal, 127, 131f, 135t
Cardiac tamponade, 169, 171
Cardiac volume and mass estimation, 133, 135f
Cardiomyopathy
dilated, 158, 160f
hypertrophic, 160, 161f
restritive, 163
Carotid-body tumor, 63–4, 64f
Cartilage, articular
abnormal, 507f, 518f, 520, 520f
normal, 500, 500f, 514, 515–16f, 521f
Cataract, 31f, 33, 35f
Cellulitis, 531
Cervix, uterine, 404f, 407, 407t
Chemodectoma
cardiac, 168
cervical, 63–4, 64f
Chiari-like malformation, 552–3f
Cholangiohepatitis and cholangitis, 194–5, 195f, 197f
Cholecystitis, 218, 219–20f, 223
Cholecystocentesis, ultrasound-guided, 236, 236f
Cholelithiasis, 219f, 223, 223f
Chondrosarcoma, 86
Chorioditis, 45f
Chylothorax, 87, 88f
Cirrhosis, hepatic, 194–6, 198f
Colon. *See also* Gastrointestinal
Colonic intussusception, 265, 268f
Colonic thickening, 268f, 281
Colonic wall, 261, 261f, 261t, 262f, 263f
Comet tail, 12f, 13. *See also* Artifact
Common bile duct
dilation of the, 213–15, 214–18f
examination of the normal, 187, 189f
wall thickening of the, 218–19, 218–19f
Congenital heart diseases, 151–5
Congenital renal malformations, 333–6, 333f
Congestion, hepatic venous, 234, 234f
Congestive heart failure, 137
Consolidation, lung, 94, 99f, 100, 102f
Contrast media and software, 481–3, 493

Contrast ultrasonography
adrenal gland, 492–3, 493f
gastrointesintal tract, 490–491, 491–2f
hepatic, 482f, 483–6, 484–5f
lymph node, 487–9
pancreas, 489–90, 490f, 491f
procedure and scanning technique for, 481, 482f
prostate, 493
renal, 487, 488–90f
safety in, 483
splenic, 486–7, 486–8f
Contusion, lung, 100, 102f
Cor pulmonale, 163, 165f, 166f
Cor triatriatum, 151, 152, 154f, 163
Cornea
disorders of the, 27, 28f, 29, 31f
normal appearance of the, 21, 23, 24f, 25, 26
Corpus cavernosum, 366, 368f, 424, 445
Corpus spongiosum, 368, 424f, 445
Cryptococcosis, 96f
Cryptorchidism, 436, 437, 438f
Crystalluria, 375f
Cushing's disease. *See* Hyperadrenocorticism
Cyst (or) cyst-like lesion
cervical, 65, 65f
choledochal, 213, 214f
cranial mediastinal, 91, 91f
hepatic, 206–9, 207f
laryngeal, 68
pancreatic, 313
prostatic cyst, 430, 430f
pulmonary, 102
renal, 12f, 340–343, 340f, 343f
thyroid, 67, 71
Cystadenoma and cystadenocarcinoma
biliary, 208–9f
renal, 345f
Cysterna chyli, 459, 459f
Cystic endometrial hyperplasia, uterine, 416, 417f
Cystic neoplasia
hepatic or biliary, 208–9f
renal, 343, 345f
thyroid, 72
Cystitis, 369–71
emphysematous, 369, 370f
polypoid, 370, 370f
Cystocentesis, ultrasound-guided, 381f, 383f, 384

D
Dehiscence, gastrointestinal, 282, 285f, 462f, 464
Diaphragm
normal, 83, 83f
rupture of the, 104, 107f
Dirofilariasis, 163, 166, 167f
Disc herniation, intraoperative assessment of, 548–50, 549–50f
Discospondylitis, 553, 553f
Diverticulum, vericourachal, 378, 380f
Doppler aliasing, 16, f1.24
Doppler flash artifact, 17, 18f
Doppler ultrasound, 7–10, 8–9f, 17f
color, 7–9, 8f
power, 8f, 9
pulsed, or spectral, 9–10, 9f
tissue, 124
Double-chamber right ventricle, 143, 144f
Drainage
pancreatic pseudocyst, 329
prostatic abscess, 431, 450, 452f
ultrasound-guided, 207f, 209, 235, 236f, 361, 531, 552
Duct(s)
biliary, 186–7, 187–9f
common bile, 187, 189f
cystic, 187–8f
Duodenitis, 280, 282f, 315f
Dysplasia
hepatic, 193t, 226
hip, 521, 522f
microvascular, 193t, 226
mitral valve, 144, 147f
occipital, 553f
renal, 335, 335f
tricuspid, 144, 147f

E
Echocardiography, normal
color flow Doppler, 122
continuous-wave Doppler, 122
measurements and indices in, 124, 127

M-mode, 120, 122–5f
pulsed-waved, 122
two-dimensional, 111–20
Echogenicity, 1, 2f, 5f
relative, 3f
Ectopic ureter, 333, 350t, 353, 356–7f
Edema
gallbladder wall, 218, 220f
gastric wall, 273, 275, 275f, 276f
interfascial, 67
pancreatic, 311, 317f
subcutaneous, 65
tracheal wall, 71
Effusion or fluid
joint, 508, 510f, 517, 518f, 519–21, 535–8
pericardial, 166, 167, 168f
peritoneal, 459–61, 460f, 461t, 462–3f
pleural, 87, 88f
retroperitoneal, 357, 357f
trapped or encapsulated, 87, 89f
Eisenmenger physiology, 152
Elbow, examination of the, 508–10
Embryonic resorption, 412, 413f
Endocardial cushion defect, 149
Endocardiosis, 155, 156f, 157
Endocarditis, infective, 156, 157, 158f
Enteritis. *See also* Intestine
Epididymis, normal, 425f, 433
Epididymitis, 436, 441, 442f, 445f
Esophagus
examination of the normal, 56f, 60–61, 61–2f
inflammation of the, 67–8, 71f
neoplasia of the, 71
perforation of the, 67–8, 69f
thickening or hypertrophy of the, 72f
Ethanol ablation of thyroid carcinoma, 78
Ethylene glycol toxicity, 336, 336f
External ear canal, 58, 59f, 63, 75
Extrapleural sign, 85
Exudate
peritoneal, 459, 461, 461t, 462f
pleural, 87
retroperitoneal, 344f, 358
Eye
anatomy of the, 23–7
examination of the normal, 19–23
fetal, 27, 27f
foreign body in the, 46, 47, 48f, 49f, 53f
trauma of the, 40, 41f
tumor of the, 46, 46f, 47, 47f, 50f

F

Fat
falciform, 184f, 185, 186f
mediastinal, 83, 84, 88
necrosis, nodular, 466, 467f
retroperitoneal, 344f, 357–8f
Feline infectious peritonitis, 339f, 345, 348f, 463f, 466, 472
Fetal abnormalities, 412, 413, 414f
Fibrosis
hepatic, 193t, 194, 197f
myocardial, 160, 163
Fibrous strands, 41, 461
Fine-needle aspiration
adrenal, 398, 400f
gastrointestinal tract, 305, 306f
kidney, 358, 360f, 361
liver, 235, 235f
musculoskeletal, 495, 531, 538
neck lesion, 67, 78
pancreas, 328, 329
peritoneal, 477
Fistular tract, 531, 534f
Flow convergence zone, 141f, 143, 144, 145f
Flow turbulence
cardiac, 148
caudal vena cava, 224, 226f, 230
Focal zone, 6, 13, f1.18
Foreign body
cervical, 67f
gastrointestinal, 268, 270f
grass awn, 67f, 542, 542f, 554f
linear foreign body(ies), 271, 272f
musculoskeletal, 531–4, 533–4f
needle, 69f
ocular, 46, 48f
peritoneal, 465f, 466f
plant, 67f, 465f, 466
porcupine quill, 534, 534f, 542, 542f
surgical sponge, retained, 466, 466f
teriyaki stick, 271
thoracic wall, 84f
wooden-stick, 463f, 466
Fracture
assessment of long bone, 538, 541f
ligament or tendon avulsion, 528f
patellar, 519, 519f
supraglenoid tubercle avulsion, 505
Fungal disease
hepatic, 209
prostatic, 430
renal, 345
testicular, 442f

G

Gain setting, 6, 6f, 9
Gallbladder
bilobed, 187f
dilation of the, 214–15, 215f, 218f
examination of the normal, 184f, 186
herniation of the, 108f
mucocele, 219–21, 221–2f
rupture of the, 221, 222f
sludge, 186–8f
wall thickening of the, 215f, 218, 220f
Gallstones. *See also* Cholelithiasis
Gas
colonic (*see* Pneumatosis)
gastric (*see* Pneumatosis)
hepatic, 209, 210f
Gastric. *See also* Stomach
Gastric distention, 269
Gastric foreign body, 269, 270f
Gastric polyp, 299
Gastric tumor(s), 287–98
Gastric ulcer, 273, 276f
Gastric wall
edema of the, 275, 276f
layering of, 260f, 261
normal appearance of, 260f, 261
thickness of, 261t
Gastritis, 273, 275f
Gastrointestinal, 282, 285f, 462f, 464
biopsy, 305, 306f
disorders, 265–305
foreign body, 269, 270f, 271, 271f, 272
inflammation, 273–81
tract
contents of the, 264, 264f
normal appearance of, 259–64
Gliding sign, lung, 88
Glomerulonephritis, 337f, 339
Granuloma or pyogranuloma
hepatic, 209, 211f
peritoneal, 466
pulmonary, 102, 105f
renal, 336, 340, 345, 348f
Granulomatous (or) pyogranulomatous process, 30f, 92, 96f, 101, 197f, 209, 227, 246f, 281, 300, 301f, 369, 370, 466, 474f
Grass awn migration, 466f, 542f, 554f

H

Halo sign, perirenal, 341f
Harmonic mode, 7, 367, 367f, 482
Heart. *See also* Cardiac
acquired diseases of the, 155–63
base tumor, 96f, 168, 170f
congenital diseases of the, 139–54
examination of the, 111–38
neoplastic disorders of the, 167–9, 169f, 170f
Heartworm disease (dirofilariasis), 163, 166, 167f
Hemangiosarcoma
bladder, 371
cardiac, 169f
hepatic, 204–5f

Hemangiosarcoma (*continued*)
metastatic, 204f
renal, 347f
retroperitoneal, 467–8, 470f
splenic, 242t, 251f, 252f
Hematoma
bladder, 378f
cervical, 67
hepatic, 209, 212f
ligament tear and, 517, 520, 530
muscular, 527, 537f
peritoneal, 236f, 461, 462f
pulmonary, 102, 104, 107f
rib, 85
tendon tear and, 503f, 505, 524
Hemoabdomen
amyloidosis and, 200
hemangiosarcoma and, 205f
Hemorrhage
bladder wall, 377, 378f
pleural, 87
post-biopsy, 236, 236f
pulmonary, 100f
retroperitoneal, 345, 347f
Hepatitis, 194–5
chronic active, 197f
emphysematous, 213f
Hepatocutaneous syndrome, 200, 201f
Hepatofugal flow, 224, 226–8f, 227, 230f, 233f
Hepatoma, 201, 202f
Hepatomegaly, 193t
Hepatopathy
steroid, 193–4, 195f
vacuolar, 193–4, 195f
Hepatopetal flow, 192
Hernia
abdominal wall, 477, 477f
diaphragmatic, 104, 107f
peritoneopericardial, 108f, 152
Hip joint
dysplasia of the, 521
examination of the, 520, 521f
luxation of the, 530
Histiocytic sarcoma
disseminated, 92f, 102f, 206f, 245, 247f, 298f, 471f
hepatic, 206, 206f
renal, 344, 347f
Horner's syndrome, 78
Hyaloid canal. *See also* Hyaloid artery
Hydronephrosis, 350t, 351–2, 352–3f
Hydroureter, 352–7, 352–7f
Hygroma, 512, 513f
Hyoid apparatus, 63, 534
Hyperadrenocorticism
adrenal changes with, 391–3
liver changes with, 193–4, 195f
Hypercalcemiam, parathyroid glands and, 74
Hyperparathyroidism, 74–5
Hyperplasia, hepatic benign nodular, 201, 201t, 202f
Hypertension
portal, 227–3, 229f, 231–3f
pulmonary, 147, 149f, 150f, 163
systemic, 168
Hyperthyroidism, ethanol or heat ablation in, 78
Hypertrophy, concentric cardiac, 140, 140f
Hypoadrenocorticism, 393, 394f
Hypothyroidism, 71, 73f
Hypovolemia, 193t

I
Incidentaloma, 398, 399f
Infarct (or) infarction
hepatic, 209, 212f
intestinal, 302
portal thrombosis and, 234, 234f
renal cortical, 346, 349f
Instability, joint, 507, 525
Insufficiency
aortic valve, 139
pulmonary, 139, 140
Insulinoma, 205f. *See also* Pancreatic tumor
Interactions between ultrasound waves and tissues, 1–2
Intestinal biopsy, 305, 306
Intestinal dehiscence, 281, 282, 285f
Intestinal foreign body, 269, 269f, 270f, 271, 272f
Intestinal perforation, 271f, 286f
Intestinal stricture, 287
Intestinal tumor(s), 287–98
Intestinal wall, 263f
Intestine
anatomy of the, 260–263, 263f
biopsy of the, 305, 306, 306f
contents, in the, 264, 264f
examination of the, 263
Intussusception
appearance of, 265
colonic, 268f
duodenogastric, 266f
jejunal, 267f, 268f
Invagination. *See* Intussusception
Iris, normal appearance of the, 20f, 21f
Ischemia
bowel, 302, 304f
myocardial, 141, 160

J
Joint mice, 506–7, 506–7f
Joint neoplasia, 535, 537f

K
Kidneys
congenital malformation of the, 333, 335f
diffuse parenchymal disorders of the, 336–40, 336–42f
disorders of the collecting system of the, 346–57, 350–357f
examination of the normal, 331–3, 332–4f
focal disorders of the, 340–346, 343–9f
neoplasia of the, 339, 341–2f, 344–5, 345–8f

L
Laryngeal paralysis, 71, 71f
Larynx
disorders of the, 67–71, 69–71f
examination of the normal, 55, 60, 60f
Left atrium, dilation of the, 144
Left ventricle
dilatation of the, 144
hypertrophy of the, 134, 144
Leiomyoma. *See also* Smooth muscle tumor(s)
gastric, 294, 296f
intestinal, 294f
uterine, 416, 418f
vaginal, 418f
Leiomyosarcoma. *See also* Smooth muscle tumor(s)
bladder, 371, 373f
intestinal, 295, 295f
Lens
luxation of the, 35, 36f
normal appearance of the, 24f, 25
posterior rupture of the, 36f
Leptospirosis
hepatic, 194, 196f
renal, 336, 336f, 338–9f
Leukemia, 193t
Leydig cell tumor, 438, 439f
Ligament(s)
collateral, 516, 520
cranial cruciate, 517, 518f
disorders of, 530, 531f
examination of, 530
falciform, 184f, 185
patellar, 514–15, 515–16f, 518–19f
Linear foreign body(ies), 269, 272f

Lipidosis, hepatic, 193–4, 194f
Lipoma
  appendicular, 535, 537f
  infiltrative, 86, 468f
  mesenteric, or abdominal, 467, 468f
Liver
  diffuse parenchymal disorders of the, 193–200, 193t
  examination of the normal, 183–92, 184–92f
  focal parenchymal disorders of the, 200–212
  neoplastic disorders of the, 196–8, 199–200f, 201–6, 202–9f
Lung. *See also* Pulmonary
  disorders of the, 94–104
  examination of the, 82f
Lymph node(s)
  abscessed, 473f
  aortic, 456f, 457–8t, 458
  cavitary, or cystic, 473f
  colic, 456f, 457–8t, 458
  cranial mediastinal, 83
  examination of the normal, 56f, 56t, 59f, 66–7, 456–9, 456f, 457–8t
  gastric, 456f, 457–8t
  hepatic, 456f, 457–8t
  inguinal, 456f, 457–8t
  jejunal (or) mesenteric, 456f, 457–8t, 458f
  mandibular, 56f, 56t, 66–7, 66f
  medial iliac, 374, 446f, 447f, 448, 456f, 457–8t, 458f
  medial retropharyngeal, 56f, 56t, 66–7, 66f
  pancreaticoduodenal, 456f, 457–8t
  sacral, 456f
  splenic, 456f
  sternal, 83, 84
  sublumbar, 456f, 457–8t, 458
Lymphadenopathy
  abdominal, 469–74, 470–474f
  cervical, 66f, 67
  cranial mediastinal, 91, 92f
  granulomatous or pyogranulomatous, 469, 474f
  inflammatory, 472
  necrotic, 473f
  neoplastic or metastatic, 469, 470f, 473f
  reactive, 469, 471f
  sublumbar, 471–2f
Lymphoma
  bladder, 371, 374f
  cervical, 65, 66–8, 66f
  cranial mediastinal, 91, 93f
  gastric, 287, 288f
  hepatic, 193t, 196, 199f, 201t, 206, 207f
  intestinal, 28, 287, 290f, 291f
  laryngeal, 70f
  mesenteric, 470f
  pancreatic, 325, 327f
  peritoneal, 467
  renal, 339, 341–2f, 346f
  subcutaneous, 535f
  ureteral, 355f
Lymphomatosis, 467

M
Mammary glands
  appearance of normal, 419, 420f
  tumor of, 420, 420f
Mandible, 56f
Mast cell tumor
  bladder, 371, 373f
  cranial mediastinal, 95f
  hepatic, 199f
Medial coronoid process
  fragmentation of the, 510, 511f
  normal, 509, 509f
Medial humeral epicondyle, avulsion (or) fragmentation, 510, 512f
Mediastinum
  abnormalities of the, 88–93
  cyst in the, 91, 91f
  mass in the, 90–92
Medullary rim sign, renal, 336–7f, 339f
Megaesophagus, 71
Melanoma, laryngeal, 70
Meniscus (or) menisci, femorotibial, 516–17, 516f, 519f
Mesentery
  inflammatory processes of the, 461–7, 463–5f
  neoplastic invasion of the, 467–9, 468–9f
  normal, 455
Mesothelial remnant, 108
Mesothelioma, 87, 168, 467
Metallic clip, 13, 201t, 209
Metastasis (or) metastatic disease
  bone, 566f
  cranial mediastinal, 92f
  lymph node, 254
  peritoneal, 467, 468f
  pleural, 87
  pulmonary, 103, 104f
  renal, 344, 346f
Microhepatica, 224f
Microvascular dysplasia, hepatic, 193t, 226
Mineralization
  adrenal, 395f, 397, 398–9f
  hepatic, 209, 212f
  neoplastic, 535
  renal, 338, 346, 350f
  tendon or muscle, 500, 501–2f, 502, 504f, 510, 521, 524, 525f, 529f
  vascular wall, 475, 476f
Mirror-image, 13, 14f. *See also* Artifact
Mitral valve
  dysplasia of the, 144, 147f
  endocardiosis, 155, 156f, 157
  regurgition of the, 136, 147f, 156
Mosaic pattern, turbulent flow, 127, 141
Mucocele, gallbladder, 219–21, 221–2f
Muscle
  biceps, 497, 499f, 529f
  brachialis, 508
  contracture, infraspinatus, 500, 502f
  cricopharyngeal, 72f
  deltoid, 497, 498f
  digastricus, 58
  examination technique of the, 526, 526f
  extensor carpi radialis, 508
  gastrocnemius, 521, 523–5f
  gluteal, 529f
  gracilis, 530f
  iliopsoas, 521, 522f
  infraspinatus, 495, 496f, 497, 498f, 500, 502f
  quadriceps femoris, 514
  sternohyoid, 58, 61
  sternothyroid, 58, 61
  supraspinatus, 495, 496f, 497, 498–9f, 500, 501–2f
  trauma, 527, 527f
  triceps, 509, 528f
Musculature, examination of the, 526, 526f
Myelolipoma
  hepatic, 201t
  splenic, 248, 248f
Myelomalacia, 553f
Myocardial disease, 158–63
Myopathy, or tendinopathy
  fibrosing and calcifying, 527, 529–30f
  iliopsoas, 521, 522f
Myositis, septic, 533f
Myxosarcoma, 205f

N
Neck, examination of normal structures in the, 55–63, 56t

Necrosis
acute tubular, 336
hepatic, 194, 198, 201, 201t, 202f, 209
Neoplasia. *See also* Mass, Nodule, Tumor
appendicular, 535–7f
bladder, 371, 373f, 374f
bone, 538, 539–40f
cardiac, 167, 168, 169f, 170f
carotid-body, 63, 64, 74
gastrointestinal, 287–98
hepatobiliary, 196, 201, 201t, 215, 218
joint, 535
laryngeal, 67
mammary glands, 420, 420f
muscle, 534–5
nerve, 558–60
ocular, 30, 31, 32f
pancreatic, 324–8
parathyroid, 74–5
penis, 448, 450f
peritoneal, 467–8
prostatic, 432, 433, 434f, 435f
pulmonary, 101–4
renal, 340–346
retroperitoneal space, 467–8
spinal, 550
splenic, 245–53
testicular, 438–41
thyroid, 74–5
urethral, 371
Nephritis, interstitial, 336, 337–8f
Nephroblastoma, 342f, 344
Nephrocalcinosis, 336, 341f
Nephrosclerosis, 338f
Nephrosis, acute tubular, 336
Nerve(s)
brachial plexus, 555, 556f
disorders of the, 557–60, 558–60f
examination of normal spinal and peripheral, 555–7, 555–7f
Nerve block (local anesthesia), 561, 561f
Neuroblastoma, renal, 342f
Neuroendocrine tumor, 63, 97
Nodular hyperplasia
adrenal, 395f
hepatic, 193, 195f, 197f, 201t, 202f
pancreatic, 324, 324f, 328
splenic, 242t, 245, 248, 249f, 250f

O

Obstruction, ureteral, 351–5, 352f, 354–5f
Omentum
inflammatory processes of the, 461, 463f, 465, 465f
neoplastic invasion of the, 462, 467, 469f
normal, 455
Optic nerve
inflammation of the, 50
normal appearance of the, 27
Orchitis, 436, 441, 442f, 443f
Os penis, 368f, 436
Osseous metaplasia, deep digital flexor muscle, 510, 513f
Osteoarthritis (or) degenerative joint disease, 510, 510f, 553, 553f
Osteochondritis dissecans
femoral condyle, 520, 520f
humeral condyle, 510
humeral head, 506–7f, 507
Osteochondroma (or) osteochondromatosis, 506
Osteomyelitis, 538, 539f
Osteophyte (or) osteophytosis, 502, 510f, 518–19f, 519, 522f
Osteosarcoma,
appendicular, 538, 539–40f
rib, 86f
splenic, 257f
vertebral, 550, 551f
Otitis media, 75, 77f
Ovarian cyst, 406f
Ovarian tumor(s), 405, 406f
Ovary
examination of, 403
normal appearance of, 404f, 405f
Overcirculation, pulmonary, 149, 150f
Overload
pressure, 139, 141, 144, 157
volume, 133, 139, 144, 151f, 157
Ovulation cycle, 404

P

Pancreas
examination of the, 312
measurements of the, 311
normal appearance of the, 309–11
Pancreatic cyst, 313
Pancreatic duct, 310–312
Pancreatic edema, 312, 317f
Pancreatic pseudocyst, 313, 316f, 318f
Pancreatic tumor(s), 324–8
Pancreatitis
acute, 311
chronic, 321f
necroticohemorrhagic, 316f
Papilla, duodenal major, 260, 262f
Paradoxical septal motion, 164
Paraprostatic cyst, 432, 433f
Parathyroid glands
abnormalities of the, 74–5, 76f
adenoma and carcinoma of the, 76f
examination of the, 56t, 61–3, 62f
intralesional ultrasound-guided treatment of the, 78, 78f
Patent ductus arteriosus, 144, 147, 148f
reversed, 149
Patent ductus venosus, 224.225, 228f
Penis
appearance of normal, 368, 423, 448f
examination of, 423
fracture of, 449f
Penrose drain, 78f
Percutaneous procedures. *See* Biopsy, Fine-needle aspiration
Perforation, gastrointestinal, 281f, 282, 284f
Pericardial effusion, 166, 167, 168f
Pericardiodentesis, ultrasound-guided, 171
Peripheral nerve(s). *See* Nerve(s)
Peripheral nerve sheath tumor, 558–60f
Peritoneal cestodiasis, 281, 284f
Peritoneocentesis, ultrasound-guided, 477
Peritonitis
bile, 222f, 464
septic, 461–5, 462–4f, 462t
Pheochromocytoma, 393, 394f
Phlegmon, 531
Piezoelectric crystals, 1–3, 5f
Pleura
abnormalities of the, 87–8
thickened, 89, 90f
Pleuritis, 87, 89f
Pneumatosis, 281, 284f
Pneumonia
abscessing, 104
aspiration, 100f
pyogranulomatous, 106f
Pneumoperitoneum, 464, 464f
Pneumothorax, 88, 102f
Polyp
bladder, 370
gallbladder wall, 221, 223f
gastric wall, 299f
Portal hypertension, 227–33, 229f, 231–3f
Portal system
Doppler assessment of the, 192, 192f, 226–33f
normal, 191–2
primary hypoplasia of the, 227
thrombosis of the, 234, 234f
Portosystemic shunt(s) or shunting
acquired, 227–33, 231–3f
congenital, 224–7, 225–31f

extrahepatic, 225–7f
general ultrasound approach to, 231f
intrahepatic, 228–9f
Postpartum uterus, 411
Pregnancy
abnormal, 412–14
gestational age in, 413t
normal progression of, 409, 410f, 411f
Pressure gradient
aortic stenosis and, 139
atrial septal defect and, 151
mitral dysplasia and, 144, 146f
patent ductus arteriosus and, 147
pulmonic stenosis and, 143
tricuspid dysplasia and, 144, 145f
ventricular septal defect and, 149, 152f
Probe (or) transducer, 2–6, 5f
Prostate, 450, 452
appearance of the normal, 424, 426f
biopsy of, 450
examination of, 423
measurement of, 427, 433
Prostatic cyst, 427, 429f
Prostatic hyperplasia, 429f, 430
Prostatic tumor, 433, 434f, 435f
Prostatitis, 427, 430f, 431f
Protein-losing glomerular disease, 339
Pseudocyst, perinephric, 358, 359f
Pseudosludge. *See also* Artifact
Pulmonary. *See* Lung
Pupil, normal appearance of the, 21
Pyelectasia, renal, 346–51, 350–351f, 350t
Pyelocentensis, 360f, 361
Pyelography, 360f, 361
Pyelonephritis, 350–351, 350–352f
Pyogranuloma, 63f, 67, 69f, 106f, 209, 211f, 219f, 246f, 276f, 336, 339f, 345, 348f, 465, 466. *See also* Granuloma
Pyonephoris, 352, 354f
Pythiosis, 300, 472, 474f

R

Ratio(s)
kidney-aorta, 331, 332f
portal vein-aorta, 191f, 192, 229f, 231f
Renal. *See* Kidneys
Renal agenesis, 333
Renal calculus(i), 350t, 352f, 353, 355f
Renal cyst(s), 340, 340f, 343–4f
Renal disease
chronic, 337–8f
diffuse parenchymal, 336–40, 336–42f
focal, 340–346, 343–9f
polycystic, 340, 343–4f
Renal granuloma or pyogranuloma, 336, 340, 345, 348f
Renal pelvis
disorders of the, 346–57, 350–357f
examination of the normal, 333
Renal tumor(s) or neoplasia, 339, 341–2f, 344–5, 345–8f
Renal-aortic ratio, 331, 332f
Reproductive tract female. *See also* Ovary, Uterus, Pregnancy
appearance of normal, 404f, 405f
examination of, 403–5
Reproductive tract male. *See also* Prostate, Testis
appearance of normal, 424f, 425f, 426f, 427f
examination of, 423–5
Resolution
contrast, 5, 5f
spatial (axial, lateral, or elevational), 2, 4–6, 4–7f, 15f
temporal, 9
Retinal detachment, 42, 43, 44f, 45f
Retrobulbar space
biopsy of the, 52, 52f, 53
mass of, 39f, 47
normal appearance of, 27, 28f
Reverberation, 12–13, 12f. *See also* Artifact
Rhabdomyosarcoma
bladder, botryoid, 371
diaphragmatic, 109
Rib(s)
aggressive lesion of the, 84, 86f
fracture, of the, 84, 85f
mass of the, 84, 86f
sarcoma, of, 86f
Right atrium, dilatation of the, 144, 166f
Right ventricle
dilation of the, 144
hypertrophy of the, 140
Roundworms, 271, 273f

S

Salivary duct cyst, 65, 65f
Salivary glands
disorders of the, 65–6, 65f
examination of the, 57f, 58, 59f
Sarcoma
histiocytic (*see also* Disseminated histiocytic sarcoma)
soft-tissue, 535
splenic, 247
Sarcomatosis, 467, 469f
Scrotal trauma, 441, 447f
Scrotum, 368f, 437
Seminoma, 438, 439f, 440f
Septal defect
atrial, 144, 147, 149, 150f, 151f
ventricular, 147, 149, 151f
Seroma
postoperative, 78, 282
subserosal, 288f
Sertoli cell tumor, 438, 440f, 444f
Shadowing, 10–11, 10–11f. *See also* Artifact
Shoulder
disorders of the, 500–508, 501–7f
examination of the normal, 495–500, 496–500f
Sialadenitis, 65, 65f
Sialocele, 65, 65f
Side-lobe and grating lobe, 13, 15f. *See also* Artifact
Sinus of Valsalva, 118, 134f, 159f
Situs inversus, 154, 155f
Smoke sign, left atrial, 162
Smooth muscle tumors, 64, 294, 295, 373
Spatial compound imaging, 6–7, 7f
Spinal cord
hemorrhage of the, 550, 550f
neoplasia of the, 550, 551f
Spine, examination of the normal, 545–8, 546–9f
Spleen, 235, 235f
appearance of the normal, 240f, 241f
examination of the, 239
extramedullary hematopoiesis of, 242t, 243, 249f
hematoma of the, 242t, 246f
histoplasmosis of the, 244f
infarction of the, 242t, 244f, 255f
myelolipoma of the, 242t, 248f
thrombus of the, 244f, 245f, 254f, 256
torsion of the, 253, 256f
tumor(s), of the, 242t, 243, 250f, 251f, 252f, 253, 253f
vessels of the, 239, 241f
Splenitis, 242, 246f
Splenomegaly, 242, 242t, 243f
Splenorenal shunt, acquired, 225f, 227, 230, 232f
Steatitis
abdominal, 461, 463f, 465, 465f
neck, 65

Stenosis
aortic or subaortic, 136, 139f, 140f, 141f, 142f
mitral, 137f, 144
pulmonic, 144f
tricuspid, 144
Steroid hepatopathy, 193–4, 195f
Stifle
disorders of the, 517–20, 518–20f
examination of the, 512–17, 514–16f
Stomach. *See also* Gastric
contents of the, 264f
examination of the, 259, 260f, 261t, 262f
normal appearance of the, 260f, 261t, 262f
Stricture, intestinal, 271, 282f, 287f
Stroke length, 136, 142f
Supraglenoid tubercle fracture, 505
Synovial cell sarcoma, 535, 537f
Syringomyelia, 552, 552f
Systolic anterior motion, 161, 162f

T
Target lesion(s)
hepatic, 201, 206f
splenic, 242t, 252f, 253
Tarsus, examination of the, 521
Telangiectasia, renal, 345f
Tendon luxation
biceps, 506, 507f
superficial digital flexor, 525, 526f
Tendon, normal
biceps brachii, 497, 499f
calcaneal (Achilles), 523, 523f
gastrocnemius, 521, 523f
infraspinatus and supraspinatus, 497, 498f
long digital extensor, 516f, 524
superficial digital flexor, 521, 523f
Tendon rupture
bicipital, 505–6f
calcaneal (Achilles), 524–5f
Tendonitis (or) tenosynovitis, tendinopathy
bicipital, 501, 503–6f
calcaneal (Achilles), 524–5f
infraspinatus, 500
supraspinatus, 500, 501–2f
Teriyaki stick, 271
Testis
appearance of, 425
atrophy of, 444, 446f
examination of, 423, 425f
measurement of, 433t
torsion of, 441, 444f, 445f
tumor(s) of, 438, 439f, 440f
Tetralogy of Fallot, 149, 150, 153f
Thoracic, 106, 107, 109f, 110f. *See also* Lung, Thorax
biopsy or fine-needle aspiration, 106, 109f
wall abscess, 84f
wall mass, 84–7
Thoracocentesis, ultrtasound-guided, 106, 109f
Thorax, examination of the, 81–4
Thromboembolism
aortic (or) iliac, 475, 476f
pulmonary, 166f, 168
Thrombus or thrombosis
aortic, 475, 476f
caudal vena cava, 348f, 396–7f, 397, 474–5, 475–6f
left atrial, 163f
malignant, 64f, 348f, 475f
portal venous, 234, 234f
Thymoma, 91, 92, 94f
Thymus, normal, 83
Thyroid gland
abnormalities of the, 71–4, 73–6f
adenoma of the, 73f
carcinoma and adenocarcinoma of the, 74–6f
examination of the, 56t, 61–3, 62f
Time-gain compensation, 6, 6f
Tongue, examination of the, 63, 64f
Torsion
liver lobe, 209, 212f
lung lobe, 101f
Toxicity
ethylene glycol, 336, 336f
grapes, 336
lily, 336
Trachea
abnormalities of the, 67–71
examination of the, 60, 61f
Transudate, pleural, peritoneal or retroperitoneal, 357–8, 460f, 461, 461t
Trichobezoar, 269, 270f
Tricuspid dysplasia, 144, 145f, 146f
Tricuspid valve regurgitation
endocardiosis and, 155
pulmonic stenosis and, 144f
Tumor(s). *See* Neoplasia
Tympanic bullae (middle ear)
disorders of the, 75, 77f
examination of the, 55, 59f, 63

U
Ulceration
gastric, 273, 276f
gastrointestinal, 273, 283f
and tumor, 288f, 291f
Ununited anconeal process, 510, 511f
Uremic gastritis, 275, 277f
Ureter
dilatation of the, 351–5, 352f, 354–7f
ectopic, 353–7, 356–7f
Ureteral jet, 355f
Ureteritis, 350t, 355f, 358
Ureterocele, 357
Urethra
disorders of the, 377, 377f
examination of the normal, 367f, 368f
Urinoma, 358, 358f
Uroliths (or) urolithiasis
bladder, 371, 375f
renal, 340, 352f
ureteral, 352, 354–5f, 360f
urethral, 371, 375, 377f
Uterine granuloma, 416, 419f
Uterine involution, 411
Uterine stump pyometra, 417f
Uterine torsion, 414f
Uterus
cystic endometrial hyperplasia of, 417f, 418f
examination of, 403
fluid filled, 416f, 418f
normal appearance of, 404f, 406, 407t, 408f, 411f
tumors of, 416

V
Vagosympathetic trunk, 56t, 58, 65
Valvular disease, chronic degenerative, 155, 156f
Vasculitis, pyogranulomatous, 336, 339f, 463f
Vein(s)
azygos, 224, 225f, 227f, 475
caudal mesenteric, 190f, 192
cranial mesenteric, 190f, 192, 225, 234
deep circumflex iliac, 456f
external and internal maxillary, 56f
external iliac, 354f, 456, 456f, 457t, 459f
external jugular, 56f, 58, 64f, 74f
gastroepiploic, 190f, 192, 224
gonadal, left, 230, 232f
hepatic, 5f, 190, 190f, 196, 224, 225f, 234f
iliac, 354f, 456, 456f, 457t, 459f
jejunal, 190, 192

left gastric, 190f, 192, 224
linguofacial, 58
maxillary, 56–7f, 58
pancreaticoduodenal, 189–90f, 192, 309–10, 310f
phrenicoabdominal, 388f, 389, 391–2f, 397
portal, 3f, 8f, 183, 184f, 188–92f, 196f, 225–34f, 456f, 457t, 471f, 473f
renal, 334f, 348f, 388f, 389, 389f, 391f, 394–6f
right gastric, 224
splenic, 192, 226f, 227, 232f, 234, 456, 457t
thyroid, 64f
Vena cava
caudal, 8f, 456, 456f, 475–6f
cranial, 83, 83f
syndrome of the, 167f
Vitreal foci, 30, 40
Vitreal retraction, 40
Vitreous body
anatomy of the, 21, 23, 24f, 25, 26
degeneration of the, 35
hemorrhage in the, 40, 43f
Vocal folds
abnormal motion of the, 68
examination of the, 55, 60
thickening of the, 70f, 71
Volvulus, gastric, 273

W
Wall layering
bladder, 363, 371f
gastrointestinal tract, 261, 262f, 263f

Y
Yolk sac membrane, 410f, 412f

Z
Zygomatic salivary gland
inflammation of the, 29f
normal appearance, 22, 22f

WILEY END USER LICENSE AGREEMENT

Go to www.wiley.com/go/eula to access Wiley’s ebook EULA.